The Institution of Engineering and Technology

SciTech Publishing
an imprint of the IET

Theory and Practice of Modern Antenna Range Measurements

2nd Expanded Edition, Volume 2

Clive Parini, Stuart Gregson, John McCormick, Daniël Janse van Rensburg and Thomas Eibert

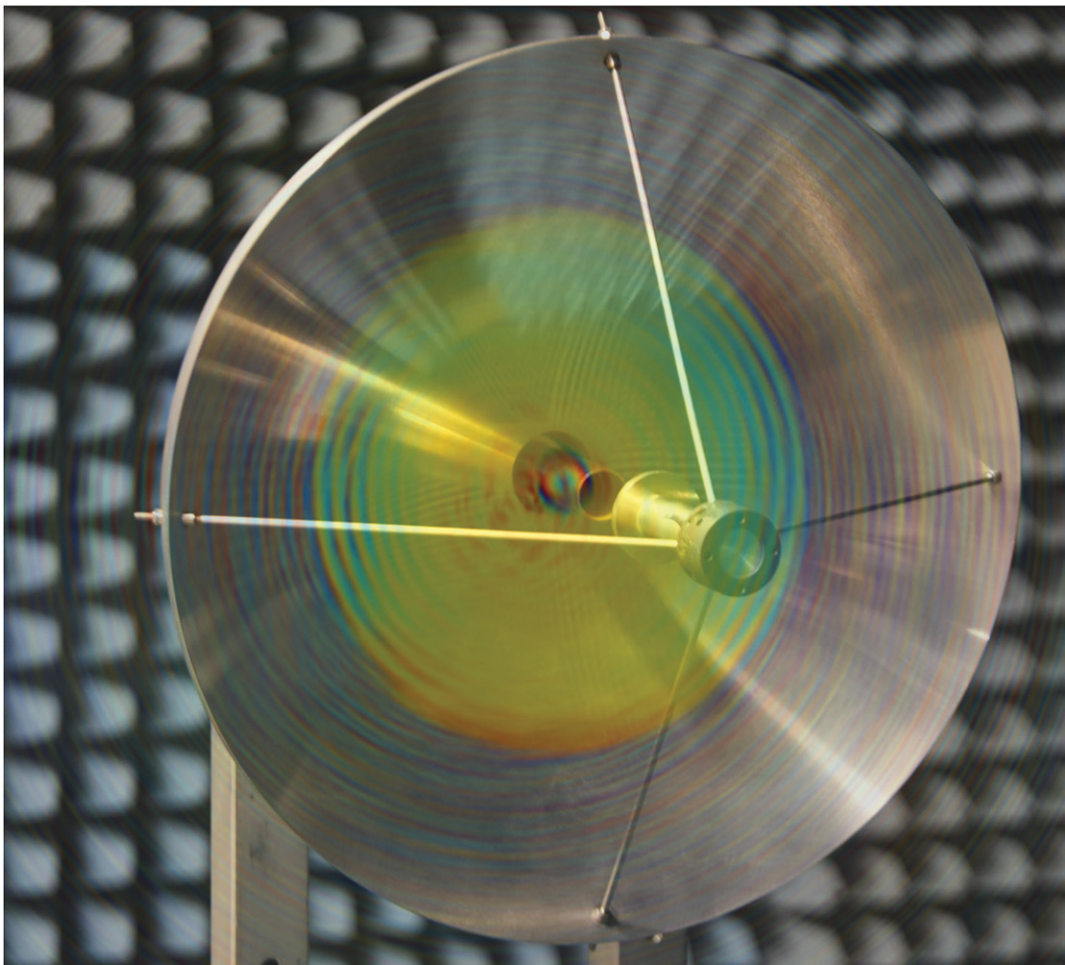

Theory and Practice of Modern Antenna Range Measurements

Related titles on electromagnetic waves

Dielectric Resonators, 2nd Edition Kajfez & Guillon
Electronic Applications of the Smith Chart Smith
Fiber Optic Technology Jha
Filtering in the Time and Frequency Domains Blinchikoff & Zverev
HF Filter Design and Computer Simulation Rhea
HF Radio Systems and Circuits Sabin
Microwave Field-Effect Transistors: Theory, design & application, 3rd Edition Pengelly
Microwave Semiconductor Engineering White
Microwave Transmission Line Impedance Data Gunston
Optical Fibers and RF: A natural combination Romeiser
Oscillator Design and Computer Simulation Rhea
Radio-Electronic Transmission Fundamentals, 2nd Edition Griffith, Jr
RF and Microwave Modeling and Measurement Techniques for Field Effect Transistors Jianjun Gao
RF Power Amplifiers Albulet
Small Signal Microwave Amplifier Design Grosch
Small Signal Microwave Amplifier Design: Solutions Grosch
2008+ Solved Problems in Electromagnetics Nasar
Antennas: Fundamentals, design, measurement, 3rd Edition Blake & Long
Designing Electronic Systems for EMC Duff
Electromagnetic Measurements in the Near Field, 2nd Edition Bienkowski & Trzaska
Fundamentals of Electromagnetics with MATLAB, 2nd Edition Lonngren *et al.*
Fundamentals of Wave Phenomena, 2nd Edition Hirose & Lonngren
Integral Equation Methods for Electromagnetics Volakis & Sertel
Introduction to Adaptive Arrays, 2nd Edition Monzingo et al
Microstrip and Printed Antenna Design, 2nd Edition Bancroft
Numerical Methods for Engineering: An introduction using MATLAB and computational electromagnetics Warnick
Return of the Ether Deutsch
The Finite Difference Time Domain Method for Electromagnetics: with MATLAB simulations Elsherbeni & Demir
Theory of Edge Diffraction in Electromagnetics Ufimtsev
Scattering of Wedges and Cones with Impedance Boundary Conditions Lyalinov & Zhu
Circuit Modeling for Electromagnetic Compatibility Darney
The Wiener-Hopf Method in Electromagnetics Daniele & Zich
Microwave and RF Design: A systems approach, 2nd Edition Steer
Spectrum and Network Measurements, 2nd Edition Witte
EMI Troubleshooting Cookbook for Product Designers Andre & Wyatt
Transmission Line Transformers Mack and Sevick
Electromagnetic Field Standards and Exposure Systems Grudzinski & Trzaska
Practical Communication Theory, 2nd Edition Adamy
Complex Space Source Theory of Spatially Localized Electromagnetic Waves Seshadri
Electromagnetic Compatibility Pocket Guide: Key EMC Facts, Equations and Data Wyatt & Jost
Antenna Analysis and Design Using FEKO Electromagnetic Simulation Software Elsherbeni, Nayeri & Reddy
Scattering of Electromagnetic Waves by Obstacles Kristensson
Adjoint Sensitivity Analysis of High Frequency Structures with MATLAB® Bakr, Elsherbeni & Demir
Developments in Antenna Analysis and Synthesis vol1 and vol 2 Mittra
Advances in Planar Filters Design Hong
Post-processing Techniques in Antenna Measurement Castañer & Foged
Nano-Electromagnetic Communication at Terahertz and Optical Frequencies, Principles and applications Alomainy, Yang, Imran, Yao & Abbasi
Nanoantennas and Plasmonics: Modelling, design and fabrication Werner, Campbell & Kang
Electromagnetic Reverberation Chambers: Recent advances and innovative applications Guillaume Andrieu
Radio Wave Propagation in Vehicular Environments Azpilicueta, Vargas-Rosales, Falcone & Alejos
Advances in Mathematical Methods for Electromagnetics Kobayashi & Smith

Theory and Practice of Modern Antenna Range Measurements

2nd Expanded Edition

Volume 2

Clive Parini, Stuart Gregson, John McCormick,
Daniël Janse van Rensburg and Thomas Eibert

The Institution of Engineering and Technology

Published by SciTech Publishing, an imprint of The Institution of Engineering and Technology, London, United Kingdom

The Institution of Engineering and Technology is registered as a Charity in England & Wales (no. 211014) and Scotland (no. SC038698).

First published 2020

The Institution of Engineering and Technology
Michael Faraday House
Six Hills Way, Stevenage
Herts, SG1 2AY, United Kingdom

www.theiet.org

British Library Cataloguing in Publication Data
A catalogue record for this product is available from the British Library

ISBN 978-1-83953-128-6 (hardback Volume 2)
ISBN 978-1-83953-129-3 (PDF Volume 2)
ISBN 978-1-83953-126-2 (hardback Volume 1)
ISBN 978-1-83953-127-9 (PDF Volume 1)
ISBN 978-1-83953-130-9 (2 volume set)

Typeset in India by MPS Limited
Printed in the UK by CPI Group (UK) Ltd, Croydon

The front cover of this volume comprises of an image of a 90GHz front fed mm-wave Cassegrain reflector antenna with a subtle overlay of the false colour plot of the reconstructed phase aperture illumination of the antenna as obtained from phase-less planar near-field antenna measurements.

Contents

Volume 1

About the authors

Professor Clive Parini is Professor of Antenna Engineering at Queen Mary University of London and heads the Antenna & Electromagnetics Research Group. He received his BSc (Eng) degree in Electronic Engineering in 1973 and PhD in 1976 both from Queen Mary University of London. After a short period with ERA Technology Ltd, he joined Queen Mary University of London as Lecturer (1977), moving to Reader (1990) and then Professor (1999). He has published over 400 papers on research topics including array mutual coupling, array beamforming, antenna metrology, antennas for mobile and on-body communications, millimetre-wave compact antenna test ranges, millimetre-wave integrated antennas, quasi-optical systems and antenna applications for metamaterials. In 1990, he was one of three co-workers to receive the IEE Measurements Prize for work on near-field reflector metrology. He is a Fellow of the IET and a past member and Chairman of the IET Antennas & Propagation Professional Network Executive Team. He is a past member of the editorial board and past Honorary Editor for the IET Journal *Microwaves, Antennas & Propagation*. In 2009, he was elected a Fellow of the Royal Academy of Engineering.

Professor Stuart Gregson is an honorary visiting professor at Queen Mary University of London and Director of Operations & Research at Next Phase Measurements. He received his BSc degree in Physics in 1994 and his MSc degree in Microwave Solid State Physics in 1995 both from the University of Portsmouth. He received his PhD degree in 2003 from Queen Mary University of London. From his time with Airbus, Leonardo, NSI-MI and the National Physical Laboratory, he has developed special experience with near-field antenna measurements, finite array mutual coupling, computational electromagnetics, installed antenna and radome performance prediction, compact antenna test range design and simulation, electromagnetic scattering, 5G OTA measurements and has published numerous peer-reviewed research papers on these topics regularly contributing to and organising industrial courses on these subject areas. He is a Fellow of the Antenna Measurement Techniques Association, a Fellow of the Institution of Engineering and Technology, a Fellow of the Institute of Physics and is a chartered Engineer and Physicist.

Dr John McCormick has extensive experience in many areas of metrology ranging from wet chemistry laboratories to free-space electromagnetic measurement facilities. His expertise relevant to these volumes relates to his involvement over a number of decades in research and development related to naval and airborne radar systems along with RCS and EW. This experience has been gained in the course of

his working relationships with DERA, BAE Systems SELEX ES and latterly Finmeccanica where he has been engineering lead on a range of advanced programmes that required the development and implementation of diverse and novel measurement techniques. He holds degrees at BA, BSc, MSc and PhD levels, is a Fellow of the Institute of Physics, a Fellow of the Institution of Engineering Technology and is a chartered Physicist and chartered Engineer. Additionally, he takes a strong and active interest in the encouragement of public awareness of all areas of Science and Engineering especially within the school environment where he acts as a schools STEM ambassador.

Dr Daniël Janse van Rensburg is Chief Technology Officer of NSI-MI Technologies in Atlanta, GA, USA. He started his career as Professor in the Department of Electrical Engineering at the University of Pretoria, South Africa in 1992. He joined the Canadian Space Agency in Ottawa, ON, Canada, as Research Engineer in 1994 and was appointed as Senior Member of Technical Staff at COMDEV in Cambridge, ON, Canada, in 1996. He joined NSI in 1998 as Applications Engineer and upon NSI merging with MI Technologies in 2016, was named CTO of the new organization, NSI-MI Technologies LLC. He specialises in microwave antenna measurement systems, computational electromagnetics and measurement uncertainty analysis. He is a graduate of the University of Pretoria, South Africa, where he earned a PhD degree in Computational Electromagnetics in 1991. He is a Senior Member of the IEEE, Licensed Professional Engineer in Ontario, Canada and Fellow of the Antenna Measurement Techniques Association (AMTA). He was the recipient of the AMTA Distinguished Achievement Award in 2015 for his contributions to near-field technology. He remains actively involved in academia and is an Adjunct Professor in the School of Information Technology and Engineering, University of Ottawa, ON, Canada.

Professor Thomas Eibert is Professor of High-Frequency Engineering at the Technical University of Munich. He received the Dipl.-Ing. (FH) degree in electrical engineering from Fachhochschule Nürnberg, Nuremberg, Germany; the Dipl.-Ing. degree in electrical engineering from Ruhr-Universität Bochum, Bochum, Germany; and the Dr.-Ing. degree in electrical engineering from Bergische Universität Wuppertal, Wuppertal, Germany, in 1989, 1992 and 1997, respectively. From 1997 to 1998, he was with the Radiation Laboratory, Electrical Engineering and Computer Science Department, University of Michigan, Ann Arbor, MI, USA. From 1998 to 2002, he was with Deutsche Telekom, Darmstadt, Germany. From 2002 to 2005, he was with the Institute for High-Frequency Physics and Radar Techniques of FGAN e.V., Wachtberg, Germany, where he was the Head of the Department of Antennas and Scattering. From 2005 to 2008, he was Professor of Radio Frequency Technology with the Universität Stuttgart, Stuttgart, Germany. His research interests include numerical electromagnetics, wave propagation, measurement and field transformation techniques for antennas and scattering, and all kinds of antenna and microwave circuit technologies for sensors and communications. He has published more than 500 scientific papers.

List of Abbreviations

Abbreviation	Definition
3D	Three Dimensional
AAPC	Advanced Antenna Pattern Correction
AC	Alternating Current
AES	Antenna Electrical System
AESA	Active Electronically Scanned Array
AMS	Antenna Mechanical System
A-MST	Advanced Modulated Scattering Technique
AMTA	Antenna Measurement Techniques Association
APC	Antenna Pattern Comparison
AR	Axial Ratio
ARC	Antenna Range Controller
AUT	Antenna Under Test
az	Azimuth
BER	Bit Error Rate
BSS	Base Station Simulator
CAE	Computer Aided Engineering
CATR	Compact Antenna Test Range
CCR	compensated compact range
CE	Current Elements
CEM	Computational Electromagnetic Modeling
CFIE	Combined Field Integral Equation
CG	Conjugate Gradient
CM	Conformal Mesh
C-MARS	Cylindrical-MARS
CMCs	Cylindrical Mode Coefficients
CMOS	Complementary Metal Oxide Semiconductor
CNF	Cylindrical Near-Field
CNFS	Cylindrical Near-Field Scanner

C_{OFF}	Off-state Capacitance
CP	Calderon Projector
CP	Circularly Polarised
CW	Continuous Wave
CS	Combined Source
dB	Decibel
dBsm	Decibel square meters
DC	Direct Current
DFT	Discrete Fourier Transform
DGBE	Diethylene Glycol Butyl Ether
DRA	Dielectric Resonator Antenna
DUT	Device under Test
DSSS	Direct-Sequence Spread Spectrum
EA	Electro Absorptive
EDFA	Erbium Doped Fibre Amplifier
EEG	Earth Equivalent Ground
EFIE	Electric Field Integral Equation
EFT	Electromagnetic Field Theory
EHF	Extremely High Frequency
EIRP	Effective Isotropic Radiated Power
El	Elevation
EM	Electromagnetic
EMI	Electromagnetic Interference
EMPL	Equivalent Multipath Level
EO	Electro-Optical
ESA	European Space Agency
ET	Edge Taper
EU	European Union
EUCAP	European Conference on Antennas and Propagation
F	Noise Figure
F/D	Focal length to diameter ratio
FCC	Federal Communications Commission
FDTD	Finite Difference Time Domain
FEA	Finite Element Analysis
FF	Far-Field
FF-MARS	Far-Field-MARS

FFT	Fast Fourier Transform
FIAFTA	Fast Irregular Antenna Field Transformation Algorithm
FIPWA	Fast Inhomogeneous Plane-Wave Algorithm
FMM	Fast Multipole Method
FOM	Figure-Of-Merit for Switching Times
FS	Free-space
GaAs	Gallium Arsenide
GBM	Gaussian Beam Mode
GO	Geometric Optics
GPIB	General Purpose Interface Bus
GRIN	Gradient Index
GSM	Global System for Mobile Communications, originally Groupe Spécial Mobile
GTD	Geometric Theory of Diffraction
HF	High Frequency
HFT	Chair of High-Frequency Engineering
HM	Least Squares Conjugate Gradient
HP	Horizontal linear
HVAC	Heating Ventilation and Air Conditioning
I	In-phase Receiver Channel
IBC	Impedance Boundary Condition
IDFT	Inverse Discrete Fourier Transform
IEEE	Institute of Electrical and Electronics Engineers
IESS	Inverse Equivalent Source Solvers
IET	Institution of Engineering and Technology
IF	Intermediate Frequency
IFFT	Inverse Fast Fourier Transform
IRUWB	Impulse Radio Ultra Wideband
ISAR	Inverse Synthetic Aperture Radar
ITU	International Telecommunication Union
JCMT	James Clerk Maxwell Telescope
JH	Huygens-Type Elementary Radiators
JM LOVE	Electric and Magnetic Surface Current Densities With Love Condition
JM	Electric and Magnetic Surface Current Densities Without Any Further Constraint
KH	Kirchhoff–Huygens

LF	Low Frequency
LHCP	Left Hand Circular Polarisation
LI	Ludwig 1st definition of cross-polarisation
LII	Ludwig 2nd definition of cross-polarisation
LIII	Ludwig 3rd definition of cross-polarisation
LO	Local Oscillator
LP	Linearly Polarised
LPDA	Log Periodic Dipole Array
LSQR	Least Squares Conjugate Gradient
MARS	Mathematical Absorber Reflection Suppression
MC	Mirror Cube
MFIE	Magnetic Field Integral Equation
MHM	Microwave Holographic Metrology
MIMO	Multiple Input Multiple Output
MLFMM	Multilevel Fast Multipole Method
MoM	Method of Moments
MRC	Minimum Radius Cylinder
MRE	Maximum Radial Extent
MRS	Minimum Radius Sphere
MST	Modulated Scattering Technique
NASA	National Aeronautics and Space Administration
NATO	North Atlantic Treaty Organization
NBS	National Bureau of Standards
NE	Normal Error
NF	Near-Field
NFFFT	Near-Field Far-Field Transformation
N_i	Input Noise
NIST	National Institute of Standards and Technology
NPL	National Physical Laboratory
NR	Normal Residual
NRL	Naval Research Laboratory
N_o	Output Noise
OEFS	Opto-Electric Field Sensor
OEWG	Open Ended Waveguide Probe
OFDM	Orthogonal Frequency Division Multiplexing
OMT	Orthogonal Mode Transducer

OTA	Over The Air
PAMS	Portable Antenna Measurement System
PEC	Perfect Electrically Conducting
PEC	Perfectly Conducting
PCU	Power Control Unit
PDF	Probability Density Function
pHEMT	Pseudomorphic High Electron Mobility Transistor
PIN	p-type Intrinsic n-type construction for diode junction
P-MARS	Planar-MARS
PMC	Perfect Magnetically Conducting
PNF	Planar Near-Field
PNFS	planar near-field scanner
PO	Physical Optics
PTD	Physical Theory of Diffraction
PTFE	Polytetrafluoro-Ethylene
PTP	Plane-to-Plane
PWS	Plane Wave Spectrum
PWSC	Plane wave Spectrum Components
Q	Quadrature receiver channel
QML	Queen Mary, London
QZ	Quiet Zone
RA	Range Assessment
RADAR	Radio Detection and Ranging
RAL	Rutherford Appleton Laboratory
RAM	Radar Absorbent Material
RCS	Radar Cross-Section
RF	Radio Frequency
RFS	Range Fixed System
RHCP	Right Hand Circular Polarisation
RI	Range Illuminator
RMS	Root Mean Square
R_{ON}	On-state Resistance
RSA	Remote Source Antenna
RSS	Root Sum Square
RSS	Received Signal Strength
RWG	Rao–Wilton–Glisson

Rx	Receive
SAR	Specific Absorption Rate
SAR	Synthetic Aperture Radar
SC	side constraint
SD	Standard Deviation
SFD	Saturating Flux Density
SGA	Standard Gain Antenna
SGH	Standard Gain Horn
SHF	Super High Frequency
S_i	Input Signal Power
SLL	Side-Lobe Level
SM	Spherical Mesh
SMA	Subminiature A
S-MARS	Spherical-MARS
SMC	Spherical Mode Coefficient
SNF	Spherical Near-Field
SNFR	Spherical Near-Field Range
SNFS	Spherical Near-Field Scanner
SNR	Signal-to-Noise Ratio
S_o	Output Signal Power
SPHNFFFT	Spherical NF FF Transformation
SPP	Single Port Probe
SRD	Step Recovery Diode
SWR	Standing Wave Ratio
TE	Transverse Electric
T_e	Equivalent Noise Temperature
TEM	Transverse Electric and Magnetic
TIS	Total Isotropic Sensitivity
TM	Transverse Magnetic
TRP	Total Radiated Power
TT	Turntable
TUM	Technical University of Munich
Tx	Transmit
UHF	Ultra High Frequency
US	United States
UTD	Universal Theory of Diffraction

UWB	Ultra Wideband
VH	Vector-Huygens
VHF	Very High Frequency
VNA	Vector Network Analyser
VP	Vertical Linear
VSWR	Voltage Standing Wave Ratio
WF	Weak-Form
WG	Waveguide

This page intentionally left blank

Foreword to volumes 1 and 2

Foreword for the 2nd Edition of *Theory and Practice of Modern Antenna Range Measurements*

Since the publishing of the First Edition of this extensive reference book, it has been the preeminent source for the theory and practical aspects of all the measurement methods that are used to characterise the extremely broad range of antennas that have been developed as critical components in modern communication, sensing and space applications. With the completion of this Second Edition, major improvements and additions have been included to keep pace with the continuing advancements in this field. The authors have the knowledge and background to provide authoritative and practical material that is very necessary for the technical challenges that are required on modern antenna measurement facilities. The new edition has increased the scope of information and the quality of presentation and will continue to be a valuable resource for technical experts working in this field for many years.

Allen C Newell
NIST Retired, Newell Near-Field Consultants
June 2019
Boulder, Colorado, USA

This page intentionally left blank

Preface to volumes 1 and 2

At the time of writing of this text, some 147 years have passed since the publication of the *Treatise on Electricity and Magnetism* by James Clerk Maxwell. This was the text that firmly established the classical theory of electromagnetism in the mainstream of science and engineering and placed Maxwell within the pantheon of greats in the fields of science and technology. The success of this classical theory is attested to by the extraordinarily good agreement that is routinely attained between theoretical prediction and physical measurement. Its initial triumph was to not only be able to summarise all previous experiences in the fields of optics, electricity and magnetism within a small* set of self-consistent equations; but also, for the first time, to admit the possibility of electromagnetic waves. Crucially, the velocity of these waves could be deduced exclusively from electrical measurements, which when compared with the then known velocity of light, the two values were found to coincide almost exactly.

This inherent accuracy and precision has enabled successive generations of workers to construct and refine ever more complex and ingenious structures for the transmission and reception of electromagnetic waves. These waves can be used for the transmission of information by means of modulating the wave-form to contrive a signal as used in the field of telecommunications. Alternatively, these modulated (i.e. radio) waves can be utilised for the remote detection and location of planes, ships, or other targets as is employed within modern radar (Radio Detection And Ranging) systems. More recently, the way in which radio waves scatter has also been harnessed, as this additional information can be used to remotely sense properties of the physical world without the need to actually visit those locations. Thus, the sheer multitude and diversity of the applications inexorably drives the ever-increasing intricacy and sophistication of the design of the devices that are used to efficiently transmit and receive these electromagnetic waves, so accurately and rigorously postulated by James Clerk Maxwell.

The achievements of Maxwell are remembered in his home town of Edinburgh in Scotland where a statue of him seated in his academic gown holding a colour wheel stands at a busy intersection, with the proud motive ‘James Clerk Maxwell Mathematical Physicist’, carved into the stone pedestal on which it sits. A more modern interpretation of the term mathematical physicist might be theoretical physicist, but in fact it should be remembered that in the opening leaf of the *Treatise on*

*It was actually Oliver Heaviside who reformulated Maxwell’s 20 equations, which were quite difficult to use, and reduced them to obtain the four very useful equations that are in common use today.

Electricity and Magnetism, Maxwell refers to himself as 'Professor of Experimental Physics in the University of Cambridge' and as if to emphasise the importance that he placed on the experimental and empirical aspects of his work he devoted the first 26 numbered paragraphs in the treatise to a preliminary to be read prior to the main text, this preliminary being entitled 'On the measurement of quantities'. Still now, after so many years as a result of the increasing intricacy and sophistication of the devices and systems designed to utilise the concept of classical electromagnetic field theory, the problem of the measurement of electromagnetic fields remains as acute as ever.

The development and proliferation of inexpensive, powerful, digital computers with large amounts of memory in the latter part of the twentieth century has enabled the use of computer-aided engineering to become commonplace in both the design and measurement of antenna assemblies. The use of full-wave three-dimensional computational electromagnetic simulation software tools has allowed the antenna designer to accurately and precisely predict the performance of a given structure. These tools harness techniques such as the finite difference time domain, or method of moments, that simply cannot be effectively deployed without the use of a digital computer. Modern, now commercially available, software packages have provided hitherto unknown levels of detail, accuracy and precision leading to their becoming an indispensable part of the antenna design and development process. Such design and prediction capabilities have become commonplace throughout academia and industry alike and have in no small way contributed towards the emergent need for the antenna metrologist to provide a broadly comparable service.

Clearly, antennas have to be mounted and attached to structures and these can influence, in some cases significantly, the installed radiation pattern as electromagnetic waves 'couple' to these structures and subsequently radiate. Additionally, variations in material properties and the influence of imperfections in manufacturing mean that in nearly all practical applications the antenna radiation characteristics have to be measured before a final design can go into commercial production. The inevitable search for more efficient and accurate techniques for the characterisation of new, increasingly complex, instruments has been the catalyst for the rapid development of modern sophisticated antenna measurement techniques. These developed first from the early direct observation techniques that were harnessed during the years of the Second World War (1939–45), and which were still commonplace until only comparatively recently, to the most advanced indirect near-field techniques.

Very often, antenna metrology is considered to be a difficult discipline that is best left to a few designated 'experts'. In part this perception is perhaps attributable to the realisation as with all science and engineering antenna metrology is fundamentally both an intellectual, and a practical activity. Thus, in order to take good measurements, the practitioner needs to be familiar with and adept at both the practical *and* theoretical aspects of the work making antenna metrology an extremely broad subject. This difficulty is further complicated as many of the concepts that are routinely used are found in the development of the theory of classical electrodynamics which, as already stated were completed in the nineteenth century[†] and which were originated centuries earlier

[†]In 1864 Maxwell published a paper entitled 'Dynamical Theory of the Electromagnetic Field'.

than that. Furthermore, and as with any discipline that becomes firmly established (i.e. entrenched), there is a danger that the principles and concepts that lie behind the terminology its workers use can become taken for granted, thereby obscuring the subject and its meaning from all but a few experienced practitioners. This is all the more acute an issue as the development of the discipline has been sufficiently rapid over the course of the past few decades that even active workers can, at times, struggle to keep abreast of the most recent developments. This text aims to address this by adopting a coherent narrative, terminology and nomenclature throughout. In this way, it is hoped that this volume can form a useful introduction and reference to graduate students, researchers and practicing engineers alike.

The first chapters of this text present an initial examination of the properties of antennas that allow them to enhance the free-space interaction of electronic systems. This is followed by an introduction to direct far-field and indirect far-field forms of antenna measurements and their implementation. Chapter 5 presents a detailed description of the compact antenna test range which is a direct far-field measurement technique before Chapters 6–8 progress to present alternative indirect planar, cylindrical and spherical techniques, respectively. Chapter 9 is devoted to field transformations from non-canonical measurement surfaces based on general inverse-source formulations. Chapter 10 discusses near-field range error budgets which are an indispensable part of antenna metrology. Chapter 11 presents a discussion of modern mobile and body-centric antenna measurements. Finally, Chapter 12 sets out some of the most recent advances in the various measurement techniques including aperture diagnostics, phase-less antenna metrology and range multi-path suppression techniques which currently are amongst some of the most active topics for researchers.

In summary, this volume will provide a comprehensive introduction and explanation of both the theory and practice of all forms of modern antenna measurements from their most basic postulates and assumptions to the intricate details of their application in various demanding modern measurement scenarios.

The authors have not attempted to identify the originators of every concept or to provide an exhaustive literary survey or historical account as this can very often obstruct the pedagogy of a text. Additionally, except where specifically stated, it should be noted that only concepts, techniques and methodologies of which at least one of the authors has direct practical experience of implementation are included for discussion in the text. The International System of Units (SI) is used exclusively with the approximation $\mu_0 = 4\pi \times 10^{-7}\ \mathrm{NA}^{-2}$. Following the redefinition of SI base units, the kilogram, ampere, kelvin and mole, on the 20th of May 2019, the difference between this value of μ_0 and the new SI (experimental) value of μ_0 is less than 1×10^{-9} in relative value which is negligible in the context of the uncertainty budgets discussed herein. However, this assumption should be noted and re-examined periodically as it does subtlety affect the permittivity of vacuum, impedance of vacuum and admittance of vacuum.

Thanks are due to a great many people who gave freely and generously of their time to review the manuscript at various stages throughout its preparation, and especially to Prof. Edward B. Joy of Georgia Tech who carefully reviewed an early

draft. However, any errors or lack of clarity must, as always, remain the responsibility of the authors alone. The authors are grateful to their wives (Claire Parini, Catherine Gregson, Imelda McCormick and Lizette Janse van Rensburg) and children (Robert Parini, Elizabeth Gregson and Suzette Janse van Rensburg) whose unwavering understanding, constant support, encouragement and good humour were necessary factors in the completion of this work. We also thank the organisations and individuals who generously provided copyright consent.

There are many useful and varied sources of information that have been tapped in the preparation of this text; however, mention must be made of the following books which have been of particular relevance and will be referred to throughout. In no special order:

M.R. Spiegel, *Theory and Problems of Vector Analysis and an Introduction to Tensor Analysis*, Schaum Publishing Company.

R.H. Clarke and J. Brown, *Diffraction Theory and Antennas*, Ellis Horwood Ltd.

J.E. Hansen, *Spherical Near-field Antenna Measurements*, Peter Peregrinus, 1988.

S.F. Gregson, J. McCormick, and C.G. Parini, *Principles of Planar Near Field Measurements*, Institution of Engineering and Technology, 2007.

Although the nomenclature and development of the theory of antenna metrology as presented within this text has not generally followed that of the National Institute of Standards and Technology (NIST), the technical publications originating from that organisation have also been a rich source of valuable information. In particular, but in no special order:

D.M. Kerns, *Plane-Wave Scattering-Matrix Theory of Antennas and Antenna-Antenna Interactions*, National Bureau of Standards Monograph 162.

A.C. Newell, *Planar Near-Field Antenna Measurements*, Electromagnetic Fields Division, National Institute of Standards and Technology, Boulder Colorado.

A.D. Yaghjian, *Near-Field Antenna Measurements on a Cylindrical Surface: A Source Scattering-Matrix Formulation*, Electromagnetics Division, Institute for Basic Standards, National Bureau of Standards, Boulder, Colorado, NBS Technical Note 696, 1977.

It is the hope of the authors that this text will act as a sound reference for all aspects of modern antenna measurements and in some small way enhance the theoretical knowledge and practical skills of the reader with relation to antenna range measurements. As it is clear from careers of the greats in science and engineering, not least Maxwell's own, that it is only through the interaction of these intellectual and practical aspects of science and engineering that effective progress can be made.

Clive Parini, Stuart Gregson, John McCormick, Daniël Janse van Rensburg
and Thomas Eibert
London, Edinburgh, Atlanta and Munich
March 2020

Chapter 8
Spherical near-field antenna measurements

8.1 Introduction

The third near-field formulation we consider is that defined in a spherical coordinate system. The process in deriving the expressions describing this formulation is analogous to that outlined in Chapter 7 and the fundamental spherical solution to Maxwell's equations presented in [1,2]. An excellent work containing the detailed formulation, as it applies to antenna measurements, was presented in [3] and two excellent overviews in [4,5]. The theoretical discussion presented here does not aim to supplant these references, but to form a cohesive presentation of the process involved when making spherical near-field (SNF) measurements and the fundamental requirements and limitations thereof. Our primary goal is therefore not to develop the SNF formulation from scratch, but review enough of the detail to provide the reader with an understanding of the process in order to become a more confident user of the technique.

Any SNF measurement process requires the sampling of tangential electrical field components on a spherical surface enclosing the antenna being characterised. From these sampled field values, we can predict far-field radiation and other associated parameters. This is conceptually simple, but tricky to implement in practice. The theory allowing us to convert measured near-field values to valid far-field radiation patterns is also quite challenging, and both of these aspects will be addressed in what follows.

The SNF measurement system is typically formed from the intersection of two rotation stages. The combined motion of these two axes of rotation allows the probe to trace out a conceptual spherical surface in three dimensions, thereby enabling the collection of samples on lines of constant longitude or latitude. Here, samples are taken at regular intervals across a spherical grid with typically the antenna under test (AUT) being rotated. The two axes of rotation have to intersect in a single point in space, and they have to be perfectly orthogonal. Several practical solutions to this are found in the industry, and these are presented in Section 8.2. The SNF measurement system is the most desirable of the three types of near-field systems since it is the only technique that can circumvent any kind of truncation. However, due to the mechanical construction of the majority[1] of these systems, one often has to contend with the effect of a continuously changing gravitational vector with

[1]We refer to the ϕ/θ configuration as described in Section 8.2.

respect to the AUT during the course of an acquisition. This can lead to unwanted dimensional changes during testing that are impossible to assess or correct for. Figure 8.1 contains a schematic representation of a typical SNF antenna test system,[1] where the conceptual, spherical raster sampling strategy is shown.

Figure 8.2 contains a colour image plot of the measured SNF amplitude of a ridged guide horn antenna. Here, complete 360° ϕ angular cuts were taken that spanned a 180° θ region, keeping with the spherical coordinate system defined below.

The corresponding far-field cardinal cuts are presented in Figure 8.3.

As will be shown within this chapter, the electromagnetic fields emanating from an arbitrary test antenna radiating into free space can be expanded into a set of orthogonal spherical modes and these modes and coefficients (SMCs) can then be used to obtain the electric and magnetic fields everywhere in space outside of a conceptual spherical surface which encloses the radiator. It will also be shown that these SMCs can be determined from the measured data in an efficient manner through the use of Fourier techniques. These mode coefficients are also corrected for the spatial filtering properties of the measuring near-field probe and used to determine the true AUT transmitting properties. Parameters such as the far-field antenna pattern function, axial ratio, tilt angle, directivity and gain of the AUT can be obtained from two orthogonal tangential near electric field components. This formulation therefore enables highly accurate, practical, SNF techniques to be implemented. The coordinate system that will be used during the development of this spherical formulation is presented in Figure 8.4.

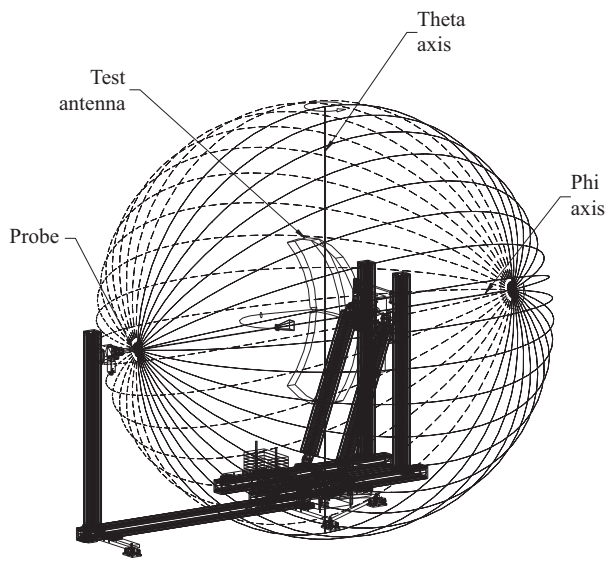

Figure 8.1 Schematic of SNF antenna test system (ϕ/θ configuration as described in Section 8.2) showing conceptual scanning surface enclosing AUT. (Picture used with permission of NSI-MI Technologies LLC.)

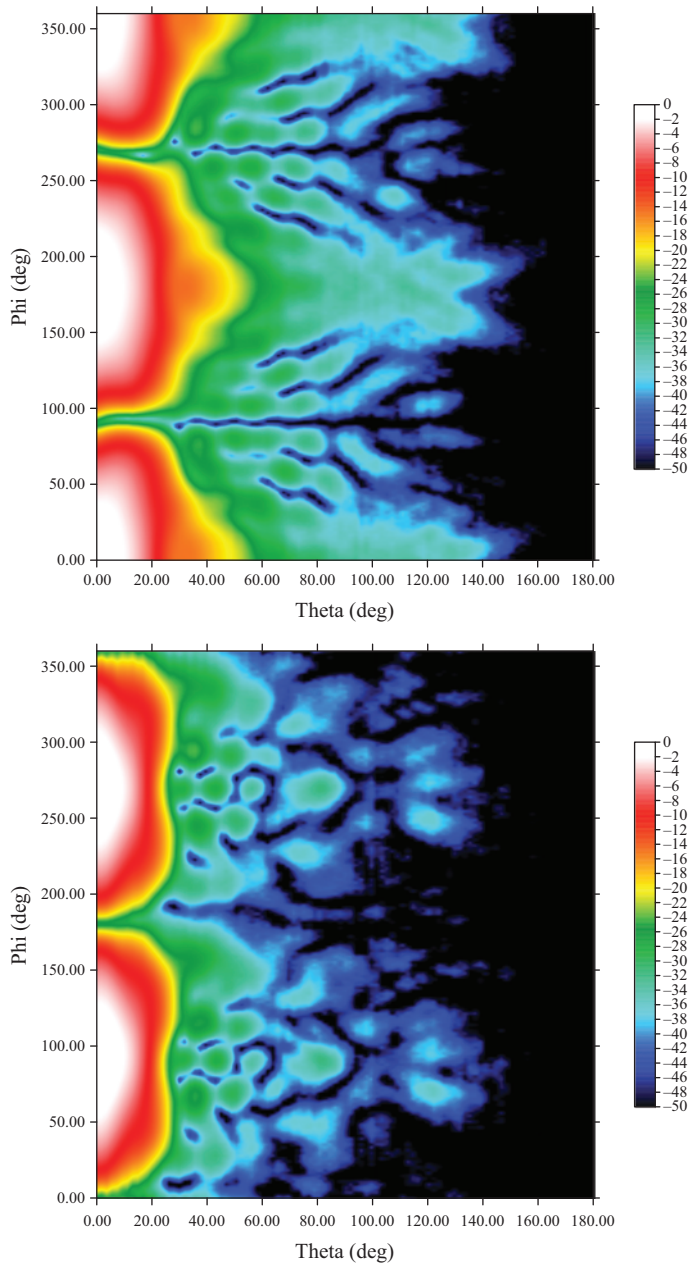

Figure 8.2 SNF colour image plot of measured amplitude pattern of ridged guide horn. Polarisation 1 is shown at the top and polarisation 2 on the bottom

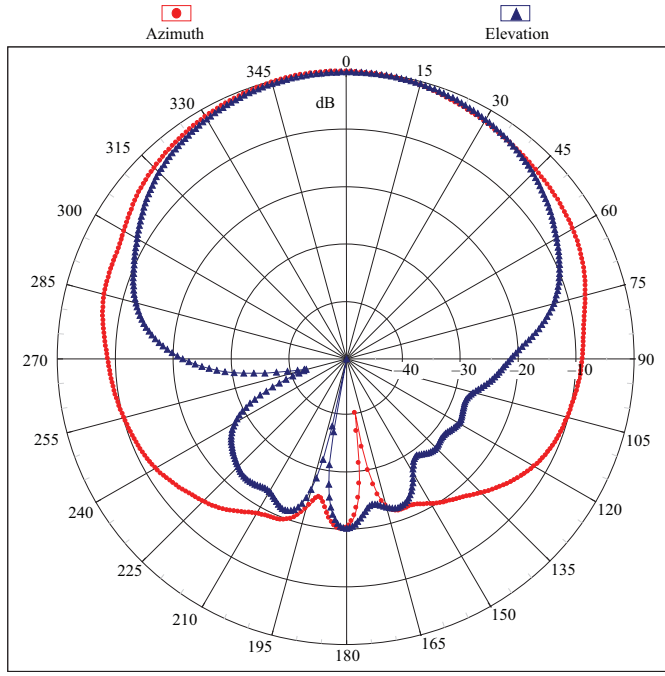

Figure 8.3 Far-field cardinal cuts obtained from SNF measurements of a ridged guide horn antenna

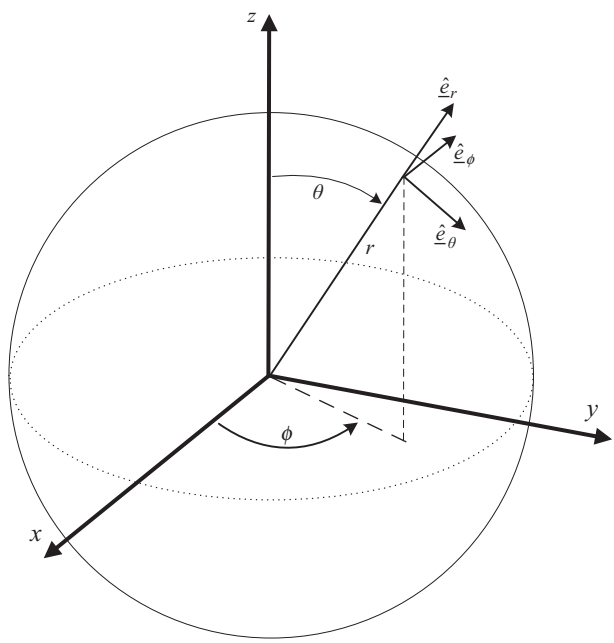

Figure 8.4 Coordinate system for the formulation of standard SNF theory

Here, for a spherical coordinate system as depicted in Figure 8.4, we can write that

$$x = r\sin\theta\cos\phi$$

$$y = r\sin\theta\sin\phi$$

$$z = r\cos\theta$$

where $r \geq 0$, $0 \leq \phi \leq 2\pi$, $0 \leq \theta \leq \pi$. In a rectangular coordinate system, point P can be expressed as $P(x, y, z)$. Conversely, in a spherical coordinate system, point P can be expressed as $P(\theta, \phi, r)$, where the relationship between the two systems is established through this triad of equations. Conversely, from rearranging the above equations, we obtain the inverse relationships, namely,[2]

$$r = \sqrt{x^2 + y^2 + z^2}$$

$$\phi = \arctan\left(\frac{y}{x}\right)$$

$$\theta = \arccos\left(\frac{z}{\sqrt{x^2 + y^2 + z^2}}\right)$$

As the electric and magnetic fields are vector quantities, we also need to obtain expressions that allow the respective vector-field components to be converted from rectangular to spherical coordinate systems and vice versa. This can be accomplished easily using the standard expression

$$\hat{\underline{e}}_1 = \left(\frac{\partial \underline{r}}{\partial u_1}\right) \Big/ \left|\frac{\partial \underline{r}}{\partial u_1}\right|$$

From Figure 8.4, it is clear that in spherical coordinates the position vector $\underline{r}$ can be expressed as

$$\underline{r} = r\sin\theta\cos\phi\,\hat{\underline{e}}_x + r\sin\theta\sin\phi\,\hat{\underline{e}}_y + r\cos\theta\,\hat{\underline{e}}_z$$

Then,

$$\frac{\partial \underline{r}}{\partial r} = \sin\theta\cos\phi\,\hat{\underline{e}}_x + \sin\theta\sin\phi\,\hat{\underline{e}}_y + \cos\theta\,\hat{\underline{e}}_z$$

As $|\partial \underline{r}/\partial r| = 1$,

$$\hat{\underline{e}}_r = \sin\theta\cos\phi\,\hat{\underline{e}}_x + \sin\theta\sin\phi\,\hat{\underline{e}}_y + \cos\theta\,\hat{\underline{e}}_z$$

Similarly,

$$\frac{\partial \underline{r}}{\partial \phi} = -r\sin\theta\sin\phi\,\hat{\underline{e}}_x + r\sin\theta\cos\phi\,\hat{\underline{e}}_y$$

[2]Where we elect to use the two-argument arctangent function so that quadrant ambiguity can be eliminated.

As $|\partial \underline{r}/\partial\phi| = r\sin\theta$,

$$\hat{\underline{e}}_\phi = -\sin\phi\hat{\underline{e}}_x + \cos\phi\hat{\underline{e}}_y$$

Similarly,

$$\frac{\partial \underline{r}}{\partial\theta} = r\cos\theta\cos\phi\hat{\underline{e}}_x + r\cos\theta\sin\phi\hat{\underline{e}}_y + r\sin\theta\hat{\underline{e}}_z$$

As $|\partial \underline{r}/\partial\theta| = r$,

$$\hat{\underline{e}}_\theta = \cos\theta\cos\phi\hat{\underline{e}}_x + \cos\theta\sin\phi\hat{\underline{e}}_y + \sin\theta\hat{\underline{e}}_z$$

Hence, we can write this in a matrix form as

$$\begin{bmatrix} \hat{\underline{e}}_\theta \\ \hat{\underline{e}}_\phi \\ \hat{\underline{e}}_r \end{bmatrix} = \begin{bmatrix} \cos\theta\cos\phi & \cos\theta\sin\phi & \sin\theta \\ -\sin\phi & \cos\phi & 0 \\ \sin\theta\cos\phi & \sin\theta\sin\phi & \cos\theta \end{bmatrix} \cdot \begin{bmatrix} \hat{\underline{e}}_x \\ \hat{\underline{e}}_y \\ \hat{\underline{e}}_z \end{bmatrix}$$

Conversely, as this is an orthogonal and normalised matrix, we can obtain the inverse relationship by taking the transpose of the square matrix thus

$$\begin{bmatrix} \hat{\underline{e}}_x \\ \hat{\underline{e}}_y \\ \hat{\underline{e}}_z \end{bmatrix} = \begin{bmatrix} \cos\theta\cos\phi & -\sin\phi & \sin\theta\cos\phi \\ \cos\theta\sin\phi & \cos\phi & \sin\theta\sin\phi \\ \sin\theta & 0 & \cos\theta \end{bmatrix} \cdot \begin{bmatrix} \hat{\underline{e}}_\theta \\ \hat{\underline{e}}_\phi \\ \hat{\underline{e}}_r \end{bmatrix}$$

As the coordinate and unit vector relationships are now established, these can be used with Maxwell's equations so that a solution to the vector wave equation can be sought using this coordinate system. The following section establishes that the general vector wave equation can be reduced to the scalar wave equation in spherical coordinates, and that this equation can be solved using the method of separation of variables. In this way, elementary spherical vector wave functions are constructed that are shown to be amenable for use as the basis of standard SNF theory.

8.2 Types of SNF ranges

In theory, an SNF measurement requires that a near-field probe be moved along a spherical surface enclosing the AUT while sampling the tangential electric field intensity. Although conceptually simple, it becomes rather challenging to implement such a device in practice, and there are various approaches that have been taken to do so. The most common configuration is what we will refer to as the ϕ-over-θ (ϕ/θ)-type systems, followed by the θ-over-ϕ (θ/ϕ) systems. Lastly, we will also describe some articulating SNF systems that allow for the AUT to remain stationary during measurement.

Roll over azimuth (ϕ/θ) *systems*[3]: These SNF scanners are the most common ones encountered in the industry today and have their origin in the so-called roll

[3]It should be noted that *roll over azimuth* is a misnomer since the lower 'azimuth' axis of rotation is not truly an azimuth axis. It is also to be noted that *roll over azimuth* is also sometimes called a 'model tower' arrangement.

over azimuth positioners used in the far-field industry for many years before the advent of near-field testing. An example of such a positioner is shown in Figure 8.5. In this configuration, two rotation stages are attached through a rigid fixture with one stage mounted on the floor (with vertical rotation axis) and the second upper rotation stage (with horizontal rotation axis) mounted to the top of the fixture. The lower stage forms the θ-axis of rotation, and the upper stage forms the ϕ-axis of rotation, thus the reference to the ϕ-over-θ positioner. This configuration is depicted in Figure 8.1, and it clearly shows that the AUT is rotated around two axes while the near-field probe remains stationary during the measurement of one polarisation component (rotated once by 90° for polarisation change).

In order for this positioner to describe a perfect sphere enclosing the antenna, the following conditions have to be met:

1. The axes of the stages have to intersect at a point.
2. The axes of the stages have to be orthogonal.
3. The stages have to be rigid and run true (no axis wobble or flexing of the stages under load).
4. The interconnecting fixture has to be rigid.
5. The near-field probe axis has to coincide (not just intersect) with the ϕ-axis when $\theta = 0°$.

Figure 8.5 A roll over azimuth (ϕ/θ) positioner. (Picture used with permission of NSI-MI Technologies LLC.)

If any of these conditions are not met, we are straying from a true SNF acquisition, and an assessment is needed to determine to what extent the measured results will be adversely affected. In reality, all of these conditions can be met fairly easily for a fixed AUT weight loading. What proves to be more challenging is to meet these conditions amidst varying weight conditions since this leads to the positioner and structure specifications that are geared for the worst-case condition, that often leads to overly bulky designs.

Another very significant limitation of the ϕ/θ scanner configuration is the fact that the AUT is rotated during acquisition in such a way that it experiences a gravity vector that is constantly changing direction. This can be very problematic for flight space antennas that are gravitationally sensitive since the antenna may deform when the gravity vector direction changes. This is often also true for testing breadboard antennas that may not have been designed mechanically to withstand an arbitrary gravity vector, and in such instances, an alternative SNF test method is needed.

Swing arm – (θ/ϕ) systems: These SNF scanners were developed to measure gravitationally sensitive antennas and have become more widely used in the industry. An example of such a positioner is shown in Figure 8.6. In this configuration, two rotation stages are again combined to describe the sphere. However, they are not interconnected, and both remain stationary during testing. One stage is mounted on the floor (with the vertical rotation axis), and the second rotation stage (with the horizontal rotation axis) is mounted on a vertical stand or even a chamber

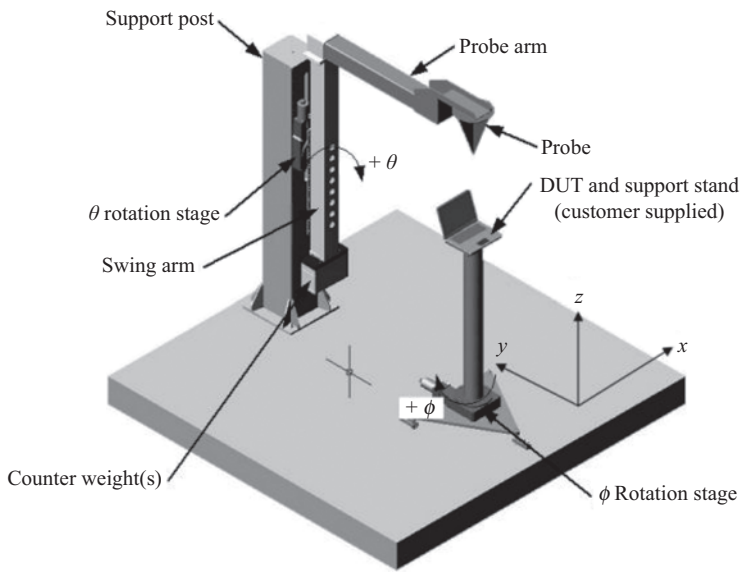

Figure 8.6 Depiction of the θ/ϕ positioner with swing arm attaching the near-field probe to the θ-stage. The AUT is supported on the ϕ-stage. (Picture used with permission of NSI-MI Technologies LLC.)

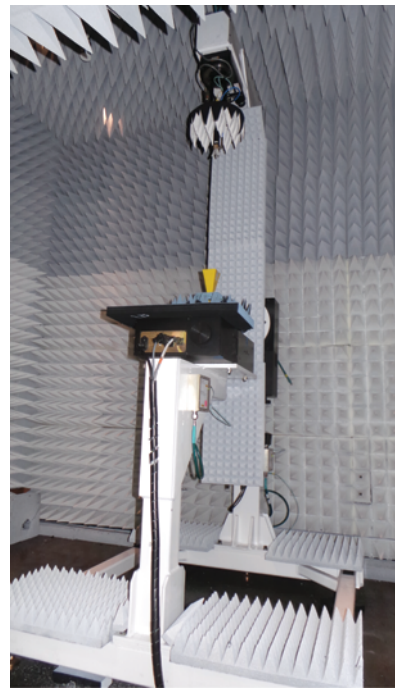

Figure 8.7 A swing arm (θ/ϕ) SNF antenna test system used for mm-wave applications. (Picture used with permission of NSI-MI Technologies LLC.)

wall. The lower stage forms the ϕ-axis of rotation in this case and the upper stage forms the θ-axis of rotation, thus the reference to a θ-over-ϕ positioner. This configuration is depicted in Figure 8.7 and it shows that the motion is now split amongst the AUT and the near-field probe. In order for this positioner to describe a perfect sphere enclosing the antenna, the same conditions as outlined for the ϕ/θ positioner have to be met.

With this alternative positioner configuration, we gain certain advantages with the most significant one being that the AUT experiences gravity in a single direction during testing. The fact that the near-field probe is being rotated implies that the swingarm structure can be designed for support of only those near-field probes to be used, which simplifies design considerably. The fact that the AUT is only rotated on an axis parallel to gravity has two benefits. It first allows for the testing of gravitationally sensitive antennas and it second simplifies the AUT mounting considerably. Fairly heavy antennas can often be supported through a simple column, which also allows for the use of dielectric columns that have certain perceived advantages when testing very low gain antennas. The latter leading to this type of SNF configuration being very popular for testing wireless devices that are often not ideally suited for mounted on a ϕ/θ type system (more details on this can be found in Chapter 11).

An alternate SNF implementation of the θ/ϕ positioner is shown in Figure 8.8. Here, an array of near-field probes replaces the mechanical swing arm, attaching a

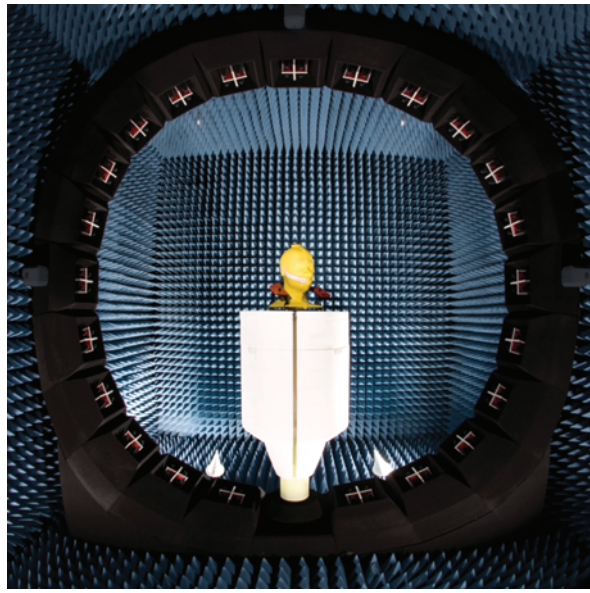

Figure 8.8 Alternate implementation of the θ/ϕ positioner with an array of near-field probes replacing the mechanical swing arm attaching the near-field probe to the θ-stage. The AUT is supported on the ϕ-stage on a dielectric column in this instance and may also be mounted on a goniometer that allows for limited rotation of the AUT in θ. (Picture used with permission of ETS Lindgren.)

single near-field probe to the θ-stage. The AUT is still supported on the ϕ-stage (in this case on a dielectric column) and the ϕ-stage can also be mounted on a goniometer that allows for limited rotation of the AUT in θ. A goniometer is a positioner that rotates an object about a fixed axis in space, where that point is located above the mounting surface of the goniometer as depicted in Figure 8.9.

The goniometer axis of rotation coincides with the θ-axis and is used to sample data points at a higher sampling density than what the array of probes allows for. The total angular span of the goniometer therefore only needs to be equal to the angular spacing of two adjacent probes in the array. The operation of this type of range is further covered in Chapter 11.

Arch-roll rotated (θ/ϕ) *systems:* This SNF scanner was developed to measure steered beam array antennas that cannot be moved and require at least a full-forward hemisphere of measurement coverage. The scanner is depicted in Figure 8.10. In this configuration, a large rotator forms the horizontal ϕ-axis, on which a 'horseshoe'-shaped hemi-spherical rail is mounted. The hemi-spherical rail forms the theta axis and the near-field probe moves along this rail. The entire 'horseshoe' structure rotates around the ϕ-axis and the specific positions for $\phi = 45°$ (left) and $\phi = 0°$ (right) are depicted in Figure 8.11.

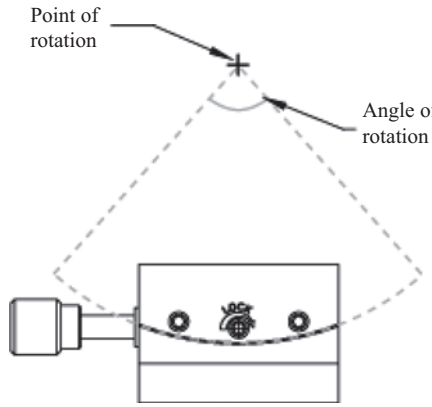

Figure 8.9 Single axis goniometer schematic

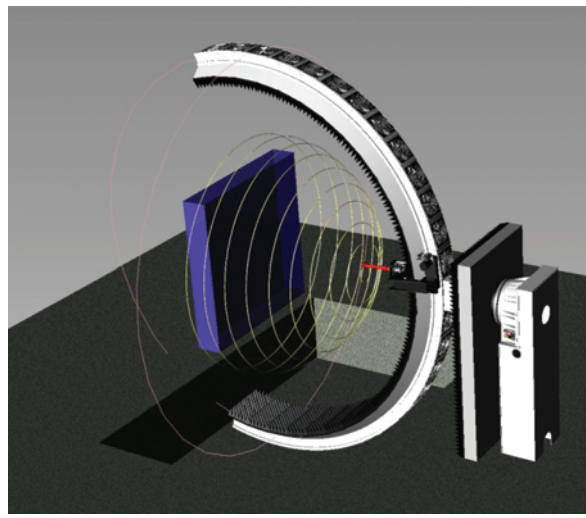

Figure 8.10 An arch-roll rotated – (θ/ϕ) positioner depicted with array antenna as a rectangular box. The horseshoe rotates on a horizontal ϕ-axis and the near-field probes rides along the inside of the horseshoe forming the θ-axis. Static AUT is represented by a large rectangular box. (Picture used with permission of NSI-MI Technologies LLC.)

The uniqueness of this design is that all SNF motion is performed by the near-field probe and the AUT remains stationary during testing. The alignment of the SNF scanner therefore becomes independent of the AUT size and weight (similar to the PNF case). An obvious disadvantage of this solution is that only a hemisphere (or marginally more) can be covered by the near-field probe during testing. The solution is therefore subject to near-field truncation in much the same way as a PNF

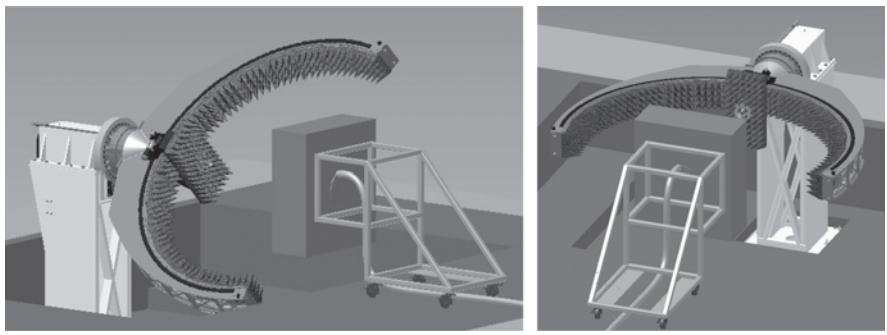

Figure 8.11 The large upper rotator forms the horizontal ϕ-axis. The horseshoe-shaped hemispherical rail forms the theta axis and the near-field probe moves along this rail. The entire horseshoe structure rotates around the ϕ-axis and the specific positions for $\phi = 45^\circ$ (left) and $\phi = 0^\circ$ (right) are depicted here. Static AUT is represented by a large rectangular box. (Picture used with permission of NSI-MI Technologies LLC.)

solution. Further, in order for this positioner to describe a perfect spherical surface, the same conditions as outlined for the ϕ/θ positioner have to be met. However, with the introduction of the 'horseshoe'-shaped rail system, some very specific and stringent mechanical requirements have to be met as described in [6]. A discussion of the mechanical performance of this structure is beyond the scope of this text and the reader is referred to [6] for an in-depth review.

With this positioner configuration, one gains the distinct advantage of the AUT remaining stationary during testing. The solution is therefore an attractive option for very sensitive or very heavy antennas. The hemispherical test region allows for the measurement of steered beam arrays, with a true truncation limit at $\pm 90^\circ$ which cannot be achieved with a PNF solution. To date, this test solution has not found widespread use in industry, principally due to the complexity of the mechanical design and construction of the scanner.

Articulating arm (θ/ϕ) systems: This SNF scanner was developed to measure on-chip antennas that cannot be moved and require as much of the spherical surface to be covered as possible. The scanner is depicted in Figure 8.12. The large upper rotator forms the horizontal ϕ-axis. The smaller travelling positioner forms the θ-axis and the near-field probe (as well as frequency converter unit) is mounted on a curved arm attached to this stage. This entire structure rotates around the ϕ-axis. The specific positions for $\phi = 0^\circ$ and $\theta = -150^\circ$ (upper left), $\phi = 180^\circ$ and $\theta = -150^\circ$ (upper right), $\phi = -90^\circ$ and $\theta = -150^\circ$ (lower left) and $\phi = 90^\circ$ and $\theta = -150^\circ$ (lower right) are depicted in Figure 8.12. The spherical region shown is the keep-out region in which the AUT can be located (not shown here).

Again, the uniqueness of this design is that all SNF motion is performed by the near-field probe and the AUT remains stationary during testing. The alignment of the SNF scanner therefore becomes independent of the AUT size and weight (similar to the PNF case). In order to assess to what extent this positioner

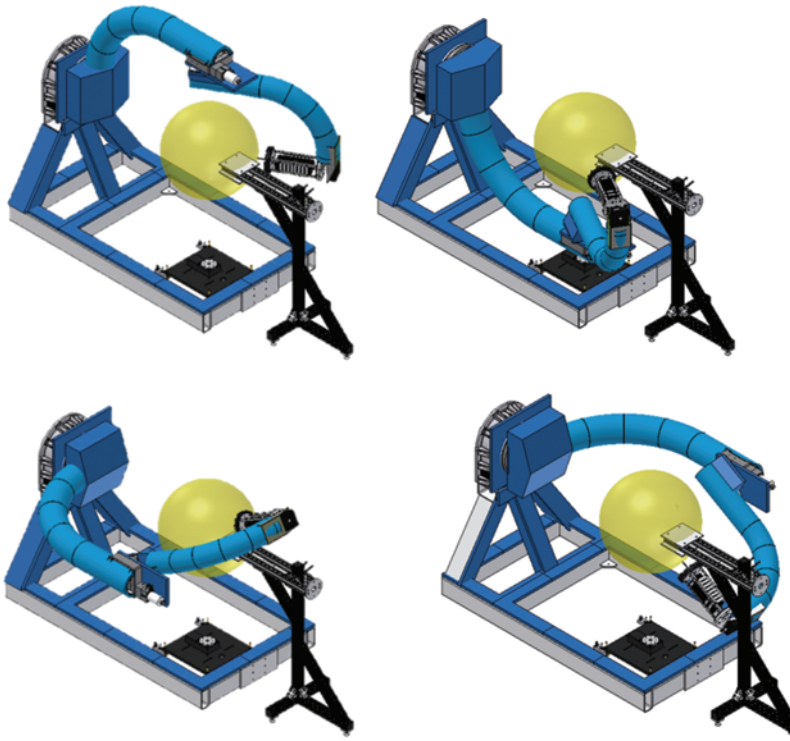

Figure 8.12 Articulating arm (θ/ϕ) scanner is shown as used for on-chip antenna testing. The large upper rotator forms the horizontal ϕ-axis. The smaller travelling positioner forms the θ-axis and the near-field probe is mounted on a curved arm attached to this stage. The entire structure rotates around the ϕ-axis. The specific positions for $\phi = 0^\circ$ and $\theta = -150^\circ$ (upper left), $\phi = 180^\circ$ and $\theta = -150^\circ$ (upper right), $\phi = -90^\circ$ and $\theta = -150^\circ$ (lower left) and $\phi = 90^\circ$ and $\theta = -150^\circ$ (lower right) are depicted here. The static AUT keep-out region is represented by the sphere shown. (Picture used with permission of NSI-MI Technologies LLC.)

describes a perfect sphere enclosing the antenna, a very careful structural analysis or three-dimensional structural assessment using a laser tracker is needed. This information can then be used to determine the limits of feasibility of using this type of scanner for SNF testing [7–10]. This solution is an attractive option for testing of very sensitive antennas (e.g. on-chip antennas where wafer probes are needed to connect to the AUT).

Robotic arm SNF systems: Agile and accurate articulated robotic arms today allow one to move a near-field probe along any conceivable measurement surface and one such a SNF application is described in [11]. A major advantage in this instance is also that the AUT remains stationary during testing. An example of such

Figure 8.13 An articulating robotic arm that can move a near-field probe along a spherical surface enclosing the stationary AUT. (Image used with permission of Electromagnetics Division of NIST, Boulder, CO, USA.)

a positioner is shown in Figure 8.13. In this implementation, there is no attempt made to align any of the robotic arm axes of rotation with the θ or ϕ axes (as shown Figure 8.14) describing the sphere and it is only the surface described by the probe tip that is of interest. This aspect complicates the control of the robotic arm considerably and especially making triggered measurements while the probe is in motion, becomes very challenging. At the time of writing, this application used stop-motion acquisition in order to ensure that the probe was stationary and at the desired location before making an RF measurement.

Another less obvious limitation of articulated robotic arms is the introduction of exclusion zones, as depicted in Figure 8.14. These are regions where the arm cannot reach or interferes with the AUT mounting. These exclusion zones therefore represent areas where the spherical surface remains open. These zones are often not circularly symmetric or simple to envision and can introduce unwanted truncation effects in the measurement.

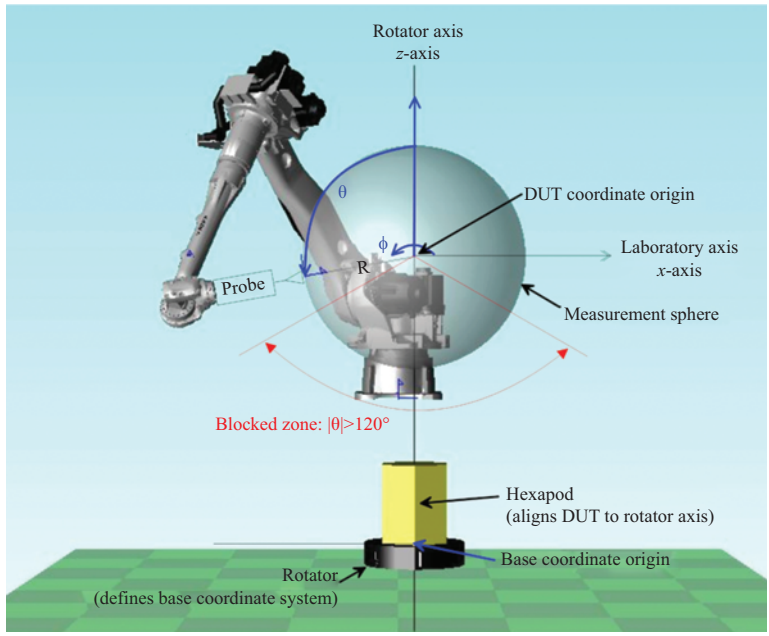

Figure 8.14 Coordinate system shown for the articulating arm of Figure 8.13 with exclusion zone shown. (Image used with permission of Electromagnetics Division of NIST, Boulder, CO, USA.)

The articulating arm solution also offers the advantage that the probe weight remains constant (or does not vary widely from one band of operation to the next). The two most attractive features of this solution is the fact that the AUT remains stationary during testing and that the system can in theory be reconfigured for testing on PNF, CNF or SNF surfaces by simply altering the acquisition control software. These solutions have not found widespread application in industry and many of the implementation challenges still have to be addressed. It is also debatable to what extent these systems can be scaled for larger applications. However, the solution seems to offer some very unique advantages like near-field acquisitions on non-canonical surfaces [12] as described in Chapter 9.

8.3 A solution to Maxwell's equations in spherical coordinates

In this section, we present a spherical wave solution to Maxwell's equations, which forms the basis of the SNF test approach widely used today. We will not present a derivation for this solution, since this is available in full detail elsewhere [1,2]. It is still worthwhile to note that one would start off by seeking a solution to the vector wave equation and applying the Laplacian operator in spherical coordinates, allowing one to reduce the problem to a set of three coupled scalar wave equations. A solution

to the vector wave equation can be constructed through the scalar wave function:

$$\psi_{mn}^{(i)}(\underline{r}) = z_n^{(i)}(kr)P_n^{|m|}(\cos\theta)e^{jm\phi}$$

for which these four versions can be explicitly written as

$$\begin{aligned}
\psi_{mn}^{(i=1)}(\underline{r}) &= z_n^{(1)}(kr)P_n^{|m|}(\cos\theta)e^{jm\phi} = j_n(kr)P_n^{|m|}(\cos\theta)e^{jm\phi}\\
\psi_{mn}^{(i=2)}(\underline{r}) &= z_n^{(2)}(kr)P_n^{|m|}(\cos\theta)e^{jm\phi} = n_n(kr)P_n^{|m|}(\cos\theta)e^{jm\phi}\\
\psi_{mn}^{(i=3)}(\underline{r}) &= z_n^{(3)}(kr)P_n^{|m|}(\cos\theta)e^{jm\phi} = h_n^{(1)}(kr)P_n^{|m|}(\cos\theta)e^{jm\phi}\\
\psi_{mn}^{(i=4)}(\underline{r}) &= z_n^{(4)}(kr)P_n^{|m|}(\cos\theta)e^{jm\phi} = h_n^{(2)}(kr)P_n^{|m|}(\cos\theta)e^{jm\phi}
\end{aligned}$$

where

$z_n^{(1)}(kr) = j_n(kr) =$ spherical Bessel function of order n
$z_n^{(2)}(kr) = n_n(kr) =$ spherical Neumann function of order n
$z_n^{(3)}(kr) = h_n^{(1)}(kr) =$ spherical Hankel function of the first kind of order n
$z_n^{(4)}(kr) = h_n^{(2)}(kr) =$ spherical Hankel function of the second kind of order n

and

$$P_n^m(x) = \frac{(1-x^2)^{m/2}}{2^n n!}\frac{d^{n+m}}{dx^{n+m}}\left(x^2-1\right)^n$$

$$\overline{P}_n^m(x) = \sqrt{\frac{2n+1}{2}\frac{(n-m)!}{(n+m)!}}P_n^m(x) \tag{8.1}$$

Here, $P_n^{|m|}$ is a Legendre function of the nth degree and the mth order and it can be evaluated using recursive expressions [13]. $\overline{P}_n^{|m|}$ is the power normalised Legendre function [14], which we select to use since it allows us to compute power based on a simple summation of spherical wave modes, as will be shown later. The variables m and n are commonly referred to as the modal indices with limits $0 \le n \le \infty$ and $-n \le m \le n$. A closer inspection of all four z_n solutions presented above shows that there is a radial variation specified through some form of the Bessel or Hankel function. There is also a θ variation specified through the Legendre function and finally there is a ϕ phase function specified through the complex exponential function.

In order to gain insight into how these functions behave, it is worthwhile plotting them. Figure 8.15 shows the first four degrees of the Legendre function $P_n^{|m|}(x = \cos\theta)$ ($n = 0$, 1, 2 and 3) plotted for all valid orders of m.

These curves therefore represent how the spherical wave functions behave as a function of $x = \cos\theta$ and they all appear to be well-behaved. We now add the phase variation function and plot these as surface grids in order to get a better understanding of what they look like in three dimensions. Figure 8.16 shows a 3D grid plot of $\left|P_n^{|m|}(\cos\theta)e^{jm\phi}\right|$ for $n = 0$, 1, 2 and 3 for all valid orders of m.

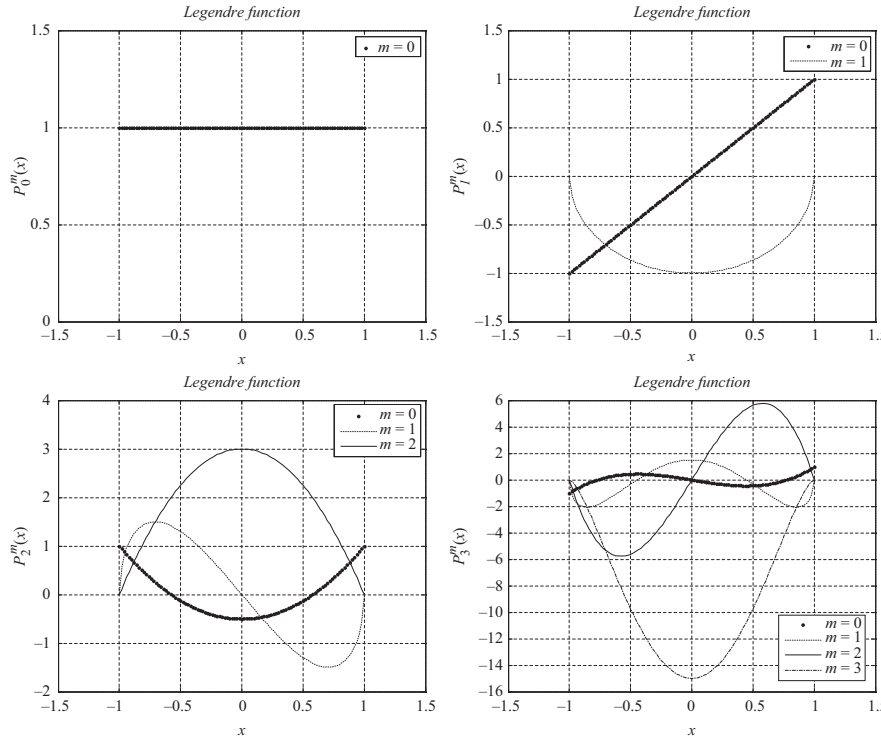

Figure 8.15 Legendre functions of zeroth, first, second and third degrees and valid orders of m in each instance shown

Analogous to the cylindrical case, spherical Bessel functions are used to represent standing waves, whereas spherical Hankel functions are used to represent travelling waves. Thus, for the case of free space measurements, we can again expect that spherical Hankel functions will be the solution of the greatest utility. The four potential solutions shown above represent standing wave solutions ($i = 1$ and $i = 2$) and travelling wave solutions ($i = 3$ and $i = 4$). For the far-field radiation case, the outward travelling wave solution[4] is of particular interest to us and that is solution 4.

The spherical Bessel (of the first kind denoted as j_n and the second kind denoted as n_n below) and Hankel functions (denoted as h_n below) can be expressed in terms of the commonly used Bessel functions $J_m(s)$, Neumann functions $Y_m(s)$,

[4]We assume a exp ($+j\omega t$) time dependency and therefore solution 3 represents an inward travelling wave and solution 4 an outward travelling wave. In [1, 3], a exp ($-j\omega t$) time dependency is assumed, in which case solution 3 represents an outward travelling wave and solution 4 an inward travelling wave.

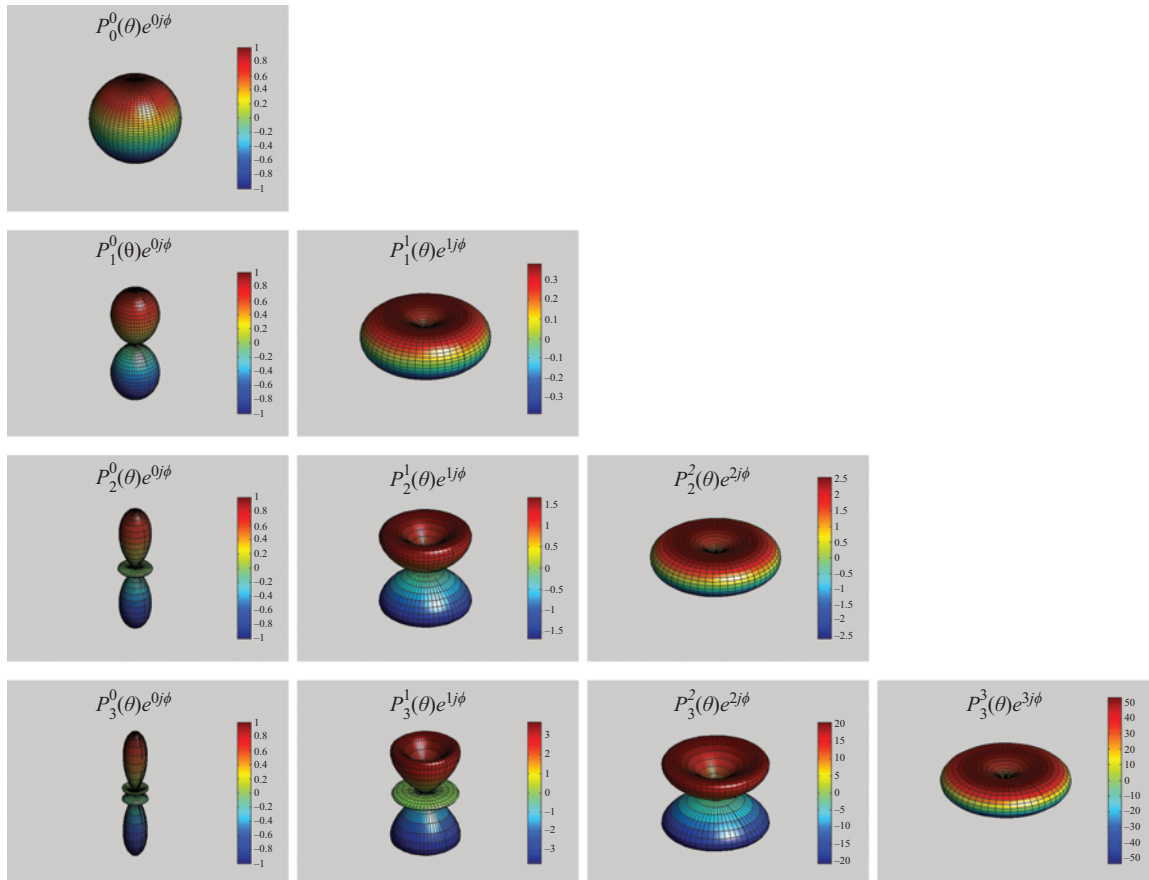

Figure 8.16 3D grid plot of $\left|P_n^{|m|}(\cos\theta)e^{jm\phi}\right|$ for n = 0, 1, 2 and 3 for all valid orders of m

Hankel functions of the first kind $H_m^{(1)}(s)$ and Hankel functions of the second kind $H_m^{(2)}(s)$ as defined in Chapter 7 and can be written as

$$\begin{aligned} j_n(x) &= \sqrt{\frac{\pi}{2x}} J_{n+1/2}(x) \\ n_n(x) &= \sqrt{\frac{\pi}{2x}} Y_{n+1/2}(x) \\ h_n^{(1)}(x) &= \sqrt{\frac{\pi}{2x}} H_{n+1/2}^{(1)}(x) \\ h_n^{(2)}(x) &= \sqrt{\frac{\pi}{2x}} H_{n+1/2}^{(2)}(x) \end{aligned} \tag{8.2}$$

By way of an illustration of the properties of these functions, Figures 8.17 and 8.18 contain plots of spherical Bessel functions of the first and second kinds for several values of positive n. The spherical Hankel functions can also be written in terms of the spherical Bessel and Neumann functions as

$$\begin{aligned} h_n^{(1)}(kr) &= j_n(kr) + jn_n(kr) \\ h_n^{(2)}(kr) &= j_n(kr) - jn_n(kr) \end{aligned}$$

As before, the order of the function is defined by the integer n.

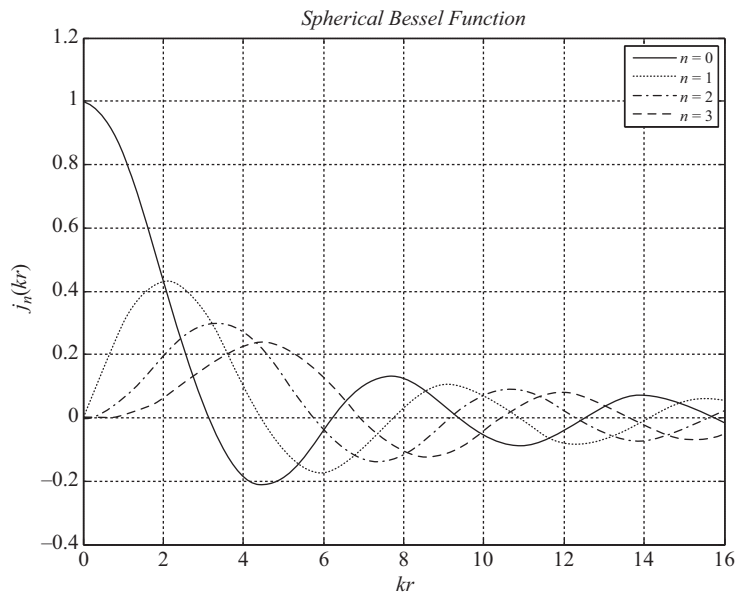

Figure 8.17 Spherical Bessel functions of the first kind plotted for several positive integer values of n

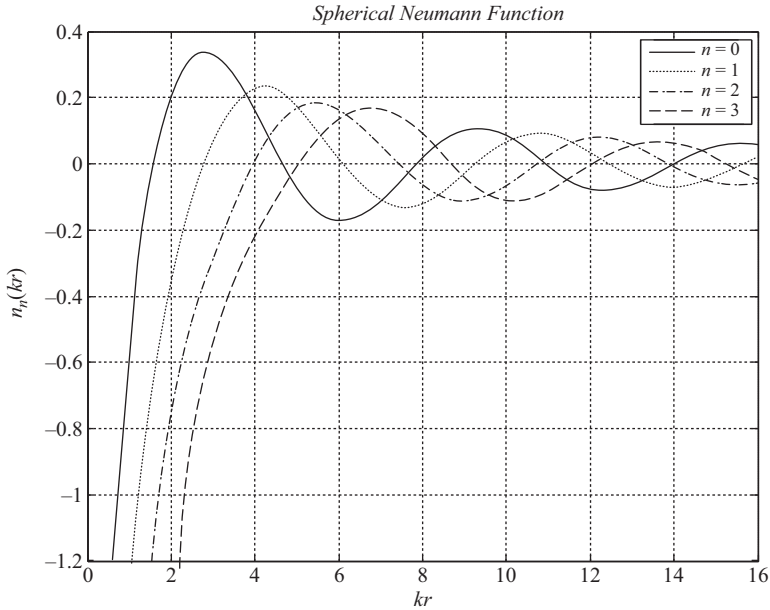

Figure 8.18 Spherical Bessel functions of the second kind (Neumann functions) plotted for several positive integer values of n

Figure 8.19 contains a plot of the magnitude of the spherical Hankel function of the first kind for various positive integer values of n. Conversely, Figure 8.20 contains a plot of the argument of the spherical Hankel function of the first kind for various positive integer values of n. Figures 8.21 and 8.22 contain equivalent plots for the spherical Hankel function of the second kind.

From inspection of Figures 8.17 to 8.22, the following qualitative analogies can be made. Spherical Bessel and Neumann functions, i.e. j_n and n_n, respectively, exhibit oscillatory behaviour for real values of kr and thus they represent standing waves. Conversely, the spherical Hankel functions of the first and second kind represent travelling waves for kr real. Spherical Hankel functions of the first kind denote waves propagating in the negative r direction, whereas spherical Hankel functions of the second kind denote waves propagating in the positive r direction. Thus, spherical Hankel functions of the second kind are the only functions which possess the appropriate behaviour as $r \rightarrow \infty$ when kr is positive real or imaginary. Specifically, when kr is real, this corresponds to an outward travelling wave, when kr is imaginary this corresponds to an evanescent field and when kr is complex this corresponds to an attenuated travelling wave. If the opposite (suppressed) time dependency had been chosen, then spherical Hankel functions of the first kind would have been the appropriate choice.

We now turn our attention to (8.1) and construct a vector-field solution from the elementary $i = 4$ spherical scalar wave function. In an analogous procedure to the cylindrical case presented in Chapter 7, the radiated electric field in free space

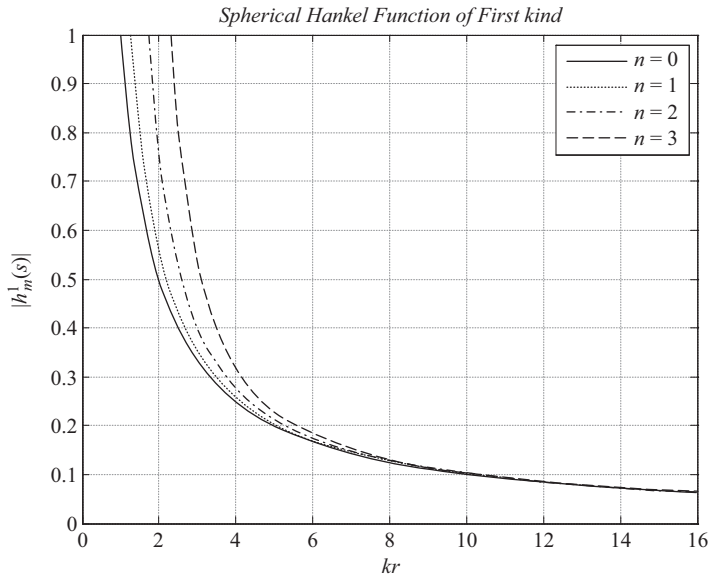

Figure 8.19 Magnitude of spherical Hankel functions of the first kind plotted for several positive integer values of n

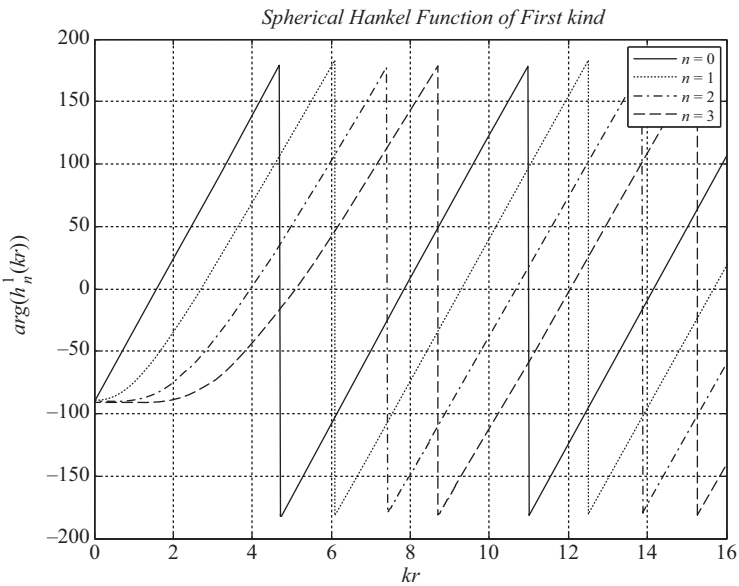

Figure 8.20 Argument of spherical Hankel functions of the first kind plotted for several positive integer values of n

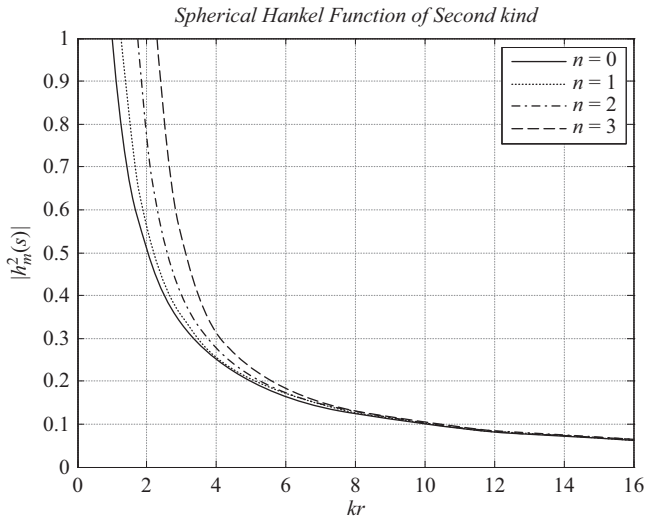

Figure 8.21 Magnitude of spherical Hankel functions of the second kind plotted for several positive integer values of n

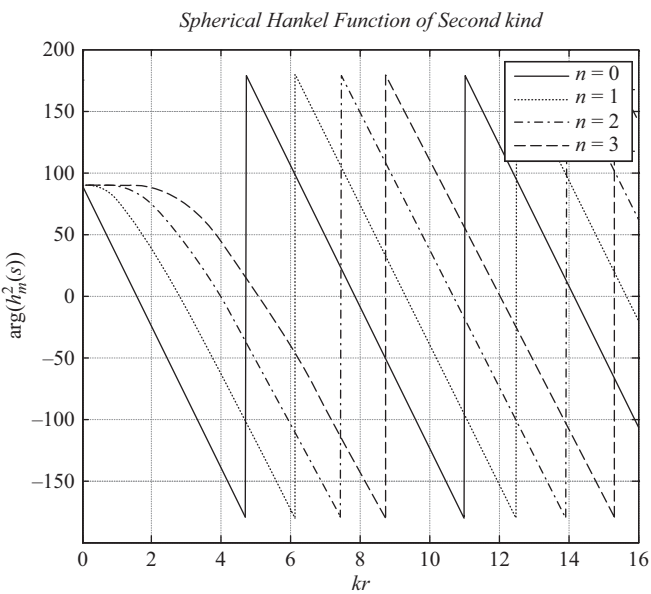

Figure 8.22 Argument of spherical Hankel functions of the second kind plotted for several positive integer values of n

can be split into a transverse electric (TE) and transverse magnetic (TM) part with respect to the radial vector $\underline{r}$. Specifically, this can be expressed as

$$\underline{E} = \nabla \times r\hat{\underline{e}}_r \psi_{mn}^4(\underline{r}) + \frac{1}{k}\nabla \times \left(\nabla \times r\hat{\underline{e}}_r \psi_{mn}^4(\underline{r})\right)$$

With the two elementary vector wave functions

$$\underline{m}_{mn}^{(4)} = \nabla \times \hat{\underline{e}}_r r\psi_{mn}^4(\underline{r})$$

$$\underline{n}_{mn}^{(4)} = \frac{1}{k}\nabla \times \left(\nabla \times r\hat{\underline{e}}_r \psi_{mn}^4(\underline{r})\right)$$

in spherical coordinates, the curl operator can be expressed as [15]

$$\nabla \times \underline{A} = \frac{1}{r\sin\theta}\left(\frac{\partial(A_\phi \sin\theta)}{\partial\theta} - \frac{\partial A_\theta}{\partial\phi}\right)\hat{\underline{e}}_r + \frac{1}{r}\left(\frac{1}{\sin\theta}\frac{\partial A_r}{\partial\phi} - \frac{\partial(rA_\phi)}{\partial r}\right)\hat{\underline{e}}_\theta$$

$$+\frac{1}{r}\left(\frac{\partial(rA_\theta)}{\partial r} - \frac{\partial A_r}{\partial\theta}\right)\hat{\underline{e}}_\phi$$

However, as in the prior equation only an r component is present, this becomes

$$\nabla \times A_r\hat{\underline{e}}_r = \frac{1}{r}\left(\frac{1}{\sin\theta}\frac{\partial A_r}{\partial\phi}\right)\hat{\underline{e}}_\theta - \frac{1}{r}\left(\frac{\partial A_r}{\partial\theta}\right)\hat{\underline{e}}_\phi$$

Thus,

$$\underline{m}_{mn}^{(4)} = \frac{1}{r}\left(\frac{1}{\sin\theta}\frac{\partial\psi_r}{\partial\phi}\right)\hat{\underline{e}}_\theta - \frac{1}{r}\left(\frac{\partial\psi_r}{\partial\theta}\right)\hat{\underline{e}}_\phi$$

Substituting this into the elemental scalar wave function yields the following expressions:

$$\underline{m}_{mn}^{(4)}(\underline{r}) = h_n^{(2)}(kr)e^{jm\phi}\left[\frac{jm}{\sin\theta}P_n^{|m|}(\cos\theta)\hat{\underline{e}}_\theta - \frac{\partial P_n^{|m|}(\cos\theta)}{\partial\theta}\hat{\underline{e}}_\phi\right]$$

$$\underline{M}_{mn}^{(4)}(\underline{r}) = norm\cdot h_n^{(2)}(kr)e^{jm\phi}\left[\frac{jm}{\sin\theta}\overline{P}_n^{|m|}(\cos\theta)\hat{\underline{e}}_\theta - \frac{\partial\overline{P}_n^{|m|}(\cos\theta)}{\partial\theta\hat{\underline{e}}_\phi}\right]$$

$$\underline{n}_{mn}^{(4)}(\underline{r}) = \frac{n(n+1)}{kr}h_n^{(2)}(kr)P_n^{|m|}(\cos\theta)e^{jm\phi}\hat{\underline{e}}_r$$

$$+\frac{1}{kr}\frac{\partial\left(krh_n^{(2)}(kr)\right)}{\partial(kr)}e^{jm\phi}\left[\frac{\partial P_n^{|m|}(\cos\theta)}{\partial\theta}\hat{\underline{e}}_\theta + \frac{jm}{\sin\theta}P_n^{|m|}(\cos\theta)\hat{\underline{e}}_\phi\right]$$

$$\underline{N}_{mn}^{(4)}(\underline{r}) = norm\cdot\frac{n(n+1)}{kr}h_n^{(2)}(kr)\overline{P}_n^{|m|}(\cos\theta)e^{jm\phi}\hat{\underline{e}}_r$$

$$+norm\cdot\frac{1}{kr}\frac{\partial\left(krh_n^{(2)}(kr)\right)}{\partial(kr)}e^{jm\phi}\left[\frac{\partial\overline{P}_n^{|m|}(\cos\theta)}{\partial\theta}\hat{\underline{e}}_\theta + \frac{jm}{\sin\theta}\overline{P}_n^{|m|}(\cos\theta)\hat{\underline{e}}_\phi\right]$$

where

$$norm = \frac{1}{\sqrt{2\pi n(n+1)}}\left(-\frac{m}{|m|}\right)^m \tag{8.3}$$

In these expressions, $\underline{m}_{mn}^{(4)}(\underline{r})$and $\underline{n}_{mn}^{(4)}(\underline{r})$ denote un-normalised spherical wave functions, while $\underline{M}_{mn}^{(4)}(\underline{r})$ and $\underline{N}_{mn}^{(4)}(\underline{r})$ denote[5] power normalised spherical wave functions and the variable *norm* is a normalisation constant. Continuing forward, we will focus our attention on the normalised spherical wave functions. The derivative expressions found in these spherical wave functions can be expressed as [16]

$$\frac{\partial \overline{P}_n^{|m|}(\cos\theta)}{\partial\theta} = \sqrt{\frac{2n+1}{2}\frac{(n-m)!}{(n+m)!}}\frac{\partial P_n^m(\cos\theta)}{\partial\theta}$$

$$= \begin{cases} -\sqrt{\dfrac{2n+1}{2}}P_n^1(\cos\theta), & m=0 \\ -\dfrac{1}{2}\sqrt{\dfrac{2n+1}{2}\dfrac{(n-m)!}{(n+m)!}}\Big\{(n-m+1)(n+m)P_n^{m-1}(\cos\theta) \\ \quad +P_n^{m+1}(\cos\theta)\Big\}, & m>0 \end{cases}$$

$$\frac{1}{kr}\frac{\partial\left(krh_n^{(2)}(kr)\right)}{\partial kr} = h_{n-1}^{(2)}(kr) - \frac{n}{kr}h_n^{(2)}(kr) \tag{8.4}$$

The vector wave function $\underline{M}_{mn}^{(4)}(\underline{r})$ only contains two vector components, both tangential to the spherical surface and orthogonal to the $\underline{r}$ vector and are referred to as the TE solution relative to $\underline{r}$. The vector wave function $\underline{N}_{mn}^{(4)}(\underline{r})$ also contains a radial vector component and is therefore referred to as the TM solution relative to $\underline{r}$. The general expression for a radiated electric field can be expressed by a linear combination of these two vector wave functions[6] and we may write that as

$$\underline{E}(\underline{r}) = \frac{k}{\sqrt{\eta}}\sum_{n=1}^{\infty}\sum_{m=-n}^{n}\left[B_{mn}^1\underline{M}_{mn}^{(4)}(\underline{r}) + B_{mn}^2\underline{N}_{mn}^{(4)}(\underline{r})\right] \tag{8.5a}$$

Coefficients $B^1{}_{mn}$ and $B^2{}_{mn}$ are complex numbers that are weighting coefficients for the vector wave functions[7]. They are functions of polarisation, the θ index m and the ϕ index n. If these coefficients were known for the test antenna, then these equations would allow the radiating electric field to be evaluated everywhere in free space. This solution would be valid outside of a conceptual sphere that is centred about the origin of the measurement coordinate system that encloses the majority of the current sources, where the radius of this sphere is defined to be a and is called the maximum radial extent (*MRE*) or also the minimum radius sphere (*MRS*).

[5]Note that we use the uppercase N to denote one of the spherical wave functions here. Later, we also use integer N as a modal index. The use of the bracketed argument for the spherical wave function should prevent confusion.

[6]When we refer to a vector wave function here, it is implied to be a spherical wave function as defined above.

[7]The factor $k/\sqrt{\eta}$ is selected here in order to ensure that the summation of the spherical wave function coefficients will have a dimension of Watt$^{1/2}$. This is selected for convenience, following [3].

A summation of coefficients $B^1{}_{mn}$ and $B^2{}_{mn}$ allows one to easily compute the total power radiated as

$$P = \frac{1}{2}\sum_{n=1}^{\infty}\sum_{m=-n}^{n}\left[\left|B^1_{mn}\right|^2 + \left|B^2_{mn}\right|^2\right]$$

The magnetic field can be calculated from the Maxwell Faraday equation and is similarly obtained from the same set of spherical mode coefficients from

$$\underline{H}(\underline{r}) = jk\sqrt{\eta}\sum_{n=1}^{\infty}\sum_{m=-n}^{n}\left[B^1_{mn}\underline{N}^{(4)}_{mn}(\underline{r}) + B^2_{mn}\underline{M}^{(4)}_{mn}(\underline{r})\right] \tag{8.5b}$$

The principal objective of this work is to determine these coefficients for a given test antenna and is where our attention is focused next.

It should be pointed out that the order of summation in the above two equations is not critical and can be reversed. When doing so, the limits of summation change:

$$\begin{aligned}&\sum_{n=1}^{\infty}\sum_{m=-n}^{n}\left[B^1_{mn}\underline{M}^{(4)}_{mn}(\underline{r}) + B^2_{mn}\underline{N}^{(4)}_{mn}(\underline{r})\right]\\ &\quad= \sum_{m=-\infty}^{\infty}\sum_{\substack{n=|m|\\ n\neq 0}}^{\infty}\left[B^1_{mn}\underline{M}^{(4)}_{mn}(\underline{r}) + B^2_{mn}\underline{N}^{(4)}_{mn}(\underline{r})\right]\end{aligned}$$

We will use this interchange of summation order at times when it is convenient to do so. Also note that for a finite number of modes[8], say N, we can simply replace the limit of $\pm\infty$ with $\pm N$. If we look at a typical mode plot as shown in Figure 8.23, one can conceptually think of the summation $\sum_{n=1}^{N}\sum_{m=-n}^{n}$ filling the triangular modal region in a column-wise fashion, starting at the apex of the triangle at the $n = 1$ column, progressing from left to right (depicted on the left in Figure 8.23). For the $\sum_{m=-N}^{N}\sum_{\substack{n=|m|\\ n\neq 0}}^{N}$ order summation, one can conceptually think of filling the triangular modal region in a row-wise manner, starting with the $m = -N$ row, progressing from bottom to top (depicted on the right in Figure 8.23).

8.4 Relating spherical mode coefficients to SNF data

In practice, one does not have the SMCs. Instead, one has to determine these from measured near-field data. In order that this can be accomplished, the expressions that were obtained within the preceding section need to be inverted so that the mode coefficients can be determined from the measured near-field. This scenario is depicted in Figure 8.24. The minimum radius sphere (*MRS*) for the AUT, centred

[8]Later on, we will relate N to the *MRE* or *MRS* and thereby derive a sampling theorem.

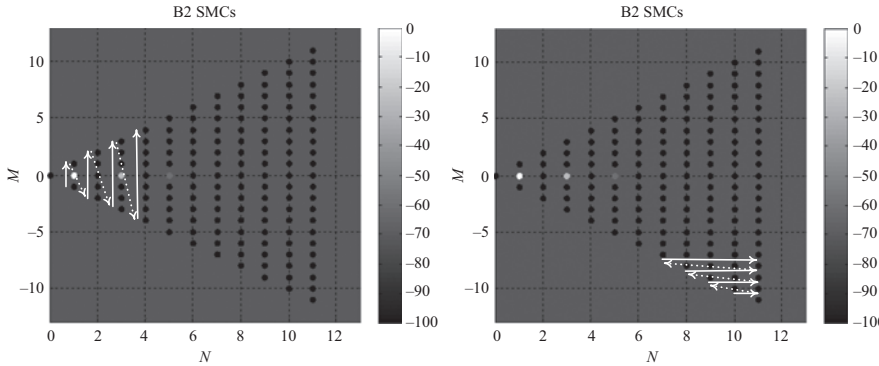

Figure 8.23 *SNF mode plot: summation $\sum_{n=1}^{N}\sum_{m=-n}^{n}$ fills the triangular modal region in a column-wise fashion, starting at the apex of the triangle (depicted by arrows on the left). Summation $\sum_{m=-N}^{N}\sum_{\substack{n=|m|\\ n\neq 0}}^{N}$ fills the triangular modal region in a row-wise fashion, starting with the $m = -N$ row (depicted by arrows on the right)*

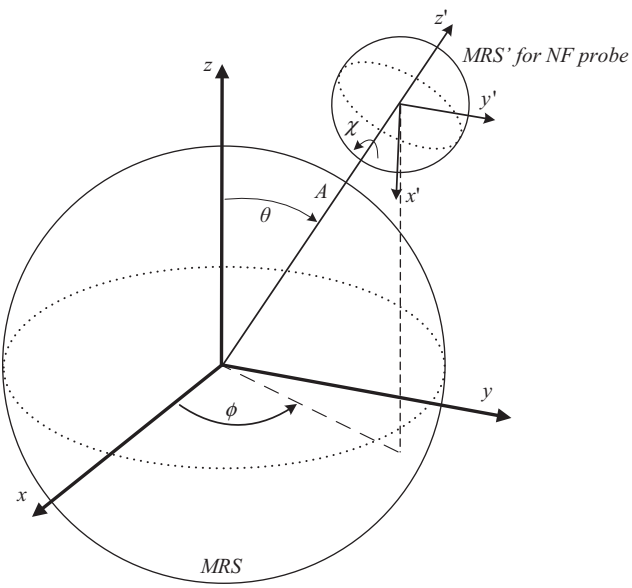

Figure 8.24 *The MRS for the AUT is shown as well as the MRS for the near-field probe at a radial distance of A*

on the unprimed coordinate system, is shown as well as the *MRS* for the near-field probe, centred on the primed coordinate system at a radial distance of A.

As pointed out in Section 8.5, the probe radial distance from the measurement coordinate system origin, denoted by A, is unrelated to the *MRS* or *MRS*′ in Figure 8.24. At the risk of stating the obvious; to avoid mechanical interference A must be greater than $MRS + MRS'$. However, in practice we also want to ensure that we do not have reactive coupling between the near-field probe and the AUT. This requirement dictates that A be selected so that the separation between the two *MRSs* is at least 1λ and a rule of thumb often used is 3λ. The latter being easy to achieve at most microwave frequencies and it is only at frequencies below 500 MHz where one can find this to become restrictive. It is important to note that these are guidelines and not absolutes. In Section 8.7, we will also show that increasing this radial distance A has the added advantage of reducing our reliance on SNF probe correction. On the opposing side, trying to minimise A can reduce facility size (important at low frequencies) and reduce free space loss.

If we assume that the AUT is transmitting and we want to calculate the energy coupled to the near-field probe, we have to translate the mode coefficients from their native coordinate system (unprimed) to that of the probe, denoted as the primed coordinate system in Figure 8.24. This process will allow us to construct a transmission formula that describes the coupling between the modes describing the AUT and the modes describing the near-field probe. It therefore also allows one to incorporate the effect of the near-field probe fully and therefore compensate for the effects of the probe.

This coordinate system mapping is achieved through a dual rotation/translation process. The rotation process can be described as follows and as depicted in Figure 8.25:

1. Rotation of the (x,y,z) coordinate system around its z-axis through an angle ϕ_0 leading to coordinate system (x_1,y_1,z_1).
2. Rotation of the (x_1,y_1,z_1) coordinate system around its y_1-axis through an angle θ_0 leading to coordinate system (x_2,y_2,z_2).
3. Rotation of the (x_2,y_2,z_2) coordinate system around its z_2-axis through an angle χ_0 (which will later be seen to be the probe polarisation angle) leading to coordinate system (x_3,y_3,z_3).

The elementary spherical wave functions defined above can be written in terms of the (x_3,y_3,z_3) coordinate system after this rotation process through the use of the addition theorem for spherical waves [17] as

$$\begin{aligned}\underline{M}_{mn}^{(4)}(\underline{r}) &= \sum_{\mu=-n}^{n} D_{\mu m}^{\mu n}(\phi_0,\theta_0,\chi_0)\underline{M}_{\mu n}^{(4)}\left(\underline{r_3}\right)\\ \underline{N}_{mn}^{(4)}(\underline{r}) &= \sum_{\mu=-n}^{n} D_{\mu m}^{\mu n}(\phi_0,\theta_0,\chi_0)N_{\mu n}^{(4)}\left(\underline{r_3}\right)\end{aligned} \tag{8.6}$$

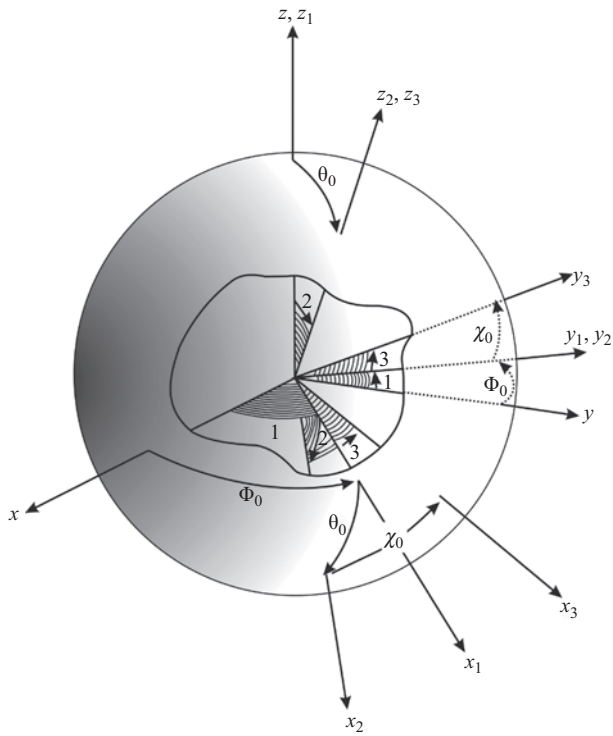

Figure 8.25 Depiction of the rotation process from coordinate system (x,y,z) to (x_3,y_3,z_3)

where vector $\underline{r_3}$ is the probe position vector within the (x_3,y_3,z_3) coordinate system and parameter D is referred to as a rotation coefficient and can be expressed as

$$D_{\mu m}^{\mu n}(\phi_0, \theta_0, \chi_0) = e^{jm\phi_0} d_{\mu m}^{(n)}(\theta_0) e^{j\mu\chi_0}$$

$$d_{\mu m}^{(n)}(\theta_0) = \sqrt{\frac{(n+\mu)!(n-\mu)!}{(n+m)!(n-m)!}} \left(\cos\frac{\theta}{2}\right)^{\mu+m} \left(\sin\frac{\theta}{2}\right)^{\mu-m} Jac_{n-\mu}^{(\mu-m,\mu+m)}(\cos\theta)$$

where

$$Jac_{n-\mu}^{(\mu-m,\mu+m)}(\cos\theta) = \frac{1}{2^{n-\mu}} \sum_{j=0}^{n-\mu} \frac{(n-m)!}{(n-m-j)!j!} \frac{(n+m)!}{(m+\mu+j)!(n-\mu-j)!} \times (\cos\theta - 1)^{n-\mu-j} (\cos\theta + 1)^{j} \tag{8.7}$$

The function $Jac_{n-\mu}^{(\mu-m,\mu+m)}(\cos\theta)$ denotes the Jacobi polynomial [18] and can be evaluated using the summation expression in (8.7). It is worthwhile to point out that (8.7) simply maps each of the spherical wave functions from the unprimed to the third coordinate system by implementing three Euler rotations (details of Euler

angles are included within Appendix Section 4.3.4). Two of these rotations (ϕ_0 and χ_0) are simple phase adjustments, while the third rotation (θ_0) is somewhat more involved as is evident by observing the expression for $d_{\mu m}^{(n)}(\theta_0)$ that requires a summation from $-n$ to $+n$. However, it should be pointed out that although somewhat convoluted, the evaluation of $d_{\mu m}^{(n)}(\theta_0)$is computationally simple. Equations (8.6) therefore show that after mapping each of the M and N wave functions they consist of not just a single expression, but a summation of modes.

Finally, the (x_3,y_3,z_3) coordinate system is translated (not depicted in Figure 8.25) by a distance A along the z_3-axis to obtain the coordinate system (x',y',z') as depicted in Figure 8.24. This translation of the (x_3,y_3,z_3) coordinate system by distance A along the z_3-axis to obtain the coordinate system (x',y',z') can be achieved through further application of the addition theorem [17] and this allows one to write the translated spherical waves as

$$\begin{aligned}
\underline{M}_{mn}^{(4)}(\underline{r}) &= \sum_{\mu=-n}^{n} \sum_{\substack{\nu=|\mu| \\ \nu\neq 0}}^{\infty} e^{jm\phi_0} d_{\mu m}^{(n)}(\theta_0) e^{j\mu\chi_0} \left\{ C_{1n\mu\nu}^{M}(kA) \frac{1}{2} \left(\underline{M}_{\mu n}^{(3)}(\underline{r}') \right.\right. \\
&\qquad \left.\left. + \underline{M}_{\mu n}^{(4)}(\underline{r}') \right) + C_{2n\mu\nu}^{M}(kA) \frac{1}{2} \left(\underline{N}_{\mu n}^{(3)}(\underline{r}') + \underline{N}_{\mu n}^{(4)}(\underline{r}') \right) \right\} \\
\underline{N}_{mn}^{(4)}(\underline{r}) &= \sum_{\mu=-n}^{n} \sum_{\substack{\nu=|\mu| \\ \nu\neq 0}}^{\infty} e^{jm\phi_0} d_{\mu m}^{(n)}(\theta_0) e^{j\mu\chi_0} \left\{ C_{1n\mu\nu}^{N}(kA) \frac{1}{2} \left(\underline{N}_{\mu n}^{(3)}(\underline{r}') + \underline{N}_{\mu n}^{(4)}(\underline{r}') \right) \right. \\
&\qquad \left. + C_{2n\mu\nu}^{N}(kA) \frac{1}{2} \left(\underline{M}_{\mu n}^{(3)}(\underline{r}') + \underline{M}_{\mu n}^{(4)}(\underline{r}') \right) \right\} \qquad (8.8)
\end{aligned}$$

where $C_{1/2n\mu\nu}^{M/N}(kA)$ is a translation coefficient along the z_3-axis over a distance A. A number of observations can be made regarding equations (8.8):

- A subset of the translation coefficients $C_{1/2n\mu\nu}^{M/N}(kA)$ is unique for a set of spherical wave functions $\left(\underline{M}_{\mu n}^{(3)}(\underline{r}') + \underline{M}_{\mu n}^{(4)}(\underline{r}') \right)$ or $\left(\underline{N}_{\mu n}^{(3)}(\underline{r}') + \underline{N}_{\mu n}^{(4)}(\underline{r}') \right)$ and this is denoted by the 1 *or* 2 subscripts.
- A subset of the translation coefficients $C_{1/2n\mu\nu}^{M/N}(kA)$ is unique for a spherical wave function $\underline{M}_{mn}^{(4)}(\underline{r})$ or $\underline{N}_{mn}^{(4)}(\underline{r})$ and this is denoted by the *M or N* superscript.
- Note the introduction of the $\underline{M}_{\mu n}^{(3)}(\underline{r}')$ and $\underline{N}_{\mu n}^{(3)}(\underline{r}')$spherical Hankel functions of the first kind. This is required since we need a finite solution at the origin of the primed coordinate system and this is fulfilled by a standing wave solution interior to the *MRS* of the probe – in this case written as the sum of the two travelling wave solutions.
- The translation process leads to cross-coupling between TE and TM spherical wave modes, since each $\underline{M}_{mn}^{(4)}(\underline{r})$ mode now contains a summation of $\underline{M}_{\mu n}^{(3/4)}(\underline{r}')$ and $\underline{N}_{\mu n}^{(3/4)}(\underline{r}')$ modes.

The translation coefficient $C^{M/N}_{1/2n\mu v}(kA)$ can now be computed from

$$C^{M/N}_{1/2n\mu v}(kA) = (-1)^{\mu}\frac{j^{n-v}}{2}\sqrt{\frac{(2n+1)(2v+1)}{n(n+1)v(v+1)}}\sqrt{\frac{(v+\mu)!(n-\mu)!}{(v-\mu)!(n+\mu)!}}$$
$$\times\sum_{p=|n-v|}^{n+v}\left[j^{-p}Ka(\mu,n,-\mu,v,p)z_p^4(kA)\right]$$

where

$$K = \delta_{s,\sigma}\{n(n+1)+v(v+1)-p(p+1)\}+\delta_{3-s,\sigma}\{2j\mu kA\}$$

$$\delta_{s,\sigma} = \begin{cases} 0 & \text{for } s\neq\sigma \\ 1 & \text{for } s=\sigma \end{cases}$$

$$a(\mu,n,-\mu,v,p) = 2(p+1)\sqrt{\frac{(n+\mu)!(v-\mu)!}{(n-\mu)!(v+\mu)!}}\begin{pmatrix} n & v & p \\ 0 & 0 & 0\end{pmatrix}\begin{pmatrix} n & v & p \\ \mu & -\mu & 0\end{pmatrix}$$

where we use the Wigner $3-j$ symbols as defined in [19], which allows us to write four specific cases

$$C^{M}_{1n\mu v}(kA) = (-1)^{\mu}\frac{j^{n-v}}{2}\sqrt{\frac{(2n+1)(2v+1)}{n(n+1)v(v+1)}}\sqrt{\frac{(v+\mu)!(n-\mu)!}{(v-\mu)!(n+\mu)!}}$$
$$\sum_{p=|n-v|}^{n+v}[j^{-p}\{n(n+1)+v(v+1)-p(p+1)\}$$
$$\times a(\mu,n,-\mu,v,p)z_p^4(kA)]$$

$$C^{M}_{2n\mu v}(kA) = (-1)^{\mu}\frac{j^{n-v}}{2}\sqrt{\frac{(2n+1)(2v+1)}{n(n+1)v(v+1)}}\sqrt{\frac{(v+\mu)!(n-\mu)!}{(v-\mu)!(n+\mu)!}}$$
$$\sum_{p=|n-v|}^{n+v}\left[j^{-p}\{2j\mu kA\}a(\mu,n,-\mu,v,p)z_p^4(kA)\right]$$

$$C^{N}_{1n\mu v}(kA) = (-1)^{\mu}\frac{j^{n-v}}{2}\sqrt{\frac{(2n+1)(2v+1)}{n(n+1)v(v+1)}}\sqrt{\frac{(v+\mu)!(n-\mu)!}{(v-\mu)!(n+\mu)!}}$$
$$\sum_{p=|n-v|}^{n+v}\left[j^{-p}\{2j\mu kA\}a(\mu,n,-\mu,v,p)z_p^4(kA)\right]$$

$$C^{N}_{2n\mu v}(kA) = (-1)^{\mu}\frac{j^{n-v}}{2}\sqrt{\frac{(2n+1)(2v+1)}{n(n+1)v(v+1)}}\sqrt{\frac{(v+\mu)!(n-\mu)!}{(v-\mu)!(n+\mu)!}}$$
$$\sum_{p=|n-v|}^{n+v}\left[j^{-p}\{n(n+1)+v(v+1)-p(p+1)\}a(\mu,n,-\mu,v,p)z_p^4(kA)\right]$$

which seems once again very intricate, but is in reality quite simple to compute. Using this notation, we can now write an expression for the electric field in terms of our original SMCs (B^1_{mn} and B^2_{mn}) but using modes defined in the primed (probe) coordinate system as

$$\underline{E}(\underline{r}') = \frac{k}{\sqrt{\eta}} \sum_{n=1}^{\infty} \sum_{m=-n}^{n} \left[\begin{array}{l} B^1_{mn} \sum_{\mu=-n}^{n} \sum_{\substack{\nu=|\mu| \\ \nu\neq 0}}^{\infty} e^{jm\phi_0} d^{(n)}_{\mu m}(\theta_0) e^{j\mu\chi_0} \left\{ C^M_{1n\mu\nu}(kA) \frac{1}{2} \left(\underline{M}^{(3)}_{\mu n}(\underline{r}') + \underline{M}^{(4)}_{\mu n}(\underline{r}') \right) \right. \\ \left. + C^M_{2n\mu\nu}(kA) \frac{1}{2} \left(\underline{N}^{(3)}_{\mu n}(\underline{r}') + \underline{N}^{(4)}_{\mu n}(\underline{r}') \right) \right\} \\ + B^2_{mn} \sum_{\mu=-n}^{n} \sum_{\substack{\nu=|\mu| \\ \nu\neq 0}}^{\infty} e^{jm\phi_0} d^{(n)}_{\mu m}(\theta_0) e^{j\mu\chi_0} \left\{ C^N_{1n\mu\nu}(kA) \frac{1}{2} \left(\underline{N}^{(3)}_{\mu n}(\underline{r}') + \underline{N}^{(4)}_{\mu n}(\underline{r}') \right) \right. \\ \left. + C^N_{2n\mu\nu}(kA) \frac{1}{2} \left(\underline{M}^{(3)}_{\mu n}(\underline{r}') + \underline{M}^{(4)}_{\mu n}(\underline{r}') \right) \right\} \end{array} \right]$$

which can be rearranged as

$$\underline{E}(\underline{r}') = \frac{k}{2\sqrt{\eta}} \sum_{n=1}^{\infty} \sum_{m=-n}^{n} \sum_{\mu=-n}^{n} \sum_{\substack{\nu=|\mu| \\ \nu\neq 0}}^{\infty} e^{jm\phi_0} d^{(n)}_{\mu m}(\theta_0) e^{j\mu\chi_0}$$

$$\left[\begin{array}{l} B^1_{mn} \left\{ C^M_{1n\mu\nu}(kA) \left(\underline{M}^{(3)}_{\mu n}(\underline{r}') + \underline{M}^{(4)}_{\mu n}(\underline{r}') \right) + C^M_{2n\mu\nu}(kA) \left(\underline{N}^{(3)}_{\mu n}(\underline{r}') + \underline{N}^{(4)}_{\mu n}(\underline{r}') \right) \right\} \\ + B^2_{mn} \left\{ C^N_{1n\mu\nu}(kA) \left(\underline{N}^{(3)}_{\mu n}(\underline{r}') + \underline{N}^{(4)}_{\mu n}(\underline{r}') \right) + C^N_{2n\mu\nu}(kA) \left(\underline{M}^{(3)}_{\mu n}(\underline{r}') + \underline{M}^{(4)}_{\mu n}(\underline{r}') \right) \right\} \end{array} \right]$$

$$= \frac{k}{2\sqrt{\eta}} \sum_{n=1}^{\infty} \sum_{m=-n}^{n} \sum_{\mu=-n}^{n} \sum_{\substack{\nu=|\mu| \\ \nu\neq 0}}^{\infty} e^{jm\phi_0} d^{(n)}_{\mu m}(\theta_0) e^{j\mu\chi_0}$$

$$\left[\begin{array}{l} \left(B^1_{mn} C^M_{1n\mu\nu}(kA) + B^2_{mn} C^N_{2n\mu\nu}(kA) \right) \left(\underline{M}^{(3)}_{\mu n}(\underline{r}') + \underline{M}^{(4)}_{\mu n}(\underline{r}') \right) \\ + \left(B^1_{mn} C^M_{2n\mu\nu}(kA) + B^2_{mn} C^N_{1n\mu\nu}(kA) \right) \left(\underline{N}^{(3)}_{\mu n}(\underline{r}') + \underline{N}^{(4)}_{\mu n}(\underline{r}') \right) \end{array} \right] \tag{8.9}$$

By comparing (8.5) and (8.9), we see that if we knew the values of the SMCs (B^1_{mn} and B^2_{mn}) we would be able to compute the electric field intensity in the unprimed coordinate system or in the primed coordinate systems. In other words, we can therefore state that in (8.9) the vector $\underline{r}'$ defines the location of the observer in the primed coordinate system. The variables θ_0, ϕ_0, χ_0 and A (and their associated quantities $d^{(n)}_{\mu m}$ and $C^{M/N}_{1/2n\mu\nu}$) define how the spherical wave functions in the unprimed coordinate system are related to those defined in the primed coordinate system and therefore allows one to use the known SMCs (native to the unprimed coordinate system) to compute the electric field intensity.

An SNF measurement will now in principle consist of sampling the tangential electric field components on a spherical surface and inverting (8.9) in order to determine the SMCs. In what follows, we continue to develop this process.

8.5 Sampling requirements and spherical mode truncation

It has been shown that a set of SMCs can be used to describe the radiation from any radiator. Equation (8.5) (duplicated below for convenience) shows how the SMCs are used in such a spherical wave expansion to achieve this. However, we also note that the upper limit of summation extends to infinity and we need to address this in order to obtain a practical solution

$$\underline{E}(\underline{r}) = \frac{k}{\sqrt{\eta}} \sum_{n=1}^{\infty} \sum_{m=-n}^{n} \left[B^1_{mn} \underline{M}^{(4)}_{mn}(\underline{r}) + B^2_{mn} \underline{N}^{(4)}_{mn}(\underline{r}) \right]$$

The approach we take here is to consider the problem as one of a spherical waveguide [2,20], which gives us the convenience of mode orthogonality, cut-off, propagation and evanescence. If we now consider a radiator enclosed within a spherical surface of radius a and centred[9] on the coordinate system origin, we can view the region exterior to this surface as a spherical waveguide extending from a to infinity. In this region, we can now use a spherical wave expansion to represent the radiated field and although there is no cut-off wavelength here, there is a cut-off radius for the modes. If one expresses the radial wave impedance for each spherical mode in terms of the ratio of its E and H field components, it is found that these impedances are predominantly reactive for $ka < n$ and predominantly resistive when $ka > n$. We can now designate $ka = N$ as the point[10] of cut-off [20]. What this implies is that reactive wave impedances represent waves bound to the radiation region and these do not contribute to the far radiation field. Resistive wave impedances represent waves that propagate and therefore contribute to the radiation field. We can therefore state that once a is known, one can evaluate $ka = 2\pi a/\lambda = N$ and this number represents the limit of n (in (8.5)) for which SMC's will have a predominantly resistive wave impedance and therefore contribute to the radiated field. Some subtle but very significant observation can be made:

1. The value of N (maximum value of the n index) is determined by the *MRS* value a, and a has a lower bound determined by the AUT size. Since N sets the limit for highest order spherical wave mode to be considered, it suggests the concept of a specific radiator only 'supporting' modes of order N or less. This

[9]The centring referred to here is that of the spherical surface and not the radiator. The radiator can be located anywhere inside this spherical surface.
[10]In this case, N is the largest integer value less than or equal to ka.

notion is incorrect since a radiator can give rise to a field distribution for which an infinite number of spherical wave modes are needed as an accurate representation. However, many of these modes may be evanescent and decay so rapidly that they may be disregarded for any practical near-field or far-field application. We are therefore stating that only modes of order N or less (and we will add a safety margin to this below) will propagate and contribute significantly to our computed far-field.

2. The value of N, as stated above, is determined by the *MRS* value a, and a has a lower bound determined by the AUT size. However, it is often true that the AUT is mounted in such a way that a is also affected by the offset of the AUT from the coordinate system origin. In such instances, higher-order spherical modes are needed to represent the radiated field as would have been required had the AUT been mounted centred on the coordinate origin. This seems somewhat counter intuitive but will be further elaborated on below.

We can therefore state that the field radiated by any finite size antenna can be described by a spherical wave expansion consisting of a discrete set of functions, limited by the electrical size of the radiator as well as the relative location of the radiator with respect to the measurement coordinate system. This concept is captured by the concept of a 'minimum radius sphere' of radius $MRS = a$, where this sphere is centred on the measurement coordinate system and encloses all contributing parts of the radiator. The concept is depicted in Figure 8.26.

We return to the fact that once a is known we can evaluate the limit $N = 2\pi a/\lambda$ and this number represents the limit of n for which spherical wave modes can contribute significantly to the radiated field. Although we like to think of this boundary as binary, it is not and although the transition from evanescent to resistive wave impedance is rapid, it has a finite slope [21] and the inclusion of some higher-order modes are in order, to insure we do not neglect any significant radiated energy in our solution. In practice, it is found for an *MRS* of less than 100λ that adding a safety margin of 10 to the number N incorporates enough of these additional modes to ensure fidelity of the modal solution [22]. The results justifying this selection are presented in [23]. We can therefore state that

$$N = [ka] + 10 = \left[\frac{2\pi a}{\lambda}\right] + 10 \tag{8.10}$$

where the square brackets indicate 'the largest integer value smaller than or equal to'. It should be noted that for cases where the *MRS* exceeds 100λ, this safety margin needs to be increased to ensure that a sufficient number of higher-order spectral modes are included in our solution. This is discussed in more detail in [22].

There are some important concepts to highlight w.r.t. the '*MRS*' concept:

1. The sphere is centred on the coordinate system origin, which is defined as the intersection of the θ- and ϕ-axes.

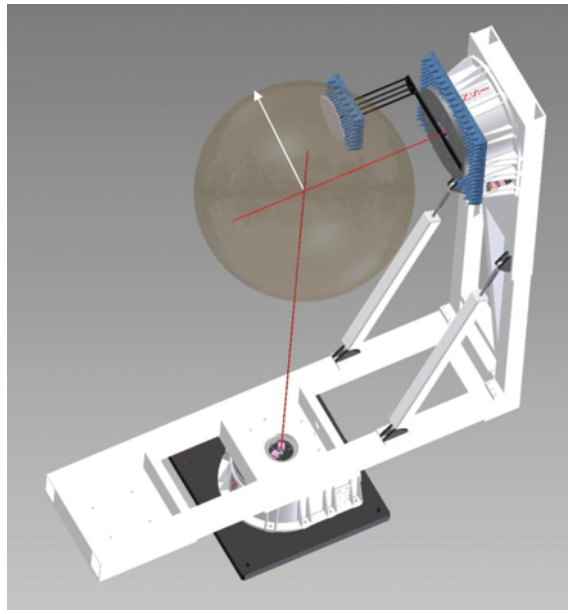

Figure 8.26 The MRS concept is illustrated. The antenna in this case is a flat plate array mounted on an offset arm on the ϕ-stage. The MRS is larger than what would have been required, had the AUT been centred on the coordinate system origin

2. The sphere must enclose all radiating parts of interest and if this condition is violated, the spherical modal expansion may not be representative of the measurement and contain the required degrees of adjustment to allow accurate representation of the measured field distribution.
3. Selecting the sphere larger than required is not a problem in theory. In practice, it is found that a slight over estimation is acceptable, but a gross over estimation allows for the inclusion of modal coefficients that are not associated with the object under test and these typically resolve external reflection sources that then lead to a loss of measurement fidelity and a significant increase in measurement time.
4. The distance between the measurement probe and the coordinate origin has no bearing on the *MRS* and therefore on the number of modes included in the modal expansion. *This is an important concept, since it implies that the near-field probe can be located at an arbitrary large distance from the radiator* (*within limits of the sensitivity of the RF sub-system*). *It also implies that all of the concepts* (*back projection, MARS*) *associated with SNF measurements can be applied to far-field antenna ranges that have positioners that allow for data acquisition on a spherical surface.*

As pointed out earlier, the *MRS* is affected by the mounting of the radiator in that if the mounting locates the radiator some distance from the coordinate system

origin, the *MRS* needs to be enlarged to accommodate this offset. It is important to realise that this is again not a problem in theory, but in practice it extends test time (since more samples are required) and it is also true that such measurements are more sensitive to system misalignment and RF instability. A way to visualise the problem is to understand that such a test case not only consists of a rotation of the radiator but also significant translation during measurement, leading to a much higher phase variation of the near-field, requiring denser spatial sampling to properly characterise and therefore more spherical modes. This is illustrated in Figure 8.28, where a z-directed $\lambda/2$ dipole is considered, first located on the coordinate origin and then offset from the origin by a distance of 2λ as depicted in Figure 8.27. The θ electric near-field vector component (amplitude left and phase right) is shown in Figure 8.28 (top row) for the centred dipole and then on the bottom row the corresponding information for the case when the dipole is offset from the coordinate system origin. The similarity in the amplitude patterns is obvious, but the significant change in phase due to the added translation is what requires higher near-field sampling density to adequately represent the field distribution with a spherical modal expansion.

For the dipole shown above, the *MRS* selected for the case where the dipole is located at the coordinate system origin is $\lambda/4$. Once the dipole has been offset this *MRS* is too small and using the same sampling density leads to erroneous far-field results shown in Figure 8.29 on the left. Extending the *MRS* to 2.25λ increases the sampling density and resolves the problem as shown in Figure 8.29 on the right.

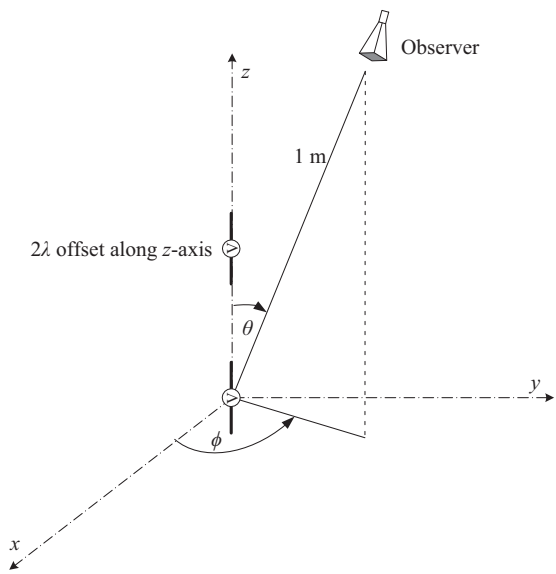

Figure 8.27 Geometry of the dipole simulations for which near-field amplitude and phase are depicted in Figure 8.28

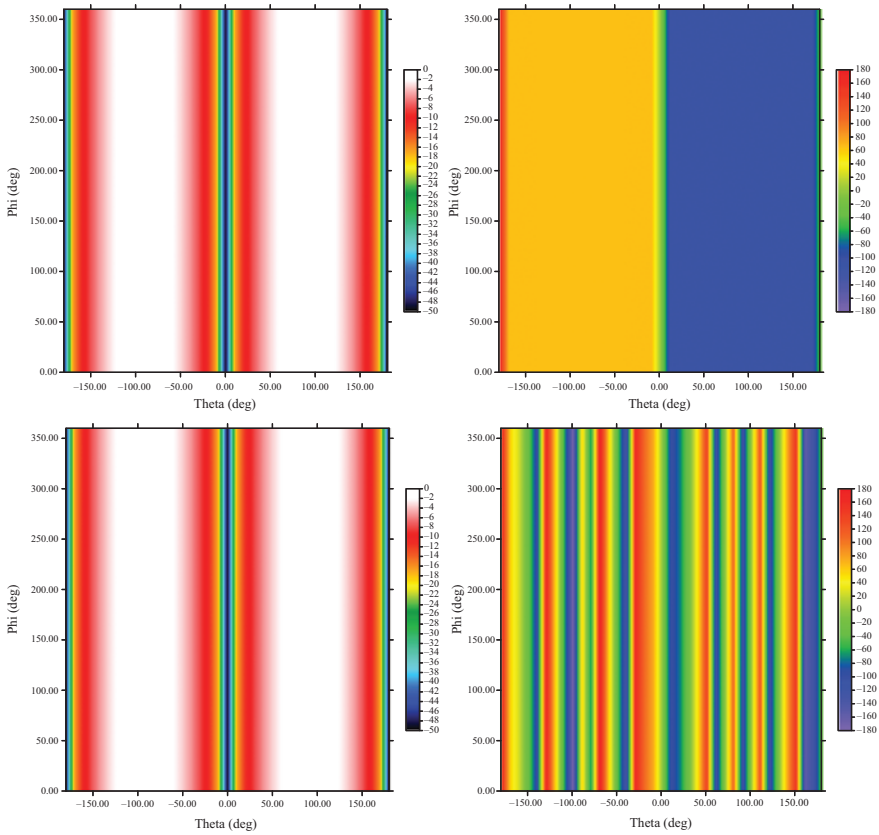

Figure 8.28 The θ electric near-field vector component (amplitude left and phase right) is shown (top row) for the centred dipole and on the bottom row, the corresponding information for the case when the dipole is offset (along the z-axis) from the coordinate system origin by 2λ

As a digression, it is worthwhile to note that although we define the concept of an *MRS* that defines N and therefore limits n and m, theory does not require these limits to be coupled. This implies that we can define two radial distances, one associated with n and the other with m. We can conceptually think of two minimum radius cylinders (MRC' and MRC'') located coaxially to the θ- and ϕ-axes and enclosing all radiating parts of the AUT. MRC' will therefore define N and MRC'' will define M (limit of m), leading to dissimilar sampling intervals in θ and ϕ. This concept is discussed in [24] and has a very practical benefit, allowing one to reduce sampling density in one dimension and therefore decreasing test

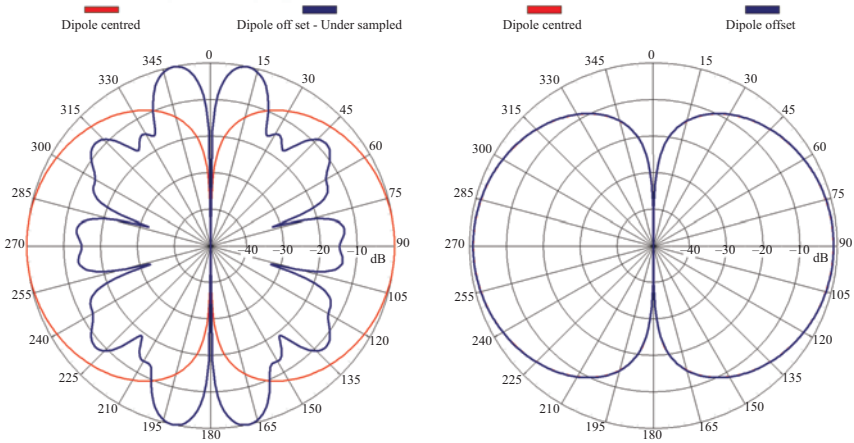

Figure 8.29 *Dipole centred far-field result is compared to offset case. The left shows an under-sampled case, leading to the disagreement of patterns. The right-hand side represents the higher sampling density case that resolves the problem and the two patterns overlay*

time. An example of a case where this may be beneficial would be a linear radiator mounted coincident with the ϕ-axis (the AUT depicted in Figure 8.44 is an applicable example). In such a case, the length (measured along the ϕ-axis) of the radiator would define MRC' and therefore N, while the width (measured along the θ-axis) of the radiator would be significantly smaller and will be reflected through MRC'' and a much reduced value of M. An SNF acquisition grid with high sampling density in θ and lower sampling density in ϕ will result. The dipole example for which modal spectra are presented in Figure 8.30 is a prime example of where this approach would be beneficial. Since the dipole is located on the ϕ-axis, we see most energy contained in the low-order m modal indices and therefore a low sampling density in ϕ would make sense. In what follows, we do not use the concept of an MRC' or an MRC'' and simply retain MRS as our SNF parameter of interest.

Returning to our dipole example depicted in Figure 8.27, we next turn our attention to the detail of the spherical wave expansion. From what has been presented above, it is clear that for any finite size antenna, the number of spherical modes required to accurately characterise its radiation will be finite and (8.10) nominally relates the antenna size to a maximum value of $n_{\max} = N$. We can therefore now write (8.5) as

$$\underline{E}(\underline{r}) = \frac{k}{\sqrt{\eta}} \sum_{n=1}^{N} \sum_{m=-n}^{n} \left[B^1_{mn} \underline{M}^{(4)}_{mn}(\underline{r}) + B^2_{mn} \underline{N}^{(4)}_{mn}(\underline{r}) \right] \tag{8.11}$$

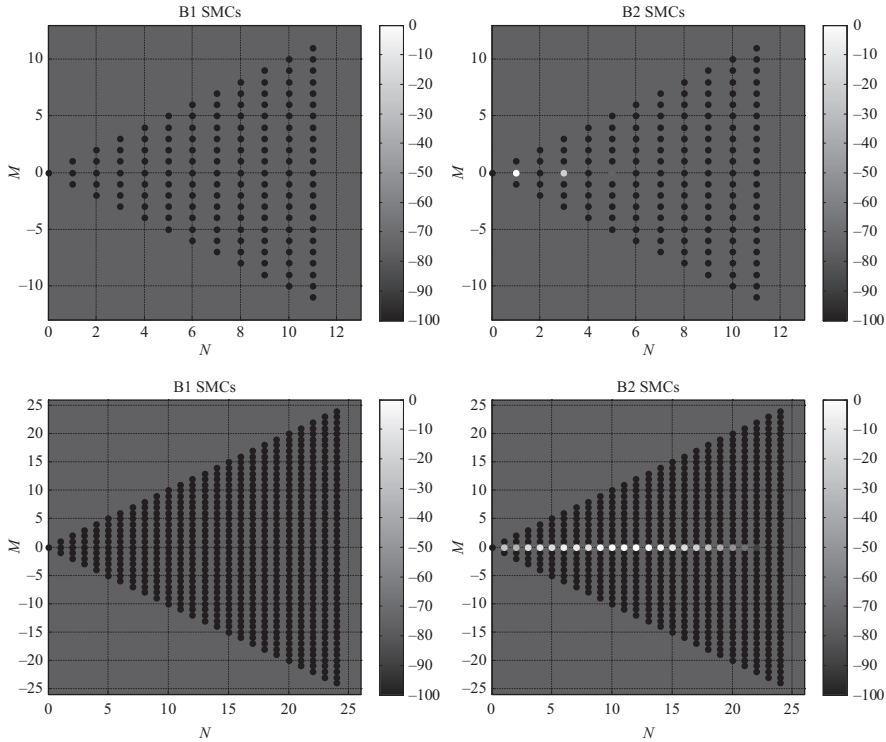

Figure 8.30 SNF Mode spectra: amplitude of the SMC's (B^1 – left and B^2 – right) for the dipole centred case (top row) and dipole offset along the z-axis (bottom row). Amplitude is displayed in dB, scales from 0 (white) to −100 dB (black)

If we now venture to solve for the SMCs by sampling tangential electric field components on a spherical surface of radius r_0, we can write the following expressions for the $\hat{\underline{e}}_\theta$ and $\hat{\underline{e}}_\phi$ field components:

$$E_\theta\left(\underline{r}_0\right) = \frac{k}{\sqrt{\eta}} \sum_{n=1}^{N} \sum_{m=-n}^{n} \left[B^1_{mn} \underline{M}^{(4)}_{mn}\left(\underline{r}_0\right) + B^2_{mn} \underline{N}^{(4)}_{mn}\left(\underline{r}_0\right) \right] \cdot \hat{\underline{e}}_\theta$$

$$E_\phi\left(\underline{r}_0\right) = \frac{k}{\sqrt{\eta}} \sum_{n=1}^{N} \sum_{m=-n}^{n} \left[B^1_{mn} \underline{M}^{(4)}_{mn}\left(\underline{r}_0\right) + B^2_{mn} \underline{N}^{(4)}_{mn}\left(\underline{r}_0\right) \right] \cdot \hat{\underline{e}}_\phi \tag{8.12}$$

By now using the orthogonality properties of the spherical modes, we can state [25]

$$\int_{\phi=0}^{2\pi}\int_{\theta=0}^{\pi}\left\{\underline{M}_{mn}^{(4)}(\underline{r})\cdot\hat{\underline{e}}_{\theta}\right\}\left\{\underline{M}_{-mn}^{(4)}(\underline{r})\cdot\hat{\underline{e}}_{\theta}\right\}+\left\{\underline{M}_{mn}^{(4)}(\underline{r})\cdot\hat{\underline{e}}_{\phi}\right\}\left\{\underline{M}_{-mn}^{(4)}(\underline{r})\cdot\hat{\underline{e}}_{\phi}\right\}$$

$$\sin\theta d\theta d\phi=(-1)^{m}\left[h_{n}^{(2)}(kr)\right]^{2}$$

$$\int_{\phi=0}^{2\pi}\int_{\theta=0}^{\pi}\left\{\underline{N}_{mn}^{(4)}(\underline{r})\cdot\hat{\underline{e}}_{\theta}\right\}\left\{\underline{N}_{-mn}^{(4)}(\underline{r})\cdot\hat{\underline{e}}_{\theta}\right\}+\left\{\underline{N}_{mn}^{(4)}(\underline{r})\cdot\hat{\underline{e}}_{\phi}\right\}\left\{\underline{N}_{-mn}^{(4)}(\underline{r})\cdot\hat{\underline{e}}_{\phi}\right\}\sin\theta d\theta d\phi$$

$$=(-1)^{m}\left[h_{n-1}^{(2)}(kr)+\frac{(1-n)}{kr}h_{n}^{(2)}(kr)\right]^{2}$$

we see that a 'mode selection' is possible by multiplying the expressions in (8.12) by each specific mode and the resulting integrals can then be equated to the closed-form expressions in terms of the spherical Hankel functions. This provides us with a method to solve for the SMCs and we can therefore multiply (8.11) by $\underline{M}_{-mn}^{(4)}(\underline{r}_0)$ and $\underline{N}_{-mn}^{(4)}(\underline{r}_0)$, integrate over θ and ϕ to obtain

$$\int_{\phi=0}^{2\pi}\int_{\theta=0}^{\pi}E_{\theta}\left(\underline{r}_0\right)\left\{\underline{M}_{-mn}^{(4)}\left(\underline{r}_0\right)\cdot\hat{\underline{e}}_{\theta}\right\}+E_{\phi}\left(\underline{r}_0\right)\left\{\underline{M}_{-mn}^{(4)}\left(\underline{r}_0\right)\cdot\hat{\underline{e}}_{\phi}\right\}\sin\theta\,d\theta\,d\phi$$

$$=\frac{k}{\sqrt{\eta}}\int_{\phi=0}^{2\pi}\int_{\theta=0}^{\pi}B_{mn}^{1}T^{1}\sin\theta\,d\theta\,d\phi=(-1)^{m}B_{mn}^{1}\left[h_{n}^{(2)}(kr_0)\right]^{2}$$

and

$$\int_{\phi=0}^{2\pi}\int_{\theta=0}^{\pi}E_{\theta}\left(\underline{r}_0\right)\left\{\underline{N}_{-mn}^{(4)}\left(\underline{r}_0\right)\cdot\hat{\underline{e}}_{\theta}\right\}+E_{\phi}\left(\underline{r}_0\right)\left\{\underline{N}_{-mn}^{(4)}\left(\underline{r}_0\right)\cdot\hat{\underline{e}}_{\phi}\right\}\sin\theta\,d\theta\,d\phi$$

$$=\frac{k}{\sqrt{\eta}}\int_{\phi=0}^{2\pi}\int_{\theta=0}^{\pi}B_{mn}^{2}T^{2}\sin\theta\,d\theta\,d\phi=(-1)^{m}B_{mn}^{2}\left[h_{n-1}^{(2)}(kr_0)-\frac{n}{kr}h_{n}^{(2)}(kr_0)\right]^{2}$$

where

$$T^{1}=\left[\left\{\underline{M}_{mn}^{(4)}\left(\underline{r}_0\right)\cdot\hat{\underline{e}}_{\theta}\right\}\left\{\underline{M}_{-mn}^{(4)}\left(\underline{r}_0\right)\cdot\hat{\underline{e}}_{\theta}\right\}+\left\{\underline{M}_{mn}^{(4)}\left(\underline{r}_0\right)\cdot\hat{\underline{e}}_{\phi}\right\}\left\{\underline{M}_{-mn}^{(4)}\left(\underline{r}_0\right)\cdot\hat{\underline{e}}_{\phi}\right\}\right]T^{2}$$

$$=\left[\left\{\underline{N}_{mn}^{(4)}\left(\underline{r}_0\right)\cdot\hat{\underline{e}}_{\theta}\right\}\left\{\underline{N}_{-mn}^{(4)}\left(\underline{r}_0\right)\cdot\hat{\underline{e}}_{\theta}\right\}+\left\{\underline{N}_{mn}^{(4)}\left(\underline{r}_0\right)\cdot\hat{\underline{e}}_{\phi}\right\}\left\{\underline{N}_{-mn}^{(4)}\left(\underline{r}_0\right)\cdot\hat{\underline{e}}_{\phi}\right\}\right]$$

after which we can rearrange to obtain expressions for the SMCs explicitly as

$$B_{mn}^{1} = \frac{k(-1)^{m}}{\sqrt{\eta}\left[h_{n}^{(2)}(kr_0)\right]^{2}} \int_{\phi=0}^{2\pi}\int_{\theta=0}^{\pi} E_{\theta}\left(\underline{r}_0\right)\left\{\underline{M}_{-mn}^{(4)}\left(\underline{r}_0\right)\cdot\hat{\underline{e}}_{\theta}\right\}$$
$$+ E_{\phi}\left(\underline{r}_0\right)\left\{\underline{M}_{-mn}^{(4)}\left(\underline{r}_0\right)\cdot\hat{\underline{e}}_{\phi}\right\}\sin\theta\, d\theta\, d\phi$$
$$B_{mn}^{2} = \frac{k(-1)^{m}}{\sqrt{\eta}\left[h_{n-1}^{(2)}(kr_0) - \frac{n}{kr_0}h_{n}^{(2)}(kr_0)\right]^{2}} \int_{\phi=0}^{2\pi}\int_{\theta=0}^{\pi} E_{\theta}\left(\underline{r}_0\right)\left\{\underline{N}_{-mn}^{(4)}\left(\underline{r}_0\right)\cdot\hat{\underline{e}}_{\theta}\right\}$$
$$+ E_{\phi}\left(\underline{r}_0\right)\left\{\underline{N}_{-mn}^{(4)}\left(\underline{r}_0\right)\cdot\hat{\underline{e}}_{\phi}\right\}\sin\theta\, d\theta\, d\phi \tag{8.13}$$

The expressions in (8.13) now give us a direct way to evaluate the SMCs based on measured tangential field components sampled on the surface of a spherical surface of radius r_0. Note that if one elect to use a Hertzian dipole as a probe, a power calibration factor needs to be introduced. It is shown in [26] that a factor $\sqrt{6\pi}\sqrt{\eta}/2k$ is required as a multiplier on the right-hand side of both expressions in (8.13) in this case.

We now turn our attention to the specific integrals in (8.13) since these have to be evaluated numerically during the measurement process. After evaluating the dot products, we see that these integrals take on the following forms where the spherical Hankel functions do not form a part of the integrands since they are not a function of either angular variable

$$B_{mn}^{1} = \frac{k(-1)^{m}}{\sqrt{\eta}\left[h_{n}^{(2)}(kr_0)\right]^{2}} \int_{\varphi=0}^{2\pi}\int_{\theta=0}^{\pi} E_{\theta}\left(\underline{r}_0\right)\left\{\underline{M}_{-mn}^{(4)}\left(\underline{r}_0\right)\cdot\hat{\underline{e}}_{\theta}\right\}$$
$$+ E_{\varphi}\left(\underline{r}_0\right)\left\{\underline{M}_{-mn}^{(4)}\left(\underline{r}_0\right)\cdot\hat{\underline{e}}_{\varphi}\right\}\sin\theta\, d\theta\, d\varphi$$
$$= \Omega\int_{\varphi=0}^{2\pi}\int_{\theta=0}^{\pi} E_{\theta}(\theta,\varphi)\overline{P}_{n}^{|m|}(\cos\theta)e^{jm\varphi}$$
$$+ E_{\varphi}(\theta,\varphi)\left(\frac{-\partial\overline{P}_{n}^{|m|}(\cos\theta)}{\partial\theta}\right)e^{jm\varphi}\sin\theta\, d\theta\, d\varphi$$
$$B_{mn}^{2} = \frac{k(-1)^{m}}{\sqrt{\eta}\left[h_{n-1}^{(2)}(kr_0) - \frac{n}{kr_0}h_{n}^{(2)}(kr_0)\right]^{2}} \int_{\varphi=0}^{2\pi}\int_{\theta=0}^{\pi} E_{\theta}\left(\underline{r}_0\right)\left\{\underline{N}_{-mn}^{(4)}\left(\underline{r}_0\right)\cdot\hat{\underline{e}}_{\theta}\right\}$$
$$+ E_{\varphi}\left(\underline{r}_0\right)\left\{\underline{N}_{-mn}^{(4)}\left(\underline{r}_0\right)\cdot\hat{\underline{e}}_{\varphi}\right\}\sin\theta\, d\theta\, d\varphi$$
$$= \Psi\int_{\varphi=0}^{2\pi}\int_{\theta=0}^{\pi} E_{\theta}(\theta,\varphi)\frac{\partial\overline{P}_{n}^{|m|}(\cos\ \theta)}{\partial\theta}e^{jm\varphi} + jmE_{\varphi}(\theta,\varphi)\overline{P}_{n}^{|m|}(\cos\ \theta)e^{jm\varphi}\, d\theta\, d\varphi$$

where

$$\Omega = \frac{k(-1)^m}{\sqrt{\eta}h_n^{(2)}(kr_0)}\frac{1}{\sqrt{2\pi n(n+1)}}\left(-\frac{m}{|m|}\right)^m$$

$$\Psi = \frac{k(-1)^m}{\sqrt{\eta}\left[h_{n-1}^{(2)}(kr_0) - \frac{n}{kr_0}h_n^{(2)}(kr_0)\right]}\frac{1}{\sqrt{2\pi n(n+1)}}\left(-\frac{m}{|m|}\right)^m$$

$$\partial\overline{P}_n^{|m|}(\cos\theta)\partial\theta = \sqrt{\frac{2n+1}{2}\frac{(n-m)!}{(n+m)!}}\frac{\partial P_n^m(\cos\theta)}{\partial\theta}$$

$$= \begin{cases} -\sqrt{\dfrac{2n+1}{2}}P_n^1(\cos\theta), & m=0 \\ \dfrac{1}{2}\sqrt{\dfrac{2n+1}{2}\dfrac{(n-m)!}{(n+m)!}}\left\{(n-m+1)(n+m)P_n^{m-1}(\cos\theta) - P_n^{m+1}(\cos\theta)\right\}, & m>0 \end{cases}$$

These expressions for the SMC's can be simplified by recognising that the dϕ integration in each case represents a Fourier transform and since we have to evaluate these integrals numerically, we can employ a discrete Fourier transform (DFT) to do so. This can be expressed as[11]

$$\int_{\varphi=0}^{2\pi} f(\varphi)e^{jm\varphi}d\varphi = DFT\{f(k\Delta\varphi)|k=0,1,2,\ldots,N-1\} = \Delta\varphi\sum_{k=0}^{N'-1} f(k\Delta\varphi)e^{jmk\Delta\varphi}$$

Allowing us to reduce the expressions for the SMC's (where we use the fact that the derivative of the Legendre polynomial [27] can be expressed as a linear combination of lower- and higher-order Legendre polynomials) to obtain

$$B_{mn}^1 = \Omega DFT\left\{\int_{\theta=0}^{\pi} E_\theta(\theta,k\Delta\phi)\overline{P}_n^{|m|}(\cos\theta)\sin\theta d\theta + \int_{\theta=0}^{\pi} E_\phi(\theta,k\Delta\phi)\left(\frac{-\partial\overline{P}_n^{|m|}(\cos\theta)}{\partial\theta}\right)\sin\theta d\theta\right\}_{k=0,1,2,\ldots,N-1}$$

$$= \sqrt{\frac{2n+1}{2}}\Omega\left\{\begin{array}{c} DFT\left\{\int_{\theta=0}^{\pi} E_\theta(\theta,k\Delta\phi)P_n^0(\cos\theta)\sin\theta d\theta + \int_{\theta=0}^{\pi} E_\phi(\theta,k\Delta\phi)P_n^1(\cos\theta)\sin\theta d\theta\right\}; m=0 \\ \sqrt{\dfrac{(n-m)!}{(n+m)!}}DFT\left\{\int_{\theta=0}^{\pi} E_\theta(\theta,k\Delta\phi)P_n^{|m|}(\cos\theta)\sin\theta d\theta\right. \\ -\dfrac{1}{2}\int_{\theta=0}^{\pi} E_\phi(\theta,k\Delta\phi)\left\{(n-m+1)(n+m)P_n^{m-1}(\cos\theta)\right. \\ \left.\left. -P_n^{m+1}(\cos\theta)\right\}\sin\theta d\theta\right\}; m>0 \end{array}\right\}_{k=0,1,2,\ldots,N-1}$$

[11]Note the use of the variable *N*' here that denotes the number of sample points to evaluate the DFT. Although related to maximum SMC order *N* and related as $N' = 2N+1$, they should not be confused.

$$B_{mn}^2 = \Psi\, DFT\left\{ \int_{\theta=0}^{\pi} E_\theta(\theta, k\Delta\phi) \frac{\partial \bar{P}_n^{|m|}(\cos\theta)}{\partial\theta} \sin\theta d\theta \right.$$
$$\left. + jm \int_{\theta=0}^{\pi} E_\phi(\theta, k\Delta\phi) \overline{P}_n^{|m|}(\cos\theta) d\theta \right\} k = 0, 1, 2, \ldots, N-1$$
$$= \sqrt{\frac{2n+1}{2}} \Psi \left\{ \begin{array}{l} DFT\left\{ -\int_{\theta=0}^{\pi} E_\theta(\theta, k\Delta\phi) P_n^1(\cos\theta) \sin\theta d\theta \right\};\ \ m = 0 \\ \sqrt{\frac{(n-m)!}{(n+m)!}} DFT\left\{ \frac{1}{2} \int_{\theta=0}^{\pi} E_\theta(\theta, k\Delta\phi) \{(n-m+1)(n+m) \right. \\ \qquad P_n^{m-1}(\cos\theta) - P_n^{m+1}(\cos\theta) \} \sin\theta d\theta \\ \qquad \left. + jm \int_{\theta=0}^{\pi} E_\phi(\theta, k\Delta\phi) P_n^{|m|}(\cos\theta) d\theta \right\}; m > 0 \end{array} \right\}_{k=0,1,2,\ldots,N-1} \tag{8.14}$$

In the DFT above, we employ a finite set of N' discrete samples in ϕ. We know that the DFT will render a non-aliased solution of the function being transformed if it is periodic and band-limited (both conditions hold true here) and N is selected as shown in (8.10). The remaining integrals in θ are of the form

$$\int_{\theta=0}^{\pi} E_{\theta/\phi}(\theta, k\Delta\phi) P_n^{|m|}(\cos\theta) \sin\theta\, d\theta$$

and

$$\int_{\theta=0}^{\pi} E_\phi(\theta, k\Delta\phi) P_n^{|m|}(\cos\theta) d\theta$$

and can be evaluated numerically. From the behaviour of the Legendre polynomials (depicted in Figure 8.15), we see that these are not difficult integrals to evaluate. Equations (8.14) therefore allow us to find the SMC's from sampled tangential electric field values, where these fields were measured on a spherical surface of radius r_0. The angular sample spacing can be calculated as

$$\Delta\theta = \Delta\phi = \frac{2\pi}{N'} = \frac{2\pi}{2N+1} \cong \frac{\pi}{N} (N \gg 1)$$

The *MRS* is related to the angular sampling density of both the θ and ϕ variables through

$$\Delta\theta = \Delta\phi \cong \frac{\pi}{\frac{2\pi MRS}{\lambda} + 10}$$

which reduces to

$$\Delta\theta = \Delta\phi \cong \frac{\lambda}{2MRS}$$

if the factor 10 safety margin is ignored.

It is important to realise that in (8.14), we assume point sampling of the electric field and there is no probe correction performed whatsoever. It is therefore not a very practical formulation, but one that does provide further insight into the process of obtaining SMC's, the use of spherical wave orthogonality properties and Fourier relations in the derivation thereof.

If we return to the example of a z-directed $\lambda/2$ dipole, first located on the coordinate origin and then offset from the origin (along the z-axis) by a distance of 2λ as depicted in Figure 8.27, we were able to extract the θ electric near-field vector component (amplitude left and phase right) as was shown in Figure 8.28 (top row) for the centred dipole and then on the bottom row for the case when the dipole is offset from the coordinate system origin. Figure 8.30 depicts the amplitude of the SMC's (B^1_{mn} and B^2_{mn}) for the dipole centred case (top row) and dipole offset along the z-axis (bottom row).

From Figure 8.30, we can make the following observations:

- These mode spectra display a higher density for the offset case than for the centred case, as expected.
- Only one of the B^1_{mn} and B^2_{mn}components contains significant energy since the dipole only has a single θ polarisation component.
- The only significant modes all have an $m = 0$ index, indicating no ϕ variation. Since this dipole is located on and aligned with the ϕ-axis, this is again as expected.
- For the dipole at the coordinate origin, we see only the $n = 1$, 3 and 5 index modes having significant energy. However, for the offset case, we note that there are many n-indices that contain higher levels of energy with the focal region being centred at roughly $n = 12$, which can be converted to a radial distance of 2λ, which coincides with the offset distance of the dipole.

If we now extend our case study of the z-directed $\lambda/2$ dipole to include the case of a dipole offset from the origin (along the y-axis) by a distance of 2λ (the three cases of interest are depicted in Figure 8.31), we can again extract near-field field values and relevant SMC's. The θ electric near-field vector component (amplitude left and phase right) is as shown in Figure 8.32 (top row) for the centred dipole and on the bottom row for the case when the dipole is offset along the y-axis from the coordinate system origin. If we now evaluate the SMC's for these two cases, we obtain the spectra depicted in Figure 8.33. These images depict the amplitude of the SMC's (B^1_{mn} and B^2_{mn}) for the dipole centred case (top row) and dipole offset along the y-axis (bottom row).

From Figure 8.33, we can make the following observations:

- The offset along the y-axis leads to a significantly more distributed mode spectrum than for the case where the offset was along the z-axis.
- Since the polarisation is now distributed between the θ and ϕ components, both the B^1_{mn} and B^2_{mn}components contain significant energy.
- Since we now lose the convenient rotational symmetry that we have when the dipole is located on the z-axis, we have modes for all values of m.

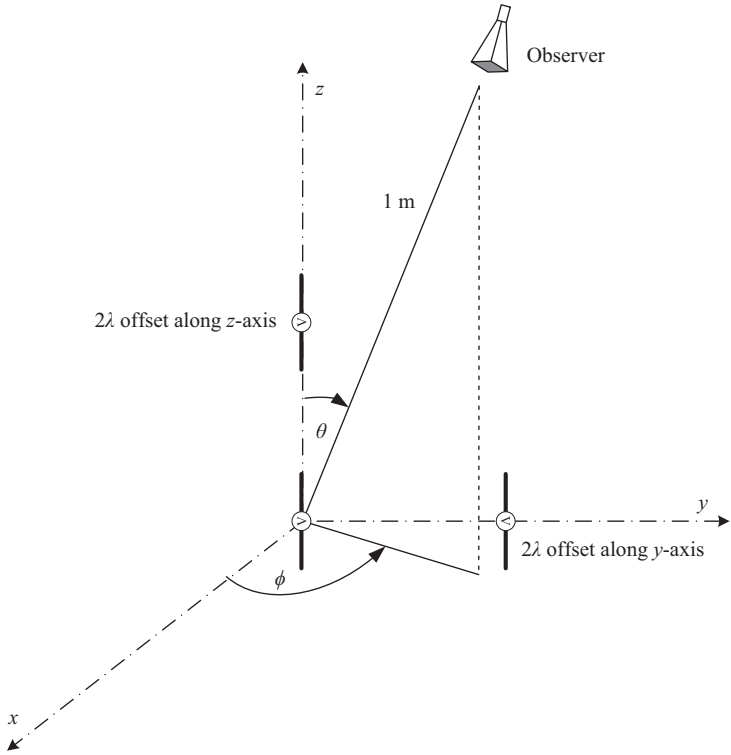

Figure 8.31 Geometry of the dipole simulations for which near-field amplitude and phase are depicted in Figure 8.28

- If we evaluate (8.10) for the offset case along the y-axis, we obtain $N = 22$, which we observe to be a sensible limit based on the amplitude values depicted in the bottom row. Were we to subtract the factor 10 safety margin in (8.10), we would clearly be excluding modes containing significant energy.

We will next venture into the complex world of probe corrected SNF formulations. In what follows, the intent again is to explain the formulation and not focus our attention on implementing a numerical solution to the equations presented. This is expertly covered in [3] and there is no need for repetition here.

8.6 Development of the transmission formula

In order to include probe correction in our SNF formulation, we need to find a coupling equation describing the interaction between the spherical modes of the AUT and those describing a near-field probe. Equations (8.9) already describe the

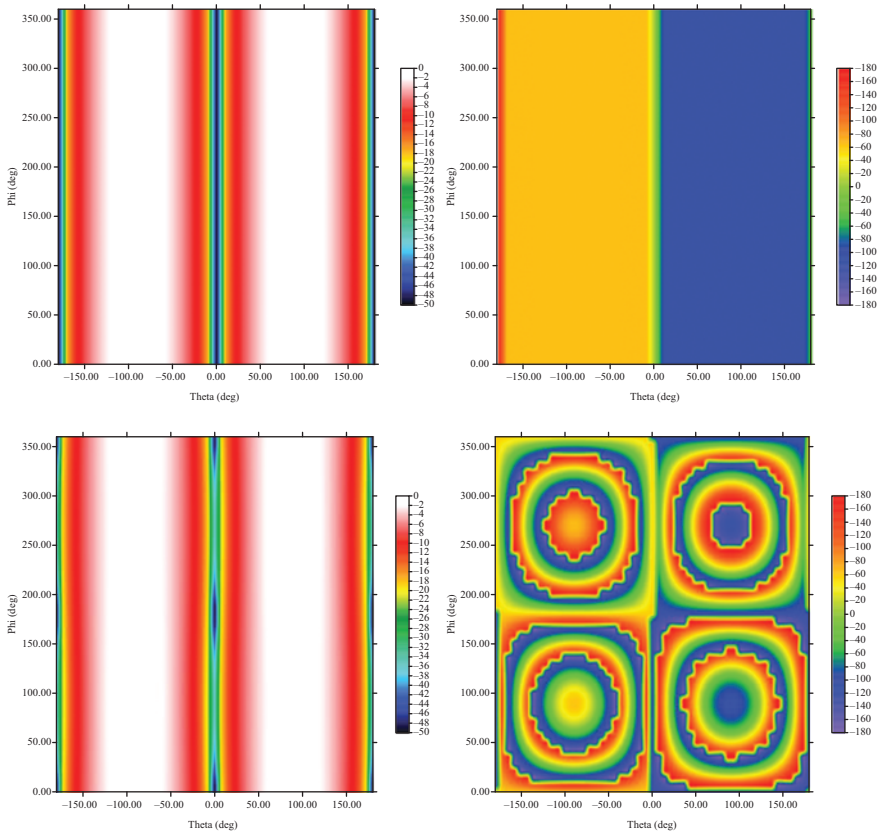

Figure 8.32 *The θ electric near-field vector component (amplitude left and phase right) is shown (top row) for the centred dipole and on the bottom row, and the corresponding information for the case when the dipole is offset (along the y-axis) from the coordinate system origin by 2λ*

electric field radiated by the AUT in terms of spherical modes in the probe (primed) coordinate system. We now need to describe the probe receive properties in terms of a separate spherical wave expansion and formulate the interaction between the two modal expansions. In order to do so, we first derive a transmission formula. This formula relates the power applied to the port of the AUT to that received at the port of the probe. If we consider Figure 8.34 which depicts an AUT (or probe), enclosed within a minimum sphere of radius $r = MRS$, we can relate spherical modes that exist external to this surface to the energy emanating from or entering the port of the device (denoted by the dashed line). We can make the following statements related to this:

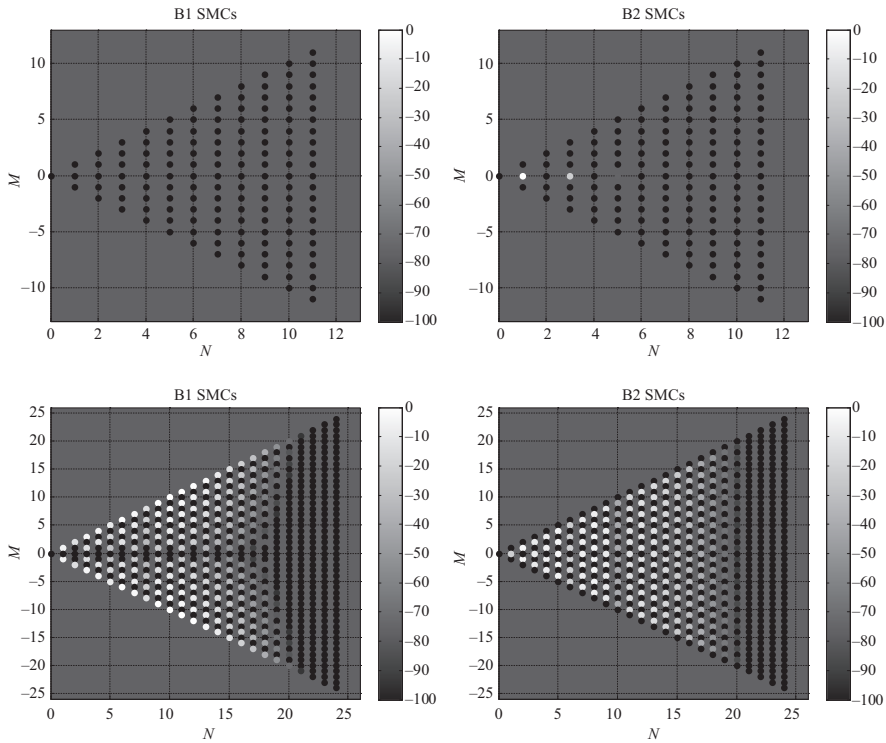

Figure 8.33 SNF mode spectra: amplitude of the SMC's (B^1 – left and B^2 – right) for the dipole centred case (top row) and the dipole offset along the y-axis (bottom row). Amplitude is displayed in dB, scales from 0 (white) to −100 dB (black)

- Voltage incident on the port is designated v and is partly reflected by port mismatch Γ, and the difference is transmitted by the AUT (we assume that the AUT has 100% efficiency).
- The field radiated into free-space by the AUT can be described by a spherical wave expansion and these modal coefficients are designated B^1_{mn} and B^2_{mn}.
- When receiving, this AUT receives energy from space and this can also be described by a spherical wave expansion and these modal coefficients are designated A^1_{mn} and A^2_{mn}.
- Of the voltage received by the AUT (if we again assume a 100% efficiency), part of it is reflected by the port reflection coefficient, and the rest is denoted as w and emerges from the port.

Using the concept of port voltage related to spherical wave expansion coefficients, we can now write the following expressions (disregarding any scattering of

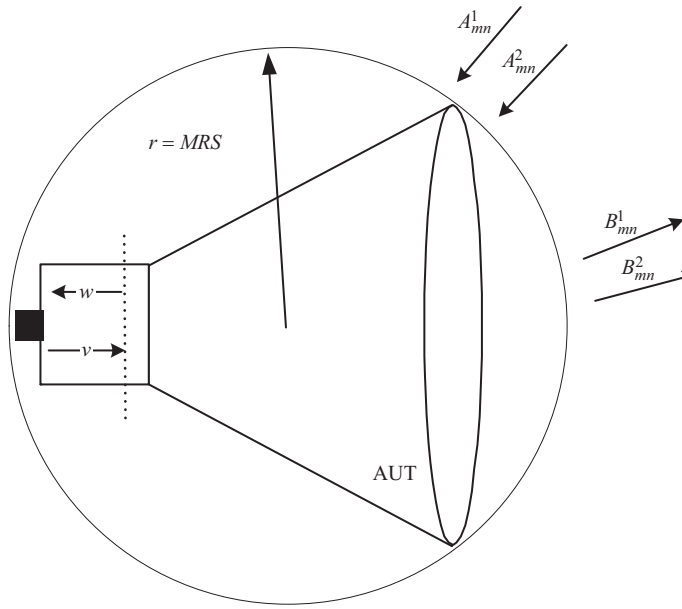

Figure 8.34 Diagram depicting AUT and near-field probe interaction during an SNF measurement

waves incident on the AUT[12]):

$$w = v\Gamma + \sum_{n=1}^{\infty}\sum_{m=-n}^{n}\left[R^1_{mn}A^1_{mn} + R^2_{mn}A^2_{mn}\right] \tag{8.15}$$

$$\sum_{n=1}^{\infty}\sum_{m=-n}^{n}\left[B^1_{mn} + B^2_{mn}\right] = v\sum_{n=1}^{\infty}\sum_{m=-n}^{n}\left[T^1_{mn} + T^2_{mn}\right] \tag{8.16}$$

where R^1_{mn} and R^2_{mn} are designated the AUT receiving coefficients and T^1_{mn} and T^2_{mn} are the AUT transmission coefficients. If we now consider the case of a receiving probe, we can use (8.15) to relate the spherical modes incident on the probe to the voltage (w) measured at the probe port as

$$w = \sum_{v=1}^{\infty}\sum_{\mu=-v}^{v}\left[R^1_{\mu v}A^1_{\mu v} + R^2_{\mu v}A^2_{\mu v}\right]$$

[12]It is worthwhile to point out that this is the only approximation that is introduced into the SNF theoretical derivation.

where we have now switched the indices to that of the primed coordinate system and we assume that the probe port is perfectly matched. Returning to the SNF system since we know what modes are transmitted by the AUT, it is logical that those are the modes incident on the probe and we can therefore relate the voltage measured at the probe port to the spherical modes transmitted by the AUT. Referring to (8.9) again (duplicated below for convenience)

$$\underline{E}(\underline{r}') = \frac{k}{2\sqrt{\eta}} \sum_{n=1}^{\infty} \sum_{m=-n}^{n} \sum_{\mu=-n}^{n} \sum_{\substack{\nu=|\mu| \\ \nu\neq 0}}^{\infty} e^{jm\phi_0} d_{\mu m}^{(n)}(\theta_0) e^{j\mu\chi_0}$$

$$\left[\begin{array}{l} \left(B_{mn}^{1} C_{1n\mu\nu}^{M}(kA) + B_{mn}^{2} C_{2n\mu\nu}^{N}(kA) \right) \left(\underline{M}_{\mu n}^{(3)}(\underline{r}') + \underline{M}_{\mu n}^{(4)}(\underline{r}') \right) + \\ \left(B_{mn}^{1} C_{2n\mu\nu}^{M}(kA) + B_{mn}^{2} C_{1n\mu\nu}^{N}(kA) \right) \left(\underline{N}_{\mu n}^{(3)}(\underline{r}') + \underline{N}_{\mu n}^{(4)}(\underline{r}') \right) \end{array} \right]$$

we can identify these modes as the $\underline{M}_{\mu n}^{(3)}(\underline{r}')$ and $\underline{N}_{\mu n}^{(3)}(\underline{r}')$ modes and their coefficients therefore represent the modes of what is impinging on the probe as

$\underline{M}_{\mu n}^{(3)}(\underline{r}')$ – TE mode coefficients

$$= \frac{1}{2} \sum_{n=1}^{\infty} \sum_{m=-n}^{n} \sum_{\mu=-n}^{n} \sum_{\substack{\nu=|\mu| \\ \nu\neq 0}}^{\infty} e^{jm\phi_0} d_{\mu m}^{(n)}(\theta_0) e^{j\mu\chi_0} \left(B_{mn}^{1} C_{1n\mu\nu}^{M}(kA) + B_{mn}^{2} C_{2n\mu\nu}^{N}(kA) \right)$$

$\underline{N}_{\mu n}^{(3)}(\underline{r}')$ – TM mode coefficients

$$= \frac{1}{2} \sum_{n=1}^{\infty} \sum_{m=-n}^{n} \sum_{\mu=-n}^{n} \sum_{\substack{\nu=|\mu| \\ \nu\neq 0}}^{\infty} e^{jm\phi_0} d_{\mu m}^{(n)}(\theta_0) e^{j\mu\chi_0} \left(B_{mn}^{1} C_{2n\mu\nu}^{M}(kA) + B_{mn}^{2} C_{1n\mu\nu}^{N}(kA) \right) \quad (8.17)$$

It is worthwhile to consider these expressions to come to terms with the notation. The coefficients $B_{mn}^{1/2}$are the sought SMC's for the AUT, the $e^{jm\phi_0} d_{\mu m}^{(n)}(\theta_0) e^{j\mu\chi_0}$ functions represent the rotation and the $C_{1/2n\mu\nu}^{M/N}(kA)$ functions represent the coordinate system translation required to map the spherical modes defined in the unprimed coordinate system to the primed coordinate system. Each *mn* mode in the unprimed coordinate system has an equivalent representation in the primed coordinate system consisting of an infinite numbers of spherical modes of which each mode is identified by the $\mu\nu$ indices. We can

therefore now write the following expression for the voltage w received by the probe:

$$w(\phi_0,\theta_0,\chi_0,A)=\frac{1}{2}\sum_{n=1}^{\infty}\sum_{m=-n}^{n}\sum_{\mu=-n}^{n}\sum_{\substack{\nu=|\mu|\\ \nu\neq 0}}^{\infty} e^{jm\phi_0}d_{\mu m}^{(n)}(\theta_0)e^{j\mu\chi_0}$$
$$\begin{bmatrix}\left(B_{mn}^{1}C_{1n\mu\nu}^{M}(kA)+B_{mn}^{2}C_{2n\mu\nu}^{N}(kA)\right)R_{\mu\nu}^{1}\\ +\left(B_{mn}^{1}C_{2n\mu\nu}^{M}(kA)+B_{mn}^{2}C_{1n\mu\nu}^{N}(kA)\right)R_{\mu\nu}^{2}\end{bmatrix} \tag{8.18}$$

where $R_{\mu\nu}^{1}$ and $R_{\mu\nu}^{2}$ are the receiving coefficients of the probe. These coefficients are obtained through a probe calibration process and can be seen as weights that apply to each incident spherical mode impinging on the probe. More information on probe calibration can be found in Chapter 12.

8.7 Near-field probe correction

Equation (8.18) is also referred to as the transmission formula and is at the core of probe corrected SNF measurements. Since we can measure values of w in an antenna range, inversion of this formula allows one to obtain the much sought-after probe corrected SMC's. We achieve this by first limiting the number of modes considered to N as outlined before. We next use the orthogonality property of the exponential function, which can be written as

$$\int_0^{2\pi} e^{j(m-m')\phi}d\phi=2\pi\delta_{mm'}$$

If we now rewrite (8.18) as

$$w(\phi_0,\theta_0,\chi_0,A)=\sum_{\mu=-n}^{n}w_{\mu}(\phi_0,\theta_0,A)e^{j\mu\chi_0}$$
$$=\sum_{\mu=-n}^{n}\left\{\frac{1}{2}\sum_{n=1}^{N}\sum_{m=-n}^{n}\sum_{\substack{\nu=|\mu|\\ \nu\neq 0}}^{\infty} e^{jm\phi_0}d_{\mu m}^{(n)}(\theta_0)\begin{bmatrix}\left(B_{mn}^{1}C_{1n\mu\nu}^{M}(kA)+B_{mn}^{2}C_{2n\mu\nu}^{N}(kA)\right)R_{\mu\nu}^{1}\\ +\left(B_{mn}^{1}C_{2n\mu\nu}^{M}(kA)+B_{mn}^{2}C_{1n\mu\nu}^{N}(kA)\right)R_{\mu\nu}^{2}\end{bmatrix}\right\}e^{j\mu\chi_0} \tag{8.19}$$

and multiply by $e^{-j\mu\chi_0}$ and integrating from 0 to 2π, we obtain

$$\int_0^{2\pi} w(\phi_0,\theta_0,\chi_0,A)e^{-j\mu\chi_0}d\chi_0=\int_0^{2\pi}\sum_{\mu=-n}^{n}w_{\mu}(\phi_0,\theta_0,A)e^{j\mu\chi_0}e^{-j\mu\chi_0}d\chi_0$$
$$=2\pi w_{\mu}(\phi_0,\theta_0,A)$$

which shows that $w_\mu(\phi_0,\theta_0,A)$ is simply the inverse Fourier transform of the $w(\phi_0,\theta_0,\chi_0,A)$ function with respect to the χ_0 variable. Using this orthogonality property again, we can from (8.19) write for $w_\mu(\phi_0,\theta_0,A)$:

$$w_\mu(\phi_0,\theta_0,A)=\sum_{m=-n}^{n} w_{\mu m}(\theta_0,A)e^{jm\phi_0}$$

$$=\sum_{m=-n}^{n}\left\{\frac{1}{2}\sum_{n=1}^{N}\sum_{\substack{\nu=|\mu|\\ \nu\neq 0}}^{N} d_{\mu m}^{(n)}(\theta_0)\left[\begin{array}{l}\left(B_{mn}^{1}C_{1n\mu\nu}^{M}(kA)+B_{mn}^{2}C_{2n\mu\nu}^{N}(kA)\right)R_{\mu\nu}^{1}\\ +\left(B_{mn}^{1}C_{2n\mu\nu}^{M}(kA)+B_{mn}^{2}C_{1n\mu\nu}^{N}(kA)\right)R_{\mu\nu}^{2}\end{array}\right]\right\}e^{jm\phi_0}$$

Multiplying by $e^{-jm\phi_0}$ and integrating from 0 to 2π allows us to write

$$\int_0^{2\pi} w_\mu(\phi_0,\theta_0,A)e^{-jm\phi_0}d\phi_0=\int_0^{2\pi}\sum_{m=-n}^{n} w_{\mu m}(\theta_0,A)e^{jm\phi_0}e^{-jm\phi_0}d\phi_0$$

$$=2\pi w_{\mu m}(\theta_0,A)$$

which similarly shows that $w_{\mu m}(\theta_0,A)$ is the inverse Fourier transform of the $w_\mu(\phi_0,\theta_0,A)$ function with respect to the ϕ_0 variable. Our final step in finding a solution to this inversion problem lies in the orthogonality property of the Legendre polynomial:

$$\int_0^{\pi} d_{\mu m}^{(n)}(\theta_0)d_{\mu m}^{(n')}(\theta_0)\sin\theta\, d\theta=\frac{2}{2n+1}\delta_{nn'}$$

By multiplying $w_{\mu m}(\theta_0,A)$ with $d_{\mu m}^{(n')}(\theta_0)\sin\theta$ and integrating from 0 to π, we obtain

$$\int_0^{\pi} w_{\mu m}(\theta_0,A)d_{\mu m}^{(n)}(\theta_0)\sin\theta_0 d\theta_0$$

$$=\frac{1}{2n+1}\sum_{\substack{\nu=|\mu|\\ \nu\neq 0}}^{N}\left[\left(B_{mn}^{1}C_{1n\mu\nu}^{M}(kA)+B_{mn}^{2}C_{2n\mu\nu}^{N}(kA)\right)R_{\mu\nu}^{1}\right.$$

$$\left.+\left(B_{mn}^{1}C_{2n\mu\nu}^{M}(kA)+B_{mn}^{2}C_{1n\mu\nu}^{N}(kA)\right)R_{\mu\nu}^{2}\right] \tag{8.20}$$

which is to be evaluated for each pair of indices (*m,n*) and all values of μ. We can now summarise and state that the transmission formula allows us to find the SMC's from measurement data by measuring field values $w(\phi_0,\theta_0,\chi_0,A)$ on a fixed grid. We then

1. Find the inverse Fourier transform of this data set with respect to χ_0, which provides us with $w_\mu(\phi_0,\theta_0,A)$.

2. Find the inverse Fourier transform of $w_\mu(\phi_0, \theta_0, A)$ with respect to ϕ_0, which provides us with $w_{\mu m}(\theta_0, A)$.
3. Evaluate integral equation (8.20), containing function $w_{\mu m}(\theta_0, A)$ to establish a set of equations for all (m,n), allowing one to solve for all B^1_{mn} and B^2_{mn} for as many probe indices μ as we want to consider.

The last statement related to probe indices μ deserves significant discussion. The theory allows us to consider as many indices as we wish, which implies using a near-field probe of high radiation complexity. However, in practice, it is common to restrict our treatment to probes that only contain the $\mu = \pm 1$ modes. An idea first introduced in [28] allowing one to simplify the SNF transmission equation and solving for the SMC's in a practical and realistic way. This restriction on the near-field probe implies a probe for which the radiation pattern variation in the circumferential direction ϕ can be fully represented by the function $e^{jm\phi_0} = e^{\pm j\phi_0}$. It is found that this condition is met by rotationally symmetric probes fed by the circular waveguide, containing the TE_{11} fundamental mode. This requirement therefore rules out rectangular horns and open-ended rectangular waveguide (OEWG) probes. (In what follows, we present results for OEWG probes to illustrate to what extent violation of this condition can introduce measurement uncertainty.) A detailed discussion on near-field probes is provided in Chapter 12.

Probes that only contain the $\mu = \pm 1$ modes are also referred to as first-order probes. The spherical mode coefficients for other modes of such carefully constructed probes are typically at least 40 dB below the first-order modes. However, such special probes increase the cost of the measurement system and the probes may have a smaller bandwidth than similar OEWG probes.

If we turn our attention to (8.20) again under the assumption that we are restricting the probe to only allow the $\mu = \pm 1$ modes, we can reduce this equation to the following two equations in two unknowns:

$$\int_0^\pi w_{-1m}(\theta_0, A) d^{(n)}_{-1m}(\theta_0) \sin\theta_0 \, d\theta_0 = \frac{1}{2n+1} \left[\begin{array}{l} \left(B^1_{mn} C^M_{1n(-1)1}(kA) + B^2_{mn} C^N_{2n(-1)1}(kA) \right) R^1_{-11} \\ + \left(B^1_{mn} C^M_{2n(-1)1}(kA) + B^2_{mn} C^N_{1n(-1)1}(kA) \right) R^2_{-11} \end{array} \right]$$

$$\int_0^\pi w_{1m}(\theta_0, A) d^{(n)}_{1m}(\theta_0) \sin\theta_0 \, d\theta_0 = \frac{1}{2n+1} \left[\begin{array}{l} \left(B^1_{mn} C^M_{1n(1)1}(kA) + B^2_{mn} C^N_{2n(1)1}(kA) \right) R^1_{11} \\ + \left(B^1_{mn} C^M_{2n(1)1}(kA) + B^2_{mn} C^N_{1n(1)1}(kA) \right) R^2_{11} \end{array} \right]$$

Under this assumption, we can now state that in order to find $w_\mu(\phi_0, \theta_0, A)$, we evaluate the inverse Fourier transform of the measured data set with respect to χ_0, for only two values of μ. This implies that two discrete measurements in χ_0(probe

polarisation angle) are needed. For convenience, we select only $\chi_0 = 0°, 90°$ and an inverse Fourier transform of the measured data set $w(\phi_0, \theta_0, \chi_0, A)$ is now evaluated for only

$$w_\mu(\phi_0, \theta_0, A) = \frac{1}{2\pi}\int_0^{2\pi} w(\phi_0, \theta_0, \chi_0, A)e^{-j\mu\chi_0}d\chi_0\Big|_{\substack{\mu=-1\\ \mu=+1}}$$

which can be reduced to

$$\begin{aligned} w_{-1}(\phi_0, \theta_0, A) &= \frac{1}{2}\left\{w(\phi_0, \theta_0, 0, A) + jw\left(\phi_0, \theta_0, \frac{\pi}{2}, A\right)\right\} \\ w_{+1}(\phi_0, \theta_0, A) &= \frac{1}{2}\left\{w(\phi_0, \theta_0, 0, A) - jw\left(\phi_0, \theta_0, \frac{\pi}{2}, A\right)\right\} \end{aligned} \tag{8.21}$$

These equations show that when a first-order probe is used, measurements are only required for two polarisation angles ($\chi = 0°$ and 90°) and numerical integration of the data for the polarisation variable is not required. This greatly reduces the measurement time and results in a fast, efficient and accurate numerical technique to perform the calculations.

Continuing on to find $w_{\mu m}(\theta_0, A)$, we evaluate the inverse Fourier transform of the $w_{\mu=\pm1}(\phi_0, \theta_0, A)$ data set with respect to ϕ_0, for $m = -N, \ldots, -1, 0, 1, \ldots, N$

$$w_{\mu=\pm1m}(\theta_0, A) = \frac{1}{2\pi}\int_0^{2\pi} w_{\mu=\pm1}(\phi_0, \theta_0, A)e^{-jm\phi_0}d\phi_0 \tag{8.22}$$

which can readily be achieved through a fast Fourier transform process [29]. Our third and final step is evaluation of the integral in θ for the function $w_{\mu=\pm1m}(\theta_0, A)$, for $n = |m|, \ldots, N$and $n \neq 0$.

We next investigate the impact of using higher-order probes when our formulation only allows for $\mu = \pm1$. We show simulation results for using an OEWG probe for SNF testing [30–32]. Since the OEWG probe is widely used, it was chosen as the probe for this study and all the simulations are for this probe. When using OEWG probes, errors will be present in the calculated AUT SMC's and the resulting far-field parameters. It has been established that if the measurement radius is large enough, probes such as the OEWG can be used for SNF measurements and the effect of their higher-order modes will be negligible, and the formulation outlined here can be used without causing a significant error in the results. Until fairly recently, there was limited information available on how large the radius must be and what the residual effects of the higher-order modes are.

In this simulation measured SNF data is used for both the AUT and an OEWG probe to calculate the far-field patterns of both the antenna and the probe over a full sphere. The AUT far-field pattern is then rotated mathematically about the z-axis to simulate a ϕ-rotation and about the y-axis to simulate a θ-rotation. The transmitting plane-wave spectrum over the forward hemisphere on a k-space (k_x,k_y) grid is then derived from the rotated pattern. This plane-wave spectrum represents the AUT rotated in ϕ and θ as it is in an SNF measurement.

The far-field probe pattern is then rotated about its z-axis to simulate a χ-rotation and its receiving plane-wave spectrum calculated on the same k-space grid as that of the AUT. The calculation of a receiving plane-wave spectrum for the rotated OEWG probe is repeated but, in this case, the spherical modes for all but the $\mu = \pm 1$ modes are set to zero in the calculation of its far-field pattern. The two spectra represent a higher-order probe and a first-order probe, respectively, with otherwise identical patterns and polarisation. Figure 8.35 shows the spherical mode amplitude plots for the B^1_{mn} SMC's for the two probes.

To obtain the results presented below, the rotated plane-wave spectra of the AUT and one of the probes are used to calculate the output of the probe for a specified x, y, z position of the probe. When $x = y = 0$, the probe is at the pole of the measurement sphere and the AUT is positioned at the origin of the sphere or along the z-axis. The z-position of the probe defines the measurement radius. The probe output is produced using the PNF transmission equation [33]. If we now add the rotation angles θ, ϕ and χ as variables to the probe output, the AUT spectrum and the probe receiving spectrum can be used to produce simulated SNF data at arbitrary (θ, ϕ)-positions on the measurement sphere with arbitrary χ rotations of the probe. The PNF transmission equation is used for the simulation rather than the SNF transmission equation since both are equally valid and accurate expressions for the transmission between a test antenna and a probe at any arbitrary near-field position and relative orientation. The planar equation is easier to calculate numerically and can be used *without* modification for both first-order and higher-order probes. (Note that it is only the spherical formulation that has this constraint on the properties of the probe, c.f. Chapter 12.)

Using the derived results, we can establish guidelines for the effect of higher-order probes in SNF measurements by comparing some near-field or far-field parameter obtained with the first-order and higher-order probes. It is not practical to simulate all the possible combinations of AUT, probe, measurement radius, AUT

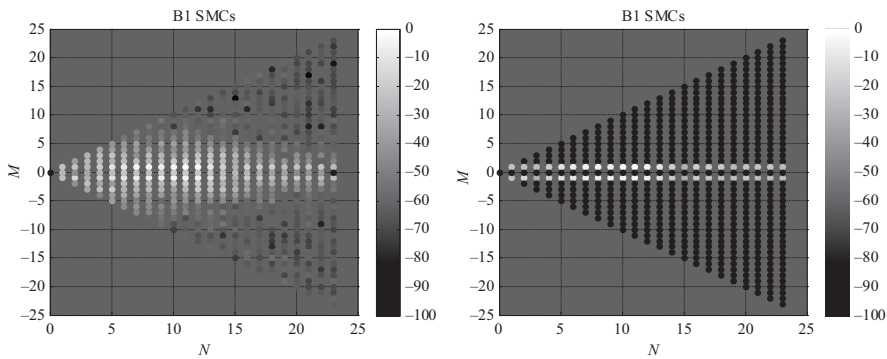

Figure 8.35 Spherical mode coefficient amplitudes for B^1_{mn} for the higher-order probe with all μ modes retained (left) and B^1_{mn} for the first-order probe with only $\mu = \pm 1$ modes (right)

offset, frequency, AUT and probe rotations and density of points used in the numerical calculations. Thus, the combinations must be reduced to a manageable size and the focus should be on the parameters that are likely to have an effect on far-field results.

In the results presented below, a narrow beam slotted waveguide array with a gain of 35 dBi was used. It is not likely that the higher-order mode effect is highly sensitive to the AUT type (in [32] another antenna type is considered to also investigate a case of lower gain). The frequency is 9.375 GHz and the AUT and the probe are linearly polarised with an on-axis axial ratio of 40 dB or more. It is known that the effect of the higher-order modes is reduced as the measurement radius is increased and it is highly desirable to perform simulations for a large enough range of radii to derive a guideline for this parameter. It is also desirable to determine the effect on the far-field results when the higher-order probe is used and to do this; a hemisphere of near-field data must be simulated and then transformed to the far-field. A hemisphere of near-field data for the slotted array has over 50,000 data points for each of the two χ angles and this requires evaluating the transmission formula on the order of 100,000 times. This cannot be done for many measurement radii, and so a complete hemisphere near-field data sets for the first-order and higher-order OEWG probes were generated for the slotted array at measurement radii of one and four times the *MRS*. These were then transformed to the far-field and both the near-field data and the far-field results for the two probes compared. Figure 8.36 show contour plots of the simulated θ-component ($\chi = 0$) and ϕ-component ($\chi = 90$) amplitudes for a measurement radius of one *MRS*.

Using the simulated amplitude and phase data, the amplitude of the complex difference between the near-fields for the two probes was calculated at each point and plotted relative to the peak near-field amplitude as shown in Figure 8.37. Using the complex difference, rather than just the amplitude difference, includes the higher-order mode's effect on both the near-field amplitude and phase and represents the upper bound effect.

There are some regions where the difference level is as high as -35 dB and other regions where it is as low as -60 to -70 dB. With this type of variation, the effect on the far-field should be less than the peak and this is confirmed when the far-field patterns are computed for the two probes and the amplitude difference converted to an error signal level. The complex difference is not used in the far-field since the far-field phase is generally not important for most antenna measurements. Figure 8.38 shows the far-field amplitude pattern and the error signal level difference between the two probes for the *MRS* radius. A peak error of -41 dB occurs in the region of the main beam and the error level in the side lobe region is below -60 dB. This characteristic of the effects of probe correction errors showing up in the main beam region is consistent with other error analysis studies. If the probe pattern used for spherical processing is changed or the probe correction is neglected, it is the main beam region of the far-field that is affected most.

The simulation of a complete near-field and processing to the far-field was also carried out for a measurement radius of 4*MRS*. Near-field complex difference

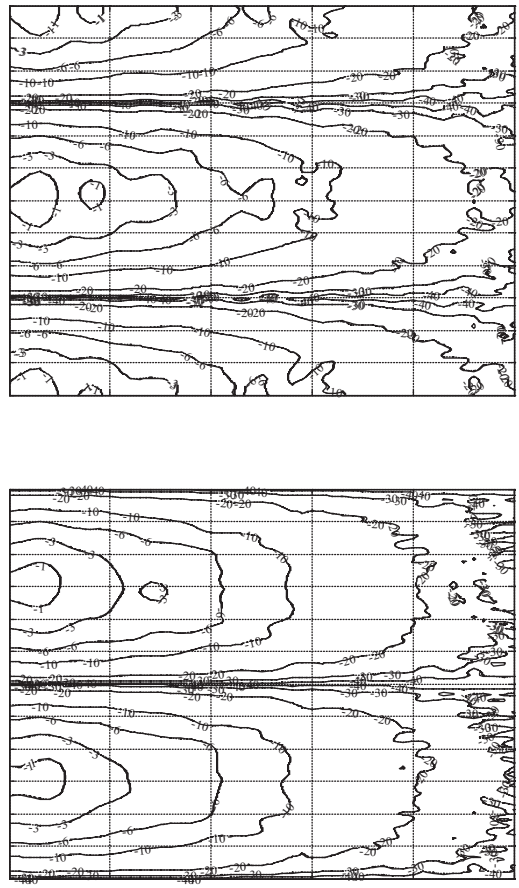

Figure 8.36 Simulated SNF amplitude for radius = 1 MRS ($\chi = 0°$ top and $\chi = 90°$ bottom). Contour levels are −1, −3, −6, −10, −20, −30, −40, −50. Solid = first-order probe and dashed = higher-order probe

results are shown in Figure 8.39 and far-field in Figure 8.40. The maximum far-field amplitude difference for this case was −53 dB.

Comparing Figures 8.37 and 8.39 clearly show that by increasing the measurement radius, the impact of neglecting the probe higher-order modes becomes less of a concern since the overall error levels are diminished. One can therefore state that the effect of the higher-order mode OEWG probe compared to an ideal first-order probe decreases with distance.

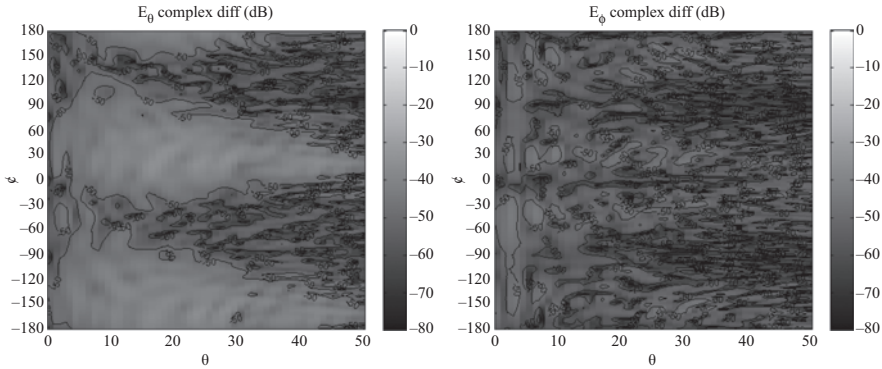

Figure 8.37 Amplitude of the complex difference relative to the peak near-field amplitude for $\chi = 0^\circ$ (left) and $\chi = 90^\circ$ (right) at measurement radius of MRS

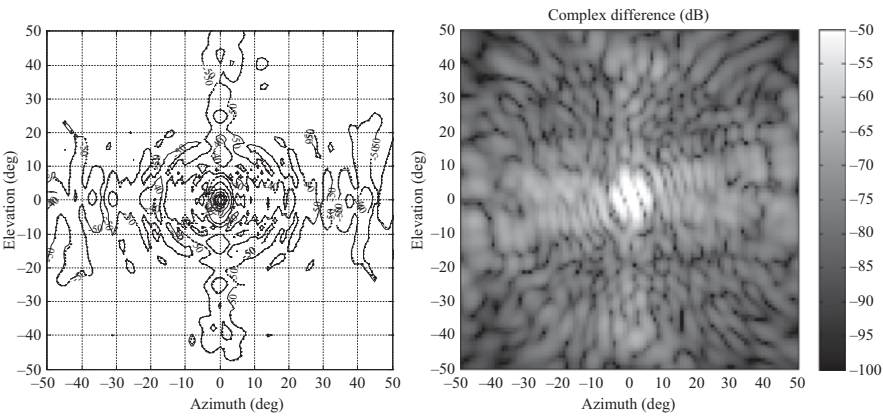

Figure 8.38 Far-field contour pattern for slotted waveguide array (solid = first-order probe and dashed = higher-order probe) and far-field error relative to the peak of the main beam (RMS level = −75 dB) due to the use of a higher-order probe for MRS measurement radius. The near-field and far-field results show acceptable results for the measurement radius as small as the MRS

The results in [32] show that for radii of 2*MRS* the differences in the near-field and far-field are on the order of −50 dB below the peak amplitudes. For larger measurement radii, the differences are below −60 dB. The difference levels are also not highly sensitive to the AUT characteristics (in [32] results are presented for a standard gain horn antenna with a gain of 21 dBi). The primary effect of the higher-order probe on the far-field pattern is in the main beam region and the side lobes are relatively unaffected.

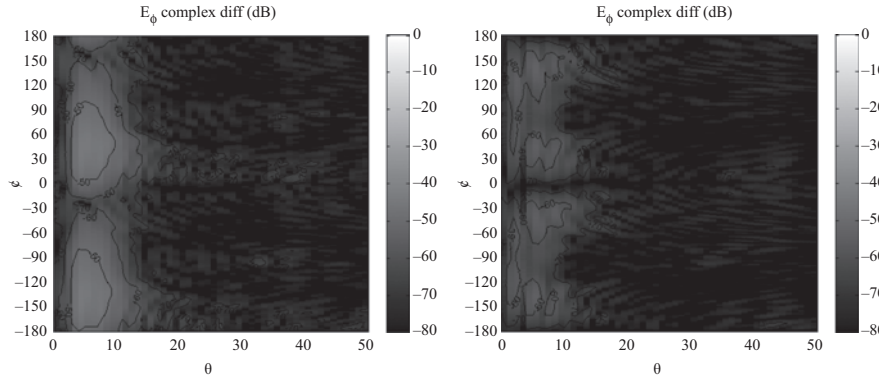

Figure 8.39 Amplitude of the complex difference relative to the peak near-field amplitude for $\chi = 0^\circ$ (left) and $\chi = 90^\circ$ (right) at a measurement radius of 4MRS

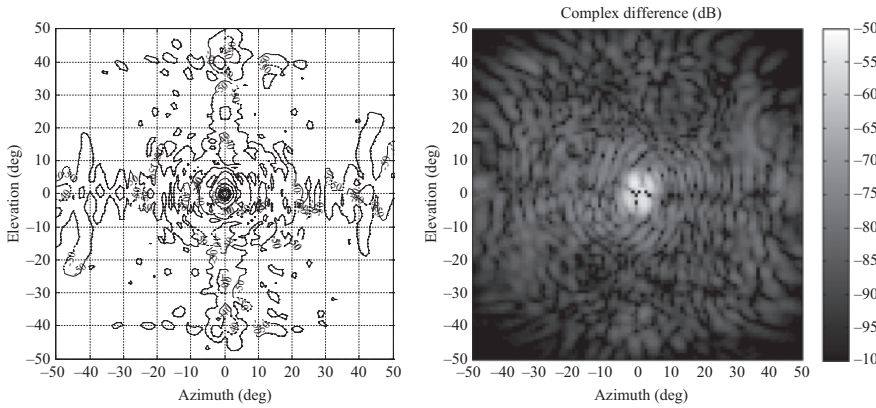

Figure 8.40 Far-field contour pattern for slotted waveguide array (solid = first-order probe and dashed = higher-order probe) and far-field error relative to the peak of the main beam (RMS level = −86 dB) due to the use of a higher-order probe for 4MRS measurement radius

We can therefore state in summary that the selection of a first-order near-field probe allows us to simplify the SNF transmission equation so that probe correction can be achieved and corrected SMC's obtained. The results above also show that if we opt to use an OEWG probe (not a first-order probe), the error introduced is small if we select a sufficiently large (i.e. $>2MRS$) probe measurement radius. Formulations do exist that allow for the use (and subsequent correction) of higher-order near-field probes and we address that below.

The use of first-order probes, as described above, make for a very efficient acquisition and processing approach. However, the limited bandwidth of such probes become very limiting and in a measurement world where wideband probes (that are non-first-order) present us with significant potential acquisition time savings, having the capability to use and probe correct for them, is highly desirable.

The probe correction formulation presented above describes spherical mode coupling between a modal expansion for the AUT and a separate modal expansion for the near-field probe. In order to describe this in terms of incident modes at the probe, the outgoing modes of the AUT must be translated into the local coordinate system of the probe. The rotation and translation functions allowing for this conversion leads to a full set of equations that are poorly conditioned and although this allows for probe correction of higher-order probes, it comes at a significant computational cost and additional measurement time. This was in the past considered to be prohibitive. However, recent work [34–41] present multiple approaches to solving this tough problem and today makes the use of higher-order wideband probes in SNF testing feasible.

In [38], the authors present a SNF probe correction technique that is valid for any higher-order near-field probe. The approach taken is to express the AUT SNF modal expansion in terms of a plane-wave expansion. The near-field probe radiation characteristics are assumed to also be known in terms of a plane-wave expansion (not unreasonable since this corresponds to a simple far-field pattern result) and the probe correction can then be achieved through coupling of plane waves, after translation of coordinate systems from the AUT coordinate to that of the probe. This is of course required for each distinct spatial location of the near-field probe w.r.t. AUT. Each plane-wave component propagating from the AUT can be translated to an incident plane wave at the probe, within the probe coordinate system. The far-field receiving pattern of the probe can therefore directly be used to weight the individual incident plane waves in order to obtain the output signal of the probe antenna. This approach enables a full correction of arbitrary field probes with realistic effort and does not require any particular near-field calibration of the probe.

A higher-order probe correction technique based on the SNF theory presented here was published in [37]. This correction technique is FFT and matrix inversion based and allows for full probe correction of any higher-order probe. The authors demonstrate the effectiveness of the probe correction by measuring a log-periodic dipole array first, by using a first-order probe and performing traditional probe correction. This radiation pattern becomes the reference. They then employ a higher-order probe that requires up to $\mu = \pm 8$ modes for proper probe characterisation and repeat their measurement. To further stress their test, they offset the log-periodic dipole array by 1.6 m (8λ). The test results reported are shown in Figure 8.41, where co- and cross-pol radiation patterns are shown for the $\phi = 0^\circ$ case on the left and the $\phi = 90^\circ$ case one the right.

The authors report in [37] that the higher-order probe correction patterns agree with the reference patterns to within a standard deviation of 0.05 dB in amplitude

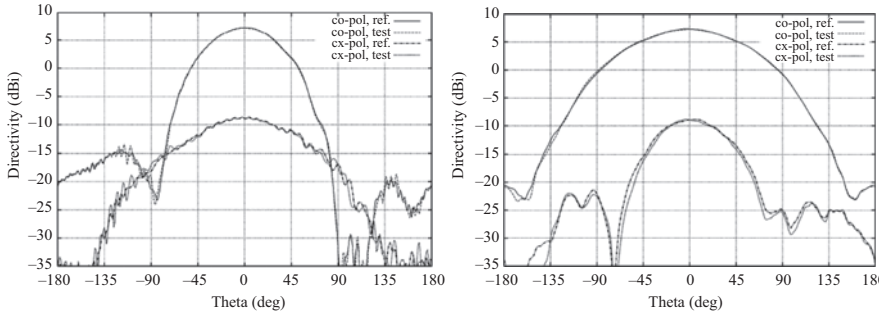

Figure 8.41 *Co- and cross-pol radiation patterns are shown for $\phi = 0°$ (left) and $\phi = 90°$ (right). Pattern overlays are for the reference pattern (solid) and the higher-order probe corrected pattern (dashed). © 2020 IEEE. Reprinted, with permission, from [37]*

and 1.16° in phase over a $-10° < \theta < +10°$ angular region. In contrast, when the higher-order probe correction is limited to only the $\mu = \pm 1$ modes (so using the higher-order probe, but not fully compensating for its behaviour), this agreement changes to a standard deviation of 0.31 dB in amplitude and 2.69° in phase over a $-10° < \theta < +10°$ angular region.

As mentioned earlier, these higher-order probe correction techniques require additional computational effort. In [41], it is reported that the FFT and matrix inversion-based technique described above requires a computational effort equivalent to O[N^4] operations, where N is the electrical radius of the AUT. The plane wave based technique of [38] requires O[N^2 log N] operations and the formulation presented in [41] requires O[N^3]. However, computational complexity does not simply translate to the computational cost, since this depends on several other factors like algorithm implementation [42]. Also, it should be stated that although promising, these techniques are fairly new and the documented experimental successes of the techniques vary in rigor and 'significance' of higher-order probes being tested. Further testing will ultimately be required to fully explore limitations of each technique.

8.8 Far-field expressions

We know that once we have obtained the SMC's, we can evaluate the electric and magnetic field intensity anywhere in space by evaluating (8.5a) and (8.5b) (repeated again below for convenience)

$$\underline{E}(\underline{r}) = \frac{k}{\sqrt{\eta}} \sum_{n=1}^{\infty} \sum_{m=-n}^{n} \left[B^1_{mn} \underline{M}^{(4)}_{mn}(\underline{r}) + B^2_{mn} \underline{N}^{(4)}_{mn}(\underline{r}) \right]$$

$$\underline{H}(\underline{r}) = jk\sqrt{\eta}\sum_{n=1}^{\infty}\sum_{m=-n}^{n}\left[B^1_{mn}\underline{N}^{(4)}_{mn}(\underline{r}) + B^2_{mn}\underline{M}^{(4)}_{mn}(\underline{r})\right]$$

and where $\underline{M}^{(4)}_{mn}(\underline{r})$ and $\underline{N}^{(4)}_{mn}(\underline{r})$ are as defined in (8.3). However, when $\underline{r}$ reaches to infinity (the true far-field case) we can use the asymptotic forms for these two functions, which allow us to write [43]

$$\underline{m}^{(4)}_{mn}(\underline{r}) = j^{n+1}\frac{e^{-jkr}}{kr}e^{jm\phi}\left[\frac{jm}{\sin\theta}P^{|m|}_n(\cos\theta)\widehat{\underline{e}}_\theta - \frac{\partial P^{|m|}_n(\cos\theta)}{\partial\theta}\widehat{\underline{e}}_\phi\right]\Bigg|_{kr\to\infty}$$

$$\underline{M}^{(4)}_{mn}(\underline{r}) = norm\, j^{n+1}\frac{e^{-jkr}}{kr}e^{jm\phi}\left[\frac{\frac{jm}{\sin\theta}\overline{P}^{|m|}_n(\cos\theta)\widehat{\underline{e}}_\theta - \partial\overline{P}^{|m|}_n(\cos\theta)}{\partial\theta\widehat{\underline{e}}_\phi}\right]\Bigg|_{kr\to\infty}$$

$$\underline{n}^{(4)}_{mn}(\underline{r}) = \frac{n(n+1)}{kr}j^{n+1}\frac{e^{-jkr}}{kr}P^{|m|}_n(\cos\theta)e^{jm\phi}\widehat{\underline{e}}_r + j^n\frac{e^{-jkr}}{kr}e^{jm\phi}\left[\frac{\partial P^{|m|}_n(\cos\theta)}{\partial\theta}\widehat{\underline{e}}_\theta + \frac{jm}{\sin\theta}P^{|m|}_n(\cos\theta)\widehat{\underline{e}}_\phi\right]\Bigg|_{kr\to\infty}$$

$$\underline{N}^{(4)}_{mn}(\underline{r}) = norm\,\frac{n(n+1)}{kr}j^{n+1}\frac{e^{-jkr}}{kr}\overline{P}^{|m|}_n(\cos\theta)e^{jm\phi}\widehat{\underline{e}}_r + norm\, j^n\frac{e^{-jkr}}{kr}e^{jm\phi}\left[\frac{\partial\overline{P}^{|m|}_n(\cos\theta)}{\partial\theta}\widehat{\underline{e}}_\theta + \frac{jm}{\sin\theta}\overline{P}^{|m|}_n(\cos\theta)\widehat{\underline{e}}_\phi\right]\Bigg|_{kr\to\infty}$$

where

$$norm = \frac{1}{\sqrt{2\pi n(n+1)}}\left(-\frac{m}{|m|}\right)^m$$

This allows us to rewrite (8.5a) and (8.5b) in the following far-field specific asymptotic forms:

$$E_\theta(\underline{r}) = \frac{norm\, k}{\sqrt{\eta}}\sum_{n=1}^{\infty}\sum_{m=-n}^{n}j^n e^{jm\phi}\left[-B^1_{mn}\left[\frac{m}{\sin\theta}\overline{P}^{|m|}_n(\cos\theta)\right] + B^2_{mn}\left[\frac{\partial\overline{P}^{|m|}_n(\cos\theta)}{\partial\theta}\widehat{\underline{e}}_\theta\right]\right]\frac{e^{-jkr}}{kr}$$

$$E_\phi(\underline{r}) = \frac{norm\, k}{\sqrt{\eta}}\sum_{n=1}^{\infty}\sum_{m=-n}^{n}j^{n+1}e^{jm\phi}\left[-B^1_{mn}\left[\frac{\partial\overline{P}^{|m|}_n(\cos\theta)}{\partial\theta}\right] + B^2_{mn}\left[\frac{m}{\sin\theta}\overline{P}^{|m|}_n(\cos\theta)\right]\right]\frac{e^{-jkr}}{kr} \tag{8.23a}$$

$$H_\theta(\underline{r}) = norm\ k\sqrt{\eta}\sum_{n=1}^{\infty}\sum_{m=-n}^{n} j^{n+1}e^{jm\phi}\left[B_{mn}^{1}\left[\frac{\partial\overline{P}_n^{|m|}(\cos\theta)}{\partial\theta}\right] - B_{mn}^{2}\left[\frac{m}{\sin\theta}\overline{P}_n^{|m|}(\cos\theta)\right]\right]\frac{e^{-jkr}}{kr}$$

$$H_\phi(\underline{r}) = norm\ k\sqrt{\eta}\sum_{n=1}^{\infty}\sum_{m=-n}^{n} j^{n}e^{jm\phi}\left[-B_{mn}^{1}\left[\frac{m}{\sin\theta}\overline{P}_n^{|m|}(\cos\theta)\right] - B_{mn}^{2}\left[\frac{-\partial\overline{P}_n^{|m|}(\cos\theta)}{\partial\theta}\right]\right]\frac{e^{-jkr}}{kr} \tag{8.23b}$$

Equations (8.23a) and (8.23b) represent two simplified expressions allowing us to evaluate the far-field from a set of SMC's in a very efficient manner.

8.9 Practical acquisition schemes and examples

The classical definition of the spherical coordinate system as presented above employs the following angular limits: $0^\circ \leq \theta \leq 180^\circ$ and $0^\circ \leq \phi \leq 360^\circ$ and we see that both angles are always positive numbers.[13] We will refer to this mode as *Phi_360*. In practice, it is often found that SNF data files are acquired using the following acquisition axis limits[14]: $-180^\circ \leq \theta \leq 180^\circ$ and $0^\circ \leq \phi \leq 180^\circ$. We will refer to this mode as *Phi_180*.

A third possible SNF acquisition scenario is where the following acquisition axis limits are used: $-180^\circ \leq \theta \leq 180^\circ$ and $0^\circ \leq \phi \leq 360^\circ$. We will refer to this mode as the *Redundant case* since the surface of the sphere is covered twice. These three scenarios can be represented graphically as shown in Figure 8.42. The grey-scale image represents measured amplitude (for only one polarisation component) with the θ angle shown on the horizontal axis and the ϕ angle on the vertical axis. The complete image represents the *Redundant case* and it is clear that the measured beam peak appears twice. The lower half of the *Redundant case* represents the *Phi_180* case and this is outlined by the solid box in Figure 8.42. The right half of the *Redundant case* represents the *Phi_360* case[15] and this is outlined by the dashed box in Figure 8.42. With the exception of unit vector reversal (and the associated phase reversal), the *Phi_180* and *Phi_360* cases are theoretically identical since each region contains all the relevant information covering the full sphere. However, in practice, it is often found that one acquisition mode has certain advantages over the other. For instance, their sensitivities to typical alignment errors or chamber

[13]More information on spherical coordinate systems and the range of spherical angles is presented within Chapter 12.

[14]This convention presumably arose from the use of legacy roll/azimuth positioner-based far-field ranges where continuous azimuth radiation pattern cuts were taken for select roll positions.

[15]It is worthwhile to note that an equivalent *Phi_360* region for $\theta < 0^\circ$ can be defined. This is represented by the left half of the *Redundant case* image in Figure 8.42, not enclosed by any box.

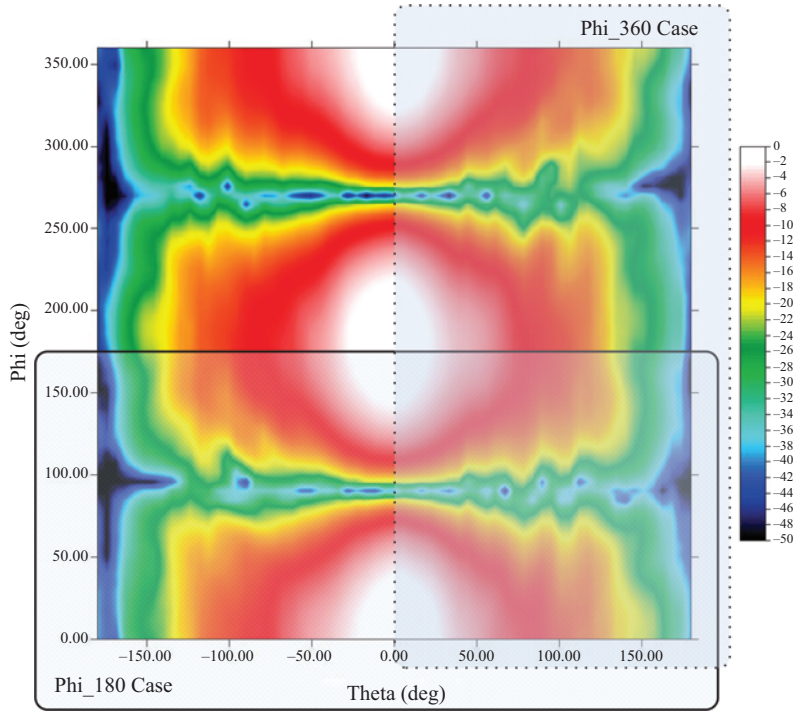

Figure 8.42 SNF data sets can be acquired in three different modes. Full image is the redundant case, the lower portion in the solid line box is the Phi_180 case and the right portion in the dashed box is the Phi_360 case

reflection effects may vary significantly and therefore it may be beneficial in some cases to select the one acquisition mode over the other. By simply inspecting the full greyscale image in Figure 8.42, it becomes obvious that the regions of duplication do differ slightly and these differences are caused by such measurement effects.

When comparing the *Phi_180* and *Phi_360* cases, one realises that when using a ϕ/θ positioner as depicted in Figure 8.1, the *Phi_180* acquisition case rotates the θ positioner a full 360° and the face of the upper ϕ-stage (and therefore the AUT) faces all four walls of the anechoic chamber during the course of the measurement. In the case of the *Phi_360* acquisition, the θ positioner only rotates 180° and the face of the upper ϕ-stage (and therefore the AUT) never faces one side wall of the anechoic chamber during the course of the measurement. In the case of the alternate *Phi_360* acquisition for $\theta < 0°$, the θ positioner again only rotates 180° and the face of the upper ϕ-stage now faces the opposite side wall of the anechoic chamber during the measurement. Barring any positioner misalignment, this aspect therefore

gives one the ability to compare reflectivity levels in one half of the chamber vs. the other. This aspect can be used as a diagnostic tool during range assessments.

When faced with a redundant data set, we have several options available to us. Simplest is to simply select that portion of the data set of interest to us and allow one to compare *Phi_180* and *Phi_360* results. Another interesting option is to average these two data sets to obtain a single sphere set containing averaged data. This is easily achieved by simply doing a complex average with a phase reversal to account for unit vectors that change direction. This technique is often employed to counter the effect of RF drift, mechanical misalignment or unwanted chamber reflections (this is often used when calibrating probes, c.f. Chapter 12). However, one should always attempt to correct problems at their root instead of relying on such a broad-brush approach.

To understand the advantages of selecting one type of SNF acquisition scheme over another, it is worthwhile to discuss the concepts of 'poles' and 'seams' in SNF data sets. In Figure 8.43, the three vertical arrows indicate sphere pole locations. The *North Pole* arrow at $\theta = 0^\circ$ is the case where the ϕ-axis is pointed at the SNF probe. The two *South Pole* arrows at $\theta = -180^\circ$ and $\theta = 180^\circ$ is the case where the ϕ-axis is pointed 180° away from the SNF probe. Both of these poles represent a single data point on the sphere where the only change is the ϕ variation from 0° to 360°.

The three horizontal lines in Figure 8.43 denote possible sphere seam locations. These are lines along the sphere where the acquired data is joined and where measurement imperfections may lead to discontinuities. The *Seam 0* line at $\phi = 0^\circ$ and the *Seam 180* line at $\phi = 180^\circ$ form such a seam for the *Phi_180* case. The *Seam 0* line at $\phi = 0^\circ = 360^\circ$ form such a seam for the redundant case. For the *Phi_360* case, only half of the *Seam 0* line at $\phi = 0^\circ = 360^\circ$ forms a seam in the sphere. When near-field data sets are inspected for fidelity, it is always worthwhile to check for amplitude and phase discontinuity across any sphere acquisition seam since measurement imperfections can introduce these. If such a discontinuity is present in a region of high energy, it may introduce unwanted artefacts in derived far-field data.

A discontinuity across the seam of a sphere must preferably be corrected by improving scanner alignment (should that be the prime cause – details of spherical alignment are presented in Chapter 12), but often RF sub-system scanner drift can be the cause and this may be impossible to address. In such instances, simply switching the acquisition scheme to relocate the seam of the sphere with respect to the region of high energy radiation can circumvent the problem by allowing the discontinuity to exist in a region of low energy and therefore have a negligible impact on the derived far-field. This is easily achieved by switching the acquisition scheme or simply offsetting the AUT in ϕ by a fixed value.

The data presented in Figure 8.43 is for a horn antenna principally radiating along the ϕ-axis and since the main beam of the horn is centred on the North pole of the sphere it is also referred to as a polar measurement. There is of course nothing preventing one from mounting the AUT such that it radiates orthogonal to the ϕ-axis and in such a case the main beam will be found along a portion of the

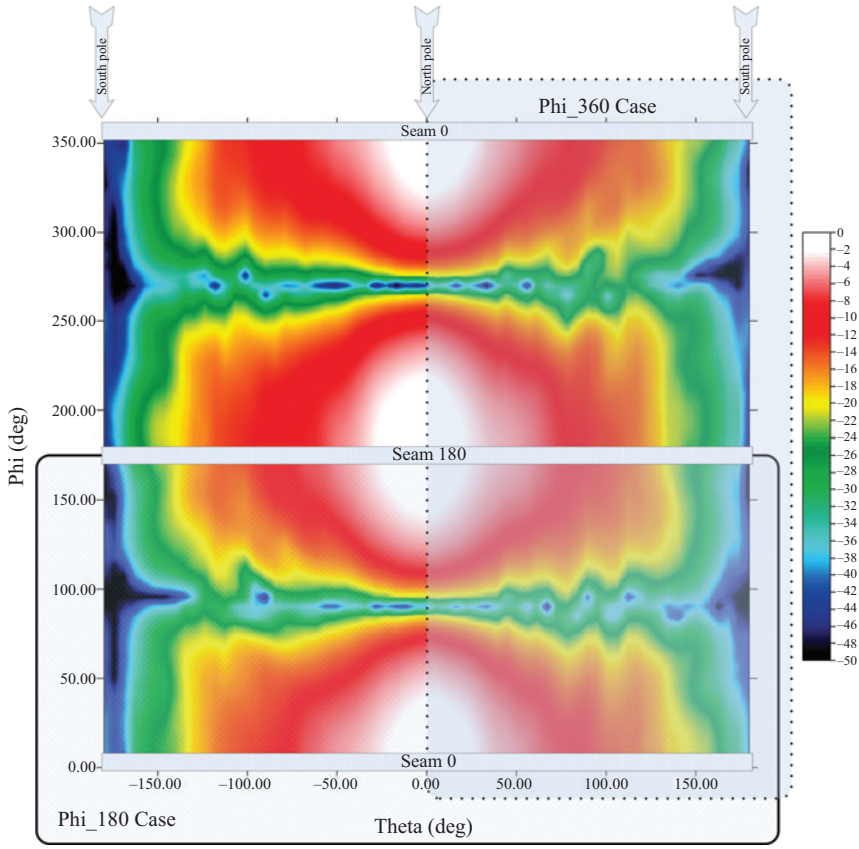

Figure 8.43 SNF data set 'poles' and 'seams' shown. Full image is the redundant case, the lower portion in the solid line box is the Phi_180 case and the right portion in the dashed box is the Phi_360 case

equator of the sphere. This type of measurement is also referred to as an equatorial measurement. A typical equatorial mounting scheme is shown in Figure 8.44. In this image, the ϕ-axis is coaxial to the circular support post behind the AUT and the θ-axis is the positioner on the floor. In this image, the AUT is shown facing the near-field probe at $\theta = 90°$ and $\phi = 180°$.

If this AUT is measured using a *Phi_180* acquisition scheme, the main beam of the AUT (which is broadside to the array face shown) will be located on *Seam 180* of the sphere and one would have to guarantee no discontinuity across this seam since the region of maximum energy will be located here. By simply switching to a *Phi_360* acquisition, the seam will be moved to the $\phi = 0° = 360°$ location, which is a region of low energy and the probability of introducing any discontinuity in the region of highest near-field energy, is minimized.

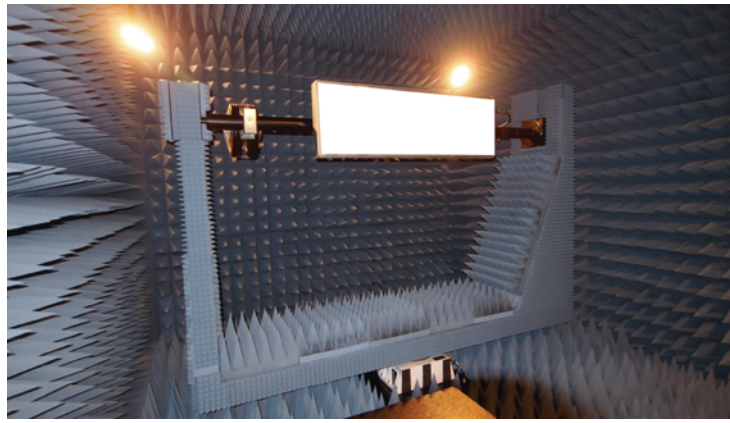

Figure 8.44 An AUT is mounted in an equatorial fashion. The ϕ-axis is coaxial to the circular support post behind the AUT, and the θ-axis is the positioner on the floor. In this image, the AUT is shown facing the near-field probe

Equatorial acquisition schemes are often employed as they can allow a larger AUT to be installed within the SNF system than would be the case for a polar measurement. The far-field data can be presented in exactly the same form, irrespective of the way in which the near-field data was acquired. Information on pattern rotation is provided in Chapter 12.

8.10 Radial distance correction

An assumption that is at the kernel of the SNF theory presented here is that near-field data is acquired at a fixed radial distance. As a result, all the practical implementation schemes described earlier, attempt to create such an ideal spherical surface. However, as with many linear parameters in the near-field process, variation in terms of wavelength is critical and one finds that when applying SNF test systems at higher frequencies, variation of radial acquisition distance becomes a limiting parameter. The articulating arm scanner presented in Section 8.2 is an example of a system where radial distance variation can become limiting. For such a system, scanner structural and positioning performance data can be obtained from laser tracker dimensional measurements (test setup depicted in Figure 8.45). These results allow one to establish a perturbed (θ', ϕ', r') grid, based on a regular (θ, ϕ, r) SNF grid. Due to visual blockage of the structure only a portion $(-110^\circ \leq \theta \leq +110^\circ)$ of the sphere can be measured. The data measured for the three spherical variables (θ', ϕ', r') are compared to (θ, ϕ, r) to assess effective errors. Figure 8.46 shows radial the distance error (variable $r' - r$) in mm as a function of variable ϕ for seven distinct values of variable θ. The curve depicting $\theta = 0^\circ$ (a solid curve without any designated symbol) represents the polar case where the SNF probe is

Figure 8.45 Structural measurement using a laser tracker. Note that only a portion of the full spherical surface can be evaluated

ideally located in one position and simply rotates its polarisation angle as a function of rotation in ϕ. Instead of observing a fixed zero error, we observe a variation that approximates a co-sinusoidal curve with a peak-to-peak amplitude of ± 0.3 mm. This behaviour is a direct consequence of structural deformation of the arms as well as the θ and ϕ rotary stages due to gravity.

Also noteworthy in Figure 8.46 are the two curves depicting $\theta = \pm 90^\circ$ (solid and dashed curves with ■ symbol). These two cases represent the equatorial motion of the SNF probe and the extreme deformation condition. We again observe a variation that approximates a co-sinusoidal curve with a peak-to-peak amplitude of ± 0.75 mm which is due to gravitational deformation. We also observe an offset between the two cases of roughly 0.25 mm and this may be attributed to non-intersection of the θ and ϕ axes and can be corrected for by shimming of the θ stage.

Figure 8.47 represents the radial distance variation for the scanner as a function of the spherical variables (θ,ϕ) and is displayed as a false colour image. This colour map is obtained through laser tracker measurement and extrapolation to approximate deformation in regions that cannot be directly measured. We can refer to this as an error map for the radial distance r. If this variation of r is repeatable, we can venture to apply a correction technique to negate the impact. This can be done by adding a mechanical translation stage to the scanner and moving the probe assembly in a radial direction to counter for this error. However, often correction for errors in r is not possible through hardware in the absence of a linear radial actuator. An alternative is to consider a near-field phase correction based upon this

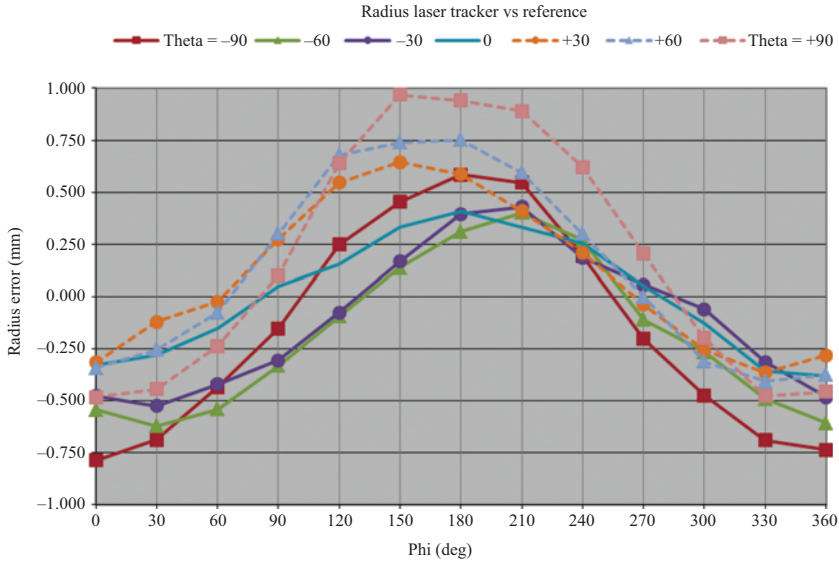

Figure 8.46 Structural laser tracker measurement showing r' error as a function of ϕ variable. Curves represent discrete values of the θ variable

error map. To implement this correction, an electrical phase value is calculated for each SNF probe position as

$$\Delta\Phi(\theta,\phi) = k[r'(\theta,\phi) - r] \tag{8.24}$$

and this phase term can then be subtracted from the measured SNF data as a first-order phase-only, correction term. The effect of this is to remove the phase impact of the radial structural variation and create a condition where variation in r' is reduced and ideally, removed.

To illustrate the impact of this radial distance variation and correction thereof on high frequency measurements, one can do the following simulation. In the first instance (case #1), we consider a half wavelength dipole radiating at 75 GHz and we locate it at the coordinate system origin. In the second instance (case #2), we consider a 6 mm $\times$ 6 mm square aperture radiating at 75 GHz, located at the coordinate origin and facing the sphere equator. In the third instance (case #3), we again consider a 6 mm $\times$ 6 mm square aperture radiating at 75 GHz, located at the coordinate origin but now facing the sphere pole. In all instances, the probe radial distance is set to 556.7 mm (139λ at 75 GHz), to coincide with the actual test hardware. For case #2, we also consider an offset of the simulated aperture by 80 mm to increase the required SNF sampling density. This is done to assess the sensitivity of the process to higher angular sampling density and to stress the test case by not having our AUT conveniently located on the coordinate origin.

The radial distance variation from laser tracker measurements were found to be approximately ± 1 mm (depicted in Figure 8.47), which translates to roughly $\pm 90^\circ$

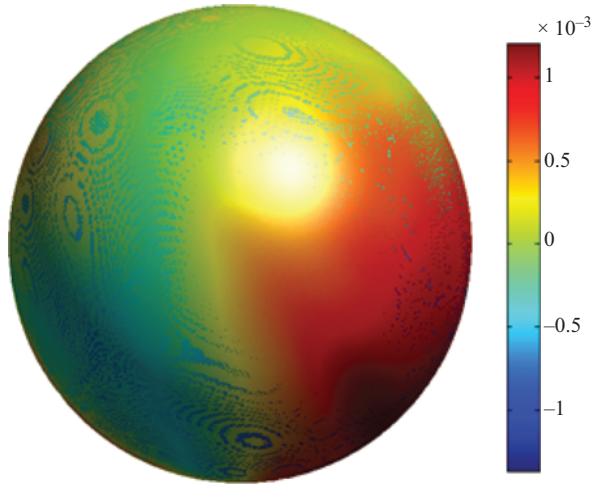

Figure 8.47 Structural laser tracker measurement showing r' error as a function of (θ,ϕ) as false colour image [m] on the spherical surface

of phase change at the simulation frequency (75 GHz). For the dipole example (case #1), we obtain the patterns shown in Figure 8.48. The solid line is the ideal dipole reference pattern and the dashed line represents the simulation, where the measured radial variation of the scanner has been imposed in our simulation. The difference between these two radiation patterns show an error-to-signal level (this concept is introduced in Chapter 10) due to this variation of roughly −12 dB, peak value. If we now apply the first-order phase correction, we see the simulated case coincides closely with the reference case and the error-to-signal level diminishes to less than −50 dB.

For case #2, we consider a higher directivity antenna and the principal radiation takes place towards the equator of the sphere, as shown in Figure 8.49. For the scanner being considered here, this is the case of the antenna radiating towards the ceiling of the chamber so as to emulate many on-chip antenna measurement cases. As for the dipole case considered first, reference and perturbed patterns are compared to assess the impact of the probe radial position error as measured using the laser tracker and we then do the first-order phase correction, so assess the success of this on the test case. The results are shown in Figure 8.50 where we again have a reference pattern, a perturbed pattern (due to the radial distance variation) and an error-to-signal pattern. On the left-hand side, we show the impact before first-order phase correction and on the right, after. Here, we see a roughly 40 dB improvement in terms of the error-to-signal level, attesting to the impact of this radial distance variation at this frequency and the success of the correction technique.

We next consider a variation of case #2, where the radiating aperture is offset from the coordinate origin by 80 mm. The aperture is still radiating towards the equator of the sphere, but a much higher SNF sampling density is now required,

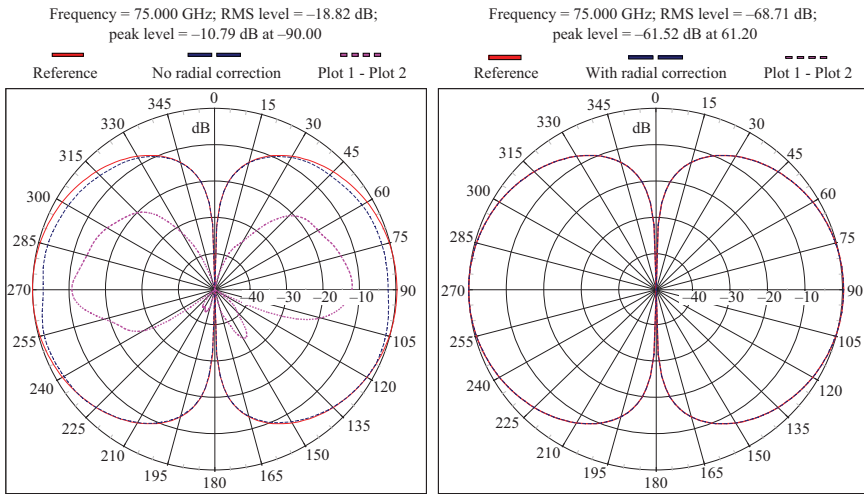

Figure 8.48 Dipole located on the z-axis (case #1) simulation. The reference pattern is shown (solid), and the simulation subject to the radial distance variation is shown as the dashed pattern, only visible on the left. An error-to-signal pattern is also shown and is only evident on the left, with a peak value of −12 dB. The patterns on the right are after the first-order phase correction

due to the increase in *MRE*. The results are shown in Figure 8.51 where we again have a reference pattern, a perturbed pattern (due to the radial distance variation) and an error-to-signal pattern. On the left-hand side, we show the impact before first-order phase correction and on the right, after. Here, we see a roughly 30 dB improvement in terms of the error-to-signal level. Except for some minor differences observed at the 160°–180° angular region, the first-order phase correction for the radial distance variation again seems to be working well.

For case #3, we consider a higher directivity antenna and the principal radiation takes place towards the pole of the sphere, as shown in Figure 8.52. For the scanner being considered here, this is the case of the antenna radiating towards the ϕ stage of the scanner so as to emulate a forward radiating measurement case, as shown. As for the two cases considered before, reference and perturbed patterns are compared to assess the impact of the probe radial position error as measured using the laser tracker and we then do the first-order phase correction, so assess the success of this on the test case. The results are shown in Figure 8.53 where we again have a reference pattern, a perturbed pattern (due to the radial distance variation) and an error-to-signal pattern. On the left-hand side, we show the impact before first-order phase correction and on the right, after. Here, we see a roughly 35 dB improvement in terms of the error-to-signal level, attesting to the impact of this

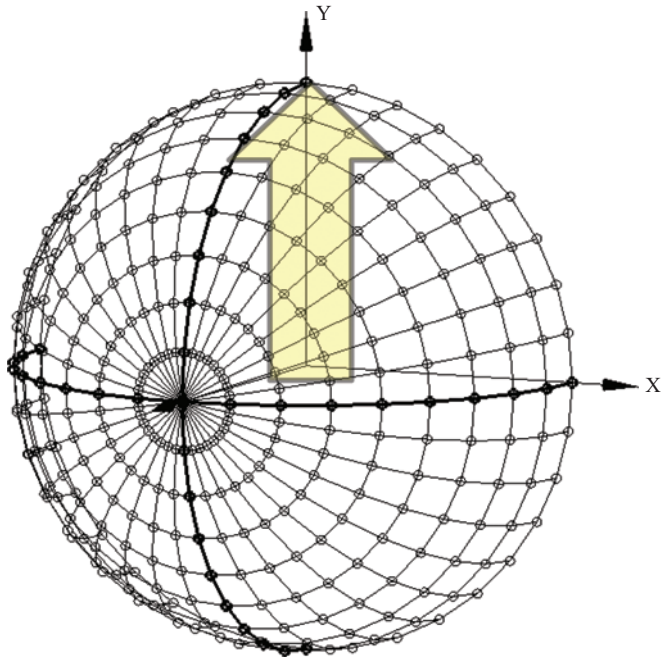

Figure 8.49 *For case #2, we consider a higher directivity antenna and the principal radiation takes place towards the equator of the sphere. For the scanner being considered here, this is the case of the antenna radiating towards the ceiling of the chamber*

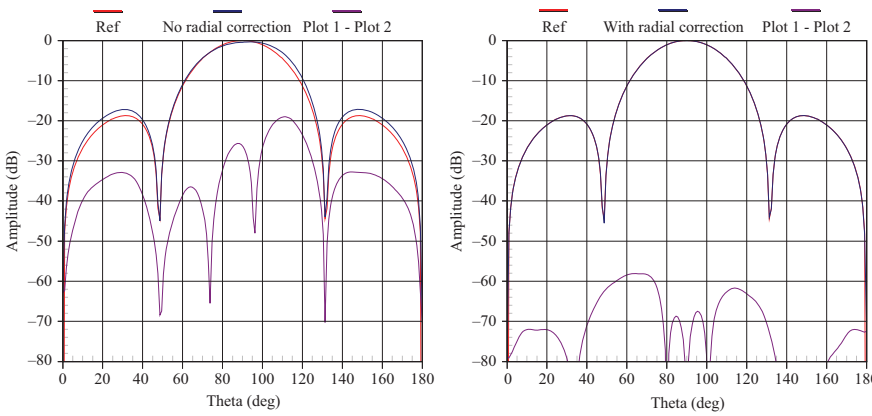

Figure 8.50 *Radiation patterns for case #2, a reference pattern, a perturbed pattern (due to the radial distance variation) and an error-to-signal pattern. On the left, we show the impact before first-order phase correction and on the right, after*

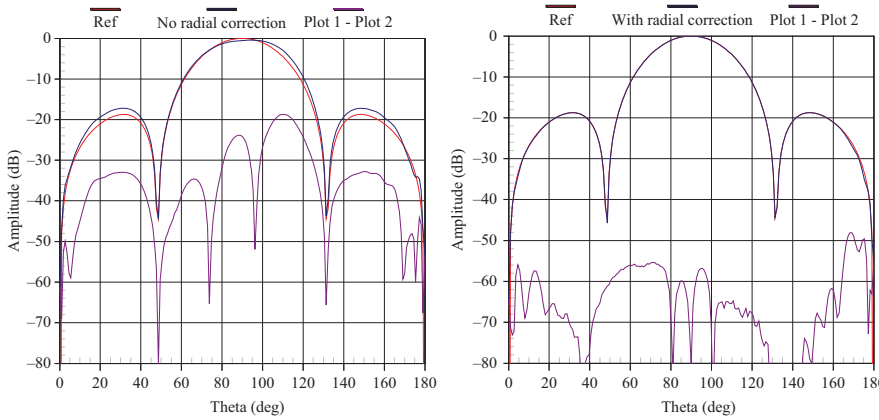

Figure 8.51 *Radiation patterns for case #2 with an 80 mm offset from the coordinate origin. A reference pattern, a perturbed pattern (due to the radial distance variation) and an error-to-signal pattern. On the left, we show the impact before first-order phase correction and on the right, after*

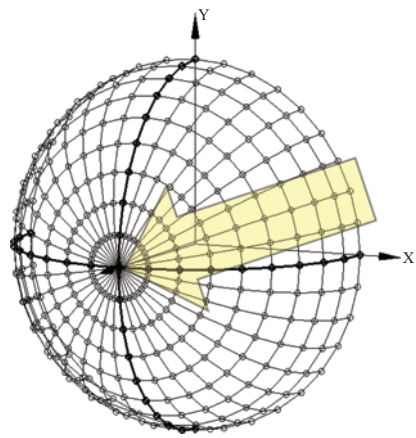

Figure 8.52 *For case #3, we consider a higher directivity antenna and the principal radiation takes place towards the pole of the sphere. For the scanner being considered here, this is the case of the antenna radiating towards the ϕ stage of the scanner*

radial distance variation at this frequency and the success of the correction technique.

As an experimental test case, we measured a horn antenna (depicted in Figure 8.54) where the principal radiation takes place towards the pole of the sphere. The test data at 90 and 110 GHz are shown in Figure 8.54. Since we did not have the

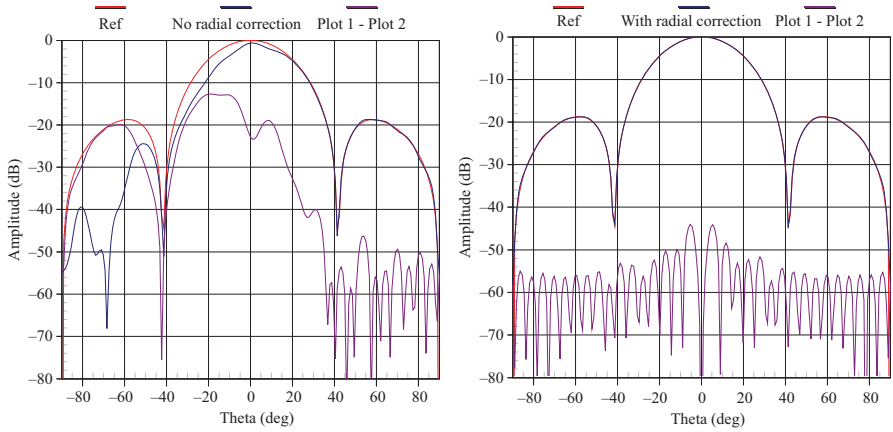

Figure 8.53 Radiation patterns for case #3, a reference pattern, a perturbed pattern (due to the radial distance variation) and an error-to-signal pattern. On the left, we show the impact before first-order phase correction and on the right, after correction

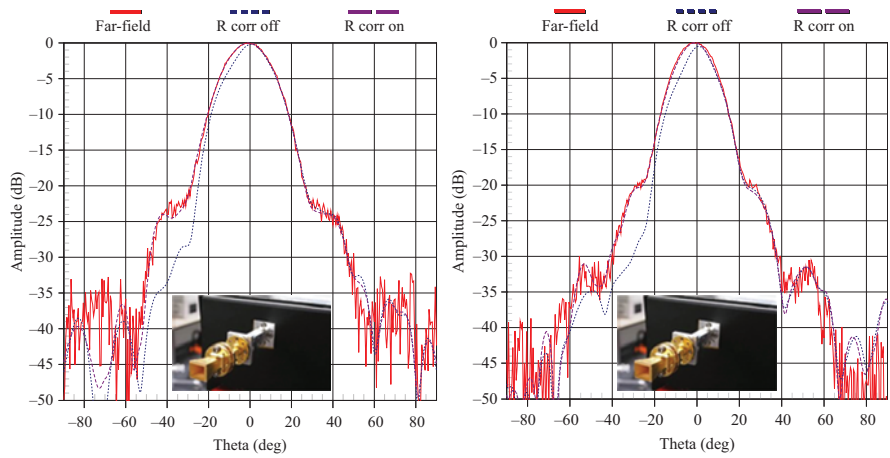

Figure 8.54 Far-field reference pattern (solid) is shown overlaid with SNF derived far-field patterns for cases where no radial phase correction is applied (–) and where radial phase correction is applied (- -). Result at 90 GHz is shown on the left and 110 GHz on the right

convenience of a computed reference pattern here, far-field radiation patterns were used for that purpose (they are shown as the solid line patterns and their noisy nature is evident). The measured SNF radiation patterns without radial distance correction are evident and unsatisfactory. This result is not surprising, given that the ± 1 mm variation will translate to $\pm 108^{\circ}$ of electrical phase at 90 GHz and to

$\pm 132^\circ$ at 110 GHz. Correcting for the measured radial distance variation leads to the corrected radiation patterns in Figure 8.54 and these resemble the far-field radiation patterns (without the noisy behaviour – a benefit of the spherical wave expansion).

As a final word on the correction of radial variations in SNF testing, an important aspect to highlight is the fact that as one considers applying near-field test methods to ever-increasing test frequencies, one inevitably runs into fabrication or implementation limitations. These limitations set an absolute limit on what can be achieved in terms of positional accuracy and repeatability. If we are to be successful in expanding these boundaries, we must become creative and instead of trying to build absolutely rigid scanners of high structural fidelity, rather record spatial coordinates of acquisition real-time and adapt our transformation technology to rely on this information. This philosophy will set us free from trying to recreate a measurement surface that conforms to our preconceived mathematical formulations (planar, cylindrical or spherical surfaces) and rather place the focus on measuring spatial coordinates during measurement. The techniques presented in Chapter 9 open the avenue for this type of approach and represents some of the newest development in antenna measurements today.

8.11 Summary

From the material presented here, it is clear that the theory underlying the SNF approach is complex and involved to implement. However, it is also very elegant and provides one with many measurement options and powerful capabilities. The numerical implementation of the theory can be efficiently deployed through the use of the fast Fourier transform (FFT) enabling transforms of even electrically large antennas to be accomplished in a matter of a few seconds on a modern powerful computer. With the advent of commercially available SNF test systems, the user can exploit these techniques, largely unimpeded by the burden of the theory or the implementation thereof. The material presented here highlighted some of the fundamental concepts and limitations the user needs to be aware of in order to use these test systems with confidence.

References

[1] J. A. Stratton, *Electromagnetic Theory*, McGraw-Hill, 1941.
[2] R. F. Harrington, *Time Harmonic Electromagnetic Fields*, McGraw-Hill, 1961.
[3] J. E. Hansen, *Spherical Near-field Antenna Measurements*, Peter Peregrinus, 1988.
[4] A. W. Rudge, K. Milne, A. D. Olver & P. Knight, *The Handbook of Antenna Design, Volumes 1 & 2*, Peter Peregrinus, 1986. (Chapter 8: Antenna Measurement by J Appel-Hansen, E S Gillespie, T G Hickman & J D Dyson.)

[5] A. D. Yaghjian, "An overview of near-field antenna measurements," *IEEE Transactions on Antennas and Propagation*, vol. 34, no. 1, pp. 30–45, 1986.
[6] G. Hindman & H. Tyler, "High accuracy spherical near-field measurements on a stationary antenna," Antenna Measurement Techniques Association Conference 2010.
[7] D. J. Janse van Rensburg & J. Wynne, "Parametric study of probe positioning errors in spherical near-field test systems for mm-wave applications," North American Radio Science Meeting Digest – URSI 2012, Chicago, USA, July 2012.
[8] D. J. Janse van Rensburg and S. F. Gregson, "Parametric study of probe positioning errors in articulated spherical near-field test systems for mm-wave applications," CAMA 1'st Annual Conference, Nice, France, Nov. 2014.
[9] P. N. Betjes, D. J. Janse van Rensburg and S. F. Gregson, "An articulated swing arm system for spherical near-field antenna measurements at millimeter wave frequencies," 36th ESA Antenna Workshop on Antennas and RF Systems for Space Science, Noordwijk, The Netherlands, Oct. 2015.
[10] D. J. Janse van Rensburg and P. Betjes, "Structural Correction of a Spherical Near-Field Scanner for mm-Wave Applications," AMTA 37th Annual Meeting & Symposium, Long Beach, CA, USA, Oct. 2015.
[11] D. Novotny, J. Gordon, J. Coder, M. Francis & J. Guerrieri, "Performance evaluation of a robotically controlled millimeter-wave near-field pattern range at the NIST," 7th European Conference on Antennas and Propagation (EuCAP), pp. 4086–4089, 8–12 April 2013.
[12] D. J. Janse van Rensburg, B. Walkenhorst, Q. Ton and J. Demas, "A robotic near-field antenna test system relying on non-canonical transformation techniques," AMTA 41st Annual Meeting & Symposium, San Diego, CA, USA, Oct. 2019.
[13] M. Abramowitz, I.A. Stegun, Eds., *Handbook of Mathematical Functions with Formulas, Graphs, and Mathematical Tables*, Dover Publications, Standard Book Number: 486-61272-4, 1964.
[14] J. E. Hansen, *Spherical Near-field Antenna Measurements*, Peter Peregrinus, 1988, p. 13.
[15] C. A. Balanis, *Antenna Theory Analsysis & Design*, Wiley, 2005, p. 1085.
[16] M. Abramowitz, I.A. Stegun, Eds., *Handbook of Mathematical Functions with Formulas, Graphs, and Mathematical Tables*, Dover Publications, Standard Book Number: 486-61272-4, 1964, p. 439, Eq. 10.2.21.
[17] J.H. Bruning & Y. Lo, "Multiple scattering of EM waves by spheres part I– Multipole expansion and ray-optical solutions," *IEEE Transactions on Antennas and Propagation,* vol. 19, no. 3, pp. 378–390, 1971.
[18] M. Abramowitz, I.A. Stegun, Eds., *Handbook of Mathematical Functions with Formulas, Graphs, and Mathematical Tables*, Dover Publications, Standard Book Number: 486-61272-4, 1964, p. 775.
[19] A. R. Edmonds, *Angular Momentum in Quantum Mechanics*, Princeton University Press, 1974, p. 46.

[20] A. Ludwig, "Near-field far-field transformations using spherical-wave expansions," *IEEE Transactions on Antennas and Propagation*, vol. 19, no. 2, pp. 214–220, 1971.
[21] J. E. Hansen, *Spherical Near-field Antenna Measurements*, Peter Peregrinus, 1988, p. 20.
[22] F. Jensen & A. Frandsen, "On the number of modes in spherical expansions," AMTA 26th Annual Meeting & Symposium, Stone Mountain, GA, Oct. 2004.
[23] J. E. Hansen, *Spherical Near-field Antenna Measurements*, Peter Peregrinus, 1988, p. 19.
[24] J. E. Hansen, *Spherical Near-field Antenna Measurements*, Peter Peregrinus, 1988, p. 129.
[25] J. E. Hansen, *Spherical Near-field Antenna Measurements*, Peter Peregrinus, 1988, p. 330.
[26] J. E. Hansen, *Spherical Near-field Antenna Measurements*, Peter Peregrinus, 1988, p. 42.
[27] J. E. Hansen, *Spherical Near-field Antenna Measurements*, Peter Peregrinus, 1988, p. 319.
[28] P.F. Wacker, "Near-field antenna measurements using a spherical scan: efficient data reduction with probe correction," Conf. on Precision Electromagnetic Measurements, IEE Conf. Publ. No. 113, pp. 286–288, London, UK, 1974.
[29] J. E. Hansen, *Spherical Near-field Antenna Measurements*, Peter Peregrinus, 1988, p. 111.
[30] A. C. Newell & S. F. Gregson, "Estimating the effect of higher order modes in spherical near-field probe correction," AMTA 34th Annual Meeting & Symposium, Seattle, WA, Oct. 2012.
[31] A. C. Newell & S. F. Gregson, "Higher order mode probes in spherical near-field measurements," EuCAP, Gothenburg, Apr. 2013.
[32] A. C. Newell & S. F. Gregson, " Estimating the effect of higher order modes in spherical near-field probe correction," AMTA 35th Annual Meeting & Symposium, Columbus, OH, Oct. 2013.
[33] S. Gregson, J. McCormick & C.G. Parini, "Principles of Planar Near Field Antenna Measurements," Appendix A, pp 347–354, IET Publications, 2007, ISBN 978-86341-736-8.
[34] T. A. Laitinen, S. Pivnenko & O. Breinbjerg, "Odd-order probe correction technique for spherical near-field antenna measurements," *Radio Science*, vol. 40, no. 5, 2005.
[35] T. A. Laitinen & O. Breinbjerg, "A first/third-order probe correction technique for spherical near-field antenna measurements using three probe orientations," *IEEE Transactions on Antennas and Propagation*, vol. 56, pp. 1259–1268, 2008.
[36] T. Laitinen, J. M. Nielsen, S. Pivnenko & O. Breinbjerg, "On the application range of general high-order probe correction technique in spherical near-

field antenna measurements," presented at the 2nd Eur. (EuCAP'07), Edinburgh, UK, Nov. 2007.

[37] T. A. Laitinen, S. Pivnenko & O. Breinbjerg, "Theory and practice of the FFT/matrix inversion technique for probe-corrected spherical near-field antenna measurements with high-order probes," *IEEE Transactions on Antennas and Propagation*, vol. 58, no. 8, pp. 2623–2631, 2010.

[38] C. H. Schmidt, M. M. Leibfritz & T. F. Eibert, "Fully probe-corrected near-field far-field transformation employing plane wave expansion and diagonal translation operators," *IEEE Transactions on Antennas and Propagation*, vol. 53, no. 3, pp.737–746, 2008.

[39] F. Saccardi, A. Giacomini & L. J. Foged, "Probe correction technique of arbitrary order for high accuracy spherical near field antenna measurements," AMTA 2016, Oct. 30–Nov. 4, Austin, TX, USA.

[40] F. Saccardi, A. Giacomini, L. M. Tancioni & L. J. Foged, "Full Probe Corrected Spherical Near Field Measurement Technique using Standard Wideband Antennas as Probes," EuCAP 2018, 9–13 April, London, England.

[41] T. B. Hansen, "Spherical near-field scanning with higher-order probes," *IEEE Transactions on Antennas and Propagation*, vol. 59, no. 11, pp. 4049–4059, 2011.

[42] S. Pivnenko, O. S. Kim, J. M. Nielson & O. Breinbjerg, "Higher-order near-field probes," DTU Report D10, ESTEC Contract No. 22812/09/NL/JD/al, 2012.

[43] J. E. Hansen, *Spherical Near-field Antenna Measurements*, Peter Peregrinus, 1988, p. 315.

Chapter 9

Antenna field transformation from non-canonical surfaces

9.1 Introduction

This chapter aims to address the need to perform near-field antenna measurements with improved flexibility as compared to the traditional approaches of canonical measurement surfaces using regular sampling. Inspired by the enormously powerful so-called fast integral equation solvers known from computational electromagnetics, we will derive computationally very efficient but still very flexible inverse equivalent source solvers (IESSs) for the transformation of measured near-field data into a set of equivalent sources, which can in turn be used to calculate near and far-fields anywhere in the solution domain. This enables near-field antenna measurements to be made on non-canonical surfaces and/or with irregular grids. A by-product of these IESSs is that they allow a very flexible modelling of the antenna under test (AUT), which can, with the inclusion of a priori knowledge about the geometric extent of the AUT, provide 'measured' currents on the antenna structure. This approach also offers the possibility of reducing measurement errors by spatial filtering as well as enabling parts of the AUT sources, or of additional echo/scattering sources within the measurement environment, to be ignored or modified in post-processing steps to achieve further improvement of the measurement results or to gain further diagnostic insight.

The antenna field transformations discussed in the previous chapters were all based on an expansion of the antenna radiation fields into modal solutions of Maxwell's equations, where field modes in Cartesian, cylindrical, and spherical coordinate systems have been considered. Such field modes represent a complete set of vector expansion functions for the radiation fields and the individual modes are mutually orthogonal when evaluated on the corresponding coordinate surfaces, e.g., on planes, cylinders, or spheres. Based on regular equidistant sampling of the measured fields on these coordinate surfaces and by utilising fast Fourier transform (FFT) algorithms, it was possible to realise highly efficient and very robust antenna field transformations for the corresponding, very specialised NF antenna measurement configurations. The enormous efficiency and accuracy of these field transformation approaches was certainly an important reason for the great success of NF antenna measurements during the past few decades, and it was very common in the antenna measurement community to adapt the measurement hardware and

configuration to the needs of the available field transformation approaches. In principle, it was certainly also clear how to perform antenna field transformations for irregularly spaced measurement samples on non-canonical surfaces. However, the available algorithms and the available computers were not powerful enough to render such field transformations and the corresponding measurements competitive.

Besides the considerable growth of computer power during the past few years, it was in particular the enormous success of fast integral equation solvers in the field of computational electromagnetics [1–3], which has eventually led to very powerful antenna field transformation algorithms for irregularly sampled non-canonical measurement surfaces. Such algorithms do not only support irregular sampling on the measurement surfaces, but they are commonly also based on very flexible radiation models of the AUT.

In this chapter, we call such transformation approaches IESSs, since they represent the AUT radiation by equivalent sources. These sources exist in a volume comprising the actual AUT volume, and knowledge about the size and shape of the AUT can thus be considered in setting up the equivalent radiation model. Most equivalent radiation models do not work with volumetric source distributions, but they assume surface sources on the surface of the equivalent AUT model, based on the well-known Huygens and/or equivalence principles of electromagnetics. First equivalent surface source solvers date back to the 1990s, where flexible planar surface current models were combined with FFT evaluations of the radiation operators for planar, equidistant measurements [4,5]. Fully three-dimensional solvers became popular not before the late 2000s, where [6] presents a general integral equation approach which was later accelerated by the Fast Multipole Method (FMM) [7,8]. In [9–13], three-dimensional IESSs have been presented which extend the basic inverse source approach by a zero-field or Love condition, and in [14] the first three-dimensional IESS accelerated based on the principles of the multi-level fast multipole method (MLFMM) [1,15] was presented. Following the work in [14] and the related approaches in [16,17], which did, however, work with expansions of the radiation fields in propagating plane waves and not with equivalent surface current densities, a series of publications evolved which report on many extensions and results, which make the IESSs very flexible, powerful, and efficient [18–24].

In the following sections, inverse equivalent source-based antenna field transformation algorithms together with the relevant background in electromagnetics and numerical algorithms are introduced, discussed, and evaluated. The considerations start from the basic measurement configuration with non-canonical surfaces and flexible equivalent source representations. Next, important fundamental electromagnetic theorems are recapitulated, before the forward transmission equation with probe correction is introduced and discussed in various forms. Spatial domain formulations are the starting point. However, spectral domain formulations with an expansion in propagating plane waves give further insight and they provide in particular also the basis for the realisation of acceleration approaches similar to the MLFMM, by utilising the concepts of operator factorisation together with

hierarchical operator evaluations. Various equivalent source representations are discussed together with their discretisation by suitable basis functions. Appropriate equivalent source representations of the measurement probes are introduced and a fully discretised representation of the forward transmission problem, from the sources to the measurement signals, is set up. The inversion of the discretised forward problem is performed by iterative linear equation system solvers, which work on a related system of normal equations. Besides the very common normal residual (NR) equations, the normal error (NE) equations are introduced which appear to exhibit certain advantages towards the solution of underdetermined equation systems as mostly encountered in IESSs. A particular focus is then put on the rapid evaluation of the forward operators by multi-level hierarchical algorithms, where a single-level algorithm is introduced first and then extended to a hierarchical multi-level approach. The concept of Gaussian-beam-based translations helps to further speed up the operator evaluation. Some short notes on the additionally required evaluation of the adjoint operators and the operators of the constraint equations follow, before a wide variety of application and evaluation examples is considered in order to demonstrate the capabilities and the performance of modern IESSs. Finally, an extension of the IESSs to transforms above ground half-spaces with arbitrary isotropic material properties is discussed and demonstrated by application examples.

9.2 Measurement configuration with non-canonical surfaces

Let us consider an antenna measurement configuration as illustrated in Figure 9.1, where the AUT is located inside of a source volume V_S and where the measurement samples are collected on a closed surface S_2, which is completely enclosing the source volume. Commonly, the measurement surface is chosen with some distance to the minimum enclosing surface S_1 of the source volume V_S in order to avoid the measurement of strong reactive fields, as well as measurement errors due to mutual interactions between the AUT and the measurement probe. The measurement probe in the following is assumed to be arbitrary within some constraints of usefulness, but its radiation or receiving behaviour is fully known. Also, it is assumed that the measurement sample locations and the orientations of the measurement probe are chosen arbitrarily on the surface S_2, again of course under the constraint of a certain usefulness and with full knowledge of the exact locations and orientations. In general, certain sampling criteria will have to be fulfilled in order to achieve useful results from the application of field transformation approaches. In the following, we will assume that the AUT is operated in transmit mode and the measurement probe in receive mode. However, as long as reciprocity is fulfilled the actual measurements can also be performed in the reverse direction.

The measurement task can be described as follows:

We want to measure sufficiently many field samples, typically in the near-field, in order to obtain the far-field of the AUT and in order to obtain diagnostic

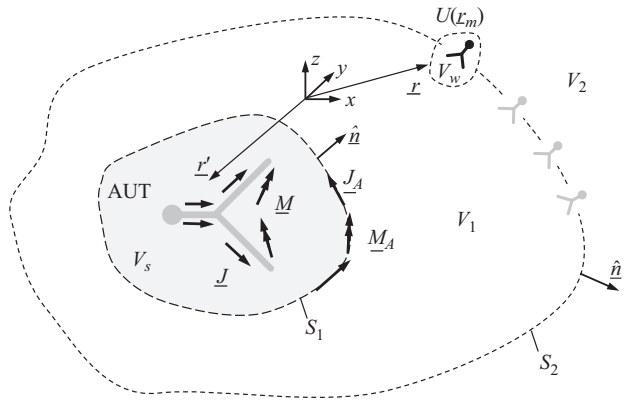

Figure 9.1 Measurement configuration with non-canonical surface: the AUT is located in the source volume V_S enclosed by a closed surface S_1 and its radiation is produced by electric $\underline{J}$ and magnetic $\underline{M}$ current densities within this volume. Near-field observations are collected at arbitrary sample locations $\underline{r}_m$ on an arbitrary surface S_2 located to completely enclose the source volume V_S (in a certain distance). Instead of the original radiation sources, equivalent electric and magnetic surface current densities $\underline{J}_A$ and $\underline{M}_A$, respectively, located on S_1 may produce the radiation fields of the AUT instead of the original sources in V_S

information about the AUT. The second task is commonly equivalent to determining the field distribution or, alternatively, equivalent surface source densities, such as $\underline{J}_A$ and $\underline{M}_A$ as shown in Figure 9.1, very close to the AUT.

In order to solve these tasks, we represent the radiation of the AUT by a set of equivalent sources which are able to correctly represent any possible radiation due to an arbitrary AUT located inside the source volume V_S. The equivalent sources can be selected from a wide collection of choices, where a couple of different options will be discussed later in this chapter. For the moment, we may assume that we work with equivalent electric $\underline{J}_A$ and magnetic $\underline{M}_A$ surface current densities located on the surface S_1 enclosing the source volume V_S, or with volumetric current densities within the volume V_S. In most cases, we may also assume that these sources radiate in a homogeneous solution space such as free space. Later in this chapter, we will see that such a configuration is able to correctly and uniquely represent the AUT radiation fields. Throughout this chapter, it is assumed that mutual interactions between the AUT and the probe antenna can be neglected.

The fundamentals of antenna radiation based on the governing Maxwell's equations have already been discussed in Chapter 2. Here, we rewrite Maxwell's equations for convenience in the form of

$$\begin{aligned}
&\nabla \times \underline{H} = j\omega \underline{D} + \underline{J} \\
&\nabla \times \underline{E} = -j\omega \underline{B} - \underline{M} \\
&\nabla \cdot \underline{D} = \rho \\
&\nabla \cdot \underline{B} = \rho_m
\end{aligned} \tag{9.1}$$

together with material properties

$$\begin{aligned}
&\underline{D} = \varepsilon \underline{E} = \varepsilon_r \varepsilon_0 \underline{E} \\
&\underline{B} = \mu \underline{H} = \mu_r \mu_0 \underline{H} \\
&\varepsilon_r = \varepsilon_r' - j\frac{\sigma}{\omega \varepsilon_0} = \varepsilon_r' - j\varepsilon_r'' \\
&\mu_r = \mu_r' - j\mu_r''
\end{aligned} \tag{9.2}$$

where we allow electric and magnetic equivalent current densities as excitation terms. Also, we note that we consider time harmonic fields with a time convention $e^{j\omega t}$ and all field and material quantities may depend on the spatial position $\underline{r}$.

$\underline{H}$ is the vector magnetic field, ω is the angular frequency related to the frequency f by $\omega = 2\pi f$, $\underline{D}$ is the displacement current density, $\underline{J}$ is the electric volume current density, $\underline{E}$ is the vector electric field, $\underline{B}$ is the vector magnetic induction, $\underline{M}$ is the vector magnetic volume current density, ρ is the electric charge density, and ρ_m is the magnetic charge density.[1] ε_0 is the permittivity of vacuum, μ_0 is the permeability of vacuum, ε_r is the relative permittivity, and μ_r is the relative permeability. The latter two are in general assumed to be complex quantities, where the real part is primed and the negative imaginary part is double primed. Also, the electric conductivity σ is in general assumed to be part of the imaginary part of the permittivity, as seen in (9.2). For our purpose, we can assume that the material properties are linear and isotropic. Also, it should be noted that the surface current densities $\underline{J}_A$ and $\underline{M}_A$ can be assumed as a special choice of volume current densities $\underline{J}$ and $\underline{M}$, e.g., in the form of

$$\underline{J} = \underline{J}_A \delta\left(\hat{\underline{n}}\left(\underline{r}_A\right) \cdot \left(\underline{r} - \underline{r}_A\right)\right), \quad \underline{M} = \underline{M}_A \delta\left(\hat{\underline{n}}\left(\underline{r}_A\right) \cdot \left(\underline{r} - \underline{r}_A\right)\right) \tag{9.3}$$

where $\hat{\underline{n}}\left(\underline{r}_A\right)$ is the unit surface normal at the location $\underline{r}_A$ on the surface S_1 and $\delta(.)$ denotes the one-dimensional Dirac delta distribution.

9.3 The reciprocity theorem

The reciprocity theorem is one of the fundamental theorems of electromagnetic fields. It is related to the mutual interaction of sources with fields, or alternatively

[1]For the considerations in this chapter, the introduced currents and charges are equivalent quantities. The physical existence, in particular of the magnetic currents and charges, is thus not required.

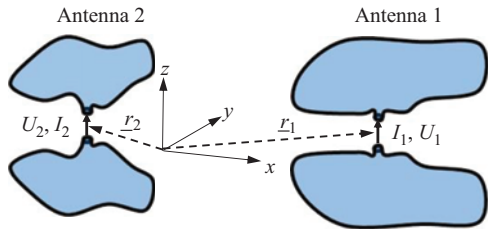

Figure 9.2 Arbitrary arrangement of two antennas: Antenna 1 may be excited by current I_1, and antenna 2 may be excited by current I_2. Excitation of antenna 1 with current I_1 causes the terminal voltage U_2 at antenna 2, when I_2 is zero. Excitation of antenna 2 with current I_2 causes the terminal voltage U_1 at antenna 1, when I_1 is zero

among antennas [2,25,26]. In our case, we consider two antennas as illustrated in Figure 9.2.

In transmit mode, antenna 1 may be excited by current I_1 and antenna 2 may be excited by current I_2, respectively. In receive mode, antenna 1 exhibits the voltage U_1 at its terminals and antenna 2 exhibits the terminal voltage U_2. Important to note is that the receive terminal voltages at the two antennas are observed when the corresponding transmit excitation current at this very antenna is zero, i.e., we can write

$$U_2 = Z_{21} I_1|_{I_2=0}, \quad U_1 = Z_{12} I_2|_{I_1=0} \tag{9.4}$$

where Z_{21} and Z_{12} are the mutual impedances between the two antennas. From the reciprocity relations of two-port networks, we can expect that $Z_{21} = Z_{12}$.

In order to obtain the connection to an electromagnetic-field-based description of the problem, we assume that

$$U_1 = -\int_{C_1} \underline{E}_{12} \cdot d\underline{s}, \quad U_2 = -\int_{C_2} \underline{E}_{21} \cdot d\underline{s} \tag{9.5}$$

$$I_1 = \iint_{A_1} \underline{J}_1 \cdot d\underline{a}, \quad I_2 = \iint_{A_2} \underline{J}_2 \cdot d\underline{a} \tag{9.6}$$

where $\underline{E}_{12}$ is the electric field in the terminal region of antenna 1 along a short curve C_1 between the terminal pins due to an impressed excitation current I_2 at antenna 2 and $\underline{J}_1$ is an impressed electric volume current density in the terminal region of antenna 1, whose integral over the terminal pin area A_1 gives the impressed current I_1. Similar definitions hold for $\underline{E}_{21}$ and $\underline{J}_2$, respectively. In order for these definitions to be reasonable, we must assume certain properties of the field and current distributions in the terminal regions of both antennas, which are commonly fulfilled for small enough terminal regions, as will be seen in the coming derivations.

Now, let us forget our antenna configuration for a moment and consider an arbitrary set of impressed sources $\underline{J}_1$ and $\underline{M}_1$ producing fields $\underline{E}_{21}$ and $\underline{H}_{21}$, as well

as a second arbitrary set of impressed sources $\underline{J}_2$ and $\underline{M}_2$ producing fields $\underline{E}_{12}$ and $\underline{H}_{12}$, where electric and magnetic sources are considered in order to maintain sufficient generality. Both fields must fulfill Maxwell's equations according to

$$\begin{aligned} \nabla \times \underline{H}_{21} &= j\omega\varepsilon \underline{E}_{21} + \underline{J}_1, \quad \nabla \times \underline{H}_{12} = j\omega\varepsilon \underline{E}_{12} + \underline{J}_2 \\ \nabla \times \underline{E}_{21} &= -j\omega\mu \underline{H}_{21} - \underline{M}_1, \quad \nabla \times \underline{E}_{12} = -j\omega\mu \underline{H}_{12} - \underline{M}_2 \end{aligned} \tag{9.7}$$

If we take the scalar product of the first equation of the two equation sets with $\underline{E}_{12}$ and $\underline{E}_{21}$, respectively, and of the second equation with $\underline{H}_{12}$ and $\underline{H}_{21}$, respectively, and take the difference of the resulting expressions, we obtain

$$-\nabla \cdot \left(\underline{E}_{21} \times \underline{H}_{12} - \underline{E}_{12} \times \underline{H}_{21} \right) = \underline{E}_{21} \cdot \underline{J}_2 + \underline{H}_{12} \cdot \underline{M}_1 - \underline{E}_{12} \cdot \underline{J}_1 - \underline{H}_{21} \cdot \underline{M}_2 \tag{9.8}$$

where the product rule for the divergence can be used in order to show that the left-hand side of this equation is correct. If this equation is integrated over a certain volume V, which is completely enclosed by a surface $A(V)$ and by utilising the Gauss integral theorem, we obtain

$$\begin{aligned} &-\oiint_{A(V)} \left(\underline{E}_{21} \times \underline{H}_{12} - \underline{E}_{12} \times \underline{H}_{21} \right) \cdot d\underline{a} \\ &\quad = \iiint_V \left(\underline{E}_{21} \cdot \underline{J}_2 + \underline{H}_{12} \cdot \underline{M}_1 - \underline{E}_{12} \cdot \underline{J}_1 - \underline{H}_{21} \cdot \underline{M}_2 \right) dv \end{aligned} \tag{9.9}$$

which is known as the general integral form of the reciprocity theorem of electromagnetic fields. For our purpose of antenna interactions in free space, it is appropriate to consider a spherical volume, whose radius r approaches infinity. With the assumption that there are no sources at infinity, we can utilise the far-field properties of the fields in form of

$$E_\vartheta = ZH_\varphi, \quad E_\varphi = -ZH_\vartheta \tag{9.10}$$

i.e., the radiated waves have the properties of locally plane waves, where $Z = \sqrt{\mu/\varepsilon}$ is the characteristic impedance of the considered medium, e.g., of free space. Utilising these relations, the surface integral in (9.9) becomes

$$\begin{aligned} &\oiint_{A(V)} \left(\underline{E}_{21} \times \underline{H}_{12} - \underline{E}_{12} \times \underline{H}_{21} \right) \cdot d\underline{a} \\ &\quad = \oiint_{A(V)} \left[ZH_{\varphi 1} H_{\varphi 2} + ZH_{\vartheta 1} H_{\vartheta 2} - ZH_{\varphi 1} H_{\varphi 2} - ZH_{\vartheta 1} H_{\vartheta 2} \right] da = 0 \end{aligned} \tag{9.11}$$

for the assumed far-field terms of the fields and the near-field terms of the fields decay so fast that their contribution to the surface integral vanishes anyways.

The general form of the reciprocity theorem for infinite space is thus

$$\iiint_V \left(\underline{E}_{21} \cdot \underline{J}_2 - \underline{H}_{21} \cdot \underline{M}_2 \right) dv = \iiint_V \left(\underline{E}_{12} \cdot \underline{J}_1 - \underline{H}_{12} \cdot \underline{M}_1 \right) dv. \tag{9.12}$$

If we come back to our antenna problem as depicted in Figure 9.2, where only electric excitation current densities $\underline{J}_1$ and $\underline{J}_2$ are present in the terminal regions of the antennas and where it is possible to factor the integral over the terminal regions according to

$$\begin{aligned}\iiint_{V_2}\left(\underline{E}_{21}\cdot\underline{J}_2\right)dv &= \underbrace{\int_{C_2}\underline{E}_{21}\cdot d\underline{s}}_{-U_2}\ \underbrace{\iint_{A_2}\underline{J}_2\cdot d\underline{a}}_{I_2}\\ &= \underbrace{\int_{C_1}\underline{E}_{12}\cdot d\underline{s}}_{-U_1}\ \underbrace{\iint_{A_1}\underline{J}_1\cdot d\underline{a}}_{I_1} = \iiint_{V_1}\left(\underline{E}_{12}\cdot\underline{J}_1\right)dv \end{aligned} \tag{9.13}$$

we finally obtain the reciprocity relation

$$\left.\frac{U_2}{I_1}\right|_{I_2=0} = Z_{21} = Z_{12} = \left.\frac{U_1}{I_2}\right|_{I_1=0} \tag{9.14}$$

as known from circuit theory.

An interesting question at this point is certainly what happens if the terminal configurations of the considered antennas do not support the factorisation of the integrals as shown in (9.13) or if we have antennas with waveguide port excitation for instance. In these cases, the unique definition of voltages and currents may not be feasible. By working with impressed electric and/or magnetic surface current densities, it is, however, possible to impress incident waves at waveguide ports and by using the orthogonality properties of the waveguide modes the common reciprocity relation $S_{21} = S_{12}$ for scattering parameters can be derived. To show this, we assume that both antennas are fed by a waveguide port, where on transmit an incident waveguide mode is impressed and on receive a waveguide mode travelling out of the port is detected. Writing (9.12) with impressed surface current densities at the planar waveguide port cross sections $A(P1)$ and $A(P2)$ gives

$$\iint_{A(P2)}\left(\underline{E}_{21}\cdot\underline{J}_{A2} - \underline{H}_{21}\cdot\underline{M}_{A2}\right)da = \iint_{A(P1)}\left(\underline{E}_{12}\cdot\underline{J}_{A1} - \underline{H}_{12}\cdot\underline{M}_{A1}\right)da. \tag{9.15}$$

The excitation of an incident waveguide mode on transmit with power wave amplitude $a_{1/2}$ can be achieved by choosing $\underline{J}_{A1/2} = a_{1/2}\sqrt{Z_{ref,1/2}}\,\underline{\hat{n}}\times\underline{\hat{H}}^{in}_{P1/2}$ and $\underline{M}_{A1/2} = -a_{1/2}\left(\underline{\hat{n}}\times\underline{\hat{E}}^{in}_{P1/2}\right)/\sqrt{Z_{ref,1/2}}$, where $\underline{\hat{n}}$ is the surface unit normal directed into the solution domain and $Z_{ref,1/2}$ is the normalisation impedance for the definition of the power wave amplitudes $a_{1/2}$ and $b_{1/2}$. The hat on top of $\underline{\hat{E}}^{in}_{P1/2}$ and $\underline{\hat{H}}^{in}_{P1/2}$ indicates that the fields are normalised to excite an incident port mode with

power wave amplitude $1\sqrt{\mathrm{W}}$ and a normalisation integral equal to 1. Moreover, it is here assumed that the feed waveguides extend to infinity outside of the solution domain in order to avoid reflection of the wave travelling out of the ports. Equation (9.15) becomes thus

$$a_2 \iint_{A(P2)} \left(\underline{E}_{21} \cdot \sqrt{Z_{ref,2}} \left(\hat{\underline{n}} \times \hat{\underline{H}}^{in}_{P2} \right) + \underline{H}_{21} \cdot \frac{\left(\hat{\underline{n}} \times \hat{\underline{E}}^{in}_{P2} \right)}{\sqrt{Z_{ref,2}}} \right) da$$

$$= a_1 \iint_{A(P1)} \left(\underline{E}_{12} \cdot \sqrt{Z_{ref,1}} \left(\hat{\underline{n}} \times \hat{\underline{H}}^{in}_{P1} \right) + \underline{H}_{12} \cdot \frac{\left(\hat{\underline{n}} \times \hat{\underline{E}}^{in}_{P1} \right)}{\sqrt{Z_{ref,1}}} \right) da. \tag{9.16}$$

With the relation between in-going and out-going waveguide mode fields [27]

$$\hat{\underline{n}} \times \hat{\underline{E}}^{in}_{P1/2} = \hat{\underline{n}} \times \hat{\underline{E}}^{out}_{P1/2}, \quad \hat{\underline{n}} \times \hat{\underline{H}}^{in}_{P1/2} = -\hat{\underline{n}} \times \hat{\underline{H}}^{out}_{P1/2} \tag{9.17}$$

and some vector algebraic manipulations, we obtain

$$-a_2 \iint_{A(P2)} \left[\left(\underline{E}_{21} \times \left(\sqrt{Z_{ref,2}} \hat{\underline{H}}^{out}_{P2} \right) \right) + \left(\frac{\hat{\underline{E}}^{out}_{P2}}{\sqrt{Z_{ref,2}}} \times \underline{H}_{21} \right) \right] \cdot \hat{\underline{n}} da$$

$$= -a_1 \iint_{A(P1)} \left[\left(\underline{E}_{12} \times \left(\sqrt{Z_{ref,1}} \hat{\underline{H}}^{out}_{P1} \right) \right) + \left(\frac{\hat{\underline{E}}^{out}_{P1}}{\sqrt{Z_{ref,1}}} \times \underline{H}_{12} \right) \right] \cdot \hat{\underline{n}} da \tag{9.18}$$

and this equation can be interpreted as

$$\frac{b_2}{a_1} = S_{21} = S_{12} = \frac{b_1}{a_2} \tag{9.19}$$

if we keep in mind that the integrals over the port areas of the two antennas in (9.18) give the received power wave amplitudes $2b_2$ and $2b_1$, respectively, due to the orthonormality properties of the port mode field distributions [27].

9.4 Mathematical formulation of the Huygens principle and equivalence principles

The Huygens principle is another fundamental theorem of electromagnetic fields, which is strongly related to the uniqueness theorem and to the equivalence principle [2,25,28,29]. In order to derive the mathematical formulation of the Huygens principle, which has already been introduced in Section 2.7 in a more intuitive way, let us consider a geometrical configuration as depicted in Figure 9.3.

Moreover, let us introduce the concept of a dyadic Green's function according to

$$d\underline{E}(\underline{r}) = \underline{\underline{G}}^{E}_{J}(\underline{r}, \underline{r}') \cdot d\underline{J}(\underline{r}') \tag{9.20}$$

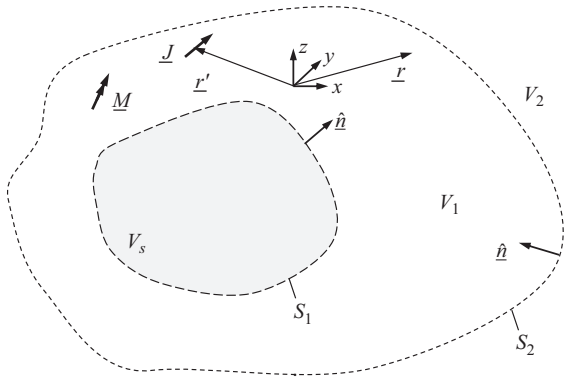

Figure 9.3 Electric and magnetic current densities $\underline{J}$ and $\underline{M}$ in a volume V_1 completely surrounded by surfaces S_1 and S_2

where the dyadic Green's function $\underline{\underline{G}}_J^E(\underline{r},\underline{r}')$ gives the electric field at any observation location r in a solution domain for excitation with an electric unit dyadic source $\underline{\underline{I}}\,\delta(\underline{r}-\underline{r}')$ at the source location $\underline{r}'$ [30]. In a similar way, dyadic Green's functions for magnetic fields (superscript H) and for excitation with magnetic unit sources (subscript M) can be defined. With this in mind and following the ideas of Monzon in [31], we consider again two sets of Maxwell's equations according to

$$\begin{aligned}\nabla\times\underline{H}(\underline{r}) &= j\omega\varepsilon(\underline{r})\underline{E}(\underline{r})+\underline{J}(\underline{r})\\ \nabla\times\underline{E}(\underline{r}) &= -j\omega\mu(\underline{r})\underline{H}(\underline{r})-\underline{M}(\underline{r})\end{aligned} \tag{9.21}$$

$$\begin{aligned}\nabla\times\widehat{\underline{H}}_e(\underline{r}) &= j\omega\varepsilon(\underline{r})\widehat{\underline{E}}_e(\underline{r})+\widehat{\underline{e}}_e\delta(\underline{r}-\underline{r}')\\ \nabla\times\widehat{\underline{E}}_e(\underline{r}) &= -j\omega\mu(\underline{r})\widehat{\underline{H}}_e(\underline{r})\end{aligned} \tag{9.22}$$

where

$$\widehat{\underline{E}}_e(\underline{r})=\underline{\underline{G}}_J^E(\underline{r},\underline{r}')\cdot\widehat{\underline{e}}_e,\quad \widehat{\underline{H}}_e(\underline{r})=\underline{\underline{G}}_J^H(\underline{r},\underline{r}')\cdot\widehat{\underline{e}}_e. \tag{9.23}$$

The hat on top of $\widehat{\underline{E}}_e$ and $\widehat{\underline{H}}_e$ indicates here that these quantities do not have the dimension of fields, but of Green's functions. The fields $\widehat{\underline{E}}_e$ and $\widehat{\underline{H}}_e$ are obviously auxiliary fields due to the unit Dirac source excitation $\widehat{\underline{e}}_e\delta(\underline{r}-\underline{r}')$.

Taking the scalar product of the first equation in (9.22) with $\widehat{\underline{E}}$ and of the second equation in (9.21) with $\widehat{\underline{H}}_e$ and subtracting both results in

$$\begin{aligned}\nabla\cdot\left(\widehat{\underline{H}}_e(\underline{r})\times\underline{E}(\underline{r})\right) &= j\omega\left[\varepsilon(\underline{r})\widehat{\underline{E}}_e(\underline{r})\cdot\underline{E}(\underline{r})+\mu(\underline{r})\widehat{\underline{H}}_e(\underline{r})\cdot\underline{H}(\underline{r})\right]\\ &\quad+\widehat{\underline{H}}_e(\underline{r})\cdot\underline{M}(\underline{r})+\underline{E}(\underline{r})\cdot\widehat{\underline{e}}_e\delta(\underline{r}-\underline{r}').\end{aligned} \tag{9.24}$$

Similarly, taking the scalar product of the first equation in (9.21) with $\widehat{\underline{E}}_e$ and of the second equation in (9.22) with $\underline{H}$ and subtracting both gives

$$\begin{aligned}&\nabla\cdot\left(\underline{H}(\underline{r})\times\widehat{\underline{E}}_e(\underline{r})\right)\\ &\quad=j\omega\left[\varepsilon(\underline{r})\widehat{\underline{E}}_e(\underline{r})\cdot\underline{E}(\underline{r})+\mu(\underline{r})\widehat{\underline{H}}_e(\underline{r})\cdot\underline{H}(\underline{r})\right]+\widehat{\underline{E}}_e(\underline{r})\cdot\underline{J}(\underline{r})\end{aligned} \tag{9.25}$$

where in both cases $-\nabla\cdot(\underline{a}\times\underline{b})=\underline{a}\cdot\nabla\times\underline{b}-\underline{b}\cdot\nabla\times\underline{a}$ was used.

Subtracting (9.24) from (9.25) gives

$$\nabla\cdot\left(\underline{H}(\underline{r})\times\widehat{\underline{E}}_e(\underline{r})-\widehat{\underline{H}}_e(\underline{r})\times\underline{E}(\underline{r})\right)$$
$$=\underline{J}(\underline{r})\cdot\widehat{\underline{E}}_e(\underline{r})-\underline{M}(\underline{r})\cdot\widehat{\underline{H}}_e(\underline{r})-\underline{E}(\underline{r})\cdot\widehat{\underline{e}}_e\delta(\underline{r}-\underline{r}'). \tag{9.26}$$

Using the Gauss integral theorem, e.g., for the volume V_1 as illustrated in Figure 9.3, results in

$$\underline{E}(\underline{r}')\cdot\widehat{\underline{e}}_e=\iiint_{V_1}\left(\underline{J}(\underline{r})\cdot\widehat{\underline{E}}_e(\underline{r})-\underline{M}(\underline{r})\cdot\widehat{\underline{H}}_e(\underline{r})\right)dv$$
$$+\oiint_{S(V_1)}\left(\underline{H}(\underline{r})\times\widehat{\underline{E}}_e(\underline{r})-\widehat{\underline{H}}_e(\underline{r})\times\underline{E}(\underline{r})\right)\cdot\underline{\hat{n}}(\underline{r})da \tag{9.27}$$

where the filter property of the Dirac delta was used. Also, it is noted that $S(V_1)=S_1+S_2$ and that the surface normal $\underline{\hat{n}}$ is here assumed to be oriented into the volume V_1.

By rearranging the vector and scalar products in the surface integral and by using (9.23), we obtain

$$\underline{E}(\underline{r}')\cdot\widehat{\underline{e}}_e=\iiint_{V_1}\left(\underline{J}(\underline{r})\cdot\underline{\underline{G}}_J^E(\underline{r},\underline{r}')\cdot\widehat{\underline{e}}_e-\underline{M}(\underline{r})\cdot\underline{\underline{G}}_J^H(\underline{r},\underline{r}')\cdot\widehat{\underline{e}}_e\right)dv$$
$$+\oiint_{S(V_1)}\left[\left(\underline{\hat{n}}(\underline{r})\times\underline{H}(\underline{r})\right)\cdot\underline{\underline{G}}_J^E(\underline{r},\underline{r}')\cdot\widehat{\underline{e}}_e-\left(\underline{E}(\underline{r})\times\underline{\hat{n}}(\underline{r})\right)\cdot\underline{\underline{G}}_J^H(\underline{r},\underline{r}')\cdot\widehat{\underline{e}}_e\right]da. \tag{9.28}$$

Utilizing the reciprocity properties of Green's functions in the form of [25,31]

$$\underline{\underline{G}}_J^E(\underline{r},\underline{r}')=\left(\underline{\underline{G}}_J^E(\underline{r}',\underline{r})\right)^T,\quad \underline{\underline{G}}_J^H(\underline{r}',\underline{r})=-\left(\underline{\underline{G}}_M^E(\underline{r}',\underline{r})\right)^T \tag{9.29}$$

with the superscript T indicating the transpose, (9.28) can be written as

$$\underline{E}(\underline{r}')\cdot\widehat{\underline{e}}_e=\iiint_{V_1}\left(\underline{J}(\underline{r})\cdot\left(\underline{\underline{G}}_J^E(\underline{r}',\underline{r})\right)^T\cdot\widehat{\underline{e}}_e-\underline{M}(\underline{r})\cdot\left(\underline{\underline{G}}_M^E(\underline{r}',\underline{r})\right)^T\cdot\widehat{\underline{e}}_e\right)dv$$
$$+\oiint_{S(V_1)}\left[\left(\underline{\hat{n}}(\underline{r})\times\underline{H}(\underline{r})\right)\cdot\left(\underline{\underline{G}}_J^E(\underline{r}',\underline{r})\right)^T\cdot\widehat{\underline{e}}_e+\left(\underline{E}(\underline{r})\times\underline{\hat{n}}(\underline{r})\right)\cdot\left(\underline{\underline{G}}_M^E(\underline{r}',\underline{r})\right)^T\cdot\widehat{\underline{e}}_e\right]da \tag{9.30}$$

By interchanging $\underline{r}$ and $\underline{r}'$ as well as by utilising the fact that the equation must be valid for arbitrary constant vectors $\widehat{\underline{e}}_e$, we finally obtain an integral representation for the electric field $\underline{E}$ in every observation location $\underline{r}$ in V_1 in the form of

$$\underline{E}(\underline{r})=\iiint_{V_1}\left(\underline{\underline{G}}_J^E(\underline{r},\underline{r}')\cdot\underline{J}(\underline{r}')+\underline{\underline{G}}_M^E(\underline{r},\underline{r}')\underline{M}(\underline{r}')\right)dv'$$
$$+\oiint_{S(V_1)}\left[\underline{\underline{G}}_J^E(\underline{r},\underline{r}')\cdot\underline{J}_A(\underline{r}')+\underline{\underline{G}}_M^E(\underline{r},\underline{r}')\cdot\underline{M}_A(\underline{r}')\right]da' \tag{9.31}$$

where the vector algebraic relation $\underline{a}\cdot\underline{\underline{G}}^T=\underline{\underline{G}}\cdot\underline{a}$ was used and where

$$\underline{J}_A(\underline{r}) = \hat{\underline{n}}(\underline{r}) \times \underline{H}(\underline{r}), \quad \underline{M}_A(\underline{r}) = \underline{E}(\underline{r}) \times \hat{\underline{n}}(\underline{r}) \tag{9.32}$$

are equivalent surface current densities, which are related to the tangential magnetic and electric fields on the surface $S(V_1)$. With similar arguments as used for (9.11), it can be shown that the surface integral contribution in (9.31) will vanish for a spherical surface with radius tending to infinity, i.e., the surface S_2 in Figure 9.3 may be shifted to infinity in the form of a sphere and then neglected.

An interesting question is what the result of (9.31) will be if the observation location $\underline{r}$ is chosen outside of V_1. Looking into the derivation of (9.31), it is clear that a key step in the derivation is from (9.26) to (9.27), where the Dirac delta will only contribute to the volume integral when $\underline{r}$ is located inside of V_1. Consequently, if $\underline{r}$ is located outside of V_1, the integral results of the volume integral and of the surface integral will cancel and (9.31) will deliver $\underline{E}(\underline{r}) = 0$ for observation locations outside of V_1.

Alternatively, we may achieve the same result by observing that the surface current densities $\underline{J}_A$ and $\underline{M}_A$ according to (9.32) cause a jump of the true field just inside of $S(V_1)$ to zero just outside of $S(V_1)$. At this point, it should be mentioned that surface current densities according to (9.32), which consequently lead to a null-field condition outside of the considered solution volume V_1, are known as Love surface current densities.

With the knowledge that (9.31) delivers a zero-field outside of the considered volume V_1, it is generally argued that the material properties outside of V_1 can be modified without modifying the result of (9.31). This is true as long as the equivalent surface current densities remain unchanged and the change of the material properties outside of V_1 is, thus, equivalent to changing the material properties for the Maxwell equations in (9.22) but not so for the equations in (9.21). That is, by changing the material properties in V_S, we change effectively the boundary conditions of the Green's functions $\underline{\underline{G}}_J^E$ and $\underline{\underline{G}}_M^E$, which do need to be set to uniquely define the Green's functions, but which have not yet been considered so far. Filling V_S in Figure 9.3, e.g., by a perfect electric conductor (PEC), the electric surface currents $\underline{J}_A$ will no longer contribute to $\underline{E}(\underline{r})$ and filling V_S with a perfect magnetic conductor (PMC), $\underline{M}_A$ will no longer contribute to $\underline{E}(\underline{r})$, but the Green's function for the remaining type of surface currents has to fulfill the boundary condition on PEC- or PMC-filling, respectively.

In antenna measurements, it is, however, in most situations convenient to work with a configuration, where the material in V_S is chosen to be identical to the (homogeneous) material in V_1. Commonly, we may also assume that there are no volume sources $\underline{J}$ and $\underline{M}$ in the solution volume V_1 and that the volume V_1 ranges to infinity.

With respect to our measurement configuration in Figure 9.1, we can thus say that the fields in V_1, which are primarily generated by the primary sources $\underline{J}$ and $\underline{M}$ in V_S, are generated by the secondary sources $\underline{J}_A$ and $\underline{M}_A$ on S_1, when we utilise (9.31) in the form of

$$\underline{E}(\underline{r}) = \oiint_{S_1} \left[\underline{\underline{G}}_J^E(\underline{r}, \underline{r}') \cdot \underline{J}_A(\underline{r}') + \underline{\underline{G}}_M^E(\underline{r}, \underline{r}') \cdot \underline{M}_A(\underline{r}') \right] da' \tag{9.33}$$

where it is, possible to work with homogeneous (free) space Green's functions $\underline{\underline{G}}_J^E$ and $\underline{\underline{G}}_M^E$. Since there are no sources in V_1 or in V_2, the surface S_2 can be chosen arbitrarily as long as it is completely outside of S_1. If S_2 is at infinity, it is clear that there is no integral contribution to (9.33) [or (9.31)] from it. If it is closer to S_1, e.g., at the position where near-field measurements may be performed, there will also be no contribution to (9.33) [or (9.31)], since an integral contribution from S_2 could only come, if there were primary sources in V_2.

If we consider the volume V_2 and calculate the field in it via a similar integral representation as given in (9.33) (now with integral over S_2), the equivalent surface sources on S_2, would carry the field information of the primary sources in V_S into the volume V_2.

From these considerations, it is also clear that the following statements hold:

- The knowledge of $\underline{J}_A$ and $\underline{M}_A$ [or of the corresponding tangential fields, see (9.32)] on S_1 is sufficient to uniquely determine the fields everywhere in V_1 and V_2.
- The knowledge of $\underline{J}_A$ and $\underline{M}_A$ [or of the corresponding tangential fields, see (9.32)] on S_2 is sufficient to uniquely determine the fields everywhere in V_2.
- With appropriately modified Green's functions, it is clear that either $\underline{J}_A$ or $\underline{M}_A$ (or either one of the corresponding tangential fields) is also sufficient in both cases, since resonance effects cannot occur in an open measurement configuration.

If the fixed relation between the surface sources and the tangential fields (Love condition) is not important, one may also work with any other kind of equivalent surface sources, which are able to correctly represent the fields on the measurement surface, i.e., on S_2 in Figure 9.1. Due to the uniqueness theorem and based on the fact that V_1 and V_2 are free of any further sources, these sources will then also produce the correct fields anywhere in V_1 and V_2. However, in contrast to the so-called Love current densities $\underline{J}_A$ and $\underline{M}_A$, other sources may also produce nonzero fields in the original source volume V_S. This violation of the zero-field condition is in general no problem since there is anyways no information about the true fields in V_S.

Furthermore, it is of course also possible to work with various kinds of equivalent sources (e.g., volume sources) inside the volume V_S. Various types and distributions of sources within V_S are able to correctly represent the fields in V_1 and V_2, where in particular a representation, e.g., with electric volume current densities $\underline{J}$ in the form of

$$\underline{E}(\underline{r}) = \iiint_{V_S} \underline{\underline{G}}_J^E(\underline{r}, \underline{r}') \cdot \underline{J}(\underline{r}')\, dv' \tag{9.34}$$

with free-space Green's function $\underline{\underline{G}}_J^E$ is advantageous in terms of simplicity of the equations. Such volume equivalent source representations are sometimes known under the name volume equivalence principle.

In summary, we can say that any equivalent source distribution inside of V_S or on the surface S_1 of V_S, which is able to correctly produce the fields on the measurement surface S_2, is also able to correctly produce the fields anywhere in V_1 and also in V_2.

At this point, it must, however, be emphasised that all the statements about the unique and correct representation of the fields and the sources are only valid under the assumption of perfect accuracy – for the measurements, for the source determination, and for the field calculation. In practice, we must be aware of the fact that the accuracy is limited. In particular, it may be impossible to determine strong evanescent fields near to the AUT with appropriate accuracy, since these fields may decay very quickly with increasing distance. The field contributions of such evanescent fields at the measurement surface may be so little that they are beyond the dynamic range of the measurement system and of the numerical field transformation approaches. In mathematical terms, we can say that our inverse source problem is at least mildly ill-conditioned and the recognition of this fact can be very important for a successful solution of such problems.

An important aspect of equivalent source representations of antennas is related to the mutual electromagnetic interaction of the antenna with its environment. After the replacement of an antenna by equivalent sources and the modification/removal of the true antenna materials, it is no longer possible to correctly account for mutual interactions, e.g., between the AUT and the probe. Therefore, the measurement configuration should always be chosen in a way that mutual interactions of the AUT with its environment are kept as little as possible, in order to avoid measurement errors.

Based on the foregoing discussion, we may ask the question: Why do we not directly work with the measured field samples on the surface S_2 in order to determine the fields in far-field distance or at any other location in V_2? The key reason for this is the influence of the measurement probes. When we measure the fields on S_2, we do only know the output signals of the probes, but not the fields incident on the probes, which would be required to obtain $\underline{J}_A = \hat{\underline{n}} \times \underline{H}$ and/or $\underline{M}_A = \underline{E} \times \hat{\underline{n}}$, or some other kind of viable sources, as necessary for the field calculation. The retrieval of these quantities from the measured signals is actually most advantageously achieved by introducing equivalent radiation sources in some distance away from S_2, e.g., on S_1. The actual determination of these sources is then achieved by solving an inverse radiation problem as discussed later in this chapter.

Even if we were able to directly measure $\underline{J}_A = \hat{\underline{n}} \times \underline{H}$ and/or $\underline{M}_A = \underline{E} \times \hat{\underline{n}}$ on S_2, i.e., probe correction would not be necessary in this case, the introduction of equivalent sources at some distance away from S_2 and solving a corresponding inverse radiation problem could be beneficial. For a direct computation of the far-fields from the measured fields or surface current densities on S_2, we would have to numerically perform the integral in the form of (9.33) over the surface S_2 based on the corresponding measurement samples. Since the measurement samples may not be collected in order to support a numerical quadrature rule over the measurement surface S_2, the solution of an inverse radiation problem for the determination of well-defined surface sources on the surface S_1, which are subsequently integrated to obtain the far-fields, can help to overcome such problems.

9.5 Forward transmission equation with probe correction

In order to set up the field transformation problem, an appropriate transmission equation from the equivalent sources representing the AUT to the output signals of the measurement probes is required and this transmission equation should be equivalent to the practically measured transmission between the AUT and the probe antenna.

9.5.1 Voltage-equivalent current formulation

In order to derive a forward transmission equation between AUT and measurement probe in a voltage-equivalent current formulation, we start from the reciprocity theorem in a form related to (9.13), given by

$$\begin{aligned} -U_2\left(\underline{r}_2\right) I_2\left(\underline{r}_2\right) &= \iiint_{V_2} \left(\underline{E}_{21}\left(\underline{r}\right) \cdot \underline{J}_2\left(\underline{r}-\underline{r}_2\right)\right) dv \\ &= \iiint_{V_1} \left(\underline{E}_{12}\left(\underline{r}\right) \cdot \underline{J}_1\left(\underline{r}-\underline{r}_1\right)\right) dv = -U_1\left(\underline{r}_1\right) I_1\left(\underline{r}_1\right) \end{aligned} \tag{9.35}$$

and consider it for a two-antenna configuration as shown in Figure 9.2, for instance. Here, we may assume that antenna 2 is the probe antenna and antenna 1 is the AUT. Next, we assume that both of the antennas are replaced by equivalent electric volume current densities radiating in free space in the form of (9.34) according to the volume equivalence principle, i.e., antenna 2, the probe, is replaced by $\underline{J}_2\left(\underline{r}-\underline{r}_2\right)$ and antenna 1, the AUT, is replaced by $\underline{J}_1\left(\underline{r}-\underline{r}_1\right)$. By writing these current densities as well as the terminal currents and voltages with respect to the antenna reference positions $\underline{r}_1$ and $\underline{r}_2$, it is indicated that the antennas, especially the probe, may have changing locations in space. Based on this, the left equation in (9.35) can be written as

$$-U_2\left(\underline{r}_2\right) = \iiint_{V_2} \left(\frac{\underline{J}_2\left(\underline{r}-\underline{r}_2\right)}{I_2\left(\underline{r}_2\right)} \cdot \iiint_{V_1} \underline{\underline{G}}_J^E\left(\underline{r},\underline{r}'\right) \cdot \underline{J}_1\left(\underline{r}'-\underline{r}_1\right) dv' \right) dv. \tag{9.36}$$

By using a free-space Green's function, it is clear that mutual interactions between both antennas are no longer considered in this equation. Also, it is clear that the influence of the probe, i.e., of antenna 2, on the measurement result is fully accounted for by evaluating the volume integral over V_2 with some kind of equivalent volume current distribution $\underline{J}_2$ representing the probe. Such a normalised equivalent volume current distribution representing the probe may be called a probe weighting function

$$\underline{w}_{Probe}\left(\underline{r}\right) = \frac{\underline{J}_{Probe}\left(\underline{r}\right)}{I_{Probe}}, \tag{9.37}$$

which is written here with the assumption that the probe reference location is in the origin of the coordinate system, and (9.36) can, thus, be written as

$$-U_2\left(\underline{r}_2\right) = \iiint_{V_2}\left(\underline{w}_{Probe}\left(\underline{r}-\underline{r}_2\right)\cdot\iiint_{V_1}\underline{\underline{G}}_J^E\left(\underline{r},\underline{r}'\right)\cdot\underline{J}_1\left(\underline{r}'-\underline{r}_1\right)dv'\right)dv. \tag{9.38}$$

The Green's function of homogeneous space involved in (9.38) can be written in the form [25]

$$\underline{\underline{G}}_J^E(\underline{r},\underline{r}') = -jkZ\left(\underline{\underline{I}}+\frac{1}{k^2}\nabla\nabla\right)\frac{e^{-jk\left|\underline{r}-\underline{r}'\right|}}{4\pi\left|\underline{r}-\underline{r}'\right|} \tag{9.39}$$

with the wavenumber of homogeneous space $k=\omega\sqrt{\varepsilon\mu}$ and the characteristic impedance of homogeneous space $Z=\sqrt{\mu/\varepsilon}$. With this knowledge, (9.36) can formally be evaluated, e.g., by numerical integration, for arbitrary volume current distributions $\underline{J}_1$ and $\underline{J}_2$. Due to the complicated functional dependence of the Green's function, this can, however, be a very cumbersome procedure. Therefore, we would like to find different representations of (9.36), which are in particular more amenable to an efficient numerical evaluation.

As a first step, let us look into the far-field formulation of (9.36), i.e., in its formulation for very large distances between the two antennas. In such a situation, we can introduce an FF approximation of the Green's function in the form of

$$\underline{\underline{G}}_J^E(\underline{r},\underline{r}') \approx -jkZ\frac{e^{-jkr_{21}}}{4\pi r_{21}}\underbrace{\left(\underline{\underline{I}}-\widehat{\underline{e}}_{r_{21}}\widehat{\underline{e}}_{r_{21}}\right)}_{\underline{\underline{I}}^{FF}}e^{jk\widehat{\underline{e}}_{r_{21}}\cdot\left(\underline{r}'-\underline{r}_1\right)}e^{-jk\widehat{\underline{e}}_{r_{21}}\cdot\left(\underline{r}-\underline{r}_2\right)} \tag{9.40}$$

where $r_{21}=\left|\underline{r}_2-\underline{r}_1\right|$ with $\underline{r}_{21}=\underline{r}_2-\underline{r}_1=r_{21}\widehat{\underline{e}}_{r_{21}}$ is the distance between the reference locations of the antennas and where the common FF approximation has been introduced with respect to the reference locations of the antennas. $\underline{\underline{I}}^{FF}$ can be seen as an FF unit dyad, which contains only transverse vector components as known from far-fields.

With this representation, (9.36) can be written as

$$U_2(\underline{r}_2) = \frac{e^{-jkr_{21}}}{4\pi r_{21}}\frac{\underline{\underline{H}}_2^{Tx}\left(\underline{r}_2,-k\widehat{\underline{e}}_{r_{21}}\right)}{jkZ}\cdot\underline{H}_1^{Tx}(\underline{r}_1,k\widehat{\underline{e}}_{r_{21}})I_1(\underline{r}_1) \tag{9.41}$$

where

$$\underline{H}_{1/2}^{Tx}(\underline{r}_{1/2},\underline{k}) = -jkZ\iiint_{V_{1/2}}\frac{\underline{J}_{1/2}\left(\underline{r}-\underline{r}_{1/2}\right)}{I_{1/2}(\underline{r}_{1/2})}\cdot\underline{\underline{I}}^{FF}e^{jk\widehat{\underline{k}}\cdot\left(\underline{r}'-\underline{r}_{1/2}\right)}dv \tag{9.42}$$

is commonly called the FF transmit antenna transfer function, here defined for antenna 1 or antenna 2, which gives the far-field of an antenna in the direction of $\widehat{\underline{k}}$.

With the definition of the FF receive antenna transfer function

$$\underline{H}_2^{Rx}(\underline{r}_2, \underline{k}) = \frac{\underline{\underline{H}}_2^{Tx}(\underline{r}_2, \underline{k})}{jkZ} \tag{9.43}$$

the transmission equation in (9.41) can be written as

$$U_2(\underline{r}_2) = \underline{H}_2^{Rx}(\underline{r}_2, -k\widehat{\underline{e}}_{r_{21}}) \cdot \underbrace{\frac{e^{-jkr_{21}}}{4\pi r_{21}} \underline{H}_1^{Tx}(\underline{r}_1, k\widehat{\underline{e}}_{r_{21}}) I_1(\underline{r}_1)}_{\underline{E}_{21}^{FF}(\underline{r}_2)} \tag{9.44}$$

which is a common form of writing the FF transmission between ultra-wideband antennas, where the phase relations dependent on frequency are important. Also, it becomes clear that the $\underline{H}^{Rx}$ receive antenna transfer function is nothing else than the (complex) effective length of an antenna on receive.

By re-writing the equation in (9.43) in the form of

$$\underline{H}_{1/2}^{Tx}(\underline{r}_{1/2}, \underline{k}) = jkZ\underline{H}_{1/2}^{Rx}(\underline{r}_{1/2}, \underline{k}) = j\omega\mu\underline{H}_{1/2}^{Rx}(\underline{r}_{1/2}, \underline{k}) \tag{9.45}$$

it becomes moreover obvious that the receive transfer function of an antenna in time domain is proportional to the temporal derivative of the corresponding transmit transfer function.

In case that an antenna is not represented by an electric current density $\underline{J}$, but by a magnetic current density $\underline{M}$, the pertinent Green's function is

$$\underline{\underline{G}}_M^E(\underline{r}, \underline{r}') = -\nabla \times \underline{\underline{I}} \frac{e^{-jk\left|\underline{r} - \underline{r}'\right|}}{4\pi\left|\underline{r} - \underline{r}'\right|} \tag{9.46}$$

with FF approximation

$$\underline{\underline{G}}_M^E(\underline{r}, \underline{r}') \approx j\underline{k} \times \underline{\underline{I}}^{FF} \frac{e^{-jkr_{21}}}{4\pi r_{21}} e^{jk\,\widehat{\underline{e}}_{r_{21}} \cdot (\underline{r}' - \underline{r}_1)} e^{-jk\,\widehat{\underline{e}}_{r_{21}} \cdot (\underline{r} - \underline{r}_2)} \tag{9.47}$$

and the corresponding FF transmit antenna transfer function thus is

$$\underline{H}_{1/2}^{Tx}(\underline{r}_{1/2}, \underline{k}) = jk \iiint_{V_{1/2}} \left(\widehat{k} \times \frac{\underline{M}_{1/2}\left(\underline{r} - \underline{r}_{1/2}\right)}{I_{1/2}\left(\underline{r}_{1/2}\right)} \right) e^{jk\widehat{\underline{k}} \cdot (\underline{r} - \underline{r}_{1/2})} dv \tag{9.48}$$

where it is still assumed that the antennas are excited by feed currents $I_{1/2}$. If an antenna is represented by a combination of electric and magnetic current densities, the contributions of both are added and both the integral representations in (9.42) and (9.48) can of course also be evaluated for surface current densities in the corresponding way.

9.5.2 Spectral representation with propagating plane waves

As already mentioned, the numerical evaluation of the near-field transmission equation in (9.36) requires an evaluation of the integrand for all necessary combinations of $\underline{r}$ and $\underline{r}'$. In contrast, the far-field transmission equation in (9.44) is obviously in a much simpler, i.e., a factorised operator form, where the source and observation integrals can be evaluated independently from each other and where the final transmission result is just obtained by multiplying several factors. The goal is now to find a similar factorised, and ideally also diagonalised, representation of the transmission equation between two antennas, which is valid under near-field conditions. There are certainly algebraic ways of achieving this goal, once a discretised representation of the transmission equation has been set up. However, one of the most successful and powerful ways of achieving a factorised and also diagonalised form of the near-field transmission equation is to follow the concepts of the FMM [1,15] and to perform a spherical multipole and subsequent propagating plane-wave expansion of the Green's function of the scalar Helmholtz equation according to

$$\frac{e^{-jk|\underline{X}+\underline{d}|}}{|\underline{X}+\underline{d}|} = \lim_{L\to\infty} \oiint e^{-j\underline{k}\cdot\underline{d}} \underbrace{\left(\frac{-jk}{4\pi}\right) \sum_{l=0}^{L} (-j)^l (2l+1) h_l^{(2)}(kX) P_l(\widehat{\underline{k}}\cdot\widehat{\underline{X}})}_{T_L(\underline{X},\underline{k})} d^2\widehat{\underline{k}} \tag{9.49}$$

valid for $|\underline{X}| > |\underline{d}|$, where P_l is the Legendre polynomial of order l and $h_l^{(2)}$ is the spherical Hankel function of order l and second kind. The term $T_L(\underline{X},\underline{k})$ is obviously multiplied with a propagating plane-wave propagator within the integrand of (9.49) and is, therefore, called a propagating plane-wave translation operator. Practically, it is computed as a truncated sum over the involved spherical multipoles, where the truncation number L is commonly computed in order to achieve a certain accuracy of the representation. An often used approximation of the required order for a certain accuracy is [1]

$$L \approx k|\underline{d}| + 1.8 d_0^{2/3} \left(k|\underline{d}|\right)^{1/3} \tag{9.50}$$

where $d_0 = \log(1/\varepsilon)$ is the number of decimal digits of the accuracy ε for the representation of the Green's function of the scalar Helmholtz equation. At this point, it must, however, also be mentioned that the expansion in (9.49) is only useful for frequencies, where $|\underline{d}|$ is larger than about one fourth of a wavelength, i.e., it will not be useable at very low frequencies, due to numerical problems in the evaluation of the involved spherical Hankel functions for small arguments and large orders. In the following, we drop the '$\lim_{L\to\infty}$', which is actually necessary to write the '=' in (9.49), and assume that sufficiently many multipole terms are considered in order to achieve accurate results in a numerical implementation of the related equations and transformations.

With $\underline{X} = \underline{r}_2 - \underline{r}_1 = \underline{r}_{21}$ and $\underline{d} = \left(\underline{r} - \underline{r}_2\right) - \left(\underline{r}' - \underline{r}_1\right)$, as well as the utilisation of (9.49) together with (9.39), the near-field transmission equation in (9.36) can be converted into

$$U_2(\underline{r}_2) = \frac{I_1\left(\underline{r}_1\right)}{jkZ} \oiint \frac{T_L(\underline{r}_{21}, \underline{k})}{4\pi} \underline{H}_2^{Tx}(\underline{r}_2, -\underline{k}) \cdot \underline{H}_1^{Tx}(\underline{r}_1, \underline{k}) d^2\widehat{\underline{k}} \tag{9.51}$$

which is a diagonalised and factorised transmission equation with full account of near-field effects as long as $|\underline{X}| > |\underline{d}|$ holds. If $|\underline{X}| > |\underline{d}|$ does not hold for a given arrangement of antennas, one or both antennas can be subdivided into smaller parts for which the interactions can be evaluated separately and finally summed up. Such approaches will be discussed later in this chapter in relation to the numerical evaluation of the transmission equations.

With the transmission equation in (9.51), the near-field interaction between the two antennas is obviously obtained by integrating over the far-fields radiated by the transmitting antenna in all directions multiplied with the far-field receive pattern of the receive antenna and the plane-wave translation operator $T_L(\underline{r}_{21}, \underline{k})$ as illustrated in Figure 9.4. Commonly, it is also said that the radiated fields of the transmit antenna are expanded in propagating plane waves. These plane waves are then translated to the receive antenna and multiplied with the receive pattern of the receiving antenna, before the result is integrated over all possible propagation directions on the Ewald sphere in *k*-space. The fact that (9.49) is a factorised representation is obviously clear. The term 'diagonal' means that every plane wave radiated by antenna 1 causes only one single incident plane wave in the same direction at antenna 2. This is for instance in contrast to spherical-multipole translations as discussed in Chapter 8, where every mode transmitted by antenna 1

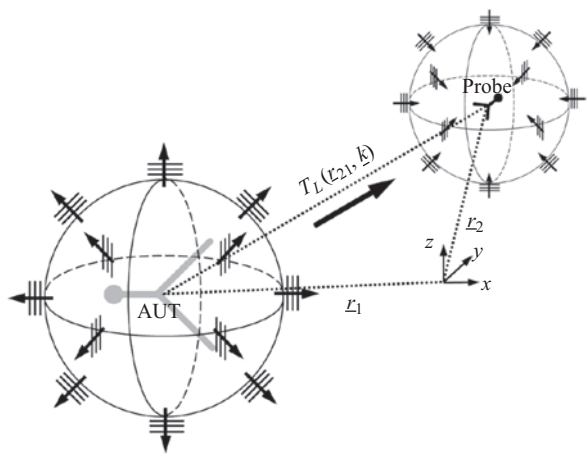

Figure 9.4 Near-field transmission between an AUT and a measurement probe based on propagating plane-wave representation and translation

causes in general a full set of receive modes at antenna 2 and where the corresponding translation operator is thus a full translation operator.

A very interesting observation is that the translation operator T_L becomes more and more like a Dirac delta impulse with its maximum in the direction of the line of sight between the two antenna centres, i.e., [32]

$$T_L(\underline{r}_{21}, \underline{k}) = T_L^{FF}(\underline{r}_{21}, \underline{k}) = \frac{e^{-jkr_{21}}}{r_{21}} \delta\left(\widehat{\underline{k}} - \widehat{\underline{r}}_{21}\right) \tag{9.52}$$

if the distance r_{21} between the two antennas is more and more increased. With the filter property of the Dirac delta in (9.52), the transmission equation in (9.51) becomes identical to the far-field transmission equation in (9.41) or (9.44), which supports the consistency of the found near-field transmission equation with propagating plane-wave representation.

9.5.3 Gain normalised transmission equation

The formulation obtained via the field and current source representation in Maxwell's equations and the common form of the reciprocity principle has led us to the propagating plane-wave-based near-field transmission equation in (9.51), which gives the terminal voltage of the receiving antenna based on the electric feed current of the transmit antenna. If we ask what kind of voltage $U_2(\underline{r}_2)$ is, we will mostly say that it is the open-circuit voltage, even though nobody measures the open-circuit voltage at a receive antenna under normal circumstances. If desired, the reciprocity considerations can also be performed for a receive antenna with a certain load resistance. However, a more natural description for antenna measurements is to work with power waves at the antenna feeding ports, as illustrated in Figure 9.5, which may not only be suitable for bipolar antenna terminals, but also for hollow waveguide or dielectric waveguide ports.

In the following, we convert the voltage–current-based transmission equation as obtained from the corresponding reciprocity considerations into a scattering-parameter-based transmission equation including gain normalised antenna transfer functions. This conversion is performed under the assumption that mutual coupling effects between the AUT and the probe are negligible, i.e., the AUT and the probe are treated as if they were located in infinite space without backscattering effects from any other object.

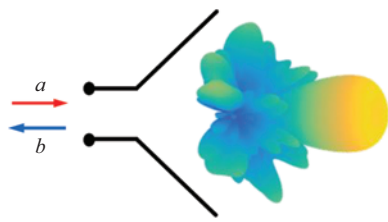

Figure 9.5 Generic antenna with power wave description at the feeding port

Let us now define the realised gain pattern of an antenna with reference position in the origin of the coordinate system in the form of

$$G(\underline{k}) = \lim_{r\to\infty} 4\pi r^2 \frac{S(r,\underline{k})}{P_0} = \frac{1}{2}\frac{\left|I(\underline{0})\underline{H}^{Tx}(\underline{0},\underline{k})\right|^2}{4\pi Z}\frac{2}{\left|a(\underline{0})\right|^2} = \left|W^{Tx}(\underline{0},\underline{k})\right|^2 \tag{9.53}$$

with

$$W^{Tx}(\underline{0},\underline{k}) = \sqrt{\frac{1}{4\pi Z}}\frac{I(\underline{0})\underline{H}^{Tx}(\underline{0},\underline{k})}{a(\underline{0})} = (1-\Gamma)\sqrt{\frac{1}{4\pi Z}}\frac{\underline{H}^{Tx}(\underline{0},\underline{k})}{\sqrt{Z_{ref}}} \tag{9.54}$$

where

$$S(r,\underline{k}) = \frac{1}{2}\frac{\left|E^{FF}(r,\underline{k})\right|^2}{Z} \tag{9.55}$$

and

$$I(\underline{0})\sqrt{Z_{ref}} = a(\underline{0}) - b(\underline{0}) = a(\underline{0})(1-\Gamma). \tag{9.56}$$

The reference of the realised gain is obviously the power

$$P_0 = \frac{1}{2}\left|a(\underline{0})\right|^2 \tag{9.57}$$

available at the antenna port which may be delivered by the ingoing power wave with amplitude $a(\underline{0})$. In the case of mismatch at the antenna port, an outgoing power wave with amplitude $b(\underline{0}) = \Gamma a(\underline{0})$ dependent on the reflection coefficient Γ may exist. Z_{ref} is the reference impedance for the definition of the power wave amplitudes.

Using (9.54) in (9.51) for both antennas results in

$$(1-\Gamma_2)\frac{U_2(\underline{r}_2)}{\sqrt{Z_{ref}}} = a_1(\underline{r}_1)\frac{1}{jk}\oiint T_L(\underline{r}_{21},\underline{k})\underline{W}_2^{Tx}(\underline{r}_2,-\underline{k})\cdot\underline{W}_1^{Tx}(\underline{r}_1,\underline{k})d^2\widehat{\underline{k}} \tag{9.58}$$

which is nothing else than

$$S_{21} = \frac{b_2(\underline{r}_2)}{a_1(\underline{r}_1)} = \frac{1}{2jk}\oiint T_L(\underline{r}_{21},\underline{k})\underline{W}_2^{Tx}(\underline{r}_2,-\underline{k})\cdot\underline{W}_1^{Tx}(\underline{r}_1,\underline{k})d^2\widehat{\underline{k}} \tag{9.59}$$

where we have used that

$$b_2(\underline{r}_2) = (1-\Gamma_2)\frac{U_2(\underline{r}_2)}{2\sqrt{Z_{ref}}} \tag{9.60}$$

if $U_2(\underline{r}_2)$ is the open circuit voltage at antenna 2.

With the transmission equation in (9.59), we have obviously a transmission equation, which is directly related to the commonly measured transmission *S*-parameter between the two antennas, i.e., between the AUT and the probe antenna.

If we write the far-field transmission equation in (9.41) in a similar form, we obtain

$$S_{21} = \frac{b_2\left(\underline{r}_2\right)}{a_1\left(\underline{r}_1\right)} = \frac{\sqrt{\pi}}{jk}\,\underline{W}_2^{Tx}(\underline{r}_2, -k\underline{\hat{e}}_{r_{21}}) \cdot \frac{e^{-jkr_{21}}}{\sqrt{4\pi}r_{21}}\,\underline{W}_1^{Tx}(\underline{r}_1, k\underline{\hat{e}}_{r_{21}}). \tag{9.61}$$

Since the power density $S_1(\underline{r}_2)$ generated by the transmit antenna at the location of the receive antenna is given by

$$S_1\left(\underline{r}_2\right) = \left|\frac{e^{-jkr_{21}}}{\sqrt{4\pi}r_{21}}\,\underline{W}_1^{Tx}(\underline{r}_1, k\underline{\hat{e}}_{r_{21}})\right|^2 \frac{|a_1|^2}{2} \tag{9.62}$$

it is obvious that the effective area normalised receive antenna transfer function of our receive or probe antenna can be written as

$$\underline{W}_2^{Rx}(\underline{r}_2, \underline{k}) = \frac{\sqrt{\pi}\underline{W}_2^{Tx}(\underline{r}_2, \underline{k})}{jk}. \tag{9.63}$$

This results in

$$A_{eff}(\underline{k}) = \left|\underline{W}^{Rx}(\underline{k})\right|^2 = \frac{\lambda^2}{4\pi}\left|\underline{W}^{Tx}(\underline{k})\right|^2 = \frac{\lambda^2}{4\pi}G(\underline{k}) \tag{9.64}$$

and shows that our derivation has provided us with the common reciprocity relation of an antenna as a by-product. In antenna text books, this relation is often derived from the reciprocity theorem under the assumption that one of the antennas is known, e.g., by assuming that one of the antennas is a Hertzian dipole.

If we transfer the gain or power normalisation to the original spatial domain transmission equation as found in (9.38), we obtain

$$\begin{aligned} S_{21} &= \frac{b_2\left(\underline{r}_2\right)}{a_1\left(\underline{r}_1\right)} \\ &= c_1 \iiint_{V_2} \left(\underline{w}_{Probe}\left(\underline{r} - \underline{r}_2\right) \cdot \iiint_{V_1} \underline{\underline{G}}_J^E\left(\underline{r}, \underline{r}'\right) \cdot \frac{\underline{J}_1\left(\underline{r}' - \underline{r}_1\right)}{I_1\left(\underline{r}_1\right)} dv' \right) dv \end{aligned} \tag{9.65}$$

with

$$c_1 = -\frac{(1-\Gamma_2)(1-\Gamma_1)}{2Z_{ref}}. \tag{9.66}$$

Equation (9.65) represents S_{21} in terms of transmission from a normalised equivalent volume current representation of the AUT to the probe in the form of spatial probe weighting with the normalised probe weighting function found in (9.37), where it is one more time noted that mutual coupling effects between the AUT and the probe have been neglected and the input reflection coefficients of the AUT and the probe, Γ_1 and Γ_2, respectively, are the input reflection coefficients in a free-space environment without any backscattering.

9.5.4 Spatial and spectral probe representation

In the previous sections, we have derived forward transmission equations, where the influence of the measurements probe has been fully accounted for. However, due to the importance of the probe correction, we want to further elaborate on this topic. Based on the derivation of (9.36) by the reciprocity theorem, we have obtained the probe weighting function

$$\underline{w}_{Probe}\left(\underline{r}\right) = \frac{\underline{J}_{Probe}\left(\underline{r}\right)}{I_{Probe}} \tag{9.67}$$

which is multiplied with the incident electric field to be measured and integrated over the probe antenna volume in order to provide the voltage at the probe terminals, the open-circuit voltage in most instances. Due to the derivation based on the free-space Green's function, it should be clear that we assume here the equivalent volume currents $\underline{J}_{Probe}\left(\underline{r}\right)$ representing the probe to exist in free space. The incident field to be measured is, therefore, also assumed to be the field existing in free space. It is noted that the concept of representing the probe by an equivalent volume current will also work with the probe material present. However, the corresponding Green's function with the probe material present would have to be used in this case, too, and this is in general not feasible. Moreover, it would also not give any benefit since the Green's function with presence of the generally unknown AUT is not known either and the consideration of mutual interactions between probe and AUT is, thus, not feasible anyways.

According to the Huygens and equivalence principles and the corresponding considerations in Section 9.4, it is clear that many different equivalent source representations may exist to correctly represent the probe behaviour. The only requirement here is that the fields produced by these sources outside of the actual probe volume must be identical to the fields produced by the real probe in transmit mode. We could even go so far that the fields produced by the equivalent probe sources must only be accurate within the entire AUT volume. Also, it is noted that the volume currents in the probe volume can be replaced by surface current densities on a Huygens surface around the probe volume, where again infinitely many different surface current distributions may be used.

Since the evaluation of a weighting integral over the probe volume or over its surface is commonly not convenient, it is desirable to evaluate the weighting integral independent from a specific incident field. This can be achieved by

expanding an arbitrary incident field into a set of known expansion functions for which the weighting integral is pre-calculated. If this is performed for propagating plane waves as found under far-field conditions, we arrive at the concept of the far-field receive antenna transfer function as given in (9.43), which is proportional to the far-field receive pattern of the probe antenna and normalised as an effective length. In the spectral representation with propagating plane waves, as introduced in Section 9.5.2, the total incident field is computed as an integral over propagating plane waves and the far-field receive function of the probe can, thus, be utilised to simplify the expressions. By utilising $\underline{H}_2^{Rx}(\underline{r}_2, \underline{k})$ according to (9.43), (9.51) becomes

$$U_2(\underline{r}_2) = I_1(\underline{r}_1) \oiint \underline{H}_2^{Rx}(\underline{r}_2, -\underline{k}) \cdot \frac{T_L(\underline{r}_{21}, \underline{k})}{4\pi} \underline{H}_1^{Tx}(\underline{r}_1, \underline{k}) d^2\widehat{\underline{k}} \tag{9.68}$$

where it is obvious that every incident propagating plane wave is multiplied by $\underline{H}_2^{Rx}(\underline{r}_2, -\underline{k})$ and then the contributions of all incident plane waves are integrated to provide the probe output signal $U_2(\underline{r}_2)$. Due to reciprocity, it is not really relevant whether we work here with the FF receive function $\underline{H}_2^{Rx}(\underline{r}_2, -\underline{k})$ of the probe or its FF transmit function $\underline{H}_2^{Tx}(\underline{r}_2, -\underline{k})$, except for a frequency-dependent factor to be considered. Also, as demonstrated in Section 9.5.3, probe representations (as well as AUT representations) with different normalisation, such as gain normalisation, may be used.

The important observation at this point is that full consideration of the probe receive behaviour, of course without mutual interactions with the AUT, is possible by just working with the far-field receive/transmit behaviour of the probe, where the far-field behaviour must be known in all directions with magnitude, phase, and polarisation. Even though we work with propagating plane waves, it should be clear that evanescent wave fields generated by the AUT are also captured by this kind of field representation as long as the condition for the utilisation of the FMM concepts according to the expansion in (9.49) is fulfilled.

In different spectral representations, probe correction is performed in a rather similar way. In planar measurements with regular sampling as discussed in Chapter 6, we work often with a planar 2D Fourier-type integral with FFT evaluation, again with propagating plane-wave representation of the incident field as well as of the probe receive behaviour. Interesting to note is that this kind of representation can capture the contribution of evanescent fields produced by the AUT only in parts, if restricted to the propagating plane-wave region. An extension to evanescent plane waves would in principle be possible, but then we would need to know the receiving behaviour of the probe for evanescent plane waves.

The transformation of spherical measurements with regular sampling, as elaborated on in Chapter 8, is often performed with FFT accelerated spherical mode expansions, where the incident fields and the probe receiving behaviour are decomposed into spherical modes. In this case, the common spectral integral representation is simplified into a discrete sum over spherical modes.

9.6 Types and discretisation of equivalent sources for representing the AUT

From the discussions of the previous sections, it should have become clear that we may work with a very large variety of different kinds of equivalent sources in order to represent the fields radiated by the AUT. The most appropriate kind of sources depends on what we want to achieve. If we are only interested in a near-field to far-field transformation, we may work with equivalent sources that are able to accurately represent the measured near-fields and, thus, also the far-fields. That is, the fields need to be accurately reproduced in the volume V_2 as found in Figure 9.1 and also on the surface S_2. The particular choice of S_1 and thus also of V_S is not that important in this case.

If we are also interested in accurate near-fields very close to the AUT, S_1 must be defined very close to the AUT such that the volume V_1, as seen in Figure 9.1, in which we can expect accurate fields, reaches also very close to the AUT. In this case, we can inspect the field distribution very close to the AUT, ideally on a surface tightly enclosing the AUT, and obtain diagnostic information about the AUT. Based on this, we may understand the AUT radiation behaviour better or we may identify faults and other problems related to the AUT.

If we restrict ourselves to the far-field case, i.e., without diagnostic intention close to the AUT, we may directly work with the spectral far-field representation of the AUT, e.g., as found in (9.59). The AUT representation $\underline{W}_1^{Tx}(\underline{r}_1, \underline{k})$ can directly be sampled on the Ewald sphere according to a numerical integration rule, which is used to evaluate the k-space integral over the Ewald sphere. The sample values of $\underline{W}_1^{Tx}(\underline{r}_1, \underline{k})$ at the k-space sample locations are in this case the unknown quantities to be determined in a corresponding NFFFT. Such a technique has been introduced in [16] and it has been used in a couple of other works, too, see, e.g., [17,33].

Instead of sampling the Ewald sphere, we can also work with a spherical-mode expansion of $\underline{W}_1^{Tx}(\underline{r}_1, \underline{k})$ and arrive at some kind of more general spherical-mode-based transformation than which is commonly used for standard spherical measurements, as discussed in Chapter 8.

Both of these, let us say, global equivalent source representations of the AUT have the disadvantage that they are only valid outside the minimum sphere around the AUT, no matter whether the AUT is really filling up the complete minimum sphere or only a part of it, as in the case of a planar antenna for instance. Moreover, these global equivalent source representations are also not well suited for setting up a very fast evaluation of the operator equations, except for the case of regular sampling on spherical measurement surfaces as considered in Chapter 8 of course.

In the following, we restrict ourselves to localised source representations, which can give more detailed diagnostic information about the AUT.

9.6.1 Surface current densities

Surface current densities on a tight surface around the AUT provide probably the most accurate but still efficient means of representing the AUT radiation under the

side constraint that the reproduced fields are accurate until very close to the AUT, i.e., also on the surface S_1 according to Figure 9.1, where S_1 can of course be chosen even closer to the AUT than implied in the figure. The radiated fields of the AUT are in this case written as in (9.33), which is given here one more time for convenience,

$$\underline{E}(\underline{r}) = \oiint_{S_1} \left[\underline{\underline{G}}_J^E(\underline{r}, \underline{r}') \cdot \underline{J}_A(\underline{r}') + \underline{\underline{G}}_M^E(\underline{r}, \underline{r}') \cdot \underline{M}_A(\underline{r}') \right] da'. \tag{9.69}$$

Obviously, we have electric $\underline{J}_A(\underline{r}')$ and magnetic $\underline{M}_A(\underline{r}')$ surface current densities, which are defined on the surface S_1. In order to set up a solvable discrete transformation problem, the surface current densities are discretised in the form of

$$\underline{J}_A(\underline{r}') = \sum_p J_p \underline{\beta}_p(\underline{r}'), \quad \underline{M}_A(\underline{r}') = \sum_q M_q \underline{\beta}_q(\underline{r}') \tag{9.70}$$

where $\underline{\beta}_{p/q}(\underline{r})$ are known expansion or basis functions for the surface current densities and J_p and M_q are the unknown expansion coefficients, which need to be found by the solution of the transformation problem. From the solution of electromagnetic radiation and scattering problems, it is nowadays well known that divergence-conforming basis functions defined on appropriate surface discretisation elements are very well suited to represent the divergence-conforming surface current densities. For triangular discretisation meshes, which give in general the best modelling flexibility, the Rao–Wilton–Glisson (RWG) basis functions [34] are in this respect the lowest order basis functions and, thus, the functions of choice. The RWG functions are defined on triangle pairs in a way that the normal current flow over the common edges is continuous and that there are no normal current components at all other edges. The corresponding current density, as also illustrated in Figure 9.6 on a triangle pair, can be written as

$$\underline{\beta}_c^{RWG}(\underline{r}) = \pm \frac{l_c}{2A_i}(\underline{r} - \underline{r}_i), \quad \nabla \cdot \underline{\beta}_c^{RWG}(\underline{r}) = \mp \frac{l_c}{2A_i} \tag{9.71}$$

where the functions are here normalised to be free of dimension. One of the signs is valid for one of the triangles, and the other sign applies then on the other triangle of

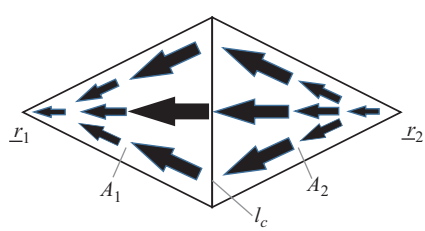

Figure 9.6 Illustration of RWG vector basis function on a pair of triangles

the triangle pair. The vector $\underline{r}$ is the position vector inside the triangles, $\underline{r}_i$ is the location of the vertex of triangle i opposite to the common edge, A_i is the area of triangle i, and l_c is the length of the common edge. As seen, the divergence of the RWG functions is a well-defined, constant expression within the triangles and the singular behaviour of the very near-fields of these functions is, thus, rather weak.

The RWG functions are so-called mixed-order basis functions, meaning that the normal component of the surface current density is constant along the common edge, but varies linearly with the perpendicular distance from the common edge. Therefore, these functions are sometimes called to be of order 0.5. Basis functions of higher order can also be utilised to represent the surface current densities [35]. However, due to the fact that the extreme near-field accuracy in inverse source formulations is first of all not that important and second not that easy to maintain anyways, higher-order discretisations of the equivalent surface currents are not recommended in most cases. This is even more the case since higher-order expansion functions lead often to a worse conditioning of the problem formulation than low-order functions. In view of this, one may even consider to work with even simpler basis functions than the RWG functions, e.g., just with electric and magnetic Dirac dipoles located at the centres of the mesh edges of the triangle pairs, i.e., with functions of the form

$$\underline{\beta}_c^{\delta}(\underline{r}) = l_c \widehat{\underline{e}}_c \delta\left(\widehat{\underline{n}}\left(\underline{r}_c\right) \times \left(\underline{r} - \underline{r}_c\right)\right) \tag{9.72}$$

where $\widehat{\underline{e}}_c$ is a unit vector along the common edge, $\widehat{\underline{n}}(\underline{r}_c)$ is the surface normal at the location $\underline{r}_c$, and $\underline{r}_c$ is the centre of the common edge, or with meshless functions as considered later on in this chapter.

As already mentioned earlier in this chapter, a formulation of the inverse equivalent source problem with electric and magnetic surface current densities at the same time, but without any further condition is redundant, i.e., it supports a null-space of non-radiating currents, but it can still deliver the correct near-field distribution in the complete volume V_1.

A formulation with electric and magnetic surface current densities is sometimes called a dual-source formulation. Single-source formulations, which do not own the mentioned kind of redundancy are possible, but should be carefully designed. For instance, one could work with either electric or magnetic surface current densities alone. However, this leads in general to a relatively badly conditioned transformation problem and is, thus, not recommended. A further single-source formulation will be discussed later on. Before this, we would like to discuss the possibility to eliminate the mentioned redundancy of the dual-source formulation by setting up a further condition, which needs to be fulfilled by the fields radiated from the equivalent dual-source representation.

9.6.2 Surface current densities with Love condition

When we look into the derivation of the Huygens principle in Section 9.4, then we find that the equivalent electric and magnetic surface current densities are related to

the tangential magnetic and electric fields on the Huygens surface S_1 (just inside the volume V_1) according to

$$\underline{J}_A(\underline{r}) = \underline{\hat{n}}(\underline{r}) \times \underline{H}(\underline{r}), \quad \underline{M}_A(\underline{r}) = \underline{E}(\underline{r}) \times \underline{\hat{n}}(\underline{r}). \tag{9.73}$$

Since the tangential fields are uniquely defined on the surface S_1, the equivalent surface current densities are, therefore, also uniquely defined, but the question is how we can enforce the fulfillment of the condition in (9.73). Formally, this is easy, since we can observe that the presence of these, so-called Love surface current densities, causes a jump of the true tangential fields at the surface S_1 within the volume V_1 to zero just on the other side of the surface currents, i.e., just inside the AUT volume V_S and due to the uniqueness theorem this leads to zero total fields throughout the complete AUT volume V_S. From this observation it is clear that we are going to obtain the Love surface current densities according to (9.73), if we perform our inverse equivalent current solution under the side constraint that the currents produce zero fields inside the volume V_S or zero tangential fields just inside the surface S_1. This kind of side condition is known as Love or zero-field condition and can be written in the form of additional integral equations. Formally, we can evaluate (9.69) and its dual version for the magnetic field for a collection of observation points inside the AUT volume V_S and force the result to zero, in order to implement the Love or zero-field condition. However, such a procedure would raise the question how to choose the observation points in V_S. More reliable appears to enforce the zero-field condition directly on the surface S_1, and implement a surface integral equation formulation of the zero-field condition in a way as known from the numerical solution of radiation and scattering problems [1,2]. However, towards this we have to take care of the singularities of the Green's functions, which occur for observation locations approaching the surface S_1. If we look into the mathematical formulation of the Huygens principle in Section 9.4, we can observe that the Dirac delta in (9.26) is directly located on the surface S_1 in these cases. The subsequent volume integration of the Dirac delta will, thus, lead to an additional ½ related to $\underline{M}_A(\underline{r})$ and $\underline{J}_A(\underline{r})$, if the surface is assumed to be smooth and the Dirac delta is assumed to be symmetric.[2] With this in mind, (9.69) and its dual version for the magnetic field can be written as

$$\underline{M}_A^L(\underline{r}) = \frac{1}{2}\underline{M}_A(\underline{r}) - \underline{\hat{n}}(\underline{r}) \times \oint\!\!\!\!\!\!\diint_{S_1} \left[\underline{\underline{G}}_J^E(\underline{r},\underline{r}') \cdot \underline{J}_A(\underline{r}') + \underline{\underline{G}}_M^E(\underline{r},\underline{r}') \cdot \underline{M}_A(\underline{r}')\right] da' \Big|_{\underline{r}\in S_1} \tag{9.74}$$

[2]Instead of relying on a symmetric Dirac delta, it is also possible to slightly deform the integration surface around the observation point and evaluate the singular integral contribution for a shrinking deformation according to the original Stratton–Chu approach [87,88].

$$\underline{J}_A^L(\underline{r}) = \frac{1}{2}\underline{J}_A(\underline{r}) + \hat{\underline{n}}(\underline{r}) \times \oiint_{S_1}\left[\underline{\underline{G}}_J^H(\underline{r},\underline{r}')\cdot\underline{J}_A(\underline{r}') + \underline{\underline{G}}_M^H(\underline{r},\underline{r}')\cdot\underline{M}_A(\underline{r}')\right]da'\Big|_{\underline{r}\in S_1} \tag{9.75}$$

where we have utilised the conditions (9.73) in order to replace the tangential fields on the left-hand side of the equations and where we indicate the corresponding surface current densities by the superscript L to make clear that these surface current densities fulfill the Love condition, whereas the surface current densities on the right-hand side of the equations can be any set of equivalent currents which solve the inverse source problem. In this sense, (9.74) and (9.75) can be seen as projectors, which are known as Calderon projectors in literature [36]. By assuming that the Love current densities are present on both sides of the equations, we may write them as constraint equations in the form of

$$\frac{1}{2}\underline{M}_A(\underline{r}) = -\hat{\underline{n}}(\underline{r}) \times \oiint_{S_1}\left[\underline{\underline{G}}_J^E(\underline{r},\underline{r}')\cdot\underline{J}_A(\underline{r}') + \underline{\underline{G}}_M^E(\underline{r},\underline{r}')\cdot\underline{M}_A(\underline{r}')\right]da'\Big|_{\underline{r}\in S_1} \tag{9.76}$$

$$\frac{1}{2}\underline{J}_A(\underline{r}) = +\hat{\underline{n}}(\underline{r}) \times \oiint_{S_1}\left[\underline{\underline{G}}_J^H(\underline{r},\underline{r}')\cdot\underline{J}_A(\underline{r}') + \underline{\underline{G}}_M^H(\underline{r},\underline{r}')\cdot\underline{M}_A(\underline{r}')\right]da'\Big|_{\underline{r}\in S_1} \tag{9.77}$$

where the superscript L indicating Love currents has been dropped. Equation (9.76) can be seen as an electric field integral equation (EFIE) and (9.77) can be seen as a magnetic field integral equation (MFIE), where already one of these equations alone would give a sufficient number of constraint equations after discretisation. However, such a formulation could possibly suffer from parasitic interior resonances, as known from the numerical solution of radiation and scattering problems [2,3]. Therefore, it is recommended to enforce both equations simultaneously or a combination of both equations in the form of a combined field integral equation (CFIE) as, e.g., given in the form

$$\begin{aligned}\frac{1}{2}\left[(1-\alpha)Z\left(\hat{\underline{n}}(\underline{r})\times\underline{J}_A(\underline{r})\right) - \alpha\underline{M}_A(\underline{r})\right] &= \alpha\hat{\underline{n}}(\underline{r}) \times \oiint_{S_1}\left[\underline{\underline{G}}_J^E(\underline{r},\underline{r}')\cdot\underline{J}_A(\underline{r}') + \underline{\underline{G}}_M^E(\underline{r},\underline{r}')\cdot\underline{M}_A(\underline{r}')\right]da'\Big|_{\underline{r}\in S_1} \\ &\quad + (1-\alpha)Z\,\hat{\underline{n}}(\underline{r})\times\hat{\underline{n}}(\underline{r}) \\ &\quad \times \oiint_{S_1}\left[\underline{\underline{G}}_J^H(\underline{r},\underline{r}')\cdot\underline{J}_A(\underline{r}') + \underline{\underline{G}}_M^H(\underline{r},\underline{r}')\cdot\underline{M}_A(\underline{r}')\right]da'\Big|_{\underline{r}\in S_1}\end{aligned} \tag{9.78}$$

where α is here the CFIE combination parameter commonly chosen in the range from 0 to 1, preferably close to one for standard discretisations with RWG basis functions in order to have a stronger weight for the commonly more accurate EFIE.

9.6.3 Surface current densities with combined-source condition

The Love or zero-field condition as discussed in the previous subsection is certainly the most popular side condition for the formulation of the inverse equivalent surface current problem, since it reliably removes the redundancy due to the dual-source formulation and it results in a well-understood definition of the surface current densities according to (9.73). However, the utilisation of the Love condition in a numerical implementation has the downside that it leads to a fully populated discretised operator equation, whose evaluation or solution can easily consume more computation time than the evaluation or solution of the inverse source operator itself. Therefore, it is of great benefit to have side conditions at hand, which are computationally less demanding.

An excellent side condition in this respect can easily be derived from the CFIE side condition as given in (9.78) by only keeping the left-hand side of the equation and setting the right-hand side of the equation to zero, resulting in

$$Z\left(\hat{\underline{n}}(\underline{r}) \times \underline{J}_A(\underline{r})\right) - \underline{M}_A(\underline{r}) = 0 \;\Rightarrow\; \underline{M}_A(\underline{r}) = Z\left(\hat{\underline{n}}(\underline{r}) \times \underline{J}_A(\underline{r})\right) \tag{9.79}$$

where the choice $\alpha = 1/2$ is here in general recommended and has been used in writing (9.79). This kind of condition is known in electromagnetics literature as a combined-source (CS) condition [20,21] and it is also strongly related to the even more popular impedance boundary condition [2,3], which is often used for scattering problems, i.e., when a wave is impinging on a material object with certain material properties. It can be easily verified that the CS condition according to (9.79) is an exact zero-field condition for the case of a planar Huygens surface and for a plane wave propagating through this surface in perpendicular direction out of the AUT volume. The CS condition can approximate the zero-field condition rather well for smooth and convex surfaces S_1.

If we wish to work with RWG basis functions for the discretisation of the surface current densities and if we wish to fulfill the CS condition in a strong form, then it is clear that we can only discretise one of the surface current types with RWG functions $\underline{\beta}_p^{RWG}(\underline{r})$, for example, the electric surface current densities $\underline{J}_A(\underline{r})$. The other type of surface currents, in the example the magnetic surface current densities $\underline{M}_A(\underline{r})$, will have to be discretised by rotated versions of the RWG functions, resulting in

$$\underline{J}_A(\underline{r}) = \sum_p J_p \underline{\beta}_p^{RWG}(\underline{r}), \quad \underline{M}_A(\underline{r}) = \sum_p J_p Z\left(\hat{\underline{n}}(\underline{r}) \times \underline{\beta}_p^{RWG}(\underline{r})\right) \tag{9.80}$$

A strong-form enforcement of the CS condition for Dirac delta basis functions as introduced in (9.72) results in elementary radiators with

$$\underline{J}(\underline{r}) = J_c l_c \hat{\underline{e}}_c \delta\left(\underline{r} - \underline{r}_c\right), \quad \underline{M}(\underline{r}) = J_c Z\left(\hat{\underline{n}}(\underline{r}) \times \hat{\underline{e}}_c \delta\left(\underline{r} - \underline{r}_c\right)\right) \tag{9.81}$$

Such elementary radiators are known in electromagnetics literature under the name Huygens radiators and they exhibit a main beam directed along the surface

normal of the surface S_1 into the volume V_1. At the same time, they have zero radiation into the opposite direction, i.e., very weak radiation into the AUT volume V_S, what is, of course, only strictly valid for AUT volumes of convex shape. Needless to mention is that the elementary radiators constructed by RWG basis functions according to (9.80) have a very similar directive radiation behaviour out of the AUT volume V_S.

A disadvantage of the strong-form CS condition with RWG function discretisation is that the divergence-conforming property of the RWG functions is lost by applying the $\widehat{\underline{n}}(\underline{r})\times$ operator. The resulting functions are curl-conforming and, therefore, very appropriate basis functions for the representation of fields. When used to represent surface current densities, curl-conforming functions produce stronger singularities than divergence conforming functions, due to line charges associated with discontinuous normal current components at the triangle edges. As mentioned earlier, the Dirac delta functions behave even worse in this respect, even without CS condition, but in general this issue is not of great relevance for inverse equivalent source solutions, since the field and current accuracy on and near to the Huygens surface S_1 is anyways restricted due to the loss of evanescent field information. Evanescent waves are commonly caused by strongly varying sources, but their magnitudes decay strongly away from the sources and in an inverse equivalent source solution evanescent wave contributions are often below the noise level at the measurement locations.

Starting from a fully divergence conforming discretisation of both surface current densities, we will present a weak-form (WF) implementation of the CS condition in Section 9.8.2.

9.6.4 Sources in complex space

The CS condition as discussed in the previous section provides an approximation of the Love or zero-field condition. In some way, the functioning of the CS condition can be explained by the directivity of the corresponding equivalent sources towards the outside of convex AUT volumes, e.g., in the form of the Huygens elementary radiators obtained after discretisation. Based on this observation, we can expect that we find better approximations of the zero-field condition by working with equivalent sources and corresponding discretisation elements which exhibit even more directivity than obtained according to the CS condition. Such more directive equivalent sources can be constructed by shifting any kind of sources from real space into complex space according to

$$\underline{r}' = \underline{r}'_{real} + j\,\widehat{\underline{n}}(\underline{r}'_{real})\Delta \tag{9.82}$$

and by replacing the common Euclidean norm of the space according to $\|\underline{r}'\|_{Eu} = \sqrt{\underline{r}' \cdot \underline{r}'^{*}}$ in the Green's functions for calculating the fields due to the sources by a complex-valued distance according to

$$\|\underline{r}'\|_c = \sqrt{\underline{r}' \cdot \underline{r}'}. \tag{9.83}$$

The star in the superscript of the Euclidean norm stands here for complex conjugation. Based on these definitions and by choosing the correct branch of the complex square root function in (9.83), the fields of the sources in complex space can be computed, where the directivity of the resulting fields can be controlled by the parameter Δ in (9.82), which defines the imaginary shift in complex space. The key effect of the imaginary shift comes from the exponential function within the Green's functions see, for instance, the Green's function of the electric field due to an electric current in (9.39). In order to conceive an understanding of this effect, let us consider the exponential in the far-field representation of the Green's function, see, e.g., (9.40), whose essential part may be written as $e^{jk\underline{\widehat{e}}_r \cdot \underline{r}'}$. As said earlier, $\underline{r}'$ is here the complex source location, k is the wavenumber of free space, and $\underline{\widehat{e}}_r$ is a unit vector pointing into the far-field radiation direction. With (9.82), this exponential can be written in the form $e^{k\Delta\underline{\widehat{e}}_r \cdot \underline{\widehat{n}}(\underline{r}'_{real})} e^{jk\underline{\widehat{e}}_r \cdot \underline{r}'_{real}}$ and it becomes obvious that the first exponential with real argument will cause a change of the radiation magnitude dependent on the radiation direction, whereas the second exponential with imaginary argument causes the common change of the phase. The magnitude is obviously maximum in the direction of $\underline{\widehat{n}}(\underline{r}'_{real})$, i.e., in the direction of the imaginary shift and minimum in the opposite direction. An illustration of the far-field magnitude dependence on the imaginary shift Δ is shown in Figure 9.7 for different values of Δ in terms of the free-space wavelength λ. From this illustration, it becomes clear that the imaginary shift must be carefully adjusted dependent on the wavelength. A value of $\Delta = 0.5\lambda$ leads already to a variation of the magnitude pattern in the far-field of close to 60 dB. In the near-field close to the source location, the field dependence is of course more complicated, where in particular

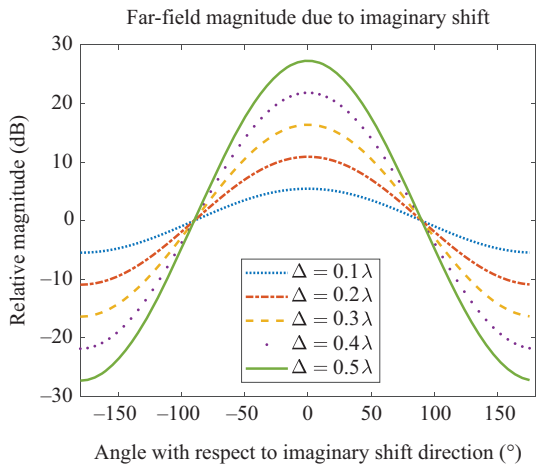

Figure 9.7 Far-field magnitude dependence on radiation angle due to imaginary shift Δ into complex space in terms of wavelength

also the singular behaviour of the fields is changed as compared to the case of real source locations.

In order to gain further insight into the far-field behaviour of equivalent surface current distributions, Figures 9.8 and 9.9 illustrate the relative far-field magnitudes of two different RWG basis function based radiators for different imaginary shifts into complex space. As seen from Figure 9.8, an RWG function electric current radiator with no imaginary shift exhibits a symmetric radiation pattern with respect to its surface normal, but by an imaginary shift along the surface normal, we obtain an adjustable directivity into the direction of the surface normal. In contrast, the Huygens type radiator as demonstrated in Figure 9.9 owns already a certain directivity into the direction of the surface normal without any imaginary shift. This directivity becomes more pronounced by an increasing imaginary shift.

Near-field distributions within the *xy*-plane for the same two elementary radiators with different imaginary shifts are found in Figures 9.10–9.15, where Figures 9.10–9.12 relate to the electric current type RWG function based radiator and Figures 9.13–9.15 give the corresponding results for the Huygens-type radiator with electric surface current density in the form of an RWG function and with the magnetic surface current density in terms of a rotated RWG function. The NF distributions show also the directive radiation behaviour as already found for the far-field magnitudes, but interesting is especially also the singular behaviour very close to the source location. For larger imaginary shifts, a somewhat irregular field distribution close to the sources is seen. If the near-fields in an inverse equivalent source solution shall be evaluated very close to the actual AUT surface, it is, therefore, recommended to stay at least outside of the distributed singularity region of the equivalent source elementary radiators in complex space.

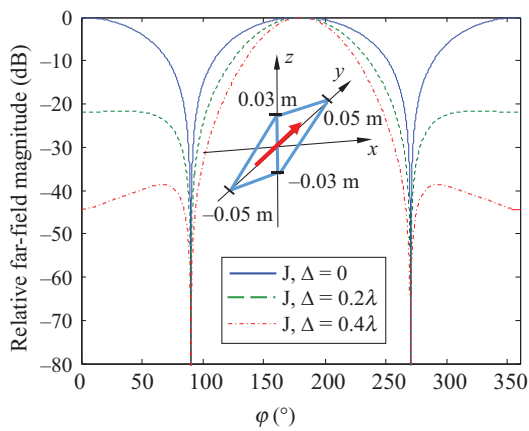

Figure 9.8 Far-field magnitude dependence on radiation angle due to imaginary shift Δ into complex space of an RWG basis function electric current radiator

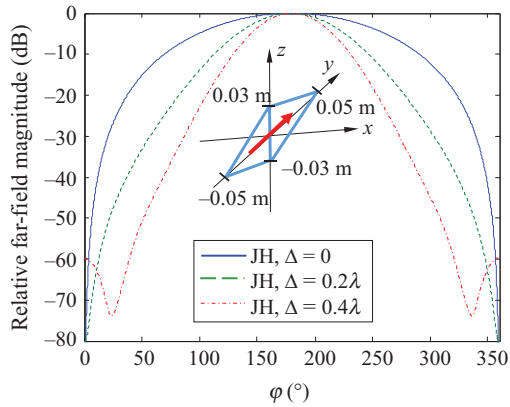

Figure 9.9 Far-field magnitude dependence on radiation angle due to imaginary shift Δ into complex space of an RWG function-based Huygens radiator with $\underline{J}_A(\underline{r}) = J_c \underline{\beta}_c^{RWG}(\underline{r})$, $\underline{M}_A(\underline{r}) = Z_0 J_c \left(\underline{\hat{n}}(\underline{r}) \times \underline{\beta}_c^{RWG}(\underline{r})\right)$

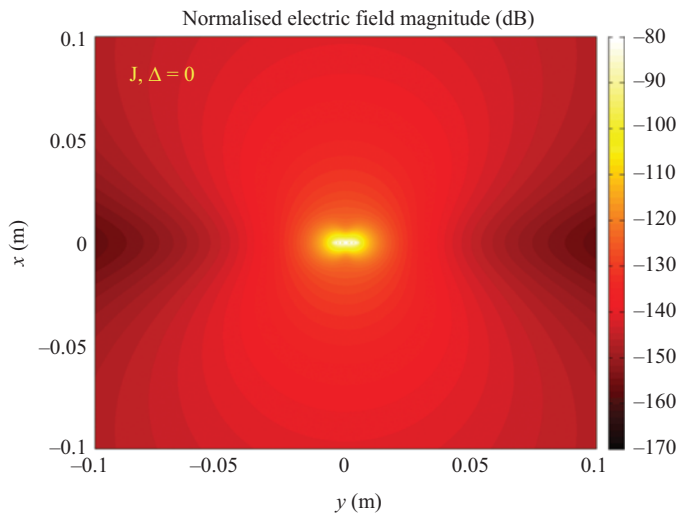

Figure 9.10 Near-field magnitude distribution of an RWG electric current radiator with imaginary shift $\Delta = 0$

9.6.5 Distributed spherical-wave or plane-wave expansion

As already mentioned earlier in this chapter, we may also work with a spectral representation of the AUT in the form of $\underline{W}_1^{Tx}(\underline{r}_1, \underline{k})$ as, e.g., utilised in the transmission equation (9.59). This spectral representation is nothing else than the

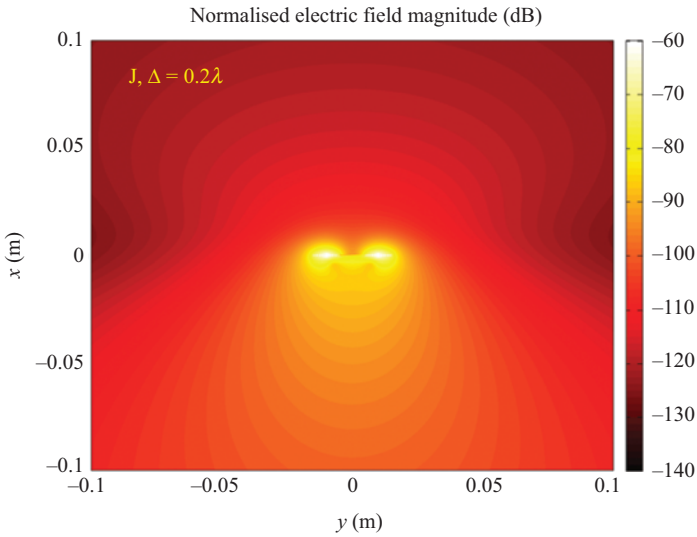

Figure 9.11 *Near-field magnitude distribution of an RWG electric current radiator with imaginary shift $\Delta = 0.2\lambda$*

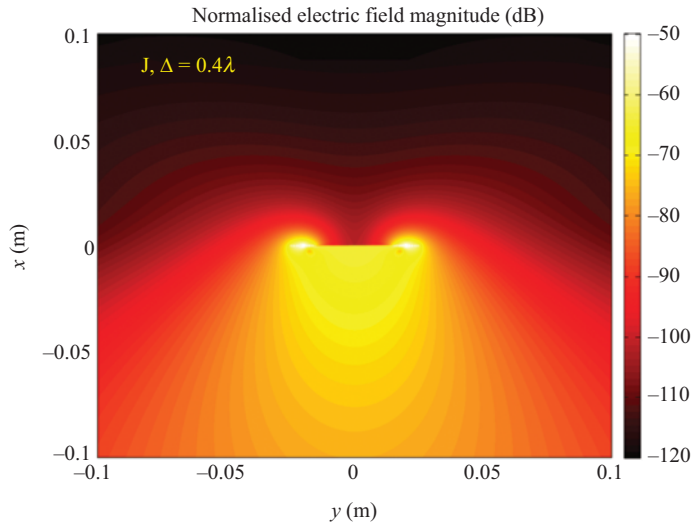

Figure 9.12 *Near-field magnitude distribution of an RWG electric current radiator with imaginary shift $\Delta = 0.4\lambda$*

far-field of the AUT with respect to its reference location $\underline{r}_1$. The downside of this representation is that it can only represent the AUT fields outside of the minimum sphere around the AUT with good accuracy. This in turn means that the equivalent volume V_S of the AUT is identical to the minimum sphere, but an AUT volume in

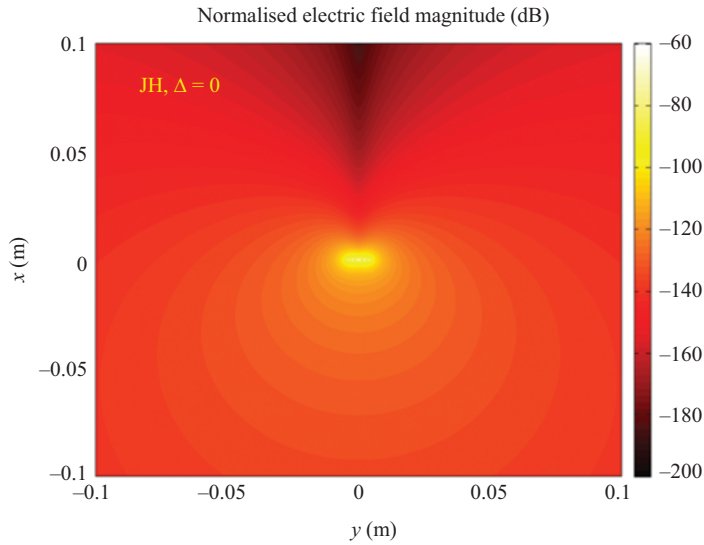

Figure 9.13 Near-field magnitude distribution of an RWG Huygens radiator with imaginary shift $\Delta = 0$

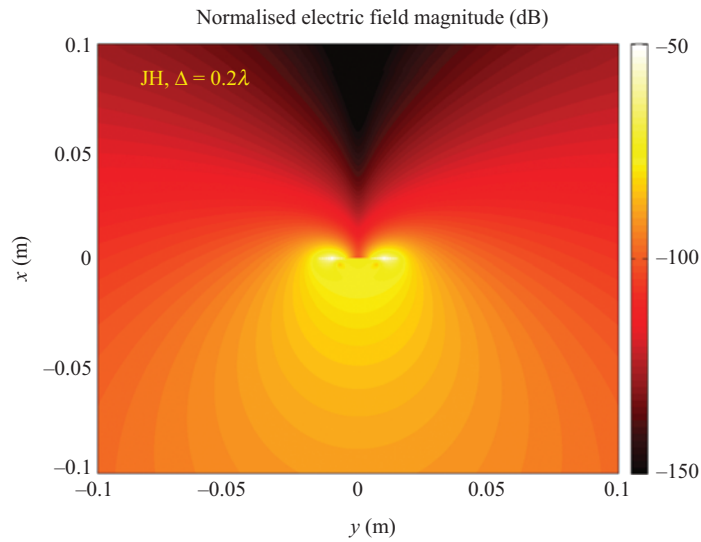

Figure 9.14 Near-field magnitude distribution of an RWG Huygens radiator with imaginary shift $\Delta = 0.2\lambda$

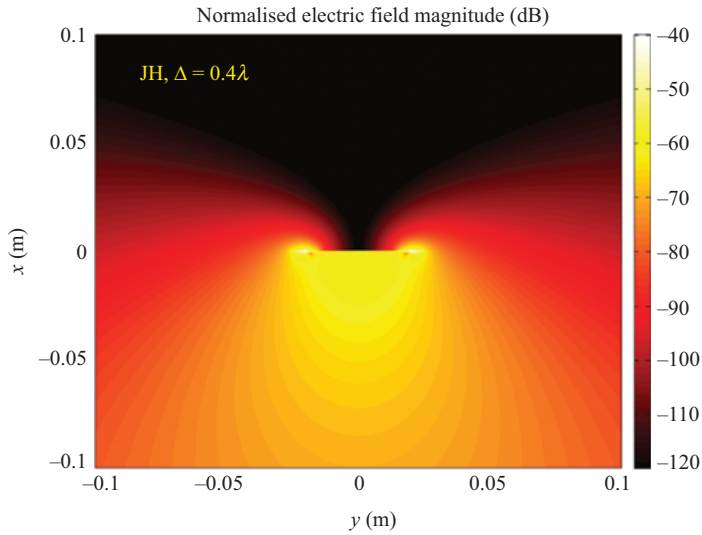

Figure 9.15 Near-field magnitude distribution of an RWG Huygens radiator with imaginary shift Δ= 0.4λ

the form of a sphere is often not very suitable, in particular not for elongated AUTs, where the measurement samples may even be located inside the minimum sphere. This issue is easily overcome by the spatial current distributions as discussed in the previous subsection, but another approach with more flexibility are distributed spectral source representations. In an implementation this means that we work with a set of spectral AUT representations $\underline{W}^{Tx}_{1,i=1,\ldots,I}(\underline{r}_1 + \Delta\underline{r}_i, \underline{k})$, where i is an index indicating the I different spectral representations and $\Delta\underline{r}_i$ is the location of the corresponding expansion centre with respect to the AUT reference location $\underline{r}_1$. As also discussed earlier, every one of these localised far-field representations can directly be sampled on the Ewald sphere in k-space or a spherical multipole expansion with a certain order may be used instead. Since now every localised FF representation models only a small portion of the entire AUT, the number of integration samples or correspondingly the spherical multipole order is chosen according to this small volume portion, and, thus, considerably smaller than for the entire AUT. However, in the course of the solution of the inverse source problem, the various expansions have, of course, to be appropriately considered altogether. Figure 9.16 illustrates the placement of distributed spectral expansion centres in a regular spatial box arrangement, where the expansion centres are located in such boxes which contain parts of the AUT geometry. Sticking to such a regular box configuration does not follow the AUT geometry as good as possible and needs also more expansion coefficients than really necessary, but it has considerable advantages in the numerical evaluation, in particular together with the efficient evaluation of the transmission equation by hierarchical concepts according to the MLFMM.

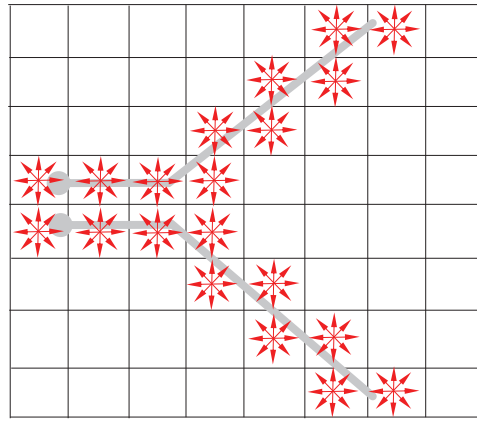

Figure 9.16 Placement of distributed spectral expansion centres in a regular box configuration adapted to the geometry of an AUT

9.7 Equivalent source representations of the measurement probe

In principle, the measurement probe antenna can be represented by exactly the same types of sources as the AUT, where the specific source distribution is, however, assumed to be completely known and does not need to be determined in the inverse problem solution. In a specific transformation problem, it is nevertheless of advantage to assume certain properties of the probe and choose an equivalent source representation of the probe, which is most suited, in particular with respect to the numerical implementation and evaluation of the inverse problem solution.

In near-field measurements, the utilised measurement probe is often electrically rather small, such that a distributed source representation of the probe is in general not necessary. Therefore, recommended representations of the probe may work directly with a discretised form of the spectral far-field representation of the probe, e.g., of $\underline{W}_2^{Tx}(\underline{r}_2, \underline{k})$ in the form of spectral samples on the Ewald sphere or by a spherical mode expansion. The number of samples for the representation of the probe pattern or the corresponding multipole order needs to be chosen according to the spectral content of the probe, which depends on the geometric extent of the probe and its properties. Super-directive effects are in general ignored in the estimation of the required sample density and of the multipole order. The discretised spectral or modal probe representation may be utilised for all situations, where the probe minimum sphere does not overlap with parts of the AUT. If this happens, a distributed source representation of the probe may be chosen, e.g., in the form of sub-spectra as discussed in [37].

Alternatively, the probe may be considered in the form of a discretised representation of the probe weighting function as given in (9.67). The simplest case here would be to place one Dirac delta like current element, i.e., a Hertzian dipole at the probe reference location. Since a Hertzian dipole senses the aligned electric field component as it is, such a probe representation would in general imply that we do not work with any kind of probe correction. The term ‘no probe correction’ means

that we assume Hertzian dipole probes, where of course, two independent, possibly orthogonal, polarisations need to be used for general measurements. More accurate spatial probe representations can be achieved by working with spatial arrangements of Hertzian dipoles or with other kinds of elementary radiators, as, e.g., discussed in Section 9.6.

An important question is how we can get the knowledge about the probe behaviour and its equivalent source representation. The most straightforward way is to measure the probe far-field radiation and/or receive behaviour and derive the equivalent source representation from these measurements. It is understood that the polarimetric probe pattern needs to be known for all directions with sufficient sampling density for magnitude and phase. With relative probe patterns, relative AUT patterns and equivalent source distributions can be found. With gain or absolute field magnitude calibrated probe patterns, similarly calibrated AUT patterns and source distributions can be determined. Dependent on how well a probe is known and understood, probe measurements may be replaced by computer simulations in order to derive the necessary data for reliable probe consideration within the inverse problem solution. Simulated or measured far-field data can directly be used in an inverse source problem, if the probe is considered by a spectral far-field representation, e.g., in the form of $\underline{W}_2^{Tx}(\underline{r}_2, \underline{k})$. Spatial probe weighting function distributions, e.g., in the form of the source types as discussed in Section 9.6, representing a given probe can for instance be obtained by solving an inverse equivalent source problem based on available far-field measurements or simulations.

In a numerical implementation of the inverse source problem solution, it is in general recommended to work with a coordinate system, which is either fixed to the AUT or to the probe. If the AUT is geometrically larger than the probe, then the recommendation can be further specified to work with an AUT related coordinate system. This in turn means that the probe antenna (or antennas, in the case of multiple different probes) needs to be moved and/or rotated within the AUT coordinate system for every measurement sample. Still, the probe behaviour will be defined in a probe specific coordinate system, e.g., in a way that the probe FF representation $\underline{W}_2^{Tx}$ is defined in the form of $\underline{W}_2^{Tx}(\underline{0}, \underline{k})$, i.e., for a reference position and for a fixed rotation angle. For example, the main beam of the probe may be directed along the x-axis. Similarly, the elementary radiators in a spatial probe representation may be located in such a local probe coordinate system.

If the inverse source problem shall now be solved in an AUT fixed coordinate system, a systematic way to consider the introduced prototype representation of the probe is to formally perform translations and rotations of the required quantities. For the spectral representation of the transmission equation in (9.59), this results in

$$\begin{aligned} S_{21} &= \frac{b_2\left(\underline{r}_2\right)}{a_1\left(\underline{r}_1\right)} \\ &= \frac{1}{2jk}\oiint T_L(\underline{r}_{21}, \underline{k})\underline{\underline{R}}^T \cdot \underline{W}_{Probe}^{Prot,Tx}(\underline{r}_2, -\underline{\underline{R}} \cdot \underline{k}) \cdot \underline{W}_1^{Tx}(\underline{r}_1, \underline{k}) d^2\widehat{\underline{k}} \end{aligned} \quad , \tag{9.84}$$

where the probe receiving behaviour in the specific measurement location $\underline{r}_2$ is considered by

$$\underline{W}_2^{Tx}(\underline{r}_2, -\underline{k}) = \underline{\underline{R}}^T \cdot \underline{W}_{Probe}^{Prot,Tx}(\underline{r}_2, -\underline{\underline{R}} \cdot \underline{k}). \tag{9.85}$$

The superscript *Prot* indicates here the prototype representation of the probe in its local coordinate system. The dyadic or tensor operator $\underline{\underline{R}}$ performs a three-dimensional rotation operation. First, the propagation direction $\underline{k}$ of a wave incident on the probe is rotated into the local probe coordinate system, afterwards the probe pattern vector components are rotated back into the AUT coordinate system by the transpose of the rotation operator $\underline{\underline{R}}^T$.

Similarly, a prototype representation of the probe antennas is of course also useful for a spatial representation of the probe, as for instance used in (9.38), which may be written as

$$\begin{aligned} -\underline{U}_2\left(\underline{r}_2\right) = \iiint_{V_2} \Big(& \underline{\underline{R}}^T \cdot \underline{w}_{Probe}^{Prot}\left(\underline{\underline{R}} \cdot \left(\underline{r} - \underline{r}_2\right)\right) \\ & \cdot \iiint_{V_1} \underline{\underline{G}}_J^E\left(\underline{r}, \underline{r}'\right) \cdot \underline{J}_1\left(\underline{r}' - \underline{r}_1\right) dv' \Big) dv \end{aligned} \tag{9.86}$$

where the operator $\underline{\underline{R}}$ performs again the appropriate rotation of the probe.

9.8 Discretisation of the forward problem

In the previous sections, we have introduced several transmission and constraint equations in continuous form, which need to be inverted or enforced in order to solve our antenna field transformation problem at hand. Since the continuous equations have formally an infinite number of degrees of freedom, we must reduce them to a finite set of unknowns together with a finite set of corresponding transmission and constraint equations. This is commonly achieved by discretisation. In the following, we restrict ourselves to method of moments (MoM) types of discretisation, which are very powerful and versatile, and thus very well suited for our antenna field transformation problem, possibly supplemented by additional constraint equations.

For the utilisation of MoM, let us assume that we have one or more operator equations in the form

$$\underline{K}\left(\underline{x}(\underline{r})\right) + \underline{L}\left(\underline{y}(\underline{r})\right) = \underline{b}(\underline{r}), \tag{9.87}$$

where $\underline{b}(\underline{r})$ is a known right-hand side vector quantity, $\underline{K}(.)$ and $\underline{L}(.)$ are linear vector operators, and $\underline{x}(\underline{r})$ and $\underline{y}(\underline{r})$ are the vector quantities, which shall be determined. As seen, the right-hand side vector quantity and the unknown quantities, in our case the equivalent sources representing the AUT, depend on $\underline{r}$, where the equivalent sources are only defined in the AUT volume V_S or on the surface S_1 enclosing the AUT volume.

In order to derive a discretised version of (9.87), we start with an expansion of the unknown quantities $\underline{x}(\underline{r})$ and $\underline{y}(\underline{r})$ in the form

$$\underline{x}(\underline{r}) = \sum_p x_p \underline{\beta}_p(\underline{r}), \quad \underline{y}(\underline{r}) = \sum_q y_q \underline{\beta}_q(\underline{r}) \tag{9.88}$$

where $\underline{\beta}_{p/q}(\underline{r})$ are a finite set of known expansion or basis functions as, e.g., already discussed in the previous section for the surface current densities $\underline{J}_A(\underline{r}')$ and $\underline{M}_A(\underline{r}')$ with x_p and y_q being the corresponding expansion coefficients to be determined. Plugging these expansions into (9.87), it can no longer exactly be fulfilled due to the finite number of degrees of freedom and we may write it as

$$\underline{K}\left(\sum_p x_p \underline{\beta}_p(\underline{r})\right) + \underline{L}\left(\sum_q y_q \underline{\beta}_q(\underline{r})\right) - \underline{b}(\underline{r}) = \underline{R}(\underline{r}) \tag{9.89}$$

where $\underline{R}(\underline{r})$ is a residual vector error term which carries the error due to the discretisation of the unknown quantities. Due to the assumed linearity of the operators $\underline{K}(.)$ and $\underline{L}(.)$, the order of the expansion summations and the operators can be interchanged resulting in

$$\sum_p x_p \underline{K}\left(\underline{\beta}_p(\underline{r})\right) + \sum_q y_q \underline{L}\left(\underline{\beta}_q(\underline{r})\right) - \underline{b}(\underline{r}) = \underline{R}(\underline{r}). \tag{9.90}$$

The goal is now to minimise this residual error by appropriately choosing the expansion coefficients x_p and y_q. In order to achieve this, we can follow different strategies. In MoM, or the more or less identical method of weighted residuals, we multiply the whole equation with vector weighting or testing functions $\underline{w}_m(\underline{r})$ and integrate over the support of the weighting functions. The results of these weighted residual integrals are forced to zero and we obtain thus a set of linear equations, one equation for every $\underline{w}_m(\underline{r})$, in the form

$$\sum_p x_p \left\langle \underline{w}_m(\underline{r}), \underline{K}\left(\underline{\beta}_p(\underline{r})\right)\right\rangle + \sum_q y_q \left\langle \underline{w}_m(\underline{r}), \underline{L}\left(\underline{\beta}_q(\underline{r})\right)\right\rangle = \left\langle \underline{w}_m(\underline{r}), \underline{b}(\underline{r})\right\rangle \tag{9.91}$$

The $\langle .,. \rangle$ operator stands here for the inner product, which comprises first a scalar product of the two input vector quantities and a subsequent integration over the common support of both input quantities. Dependent on the type of operator equation and the representation of the weighting functions (e.g., in spatial domain or in spectral domain), the integration domain can be different. Typically, the known right-hand side vector quantity $\underline{b}(\underline{r})$ is important in this respect, in particular the domain on which it shall be evaluated or where it is known.

9.8.1 Discretisation of the transmission equations

If we first look into the transmission equations of our antenna measurement problem, the weighting or testing process is carried out by the measurement probe,

when it measures the antenna fields at a certain location in space. The result of this measurement process is commonly the $S_{21,m}(\underline{r}_m)$ transmission parameter between the probe at the measurement location and the AUT, which can be measured with transmitting probe or with transmitting AUT, due to reciprocity. Alternatively, the measurement signal might be the voltage at the probe output for a transmitting AUT, as found in several of the transmission equations as discussed in this chapter. For a spatial probe representation as utilised, e.g., in (9.38) or in the form of a prototype probe in (9.86), the weighting integral is a volume integral over the probe volume at the measurement location $\underline{r}_m$. In contrast, for a spectral domain transmission equation as, e.g., utilised in (9.51), (9.59), or (9.84), the weighting integral is finally performed over the Ewald sphere in k-space and the corresponding spectral representation of the measurement probe is used.

The transmission equation, which is most convenient for a numerical solution of the inverse source problem with full probe correction and more or less arbitrary location of the measurement samples, is (9.84), but with the AUT far-field transmit antenna transfer function represented in terms of electric and magnetic surface current densities. Starting from (9.84) with $\underline{\underline{W}}_1^{Tx}$ replaced by H_1^{Tx} according to (9.54) and this one subsequently replaced by its integral representation in terms of electric and magnetic surface current densities according to (9.42) and (9.48), respectively, we obtain first

$$S_{21,m}\left(\underline{r}_m\right) = c_2 \oiint T_L(\underline{r}_{m1}, \underline{k}) \underline{\underline{R}}_m^T \cdot \underline{\underline{W}}_{Probe}^{Prot,Tx}(\underline{r}_m, -\underline{\underline{R}}_m \cdot \underline{k}) \cdot \underline{H}_1^{Tx}(\underline{r}_1, \underline{k}) d^2\widehat{\underline{k}} \tag{9.92}$$

with

$$c_2 = \frac{1}{2jk} \frac{(1-\Gamma_1)}{\sqrt{Z_{ref}}} \sqrt{\frac{1}{4\pi Z}} \tag{9.93}$$

and then

$$\begin{aligned} S_{21,m}\left(\underline{r}_m\right) = c_3 \oiint & T_L(\underline{r}_{m1}, \underline{k}) \underline{\underline{R}}_m^T \cdot \underline{\underline{W}}_{Probe}^{Prot,Tx}(\underline{r}_m, -\underline{\underline{R}}_m \cdot \underline{k}) \cdot \underline{\underline{I}}^{FF} \\ & \cdot \iint_{S_1} \left[\frac{Z \underline{J}_{A,1}\left(\underline{r}' - \underline{r}_1\right)}{Z I_1\left(\underline{r}_1\right)} - j \frac{\left(\widehat{\underline{k}} \times \underline{M}_{A,1}(\underline{r}' - \underline{r}_1)\right)}{Z I_1\left(\underline{r}_1\right)} \right] \\ & e^{jk\,\widehat{\underline{k}} \cdot (\underline{r}' - \underline{r}_1)} da' d^2\widehat{\underline{k}} \end{aligned} \tag{9.94}$$

with

$$c_3 = -\frac{(1-\Gamma_1)}{2\sqrt{Z_{ref}}} \sqrt{\frac{Z}{4\pi}}. \tag{9.95}$$

The next step is to represent the electric and magnetic surface current densities by an expansion as given in (9.70) resulting in

$$S_{21,m}\left(\underline{r}_m\right) = c_3 \oiint T_L(\underline{r}_{m1}, \underline{k}) \underline{\underline{R}}_m^T \cdot \underline{W}_{Probe}^{Prot,Tx}(\underline{r}_m, -\underline{\underline{R}}_m \cdot \underline{k}) \cdot \underline{\underline{I}}^{FF} \cdot \iint_{S_1} \left[\sum_p Z J_p \underline{\beta}_p(\underline{r}') - j \sum_q M_q \left(\widehat{\underline{k}} \times \underline{\beta}_q(\underline{r}') \right) \right] e^{jk\widehat{\underline{k}} \cdot (\underline{r}' - \underline{r}_1)} da' d^2\widehat{\underline{k}} \tag{9.96}$$

where the expansion in basis functions is performed in a way that the normalisation by the product of the AUT feed current with the characteristic impedance of free space $ZI_1\left(\underline{r}_1\right)$ is appropriately considered. The expansion coefficients J_p are multiplied with the characteristic impedance of free space Z in order to achieve a better balanced system of equations with unknowns ZJ_p and M_q, which are on the same order of magnitude.

Utilising again the linearity of the operators and rearranging summations and integrations, we obtain

$$S_{21,m}\left(\underline{r}_m\right) = \sum_p ZJ_p \underbrace{\oiint c_3 T_L(\underline{r}_{m1}, \underline{k}) \underline{\underline{R}}_m^T \cdot \underline{W}_{Probe}^{Prot,Tx}(\underline{r}_m, -\underline{\underline{R}}_m \cdot \underline{k}) \cdot \tilde{\underline{\beta}}_p(\underline{r}_1, \underline{k}) d^2\widehat{\underline{k}}}_{L_{mp}}$$

$$+ \sum_q M_q \underbrace{\oiint (-jc_3) T_L(\underline{r}_{m1}, \underline{k}) \underline{\underline{R}}_m^T \cdot \underline{W}_{Probe}^{Prot,Tx}(\underline{r}_m, -\underline{\underline{R}}_m \cdot \underline{k}) \cdot \left(\widehat{\underline{k}} \times \tilde{\underline{\beta}}_q(\underline{r}_1, \underline{k}) \right) d^2\widehat{\underline{k}}}_{K_{mq}} \tag{9.97}$$

with

$$\tilde{\underline{\beta}}_{p/q}\left(\underline{r}_1, \underline{k}\right) = \underline{\underline{I}}^{FF} \cdot \iint_{S_1} \underline{\beta}_{p/q}(\underline{r}') e^{jk\widehat{\underline{k}} \cdot (\underline{r}' - \underline{r}_1)} da'. \tag{9.98}$$

If we perform a set of measurements for different probe positions with respect to the AUT, we obtain a corresponding set of linear equations, which may be written in matrix form as

$$\left[L_{mp}\right]\left[ZJ_p\right] + \left[K_{mq}\right]\left[M_q\right] = \left[S_{21,m}\right], \quad m = 1, \ldots, M, p = 1, \ldots, P, \quad q = 1, \ldots, Q. \tag{9.99}$$

The number of equations M is equal to the number of performed measurements, P is the number of electric surface current unknowns, and Q is the number of magnetic surface current unknowns. From the definition of the matrix elements, it is immediately obvious that the linear equation system is fully populated and it is also clear that the computation of the matrix elements in the form of the multiple integral representations can be very demanding. An analytical calculation of the matrix elements is in general not possible. The Fourier-type integral in (9.98) can in principle be calculated analytically for polynomial basis functions on polyhedral

domains such as the RWG basis functions on triangles, but a simple Gauss quadrature with very few points gives also very accurate results. The computation of the translation operator $T_L(\underline{k}, \underline{r}_{m1})$ requires to evaluate the series representation as given in (9.49) with the corresponding special functions. It is noted that the order L for the computation of the translation operator must be chosen very carefully according to the sizes of the source regions and the observation regions in order to achieve the desired accuracy. The probe pattern is in general known from measurements or from simulations and should be represented with sufficiently fine sampling according to its electrical size, and the rotation dyads can be computed according to the probe orientation with respect to the AUT. As already said, in most cases it will be convenient to assume an AUT-fixed coordinate system and a probe which is moving and/or rotating around the AUT.

The k-space integral over the Ewald sphere is commonly evaluated numerically. The φ-integration can be performed accurately by a trapezian rule with equidistant sampling, due to the periodicity in φ. The ϑ-integration is in most cases performed by Gauss–Legendre quadrature after the substitution $u = \cos\vartheta$, see for instance [1,8,38], but it is also possible to extend the ϑ-range from 0 to π to 0 to 2 π and work then with regular sampling as for φ, see, e.g., [39,40].

As shown later in this chapter, the matrix elements in (9.99) will in general not be computed in a one by one fashion, but the matrix products of the complete matrices with a specific input vector will be computed on the fly according to the principles of the FMM and its multi-level version (MLFMM).

Finally, it is noted that all the discretised transmission equations may also be evaluated for source currents which are shifted into complex space, as discussed in Section 9.6.4, or for distributed spherical-wave or plane-wave expansions.

9.8.2 Discretisation of supplementary constraint equations

In addition to the transmission equations representing the actual antenna measurements, we have introduced the so-called Love and CS condition in Sections 9.6.2 and 9.6.3, respectively. In a numerical evaluation, these additional constraint equations need to be discretised, too. Discretising the Love condition according to the CFIE in (9.78) in a fashion as demonstrated for (9.91), we obtain a system of linear equations in matrix form as

$$\left[L_{sp}^{C}\right]\left[ZJ_p\right] + \left[K_{sq}^{C}\right]\left[M_q\right] = [0], \quad s = 1,\ldots,S, p = 1,\ldots,P, q = 1,\ldots,Q \tag{9.100}$$

where the superscript C indicates that the equations have been derived from the CFIE. In a normal situation, the number of electric current coefficients P will be identical to the number of magnetic current coefficients Q, and the number of equations S will also be the same. However, different numbers of expansion coefficients for the two types of currents can be thought of and the number of equations will in these cases commonly either be equal to P or equal to Q, dependent on how the equation is tested. If one works with RWG basis functions to represent the

surface current densities in (9.78), the classical way of testing the equation is to work with weighting functions $\underline{w}_s(\underline{r}) = \underline{\hat{n}}(\underline{r}) \times \underline{\beta}_{p/q}^{RWG}(\underline{r})$ and the weighting integrals are thus evaluated over the discretised surface S_1 enclosing the AUT. However, other ways of testing can also be implemented. The discretisation of both the equations in (9.76) and (9.77) in side constraint form gives even more flexibility in the choice of the testing schemes, but this results also in a larger number of equations. If we choose again testing functions $\underline{w}_s(\underline{r}) = \underline{\hat{n}}(\underline{r}) \times \underline{\beta}_{p/q}^{RWG}(\underline{r})$, the result of the testing procedure is

$$\left[L_{tp}^{E}\right]\left[ZJ_p\right] + \left[K_{tq}^{E}\right]\left[M_q\right] = [0], \quad t = 1,\ldots,T, p = 1,\ldots,P, q = 1,\ldots,Q \tag{9.101}$$

$$\left[K_{sp}^{M}\right]\left[ZJ_p\right] + \left[L_{sq}^{M}\right]\left[M_q\right] = [0], \quad s = 1,\ldots,S, p = 1,\ldots,P, q = 1,\ldots,Q \tag{9.102}$$

where the superscript E indicates the origin EFIE and the superscript M the origin MFIE, respectively. Also, in most cased we will have $S = T = P = Q$. The MFIE is here tested differently than the MFIE part in the CFIE in (9.100), which is commonly of advantage for the accuracy when low-order RWG functions are used.

In the field of the numerical solution of radiation and scattering problems by related surface integral equation approaches, a lot of work has been done to understand the effects of different basis and testing functions and we can only refer to the relevant literature (for some examples see [2,41,42]). Similarly, the computation of the matrix elements in (9.100), (9.101), (9.102), or even other forms of the Love condition side constraint is a topic on which a vast amount of literature can be found (see, e.g., [2]). Whereas the radiation integrals in the transmission equations are in general not evaluated close to the actual sources, but only some distance away at the measurement locations, the integrals here need to be evaluated exactly on the surface S_1, where the source current densities are located. Therefore, the evaluation of the double surface integrals is commonly performed by numerical quadrature in a spatial domain representation, where the key difficulties of these integrals are the singular kernels due to the singularities of the involved Green's functions. Nowadays, a variety of techniques is available to compute these integrals up to machine precision. However, for our field transformation problem at hand, the accuracy is not that essential as for radiation or scattering problems. Equation (9.78) is 'only' a side condition to remove redundancy out of the field transformation problem. Even if it is not implemented with high accuracy, the field transformation problem can still be solved with high accuracy. For cases, where the sources and the testing locations have a large enough separation, these integrals can also be evaluated according to spectral domain representations, e.g., in the form of propagating plane waves according to the principles of FMM and MLFMM [1,15,43].

The projector equations (2.74) and (2.75) can be treated in a similar way as (9.76)–(9.78), where, however, even four sets of unknown quantities are involved.

The MoM procedure leads to a linear system of equations in the form

$$-\frac{1}{2}\left[G_{sq}\right]\left[M_q^L\right] = \left[B_{sp}^J\right]\left[ZJ_p\right] + \left[D_{sq}^M\right]\left[M_q\right], \quad s = 1,\ldots,S, p = 1,\ldots,P, \quad q = 1,\ldots,Q \tag{9.103}$$

$$\frac{1}{2}\left[G_{tp}\right]\left[ZJ_p^L\right] = \left[D_{tp}^J\right]\left[ZJ_p\right] + \left[B_{tq}^M\right]\left[M_q\right], \quad t = 1,\ldots,T, p = 1,\ldots,P, \quad q = 1,\ldots,Q. \tag{9.104}$$

The elements of the matrix $\left[G_{s/tq/p}\right]$ are here given as

$$G_{s/tq/p} = \frac{1}{c_4}\iint_{S_1} \underline{w}_{s/t}(\underline{r}) \cdot \underline{\beta}_{p/q}(\underline{r})\, da \tag{9.105}$$

where c_4 is Z or 1 dependent on the specific equation. The weighting and expansion functions should be chosen in a way that these matrices, which are known as Gram matrices, can be easily inverted in order to obtain Love surface current densities out of any other kind of surface current densities. In case of RWG expansion functions, the weighting functions are commonly also chosen as RWG functions and the matrix elements can in this case easily be computed analytically. The testing of the operators on the right-hand side of the equations is in this case not optimal according to the theory of the involved function spaces, where in terms of accuracy, however, the Gram matrices on the left- and right-hand side of the equations are more important. Especially with RWG functions, these Gram matrices limit the achievable accuracy, where, however, more advanced testing schemes may be thought of [42]. In contrast to the side-constraint equations (9.78)–(9.80), the projectors are directly applied to the system of transmission equations of the inverse source problem and they should, therefore, be evaluated with high accuracy.

If we finally come to the CS condition in (9.79), it should be noted that this condition can be implemented without any discretisation, i.e., in strong form as already shown in Section 9.6.3, where, however, the basis functions for the representation of one type of surface current densities are rotated around the surface normal by 90°. If this is done with RWG functions, they lose their divergence-conforming properties and become curl-conforming, and are thus no longer the appropriate basis functions for the representation of the other type of surface current density. This issue, which is again not really severe in an IESS, can be overcome by a WF representation of the CS condition, e.g., in a form as [21]

$$\left[G_{sq}\right]\left[M_q\right] = \left[G'_{sp}\right]\left[Z_F J_p\right], \quad s = 1,\ldots,S, \quad p = 1,\ldots,P, \quad q = 1,\ldots,Q \tag{9.106}$$

where the elements of the matrix $\left[G'_{sp}\right]$ are here given as

$$G'_{sp} = \iint_{S_1} \underline{w}_s(\underline{r}) \cdot \left(\hat{\underline{n}}(\underline{r}) \times \underline{\beta}_p(\underline{r})\right) da. \tag{9.107}$$

If it is intended to work with sources, which are shifted into complex space (see Section 9.6.4), then the enforcement of the Love condition is not that straightforward anymore, since the near-field behaviour of the sources is modified, but the CS condition, especially as strong-form condition, can still be enforced without complication.

For the case of distributed spherical-wave or plane-wave expansions, the discussed surface current density-based constraint equations cannot be enforced directly, but certain supplementary side constraints can of course still be defined, which is, however, not further discussed.

9.9 Inversion of the discretised forward problem

The solution of linear systems of equations as obtained from the discretisation of the forward problem is in general a standard task in numerical mathematics. However, in the case of the inverse problem at hand, certain peculiarities need to be considered. First of all, it should be noted that the discretised transmission equations are in general ill-conditioned in a way that evanescent wave terms, which determine the equivalent source distribution of the AUT at least in part, can no longer be measured in some distance away from the AUT. The magnitudes of these waves decay so fast that unavoidable measurement errors and noise make their measurement with sufficient accuracy impossible. A second form of ill-conditioning is related to the dual-source formulations without additional side constraint, which may even support a null-space of non-radiating currents. If a possible null-space and all AUT sources related to unmeasurable field contributions are removed from the equivalent source representation, then a well-posed problem can be obtained, as common in standard spherical-mode-based transformations in spherical measurements. However, for measurements and transformations with a maximum degree of flexibility and with the direct capability to provide diagnostic information about the AUT, this is in general neither feasible nor desirable. Consequently, for the solution of the inverse problem in this chapter, we need linear system of equations solvers which can handle ill-posed problems and which have certain regularisation properties. In most cases, it is even the case that we have considerably more source unknowns than field measurement samples, especially when we work with surface source expansions on complex shaped surfaces around the AUT. Under such circumstances, it is recommend to solve a so-called system of normal equations instead of the original system of equations, which leads to a least-mean-square solution of the original system of equations, possibly together with an additional constraint, which is commonly inherent to the utilised linear system of equations solver. Such an additional constraint may for instance require that the energy of the obtained solution vector is minimised together with the mean-square solution error. Alternatively, it is also possible to directly solve the original, possibly over-determined or under-determined, system of equations by utilising the concept of the pseudo inverse, which is commonly based on a singular value decomposition of the equations. Since the computation of the singular value

decomposition is in general a very costly procedure and thus not really feasible for large problems, we do not further consider this option in the following.

In order to arrive at a solution of the inverse problem, let us first assume a general linear system of equations in the form

$$\left[A_{mp}\right]\left[x_p\right] = \left[b_m\right], \quad m = 1, \ldots, M, \quad p = 1, \ldots, P, \tag{9.108}$$

where M is the number of equations and P the number of unknowns, both of which can be different. The solution accuracy of such a system of equations, in particular when it is solved by an iterative solver, is commonly evaluated based on the residual error

$$\varepsilon_{res} = \frac{\left|\left[A_{mp}\right]\left[x_p\right] - \left[b_m\right]\right|}{\left|\left[b_m\right]\right|} \tag{9.109}$$

with $\left|\left[b_m\right]\right| = \sqrt{\left[b_m\right]^T\left[b_m\right]^*}$ where the superscript * indicates complex conjugation and the superscript T the transpose of a vector or a matrix.

A system of normal equations related to (9.108) can be formed by multiplying the complete system with the adjoint matrix operator resulting in

$$\left[A^*_{pm}\right]\left[A_{mp}\right]\left[x_p\right] = \left[A^*_{pm}\right]\left[b_m\right], m = 1, \ldots, M, p = 1, \ldots, P \tag{9.110}$$

where the flipping of row and column indices indicates the transpose of a matrix.

A second set of normal equations can be formed by setting

$$\left[x_p\right] = \left[A^*_{pm}\right]\left[u_m\right] \tag{9.111}$$

resulting in

$$\left[A_{mp}\right]\left[A^*_{pm}\right]\left[u_m\right] = \left[b_m\right], \quad m = 1, \ldots, M, p = 1, \ldots, P. \tag{9.112}$$

According to [44], the normal equations in (9.110), which are often referred to as normal residual (NR), are typically used to solve over-determined systems of equations with $M > P$. In contrast, the normal equations in (9.112) are often denoted as normal error (NE) and they are in particular useful to solve under-determined systems of equations with $M < P$. The operation in (9.111) can actually be seen as a step towards an up-sampling scheme as advised in [45] in order to arrive at a well-conditioned system of normal equations. The NR equations seem to be more common in literature, even for the solution of under-determined systems, even though they work in this case on a solution vector which is longer than in the case of the NE equations. Whereas the NR equations work on the residual of the system of equations in the space of the solution vector $\left[x_p\right]$ according to

$$\varepsilon^{NR}_{res} = \frac{\left|\left[A^*_{pm}\right]\left[A_{mp}\right]\left[x_p\right] - \left[A^*_{pm}\right]\left[b_m\right]\right|}{\left|\left[A^*_{pm}\right]\left[b_m\right]\right|} \tag{9.113}$$

the NE equations work directly on the error in the space of the field observations on the right-hand side vector $[b_m]$ in the form of

$$\varepsilon_{res}^{NE} = \frac{\left| \left[A_{mp}\right] \left[A_{pm}^{*}\right] [u_m] - [b_m] \right|}{|[b_m]|} = \varepsilon_{res}, \tag{9.114}$$

which is obviously identical to the residual error ε_{res} of the original system of equations in (9.108). Since the primary degrees of freedom of the NE equations exist in the space of the observations of the right-hand side vector $[b_m]$, for our inverse source problem NF or FF observations, the NE equations have a more direct control of these degrees of freedom than the NR equations, which perform first a mapping of the right-hand side vector into the space of the solution vector by applying the adjoint operator. If the original system of equations is underdetermined, it is intuitively clear that the control of the original degrees of freedom is now less direct. Once, the NR system of equations is solved, it is, however, also possible to compute the residual error ε_{res} of the original system of equations and evaluate thus the observation error of our inverse equivalent source problem. This observation error is obviously a measure of how well the found equivalent sources can reproduce the measurement samples or observations.

If we write our discretised transmission equation in (9.99) in the form of the NR equations, we obtain

$$\begin{bmatrix} L_{pm}^{*} \\ K_{qm}^{*} \end{bmatrix} [\, L_{mp} \quad K_{mq}\,] \begin{bmatrix} ZJ_p \\ M_q \end{bmatrix} = \begin{bmatrix} L_{pm}^{*} \\ K_{qm}^{*} \end{bmatrix} \left[S_{21,m}\right] \tag{9.115}$$

where we have omitted the ranges of the indices. The corresponding NE equations are

$$[\, L_{mp} \quad K_{mq}\,] \begin{bmatrix} L_{pm}^{*} \\ K_{qm}^{*} \end{bmatrix} [u_m] = \left[S_{21,m}\right] \tag{9.116}$$

with

$$\begin{bmatrix} ZJ_p \\ M_q \end{bmatrix} = \begin{bmatrix} L_{pm}^{*} \\ K_{qm}^{*} \end{bmatrix} [u_m]. \tag{9.117}$$

Both of these systems of equations can of course also be written for surface current densities with strong-form CS condition as discussed in Section 9.6.3, for sources with shift into complex space as introduced in Section 9.6.4, or with distributed propagating plane-wave or spherical-multipole expansions as mentioned in Section 9.6.5, where in these cases the unknowns and the system matrix elements may of course be different.

The supplementary constraint equations can be considered in a variety of ways. Since their purpose is to remove the redundancy due to the equivalent source representation with electric and magnetic surface currents densities, we may take one of the supplementary constraint equations, solve them for one of the current sets, and plug the outcome into the system of equations resulting from the transmission equation.

Starting, e.g., from the WF CS condition according to (9.106), the inversion of the Gram matrix in front of the magnetic surface current coefficients gives

$$\left[M_q\right] = \left[G_{sq}\right]^{-1}\left[G'_{sp}\right]\left[ZJ_p\right] \tag{9.118}$$

which can be appropriately considered in the solution of (9.115) or (9.116).

Performing an inversion of the Gram matrices of the Calderon or Love projector in (9.103) and (9.104) results into

$$\begin{bmatrix} ZJ_p^L \\ M_q^L \end{bmatrix} = 2\begin{bmatrix} G_{sp}^{-1}D_{sp}^J & G_{sp}^{-1}B_{sq}^M \\ G_{tq}^{-1}B_{tp}^J & G_{tq}^{-1}D_{tq}^M \end{bmatrix}\begin{bmatrix} ZJ_p \\ M_q \end{bmatrix} \tag{9.119}$$

and this equation can be utilised as a left-hand side preconditioner of the NR equation system in (9.115) resulting in

$$\begin{bmatrix} G_{sp}^{-1}D_{sp}^J & G_{sp}^{-1}B_{sq}^M \\ G_{tq}^{-1}B_{tp}^J & G_{tq}^{-1}D_{tq}^M \end{bmatrix}\begin{bmatrix} L_{pm}^* \\ K_{qm}^* \end{bmatrix}\left[L_{mp}K_{mq}\right]\begin{bmatrix} J_p \\ M_q \end{bmatrix}$$

$$= \begin{bmatrix} G_{sp}^{-1}D_{sp}^J & G_{sp}^{-1}B_{sq}^M \\ G_{tq}^{-1}B_{tp}^J & G_{tq}^{-1}D_{tq}^M \end{bmatrix}\begin{bmatrix} L_{pm}^* \\ K_{qm}^* \end{bmatrix}\left[S_{21,m}\right]. \tag{9.120}$$

If one works with the NE equations in (9.116), the Calderon projector can be applied after the adjoint operator resulting in

$$\left[L_{mp}K_{mq}\right]\begin{bmatrix} G_{sp}^{-1}D_{sp}^J & G_{sp}^{-1}B_{sq}^M \\ G_{tq}^{-1}B_{tp}^J & G_{tq}^{-1}D_{tq}^M \end{bmatrix}\begin{bmatrix} L_{pm}^* \\ K_{qm}^* \end{bmatrix}\left[u_m\right] = \left[S_{21,m}\right] \tag{9.121}$$

and finally also on the currents in (9.117) according to

$$\begin{bmatrix} ZJ_p^L \\ M_q^L \end{bmatrix} = \begin{bmatrix} G_{sp}^{-1}D_{sp}^J & G_{sp}^{-1}B_{sq}^M \\ G_{tq}^{-1}B_{tp}^J & G_{tq}^{-1}D_{tq}^M \end{bmatrix}\begin{bmatrix} L_{pm}^* \\ K_{qm}^* \end{bmatrix}\left[u_m\right]. \tag{9.122}$$

The inversion of the very sparse Gram matrices can be performed by a specifically optimised direct solver, but more convenient appears here the use of an iterative system of equations solver such as a conjugate gradient (CG) solver [44].

Trying to perform the same exercise with the fully populated Love or zero-field conditions in (9.100), (9.101), or (9.102) is in practice most likely not recommended due to the large effort for inverting the fully populated matrices. Instead, it might be more feasible to solve the systems of equations in (9.99) and for instance the one in (9.100) in a joint effort, e.g., in the form of a system of NR equations

$$\begin{bmatrix} L_{pm}^* & L_{ps}^{C*} \\ K_{qm}^* & K_{qs}^{C*} \end{bmatrix}\begin{bmatrix} L_{mp} & K_{mq} \\ \lambda_{SC}L_{sp}^C & \lambda_{SC}K_{sq}^C \end{bmatrix}\begin{bmatrix} Z_F J_p \\ M_q \end{bmatrix} = \begin{bmatrix} L_{pm}^* \\ K_{qm}^* \end{bmatrix}\left[S_{21,m}\right] \tag{9.123}$$

where we have introduced the constant multiplier λ_{SC} to scale the constraint equations appropriately with respect to the actual inverse source equations within the least mean square solution of the system of equations. This multiplier can be chosen empirically for a certain measurement configuration, but it can also be retrieved by first analysing certain properties of the submatrices prior to the actual solution, where it is in general recommended to consider also the noise level of the available data as, for example, done in the L-curve approach [11,12].

The corresponding solution in the form of NE equations can be written as

$$\begin{bmatrix} L_{mp} & K_{mq} \\ \sqrt{\lambda_{SC}}L^{C}_{sp} & \sqrt{\lambda_{SC}}K^{C}_{sq} \end{bmatrix} \begin{bmatrix} L^{*}_{pm} & \sqrt{\lambda_{SC}}L^{C*}_{ps} \\ K^{*}_{qm} & \sqrt{\lambda_{SC}}K^{C*}_{qs} \end{bmatrix} \begin{bmatrix} u_m \\ v_s \end{bmatrix} = \begin{bmatrix} S_{21,m} \\ 0_s \end{bmatrix} \tag{9.124}$$

where the scaling parameter has here been considered in symmetric form. The final solution for the current expansion coefficients can be obtained by the solution of

$$\begin{bmatrix} ZJ_p \\ M_q \end{bmatrix} = \begin{bmatrix} L^{*}_{pm} & \sqrt{\lambda_{SC}}L^{C*}_{ps} \\ K^{*}_{qm} & \sqrt{\lambda_{SC}}K^{C*}_{qs} \end{bmatrix} \begin{bmatrix} u_m \\ v_s \end{bmatrix}. \tag{9.125}$$

In addition to the degrees of freedom u_m in the space of the NF measurements, we have now also introduced degrees of freedom v_s in the space of the side constraint equations.

Instead of solving the inverse source equations in (9.99) together with the constraint equations due to the CFIE in (9.100), it is also possible to work with the discretised forms of the EFIE and the MFIE in (9.101) and (9.102), respectively. For the NR case, this results in

$$\begin{bmatrix} L^{*}_{pm} & K^{E*}_{tq} & L^{M*}_{sp} \\ K^{*}_{qm} & L^{E*}_{tp} & K^{M*}_{sq} \end{bmatrix} \begin{bmatrix} L_{mp} & K_{mq} \\ \lambda_{SC}L^{E}_{tp} & \lambda_{SC}K^{E}_{tq} \\ \lambda_{SC}K^{M}_{sq} & \lambda_{SC}L^{M}_{sp} \end{bmatrix} \begin{bmatrix} Z_F J_p \\ M_q \end{bmatrix} = \begin{bmatrix} L^{*}_{pm} \\ K^{*}_{qm} \end{bmatrix} \begin{bmatrix} S_{21,m} \end{bmatrix} \tag{9.126}$$

and for the NE case the resulting equations are

$$\begin{bmatrix} L_{mp} & K_{mq} \\ \sqrt{\lambda_{SC}}L^{E}_{sp} & \sqrt{\lambda_{SC}}K^{E}_{sq} \\ \sqrt{\lambda_{SC}}K^{M}_{sq} & \sqrt{\lambda_{SC}}L^{M}_{sp} \end{bmatrix} \begin{bmatrix} L^{*}_{pm} & \sqrt{\lambda_{SC}}L^{E*}_{pt} & \sqrt{\lambda_{SC}}K^{M*}_{qs} \\ K^{*}_{qm} & \sqrt{\lambda_{SC}}K^{E*}_{qt} & \sqrt{\lambda_{SC}}L^{M*}_{ps} \end{bmatrix} \begin{bmatrix} u_m \\ v_t \\ v_s \end{bmatrix} = \begin{bmatrix} S_{21,m} \\ 0_t \\ 0_s \end{bmatrix}. \tag{9.127}$$

The final surface-source solution is now obtained by solving

$$\begin{bmatrix} ZJ_p \\ M_q \end{bmatrix} = \begin{bmatrix} L^{*}_{pm} & \sqrt{\lambda_{SC}}L^{E*}_{pt} & \sqrt{\lambda_{SC}}K^{M*}_{qs} \\ K^{*}_{qm} & \sqrt{\lambda_{SC}}K^{E*}_{qt} & \sqrt{\lambda_{SC}}L^{M*}_{ps} \end{bmatrix} \begin{bmatrix} u_m \\ v_t \\ v_s \end{bmatrix} \tag{9.128}$$

and we have degrees of freedom v_t and v_s in the space of the side constraint equations together with the original degrees of freedom u_m in the space of the

observations. The explicit number of matrix elements to be considered is now larger for both the NR and the NE equations, but we should keep in mind that EFIE and MFIE matrix elements are also needed within the CFIE and the achievable accuracy with a separate consideration of the EFIE and of the MFIE is often better than for the CIFE. The residual error according to (9.114) of the NE equations in (9.124) and (9.127) is not anymore the residual of the original inverse source problem, but it is comprising additional error contributions related to the fulfillment of the constraint equations. The pure observation error can be retrieved by performing the summation for the error calculation only for $m = 1, \ldots, M$. Moreover, it can be observed that in particular the NE system of equations in (9.127) has even more unknowns than the corresponding NR equation in (9.126).

As mentioned earlier, the recommended linear system of equations solvers to be used for any of the obtained systems of normal equations, either with side constraint or not, are iterative solvers, which do in general only need repeated computations of the forward operators instead of explicitly inverting the systems of equations. Such iterative solvers can advantageously be combined with algorithms for the rapid and memory-efficient evaluation of the forward operators as discussed in the following section. This is important due to the fact that the forward operators are fully populated and their efficient computation is, therefore, of paramount importance for the practical utility of the inverse source-based field transformations.

Since the derived systems of normal equations are in general positive definite, a relatively large collection of iterative equation solvers can be used for its solution. A wide collection of solvers are for instance found in the book by Saad [44] or in [46], where in particular Krylov subspace solvers appear to be useful. For the inversion examples presented later on in this chapter the generalised minimal residual solver (GMRES) has been used, which can be considered as one of the most powerful iterative system of equations solvers. A disadvantage of this solver is that it has rather large memory requirements due the fact that it performs an explicit orthogonalisation of the search vectors. However, this orthogonalisation is also a key reason for its superior performance compared to many other solvers. Also, the GMRES solver is based on a minimisation of the energy contained in the solution vectors, which is considered to be a suitable regularisation constraint for the solution of the ill-conditioned systems of equation, as mentioned earlier. Other variants of Krylov subspace-based solvers, such as the very popular CG solver, are for instance also discussed in [44] and may be considered for the solution of the encountered inverse source linear systems of equation, too.

9.10 Rapid computation of the forward operator

As already discussed in the previous sections and as common for integral radiation operators in electromagnetics, the discretised forward operators of our inverse problem and of the Love condition result in fully populated linear systems of equations or correspondingly fully populated matrices. If we assume a discrete

operator with M rows and P columns, corresponding to, e.g., M equations and P unknowns, the memory to store this matrix is proportional to MP, i.e., its memory complexity is of order $O(MP)$, which is quadratic in M or P for $M = cP$, $c = \text{const}$. Similarly, the computational or numerical complexity for the computation of a corresponding matrix-vector product is also $O(MP)$. Since both M and P are proportional to the number of measurement samples, the computational complexity for the iterative solution of our inverse problems by iterative solvers, which evaluate a series of matrix-vector products, is at least quadratic in the number of measurement samples and in general of $O(D^4)$, if D is the diameter of the AUT. This is due to the fact that the number of measurement samples needed to appropriately sample the radiation field of an AUT is in general proportional to D^2. For the overall solution of the inverse source problem systems of equations, we may further expect a slightly increasing number of iterations with problem size until convergence and thus the overall solution complexities can even be worse.

In order to be able to solve large inverse source problems with millions of measurement samples within acceptable computation times, it is mandatory to reduce the memory and computation complexities of the forward operators. One way of achieving such a complexity reduction would be to specialise our inverse source formulation to the planar, cylindrical, or spherical configurations as discussed in Chapters 6, 7, and 8. For these configurations, the corresponding eigenmodes pertinent to Maxwell's equations with its beneficial orthogonality properties are utilised to represent the AUT fields, and may allow even a direct inversion of the forward operator. Furthermore, the FFT algorithm with its implicit hierarchical multi-level representation helps to considerably speed-up the solution of the inverse source problem.

In more general terms, we can say that a fast operator evaluation can be achieved by removing redundancy out of the formulation, by working with a regular discretisation of the operator equation, and/or by working with a factorised and possibly diagonalised representation of the forward operator. The latter can be achieved based on purely algebraic approaches such as adaptive cross approximation [47,48] or the so-called H-matrices [49], or by analytical concepts such as the utilisation of eigenmode representations.

In the following, we present first a single-level and then a multi-level algorithm for fast evaluation of the forward operators, which are based on the spectral plane-wave representation with propagating plane waves corresponding to an integration in k-space over the Ewald sphere.

9.10.1 Single-level algorithm

Since we are interested in efficient field transformations for measurement configurations with non-canonical measurement surfaces and with non-canonical surface source distributions representing the AUT, we must have a fast algorithm, which supports full flexibility with respect to these requirements. Therefore, we make use of the ideas of the FMM [8] for high-frequency field problems, which has proven its performance and flexibility for the solution of electromagnetic integral

equations in scattering and antenna problems over many years and more recently also for antenna field transformations. In the next section, this algorithm will be further extended to a multi-level algorithm by following the ideas of the MLFMM [1,15,43].

The algorithm is based on a propagating plane-wave representation of the radiation operators, as, for example, found in (9.97), and in Section 9.5.2, it was shown that such a formulation can be derived from a spherical-multipole expansion of the involved Green's function of the Helmholtz equation together with a subsequent plane-wave expansion of parts of the multipole representation. The key properties of a spectral representation as in (9.97) are factorisation and diagonalisation. Factorisation means here that the actual source integration according to (9.98) can be computed independent from the observation locations $\underline{r}$ and $\underline{r}_m$, once the reference location $\underline{r}_1$ has been fixed, and similarly the actual observation process is independent from $\underline{r}'$ and $\underline{r}_1$. The source integration means to obtain the plane-wave representation of the fields radiated by the sources. The observation process means to weight the plane waves incident on the measurement probe by plane-wave receiving coefficients of the probe, which have been obtained before, e.g., by simulation and far-field integration of the obtained probe sources or by a calibration measurement of the probe. The interrelation between the fields radiated by the sources and the plane waves received by the probes is given by translation with the translation operator $T_L(\underline{k}, \underline{r}_{m1})$. Since this translation operator translates every radiated plane wave into just one corresponding incident plane wave at every receiving probe position, we have a diagonal translation process, which is essential to achieve a low numerical complexity of the forward operator evaluation. In contrast, a non-diagonal translation process would produce several incident plane waves out of every radiated plane wave. Non-diagonal translations are for instance encountered with the spherical-mode representation as discussed in Chapter 8.

In order to finalise the forward operator computation according to the spectral representation in (9.97), a spectral integration over the Ewald sphere must be performed in order to sum up all signal contributions received at the probe according to individual plane-wave components. This integration is commonly performed by some numerical quadrature rule which is appropriate for integration over a sphere. Due to the periodic nature, the integration in φ is ideally performed by a trapezoidal rule, i.e., by equidistant sampling with constant integration weights. The integration in ϑ is often evaluated by Gaussian quadrature with the substitution $x = \cos\vartheta$, which helps to get rid of the $\sin\vartheta$-factor coming from the integration in spherical coordinates. Alternatively, the ϑ-range can also be extended to 2π and thus be made periodic; by similar concepts as discussed for the spherical transformations in Chapter 8 or as found in [39,40]. If this is done, a trapezoidal rule can also be utilised to perform the integration over ϑ. Important to note here is that the spectral functions, which need to be integrated by numerical quadrature, are band-limited and can thus be integrated with a controllably low error. In the case of the periodic extension of the ϑ-range, however, some care must be exercised in order to control the bandwidth of the involved (and not removed) $|\sin\vartheta|$-factor.

In order to facilitate an efficient evaluation of the translation process in (9.97), it is also important that the reference locations for the spectral representations of the sources and the probes are chosen on a regular grid. To account for this, we rewrite (9.97) in the form of

$$S_{21,m}\left(\underline{r}_m\right) = c_3 \oiint \underline{\underline{W}}^{Tx}_{Probe,m}(\underline{r}_{R(m)}, -\underline{k}) \cdot T_L(\underline{r}_{RS}, \underline{k}) \sum_p J_p \underline{\tilde{\beta}}_p\left(\underline{r}_{S(p)}, \underline{k}\right) d^2\widehat{\underline{k}} \tag{9.129}$$

where the spectral probe representation with a probe prototype has been replaced by the representation

$$\underline{\underline{W}}^{Tx}_{Probe,m}(\underline{r}_{R(m)}, \underline{k}) = T_{FF}(\underline{r}_{R(m)m}, \underline{k}) \underline{\underline{R}}^T_m \cdot \underline{\underline{W}}^{Prot,Tx}_{Probe}(\underline{r}_m, \underline{\underline{R}}_m \cdot \underline{k}) \tag{9.130}$$

defined with respect to a reference location $\underline{r}_R$, with

$$T_{FF}(\underline{r}_{R(m),m}, \underline{k}) = e^{-jk\widehat{\underline{k}} \cdot (\underline{r}_{R(m)} - \underline{r}_m)}. \tag{9.131}$$

The subscript $S(p)$ of $\underline{r}_{S(p)}$ indicates that the source box is chosen according to the location of the basis function with index p and similarly $R(m)$ indicates that the receive box is chosen according to the reference location of the measurement probe with index m.

The reference-location specific spectral representation of the probe in (9.130) is ideally pre-computed prior to the actual solution of the inverse problem or it may be computed on the fly, e.g., if the necessary memory for the pre-computed representation cannot be afforded.

For simplicity, we consider only electric surface current densities at this point, since the treatment of magnetic current densities is more or less identical and thus not important for the explanation of the algorithm. Similar to the reference-location specific spectral representation of the probe, it is recommended to also pre-compute the spectral representation $\underline{\tilde{\beta}}_p(\underline{r}_S, \underline{k})$ of the current basis functions with respect to a corresponding source reference location $\underline{r}_S$.

For the evaluation of (9.129), we introduce a regular box structure as illustrated in Figure 9.17,[3] where $\underline{r}_{S(m)}$ and $\underline{r}_{R(p)}$ are chosen as the box centres, which are as close as possible to the basis function with index p and the measurement location with index m, respectively. Assuming, for example, two given source expansion coefficients J_{p1} and J_{p2}, the receive signals of the probes or correspondingly the S-parameters $S_{21,m}$ can be computed in three subsequent steps:

First, the radiated plane-wave spectrum of all sources in a source box is computed by summing up all plane waves aggregated with respect to the box centre.

Next, the entire plane-wave spectrum is translated to the centre of the receive box.

[3]If desired, separate box structures for the sources and the measurement locations may be used.

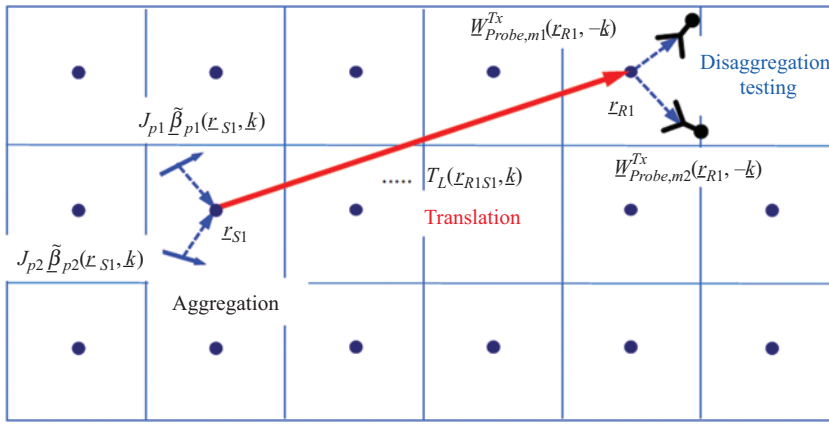

Figure 9.17 Illustration of the computation steps of the single-level propagating plane-wave-based algorithm for the computation of the source-probe interactions: the plane-wave expansions of the source basis functions and of the probes are computed with respect to reference locations chosen as centres of a regular box partitioning of the computational domain. With known basis function expansion coefficients J_{p1} and J_{p2}, the radiated plane-wave spectra are aggregated with respect to the corresponding box centre. The aggregated spectrum is translated to the box centre containing the receiving probes. Then, the receive signals at the probes are computed by summing up the receive spectra multiplied with the probe plane-wave transmit patterns

Finally, the waves received at the receive box are disaggregated to the probes, i.e., tested or weighted by the receive patterns of the probes with respect to the box centre, and summed up in order to give the probe receive signals.

In order to better understand this single-level algorithm, let us look into its computational complexity. As already discussed earlier in this section, the combined radiation/measurement operator is a full operator, since every source basis function contributes to the signal received by every probe. Therefore, the direct evaluation of the combined radiation/measurement operator has a numerical complexity of $O(M^2)$, if we assume that the number of source basis functions P is proportional to the number of measurements M.

For the discussed single-level algorithm, the spectral integral over the Ewald sphere is evaluated by numerical quadrature with a fixed number of, let us say Q, quadrature samples, where the value of Q depends on the size of the boxes. If all spectral quantities are computed at exactly these quadrature samples, the computational complexity of the algorithm is as follows. The aggregation process is proportional to the number of basis functions P multiplied with Q, i.e., it is of

complexity $O_A(PQ) = O_A(MQ)$. Correspondingly, the complexity of the disaggregation/testing process is $O_D(MQ)$. Finally, the computational complexity of the translation process is $O_T(P_{box}M_{box}Q) = O_T(M_{box}M_{box}Q)$, where P_{box} is the number of boxes containing sources and M_{box} is the number of boxes containing measurement locations. Similar to P and M, it was assumed here that P_{box} is proportional to M_{box}. In general, it is here assumed that the spectral representations of the basis functions and of the probes, as well as the translation operators have been pre-computed at the required sample locations.

The overall computational effort of the algorithm is given as the sum of the efforts of the three steps and the computational complexity is thus dominated by the step with the largest computational complexity. The optimum complexity is achieved by choosing the size of the boxes such that $O_A(MQ) = O_D(MQ) = O_T(M_{box}M_{box}Q)$ and this is achieved by selecting $M_{box} = \sqrt{M}$. For this consideration, it is assumed that the source basis functions are more or less evenly distributed on a surface and that the same is true for the measurement samples. If such a surface would be a simple square with side length l_S, then the box side lengths would be $\sqrt{l_S}$. With $M_{box} = \sqrt{M}$, we have $Q \sim \sqrt{M}$ and thus $O_A(M^{3/2}) = O_D(M^{3/2}) = O_T(M^{3/2})$, i.e., the complexities of the three steps are equally balanced and the complexity of the overall single-level algorithm is thus also $O(M^{3/2})$ in contrast to the $O(M^2)$ of the direct straightforward computation. The storage complexity of the precomputed plane-wave spectra of the expansion functions and of the probes will be on the same order. Due to the chosen regular box structure and the corresponding translation invariance, only relatively few different translation operators need to be computed and stored, if they are pre-computed. For the inverse problem at hand, with typically well-separated regions containing measurement samples and sources, one may even think of constructing separate box structures for the sources and for the measurement locations. This would give more flexibility in choosing the box sizes appropriately, but may require computing considerably more translation operators. One aspect to consider here is that the basis function distribution is commonly considerably denser than the distribution of the measurement locations.

Important to note is that the described algorithm can only be employed, if it delivers the probe signals or the corresponding S-parameters with sufficient accuracy. To this end, the multipole order L of the translation operator must be chosen appropriately, see, e.g., the approximation formula in (9.50) found also in [1], where d is two times the diameter of the minimum sphere around one box, since the sizes of the source box and of the receiver box must be added. The multipole order must be chosen with care according to the accuracy requirements, since increasing L further and further will finally lead to a break-down of the algorithm and a complete loss of accuracy. Appreciable accuracy can only be achieved if the source and observation boxes are well separated, see the requirement $|\underline{X}| > |\underline{d}|$ given just after the scalar Green's function expansion in (9.49). In the case of a common box grid for the sources and the measurement samples, the translation can only be accurate if at least one empty box, a so-called buffer box, is between the source box and the receive box. Better accuracy can be achieved with more than one buffer boxes. For very short interaction distances between the sources and the

measurement probes, the algorithm can be supplemented by a direct spatial domain integration of the interaction integrals related to those source–probe interactions with too little separation.

In the implementation of the algorithm, the spectral integrals are computed by numerical quadrature based on appropriately chosen discrete samples of the integrand. The choice of the appropriate number of quadrature samples depends on the spectral content of the integrand and the spectral content of the integrand depends on the spectral contents of the various factors in the integrand. In order to represent the translation operator of order L accurately by discrete samples in spherical coordinates ϑ and φ, we need $2L$ samples in φ and in ϑ the number of samples is commonly chosen as $L + 1$ [1,50]. The spectral bandwidths of the translated source and receive spectra on the translation level are only half of the bandwidth of the translation operator and the spectra can thus be discretised with fewer samples. However, in common implementations of the algorithm the source and receive spectra are often sampled with the same number of samples as the translation operators, which simplifies the algorithm for the cost of increased memory requirements.

In order to derive an appropriate quadrature rule, the spectral integral in (9.129) is written in spherical coordinates according to

$$\oiint \ldots d^2\underline{\hat{k}} = \int_{\vartheta=0}^{\pi}\int_{\varphi=0}^{2\pi} \ldots d\varphi \sin(\vartheta) d\vartheta = \int_{u=-1}^{+1}\int_{\varphi=0}^{2\pi} \ldots d\varphi\, du, \quad u = \cos(\vartheta). \tag{9.132}$$

The two-dimensional integral is then evaluated by approximating the integration by a double sum in the form of

$$\int_{u=-1}^{+1}\int_{\varphi=0}^{2\pi} f(u,\varphi) d\varphi\, du = \sum\nolimits_{m=1}^{M}\sum\nolimits_{n=1}^{N} f(u_m,\varphi_n) w_n(\varphi_n) w_m(u_m) \tag{9.133}$$

where the two one-dimensional integrations are treated in factorised form. The symbols u_m and φ_n are the sample locations and w_m and w_n are the weights of the numerical quadrature rules.

The integration in φ is commonly performed by a trapezoidal rule with equidistant samples, which converges here very quickly due to the periodicity of the integrand in φ. In the implementation of the algorithm, employing the trapezoidal rule with the $2L$ samples mentioned above gives integration results with negligible error [50]. The numerical quadrature in ϑ is more tricky. As already introduced in (9.133), it is common to work here with the substitution $u = \cos(\vartheta)$ and evaluate the integration in u by Gauss–Legendre quadrature, where again the $L + 1$ samples mentioned above give results with negligible error [50]. The Gauss–Legendre quadrature optimises the sample locations together with the quadrature weights in order to exactly integrate polynomials with an as large as possible order with as few as possible sample points. The result of this nonlinear optimisation process is that the sample locations are chosen as the zeroes of Legendre polynomials [38].

In order to better understand what happens in the discrete evaluation of the integrand and in the quadrature of the integrals, Figure 9.18 illustrates the Fourier spectra of the φ-dependence of the factors within the integrand of (9.129).

As mentioned earlier, the translation operator has a certain spectral bandwidth with respect to the spectral integration variables, as for instance φ, characterised by the corresponding corner frequency $f^{T}_{\varphi,B} \sim L$, given here for the φ-dependence. In contrast, the source spectra and the probe spectra have a corresponding spectral bandwidth in φ with a corner frequency $f^{S/W}_{\varphi,B} \sim L/2$. Also, it should be noted that we observe a periodic repetition of all spectra with multiples of the sampling frequency $f_{\varphi,sample}$ due to the discrete representation. The common choice of the sampling frequency is $f_{\varphi,sample} = 2f^{T}_{\varphi,B}$, which means that the translation operator is sampled at the sampling limit and the source spectra as well as the probe spectra are oversampled by a factor of two. The multiplication of the source spectra with the translation operator results in spectra with a corner frequency of $\sim 3L/2$ as also indicated in Figure 9.18. Since the sampling frequency is no longer sufficient to correctly represent these spectra, we observe aliasing errors, which do, however, not affect the range of $F_{\varphi}(.)$ from $-f^{S/W}_{\varphi,B}$ to $f^{S/W}_{\varphi,B}$. An example φ-integration with scalar quantities, as also illustrated in Figure 9.18, can now be written in the form

$$\begin{aligned}\int_{\varphi=0}^{2\pi} W^{Tx}_{Probe}(\varphi)\left\{T_L(\varphi)\tilde{J}(\varphi)\right\}d\varphi &= \int_{\varphi=0}^{2\pi}\sum_{k_\varphi=-L_W}^{L_W} W^{Tx}_{Probe,k_\varphi} e^{jk_\varphi\varphi}\sum_{l_\varphi=-2L_W}^{2L_W}\left\{T_L\tilde{J}\right\}_{l_\varphi} e^{-jl_\varphi\varphi}d\varphi \\ &= \sum_{k_\varphi=-L_W}^{L_W} W^{Tx}_{Probe,k_\varphi}\sum_{l_\varphi=-2L_W}^{2L_W}\left\{T_L\tilde{J}\right\}_{l_\varphi}\int_{\varphi=0}^{2\pi} e^{j(k_\varphi-l_\varphi)\varphi}d\varphi \\ &= \sum_{k_\varphi=-L_W}^{L_W} W^{Tx}_{Probe,k_\varphi}\left\{T_L\tilde{J}\right\}_{k_\varphi}\end{aligned} \tag{9.134}$$

where the two factors in the integrand have been expanded in Fourier series in φ with Fourier coefficients W^{Tx}_{Probe,k_φ} and $\left\{T_L\tilde{J}\right\}_{l_\varphi}$ in order to facilitate the integral evaluation. By re-arranging the different terms, it becomes obvious that the integration reduces now to an integral over the product of the exponentials of the

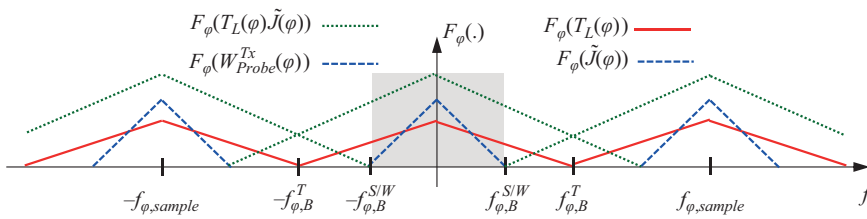

Figure 9.18 Principal illustration of the Fourier spectra $F_\varphi(.)$ with respect to φ of the factors in the integrand of (9.129), where the factors with vector character are only considered as scalar quantities

Fourier series. Finally, due to the orthogonality of the Fourier exponentials, the double series reduces to a single series, which comprises the range of the Fourier spectrum of the probe only, i.e., the shaded area in Figure 9.18. This in turn means that the portions of the spectra, which have been distorted by aliasing errors, do not contribute to the result of the integration. Thus, the sampling rate in φ was chosen large enough for an accurate evaluation of the integral.

In the numerical implementation, the integral over φ is evaluated by numerical quadrature and one may ask whether higher-order Fourier terms, which are present due to the discrete representation, may contribute to the integration result. Here, we can say that such contributions are effectively suppressed by the low-pass and smoothing character of the quadrature rule. The consideration performed here for the φ-dependence can be performed in a similar way for the ϑ-dependence, too.

A direct consideration of the two-dimensional integrations can for instance be done by introducing spherical multipole expansions of the factors in the integrand, as shown in [15]. To demonstrate this, let us consider (9.129) in the form

$$S_{21,m}\left(\underline{r}_m, \underline{r}_S\right) = c_3 \oiint \underline{W}^{Tx}_{Probe,m}(\underline{r}_R, -\underline{k}) \cdot \left\{ T_L(\underline{r}_{RS}, \underline{k}) \underline{\tilde{J}}(\underline{r}_S, \underline{k}) \right\} d^2\widehat{\underline{k}} \tag{9.135}$$

where $\underline{\tilde{J}}\left(\underline{r}_S, \underline{k}\right) = \sum_p J_p \underline{\tilde{\beta}}_p \left(\underline{r}_S, \underline{k}\right)$ represents the radiated plane-wave spectrum from all the sources in one box and $S_{21,m}\left(\underline{r}_m, \underline{r}_S\right)$ indicates that we consider only the transmission from these sources to the measurement location. Now, we introduce

$$\underline{W}^{Tx}_{Probe,m}\left(\underline{r}_R, -\underline{k}\right) = \sum_{r=0}^{R} \sum_{s=-r}^{r} \underline{W}^{*}_{m,rs} Y^{*}_{rs}(\vartheta, \varphi) \tag{9.136}$$

where $Y_{pq}(\vartheta, \varphi)$ are normalised spherical harmonics and the * indicates complex conjugation, and

$$\left\{ T_L(\underline{r}_{RS}, \underline{k}) \underline{\tilde{J}}(\underline{r}_S, \underline{k}) \right\} = \sum_{r'=0}^{2R} \sum_{s'=-r'}^{r'} \left\{ T_L \tilde{J} \right\}_{r's'} Y_{r's'}(\vartheta, \varphi) \tag{9.137}$$

where the multipole order is chosen to be twice the value of the order P required to appropriately represent the probe and source plane-wave spectra, i.e., appropriate to represent the translation operator and comparable to $f^{T}_{\varphi,B} \sim L$ in the consideration of the φ-dependence only, as illustrated in Figure 9.18. Plugging the multipole expansion into (9.135) results in

$$\begin{aligned} S_{21,m}\left(\underline{r}_m, \underline{r}_S\right) &= c_3 \oiint \sum_{r=0}^{R} \sum_{s=-r}^{r} \underline{W}^{*}_{m,rs} Y^{*}_{rs}(\vartheta, \varphi) \cdot \sum_{r'=0}^{2R} \sum_{s'=-r'}^{r'} \left\{ T_L \tilde{J} \right\}_{r's'} Y_{r's'}(\vartheta, \varphi) d^2\widehat{\underline{k}} \\ &= c_3 \sum_{r=0}^{R} \sum_{s=-r}^{r} \underline{W}^{*}_{m,rs} \cdot \sum_{r'=0}^{2R} \sum_{s'=-r'}^{r'} \left\{ T_L \tilde{J} \right\}_{r's'} \oiint Y^{*}_{rs}(\vartheta, \varphi) Y_{r's'}(\vartheta, \varphi) d^2\widehat{\underline{k}} \\ &= c_3 \sum_{r=0}^{R} \sum_{s=-r}^{r} \underline{W}^{*}_{m,rs} \cdot \left\{ T_L \tilde{J} \right\}_{rs} \end{aligned} \tag{9.138}$$

where the orthogonality relation of the spherical harmonics

$$\oint\!\!\!\oint Y_{rs}(\vartheta,\varphi)\,Y^{*}_{r's'}(\vartheta,\varphi)\,d\widehat{\underline{k}} = \delta_{rr'}\delta_{ss'} \tag{9.139}$$

has been utilised. $\delta_{ss'}$ is here the Kronecker delta, which is zero except for $s = s'$ where it is one. As already observed for the φ-dependence only, the band-limited probe spectra filter out only the spherical modes up to order R in the incident wave fields and this knowledge can be used to directly restrict the expansion of the incident wave fields to a modal order of R.

Another way to evaluate the ϑ-integration in (9.132) is to keep ϑ instead of u and extend the ϑ-range from 0 to π to 0 to 2 π, resulting in [39,40]

$$\begin{aligned}\oint\!\!\!\oint \ldots d^2\widehat{k} &= \int_{\vartheta=0}^{\pi}\int_{\varphi=0}^{2\pi} \ldots d\varphi\,\sin(\vartheta)d\vartheta \\ &= \frac{1}{2}\int_{\vartheta=0}^{2\pi}\int_{\varphi=0}^{2\pi} \ldots d\varphi|\sin(\vartheta)|d\vartheta.\end{aligned} \tag{9.140}$$

where it is, however, necessary to replace the $\sin(\vartheta)$ by $|\sin(\vartheta)|$. Also, the integration result needs to be divided by 2 in order to account for the fact that the integration is now performed twice over the original integration range in ϑ and φ. The key advantage of this representation is that the integrand is now also periodic in ϑ allowing to work with the trapezoidal integration rule with equidistant sampling in ϑ. The downside of this representation is, however, the factor $|\sin(\vartheta)|$ within the integrand, which is not band-limited leading to a more complicated numerical quadrature of the integral. The approach to handle this situation is to appropriately increase the sampling rate and perform a band-limitation of the $|\sin(\vartheta)|$-term. It turns out that aliasing errors can be completely avoided by doubling the sampling rate as compared to the case of the φ-integration and by low-pass filtering the $|\sin(\vartheta)|$-term exactly to this corresponding low-pass band as illustrated in Figure 9.19. If now the $|\sin(\vartheta)|$-term is multiplied with the incident plane-wave

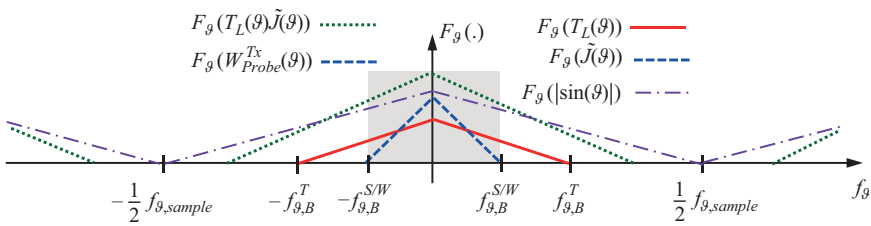

Figure 9.19 Principal illustration of the Fourier spectra $F_\vartheta(.)$ with respect to ϑ of the factors in the integrand of the spectral integral according to (9.129), where the factors with vector character are only considered as scalar quantities and where the factor $|\sin(\vartheta)|$ is now also considered, in contrast to the situation in Figure 9.18

spectrum in the receive box, corresponding to a convolution of the ϑ-spectra, the result of the multiplication is fully correct in the range of $F_\vartheta(.)$ from $-f_{\vartheta,B}^{S/W}$ to $f_{\vartheta,B}^{S/W}$, which is finally filtered out in the evaluation of the integral due to the band-limitation of the probe receive spectrum, similar as shown for the φ-integration before.

9.10.2 Multi-level algorithm

In the multi-level algorithm, the regular box configuration is extended to a multi-level hierarchical oct-tree structure, where in a three-dimensional arrangement, as exclusively considered in this chapter, the boxes on a coarser level are obtained by combining eight boxes on the next finer level. The construction of the oct-tree can be done by starting from the finest level with a given box size, or it can be done by starting from the coarsest level, where commonly just one box is chosen, which covers the entire computational volume, and by sub-dividing this box into smaller boxes on the finer levels. In the latter case, the resulting size of the boxes on the finest level is kind of arbitrary, where, however, the box construction can of course also be controlled in a way that a pre-specified box size on the finest level is achieved. The multi-level algorithm is typically implemented in a way that the plane-wave spectra of the basis functions and of the measurement probes are first pre-computed on the finest level. In the actual forward operator evaluation as illustrated in Figure 9.20 for a two-level situation, the source spectra are then aggregated for all non-empty source boxes by multiplying the spectra $\underline{\tilde{\beta}}_p\left(\underline{r}_S, \underline{k}\right)$ with the expansion coefficients J_p and adding the results for all basis functions in a box. Next, the spectra of the non-empty source boxes on the finest level are all aggregated into the centres of the corresponding boxes on the next coarser level. In the considered example, the source spectrum on this coarser level is then translated to one receiver box on this level. The received plane-wave spectrum is next disaggregated to two receive boxes on the finer level, where the received spectra are disaggregated to the measurement probes. The disaggregation of the spectra on the fine level to the measurement probes can also be considered as testing the received spectra with the receive patterns of the measurement probes. In order to obtain the output signals at the probes, all received plane-wave contributions are summed up.

In Figure 9.20, the $\underline{r}_{S/R}^{li}$ indicate the locations of the box centres on the various levels. $\underline{r}_{S1}^{l1}$ is for instance the position of the first source box on level 1 containing sources, i.e., the subscript numbers the box centres on the level defined by the superscript, where larger numbers indicate coarser levels. The aggregation, translation, and disaggregation events are indicated with arrows pointing from the source centre to the destination centre.

Starting from (9.129), the multi-level approach can be written in a somewhat simplified form as

$$S_{21,m}\left(\underline{r}_m\right) = c_3 \oiint \underline{W}_{Probe,m}^{Tx}(\underline{r}_{R(m)}^{l1}, -\underline{k}) T_{FF}(\underline{r}_{R(m)}^{l1} - \underline{r}_{R(m)}^{l2}, \underline{k}) T_L(\underline{r}_{R1S1}^{l2}, \underline{k}) \cdot \sum_p T_{FF}(\underline{r}_{S(p)}^{l2} - \underline{r}_{S(p)}^{l1}, \underline{k}) J_p \underline{\tilde{\beta}}_p\left(\underline{r}_{S(p)}^{l1}, \underline{k}\right) d^2\widehat{\underline{k}} \tag{9.141}$$

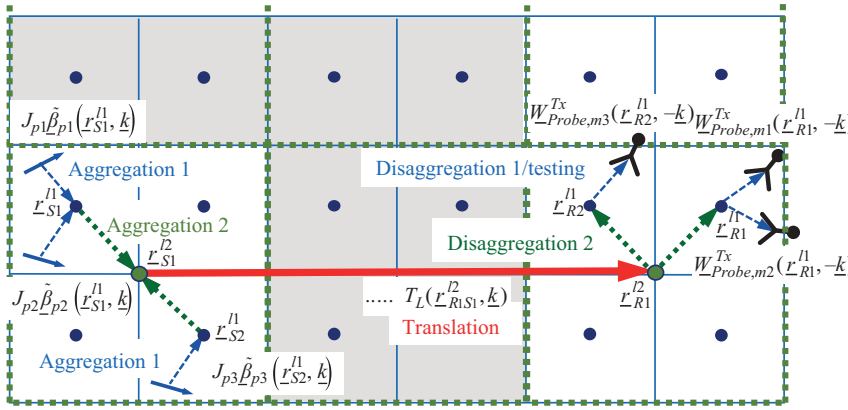

Figure 9.20 Illustration of the computation steps of the multi-level propagating plane-wave-based algorithm for the computation of source-probe interactions (two-level case): the plane-wave expansions of the source basis functions and of the probes are computed with respect to box centres on the finest level. With known basis function expansion coefficients J_{p1} and J_{p2}, the radiated plane-wave spectra are aggregated with respect to the corresponding box centre. The aggregated spectrum on the finest level is aggregated with respect to the box centre of the next coarser level. The plane-wave spectrum is translated to the box centre on the same level containing the receive probes. Next, the received plane-wave spectrum is disaggregated to the next finer level. Finally, the receive signals at the probes are computed by summing up the receive spectra multiplied with the probe plane-wave transmit patterns

where this equation needs to be evaluated for all m. Similar to the single-level algorithm, the subscript $S(p)$ of $\underline{r}_{S(p)}$ indicates that the source boxes on the involved levels are chosen according to the location of the basis function with index p and $R(m)$ indicates that the receive boxes on the involved levels are chosen according to the reference location of the measurement probe with index m. Since the numerical quadrature of the spectral integral is not considered in detail at this point, there is no discrete representation of the plane-wave spectra and the aggregation/disaggregation processes are just translations of plane waves from one reference location to another, by multiplying with $T_{FF}(\underline{r}_{S(p)/R(p)}^{l2/1} - \underline{r}_{S(p)/R(p)}^{l1/2}, \underline{k})$ as defined in (9.131), after all spectral contributions in a source/receive box have been summed up. As also seen in Figure 9.20, the summation over p needs to be organised in a box-wise manner, i.e., all spectra from basis functions in a box need to be summed up first, before the aggregation to the next coarser level can be performed. Similarly, the translation on the coarser level is not performed before all spectra from non-empty boxes on the

finer level have been aggregated. In the example in Figure 9.20, there is only one translation. However, in realistic situations many translations need to be performed and such translations may also happen on various levels. As noted earlier, a sufficiently large relative distance with respect to the box sizes must be maintained between the source box and the receive box and short translation distances can, therefore, only be realised on finer levels. Overall, there are quite some parameters which need to be chosen appropriately in order to achieve an accurate but still very efficient multi-level algorithm.

Similar to the single-level algorithm, the performance of the multi-level algorithm depends strongly on the numerical quadrature of the spectral integrals over the Ewald sphere and the corresponding discrete representation of the plane-wave spectra on the various levels. The appropriate choice of the numbers of sample locations for the representation of the spectra and the translation operator has been discussed already for the single-level algorithm. Important for the multi-level algorithm is that the bandwidths of the plane-wave spectra and of the translation operators are smaller on finer levels, due to the smaller box sizes, and larger on coarser levels. This fact must be carefully utilised in an implementation of the algorithm in order to achieve an efficient evaluation of the forward operators. As a result, the plane-wave spectra on finer levels are represented with fewer discrete samples than the plane-waves spectra on coarser levels. In turn, this means that the sample density of a source spectrum must be first interpolated to the sample density on the coarser level before it can be translated to the centre of the box on the coarser level and added to the spectrum of the corresponding box. Similarly, on the receive side the plane-wave spectra are first translated to the box centre on the finer level, before the spectral content can be reduced to match the sample density on the finer level by a so-called anterpolation step. Commonly, the anterpolation operation is considered to be an adjoint interpolation operation. In effect, anterpolation is a low-pass filtering process, which maintains the integration or summation result over the function. This property is important, since the quadrature rule for the evaluation of the spectral integral is set up on the translation level, i.e., with appropriately many quadrature samples, and the integration result must remain correct through the whole disaggregation process including the anterpolations. Interpolation and anterpolation can be performed in different ways, where we assume in the following that the functional dependencies in ϑ and φ are treated separately, i.e., only one-dimensional interpolations need to be performed. If the plane-wave spectra are sampled by the same number of discrete samples as the translation operators, as commonly done in order to simplify the algorithm, they are oversampled by a factor of about two and this property allows to perform the interpolations and anterpolations with appropriate rules or algorithms of relatively low order.

A very popular and powerful interpolation rule is Lagrange interpolation. Lagrange interpolation is a polynomial interpolation rule, which constructs the polynomial of lowest possible order, which fulfills a set of L_G given data points (x_l, y_l) of a function $y = f(x)$ exactly. A new function value at a new sample

location x is found by evaluating the constructed polynomial at this position. In the form of Lagrange, the new interpolated function value can be written as [38]

$$I_{L_G}(x) = \sum_{l=1}^{L_G} y_l L_l(x), \tag{9.142}$$

with

$$L_l(x) = w_l(x) = \frac{(x - x_1)\cdots(x - x_{l-1})(x - x_{l+1})\cdots(x - x_{L_G})}{(x_l - x_1)\cdots(x_l - x_{l-1})(x_l - x_{l+1})\cdots(x_l - x_{L_G})}$$

Such a polynomial interpolation rule is called a local interpolator, since it works only with data values within a limited range, dependent on the order or number of sample points L_G. A local interpolator can only deliver accurate results, if the target function is oversampled, where the interpolation accuracy increases with the number of interpolation points. Instabilities as sometimes reported with higher-order polynomial interpolation rules, and known under the name Runge phenomenon, are in general not observed, if the interpolator is applied to periodic functions as found for our spectral integrals over the Ewald sphere. Figure 9.21 illustrates the interpolation of a function $y = f(x)$ given by its samples on level l to closer spaced samples on level $l + 1$. Then new function values are obtained by taking the weighted sum of given function values on level l, where the weights can for instance be computed by the Lagrange interpolation rule as given in (9.142). As mentioned earlier, anterpolation is the adjoint process of interpolation and the anterpolation process corresponding to the interpolation process in Figure 9.21 is illustrated in Figure 9.22. Anterpolation performs the interpolation process just in reverse order, where, however, the multiplications with the weights are not reversed to divisions, but just retained as multiplications. In case, the weights are complex numbers they are taken as complex conjugate and as such we obtain the phase conjugation operation as known from adjoint operators. Interesting to note is that anterpolation retains the shape of a low-pass function with sufficiently small bandwidth, but it changes its absolute values according to the sample densities on

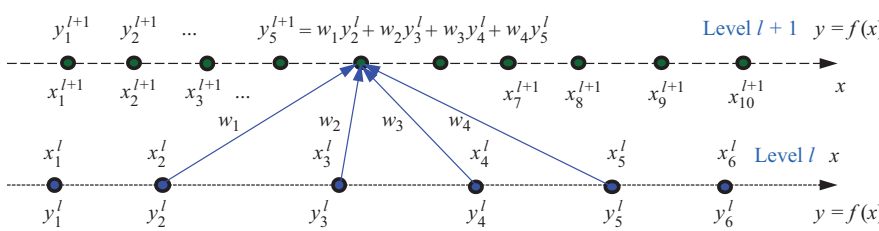

Figure 9.21 Illustration of the interpolation of a new function value of a function $y = f(x)$ by a four-point local interpolator such as the Lagrange interpolator. The new function value on level $l + 1$ is obtained from given function values on level l by adding the four nearest function values multiplied with corresponding interpolation weights. The sum of all interpolation weights is one

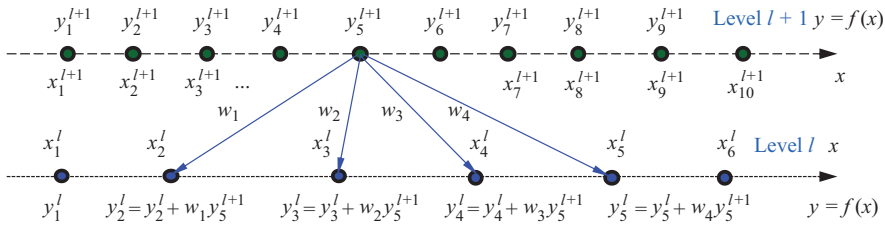

Figure 9.22 Illustration of the anterpolation of a given function value of a function $y = f(x)$ as adjoint interpolation. The shown situation corresponds to the interpolation shown in Figure 9.21 and is actually nothing else than the reversal of the interpolation process. The function value on level $l + 1$ with finer sampling is distributed onto the function values on level l with coarser sampling according to the interpolation weights

the different levels. Important for the multi-level algorithm is that anterpolation maintains the integration or summation result over the function as obtained with the finer sampling. If anterpolation is applied to a function whose bandwidth is larger than the bandwidth, which can be correctly represented by the samples on the target level, then this function is low-pass filtered during the anterpolation process. The low-pass filter function of a polynomial local interpolator is a smooth filter function as observed for the well-known Butterworth filters, where the filter order increases with the number of interpolation samples. Increasing the interpolation order further and further will decrease the interpolation error further and further and if all given samples are taken into account, the interpolation error should go to zero. For arbitrary functions, this is certainly not practical. However, for periodic functions as encountered in our case, a finite number of function samples are sufficient to represent band-limited functions and an exact global interpolator can be constructed.

Exact interpolation and anterpolation can be realised via a discrete Fourier transform, commonly performed by a FFT and its inverse, in the form of

$$\begin{aligned}\left[F\left(y_{k=1,\ldots,L_l}\right)_{k=1,\ldots,L_l}\right] &= \mathrm{FFT}\left(\left[y_{k=1,\ldots,L_l}\right]\right)\\ \left[y_{k=1,\ldots,L_{l+1}}\right] &= \mathrm{IFFT}\left(\left[F\left(y_{k=1,\ldots,L_l}\right)_{k=1,\ldots,L_l/2}, 0_{k=L_l/2+1,\ldots,L_{l+1}-L_l/2},\right.\right.\\ &\qquad \left.\left. F\left(y_{k=1,\ldots,L_l}\right)_{k=L_{l+1}-L_l/2+1,\ldots,L_{l+1}}\right]\right).\end{aligned} \tag{9.143}$$

First, the FFT of the discrete vector of function values $\left[y_{k=1,\ldots,L_l}\right]$ is computed, where the number of samples is according to the sample density on the level l. Next, the vector in the Fourier domain is zero-padded by adding higher-frequency components with zero magnitude and finally the inverse FFT is computed to obtain the interpolated vector $\left[y_{k=1,\ldots,L_{l+1}}\right]$ with the required number of sample values according to the sample density on level $l + 1$. Since the FFT works commonly

only on equidistant sampling grids, global interpolation is not feasible, if the ϑ-integration is performed by Gauss quadrature. Therefore, global interpolation is often only used for the φ-dependence and for cases, where the ϑ-range is extended to 2π in order to make it periodic and suitable for equidistant sampling [39,40].

As for the single-level algorithm, the spectral integral over the Ewald sphere is evaluated by numerical quadrature with a fixed number of, for example, Q, quadrature samples, where the value of Q depends on the size of the boxes. In order to obtain accurate results, the numerical quadrature is performed on the level on which the translation is performed. Since translations are commonly performed on several different levels, there are quadrature rules of different orders involved in the multi-level algorithm. In general, it is recommended to set up the algorithm in a way that the box size on the finest level is chosen in order to have a good compromise of algorithm accuracy and algorithm efficiency. As a lower bound for the box size on the finest level, 0.2λ is often recommended. Below this size, the achievable accuracy deteriorates. Larger box sizes can help to achieve better accuracy. However, also the necessary sample point density of the source spectra increases, in particular for the spectra of the basis functions and the probes, which are preferably pre-computed and stored in memory. Therefore, the size of the finest boxes should not be too large. Finest box sizes on the order of 0.2λ to 0.5λ appear to be a good compromise in many situations. For relatively small measurement distances between the AUT and the probes, the finest box size needs to be chosen as small as possible. If the algorithm shall work with distributed spherical wave expansions located in the centres of the boxes, a good choice for the box size is 0.5λ, since the sources located in neighbouring boxes are well decoupled with this distance. Another aspect to consider is the geometric extent of the basis functions and in particular also of the probe antennas. In order to deliver accurate results, the extent of the smallest boxes used to carry the plane-wave spectra, should be large enough compared to the extent of the basis functions or the probes. In particular, for translations on the finest level, it must be ensured that the geometric supports of the source and of the weighting functions, i.e., of the probes, do not overlap in order for (9.49) to be convergent. In general, it is recommended that the geometric extent of the probes and of the basis functions should be smaller than the geometric extent of the finest boxes, dependent on the chosen accuracy and sampling parameters. In order to work with large probe antennas, it is possible to handle the probes on a coarser level than the basis functions and it is also possible to subdivide the probes into smaller subprobes, which are handled in several boxes and combined afterwards [37].

In the multi-level algorithm, translations are performed on different levels and, dependent on the choice of parameters, certain interactions can be treated by translations on finer or coarser levels. It is clear that all interactions must be captured and it is also clear that a certain interaction should only be captured once. In general, we can say that translations over larger distances can and should be performed on coarser levels, whereas short translation distances must or should be treated on finer levels. For the situation in Figure 9.20, one translation starting from box $\underline{r}_{S1}^{l2}$ on level $l2$ is performed. If we want to maintain one buffer box on this level, i.e., translations only over distances with at least one empty box in between,

then the grey-shaded boxes in the figure cannot be treated by translations on level *l*2 and must be handled on the level below or even by direct interaction computation. In order to set up a suitable translation plan for the multi-level algorithm, we may define a maximum translation distance in number of boxes on a certain level together with the number of desired buffer boxes. Then, we identify the coarsest level on which translations need to be performed and we set up a translation table. Once the translations on the coarsest necessary level have been identified, we move one level below and identify the possible and necessary translations on this level and so on, until all necessary translations have been treated.

Once the translation plan has been set up, the necessary translation operators can be pre-computed and stored in memory. Also, the necessary aggregations and disaggregations can be identified and the required aggregation operators can also be precomputed. If a regular oct-tree structure is used covering the sources and also the observation region including the measurement locations, only relatively few aggregation and translation operators need to be pre-computed due to the symmetry properties of the configuration. For the computation of the translation operators, it is recommended to follow a scheme where the rotationally symmetric translation operators are first pre-computed for translations along the *z*-direction on a relatively fine sampling grid and then interpolated on the corresponding grid for translations in arbitrary directions [1].

In a numerical implementation, the aggregations and disaggregations in the form of the operators $T_{FF}(\underline{r}^{l2/1}_{S(p)/R(p)} - \underline{r}^{l1/2}_{S(p)/R(p)}, \underline{k})$ in (9.141) must be combined with appropriate interpolation and anterpolation steps in order to achieve an efficient multi-level algorithm, where the discussed interpolation algorithms can be used. If the source spectra are handled in an over-sampled representation as needed with local interpolators, then it is recommended to represent the spectra of the basis functions on the finest level in a compressed form in order to save memory. For this purpose, the spherical-multipole expansion

$$\underline{\tilde{\beta}}_p\left(\underline{r}_S, \underline{k}\right) = \sum_{r=0}^{R} \sum_{s=-r}^{r} \underline{\tilde{\beta}}_{p,rs} Y_{rs}(\vartheta, \varphi) \tag{9.144}$$

of the basis function spectra may be used [15], where the scalar multipoles can also be replaced by TE and TM vector multipoles [30,51]. The multipole order R can here be chosen according to the spectral content of the spectra and a conversion to the oversampled source-spectra representation can be performed without loss of accuracy after the collection of all source contributions in a box by evaluating the spherical multipoles at the necessary sample locations. For the small multipole orders on the finest level, this step can be performed with little numerical effort.

If equidistant sampling with exact global interpolation is used, then the source, receive, and probe spectra can always be kept at a minimum sampling representation, where, however, the treatment of the increasingly finer sample densities in φ towards the poles of a grid with equidistant sampling can be very cumbersome and

many extra interpolation and anterpolation steps may become necessary in order to provide the appropriate sample densities for the translations [39,40].

In order to derive the numerical complexity of the multi-level algorithm, we go through all the computational steps required to evaluate the complete forward operator according to (9.141), where we assume that the basis function and probe spectra with respect to the box centres on the finest level have already been pre-computed. On the finest level, the spectra of all basis functions in the boxes are first collected with consideration of given expansion coefficients. With a fixed size of the boxes on the finest level and thus also a fixed number of plane-wave samples, this step has a complexity of $O(P) = O(M)$, where P is the number of basis functions and M is the number of measurement samples. Both of these numbers can be assumed to be proportional to each other. With a fixed box size on the finest level, we observe also that the number of boxes on the finest level is proportional to P and thus also to M. If translations are necessary on the finest level, then the numerical effort of these translations has a complexity of $O(P) = O(M)$, since the maximum number of translations for every source box is constant for a fixed maximum translation distance and the number of boxes is proportional to P. Aggregation to the next coarser level has again a complexity of $O(P) = O(M)$, if it is assumed that the interpolation is performed with a local interpolator working with a fixed number of interpolation samples, since every box on the finest level needs to be aggregated for the given constant number of plane-wave samples. If we represent our AUT with a surface source distribution, we can assume that the number of non-empty source boxes on the next coarser level is four times less than the number of boxes on the finest level.[4] However, due to double the size of the boxes on the next coarser level, we need also a plane-wave sample density on the next coarser level, which requires four times more sample locations than on the level below (two times in ϑ and two times in φ). Consequently, the numerical complexity of all operations, which need to be performed on the next coarser level are all of $O(P) = O(M)$, too, since the reduction in the number of boxes by the factor of four is compensated by the increase in the number of plane-wave samples by the same factor of four. If we need to move to even coarser levels, we make again the same observation, i.e., the number of boxes decreases by a factor of four and the number of samples increases by a factor of four. After receiving the translated source spectra, they are disaggregated to finer levels and here we observe again that all operations on every involved level, including the final testing on the finest level, are of $O(M)$ if a local interpolator/anterpolator is assumed. In summary, the operations on every single level of the multi-level algorithm have a numerical complexity of $O(M)$. Together with the fact that the number of required levels increases for larger solution domains (the next coarser level is in general needed if the solution domain extent doubles), the overall numerical complexity of the multi-level algorithm is found to be of $O(M \log(M))$, where this complexity law can in general only be observed for relatively smooth surface-source expansion and measurement surfaces in rather large problem configurations. Also, in reality, the absolute numerical efforts of the algorithm are often more important than

[4]Such a statement is of course only true on average for typical smooth surfaces of large enough extent.

the complexities. Dependent on the applicable multiplication constants in front of the complexity laws in order to achieve absolute computation times, an algorithm with small computation complexity can still have a large computation time and dependent on the particular problem configuration, there is a lot of room to adapt an algorithm for optimum performance under the constraint of certain accuracy requirements. If global interpolations with FFT acceleration are used within the multi-level algorithm, then the interpolations itself are of $O(M \log(M))$ and the overall complexity is thus of $O(M \log^2(M))$, where, dependent on the configuration, the total computation time can of course be smaller than with local interpolators.

9.10.3 Far-field translations

The major workload of the single and multi-level algorithms comes from the processing of the spectral samples of the source and receive spectra as well as of the translation operators. In general, it is observed that the translation operators due to the spectral expansion in (9.49) exhibit a maximum into the direction from the source towards the observation location. However, the decay of the translation operators with increasing angular distance from its maximum is slow and the spectral integrals must be evaluated over the entire Ewald sphere. The magnitude of a typical FMM translation operator is illustrated in Figure 9.23 and it is seen that the magnitude does not fall much below −30 dB. Since it is clear that under FF conditions a single plane-wave contribution is sufficient to compute the interaction of sources with a receiving antenna, one may try to compute all necessary source-

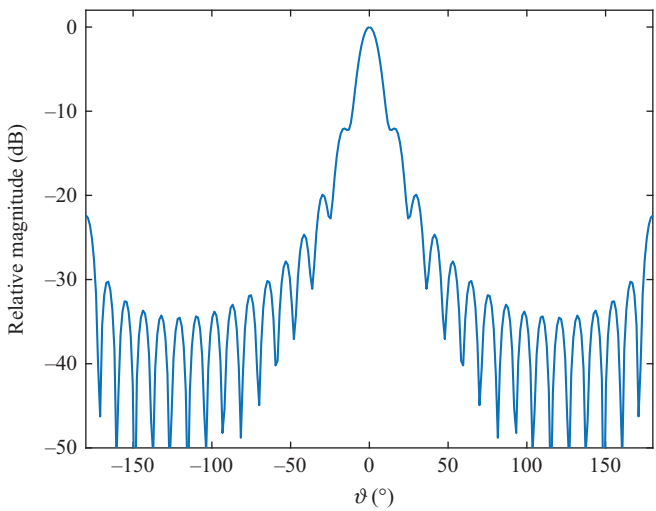

Figure 9.23 Illustration of a typical FMM translation operator for a box size of λ, a translation distance of 10λ and a multipole order of L = 15. The translation direction is here along the positive z-axis

observation interactions based on FF translation operators according to (9.52), i.e., by a spectral translation operator in the form of a Dirac delta.

Writing (9.141) with the FF translation operator results in

$$\begin{aligned} S_{21,m}\left(\underline{r}_m\right) &= c_3 \oiint \underline{W}^{Tx}_{Probe,m}(\underline{r}^{l1}_{R(m)}, -\underline{k}) T_{FF}\left(\underline{r}^{l1}_{R(m)} - \underline{r}^{l2}_{R(m)}, \underline{k}\right) \frac{e^{-jkr^{l2}_{R(m)S(p)}}}{r^{l2}_{R(m)S(p)}} \\ &\quad \cdot\delta\left(\widehat{\underline{k}} - \widehat{\underline{r}}^{l2}_{R(m)S(p)}\right) \sum_p T_{FF}(\underline{r}^{l2}_{S(p)} - \underline{r}^{l1}_{S(p)}, \underline{k}) J_p \tilde{\underline{\beta}}_p\left(\underline{r}^{l1}_{S(p)}, \underline{k}\right) d^2\widehat{\underline{k}} \\ &= c_3 \underline{W}^{Tx}_{Probe,m}(\underline{r}^{l1}_{R(m)}, -k\widehat{\underline{r}}^{l2}_{R(p)S(p)}) T_{FF}(\underline{r}^{l1}_{R(m)} - \underline{r}^{l2}_{R(m)}, k\widehat{\underline{r}}^{l2}_{R(m)S(p)}) \\ &\quad \cdot \frac{e^{-jkr^{l2}_{R(m)S(p)}}}{r^{l2}_{R(m)S(p)}} \sum_p T_{FF}(\underline{r}^{l2}_{S(p)} - \underline{r}^{l1}_{S(p)}, k\widehat{\underline{r}}^{l2}_{R(m)S(p)}) J_p \tilde{\underline{\beta}}_p\left(\underline{r}^{l1}_{S(p)}, k\widehat{\underline{r}}^{l2}_{R(m)S(p)}\right) \end{aligned} \tag{9.145}$$

where the filter property of the Dirac delta has been employed in order to evaluate the spectral integral. However, in order to make such an approach feasible, it must be guaranteed that FF translations can provide the desired accuracy and this is in general only possible if the FF translations are performed on a fine enough level. Here, it should be kept in mind that the necessary FF distance increases with the square of the box sizes and for good accuracies of the algorithm, the FF distance must be chosen so large that an efficient and accurate algorithm is hard to achieve with FF translations. However, FF translations can advantageously be utilised if the input (measurement) data for the algorithm is already in the FF, as, e.g., in the case of FF measurements, or if the NF to FF transformation has already been performed with another algorithm and the inverse source solver shall be utilised for the retrieval of diagnostic information by determining equivalent surface-source distributions.

9.10.4 Gaussian-beam translations

As discussed in the section earlier, FF translations are commonly not an efficient choice to solve the inversion problem for NF data, if good accuracies are required. Since FF translations with only one plane-wave sample are obviously not accurate enough, the question may be asked whether it is possible to find suitable translation operators which allow one to achieve good enough accuracies but require still less plane-wave samples than the full standard translation operators. The answer is here certainly yes and first attempts into this directions were based on windowing approaches employed during the multipole summation for the computation of the FMM translation operator in (9.49) [52]. Such approaches have never achieved much popularity; however, the so-called concept of Gaussian-beam-based translation operators, introduced by Thorkild Hansen [53], can be considered as a major breakthrough in this respect. The idea of the Gaussian-beam-based translation operator is to rewrite the expansion in (9.49) by choosing $\underline{X} + \underline{d} = (\underline{X} - j\Delta\hat{\underline{X}}) + (\underline{d} + j\Delta\hat{\underline{X}})$,

where Δ is obviously an imaginary shift in the direction of the translation, which is on the one hand applied within the multipole summation of the operator, and on the other hand also multiplied as an angle-dependent exponential to the plane-wave spectra in order to compensate for the effect of the shift within the multipole summation. The resulting expansion is, therefore,

$$\frac{e^{-jk|\underline{X}+\underline{d}|}}{|\underline{X}+\underline{d}|} = \lim_{L\to\infty} \oiint e^{-j\underline{k}\cdot\underline{d}} \underbrace{\left(\frac{-jk}{4\pi}\right) e^{k\Delta\left(\hat{k}\cdot\hat{X}\right)} \sum_{l=0}^{L} (-j)^l (2l+1) h_l^{(2)}(kX - jk\Delta) P_l(\widehat{\underline{k}}\cdot\widehat{\underline{X}})}_{T_L\left(\underline{X},\underline{k},\Delta\right)} d^2\widehat{\underline{k}} \tag{9.146}$$

where it is seen that the angle-dependent exponential outside of the multipole summation can be treated in the form of a factor in front of the translation operator. The effect of the imaginary shift introduced in this way is illustrated in Figure 9.24 with $\Delta = \lambda$, for the same translation situation as already considered in Figure 9.23. It is obvious that the translation operator is now much more directive and strongly attenuated for increasing angular distances with respect to the main-beam direction,

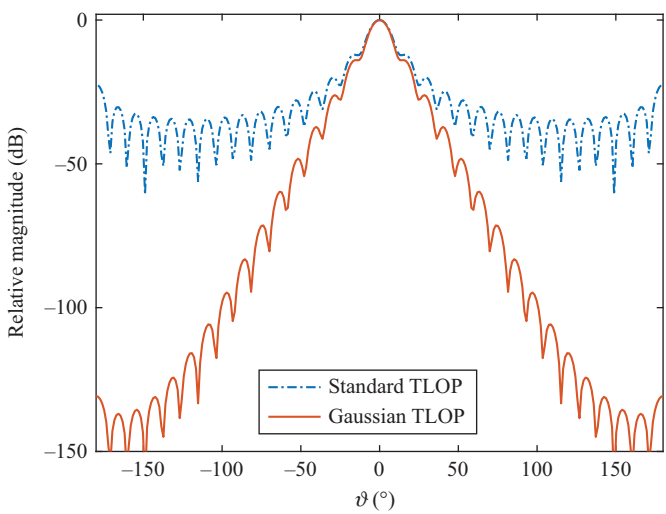

Figure 9.24 Illustration of a typical Gaussian-beam-based translation operator in comparison to the corresponding standard FMM translation operator, for a box size of λ, a translation distance of 10λ and a multipole order of L = 15. The translation direction is here along the positive z-axis. The imaginary shift in the computation of the Gaussian-beam-based translation operator was chosen to be λ

where the rate of decay, i.e., the directivity can be controlled by Δ. In a numerical implementation, care must be exercised in choosing the imaginary shift Δ, since a too large imaginary shift can prevent the convergence of the expansion in (9.146). Even if it is not so large that the convergence breaks down, it may become necessary to adjust the multipole order L and correspondingly also the sampling densities of the translation operators as well as of the source and receive plane-wave spectra. More information on the appropriate choice of the available parameters can be found in [53,54].

The numerical evaluation of the forward operator can benefit from the utilisation of Gaussian-beam-based translation operators in several ways. First of all, translation operator values below a certain magnitude threshold, e.g., below -80 or -90 dB, can be dropped completely and there is no more need to either compute the corresponding translations or pre-compute and store the corresponding translation operator values. Second, the spectra of the source and receive boxes can be restricted to those values, which are needed to perform translations, leading again to memory and computation time reductions. However, at this point, we should keep in mind that the extent of the plane-wave spectra must be chosen in a way that all relevant translations between the various boxes are supported. In order to realise the possible savings in computation time and memory, which are very remarkable, the implementation complexity of the multi-level algorithm increases considerably. In particular, a multilevel algorithm with global interpolation is no longer possible in a straightforward manner due to the fact that global interpolation leads also to a global spread of the function values. In contrast, local interpolation with appropriate oversampling is still feasible without particular complication.

9.11 Evaluation of constraint equations and adjoint operators

The various techniques, which have been discussed in Section 9.10 for the computation of the inverse problem forward operator, can in principle also be employed for the evaluation of the forward operators in the constraint equations as, e.g., in (9.100). However, not all of the techniques behave in the same way for the constraint equations as for the inverse problem equations. The key difference is that the inverse problem equations relate the sources to distant observers, whereas the constraint equations work on the sources only. Therefore, in the inverse problem equations, there are mostly translations over large distances and the observer density is rather sparse. In contrast, in the constraint equations, there are a large number of short translation distances and even the singular self-interactions need to be carefully computed, which are not encountered at all within the inverse problem equations. Also, the observer density is the same as the source density within the constraint equations. Nonetheless, we do not intend to further discuss the computation of the operators within the constraint equations, since there is a vast amount of literature available on this topic. The constraint equations are more or less identical to the equations, which are obtained from the MoM solution of surface integral equations

related to scattering and radiation problems. Such solution methods have been well established since the 1980s and even its solution by FMM and MLFMM has been around since the late 1990s. Some textbooks covering the relevant topics are [1–3].

Another important aspect for the solution of the inverse problem is the computation and evaluation of the adjoint operators which have been used to set up the systems of normal equations in (9.110) and (9.112). If the forward operator is available in matrix form, then it is clear that the adjoint operator is obtained by transposing the complex conjugate matrix of the forward operator. When the operators are computed on the fly, as in the techniques for rapid operator evaluation in Section 9.10, the adjoint operator computation can be a bit more challenging. A feasible and relatively easy to comprehend procedure is to perform the algorithm for the computation of the forward operator in a reverse manner and utilise all the involved quantities, except for the input coefficients, as its adjoint values. The transmission equation in (9.141) used to illustrate the multilevel algorithm for the example of two levels can thus be written in the form of

$$\left(S_{12,p}\left(\underline{r}_p\right)\right)^* = c_3^* \oiint \underline{\beta}_p^*\left(\underline{r}_{S(p)}^{l1}, -\underline{k}\right) T_{FF}^*(\underline{r}_{S(p)}^{l2} - \underline{r}_{S(p)}^{l1}, \underline{k}) T_L^*(\underline{r}_{R1S1}^{l2}, \underline{k}) \cdot \sum_m T_{FF}^*(\underline{r}_{R(m)}^{l1} - \underline{r}_{R(m)}^{l2}, \underline{k}) W_m \underline{W}_{Probe,m}^{Tx*}(\underline{r}_{R(m)}^{l1}, \underline{k}) d^2\widehat{\underline{k}} \tag{9.147}$$

where this equation needs to be evaluated for all relevant p. Now, the input vector represents probe excitation coefficients W_m and the probes radiate conjugate complex plane-wave spectra. Also, the aggregations, translations, and disaggregations are performed in an adjoint manner, where adjoint aggregation is disaggregation and vice versa, including the interpolation and anterpolations, which become anterpolations and interpolations, respectively.

9.12 Applications and evaluations

The antenna field transformation approaches discussed in the previous sections support a great variety of antenna measurement applications and they can provide very useful diagnostic information about the considered antenna and its measurement environment. The primary goal of many antenna measurements is to provide the far-field antenna pattern of the AUT with certain accuracy. This accuracy is in general quantified by an appropriate error measure. In the following, we quantify the accuracy of the obtained antenna patterns by their normalised magnitude error in a linear scale, which is commonly still given in dB, and calculated as

$$\Delta|E|\ (\mathrm{dB}) = 20 \log\left(\frac{|E| - \left|E_{ref}\right|}{\max\left\{\left|E_{ref}\right|\right\}}\right) \tag{9.148}$$

i.e., the difference of the magnitudes of both fields is normalised with respect to the maximum of one of the fields, typically the reference field. In most cases, the errors are given for individual field components, e.g., $E = E_\varphi$ or $E = E_\vartheta$, but it is also

possible to give the error for the complete electric field vector $\underline{E}$. Since the true antenna reference pattern is often not known in antenna measurements and also not in the following considerations, we will mostly use the term 'difference' or 'deviation' of two antenna patterns, e.g., if both fields are obtained from different NF to FF transformation approaches or if one field has been obtained from measurements and one from simulation.

In the following, we will consider a variety of antenna field transformations for different antennas and for different measurement configurations, in order to demonstrate the applicability and functionality of the inverse equivalent source-based field transformation for non-canonical measurement surfaces, but, of course, also for canonical measurement surfaces. Moreover, we will evaluate the performance of such transformations with respect to achievable transformation accuracies and with respect to the retrieval of diagnostic information. In particular, for the error considerations, we will work with synthetic measurement data, i.e., with measurement data which has not been measured, but which has been computed numerically from a given source distribution. To this end, we may consider a collection of dipole sources, which represent a certain antenna [55] or we may take a computational electromagnetics solver, such as FEKO [56], simulate an antenna, and export appropriate NF and FF data. With a dipole model, the achievable accuracy is close to the machine accuracy of the utilised computer. With a computational EM solver, the accuracy has commonly limitations on a considerably worse level, but with a current-based solver, such as FEKO, the near-fields and the far-fields are computed from the same source distribution and they are thus very accurate with respect to our antenna field transformation evaluations.

9.12.1 Pyramidal horn antenna – synthetic measurement data

The first considered AUT is an ideally conducting pyramidal horn antenna with infinitely thin walls, where NF measurement data and the FF pattern have been obtained from FEKO simulations [56]. The utilised FEKO mesh is illustrated in Figure 9.25. It shows the geometry of the AUT and gives the geometric dimensions. The simulations have been performed for a frequency of $f = 11.0$ GHz and all results will also be given for this frequency. The wavelength at this frequency is $\lambda = 27.3$ mm and the commonly accepted FF distance according to $r_{FF} = 2D_{AUT}^2/\lambda$ is around 0.7 m, where D_{AUT} is the diameter of the minimum sphere around the AUT. The vertical FF cut of this AUT in the E-plane obtained by FEKO is given in Figure 9.26 together with results from an inverse equivalent source solution.

We consider here a spherical measurement configuration with equidistant sampling in ϑ and φ, where synthetic NF data has been computed for different observation radii with 30 samples in ϑ and 60 samples in φ, two orthogonal polarisations, without considering the influence of a specific measurement probe, i.e., the probe is a Hertzian dipole. Overall the number of the virtual measurement samples is 3,600, where samples at the poles are avoided by starting the sampling in ϑ at 3°. For the IESS, we used the closed triangular mesh consisting of 6,322

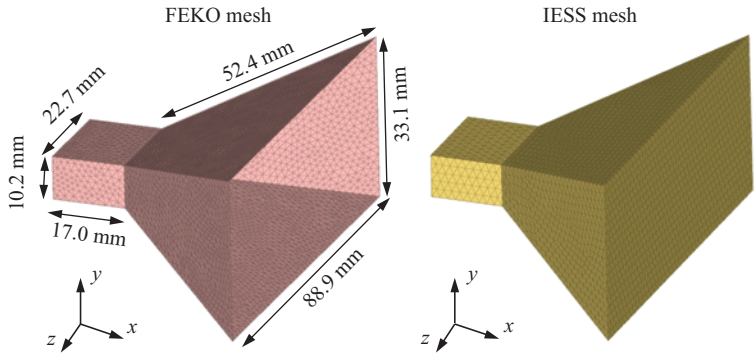

Figure 9.25 Ideally conducting pyramidal horn antenna for a frequency of 11.0 GHz. The illustration shows the triangular mesh as used for FEKO simulations and the triangular mesh as used for the IESS. The FEKO mesh is open at the radiation aperture, whereas the IESS mesh is closed

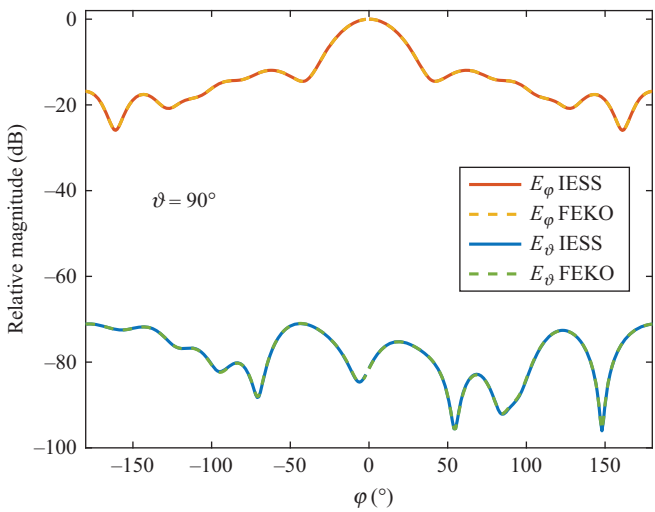

Figure 9.26 E-plane FF cut of the AUT in Figure 9.25. Transformation results of the IESS are compared to the corresponding FEKO data. The shown vertical cut has been chosen since the largest transformation errors are observed in this cut. The IESS results have here been obtained by computing the inverse source solution from FEKO FF data on a complete sphere around the AUT

triangles as shown on the right-hand side of Figure 9.25. IESS transformation accuracies for the vertical FF cut according to the error definition in (9.148) are shown in Figures 9.27 and 9.28.

For the results in Figure 9.27, the IESS has been configured to achieve as good as possible transformation accuracy for the given mesh with low-order RWG current basis functions, whereas the results in Figure 9.28 have been obtained with realistic standard settings providing a good compromise between transformation time and transformation accuracy. For both cases, equivalent surface sources with Huygens-type RWG elementary radiators with outward directed radiation pattern have been used. With the standard settings, the transformation time for one set of NF data and one frequency (without additional side constraint such as a zero-field condition) is on the order of half a minute on a typical desktop computer (Intel® Core™ i7-4820K @ 3.70 GHz, four cores). The pattern accuracy with the standard settings is below −80 dB and is considered to be more than sufficient for practical antenna measurements, where it is hardly possible to achieve pattern accuracies on the order of −60 dB. The maximum achieved pattern accuracy in Figure 9.27 is on the order of 20 dB better than the standard accuracy in Figure 9.28. The observed accuracy on the order of −100 dB can be considered as a very good value, which is not always observed together with generally available numerical solution approaches. Figure 9.29 shows Love surface current densities obtained with the IESS under

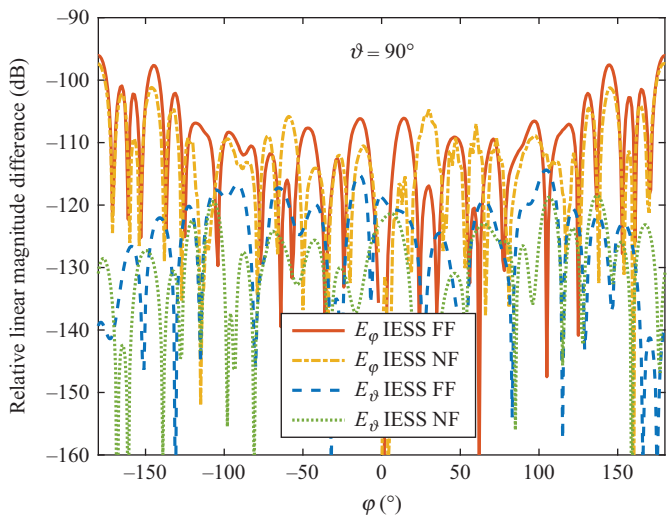

Figure 9.27 E-plane cut FF pattern deviations with respect to the FEKO reference data for the AUT in Figure 9.25. The deviations are shown for IESS results obtained from FF data and obtained from NF data with a measurement radius of 0.1 m. The IESS has been configured to obtain as good as possible transformation accuracy

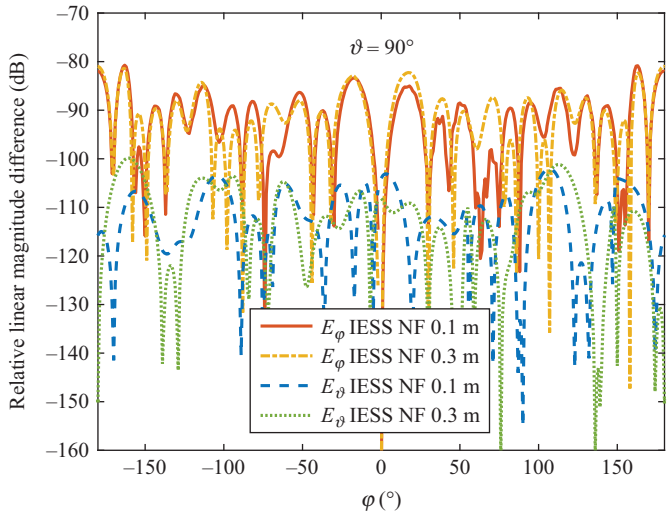

Figure 9.28 E-plane cut FF pattern deviations with respect to the FEKO reference data for the AUT in Figure 9.25. The deviations are shown for IESS results obtained from NF data with a measurement radius of 0.1 and of 0.3 m, respectively. The IESS has been configured with recommended standard settings

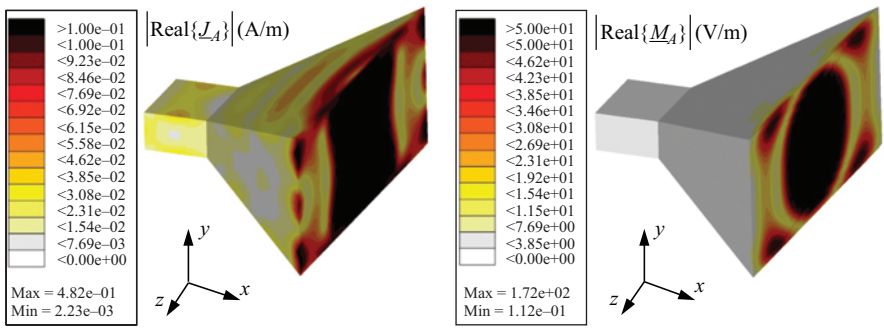

Figure 9.29 Love surface current densities obtained with the IESS solver from NF data with a measurement radius of 0.1 m, for the AUT in Figure 9.25, on the mesh on the right-hand side of Figure 9.25

imposition of the Love condition as a Calderon projector according to (9.119). From the illustration, the appropriate functioning of the antenna becomes obvious.

In Figure 9.30, the IESS iterative solver convergence is depicted for several solver choices. The graph on the left-hand side of the figure shows the solver residual for NE systems of normal equations and the graph on the right-hand side of the figure shows the same results for the corresponding NR systems of normal

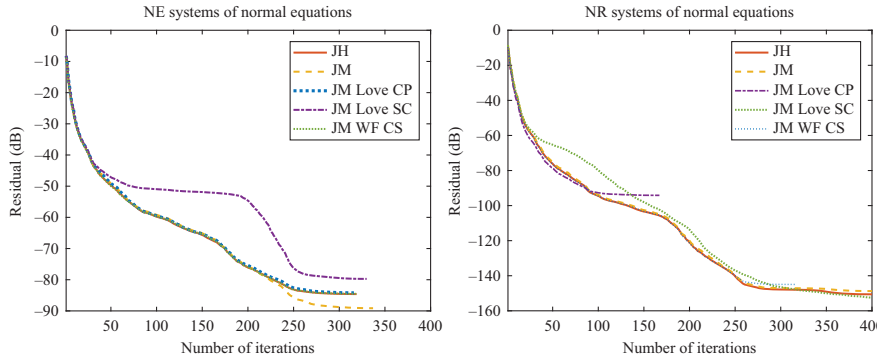

Figure 9.30 IESS iterative solver convergence for NE systems of normal equations (left-hand side) and for NR systems of normal equations (right-hand side), with the mesh on the right-hand side of Figure 9.25. JH: Huygens-type elementary radiators, JM: electric and magnetic surface current densities without additional side constraint, JM WF CS: electric and magnetic surface current densities with WF CS condition, see (9.106), JM Love CP: electric and magnetic surface current densities with Love condition in the form of the Love projectors according to (9.103) and (9.104), JM Love SC: electric and magnetic surface current densities with Love condition in the form of an additional side constraint according to (9.101) and (9.102)

equations. The NE residual is directly the observation error (except for the JM Love SC solution), whereas the NR residual is related to the space of the solution vector (see Section 9.9). The NE residual, i.e., the observation error reaches here to a similar level as the FF error in Figure 9.28 and also the NR solvers reach this observation error level, except for the solver with the Love condition in the form of Calderon projectors. However, it is to note that the NR residual needs to reach until below −140 dB before the observation error level of somewhat below −80 dB is reached. The stopping criterion for all solver runs was relative in a way that the solver stopped, when 3 iterations in a row did not give a relative residual improvement of better than 0.9999. All solver choices stopped with this criterion and also all of them needed about the same number of iterations to reach the stopping criterion, where the observation error was about the same for all of them, except for the NR solver with the Calderon projectors. Obviously, the Calderon projectors introduce additional errors, which limit the achievable observation and thus also the FF error to around −65 dB when utilised within the NR system of equations. In the NE system of equations, the Calderon projector does not show any notable effect. When the Love condition is included in the form of an additional side constraint as in (9.126) for the NR systems of equations and in (9.127) for the NE systems of equations, respectively, then it is obvious that the convergence

behaviour of the solvers changes, where, however, still similar values of the residuals are achieved, if the weighting of the Love condition via the scaling parameter λ_{SC} is not too strong. In addition to the solver residuals, Figure 9.31 compares the observation errors of IESS solutions obtained with NE and NR systems of equations. Here, it should be noted that the observation error is in general not computed in the solution of the NR equations and its generation causes a considerable amount of extra computations. For the NE solutions with Love condition in the form of a side constraint, the residual comprises the observation error together with an error contribution related to the fulfillment of the Love condition side constraint equations. Therefore, the pure observation error as seen in Figure 9.31 is here also computed in an additional step. The NE solvers with no or a simple CS side constraint show obviously the best convergence behaviour with respect to the observation error, where, however, the NR solutions are not much worse. In both cases, the solvers with Love condition behave worse than the solvers with no or a simple side constraint. For the solutions with Love condition as a side constraint, the convergence behaviour depends strongly on the chosen weighting of the side constraint, which is, however, not further investigated. The given results are for a typical value of the weighting parameter.

In summary, we can say that the simple IESSs without additional side constraint, or with the simple CS condition, show the best behaviour for the lowest computational effort and the solution of the NE systems of normal equations allows for a more direct control of the solution accuracy. For the NR systems, it would

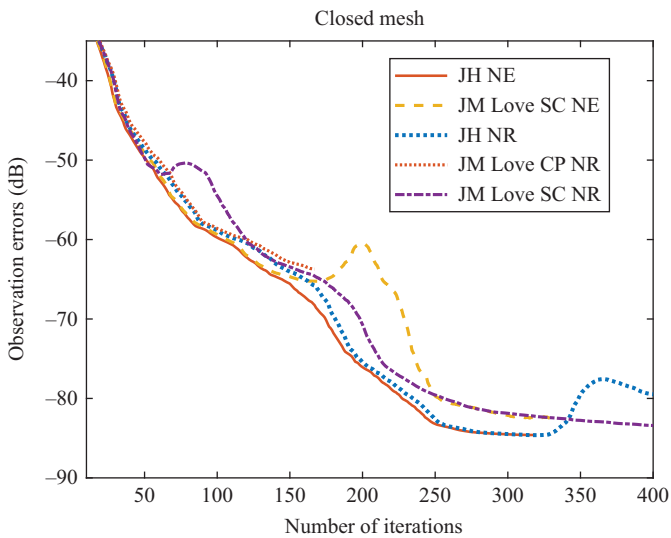

Figure 9.31 IESS observation errors dependent on the number of iterations for several solver choices as already shown in Figure 9.30, where the goal is to compare the observation errors of NE and NR systems of normal equations

certainly also be possible to control the convergence dependent on the observation error and not dependent on the residual in order to avoid too many iterations and possibly occurring observation error instabilities, but this would in general need extra computations within the solver.

9.12.2 Planar aperture antennas – synthetic measurement data

The next considered AUTs are circular planar aperture radiators where the synthetic measurement data in an NF observation plane has been computed from a Hertzian dipole representation of the radiation aperture distribution [55]. The first measurement configuration is depicted in Figure 9.32. The FF distance of the AUT with a diameter of 48 cm is more than 60 m at the considered frequency of 40 GHz. Even though the measurement distance is several hundred wavelengths, it is still only a small fraction of the FF distance. IESS transformation results are shown in Figure 9.33 and compared to the reference data from the dipole model. The achieved linear pattern error is below −100 dB in the main beam and is getting worse away from the main beam, which is expected due to the truncated scan aperture. The decay of the NF magnitude towards the edges of the scan plane is on the order of −37 dB and the commonly assumed valid pattern angle around the main beam for the considered measurement configuration is around $\theta_{valid} = 6.3^{\circ}$, see also Figure 9.32. As, for example, discussed in [57], the error due to scan plane truncation is commonly relatively small for an IESS, as compared to the common plane-wave based and FFT accelerated planar transformation schemes as discussed in Chapter 6. The reason for the better performance of the IESS is the assumption of a localised source distribution just in the aperture of the AUT, whereas the planar plane-wave-based transformation approaches do not assume an a priori localisation of the sources. In the given case, we worked with a planar triangular surface mesh

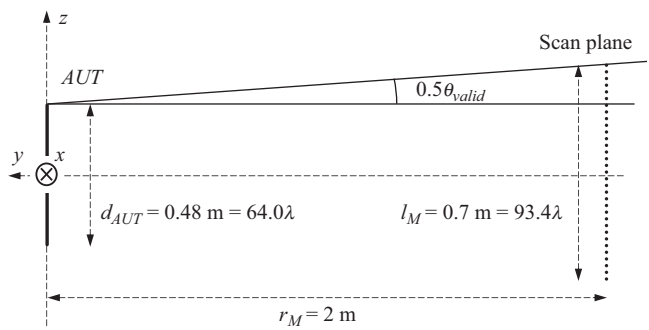

Figure 9.32 Planar measurement configuration for a 40 GHz circular aperture antenna. The square scan plane is regularly sampled with 34,969 sample locations, two polarisations each, where a horn-like probe antenna has been used

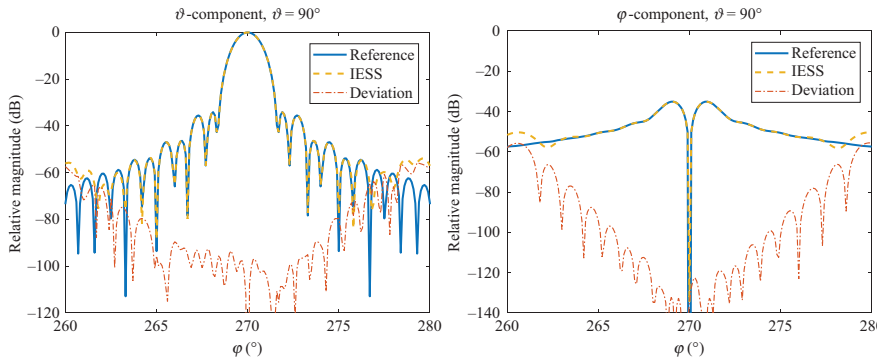

Figure 9.33 H-plane FF pattern cut of the 40 GHz aperture antenna as considered in Figure 9.32. IESS transformation results are compared to reference results directly obtained from the assumed Hertzian dipole source distribution

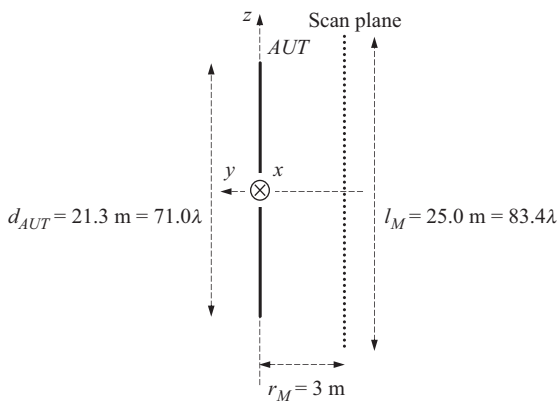

Figure 9.34 Planar measurement configuration for a 1 GHz circular aperture antenna. The square scan plane is regularly sampled with 27,889 sample locations, two polarisations each, where a horn-like probe antenna has been used

consisting of 1,575,882 triangles and Huygens elementary radiators based on RWG functions have been used as equivalent sources.

The second measurement configuration is shown in Figure 9.34. The FF distance of the AUT with a diameter of 21.3 m is more than 3,000 m at the considered frequency of 1 GHz. The measurement distance is here 3 m (around ten times the wavelength) and thus only a fraction of the aperture diameter. IESS transformation results are shown in Figure 9.35 and compared with the reference data from the dipole model. The achieved linear pattern error is here slightly worse than before, but still close to −100 dB in the main beam. The decay of the NF magnitude

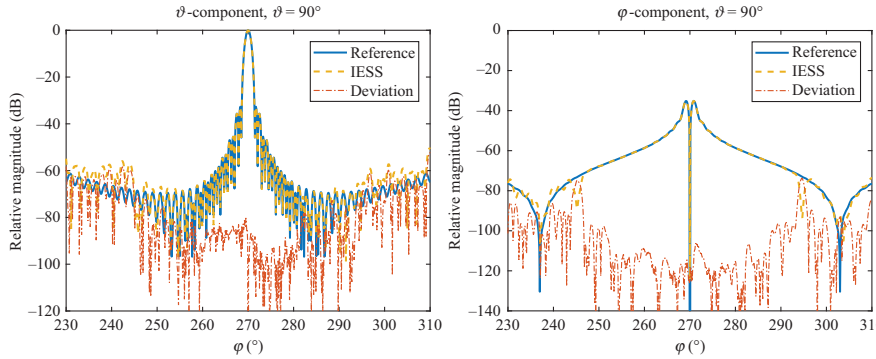

Figure 9.35 H-plane FF pattern cut of the 1 GHz aperture antenna as considered in Figure 9.34. IESS transformation results are compared to reference results directly obtained from the assumed Hertzian dipole source distribution

towards the edges of the scan plane is on the order of close to −40 dB and the geometrically estimated valid pattern angle around the main beam is here around $\theta_{valid} = 63.6°$, see Figure 9.32 for the definition. To model this aperture antenna within the IESS, a pillbox-shaped mesh with 3,152,660 triangles was utilised and Huygens elementary radiators based on RWG functions have been used as equivalent sources. The pillbox-shaped closed surface mesh was here certainly not necessary and leads to many more unknowns than actually required. However, with an appropriate solver of the resulting linear system of equations, such a model can well be handled and reliably be solved.

The magnitude of the obtained equivalent surface sources on the radiating side of the pillbox mesh is depicted in Figure 9.36. It shows nicely the aperture tapering, but also a ring structure, which resembles the original source distribution consisting of rings of Hertzian dipoles, which had a distance as recovered by the IESS. This result is a clear demonstration of the diagnostic capabilities of an IESS.

9.12.3 *Double-ridged waveguide antenna – spherical and multi-planar near-field measurements*

In this subsection, first spherical near-field measurements of a double-ridged waveguide antenna, as shown in Figure 9.37 are considered. The antenna is a DRH18 from RFSpin [58] and it has been measured in the anechoic chamber at the Technical University of Munich. The figure gives also an impression of the geometric dimensions of the antenna and it shows its location with respect to the scan centre and the coordinate system of the measurement setup.

The antenna is specified for a frequency range of about 1–18 GHz. In the following, we consider measurements at the upper frequency limit at 18 GHz. The common FF distance of the DRH18 at 18 GHz is around 7.5 m, and the NF measurements have been performed at a distance of 2.68 m, utilising an open-ended

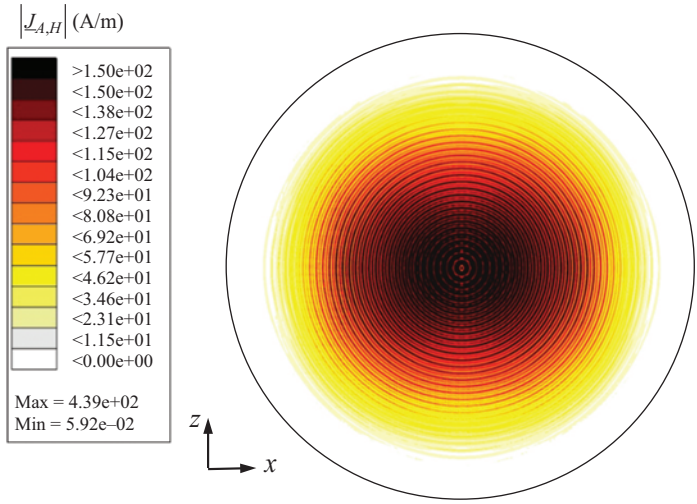

Figure 9.36 Magnitude of the surface current distribution (elementary Huygens radiators based on RWG functions) of the IESS solution for the 1 GHz aperture antenna according to Figure 9.34. The source magnitude decays towards the circumference of the mesh and the visible ring pattern is due to the assumed original source distribution consisting of rings of Hertzian dipoles

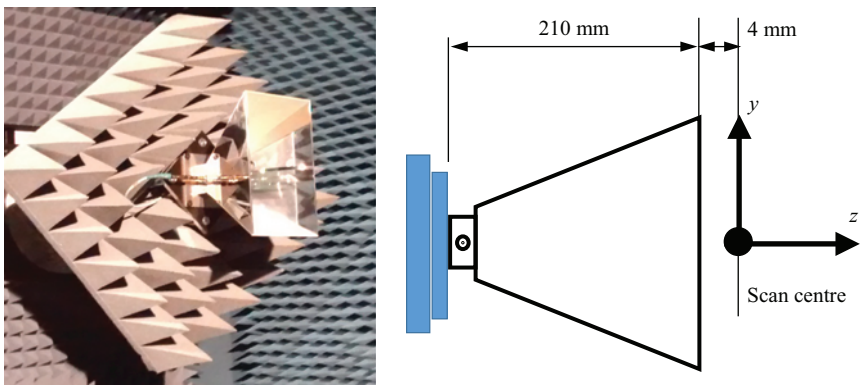

Figure 9.37 Double-ridged waveguide antenna DRH18 mounted on the spherical positioner in the anechoic antenna measurement chamber at the Technical University of Munich

rectangular hollow waveguide probe OEWG WR62 from NSI-MI [59]. The measurements have been performed with equidistant sampling in ϑ and φ with an angular spacing of 1.25°, resulting in a total of 41,905 measurement locations with two orthogonal polarisations each. The principal FF pattern cuts obtained from the

NF measurements are shown in Figure 9.38, where IESS transformation results from different meshes are compared to modal spherical transformation results obtained with the Software from NSI-MI [59]. The observed deviations between the different patterns on the order of −40 dB to −50 dB are on the order of accuracy which can be expected with this measurement setup. The spherical mesh IESS results are closer to the spherical mode results, since the sources of the spherical mesh are less localised than the sources of the conformal mesh shown in Figure 9.39, as it is also the case for the spherical mode expansion. Both meshes are centred around the AUT and are offset with respect to the rotation centre of the measurements, whereas the modal expansion assumes a minimum sphere around the scan centre of the measurements, which is larger than the extent of the spherical mesh. Further FF pattern comparisons are given in Figure 9.40, where both polarisations in the E-plane are considered. Only IESS results obtained with the conformal mesh in Figure 9.39 are shown. However, different equivalent sources have now been used to perform the transformation: electric and magnetic surface current densities without any further constraint (JM), electric and magnetic surface current densities with Love condition (JM Love), and Huygens-type elementary radiators (JH). The Love-constrained result is taken as reference for the illustration, but the observed differences between the three patterns can be considered as very low. Here, we should keep in mind that we have various parasitic echo field contributions in the measurement data, e.g., due to the antenna fixture and absorbers as seen in Figure 9.37, and due to room echoes.

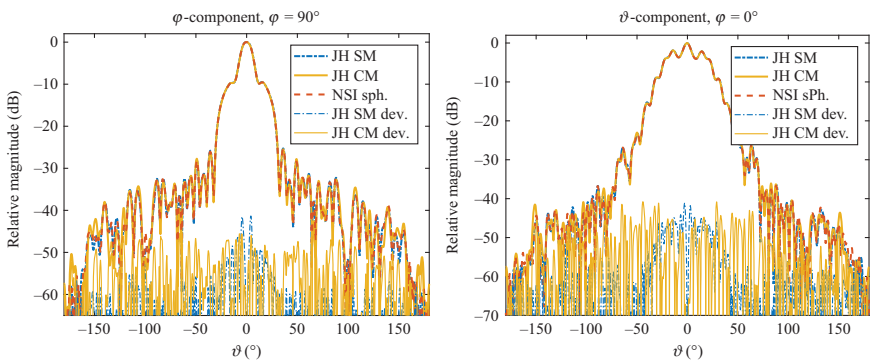

Figure 9.38 *H-plane (left) and E-plane (right) FF pattern cuts at 18 GHz of the DRH18 antenna as depicted in Figure 9.37. IESS transformation results are compared to results obtained by the modal spherical transformation software from NSI-MI [59]. The IESS transformations have been performed with Huygens-type elementary radiators (JH) based on RWG functions for a spherical mesh (SM) with 340 mm diameter around the AUT and with conformal mesh (CM) as shown in Figure 9.39*

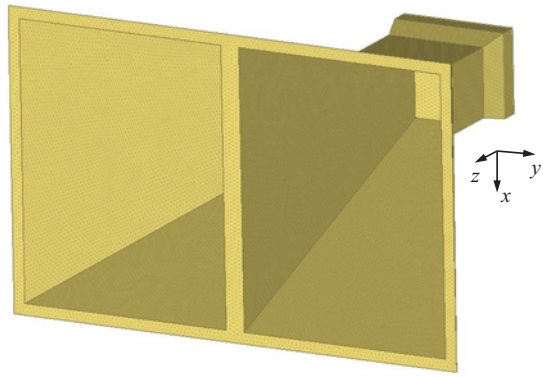

Figure 9.39 Closed conformal triangular surface mesh used to perform IESS transformations for the DRH18 antenna shown in Figure 9.37. The mesh comprises 129,020 triangles

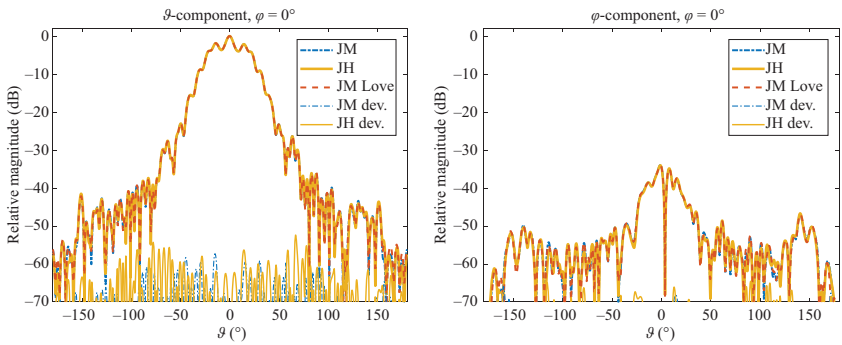

Figure 9.40 E-plane FF pattern cut for 18 GHz of the DRH18 antenna as depicted in Figure 9.37. Comparison of different IESS transformation results obtained with the CM as shown in Figure 9.39

Since the observed differences between the different source models are mostly dependent on the specific numbers of iterations that were performed during the solution of the inverse problem, it can be concluded that the chosen source model is not really important for the obtained FFs. These computations have been performed with the NE system of normal equations as introduced in (9.116) but very similar results are also obtained with the NR system of normal equations in (9.115), if the iterative solver is continued until it reaches the same observation error. An advantage of the NE equations as compared to the NR equations is that they work directly on the observation error and the degrees of freedom are also in the space of the observations, which are often less than the degrees of freedom in the equivalent sources. Based on this, a relative stopping criterion of the iterative solver appears to be more predictable and often slightly fewer iterations are required to achieve a

certain observation error. The electric and magnetic surface current densities obtained from the IESS transformation with imposition of the Love condition in the form of a Calderon projector are shown in Figure 9.41. They give a clear insight into the radiation mechanisms of this antenna and they relate to the magnetic and electric fields as expected.

Figure 9.42 shows surface source densities obtained from IESS transformations with Huygens-type elementary radiators (left-hand side) and obtained with unconstrained electric and magnetic surface current densities (right-hand side). Both show also the wave behaviour of the radiation, but do not have the clarity of the Love surface current densities. The physical insight into the antenna mechanisms is certainly also not as clear as for the Love surface current densities. If desired, Love surface current densities or magnetic and electric fields can,

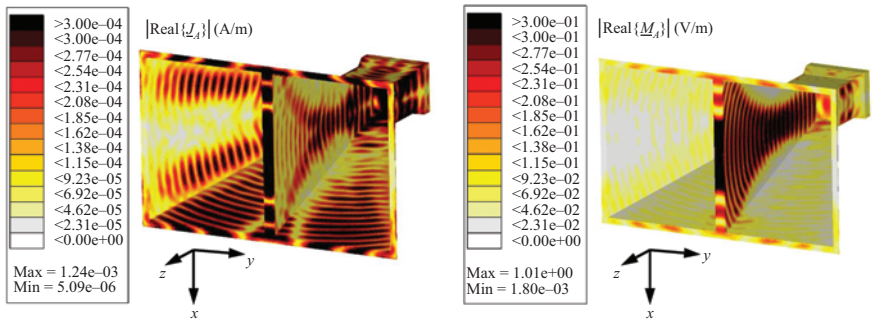

Figure 9.41 Electric and magnetic surface current densities on the conformal mesh from Figure 9.39, obtained by IESS transformations with enforcement of the Love or zero-field condition in the form of a Calderon projector

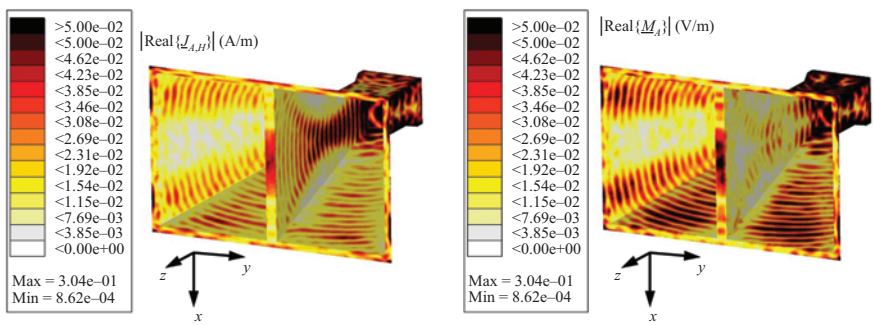

Figure 9.42 Huygens surface-source density (left-hand side) and magnetic surface current density from unconstrained electric and magnetic current densities (right-hand side), shown on the conformal mesh from Figure 9.39, obtained by IESS transformations

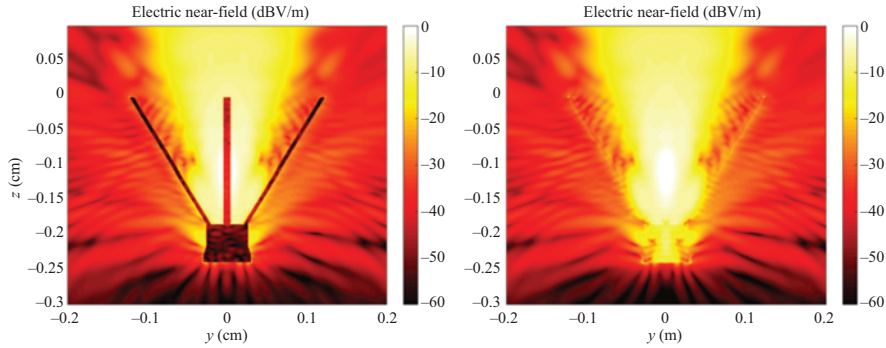

Figure 9.43 Electric NF magnitude in the yz-cut plane through the AUT model computed from surface-source densities obtained by IESS solutions. Left-hand side: electric and magnetic surface current densities obtained from IESS solution with Love-projectors as shown in (9.103) and (9.104), and right-hand side: electric and magnetic surface current densities obtained from IESS solution without additional side constraint

however, easily be computed from these sources in a post-processing step in order to provide the full diagnostic information. Near-fields computed in a post-processing step from the obtained source distributions are shown in Figures 9.43 and 9.44. Figure 9.43 shows NFs computed from electric and magnetic surface current densities obtained from an IESS solution with Love constraint in the form of projector equations as found in (9.119) (left-hand side) and from electric and magnetic surface current densities obtained from an IESS solution without any additional side constraint. Figure 9.44 shows fields which have been computed from Huygens-type elementary radiators obtained from a corresponding IESS solution. Corresponding relative field magnitude differences in linear scale with respect to the magnitude of the Love-constrained fields are seen in Figure 9.45 within the *yz*-plane.[5] The results show that the Love-constrained solution suppresses the field inside the closed mesh, whereas the unconstrained electric/magnetic surface current solution does not at all show this effect. The Huygens-type elementary radiators cannot show much field suppression inside the AUT model for this rather complex and non-convex shape. Some field suppression is visible near the support of the antenna, and, of course, an important advantage of the Huygens-type elementary radiators is that only half the number of unknowns are needed as compared to the case of working with electric and magnetic surface sources.

[5]The normalisation of the field differences is here performed with respect to the average of the reference field magnitude in a linear scale over the entire illustration area. This is certainly an arbitrary choice, but to be preferred over a pointwise normalisation, which leads to very large relative errors for very small field magnitudes.

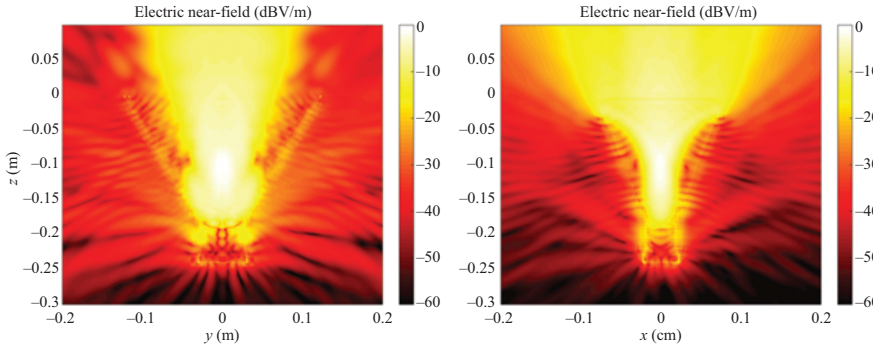

Figure 9.44 *Electric NF magnitude in cut planes through the AUT model computed from Huygens-radiator-type surface-source densities obtained by IESS solution. Left-hand side: yz-plane, and right-hand side: xz-plane*

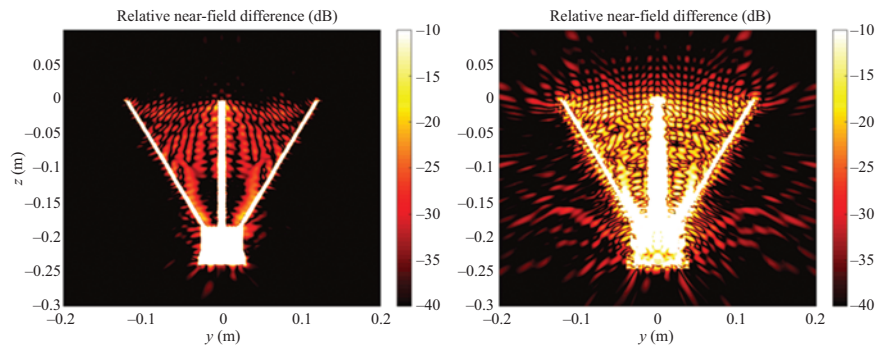

Figure 9.45 *Relative linear differences of NF magnitudes in the yz-plane through the AUT model computed from different equivalent surface–source distributions, where the Love-constraint fields as shown on the left-hand side of Figure 9.43 are taken as reference. Left-hand side: electric and magnetic surface current densities obtained from IESS solution without additional side constraint, seen on the right-hand side of Figure 9.43; and right-hand side: Huygens-radiator-type surface-source densities obtained by IESS solution, seen in left-hand side of Figure 9.44*

The NF magnitude field differences in Figure 9.45 show good agreement of all fields within the main beam of the radiation and also in the outside regions of the mesh. The largest differences are of course observed in the inner of the AUT mesh, where the fields are not well defined anyways. Interesting is the difference behaviour of the NF magnitude in the centre of the plots, near the ridges of the AUT. The field magnitudes with the Huygens-type radiators show here larger differences

than the electric/magnetic currents solution, which is, however, expected due to the different NF behaviour of both models very close to the sources, in particular due to the different basis functions for the magnetic current part within the Huygens-type basis functions. Figure 9.46 shows the NF electric field magnitude obtained from an IESS solution with WF CS side condition between the electric and magnetic surface current densities [see (9.106)] on the left-hand side of the figure and the deviation to the field magnitude obtained with the Love-projector on the right-hand side of the figure. As expected, the deviations close to the Huygens surface, especially in the centre of the figure near to the ridges, are now considerably reduced as compared to the strong-form CS condition in terms of the Huygens-elementary-radiator-type basis functions. Figures 9.47 and 9.48 show the electric NF magnitude obtained with a mesh similar to the one in Figure 9.39, where the aperture was, however, closed by a planar mesh, i.e., the mesh is not following the ridges to the inside. These illustrations are intended to show the influence of an imaginary shift of the basis functions normal to the Huygens surface as discussed in Section 9.6.4.

Figures 9.49 and 9.50 illustrate the IESS convergence behaviours for different solver options. Figure 9.49 relates to the conformal mesh as shown in Figure 9.39, whereas Figure 9.50 relates to the spherical mesh around the AUT, which has already been used to obtain some of the results in Figure 9.38. The left-hand side graph in both figures shows results for NE systems of normal equations, and the right-hand side graph is for NR systems of normal equations.

As already found for the simulated example in Section 9.12.1, the NE solutions exhibit a considerably better control of the true solution error and stop reliably with the applied relative stopping criterion, which stops the solver after three consecutive iterations with a worse relative improvement of the residual than 0.999. Remarkable is, however, that also the NR solutions achieve about the same

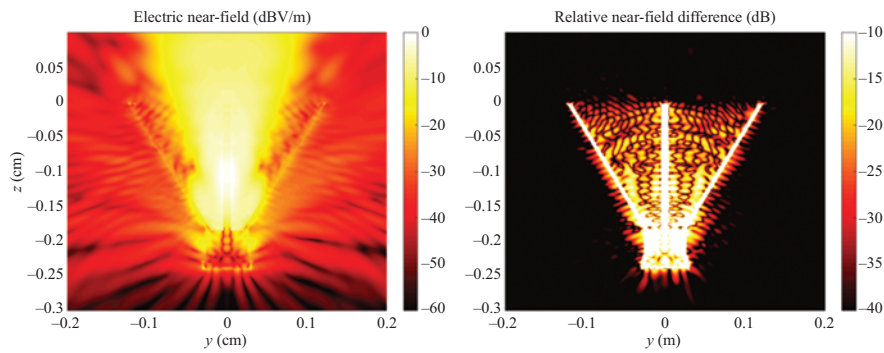

Figure 9.46 Electric NF magnitude in the yz-plane through the AUT model computed from surface-source densities obtained by IESS solutions. Left-hand side: electric and magnetic surface current densities obtained from IESS solution with WF CS condition as given in (9.106), and right-hand side: deviation to field magnitude obtained from IESS with Love-projectors as shown in (9.103) and (9.104)

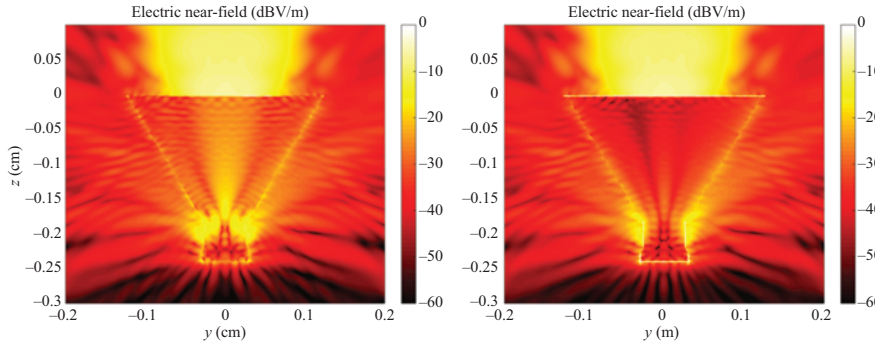

Figure 9.47 *Electric NF magnitude in the yz-plane through the AUT model computed by IESS solution with Huygens-type elementary radiators with a mesh similar to the one in Figure 9.39, where the aperture is, however, closed by a plane. Left-hand side: no imaginary shift of basis functions, and right-hand side: imaginary shift of 0.2λ*

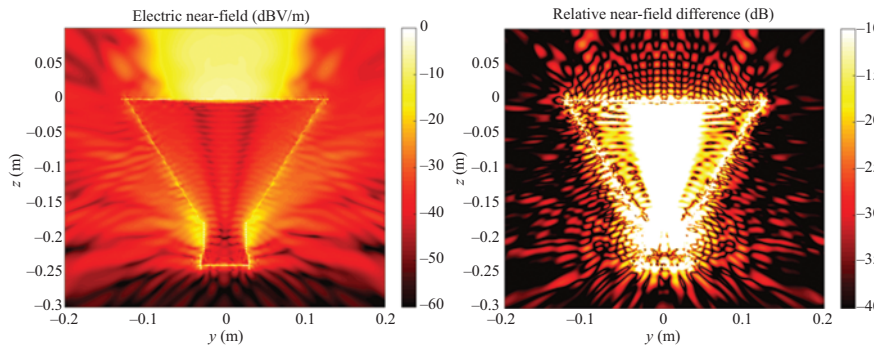

Figure 9.48 *Electric NF magnitude in the yz-plane through the AUT model computed by IESS solution with Huygens-type elementary radiators with a mesh similar to the one in Figure 9.39, where the aperture is, however, closed by a plane. Left-hand side: imaginary shift of basis functions 0.4λ, and right-hand side: deviation between case with no imaginary shift and imaginary shift of 0.4λ*

observation errors as the NE solutions, no matter whether they stop with fewer or more iterations. The additional NR iterations decrease obviously the residual of the solution further without notable improvement of the observation error. A direct comparison of the iteration-dependent behaviour of the observation error for both types of equation systems is shown in Figure 9.51, where it becomes obvious that the NE solutions show a slightly better performance, and, as already seen for the simulated example in Section 9.12.1, the solutions with Love constraint behave

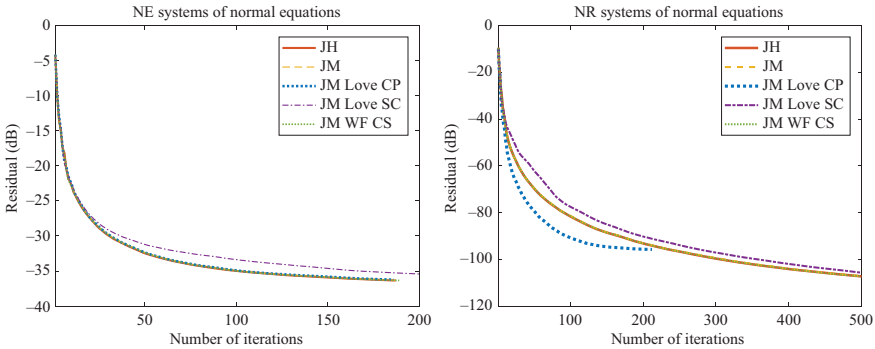

Figure 9.49 IESS iterative solver convergence for NE systems of normal equations (left-hand side) and for NR systems of normal equations (right-hand side), with the mesh on the right-hand side of Figure 9.25. JH: Huygens-type elementary radiators, JM: electric and magnetic surface current densities without additional side constraint, JM WF CS: electric and magnetic surface current densities with WF CS condition, see (9.106), JM Love CP: electric and magnetic surface current densities with Love condition in the form of the Calderon projectors according to (9.103) and (9.104), JM Love SC: electric and magnetic surface current densities with Love condition in the form of an additional side constraint according to (9.101) and (9.102)

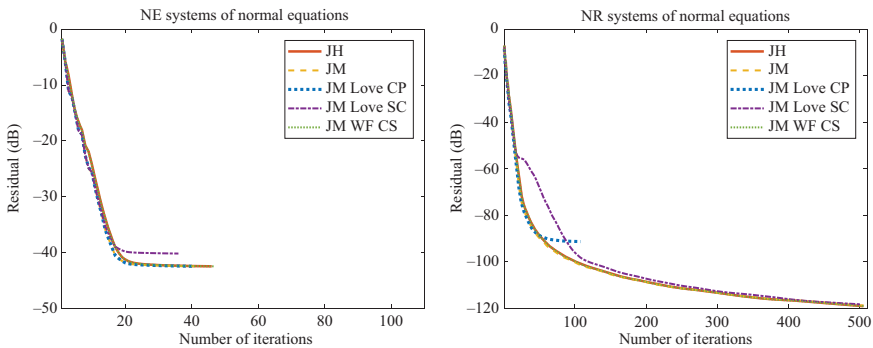

Figure 9.50 IESS iterative solver convergence for NE system of normal equations (left-hand side) and for NR system of normal equations (right-hand side), for the SM with 340 mm diameter around the AUT as already considered in Figure 9.38. For the definition of the legends, see the caption of Figure 9.49

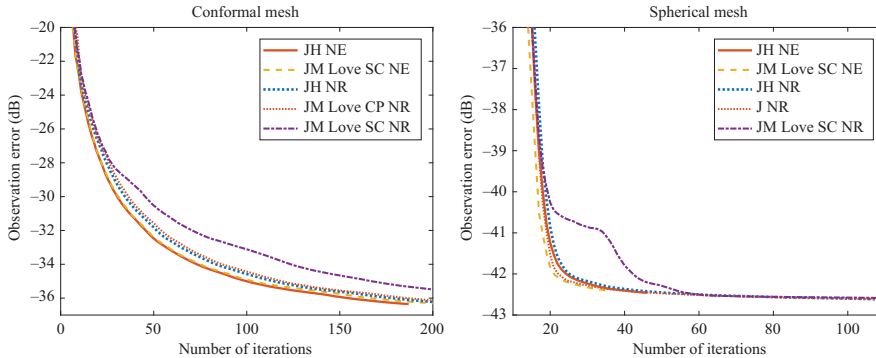

Figure 9.51 IESS observation errors dependent on the number of iterations for several solver choices as already shown in Figures 9.49 and 9.50 for the CM (left-hand side) and for the SM (right-hand side), where the goal is to compare the observation errors of NE and NR systems of normal equations

worse, where the Love side constraint solutions depend again strongly on the chosen weighting of the side constraint. Interesting, but of course expected, is that the spherical mesh requires considerably less iterations. Here it is to note that the Love condition helps to achieve a rather early stop of the NR solutions. Finally, it should be emphasised that the solutions with the spherical mesh lead to smaller observation errors than the solutions with the conformal mesh. This is also expected since the spherical mesh has a larger extent around the AUT and is thus able to represent also the scattering contributions coming from the fixture and the absorbers behind the AUT. Due to the spatial filtering behaviour of the conformal mesh, it is expected that the results obtained with this mesh are more appropriate to characterise the antenna alone.

In summary, it is concluded that the NE solutions provide again considerably better controllability of the solution accuracy and that the solver choices without additional constraint, or with a simple side constraint in the form of the combined-source condition, are the better choice, due to their lower computation cost and their good accuracy.

Next, we consider NF measurements of the double-ridged waveguide antenna, which were collected with the planar NF scanner in the antenna test range of the Technical University of Munich. These measurements were performed at a frequency of 10 GHz with an OEWG WR90 as probe antenna. In an initial step, measurement data was collected on the primary scan plane with an extent of 2.4 m by 1.5 m in x- and y-directions, respectively, as seen in Figure 9.52.

In order to extend the valid range of the FF pattern after the NFFF transformation, measurement data was collected on four further scan planes, which were obtained by rotating the AUT on the spherical positioner into new positions, which were fixed during the planar measurement on the respective plane. The distance of

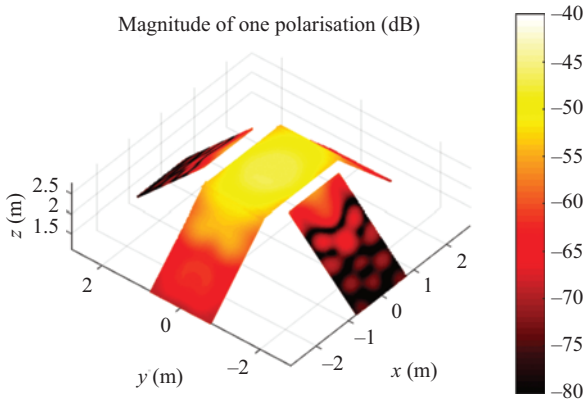

Figure 9.52 Illustration of multi-planar NF measurement of the double-ridged waveguide antenna. The primary scan plane is parallel to the xy-plane and has an extent of 2.4 m by 1.5 m in x- and y-directions, respectively. In order to extend the scan range, four additional scan planes have been generated by rotating the primary scan plane ±45° in the xz- and yz-planes, respectively, with a rotation radius of 9.73 m around the AUT

the scan plane from the rotation centre of the spherical positioner was 2.73 m. The number of equidistant sample locations in the primary scan plane was 36,391 with two polarisations each, resulting into 181,955 sample locations for all five scan planes. For comparison, spherical measurements with 32,942 sample locations with two polarisations each have also been performed with the same probe antenna. The NFFFTs for the three considered configurations have been performed by an IESS with the conformal mesh as found in Figure 9.39. The obtained FF pattern results are depicted in Figures 9.53 and 9.54, where the planar and multi-planar measurement results are compared to the results obtained from the spherical measurements. The restricted valid angular range of the one-plane measurements is clearly seen in the pattern cuts and corresponds to the valid range to be expected by a geometrical consideration as for instance illustrated in Figure 9.32. With the five-plane measurements, the valid angular range of the obtained FF patterns is considerably increased and even the gap in the measurements in *y*-direction is almost without influence in the FF pattern.

9.12.4 Parabolic reflector with defect – synthetic measurement data

We consider the hollow-waveguide-horn fed parabolic reflector as shown in Figure 9.55. The reflector has a defect in the form of a slot shaped as the logo of the Technical University of Munich (TUM), where the width of the slot is one wavelength. As also seen in the figure, the horizontal width of the reflector is 60λ for the

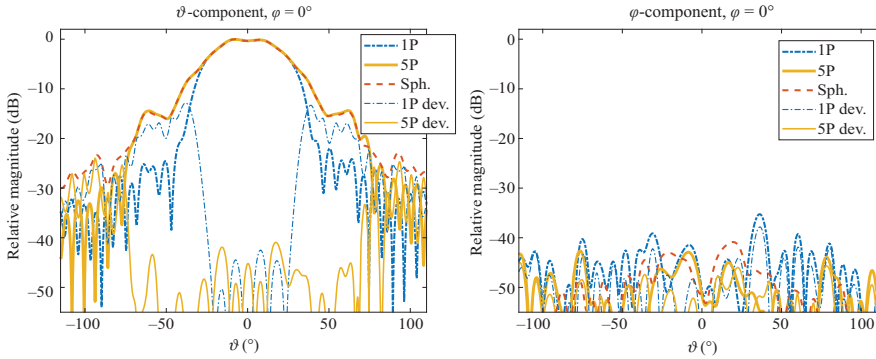

Figure 9.53 *E-plane FF pattern cut for 10 GHz of the DRH18 antenna as depicted in Figure 9.37. Comparison of IESS transformation results obtained for one measurement plane (1P) and for five measurement planes (5P) with respect to results obtained by a full spherical measurement. The IESS results have been obtained with the CM as shown in Figure 9.39*

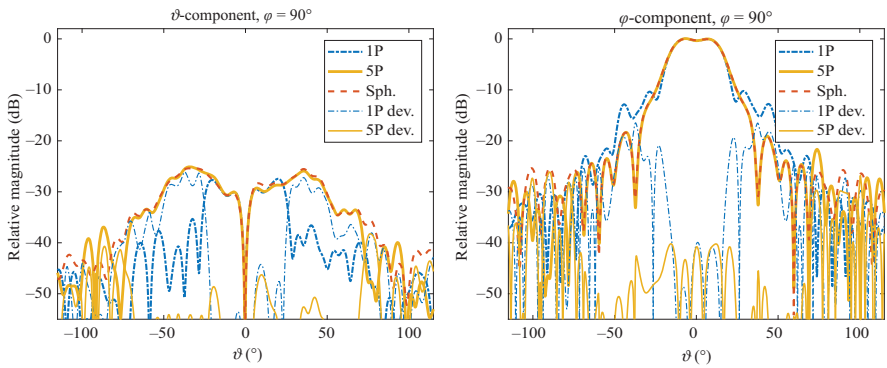

Figure 9.54 *E-plane FF pattern cut for 10 GHz of the DRH18 antenna as depicted in Figure 9.37. Comparison of IESS transformation results obtained for one measurement plane (1P) and for five measurement planes (5P) with respect to results obtained by a full spherical measurement. The IESS results have been obtained with the CM as shown in Figure 9.39*

operation frequency of $f = 12$ GHz. The reflector has been modelled by a MoM integral equation solver [15,43] and the reference FF patterns as well as NF samples (114,756 sample locations, two orthogonal polarisations) on a spherical measurement surface with a radius of 180λ have been computed from the obtained MoM

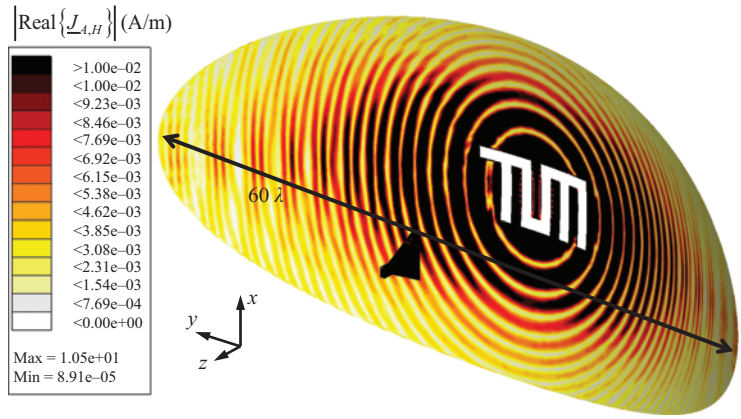

Figure 9.55 Electric surface current density on an infinitely thin ideally metallic reflector with a TUM-shaped slot defect with slot width λ, obtained by a MoM solver [15,43]

current distributions. Some results related to this simulated reflector antenna have already been published in [18].

In the following, we consider IESS solutions obtained with a closed triangular mesh around the reflector, where the undistorted reflector surface is shifted 1 cm forward and backward and closed at the edges. The mesh consists of 576,383 triangles and IESS solutions with Huygens-radiator-type surface sources as well as with electric and magnetic surface current densities and imposition of the Love condition in the form of a Calderon projector, see (9.119), have been computed. The resulting surface-source distributions are illustrated in Figures 9.56 and 9.57. Figure 9.56 shows the two Love surface current densities on the front side of the reflector and Figure 9.57 the Huygens-type surface sources on the front side and on the rear side of the reflector. All the surface-source densities show clearly the influence of the slot defect and provide thus valuable diagnostic information about the antenna. The H-plane FF pattern cut of the defected reflector is seen in Figure 9.58. The two IESS solutions show very good agreement (−80 dB linear magnitude difference) with the MoM reference solution. The IESS solution with the Huygens-radiator-type sources was obtained in about 28 min on a standard desktop computer (Intel® Core™ i7-4820K @ 3.70 GHz, four cores), where the IESS solver could, however, easily be stopped after 10 min or less, if a somewhat worse error level can be accepted. The imposition of the Love condition needs considerable extra computation time and leads to a computation time which is several times longer.

9.12.5 *Satellite mock-up with Ku-band reflectors – synthetic measurement data*

As an example for a modern communication satellite, the generic mock-up as illustrated in Figure 9.59 is considered. The feed horn is operated at a frequency of

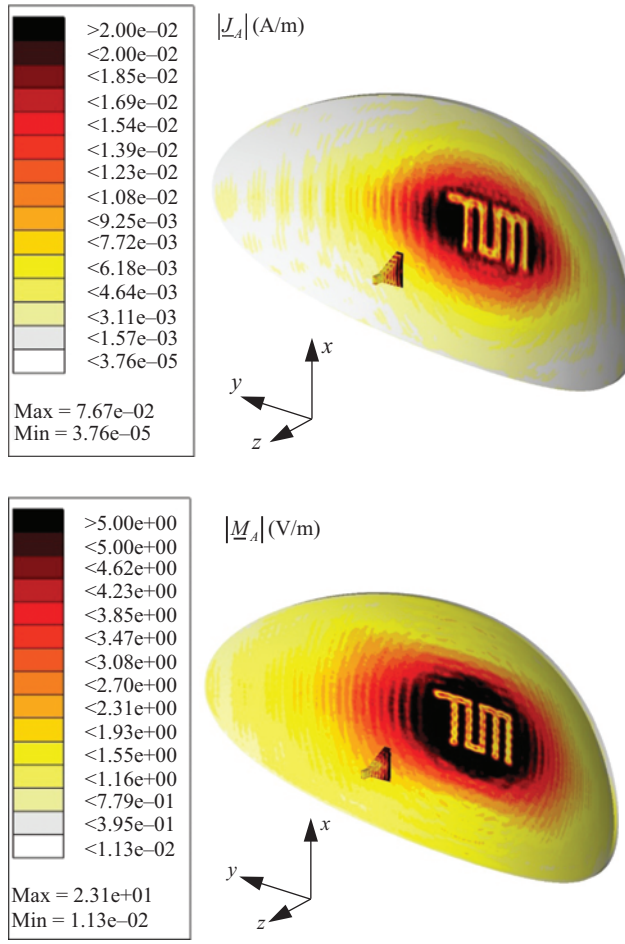

Figure 9.56 Electric (top) and magnetic (bottom) surface current densities on a closed Huygens surface around the reflector and the horn feed from Figure 9.55. The surface current densities have been obtained from an IESS solution with Love condition in the form of a Calderon projector. In both types of surface currents (from one IESS solution), the effect of the slot defect is clearly seen

$f = 12$ GHz and it illuminates the reflector on the right-hand side of the figure, where there is, however, also considerable illumination of the left-hand side reflector and of the fixtures.

The complete mock-up has been simulated by the GRASP simulation package from TICRA [60] and the far-field has been generated at 142,129 sample locations (two orthogonal polarisations each) according to the Ticra Grid format, i.e., an equidistant grid in the *xy*-plane is projected onto an FF sphere with a normalised

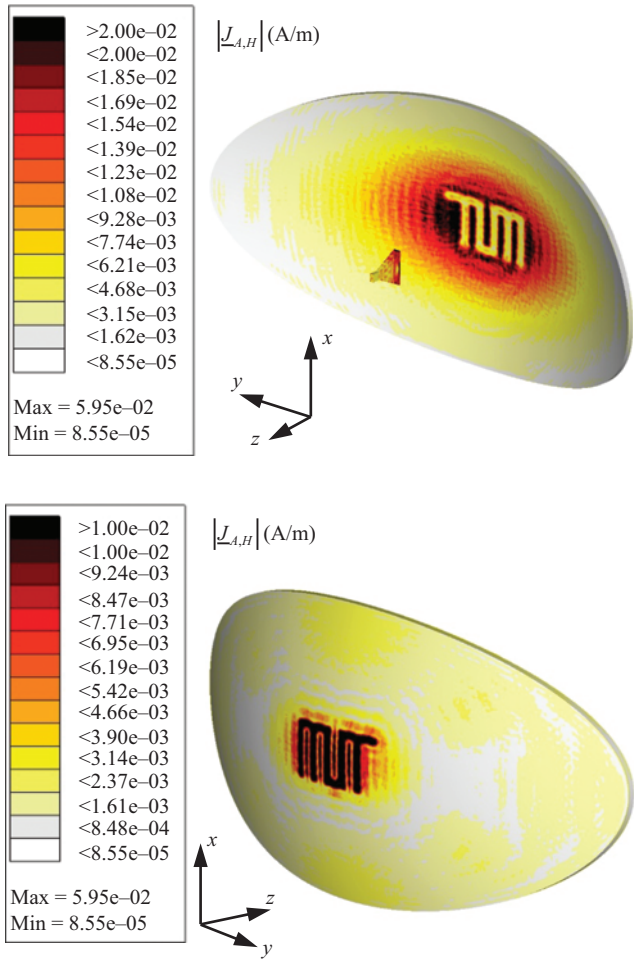

Figure 9.57 Huygens-radiator-like surface-source density from an IESS solution on a closed Huygens surface around the reflector and the horn feed from Figure 9.55. Top: front side of reflector and bottom: rear side of the reflector. On both sides, the slot defect is clearly seen in the reconstructed source distribution

radius of 1 m. Both polarisations of the FF in normalised representation are illustrated in Figure 9.60 showing the quite versatile radiation behaviour of this arrangement.

For the IESS solution, the FF has been assumed to be measured at a distance of 50,000 m and the complete mock-up was modelled with a mesh consisting of 5,224,024 triangles. The IESS solutions have been computed by a spectral transmission equation based on FF translation operators as given in (9.52). The surface-source distribution of an IESS solution with Huygens-radiator-like surface sources is shown in Figure 9.61 with two different colour scales in both sides of the figure.

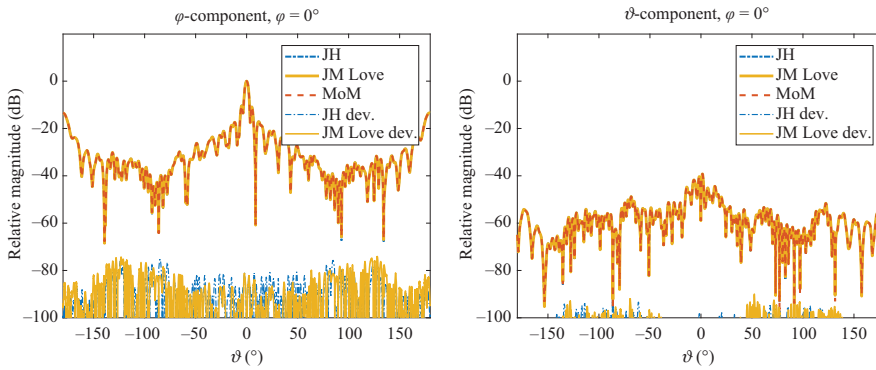

Figure 9.58 H-plane FF pattern cut of the parabolic reflector with defect as shown in Figure 9.55. IESS solutions with Huygens-radiator-type sources as well as with electric and magnetic surface current densities and Love projectors are compared to MoM results

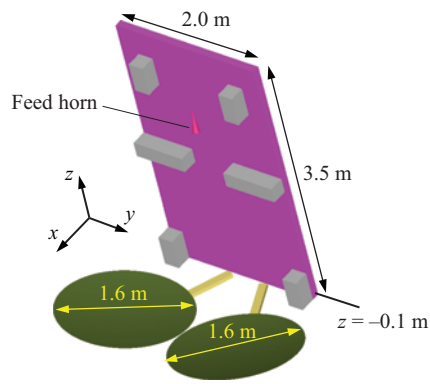

Figure 9.59 Communication satellite mock-up with two reflectors and a feed horn for one of the reflectors

It is obvious that the feed horn beam width is too large for the illumination of the right-hand side reflector and the left-hand side reflector as well as the reflector fixtures are thus illuminated, too. Also, it is obvious that further parts of the mock-up are illuminated by the waves coming from the reflector, causing further distortions of the radiation pattern. At this point, it should be noted that this mock-up has purposely been designed to malfunction and to demonstrate the behaviour of an IESS for such a configuration. The authors are grateful to Dr. Dennis Schobert from ESA ESTEC for generating the mock-up model and for performing the simulations with the TICRA GRASP software package [60].

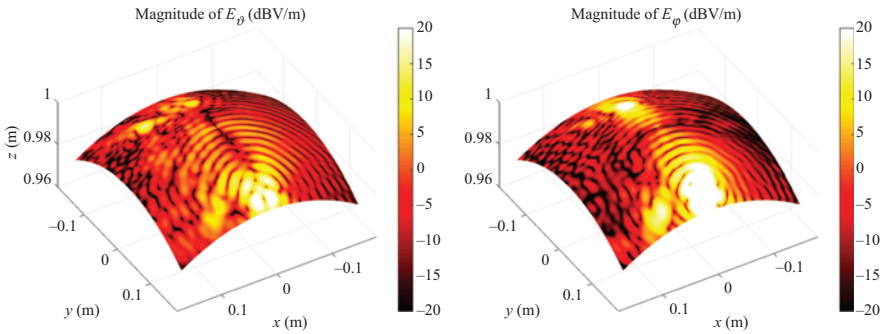

Figure 9.60 Simulated FF of the satellite mock-up in Figure 9.59. The FF is shown for a normalised FF distance of 1 m and it is regularly sampled (377 samples in one dimension) in the xy-plane on a square of 0.4 m by 0.4 m

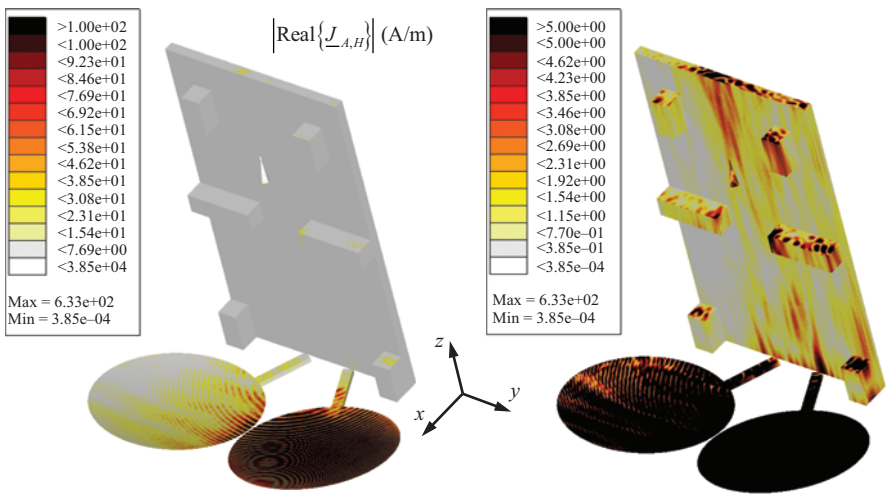

Figure 9.61 Huygens-radiator like surface-source density from an IESS solution on the mesh of the satellite mock-up in Figure 9.59, in different colour scales on the left- and right-hand sides of the figure

9.12.6 Reflector antenna – irregular near-field measurements

Another reflector antenna has been measured by the overhead crane-based portable antenna measurement system (PAMS) [61,62] of Airbus Defence and Space. The measurement set-up together with the AUT and the PAMS gondola is

seen in Figure 9.62. The measurements have been performed with a quad-ridged dual-polarised waveguide probe at a frequency of $f = 6.05$ GHz. A part of the collected measurement samples of one polarisation is shown in Figure 9.63, where the dots indicate individual measurement samples and the colour represents the magnitude of the measured field values. The measurements have been collected in

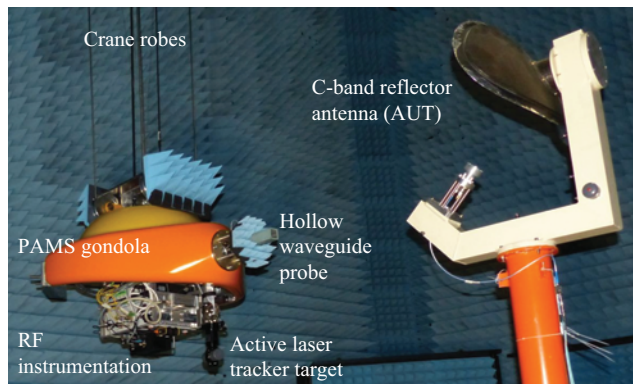

Figure 9.62 NF measurement of a C-band reflector antenna with the PAMS of Airbus Defence and Space in the anechoic chamber of Airbus Defence and Space in Taufkirchen close to Munich (Photo courtesy by Airbus Defence and Space)

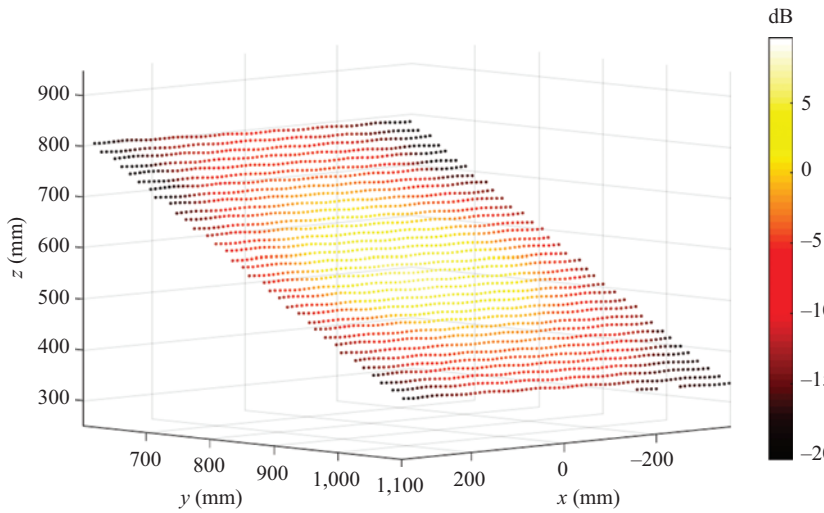

Figure 9.63 Illustration of the measurement values and locations of one polarisation according to the NF measurement in Figure 9.62

a quasi-planar fashion where, however, certain deviations from an ideal plane are observed due to the dynamics of the crane and its control. Overall, the deviations from the intended plane are not very large and the accurate position of the measurement samples together with the orientation of the gondola and, thus, also of the probe are measured by a laser tracking device, where the active target of the utilised laser tracker is also seen in Figure 9.63. A total of 52,400 samples with two polarisations each have been collected and the IESS transformation from the near-field to the far-field has in this case been performed by working with distributed spherical multipole expansions as discussed in Section 9.6.5. The obtained FF is compared to FF pattern results obtained from measurements in the compensated compact range (CCR) [63] of Airbus Defence and Space in Taufkirchen near Munich for one cut in Figure 9.64. The observed normalised linear pattern difference is well below −40 dB for the shown left-handed circular polarised (LHCP) and right-handed circular polarised (RHCP) components. Further information on the PAMS system and the performed measurements can be found in [62,64].

9.13 Antenna field transformations above ground

9.13.1 Introduction

When it comes to NF antenna measurements above ground, the ground should be considered within the NFFFT, if its influence is important. If the AUT radiation is, for instance, directed predominantly away from the ground, it is clear that the ground is not really relevant. Such a situation may, e.g., occur with automobile antennas for satellite communications or satellite navigation. In this case, NF measurements on a scan plane above the AUT or on a spherical or otherwise curved sector above the AUT can be sufficient to determine the relevant portion of the

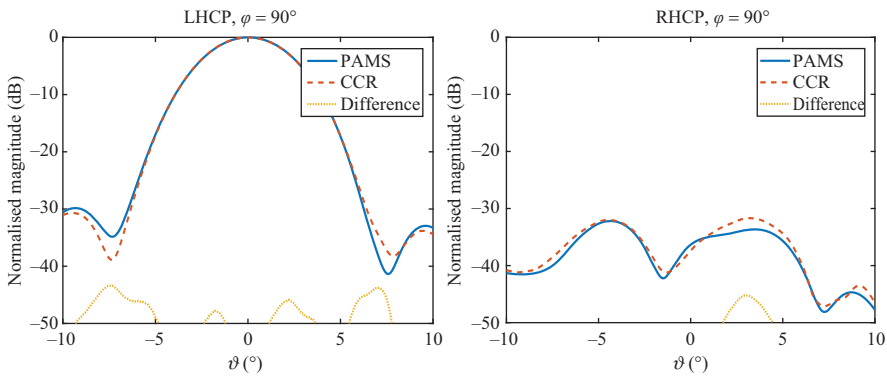

Figure 9.64 FF pattern cut of the C-band reflector antenna as shown in Figure 9.62. The IESS solution is compared to measurement results obtained in the CCR of Airbus Defence and Space, Taufkirchen close to Munich. Left: LHCP component and right: RHCP component

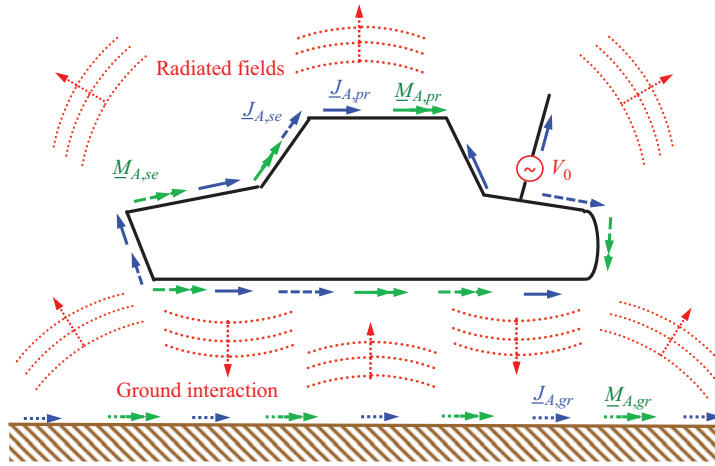

Figure 9.65 Antenna radiation mechanisms for an antenna on a car: in a free-space situation, the primary excitation of the antenna, here given by a voltage source with V_0, causes primary (equivalent) radiation sources on the car. Above ground, the backscattering from the ground interface induces secondary (equivalent) radiation sources on the car and the antenna (together the AUT)

radiation pattern. The ground consideration becomes important whenever the NF measurement values are influenced by the ground, i.e., when the primary sources of the AUT[6] produce radiation towards the ground. In this case, secondary sources may be induced on the AUT due to the back-scattered waves from the ground and the measured NF values are therefore modified as compared to the free-space case. A principle illustration of such a configuration is given in Figure 9.65, where the focus of antenna measurements above ground is on automobile antennas.

Since an antenna measurement over ground will measure the field values with the presence of the ground, an IESS can only determine the sum of the primary and the secondary sources on the AUT, or some other set of equivalent sources on a Huygens surface around the AUT which are equivalent to these sources.[7] As already mentioned, this can be desired or not, but it should be kept in mind, whenever antenna measurements are performed over ground.

Formally, there are two approaches towards the consideration of the ground within the NF to FF transformation. First, the ground influence may be included by additional equivalent sources representing its influence, e.g., the surface current densities $\underline{J}_{A,gr}$ and $\underline{M}_{A,gr}$ as drawn in Figure 9.65. Second, the ground effect can be considered by modifying the forward radiation operator appropriately. Further

[6]The AUT is here the actual antenna together with its carrier platform, e.g., an automobile.

[7]Here, it is assumed that measures such as time gating or other means of separating multi-path components are not feasible due to the close distance of the AUT to the ground.

approaches might be to pre-process the measured data prior to the NFFFT in order to consider the ground or to post-process the transformation results in order to obtain the desired results.

In an inverse equivalent source approach, both of the first two options can be pursued with full flexibility. An extension of the equivalent sources can be realised by placing surface-source densities on the ground interface, which are determined together with the sources representing the AUT. Such an approach may have the advantage that the sources representing the ground can adapt to the particular properties of the ground and the ground can basically be of arbitrary material and of arbitrary geometric shape – within certain constraints of course. Disadvantages are that it might be complicated to determine the two types of sources correctly, in particular, the transformation algorithm may not have enough information in a standard measurement configuration in order to separate the radiation contributions coming from the ground and coming from the AUT. Since the equivalent sources representing the ground may reach very close to the measurement locations, the effective electrical size of the AUT can be very large and a very dense sampling step size on the order of half a wavelength may be required.

The second option of modifying the radiation operator is also possible within an IESS as long as it is possible to find an appropriate and practically feasible representation of the pertinent Green's functions and in particular also a representation which fits into the hierarchical plane-wave-based representation of the operators. For infinite PEC ground, an exact image theory is available [23] and for more complex PEC ground shapes or objects, ray-optical extensions of Green's functions can, e.g., be considered as already demonstrated in [22,65].

Pre-processing of the measurement data prior to the NFFFT is in particular a useful choice for the treatment of infinite planar PEC ground within spherical-mode-based NFFFTs. The idea here is, e.g., to mirror the NF measurement values based on the image principle in order to achieve an equivalent free-space configuration [66–68]. However, as discussed in [68] the application of the image principle is only possible (or correct) for measurement probes with certain symmetries, and highest efficiency of the modal approaches can only be achieved if the PEC interface is located exactly in the rotation centre of the spherical measurements.

For infinite planar PEC ground, an exact image theory for electromagnetic sources and its radiation is available and can be utilised within the NFFFT. If the necessary conditions are fulfilled, it is most straightforward to mirror directly the measured NF values [66–68] and apply a standard NFFFT for free-space measurements. However, as mentioned earlier the probes must fulfill certain symmetry conditions and for standard spherical-mode NFFFTs it is required that the PEC interface is located exactly in the spherical rotation centre [68]. The result of a standard spherical-mode NFFFT is commonly the FF radiation pattern of the primary and secondary sources with the presence of the infinite PEC ground. An extraction of the corresponding free-space pattern, i.e., a separation of the original sources from its image sources, is commonly not possible with a standard spherical-mode-based transformation approach. However, with an advanced spherical-mode-based transformation approach as, e.g., described in [68] such a separation is at

least possible if the original sources have a certain separation from the ground interface. Also, this approach is able to consider the image principle within the NFFFT. Thus, it is not limited to probes with the before mentioned symmetries and it does also not require that the ground interface is exactly located in the rotation centre of the spherical measurements.

In realistic measurement configurations, the ground is of course always of finite extent. However, if the measurement setup is carefully designed the edge effects of finite ground or of a slot in the ground due to a turntable can in general be kept so small that they can be neglected, at least for not too high frequencies. If an accurate consideration of finite ground is really needed, completely modelling the ground within the NFFFT cannot be avoided. As an approximate solution, it is possible to employ the image principle in a way as, e.g., discussed in [69–71].

If NF measurements are performed over realistic ground, here called earth-equivalent ground (EEG), the NFFFT becomes considerably more complicated as for the case of PEC ground. In the following, it is assumed that the EEG is a planar half-space of infinite extent and that the electromagnetic behaviour of the EEG can be described by a homogeneous complex-valued permittivity and a homogeneous complex-valued permeability.

In contrast to infinite PEC ground, an exact image theory is not available for EEG. However, it is still possible to find analytical forms of the pertinent Green's functions, at least in integral form, which can be used within the necessary radiation operators. Also, a direct equivalent source modelling of EEG is possible in the same way as for PEC ground and suffers also from the same limitations. The source distribution extends typically until close to the measurement probes and, thus, the effective size of the measurement configuration is very large and may need appropriately fine measurement sampling. Also, it may happen that standard measurement configurations, e.g., measurements on just a hemispherical surface around the AUT, may not deliver sufficient information in order to be able to separate the AUT sources from the sources used to represent the EEG. In such a situation, it would be desirable to measure on a closed surface around the actual AUT, i.e., also between the AUT and the ground that does not really seem to be feasible.

The investigation of the radiation of electromagnetic sources above planar material half-spaces goes back to Sommerfeld, who investigated first the radiation of a vertical Hertzian dipole [72,73] and later also the radiation of a horizontal Hertzian dipole [74]. The key approach to treat such a problem is to work with an expansion of the pertinent Green's function into plane waves or into cylindrical waves. This is achieved by an infinite planar integral in the wavenumber domain of plane waves, where the case of cylindrical waves requires only a one-dimensional integration. Such one-dimensional cylindrical wave integrals are known as Sommerfeld integrals. The key of this approach is that incident plane or cylindrical waves on EEG just cause a reflected wave and a transmitted wave of the same type, where the reflection and transmission coefficients are known analytically. Thus, the integrand of the wavenumber domain integrals can be constructed analytically dependent on the appropriate reflection coefficient. The key problem is then the

evaluation of the spectral integrals, which can in general not be computed analytically and need to be performed numerically. Over the past few decades, a vast collection of methods have been established for the evaluation of Sommerfeld-type integrals, but the methods are mostly complex and computationally expensive [75].

The complex image theory is an attempt to establish an image theory for multilayered dielectric and lossy materials [76,77]. The idea is here to work with image sources in complex space, whose Sommerfeld integral solutions are known analytically. A certain number of such complex image sources are chosen and its parameters are optimised in a way that all of them together with the primary source and possibly further real sources give a good approximation of the integrand of the Sommerfeld integral. For multi-layered planar material spaces, it is commonly necessary to extract surface wave pole contributions out of the Sommerfeld integral, if the corresponding surface wave pole is located close to the integration path. For lossy half-spaces, good accuracy of the Green's functions can be achieved with relatively few complex images and without surface wave pole extraction.

As an approximation, an asymptotic steepest descent path evaluation of the Sommerfeld integrals can be performed, which results just in one reflected ray optical contribution together with the direct line of sight contribution. This so-called reflection coefficient model is, however, only accurate, if source and observation locations are rather far away from each other and also from the ground interface.

Since the IESS considered in this chapter, in its spectral representation with propagating plane waves, is strongly related to the MLFMM [1], it would be very desirable to extend the MLFMM for the treatment of lossy dielectric planar ground. A series of papers have been published by the group of L. Carin from Duke University starting in the mid-1990s [78,79] and an application of these findings for wave propagation above the sea surface is found in [80]. These works seem to employ sophisticated Sommerfeld integral representations of the near-interactions between sources and observers and purely asymptotic reflected ray contributions for larger interaction distances. An interesting extension of these considerations was outlined in [81], where, however, not many details are provided.

An obviously very powerful approach has been published by the group of Weng Chew in [82]. However, this approach is based on the so-called fast inhomogeneous plane-wave algorithm (FIPWA) and thus not directly compatible with our propagating plane-wave representation. The FIPWA starts directly from Sommerfeld integrals and employs a saddle point solution for its evaluation over large interaction distances.

9.13.2 Inverse equivalent source formulation above ground

When we look back into the derivation of our IESS, we may recognise that the fundamental equations, as, e.g., found in (9.31) and (9.33), are written with the pertinent Green's functions of the considered solution environment. In the previous sections, the considered solution environment was just free space, since the AUT materials have been removed by invoking the Huygens or equivalence principle.

Formally, an extension of the derived IESS is possible by just replacing the Green's functions of free space by the Green's functions of another solution environment, e.g., by the Green's functions pertinent to a ground half-space with certain material parameters. As already mentioned, the Green's functions of ground half-spaces with arbitrary material parameters of infinite extent are known in principle, even though their computation can be demanding in terms of computational requirements. For a PEC half-space, an exact image principle is available.

In the following, we focus on the spectral domain representation with propagating plane waves of the transmission equation of our IESS and discuss its extension towards the consideration of a homogeneous material half-space of infinite extent. If we start from our spectral transmission equation as given in (9.59)

$$S_{21} = \frac{1}{2jk} \oiint T_L(\underline{r}_{21}, \underline{k}) \underline{W}_2^{Tx}(\underline{r}_2, -\underline{k}) \cdot \underline{W}_1^{Tx}(\underline{r}_1, \underline{k}) d^2\widehat{\underline{k}} \tag{9.149}$$

then a formal consideration of the ground influence may be written as

$$\begin{aligned} S_{21} = \frac{1}{2jk} \oiint & \underline{W}_2^{Tx}(\underline{r}_2, -\underline{k}) \\ & \cdot \left[T_L(\underline{r}_{21}, \underline{k}) \underline{W}_1^{Tx}(\underline{r}_1, \underline{k}) + T_L(\underline{r}_{21Im}, \underline{k}) \underline{\underline{\Gamma}}(\underline{k}) \cdot \underline{W}_{1Im}^{Tx}(\underline{r}_1, \underline{k}) \right] d^2\widehat{\underline{k}} \end{aligned} \tag{9.150}$$

where $\underline{\underline{\Gamma}}(\underline{k})$ is a dyadic reflection coefficient, which considers the ground influence, and where $T_L(\underline{r}_{21Im}, \underline{k})$ is a plane-wave translation operator from an image location below the ground interface. Also, $\underline{W}_{1Im}^{Tx}(\underline{r}_1, \underline{k})$ indicates that for reflected waves, which are transmitted from the image location, the z-components of the k-vectors are flipped in sign.

This formulation is exact if an exact image principle is valid as for the case of an infinite PEC or PMC material half-space. For the case of the PEC half-space, the reflection coefficient for the φ-component of $\underline{W}_{1Im}^{Tx}(\underline{r}_1, \underline{k})$ is -1 and for the ϑ-component it is $+1$. For the case of a lossy dielectric material half-space, it would be desirable to work with a similar formulation, where it can, however, be accepted that the reflection coefficient $\underline{\underline{\Gamma}}(\underline{k})$ depends on $\underline{k}$.

An exact formulation for material half-spaces with arbitrary material properties can be achieved by working with the so-called Weyl identity [51]

$$\begin{aligned} \frac{1}{4\pi} \frac{e^{-jk|\underline{r} - \underline{r}'|}}{|\underline{r} - \underline{r}'|} &= \frac{-j}{8\pi^2} \int\int_{-\infty}^{+\infty} \frac{e^{-jk_z|z-z'|}}{k_z} e^{-jk_x(x-x')} e^{-jk_y(y-y')} dk_x dk_y \\ &\text{with } k_z = \sqrt{k_0^2 - k_x^2 - k_y^2} \end{aligned} \tag{9.151}$$

which decomposes the free-space Green's function in plane waves, where the key property of this representation is that it produces only plane waves propagating towards the half-space interface, if the source is located above the half-space interface. In contrast, the formulation in (9.150) works with all propagating plane

waves on the Ewald sphere, i.e., also upward propagating plane waves impinging on the half-space interface do exist, even when the source is located above the interface. A disadvantage of the representation in (9.151) with respect to our purpose is that it works with propagating and evanescent plane waves, where the evanescent plane waves are not directly available within our spectral formulation with all propagating plane waves according to the complete Ewald sphere. Nevertheless, the ground reflected contribution according to (9.151) can be written exactly in the form of

$$g_\Gamma(\underline{r},\underline{r}') = \frac{-j}{8\pi^2}\int\int_{-\infty}^{+\infty}\Gamma(k_z)\frac{e^{-jk_z|z+z'|}}{k_z}e^{-jk_x(x-x')}e^{-jk_y(y-y')}dk_xdk_y \tag{9.152}$$

where $\Gamma(k_z)$ is the corresponding plane-wave reflection coefficient at the ground. Also, the ground interface has been assumed at $z=0$ and $z,z'>0$.

Compared to the full vector formulation in (9.150), we consider at this point only a scalar reflection coefficient, which will be later one component of the reflection dyad. Following the concepts in [81], the reflection coefficient in the spectral integral may be represented by a Taylor series around the specular reflection direction k_{z0} in the form of[8]

$$\Gamma(k_z) \approx \sum_{n=0}^{N}\frac{1}{n!}\frac{\partial^n}{\partial k_z^n}\Gamma(k_z)\bigg|_{k_z=k_{z0}}(k_z-k_{z0})^n = \sum_{n=0}^{N}\Gamma_n(k_z-k_{z0})^n \tag{9.153}$$

where the Taylor series may be truncated after the term with index N.

Plugging this expression into (9.152) yields

$$\begin{aligned} g_\Gamma(\underline{r},\underline{r}') \approx{}& \frac{-j}{8\pi^2}e^{-jk_{z0}|z+z'|}\int\int_{-\infty}^{+\infty}\sum_{n=0}^{N}\Gamma_n(k_z-k_{z0})^n\frac{e^{-j(k_z-k_{z0})|z+z'|}}{k_z} \\ & e^{-jk_x(x-x')}e^{-jk_y(y-y')}dk_xdk_y \end{aligned} \tag{9.154}$$

which can be further written as

$$\begin{aligned} g_\Gamma(\underline{r},\underline{r}') \approx{}& e^{-jk_{z0}|z+z'|}\sum_{n=0}^{N}\Gamma_n\frac{\partial^n}{(\mp j)^n\partial z^n}\frac{(-j)}{8\pi^2}\int\int_{-\infty}^{+\infty}\frac{e^{-j(k_z-k_{z0})|z+z'|}}{k_z} \\ & e^{-jk_x(x-x')}e^{-jk_y(y-y')}dk_xdk_y \\ \approx{}& e^{-jk_{z0}|z+z'|}\sum_{n=0}^{N}\Gamma_n\frac{\partial^n}{(\mp j)^n\partial z^n}e^{+jk_{z0}|z+z'|}\frac{1}{4\pi}\frac{e^{-jk|\underline{r}-\underline{r}_{Im}|}}{|\underline{r}-\underline{r}_{Im}|} \end{aligned} \tag{9.155}$$

where $\underline{r}_{Im}$ is the common image location below the ground and where the $-$ within the $\mp$ would correspond to $z+z'\geq 0$ and the plus sign to $z+z'<0$, which can, however, not occur due to $z,z'>0$. If we now replace the scalar Green's function

[8] A Taylor expansion around the specular reflection direction is useful, since the largest integral contributions are expected for this direction, but other expansion directions can be chosen, too.

of the Helmholtz equation by a spectral representation with propagating plane waves as introduced in (9.49), which is also the basis for the transmission equation in (9.150), and take the derivatives with respect to z on the basis of this representation, the Taylor polynomials in $(k_z - k_{z0})$ as found in (9.154) are retrieved and we can rewrite (9.150) as

$$S_{21} \approx \frac{1}{2jk} \oiint \underline{W}_2^{Tx}(\underline{r}_2, -\underline{k}) \cdot \left[T_L(\underline{r}_{21}, \underline{k}) \underline{W}_1^{Tx}(\underline{r}_1, \underline{k}) + T_L(\underline{r}_{21Im}, \underline{k}) \sum_{n=0}^{N} \underline{\underline{\Gamma}}_n \left(k_z - k_z^0\right)^n \cdot \underline{W}_{1Im}^{Tx}(\underline{r}_1, \underline{k}) \right] d^2\widehat{\underline{k}} \tag{9.156}$$

where we have found a representation which just works with a single image location below the ground interface. Formally, it seems that the Taylor series expansion of the reflection coefficient can just be replaced by the original representation of the reflection coefficient leading to our original equation (9.150)

$$S_{21} = \frac{1}{2jk} \oiint \underline{W}_2^{Tx}(\underline{r}_2, -\underline{k}) \cdot \left[T_L(\underline{r}_{21}, \underline{k}) \underline{W}_1^{Tx}(\underline{r}_1, \underline{k}) + T_L(\underline{r}_{21Im}, \underline{k}) \underline{\underline{\Gamma}}(k_z) \cdot \underline{W}_{1Im}^{Tx}(\underline{r}_1, \underline{k}) \right] d^2\widehat{\underline{k}} \tag{9.157}$$

where the ground reflection coefficient is now, however, known as the one found with the Sommerfeld or Weyl representations.

The obtained formulation is certainly not fully correct, since the involved derivatives with respect to z are taken from different integral representations during the derivation. Also, it is noted that the order of the Taylor series and of the spectral integration have been interchanged in (9.155), which is only feasible, if all expressions converge correctly. Finally, we must assume that the Taylor series is convergent.

An interesting aspect is the interpretation of $\underline{\underline{\Gamma}}(k_z)$ while the integral over the Ewald sphere is evaluated. Obviously, positive k_z-values correspond to waves propagating towards the material interface. Grazing waves propagating in parallel to the material interface have $k_z = 0$ and waves propagating away from the interface will, thus, have negative values. This becomes, e.g., clear from the Taylor series expansion of the reflection coefficient, which will smoothly continue the reflection coefficient beyond zero. With an isotropic and homogeneous ground material, the dyadic reflection coefficient in (9.157) has only entries on its main diagonal corresponding to *TE*-waves for the φ-components and to *TM*-waves for the ϑ-components. The scalar reflection coefficients for these two cases are given as [25,51]

$$\Gamma_{TX} = \frac{W_{t,TX} - W_{i,TX}}{W_{t,TX} + W_{i,TX}} \tag{9.158}$$

where i and t indicate the air and ground half-spaces, respectively, TX can be TE or TM and

$$W_{i/t,TM} = Y_{i/t,TM} = \frac{\omega_{i/t}}{k_{z,i/t}} \tag{9.159}$$

$$W_{i/t,TE} = Z_{i/t,TE} = \frac{\omega_{i/t}}{k_{z,i/t}}. \tag{9.160}$$

Checking out the reflection coefficient dependence on $k_z = k_{z,i}$ shows that

$$\Gamma_{TE/TM}(-k_z) = \frac{1}{\Gamma_{TE/TM}(k_z)} \tag{9.161}$$

This can intuitively be interpreted in a way that an incident plane wave at the interface, which propagates away from the interface, requires a reflected wave at the interface, which propagates towards the interface. For such a situation, it is intuitively clear that the incident wave with the incorrect propagation direction away from the interface can be divided by the 'normal' reflection coefficient, computed for positive k_z, in order to fulfill the boundary conditions at the interface. An obvious problem is that $\underline{\underline{\Gamma}}(-k_z)$ will become singular at zeros of the 'normal' reflection coefficient, leading us to the conclusion that an incident wave propagating away from the interface cannot only produce a reflected wave propagating towards the interface together with a transmitted wave propagating away from the interface. There must also be a transmitted wave, which propagates towards the interface, where it is not really clear how the amplitude of this wave can be correctly determined. Zeroes of the reflection coefficient occur, e.g., for the Brewster angle. If singularities occur near the integration path over the Ewald sphere, the obtained integral representation will certainly not be correct and an appropriate numerical treatment must be implemented to avoid a complete failure of the expressions. In particular, the implementation should guarantee that the results become equal to the homogeneous-space results, if the material parameters of the material half-space become identical to the parameters of the upper half-space.

In the realisation of an IESS for field transformations above material half-spaces, the presented formulation can be utilised to realise an approximation which allows to perform NFFFTs with good accuracy and which should be sufficient for most practically relevant NF measurements. For transformations above a PEC half-space the formulation is exact [83,84].

Towards an IESS solution, the unknown quantity in (9.157) is $\underline{\underline{W}}_1^{Tx}(\underline{r}_1, \underline{k})$, which can of course be replaced by H_1^{Tx} according to (9.54), and subsequently H_1^{Tx} can be replaced by its integral representation in terms of electric and magnetic surface current densities according to (9.42) and (9.48) as already done in Section 9.8.1, in order to arrive at a formulation with the discussed equivalent sources in Section 9.6. In the implementation of the IESS according to the single-level and multi-level algorithms as discussed in Section 9.10, the grouping of the source and receive boxes is aligned to the half-space interface as illustrated in Figure 9.66, where the shown arrangement is for a single-level algorithm but its

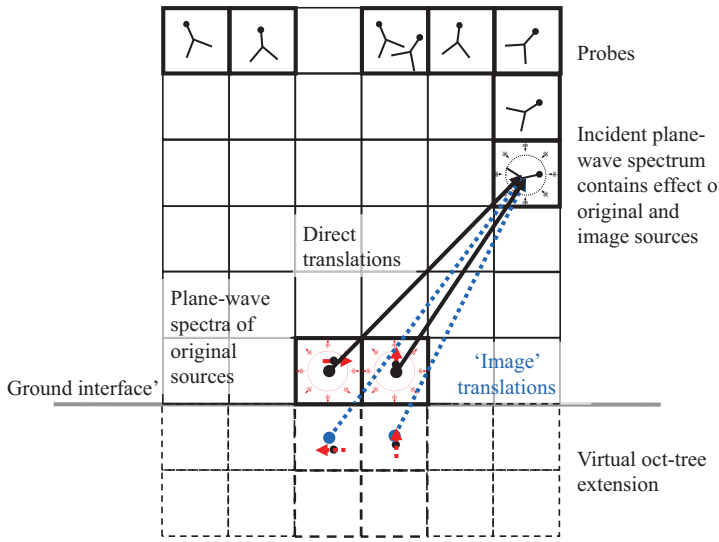

Figure 9.66 Illustration of propagating plane-wave translations for source and receive probes above a ground half-space

extension to multi-level is straightforward. The source spectra are only computed for the boxes above the interface and aggregations to coarser levels also need to be performed only for these boxes. The direct translations are performed as for the case of a free-space situation. For the image translations, first the image-source spectra are obtained and these are then multiplied with the pertinent reflection coefficients and translated to the receive boxes by multiplication with the corresponding translation coefficients. At the receive side, everything is as in a situation without reflected contributions, i.e., disaggregation and testing is performed only for the receive boxes above the ground interface.

An interesting question is how the probe behaviour changes, when the probe location is close to the ground. This depends certainly on the type of the probe and the required accuracy. In general, however, it is not expected that the probe behaviour changes a lot as long as the distance to the ground is on the order of a few wavelengths, which can easily be realised for not too short measurement distances. If necessary, an IESS solver can easily be implemented in a way that it has the capability to consider changing probe receive behaviours dependent on the distance from the ground interface.

9.13.3 Post-processing of equivalent sources above different ground materials

Once an inverse equivalent source problem has been solved under consideration of a certain ground half-space, the obtained equivalent sources can be utilised to evaluate the FF radiation (and also the NF radiation) of the AUT exactly above the

same half-space, but it is of course also possible to evaluate the AUT radiation in different environments. The corresponding procedure is illustrated in Figure 9.67. First, the equivalent sources are obtained by an IESS solution with consideration of the Green's function of the half-space over which the measurements had been performed. Next, the equivalent sources are placed in a new environment such as free space or above a ground half-space with modified material properties. Finally, the far-field is computed in the new environment with consideration of the Green's function belonging to this environment.

In order to perform such post-processing tasks, the found equivalent sources can for instance be loaded into one of the commercial electromagnetic software packages for further investigations, but especially the FF radiation in free space or above ground half-spaces with arbitrary material parameters can be computed relatively easily, since the necessary FF Green's functions are relatively simple. The FF Green's function of free space has for instance been given in Section 9.5.2 and the FF Green's function above an arbitrary material half-space can be calculated analytically by a saddle point evaluation of the Sommerfeld- or Weyl-type integral representations [85,86]. Based on these considerations, the far-field can easily be extracted from our common propagating plane-wave-based spectral representations over the Ewald sphere via

$$\underline{E}^{FF}(r_{FF},\vartheta,\varphi) = jk\cos\vartheta\underline{\tilde{E}}\left(\underline{r}_{ref},\underline{k}\right)\Big|_{\underline{k}=(k\sin\vartheta\cos\varphi,k\sin\vartheta\sin\varphi,k\cos\vartheta)} \tag{9.162}$$

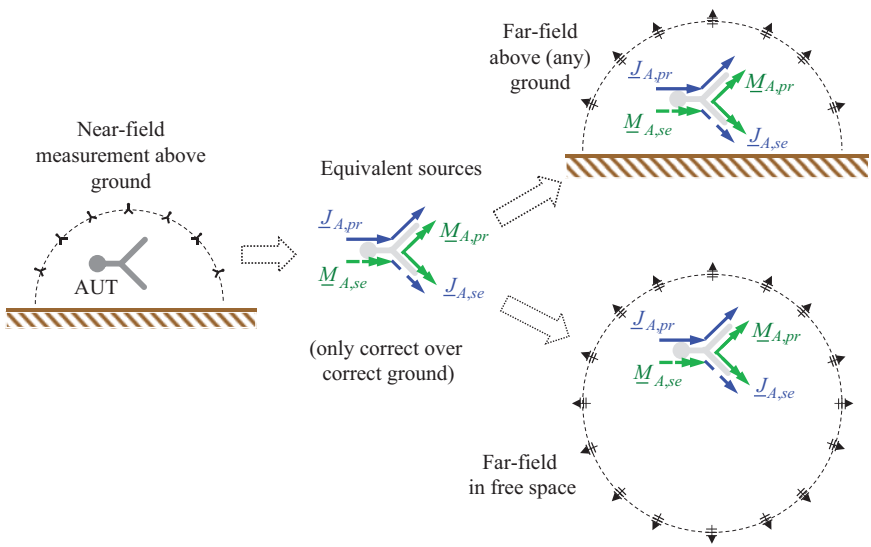

Figure 9.67 Post-processing of equivalent-source radiation in different environments

where $\underline{\tilde{E}}$ is the propagating plane-wave-based representation of the electric field according to an integral as in (9.98) within the corresponding environment, with respect to a reference location $\underline{r}_{ref}$.

9.13.4 *Field transformation results above ground – synthetic measurement data*

As an example for a measurement configuration above ground, we consider the car body with a vertical monopole antenna on its roof as depicted in Figure 9.68. This car body model is provided within the FEKO modelling package [56] and FEKO has also been used for the computation of synthetic NF measurement data for the configuration together with FF reference results. As a measurement surface we consider a hemispherical shell with a radius of 5 m above the car and the probe antennas are Hertzian dipoles which sample directly the ϑ- and φ-components of the electric field. All IESS solutions discussed in the following have been performed by using the triangular mesh as shown in Figure 9.69, where the bottom is missing, unless otherwise stated, in order to improve the conditioning of the transformation problem. Since the hemispherical scan surface is not fully enclosing the actual AUT, i.e., the car body with the antenna, the solver cannot easily separate vertical-up radiation contributions coming directly from the car or bouncing back from the ground. The missing bottom mesh together with the use of Huygens-type-radiator sources with an imaginary shift of 0.1λ avoid primary radiation towards the ground directly below the car body and thus also reflected waves vertically up.

First, we consider synthetic NF measurements above PEC ground for $f = 1$ GHz, where the measurement samples are collected by a virtual spiral scan over the scan surface resulting into 3,844 measurement samples with two polarisations each. The primary radiation of the monopole antenna is clearly seen on the upper side of the mesh in the surface source illustration in Figure 9.70, and near to the PEC ground half-space, the influence of the ground interactions is visible. Figures 9.71 and 9.72 show FF pattern cuts obtained by the IESS solution with

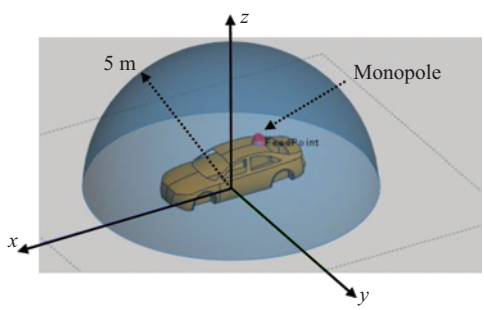

Figure 9.68 NF antenna measurement scenario above ground half-space: car body with monopole antenna on its roof with a hemispherical NF measurement surface with a radius of 5 m, rotation centre in the ground interface at $z = 0$

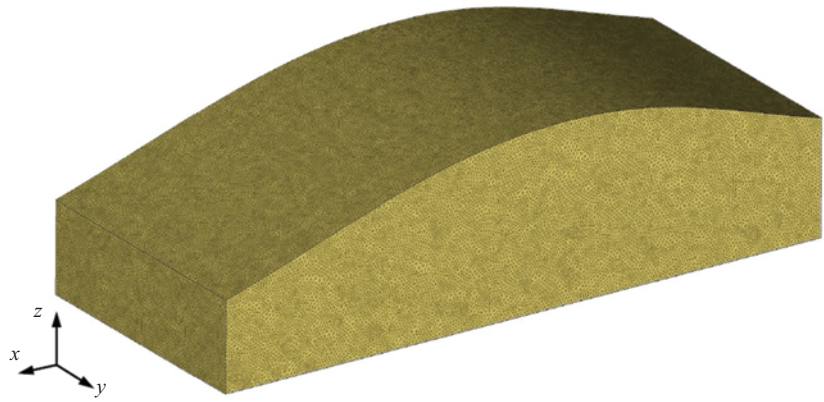

Figure 9.69 Simplified triangular mesh around the car body in Figure 9.68 consisting of 90,846 triangles where the bottom of the mesh is missing, i.e., the meshed surface is not closed

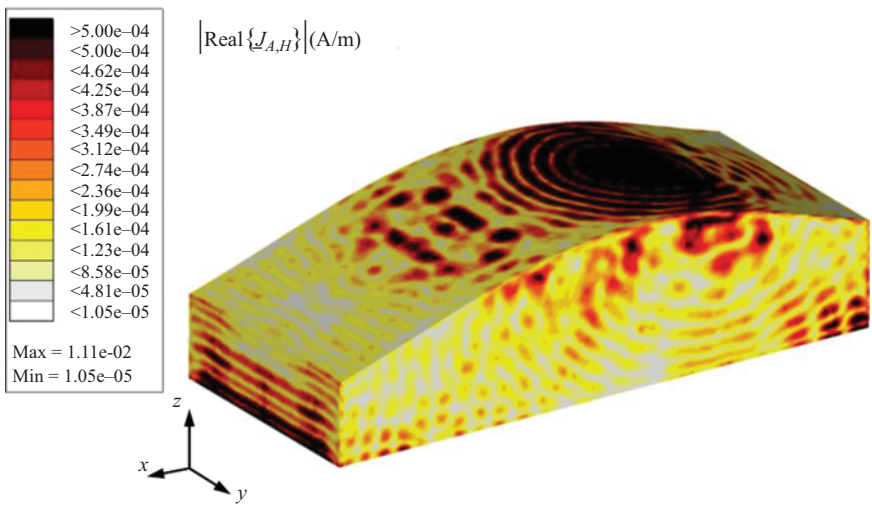

Figure 9.70 Surface-source distribution (elementary Huygens radiators based on RWG functions with imaginary shift of 0.1λ) on the triangular mesh as seen in Figure 9.69 for the virtual NF measurement with spiral scan above PEC ground

exact consideration of the PEC ground half-space by the image principle in comparison to the FEKO reference results, where the difference between the IESS results and the FEKO results of around −60 dB is good. Additionally, quasi-free-space patterns obtained from the IESS sources in a post-processing step are shown, which do not exhibit the strong ripples due to the ground interactions any more.

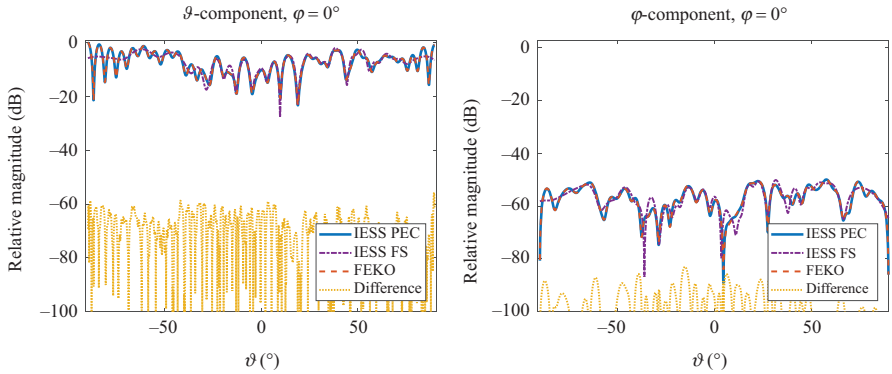

Figure 9.71 FF pattern cut in the xz-plane for 1 GHz of the monopole antenna on the car body above PEC ground in Figure 9.68. The IESS transformation result obtained with the mesh in Figure 9.69 is compared to the FEKO reference. Additionally, the free-space (FS) FF pattern obtained in a post-processing step from the IESS equivalent sources is shown

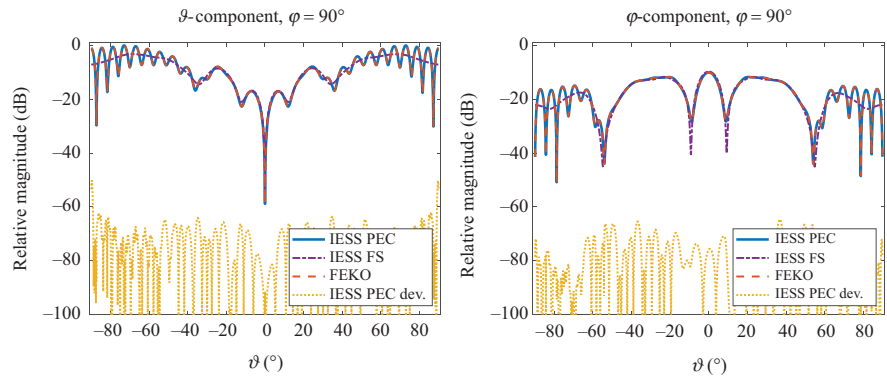

Figure 9.72 FF pattern cut in the yz-plane for 1 GHz of the monopole antenna on the car body above PEC ground in Figure 9.68. The IESS transformation result obtained with the mesh in Figure 9.69 is compared to the FEKO reference. Additionally, the FS FF pattern obtained in a post-processing step from the IESS equivalent sources is shown

Next, a measurement and transformation scenario over a lossy dielectric ground half-space ($\varepsilon_r = 5.0 - j0.25$) with the same AUT and again for $f = 1$ GHz is considered, where the measurement samples are now regularly spaced with a step size of 2.4° resulting into 5,700 sample locations with two polarisations each. The

primary radiation of the monopole is again clearly seen in the surface-source illustration in Figure 9.73, but the effects due to the ground interactions are now less pronounced than for the case of the PEC ground.

Figures 9.74 and 9.75 show FF pattern cuts obtained by the IESS solution with approximate consideration of the lossy dielectric ground half-space by the spectral image principle according to (9.157) in comparison to the FEKO reference results, where the difference between the IESS results and the FEKO results of well below −40 dB is quite satisfactory in view of the fact that the employed spectral image principle is not exact. Again, quasi-free-space patterns obtained from the IESS sources in a post-processing step are also shown.

The obtained quasi-free-space pattern cuts obtained with the PEC ground and with the lossy dielectric ground are shown one more time in Figures 9.76 and 9.77, but now for the complete angular range and in comparison to the FEKO reference results. The restricted accuracy is expected, since the equivalent sources used to compute the FF patterns are not the correct ones for the FS case, due to the multiple interactions with the ground interface in their respective measurement environment. Kind of interesting is that the patterns from the two measurement environments show rather different error behaviours, which may lead us to the conclusion that the achieved accuracy level depends strongly on the particular antenna configuration. The extrapolation of the FS pattern to downward directions is rather satisfactory and most likely due to the spatial filtering properties of the IESS.

In Figures 9.78 and 9.79, FF pattern results of two more measurement scenarios are shown. In the scenario FS Diel., the antenna together with the car was

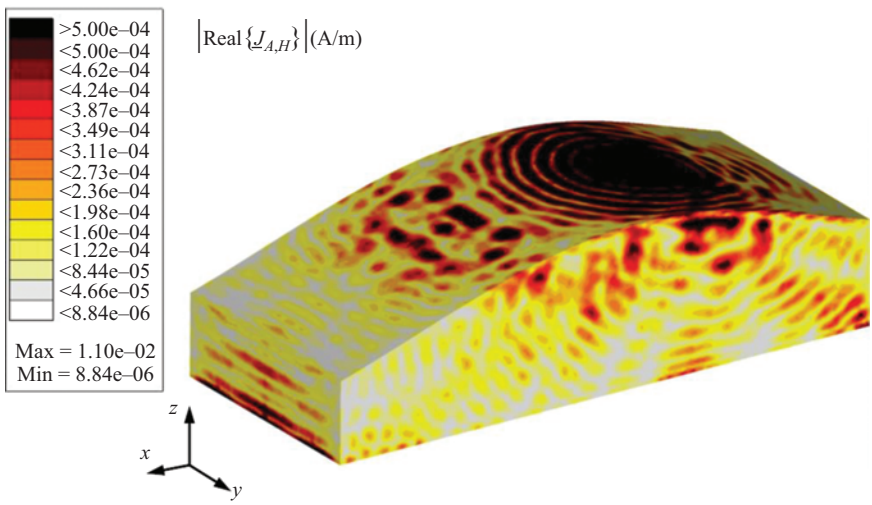

Figure 9.73 Surface-source distribution (elementary Huygens radiators based on RWG functions with an imaginary shift of 0.1λ) on the triangular mesh as seen in Figure 9.69 for the virtual NF measurement with regular sampling above lossy dielectric ground

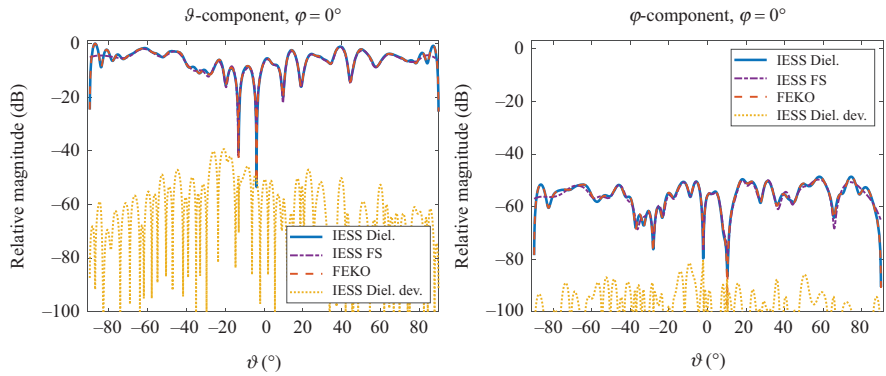

Figure 9.74 *FF pattern cut in the xz-plane for 1 GHz of the monopole antenna on the car body above lossy dielectric ground in Figure 9.68. The IESS transformation result obtained with the mesh in Figure 9.69 is compared to the FEKO reference. Additionally, the FS FF pattern obtained in a post-processing step from the IESS equivalent sources is shown*

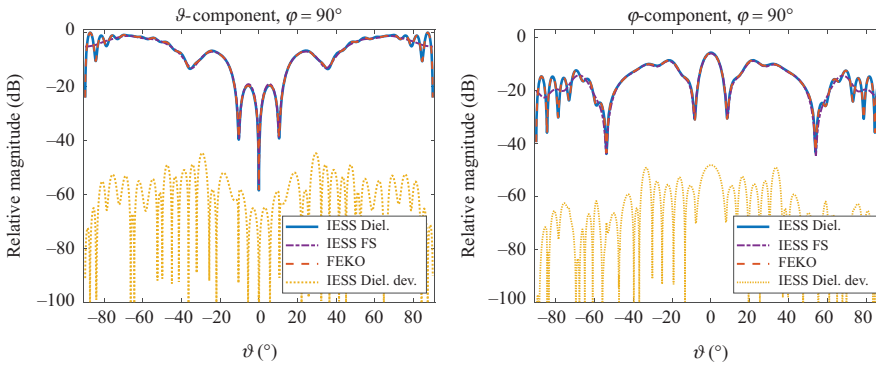

Figure 9.75 *FF pattern cut in the yz-plane for 1 GHz of the monopole antenna on the car body above lossy dielectric ground in Figure 9.68. The IESS transformation result obtained with the mesh in Figure 9.69 is compared to the FEKO reference. Additionally, the FS FF pattern obtained in a post-processing step from the IESS equivalent sources is shown*

first measured under FS conditions (NF, full sphere), and then the equivalent sources have been obtained by an IESS with the mesh shown in Figure 9.69, but now containing a bottom mesh, too, and finally, the obtained sources where placed above the dielectric ground half-space in order to compute the FF pattern. In the scenario PEC Diel., a similar procedure was followed, except that the NF

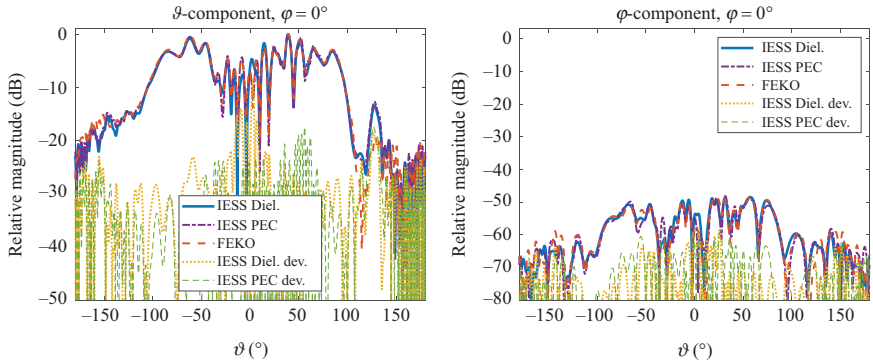

Figure 9.76 (Quasi) FS FF pattern cut in the xz-plane for 1 GHz of the monopole antenna on the car body in Figure 9.68. The patterns are the same as those in Figures 9.71–9.74 but show the full angular range and are compared to the FEKO FS reference results

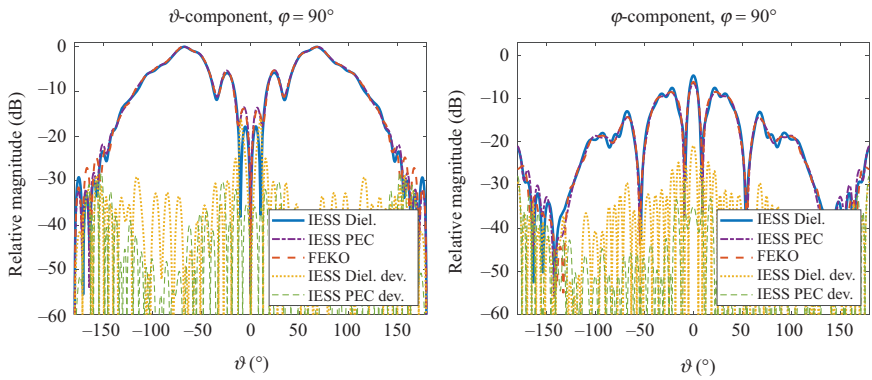

Figure 9.77 (Quasi) FS FF pattern cut in the yz-plane for 1 GHz of the monopole antenna on the car body in Figure 9.68. The patterns are the same as those in Figures 9.72 and 9.75 but show the full angular range and are compared to the FEKO FS reference results

measurements were collected above a PEC ground (hemisphere) and that the mesh did not have a bottom. Close to grazing, both scenarios give remarkably good results, but vertical-up the accuracy deteriorates.

Since full-sphere NF measurements of a car are not easy to perform, we consider two more cases of the spherical NF measurements, now with truncated spherical FS NF measurements. The achieved results are depicted in Figures 9.80 and 9.81. In the case of Cut1, the NF measurements were performed on a hemisphere above the car which was extended by 3.6° below the horizontal and in the

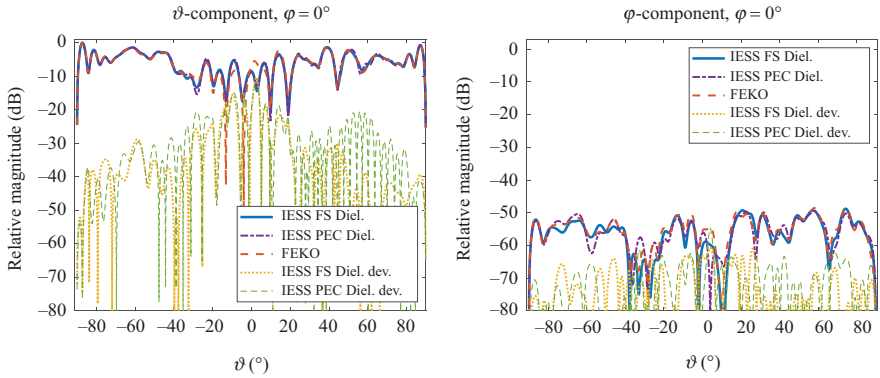

Figure 9.78 *FF pattern cut in the xz-plane for 1 GHz of the monopole antenna on the car body above lossy dielectric ground in Figure 9.68. The IESS FS Diel. and the IESS PEC Diel. patterns have been obtained from full-sphere FS NF and hemispherical PEC NF measurements, respectively, with IESS processing, where the obtained equivalent sources were placed above the dielectric ground in a post-processing step, mesh according to Figure 9.69, including also a meshed bottom in the case of the FS measurement*

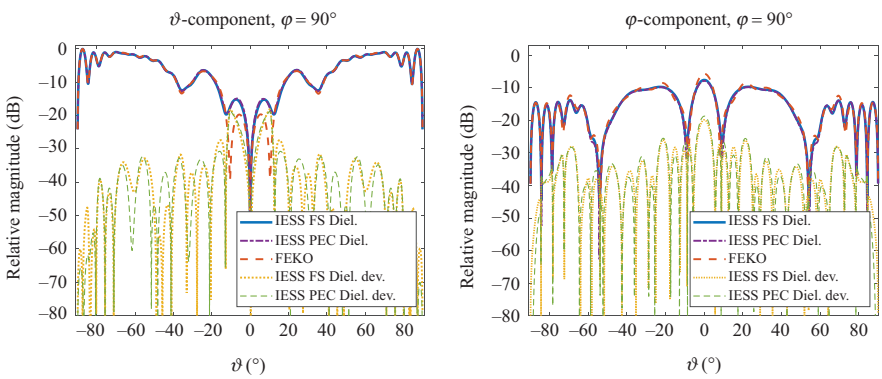

Figure 9.79 *FF pattern cut in the yz-plane for 1 GHz of the monopole antenna on the car body above lossy dielectric ground in Figure 9.68. The IESS FS Diel. and the IESS PEC Diel. patterns have been obtained from full-sphere FS NF and hemispherical PEC NF measurements, respectively, with IESS processing, where the obtained equivalent sources were placed above the dielectric ground in a post-processing step, mesh according to Figure 9.69, including also a meshed bottom in the case of the FS measurement*

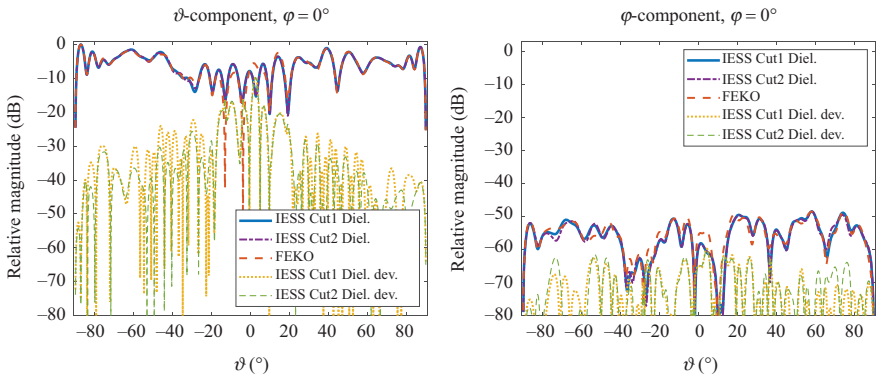

Figure 9.80 *FF pattern cut in the xz-plane for 1 GHz of the monopole antenna on the car body above lossy dielectric ground in Figure 9.68. The patterns have been obtained from truncated spherical FS NF measurements with IESS processing, where the obtained equivalent sources were placed above the dielectric ground in a post-processing step, mesh according to Figure 9.69 including also a meshed bottom. The Cut1 measurements were truncated 3.6° below the horizontal, and the Cut2 measurements 10.6° below the horizontal*

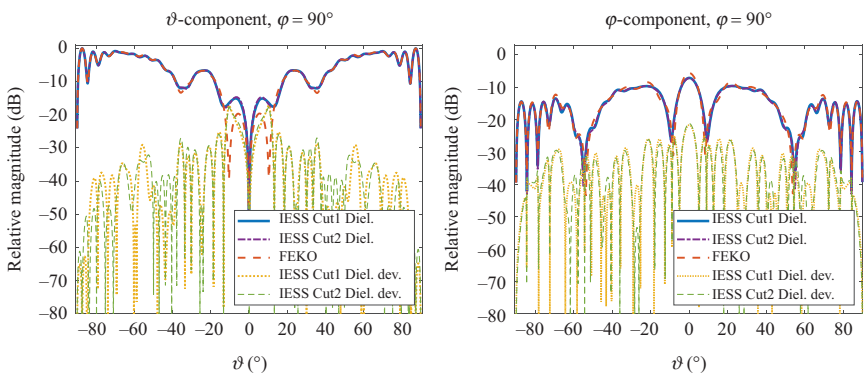

Figure 9.81 *FF pattern cut in the yz-plane for 1 GHz of the monopole antenna on the car body above lossy dielectric ground in Figure 9.68. The patterns have been obtained from truncated spherical FS NF measurements with IESS processing, where the obtained equivalent sources were placed above the dielectric ground in a post-processing step, mesh according to Figure 9.69 including also a meshed bottom. The Cut1 measurements were truncated 3.6° below the horizontal, and the Cut2 measurements 10.6° below the horizontal*

case of Cut2, the extension of the hemisphere was 10.6° below the horizontal. Compared to the full-sphere FS measurements, some slight deteriorations are visible, but overall the influence of the truncation is very little. A reason for this is certainly the good extrapolation property of an IESS, due to the localisation of the sources, but the placement of the antenna on top of the car roof is certainly also beneficial for the truncated FS measurements. With antennas closer to the ground, e.g., in the bumper of a car, the situation may be worse. In order to give further insight into the two-step procedure, the FS patterns obtained from the truncated FS measurements are shown in Figures 9.82 and 9.83.

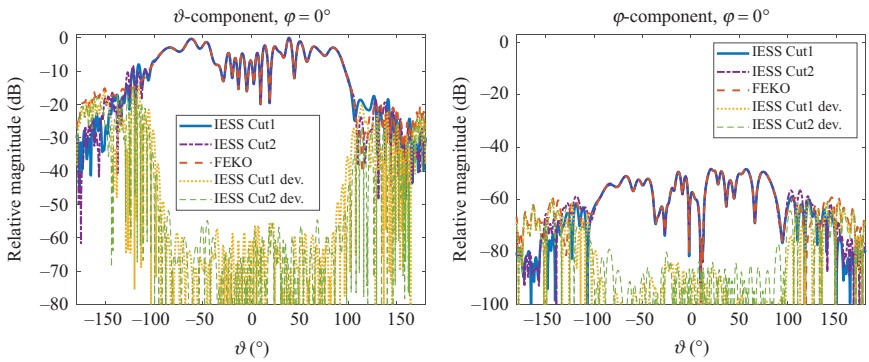

Figure 9.82 FS FF pattern cut in the xz-plane for 1 GHz of the monopole antenna on the car body in Figure 9.68. The shown patterns are obtained from the truncated FS measurements as considered in Figure 9.80

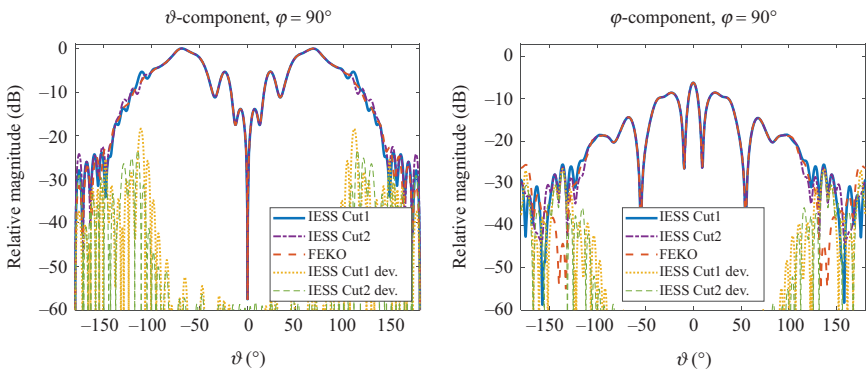

Figure 9.83 FS FF pattern cut in the yz-plane for 1 GHz of the monopole antenna on the car body in Figure 9.68. The shown patterns are obtained from the truncated FS measurements as considered in Figure 9.80

9.14 Summary

The chapter was inspired by the increasing need and wish to perform near-field antenna measurements with improved flexibility as compared to the traditional approaches, discussed in Chapters 6–8, which were based on canonical measurement surfaces with regular sampling. To overcome these restrictions, we started in this chapter with a general and flexible integral-equation and equivalent-source-based field transformation approach, which provides full flexibility, but is numerically intensive. Inspired by the enormously powerful fast integral equation solvers known from computational electromagnetics, we derived computationally very efficient but still very flexible IESSs for the transformation of measured near-field data into a set of equivalent sources, which can in turn be used to calculate near and far-fields anywhere in the solution domain. A by-product of these IESSs is that they allow a very flexible modelling of the AUT, too, and, thus, the inclusion of a priori knowledge about the geometric extent of the AUT. The resulting AUT adapted equivalent source model can help to reduce measurement errors by spatial filtering and the illustration of the equivalent sources on the AUT model gives diagnostic insight into the AUT functioning. If desired, parts of the AUT sources, or of additional echo/scattering sources within the measurement environment, can even be ignored or modified in post-processing steps in order to achieve further improvement of the measurement results or to gain further diagnostic insight.

A variety of equivalent sources were discussed, where the focus was on equivalent surface-source densities, such as electric and magnetic surface current densities. Since both of these source types together form an underdetermined inverse source problem, side constraints such as the zero-field/Love condition or the CS condition were discussed.

The discretised inverse equivalent source problems were solved in the form of systems of normal equations, which lead in general to a least mean square solution of the inverse problem. In addition to the very popular NR set of equations, we discussed and investigated also the NE set of equations, which is known to be more suitable for under-determined systems of equations. For our inverse equivalent source problem, the NE set of equations turned out to give a more direct control of the transformation errors, since the residual of the equation system is directly the error in the space of the near-field measurements, and for the investigated examples, the NE-based solution by the iterative GMRES-solver gave always a very clear relative stopping criterion, when the achievable observation error was reached or almost reached. Since the consideration of the zero-field/Love constraint rather leads to a worse convergence behaviour of the iterative solver than to an improvement, the recommendation is to work with rather simple inverse source formulations without extra side constraint for the equivalent sources or with a computationally cheap side constraint such as the CS condition, either in strong or in weak form. If Love surface current densities are desired for diagnostic or other

purposes, they can more easily be computed from the obtained equivalent sources in a post-processing step.

As a final scenario, antenna field transformations for near-field measurements above a ground half-space were considered. The consideration of the ground half-space within the IESS was achieved by working with the pertinent Green's functions within the radiation integrals, where a PEC ground half-space was accounted for by exact image theory for the sources and possibly lossy dielectric half-spaces were modelled by an approximate spectral image principle for the propagating plane-wave-based representation of the radiation fields. The feasibility of these approaches was demonstrated by a virtual measurement scenario of a monopole antenna on the roof of a car body, where the near-field measurement samples and the reference far-fields were obtained by full-wave electromagnetic simulation.

References

[1] W. C. Chew, J.-M. Jin, E. Michielssen and J. Song, Fast and Efficient Algorithms in Computational Electromagnetics, Boston: Artech House, 2001.

[2] J.-M. Jin, Theory and Computation of Electromagnetic Fields, New York: John Wiley & Sons, Inc., 2015.

[3] A. F. Peterson, S. L. Ray and R. Mittra, Computational Methods for Electromagnetics, Wiley-IEEE Press, 1997.

[4] P. Petre and T. K. Sarkar, "Planar Near-field to Far-field Transformation Using an Equivalent Magnetic Current Approach," *IEEE Transactions on Antennas and Propagation*, vol. 40, no. 11, pp. 1348–1356, 1992.

[5] T. Sarkar and A. Taaghol, "Near-field to Near/Far-field Transformation for Arbitrary Near-field Geometry Utilizing an Equivalent Electric Current and MoM," *IEEE Transactions on Antennas and Propagation*, vol. 47, pp. 1178–1185, 1999.

[6] Y. Alvarez, F. Las-Heras and M. R. Pino, "Reconstruction of Equivalent Currents Distribution Over Arbitrary Three-dimensional Surfaces Based on Integral Equation Algorithms," *IEEE Transactions on Antennas and Propagation*, vol. 55, no. 12, pp. 3460–3468, 2007.

[7] Y. Alvarez, F. Las-Heras and M. R. Pino, "Acceleration of the Sources Reconstruction Method Via the Fast Multipole Method," in *IEEE Antennas and Propagation International Symposium*, San Diego, CA, USA, 2008.

[8] R. Coifman, V. Rokhlin and S. Wandzura, "The Fast Multipole Method for the Wave Equation: A Pedestrian Prescription," *IEEE Antennas and Propagation Magazine*, vol. 35, no. 3, pp. 7–12, 1993.

[9] J. L. A. Quijano and G. Vecchi, "Field and Source Equivalence in Source Reconstruction on 3D Surfaces," *Progress in Electromagnetics Research*, vol. 103, pp. 67–100, 2010.

[10] J. L. A. Quijano, L. Scialacqua, J. Zackrisson, L. Foged, M. Sabbadini and G. Vecchi, "Suppression of Undesired Radiated Fields Based on Equivalent Currents Reconstruction from Measured Data," *IEEE Antennas and Wireless Propagation Letters*, vol. 10, pp. 314–317, 2011.

[11] E. Jorgensen, P. Meincke and C. Cappellin, "Advanced Processing of Measured Fields Using Field Reconstruction Techniques," in *European Conference on Antennas and Propagation*, Rome, 2011.

[12] E. Jorgensen, D. W. Hess, P. Meincke, O. Borries and C. Cappellin, "Antenna Diagnostics on Planar Arrays Using a 3D Source Reconstruction Technique and Spherical Near-field Measurements," in *European Conference on Antennas and Propagation*, Prague, 2012.

[13] E. Kilic and T. F. Eibert, "Solution of 3D Inverse Scattering Problems by Combined Inverse Equivalent Current and Finite Element Methods," *Journal of Computational Physics*, vol. 288, pp. 131–149, 2015.

[14] T. F. Eibert and C. H. Schmidt, "Multilevel Fast Multipole Accelerated Inverse Equivalent Current Method Employing Rao–Wilton–Glisson Discretization of Electric and Magnetic Surface Currents," *IEEE Transactions on Antennas and Propagation*, vol. 57, no. 4, pp. 1178–1185, 2009.

[15] T. F. Eibert, "A Diagonalized Multilevel Fast Multipole Method With Spherical Harmonics Expansion of the *k*-Space Integrals," *IEEE Transactions on Antennas and Propagation*, vol. 53, no. 2, pp. 814–817, 2005.

[16] C. H. Schmidt, M. M. Leibfritz and T. F. Eibert, "Fully Probe-corrected Near-field Far-field Transformation Employing Plane Wave Expansion and Diagonal Translation Operators," *IEEE Transactions on Antennas and Propagation*, vol. 56, no. 3, pp. 737–746, 2008.

[17] C. H. Schmidt and T. F. Eibert, "Multilevel Plane Wave Based Near-field Far-field Transformation for Electrically Large Antennas in Free-space or above Material Halfspace," *IEEE Transactions on Antennas and Propagation*, vol. 57, no. 5, pp. 1382–1390, 2009.

[18] T. F. Eibert, E. Kilic, C. Lopez, R. A. M. Mauermayer, O. Neitz and G. Schnattinger, "Electromagnetic Field Transformations for Measurements and Simulations (Invited Paper)," *Progress in Electromagnetics Research*, vol. 151, pp. 127–150, 2015.

[19] T. F. Eibert, C. Lopez and T. B. Hansen, "Irregular Probe Corrected Antenna Field Transformations Utilizing Gaussian Beam Based Fast Multipole Translation Operators," in *European Conference on Antennas and Propagation*, Davos, 2016.

[20] T. F. Eibert, D. Vojvodic and T. B. Hansen, "Fast Inverse Equivalent Source Solutions with Directive Sources," *IEEE Transactions on Antennas and Propagation*, vol. 151, no. 11, pp. 4713–4724, 2016.

[21] T. F. Eibert and T. B. Hansen, "Inverse-source Algorithm for Antenna-field Transformations Using the Weak Form of the Combined-source Condition," in *European Conference on Antennas and Propagation*, Paris, 2017.

[22] R. A. M. Mauermayer and T. F. Eibert, "Combining the Fast Irregular Antenna Field Transformation Algorithm with Asymptotic High Frequency Methods," in *European Conference on Antennas and Propagation*, Lisbon, 2015.

[23] R. A. M. Mauermayer and T. F. Eibert, "Fast Irregular Antenna Field Transformation above Perfectly Conducting Ground Planes," in *European Conference on Antennas and Propagation*, Davos, 2016.

[24] O. Neitz, R. A. M. Mauermayer, Y. Weitsch and T. F. Eibert, "A Propagating Plane-wave Based Near-field Transmission Equation for Antenna Gain Determination from Irregular Measurement Samples," *IEEE Transactions on Antennas and Propagation*, vol. 65, no. 8, pp. 4230–4238, 2017.

[25] J. A. Kong, Electromagnetic Wave Theory, 2nd ed., New York: John Wiley & Sons, 1990.

[26] C. A. Balanis, Antenna Theory, 3rd ed., New York: John Wiley & Sons, 2005.

[27] R. E. Collin, Field Theory of Guided Waves, Picataway, NJ: IEEE Press, 1990.

[28] A. E. H. Love, "The Integration of the Equations of Propagation of Electric Waves," *Philosophical Transactions of the Royal Society A*, vol. 197, pp. 1–43, 1901.

[29] S. Schelkunoff, "Some Equivalence Theorems of Electromagnetics and Their Application to Radiation Problems," *Bell System Technical Journal*, vol. 15, pp. 92–112, 1936.

[30] C.-T. Tai, Dyadic Green Functions in Electromagnetic Theory, 2nd ed., Piscataway, NJ: IEEE, 1994.

[31] J. C. Monzon, "On Surface Integral Representations: Validity of Huygens' Principle and Equivalence Principle in Inhomogeneous Bianistropic Media," *IEEE Transactions on Microwave Theory and Techniques*, vol. 41, no. 11, pp. 1995–2001, 1993.

[32] W. C. Chew, T. J. Cui and J. M. Song, "A FAFFA-MLFMA Algorithm for Electromagnetic Scattering," *IEEE Transactions on Antennas and Propagation*, vol. 50, no. 11, pp. 1641–1649, 2002.

[33] C. H. Schmidt and T. F. Eibert, "Near-field to Far-field Transformation Utilising Multilevel Plane Wave Representation for Planar and Quasi-planar Measurement Contours," *IET Microwaves, Antennas & Propagation*, vol. 4, no. 11, pp. 1829–1837, 2010.

[34] S. M. Rao, D. R. Wilton and A. W. Glisson, "Electromagnetic Scattering by Surfaces of Arbitrary Shape," *IEEE Transactions on Antennas and Propagation*, vol. 30, no. 5, pp. 409–418, 1982.

[35] T. F. Eibert, Ismatullah, E. Kaliyaperumal and C. H. Schmidt, "Inverse Equivalent Surface Current Method with Hierarchical Higher Order Basis Functions, Full Probe Correction and Multilevel Fast Multipole Acceleration (Invited Paper)," *Progress in Electromagnetics Research*, vol. 106, pp. 377–394, 2010.

[36] G. C. Hsiao and R. E. Kleinman, "Mathematical Foundations for Error Estimation in Numerical Solutions of Integral Equations in Electromagnetics," *IEEE Transactions on Antennas and Propagation*, vol. 45, no. 3, pp. 316–328, 1997.

[37] R. A. M. Mauermayer, G. Schnatting and T. F. Eibert, "Multi-Spectral Representation of Measurement Probes for Antenna Field Transformations," in *European Conference on Antennas and Propagation*, The Hague, 2014.

[38] M. Abramowitz and I. E. Stegun, Handbook of Mathematical Functions, 9th ed., New York: Dover Publications, Inc., 1972.

[39] J. Sarvas, "Performing Interpolation and Anterpolation Entirely by Fast Fourier Transform in the 3-D Multilevel Fast Multipole Algorithm," *SIAM Journal on Numerical Analysis*, vol. 41, pp. 2180–2196, 2003.

[40] S. Järvenpää and P. Ylä-Oijala, "A Global Interpolator With Low Sample Rate for Multilevel Fast Multipole Algorithm," *IEEE Transactions on Antennas and Propagation*, vol. 61, no. 3, pp. 1291–1300, 2013.

[41] J. Kornprobst and T. F. Eibert, "A Combined Source Integral Equation with Weak Form Combined Source Condition," *IEEE Transactions Antennas Propagation*, vol. 66, no. 8, pp. 2151–2155, 2018.

[42] J. Kornprobst and T. F. Eibert, "An Accurate Low-order Discretization Scheme for the Identity Operator in the Magnetic Field and Combined Field Integral Equations," *IEEE Transactions on Antennas and Propagation*, vol. 66, no. 11, pp. 6146–6157, 2018.

[43] T. F. Eibert, "Some Scattering Results Computed by the Hybrid Finite Element – Boundary Integral – Multilevel Fast Multipole Method," *IEEE Antennas and Propagation Magazine*, vol. 49, no. 2, pp. 61–69, 2007.

[44] Y. Saad, Iterative Methods for Sparse Linear Systems, 2nd ed., Society for Industrial and Applied Mathematics, 2003.

[45] T. B. Hansen, A. Paulus and T. F. Eibert, "On the Condition Number of a Normal Matrix in Near-Field to Far-Field Transformations," *IEEE Transactions on Antennas and Propagation*, vol. 67, no. 3, pp. 2028–2033, 2019.

[46] A. Björck, Numerical Methods for Least Squares Problems, Philadelphia, PA: SIAM, 1996.

[47] K. Zhao, M. N. Vouvakis and J.-F. Lee, "The Adaptive Cross Approximation Algorithm for Accelerated Method of Moments Computations of EMC Problems," *IEEE Transactions on Electromagnetic Compatibility*, vol. 47, no. 11, pp. 763–773, 2005.

[48] Y. Wang, T. F. Eibert and Z. Nie, "Adaptive Cross Approximation Algorithm Accelerated Inverse Equivalent Current Method for Near-Field Antenna Measurement," *IEEE Transactions on Antennas and Propagation*, vol. 67, no. 3, pp. 1874–1883, 2019.

[49] W. Hackbusch and S. Boerm, "H2-Matrix Approximation of Integral Operators by Interpolation," *Applied Numerical Mathematics*, vol. 43, pp. 129–143, 2002.

[50] S. Koc, J. Song and W. C. Chew, "Error Analysis for the Numerical Evaluation of the Diagonal Forms of the Scalar and Spherical Addition Theorem," *SIAM Journal on Numerical Analysis*, vol. 36, pp. 906–921, 1999.

[51] W. C. Chew, Waves and Fields in Inhomogenous Media, D. G. Dudley, Ed., Piscataway, NJ: IEEE, 1995.

[52] T.-J. Cui, W. C. Chew and J. Song, "Efficient MLFMA, RPFMA, and FAFFA Algorithms for EM Scattering by Very Large Structures," *IEEE Transactions on Antennas and Propagation*, vol. 52, no. 3, pp. 759–770, 2004.

[53] T. B. Hansen, "Translation Operator Based on Gaussian Beams for the Fast Multipole Method in Three Dimensions," *Wave Motion*, vol. 50, no. 7, pp. 940–954, 2013.

[54] T. B. Hansen and O. Borries, "Gaussian Translation Operator in a Multilevel Scheme," *Radio Science*, vol. 50, pp. 754–763, 2015.

[55] C. H. Schmidt, D. T. Schobert and T. F. Eibert, "Electric Dipole Based Synthetic Data Generation for Probe-corrected Near-field Antenna Measurements," in *5th European Conference on Antennas and Propagation*, Rome, 2011.

[56] Altair, "FEKO," Altair Engineering, 2019.

[57] M. A. Qureshi, C. H. Schmidt and T. F. Eibert, "Near-field Error Analysis for Arbitrary Scanning Grids Using Fast Irregular Antenna Field Transformation Algorithm," *Progress in Electromagnetics Research B*, vol. 48, pp. 197–220, 2013.

[58] RFspin, "DRH18 Double Ridged Waveguide Horn," http://www.rfspin.cz/en/antennas, 2016.

[59] NSI-MI, "Microwave Test Systems," https://www.nsi-mi.com, 2019.

[60] TICRA, "GRASP," https://www.ticra.com/software/grasp/, Kopenhagen, 2018.

[61] T. Fritzel, A. Geise, C. H. Schmidt, *et al.*, "Concept of a Portable Antenna Measurement System for Large-scale and Multi-contour Near-field Measurements," in *35th ESA Antenna Workshop on Antenna and Free Space RF Measurements*, Noordwijk, 2013.

[62] A. Geise, O. Neitz, J. Migl, H.-J. Steiner, *et al.*, "A Crane Based Portable Antenna Measurement System – System Description and Validation," *IEEE Transactions on Antennas and Propagation*, vol. 67, no. 5, pp. 3346–3357, 2019.

[63] D. Fasold and G. Radig, "The New Antenna Test Centre at MBB, Ottobrunn," in *Proc. 11th ESTEC Antenna Workshop on Antenna Measurements*, Gothenburg, 1988.

[64] A. Geise, T. Fritzel and M. Paquay, "Ka-band Measurement Results of the Irregular Near-field Scanning System PAMS," *Annual Symposium of the Antenna Measurement Techniques Association, Atlanta, GA*, 2017.

[65] A. Tzoulis and T. F. Eibert, "A Hybrid FEBI-MLFMM-UTD Method for Numerical Solutions of Electromagnetic Problems Including Arbitrarily Shaped and Electrically Large Objects," *IEEE Transactions on Antennas and Propagation*, vol. 53, no. 10, pp. 3358–3366, 2005.

[66] J. R. Camacho-Perez and P. Moreno, "Initial Considerations Towards Hemispherical Near-field Antenna Measurements," *IEEE Antennas and Wireless Propagation Letters*, vol. 13, pp. 1441–1444, 2014.

[67] J. R. Camacho-Perez and P. Moreno, "Spherical Near-field to Far-field Transformations for the Half-space Problem with a PEC Boundary," in *IEEE MTT-S International Microwave Workshop Series on Signal Integrity and High-Speed Interconnects*, 2009.

[68] R. A. M. Mauermayer and T. F. Eibert, "Spherical Field Transformation above Perfectly Electrically Conducting Ground Planes," *IEEE Transactions on Antennas and Propagation*, vol. 65, no. 3, pp. 1465–1478, 2018.

[69] J. T. Williams, H. J. Delgado and S. A. Long, "An Antenna Pattern Measurement Technique for Eliminating the Fields Scattered from the Edges of a Finite Ground Plane," *IEEE Transactions on Antennas and Propagation*, vol. 38, no. 11, pp. 1815–1822, 1990.

[70] L. J. Foged, F. Mioc, B. Bencivenga, M. Sabbadini and E. D. Giampaolo, "Accurate Infinite Groundplane Antenna Measurements," in *31th Annual Symposium of the Antenna Measurement Techniques Association*, Salt Lake City, UT, USA, 2009.

[71] L. J. Foged, F. Mioc, B. Bencivenga, M. Sabbadini and E. D. Giampaolo, "Infinite Ground Plane Antenna Characterization from Limited Groundplane Measurements," in *European Conference on Antennas and Propagation*, Barcelona, 2010.

[72] A. Sommerfeld, "Über die Ausbreitung der Wellen in der drahtlosen Telegraphie," *Annalen der Physik*, vol. 28, pp. 665–737, 1909.

[73] A. Sommerfeld, "Über die Ausbreitung der Wellen in der drahtlosen Telegraphie," *Annalen der Physik*, vol. 81, pp. 1135–1153, 1928.

[74] A. Sommerfeld, Partielle Differentialgleichungen der Physik, Thun: Verlag Harri Deutsch, 1978.

[75] K. A. Michalski and J. R. Mosig, "The Sommerfeld Halfspace Problem Redux: Alternative Field Representations, Role of Zenneck and Surface Plasmon Waves," *IEEE Transactions Antennas Propagation*, vol. 63, no. 12, pp. 5777–5790, 2018.

[76] D. G. Fang, J. J. Yang and G. Y. Delisle, "Discrete Image Theory for Horizontal Electric Dipole in a Multilayer Medium," *Proceedings of the Institute of Electrical Engineers H*, vol. 135, no. 5, pp. 297–303, 1988.

[77] M. I. Aksun, "A Robust Approach for the Derivation of Closed-form Green's Functions," *IEEE Transactions on Antennas and Propagation*, vol. 44, no. 5, pp. 651–658, 1996.

[78] N. Geng, A. Sullivan and L. Carin, "Multilevel Fast-Multipole Algorithm for Scattering from Conducting Targets Above or Embedded in a Lossy Half Space," *IEEE Transactions on Antennas and Propagation*, vol. 38, pp. 1561–1573, 2000.

[79] N. Geng, A. Sullivan and L. Carin, "Fast Multipole Method for Scattering from an Arbitrary PEC Target Above or Buried in a Lossy Half Space," *IEEE Transactions on Antennas and Propagation*, vol. 39, pp. 740–748, 2001.

[80] X. W. Zhao, C. H. Liang and L. Liang, "Multilevel Fast Multipole Algorithm for Radiation Characteristics of Shipborne Antennas above Seawater," *Progress in Electromagnetics Research*, vol. 81, pp. 291–302, 2008.

[81] Z. Liu, J. He, Y. Xie, A. Sullivan and L. Carin, "Multilevel Fast Multipole Algorithm for General Targets on a Half-space Interface," *IEEE Transactions on Antennas and Propagation*, vol. 50, no. 12, pp. 1838–1849, 2002.

[82] B. Hu and W. C. Chew, "Fast Inhomogeneous Plane Wave Algorithm for Scattering from Objects Above the Multilayered Medium," *IEEE Transactions on Geoscience and Remote Sensing*, vol. 39, pp. 1028–1038, 2001.

[83] T. F. Eibert and R. A. M. Mauermayer, "Near-field Far-field Transformations for Automobile Antenna Measurements," in *Applied Computational Electromagnetics Society Conference*, Denver, 2018.

[84] T. F. Eibert and R. A. M. Mauermayer, "Equivalent Sources Based Near-field Far-field Transformation above Dielectric Half Space," in *Annual Symposium of the Antenna Measurement Techniques Association (AMTA)*, Williamsburg, 2018.

[85] L. B. Felsen and N. Marcuvitz, Radiation and Scattering of Waves, D. G. Dudley, Ed., Piscataway, NJ: IEEE Press, 1994.

[86] V. W. Hansen, Numerical Solution of Antennas in Layered Media, Taunton, Sommerset: Research Studies Press Ltd., 1989.

[87] J. A. Stratton, Electromagnetic Theory, Piscataway, NJ: IEEE Press, 2007.

[88] T. F. Eibert and V. Hansen, "3-D FEM/BEM-Hybrid Approach Based on a General Formulation of Huygens' Principle for Planar Layered Media," *IEEE Transactions on Microwave Theory and Techniques*, vol. 45, no. 7, pp. 1105–1112, 1997.

This page intentionally left blank

Chapter 10

Near-field range assessment

10.1 Introduction

The range assessment (RA) concept establishes a formalised process for identifying and evaluating measurement errors[1] within a given test facility. A significant portion of the groundwork related to RAs was conducted in an effort to allay the fears of the engineering community in the early days of near-field antenna testing. At the time, far-field testing was the norm and the truth model for all other methods of testing. Needless to say, the new-fangled concept of near-field testing was regarded with a healthy degree of scepticism, and this led to contributions that today form the foundation for most of the RA work being performed [1–5].

Although initially focussed on planar near-field (PNF) testing, RA concepts have been expanded to cylindrical near-field (CNF) [6] and spherical near-field (SNF) [2] test systems and are today readily applied to far-field test systems as well. Driven by demanding needs in the defence and communications industry, the need for ever-higher fidelity in measurement has led to the significant effort being spent on the reduction of measurement uncertainty and an improved understanding of their sources. Today, the measurement community has started to adopt the principle that any measurement being reported without some indication of the associated uncertainty is not worth being reported at all.

It is important to realise that any measured parameter has an associated uncertainty and a RA therefore has to be conducted for each one of these. These RAs can be costly and time consuming, but are essential in understanding a measurement process and potentially improving it. RAs are typically done for gain, directivity, side lobe level, cross-polarisation or beam pointing error.

10.2 A framework for measurement uncertainty

Once specific sources of measurement uncertainty are listed, one can easily become overwhelmed with the enormity of the task and it is therefore worthwhile to define

[1]If we distinguish between the concept of a 'measurement error' and a 'measurement uncertainty', the former is in general regarded as a known quantity and can therefore be removed or compensated for, whereas the latter is an unknown quantity that we are trying to bound. Measurement uncertainty therefore establishes a region of 'fuzziness' within which the true measurement lies. We will use these terms interchangeably here.

Table 10.1 The broad classes of errors and their potential impact on near-field, far-field and CATR's

	Class	Near-field range	Far-field range and CATR
1	Probe/illuminator-related errors	Yes	Yes
2	Mechanical/positioner-related errors	Yes	Yes
3	Absolute power level-related errors	Gain, EIRP and SFD only	Gain, EIRP and SFD only
4	Processing-related errors	Yes	No
5	RF sub-system-related errors	Yes	Yes
6	Environmental errors	Yes	Yes

a simple classification framework within which these terms can be grouped. The following general classes of errors form such a framework within which all specific error sources can be categorised:

1. Probe/illuminator-related errors
2. Mechanical/positioner-related errors
3. Absolute power level-related errors
4. Processing-related errors
5. RF sub-system-related errors
6. Environmental-related errors

Considering these broad classes, one can compile the table of inter-dependencies as shown in Table 10.1. We can now list each specific error term within this framework of six classes as in Table 10.2.

The error terms listed in Table 10.2 are almost exclusively systematic in nature and all of these have a small random component. We do not attempt to resolve this random component for each and instead lump the random component into term #18. All of these error terms are assumed to be independent and uncorrelated and their effect can therefore be assessed independently. It is also important to state that we assume that there is no error within the near-field theory. The only aspects from a theoretical stand point where this does not hold are AUT-to-probe multiple reflections and scan plane truncation and both of these are included as specific terms within this budget.

10.3 The effects of unwanted signals on vector measurements

When evaluating measurement uncertainties, the usual method for determining errors through measurement is to isolate and vary a single parameter of the test and

Table 10.2 List of 18 error terms and their associated categories

	Specific error term	Class	Error type
1	Probe relative pattern	Probe/illuminator-related errors	Systematic
2	Probe polarisation purity	Probe/illuminator-related errors	Systematic
3	Probe alignment	Probe/illuminator-related errors	Systematic
4	AUT alignment	Mechanical/positioner-related errors	Systematic
5.1	Probe (x, y) positioning	Mechanical/positioner-related errors	Systematic
5.2	Probe (ϕ, z) positioning	Mechanical/positioner-related errors	Systematic
5.3	Probe (θ, ϕ) positioning	Mechanical/positioner-related errors	Systematic
6.1	Probe z positioning	Mechanical/positioner-related errors	Systematic
6.2	Probe ρ positioning	Mechanical/positioner-related errors	Systematic
6.3	Probe r positioning	Mechanical/positioner-related errors	Systematic
7	Gain reference uncertainty	Absolute power level-related errors	Systematic
8	Normalisation constant	Absolute power level-related errors	Systematic
9	Impedance mismatch	Absolute power level-related errors	Systematic
10	Aliasing	Processing-related errors	Systematic
11	Truncation	Processing-related errors	Systematic
12	Receiver linearity	RF sub-system-related errors	Systematic
13	Systematic phase	RF sub-system-related errors	Systematic
14	Leakage	RF sub-system-related errors	Systematic
15	Receiver dynamic range	RF sub-system-related errors	Systematic
16	Multiple reflection	Environmental errors	Systematic
17	Chamber reflection	Environmental errors	Systematic
18	Random	Environmental errors	Random

observe pattern changes. The change in the measurement parameter is designed to focus on a single error source such as chamber scattering or receiver linearity. Differences in pattern characteristics, i.e. gain, side lobe level, cross-polarisation level and pointing, are then recorded. Often it is possible to describe small pattern differences by computing a signal-to-error level. This signal-to-error ratio can then be used to evaluate the effects of the same error at a different pattern level. Figures 10.1 and 10.2 contain a schematic representation of a signal S being combined with an error E. Here, the true value, designated by S is taken to mean the value obtained after an infinite series of measurements have been performed under the same conditions with an instrument not affected by systematic errors. The error is the result of a measurement, i.e. the measured value, minus the true value. The measured value is the vector *addition* of the true value and the error. In practice, the uncertainty/error in a measurement can never be determined it can only be estimated.

Here, both E and S are assumed to be complex quantities. The combination of these vectors can be represented by using free vectors plotted in the Argand plane with the measured signal being formed from the vector addition using the parallelogram law. The dotted circle represents the locus of possible measured values. Figure 10.1 shows the case of S and E being added such that the phases of the error and signal are in phase or exactly 180° out of phase which would result in the

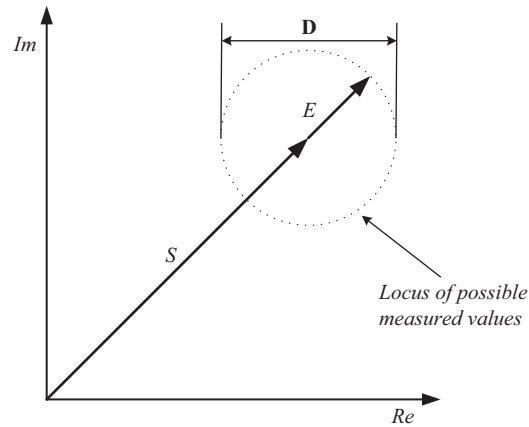

Figure 10.1 Worst case amplitude error, S and E are in (or exactly out of) phase. $D = 2E$

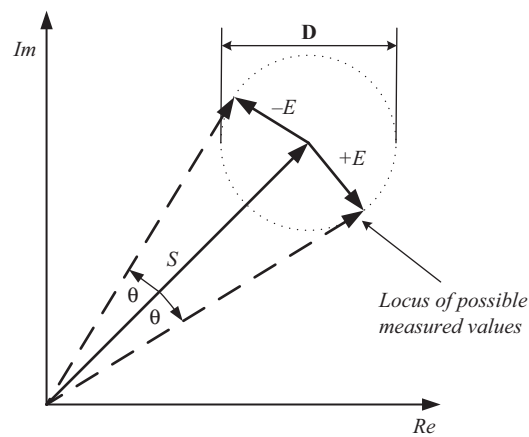

Figure 10.2 Worst-case phase error when the resulting signal $E + S$ is in quadrature with E

largest change in the measured amplitude. From Figure 10.1, it is clear that the maximum signal is recorded at $S + E$ and the minimum signal is recorded at $S - E$, whereupon the envelope of the measured amplitude value can be expressed as

$$\text{Measured}|_{\text{dB}} = 20\log_{10}(S \pm E) \tag{10.1}$$

Conversely, Figure 10.2 contains a combination of S and E where signals are combined such that the maximum phase change occurs. This happens when the measured signal ($E + S$) is in quadrature with the error signal E, with E either leading or lagging S. Thus, from inspection of Figure 10.2 it is clear that the maximum phase error can be written as

$$\theta_{\max} = \pm\arcsin\left(\frac{E}{S}\right) \tag{10.2}$$

Usually, we do not know the value of the error as in practice it is the ratio of the signal to the error that is available. Thus, taking (10.1) and expressing it in terms of the signal-to-error ratio E/S (where E/S is a relative error), we obtain

$$\text{Measured}|_{\text{dB}} = 20\log_{10}\left(S \pm \frac{S}{S/E}\right)$$

Factorising this and using the law of logarithms yields

$$\text{Measured}|_{\text{dB}} = 20\log_{10}(S) + 20\log_{10}\left(1 \pm \frac{1}{S/E}\right)$$

Thus, the measured value can be expressed as

$$\text{Measured}|_{\text{dB}} = \text{Signal}|_{\text{dB}} + \text{Uncertainty}|_{\text{dB}}$$

Here, the term uncertainty is used to mean an estimate or approximation of the error. Thus, when assuming the E/S ratio is expressed in logarithmic form, which it usually is, we can write the upper and lower bound uncertainties as

$$\text{Uncertainty}|_{\text{dB}} = 20\log_{10}\left(1 \pm 10^{-((S/E|_{\text{dB}})/20)}\right) \tag{10.3}$$

or

$$\text{Upper bound uncertainty}|_{\text{dB}} = 20\log_{10}\left(1 + 10^{-((S/E|_{\text{dB}})/20)}\right) \tag{10.4}$$

$$\text{Lower bound uncertainty}|_{\text{dB}} = 20\log_{10}\left(1 - 10^{-((S/E|_{\text{dB}})/20)}\right) \tag{10.5}$$

In practice, when computing the lower bound uncertainty, the absolute part of the argument of the logarithm is used as the logarithm of a negative number results in a complex value, which in this case is unwanted.

Figure 10.3 contains a plot of the upper bound uncertainty plotted as a function of the signal-to-error ratio, whereas Figure 10.4 contains a plot of the phase error

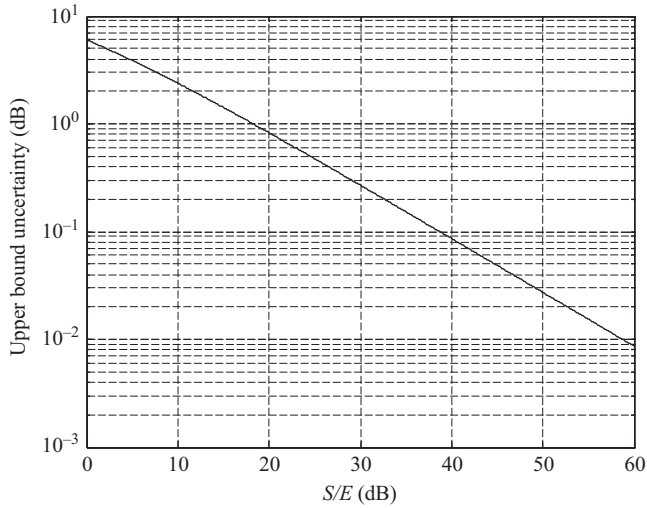

Figure 10.3 Amplitude measurement error due to signal-to-error ratio

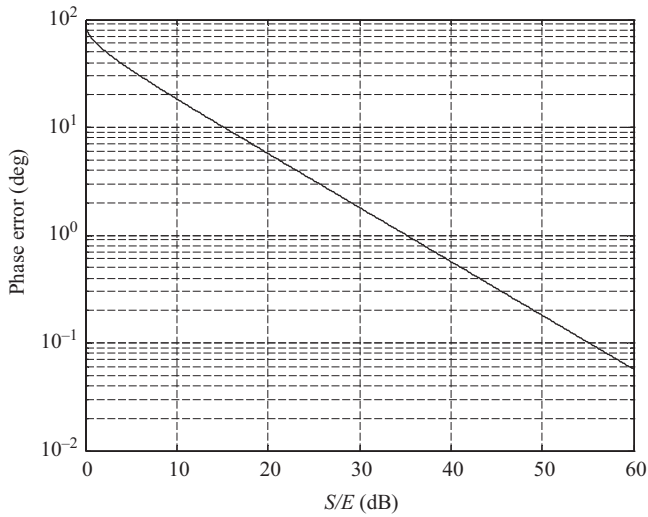

Figure 10.4 Phase measurement error due to signal-to-error ratio

when plotted as a function of the signal-to-error ratio, thereby illustrating their respective relationships. By comparing these plots, it is clear that a maximum phase error of 10° or a maximum amplitude error of 1 dB could be produced by roughly the same error level. When taking measurements, this is an approximate relationship, i.e. rule of thumb, which is often observed.

Table 10.3 shows several examples of the conversion between E/S and uncertainty.

Figure 10.5 illustrates the conversion between E/S and upper and lower bound uncertainties using (10.4) and (10.5), respectively. When the E/S is high, i.e. greater than 25 dB, the difference between the lower and upper bounds is negligible. As the E/S reduces, the difference becomes more pronounced.

The measurement uncertainty means that the true value falls somewhere between the upper and lower bounds plus the measurement value. Even though the AUT may not actually have a side lobe, or cross-polarisation value at a particular level, the error can still be evaluated at that level. To illustrate this procedure, consider a side lobe measured at -45 dB with a 10 dB E/S ratio. From (10.4) and (10.5), we can see that this will have a true value that lies between the lower bound of -48.3 dB ($-45 + -3.3$) and the upper bound of -42.6 dB ($-45 + 2.4$). Thus, for a fixed error level, as the signal level increases, the uncertainty bounds correspondingly decrease. This can be seen illustrated further in Table 10.4 where an error level of -55 dB has been assumed, and the effect that this has on a side lobe at varying levels S dB has been calculated.

This can also be seen illustrated further in Figure 10.6 which contains a graphical representation of the side lobe level upper and lower bounds as a function of signal level for a fixed error level of -55 dB showing the effect that this has on a side lobe at varying levels S.

Table 10.3 S/E versus uncertainty

E/S* (dB) at 0 dB *S	**Lower bound uncertainty (dB)**	**Upper bound uncertainty (dB)**
80.0	−0.001	+0.001
75.0	−0.002	+0.002
70.0	−0.003	+0.003
65.0	−0.005	+0.005
60.0	−0.009	+0.009
55.0	−0.015	+0.015
50.0	−0.028	+0.027
45.0	−0.049	+0.049
40.0	−0.087	+0.086
35.0	−0.156	+0.153
30.0	−0.279	+0.270
25.0	−0.503	+0.475
20.0	−0.915	+0.827
15.0	−1.701	+1.421
10.0	−3.302	+2.387
5.0	−7.177	+3.876
3.0	−10.691	+4.649
2.0	−13.737	+5.078
1.0	−19.271	+5.535
0.5	−25.046	+5.774
0.0	$-\infty$	+6.021

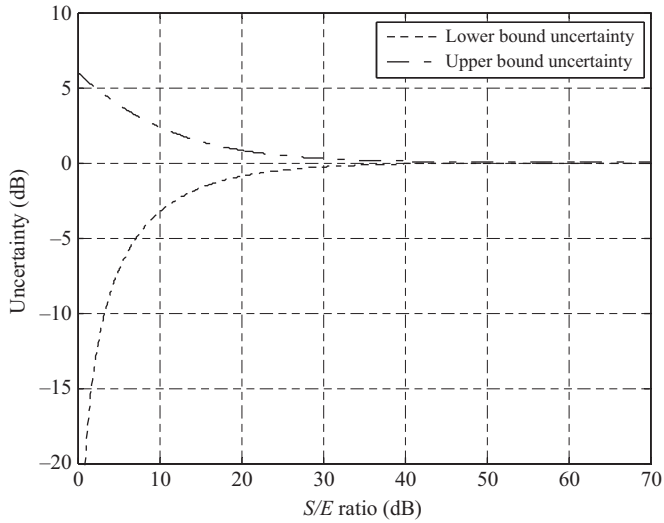

Figure 10.5 Upper and lower bound uncertainties plotted as a function of the S/E level

Table 10.4 Error levels at varying side lobe levels for a −55 dB error level

SLL, *S* (dB)	Lower bound uncertainty (dB)	Upper bound uncertainty (dB)	Lower bound value (dB)	Upper bound value (dB)
0	−0.02	0.02	−0.02	0.02
−5	−0.03	0.03	−5.03	−4.97
−10	−0.05	0.05	−10.05	−9.95
−15	−0.09	0.09	−15.09	−14.91
−20	−0.16	0.15	−20.16	−19.85
−25	−0.28	0.27	−25.28	−24.73
−30	−0.50	0.48	−30.50	−29.52
−35	−0.92	0.83	−35.92	−34.17
−40	−1.70	1.42	−41.70	−38.58
−45	−3.30	2.39	−48.30	−42.61
−50	−7.18	3.88	−57.18	−46.12
−55	$-\infty$	6.02	$-\infty$	−48.98

Since there is often a 'not-to-exceed' specification on side lobes or cross-polarisation performance, the upper bound value is usually chosen when the E/S is low. Since the lower bound can approach $-\infty$, choosing the upper bound uncertainty makes sure that the highest level the true value can be compared to is the 'not-to-exceed' specification. Although it is erroneous to do so, for the sake of simplicity, although perhaps at the expense of clarity, many workers state only the upper bound value and ignore the asymmetric nature of the upper and lower bounds.

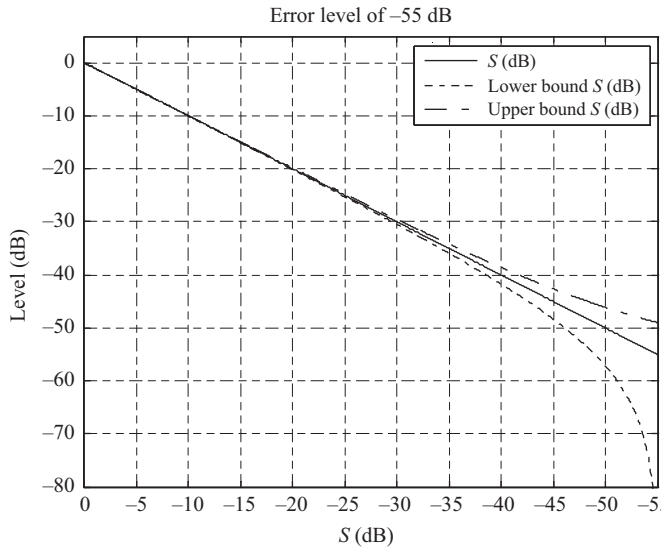

Figure 10.6 Error levels at varying side lobe levels for a −55 dB error level

As will be shown below, once the measurement uncertainty is known from completing an 18-term range assessment, and by using the antenna pattern function, it is possible to plot the measurement uncertainty in the form of a pattern cut, etc., with an example plot being illustrated in Figure 10.7.

In this way, the upper and lower uncertainty levels can be used to enable 'error bars' to be plotted with the antenna pattern. Here, the actual lower bound was used as opposed to choosing the lower bound to be the negative of the upper bound. Conversely, by manipulation of (10.4) and (10.5), it can be shown that the E/S ratio can be obtained from the upper and lower bound uncertainties using

$$S/E|_{\text{dB}} = -20\ \log_{10}\left(10^{(\text{upper bound uncertainty}|_{\text{dB}}/20)} - 1\right) \tag{10.6}$$

$$S/E|_{\text{dB}} = -20\ \log_{10}\left(1 - 10^{(\text{lower bound uncertainty}|_{\text{dB}}/20)}\right) \tag{10.7}$$

Some workers prefer instead to use the inverse ratio, error to signal, i.e. E/S, in which case the values would be negative which follows from the law of logarithms. In this case, (10.4) and (10.5) can be expressed, respectively, as

$$\text{Upper bound uncertainty}|_{\text{dB}} = 20\ \log_{10}\left(1 + 10^{((E/S|_{\text{dB}})/20)}\right) \tag{10.8}$$

$$\text{Lower bound uncertainty}|_{\text{dB}} = 20\ \log_{10}\left(1 - 10^{((E/S|_{\text{dB}})/20)}\right) \tag{10.9}$$

Similarly, (10.6) and (10.7) can be expressed as

$$E/S|_{\text{dB}} = 20\ \log_{10}\left(10^{(\text{upper bound uncertainty}|_{\text{dB}}/20)} - 1\right) \tag{10.10}$$

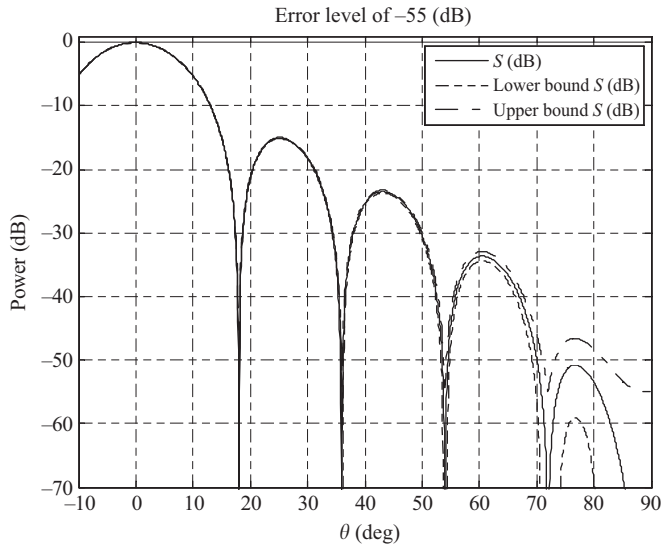

Figure 10.7 Example of a pattern cut showing upper and lower bound uncertainties

$$E/S|_{\text{dB}} = 20\ \log_{10}\left(1 - 10^{(\text{lower bound uncertainty}|_{\text{dB}}/20)}\right) \tag{10.11}$$

This provides the expressions in the form that will be used below. By way of further illustration of the use of (10.10) and (10.11) in the translation of uncertainties in the context of pattern comparison, let us consider the upper uncertainty at the −25 dB SLL. Using (10.10), we can show that an upper bound uncertainty of, say, 0.098 dB at 0 dB equates to an *E*/*S* level of −38.876 dB relative to a 0 dB side lobe. Clearly, relative to a −25 dB side lobe, this equates to an *E*/*S* level of −13.876 dB. Using (10.11), we can see that this corresponds to a 1.601 dB upper uncertainty bound at the −25 dB SLL and using (10.11) a −1.964 lower uncertainty bound.

For the case of the *E*/*S* ratio repeating Table 10.3 for this convention, the table becomes as in Table 10.5.

As can be seen from inspection of this table, for smaller values of *E*/*S*, and when rounded to a few decimal places only, it can be seen that the upper and lower bounds are equal (that is to say symmetrical). Thus, taking the −55 dB *E*/*S* case as an example, when rounded to three decimal places the upper and lower bound uncertainties are equal. Thus, for the sake of brevity (if perhaps not for the sake of clarity), many workers simply take the upper bound uncertainty (which is the tighter more conservative bound) and simply state that the uncertainty is ± that amount. Figure 10.8 contains a repeat of Figure 10.5 only here; the uncertainties are plotted as a function of the *E*/*S* level with the plot also being extended to include the region where the error is larger than the signal.

Table 10.5 E/S versus uncertainty

E/S* (dB) at 0 dB *S	**Lower bound uncertainty (dB)**	**Upper bound uncertainty (dB)**
−10.0	−3.302	+2.387
−15.0	−1.701	+1.421
−20.0	−0.915	+0.827
−25.0	−0.503	+0.475
−30.0	−0.279	+0.270
−35.0	−0.156	+0.153
−40.0	−0.087	+0.086
−45.0	−0.049	+0.049
−50.0	−0.028	+0.027
−55.0	−0.015	+0.015
−60.0	−0.009	+0.009
−65.0	−0.005	+0.005
−70.0	−0.003	+0.003
−75.0	−0.002	+0.002
−80.0	−0.001	+0.001

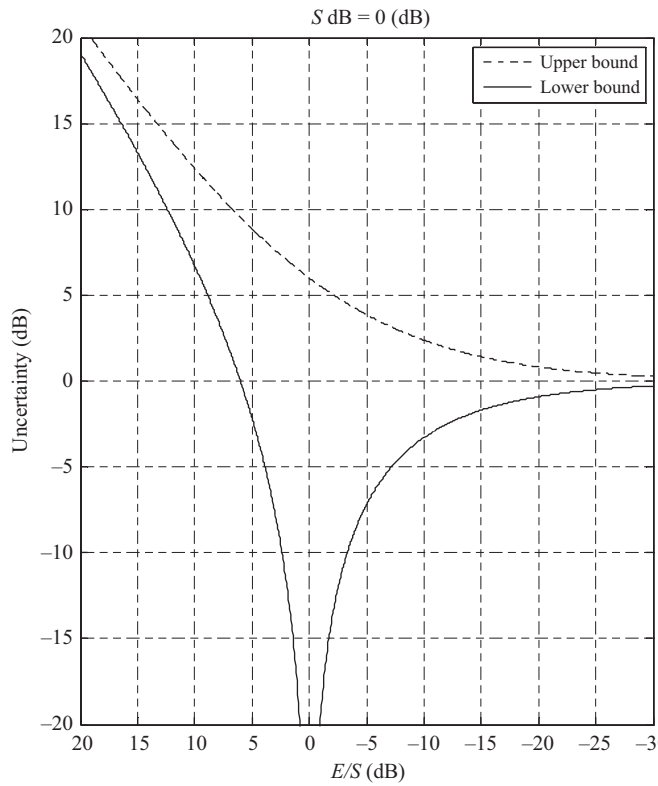

Figure 10.8 Upper and lower bound uncertainties plotted as a function of E/S level

10.4 The statistical nature of error signals

When we consider unwanted signals as described in the previous section, we like to think of these as being 'random'. However, as stated earlier, most of the error terms considered here are not random in nature, but rather systematic and can therefore be assessed and repeated with high confidence. What one does find though is that the signals are highly angular dependent and this dependency requires the application of some level of statistical processing in order to predict bounds of uncertainty.

In the previous section, we related E/S to a measurement uncertainty and vice versa. A powerful technique in RA work is to conduct two measurements and to observe any differential between the two sets (i.e. subtract the results) and from that obtain an E/S function versus angle [7] as shown in Figure 10.9. This E/S function can be calculated as a function of angle as

$$\left|\frac{E}{S}(\theta)\right|_{\text{dB}} = 20\ \log_{10}\left|\frac{f_1(\theta) - f_2(\theta)}{f_{\max}(\theta_0)}\right|$$

where $f_1(\theta)$ is the first radiation pattern of interest, $f_2(\theta)$ is the second radiation pattern of interest and $f_{\max}(\theta_0)$ is the maximum value of both radiation patterns. This E/S function as depicted in Figure 10.9 displays the high angular dependency noted above.

It is worthwhile pointing out that in Figure 10.9, pattern 1 has the higher amplitude value and therefore becomes our reference. Once the E/S curve has been

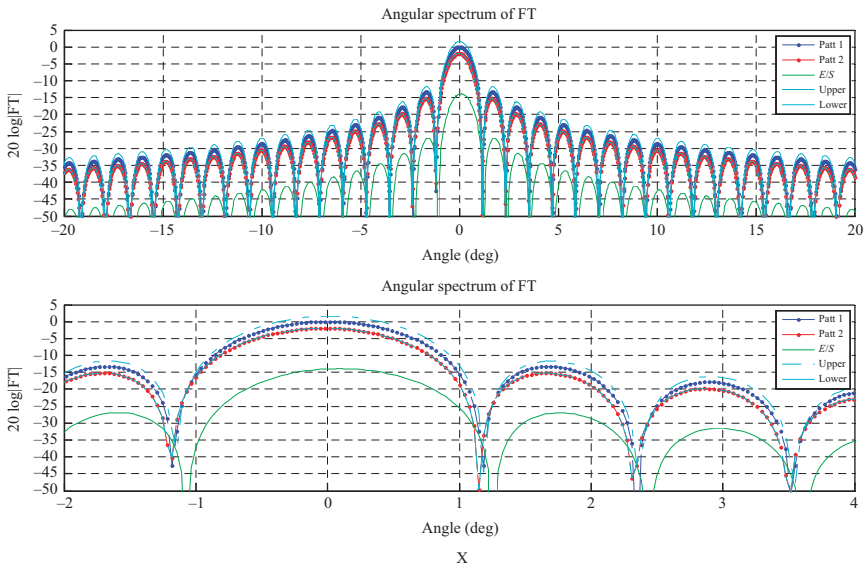

Figure 10.9 Example pattern comparison between two far-field pattern data sets with associated E/S function. The full pattern is shown at the top and −2° to 4° span is shown at the bottom for clarity

calculated, we can use (10.8) and (10.9) to calculate upper and lower bounds relative to pattern 1 and these are also shown in Figure 10.9. If we look at the peak of the main beam, we see the upper limit at a level higher than pattern 1 and the lower limit at a level below pattern 1 and coincident with pattern 2.

Using this technique, we can now consider a single error source in an 18-term RA uncertainty analysis and we can perform a self-comparison test which does not depend on knowing the true antenna parameters or even assuming that the results of a given measurement are free from other sources of error. The tests are designed to be sensitive to only a single error source and ideally the difference between two or more measurements will quantify the uncertainty for the single term. For instance, in the case of a SNF range that has an error in the intersection alignment of the θ and ϕ axes, the antenna patterns calculated from measured SNF data will not produce the correct results because of this alignment error. However, if the alignment errors and all the other systematic errors are repeatable for a given measurement configuration, the far-field results should also be repeatable and when (for instance) pattern comparison is used to estimate the uncertainty due to one specific introduced error source (e.g. a piece of absorber being changed), the effect of the alignment errors and all the other systematic errors should remain constant and the changes in the far-field results are due primarily to the introduced single error source. This term can therefore be quantified even though there may also be a larger but constant error term due to the misalignment. We do therefore rely on high precision to quantify the accuracy.

In each of these self-comparison tests, graphs like Figure 10.9 are produced and the E/S pattern is computed. The graph shows that the function will have large variations over most angular regions and a decision must be made on what value to use as the uncertainty for a given side lobe level or angular location. As an example, if the focus is on a particular side lobe, such as that between 1° and 2°, we would expect using the value of the E/S function at that specific side lobe peak location. However, a problem arises in that neither of the patterns being compared is the 'truth' and we see in Figure 10.9 more than 25 dB variation in the E/S level between 1° and 2°. We therefore need to define a technique to interpret the E/S distribution in a way to increase the usefulness of this function and reducing its extreme angular sensitivity.

In [7], the E/S pattern is viewed as an estimated uncertainty distribution function of angle and one can therefore compute a standard deviation (σ) or root-mean-square (RMS) value[2] that is a single number, valid across all angles. Assuming a set of N discrete angular values, we can compute σ as

$$\sigma|_{\text{dB}} = 20\ \log_{10}\left(\sqrt{\frac{1}{N}\sum_{i=1}^{N}\left(\frac{E}{S}(\theta_i) - \frac{\overline{E}}{S}\right)^2}\right)$$

[2]We can use σ and RMS interchangeably here since the functions in question will all have a zero mean value, in which case the RMS value reduces to σ.

where

$$\frac{\overline{E}}{S} = \frac{1}{N}\sum_{i=1}^{N}\frac{E}{S}(\theta_i)$$

This is an extreme simplification since this number will be constant over the full angular region, however, we can opt to only apply this over limited angular regions of interest.

In Figure 10.10, we show the σ value of an E/S distribution calculated from the two radiation patterns depicted. The value is -34 dB and since the σ value is associated with a confidence level of 68%, we know that in order to make this number more representative, we need to consider a 2σ (for 95% confidence) or even a 3σ value (for 99% confidence). These values are also shown in Figure 10.10.

By using the 2σ or 3σ values, we raise our confidence in the single E/S value, but we also simultaneously become more conservative in our estimates and this may come at an unacceptably high price. It is worthwhile to note that on a dB scale converting a σ value to a 2σ or 3σ value one can simply add 6 dB or 9.5 dB, respectively, to the calculated σ value.

Before continuing our discussion on the conversion of the E/S function to a σ value, we have to pause and consider the question of pattern normalisation. Normalisation to a global maximum when comparing two radiation patterns retains

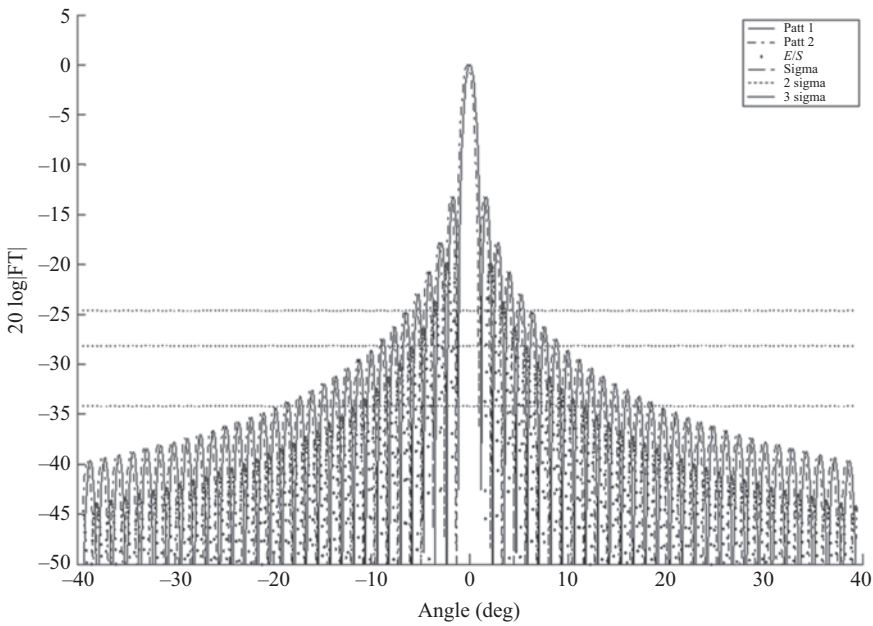

Figure 10.10 Example pattern comparison between two far-field pattern data sets with associated E/S function, σ, 2σ (higher) and 3σ (highest) levels

absolute power level changes since a relative difference in beam peak values is not lost. However, when we are interested in parameters that are measured relative to a radiation pattern beam peak (e.g. side lobe level), local pattern normalisation is appropriate and when this is done, the E/S distribution becomes

$$\left.\frac{E}{S}(\theta)\right|_{\text{dB}} = 20\log_{10}\left|\frac{f_1(\theta)}{f_{1\_\max}(\theta_0)} - \frac{f_2(\theta)}{f_{2\_\max}(\theta_0)}\right|$$

We highlight the impact of this below. In what follows, the reference to *normalisation* refers to this type of normalisation where each radiation pattern is normalised relative to its beam peak value.

In Figure 10.11, we overlay two similar radiation patterns (example #1), one denoted as Pattern1 = Sinc(x) and the second as Pattern2 = Sinc(x) − 0.05. We also show the difference pattern (E/S function) as well as the σ and RMS values. The two images on the left are plotted on linear amplitude axes and the two on the right on logarithmic axes. The images on the top row represent subtraction of the two radiation patterns without normalisation and the second row shows the normalised case. It is worthwhile to note the following in these images:

- In the upper left-hand corner, the difference value is simply a constant value of 0.05, as expected and this difference is simply equal to the RMS value. Since the difference function has no variation, the standard deviation is zero.

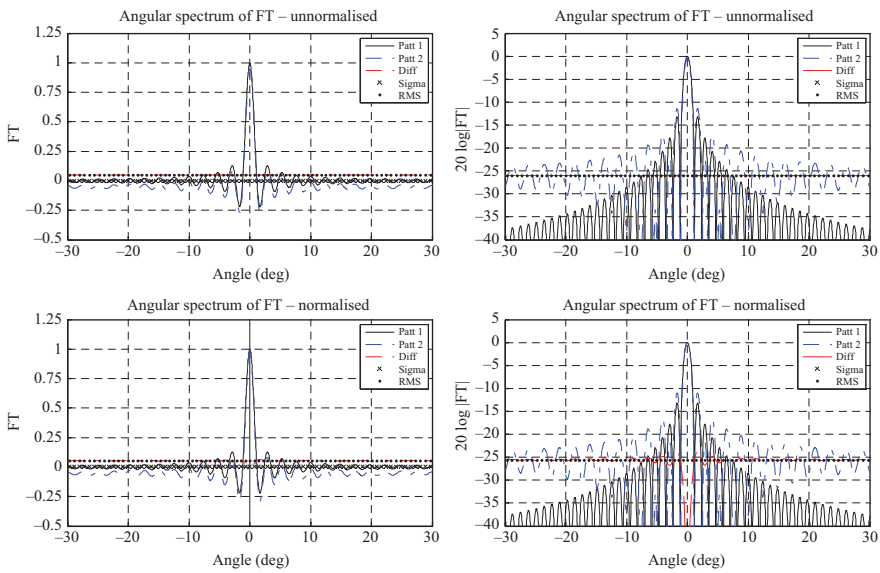

Figure 10.11 Pattern subtraction example #1 [Pattern1 = Sinc(x) and Pattern2 = Sinc(x) − 0.05], linear axes are shown on the left and logarithmic on the right. Radiation patterns are normalised in the bottom row

- In the upper right-hand corner, we see what appears to be very significant differences in the two radiation patterns, all due to the small 0.05 constant linear offset between Pattern1 and Pattern2. A seemingly insignificant result, but instructional and aids in the understanding of the difference calculation.[3] Again, since the difference function has no variation, the standard deviation is $-\infty$.
- In the lower right-hand corner is the most important observation to be made in that the two radiation pattern peaks are now of identical amplitude and the difference function approaches $-\infty$ at 0°.

In Figure 10.12, we overlay two similar radiation patterns (example #2), one denoted as Pattern1 = Sinc(x) and the second as Pattern2 = 0.9 Sinc(x). We also show the E/S distribution as well as the σ and RMS values. The two images on the left are again plotted on linear amplitude axes and the two on the right on logarithmic axes. The images on the top row represent subtraction of the two radiation patterns without normalisation and the second row shows the normalised case. It is worthwhile to note the following in these images:

- In the top row, we observe that the difference curves are simply attenuated versions of the original radiation patterns. Also, the RMS value and the σ values coincide, since the mean value of the difference curve is now zero.
- In the bottom row, one can make the important observation in that the normalisation removes the pattern differences and the difference pattern reduces to zero or $-\infty$ on the logarithmic scale. This is another way of stating that the addition of an amplifier or attenuator in the measurement system will affect absolute power level measurements, but relative pattern levels will remain unchanged. Again, a seemingly insignificant result, but very worthwhile to observe.[4]

Our third example is shown in Figure 10.13 and here we again overlay two similar radiation patterns (example #3), one denoted as Pattern1 = Sinc(x) and the second as Pattern2 = 0.9 Sinc($x + 0.2$). We again show the difference pattern, the σ and RMS values. The two images on the left are again plotted on linear amplitude axes and the two on the right on logarithmic axes. The images on the

[3]The simple subtraction of a constant to introduce a difference between the two radiation patterns is a non-physical radiation phenomenon in that it represents the addition of an angularly independent source of radiation. The circuit equivalent will be a DC offset to a time-varying signal. This constant value therefore introduces a non-zero mean value observed in the difference pattern and also highlights the difference between the calculated RMS and σ values. As stated, an insignificant result but instructional nevertheless.

[4]The simple multiplication by a constant to introduce a difference between the two radiation patterns is common in any measurement system in that it represents an amplifier or attenuator that may be present in the system. This amplifier or attenuator therefore does not change the zero mean value observed in the difference pattern and there is therefore no difference between the calculated RMS and σ values.

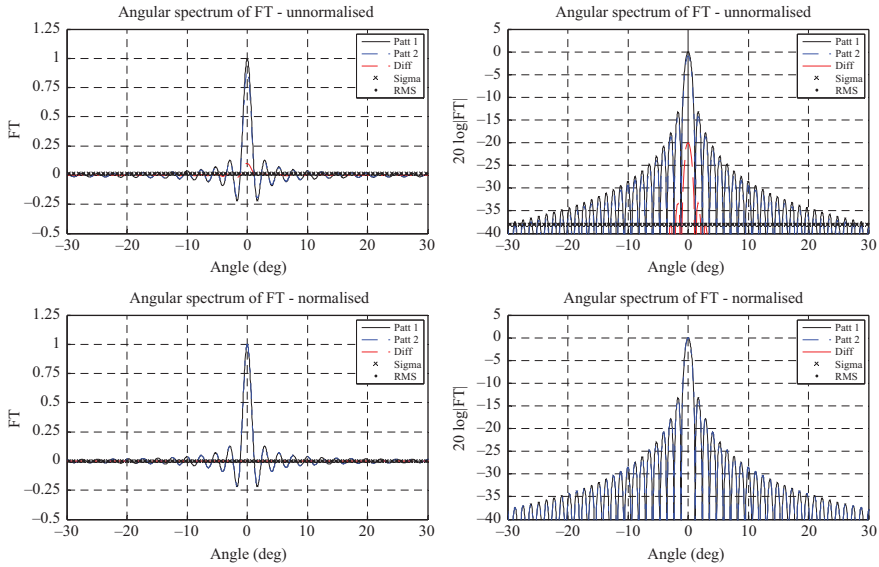

Figure 10.12 Pattern subtraction example #2 [Pattern1 = Sinc(x) and Pattern2 = 0.9 Sinc(x)], linear axes are shown on the left and logarithmic on the right. Radiation patterns are normalised in the bottom row

top row represent subtraction of the two radiation patterns without normalisation and the second row shows the normalised case. We note the following in these images:

- In all of these graphs, we note the relative shift of Pattern1 with respect to Pattern2, which is a phenomenon often encountered when comparing real measured radiation patterns.
- In all cases, the RMS value and the σ values coincide, since the mean value of the difference curve is zero.
- Most importantly, we note that the E/S distributions all have a zero value at exactly 0° in the normalised cases and in the un-normalised cases only at the angle where the main beams overlap.

Figure 10.14 shows a magnified portion of the logarithmic graphs of Figure 10.13 for clarity. When comparing the different curves in the region of the main beam (around 0°) for the two logarithmic scale graphs, the difference in magnitude is evident. The significance of this observation is that for parameters related to the absolute power level of the AUT main beam (i.e. gain, directivity and

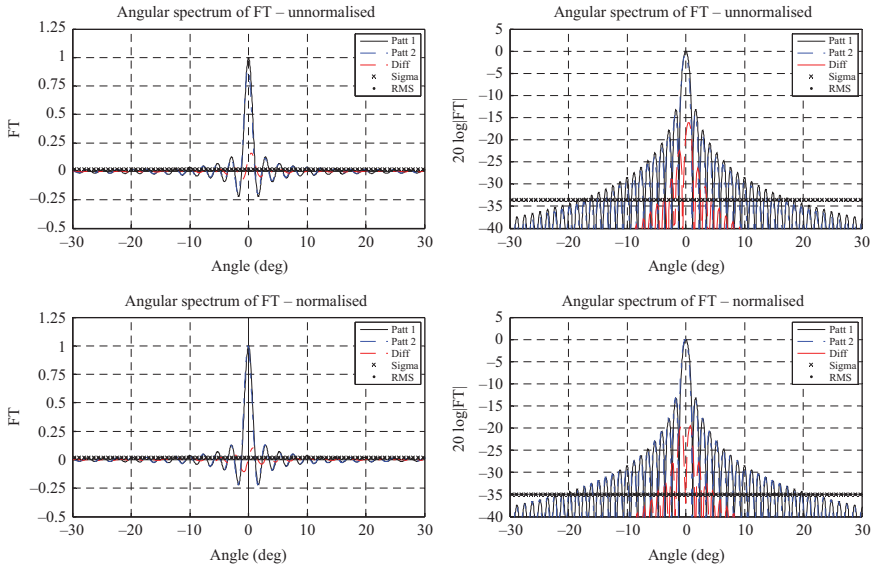

Figure 10.13 Pattern subtraction example #3 [Pattern1 = Sinc(x) and Pattern2 = 0.9 Sinc(x + 0.2)], linear axes are shown on the left and logarithmic on the right. Radiation patterns are normalised in the bottom row

peak far-field) we do NOT want to normalise radiation patterns when generating *E*/*S* distributions. However, for parameters that are measured relative to the main beam (i.e. side lobe level, cross-polarisation) we DO want to normalise radiations patterns when we generate *E*/*S* distributions. Figure 10.14 also shows the lower RMS value resulting from the normalisation of the two radiation patterns. The patterns being compared are therefore normalised to the peak of the main beam of each pattern so that the comparison is between relative rather than absolute side lobe levels.

To further increase confidence in the RMS or σ values derived from the *E*/*S* curves, the main beam region of the compared radiation patterns can be excluded from the calculation. As previously mentioned, the main beam parameters of gain, directivity and peak far-field are used to characterise the main beam region. By excluding the main beam region in the calculation of the σ value, the residual effect of main beam misalignment is eliminated and the calculated σ value is focussed on the side lobe region. Figure 10.15 shows the calculated σ value for the un-normalised and normalised cases where the main beams of the two radiation patterns being subtracted have been suppressed in the calculation. Comparing Figure 10.15 to Figure 10.14 clearly shows that the σ level reduced from -35 dB to -42 dB by excluding the main beam from the calculation. Another very useful technique is to use an *n*-point boxcar mean average to reveal the underlying trend of a highly oscillatory difference pattern (e.g. $n = 11$). This works well in as much as it can reveal trends in the patterns.

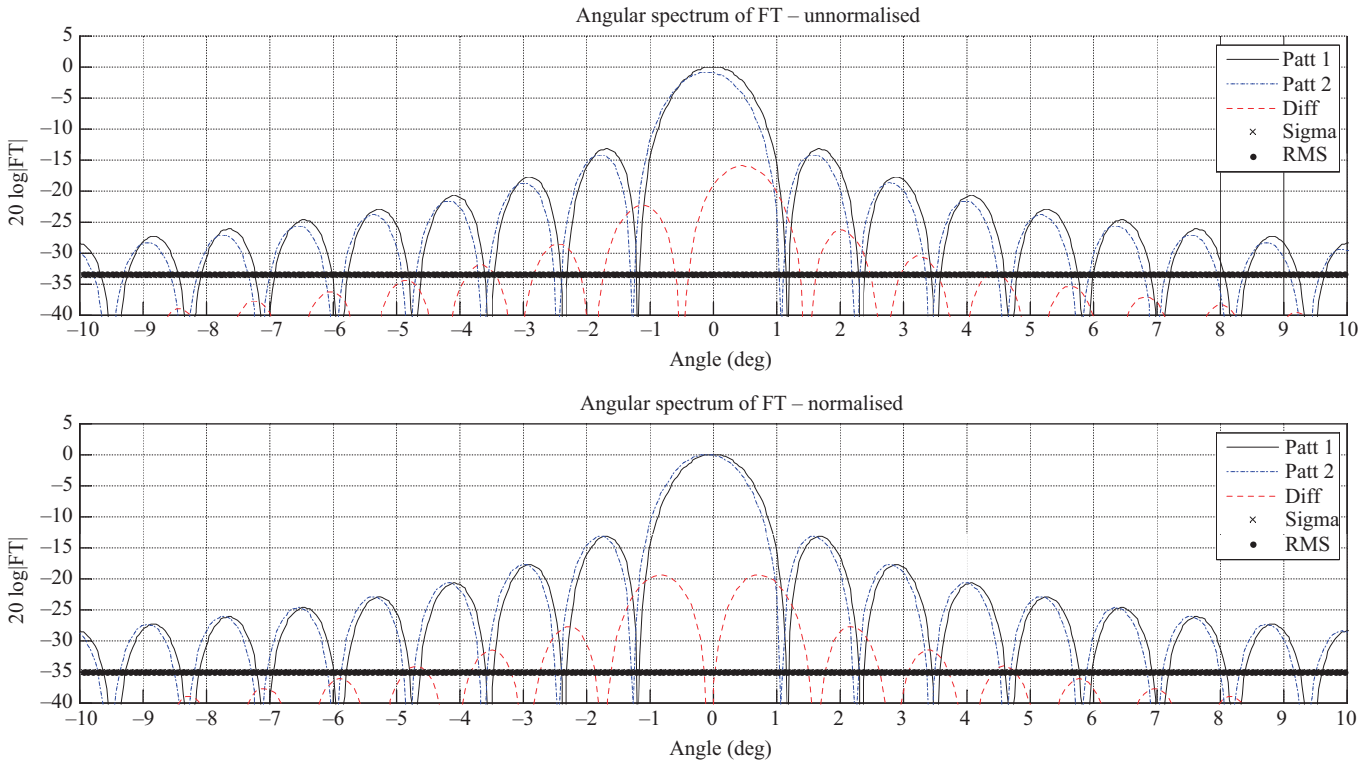

Figure 10.14 Pattern subtraction example #3 [Pattern1 = Sinc(x) and Pattern2 = 0.9 Sinc(x + 0.2)] enlarged view of logarithmic graphs; normalised at the bottom

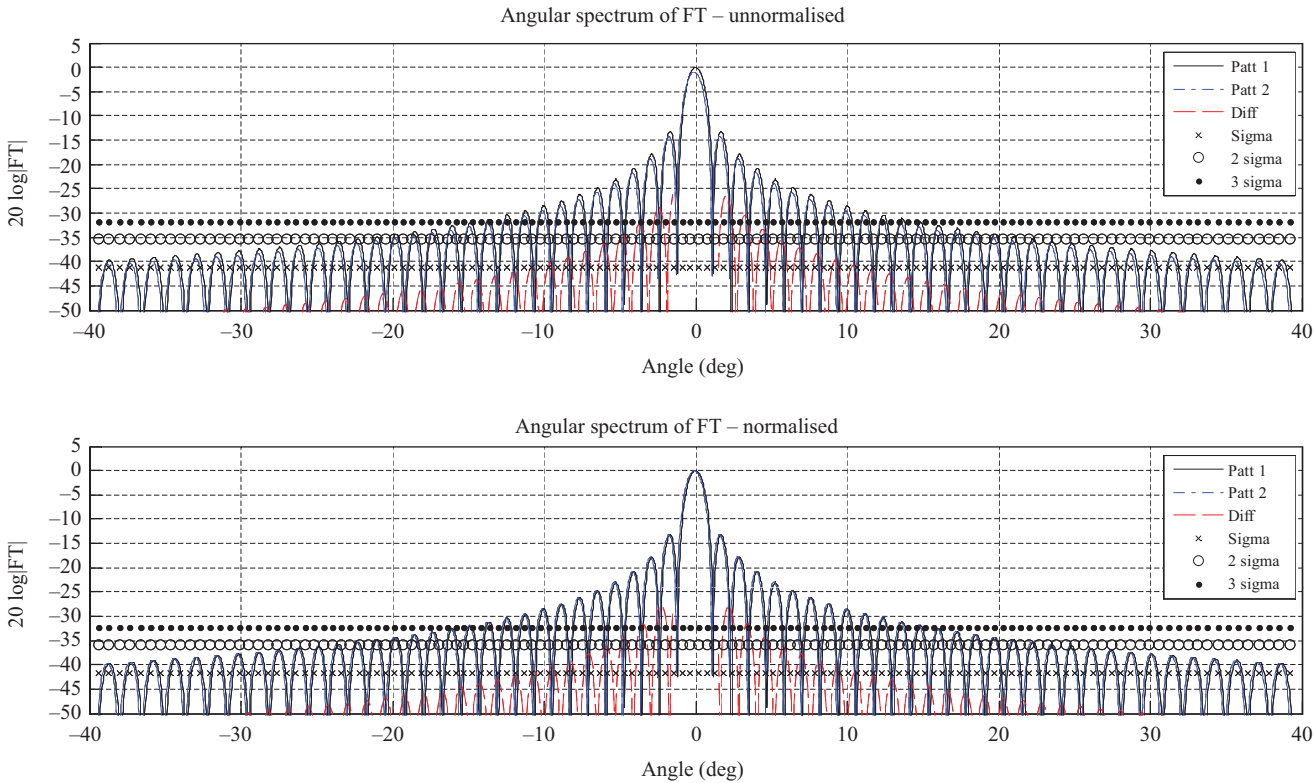

Figure 10.15 Pattern subtraction example #3 [Pattern1 = Sinc(x) and Pattern2 = 0.9 Sinc(x + 0.2)] showing normalised patterns at the bottom. Also shown are σ, 2σ and 3σ values extracted after suppression of the main beams in the difference pattern calculation

10.5 Probe/illuminator-related errors

The three error terms addressed in this section relate uncertainty in the near-field probe parameters to the measured far-field. More specifically, the uncertainty in the probe co-polarisation and cross-polarisation radiation patterns used for probe correction and any mechanical probe misalignment; the latter leading to an offset between what is used for probe correction in software during processing and what is actually affected during measurement. Near-field probe correction is required for all near-field measurements and is even applicable to far-field testing if one is interested in correction of the finite polarisation ratio of the range illuminator. In what follows, we divide probe correction into probe pattern correction and probe polarisation correction. Strictly speaking both of these concepts fall within the domain of 'probe correction', but due to approximations that are often made in practice, this division has value.

10.5.1 Probe relative pattern

When comparing the impact of probe correction on PNF, CNF or SNF measurements, one finds that this listed order also represents the order of decreasing significance. That is, PNF testing is affected most significantly by probe correction and SNF testing least and in many instances no probe correction is even performed for the latter. It therefore makes sense to use the PNF instance as a case study. For the purpose of this discussion, we opt to use the PNF formulation as presented in [8], where an azimuth/elevation coordinate system (and associated azimuth/elevation polarisation definition) is adopted (cf Sections 4.1 and 4.2). This formulation offers a unique framework for gaining insight into the factors influencing probe correction and we can write the fundamental equations relating measured spectra, probe spectra and desired AUT spectra for the PNF case as

$$\begin{aligned} D_A &= t_A s_A^{'} + t_E s_E^{'} = \text{Measured\_Spectrum\_}A \\ D_E &= t_A s_A^{''} + t_E s_E^{''} = \text{Measured\_Spectrum\_}E \end{aligned} \tag{10.12}$$

where

- t_A is the probe corrected complex spectrum of the AUT containing the azimuth-polarised component.
- t_E is the probe corrected complex spectrum of the AUT containing the elevation-polarised component.
- D_A is the measured (uncorrected) complex spectrum of the AUT containing the azimuth-polarised component.
- D_E is the measured (uncorrected) complex spectrum of the AUT containing the elevation-polarised component.
- $s_A^{'}$ is the complex spectrum of probe 1, usually selected to align with the AUT azimuth-polarised (H on axis) component.
- $s_A^{''}$ is the complex spectrum of probe 2, usually selected to align with the AUT elevation-polarised (V on axis) component.

We can now rewrite these equations to solve for t_A and t_E as

$$t_A = \frac{\frac{D_A}{s_A^{'}} - \frac{s_E^{'}}{s_A^{'}}\frac{D_E}{s_E^{''}}}{1 - \frac{s_E^{'}}{s_A^{'}}\frac{s_A^{''}}{s_E^{''}}} = \frac{\frac{D_A}{s_A^{'}} - \rho_s^{'}\frac{D_E}{s_E^{''}}}{1 - \frac{\rho_s^{'}}{\rho_s^{''}}} = \text{AUT\_Spectrum\_}A$$

$$t_E = \frac{\frac{D_E}{s_E^{''}} - \frac{D_A}{s_A^{'}}\frac{s_A^{''}}{s_E^{''}}}{1 - \frac{s_E^{'}}{s_A^{'}}\frac{s_A^{''}}{s_E^{''}}} = \frac{\frac{D_E}{s_E^{''}} - \frac{D_A}{s_A^{'}\rho_s^{''}}}{1 - \frac{\rho_s^{'}}{\rho_s^{''}}} = \text{AUT\_Spectrum\_}E \tag{10.13}$$

where we introduce the concept of a polarisation ratio, denoted as

- $\rho_s^{'}$ is the complex polarisation ratio of probe 1, nominally aligned to the AUT azimuth-polarised component and is $\ll 1$ if the probe is H-polarised.
- $\rho_s^{''}$ is the complex polarisation ratio of probe 2, nominally aligned to the AUT elevation-polarised component and is $\gg 1$ if the probe is V-polarised.

and these can be written as

$$\rho_s^{'} = \frac{s_E^{'}}{s_A^{'}}$$

$$\rho_s^{''} = \frac{s_E^{''}}{s_A^{''}}$$

The polarisation ratio can also be expressed in terms of two orthogonal linearly polarised (LP) components as

$$\rho = \frac{E_y}{E_x} e^{j\delta}$$

where

E_x = amplitude of electric field in the x-direction
E_y = amplitude of electric field in the y-direction
δ = phase by which the y-component leads the x-component

Table 10.6 [9] shows typical values for the polarisation ratio and how they relate to common polarisation states.

If we do assume that probe 1 is H-polarised and probe 2 is V-polarised, we see that the ratio of $\rho_s^{'}/\rho_s^{''}$ approaches 0 and then t_A can be simplified to

$$t_A = \frac{\frac{D_A}{s_A^{'}} - \rho_s^{'}\frac{D_E}{s_E^{''}}}{1 - \frac{\rho_s^{'}}{\rho_s^{''}}} \approx \frac{D_A}{s_A^{'}} - \rho_s^{'}\frac{D_E}{s_E^{''}} \tag{10.14}$$

and t_E can be simplified to

$$t_E = \frac{\frac{D_E}{s_E^{''}} - \frac{D_A}{\rho_s^{''}s_A^{'}}}{1 - \frac{\rho_s^{'}}{\rho_s^{''}}} \approx \frac{D_E}{s_E^{''}} - \frac{D_A}{\rho_s^{''}s_A^{'}} \tag{10.15}$$

Table 10.6 Definition of different states of the polarisation ratio and common polarisation states encountered. Reproduced with permission from Warren L. Stutzman, Polarization in Electromagnetic Systems, Norwood, MA: Artech House, Inc., 1993. © 1993 by Artech House, Inc. [9]

ρ_L	**State of polarisation**	**Comment**
0	Horizontal linear (HP)	$E_y = 0$
∞	Vertical linear (VP)	$E_x = 0$
$+j$	LHCP	$E_x = E_y$, $\delta = 90°$
$-j$	RHCP	$E_x = E_y$, $\delta = -90°$
$\text{Imag}(\rho_L) = 0$	Linear	$\delta = 0°$
$\text{Imag}(\rho_L) > 0$	Left-hand elliptical	$0° < \delta < 180°$
$\text{Imag}(\rho_L) < 0$	Right-hand elliptical	$-180° < \delta < 0°$
1	LP, $\tau = 45°$	$E_x = E_y$, $\delta = 0°$
-1	LP, $\tau = -135°$	$E_x = E_y$, $\delta = 180°$

Both of these equations now consist of two terms, the first being what can be called a 'pattern correction term' and the second a 'polarisation correction term' (cf Chapter 7). Their combined effect is best illustrated through a numeric example: Consider a probe 1 with 50 dB cross-polarisation suppression at some angle, the polarisation ratio $\rho_s^{'}$ will have a magnitude of 50 dB. If that same probe is rotated by 90° (to serve as probe 2) to measure the cross-polarisation component, $\rho_s^{''}$ will have a magnitude of −50 dB. We illustrate the effect of probe pattern and probe polarisation correction through the far-field radiation patterns shown in Figure 10.16 (AUT co-polarisation is shown at the top and cross-polarisation at the bottom). These patterns show the AUT co-polarisation radiation pattern without probe correction, with only probe pattern correction and with probe pattern and polarisation correction. The probe co- and cross-polarisation patterns are also shown superimposed, for reference. The effect of the probe pattern correction (complex division, logarithmic subtraction) is obvious in that the side lobes are raised.

The effect of the polarisation correction is more subtle and it is worthwhile to compute some numbers to gain further insight. If we consider the AUT co-polarisation pattern at −60° elevation, we see an uncorrected level of –64 dB, a partially corrected (probe pattern only) value of –57 dB and a probe co-polarisation pattern value of –7 dB. The AUT pattern is therefore raised by 7 dB to obtain the −57 dB pattern level. To now add the probe polarisation correction as well, we consider the polarisation correction term and at the –60° elevation angle the relevant values can be determined as

$$D_E = -70 \text{ dB}, s_E{}'' = -7 \text{ dB} \quad \text{and} \quad \rho_s{}' = 3 \text{ dB}$$

for a total $-\rho_s^{'}(D_E/s_E^{''})$ correction value of –66 dB or 501.2 μV. If we now convert the partially corrected signal level of –57 dB to a linear value, we obtain 1.413 mV. Depending on phasing, the corrected signal can therefore vary from

$$1.413 \text{ mV} - 501.2 \text{ μV} = 911.8 \text{ μV}(-61 \text{ dB})$$

to

$$1.413 \text{ mV} + 501.2 \text{ μV} = 1.914 \text{ mV}(-54 \text{ dB})$$

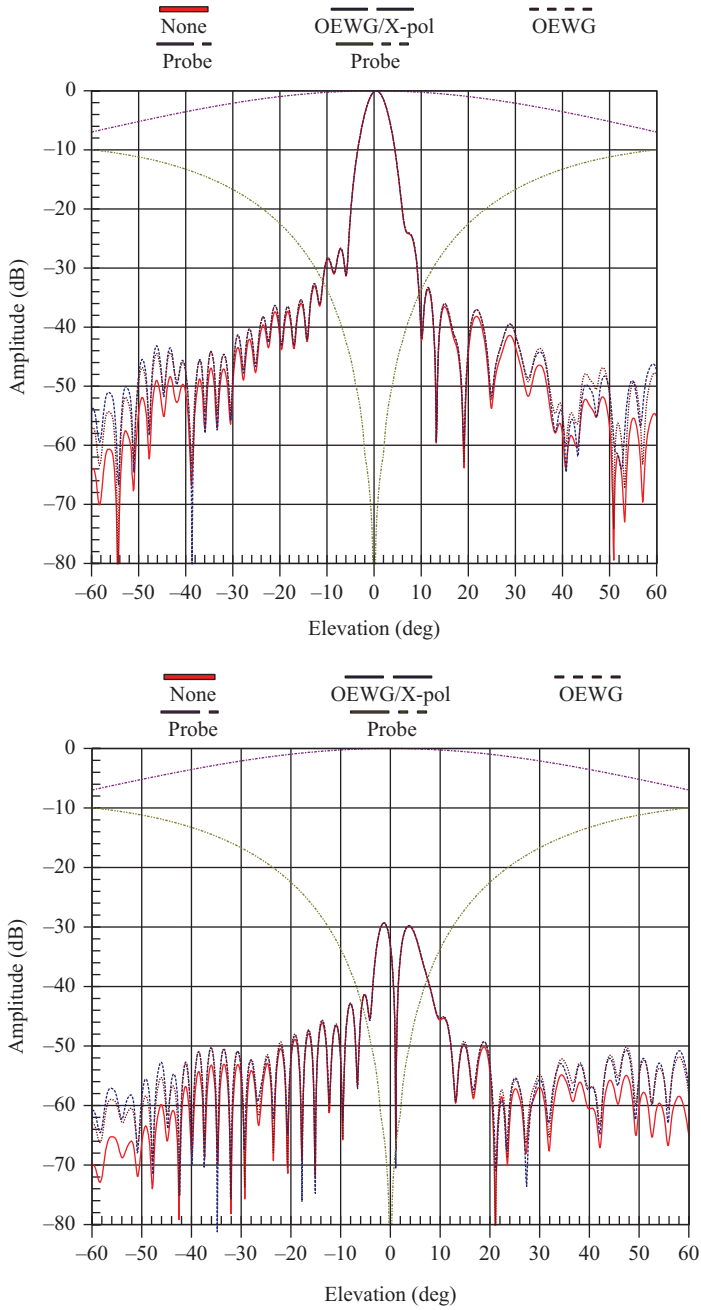

Figure 10.16 Far-field patterns are shown for the AUT without probe correction (none), with only probe pattern correction (OEWG) and with probe pattern and polarisation correction (OEWG/X-pol). AUT co-polarisation is shown at the top and cross-polarisation at the bottom

and this is confirmed in the cross-polarisation and co-polarisation results, respectively, shown in Figure 10.16.

If we also consider the cross-polarisation pattern at, say, $+60^\circ$ elevation, we see an uncorrected level of –65 dB, a probe pattern only corrected value of –58 dB and a probe co-polarisation pattern value of –7 dB. The AUT pattern is therefore raised by 7 dB to obtain the –58 dB pattern level. (Keep in mind that the probe has been rotated and that the probe co-polarisation pattern now applies to the cross-polarisation AUT pattern.) If we now want to add the probe polarisation correction as well, we have to evaluate the relevant terms as

$$D_A = -55 \text{ dB}, s_A'' = -7 \text{ dB and } \rho_s'' = -3 \text{ dB}$$

for a total $-D_A/\rho_s'' s_A'$ correction value of –51 dB or 2.818 mV. If we now convert the partially corrected signal level of –58 dB to a linear value, we obtain 1.259 mV. Depending on phasing, the corrected signal can therefore vary from

$$1.259 - 2.818 \text{ mV} = -1.559 \text{ mV } (-56 \text{ dB})$$

to

$$1.259 + 2.818 \text{ mV} = 4.077 \text{ mV} (-48 \text{ dB})$$

and this is again confirmed in Figure 10.16. We can therefore state that the AUT cross-polarisation pattern is affected by the AUT co-polarisation probe pattern corrected data, suppressed by the probe polarisation ratio of the probe used to measure the cross-polarisation data. It is therefore clear that without probe polarisation correction the performance of the probe can be crucial if reliable cross-polarisation data is to be measured in angular regions of high co-polarisation amplitudes.

The results presented in Figure 10.16 illustrate how the probe spectra affect the far-field result in the PNF case. This gives us the tools to assess the impact of uncertainty in the near-field probe spectra on far-field radiation patterns and we can divide this into an investigation of probe pattern correction and probe polarisation separately. The same process can be applied to CNF or SNF test cases with equal efficiency.

We now proceed to consider the case when neglecting the polarisation correction terms, in which case (10.14) and (10.15) can be reduced to

$$t_A \approx \frac{D_A}{s_A'}$$
$$t_E \approx \frac{D_E}{s_E''} \tag{10.16}$$

These equations show that PNF probe correction now simply reduces to a complex division in the spectral domain and involves separate and isolated pattern corrections for the azimuth and elevation spectra using probe 1 and 2 spectra, respectively. This part of the PNF probe correction is referred to as probe pattern only correction and neglects any probe polarisation leakage correction (which is

considered in the next section). Any uncertainty in the spectra of the probes only affect the measured far-field result in as far as the complex division process above describes. Figure 10.17 illustrates the effect of probe pattern uncertainty on the far-field; two far-field radiation patterns are overlayed. The first (designated Plot 1) is obtained with probe pattern shown as probe 1. A second (designated Plot 2) is obtained with a probe pattern shown as probe 2. The difference between the two probe patterns is subtle and is equivalent to the uncertainty in the measured or calculated probe pattern. We observe the resulting impact on the far-field and subtraction of the two far-field patterns allows us to extract an *E*/*S* curve as shown. The RMS value for this *E*/*S* curve is −78 dB and it is evident that there is no need to remove the effect of the AUT main beam in this case and this value (or multiples therefore if the 2σ or 3σ case is to be considered) can be used to estimate any side lobe uncertainty.

The result presented in Figure 10.17 is for a PNF case and would also apply to the elevation plane of a CNF system. A similar procedure can be applied for the CNF azimuthal plane and for the SNF case. However, as stated earlier, the impact

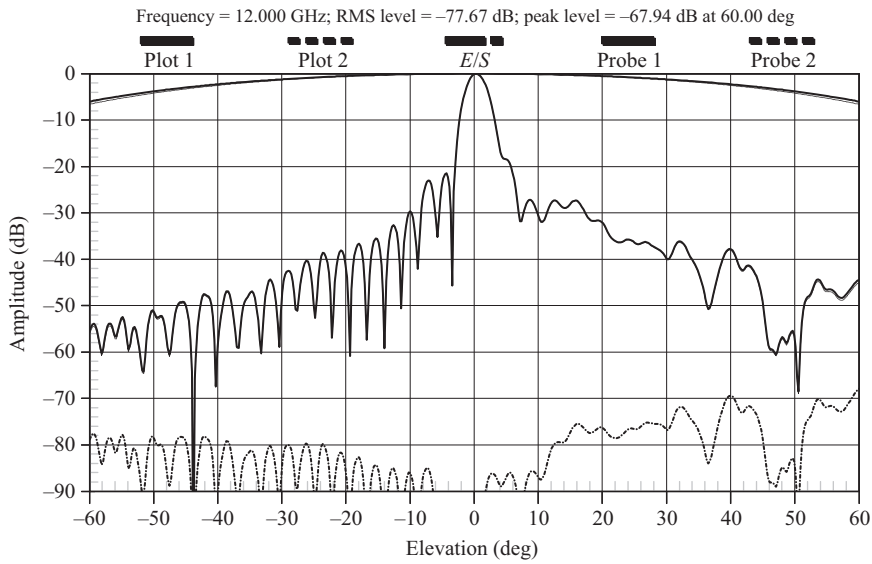

Figure 10.17 Two far-field radiation patterns are overlayed, one designated as Plot 1 is obtained with the probe pattern shown as probe 1. A second designated as Plot 2 is obtained with the probe pattern shown as probe 2. The difference between the two probe patterns is equivalent to the uncertainty in the measured or calculated probe pattern. Subtraction of the two far-field patterns gives rise to the E/S curve with a peak value of −68 dB and an RMS value of −78 dB

of probe pattern variation in both of these instances is much less significant than that observed here for the PNF case.

10.5.2 Probe polarisation purity

The probe polarisation ratio forms part of the full PNF probe correction process as expressed by (10.13). If complete probe correction is performed (complex co-polarisation and cross-polarisation probe pattern correction), the probe polarisation ratio is taken into account and this error term focusses simply on the impact of the uncertainty of the probe polarisation ratio on the derived far-field result. However, since polarisation correction is often neglected in near-field measurements, we can also assess the uncertainty introduced by this omission, which is often of more significance to the user.[5] In (10.14) and (10.15), we identified the polarisation correction terms as

$$t_{A\_\mathrm{Pol\_Correction}} \approx -\rho_s^{'} \frac{D_E}{s_E^{''}} \tag{10.17}$$

$$t_{E\_\mathrm{Pol\_Correction}} \approx -\frac{D_A}{s_A^{'}\rho_s^{''}} \tag{10.18}$$

These polarisation correction terms therefore consist of the probe pattern corrected spectrum of the **orthogonal polarisation**, weighted by the probe polarisation ratio of the probe used to measure the polarisation of interest. In other words, whatever signal is leaking through the probe (due to its finite cross-polarisation behaviour) is being removed.

To better understand the impact of the polarisation correction, it is worthwhile to momentarily look at the case where the near-field probe is facing the AUT (where $S_A^{'} = 1$ and $S_A^{''} = 1$) where (10.14) and (10.15) can be simplified to

$$t_A \approx D_A - \rho_s^{'} D_E \tag{10.19}$$

$$t_E \approx D_E - \frac{D_A}{\rho_s^{''}} \tag{10.20}$$

since the on-axis probe pattern correction terms are simply unity. If we now evaluate these two equations for a near-field probe with say 30 dB on-axis cross-polarisation performance (and used for measuring both polarisations by rotating the probe), we obtain

$$t_A \approx D_A - 0.032 D_E \tag{10.21}$$

$$t_E \approx D_E - 0.032 D_A \tag{10.22}$$

[5]It is also worthwhile to consider that probe polarisation correction without probe pattern correction is a feasible technique for correction of far-field range test data. For instance, if the on-axis polarisation ratio of a range illumination antenna is known, this type of correction can be applied to counter the effect of cross-polarisation leakage.

since[6] $\rho_s^{'} = 0.032 = 1/\rho_s^{''} = 1/31.623$. These equations therefore show how the measured result can be corrected for leakage through the near-field probe. It is worthwhile to note that if the AUT is nominally azimuth-polarised, with a **measured uncorrected** −20 dB suppressed elevation-polarised pattern, the corrected spectrum t_A will not be affected significantly by this correction, but the elevation-polarised spectrum t_E will. This can be demonstrated by evaluating the relative signal levels as

$$t_A \approx D_A - 0.032D_E = 1 - 0.032(0.1) = 0.997 = -0.028 \text{ dB}$$
$$t_E \approx D_E - 0.032D_A = 0.1 - 0.032(1) = 0.068 = -23.35 \text{ dB}$$

If the probe was characterised, the uncertainty in the co-polarisation and cross-polarisation patterns allows one to calculate a $\Delta\rho_s^{'}$ and a $\Delta\rho_s^{''}$ from which a corresponding far-field uncertainty can be obtained. As mentioned earlier, the other case of interest is the case when the probe polarisation ratio is neglected. This condition obviously requires a near-field probe that is nominally polarisation matched to the AUT (e.g. a V-polarised AUT and a V-polarised near-field probe) and one relies on the cross-polarisation rejection of the near-field probe to suppress the unwanted cross-polarisation signal of contaminating the co-polarised measurement. If we again consider the case of an AUT that is nominally azimuth-polarised, with a **measured uncorrected** −20 dB suppressed elevation-polarised pattern, we can calculated the uncertainty in the corrected spectra t_A and t_E due to the finite polarisation ratio of the near-field probe as[7]

$$t_A \approx D_A \pm 0.032D_E = 1 \pm 0.032(0.1) = 0 \pm 0.028 \text{ dB}$$
$$t_E \approx D_E \pm 0.032D_A = 0.1 \pm 0.032(1) = -20 \text{ dB} \pm 3.35 \text{ dB}$$

It is important to realise that although the result above was derived for the PNF spectral case (this was also done in Chapter 7 for the CNF case), when probe pattern correction is neglected (which is often very feasible for SNF testing and applicable to all far-field test cases) these equations can be applied to do polarisation correction to the measured co-polarisation and cross-polarisation signals if the complex polarisation ratios are known. On a far-field range, we can use this to correct for finite cross-polarisation performance of the range illuminator (in this case we simply substitute the polarisation ratio of the range illuminator for that of the near-field probe). These equations show that if the finite polarisation ratio of the range illuminator is known, the unwanted leakage of the orthogonal polarisation during measurement can be removed. It is important to keep in mind that this correction term is complex and therefore amplitude and phase is to be acquired during measurement and phase stability needs to be maintained; all aspects that are usually complied with in a near-field measurement, but not necessarily for far-field testing.

[6]It is important to remember that the polarisation ratio is complex and that relative phase of the polarisation components are needed to do this correction. In this simple example, we assume that the phases of the polarisation components are identical.

[7]As mentioned earlier, the logarithmic measurement uncertainty bounds are not symmetrical. Here, we selected the largest value and show that as the symmetrical uncertainty bound.

It is worthwhile to point out that our assumption of an AUT which is nominally Azimuth polarised (and linear) only aids in the understanding of the equations and does not in any way reduce the general validity of the probe correction formulation. In cases where the AUT polarisation does not align with one of the near-field probes being used, the simplifying isolation of terms we performed here cannot be made blindly and both probe pattern and polarisation correction terms become equally important. Examples of this would be when a slant linear or circularly polarised AUT is measured using linearly polarised probes.

10.5.3 Probe alignment

Probe mechanical misalignment introduces an angular uncertainty between the probe as used during measurement and the expected performance of the probe. In alternate terms, the near-field probe correction being performed and the actual near-field performance of the probe may not match due to mechanical misalignment. This misalignment can be in pointing of the probe axis (leading to an angular pattern shift of the probe) and a rotation of the probe polarisation axis (leading to misalignment of the polarisation vector).

Probe axial pointing misalignment: Since most near-field probes have fairly broad beams, this type of misalignment is usually not a significant contributor to measurement uncertainty. It further affects PNF measurements most (and also CNF measurements along the elevation axis). This error is almost never a concern for SNF or far-field measurements since the AUT is only illuminated by a limited angular region of the probe pattern and is therefore inconsequential unless the pointing misalignment is very severe. The impact on PNF and CNF measurements can be assessed by first estimating the actual probe angular misalignment and this is best achieved by considering the actual method of probe alignment during mounting. In the case of a vertical PNF or CNF scanner, a spirit level can be used to determine the probe alignment w.r.t. gravity and this is easily achieved within $\pm 0.05^\circ$ uncertainty. In the orthogonal plane, alignment may require alternative methods or specialised fixtures. However, alignment to within the stated angular uncertainty is achievable and this number can therefore be used to assess the impact of this error source.

If we observe the probe pattern in Figure 10.16, it is clear that the slope of the pattern is highest at the angular extremes and the slope is roughly 0.2 dB/°. Using this slope and the estimated angular alignment uncertainty of the probe, we can calculate that the far-field measurement uncertainty will be $\pm 0.05/^\circ \times 0.2$ dB/° $= \pm 0.01$ dB, worst case. This number will of course increase if probe alignment is worse than that assumed here or if the probe slope pattern increases. However, it is clear that this error term is fairly easy to assess and mitigate for co-polarised patterns, in case it proves to be a concern.

When considering cross-polarisation AUT patterns, we also have to consider the shape of the cross-polarisation pattern of the probe since these often contain deep nulls that can be highly sensitive to small angular variations. Looking at the

measured pattern data for an open-ended rectangular waveguide shown in Figure 10.18, we see a minimum cross-polarisation level of −98 dB and a steep pattern slope of about 15 dB/°, which implies an induced cross-polarisation error of ±0.75 dB in cross-pol null depth for the stated ±0.05° alignment uncertainty.

We can now evaluate (10.19) and (10.20) in order to assess the uncertainty induced in the measured AUT co and cross-polarisation pattern level due to this induced cross-polarisation uncertainty caused by probe misalignment. One immediately observes that the impact on measured co-polarisation pattern is negligible and the cross-polarisation term remains the only one to be evaluated and this can be done as before. Since probe polarisation ratio phase is often not known or may be unreliable since these are very low level signals to measure we simply assess this uncertainty as if no phase information is available.

Probe polarisation tilt misalignment: This error term relates the uncertainty in alignment of the probe polarisation reference to the uncertainty in the measured far-field. To help gain insight into the factors at work here, we can consider a near-field probe that is nominally horizontally polarised and has an on-axis cross-polarisation level of −50 dB. This probe will therefore have a horizontally polarised field component as well as a vertically polarised field component that is suppressed by 50 dB. We therefore see that if the two vector components are in phase, the electrical polarisation tilt of the probe will be 0.18° (we can refer to this as angle τ).

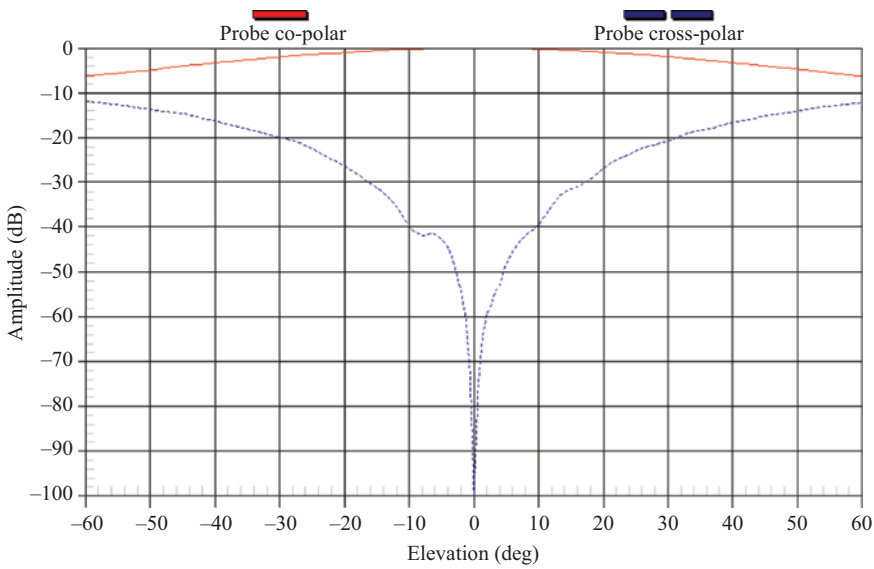

Figure 10.18 Measured rectangular open ended waveguide probe co-polarisation and cross-polarisation patterns

This number is obtained from

$$\text{Tilt} = \tau = \arctan\frac{E_y}{E_x} = \arctan\frac{10^{-50/20}}{10^{0/20}} = 0.18^\circ$$

If we mount the probe and there is any mechanical polarisation misalignment introduced, we are perturbing angle τ. If our mounting is perfect and there is no perturbation of τ, our probe correction will take care of the 0.18° electrical tilt of the polarisation vector. However, if we do introduce a polarisation tilt uncertainty, we will effectively introduce unwanted co-polar/cross-polarisation coupling into our measurement and we can estimate the effect of this as follows. If we now look at the polarisation ratio again, which was expressed as

$$\rho = \frac{E_y}{E_x}e^{j\delta}$$

we can define a $\Delta\tau$ angular polarisation alignment uncertainty and we can assess the impact on the measured far-field pattern by estimating the perturbed probe polarisation ratio as

$$\rho_{\text{Perturb}} = \frac{E_y \cos\ \Delta\tau + E_y \sin\ \Delta\tau}{E_x \cos\ \Delta\tau + E_x \sin\ \Delta\tau}e^{j\delta}$$

where we simply calculate the field component cross-coupling due to the $\Delta\tau$ uncertainty. If we now consider a horizontally polarised probe with −50 dB cross-polarisation (and $\delta = 0$) and $\Delta\tau = \pm 0.05^\circ$, we see that

$$\rho_{\text{Perturb}} = \frac{0.0032 \pm 0.001}{1 \pm 0.0032\ (0.001)} = -50\ \text{dB} \pm 2.77\ \text{dB}$$

By evaluating (10.19) and (10.20), one can now assess the impact on both the co-polarisation and cross-polarisation measurement values due to this polarisation vector alignment uncertainty. One should note that this error term is usually only a concern for cross-polarisation measurements, since it is negligible for most co-polarised quantities.

10.6 Mechanical/positioner-related errors

As the title of this section suggests, we have to assess all types of positioning errors when conducting any type of range assessment, and these can be listed as follows:

Type of tests system	Scanning axis positioning errors	Distance errors
PNF	(x, y) – Linear	z – Linear
CNF	(ϕ, z) – Angular and linear	ρ – Linear
SNF	(θ, ϕ) – Angular	r – Linear
Far-field	(θ, ϕ) – Angular	r – Linear

Of these positioning errors, the angular terms related to far-field testing have a one-to-one correspondence to the measured data and are therefore easy to assess. Any uncertainty in angle will translate directly to an angular measurement uncertainty and the slope of the radiation pattern will determine the measured amplitude uncertainty. Any radial distance variation will affect measured far-field phase, but since phase is rarely of interest in a far-field measurement this is not of concern to us.

For the near-field techniques, the PNF (x, y, z) positioning uncertainties have been studied extensively and will be discussed at length below. Limited work has been done on the CNF probe (ϕ, z, ρ) positioning uncertainties [10] and we will present results illustrating assessment of radial distance uncertainty. However, the work presented here should only be regarded as a proposed methodology for studying these parameters and certainly do not represent the final word on this subject. Further investigation into this matter is warranted. A similar statement can be made regarding SNF probe (θ, ϕ, r) positioning uncertainties [2,11,12] and we will present limited results illustrating assessment of axis non-intersection errors below. This work should again be regarded as a proposed methodology for studying these parameters and is not exhaustive.

10.6.1 AUT alignment

This error term applies equally to PNF, CNF, SNF and far-field test systems. AUT alignment impacts measured beam pointing and is regarded as the difference between the electrical and mechanical pointing directions of the AUT. This parameter is usually of interest for high gain antennas where a very narrow beamwidth makes physical pointing of the AUT critical. In cases where an antenna is being used as part of a tracking radar, the significance of the difference between the mechanical pointing direction of the AUT and the corresponding electrical pointing direction becomes obvious.

Conceptually AUT alignment uncertainty is directly related to the uncertainty associated with mounting an antenna in a test range and aligning the mechanical references of the antenna with the mechanical reference within the test range. Due to the many different ranges and AUT configurations encountered, a detailed description of alignment procedures and techniques is not feasible or practical. However, an understanding of the fundamental surfaces or axes within an antenna test range that form the mechanical references are sufficient to allow one to construct an alignment procedure within a specific antenna test range for a specific AUT. For the different types of facilities, we can describe these as follows:

PNF: In the case of PNF measurements, we make the assumption that the scan plane is perfectly flat and this plane itself becomes our reference surface for alignment purposes. Although there is no fundamental need for this plane to be parallel or orthogonal to gravity, it is most often the case and this can simplify the alignment process considerably. The definition of the scan plane is often established with a laser tracker or theodolite and the vector normal (z-axis) to this plane then becomes our mechanical reference axis for alignment. The specific location of the probe (0, 0, 0) position defines the

coordinate system origin but is not relevant for the AUT pointing alignment. Detailed information on the measurement and subsequent correction of antenna-to-range alignment can be found in [13].

CNF: In the case of CNF measurements, we make the assumption that the scan plane is described by a perfect cylinder. The coaxial axis of the cylinder becomes one reference for alignment purposes. Although there is no fundamental need for this axis to be parallel to gravity, it is most often the case and this can simplify the alignment process considerably. Our second alignment reference is the $\phi = 0$ position of the phi positioner. We therefore align the AUT w.r.t. this zero position mechanically for alignment purposes. Any misalignment of the AUT w.r.t. the $\phi = 0$ position will manifest as a far-field angular beam shift in the ϕ-plane.

SNF and far-field: In the case of both SNF and far-field measurements, a spherical coordinate system is defined and the mechanical alignment of the AUT with respect to the $\theta = \phi = 0$ location within this coordinate system is our objective. If we consider a traditional ϕ/θ (roll/azimuth) positioner, the θ-axis is a vertical axis of rotation and the ϕ-axis is a horizontal axis of rotation and alignment of the AUT mechanical reference w.r.t. the angular zero positions is our objective. We therefore align the AUT w.r.t. this zero position mechanically for alignment purposes and any angular shift within this coordinate system will manifest itself as an identical angular shift in the far-field.

CATR: AUT alignment for a CATR is identical to that of any far-field range with the added complexity of establishing the exact angle of incidence of the plane wave emanating from the CATR reflector. This can be achieved through precise rotation of the AUT as described in [14] or by measuring the phase of the field distribution across the aperture of the AUT. This can be achieved by using a linear scanner and determining the angle of incidence based on the slope of the measured phase. By repeating this for two orthogonal planes, the plane wave angle of incidence can be uniquely determined and compensated for. This can be done through mechanical alignment adjustment of the AUT or correction in software after completion of the measurement. It can also be undertaken using the RCS of a 'flat plate' as the AUT (see Section 5.4.4 in Chapter 5).

10.6.2 PNF probe (x, y) position error

When PNF data is acquired, it is usually assumed that the acquisition grid is regular. That is, that samples are spaced at equal intervals along the x or y axes (Δx does not have to be equal to Δy). The requirement for such a regular grid is a result of using an FFT to perform the spectral transformation implicit in the PNF process and any deviation from this grid introduces an inherent uncertainty in the measurement. A way to overcome this limitation is to record actual probe x and y location information and using a DFT (that does not rely on a regular grid) for the spectral transformation process. However, even if this approach is taken, any uncertainty in probe x and y location with respect to that reported by the device

used to measure position will result in a similar (albeit reduced) measurement uncertainty. This uncertainty term assesses the impact of this probe position information on measured far-field results.

The angular spectrum of interest is computed from a partial knowledge of the tangential components of the aperture field distribution of the AUT or the tangential components of the field distribution over a finite parallel plane at $z = d$ in front of the radiator (i.e. the scan plane). As shown in [13], the angular spectrum can be immediately obtained from the tangential electric field components using

$$\underline{F}_T\left(k_x, k_y, z = d\right) = \int_{-\infty}^{\infty}\int_{-\infty}^{\infty} \underline{E}_T(x, y, z = d)e^{j\left(k_x x + k_y y\right)}dxdy$$

which becomes

$$\underline{F}_T\left(k_x, k_y, z = d\right) = \int_{-\frac{1}{2}L_y}^{\frac{1}{2}L_y}\int_{-\frac{1}{2}L_x}^{\frac{1}{2}L_x} \underline{E}_T(x, y, z = d)e^{j\left(k_x x + k_y y\right)}dxdy$$

if the finite region of the scan plane is considered. Here, L_x and L_y are the linear dimensions of the scan plane in the x and y directions, respectively. Without a loss of generality, we can continue studying this source of measurement uncertainty by considering only the single dimensional case of

$$\underline{F}_T(k_x, z = d) = \int_{-\frac{1}{2}L_x}^{\frac{1}{2}L_x} \underline{E}_T(x, z = d)e^{jk_x x}dx$$

If we now assume a constant measured field distribution (and zero phase) across the entire scan plane, this Fourier integral reduces to the familiar Sinc function

$$\underline{F}_T(k_x, z = d) = \int_{-\frac{1}{2}L_x}^{\frac{1}{2}L_x} e^{jk_x x}dx = L_x \frac{\sin\left(\frac{k_x L_x}{2}\right)}{\frac{k_x L_x}{2}}$$

which can also be expressed in terms of angular space as

$$\underline{F}_T(k_0 \sin\theta, z = d) = \int_{-\frac{1}{2}L_x}^{\frac{1}{2}L_x} e^{jk_0 x \sin\theta}dx = L_x \frac{\sin\left(\frac{\pi \sin\theta L_x}{\lambda}\right)}{\frac{\pi \sin\theta L_x}{\lambda}}$$

If we again consider the case of an arbitrary measured field distribution and know the exact positions along the x-axis where these electric field values were acquired, this Fourier integral can be evaluated numerically to obtain the spectrum $\underline{F}_T$ as

$$\underline{F}_T(k_0 \sin\theta, z = d) = \int_{-\frac{1}{2}L_x}^{\frac{1}{2}L_x} \underline{E}_T(x, z = d)e^{jk_0 x \sin\theta}dx$$

and in the case where there is some uncertainty Δx associated with the measurement locations as

$$\underline{F}'_T(k_0 \sin\theta, z = d) = \int_{-\frac{1}{2}L_x}^{\frac{1}{2}L_x} \underline{E}_T(x', z = d)e^{jk_0 x \sin\theta}dx$$

where $x' = x \pm \Delta x$. Using a DFT to evaluate both integrals then allows for the evaluation of an error term

$$\frac{E}{S}(\theta) = |\underline{F}_T^{'}(\theta)| - |\underline{F}_T(\theta)|$$

This is illustrated below where a $L_x = 2.4$ m linear aperture and scan plane is considered and a random position uncertainty of ± 1 mm is introduced. The position error is shown as the top graph in Figure 10.19 with the spectra (calculated at 3 GHz) shown at the bottom.[8] There are four spectra overlaid, the Sinc function as a reference, the spectrum extracted using an FFT (so no position error introduced), the spectrum F_T (DFT evaluated using the precise locations of each measurement point) and the spectrum $F_T^{'}$ (DFT evaluated using the approximate locations of each measurement point). It is clear that all of these results match closely to the observer comparing the graphs. Evaluation of the difference between F_T and $F_T^{'}$ provides the signal to error response shown as E/S at a level of <-65 dB. In this instance, the position uncertainty introduced is $\pm 1/100\lambda$ and the resulting E/S level is fairly low. However, one should be cognisant of the fact that the direction of radiation in this case is orthogonal to the linear axis of motion and in order to fully assess the impact of the position uncertainty one has to consider radiation in non-orthogonal directions as well.

This error term can be evaluated for arbitrary angles of radiation by simply introducing a phase slope across the radiating aperture. This can be expressed as

$$\underline{F}_T(k_0 \sin\theta, z = d) = \int_{-\frac{1}{2}L_x}^{\frac{1}{2}L_x} \underline{E}_T(x, z = d) e^{jk_0 x \sin\theta_0} e^{jk_0 x \sin\theta} dx$$

where θ_0 is the direction of propagation of interest. If an angle of -30° is selected and we retain the random position uncertainty of ± 1 mm we can extract the corresponding spectra (calculated at 3 GHz) shown in Figure 10.20. There are again four spectra overlaid, the Sinc function as a reference (here still shown at 0°), the spectrum extracted using an FFT (so no position error introduced), the spectrum F_T (DFT evaluated using the precise locations of each measurement point) and the spectrum $F_T^{'}$ (DFT evaluated using the approximate locations of each measurement point). Evaluation of the difference between F_T and $F_T^{'}$ provides the error to signal response shown as E/S at a level of <-50 dB in this instance. The reason for this increase lies in the fact that there is now a phase slope associated with the measured aperture distribution and therefore any positional uncertainty is directly translated to a measured phase uncertainty. Since this phase slope increases for larger angles θ_0, one would expect higher sensitivity to probe positional uncertainty in x (or y) as θ_0 approaches $\pm 90^\circ$. This is evident when we extract the maximum E/S value for $-80^\circ < \theta_0 < 80^\circ$ as shown in Figure 10.21.

[8]In this analysis, we assume that E_T is simply a constant with no phase variation. As shown below, we do introduce a phase slope to consider arbitrary directions of propagation to consider all instances of phase variation. In reality, the technique described here can be applied to any measured E_T and the impact of probe position uncertainty assessed for the actual AUT of interest.

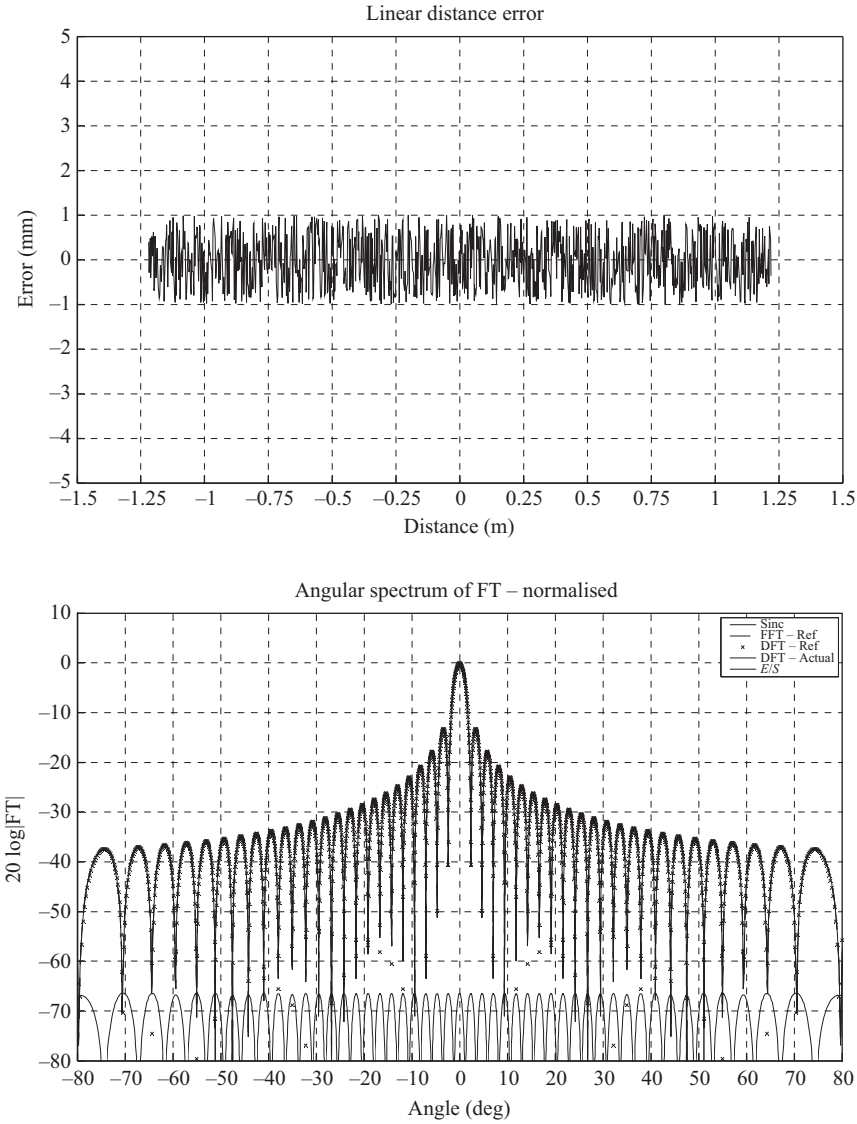

Figure 10.19 Random position error of ±1 mm introduced (top). Four spectra are shown overlaid for $\theta_0 = 0°$ (bottom); Sinc function, spectrum extracted using an FFT (so no position error introduced), the spectrum F_T and the spectrum F_T' and E/S at a level of <-65 dB

The random position uncertainty considered up to this point is interesting to assess and one can observe that the PNF measurement process is actually fairly tolerant to large uncertainty values. However, in practice, such purely random uncertainties are quite rare and most uncertainties observed are actually systematic

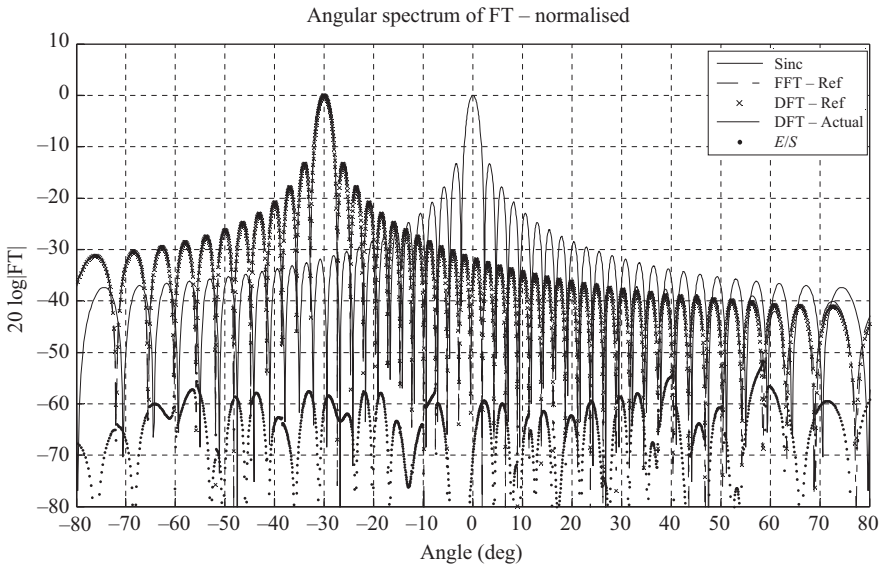

Figure 10.20 Random position error of ±1 mm introduced. Four spectra are shown overlaid for $\theta_0 = 0°$; Sinc function, spectrum extracted using an FFT (so no position error introduced), the spectrum F_T and the spectrum F_T' and E/S at a level of <-55 dB

in nature. One such uncertainty is that due to a faulty scale factor (this can be as simple as an incorrectly tuned control system or set scale factor, or a more subtle effect of a stretching drive belt).

This is illustrated below where an $L_x = 2.4$ m linear aperture and scan plane is considered and a linear position uncertainty of ±1 mm per metre is introduced. The position error is shown as the top graph in Figure 10.22 with the spectra (calculated at 3 GHz) shown at the bottom. In this case, a direction of radiation of $-30°$ is again selected and there are two spectra overlaid, F_T, F_T' and the difference shown as E/S at a level of <-35 dB in this instance. Also shown are the maximum E/S values for $-80° < \theta_0 < 80°$ where the latter again shows the increased sensitivity to probe positional uncertainty in x (or y) as θ_0 approaches $\pm 90°$. Also of interest to observe here is that this type of positional error introduces an apparent broadening of the measured main beam of the AUT as is evident from the E/S curve.

Another positional uncertainty that is common for rack and pinion driven scanners is a cyclical one, usually as a result of rack pitch variations. This can be modelled by introducing a sinusoidal position error in the probe position. This is illustrated below where an $L_x = 2.4$ m linear aperture and scan plane is considered and a sinusoidal position uncertainty of ±1 mm amplitude is introduced. The position error is shown as the top graph in Figure 10.23 with the spectra (calculated at 3 GHz) shown at the bottom. In this case, a direction of radiation of 60° is selected and there are two spectra overlaid, F_T and F_T', and the difference shown as

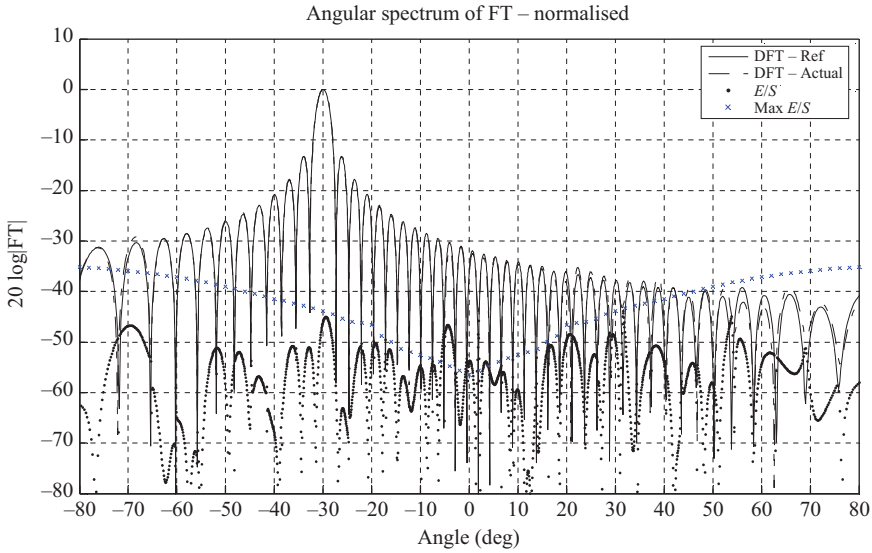

Figure 10.21 Random position error of ±5 mm introduced. Two spectra are shown overlaid; F_T and the spectrum F_T' and E/S at a level of <−45 dB. Also shown (×) are maximum E/S values for $-80° < \theta_0 < 80°$

E/*S* at a level of <−30 dB in this instance. Also shown are the maximum *E*/*S* values for $-80° < \theta_0 < 80°$.

It is worthwhile to observe in this case the impact of the sinusoidal position uncertainty at a very specific spectral location (roughly −10°) as shown by the *E*/*S* curve. If the period of the sinusoidal variation is extended (i.e. slower spatial variation), this position translates closer to the spectrum maximum.

If we now turn our attention to measured positional errors for a linear axis of motion with rack and pinion drive (results are provided courtesy of NSI-MI Technologies LLC), the error curve shown in Figure 10.24 is obtained.

This positional uncertainty can now be used to assess scanner performance without making any assumptions related to the behaviour of the mechanical positioner. This is illustrated below where an $L_x = 2.4$ m linear aperture and scan plane is again considered at 3 GHz and now also 6 GHz. In this case, a direction of radiation of 45° is selected and there are two spectra overlaid, F_T, F_T' and the difference shown as *E*/*S*. The results are presented in Figure 10.25 with the 3 GHz result shown at the top and the 6 GHz result at the bottom. In both cases, the maximum *E*/*S* values are also shown for $-80° < \theta_0 < 80°$. It is clear by comparing these two results that probe *x* (or *y*) position uncertainty not only becomes a bigger concern at larger angles of radiation, but also at higher frequencies.

10.6.3 PNF probe z-position (planarity) error

When PNF data is acquired, it is assumed that the probe *z*-position is fixed, or alternatively that the scanner describes a perfectly flat plane. This is a crucial

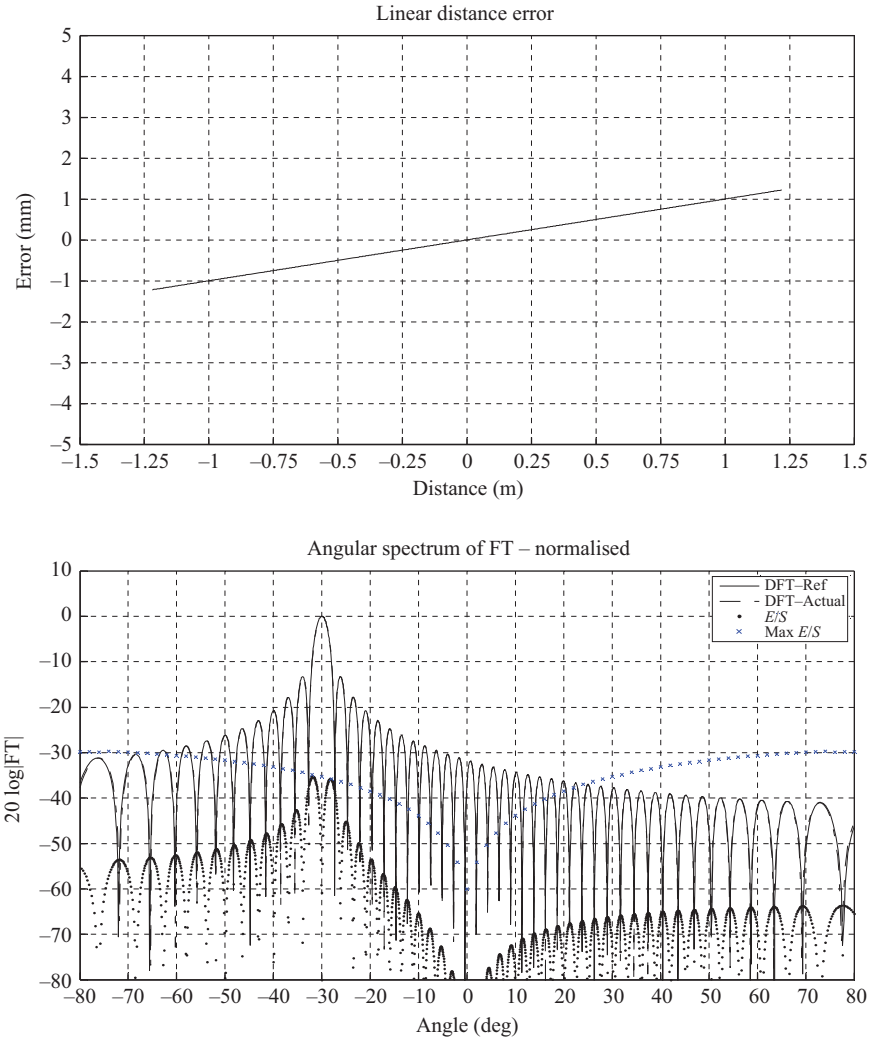

Figure 10.22 Linear position error of ±1 mm/m introduced (top). Two spectra are shown overlaid (bottom); F_T and the spectrum $F_T^{'}$ and E/S at a level of <-35 dB. Also shown (×) are maximum E/S values for $-80° < \theta_0 < 80°$

performance specification for PNF systems and is in general described by the scanner planarity specification as a peak-to-peak or RMS value; this number indicating by how much the probe tip translates in z during motion of the scanner in x and y.

The impact on the PNF measurement is what this error term aims to assess. In terms of practical impact scanner non-planarity introduces a phase error in our

acquired near-field data set and even though an amplitude error is also introduced, typical non-planarity translation values are in the order of 0.1 mm RMS and amplitude variation due to such small distances can be neglected at most operational frequencies of interest. We therefore find that change in phase is where our attention needs to be focussed.

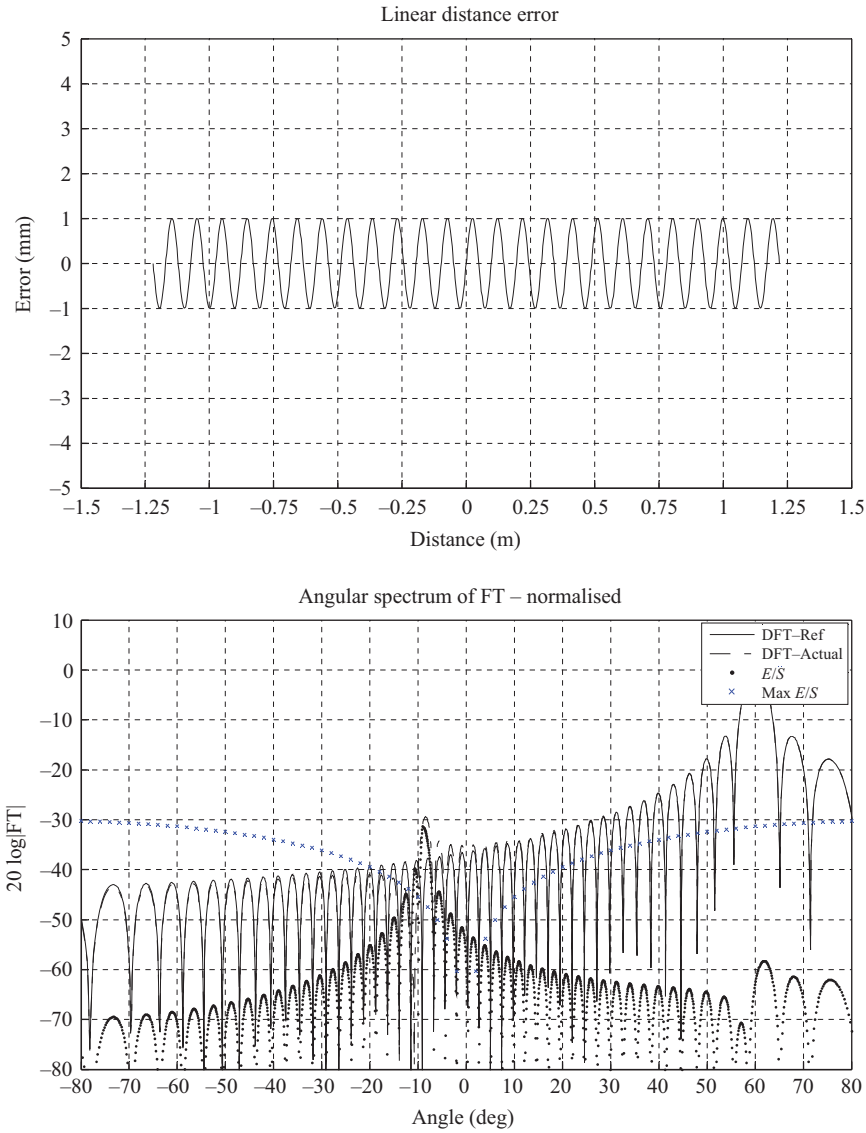

Figure 10.23 Sinusoidal position error of ±1 mm introduced (top). Two spectra are shown overlaid (bottom); F_T and the spectrum F_T' (for $\theta_0 = 60°$) and E/S at a level of <-30 dB. Also shown (×) are maximum E/S values for $-80° < \theta_0 < 80°$

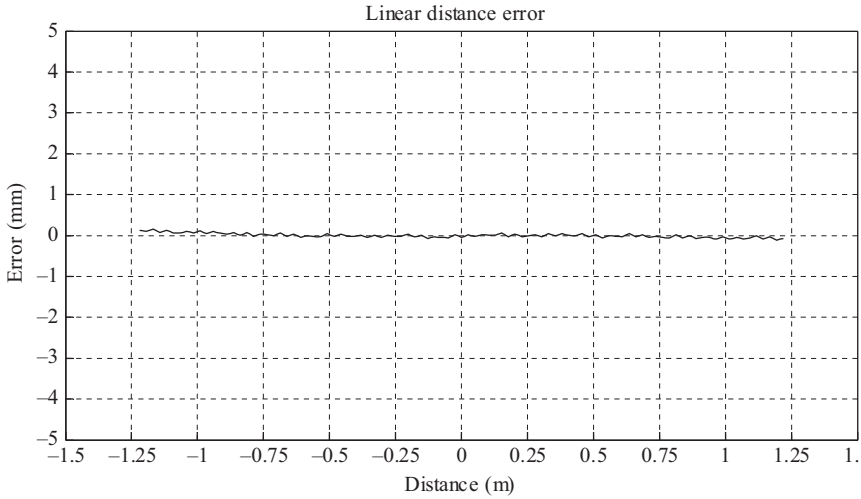

Figure 10.24 Laser interferometer measured x-axis positioner error for NSI-MI Technologies 2.4 m × 2.4 m PNF scanner

In practice, it is fairly straightforward to assess scanner planarity today. It can be achieved through the use theodolites or laser trackers and a complete surface map of the scanner performance can be generated as shown at the top in Figure 10.26. This data shows a peak-to-peak probe deviation of roughly −0.2 mm to 0.1 mm. Using a linear actuator that allows for translation of the near-field probe in z, this error map of the scanner planarity allows one to compensate for the inherent mechanical errors in the scanner and this leads to the concept of a corrected planarity map, shown on the bottom in Figure 10.26. The corrected planarity is much improved over that of the uncorrected planarity, but is still not perfect. This is due to actuator resolution and the finite capabilities of the optical measurement system.

The challenge here is therefore to assess what the impact of scanner planarity imperfection is on our measurement, albeit corrected or uncorrected.

In [1], expressions are presented that allow us to assess gain variation and side lobe level uncertainty (in dB) based on scanner non-planarity values. These expressions are based on the non-planarity function and allow for a quick approximate assessment. However, with the measurement capabilities and processing tools at our disposal, we can assess the impact of actual measured scanner planarity on each antenna we measure in a facility. In fact, we can also use the measured planarity information to correct PNF data, but as we shall see below, this effort hardly seems worthwhile in general. In reality, we find that aspects like cable flexure and facility temperature variation are bigger contributors to an effective scanner planarity error than any imperfections that a correction scheme for mechanical imperfections can help to mitigate.

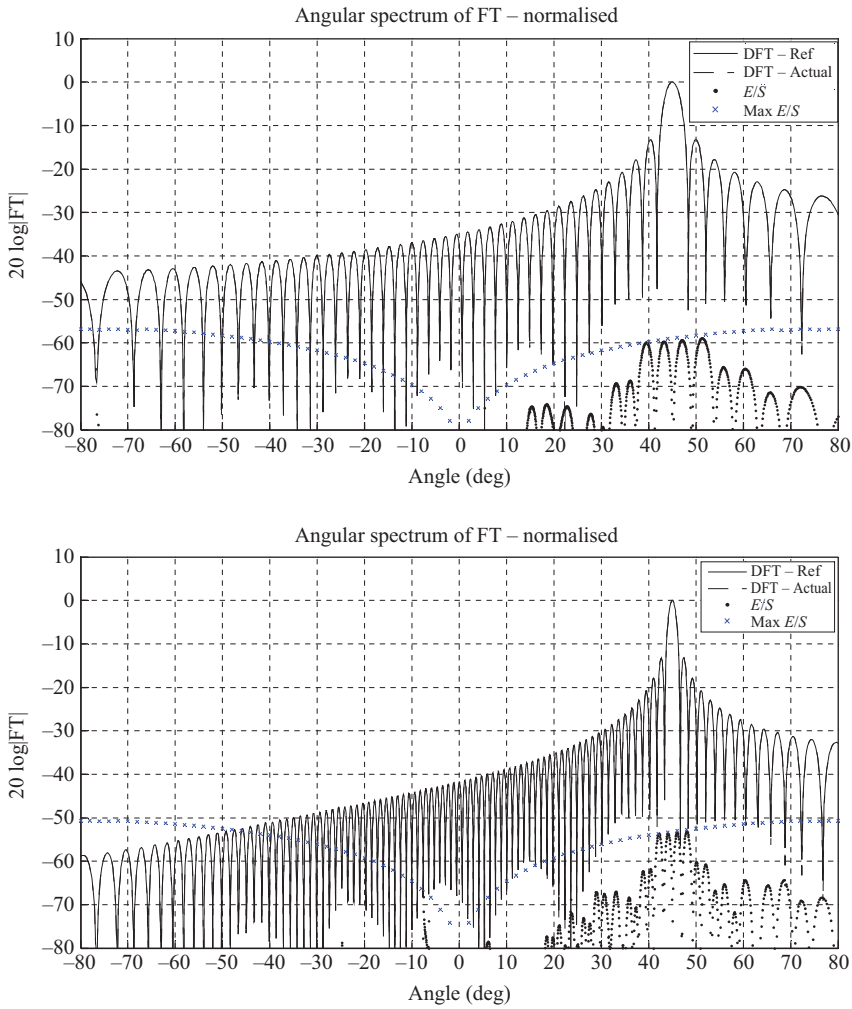

Figure 10.25 Two spectra are shown overlaid (3 GHz top and 6 GHz bottom); F_T and the spectrum F'_T (for $\theta_0 = 45°$) and E/S. Also shown (×) are maximum E/S values for $-80° < \theta_0 < 80°$

The angular spectrum of interest is computed from a partial knowledge of the tangential components of the aperture field distribution of the AUT, or from the tangential components of the field distribution over a finite parallel plane at $z = d(x, y)$ in front of the radiator (i.e. the scan plane) and the angular spectrum is obtained from

$$\underline{F}_T\left(k_x, k_y, z = d(x,y)\right) = \int_{-\infty}^{\infty}\int_{-\infty}^{\infty} \underline{E}_T(x, y, z = d(x,y)) e^{j\left(k_x x + k_y y\right)} dxdy$$

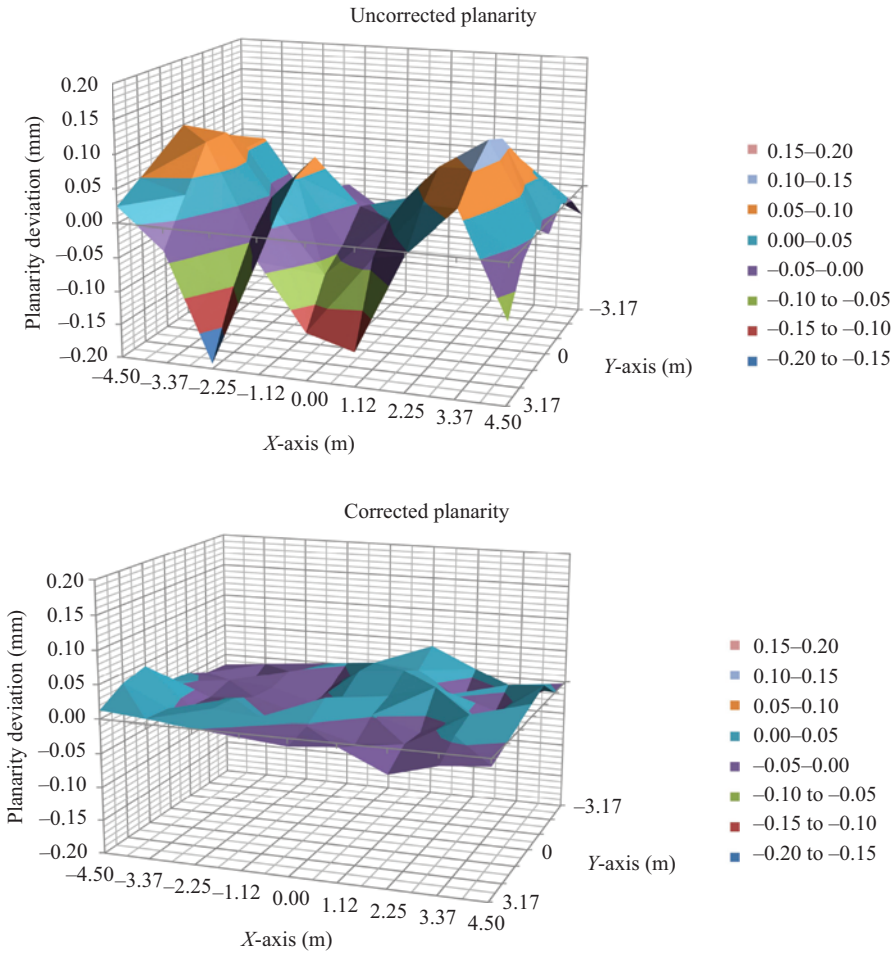

Figure 10.26 Planarity data for a 9 m × 6.4 m PNF scanner with z-distance variation shown on the vertical axis in units of 50 μm. Uncorrected planarity is shown at the top and corrected planarity at the bottom

where we have now introduced d as a variable of x and y and becomes

$$\underline{F}_T\left(k_x, k_y, d(x,y)\right) = \int_{-\frac{1}{2}L_y}^{\frac{1}{2}L_y} \int_{-\frac{1}{2}L_x}^{\frac{1}{2}L_x} \underline{E}_T(x,y,d(x,y)) e^{j\left(k_x x + k_y y\right)} dxdy \tag{10.23}$$

if the finite region of the scan plane is considered. We see in this equation that we evaluate the electric field not at a constant z-distance, but at a varying distance and we have three options to assess the impact of this. The first is known as a zero-order planarity assessment, the second option is an experimental planarity correction

assessment and the third is a simulation assessment. We describe these approaches below:

1. *Zero-order assessment*: A simple though effective planarity correction technique is to apply an electrical phase adjustment to all near-field data, based on the measured scanner planarity and the frequency of measurement. This can be expressed mathematically as

$$\underline{F}_T\left(k_x, k_y, d(x,y)\right)|_{\text{Corrected}} = \int_{-\frac{1}{2}L_y}^{\frac{1}{2}L_y} \int_{-\frac{1}{2}L_x}^{\frac{1}{2}L_x} \underline{E}_T(x,y,d(x,y)) e^{-jkd(x,y)} e^{j\left(k_x x + k_y y\right)} dxdy$$

   Where we are compensating the phase of the measured near-field by $e^{-jkd(x,y)}$ to counter the effect of the probe motion in z. The problem with this approach is that the phase correction is only accurate for the plane wave component incident at 0° and hence the name 'zero-order correction'. If we have an AUT that is principally radiating in this direction (and this often is the case during PNF testing), this approximate correction scheme works well. The weakness of this approach is that the phase correction being applied is equal for all spectral components, regardless of their angular location and this is not accurate. However, it works well for AUT's with spectra focussed around the $k_x = k_y = 0$ point and is simple to implement. We can also assess the impact of both corrected and uncorrected planarity easily. More information on post-processing-based planarity correction schemes can be found in [13].
2. *Experimental planarity correction assessment*: This technique relies on having the ability to do scanner planarity correction using a linear actuator. The approach is to make a measurement with and without planarity correction, compare the far-field results and assess the impact of scanner planarity [15]. The data depicted in Figure 10.26 would represent the two planarity scenarios one would be comparing. A straightforward, experimental approach that needs little explanation. Two weaknesses of this approach are that measurement repeatability is embedded in our result, and there is no way to assess the impact of the corrected planarity, since it becomes our reference in this case.
3. *Simulation assessment*: This approach relies on a simulated radiation source for which we can extract electric field values at any point in space. We can then evaluate (10.23) on a regular (x, y) grid, while positioning the simulated near-field probe at the z-distance prescribed by the scanner planarity measured. It therefore allows us to simulate the perfect case and a case based on actual scanner measured planarity performance and assess the impact. The weakness of this approach is that the actual antenna being measured is not assessed for planarity impact and that a representative simulation source is being used. However, on the upside, there is no concern about measurement repeatability embedded in our result and we can assess the impact of both corrected and uncorrected planarity. An example of this is depicted in Figure 10.27. In this instance, a simulated planar array is considered and when comparing the far-field radiation pattern for the reference case and the uncorrected planarity case,

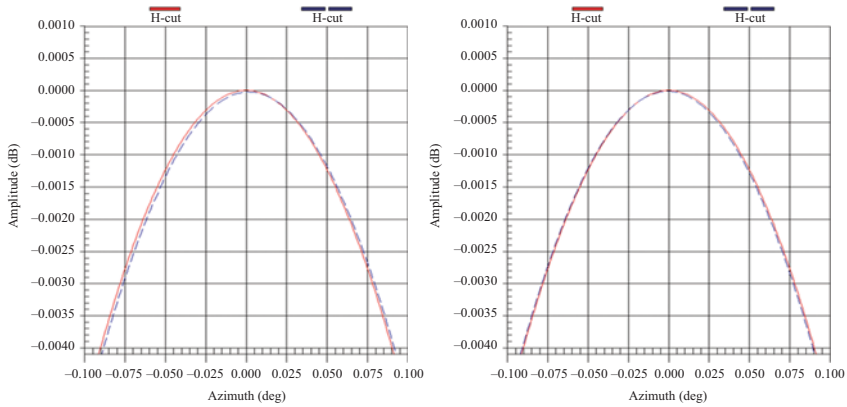

Figure 10.27 X-band simulation assessment of scanner planarity data depicted in Figure 10.26. Far-field beam peak locations are compared with reference versus uncorrected planarity (left) and beam peak comparisons of reference versus corrected planarity (right)

we obtain results that are virtually identical, proving no significant impact due to the scanner planarity imperfection. Examining the beam peaks closer a slight angular shift of the radiation patterns is detected. We see that the uncorrected case (shown as the left image in Figure 10.27) displays a beam peak shift of roughly 0.0025° (44 μrad) and the corrected case (shown as the right image in Figure 10.27) displays a beam peak shift of roughly 0.001° (17 μrad). Small changes indeed, which emphasise the fact that the mechanical planarity achievable for large PNF scanners today is excellent.

10.6.4 CNF probe ρ-position error

This term assesses the impact of uncertainty in the radial distance parameter (the azimuth axis to probe distance) in far-field results obtained in CNF test systems. The results presented here help to establish a base for understanding the necessity of accurate alignment of CNF scanners, and more importantly, it serves to quantify the tolerance required for the radial distance parameter.

In a typical dual-axis cylindrical acquisition system (as described in Chapter 7), there is a vertical axis of rotation and a vertical axis of probe motion parallel to this axis. During the data acquisition, the probe is moved parallel to the axis of rotation and the AUT is rotated around this axis so that data points can be acquired on a regular grid (ϕ, z). Variable ϕ is the azimuth angle of rotation of the AUT and z is the linear distance of probe motion. The separation distance between the probe coordinate system origin and the axis of rotation is denoted by ρ and is referred to here as the radial distance parameter. This distance has to be specified for the CNF

transformation algorithm, and its accuracy is dependent on the actual measurement process used during system calibration and also the coordinate system origin of the probe being used. (Note that when one is using measured probe patterns for probe correction, this point will be defined by the coordinate system origin that was used during the probe calibration process. When computed probe patterns are used, this point is defined by the far-field coordinate system origin used during the computation.) The latter is not always known for a given probe, and this fact therefore contributes to the uncertainty associated with this parameter. In what follows, data is shown where known error values were introduced in the radial distance parameter, to study the far-field radiation pattern sensitivity to this variation.

For the radial distance parameter test, the system configuration as shown in Figure 10.28 was used. Here, an AUT is shown mounted on a rotary positioner, mounted on an automated linear slide which allows variation of the radial distance parameter. The X-band AUT with sum and difference patterns was first measured using a planar scanning configuration for reference purposes and then using a cylindrical scanning configuration with a scan size of 100° rotation (0.5° step size) and 2 m vertical probe motion (16.5 mm step size).

The probe to AUT axis of rotation distance was set to 1.1 m. For the cylindrical parametric study test, the AUT linear slide was set at radial distance offsets of 0, $-0.2\,\lambda$, $-0.4\,\lambda$, …, $-1.6\,\lambda$. The radiation pattern data shown in Figures 10.29 and 10.30 represent the far-field derived patterns from these multiple CNF acquisitions as described. Note that during processing, the radial distance parameter was kept fixed at 1.1 m for all cases, thus inducing an error in the processing since the radius was indeed changed. The relative insensitivity of the elevation pattern data on this parameter is evident.

When comparing AUT difference pattern data (that typically contain deep nulls), similar behaviour is noticed for azimuth and elevation patterns. However, for the azimuth pattern, a significant difference pattern null position variation is noticed (0.05°) as is evident in Figures 10.31 and 10.32.

From these results, it is clear that uncertainty in the radial distance parameter ρ has almost no impact on CNF derived elevation pattern data. However, the impact on the azimuth pattern data is significant. Based on the results presented here, it appears that a target accuracy for determining this radial distance parameter should be better than 0.1λ. However, if parameters like difference pattern null position are to be measured, more stringent limits may be required. In reality, CNF sensitivity to this parameter diminishes for larger ρ/MRC ratios and what we present here simply illustrates how one can assess the impact of any uncertainty in this parameter for a given AUT.

10.6.5 SNF (θ, ϕ, r) positioning uncertainty

We investigate the sensitivity of far-field derived data for a SNF system in the presence of θ (swing arm axis) positioning uncertainty and radial distance variation. As an example, we use measured data for a θ/ϕ swing arm type scanner as depicted in Figure 10.33.

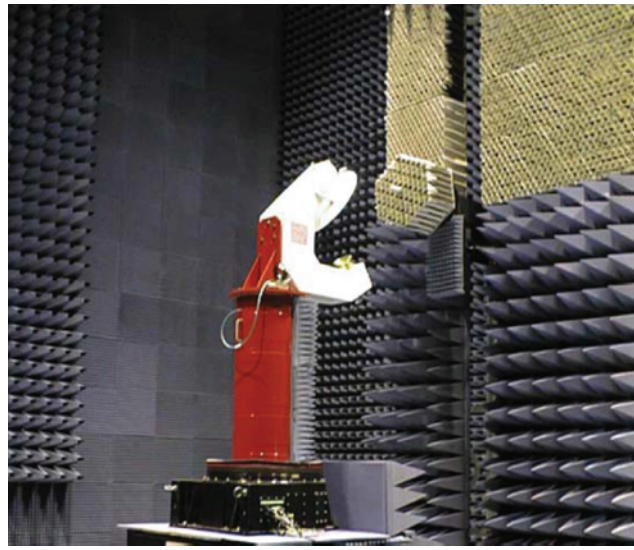

Figure 10.28 Cylindrical near-field measurement test configuration. (Picture used with permission of NSI-MI Technologies LLC)

The results presented here were obtained from a mechanical finite element analysis (FEA) of the structure and simulated electromagnetic data based on the introduction of these mechanical tolerances in the acquisition process of the system. The angles θ and ϕ correspond to the motion of the swingarm and turntable, respectively.

A FEA model as depicted on the left in Figure 10.34 was analysed [11], with the resulting deformations (shown exaggerated) as depicted on the right.

From the FEA, the results shown below could be extracted. Figure 10.35 shows θ error as a function of θ angle at the FEA probe tip. The sinusoidal behaviour is as expected (worst case for $\theta = \pm 90^\circ$) and a maximum number of $\pm 0.062^\circ$ is noted (RMS value of 0.044°).

Figure 10.36 shows radial error as a function of θ angle at the FEA probe tip. The cosinusoidal behaviour is again as expected (zero value for $\theta = \pm 90^\circ$) and the maximum number of $\pm 0.007''$ (± 0.18 mm) is evident (RMS value of $0.005''$ (0.13 mm)).

Figure 10.37 shows z-distance error as a function of θ angle at the FEA probe tip. It is noted that this value is negative for all θ angles and the maximum value is $-0.005''$ (-0.13 mm). Figure 10.38 shows the FEA probe axis pointing error w.r.t. the coordinate system origin. The minimum value for $\theta = 0^\circ$ is as expected with deviation in the same direction for both positive and negative angles of θ rotation. The data of both Figures 10.37 and 10.38 are difficult to visualise and Figure 10.39 helps with the interpretation.

Figure 10.39 shows an exaggerated rendering of the θ and ϕ axis deformations for the $\theta = 0^\circ$ position and the $\theta = 180^\circ$ position and it is from this analysis that the

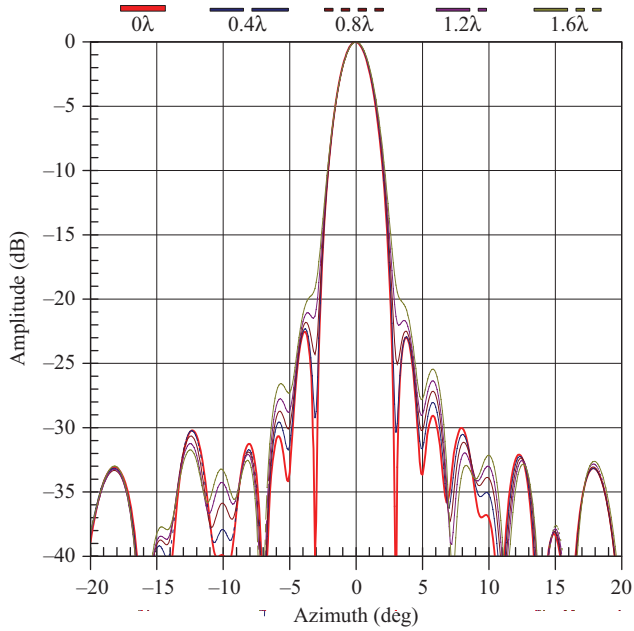

Figure 10.29 Azimuth radiation pattern data for multiple CNF data sets with radial distance parameter offset values introduced

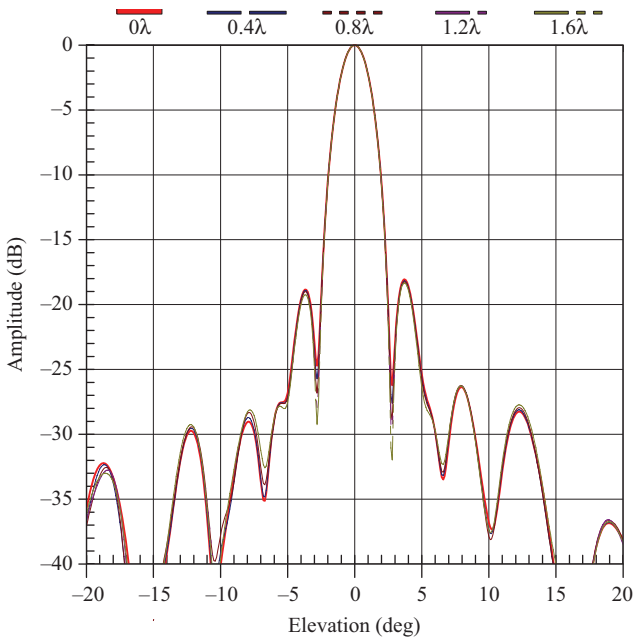

Figure 10.30 Elevation radiation pattern data for multiple CNF data sets with radial distance parameter offset values introduced

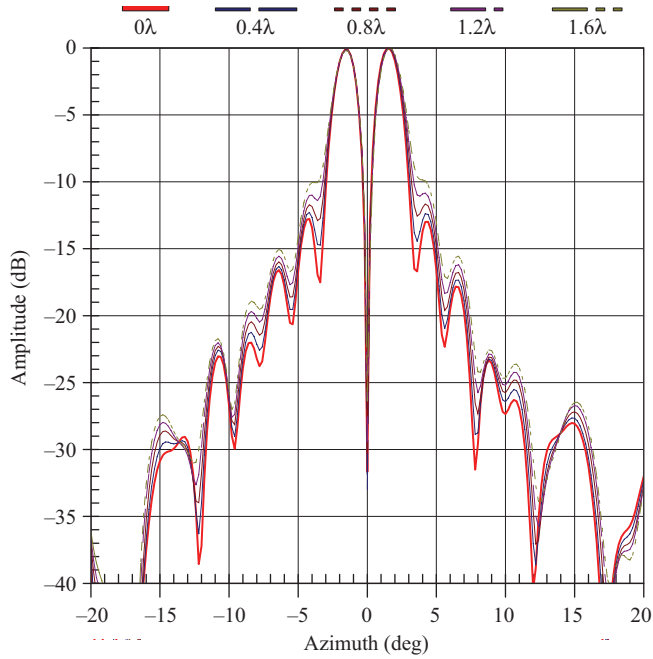

Figure 10.31 Azimuth difference pattern data for multiple CNF data sets with radial distance parameter offset values introduced

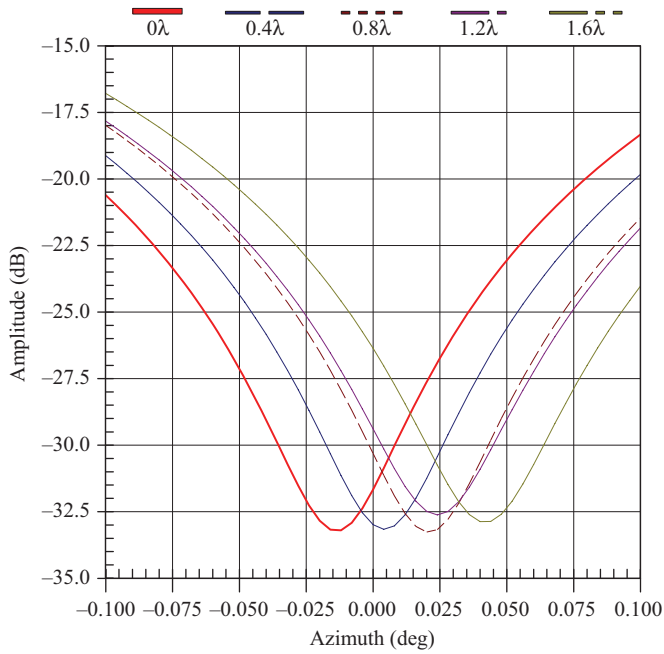

Figure 10.32 Enlarged section of null detail of Figure 10.31

data depicted in Figures 10.37 and 10.38 were extracted. It is also important to realise that this deformation leads to axis non-orthogonality and this is evident by the images shown in Figure 10.39. Figure 10.40 shows probe tip y-axis location versus z-axis location for all θ angles of motion. Ideally, this graph should be a vertical straight line and the slope indicates a theta axis that is not horizontal. Also, the fact that the projection is not a perfect straight line is an indication that the condition changes as θ changes and this is due to the fact that the deformation changes as the θ axis moves (effective axis wobble). The slope of a best fit straight line through this curve allows one to measure an average angle of 0.025°. Considering the ϕ stage mount and the fact that it tilts in the opposite direction relative to an ideal vertical plane at an angle of 0.011°, these two values can be added as a measure of the total axis non-

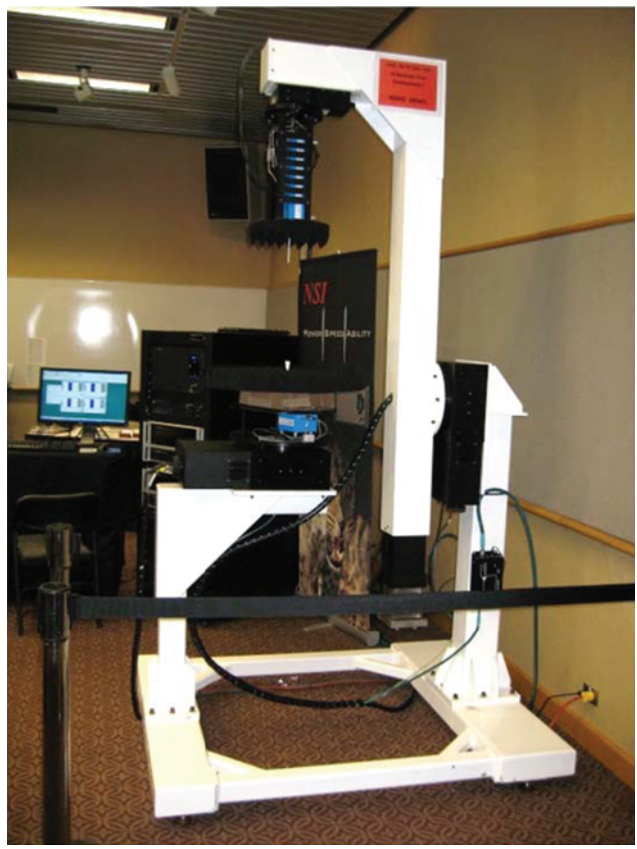

Figure 10.33 SNF swing-arm scanner shown with 75 GHz RF sub-system. Arm is parked in the $\theta = 0°$ location. Frequency up- and down-conversion units are mounted immediately behind the probe and AUT (Picture used with permission of NSI-MI Technologies LLC)

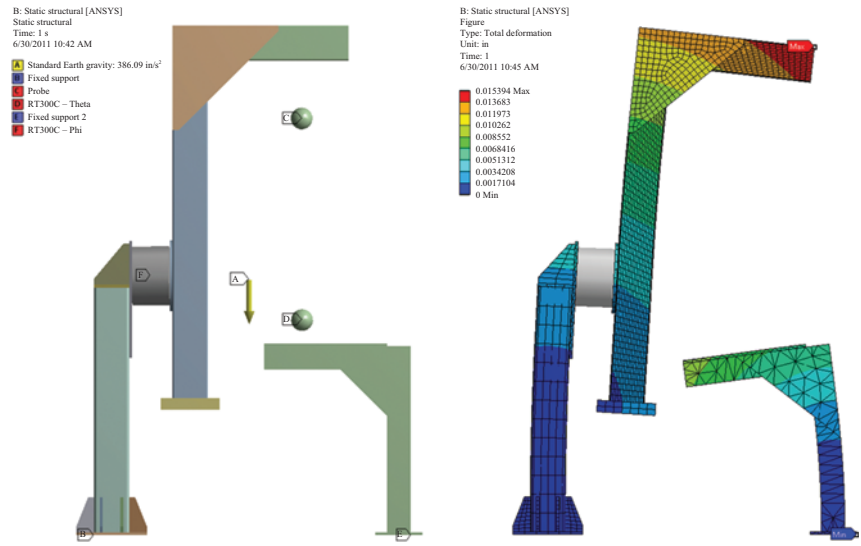

Figure 10.34 FEA model used is shown on the left and FEA deformation result is shown on the right (Deformations have been exaggerated in these figures to illustrate the sense and relative magnitudes of the mechanical changes)

orthogonality of 0.036°. If desired the ϕ stage can be tilted to counter this effect (assuming that AUT weight has no impact on ϕ stage deflection).

These coordinate system deviations can now be used in an electromagnetic simulation tool to assess the impact of the mechanical deformations on the SNF measurement. Three simulated sources are considered, the first (source #1) a 15 mm × 15 mm aperture radiating at 60 GHz, the second (source #2), a 6 mm × 6 mm aperture radiating at 150 GHz (same electrical size as #1) and the third (source #3) a half wavelength dipole radiating at 60 GHz. In all instances, the probe radial distance was set to 17″ (432 mm) to correspond with the scanner dimensions. These simulated source distributions were selected to represent two high-gain cases at typical operational frequencies and a low-gain case with radiation into regions not illuminated by the high gain cases. The cases are compared in Table 10.7.

For source #1, typical far-field pattern data at 60 GHz is shown in Figure 10.41.

The first case considered is that of a systematic error (as depicted in Figure 10.35) with peak value of ±0.062°, applied as a sinθ function to the absolute θ value. For source #2, a SNF sampling density of 10° is required to make a valid acquisition. By now introducing a probe positional θ error as shown in Figure 10.35, two far-field patterns can be generated to assess the impact of the theta-axis deformation. This data is depicted in Figure 10.42 (left) below and a resultant −60 dB error level is observed. If source #2 is offset from the coordinate system origin by

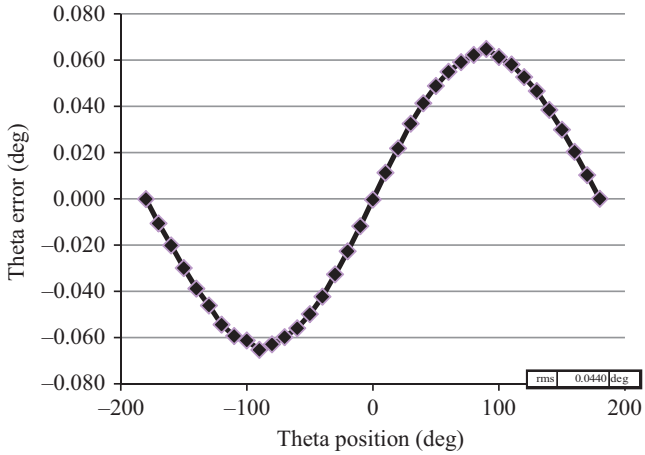

Figure 10.35 Theta error as a function of θ angle at the FEA probe tip

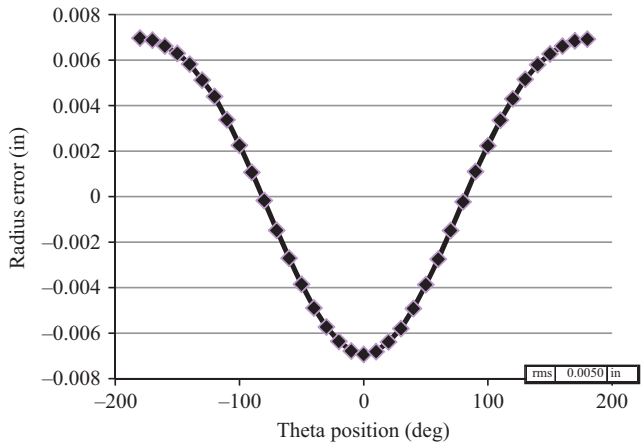

Figure 10.36 Radial error as a function of θ angle at the FEA probe tip

80 mm, a higher sampling density is required for making valid SNF acquisition and the interval becomes 0.5°. If the same θ positional error is introduced, the data depicted in Figure 10.42 (right) is obtained and a resultant −50 dB error level is observed. This result seems to indicate a higher sensitivity to θ-axis positional error for smaller angular increments, although similar error values are observed for an AUT offset of 40 mm and a sampling interval of 1.25°.

For source #1, a SNF sampling density of also 10° is required to make a valid acquisition. By introducing the same probe positional θ error as shown in Figure 10.35, two far-field patterns can again be generated to assess the impact of the θ-axis deformation. Data similar to that depicted in Figure 10.42 is obtained and

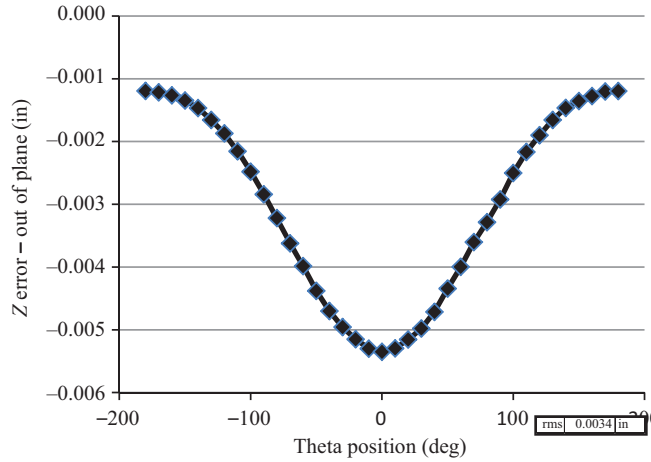

Figure 10.37 Predicted z-distance error as a function of θ angle at the FEA probe tip (refer to Figure 10.39 for interpretation)

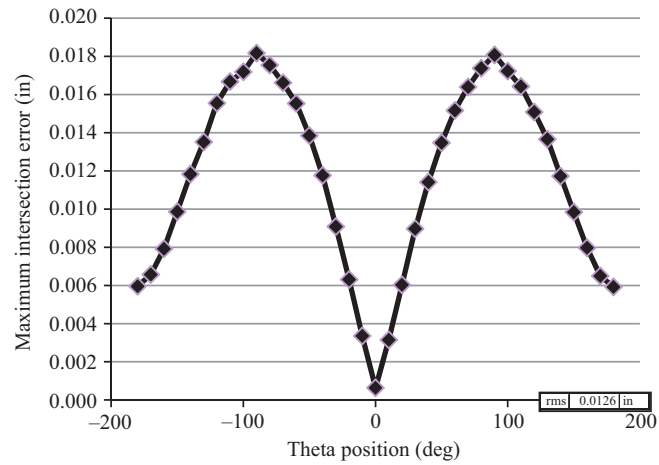

Figure 10.38 FEA probe axis pointing error w.r.t. the coordinate system origin (refer to Figure 10.39 for interpretation)

a resultant −60 dB error level is observed. If source #1 is offset from the coordinate system origin by 100 mm, a higher sampling density is required for making a valid SNF acquisition and the interval becomes 1.25°. Data similar to that depicted in Figure 10.42 (right) is again obtained and a resultant −50 dB error level is observed. This result also indicates a higher sensitivity to θ-axis positional error for smaller angular increments.

Figure 10.43 shows near-field phase differences for two test cases with and without the sinusoidal theta angular error introduced. The difference curve is an

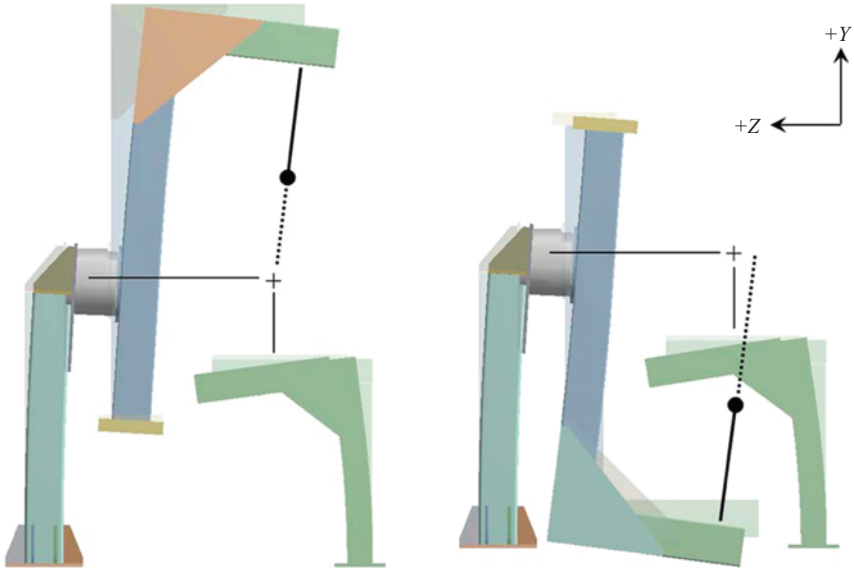

Figure 10.39 FEA probe axis pointing error with respect to the coordinate system origin (Deformations have been exaggerated in these figures to illustrate the sense and relative magnitudes of the mechanical changes)

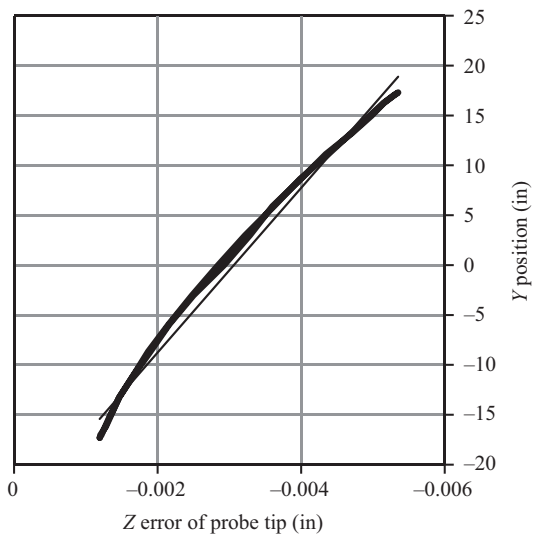

Figure 10.40 Projection of probe tip location onto the yz-plane with the best fit line shown

Table 10.7 Simulated test sources for SNF angular and radial distance error assessment

Source #	Size (mm)	Freq (GHz)	λ (mm)	Offset (mm)	MRS (mm)	Sample spacing (Deg)	MRS (λ)	Probe distance (λ)	$2D^2/\lambda$ (mm)
1	15 × 15	60	5	0 100	11 106	10 1.25	2.2 21.2	86	180 18 000
2	6 × 6	150	2	0 40 80	4 50 100	10 1 0.5	2 25 50	216	72 2 500 10 000
3	2.5	60	5	0 100	3 103	10 1.25	0.6 20.6	86	15 17 000

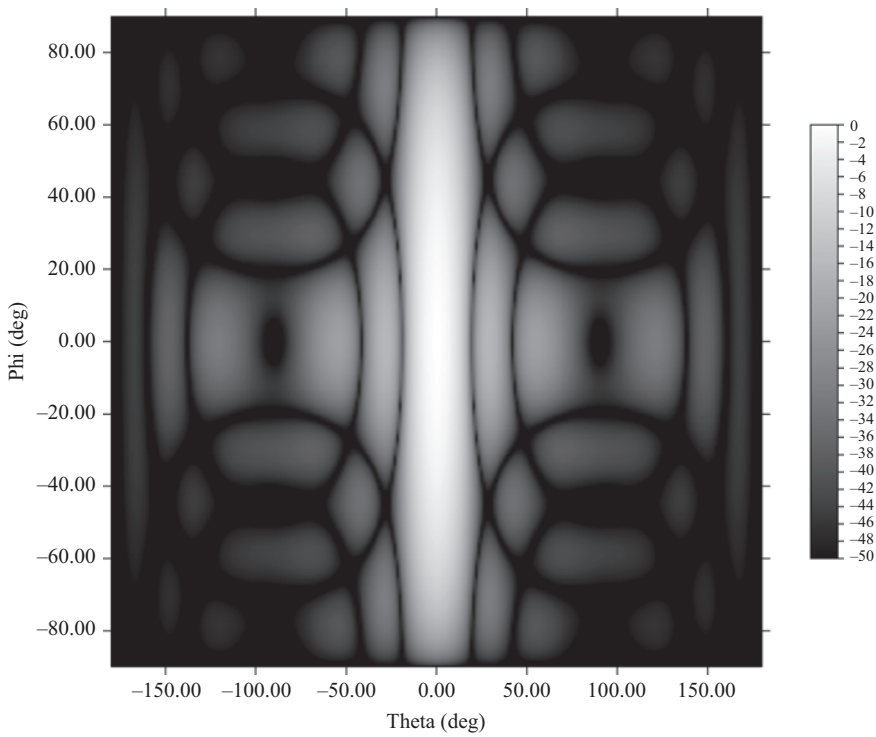

Figure 10.41 15 mm × 15 mm aperture reference near-field amplitude data set at 60 GHz

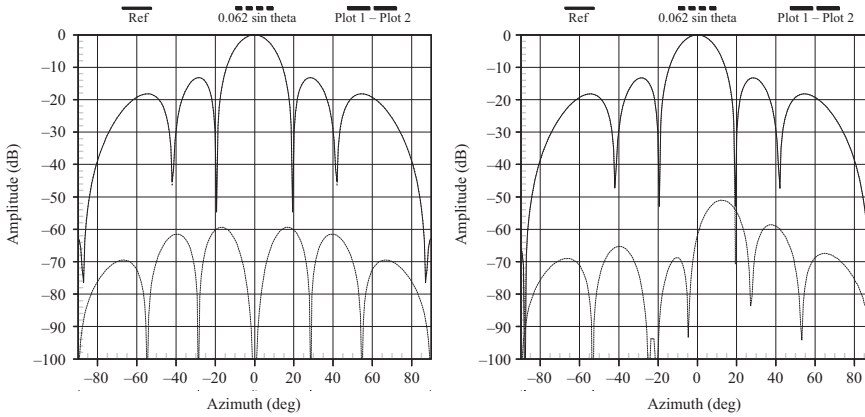

Figure 10.42 Error induced by 0.062° sinusoidal theta error (swing arm droop) at 150 GHz for AUT with 10° sampling interval (left) and offset (by 80 mm) AUT with 0.5° sampling interval (right). Results remain unchanged for 60 GHz

indication that the error is correctly introduced with maximum effect at ±90° (note that the zero crossing at close to ±90° is where the angular shift is a maximum and the two-phase curves cross).

For source #3 (z-directed dipole), a SNF sampling density of 10° is required to make a valid acquisition. By now introducing a probe positional θ error as shown in Figure 10.35, two far-field patterns can again be generated to assess the impact of the θ-axis deformation. This data is depicted in Figure 10.44 (left) and a resultant <-60 dB error level is observed. If source #3 is offset from the coordinate system origin by 100 mm, a higher sampling density is required for making a valid SNF acquisition and the interval becomes 1.25°. If the same θ positional error is introduced, the data depicted in Figure 10.44 (right) is obtained and a resultant <-60 dB error level is observed. This result *does not* indicate a higher sensitivity to θ-axis positional error for reduced angular increments in this instance.

The random θ error case considered assumes a maximum value of ±0.062° (not based on an actual measurement, but simply on the peak value of the systematic error investigated above). Figure 10.45 shows the resultant effect on the near-field data of source #1 (60 GHz) for no source offset (10° sampling interval shown on the left) and 100 mm offset (1.25° sampling interval shown on the right). The respective residual error levels detected are –55 dB in the first case and −33 dB in the second. Figure 10.46 shows the resultant effect on the near-field data of source #2 (150 GHz) for a source offset of 40 mm (1° sampling interval shown on the left) and 80 mm offset (0.5° sampling interval shown on the right). The respective residual error levels detected are –33 dB in the first case and −23 dB in

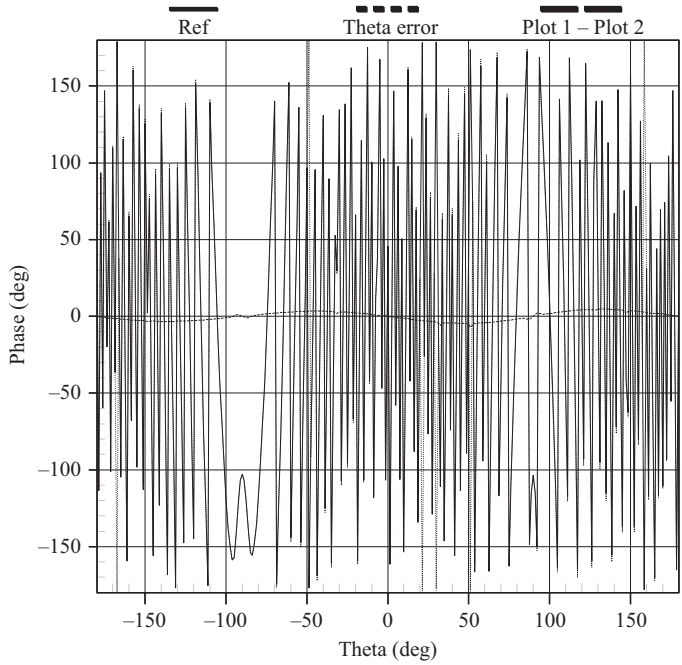

Figure 10.43 Near-field phase for reference and test case for a θ error (as depicted by Figure 10.35 with a peak value of 0.062°) induced. The dashed sinusoidal curve is the difference curve and clearly shows the impact of the positional error on the raw near-field phase

the second. These results support the idea of a random θ error affecting test results significantly more than a systematic error and further also affecting measurements with higher sampling density more severely.

Turning to radial distance variation of the probe due to swing arm flexing, we can model these through the introduction of a phase perturbation added to the near-field data. As such, simulated or measured data sets can be used. Since this error will most likely be systematic for a swing arm scanner (per Figure 10.36), no random component is investigated here. The thought behind this simple cosine model is that swing arm sag will cause the maximum radial deflection at 0° and 180° and this is supported by the results depicted in Figure 10.36. The investigations below using all three simulated sources show a very high level of tolerance to radial error introduced in this fashion. (Results presented in [16] show a very high sensitivity to a radial error with spatial period in the order of a sampling interval. This will not be true for a swing arm system, but may hold true for scanners constructed from curved rail segments.)

Figure 10.47 shows the net far-field induced error for this radial distance variation for source #3 (60 GHz). The source with no offset is shown in the left and the 100 mm offset case is shown on the right. The net result is the same in both instances (in this case the $\pm 0.007''$ (± 0.18 mm) radial distance perturbation translates to

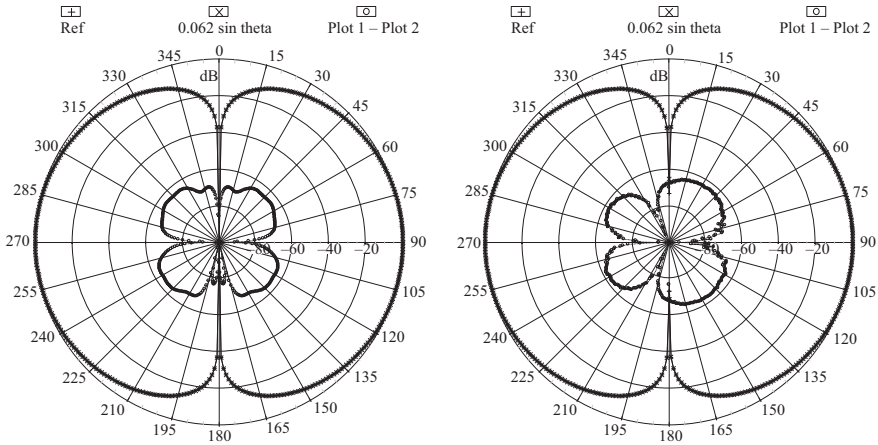

Figure 10.44 Error induced by 0.062° sinusoidal θ error (swing arm droop) at 60 GHz for dipole with 10° sampling interval (left) and dipole offset by 100 mm with 1.25° sampling interval (right)

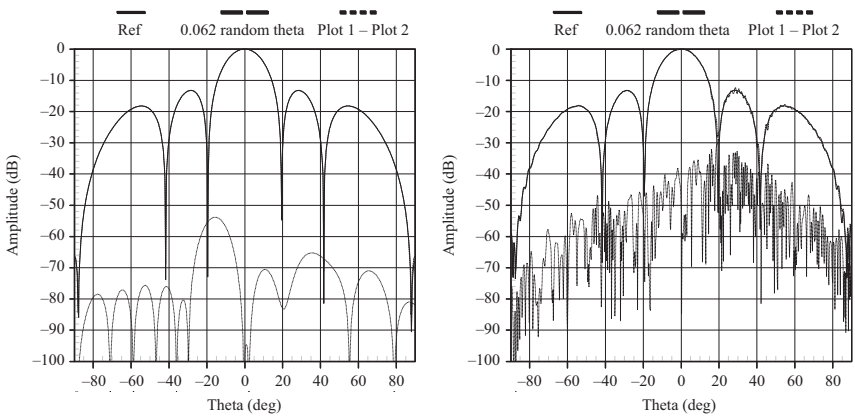

Figure 10.45 Error induced by 0.062° peak random θ error (swing arm) at 60 GHz for AUT with 10° sampling interval (left) and AUT with 1.25° sampling interval (right)

±12.8° of phase). These results remain unchanged for source #1 (60 GHz). The radial distance is 432 mm.

Figure 10.48 shows the net far-field induced error for this radial distance variation for source #2 (150 GHz). The source with no offset is shown at the top and the 40 mm offset case is shown in the middle with 80 mm offset case on the

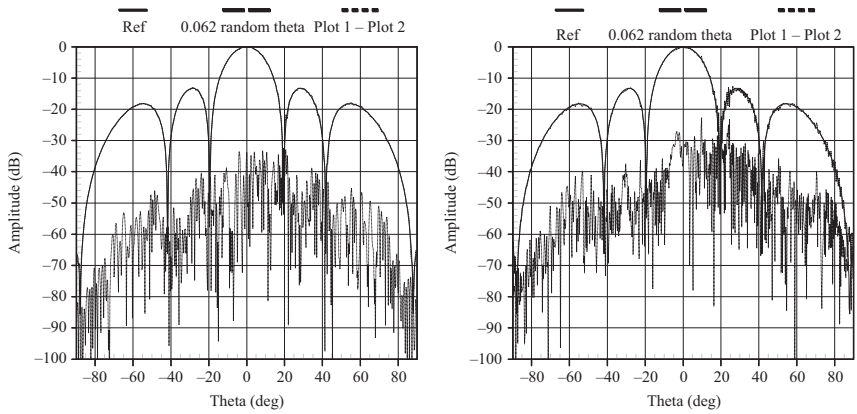

Figure 10.46 Error induced by 0.062° peak random theta error (swing arm) at 150 GHz for AUT with 1° sampling interval (left) and AUT with 0.5° sampling interval (right)

bottom. The net results for the offset cases are slightly worse (in this case the $\pm 0.007''$ (± 0.18 mm) radial distance perturbation translates to $\pm 32°$ of phase).

In order to investigate the sensitivity of radial distance error for reduced radial distances,[9] the following simulation results are presented. Figure 10.49 shows the net far-field induced error for this radial distance variation for source #2 (150 GHz), but for a reduced radial distance of 232 mm. The source with no offset is shown in the left and the 80 mm offset case is shown on the right. The net result for the offset case is slightly worse again, but similar to the larger $R = 432$ mm case shown in Figure 10.48.

Figure 10.50 shows the net far-field induced error for the same radial distance variation for source #2 (150 GHz), but for a reduced radial distance of 132 mm. The source with no offset is shown in the left and the 80 mm offset case is shown on the right. The net result for the offset case is clearly worse than before.

The results in Figures 10.47–10.50 support the conclusion that a radial distance variation of up to $\lambda/10$ will guarantee an induced far-field error of < -45 dB as the measurement radius approaches the *MRS* sphere as a worst-case scenario. As the radius increases w.r.t. the *MRS* this sensitivity decreases and a -60 dB error level becomes typical. The crucial issue to take note of here is the slow spatial variation of the radius (period of 360°). If this spatial period was in the order of a sampling interval, this sensitivity will be significantly higher.

In the analysis presented here, we combined the use of a mechanical FEA and an electromagnetic simulation tool to characterise a SNF test system in terms of θ-axis deflection and radial distance variation. The results show that the sensitivity

[9]It has been observed that as the measurement radius is reduced and approaches the *MRS* sphere (typically $R/MRS < 2$), sensitivity to SNF alignment is increased as well as sensitivity to errors in the radial distance.

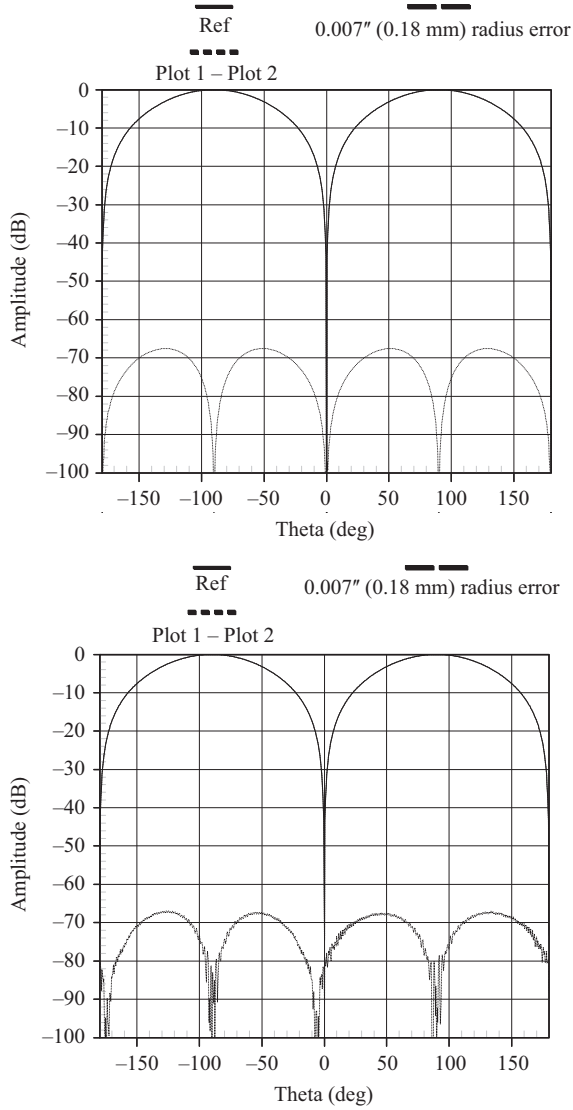

Figure 10.47 Impact of radial distance errors of ±0.007″ (±0.18 mm − ±12.8° of electrical phase at 60 GHz). The error was added as a cos θ function (i.e. maximum for gantry vertical). Source #3 with zero offset at the top and 100 mm offset at the bottom. Results for source #1 are identical

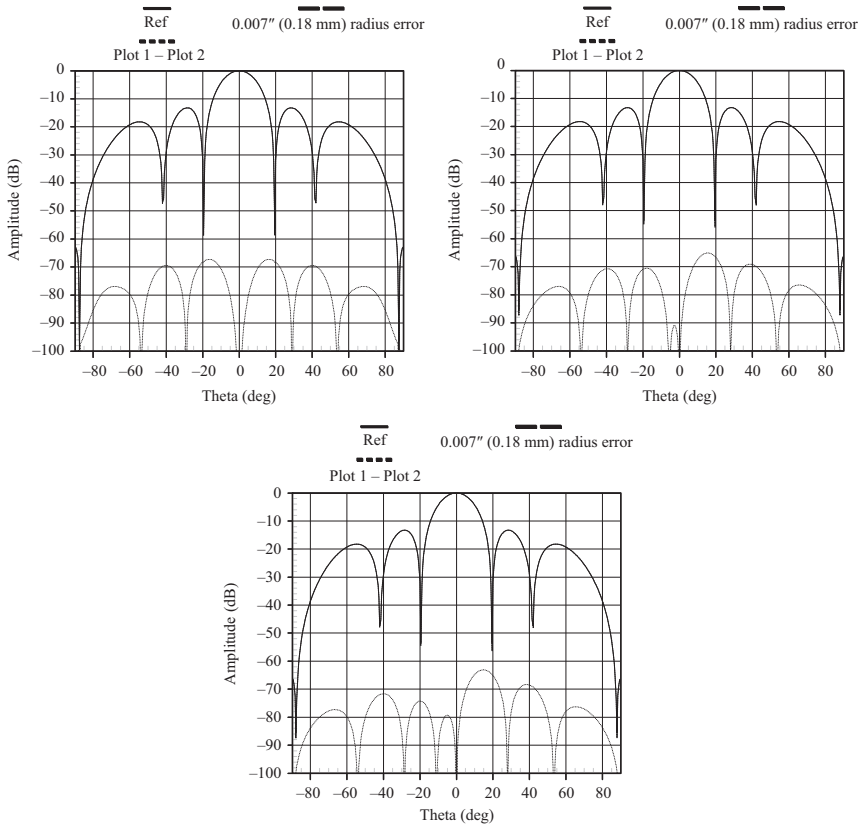

Figure 10.48 Impact of radial distance errors of ±0.007″ (±0.18 mm) (±32° of electrical phase at 150 GHz). The error was added as a cos θ function (i.e. maximum for gantry vertical). Source #2 with zero offset at the top left (R/MRS = 216), 40 mm offset at the top right (R/MRS = 8.6) and with 80 mm offset at the bottom (R/MRS = 4.3)

of the far-field data on the θ-axis angular location (θ angle) is considerably higher for random errors than for systematic errors with a 360° spatial period. A very important observation is that this sensitivity is frequency independent and driven by the *MRS* and corresponding sampling interval. Random angular and systematic angular errors of up to ±0.062° were considered.

The results also show that the derived far-field results are fairly insensitive to phase variations that are introduced as a measure for radial variation of the probe location. A phase variation corresponding to a total radial variation of up to

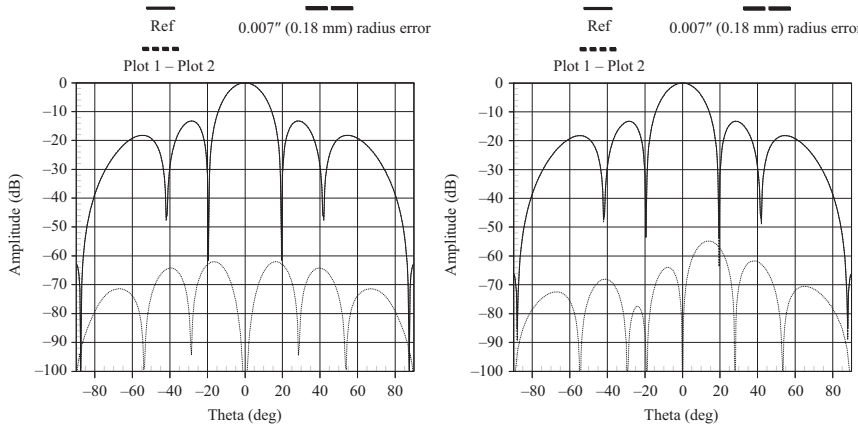

Figure 10.49 Impact of radial distance errors of ±0.007″ (±0.18 mm) (±32° of electrical phase at 150 GHz) for case where radial distance is reduced to 232 mm. The error was added as a cos θ function (i.e. maximum for gantry vertical). Source #2 with zero offset on left (R/MRS = 116) and 80 mm offset on right (R/MRS = 2.3)

±0.007″ (±178 μm) can be tolerated in most of the cases shown here without a noticeable change in the far-field pattern level. This distance corresponds to $\lambda/10$ at 150 GHz and the results presented here support the conclusion that this radial distance variation will guarantee an induced far-field error of <-45 dB as the measurement radius approaches the *MRS* sphere as a worst-case scenario. As the radius increases w.r.t. the *MRS* this sensitivity decreases and a -60 dB error level becomes typical [12].

10.6.6 SNF axis non-orthogonality

The θ/ϕ swing arm scanner example considered in the previous section is again the topic of discussion here. The FEA analysis described predicted a θ-axis deviation from horizontal as depicted in Figure 10.39 and estimated a total axis non-orthogonality of 0.036°. In the simulation results presented here, this error is modelled by perturbing the orthogonality of the ϕ-axis with respect to the θ-axis as described in [17]. Figure 10.51 shows the impact of this axis non-orthogonality error on the far-field for source #2 at 150 GHz. Data for source #2 with zero offset is shown on the left and with a 40 mm offset on the right. It is clear that the error becomes more pronounced for smaller sampling intervals. Figure 10.52 shows the impact of this axis non-orthogonality error on the far-field for source #1 at 60 GHz. Data for source #1 with zero offset is shown on the left and with a 100 mm offset on the right. Similar conclusions to that drawn at 150 GHz apply here.

The data presented here represent a methodology of assessing SNF scanner axis non-orthogonality by using results obtained from a mechanical FEA. The results show that the sensitivity of the far-field data to axis non-orthogonality is

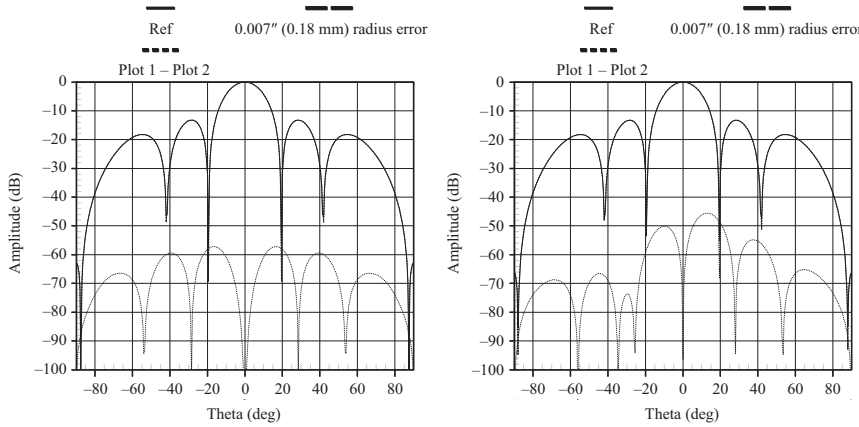

Figure 10.50 Impact of radial distance errors of ±0.007″ (±0.18 mm) (±32° of electrical phase at 150 GHz) for case where radial distance is reduced to 132 mm. Error was added as a cos θ function (i.e. maximum for gantry vertical). Source #2 with zero offset on left (R/MRS = 66) and 80 mm offset on right (R/MRS = 1.3)

high for the errors that were considered here. This error can be corrected successfully by shimming the θ and ϕ stages and the results shown here can be used as a guide for establishing alignment tolerances.

10.6.7 SNF axis (θ, ϕ) non-intersection error

A very practical aspect of SNF acquisition systems is alignment of the positioners with respect to one another and an aspect that warrants discussion is that of misalignment of the θ- and ϕ-axes so that they do not intersect in a point, also referred to as axis non-intersection error (also discussed at length in Chapter 12, Section 12.5.1). The impact of axis non-intersection is most often seen when testing broad beam antennas or narrow beam antennas tested in equatorial mode.

We will present simulated data to demonstrate the problem and also a simple mathematical model that can be used to assess and subsequently correct for the error. We will also show that *Phi_360* and *Phi_180* acquisition schemes (as described in Chapter 8) are affected differently by this error.

When a ϕ/θ SNF test system is constructed using two rotary positioners (see Figure 8.1), it is required that the two axes intersect in a point and are orthogonal. These conditions are fundamental in that if they are not met, the coordinate system being described is not truly spherical and the assumptions implicit in the spherical wave transformation are violated. If one were to measure a perfect half-wavelength dipole in a SNF range, the expected and ideal co-polarisation result will be the pattern as depicted in Figure 10.53 (3D image shown in Figure 10.54). If an axis non-intersection error of 0.1λ is introduced, the far-field radiation pattern depicted

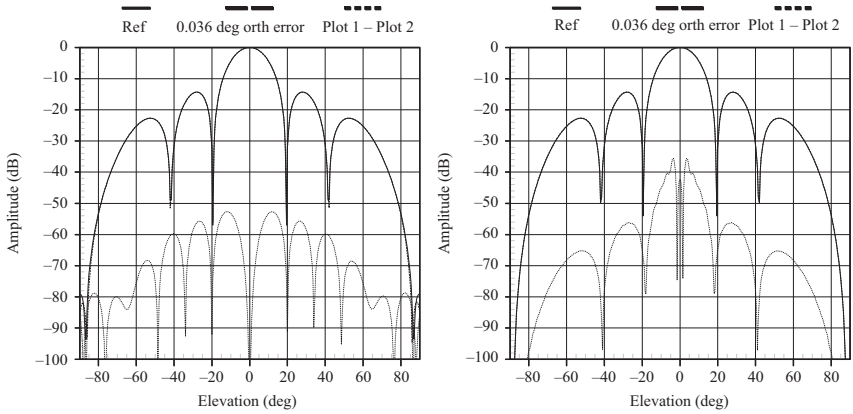

Figure 10.51 Impact of axis non-orthogonality error of 0.036° at 150 GHz. Source #2 with zero offset on the left and 40 mm offset on the right

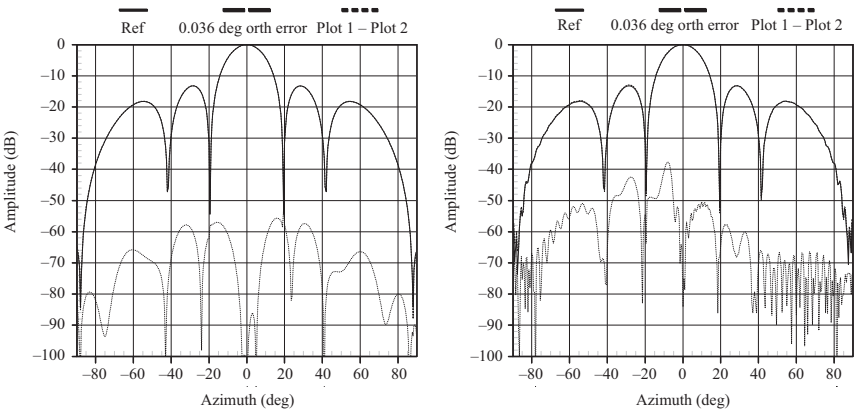

Figure 10.52 Impact of axis non-orthogonality error of 0.036° at 60 GHz. Source #1 with zero offset on the left and 100 mm offset on the right

(dashed) in Figure 10.53 results (3D image shown in Figure 10.55) and the deterioration in measurement quality is evident.

When one inspects the raw near-field data of these two data sets the amplitude information seems identical. However, the phase displays a very distinct behaviour and this is observed in Figure 10.56. The flat phase curve shows the near-field phase of the non-offset case as a function of θ rotation. The sinusoidal curve represents the near-field phase of the 0.1λ offset case as a function of theta. The sinusoidal behaviour of the phase is evident and the amplitude of this sinusoidal

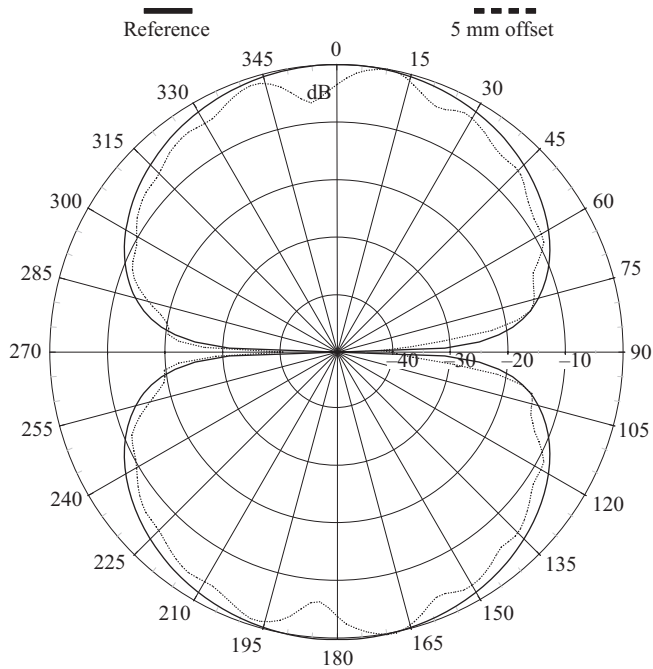

Figure 10.53 Simulated dipole radiation pattern. Reference (solid) pattern versus perturbed (dashed) pattern with a 0.1λ (5 mm) axis non-intersection error introduced

deviation is proportional to the axis non-intersection distance (say c), with an absolute phase value of ck in radians. This observation therefore allows one to correct for positioner axis non-intersection error by phase correcting each individual near-field data point using the expression

$$\text{Phase\_correction} = \Delta_\phi = -c\frac{2\pi}{\lambda}\sin\theta$$

Note that this correction is independent of angle φ. A physical interpretation of this expression is that for angles close to $\theta = 0°$, axis non-intersection causes cross-range translation of the AUT and it therefore has a negligible impact on the near-field phase data. For angles close to $\theta = 90°$, axis non-intersection causes down range translation of the AUT and it therefore has a maximum impact on the near-field phase data with the phase change being directly proportional to the distance of motion c.

Correction for axis non-intersection now becomes very simple once the distance c is known. If this distance is not known, it can be derived from the near-field phase data.

Correcting for the axis non-intersection using the simple mathematical model leads to the comparative data depicted in Figure 10.57 where the corrected pattern is indistinguishable from the reference pattern and the difference is <-50 dB.

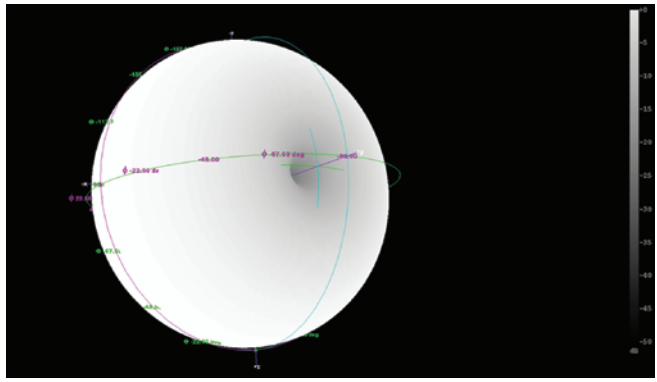

Figure 10.54 3D image of dipole reference pattern

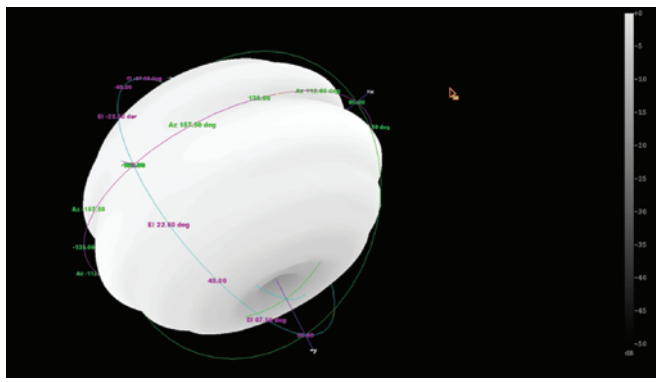

Figure 10.55 3D image of dipole pattern affected by 0.1λ axis non-intersection error (Note that the viewing angle was changed from that shown in Figure 10.54 to better show the equatorial ripple)

Figure 10.58 shows a dipole that was measured in a SNF facility. Due to the fact that the dipole illuminates the support structure strongly, the mounting configuration was changed from that depicted in Figure 10.58 to the dipole rotated to be collinear to the ϕ-axis.

The resulting far-field radiation pattern (for the omnidirectional plane) is shown in Figure 10.59 as the solid line. The slight anomaly observed at 0° (detail shown in rectangular plot) is due to a 6 mm axis non-intersection error and can be corrected as described above. The corrected radiation pattern is depicted by the dashed line.

Returning to our simulated dipole example presented above, the mode of acquisition was *Phi_180*. When the same simulation is performed for an axis non-intersection of 0.1λ and the acquisition mode *Phi_360* is selected, a significantly higher tolerance for the error is observed. Comparing the far-field radiation patterns of the three cases, we obtain the patterns shown in Figure 10.60. The reference (solid),

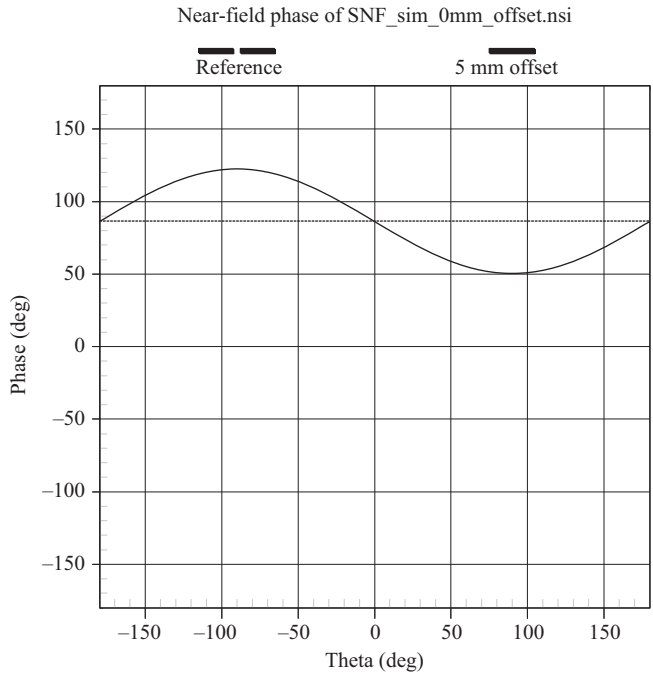

Figure 10.56 Near-field phase of the simulated dipole: flat phase (dashed) is the reference case and sinusoidal (solid) is the 5 mm (0.1 λ) axis non-intersection offset case

Phi_180 (dashed) and *Phi_360* (dashed – but covered by reference) patterns are shown. A closer comparison between the reference and *Phi_360* cases show very small differences. This observation is significant in that it highlights that at least in this one instance, a higher tolerance of the *Phi_360* acquisition scheme to axis non-intersection error.

10.7 Absolute power level-related errors

The errors described in this section are all related to establishing an absolute power level and therefore impact gain uncertainty budgets. They do not affect relative level measurements like side lobe level or cross-polarisation. These absolute power level terms are therefore omitted when gain uncertainty is not required.

10.7.1 Gain standard uncertainty

Any comparison (or direct connect [18]) gain measurement relies on the calibrated gain of the gain reference antenna (or near-field probe) as an absolute power

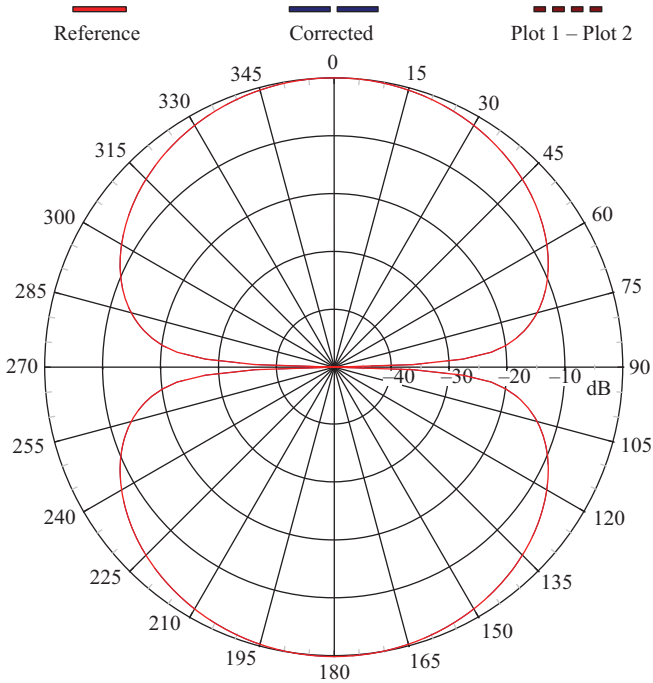

Figure 10.57 Simulated dipole radiation patterns: reference and 0.1λ axis non-intersection error-corrected cases overlay perfectly. The difference pattern is <−50 dB and not visible here

reference. Such a gain calibration is obtained through a separate measurement process (and often performed by a third party) with a relevant measurement uncertainty that applies. For instance, when a gain calibration is performed by a National Calibration Laboratory, the gain standard is delivered with a calibration certificate and a calibration report that states the associated calibration uncertainty. It is this uncertainty that is taken into consideration here and it applies equally to all near-field and far-field measurements. Since this uncertainty figure contains within it an entire measurement process, it is often the driving factor in a gain RA uncertainty budget.

10.7.2 Normalisation constant

When a gain calibration is performed, there are uncertainties associated with that measurement. For instance, when a *direct connect* [18] measurement is made, an

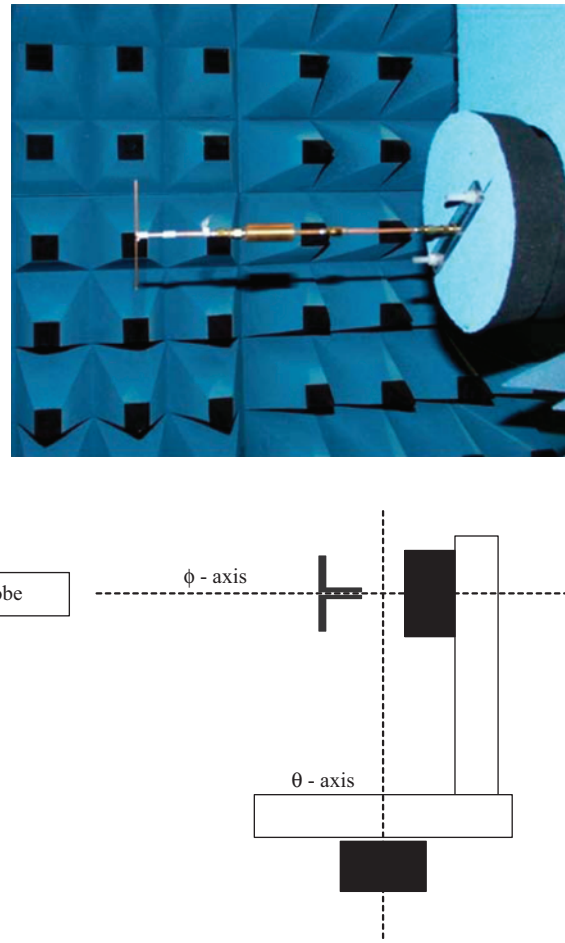

Figure 10.58 Dipole SNF test setup (Due to the fact that the dipole illuminates the support structure strongly, the mounting configuration was changed from that shown, to the dipole rotated to be collinear to the ϕ-axis)

attenuator is often introduced in the through measurement to ensure that the receiver is not saturated and to normalise the power level between the radiation and coaxial measurements. (This is to minimise the effects of receiver non-linearity and to mitigate any impedance mismatch effects. The logic of the former being that measuring signals of roughly the same magnitude can be done with more precision than measuring signals that differ greatly.) This process of introducing an

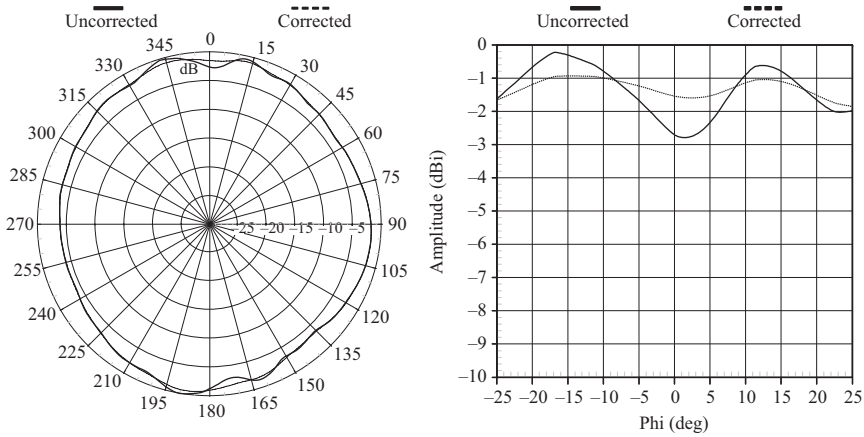

Figure 10.59 Dipole omni-directional pattern. Effect of 6 mm axis non-intersection error (solid) and corrected (dashed)

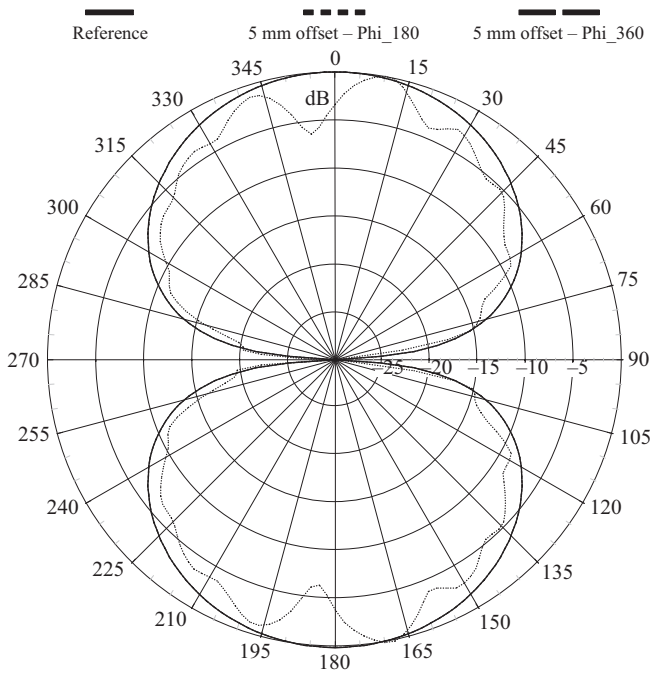

Figure 10.60 Simulated dipole radiation pattern. Solid curve is reference, dashed line is with a 0.1λ axis non-intersection error introduced for Phi_180 acquisition and Phi_360 acquisition is indistinguishable form reference

attenuator, disconnecting and connecting cables all introduce uncertainty. The value of the attenuator[10] will have some uncertainty associated with it and the repeatability of the coaxial connectors being mated as well. The combined effect of these is what we would assign as the *Normalisation constant* uncertainty.

When gain calibration is performed by a *comparison technique*, we have to measure the gain standard and a known gain value of that standard now becomes our reference that determines the normalisation that has to be performed to calibrate our system. The uncertainty in the known reference value is taken into account by the *Gain standard uncertainty* mentioned earlier, and what is to be addressed here are all other factors contributing to uncertainty in our normalisation measurement. Since our gain standard is measured exactly like an AUT we have to consider factors like truncation and leakage to assess this uncertainty. Since it is the value of the far-field beam peak for our gain reference that is most critical, we focus on factors that may affect this value significantly. We can of course complete a full 18-term range assessment for the gain standard measurement but in practice we usually focus on near-field truncation, probe structure reflections, chamber reflections and receiver leakage. Each one of these terms is assessed as described below and collectively (in essence we do a mini-RA for the gain standard) becomes our *Normalisation constant* uncertainty.

10.7.3 Impedance mismatch

This error term is simple to understand in principle, but many hours can be consumed during a test campaign due to confusion about the precise procedure to successfully correct for it. In what follows, we give a verbose analysis of the problem and step by step direction of the implementation of the correction procedure, in an effort to clarify matters. The most extensive and complete body of the work on this topic is presented in [19] and the work presented here is to a large extent based on this reference. This error term applies to absolute power measurements and therefore applies equally to PNF, CNF, SNF and far-field test systems. It pertains to the impedance mismatch[11] difference between the AUT and the gain standard being used and impacts absolute level measurements, like gain. If we consider the case of an AUT connected to a test system transmit port (or receive) and a near-field probe (also applies to a far-field source antenna) connected to the receive (or transmit) test system port, we know that at both of these interfaces some level of impedance mismatch will exist, reducing the efficiency of power transfer. However, for the duration of the measurement, this condition will remain constant for a fixed frequency and the measurement can be made without consideration given to this fact. It is once the AUT is replaced with a gain standard that the impedance equilibrium of our measurement is disturbed and compensation for the

[10]This attenuator would need to be calibrated using a VNA and this measurement will have an uncertainty associated with it.

[11]When we refer to 'impedance mismatch', we mean an 'acceptable' mismatch and not something pathological that would degrade the signal-to-noise ratio (SNR) to a point that no meaningful measurement can be made.

changing of impedances is required. Since we are attempting to establish the AUT gain w.r.t. the gain standard, we have to compensate for this change since it impacts the power transfer efficiency and this will impact our absolute gain result. In the unlikely eventuality that the AUT and the gain standard have the exact same input impedances (this requires the exact same amplitude AND phase), the power transfer efficiency will not change and this impedance mismatch error term becomes zero.

If we consider an impedance interface as shown in Figure 10.61, the impedance mismatch at the interface allows us to calculate a complex voltage reflection coefficient Γ_{Right}, looking towards the right as

$$\Gamma_{\text{Right}} = \frac{Z_1 - Z_0}{Z_1 + Z_0}$$

and a corresponding complex voltage reflection coefficient Γ_{Left}, looking to the left as

$$\Gamma_{\text{Left}} = \frac{Z_0 - Z_1}{Z_0 + Z_1} = -\Gamma_{\text{Right}}$$

The ratio of the impedance interface is also often encountered in the literature and can be written as

$$\frac{Z_1}{Z_0} = \frac{1 + \Gamma_{\text{Right}}}{1 - \Gamma_{\text{Right}}} \tag{10.24}$$

From the complex voltage reflection coefficient, one can then also compute the voltage standing wave ratio (VSWR) as

$$\text{VSWR} = \frac{1 + |\Gamma|}{1 - |\Gamma|}$$

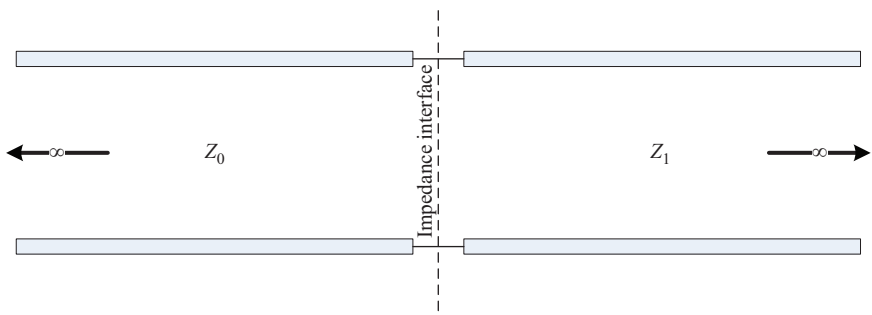

Figure 10.61 Two transmission lines of dissimilar impedance connected to form an impedance interface

Conversely, the magnitude of the complex voltage reflection coefficient can be obtained from the VSWR as

$$|\Gamma| = \frac{\text{VSWR} - 1}{\text{VSWR} + 1}$$

Note, as the current reflection coefficient is merely the negative of the voltage reflection coefficient, we shall avoid its use. Return loss in dB is defined as

$$\text{RL}|_{\text{dB}} = -20\log_{10}|\Gamma|$$

Transmission loss in dB is therefore defined as

$$\text{TL}|_{\text{dB}} = -10\log_{10}(1 - |\Gamma|^2)$$

The percentage of the reflected power can be obtained from the voltage reflection coefficient using

$$P_R|_{\%} = 100|\Gamma|^2$$

Similarly, the percentage of the power transmitted can be obtained using

$$P_T|_{\%} = 100\left(1 - |\Gamma|^2\right)$$

These expressions were used to generate Table A.6 in the Appendix. Note: in some texts, transmission loss can be referred to as mismatch loss.

With the complex voltage reflection coefficient defined, we can now also look at power flow on the transmission line. If we again consider the impedance interface as shown in Figure 10.62, where we now depict an incident voltage V_i, which, when reflected at the impedance interface gives rise to the reflected voltage V_R, we

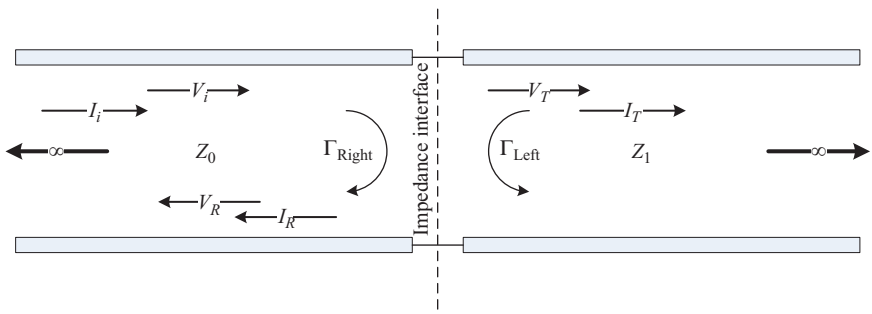

Figure 10.62 Two transmission lines of dissimilar impedance connected to form an impedance interface. Relevant voltages and currents are depicted

can relate this to the incident voltage as

$$V_R = V_i \Gamma_{\text{Right}}$$

It should be noted that at the interface the total line voltage must be equal to the transmitted voltage

$$V_T = V_i + V_R$$

leading to one being able to express the transmitted voltage V_T in terms of the incident voltage as

$$V_T = V_i(1 + \Gamma_{\text{Right}})$$

We can now also define a set of currents corresponding to the voltages defined above where they are related as follows:

$$I_i = \frac{V_i}{Z_0}$$
$$I_R = \frac{V_R}{Z_0} = \frac{V_i \Gamma_{\text{Right}}}{Z_0}$$

As for the voltage, the current has a continuity condition at the interface in that the total line current must be continuous, therefore

$$I_T = I_i - I_R$$

leading one to be able to express the transmitted current I_T in terms of the incident current as

$$I_T = I_i(1 - \Gamma_{\text{Right}})$$

With the voltages and currents defined, we can now proceed to calculate power flow at the interface. The time-averaged incident power can be written as

$$\begin{aligned} P_i &= \frac{1}{2}\text{Re}\left[V_i I_i^*\right] \\ &= \frac{1}{2}\text{Re}[V_i (V_i/Z_0)^*] \\ &= \frac{1}{2}|V_i|^2 \text{Re}[1/Z_0] \end{aligned}$$

and the time averaged reflected power can be written as

$$\begin{aligned} P_R &= \frac{1}{2}\text{Re}\left[V_R I_R^*\right] \\ &= \frac{1}{2}\text{Re}\left[V_i \Gamma_{\text{Right}} \left(\frac{V_i \Gamma_{\text{Right}}}{Z_0}\right)^*\right] \\ &= \frac{1}{2}|V_i \Gamma_{\text{Right}}|^2 \text{Re}\left[\frac{1}{Z_0}\right] \end{aligned}$$

where the asterisk denotes complex conjugation. The time-averaged transmitted power can then be written as

$$\begin{aligned} P_T &= \frac{1}{2}\mathrm{Re}\left[V_T I_T^*\right] \\ &= \frac{1}{2}\mathrm{Re}\left[V_i(1+\Gamma_{\mathrm{Right}})(I_i(1-\Gamma_{\mathrm{Right}}))^*\right] \\ &= \frac{1}{2}\mathrm{Re}\left[V_i(1+\Gamma_{\mathrm{Right}})\left(\frac{V_i(1-\Gamma_{\mathrm{Right}})}{Z_0}\right)^*\right] \\ &= \frac{1}{2}|V_i|^2\left(1-|\Gamma_{\mathrm{Right}}|^2\right)\mathrm{Re}\left[\frac{1}{Z_0}\right] \end{aligned} \tag{10.25}$$

which supports the principle of the conservation of power, since the power transmitted is equal to the incident power minus the reflected power as

$$P_T = P_i - P_R$$

We can now consider the case of a generator (with an internal impedance of Z_G) attached to a lossless transmission line of length l and impedance Z_0, which is in turn terminated in a load impedance Z_L, as depicted in Figure 10.63. This case represents what we face in an antenna range when an antenna is connected to a source or receiver via some transmission line.

Assuming an impedance mismatch at the generator to transmission line interface, as well as the transmission line to load interface, we know that this will lead to inefficiency in power transfer. At the generator end, we can calculate a voltage reflection coefficient looking into the generator as

$$\Gamma_G = \frac{Z_G - \mathrm{Z}_0}{Z_G + Z_0}$$

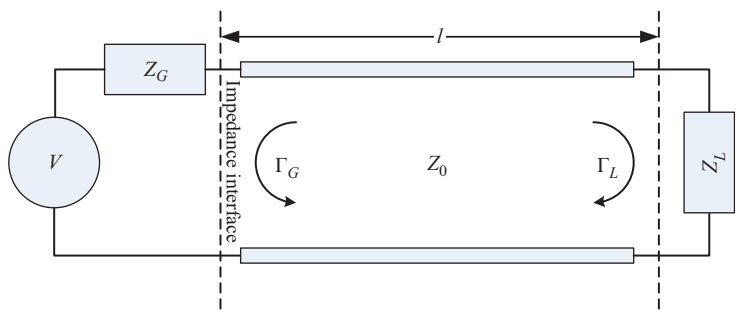

Figure 10.63 A source is shown connected to a transmission line and load impedance

and at the load end, we can calculate a voltage reflection coefficient looking into the load as

$$\Gamma_L = \frac{Z_L - Z_0}{Z_L + Z_0}$$

In order to compute the power being dissipated in the load (or antenna), we have to simplify this diagram further and we can do that by transforming the load impedance through the section of the transmission line (length l and propagation constant β) to find an equivalent impedance $Z_{L'}$ [20] as

$$Z_{L'} = Z_0 \frac{Z_L + jZ_0 \tan \beta l}{Z_0 + jZ_L \tan \beta l} = Z_0 \frac{1 + \Gamma_L e^{-2j\beta l}}{1 - \Gamma_L e^{-2j\beta l}} \tag{10.26}$$

Using this equivalent impedance,[12] Figure 10.63 can be simplified to a lumped element circuit, as depicted in Figure 10.64.

We can now compute the power being dissipated in the equivalent load $Z_{L'}$ using the power expression of (10.25). In order to do so, we need to relate the source voltage V to the incident voltage V_i [19] and we can do so by first calculating the voltage $V_{L'}$ across the equivalent load impedance $Z_{L'}$ in terms of a simple voltage divider

$$V_{L'} = V \frac{Z_{L'}}{Z_{L'} + Z_G}$$

Note that this voltage is the line voltage at the source side impedance interface of Figure 10.63 and since the transmission line is lossless, power flow calculated at this interface will represent power flow dissipated by the load Z_L. If we now compare this impedance interface to that shown in Figure 10.62 (between two infinite transmission lines), we see that the voltage $V_{L'}$ applied across the equivalent load impedance $Z_{L'}$ corresponds to the line voltage (consisting of incident and a reflected waves) applied across the impedance interface in Figure 10.62 and this allows us to write

$$V_{L'} = V_i + V_R = V \frac{Z_{L'}}{Z_{L'} + Z_G}$$

which in turn allows us to relate V and V_i directly as

$$V_i(1 + \Gamma_{L'}) = V \frac{Z_{L'}}{Z_{L'} + Z_G}$$

where $\Gamma_{L'}$ corresponds to the equivalent load reflection coefficient

$$\Gamma_{L'} = \frac{Z_{L'} - Z_0}{Z_{L'} + Z_0}$$

[12]We use the prime notation here to indicate an impedance or voltage reflection coefficient related to the load (or later the source) transformed through a section of transmission line as defined by (10.26).

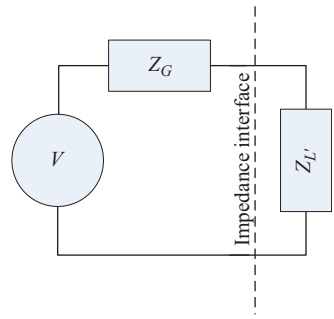

Figure 10.64 A lumped element circuit, allowing one to calculate the voltage across the equivalent load impedance

We can now solve for V_i, by substituting impedance values with their reflection coefficient forms by using (10.24)

$$V\frac{(1+\Gamma_{L'})}{(1-\Gamma_{L'})}Z_0 = V_i(1+\Gamma_{L'})\left[\frac{(1+\Gamma_{L'})}{(1-\Gamma_{L'})}Z_0 + \frac{(1+\Gamma_G)}{(1-\Gamma_G)}Z_0\right]$$

which can then be simplified further as follows:

$$\begin{aligned}
V_i &= V\frac{(1+\Gamma_{L'})}{(1-\Gamma_{L'})}\frac{1}{(1+\Gamma_{L'})}\left[\frac{(1+\Gamma_{L'})}{(1-\Gamma_{L'})}+\frac{(1+\Gamma_G)}{(1-\Gamma_G)}\right]^{-1} \\
&= V\frac{1}{(1-\Gamma_{L'})}\left[\frac{(1+\Gamma_{L'})(1-\Gamma_G)+(1+\Gamma_G)(1-\Gamma_{L'})}{(1-\Gamma_{L'})(1-\Gamma_G)}\right]^{-1} \\
&= V\frac{1}{(1-\Gamma_{L'})}\left[\frac{(1-\Gamma_{L'})(1-\Gamma_G)}{(1+\Gamma_{L'})(1-\Gamma_G)+(1+\Gamma_G)(1-\Gamma_{L'})}\right] \\
&= V\left[\frac{(1-\Gamma_G)}{(1+\Gamma_{L'})(1-\Gamma_G)+(1+\Gamma_G)(1-\Gamma_{L'})}\right] \\
&= \frac{V(1-\Gamma_G)}{(1+\Gamma_{L'})(1-\Gamma_G)+(1+\Gamma_G)(1-\Gamma_{L'})} \\
&= \frac{V(1-\Gamma_G)}{1-\Gamma_G+\Gamma_{L'}-\Gamma_{L'}\Gamma_G+1+\Gamma_G-\Gamma_{L'}-\Gamma_{L'}\Gamma_G}
\end{aligned}$$

which leads to a result allowing one to relate the source voltage V to the incident wave voltage V_i as

$$V_i = \frac{V(1-\Gamma_G)}{2(1-\Gamma_{L'}\Gamma_G)}$$

This expression is a fundamental expression for relating voltages for a source connected to a load impedance [19]. If we now define this expression as the voltage

amplitude emerging from the source with internal impedance Z_G and denote it as V_G, when a non-reflecting load is connected to the source, we can write

$$V_i = V_G = \frac{V}{2}(1 - \Gamma_G)|_{\Gamma_{L'}=0}$$

which allows us to write

$$\begin{aligned} V_i &= \frac{V_G}{(1 - \Gamma_{L'}\Gamma_G)} \\ &= V_G + V_i\Gamma_{L'}\Gamma_G \\ &= V_G + V_{L'}\Gamma_G \end{aligned}$$

If we now again turn our attention to the source side impedance interface of Figure 10.63, we can write the following expression for the power delivered to the transmission line and load by substituting the expression for the incident voltage V_i above, into (10.25) as

$$\begin{aligned} P_T &= \frac{1}{2}|V_i|^2(1 - |\Gamma_{L'}|^2)\mathrm{Re}[1/Z_G] \\ &= \frac{1}{2}\left|\frac{V_G}{(1 - \Gamma_{L'}\Gamma_G)}\right|^2(1 - |\Gamma_{L'}|^2)\mathrm{Re}[1/Z_G] \\ &= \frac{1}{2}\frac{|V_G|^2}{\mathrm{Re}[Z_G]}\frac{1 - |\Gamma_{L'}|^2}{|1 - \Gamma_{L'}\Gamma_G|^2} \end{aligned}$$

It is now worthwhile to rewrite the incident and reflected power components as

$$\begin{aligned} P_T &= P_i - P_R \\ P_i &= \frac{1}{2}\frac{|V_G|^2}{\mathrm{Re}[Z_G]}\frac{1}{|1 - \Gamma_{L'}\Gamma_G|^2} \\ P_R &= \frac{1}{2}\frac{|V_G|^2}{\mathrm{Re}[Z_G]}\frac{|\Gamma_{L'}|^2}{|1 - \Gamma_{L'}\Gamma_G|^2} \end{aligned}$$

We can now also identify the maximum power that can be delivered by the source to the load when the load is a conjugate match to the source ($\Gamma_{L'} = \Gamma_G^*$) as

$$\begin{aligned} P_{\max} &= \frac{1}{2}\frac{|V_G|^2}{\mathrm{Re}[Z_G]}\frac{1 - |\Gamma_G^*|^2}{|1 - \Gamma_G^*\Gamma_G|^2} \\ &= \frac{1}{2}\frac{|V_G|^2}{\mathrm{Re}[Z_G]}\frac{1 - |\Gamma_G|^2}{|1 - |\Gamma_G|^2|^2} \\ &= \frac{1}{2}\frac{|V_G|^2}{\mathrm{Re}[Z_G]}\frac{1}{1 - |\Gamma_G|^2} \end{aligned}$$

which in turn allows us to rewrite the delivered power expression as

$$P_T = P_{\max}\frac{(1-|\Gamma_G|^2)(1-|\Gamma_{L'}|^2)}{|1-\Gamma_{L'}\Gamma_G|^2} \tag{10.27}$$

This expression can also be rewritten as

$$P_T = P_{\max}\left[1-\left|\frac{\Gamma_{L'}-\Gamma_G^*}{1-\Gamma_{L'}\Gamma_G}\right|^2\right] \tag{10.28}$$

which has the advantage of illustrating the maximum property of $P_{\max}$, since the term in brackets is bounded by zero and unity.

At this point, we have to address the fact that the power expressions above describe power flow at the source side impedance interface of Figure 10.63 and in many instances this may not be the interface of interest to one and in fact, we often disconnect the transmission line at the antenna under test (load) to exchange that with a gain standard for calibration purposes. We are therefore in need of impedance mismatch correction equations at an interface of our choosing. This can be addressed by realising that the power flow expressions above can be applied to the load side impedance interface of Figure 10.63 and in that instance $\Gamma_{L'}$ is simply equal to Γ_L, Γ_G needs to be replaced by $\Gamma_{G'}$ and Z_G needs to be replaced by $Z_{G'}$ where the primes denote transformation through the section of the transmission line as defined by (10.26), but ensuring the length l is adjusted as appropriate. These modifications allow us to change the power flow expressions to describe power flow at any transmission line impedance interface and we simply need to measure the impedance (and associated reflection coefficients) looking into both ends of the transmission line to evaluate them. This is of significant practical value and we can now rewrite (10.27) to show these modified variables as

$$P_T = P_{\max}\frac{(1-|\Gamma_{G'}|^2)(1-|\Gamma_{L'}|^2)}{|1-\Gamma_{L'}\Gamma_{G'}|^2} \tag{10.28}$$

which can in turn be used to write an impedance mismatch correction factor as

$$\frac{P_T}{P_{\max}} = \frac{(1-|\Gamma_{G'}|^2)(1-|\Gamma_{L'}|^2)}{|1-\Gamma_{L'}\Gamma_{G'}|^2}$$

or as a dB correction factor as

$$\frac{P_T}{P_{\max}}|_{\text{dB}} = 10\log\left[\frac{(1-|\Gamma_{G'}|^2)(1-|\Gamma_{L'}|^2)}{|1-\Gamma_{L'}\Gamma_{G'}|^2}\right]$$

where $\Gamma_{L'}$ is the voltage reflection coefficient measured looking towards the load (or antenna) and $\Gamma_{G'}$ is the voltage reflection coefficient measured looking towards the source (or receiver). In the expressions above $0 \leq P_T/P_{\max} \leq 1$ and once converted to dB is a negative number and is SUBTRACTED from the measured

gain of an AUT (or SGA), to obtain the higher, corrected value. Since the IEEE definition of gain [21] assumes that the AUT is connected to a matched network, this impedance mismatch correction always raises the gain value of the AUT, since it is typically not matched during testing.

After this lengthy derivation of the impedance mismatch expression, we can now compute the ***ratio*** of the mismatch between AUT and standard gain antenna (SGA) as

$$\begin{aligned} M &= \frac{P_{T\_\mathrm{AUT}}}{P_{T\_\mathrm{SGA}}} \\ &= \frac{P_{\max}\dfrac{(1-|\Gamma_{G'}|^2)(1-|\Gamma_{\mathrm{AUT}}|^2)}{|1-\Gamma_{\mathrm{AUT}}\Gamma_{G'}|^2}}{P_{\max}\dfrac{(1-|\Gamma_{G'}|^2)(1-|\Gamma_{\mathrm{SGA}}|^2)}{|1-\Gamma_{\mathrm{SGA}}\Gamma_{G'}|^2}} \\ &= \frac{|1-\Gamma_{\mathrm{SGA}}\Gamma_{G'}|^2[1-|\Gamma_{\mathrm{AUT}}|^2]}{|1-\Gamma_{\mathrm{AUT}}\Gamma_{G'}|^2[1-|\Gamma_{\mathrm{SGA}}|^2]} \end{aligned} \tag{10.29}$$

Equation (10.29) can be expressed as a dB correction term as

$$M_{\mathrm{dB}} = 10\log\left[\frac{|1-\Gamma_{\mathrm{SGA}}\Gamma_{G'}|^2[1-|\Gamma_{\mathrm{AUT}}|^2]}{|1-\Gamma_{\mathrm{AUT}}\Gamma_{G'}|^2[1-|\Gamma_{\mathrm{SGA}}|^2]}\right]$$

Since the AUT gain is determined in comparison to that of the SGA, the ratio of the two correction values for the AUT and the SGA is given by M, and M_{dB} is the gain correction term due to mismatch loss relative to the SGA and this number can be positive OR negative, depending on the relative mismatches of the AUT and SGA. M_{dB} is SUBTRACTED from the measured gain value of the AUT, to obtain the corrected value. Since the correction value M_{dB} can be positive OR negative, it can therefore increase or decrease the AUT gain value since it relates the relative match of the AUT and SGA. It is worthwhile to step through the reasoning process here:

1. Port connecting source/receiver to device under test reflection coefficient is measured as complex $\Gamma_{G'}$ using calibrated VNA.
2. AUT reflection coefficient is measured as complex Γ_{AUT} using calibrated VNA.
3. SGA reflection coefficient is measured as complex Γ_{SGA} using calibrated VNA.
4. We typically measure return loss and in Table 10.8 we show three typical cases and the corresponding reflection coefficient magnitudes. By now considering arbitrary phase values for each, we can calculate the factors P_T and M for the corresponding return loss values.
5. Case 1: If we assume that the SGH reflection coefficient is almost matched to the source/receiver impedance and the AUT is matched poorly, the power transfer to

Table 10.8 Typical measured return loss values and their corresponding reflection coefficient magnitudes

Case no.	$RL_{G'}$ (dB)	RL_{SGA} (dB)	RL_{AUT} (dB)	$\lvert\Gamma_{G'}\rvert$	$\lvert\Gamma_{SGA}\rvert$ (dB)	$\lvert\Gamma_{AUT}\rvert$ (dB)
1	20	25	10	0.1	0.056	0.316
2	20	12	10	0.1	0.251	0.316
3	20	12	25	0.1	0.251	0.056

the SGH will be much more efficient than to the AUT and the correction term M_{dB} is almost solely due to the AUT mismatch. This is depicted in Figure 10.66 (top). In this diagram the phase for Γ_{AUT} is varied from -180° to $+180^\circ$ and the phase for Γ_{SGA} is assumed to be double[13] that of Γ_{AUT}. We see that for a phase value of 0° the corresponding correction term is roughly equal to -0.2 dB.

6. Case 2: If we assume that the SGH reflection coefficient is similar to the AUT reflection coefficient, the power transfer to both is similar and simply a function of specific phasing and the correction term M_{dB} can actually lower the measured gain of the AUT in some instances. This is depicted in Figure 10.66 (middle) and the correction term M_{dB} is seen to be positive in some of the phase regions.
7. Case 3: If we assume that the AUT reflection coefficient is almost matched to the source/receiver impedance and the SGA is matched poorly, the power transfer to the AUT will be much more efficient than to the SGA and the correction term M_{dB} is almost solely due to the SGA mismatch. This is depicted in Figure 10.66 (bottom). We see that for a phase value of 0°, the correction term is roughly equal to 0.1 dB, and since it is a positive number, it will effectively lower the measured gain of the AUT.

One last aspect of the impedance correction to be considered is that of the unavailability of phase information. This is relevant since antennas are often supplied with VSWR values only and therefore only the magnitude of the reflection coefficient is available. In such instances, we cannot correct for impedance mismatch, but only estimate worst-case bounds. If we again consider (10.28), shown below for convenience

$$P_T = P_{\max}\frac{(1-|\Gamma_{G'}|^2)(1-|\Gamma_{L'}|^2)}{|1-\Gamma_{L'}\Gamma_{G'}|^2}$$

We see that the numerator is phase independent and only the denominator is affected by phase through the complex multiplication of the two reflection

[13]These phase variations are arbitrary and is simply shown here to sensitise the reader to the fact that the relative phase between these reflection coefficients strongly affect the magnitude of the correction factor calculated.

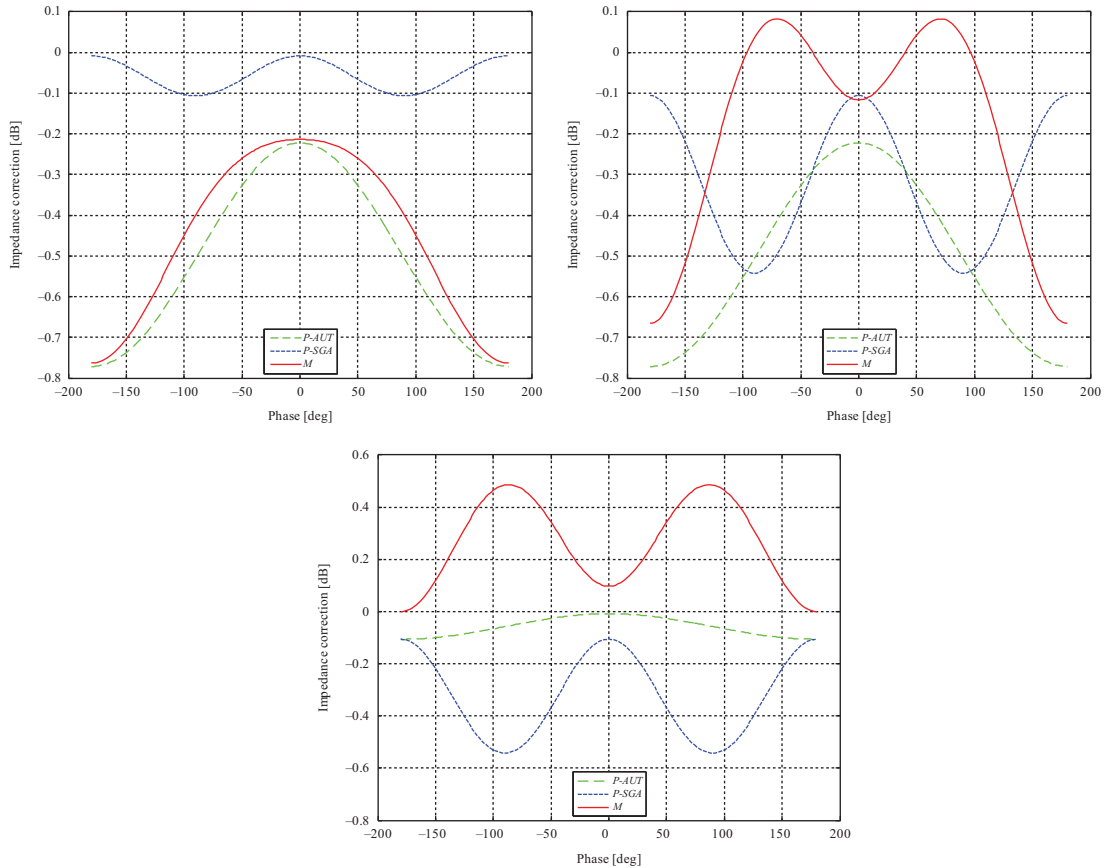

Figure 10.65 The factors P_AUT, P_SGA and M are shown as a function of phase for Cases 1, 2 and 3 as defined in Table 10.8

coefficients. If we expand the denominator into real and imaginary components, we can write the following expression for bounding the term:

$$\frac{(1-|\Gamma_{G'}|^2)(1-|\Gamma_{L'}|^2)}{[1+|\Gamma_{L'}||\Gamma_{G'}|]^2} \leq \frac{P_T}{P_{\max}} \leq \frac{(1-|\Gamma_{G'}|^2)(1-|\Gamma_{L'}|^2)}{[1-|\Gamma_{L'}||\Gamma_{G'}|]^2}$$

If we again consider the three cases above, we can evaluate these limits as shown in Table 10.9 and can be visually confirmed in Figure 10.65.

These expressions therefore allow us to estimate limits for the correction term M as

$$M_{\max} = \frac{P_{T\_\mathrm{AUT}\_\max}}{P_{T\_\mathrm{SGA}\_\min}}$$

and

$$M_{\min} = \frac{P_{T\_\mathrm{AUT}\_\min}}{P_{T\_\mathrm{SGA}\_\max}}$$

We can therefore write the limits for M as

$$\frac{(1-|\Gamma_{\mathrm{AUT}}|^2)}{[1+|\Gamma_{\mathrm{AUT}}||\Gamma_{G'}|]^2}\frac{[1-|\Gamma_{\mathrm{SGA}}||\Gamma_{G'}|]^2}{(1-|\Gamma_{\mathrm{SGA}}|^2)} \leq M \leq \frac{(1-|\Gamma_{\mathrm{AUT}}|^2)}{[1-|\Gamma_{\mathrm{AUT}}||\Gamma_{G'}|]^2}\frac{[1+|\Gamma_{\mathrm{SGA}}||\Gamma_{G'}|]^2}{(1-|\Gamma_{\mathrm{SGA}}|^2)}$$

which are also evaluated for the three cases above and are shown in Table 10.10. These numbers can partially (subject to relative phase relationships) be confirmed visually in Figure 10.65.

It must also be stated that when considering an AUT and probe pair, we usually only think about the guided wave mismatches. However, one should be cognisant of

Table 10.9 Typical measured return loss values, their corresponding reflection coefficient magnitudes and associated impedance mismatch correction (P) limits

Case no.	$RL_{G'}$ (dB)	RL_{SGA} (dB)	RL_{AUT} (dB)	$\lvert\Gamma_{G'}\rvert$	$\lvert\Gamma_{SGA}\rvert$	$\lvert\Gamma_{AUT}\rvert$	P_{min_SGA} (dB)	P_{max_SGA} (dB)	P_{min_AUT} (dB)	P_{max_AUT} (dB)
1	20	25	10	0.1	0.056	0.316	−0.106	−0.008	−0.772	−0.222
2	20	12	10	0.1	0.251	0.316	−0.542	−0.106	−0.772	−0.222
3	20	12	25	0.1	0.251	0.056	−0.542	−0.106	−0.106	−0.008

Table 10.10 Typical measured return loss values, their corresponding reflection coefficient magnitudes and associated impedance mismatch correction (M) limits

Case no.	$RL_{G'}$ (dB)	RL_{SGA} (dB)	RL_{AUT} (dB)	$\lvert\Gamma_{G'}\rvert$	$\lvert\Gamma_{SGA}\rvert$	$\lvert\Gamma_{AUT}\rvert$	M_{min} (dB)	M_{max} (dB)
1	20	25	10	0.1	0.056	0.316	−0.763	−0.116
2	20	12	10	0.1	0.251	0.316	−0.666	0.320
3	20	12	25	0.1	0.251	0.056	0	0.534

the fact that a free-space mismatch also exists between the AUT and the probe. A standing wave pattern therefore exists in free space between the AUT and the probe and this effect becomes more pronounced for reduced separation distances. This implies that even if the AUT and gain standard have identical input impedances, this standing wave pattern will change when the AUT and gain standard is exchanged and still introduce an uncertainty. The impact of this free-space mismatch is most significant for PNF test systems where the AUT to probe separation distance is usually a minimum. The impact of this effect is regarded as part of the *multiple reflection* error term and is not considered part of the impedance mismatch error term.

10.8 Processing-related errors

The errors addressed in this section are all related to the application of near-field theory in practice. That is, reducing scan sizes from infinity to a finite and practical acquisition region or the assumption of the AUT being band limited and using finite sampling densities to solve for a finite number of modal coefficients.

10.8.1 Aliasing

All the near-field theory presented relies on a modal expansion of some sort and these dictate an infinite number of modes. We then make the assumption that the AUT is band limited (as this concept applies to each of the formulations presented) and this step allows us to reduce our problem from one with an infinite number of modes to a finite number. This finite number then also dictates our near-field sampling density as described earlier. If we now under sample our near-field data, we end up with a violation of the Nyquist sampling rate and we cannot construct a solution to solve for the modal coefficients we require to fully represent the AUT.

In the case of CNF and SNF solutions, where we have modal functions defined in angular space (only in one plane for CNF), this type of under sampling leads to an insufficient expansion function and the representation is poor over all of angular space. This failure is therefore very evident and nothing is to be gained by under sampling. In the case of PNF and CNF solutions (elevation axis only), where we have modal functions defined in linear space, this type of under sampling leads to aliasing in the spectral domain and this type of result may still be useful if the aliasing is not affecting angular regions of interest. This aliasing is typically encountered when linear sampling exceeds $\lambda/2$ spacing and can be used as a test time reduction technique for cases where only limited regions of far-field angular extent are of interest. A sample spacing of slightly less than $\lambda/2$ produces patterns over a full hemisphere. In some cases, error signals in the measured data due to multiple reflections can produce higher frequency variations and require near-field sampling of less than $\lambda/2$.

To determine the impact of this data point spacing (and the resulting aliasing) on far-field results experimentally, a full near-field measurement is performed using a spacing of $\lambda/4$. The far-field spectrum is calculated and patterns are

compared to measurements taken with larger sample spacings. From these tests, it becomes a simple process to assess if a given data point spacing results in an acceptable level of far-field error due to aliasing effects. An example of this type of result is shown in Figure 10.66. It is also important from a practical point of view to make a $\lambda/4$ spaced measurement and to then decimate this data to obtain the $\lambda/2$ data set. This approach avoids measurement drift and repeatability effects to come into play and gives one the best indication of true aliasing.

10.8.2 Measurement area truncation

Measurement area truncation [22,23] is mostly associated with PNF and CNF test systems since it is an ever-present threat. However, in many instances, SNF data sets are also truncated (often times blockage due to an AUT mount also causes an effective truncation region) to reduce measurement times and it is therefore required to assess the impact of truncation on any near-field truncated measurement. We will focus our attention here on the PNF case.

A typical PNF data set, acquired over a rectangular region, contains amplitude and phase distributions for two orthogonal polarisation components. The amplitude distribution for one polarisation component of an example data set (pyramidal horn) is shown in Figure 10.67. From this amplitude distribution, it is clear that regions of low field intensity, approaching −50 dB below the peak, are present at the edge of the scan plane. Traditionally, scan plane truncation is performed by geometric reduction of the rectangular scan area. This technique relies on the

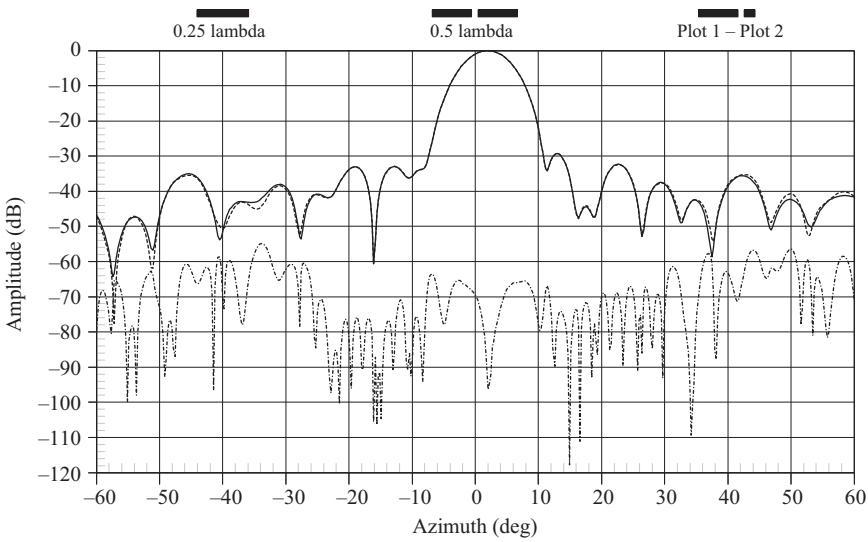

Figure 10.66 PNF derived far-field result for λ/4 near-field spacing (solid line) versus λ/2 near-field spacing (dashed line) and derived E/S level (<−55 dB)

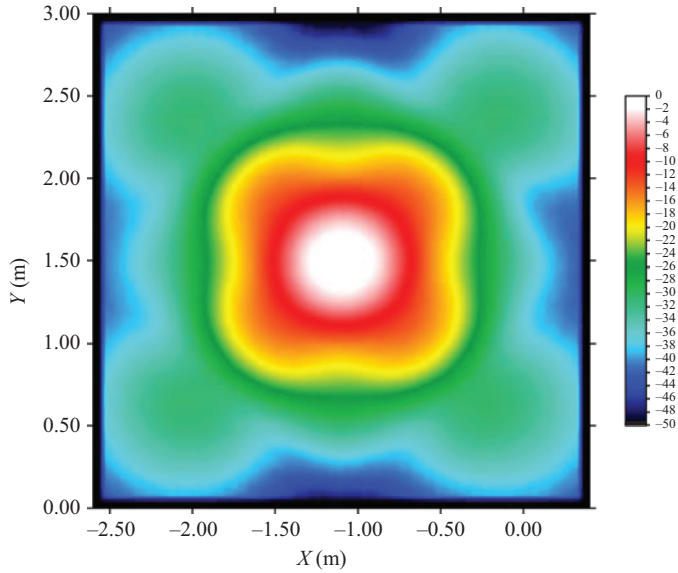

Figure 10.67 Typical PNF amplitude distribution, truncation at roughly −45 dB

judgement of the operator and is oftentimes driven by the truncation error observed in the principal plane radiation patterns only. An example of this type of scan plane reduction is shown as the truncation region in Figure 10.67 where a uniform section of data is omitted along the circumference of the data set. Although not explicitly shown here, this type of truncation is also applied to the orthogonal polarisation data set. The estimated data acquisition time reduction as a result of the truncation shown in this particular example is about 10%.

For the near-field data presented, extraction of the far-field radiation patterns from both the full (3 m × 3 m) and truncated (2.8 m × 2.8 m) data sets provides radiation patterns as shown in Figure 10.68. The reference radiation pattern based on the full data set is shown as a solid red line and the pattern based on the truncated data set is shown as the blue pattern that almost overlays the reference. These patterns clearly show the impact of the truncation and an error pattern can be calculated as shown, with a peak value of roughly –48 dB below the beam peak value.

As a second higher gain AUT example we consider a reflector antenna for which we show the near-field amplitude distribution of the dominant polarisation in Figure 10.69. Rectangular truncation corresponding to roughly a 20% acquisition time reduction is also depicted. Extraction of the far-field radiation patterns from both the full and rectangular truncated data sets again provides comparative radiation patterns and an error level, as shown in Figure 10.70. These patterns show

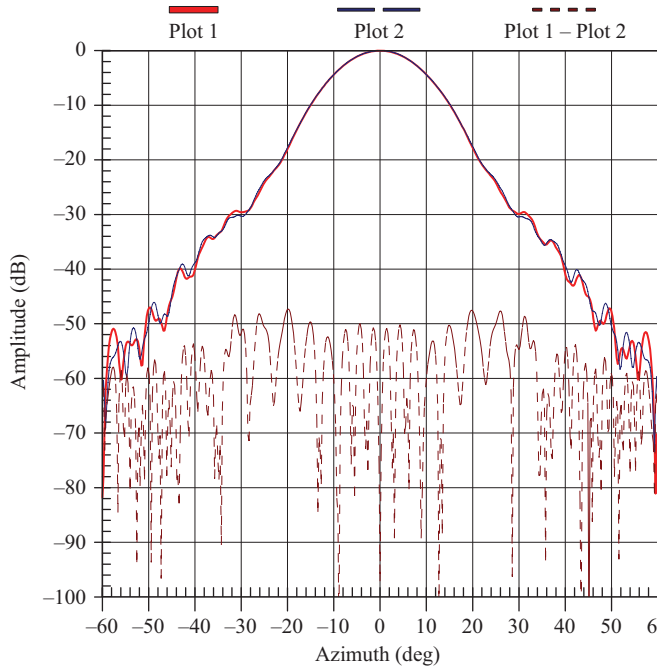

Figure 10.68 Far-field radiation patterns and E/S level for full and rectangular truncated data sets for near-field data depicted in Figure 10.67

the impact of the truncation and an error pattern with a maximum value of less than –62 dB below the beam peak value.

Visual inspection of this near-field distribution for the reflector suggests that the rectangular scan plane truncation is not optimal for the distribution and suggests using an irregular truncation region. Figure 10.71 depicts a truncated data set, where the truncation boundary is established by the amplitude value of the near-field data. It is seen that the boundary is now not a straight line, but a boundary region beyond which the near-field data is negligible.

This truncation is only applied along the *y*-axis and also results in an estimated data acquisition time reduction of 20%.

Extraction of the far-field radiation patterns from both the full and truncated data sets of Figure 10.71 provides comparative radiation patterns, as shown in Figure 10.72. These patterns show the impact of the truncation and an error pattern with a maximum value of roughly –66 dB below the beam peak, a slight improvement over that of the rectangular truncated case. This example illustrates the fact that truncation boundaries need not be simple boundaries, although that

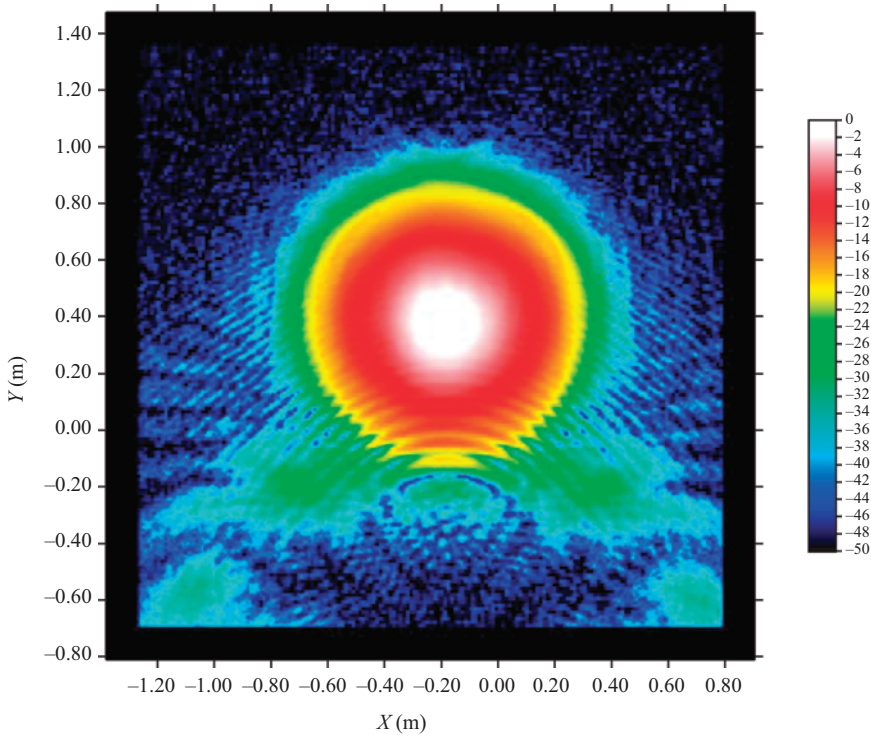

Figure 10.69 Near-field data set for reflector antenna with the truncated region shown along a rectangular region

does simplify practical acquisition systems and there are benefits by selecting irregular truncation boundaries in near-field testing [22].

Some final insight into the truncation process can be gained from the PNF scan plane and spectral domain images depicted in Figure 10.73. These images represent normalised PNF amplitude distributions for a dominant polarisation component. Near-field amplitude values are shown in the top row and spectral domain images are shown in the bottom row. The top row represents a near-field amplitude distribution extending to infinity (top left), the square truncation function (top middle) and the finite, measured near-field amplitude distribution (top right). The top right image is the result of a multiplication of the values in the top left and top centre data sets.

The top and bottom rows are Fourier transform pairs. The bottom left image is the spectral domain representation of the infinite near-field data set. The bottom middle image is the spectral domain representation of the truncation function, and the bottom right image is the spectral domain representation of the finite near-field data set. The bottom right image is therefore the result of a 2D convolution of the bottom left and bottom centre data sets.

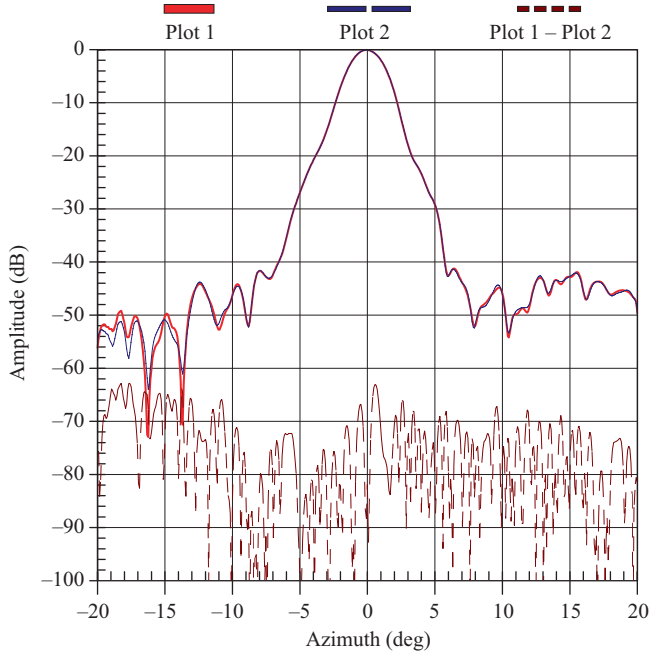

Figure 10.70 Far-field radiation patterns and E/S level for full and rectangular truncated data sets for near-field data depicted in Figure 10.69

The last observation to be made in Figure 10.73 is that the truncation function spectrum (bottom centre) is simply a two-dimensional Sinc function with 13.5 dB principal plane side lobes. It is these side lobes that cause the familiar ripple effect in the spectral domain data. Since the truncation region is a rectangular function (top centre), tapering of this region can lower these side lobes and soften the effect of truncation. These types of truncation reduction techniques can be used with significant success in some instances [22].

10.9 RF sub-system related errors

10.9.1 Receiver amplitude linearity

Receiver amplitude linearity refers to the ability of the RF sub-system to measure signals of widely varying dynamic range accurately. This was a particularly challenging problem with analogue receivers but has become less of a concern with the advent of modern digital receivers. These receivers still contain some degree of analogue conversion circuitry, but any non-linearity of these can easily be compensated for in the digital portion of the receiver through effective calibration procedures. The method used to assess the impact of receiver non-linearity is the exact same process used in the receiver calibration process and therefore we find

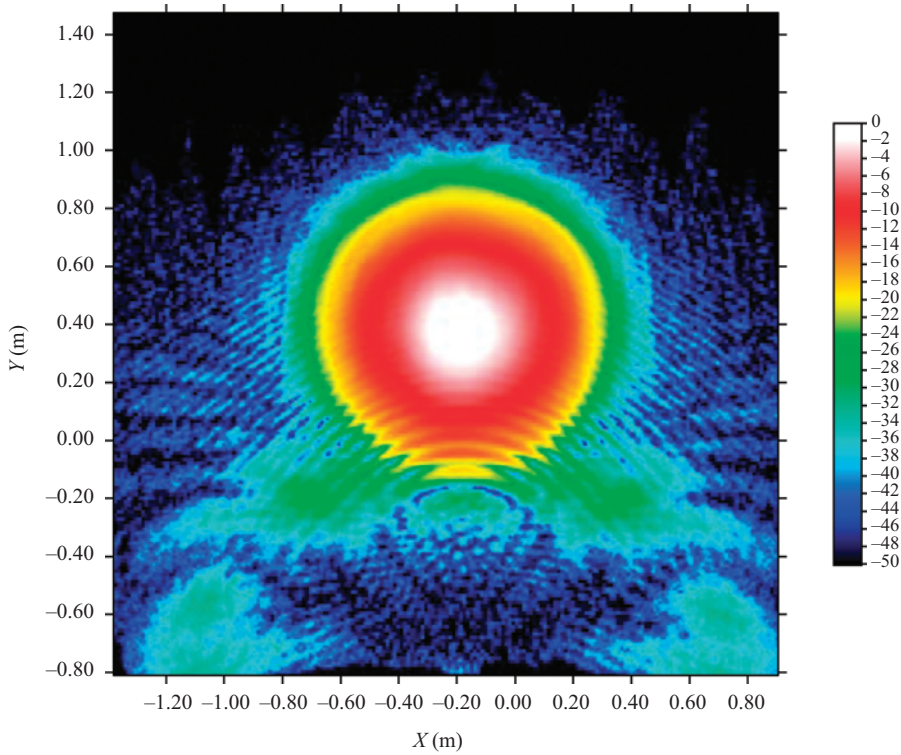

Figure 10.71 Near-field data set for reflector antenna with truncation boundary established by near-field amplitude

that residual receiver non-linearity today is subject to the stability of the calibration and linearity characterisation processes.

Receiver non-linearity is often specified as a dB/dB number, indicating to what extent a signal that is x dB higher or lower than the reference signal will be misrepresented by the receiver due to its non-linear behaviour. For modern receivers, this number is as small as 0.3 dB over a 100 dB range (after calibration), corresponding to 0.003 dB/dB value (which we designate ψ_{dB}), which is indeed very small. The error due to this non-linearity is easily assessed for any measured pattern, since the raw measured data is simply perturbed (in dB) as

$$E'_{\mathrm{dB}}(x,y) = \psi_{\mathrm{dB}}(E_{\mathrm{dB}}(x,y) - E_{\mathrm{dB}}(x_0,y_0)) + E_{\mathrm{dB}}(x,y)$$

where (x_0, y_0) refers to the point of data normalisation. Also, note that (x, y) can be substituted by any two acquisition variables, so that these expressions also apply to raw measured CNF, SNF or far-field data sets. We can write the equivalent linear

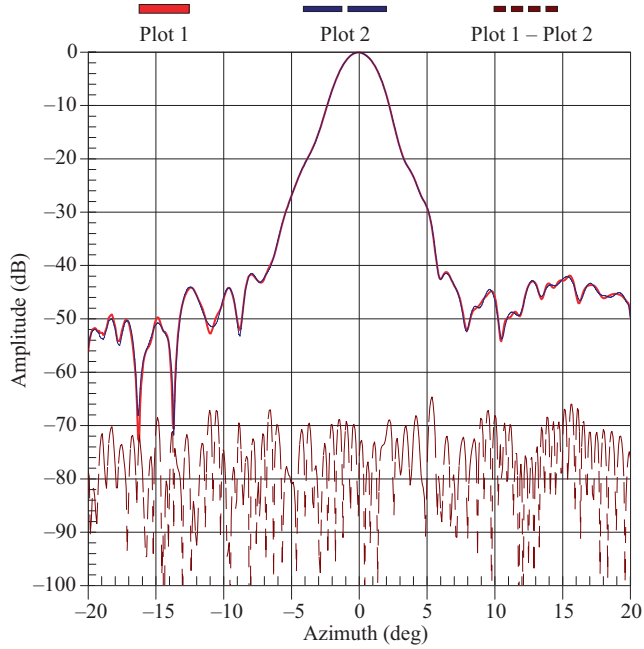

Figure 10.72 Far-field radiation patterns and E/S level for full and irregular truncated data sets for near-field data depicted in Figure 10.71

domain expressions as

$$E'(x,y) = \psi^{(E_{\mathrm{dB}}(x,y) - E_{\mathrm{dB}}(x_0,y_0))} E(x,y)$$
$$= \psi^{20 \log\left[\frac{E(x,y)}{E(x_0,y_0)}\right]} E(x,y)$$

where ψ is the linear version of ψ_{dB}. A simple subtraction of the far-field result obtained from the perturbed data set from that of the far-field result obtained from the reference data set provides one with a complete error to signal equivalent noise floor for this error term. Typical values are $<$70 dB below the beam peak with the result that this term is rarely of concern to one.

10.9.2 Systematic phase

The measurement of phase became essential with the implementation of near-field test systems since the near-field to far-field transformation processes require complex information. This is often not a concern on far-field ranges if amplitude only patterns are measured. (However, in the modern world of antennas where spherical wave post-processing of data for reflection suppression is of interest, phase measurements are common even on far-field ranges where we can obtain

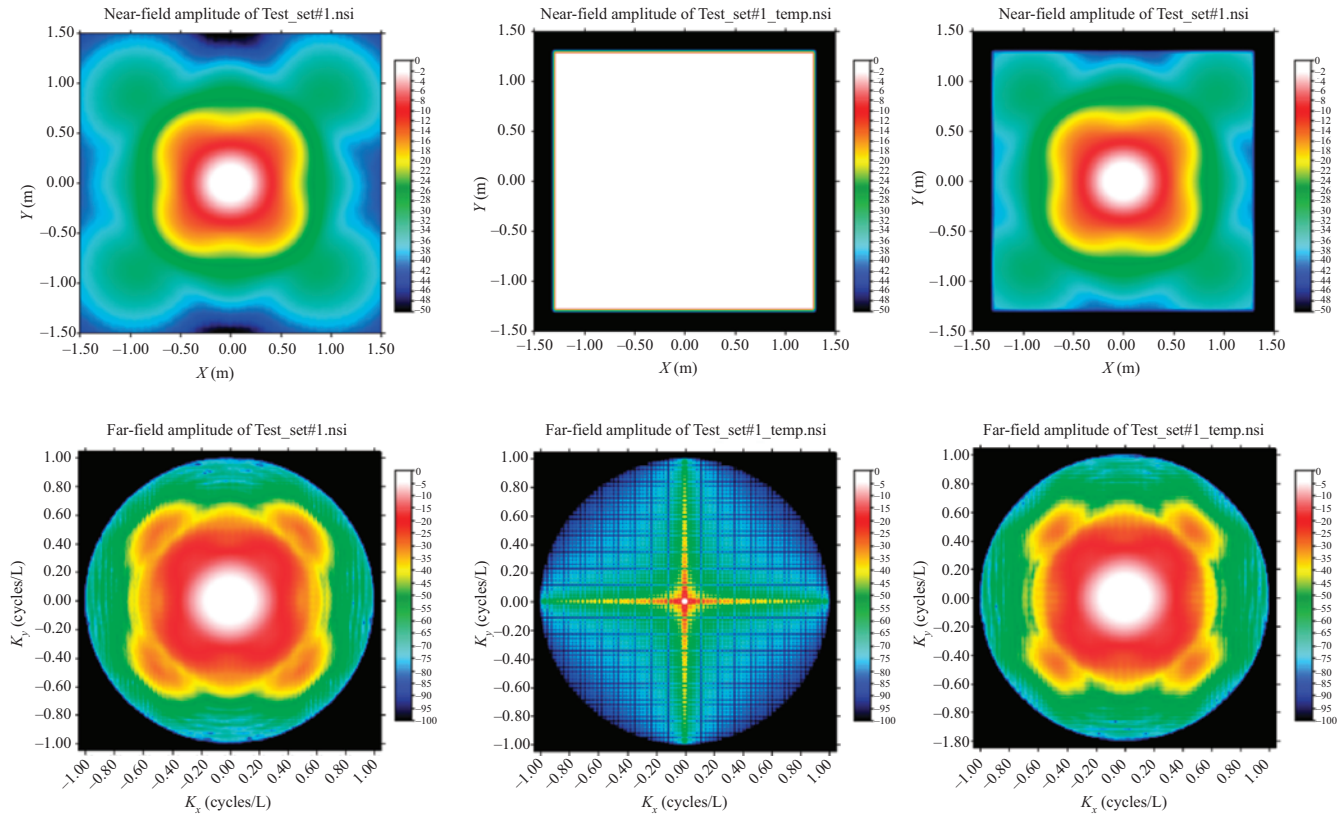

Figure 10.73 PNF scan plane amplitude values are shown in the top row. PNF spectral domain images are shown in the bottom row. Top/bottom images are Fourier transform pairs. Top right image is the result of a 2D multiplication of top left and top centre data sets. Bottom right image is the result of a 2D convolution of bottom left and bottom centre data sets

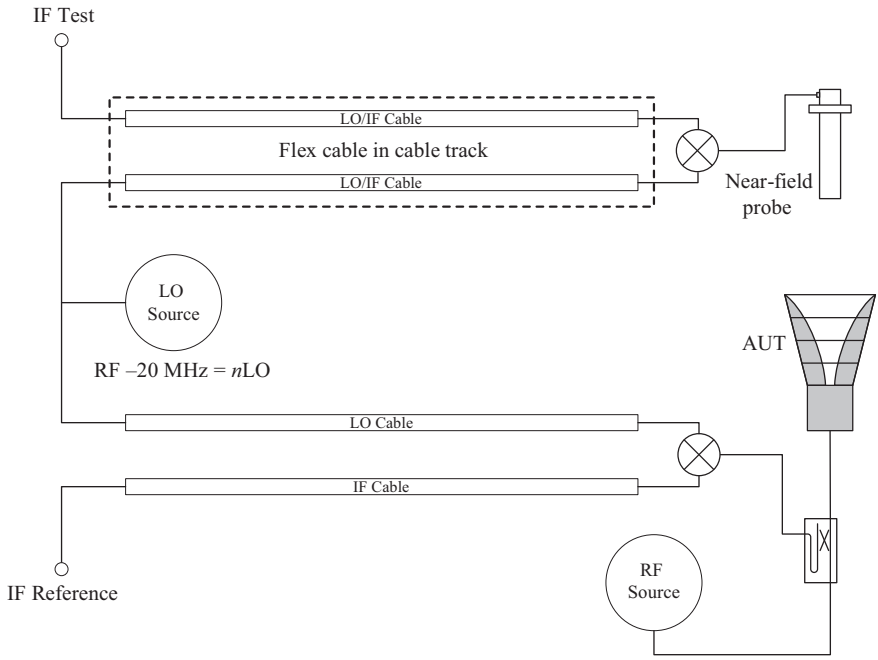

Figure 10.74 Typical RF system diagram for a system with one linear axis of motion. A single RF cable (denoted by the dashed box) conveys the LO and IF signals, which are separated through diplexers at both ends of the cable

polarisation information from measurements made using a linearly polarised range illuminator.) It is obvious that the electrical phase is affected by almost all aspects of a test system. As part of this term, we consider receiver stability, RF cables and rotary joints. Of these, RF cables and rotary joints are found to be by far the dominant terms to consider. Since mechanical positioners require rotation or linear motion, the effect of both RF cables and rotary joints are always observed during measurement.

A typical RF diagram for a system with at least one linear axis of motion is depicted in Figure 10.74. A reference channel mixer is shown on the AUT side and a test channel mixer on the probe side. Both are fed by a common LO source that is phase locked to the RF source that provides a stable reference allowing for phase

measurement. A single RF cable (denoted by the dashed box) conveys the LO and IF signals, which are separated through diplexers on the ends of the cable. This cable is passed through a cable track and may also pass through a rotary joint, if needed and is our primary concern when evaluation cable impact due to flexing or motion on phase.

As frequency increases, the electrical length of the RF path typically increases and this further compounds the problem. Unlike amplitude attenuation where one can employ amplifiers or remote mixers for low-frequency distribution of the measured signal, phase sensitivity cannot be mitigated [24]. Even though down-conversion of a signal (as depicted in Figure 10.74) has the obvious advantage of lower loss and a longer wavelength, the phase change effected by cable flexure is again reintroduced by the harmonic up-/down-conversion factor once the signal is converted back to the original frequency of measurement within the receiver. RF cable and rotary joint impact on the measured phase therefore remains a significant concern on measurement uncertainty and has to be evaluated carefully.

In the case of a PNF system or the vertical axis of a CNF system, the effect of an RF cable being flexed during acquisition is to effectively disturb the flatness of that axis. The PNF scanning surface therefore becomes a noisy approximation of a perfectly flat Cartesian plane. If this cable impact is repeatable and stable, one can in principle measure this response (assuming it was feasible) and remove the effect from the cable through an electrical calibration process. In practice, there are two problems though; firstly, measurement of the cable response is problematic and secondly, the cable behaviour is usually not very repeatable. In [24], a 'loopback cable' technique is described to assess the impact of the flexing cable. The loop-back cable tests are performed using a stable, coiled semi-rigid feedback cable that connects the AUT port to the probe port. This approach introduces the possibility of adding extra cable errors due to movement of this loopback cable, but since this cable is not inserted in the cable track and is hung directly from the probe carriage for the test, flexure of this cable is minimised during testing. Several repeat tests with variations of the loopback cable can also be used to mitigate uncertainty due to the impact of the loopback cable. This cable is often long and made of copper, so it is very sensitive to temperature variations. As such, these measurements need to be made over only short periods of time so as to minimise thermal drift instability. In Figure 10.75, the measured amplitude and phase response at 4 GHz of x- and y-cables on a 7 m $\times$ 7 m PNF scanner using a loopback cable technique are shown. It can be seen that the amplitude variation is negligible (peak-to-peak variation of $<\pm 0.025$ dB). The phase response of the x-axis cable is good, showing almost zero average slope and a peak-to-peak variation of $< \pm 0.5^\circ$. The phase response of the y-axis cable is questionable showing a significant variation in phase of up to $\pm 1^\circ$ and this aspect has to be assessed. It is important to realise that since the x- and y-axis motions are orthogonal in a PNF scanner, the linear response of the two cables can be combined to obtain a two-dimensional normalisation function for the entire scan plane that allows for the compensation of the near-field data in both amplitude and phase at any (x, y) location of the near-field probe.

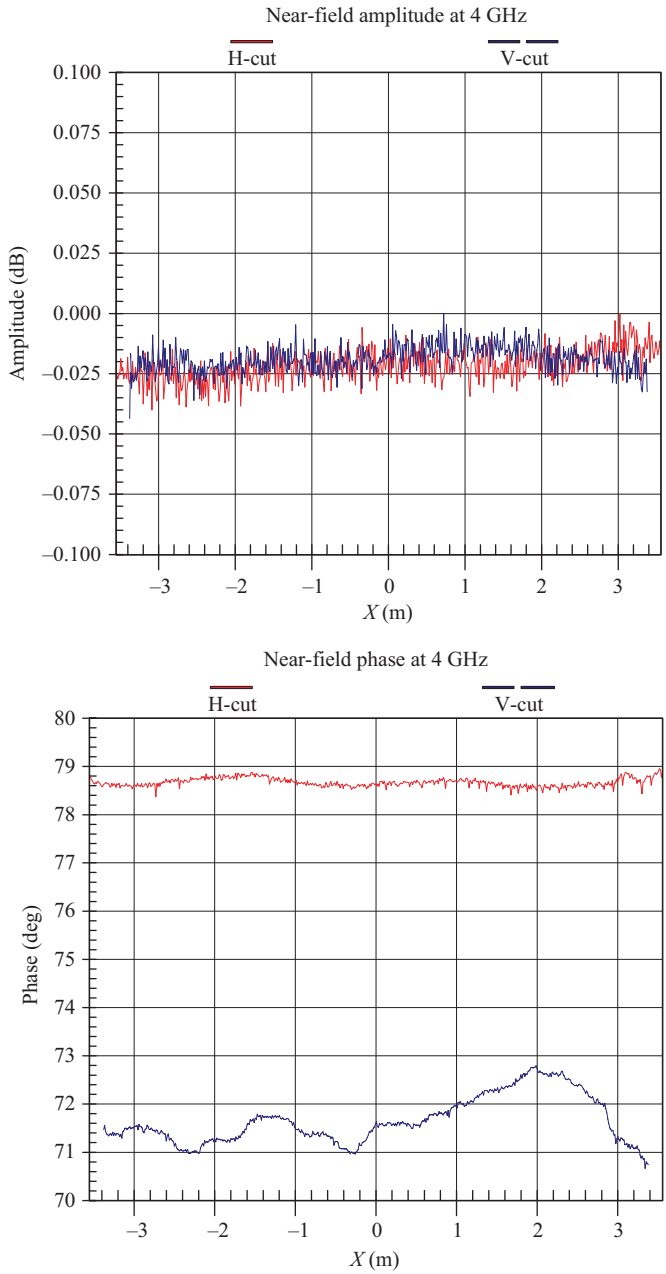

Figure 10.75 Measured amplitude and phase response of x (red) and y (blue) cables on a 7 m × 7 m PNF scanner using a loopback cable technique

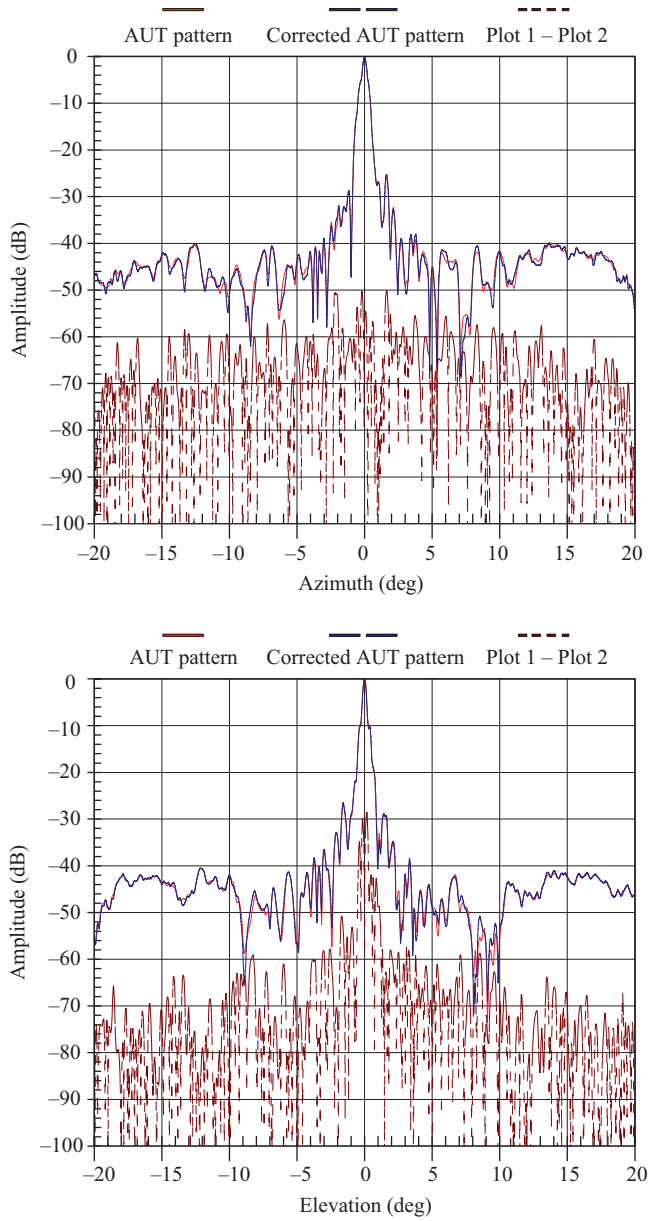

Figure 10.76 Far-field results are shown for azimuth and elevation patterns for an AUT with and without flex cable correction. Effective measurement uncertainty E/S is also shown as a dashed curve

In [24], two techniques are described to assess the impact of the measured cable responses; a constant aperture technique and measured aperture technique. Of these, the measured aperture technique is preferred and we assume the cable responses are repeatable and stable and we remove their effect from an actual PNF measured aperture. An uncorrected near-field data set can therefore be compared to a corrected near-field data set and the effective far-field induced uncertainty evaluated. Typical results are presented in Figure 10.76. It should be noted that these results are for a mm-Wave antenna and the 4GHz phase uncertainty shown in Figure 10.75 impact a higher order harmonic RF up/down conversion process.

The results show a low-level impact in the azimuth plane result and a significant effect in the elevation plane and this is principally due to the average phase slope introduced by the *y*-axis cable. In this instance (since the AUT main beam is orthogonal to the scan plane), the *x*-axis cable dominates the azimuth plane data and the *y*-axis cable the elevation plane data. The average phase slope introduced by the *y*-axis cable is therefore an effective tilt of the PNF scan plane and introduces a slight boresight shift of the measured main beam of the AUT in elevation, leading to the measurement uncertainty depicted. Replacement of the *y*-axis cable to obtain performance similar to that of the *x*-axis cable would be recommended to correct for this.

The loopback cable technique described above has its obvious limitations. Two other viable alternatives that have been proposed and have merit but have not been widely implemented are; the three-cable technique [25] and the modulation technique described in [26]. Of these, the three-cable technique uses three cables instead of a single cable in each flexure path and by measuring the signal through the three paths, the insertion loss can be solved for exactly (similar to the three antenna gain calibration processes). This method although very attractive from a theoretical viewpoint has serious implementation cost and complexity limitations and due to progress in the stability of RF cables, has become of lesser interest.

In the case of a SNF system or the rotary axis of a CNF system, potential insertion loss variation of a moving rotary joint can adversely affect measurement. Assessment of rotary joints is difficult and is often limited to a benchtop health check with a VNA (and even this exercise can be tricky). There are some select cases (like when an AUT is mounted on a ϕ/θ positioner and the phi axis is pointing directly at the near-field probe or far-field illuminator) where an AUT can be mounted and rotated on the ϕ-axis and any signal variation observed should be due to polarisation variation and rotary joint induced uncertainty only. In such instances, the argument can be made that compensation for any polarisation variation would allow one to assess the performance of the rotary joint. However, such correction schemes are prone to be affected by positioner alignment imperfections and chamber reflections and most of all, do not allow for the assessment of all rotary joints in a system and are therefore of limited use. In reality, swapping of rotary joints between axes (or spares if they are available) is usually a good method of identifying a failing unit and assessing effective levels of uncertainty due to a specific rotary joint.

10.9.3 Leakage

The phenomenon of leakage in an antenna test system can be described as an unwanted RF source signal finding its way into the test channel. In Figure 10.74, this can happen when the reference signal leaks through to the test channel internal to the receiver (often referred to as bias error [27] – further information on bias leakage error correction can be found presented below in Chapter 12). It can also happen when the signal feeding the AUT is radiated from elsewhere than the AUT and detected on the test channel of the receiver via the near-field probe. This can happen when amplifiers are used in the anechoic chamber and are not shielded from the near-field probe.

The common technique used to assess measurement uncertainty due to leakage is to

- measure the AUT of interest;
- terminate the AUT port in a matched load and repeat the measurement – designate as *AUT-terminated*;
- terminate the near-field (or range illuminator) port in a matched load and repeat the measurement – designate as *Probe-terminated*; and
- terminate the AUT and near-field (or range illuminator) port in matched loads and repeat the measurement – designate as *All-terminated*.

By now comparing the initial reference measurement to the three terminated cases, the following leakage assessments can be made

1. AUT-ref versus *AUT-terminated* case provides a measure of the leakage internal to the receiver AND leakage in the RF path leading to the AUT.
2. AUT-ref versus Probe-*terminated* case provides a measure of the leakage internal to the receiver AND leakage in the RF path leading to the probe.
3. AUT-ref versus *All-terminated* case provides a measure of the leakage internal to the receiver (receiver bias) – This test is optional since this leakage term will be contained in both the *AUT* and *Probe-terminated* cases.

The comparison of these measurements will provide one with a picture of the severity of the leakage problem and typically the worst-case result is selected to assess the impact of this term on the far-field uncertainty. Figure 10.77 shows a far-field radiation pattern for the reference measurement in solid and the corresponding far-field results for the *AUT-terminated* and *Probe-terminated* cases. The worst-case E/S is observed at a level of 80 dB below the peak of the beam, and there is no low-level distinct peak at the 0° location, which is usually an indication of leakage internal to the receiver.

Some general comments that can be made; Leakage is a term that needs to be assessed early in a range assessment cycle since if found to be unacceptable, needs to be dealt with before any other parameters can be evaluated reliably. Leakage internal to the receiver can typically not be addressed by the user and is something that can only be fixed by the manufacturer. Leakage external to the receiver can be time consuming to track down and can often be avoided by making sure that all

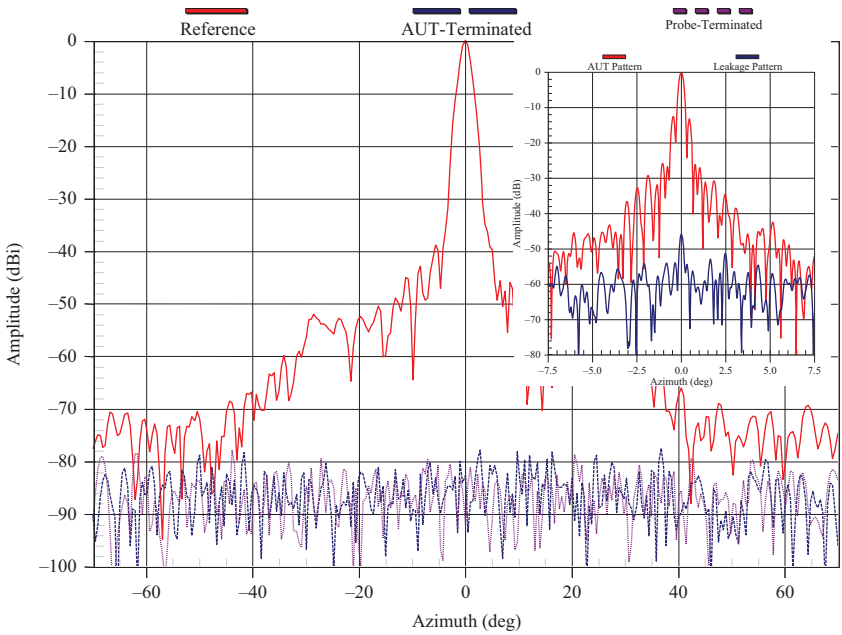

Figure 10.77 Leakage data acquired in a PNF range. Reference pattern shown as solid red lines, and AUT-terminated and probe-terminated as dashed lines. (Insert depicts typical leakage internal to the receiver at 0°)

connectors are torqued, active components are covered with absorber and RF cables are pristine. Leakage is generally more of a concern in PNF and CNF antenna test ranges. This is due to the fact that the PNF and CNF process gain (as described below) amplifies the leakage internal to the receiver. For larger scan planes, the process gain does not increase for the desired measured signal (since it diminishes in strength as the scan plane size increases) but this does not hold true for leakage internal to the receiver. Since this signal is constant in phase and of equal amplitude for all measured data points, the process gain continues to increase as the scan plane size is increased and at some point this error signal will swamp the desired measured signal. One should therefore be aware of this danger of over scanning in PNF and CNF cases. On a practical note, it is worth using good quality matched loads to terminate the RF cables. These need to be wrapped in copper tape and buried in the RF absorber to minimise the impact of unwanted leakage during the assessment.

10.9.4 Receiver dynamic range

The dynamic range of the receiver being used is usually a published specification. However, this number is valid for the device as a standalone unit and the addition of RF cables and/or a remote RF up-/down-conversion network and amplifiers will

change this dynamic range significantly. Adding to this picture is also the gain of the near-field probe (or far-field range illuminator) and the AUT. It is therefore imperative that the RF sub-system is assessed as it will be used in the antenna test range to determine the effective dynamic range (or signal-to-noise ratio) and associated uncertainty.

Table 10.11 shows a typical RF power budget for a small 0.5 m length test range and it illustrates how the effective dynamic range (or signal-to-noise ratio as labelled below) can be determined. Following the 40 GHz column, the source output power is specified as −5 dBm. Taking the loss of various components into account, as well as the amplification of an amplifier leads to a power level of +5.11 dBm at the port of the AUT. After transmission through the AUT, path loss of 58.47 dB and being received by the probe the power available at the probe port is only −41.36 dBm. Accounting for the loss of the remaining components leads to a received power at the receiver port of −62.03 dBm. The receiver noise floor at this frequency is specified as −77 dBm for an IF bandwidth of 1 kHz, which leads to a signal-to-noise ratio of 15 dB. By narrowing the receiver IF bandwidth this noise floor can be improved and therefore the SNR as well. It should be noted that there is a trade-off between dynamic range and measurement speed. Every factor of 10 increase in the number of receiver averages, decreases the receiver effective IF bandwidth by a factor of 10 and this results in a 10 dB improvement in dynamic range.[14] One therefore needs to choose the IF bandwidth (or averaging factor) to give one an acceptable dynamic range while being cognisant of the decrease in measurement speed this introduces. Having a receiver with a fast sampling rate allows one to trade dynamic range for measurement speed.

The power budget shown in Table 10.11 therefore illustrates that for the RF sub-system, AUT and probe considered in this instance a SNR of only 15 dB is possible at 40 GHz for a 1 kHz IF bandwidth. This can be improved to a value of 35 dB for a 10 Hz IF bandwidth. These SNR values represent E/S ratios as shown in Table 10.3. It therefore becomes clear that an E/S ratio of 15 dB leads to a measurement power level uncertainty of roughly ±1.5 and an E/S of 35 dB leads to a measurement power level uncertainty of roughly ±0.15.

These numbers show how the RF sub-system dynamic range (or effective measurement SNR) directly affects measurement uncertainty for the beam peak (gain) measurement. For SLL measurements, the specific SLL needs to be subtracted from the SNR value to obtain the effective E/S ratio and the associated uncertainty derived.

The RF sub-system dynamic range as described above determines the dynamic range of all far-field and SNF test systems. For CNF and PNF test systems, there is process gain that increases the effective dynamic range of the measurement by virtue of the synthetic aperture gain increase. For CNF cases, this gain increase in dB can be estimated as 10 log N and for PNF cases 10 log($M \times N$) [28], where M is the number of 'significant' (i.e. of significant power) data points along the x-axis

[14]An increase in receiver averages improves the dynamic range by 10 log (number of samples), ultimately limited by the receiver noise floor.

Table 10.11 A typical 1–40 GHz RF power budget for a small SNF range

Frequency	**1**	**6**	**10**	**15**	**18**	**25**	**30**	**35**	**40**	**GHz**
RF harmonic	1	1	1	1	1	1	1	1	1	
LO harmonic	1	1	1	1	1	1	1	1	1	
PNA power	0.00	0.00	0.00	0.00	0.00	–5.00	–5.00	–5.00	–5.00	dBm
Cable to chamber thrupanel	–0.90	–2.25	–2.92	–3.60	–3.96	–4.70	–5.17	–5.60	–6.01	dB
Cable, Chamber Thrupanel to Az RJ	–1.10	–2.73	–3.55	–4.38	–4.82	–5.72	–6.29	–6.83	–7.33	dB
40 GHz RJ	–0.50	–0.50	–0.50	–0.50	–0.50	–0.75	–1.00	–1.00	–1.00	dB
Cable, input to amp	–0.61	–1.51	–1.97	–2.42	–2.66	–3.16	–3.48	–3.77	–4.04	dB
Amplifier input					–11.94	–19.33	–20.94	–22.20	–23.38	dBm
Amplifier output					+17.00	+15.67	+14.06	+12.80	+11.62	dBm
Cable, amp to pol RJ	–	–	–	–	–1.50	–1.83	–2.06	–2.27	–2.47	dB
40 GHz RJ	–0.50	–0.50	–0.50	–0.50	–0.50	–0.75	–1.00	–1.00	–1.00	dB
Cable, pol RJ to AUT	–0.35	–0.95	–1.28	–1.63	–1.83	–2.24	–2.52	–2.79	–3.04	dB
Transmit power at AUT	–3.97	–8.44	–10.72	–13.04	+13.18	+10.85	+8.49	+6.75	+5.11	dBm
AUT gain	6.00	6.00	6.00	6.00	6.00	6.00	6.00	6.00	6.00	dBi
Space loss	–26.43	–41.99	–46.43	–49.95	–51.53	–54.39	–55.97	–57.31	–58.47	dBi
Probe gain (N/A)	6.00	6.00	6.00	6.00	6.00	6.00	6.00	6.00	6.00	dBi
Received power at probe	–18.39	–38.43	–45.15	–50.99	–26.36	–31.54	–35.48	–38.56	–41.36	dBm
Probe Rx cable	–	–	–1.28	–1.63	–1.83	–2.24	–2.52	–2.79	–3.04	dB
40 GHz RJ	–0.50	–0.50	–0.50	–0.50	–0.50	–0.75	–1.00	–1.00	–1.00	dB
Cable, pol RJ to W05	–1.59	–3.95	–5.14	–6.34	–6.97	–8.28	–9.11	–9.89	–10.61	
Cable chamber thrupanel to VNA	–0.90	–2.25	–2.92	–3.60	–3.96	–4.70	–5.17	–5.60	–6.01	dB
Power level at VNA	–21.39	–45.13	–54.99	–63.06	–39.61	–47.51	–53.29	–57.84	–62.03	dBm
RF power OK?	OK	OK	OK	OK	OK	OK	OK	OK	OK	
Power level at VNA	–21.39	–45.13	–54.99	–63.06	–39.61	–47.51	–53.29	–57.84	–62.03	dBm
Specified IF noise floor (1 kHz IFBW)	–84.00	–84.00	–82.00	–82.00	–82.00	–77.00	–77.00	–77.00	–77.00	dBm
Specified VNA compression power	10.00	10.00	10.00	10.00	10.00	10.00	10.00	10.00	10.00	dBm
***S/N* level (1 kHz IFBW), dB**	**62.6**	**38.9**	**27.0**	**18.9**	**42.4**	**29.5**	**23.7**	**19.2**	**15.0**	**dB**
***S/N* level (10 Hz IFBW), dB**	**82.6**	**58.9**	**47.0**	**38.9**	**62.4**	**49.5**	**43.7**	**39.2**	**35.0**	**dB**

and N along the y-axis. For a typical data set with 100 samples in x and 100 in y, this leads to a process gain increase of 40 dB in PNF and 20 dB in CNF.

10.10 Environmental-related errors

In this section, we look at sources of reflection within the test environment (i.e. anechoic chamber) that lead to measurement uncertainty. Within this domain, we partition these into AUT/probe interaction and chamber reflection terms. The reason for this partitioning is practicality. If we can identify specific unwanted regions of reflection, we can focus our attention on addressing them and improving the quality of our measurement. Since precision computer-controlled translation stages are available in modern antenna ranges, it becomes practical to assess reflection from the probe structure in an isolated fashion and therefore this partitioning makes sense.

10.10.1 Probe structure reflection

This error term refers to an unwanted interaction between the AUT and the near-field probe or range illuminator and is most often described as 'multiple reflections'. Since the direct signal from the AUT to near-field probe is the desired signal, the unwanted signal impinging on the probe due to signal travel from the AUT to probe structure, to AUT and back to the probe, is what this term refers to. It is an error associated with near-field testing since the error term becomes more pronounced with reduced AUT to probe separation distance, but it can exist in any measurement facility regardless of this separation distance (particularly in the case of a CATR where the 'probe' has high gain). Yaghjian presents an extensive theoretical analysis to estimate upper and lower bounds for this error term in [29] and these results are also reported in [1]. However, these estimates tend to be overly conservative and as stated in [29] '... it is impossible to derive an accurate estimate of the far-field errors analytically without knowing the phase of the multiply reflected fields throughout the scan area. Thus the only reliable way to get an accurate estimate ... is through measurement.' We do therefore not report on the detail of the expressions derived and presented in [29] and take the approach of measurement here.

In Figure 10.78, an AUT and near-field probe are shown with the direct wanted signal 'S' as well as an unwanted reflected signal 'R' returning from the probe structure towards the AUT and re-reflected back towards the near-field probe (the process can of course be repeated ad infinitum, but we focus on the first and dominant term since that illustrates the principle adequately). This multiply reflected signal is our source of uncertainty and concern here. It is important conceptually to realise that the reflected signal can be due to imperfect absorber covering around and behind the probe, imperfect absorber performance and also a complex mismatch at the probe aperture and port (more information is provided below in Chapter 12). The error term can be reduced by using a smaller probe, probe structure or by increasing the AUT to probe separation distance.

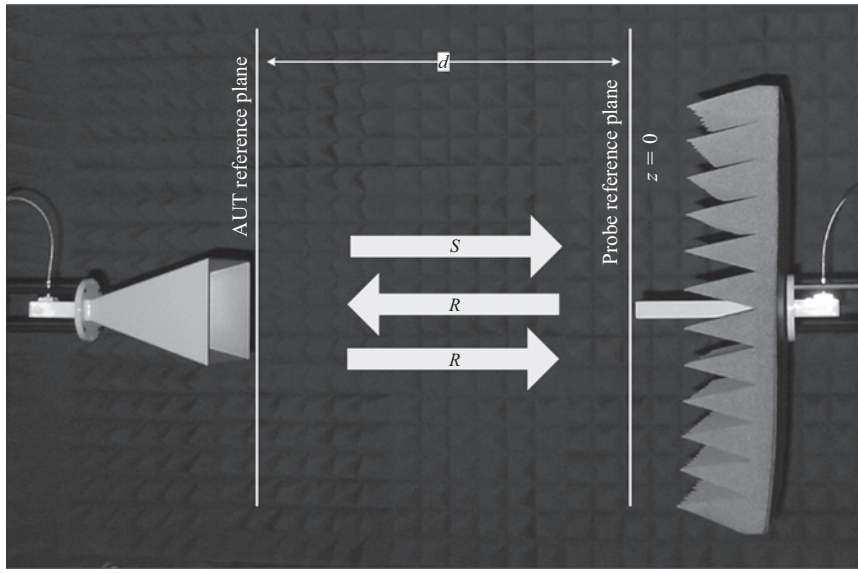

Figure 10.78 Direct desired signal 'S' and unwanted reflection 'R' from the probe structure

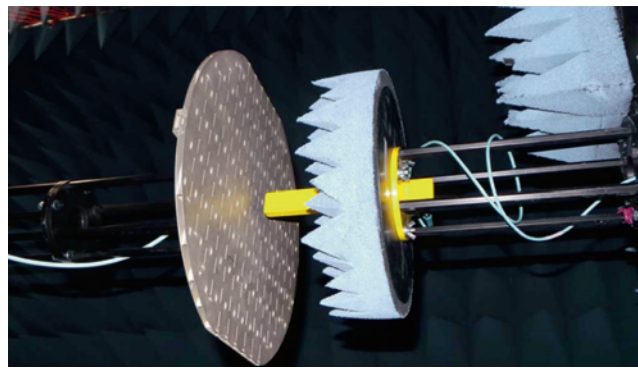

Figure 10.79 Measurement setup for results depicted in Figure 10.80. Probe to AUT spacing minimum is 13 mm = 0.4λ

The technique for assessing this unwanted reflected signal is to change the separation distance d between the AUT and the near-field probe. Changing the separation distance by ΔR changes the phase of the wanted signal by $k\Delta R$, but the phase of the multiply reflected signal by $3k\Delta R$. This differential phase change between the wanted and unwanted signals allows one to characterise the impact of the reflected signal, and the process can be automated by mounting the near-field probe assembly on a precision linear translation stage. Figure 10.79 shows a test setup for which results are presented in Figure 10.80. The latter shows measured

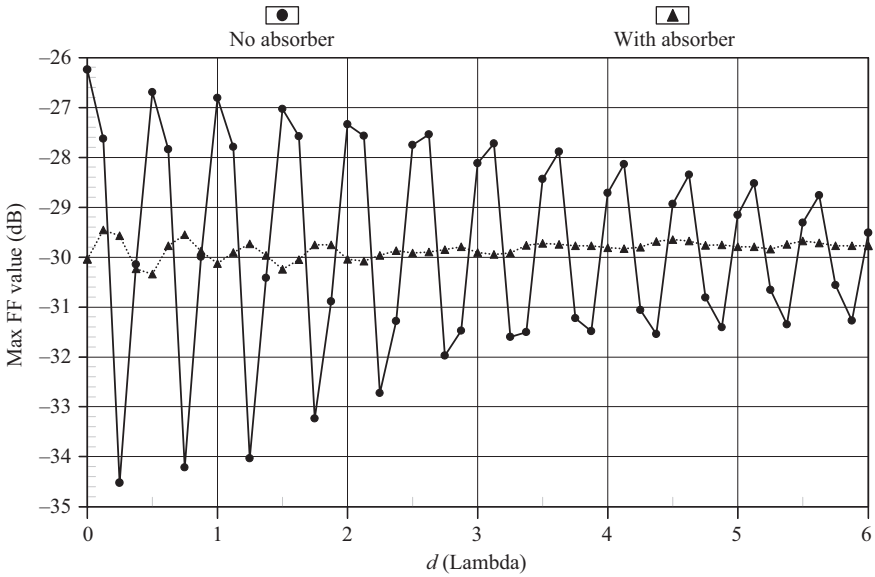

Figure 10.80 A comparison of the far-field main beam peak variation as a function of the probe to AUT separation distance. The solid curve is without probe absorber panel and the dashed curve has the absorber panel in place. Markers are at λ/8 intervals. d = 0 corresponds to a minimum AUT to a probe separation distance of 13 mm = 0.4λ

signal (far-field beam peak) as a function of AUT to probe separation distance d (the solid curve is without the probe absorber panel and the dashed curve has the absorber panel removed) in steps of $\lambda/8$.

Figure 10.80 shows the effect of the probe absorber and it is seen to reduce the peak-to-peak signal variation as well as lead to a fairly smooth sinusoidal response. The peak-to-peak amplitude variation diminishes from about 1 dB to 0.1 dB at a distance of 3λ. The period of the sinusoidal response is seen to be $\lambda/2$.

The assessment process is identical for all types of antenna ranges, but it is found that it is of greater importance on PNF ranges, simply based on the fact that this is the application where AUT to probe separation distance is a minimum. A useful correction technique for PNF ranges was presented in [30] and consists of a data averaging technique. If we consider a second PNF measurement where the separation distance is changed by $\Delta R = \lambda/4$ as shown in Figure 10.81.

We can write the following expressions for the first and second voltages measured, respectively

$$V_1 = [S + R]_d$$
$$V_2 = [S' + R']_{d+\Delta R}$$

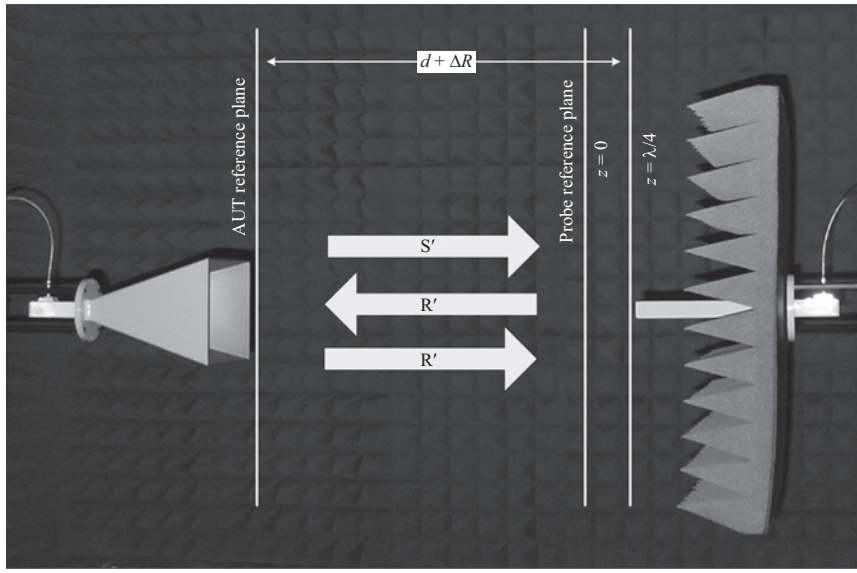

Figure 10.81 Direct desired signal S′ and unwanted reflection R′ from the probe structure after changing the separation distance by $\Delta R = \lambda/4$

If we now assume that S and S' are equal in magnitude and only differ in phase and that the same assumption can be made about R and R', we can write

$$V_2 = \left[Se^{-jk\Delta R} + Re^{-jk3\Delta R}\right]_{d+\Delta R}$$

If we now phase correct V_2 for the $\Delta R = \lambda/4$ change in AUT to probe separation distance, we can write

$$\begin{aligned} V_2 &= \left[Se^{-jk\Delta R}e^{+jk\Delta R} + Re^{-jk3\Delta R}e^{+jk\Delta R}\right]_d \\ &= [S - R]_d \end{aligned}$$

which we can then average with V_1 to obtain a result for which the unwanted reflected signal R has been largely suppressed as

$$\frac{V_1 + V_2}{2} = \frac{[S + R] + [S - R]}{2} = S$$

This simple correction technique works well within the assumption (as stated above) that the two signals do not change in amplitude when changing the AUT to probe separation distance. We know this assumption to be subject to the change in space loss based on the increasing propagation distance and therefore an approximation at best. The technique also relies on the fact that the reflection signal propagates along the z-axis and for off-axis suppression the improvement will be degraded proportional to $\sin(\theta)$.

10.10.2 Chamber reflection

Once one understands the unwanted scattering mechanism between the AUT and the probe, other unwanted sources of scattering also deserve attention. The *room scattering* term refers to any unwanted interaction between the AUT and the environment in which it is being tested, excluding the near-field probe and it's support structure. It therefore includes reflection from all surfaces (exposed or absorbed) within the chamber and begs the question, how do we ensure that the reflection from the probe and probe support structure is not included as part of this *room scattering* term?

The mechanism for isolating scattering sources is the relative motion of such sources w.r.t. the AUT. This is illustrated in Figure 10.82. Here, the AUT and probe are both mounted on independent precision linear translation stages. The motion of the probe w.r.t. the AUT allows us to identify the unwanted AUT/probe interaction as described in the prior section. To now identify AUT/chamber interaction, the probe and AUT can be moved in unison using the two translation stages, so that the chamber is effectively translated w.r.t. the AUT and thus the unwanted AUT/chamber interaction can be identified. In Figure 10.82, the user would first acquire a reference measurement depicted as 'Case 1', where the AUT and the probe are separated by a distance R_1. A second acquisition depicted as 'Case 2' below is then made where the AUT and the probe are translated in unison by $\lambda/4$, still separated by a distance R_1. The change observed between the result from the reference pattern and the second case will be due to the chamber reflection changing phase relative to the desired measured signal and NOT the AUT/probe interaction since this remains constant. Results for a typical case are shown in Figure 10.83. A third acquisition depicted as 'Case 3' below is now made where the AUT is translated back to its original position by $-\lambda/4$, increasing the separation distance to R_2. The change observed between the result from the reference pattern and this third case will be due to *AUT/probe scattering* only and is depicted in Figure 10.84.

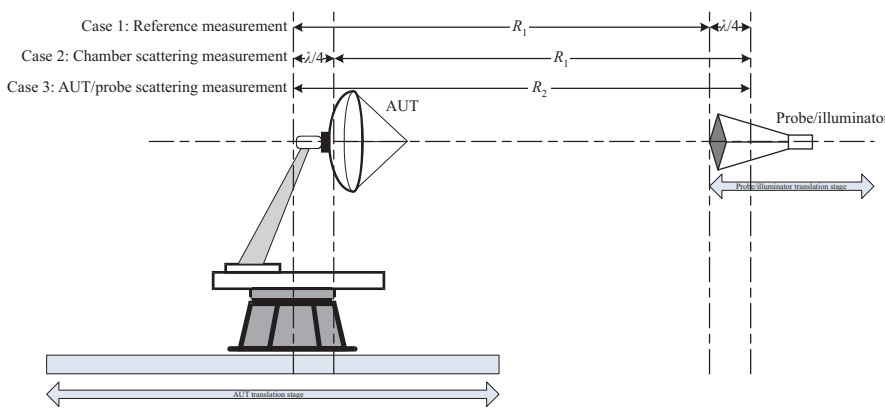

Figure 10.82 Schematic showing AUT and probe/illuminator linear translation

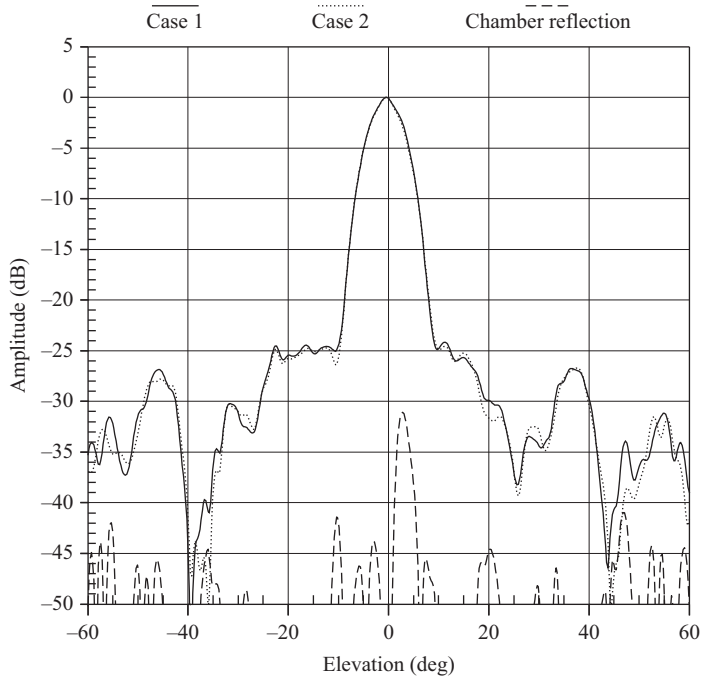

Figure 10.83 Test result for 'Case 1' and 'Case 2' and the resulting E/S showing the impact of chamber scattering

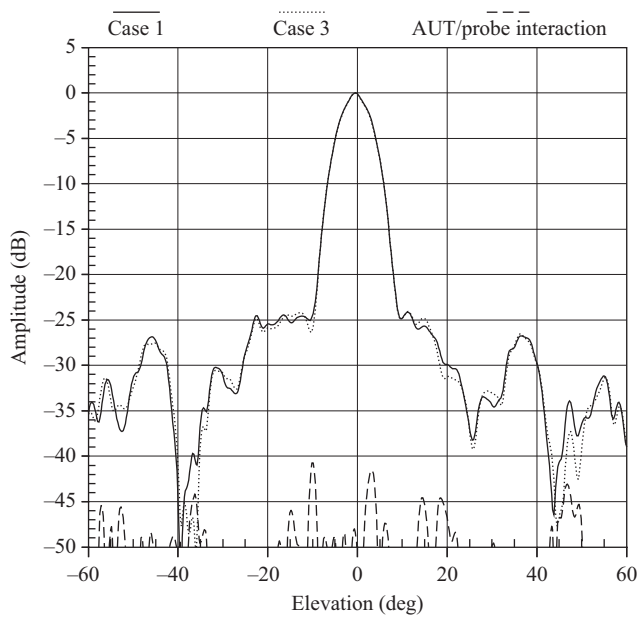

Figure 10.84 Test result for 'Case 1' and 'Case 3' and the resulting E/S showing the impact of AUT/probe interaction

Note that this approach works well for PNF testing and can also be used for CNF, SNF and far-field testing, as long as AUT translation is feasible. This method can of course also be employed conceptually for CATRs. However, in practice, the translation of the entire feed and reflector in unison is impractical (to say the least) and defeats the implementation.

In the absence of a lower AUT translation stage, evaluating *room scattering* can become challenging. For the PNF case, translation of the AUT without such a stage is often time wasted, since a manual translation usually disturbs the AUT pointing and alignment sufficiently, to render the end result worthless. For all test cases that require rotation of the AUT (CNF, SNF and far-field test systems), a translation of the AUT using an upper translation stage will also work. It is important in such cases to realise that the phase pattern of the AUT will change since the AUT is relocated w.r.t. the coordinate system origin. However, as long as the probe or illuminator is translated in synchronisation with the AUT, the effect of the chamber scattering will be evaluated.

In practice, one finds that the *room scattering* term is driven by the quality and suitability of the absorber used for lining the chamber walls, floor and ceiling and we list some common misconceptions w.r.t. chamber absorber:

- Pyramidal absorber size determines low-frequency performance. For a fixed size of the absorber, reflectivity becomes gradually worse for lower frequencies and there is no sharp 'point of failure'.
- AUT directivity can drive the chamber absorber layout. For testing low directivity antennas that direct energy everywhere in the chamber, uniform absorber coverage is needed. However, for high directivity antennas, often absorber coverage in only the illuminated regions is needed for making adequate measurements (e.g. for PNF testing, it is often sufficient to only cover that scanner structure and wall behind the scanner with absorber).
- Absorber paint has been shown to be transparent at frequencies below 50 GHz. Claims are often made that the paint has no impact at higher frequencies. However, this claim is not well supported and one should be aware that at higher frequencies absorber paint can cause higher than expected levels of reflection.
- The absorber is often thought of as magic material that makes things 'disappear' in an RF sense. It is wise to consider absorber as RF attenuating material that reduces reflections and depending on what one is trying to observe, may be sufficient for doing so, or be wholly inadequate.
- Often chambers with exposed door frames or light fixtures appear to be functioning well and are deemed suitable for all test purposes, only to be exposed as deficient when the AUT directivity changes or illuminates these regions strongly.
- Humidity is the enemy of microwave absorber. High humidity can cause absorber to absorb moisture (in addition to the intended RF) and lead to leaching of carbon and chemicals from the material, rendering it useless. The absorber can also change dimensionally by shrinking and swelling with changes in humidity, opening up reflecting gaps in chamber lined surfaces.

- Chamber absorber heats up during operation (since it is a lossy material) and has a power threshold driven by the rate of heat dissipation. This is not a problem for most applications where the power levels from commercial synthesisers are limited. However, once power amplifiers are inserted in the test setup one should pay careful attention to the power densities generated and ensure that the safe level for the chamber absorber is not exceeded. A special high power absorber that allows for forced air cooling is available for such applications.

10.10.3 Random errors

This final error term represents random variation in amplitude and phase due to all aspects of the measurement system combined. A mathematical analysis [31] has been developed to address this term, but we prefer to take an experimental approach. What we are attempting to capture here is the combined effect of all non-repeatable errors and these can include RF stability, cable changes, temperature variation, leakage and AUT variation. The most direct way of assessing this error term is to compare far-field results of multiple acquisitions, taken with the exact same parameters. One would therefore simply repeat the same measurement multiple times and this can even be done in an automated fashion if the acquisition software allows for that. Variation from one data set to the next then gives one an idea of the variation observed.

One would typically acquire five or more of these repeat measurements (taking care not to change anything between sets) and then average these data sets to obtain a baseline or reference measurement. We then calculate the difference between this reference data set and any of the single measurements to obtain an error signal that we designated as the *random error* term.

10.11 Combining uncertainties

The uncertainty terms defined in the previous section cannot realistically be added in a linear sense since they are to a large degree uncorrelated. On this topic, Newell aptly states [1]:

> The problem of combining systematic and random errors to provide an overall estimate of accuracy has evoked heated discussion, and various viewpoints have evolved concerning this topic. Choosing the correct method for combining the systematic errors requires some knowledge about their error distribution. This information is not normally available from experimental tests and, at best, is obtained through an educated guess. We do know that to a first approximation the systematic errors are independent. Our viewpoint is that the method of combination assumes secondary importance if the estimates for each error source are tabulated and the formula used in the combined estimate is explicitly stated.

We concur with this position and therefore combine the impact of the defined terms of uncertainty in a root sum square (RSS) sense. The validity of this rests

upon the fundamental assumption that all of the uncertainty sources considered are independent and have a normal distribution.[15] When adding variables with normal probability density functions, the central limit theorem [33] states that the resultant will also have a normal probability density function and the standard deviation σ of this function, will be given by

$$\sigma = \sqrt{\sum_{i=1}^{18} \left(\frac{\varepsilon_i}{3}\right)^2} \tag{10.30}$$

where ε_i refers to the uncertainty of each individual error term and corresponds to a 3σ equivalent value as stated earlier. This expression is also known as a RSS summation of terms. Table 10.12 lists all the terms as described above and the measurement uncertainty introduced by these are combined in an RSS sense in the linear domain. The goal being to obtain a single bounding measurement uncertainty number. In Table 10.12, all values shown are in dB (they do not represent typical error values, but simply serve as placeholders). It is also important to state that if we have an E/S ratio of say -52 dB (like for term 18), we calculate the associated uncertainty value of ± 0.02 dB using (10.3). To be precise, we have to state upper and lower error bounds but as stated earlier, we often state the bounds as a single symmetrical value for convenience. In cases where we have an uncertainty value of say ± 0.24 dB (like for term 1), we calculate the associated E/S value as -31 dB using (10.7). We finally convert all logarithmic E/S values to their linear equivalent values and evaluate (10.30) to obtain a single linear E/S value, which is then converted to a logarithmic value (-24 dB in Table 10.12), from which associated uncertainty value is calculated (± 0.53 dB in Table 10.12).

10.12 Inter-range comparisons

A topic that is closely related to range assessment is inter-range comparison. That is, comparing measured results from one facility to those obtained in another. This is often done to verify or evaluate a new facility or simply confirm operation after maintenance or refurbishment. However, since we are now familiar with the concept of a measurement uncertainty we give consideration to developing a comparison strategy that takes account of the finite, non-zero, measurement uncertainties that inevitably complicate the comparison process.

Knowledge of these uncertainties becomes all the more crucial when measurements are to be compared since the degree of agreement achieved can only be successfully interpreted when this information is taken into account. The method that underpins this comparison therefore utilises results from two RAs, one RA being derived for each of the measurement data sets being compared. This comparison can be determined by performing repeat measurements where only a single parametric change has been introduced (although in principle it can also be different

[15] A detailed discussion of probability density functions in measurement is given in [32] and we do not attempt to sub-categorise sources of measurement uncertainty here.

Table 10.12 A summary of the terms contributing to the uncertainty budget is shown as well as which ones are to be included (x) for the PNF, CNF, SNF or far-field. We also indicate which ones are to be considered (x) when gain, side lobe level (SLL), cross-polarisation or pointing budgets are compiled

Uncertainty budget overview													
#	**Item – uncertainty**	**Uncertainty +/– dB**	***E/S* level – dB**	**PNF**	**CNF**	**SNF**	**FF**	**Basis of estimate or evaluation**	**Gain**	**SLL**	**Cross-pol**	**Pointing**	**Ref**
1	Probe relative pattern	0.24	–31	x	x	x		Probe characterisation data uncertainty	x	x	x	x	Section 10.5.1
2	Probe polarisation purity	0.22	–32	x	x	x	x	Probe characterisation data uncertainty	x	x	x	x	Section 10.5.2
3	Probe alignment	0.19	–33	x	x	x	x	Probe alignment uncertainty	x	x	x	x	Section 10.5.3
4	AUT alignment	0.17	–34	x	x	x	x	AUT alignment uncertainty				x	Section 10.6.1
5.1	PNF (x, y) position	0.15	–35	x				Scanner positioning uncertainty	x	x	x	x	Section 10.6.2
5.2	CNF (ϕ, v) position	0.14	–36		x			Scanner positioning uncertainty	x	x	x	x	Section 10.6.3
5.3	SNF (θ, ϕ) position	0.12	–37			x		Scanner positioning uncertainty	x	x	x	x	Section 10.6.4
6.1	PNF z position	0.11	–38	x				Scanner positioning uncertainty	x	x	x	x	Section 10.6.5
6.2	CNF radial position	0.10	–39		x			Scanner positioning uncertainty	x	x	x	x	Section 10.6.6
6.3	SNF radial position	0.09	–40			x		Scanner positioning uncertainty	x	x	x	x	Section 10.6.7
7	Gain standard	0.08	–41	x	x	x	x	SGH reference or probe reference gain uncertainty	x				Section 10.7.1
8	Normalisation constant	0.07	–42	x	x	x	x	Network correction measurement uncertainty	x				Section 10.7.2
9	Impedance mismatch	0.06	–43	x	x	x	x	Network correction measurement uncertainty	x				Section 10.7.3
10	Aliasing	0.05	–44	x	x	x		Finite sampling impact	x	x	x	x	Section 10.8.1
11	Truncation	0.05	–45	x	x	x		Finite measurement area impact	x	x	x	x	Section 10.8.2
12	Receiver amplitude linearity	0.04	–46	x	x	x	x	RF sub-system capability	x	x	x	x	Section 10.9.1
13	Systematic phase	0.04	–47	x	x	x		Phase measurement capability and stability	x	x	x	x	Section 10.9.2
14	Leakage	0.03	–48	x	x	x	x	RF sub-system capability	x	x	x	x	Section 10.9.3
15	Receiver dynamic range	0.03	–49	x	x	x	x	RF sub-system capability	x	x	x	x	Section 10.9.4
16	Probe structure reflection	0.03	–50	x	x	x	x	Unwanted reflection from probe/scanner structure	x	x	x	x	Section 10.10.1
17	Chamber reflection	0.02	–51	x	x	x	x	Unwanted reflection from chamber walls	x	x	x	x	Section 10.10.2
18	Random	0.02	–52	x	x	x	x	Random measurement errors – repeatability	x	x	x	x	Section 10.10.3
	RSS total =	**0.53**	**–24**										

facilities or multiple changes that have been made). For the case being considered here, that change corresponded to the substitution of a 'model tower' ϕ/θ-type SNF positioning system with an alternative 'overhead scanning arm' θ/ϕ-type SNF system. All other parameters remained fixed. That is to say, the comparison was made using the same: AUT, beam, frequency, SGH, near-field probe, acquisition and processing software, RF subsystem, chamber, tabulating coordinate system, polarisation basis and definition of cross-polarisation. The degree of agreement between the two 'equivalent' measurements can be assessed qualitatively, through visual inspection, of graphical representations of the measured data using for, example, one-dimensional cuts, or two-dimensional greyscale plots, etc. Alternatively, quantitative measures of adjacency can be obtained through the extraction of various statistical metrics [13,34]. Figures 10.85 and 10.86 contain typical colour pattern plots that can be used to qualitatively assess agreement through inspection. Here, the patterns have been resolved onto a circularly polarised Ludwig II [35] azimuth over elevation polarisation basis and have been tabulated using a regular azimuth over elevation coordinate system [34]. The same colour range and contour levels have been used during the preparation of each figure.

From the inspection of these figures, it is clear that the respective principal polarised patterns are in good agreement. However, without considering the respective uncertainty budgets, it is not possible to say whether these patterns agree to within the determined experimental bounds. The remainder of this section is devoted to answering this question, commencing using the concept of a E/S ratio concept (as developed in Section 8.3) which, as will be shown, can be used to address this issue and follows the treatment presented in [36].

When comparing measurements taken using separate antenna test ranges, it is clear that each individual measurement has an uncertainty associated with it, and that those uncertainties must be considered when comparing the respective antenna patterns. When combining the 18 individual terms within the range assessment, as expounded above, a total value is obtained by taking the RSS of the individual terms. This is valid as each of the terms is assumed to be independent, i.e. orthogonal, from one-another. Thus, as each of the antenna pattern measurements that are to be compared can also be considered to be independent, as they are taken using different facilities, it is possible to combine the respective uncertainties again using an RSS. This enables a total uncertainty to be determined that can be used when comparing one measurement to the other. This one-dimensional measurement comparison can be seen illustrated in Figures 10.87 and 10.88 for co- and cross-polarised patterns, respectively. Here, a 130° inter-cardinal cut was chosen for the sake of generality; however, other cuts can be used and when this was done, a similar degree of agreement was attained across all other cuts.

Here, the solid trace is used to denote the results from the second measurement (θ/ϕ system) and the solid trace with circle markers the first measurement (ϕ/θ system). The curves are very similar, and differences are minor, thereby underlining the very high degree of agreement attained. The upper and lower uncertainties are obtained from the combined range assessments and are plotted as dashed traces with the first measurement being used to compute the upper and

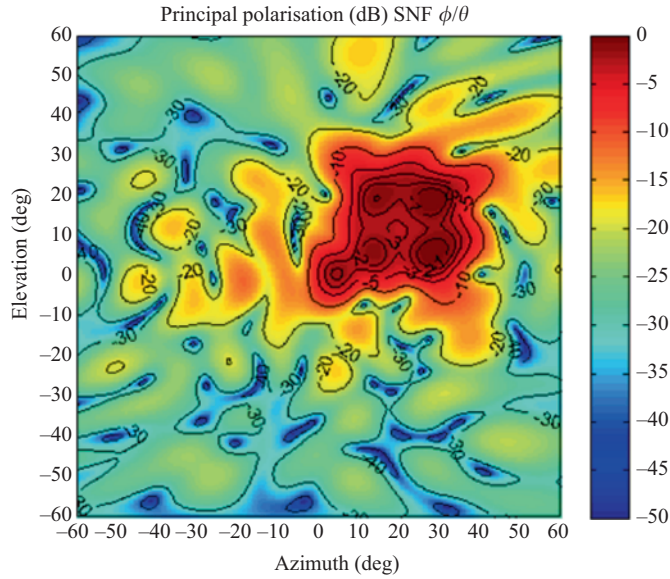

Figure 10.85 Measurement 1 far-field, co-polarised result based on ϕ/θ SNF measurement

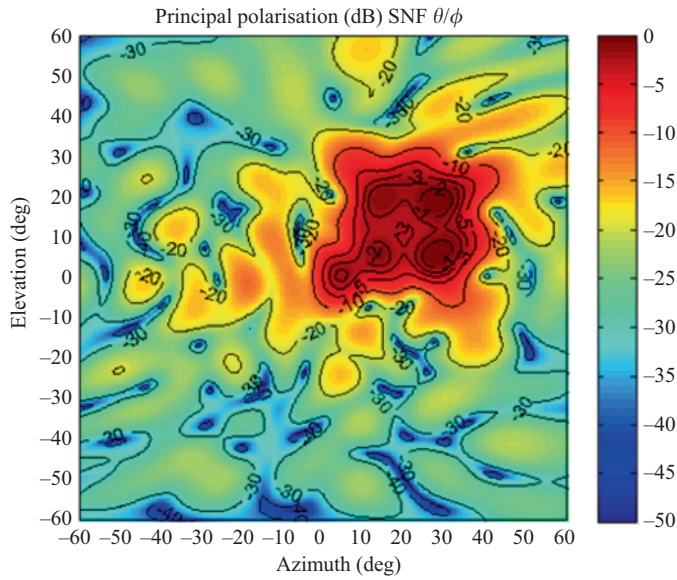

Figure 10.86 Measurement 2 far-field, co-polarised result based on θ/ϕ SNF measurement

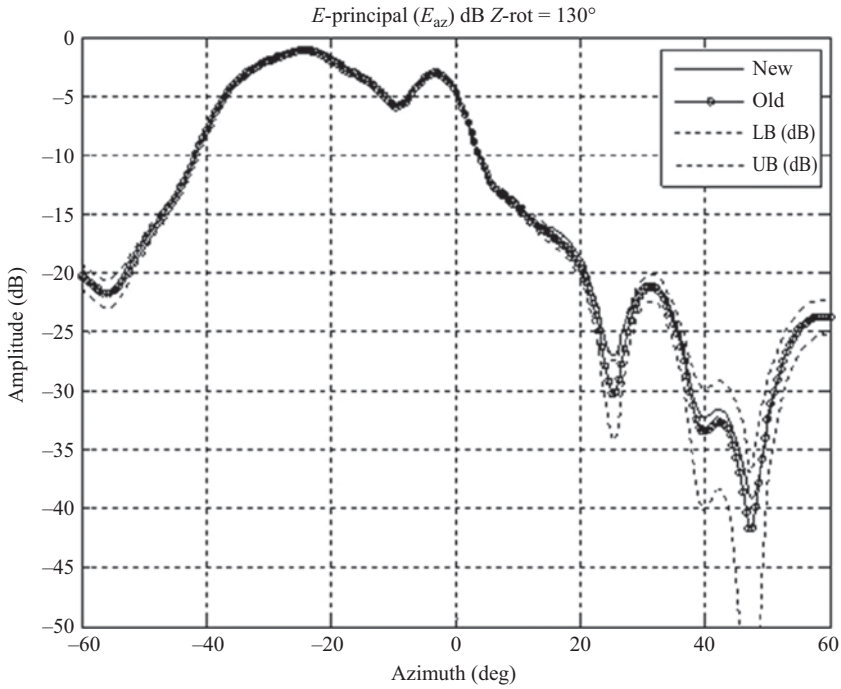

Figure 10.87 Comparison of co-polarisation showing uncertainty bounds (dashed traces). The solid trace is used to denote the results from the second measurement (θ/ϕ system) and the solid trace with circle markers the first measurement (ϕ/θ system)

lower bounds shown. As these upper and lower bounds are computed from the first measurement and since those uncertainties contain the combination of uncertainties from both the first and second measurements, then it is possible to say that the measurements agree to within the experimental uncertainties when the second (solid trace) falls within these uncertainty levels. That is to say, if the second measurement (solid trace) falls between the dashed traces, the two measurements agree to within the experimental uncertainties. From inspection of the co-polar and cross-polar plots, it is clear that the results agree well and that for almost every angle of interest this condition was satisfied.

Providing each cut contains a large number of data points, a quantitative assessment of the degree of agreement can be obtained by calculating the percentage of points on the second measurement trace that lies between the upper and lower uncertainty traces. This statistical treatment can be taken further, it is in principle possible to compute the mean average across every point in the far-field pattern within the, in this case, 60° maximum pattern angle. For this example, it was found that 95.4% of the far-field co-polarised pattern points from the second measurement

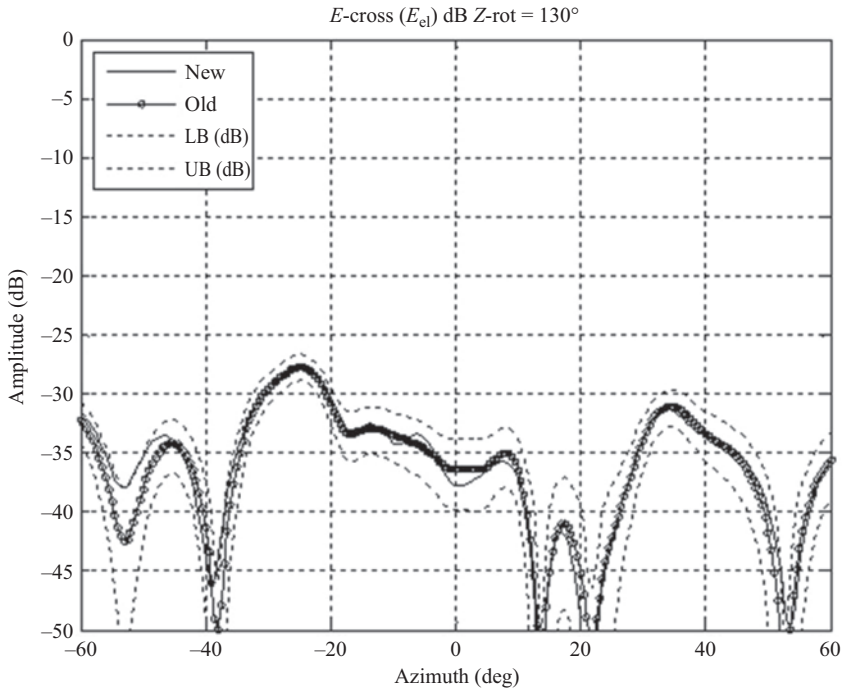

Figure 10.88 Comparison of cross-polarisation showing uncertainty bounds (dashed traces). The solid trace is used to denote the results from the second measurement (θ/ϕ system) and the solid trace with circle markers the first measurement (ϕ/θ system)

fell within the upper and lower limits. This suggests that the agreement attained between the respective pattern measurements was within two standard deviations. That is to say, the agreement between the pattern measurements was circa $2\sigma \sim 95.5\%$. This analysis can be repeated for the cross-polarised pattern and when that was done it was found that 94.1% of the far-field pattern points from the second measurement fell within the upper and lower bounds which again mean that the cross-polarised patterns agree to within 2σ. By assuming that the error on this assessment is randomly distributed, then a measure of the uncertainty on this result can be approximated from taking the square root of the sample size. As such, the associated uncertainty on this assessment can be seen to be approximately 0.45%, which is an encouragingly small quantity thereby confirming that the sample size was sufficiently large to enable meaningful statistical analysis to be performed.

As has been mentioned earlier, these far-field patterns must be presented in the same way so that the degree of similarity can be gauged. As it is in general impossible to install an antenna within a given antenna measurement system and to perfectly align its axes to those of the range, a correction for imperfections in the antenna to range alignment must be performed. Techniques for implementing these sorts of

vector isometric rotations are well understood and their use has become commonplace with an extensive treatment of the antenna-to-range alignment correction being found in the open literature [13]. Once each measured far-field pattern has been corrected for imperfections in the antenna-to-range alignment the patterns can be compared. In this example, the antenna-to-range alignment information was obtained from an optical survey of the AUT with the relationship between the antenna and the range coordinate systems being described by a nine element (orthogonal and normalised) direction cosine matrix, more details on this can be found presented in Chapter 4 and in [13]. In this way, all antenna patterns that are presented within this inter-range comparison can be considered to be presented in a single (fiducial) antenna mechanical coordinate system. Failure to do this can result in very large apparent differences, particularly in the main beam region.

The task of assessing pattern pointing can become complicated if the antenna in question has a particularly broad beam pattern. For the case of a broad beam (e.g. isoflux) antenna the exact location of the peak in the pattern can be disturbed by low-level noise or scattering resulting in recourse to alternative assessments. As the gain slope in the vicinity of the greatest region of field intensities is very shallow, this implies that any small change in the pattern (e.g. resulting from random noise, etc.) can result in the peak of the pattern appearing to be shifted by a large angular distance. Thus, denoting the peak of the pattern by the location of the largest element within the respective far-field pattern arrays can be very misleading and as such an alternative technique that is more applicable to broad antenna patterns must be utilised.

One technique for assessing the direction of the pattern is to compute the centre of gravity of a lamina that is formed from an iso-level. That is to say, a $-n$ dB centroid is used to compare the electric direction of the antenna patterns. Selecting an iso-level such as this means that the deleterious effects of low-level noise on a very flat pattern are mitigated thereby enabling useful comparisons to be made. It is possible to select different levels and often the half power (-3 dB) contour is chosen. In some cases where the pattern is very broad lower levels are needed and typically selected where the pattern slope is steep. An example is shown in Figure 10.89 where data is shown for a pattern containing a beam peak at 2° in x and 1° in y and the beam peak using traditional interpolation techniques is found at 1.999° in x and 1.001° in y. If a -3 dB contour is generated and the beam peak is found based on the centre of gravity of this lamina, we obtain a beam peak estimate at 1.987° in x and 0.998° in y. If we now add noise to this picture we obtain the example as shown in Figure 10.90 where a -40 dB noise signal has been introduced. The beam peak using traditional interpolation techniques is now found at 1.828° in x and 0.655° in y. If a -3 dB contour is generated and the beam peak is found based on the centre of gravity of this lamina, we obtain a beam peak estimate at 1.994° in x and 0.997° in y, showing a much higher degree of tolerance to the introduction of noise. This agreement between the respective pattern's pointing as derived from the -3 dB centroid is encouraging and illustrates how this technique can be applied to not only assess pointing error during RA, but also remove the impact of electrical pointing variation when assessing other parameters during RA.

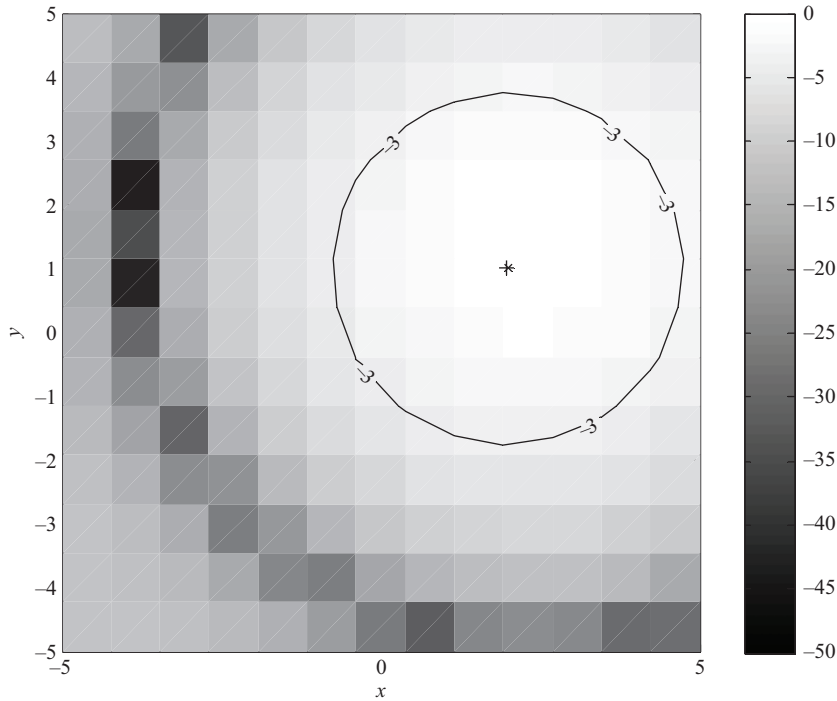

Figure 10.89 Pattern data containing a beam peak at 2° in x and 1° in y. Peak is detected using traditional interpolation techniques at 1.999° in x and 1.001° in y (denoted by '×') and at 1.987° in x and 0.998° in y (denoted by '+') using the centre of gravity of the −3 dB contour

A detailed description of the computation of the beam pointing direction from the centre of gravity of a lamina can be found presented in [13].

10.13 Summary

The uncertainty concepts described in this chapter form the basis of any RA, regardless of the type of test facility and therefore allow us to create a framework within which the quality of any antenna measurement result can be expressed. It also allows us to do meaningful range inter-comparisons that have become such an integral part of modern test programs.

Although most of the groundwork related to RA's was conducted in an effort to validate near-field testing in the early days, this work has found wider application and can today be applied to far-field and CATR test systems with equal success. It is safe to say that the antenna measurement community (for the most part) have adopted the principle that measurement results need to be reported with an associated uncertainty, to make them credible.

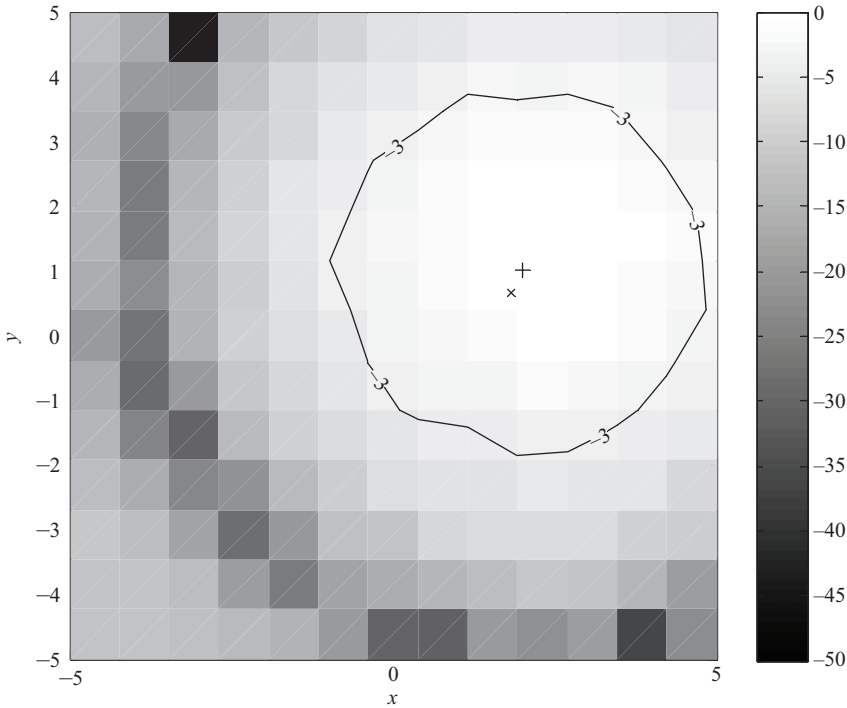

Figure 10.90 Pattern data with –40 dB noise introduced, containing a beam peak at 2° in x and 1° in y. Peak is detected using traditional interpolation techniques at 1.828° in x and 0.655° in y (denoted by '×') and at 1.994° in x and 0.997° in y (denoted by '+') using the centre of gravity of the −3 dB contour

Finally, a very welcome side effect of doing any RA is a greater understanding of the measurement process and associated weaknesses. This often leads to a clear definition of exactly what aspect needs to be addressed if uncertainty is to be reduced, making for a very efficient use of resources in the process.

References

[1] A. C. Newell, "Error analysis techniques for planar near-field measurements", *IEEE Trans. Antennas & Propagat.*, Vol. 36, No. 6, pp. 754–768, 1988

[2] J. E. Hansen, *Spherical Near-field Antenna Measurements*, Peter Peregrinus, 1988, Chapter 6

[3] D. Slater, *Near-Field Antenna Measurements*, Artech House, 1991, Chapter 9

[4] D. W. Hess, "An expanded approach to spherical near-field uncertainty analysis", AMTA Annual Meeting & Symposium, Cleveland, OH, USA, 2002

[5] Lars Jacob Foged, Antonis Alexandridis, Christian Sabatier, Hakan Eriksson, Jan Zackrisson, Ludovic Durand, Manuel Sierra Castener, Martin Boettcher, Sara Burgos and Sergey Pivnenko, *Recommendations and Comparative Investigations for Near-Field Antenna Measurement Techniques and Procedures*, ACE Report # FP6-IST-026957-A1.2D2, 31 Dec. 2007

[6] A. C. Newell and D. Lee, "Application of the NIST 18 term error model to cylindrical near-field antenna measurements", AMTA Annual Meeting & Symposium, Philadelphia, PA, 2000

[7] A. C. Newell and G. E. Hindman, "Antenna pattern comparison using pattern subtraction and statistical analysis", EuCAP, Rome, April 2011

[8] D. M. Kerns, *Plane-Wave Scattering-Matrix Theory of Antennas and Antenna-Antenna Interactions*, National Bureau of Standards Monograph 162, June 1981

[9] W. L. Stutzman, *Polarization in Electromagnetic Systems*, Artech House, 1993

[10] D. J. Janse van Rensburg, A. Newell and G. M. Hagenbeek, "The impact of alignment errors on cylindrical near-field antenna measurements", AMTA 22nd Annual Meeting & Symposium, Philadelphia, PA, USA, Nov. 2000

[11] D. J. Janse van Rensburg and J. Wynne, "Parametric study of probe positioning errors in spherical near-field test systems for mm-wave applications", North American Radio Science Meeting Digest – URSI 2012, Chicago, USA, July 2012

[12] D. J. Janse van Rensburg, "Parametric study of angular and radial probe positioning errors in a large spherical near-field automotive antenna test system", ANTEM 2004 Symposium, Ottawa, ON, Canada, July 2004

[13] S. Gregson, J. McCormick and C. G. Parini, "Principles of Planar Near Field Antenna Measurements", Appendix A, pp. 347–354, IET Publications, 2007, ISBN 978-86341-736-8

[14] D. W. Hess, *Antenna Boresighting*, 1987

[15] D. J. Janse van Rensburg, "Phased-array simulation for antenna test range design", AMTA 20th Annual Meeting & Symposium, Montreal, Quebec, Canada, Nov. 1998

[16] M. Francis, "Estimating far-field errors due to mechanical errors in spherical near-field scanning", APS/URSI Symposium, Chicago, IL, 2012

[17] D. J. Janse van Rensburg, S. R. Mishra and Guy Séguin, "Simulation of errors in near-field facilities", AMTA 17th Annual Meeting & Symposium, Williamsburg, Virginia, USA, Nov. 1995

[18] A. C. Newell, R. D. Ward and E. J. McFarlane, "Gain and power parameter measurements using planar near-field techniques", *IEEE Trans. Antennas Propagat.*, Vol. 36, No. 6, 1988

[19] D. M. Kerns and R. W. Beatty, *Basic Theory of Waveguide Junctions and Introductory Microwave Network Analysis*, NBS Report 8807, 1965

[20] D. M. Pozar, *Microwave Engineering*, Addison-Wesley, 1990, p. 79
[21] IEEE Standard for Definitions of Terms for Antennas, 145, IEEE, 2013.
[22] D. J. Janse van Rensburg, "Scan plane reduction techniques for planar near-field antenna measurements", *Antennas Propagat. Mag.*, Vol. 46, No. 6, pp. 179–184, 2004
[23] E. B. Joy and C. A. Rose, "Windows 96 for planar near-field measurements", AMTA 18th Annual Meeting & Symposium, Seattle, September 30–October 3, 1996
[24] D. J. Janse van Rensburg, "A technique to evaluate the impact of flex cable phase instability on mm-wave planar near-field measurement accuracies", ESTEC Antenna Conference, Noordwijk, The Netherlands, May 1999
[25] D. W. Hess, "Principle of the three-cable method for compensation of cable variations", AMTA Annual Meeting & Symposium, Columbus, OH, USA, Oct. 1992
[26] J. Tuovinen, A. Lehto and A. Raisanen, "A new method for correcting phase errors caused by flexing of cables in antenna measurements", *IEEE Trans. Antennas Propagat*., Vol. 39, No. 6, pp. 859–861, 1991
[27] A. C. Newell, J. Guerrieri and K. MacReynolds, "Methods to estimate and reduce leakage bias errors in planar near-field antenna measurements", AMTA Annual Meeting & Symposium, Cleveland, OH, USA, 2002
[28] D. Slater, *Near-Field Antenna Measurements*, Artech House, 1991, p. 230
[29] A. Yaghjian, *Upper-Bound Errors in Far-Field Antenna Parameters Determined From Planar Near-Field Measurements. Part 1*, National Bureau of Standards Technical Note 667, Oct. 1975
[30] G. H. Hindman and D. Slater, "Error suppression techniques for near-field antenna measurements", AMTA Annual Meeting & Symposium, Monterey, CA, USA, Oct. 1989
[31] A. C. Newell and C. F. Stubenrauch, "Effect of random errors in planar near-field measurement," *IEEE Trans. Antennas Propagat.*, Vol. 36, No. 6, pp. 769–773, 1998
[32] UKAS Document, "The expression of uncertainty and confidence in measurement", United Kingdom Accreditation Service, M3003, Edition 1, Dec. 1997
[33] H. Taub and D. L. Schilling, *Principles of Communications Systems*, McGraw-Hill, 1971
[34] McCormick, S. F. Gregson and C. G. Parini, "Quantitative measures of comparison between antenna pattern data sets", *IEE Proc. Microw. Antennas Propag*., Vol. 152, No. 6, pp. 539–550, 2005
[35] W. L. Stutzman, *Polarization in Electromagnetic Systems*, Artech House, 1993
[36] S. F. Gregson, A. C. Newell, C. Feat and F. Viguier, "The Use of Statistical Image Classification in Assessing Antenna Pattern Measurements", AMTA, Columbus, OH, Oct. 2013

Chapter 11

Mobile and body-centric antenna measurements

11.1 Introduction

During the past ten years there has been a very rapid development of wireless mobile systems including 3G/4G cellular systems, smart-phones, Wi-Fi, Bluetooth, SatNav, ultra-wideband (UWB), etc. All these require antennas and often the antenna needs to support more than one (if not all!) of these applications, so measurement of these, largely low gain, antennas is an important issue for the antenna measurement engineer. In this chapter we look at the key issues that are unique to the measurement of this class of antenna, and we start by considering both far-field and near-field techniques for radiation pattern measurement. We then consider the measurement of return loss and hence the antennas' operating bandwidth. In the practical use of mobile devices, there are no RF cables connecting them, but for *S*-parameter and pattern measurements a cable usually exists and it can have significant influence on the resulting measurements, and in Section 11.5 we show how the use of optical fibre connections is solving this problem. The human body has a high dielectric constant and so antennas mounted close to the body operate differently than in 'free space', so in Section 11.6 we consider the issue of 'on-body' antenna measurements both on a live subject and on the use of phantoms. For electrically small antennas efficiency is very important and in Section 11.7 we consider the measurement of efficiency via both radiation pattern measurement and the Wheeler Cap method, where we report an improved method well suited to body-centric measurements. Finally we consider the measurement of UWB antennas, noting that 'radiation pattern' has less importance than pulse fidelity in many UWB applications.

11.2 Indoor far-field antenna measurements

Because antennas for mobile terminals require generally near-omni coverage radiation patterns and are of small size they are inevitably electrically small and of low gain. They are thus well suited for measurement in an indoor far-field anechoic chamber where the $2D^2/\lambda$ condition is met with very modest chamber dimensions. The basic concept of the far-field range has been covered in Section 3.3, and the use of shielded anechoic chambers in Section 3.4. Because this class of antennas is usually being tested in commercially operational bands, suppression of interference

from and to outside users needs to be prevented and hence the importance of fully shielded chambers for antenna testing.

The chamber transmit/receive horn for such facilities is usually a wideband, dual-linear polarisation double ridged horn of the type shown in Figure 11.1, where these can cover wide operating bandwidths, e.g. 0.4–10 GHz. They can also be fed with a 90° hybrid to achieve circular polarisation.

For the AUT the antenna positioner needs to avoid any metal that would act as an additional ground plane to the test antenna (so affecting its radiation pattern) as well as having a low profile to ensure that the often near omnidirectional patterns can be taken without masking the antenna with the positioner. One such configuration is shown in Figure 11.2, where the positioner has a low-reflection support made of plastic, with phi (polarisation) rotation (for far-field coordinate system see Figure 11.3) provided by toothed belt-driven pulley operating through the hollow support column with the drive motor at the base. AUT connection to RF can be made through a single coaxial rotary joint with cable feed down the hollow support column, or a flexible cable with the position controller limiting phi rotation to $\pm 100°$ to avoid cable twisting. Such a system can take full coverage of linear polarisation patterns by taking a series of full 360° azimuth (θ in Figure 11.3) patterns and stepping the phi angle ($-90°$ to $+90°$) in synchronisation with the phi angle for the range transmit/receive horn, thus providing the co-polar pattern. The cross-polar pattern is obtained by repeating the above with the AUT and range horn orthogonal in phi to start with.

If the AUT is circularly polarised (CP), then either a CP range horn is required or a linear polarisation range horn can be used and the AUT measured using the 'spin linear' technique. Here, the linearly polarised range horn is rotated in phi at a

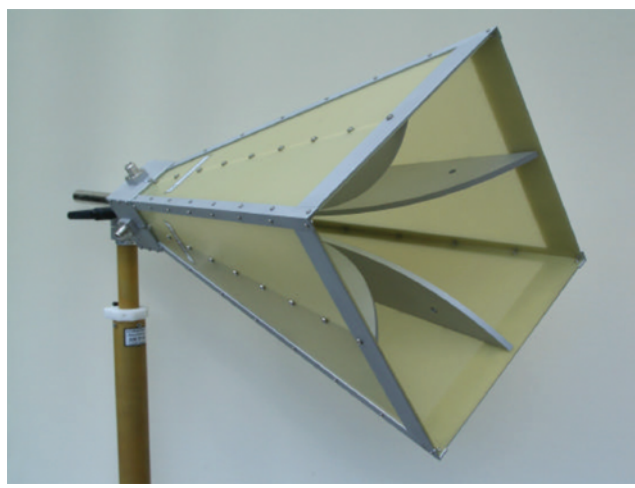

Figure 11.1 Typical anechoic chamber wideband dual polarised horn covering 0.4–10 GHz

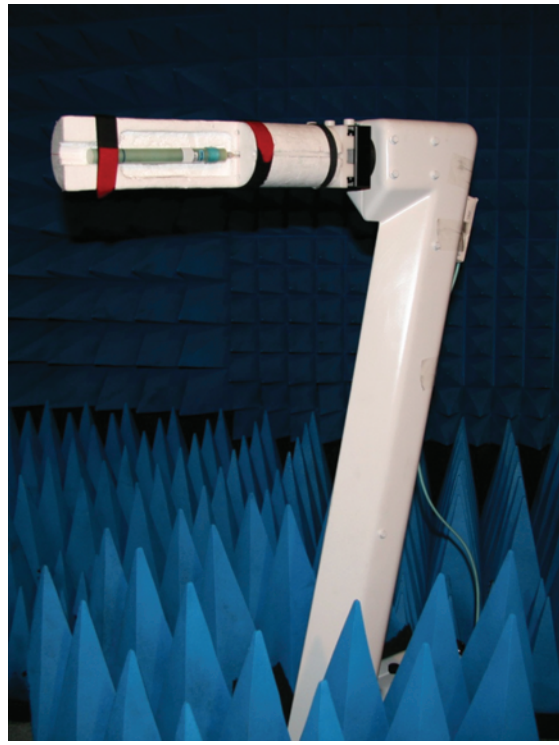

Figure 11.2 Low profile antenna positioner for low gain mobile antenna radiation pattern measurement (Courtesy of NSI-MI Technologies LLC)

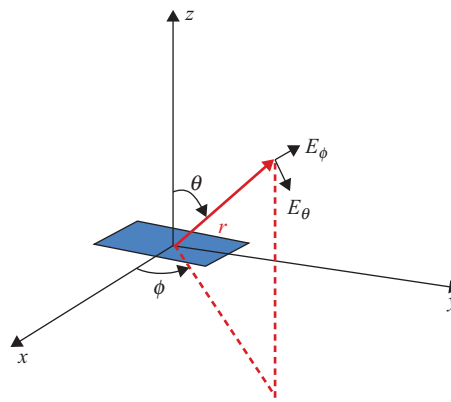

Figure 11.3 Coordinate system for E_θ and E_ϕ

much faster rate than the azimuthal rotation of the AUT, and the measured pattern simultaneously displays both the axial ratio (from the peak to peak level of the ripple) and the beam pattern, and a typical pattern can be found in Figure 4.40 along with the mathematics of the process described in Section 11.2.7 (see also [1,2]). Another method suitable for automated measurement facilities with a VNA as receiver is the phase-amplitude method. The method uses a linearly polarised range horn to measure both the amplitude and phase across one or more cuts of the CP radiation pattern. The method consists of measuring both E_θ and E_ϕ in Figure 11.3 for a given theta pattern cut. Thus with the phi angle of both the AUT and range horn aligned take theta (azimuth pattern) then repeat with range horn polarisation rotated by 90°. The measured data is post-processed in order to reconstruct the CP co- and cross-polarisation patterns (or right-and left-hand polarised components E_{RH} and E_{LH}) through (11.1) and (11.2).

$$E_{RH} = 1/\sqrt{2}\left(E_\theta + jE_\phi\right) \tag{11.1}$$

$$E_{LH} = 1/\sqrt{2}\left(E_\theta - jE_\phi\right) \tag{11.2}$$

The axial ratio (AR) can then be found from

$$AR = \frac{||E_{RH}| + |E_{LH}||}{||E_{RH}| - |E_{LH}||} \tag{11.3}$$

11.3 Spherical near-field measurements

The measurement of full 3D radiation patterns and the associated calculation of directivity and hence efficiency are a frequent requirement for mobile antennas. This can be achieved using a conventional far-field range as described in the previous section, but can be a time-consuming process. We have already seen in earlier chapters the spherical near-field approach offers an attractive alternative when full 3D characterisation is required. For electrically small low-gain mobile antennas such facilities can be very compact minimising the size (and cost) of the anechoic chamber. Even if the effect of the human operator is to be included (either directly of via a phantom) then spherical near-field measurement offers a significantly more compact solution than the far-field approach (taking into account the $2D^2/\lambda$ size including the human or phantom). Conventional spherical near-field, as discussed in Chapter 8, is one such method and suitable small scanners have been developed, see e.g. Figure 11.4, where the Theta-over-Phi scanner (often called an overhead swing-arm) requires just an azimuthal rotation of the AUT for full (nearly) 3D coverage. Figure 11.4 shows the use of a dual polarisation probe for rapid measurements, the AUT is a calibration probe. Alternatively a Phi-over-Theta spherical NF measurement can be made with a fixed probe (dual or single polarisation) and AUT scanned using a positioner of the type shown in Figure 11.2.

Figure 11.4 Overhead swing-arm spherical scanner. AUT is a monopole and the probe is a dual polarised, log-periodic 500 MHz to 18 GHz probe (Courtesy of NSI-MI Technologies LLC)

Where speed of measurement is required, it would be very desirable to use an array of receivers on an arch to perform the phi scan electronically and then just a mechanical scan for the theta (azimuthal) axis. Using conventional RF array switching electronics can be expensive, particularly if wideband operation is required. However, the modulated scattering technique (MST), first proposed in 1982 [3], offers a viable solution, and has been commercially well established, developing to the method termed 'Advanced Modulated Scattering Technique' (A-MST). In the original modulated scattering near-field approach, the probe acts simply as a scatterer of the incident field from the AUT, $Ee^{j\theta}$, the scattered field being modulated by an LF (low frequency) source that is connected to the 'active probe'. In the monostatic system the AUT receives the modulated scattered field from the probe, the amplitude and phase of the modulated signal being directly related to the AUT field at the probe by ($E^2e^{j2\theta}$), see e.g. [4] and [5]. The probe can be moved around the AUT to provide either spherical, cylindrical or planar scanning with no issues concerning RF cables and phase stability, etc. By employing an array of scatters (a linear array is shown in Figure 11.5 for a cylindrical near-field

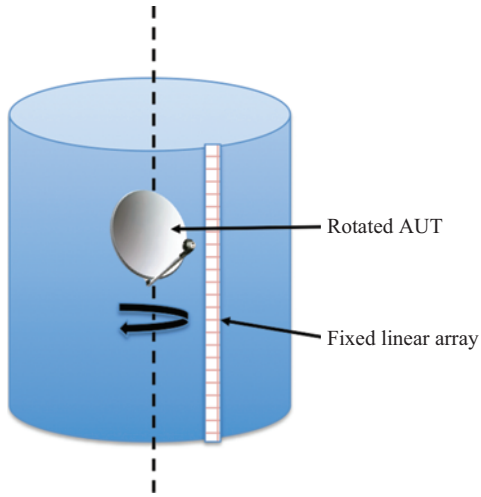

Figure 11.5 Linear modulated scattering array offering a cylindrical near-field measurement system

system), the field is probed by just selecting which array element has the LF modulation applied to it.

The concept of the A-MST approach is to apply the modulation at the probe and to transmit the probe-received signal to the receiving equipment via a passive power dividing network connecting every probe. By sequentially applying the LF modulation to each probe, the received modulated signal amplitude and phase are directly related to the signals at each of the probes. The concept was reported in an AMTA paper in 1999 [6] and a current commercial realisation can be seen in Figure 11.6, which employs dual polarisation probes for full electronic scanning in phi, with mechanical single axis scanning for theta (azimuth). The AUT is positioned at the centre of the arch.

Shows an example of a system with dual polarised measurement probes spaced 22.5° apart. These probes contain a pair of orthogonal printed antennas designed to provide broadband characteristics covering 400 MHz to 6 GHz. The two antennas are linearly polarised and aligned according to vertical and horizontal polarisations. The probes are completely reciprocal and can be used in both receive and transmit modes. The probe assembly also houses the circuit board containing the control electronics for the LF modulation of the probe. The probes are covered in a conformal multilayer absorber to reduce mutual coupling effects. The concept has been extended to operate additionally from 6 to 18 GHz by the inclusion of 16 probes interleaved with those operating at the 0.4–6 GHz band [7]. An example of the measurement speed that can be achieved is a full 3D pattern measurement with 22.5° samples at six frequencies taking 90 seconds. Because the antenna array is connected via a passive power dividing network, the measurement system can be

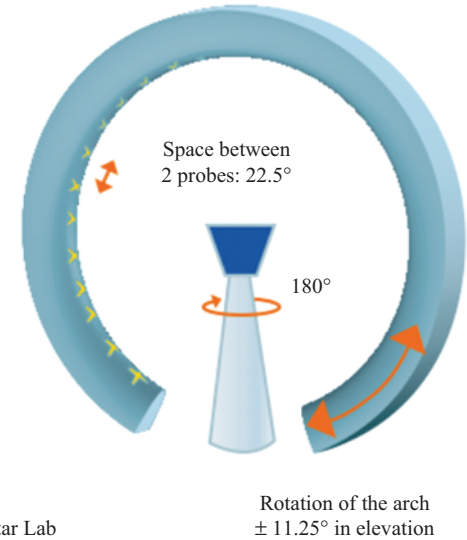

Figure 11.6 Spherical A-MST system (Courtesy of Microwave Vision Group)

operated in both transmit and receive modes; it thus offers considerable capability for production line testing.

With the development of wideband PIN diode switch matrices, the use of a circular array with RF switching has been deployed and an example of a 700 MHz to 6 GHz system is shown in Figure 11.7, offering three-channel active measurements in less than 2 minutes per frequency.

All of the above multi-probe systems suffer with channel imbalance and need regular calibration to enable the relative electrical path lengths to be equalised. This can be time-consuming since it requires an auxiliary RF measurement to be made across the frequency band for every probe within the array.

11.3.1 Over-the-air measurements

These spherical NF systems can be used to make direct 'over-the-air' (OTA) measurements of mobile handsets where the mobile-inbuilt RF transmit/receive section along with the antenna can be tested in conjunction with a radio communication tester (Base Station Simulator) connected to the array elements (rather than a VNA). This permits measurement of a full production handset as well as such additional parameters as total radiated power (TRP) and total isotropic sensitivity (TIS). An example of a typical measurement set-up is shown in Figure 11.8, where narrow-band standard gain antennas such as resonant loop and sleeve dipoles offer good calibration accuracy.

TRP is a measurement of the total radiated power from the mobile antenna compared to that from the mobile with an isotropic radiator. It is made using a Base Station Simulator (BSS) to establish a call with the test device and then measuring

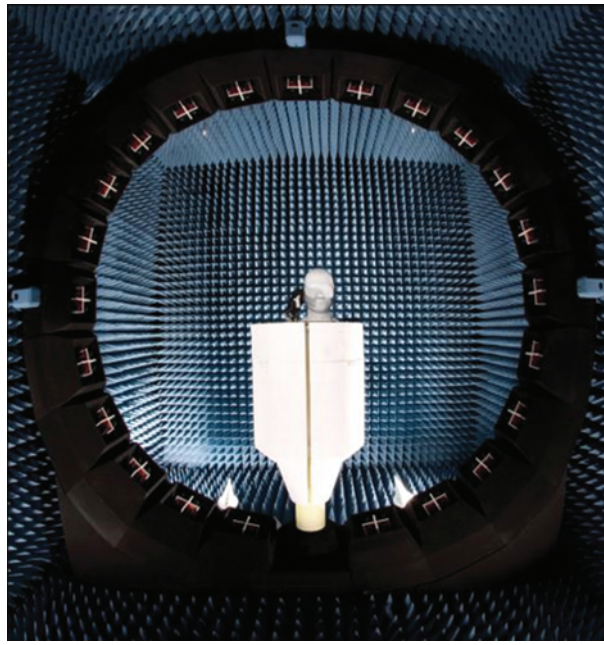

Figure 11.7 PIN-switched array for spherical NF measurements (Courtesy of ETS-Lindgren)

the power from the device as the receive probe traverses the sphere surrounding the device. TRP is then calculated by integrating over the complete sphere as

$$TRP = \frac{1}{4\pi}\int_{\theta=0}^{\pi}\int_{\phi=0}^{2\pi}(EIRP_{\theta}(\theta,\phi) + EIRP_{\phi}(\theta,\phi))\sin(\theta)d\theta d\phi$$

The near-horizon partial radiated power measured over a cap covering either 45° or 30° from the horizon (NHPRP45, NHPRP30) can be calculated using

$$NHPRP45 = \frac{1}{4\pi}\int_{\theta=\pi/4}^{3\pi/4}\int_{\phi=0}^{2\pi}(EIRP_{\theta}(\theta,\phi) + EIRP_{\phi}(\theta,\phi))\sin(\theta)d\theta d\phi$$

$$NHPRP30 = \frac{1}{4\pi}\int_{\theta=\pi/3}^{2\pi/3}\int_{\phi=0}^{2\pi}(EIRP_{\theta}(\theta,\phi) + EIRP_{\phi}(\theta,\phi))\sin(\theta)d\theta d\phi$$

An example of a TRP measurement is shown in Figure 11.9, which was made using the swing arm system of Figure 11.4 with a measurement time of approximately 15 minutes.

TIS quantifies the RF receiver performance and is the antenna sensitivity integrated over a sphere [8]. Here the BSS establishes a call with the device and then places the device in loop-back mode, and it then transmits a bit-pattern to the

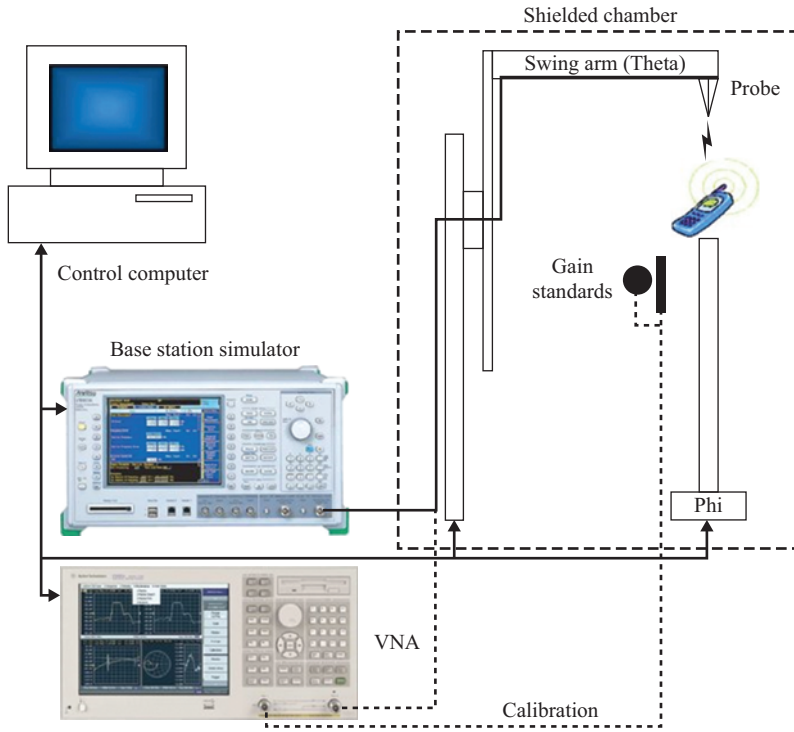

Figure 11.8 Over-the-air measurement system

device and receives the re-transmitted pattern back from the device. Finally the BSS compares the bit-patterns and computes a BER. The control software iterates the BSS Tx power to determine the sensitivity. Sensitivity is defined as the power level at which the BER matches the target BER, which for GSM is 2.44%. The total isotropic sensitivity, integrated over the complete sphere, is

$$TIS = \frac{4\pi}{\int_{\theta=0}^{\pi}\int_{\phi=0}^{2\pi}\left[\frac{1}{EIS_{\theta}(\theta,\phi)}+\frac{1}{EIS_{\phi}(\theta,\phi)}\right]\sin(\theta)d\theta d\phi}$$

The near-horizon partial isotropic sensitivity integrated over 30° from the horizon would be

$$NHPIS30 = \frac{4\pi}{\int_{\theta=\pi/3}^{2\pi/3}\int_{\phi=0}^{2\pi}\left[\frac{1}{EIS_{\theta}(\theta,\phi)}+\frac{1}{EIS_{\phi}(\theta,\phi)}\right]\sin(\theta)d\theta d\phi}$$

Each BER measurement can take up to 10 seconds with a full grid measurement time of about 2 hours. A typical measured result is shown in Figure 11.10.

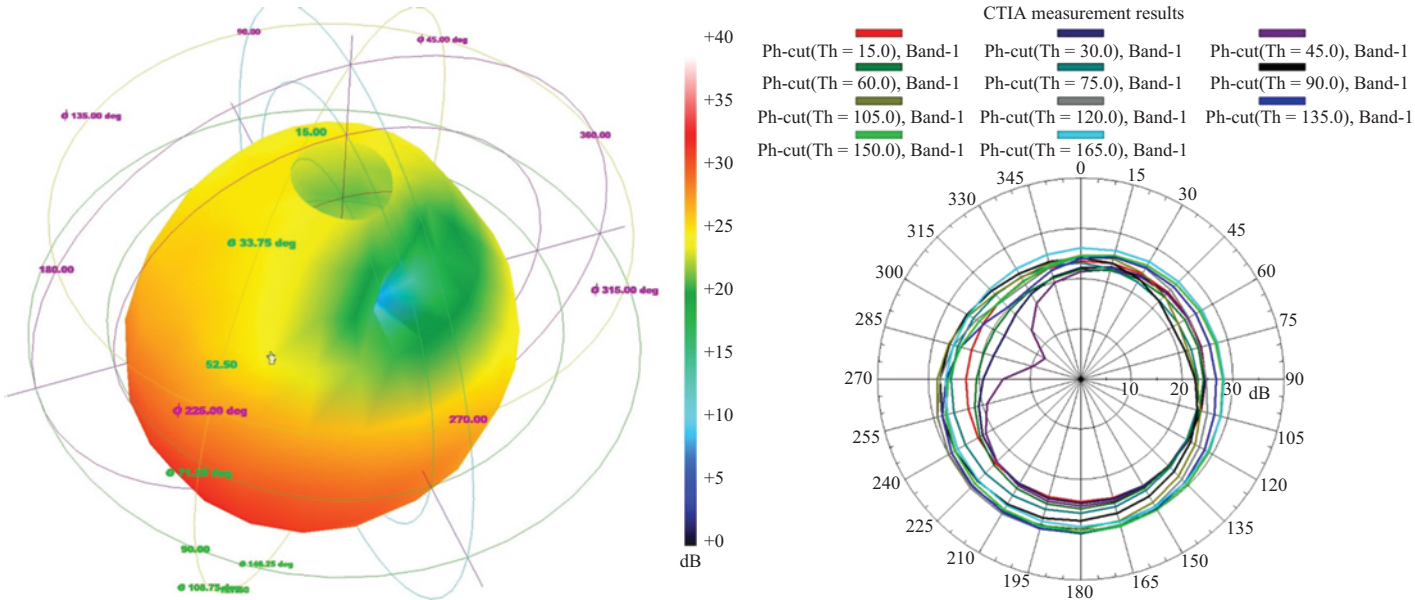

Figure 11.9 Typical TRP measured result

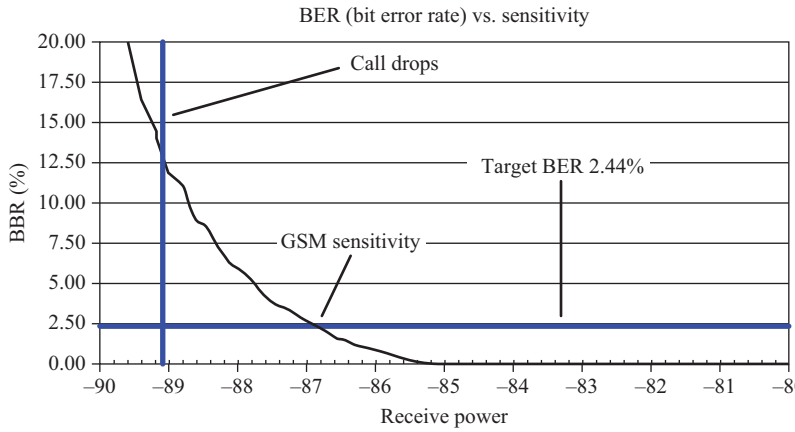

Figure 11.10 Typical TIS measurement

11.4 Low-gain antenna and *S*-parameter measurement methods

For low-gain antenna testing the cable connecting the AUT to the receiver system is a critical component. Coaxial cable is thus a natural choice since it offers intrinsic shielding ensuring there is no radiation from the cable contributing to the measured AUT signal. If the AUT has a balanced feed (e.g. a simple half wavelength dipole), then feeding the dipole using a coaxial cable means that undesirable currents will flow on the outer conductor of the cable. This leakage current can be suppressed by using a balun, see Figure 11.11, which exhibits suppression of the outer current I_3 via the quarter-wave, short-circuited transmission line in the form of an outer coaxial sleeve (often called the sleeve balun). This is of course a narrow-band device.

This impedance transformation is often not needed in the final version of the antenna because it is directly attached to the amplifier in a handset or other mobile device.

As mentioned earlier, where an antenna uses a ground plane the size of the ground plane will affect the antennas performance. Both the return loss and radiation pattern of a monopole antenna are affected by a finite-sized ground plane and in [2] it is shown that the ground plane edge needs to be at least 1.5 λ from the monopole where the antenna input impedance then converges to within 5 per cent of the infinite ground plane value. A square rather than circular-shaped ground plane was shown to perform better, due to the varying length of the edge diffraction component with respect to the monopole. However, it was found that the square ground plane creates large cross-polar components in the plane of the ground plane (-16 dB peaks compared to -25 dB peaks for the circular ground plane of same 1.5 λ radius).

The influence of the AUT positioner on the measured radiation pattern of a low gain antenna should also be considered. Figure 11.12 shows a dipole antenna

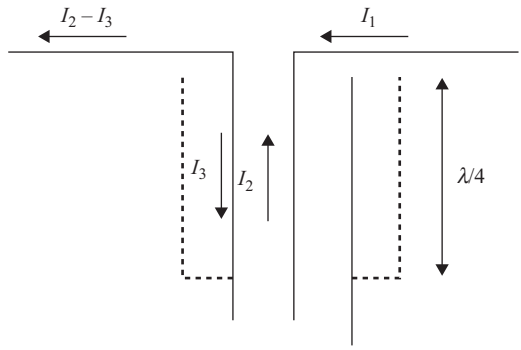

Figure 11.11 Dipole antenna fed via a balun, showing suppression of the outer current I_3 via the quarter-wave, short-circuited transmission line (dotted)

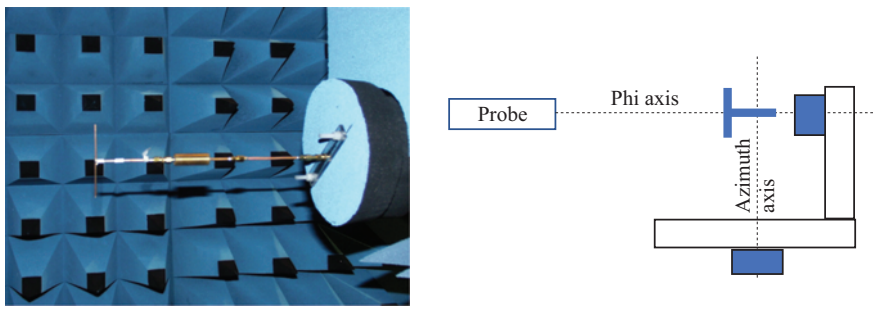

Figure 11.12 Dipole antenna mounted on azimuth/phi axis SNF positioner

mounted on an azimuth/phi axis positioner, and Figure 11.13 shows the SNF measured principal plane cuts of the radiation pattern, clearly showing the aperture blocking resulting for the AUT support. Such effects can often be mitigated by re-locating the AUT such that the direction of minimum illumination is directed towards the AUT support structure. For the case of the dipole, this is shown in Figure 11.14(a), with the corresponding SNF measured radiation patterns shown in Figures 11.14(b) and (c). Clearly, the omni-directional pattern of the AUT about the dipole axis is now much improved, with now the 'figure-of-eight' pattern effected by the positioner blockage.

The AUT is connected to the transmitter or receiver by some form of transmission line. The impedance presented to the transmission line by the antenna is termed the antenna input impedance, which itself is the sum of the self-impedance and the mutual impedance:

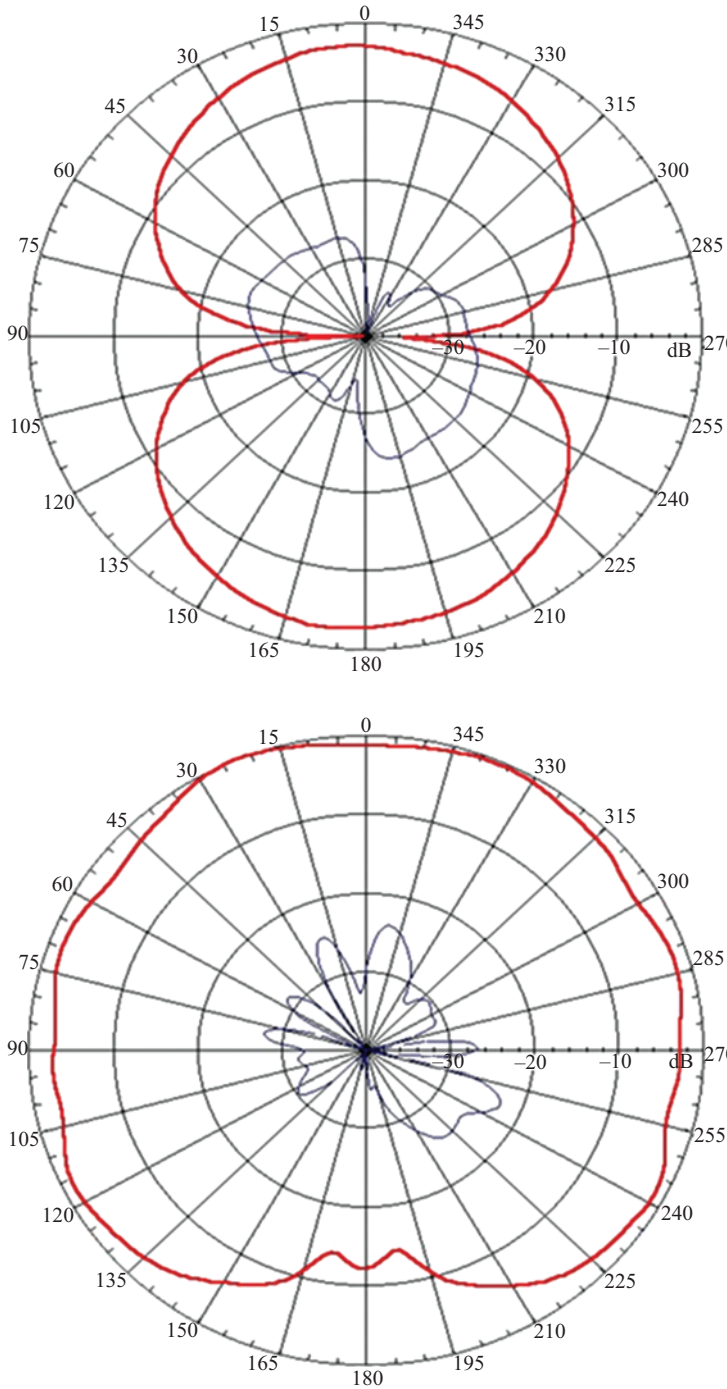

Figure 11.13 SNF measured radiation patterns of dipole antenna shown in Figure 11.12

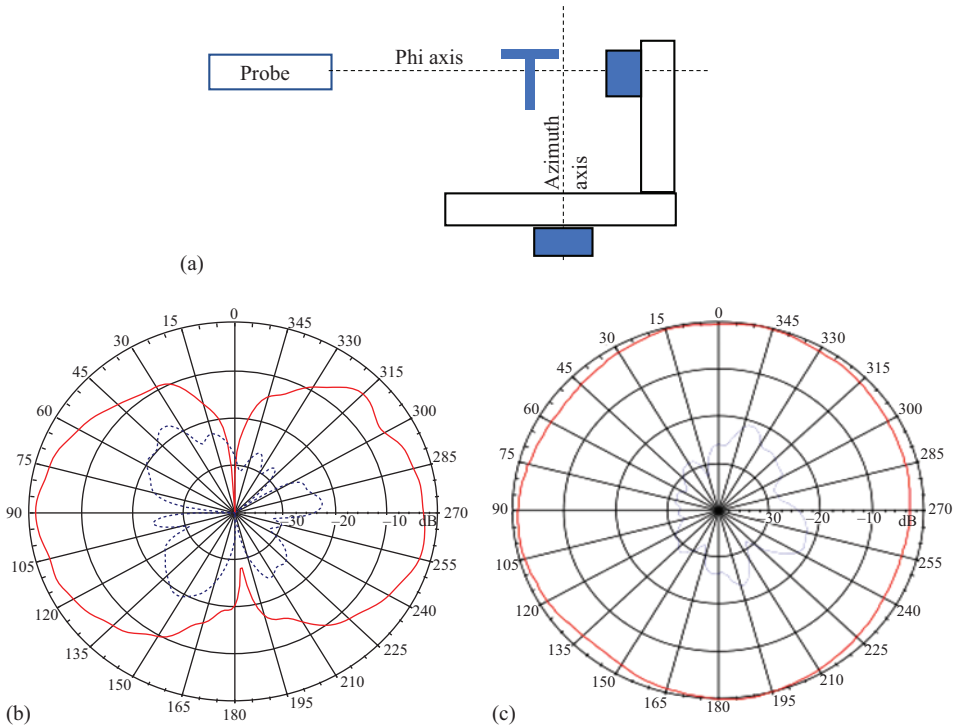

Figure 11.14 *(a) Dipole antenna relocated on positioner system; (b and c) SNF measured radiation patterns of dipole antenna shown in (a)*

Self-impedance is the impedance which would be measured at the antenna terminals with the antenna radiating into free space in the absence of other antennas or reflecting obstacles.

Mutual impedance accounts for the radiative coupling to the antenna by any other outside source such as a reflecting object or other passive antenna. This is illustrated in Figure 11.15 where the passive directors of a Yagi antenna are the mutual impedance component of the overall Yagi input impedance.

$$\text{Self-impedance} = \text{Self-resistance} + j\ \text{Self-reactance}$$

Self-reactance arises from the reactive energy which is stored in the reactive near-field region of the antenna.

Self-resistance accounts for all the power absorbed by the antenna as seen at its input terminals (transmit mode).

$$\text{Self-resistance} = \text{Radiation resistance} + \text{Loss resistance}$$

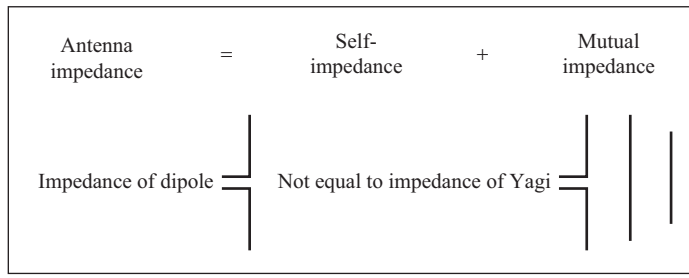

Figure 11.15 Self- and mutual impedance with respect to the dipole and Yagi antenna

Radiation resistance: Power ultimately radiated by the antenna and is the equivalent resistance which would dissipate a power P_r equal to that radiated when the current at the antenna input terminals is I_0

$$R_r = P_r / I_0^2 \tag{11.4}$$

Loss resistance: Dissipative and ohmic losses in the antenna structure. This needs to be kept low compared to the radiation resistance for an efficient antenna.

A practical half-wave dipole has a radiation resistance of approximately 73 Ω with a loss resistance of a couple of ohms. An electrically small dipole (length $<$ 0.1 λ) will have a very low radiation resistance and will be dominated by its loss resistance, hence is inefficient as little of the power supplied to it will be radiated in transmit mode. Like any other load impedance connected to a transmission line, maximum power transfer occurs when the source (load) presents a conjugate match to the antenna. The input impedance can be measured with the antenna radiating in free space by measuring its reflection coefficient (S_{11}).

The measurement of *S*-parameters of mobile antennas is ideally done with the AUT in an anechoic chamber and the measurement undertaken using a VNA employing vector error correction to calibrate the VNA with reference points at the end of the coaxial cable that will connect to the AUT. Vector-error correction is the process of characterising systematic error terms by measuring known calibration standards and then removing the effects of these errors from subsequent measurements. One-port calibration is used for reflection measurements and can measure and remove three systematic error terms (directivity, source match and reflection tracking). This is achieved by measuring three known calibration standards, e.g. a short-circuit, an open-circuit and a matched load. From these measurements the equations yielding the systematic error terms can be derived and so enable the calculation of the actual reflection of *S*-parameter of the subsequently connected AUT [9]. Most modern VNAs undertake the calculations internally and guide the operator through the calibration process of connecting the various known calibration standards. In addition fast 'Electronic Calibration' systems using

calibration modules which are solid-state devices with programmable, repeatable impedance states, with manufacturer calibrated data that is fed directly to the VNA are available. These various impedance states are achieved by PIN-diode switches which shunt the transmission line to ground. Four different states are used to compute the error terms at each frequency point, and it offers a fast calibration process by simply connecting the one device to the RF cable end [9].

When using a VNA for antenna pattern measurements a two-port calibration can be undertaken that usually requires twelve measurements on four known standards (short-circuit, open-circuit, matched load, through line), to recover all twelve error terms [9].

11.5 Corruption by cables: the use of optical fibre links

For antennas that need an external power supply or RF or data cables, a hugely important factor is the effect that wires or cables can have on the measured radiation pattern. For reasons of space or economics, a small antenna may not have a sufficient balun (see Section 11.4) to prevent common mode current appearing on the outer surface of the wires and hence contributing to the radiation. For mobile devices it is most likely that the wires or cables are needed only for the testing of the antennas but will not be used in the final product. The undesirable radiation caused by the common mode current will interact with the intended antenna radiation and give a distorted measurement of the actual pattern. An example of this is shown in Figure 11.16 where a small UWB antenna [10] is measured and compared with the EM simulated patterns [12].

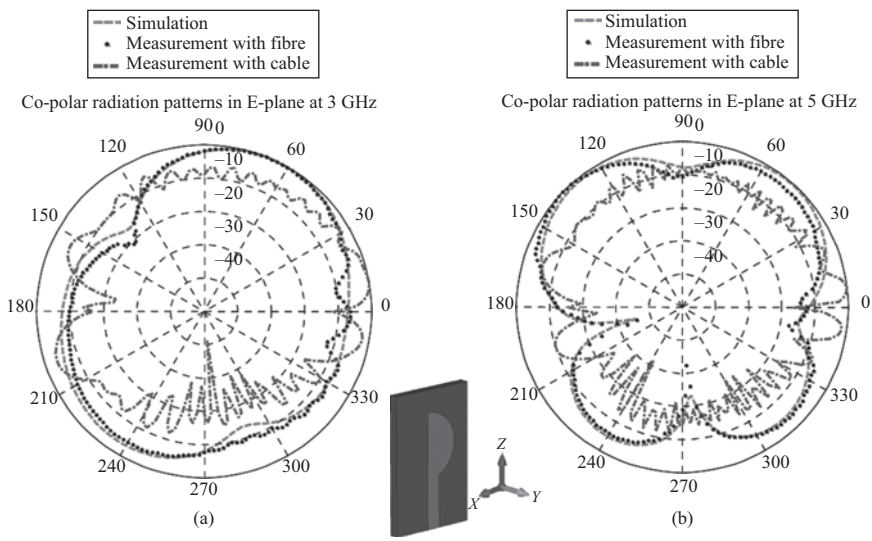

Figure 11.16 Simulated (dashed), measured with fibre (dotted), measured with cable (dot-dash) UWB antenna (shown inset) co-polar radiation pattern in E-plane (i.e. XZ cut). (a) 3 GHz, (b) 5 GHz [10,12]

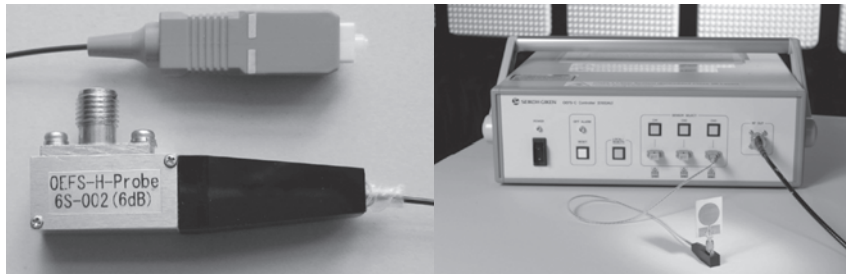

Figure 11.17 Left: electro-optic transducer with SMA connector. Right: OEFS controller and OEFS-PR-7G transducer and 25 mm diameter microstrip-fed top-loaded monopole antenna (Courtesy of National Physical Laboratory, UK)

To overcome this issue the metal coaxial line can be replaced by an optical fibre, which being fully dielectric is not invasive to the fields being measured and will not support common mode currents. An example of such a system is the Seikoh-Giken OEFS-PR-7G transducer (shown in Figure 11.17) which has an RF to optical transducer that comprises a laser-activated lithium niobate crystal and is contained in an aluminium case 20 mm $\times$ 10 mm $\times$ 10 mm on which is mounted an SMA connector to which the receive AUT (as shown in Figure 11.17) is connected. The transducer connects to an opto-electric field sensor (OEFS) controller, which supplies optical power to the transducer and converts the returned RF-modulated detected optical signal into an RF electric signal. The controller comprises a semiconductor laser, an optical circulator, a photo-detector and a 30 dB RF amplifier. The measurement system is shown in Figure 11.18 where the OEFS connects to the test port of a VNA [11,12]. This system has been used to measure the radiation patterns of the small UWB shown in Figure 11.16, in the UK National Physical Laboratories (NPL) 'small antenna test range' [12]. Figure 11.19 shows the measured 3D radiation patterns with the optical cable, conventional metallic coaxial cable and simulation results where the simulation included the SMA adaptor and the metallic cased electro-optic transducer (shown in Figure 11.17) [11]. The closeness of the OEFS measured patterns to the simulation is clear, as is the effect of the cable.

The OEFS system shown in Figure 11.17 operates up to 6.2 GHz and has a detected RF power range from $+20$ dBm to -60 dBm.

In [13] the National Metrology Institute of Japan reported a fully optical antenna measurement system with transmit AUT antenna fed by three fibres, one being the RF-modulated transmit source amplified by a Erbium-doped fibre amplifier, the other two fibres being detected reference and reflection obtained from RF photonic sensors in the RF transmit head, thus offering full *S*-parameter testing of the AUT with an all fibre connection (Figure 11.20). The range antenna operates in receive mode and is also connected via an optical fibre receive system similar to that described in Figure 11.17. The whole system offers an S_{21} dynamic

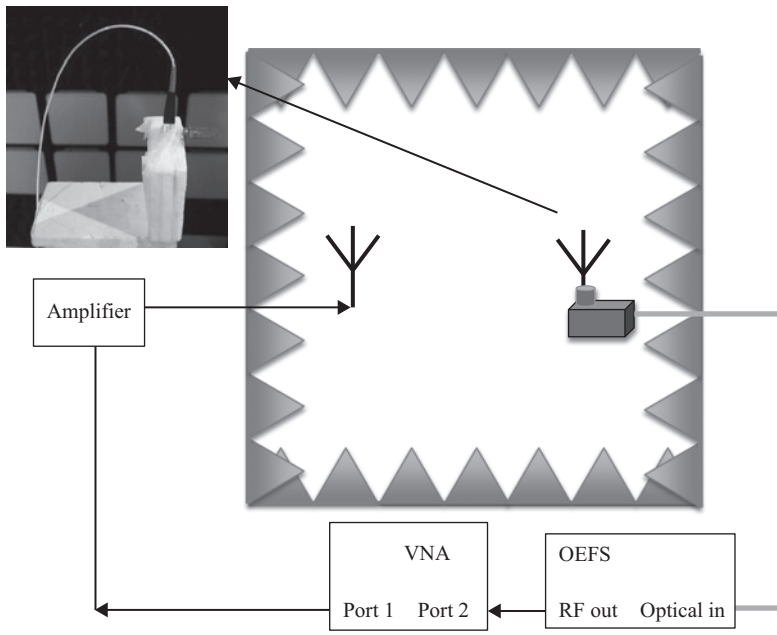

Figure 11.18 Connection of OEFS system in the antenna measurement range; inset shows mounted UWB antenna of Figure 11.16 [12]

range of better than 60 dB. In a recent development of this work [14], an optical-link receiving system that consists of an RF amplifier with photovoltaic power converter (fed by one fibre) and a zero-biased electro-absorptive (EA) optical intensity modulator that feeds a second fibre, has been developed into a very compact SMA to fibre connector shown in inset of Figure 11.21. Using this system it is possible to measure signals less than −100 dBm RF input level in frequency range from 1 GHz to 6 GHz, resulting in a near 100 dB dynamic range. Such a system offers an 'all optical' antenna measurement range suitable for highly sensitive EMI measurements.

11.6 On-body measurements

On-body communication channels are of increasing interest for a number of applications, such as medical-sensor networks, emergency-service workers and personal communications. We have already seen how low-gain antenna radiation characteristics can be affected by mutual impedance effects as well as the effects of any cables associated with the antenna test that are not part of the final antenna configuration. Another important effect on an electrically small antenna is the mutual impedance effect of the human body when antennas are placed on or close

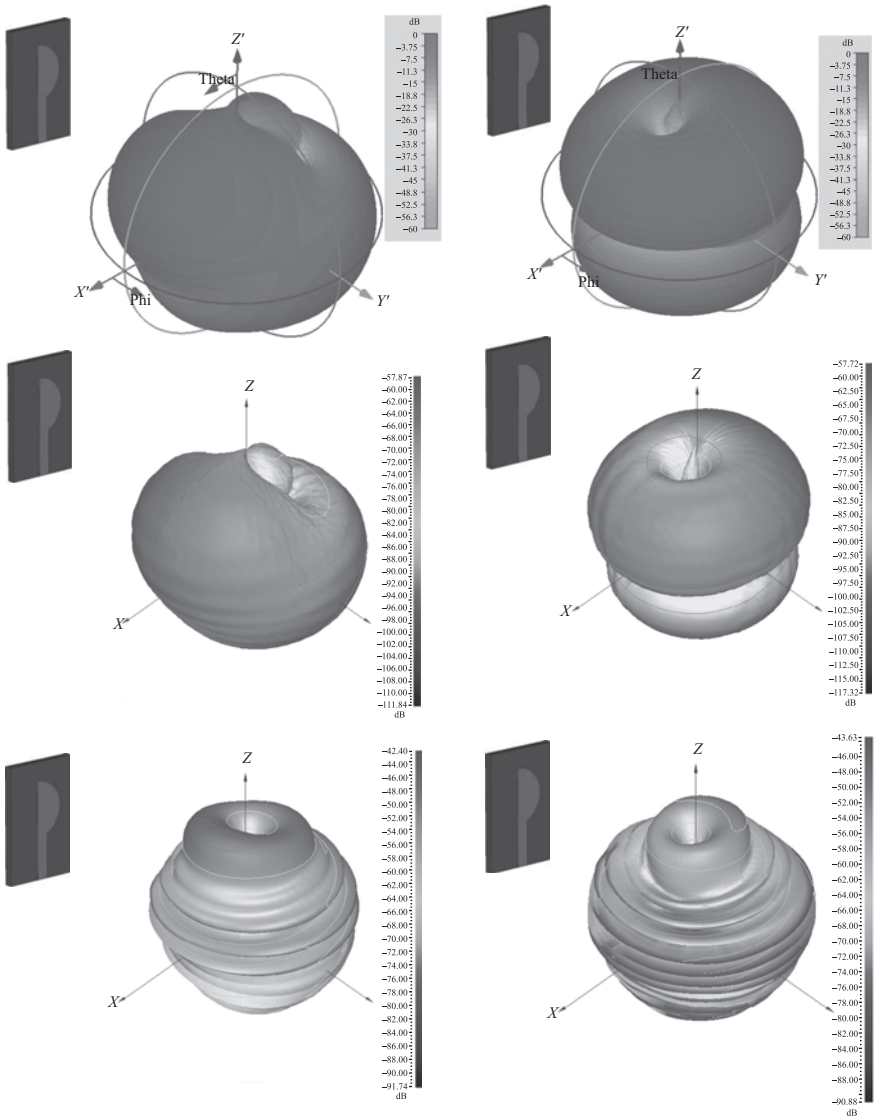

Figure 11.19 The horizontally polarised radiation pattern of the UWB antenna of Figure 11.16 measured at 3 GHz (left) and 5 GHz (right). Top: simulation results; middle: OEFS system; bottom: conventional metallic cable [12]

to human tissue. A typical example is shown in Figure 11.22 where the effects on the resonant frequency of a dual-band planar antenna mounted in isolation and then close to the human body are compared. The radiation pattern of this antenna is also similarly affected by the human body (see Figure 11.23).

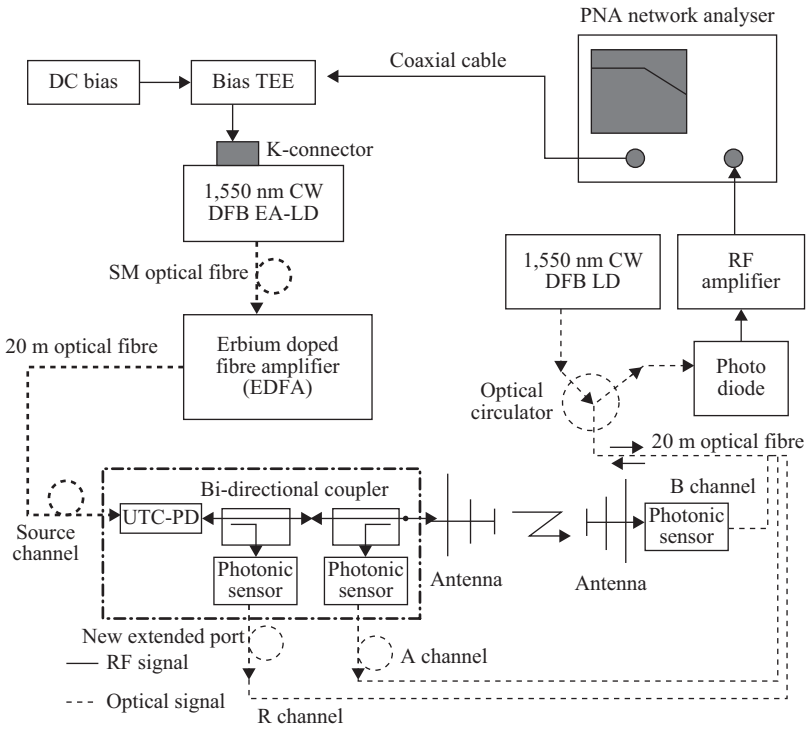

Figure 11.20 Fully optical transmit and receive antenna measurement range [13]

Such an effect should not be surprising since the electrical properties of human tissue are both lossy (Figure 11.25) and have high dielectric constant (Figure 11.24) as well as exhibiting a frequency dependency of these parameters [16–18].

Even the way the human hand is placed to hold and operate a particular design of mobile phone handset can reduce the TRP from −4.1 dB to −11.6 dB compared to the free-space value [19]. In [20] it is shown that body-mounted antennas undergo significant channel fading during normal human activity, due primarily to the dynamic nature of the human body, but also due to multipath around the body and from scattering by the environment. Separation of the antennas' performance from the channel characteristics is difficult, but results show that for many channels, an antenna polarised normal to the body's surface gives the best path gain. Like any low-gain antenna key measurements are the radiation pattern, input impedance and efficiency; however, for many applications additional information is often required such as specific absorption rate (SAR) and body-centric propagation channel characterisation. In this text we will limit ourselves to radiation pattern, input impedance and efficiency, the latter being covered in Sections 11.3 and 11.7. SAR is the measure of the amount of microwave energy absorbed by the tissue surrounding the antenna and for human subject must meet strict national/international limits to prevent excessive cell

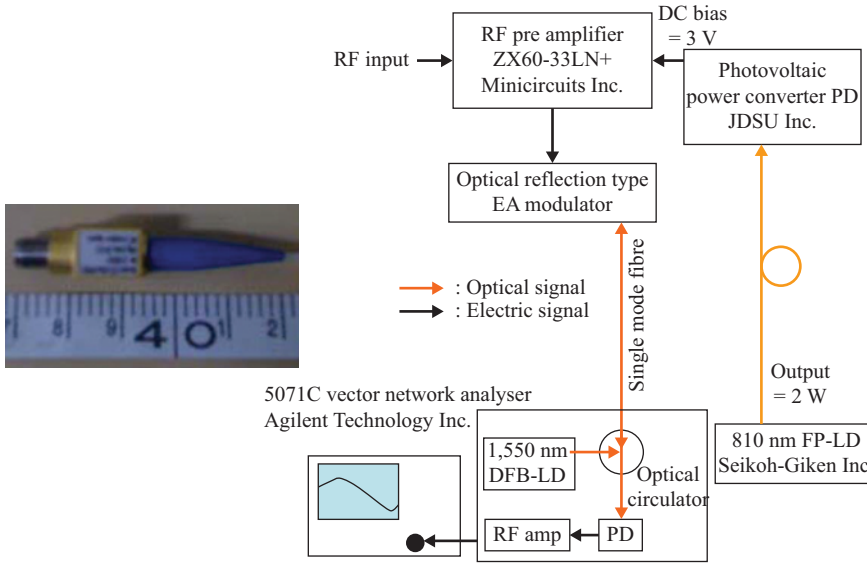

Figure 4.21 Optical fibre receive system with inbuilt RF amplifier powered by a fibre-driven photovoltaic converter. Inset picture on left shows the detector and integrated RF amplifier in a compact SMA to fibre package [14]

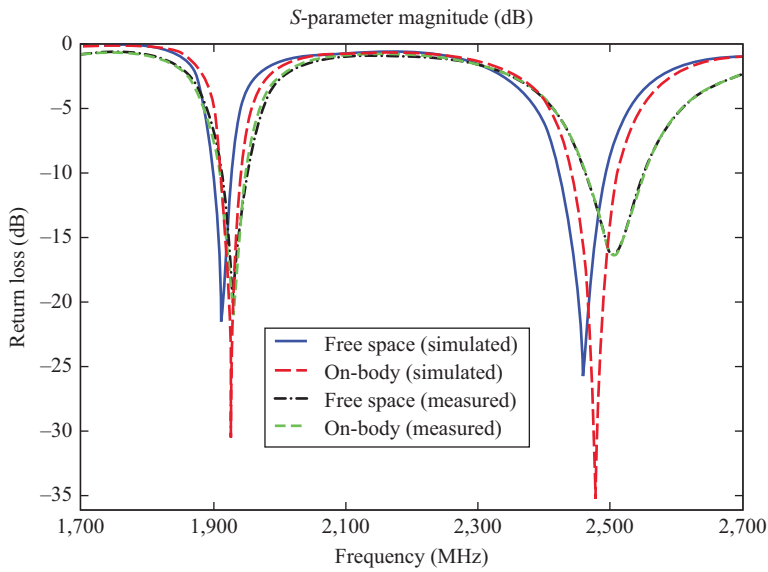

Figure 11.22 Simulated and measured free space and on-body return loss curves of a dual-band antenna [15]

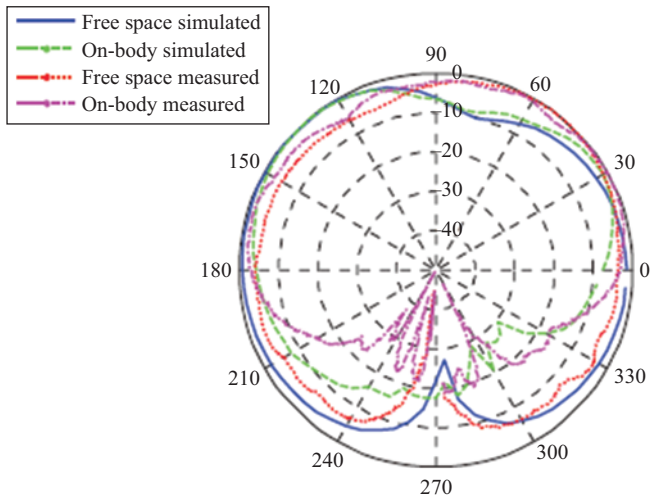

Figure 11.23 2.45 GHz simulated and measured free space and on-body radiation pattern corresponding to Figure 11.22 [15]

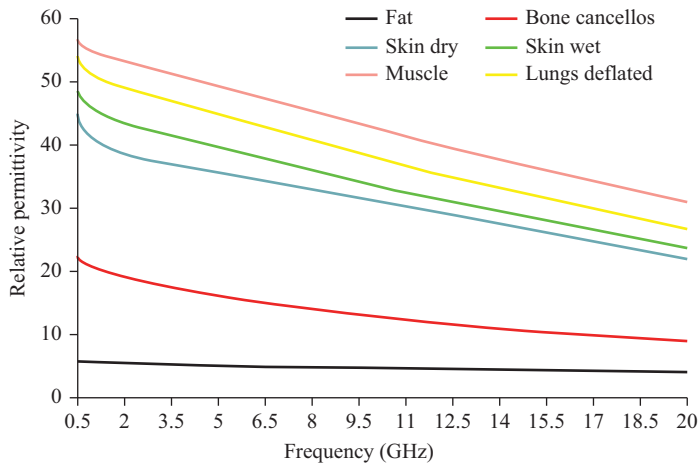

Figure 11.24 Relative permittivity of human tissue types, complied from data in [16] and [17]

heating (see e.g. [21]). There are a variety of texts on this complex subject, see, e.g., [2] for an introduction and [22] for a comprehensive text. A good introduction to the issues of the body-centric radio communications channel can be found in [20] and a comprehensive text can be found in [19].

To experimentally measure the radiation pattern and input impedance of a body-worn antenna, there are essentially two options, to use a human subject or to

use some form of phantom that replicates the complex dielectric properties and geometric shape of the human body. Whichever method is used, the effects of any cable associated with the measurement system that would not be present under normal mobile operating conditions are a significant source of error, and is an issue that has been considered in the previous section, where an optical fibre cable solution is presented. An alternative solution is to connect the AUT to an integrated circuit-based radio transceiver combined with an ultra-low power microcontroller plus battery to configure and control the transceiver chip as well as acting as a data logger for the received signal strength (RSS). Such a system is described in [23] where the 'wireless module' can be used in a variety of ways. For radiation pattern measurements of a body-mounted AUT, the module is used in transmit mode with the range antenna connected to a spectrum analyser to detect the RSS as the AUT and subject are rotated. Alternatively the range antenna can be connected to a fixed RF source and the AUT measured in receive mode with the module recording the RSS as a function of time using the microcontroller as a data logger. This can be linked with a camera or camera-based motion tracking system to record the measured signal as a human subject makes a variety of movements such as turning, sitting, walking and so on. The system can also be used to measure the RSS between two points on the human body as the subject moves around naturally. In [24] a number of wireless-based measurement nodes are used to measure the propagation channel between a number of points on the human body.

For a variety of reasons it is often difficult to operate with human subjects and so the use of phantoms is a popular option, particularly as they offer repeatability as they don't move! Phantoms aim to simulate the human body dielectric characteristics and can be classified as either 'wet' or 'dry' phantoms. Dry phantoms are often more convenient but are difficult to make with materials that model both the complex permittivity and conductivity values as illustrated in Figures 11.24 and 11.25. Wet phantoms can provide better models but are inconvenient to use and have a finite 'shelf life' of just a several weeks at most. These are often made of one material only; therefore, their physical characteristics are homogenous over the entire volume of the phantom. Since the human body is inhomogeneous, equivalent parameters have to be considered when manufacturing the phantom. Usually, a weighted average of the electrical properties of the various tissues involved in the investigation is considered [20,25]. Fully liquid phantoms are usually used in SAR measurements as the SAR probe can be placed inside the liquid (i.e. inside the body). A relatively simple liquid-filled phantom that simulates the human trunk is shown in Figure 11.26, and is constructed from Nylon 66 ($\varepsilon_r = 3.4$, $\sigma = 0.04$ S/m) with a wall thickness of 2 mm. The filling liquid used for 2.45 GHz operation to simulate human muscle tissue ($\varepsilon_r = 53.58$, $\sigma = 1.81$ S/m) was made from deionised water 79.7 per cent, sodium chloride 0.25 per cent, Triton X-100 (polyethylene glycol mono phenyl ether) 16 per cent, diethylene glycol butyl ether (DGBE) 4 per cent and boric acid 0.05 per cent [26].

Semisolid phantoms are gel based and are often more suited to antenna measurements, various recipes have been reported (e.g. [27]) mainly for use up to about 11 GHz. In [28] a semisolid phantom representing the electrical characteristics of

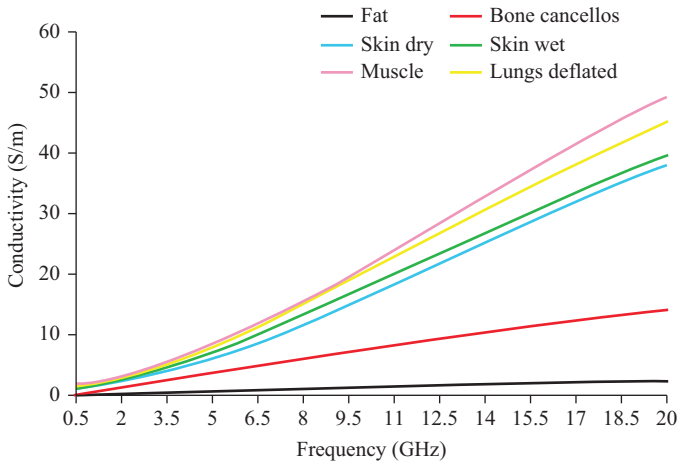

Figure 11.25 Conductivity of human tissue types, complied from data in [16] and [17]

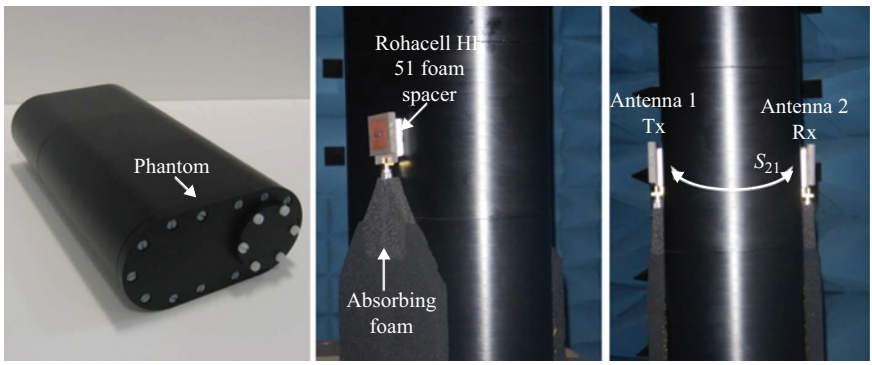

Figure 11.26 Solution-filled phantom simulating the human trunk [26] (Courtesy of Queens University Belfast)

skin between 55 and 65 GHz was reported. Various solid phantoms working at frequencies up to 6 GHz have been proposed, based on various materials including carbon fibres and silicon rubber [29,30], ceramic and graphite powder [31], and a conductive plastic [32]. Although they have longer lifespan than semisolid phantoms, they are also more expensive and require advanced and complex manufacturing processes involving extremely high pressures and temperatures.

The wavelength of operation tends to determine if it is necessary to use a whole-body phantom, or if just a head, upper torso or even hand phantom is sufficient. It is certainly possible to get useful body-mounted antenna measurement with just a small slab of phantom material mounted next to the AUT as illustrated in [33], where the importance of the size of air-gap (simulating clothing) between

the human or phantom and the AUT is also demonstrated. A good summary of the use of phantoms in mobile antenna measurement can be found in [2].

Most body-centric antenna measurement work has been undertaken in the microwave region; however, a limited amount of experimental work has been undertaken in the millimetrewave band, see e.g. [34].

11.7 Efficiency measurement using Wheeler Cap

In a low-gain-printed antenna, input power can be divided into

- Radiated power (P_{rad})
- Power dissipated in the dielectric (P_d)
- Power dissipated in the conductors (P_c)
- Power delivered to surface waves (P_{sw})

In addition, spurious power may be radiated from the feed network. The surface wave power may diffract from the substrate edges to become part of the radiation pattern of the antenna, as may the feed network radiation. These powers then become part of the radiated power, and may not show up as a loss in a measurement of efficiency.

To measure the directivity of a low-gain antenna, a far-field anechoic chamber or a spherical near-field system can be used to perform full 3D radiation pattern plots to enable the directivity to be found by pattern integration. Directivity is defined as

$$D = \frac{\text{Radiation intensity at maximum radiation pattern direction } (W/\text{unit solid angle})}{\frac{\text{Total radiated power}}{4\pi} (W/\text{unit solid angle})} \tag{11.5}$$

The efficiency of an antenna is defined as

$$\text{Radiation efficiency} = \frac{G(\theta, \phi)}{D(\theta, \phi)} \tag{11.6}$$

where $G(\theta, \phi)$ and $D(\theta, \phi)$ are the gain and directivity, respectively, in the (θ, ϕ) direction. This gain can be measured using the Friis transmission formulae directly, the three-antenna method, or the gain transfer method (see Section 5.5.2) and by definition gain includes the dissipative losses in the antenna. Hence the efficiency is a measure of these losses in the antenna. An alternative approach to efficiency measurement is to use a reverberation chamber (see Section 11.9.2).

In this section we look at measuring efficiency directly using the Wheeler Cap method, which is applicable to antennas on a ground plane. The method involves measuring the input impedance of the AUT on a ground plane, both with and without being fully enclosed by a metallic hemisphere. If the loss mechanism of the AUT can be modelled as a series resistance R_L, the effect of the cap is to short out the radiation resistance R_r allowing the resistance R_L to be separated from the total input impedance.

Figure 11.27 Wheeler Cap method for antenna efficiency measurement

The efficiency is then calculated by

$$\eta = \frac{R_1 - R_2}{R_1} = \frac{R_r}{R_r + R_L} \tag{11.7}$$

where R_1 is the real part of measured input impedance without cap; R_2 is the real part of measured input impedance with cap.

Figure 11.27 depicts the process and the method assumes that the presence of sphere does not change the current distribution on antenna, which is reasonable for electrically small antennas. The size of cap is not critical and the shape of the cap need not be spherical, cubic caps have been successfully used. Indeed measurements at 5 GHz have been successfully made using a 35 cm diameter cooking wok! Good electrical contact between ground plan and cap is essential and use of conducting tape between the cap and the ground plane is a good solution. Centring the cap over the AUT is also important [35]. The basic method works well when antennas are directly mounted on a ground plane (e.g. patch antenna) but is only valid as long as the inner losses of the AUT can be interpreted as a series resistance. Antennas of small mobile devices, however, do not use large ground planes. They are typically mounted on the top side or the back side of the mobile device, and so some revision of the basic method is required to account for this. In [36] a study of the Wheeler Cap method for mobile device antennas was undertaken and an improved formulation for calculating the efficiency was developed. This described the cap as a small ohmic resistance R_{cap}, connected via a transmission line of length L_{cap} so describing the effective electrical distance between the device and the cap. R_{cap} is typically negligible when compared to the measured resistances. However, the transformed impedance at the antenna output port can become quite large depending on L_{cap} and thus the cap to AUT distance should not be neglected. The method is based on an earlier paper by Johnston and McRory [37] where L_{cap} is varied in order to determine the effect of the cap distance on the measured S_{11} by determining ΔS_{max} and ΔS_{min} on the Smith chart (Figure 11.28) and a formulation for the efficiency becomes

$$\eta = \frac{2}{(\Delta S_{max})^{-1} + (\Delta S_{min})^{-1}} \frac{1}{1 - |S_{11}|^2} \tag{11.8}$$

where S_{11} is the value at the desired frequency of the efficiency calculation.

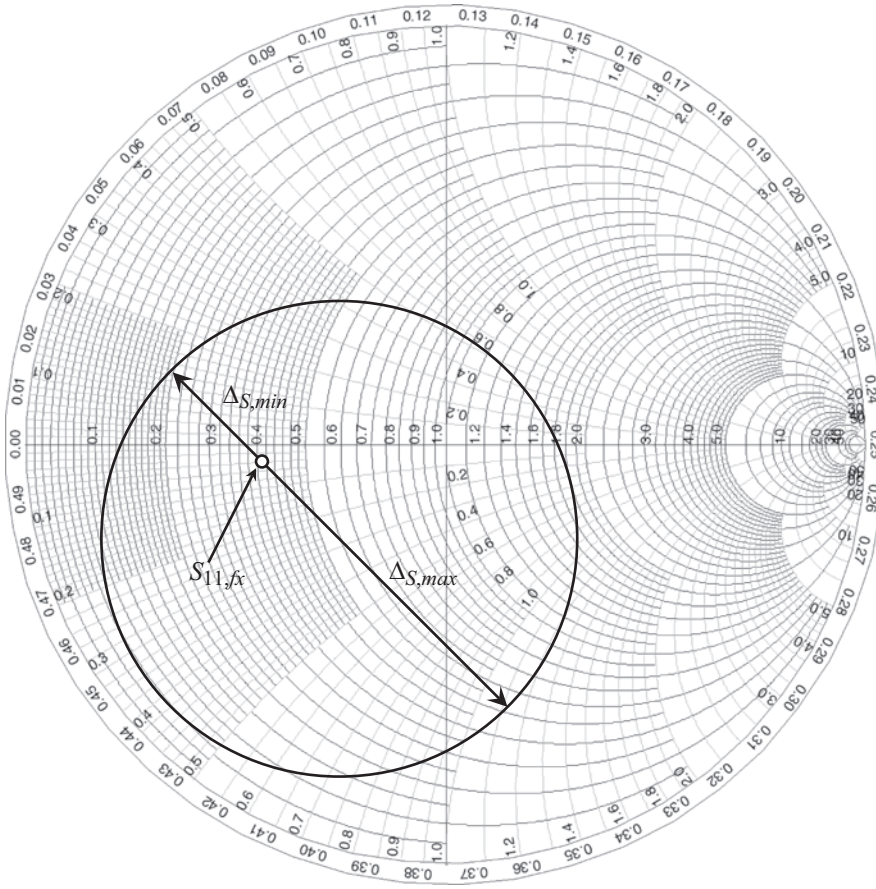

Figure 11.28 Modified Wheeler Cap formulation requiring the determination of ΔS_{max} and ΔS_{min} on the Smith chart

In the improved version of [36], the variation in L_{cap} and hence rotation round the Smith chart is achieved by frequency sweeping with a fixed L_{cap}. This method has been demonstrated successfully in [38] where this revised Wheeler Cap method has been used to calculate the efficiency of a 2.45 GHz monopole antenna mounted on a body phantom, using a cylindrical 'cap' of 200 mm diameter and height of 200 mm (Figure 11.29). Results were compared with both simulation and radiation pattern integration, both with and without the phantom 'ground plane', and these are summarised in Table 11.1, showing good agreement with the far-field pattern integration method. Note in this case the antenna had a small ground plane and so connection to this with the Wheeler Cap was not required but it was earthed to the outer conductor of the coaxial cable.

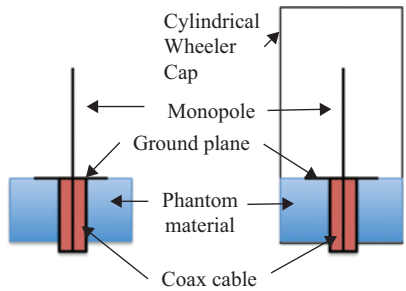

Figure 11.29 Wheeler Cap method applied to monopole antenna mounted on a body phantom (from [38])

Table 11.1 Results for Wheeler Cap method applied to Figure 11.29 [38]

	Wheeler Cap (%)	Far-field patterns (%)	Simulation (%)
Free space	92.3	91	96.70
Phantom	58	60.60	52.2

11.8 UWB antenna measurements

Ultra-wideband (UWB) technology has emerged in the past 15 years for short–range, low-power and high-data rate applications in radar sensing, locating objects and communications after the US FCC issued a ruling for its unlicensed operation in the 3.1–10.6 GHz band in 2002. With a maximum radiated power in the band restricted to −41.3 dBm/MHz effective isotropic radiated power (EIRP), narrow-band communication systems see this very low-power spectral density signal as simply noise. The agreed definition for UWB is the simultaneous radiation of an absolute bandwidth over 500 MHz or a relative bandwidth of at least 25 per cent, and there are now additional UWB bands at both 60 and 76 GHz. Numerous other countries have now also permitted UWB operation, but the spectral peak power footprints are slightly different for different regions of the world. The requirement for simultaneous usage of the frequency band limits the applicable transmit signals to (i) impulse-driven systems (impulse radio UWB, IRUWB); (ii) parallel frequency coding (orthogonal frequency division multiplexing [OFDM]); (iii) spread spectrum (direct-sequence spread spectrum [DSSS]).

In measuring the performance of UWB antennas, there are the familiar measurements we undertake for narrow-band devices such as return loss and radiation pattern, but there are also specific parameters such as *fidelity factor* and *mean gain* which relate specifically to the wideband nature of the antennas operation. Fidelity factor recognises that a UWB antenna often needs to radiate pulses with ideally

similar shape in all directions. Mean gain recognises that over such a wide band, the conventional antenna gain will change considerably over the band as the electrical size of the antenna increases from the low to high end of the frequency band. Further we look at the various AUT measurements to be made for UWB antennas.

11.8.1 Return loss

This defines the UWB antenna's bandwidth and is generally specified by the AUT's −10 dB return loss bandwidth, and an example is shown in Figure 11.30 for a miniature UWB antenna designed for motion capture applications and operating on the 5–10.6 GHz band [39].

11.8.2 Radiation pattern

As mentioned earlier the radiation pattern will change as the frequency is increased, as illustrated in Figure 11.31, so the concept of radiation pattern is somewhat redundant for UWB antennas.

There is a wide selection of texts on UWB (e.g. [40,41]) and a valuable review of UWB antennas can be found in [42].

11.8.3 UWB pseudo-time domain measurements

The successful transmission and reception of UWB pulse signals entails minimisation of ringing, spreading and distortion of the pulses in the time domain. The choice of pulse determines the bandwidth of the transmission, and a fourth-order Rayleigh pulse fits to the FCC bandwidth mask well, as shown in Figure 11.32. The pulse is described mathematically as [43].

$$f(t) = \left[\frac{12}{a^4} - \frac{48}{a^6}(t-1)^2 + \frac{16}{a^8}(t-1)^4\right] e^{-(t-1/a)^2} \tag{11.9}$$

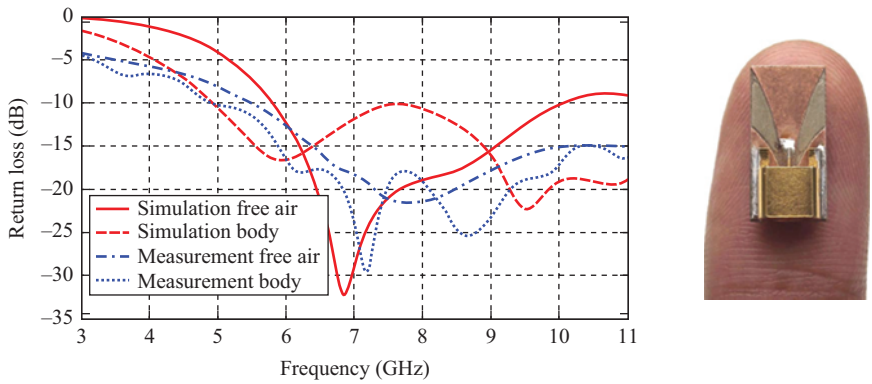

Figure 11.30 Simulated and measured return loss curves of the miniature tapered-slot UWB antenna shown on the right

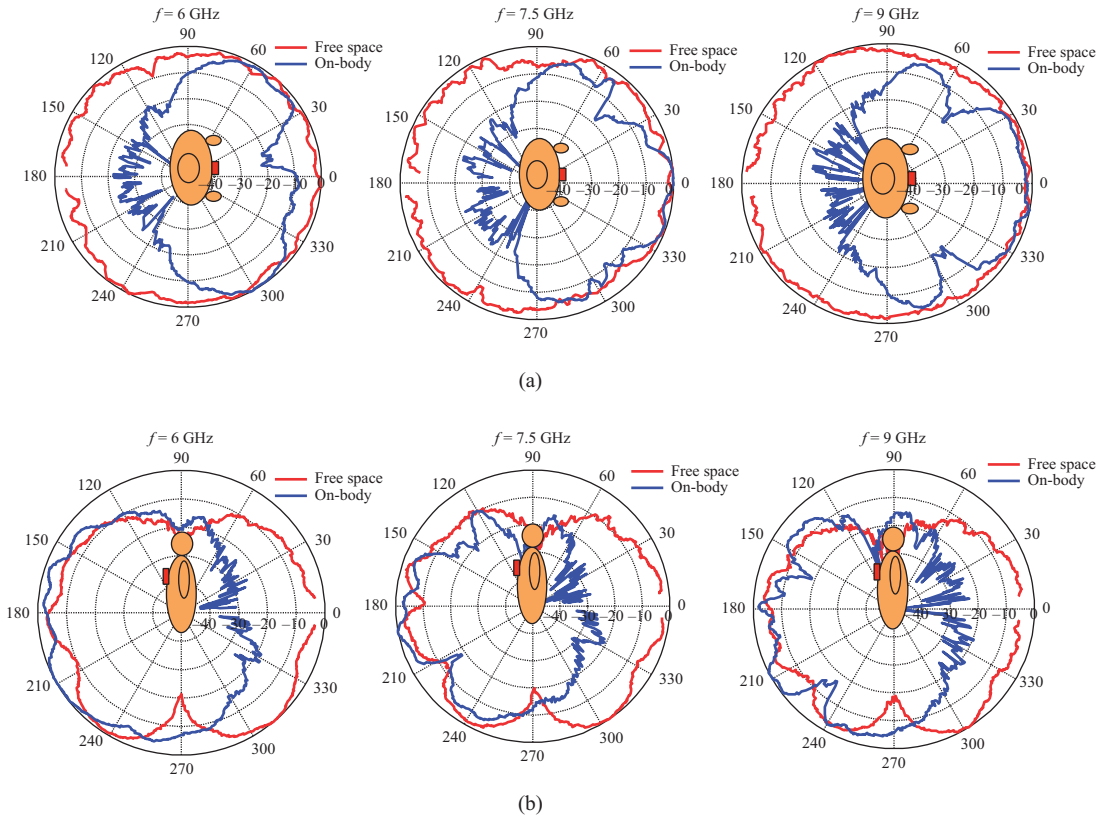

Figure 11.31 Measured free space and on-body radiation patterns of the UWB antenna shown in Figure 11.30 at 6, 7.5 and 9 GHz in (a) XY-plane, (b) YZ-plane. The radiation patterns have been normalised (maximum = 0 dB)

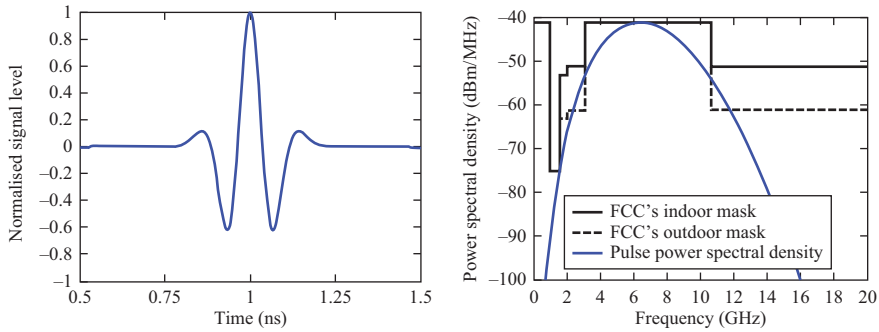

Figure 11.32 Left: fourth-order Rayleigh pulse with $a = 70$ ps; right: power spectral density of fourth-order Rayleigh pulse superimposed of FCC EIRP mask

It is feasible to shift the spectra of the first-order Rayleigh pulse to fully satisfy the FCC's emission limits by using a continuous sine wave carrier if the carrier frequency and the pulse parameter are properly chosen [44]. Despite the fact that the power spectral density of the unmodulated first-order Rayleigh pulse, given by

$$f(t) = -\frac{2t}{a^2} e^{-(t/a)^2} \tag{11.10}$$

cannot completely meet the FCC's emission mask, it is widely employed in UWB systems because of its simple monocycle waveform which can be easily produced by RF circuits (see Figure 11.35). Another useful pulse shape with well-defined bandwidth is modulated Gaussian pulse

$$f(t) = \sin(2\pi f_c t) \cdot e^{-(t/a)^2} \tag{11.11}$$

which is shown in Figure 11.33, where a carrier frequency $f_c = 6$ GHz and pulse parameter $a = 350$ ps are chosen.

As an example of the measurement process two identical tapered-slot UWB antennas (antenna shown inset to Figure 11.30) are aligned in two different orientations, namely face-to-face and side-by-side to each other to form a transmission system (Figure 11.34). The distance between the two antennas is 40 cm for both the orientations. The measurements of the antenna system S_{21} is carried out by using a VNA. For this example, a first-order Rayleigh pulse with pulse parameter $a = 45$ ps is chosen, as it is a simple pulse that covers the entire UWB band of 3.1–10.6 GHz defined by the FCC (see Figure 11.35). Since the antenna system can be modelled as a linear, time-invariant system, the received signal can be calculated by convolving the input pulse and impulse response of the antenna system. To undertake this measurement, the transfer function (S_{21} magnitude together with phase) is measured using a VNA across a suitably wide frequency band, and it is firstly transformed to the time domain by performing the inverse Fourier transform (usually within the VNA). It is then convolved with the input pulse, and the

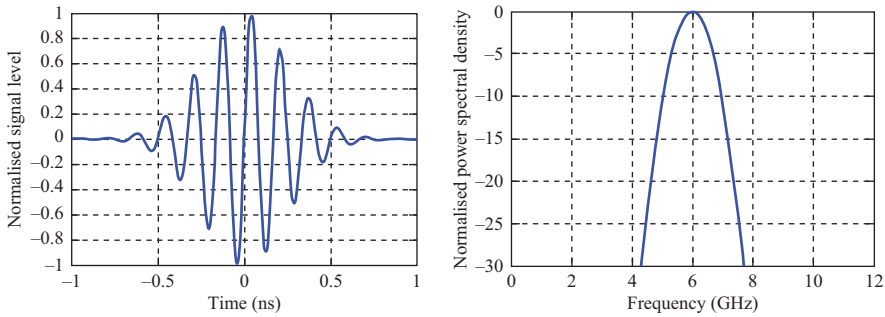

Figure 11.33 Sine-modulated Gaussian pulse (left) in time domain and its (right) power spectral density in frequency domain

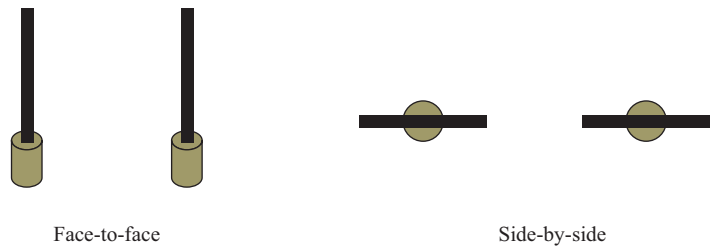

Figure 11.34 Measurement configuration of pair of identical UWB antennas

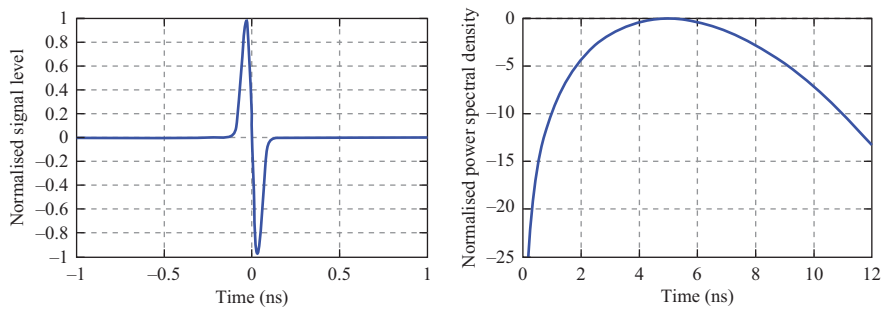

Figure 11.35 First-order Rayleigh pulse (left) in time domain and its (right) power spectral density in frequency domain

measured UWB pulse response of the wireless system is consequently obtained. Note that the *system* consists of a pair of identical transmit and receive antennas. The Hermitian processing used for this data conversion is illustrated in Figure 11.36 and described in detail in [45]. First, the pass-band signal is obtained with zero padding from the lowest frequency down to DC (direct current). Second,

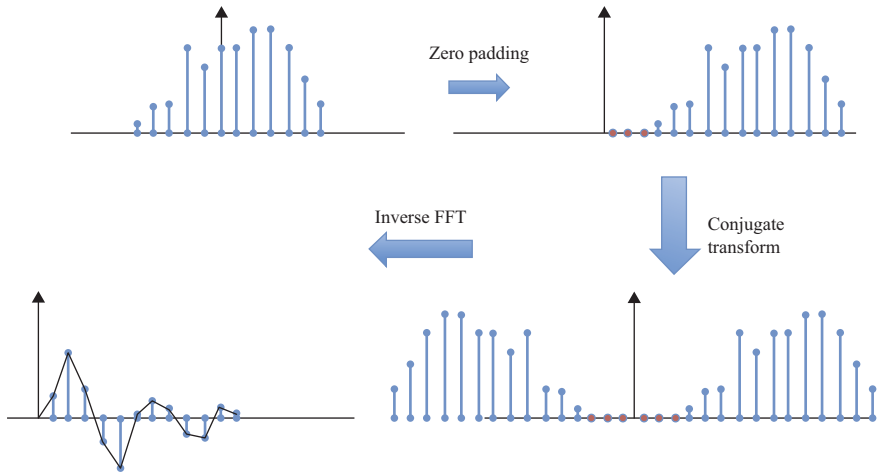

Figure 11.36 Flow diagram for Hermitian processing

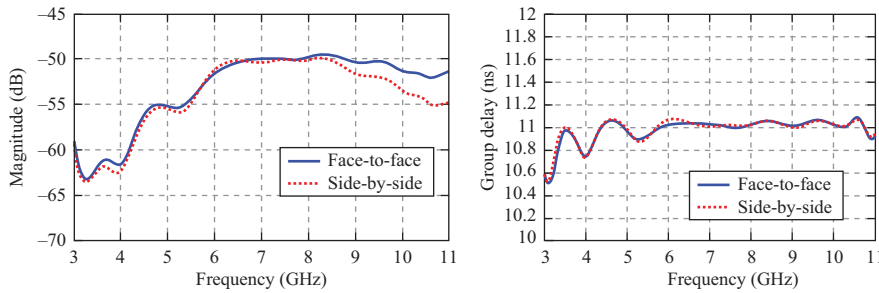

Figure 11.37 Left: measured transfer function magnitude; right: group delay for the tapered-slot UWB antenna (shown in Figure 11.26) for both antenna

the conjugate of the signal is taken and reflected in the negative frequency axis. The resulting double-sided spectrum corresponds to a real signal, i.e. the *system* impulse response. It is then transformed to the time domain using inverse fast Fourier transform (IFFT). Finally, the system impulse response is convolved with the input signal to obtain the received pulse.

The measured magnitude of the transfer function as well as the group delay for both the orientations in free space (shown in Figure 11.34) is shown in Figure 11.37. In order to have minimal distortion in the received signal, the transfer function should have a flat magnitude and linear phase response across the operating frequency band. To compute the phase response of the transfer function, group delay is commonly used, as this is now available as a direct measured output

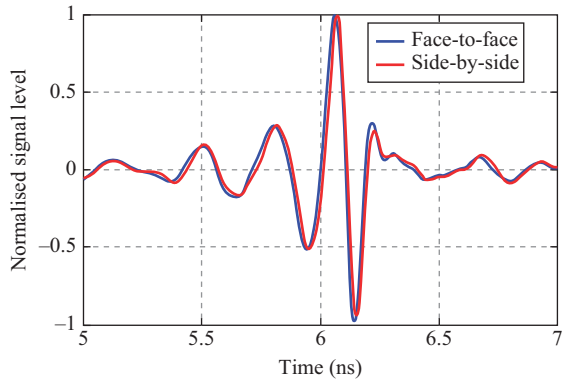

Figure 11.38 Received signal waveforms for the face-to-face and side-by-side orientation scenarios for first-order Rayleigh pulse, AUT shown in Figure 11.26

from most modern VNAs. Group delay gives the rate of change of the transmission phase angle with respect to frequency, so a constant group delay is required for a UWB antenna, which indicates a linear phase response with frequency. In Figure 11.37 the magnitude of the transfer function is relatively flat within the 6–10.6 GHz frequency range and from the group delay plot it can be seen that the phase response is almost linear across the 6–10.6 GHz frequency range. The operating band for both the measurement scenarios is nearly the same, which shows the omnidirectional characteristics of the antenna. The group delays of the two cases are quite stable with variation of less than 0.3 ns within the frequency range from 4.5 to 11 GHz, which corresponds to a linear phase response within this frequency range.

The measured received pulse is obtained by using the convolution approach mentioned earlier. A comparison between the measured received pulses for the different antenna pair orientations, namely face-to-face and side-by-side, has been plotted in Figure 11.38. It can be seen that the received waveforms for both the cases, face-to-face and side-by-side, match with each other well, indicating the omnidirectional pulse characteristics of the UWB antenna. The received pulses generally follow the shape of source pulse (Figure 11.35) but have some distortions and ringing effects. These slight distortions can be attributed to the filtering characteristics of the antenna system that acts as a band pass filter, since some of the energy of the first-order Rayleigh pulse is distributed outside the operating band of the antenna system.

11.8.4 Fidelity analysis

Since for many UWB antenna applications we wish to transmit a pulse such that it achieves minimum distortion, a quantitative measure of the similarity between the received pulse and the input pulse is a highly desirable performance measure.

Fidelity is a well-defined parameter used to evaluate the quality of a received pulse waveform. In time-domain formulation, the fidelity between waveforms $x(t)$ and $y(t)$ is generally defined as a normalised correlation coefficient [46]

$$F = \max_{\tau} \left[\frac{\int_{-\infty}^{+\infty} x(t) \cdot y(t-\tau) \cdot dt}{\sqrt{\int_{-\infty}^{+\infty} |x(t)|^2 \cdot dt \int_{-\infty}^{+\infty} |y(t)|^2 \cdot dt}} \right] \tag{11.12}$$

where the source pulse $x(t)$ and the received pulse $y(t)$ are normalised by their energy. The *fidelity factor* F is the maximum correlation coefficient of the two signals by changing the time delay τ. It denotes the similarity between the source pulse and the received pulse. When the two signal waveforms are equivalent to each other, the fidelity reaches its peak of unity. In the extreme scenario that the two pulses are totally different in shape, the fidelity reduces to the minimum value of zero. In practice, signal fidelity is calculated for a given direction in space in order to fully characterise the spatial radiation properties of an antenna. The fidelity depends not only on the antenna characteristics, but also on the excitation pulse; thus, it is also a system-dependent parameter.

As an example for the antenna shown inset to Figure 11.30, the fidelity factor was calculated for five different pulse types, both in face-to-face and side-by-side orientations (see Figure 11.34) in Table 11.2.

The highest fidelity values (Figure 11.39) are achieved for this miniature UWB antenna when the modulated Gaussian pulse is used as the source pulse (Figure 11.33). This is expected because the pulse spectrum is fully located within the band of the system transfer function, so most of frequencies are received efficiently and equally. The fidelity is greater than 0.95 even when the antennas are mounted on the human body (a finger, as shown in Figure 11.30). The fidelity factor of the antenna decreases only marginally due to the human body. There is minimal effect to the received pulse when the antenna is both in free space and on human body.

11.8.5 True time domain measurements

It is also possible to measure the time response of a UWB antenna pair directly in the time domain, as shown in Figure 11.40. In [47] both the direct measurement method and an alternative frequency domain method are compared for the same AUTs, the

Table 11.2 Calculated fidelity factor values for the miniature tapered-slot antenna

	First-order Rayleigh pulse $a = 45$ ps	**Second-order Rayleigh pulse $a = 70$ ps**	**Fourth-order Rayleigh pulse $a = 70$ ps**	**Modulated Gaussian pulse (free space) $a = 350$ ps**	**Modulated Gaussian pulse (on-body) $a = 350$ ps**
Face-to-face	0.8202	0.8832	0.9083	0.9689	0.9634
Side-by-side	0.8222	0.8765	0.9007	0.9633	0.9544

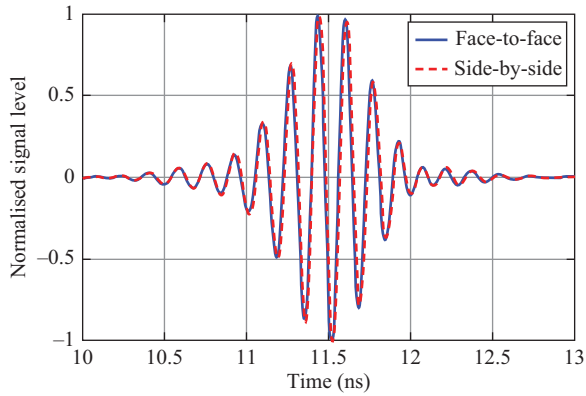

Figure 11.39 Received signal waveforms in free space for two different antenna orientations for sine-modulated Gaussian pulse input

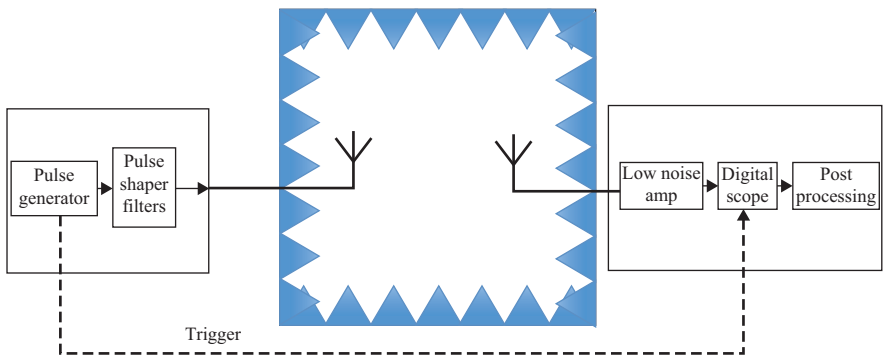

Figure 11.40 A time domain measurement system for UWB antenna pair

frequency domain measurements being obtained via the full 3D radiation pattern measurement of a single AUT in a near-field facility for frequency values contained in a band of 3.0–6.0 GHz. Results corresponding to the two antenna measurement scenario of Figure 11.40 are then calculated via a process termed *Friis Synthesis*, which uses the far-field measured radiation pattern at (θ, ϕ) across the frequency band f, $E(\theta, \phi, f)$ and the Friis transmission formulation to create a transfer function for the two antenna links, plus an IFFT. The time domain results for both direct and indirect method approaches are compared showing good agreement, so long as the limited bandwidth of the frequency domain measurement approach (3 GHz in this case) is taken into account. This is a critical point as the frequency domain result will always be to some extent a band-limited version of the channel impulse response. However, the VNA approach does offer much better sensitivity than the digital sampling scope. In [48] a UWB body-centric propagation study was undertaken using true time domain measurements using a Picosecond Pulse Labs 3500D impulse generator [49].

The key issue in this measurement method is the generation of the UWB pulse, and there are a variety of options available to achieve this, e.g.

1. *Single-chip CMOS pulse generator*: The basic concept is to combine different delayed edges using CMOS flip-flop logic circuits in order to form a very short-duration pulse, and then filter it, so as to obtain an UWB pulse. It is possible to vary the output pulse shape, and thus the corresponding spectrum by using multiple 'logic' edges, so, e.g., a pulse produced by combining four edges close together through a filter can produce something like the sine-modulated pulse of 9.30 [50].
2. *Step generator and microstrip band pass filter*: Different Gaussian pulses have been generated by sending a step pulse through various differentiating circuits (high-pass filters). The step pulse can be created on the rising edge of an input pulse train by employing a pHEMT and diode using the circuit shown in Figure 11.41 [51]. To generate an approximate Gaussian pulse shape, the same circuit was used to produce a positive step of peak amplitude 10 V and a rise time of 45 ps is sent through a high-pass filter circuit in [52].

   By sending this Gaussian pulse through subsequent differentiators, approximations to first- and second-derivative Gaussian pulses have been generated (Figure 11.42) [53].
3. *Step-recovery diodes (SRDs) plus tunable reflection transmission lines*: SRDs are promising devices for UWB pulse generation, as they are simple to design, inexpensive, and have low power consumption with relatively high-output voltage swings. In [54] a tunable narrow pico-pulse generator using a 60 ps SRD is described. Both the pulse duration and shape are electronically controllable using PIN diodes that switch in different lengths of reflection line forming the duration of the Gaussian shaped pulse (Figure 11.43). The developed pulse generator circuit has a wide adjustable pulse duration covering a 300 ps to 1 ns range and produces either monocycle or Gaussian pulses and can be reconfigured to include more complicated pulse shapes such as the polycycle signals described earlier.

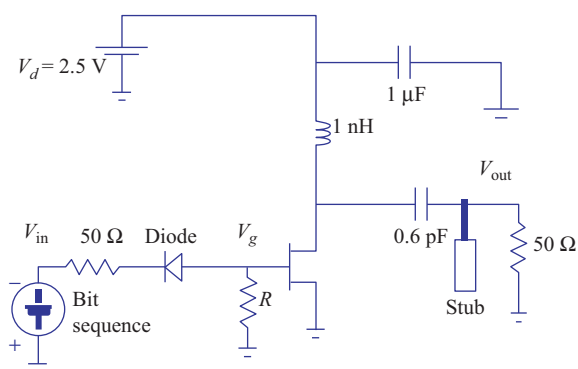

Figure 11.41 UWB pulse circuit using pHEMT and diode [51]

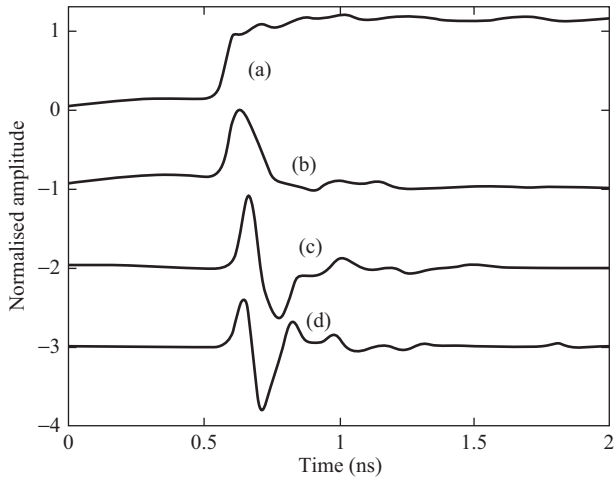

Figure 11.42 Measured Gaussian pulses obtained with the circuit based on Figure 11.41: (a) step function; (b) Gaussian pulse; (c) first-order time-derivative Gaussian pulse; and (d) second-order time-derivative Gaussian pulse [53]

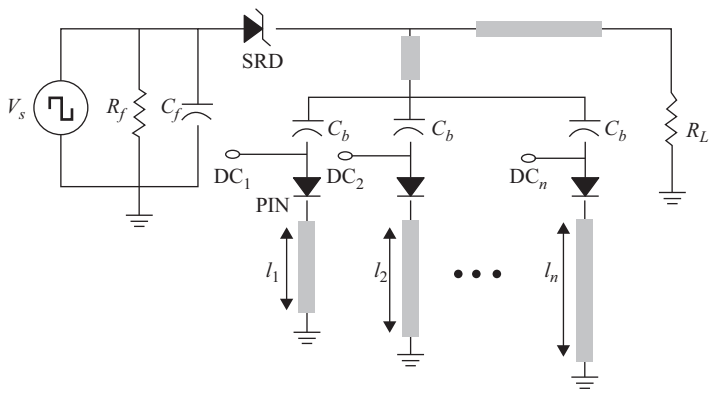

Figure 11.43 Step recovery diode pulse generator with tunable duration [54]

Commercial test instruments providing short-duration pulses with various shaping suitable for UWB applications capability are available, see e.g. [49].

11.8.6 Mean gain

The mean gain G_m is a simple quantity for the evaluation of the efficiency of the radiation properties of a broadband antenna over large frequency range with one single value. For that purpose, an arithmetical mean is used, according to

$$G_m(\theta,\phi) = \frac{1}{f_h - f_l}\int_{f_l}^{f_h} G(f,\theta,\phi)df \tag{11.13}$$

where f_l and f_h, respectively, are the low- and high-edge frequencies of the respective frequency range [42].

11.9 Special facilities

Here we look at several special facilities that can assist the measurement campaigns for mobile antennas.

11.9.1 Over-the-air multipath environment simulation for MIMO testing

In Section 11.3.1 the use of a spherical near-field chamber to undertake over-the-air (OTA) measurements for full production handsets was described. With the increasing use of multiple input multiple output (MIMO) techniques to increase link capacity in mobile communication systems, there is a related need to be able to test these multiple antenna systems in an OTA environment to ensure that parameters such as data throughput vs path loss can be measured in a realistic and controlled environment. To undertake this test, the illumination of the N antennas forming the MIMO AUT requires that the true multipath environment in a 'real-world' scenario be recreated in the test chamber. Thus each antenna element of the MIMO device under test will see signals coming from a variety of sources with low spatial correlation through varying levels of power, polarisation, Doppler shift and signal delay. Producing a near infinite number of sources, which are highly uncorrelated, can be achieved by undertaking measurements in a reverberation chamber (see Section 11.9.2) using mode stirrers plus averaging over a time related to the mode stirrer rotation. However, this significantly departs from the 'real-world' situation where a relatively small finite number of significant low-correlation signals would be practically received by the MIMO array. In [55] a circular array of near-field sources is used to simulate a given multipath environment, where the spatial channel emulator provides (Figure 11.44) signals to each array element that have a given delay, Doppler shift, amplitude and polarisation excitation of the test signal so that at the AUT the 'real-world' multipath environment can be received by each of the N antenna elements. To fully recreate the true environment would need a spherical array of many elements, so the use of a single horizontal circular array with (in this case 8 elements) is an approximation of the true environment, but has the merit that it is completely reproducible and so direct comparison of device under test performance can be made. A practical implementation of such a system is shown in Figure 11.45 where a horizontal 8-element array has been added to a spherical near-field array measurement system of the type shown in Figure 11.7.

The use of a CATR in OTA testing of MIMO 5G basestation antennas is covered in Section 5.9.

11.9.2 Reverberation chamber measurements

The reverberation chamber has become established as an accurate tool for measuring the radiation efficiency of small antennas, as well as complete mobile terminals [56]. A reverberation chamber (Figure 11.46) is a large metal cavity

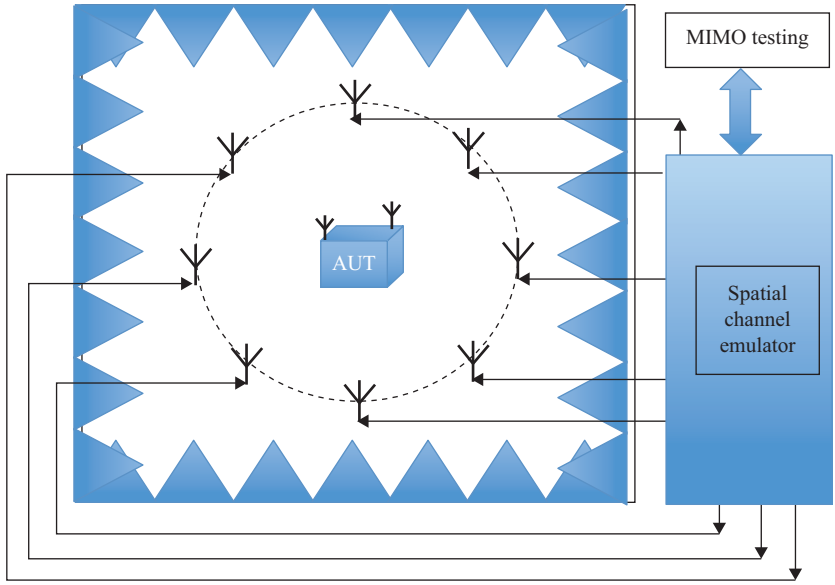

Figure 11.44 Plan view of array of antennas in an anechoic chamber used to simulate low correlation signals from different directions at the AUT

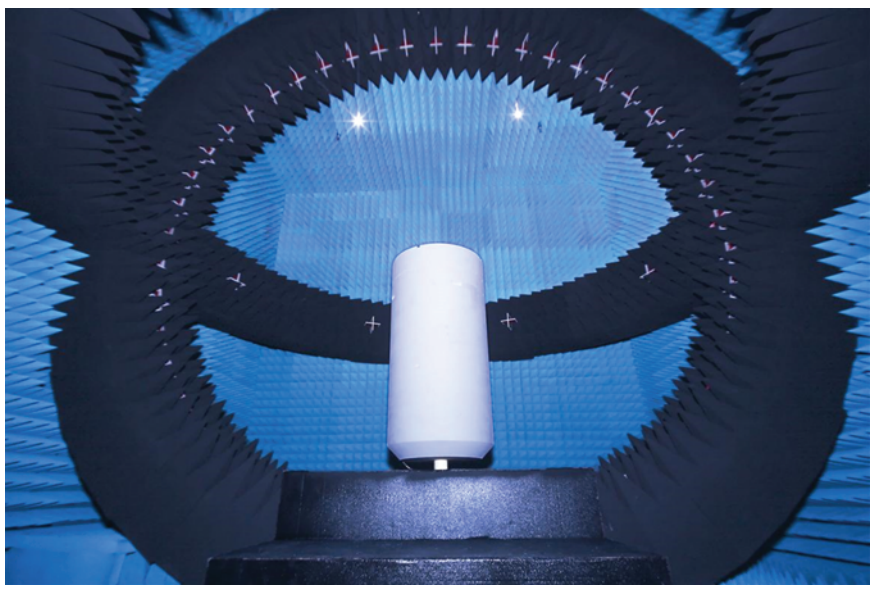

Figure 11.45 Practical realisation of concept in Figure 11.44 (Courtesy of ETS-Lindgren)

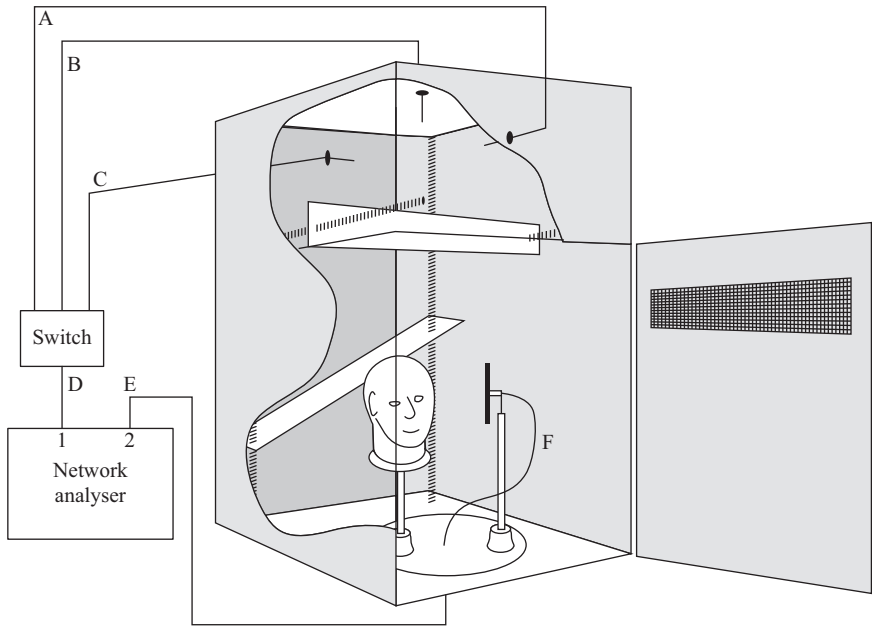

Figure 11.46 Reverberation chamber [58]

containing rotating metal plate(s) which act as mode stirrers, excitation is via switched antennas to act as polarisation stirrers and finally the frequency of operation is switched by a small amount (e.g. 25 MHz) to act as a frequency stirrer. The aim of the stirring processes is to achieve an isotropic plane-wave incident environment to the AUT. This uniform isotropic environment enables the AUT to be characterised in terms of classical antenna quantities such as radiation efficiency and TRP. In [57] a large chamber (a 2.4 m cube) was used to measure the radiation efficiency and antenna S_{11} for body-mounted antennas on both human subjects and part-body phantoms. The results for both S_{11} and radiation efficiency were compared to measurements made in a near-field facility using the same antenna plus phantom (or human) for five different antennas, and for all cases radiation efficiency losses were within 0.5 dB and excellent agreement between the S_{11} plots were demonstrated. It has been shown [58] that the reverberation chamber generates a Raleigh distribution at the AUT and so can be used to undertake over-the-air characterisation of multipath-based test devices (e.g. MIMO), such as diversity gain measurement.

References

[1] Golio M., Golio J., *RF and Microwave Passive and Active Technologies*. CRC Press; December 2007 (Chapter 9)

[2] Arai H., *Measurement of Mobile Antenna Systems*. Artech House; 2001. ISBN 1-58053-065-6

[3] Collignon G., Michel Y., Robin F., Saint J., Bolomey J., Ch. 'Quick microwave field mapping for large antennas', *Microwave Journal*. 1982;**25**(12):129–32
[4] Bolomey J.-C., Cown B.J., Fine G., *et al.*, 'Rapid near-field antenna testing via arrays of modulated scattering probes', *IEEE Transactions Antennas and Propagation*. 1988;**36**(6):804–14. doi:10.1109/8.1182
[5] Bolomey J.-C., Gardiol F.E., *Engineering Applications of the Modulated Scatterer Technique*. Artech House; 2001
[6] Iversen P.O., Garreau P., Englund K., Pasalic E., Edvardsson O., Engblom G., 'Real time spherical near field antenna test range for wireless applications', *AMTA*, 4–8 October 1999, pp. 363–8, Monterey Bay, California, Session 11
[7] Foged L.J., Duchesne L., Durand L., Herbiniere F., Gross N., 'Small antenna measurements in spherical nearfield systems', *Second European Conference on Antennas and Propagation, EuCAP*, 2007, pp. 1–4
[8] Rowell C., Lam E.Y., 'Mobile-phone antenna design', *Antennas and Propagation Magazine, IEEE*. 2012;**54**(4):14–34. doi:10.1109/MAP.2012.6309152
[9] Agilent Technologies Inc., Network Analyzer Basics, 5965-7917E, 2004
[10] Guo L., Wang S., Chen X., Parini C.G., 'A small printed quasi-self-complementary antenna for ultrawideband systems', *IEEE Antennas and Wireless Propagation Letters*, 2009;**8**:554–7
[11] Hong Loh T., Alexander M., Miller P., López Betancort A., 'Interference minimisation of antenna-to-range interface for pattern testing of electrically small antennas', *Proceedings of European Conference on Antennas and Propagation (EuCAP)*, 2010, pp. 1–5
[12] Loh T.H. 'Non-invasive measurement of electrically small ultra-wideband and smart antennas', *Antennas and Propagation Conference (LAPC)*, Loughborough, 2013, pp. 456–60. doi:10.1109/LAPC.2013.6711941
[13] Kurokawa, S., Hirose M., Komiyama K., 'Optical fiber link 1-pass 2-port antenna measurement system', *ARFTG Conference*, 2006, pp. 246–50. doi:10.1109/ARFTG.2006.4734395
[14] Kurokawa S., Ameya M., Hirose M., Hayashi D., Arata S., 'Optical fiber link antenna and EMI measurement system using optical biased devises', *European Conference on Antennas and Propagation (EUCAP)*, 2012, pp. 2158–60. doi:10.1109/EuCAP.2012.6206322
[15] Khan M.M., Abbasi Q.H., Alomainy A., Parini C., Yang H. 'Dual band and dual mode antenna for power efficient body-centric wireless communications', *IEEE International Symposium on Antennas and Propagation (APSURSI)*, 2011, pp. 396–9. doi:10.1109/APS.2011.5996727
[16] Andreuccetti D., Fossi R., Petrucci C., 'An Internet resource for the calculation of the dielectric properties of body tissues in the frequency range 10 Hz–100 GHz', IFAC-CNR, Florence (Italy), 1997. Available from http://niremf.ifac.cnr.it/tissprop/. Based on data published by Gabriel *et al.* (1996)
[17] Gabriel C., Gabriel S., 'Compilation of the dielectric properties of body tissues at rf and microwave frequencies', Internet document. Available from http://www.brooks.af.mil/AFRL/HED/hedr/reports/dielectric/home.html (authorized mirror at http://niremf.ifac.cnr.it/docs/DIELECTRIC/home.html)

[18] Sani A., 'Modeling and characterization of antennas and propagation for body-centric wireless communication', Ph.D. thesis, School of Electronic Engineering and Computer Science, Queen Mary University of London, UK, 2010

[19] Hall P.S., Hao Y., *Antennas and Propagation for Body-centric Wireless Communications*. 2nd edn. Norwood, MA: Artech House; 2012. ISBN 1608073769

[20] Hall P.S., Hao Y., Nechayev Y.I., *et al.*, 'Antennas and propagation for on-body communication systems', *IEEE Antennas and Propagation Magazine*. 2007;
49(3):41–58. doi:10.1109/MAP.2007.4293935

[21] ICNIRP Statement: 'Guidelines for limiting exposure to time-varying electric, magnetic, and electromagnetic fields (up to 300 GHz)', *Health Physics*. 2009;**97**(3):257–8. doi:10.1097/HP.0b013e3181aff9db

[22] Lin J.C., *Electromagnetic Fields in Biological Systems*. Boca Raton, FL: CRC Press; 2012. ISBN 978-1-4398-5999-5

[23] Munoz M.O., Foster R., Hao Y., 'Physiological features from an on-body radio propagation channel', *Ninth International Conference on Wearable and Implantable Body Sensor Networks (BSN)*, 2012, pp. 52–7. doi:10.1109/BSN.2012.29

[24] Cotton S.L., Scanlon W.G., 'An experimental investigation into the influence of user state and environment on fading characteristics in wireless body area networks at 2.45 GHz', *IEEE Transactions on Wireless Communications*. 2009;**8**(1):6–12. doi:10.1109/T-WC.2009.070788

[25] Kim J., Rahmat-Samii Y., 'Implanted antennas inside a human body: simulations, designs, and characterizations', *IEEE Transactions on Microwave Theory and Techniques*. 2004;**52**(8):1934–43

[26] Conway G.A., Scanlon W.G., 'Antennas for over-body-surface communication at 2.45 GHz', *IEEE Transactions on Antennas and Propagation*. 2009;**57**(4):844–55, Part: 1. doi:10.1109/TAP.2009.2014525

[27] Ito K., Furuya K., Okano Y., Hamada L., 'Development and characteristics of a biological tissue-equivalent phantom for microwaves', *Electronic Communications in Japan Part I: Communications*. 2011;**84**(4):67–77

[28] Chahat N., Zhadobov M., Alekseev S., Sauleau R., 'Broadband tissue-equivalent phantom for BAN applications at millimeter waves', *IEEE Transactions on Microwave Theory and Techniques*. 2012;**60**(7):2259–66

[29] Nikawa Y., Chino M., Kikuchi K., 'Soft and dry phantom modeling material using silicone rubber with carbon fiber', *IEEE Transactions on Microwave Theory and Techniques*. 1996;**44**(10):1949–52

[30] MCL-T website http://www.mcluk.org

[31] Kobayashi T., Nojima T., Yamada K., Uebayashi S., 'Dry phantom composed of ceramics and its applications to SAR estimation', *IEEE Transactions on Microwave Theory and Techniques*. 1993;**41**(1):136–40

[32] Chang J.T., Fanning M.W., Meaney P.M., Paulsen K.D., 'A conductive plastic for simulating biological tissue at microwave frequencies', *IEEE Transactions on Electromagnetic Compatibility*. 2000;**42**(1):76–81. doi:10.1109/15.831707

[33] Khattak M.I., Edwards R.M., Ma J., Ullah A., Panagamuwa C.J., 'A study of perturbations in linear and circular polarized antennas in close proximity to the human body and a dielectric liquid filled phantom at 1.8 GHz', *Proceedings of the fourth European Conference on Antennas and Propagation (EuCAP)*, 2010, pp. 1–4

[34] Brizzi A., Pellegrini A., Lianhong Z., Yang H., 'Statistical path-loss model for on-body communications at 94 GHz', *IEEE Transactions on Antennas and Propagation*. 2013;**61**(11):5744–53. doi:10.1109/TAP.2013.2277718

[35] Pozar D.M., Kaufman B., 'Comparison of three methods for the measurement of printed antenna efficiency', *IEEE Transactions on Antennas and Propagation*. 1988;**36**(1):136–9

[36] Geissler M., Litschke O., Heberling D., Waldow P., Wolff I., 'An improved method for measuring the radiation efficiency of mobile devices', *IEEE Antennas and Propagation Society International Symposium*. 2003;**4**:743–6. doi:10.1109/APS.2003.1220380

[37] Johnston R.H., McRory J.G., 'An improved small antenna radiation-efficiency measurement method', *IEEE Antennas and Propagation Magazine*. 1998;**40**(5):40–8. doi:10.1109/74.735964

[38] Salim T.Z., Hall P.S., 'Efficiency measurement of antennas for on-body communications', *Microwave and Optical Technology Letters*. 2006;**48** (11):2256–9

[39] Sharma M., Parini C.G., Alomainy A., 'Time domain analysis of a miniature tapered-slot UWB antenna', *International Workshop on Antenna Technology (iWAT)*, Australia, 2014

[40] Valderas D., Sancho J.I., Puente D., Ling C., Chen X., *Ultrawideband Antennas: Design and Applications*. London: Imperial College Press; 2010. ISBN 1848164912

[41] Allen B., Dohler M., Okon E., Malik W., Brown A., Edwards D., *Ultra Wideband: Antennas and Propagation for Communications, Radar and Imaging*. Chichester, UK: Wiley; 2007. ISBN 047003255

[42] Adamiuk G., Zwick T., Wiesbeck W., 'UWB antennas for communication systems', *Proceedings of the IEEE*. 2012;**100**(7):2308–2321. doi:10.1109/JPROC.2012.2188369

[43] Chen Z., Wu X., Li H., Yang N., Chia M., 'Considerations for source pulses and antennas in UWB radio systems', *IEEE Transactions on Antennas and Propagation*. 2004;**52**(7):1739–48

[44] Siwiak K., McKeown D., *Ultra-wideband Radio Technology*. Chichester, UK: John Wiley & Sons; 2004. ISBN 0470859318

[45] Oppermann I., Hamalainen M., Iinatti J., *UWB Theory and Applications*. Chichester, UK: John Wiley & Sons; 2004. ISBN 0470869178

[46] Lamensdorf D., Susman L., 'Baseband-pulse-antenna techniques', *IEEE Antennas and Propagation Magazine*. 1994;**36**:20–30. doi:10.1109/74.262629

[47] Talom F.T., Uguen B., Rudant L., Keignart J., Pintos J.-F., Chambelin P., 'Evaluation and characterization of an UWB antenna in time and frequency domains', *The 2006 IEEE 2006 International Conference on Ultra-Wideband*, 24–27 September 2006, pp. 669–73. doi:10.1109/ICU.2006.281628

[48] Chen Y., Teo J., Lai J.C.Y., Gunawan E., Low K.S., Soh C.B., Rapajic P.B., 'Cooperative communications in ultra-wideband wireless body area networks: channel modeling and system diversity analysis', *IEEE Journal on Selected Areas in Communications*. 2009;**27**(1):5–16. doi:10.1109/JSAC.2009.090102

[49] www.picosecond.com

[50] Smaini L., Tinella C., Helal D., *et al.*, 'Single-chip CMOS pulse generator for UWB systems', *Solid-State Circuits, IEEE Journal*. 2006;**41**(7):1551–61. doi:10.1109/JSSC.2006.873896

[51] Kumar M., Basu A., Koul S.K., 'Electromagnetic short pulse generation techniques', *URSI International Symposium on Electromagnetic Theory (EMTS)*, 2010, pp. 299–302. doi:10.1109/URSI-EMTS.2010.5636994

[52] Rambabu K., Tan A.E.-C., Chan K.K.-M., Chia M.Y.-W., 'Estimation of antenna effect on ultra-wideband pulse shape in transmission and reception', *IEEE Transactions on Electromagnetic Compatibility*. 2009;**51**(3):604–10, Part: 2. doi:10.1109/TEMC.2009.2023364

[53] Tan A.E.-C., Chia M.Y.-W., Chan K.K.-M., Rambabu K., 'Modeling the transient radiated and received pulses of ultra-wideband antennas', *IEEE Transactions on Antennas and Propagation*. 2013;**61**(1):338–45. doi:10.1109/TAP.2012.2215293

[54] Zhang C., Fathy A.E., 'Reconfigurable pico-pulse generator for UWB applications', *IEEE MTT-S International Microwave Symposium Digest*, 2006, pp. 407–10. doi:10.1109/MWSYM.2006.249557

[55] Foegelle M.D., 'Creating a complex multipath environment simulation in an anechoic chamber', *Microwave Journal*. 2010. Available from http://www.microwavejournal.com/articles/9872-creating-a-complex-multipath-environment-simulation-in-an-anechoic-chamber

[56] Kildal P.-S., Orlenius C., Carlsson J., Carlberg U., Karlsson K., Franzen M., 'Designing reverberation chambers for measurements of small antennas and wireless terminals: Accuracy, frequency resolution, lowest frequency of operation, loading and shielding of chamber', *Proceedings of 1st EU Conference on Antennas Propagation. (EuCAP 2006)*, Nice, France, November 2006

[57] Conway G.A., Scanlon W.G., Orlenius C., Walker C., 'In situ measurement of UHF wearable antenna radiation efficiency using a reverberation chamber', *IEEE Antennas and Wireless Propagation Letters*. 2008;**7**:271–4. doi:10.1109/LAWP.2008.920753

[58] Kildal P.-S., Chen X., Orlenius C., Franzen M., Patane C.S.L., 'Characterization of reverberation chambers for ota measurements of wireless devices: Physical formulations of channel matrix and new uncertainty formula', *IEEE Transactions on Antennas and Propagation*. 2012;**60**(8):3875–91. doi:10.1109/TAP.2012.2201125

This page intentionally left blank

Chapter 12
Advanced antenna measurement topics

12.1 Introduction

This chapter encompasses a number of disparate antenna measurement topics that do not naturally fall within the strict purview of any one of the preceding chapters. A number of these topics, such as aperture diagnostics and channel balance correction, are applicable to all forms of modern antenna range measurements. Conversely, other topics such as the sections on reflection suppression are far more intimately associated with a particular geometric implementation of a particular antenna test system. Consequently, as the topics are divided, so too are the sections within this chapter; general techniques are treated first, with measurement-specific techniques being distributed amongst the appropriate implementation sections.

12.2 Common topics

12.2.1 Probes and probe selection

Within the development of the standard planar, cylindrical, and spherical near-field theories as presented above, a significant amount of effort and ingenuity was devoted to establishing ways by which near-field measurements can be compensated for the directive properties of the measuring probe. Crucially, as was shown in Chapter 10, probe pattern characterisation uncertainties contribute fundamentally to the overall system level uncertainty budget and potentially constitute one of the largest, and most repeatable, components therein. While it is true that the behaviour of the probe is manifestly different between the respective measurement geometries, the effect remains ever present. Thus it is clear that in order to obtain reliable far-field data from practical near-field measurements, the electromagnetic properties of the probe must be known and they must be known accurately and precisely. Although the details and impact of the probe compensation formula do differ between the various near-field measurement geometries, in each case the probe pattern compensation procedure can be divided conceptually into two parts: first a probe pattern correction which is primarily due to the probe's main component pattern, and second a polarisation correction which is mainly due to probe's cross-polar component pattern. This behaviour was illustrated within Chapter 10. Thus the AUT pattern requirements for principal and cross-polar

performance will in general determine the design of probe that is most appropriate for a particular measurement application. A detailed list of desirable properties for a near-field probe is first presented in Chapter 6, Section 6.5.2, and these are only summarised here:

1. Time invariant.
2. No pattern nulls in the forward hemisphere corresponding to a low directivity.
3. Wide bandwidth.
4. Low scattering cross-section and reflection coefficient.
5. Good polarisation purity.
6. Good front to back ratio.

It is not possible to simultaneously satisfy all of these requirements with a single device (as some of these properties are mutually exclusive); however, depending upon the specific application and test system concerned, certain choices can be prioritised thereby guiding the selection of a particular probe. It is worth noting that the effect that a probe has on a particular near-field measurement can be minimised by utilising a probe with a pattern that approximates that of a Hertzian dipole, i.e. a linearly polarised infinitesimal current element. This observation is equally valid for planar, cylindrical, and spherical near-field measurement cases; however the use of such a low directive gain probe antenna increases the susceptibility of the measurement to the egregious effects of noise as the RF link budget is largely compromised by the excessively low probe gain, and therefore also by the lack of immunity to indirect, scattered, fields.

Thus far, it has been assumed that only relative measurements are taken, that is to say without reference to an absolute gain standard. If however absolute gain measurements are needed then, as will be shown in Section 12.6.2.1, the gain of the probe is also needed, but only if a direct connection gain calibration measurement technique is used. In such cases, typically an extrapolation gain measurement technique is used to obtain the gain of the probe. More information on probe characterisation is given in Section 12.2.1.5. For other cases, only relative probe pattern data is needed and as a consequence, probe amplitude patterns are typically normalised to unity on boresight.

The remainder of this section provides an overview of the most commonly encountered near-field probes, together with a summary of the characteristics of these probes and concludes with a broad generalisation as to which types of antennas and near-field test systems they are most commonly used with.

12.2.1.1 Open-ended rectangular waveguide probes

Many different types of antennas are employed as near-field probes. However, as noted above, probably the most widely used and generally applicable probe is the open-ended rectangular waveguide (OEWG) probe. Figure 12.1 contains a picture of a typical OEWG probe that is used for microwave antenna testing.

These probes are low gain (typically in the range of 4–6 dBi across their respective frequency bands), inexpensive to fabricate, easy to mount on the measurement system, and their far-field radiation patterns can be modelled fairly

Figure 12.1 OEWG probe specifically designed for near-field measurements. Probes typically include absorber collar and chamfered aperture which are used to reduce the scattering cross-section of the probe

accurately to provide the data needed for probe correction processing using a full-wave three-dimensional computational electromagnetic modelling (CEM) modelling tool or an analytic model [1]. A comparison of measured and analytical patterns for the cardinal cuts of a WR284 OEWG probe is presented in Figures 12.2 and 12.3 together with the equivalent multipath level (EMPL [2]) at 3.9 GHz.

Here, errors within the measurement and the analytical model have been lumped together into a single-error term, plotted as a dashed black trace. The slightly higher EMPL present within the elevation cut is probably attributable to the larger field intensities that illuminate the walls of the measurement facility in this plane. The very low EMPL is encouraging as this can be used to confirm both the modelling technique and the measurement process. In general an accuracy of circa 0.15–0.4 dB over $\pm 60^\circ$ in azimuth and elevation can be achieved with this simple analytical model. Similar EMPL levels are obtained when using the CEM probe model although this offers the ability to simulate more complex probes, with this approach perhaps being best suited for research and development projects where calibrated far-field pattern files or predictions from full-wave solvers are not available, or for more cost-sensitive applications. For more demanding applications, recourse to a traceable standards laboratory probe pattern calibration becomes unavoidable.

As the internal dimensions are proportional to the guide wavelength, cf. Appendix 1.2, such probes can become excessively large and heavy at low frequencies, e.g. below several hundred MHz, and impractically small, delicate, and difficult to align at high frequencies, e.g. above WR03 (325 GHz). For a given OEWG probe, the useable frequency range is limited at the bottom of the band by the cut-off frequency of the fundamental TE_{10} mode, and at the top of the band by

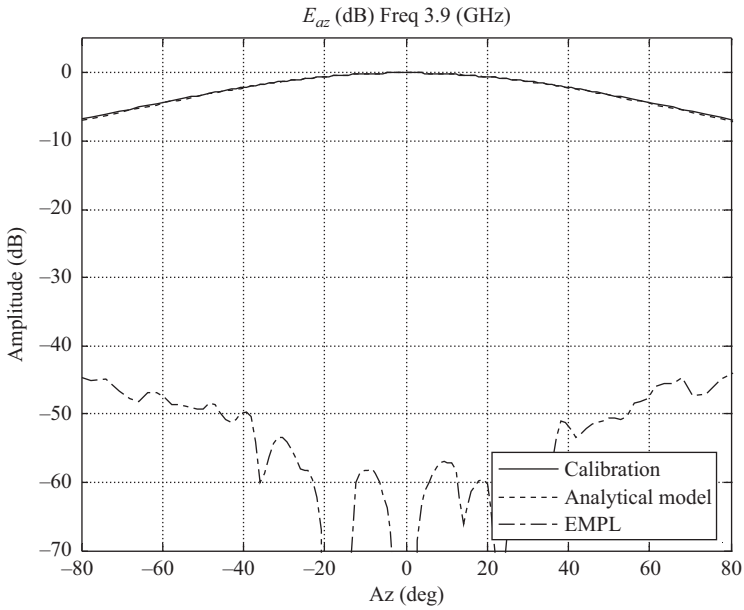

Figure 12.2 Comparison of measured and modelled co-polar probe patterns, azimuth cut

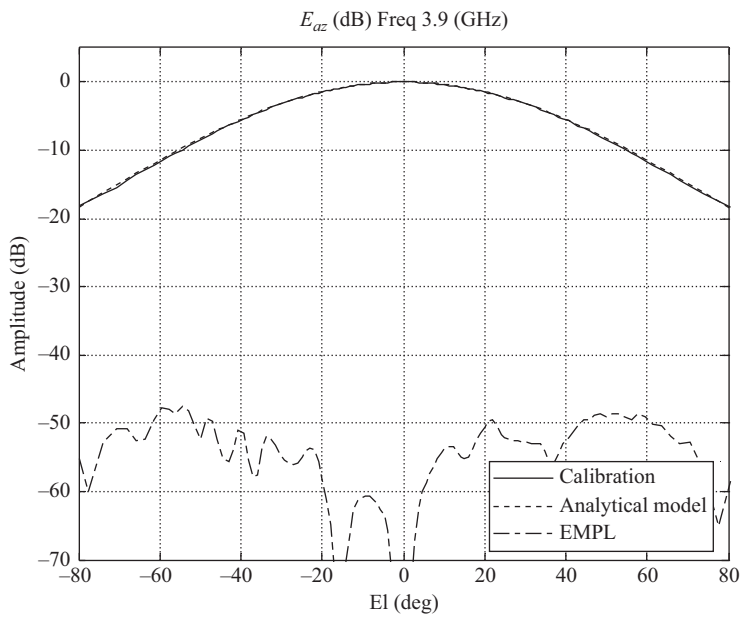

Figure 12.3 Comparison of measured and modelled co-polar probe patterns, elevation cut

the cut-on frequency of the next propagating mode for the rectangular waveguide section concerned [3]. This therefore prohibits broadband testing with only a single OEWG probe and instead a family of probes must be available if broadband testing is required. Switching probes to span a large AUT instantaneous bandwidth is one of the more significant disadvantages of these probes.

The (generally extrusion moulded) rectangular WG section and TE_{10} fundamental mode excitation result in a polarisation purity of circa 50–60 dB on boresight enabling these probes to measure many types of AUTs without recourse to sophisticated polarisation calibration and correction procedures. The single TE_{10} mode operation also means that rectangular OWEG probes are not able to simultaneously sample two orthogonal tangential near electric field components and as such are said to be 'single polarised' probes. Therefore the second polarisation is typically sampled by mechanically rotating the probe about its *z*-axis (which is at a normal to the aperture of the OEWG probe). This means that measurement times are roughly doubled when compared to those where a dual polarised probe has been utilised. This is the second most significant limitation of this probe design. As these are singularly polarised probes, this implies that the orthogonally polarised fields will be reflected at the aperture of the probe, and this can also lead to an increase in the standing wave ratio (SWR) between the AUT and the probe which, in particular, tends to compromise the accuracy of gain, and cross-polar measurements.

These probes are typically equipped with a mounting flange, coaxial to rectangular waveguide transition (for probes below 50 GHz, above 50 GHz waveguide flanges are a more commonly used interface), circular RF absorber collar, and chamfered aperture (i.e. tapered waveguide opening). Such probes are specifically designed for use with near-field test systems as the close proximity of the probe to the AUT means that mismatch in the probe increases the SWR between the AUT and the probe. The chamfered aperture and small circular RF absorber collar are commonly used design features that aim to minimise diffraction effects and the scattering cross-section of the probe. Since these probes have a very broad pattern (which is intentional by design), an absorber collar must be placed behind the probe to prevent reflections from the metal flange, the coax adapter, and mounting structures behind the probe being received by the probe. The circular profile arguably means that edge diffraction effects are spread out over a broad range of far-field directions rather than being concentrated in specific (sacrificial) directions, but these should be second-order effects. Minimising the size of the absorber collar has another, potentially more significant benefit, which is to maximise the angle of incidence of fields illuminating the edges as subtended from the aperture of the probe. In the event that the angle of illumination is too shallow, i.e. closer to a grazing angle, then the effectiveness of the absorber degrades (as the reflectivity is typically a function of incidence angle with the best match, and therefore greatest absorption, obtained close to normal incidence), that is to say larger 'absorber shadow angles' [4]. Incorrect selection of probe absorber collar size and absorber thickness can therefore significantly impact the RF performance of the probe, e.g., through the introduction of high angular frequency spurious ripple, which can

lead to errors being introduced into probe compensated measurements that are taken using these probes for which the theoretical model or calibration does not include these characteristics. Thus, if the probe is calibrated with a specific absorber configuration, the pattern may change if the collar is damaged, replaced with a different size or moved relative to the aperture of the probe. Changes to the probe pattern at wide angles would have the largest effect on planar measurements where there is a one-to-one mapping between the probe pattern and the correction to the far-field. The absorber collar could possibly affect the on-axis gain as well as the pattern of the probe. This would not produce errors for comparison gain measurements where the same probe/absorber configuration was used for both the gain standard and the AUT. But this would cause problems if the probe is used as the gain standard in a direct gain measurement and the collar had been moved or changed after it was calibrated. The potential effect on gain can be inferred from the pattern measurements by examining the pattern in the on-axis region and looking for small ripples in this region [4]. Thus extra care should be taken when handling probes and their absorber collars as generally this is the single most important piece of absorber within the test chamber.

Although rectangular OEWG probes can be used with planar and cylindrical near-field test systems, the standard spherical near-field theory (as expounded within Chapter 8) requires the use of a rotationally symmetrical, first-order, probe. That is to say a probe for which the spherical mode spectra are limited to the $\mu = \pm 1$ modes. However, as was shown in Chapter 8, although these rectangular OEWG probes do not strictly satisfy this requirement, providing the measurement radius is more than twice the MRS, then the error that this introduces into an SNF measurement is typically smaller than the other error terms within the range uncertainty budget. Thus, as these errors are small, rectangular OEWG probes are routinely used to take SNF data. This arises from noting that the pattern of the OEWG probe approximates a first-order probe sufficiently well over the angular range that is subtended by the MRS at the probe for sufficiently large range lengths. However, for very demanding applications, or for cases where test times are at a premium, the use of dual polarised circular waveguide probes is a popular choice. These probes are the subject of the next section.

12.2.1.2 Dual polarised circular waveguide probes

Circular waveguide probes are often used with spherical near-field test systems when highly accurate measurements are needed and a first-order probe is required, cf. Chapter 8. Figure 12.4 presents a picture of a typical circular choked waveguide probe which when excited by the TE_{11} waveguide mode (assuming that higher order modes introduced by the aperture discontinuity are negligible) satisfies the requirements for a first-order probe. As was the case with the rectangular OEWG probes, an absorber collar, waveguide to coaxial transform and fixturing are needed. Typically, these probes are higher gain than their rectangular OEWG counterparts with gain values of typically 10 dBi or more across the band. This implies that the design of the absorber collar is less critical (but far from unimportant) than was the case for the OEWG probe. Unlike the OEWG probe, analytic expressions

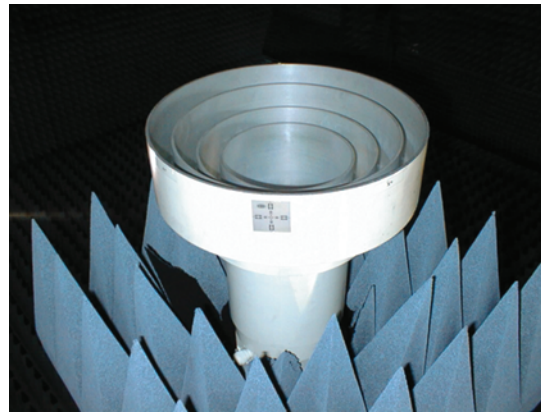

Figure 12.4 Circular choked waveguide probe. The use of chokes to improve bandwidth can increase the scattering cross-section of the probe

for the far-field pattern of these probes are less common and typically CEM predictions [5] or probe calibrations are used to correct measured near-field data.

As these probes are typically manufactured using circular waveguide, they can support two orthogonal TE_{11} waveguide modes at the same frequency and therefore offer the attractive attribute of enabling the construction of 'dual polarised' probes. These probes typically combine a choked circular waveguide section, with an orthogonal mode transducer (OMT). An OMT is in essence a mode filter (or mode duplexer) which separates the two perpendicular dominant modes in square or circular waveguide to two separate waveguide transmission lines. These waveguide sections then each have a coaxial to waveguide transformer. Thus, with the use of a two-port PIN switch, these probes can allow measurement times to be halved by taking multiplexed near-field measurements. That is to say, the E_θ and E_ϕ (or E_x and E_y) near electric field components are acquired within a single mechanical scan. A network (i.e. channel balance) correction is usually needed to compensate for the difference in electrical path length through the cabling, PIN switch and probe. Detailed information on how to determine and subsequently compensate for this is given in Section 12.2.2. This channel balance correction is usually needed as the two orthogonal waveguide ports within the OMT are at different positions along the z-axis (i.e. along the length) of the probe; thus this channel balance correction is needed even in the extremely unlikely case that the two-port PIN switch and two RF coaxial cables are perfectly amplitude and phase matched. This correction becomes especially important when testing circularly polarised[1] (CP) antennas, or when looking at cross-polar patterns. When testing CP antennas, the requisite linear polarisation to circular polarisation conversion is often accomplished within the post-processing. However, through the use of a hybrid, it is possible to implement

[1]Also more specifically right-hand circular polarisation (RHCP) and left-hand circular polarisation (LHCP).

this in hardware, whereupon circularly polarised probes can be produced. These probes also have two, typically coaxial, ports that correspond to the RHCP and LHCP polarisations. For the linearly polarised probe the ports correspond to horizontal and vertical polarisations. Although these probes have a larger physical aperture size than an equivalent rectangular OEWG probe, as the chokes improve the match, and the dual polarised nature of the device means that the cross-polarised fields are absorbed (rather than being reradiated), this results in the scattering cross-section of the probe being manageable. Figure 12.5 shows the OMT and dual coaxial ports of a choked circular waveguide probe.

The complexity, cost, and comparatively narrow bandwidth of these probes mean that they are relatively uncommon; however they are routinely used for demanding, typically aerospace, antenna test campaigns. Another benefit of the circular aperture fed by a TE_{11} mode is the lower cross-polar levels seen in the inter-cardinal axes, meaning that these probes are particularly well suited to characterising low cross-polar test antennas as they are less dependent upon the quality of the probe calibration when correcting the measured data. Here, one complete pattern calibration is needed for each port, and at each frequency which further increases the cost.

Although the rotational symmetry is not a prerequisite for planar or cylindrical testing, the aforementioned benefits mean that these probes are often used with

Figure 12.5 Picture showing back of choked circular waveguide probe showing OMT and dual coaxial ports

these test systems. The frequency band of these probes can be increased through aperture-reuse and dual band, dual polarised probes are available provided the respective WG bands are not too dissimilar in frequency [6]. Thus the increase in bandwidth is obtained through an increase in cost and complexity. An alternative class of 'frequency-independent' broadband probes are the subject of Section 12.2.1.3.

12.2.1.3 Broadband probes

Two types of commonly used broadband probes can be seen presented in Figures 12.6 and 12.7. The wide bandwidth of these probes allows replacement of several standard OEWG probes, thereby eliminating the need to change probes frequently. No probe is truly frequency-independent and the probe shown in Figure 12.6 spans the broad 750 MHz to 10 GHz bandwidth with scaled versions (and even dual polarised variations) of this design being available to cover other frequency ranges. Conversely, the dual polarised log-periodic dipole array antenna (LPDA) presented in Figure 12.7 spans the broader 500 MHz to 18 GHz band again with other scaled designs available to cover higher and lower frequencies.

In general, both of these broadband probes have too much directivity to be routinely used with planar or cylindrical test systems (circa 3–16 dBi for the dual-ridge horn, and 7–10 dBi for the LPDA); however they are better suited for use as a probe when taking spherical near-field measurements. These devices are most commonly encountered in cases where measurement speed is of greatest importance, and where uncertainty requirements can be relaxed. Or, in low-frequency applications where the excessive size and mass of corresponding waveguide probes result in there being little or no alternative. In planar measurements the probes for measuring the two polarisation components may have different patterns and therefore two probe patterns are required. One file contains the data for the

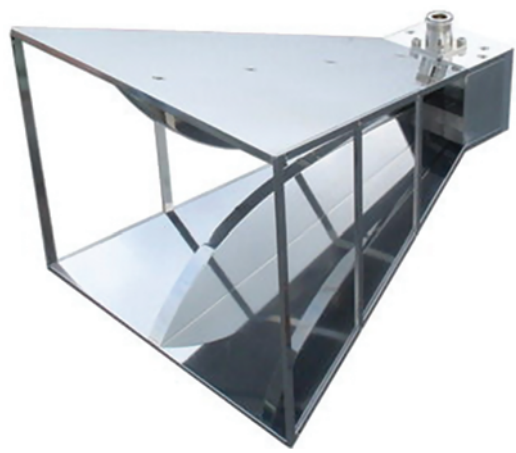

Figure 12.6 Dual-ridge broadband probe (Picture courtesy of RF-Spin)

Figure 12.7 Dual polarised log-periodic dipole array (LPDA) antenna (Picture courtesy of NSI-MI Technologies LLC)

nominally horizontally polarised probe, and the other for the nominally vertically polarised probe. This is also true for the cylindrical near-field case. However, for standard spherical near-field theory, a single linearly polarised probe is used and the standard *theory* assumes that a single probe is rotated by 90° to produce the second polarisation. Thus two complete probe patterns for two different probes are *not* allowed and so data is typically provided for a single linearly polarised probe. Thus, when using a dual-port probe (for spherical near-field testing) where each port has a unique probe pattern associated with it, differences between these respective patterns manifest themselves as additional errors in the measurement process. As probe pattern correction in spherical near-field is typically concerned with second-order effects, this is an uncertainty that can in some applications be tolerated. Transforming a single near-field measurement using each of the probe patterns in turn can provide an estimate as to the magnitude of this error term whereupon it can be incorporated into the range uncertainty budget.

Figures 12.8 and 12.9 illustrate the co-polarised and cross-polarised probe pattern for the dual-ridge horn at the bottom of its frequency band. Here, the patterns are presented as grey-scale plots where the data has been tabulated on a polar spherical coordinate system and the electric fields are resolved onto a Ludwig III polarisation basis. From inspection of these figures it is evident that the co-polar pattern is comparatively broad, as evidenced by the −3 dB contour, and the polarisation purity is good on boresight. The measured root mean square (RMS) cross-polar discrimination is −47 dB across the frequency band for this probe, which is good. However this is not the whole story as at inter-cardinal angles away from boresight, the polarisation purity is far less well behaved with the cross-polar

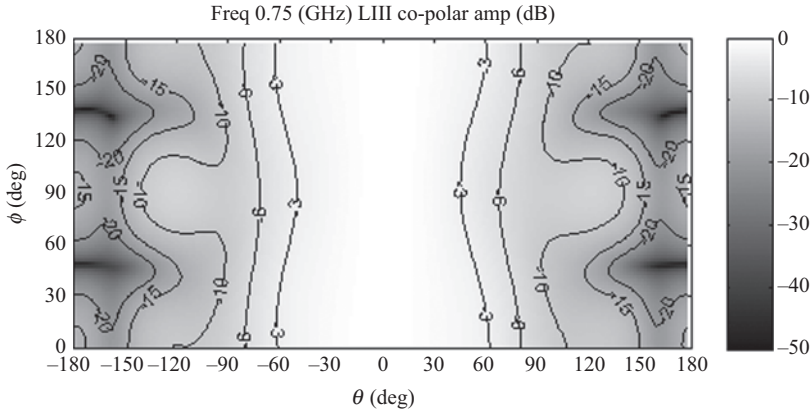

Figure 12.8 Ludwig III co-polar pattern at bottom of band

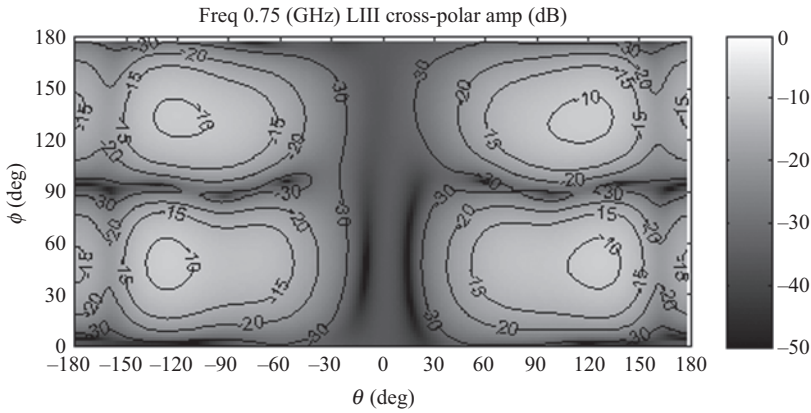

Figure 12.9 Ludwig III cross-polar pattern at bottom of band

pattern being comparable in level with the co-polar pattern in some directions. Similarly, Figures 12.10 and 12.11 contain equivalent plots for the probe at the centre of the band and Figures 12.12 and 12.13 show the results at the top of the band. Thus it is clear that the gain of the probe increases as a function of frequency with the corresponding −3 dB beamwidth progressively narrowing. Thus at the top of the band this probe is potentially too directive for many practical test applications. This is not a fault *per se* of this particular probe, but rather is an observation that can be made across this class of probes.

Also, it is worth noting that the wider the probe pattern beamwidth, the larger the aperture diameter of AUT that can be tested on a spherical system at a fixed probe-to-AUT separation, i.e. range length. As the probe pattern drops off, this corresponds to the probe becoming progressively less sensitive to fields incident

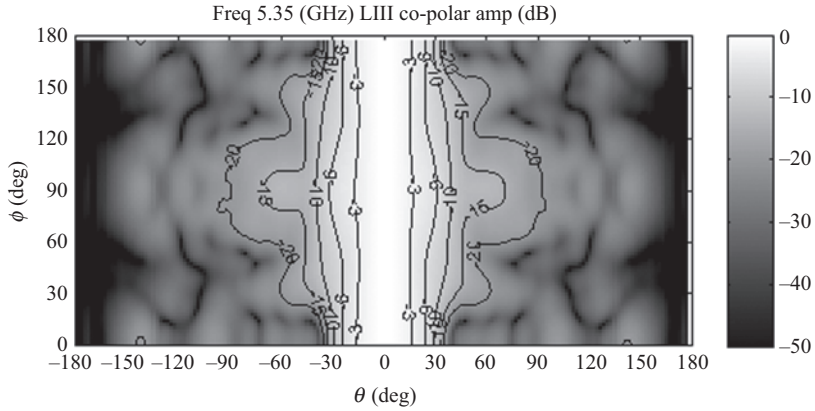

Figure 12.10 Ludwig III co-polar pattern at centre of band

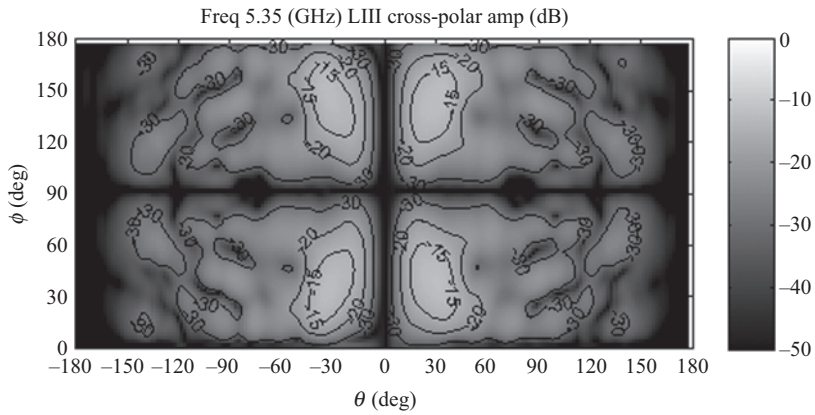

Figure 12.11 Ludwig III cross-polar pattern at centre of band

from those angles which results in excessively large correction terms being needed within the probe compensation, which can increase the measurement uncertainty.

As the pattern functions of these probes are a function of frequency and as convenient accurate analytical models are not available, if these probes are to be successfully used then measured pattern data must be available for use by the transformation software. Thus the calibration of these probes can become expensive as the frequency band is large and the number of frequency points across that band can become significant. However, there are further difficulties associated with calibrating this sort of antenna that can arise from the way in which the antenna is fabricated. Typically, this class of probe can be constructed from separate parts that are screwed or bolted together, resulting in it being susceptible to changes in the gain and pattern if the relative positions of the parts change. Thus care must be taken to guarantee the rigidity of the probe, and to minimise acceleration experienced

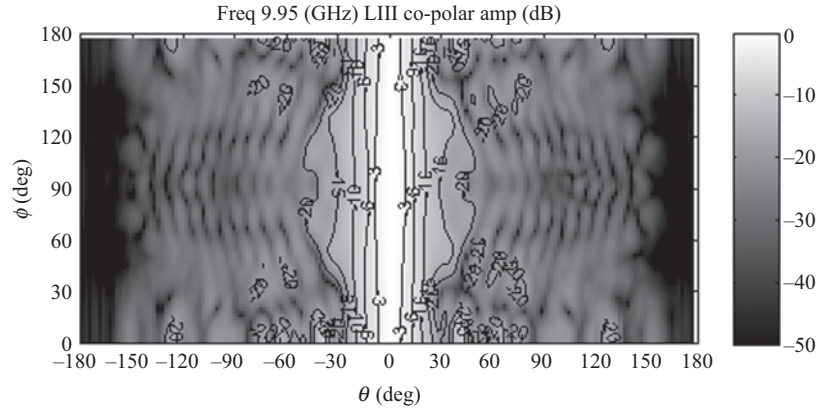

Figure 12.12 Ludwig III co-polar pattern at top of band

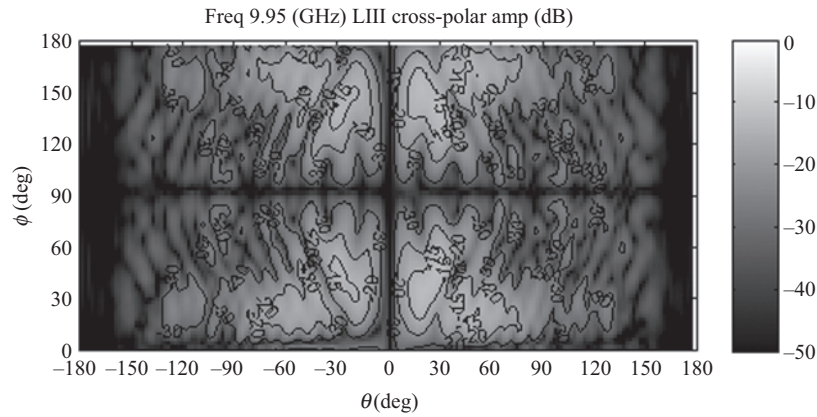

Figure 12.13 Ludwig III cross-polar pattern at top of band

during transportation or any other factors that may affect structural integrity. This is also a problem for the type of antennas like LPDA as the individual dipole elements within the array are often exposed and are therefore vulnerable to being deformed, e.g. bent, during use or while being transported. Clearly, any mechanical variation in the antenna's structure between the time when the probe was calibrated and the time when the probe is used will, to some extent at least, invalidate the precious calibration data. That being said, proper calibration of a broadband probe can largely compensate for the cross-component properties of these and other broadband probes, significantly increasing their ability to measure low-level cross-polarisation of the test antennas. More information on this is available in the open literature [7], where it was reported that a broadband LPDA probe with an axial ratio on the order of only 15–20 dB was successfully calibrated using a good polarisation standard

(e.g. open-ended waveguide probe) and its effective calibrated axial ratio was shown to be approximately 3 dB less than that of the standard. Thus, provided the aforementioned precautions are taken, broadband probes can be used in near-field measurements and produce high-accuracy polarisation results.

12.2.1.4 Far-field anechoic chamber measurements

When taking far-field measurements, the 'probe' is more commonly referred to as being a remote source antenna (RSA) or a range illuminator (RI). Whatever terminology is adopted, the meaning is the same. The choice of RI when testing in the (quasi) far-field can be determined by many factors, particularly when testing outdoors. However, outdoor far-field testing is not the subject of this text, and as such this section will concern itself purely with indoor far-field chamber measurements. CATR feeds are also omitted here as that is a separate, very specialised topic that is specifically dealt with in Chapter 5. Figure 12.14 contains a picture of a typical indoor 'far-field' test system that has been installed within an anechoic chamber.

As measurements taken in the far-field using a system such as this are assumed not to require probe pattern correction, only probe polarisation correction need be considered. As such, rectangular pyramidal horns, e.g. standard gain horns (SGHs), are often used as RIs as they have excellent polarisation purity, have a well-behaved broad pattern with a gain of between 15 and 25 dBi (depending upon the particular SGH) in order that the RF link budget is maximised. This also has the additional benefit of reducing the field intensities illuminating the walls of the chamber thereby minimising the effects of range reflections. Furthermore, SGHs are inexpensive to fabricate, and are easy to mount and align on the measurement system. Unfortunately, SGHs are limited to operating within the same waveguide bands as previously noted when using rectangular OEWG probes. Further detailed information regarding the measurement of gain using SGHs is provided in

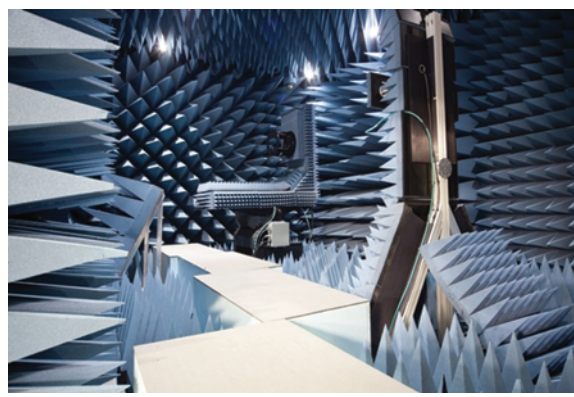

Figure 12.14 Far-field test system installed within an anechoic chamber (Picture courtesy of NSI-MI Technologies LLC)

Section 12.7.2. For low-frequency operation dual-ridge horns of the type shown in Figure 12.6 are frequently used as are log-periodic antennas shown in Figure 12.7.

12.2.1.5 Probe calibration

Probe calibration by a traceable national standards laboratory typically comprises the following measurements [8]:

1. Measurement of reflection coefficient at the port(s). Port-to-port isolation is also measured when characterising a dual-port probe. This is accomplished using a calibrated VNA.
2. Measurement of on-axis gain and polarisation (including tilt angle, axial ratio and sense of polarisation). This is often accomplished using an extrapolation range [9].
3. Measurement of relative probe far-field pattern data for each port. This is usually accomplished using a spherical far-field measurement system installed within an anechoic chamber.

Items 1 and 2 are specialised, auxiliary measurements; further details of these are left to the open literature [8,9]. It is important that the probe is fitted with metrology grade connector(s) otherwise repeatability when mating can be problematic yielding unreliable S-parameter and gain data.

To accomplish pattern probe correction, the probe used in the near-field measurement must be accurately and precisely characterised to determine its receiving pattern, as noted within item 3 above. This measurement is usually carried out on a spherical far-field range, which for the case of an electrically small probe has a range length of only a few metres. Following the measurement, the pattern data is further processed to convert it into a form that can be used by the data transformation processing chain.

Probes are typically characterised by taking far-field measurements, which is a consequence of the requirement to fully characterise the probe over the entire forward half space (and for spherical case out to wider angles) and for the need to minimise truncation effects which could disturb the pattern as a result of positioner blockage. A typical measurement arrangement is shown in Figure 7.1. Here, the benefit of the polar-mode arrangement is obvious as the blockage which results from the positioning system is placed behind the antenna in the back half space, thus minimising any truncation of the measured pattern that would otherwise result. The polar mode also results in an over-sampling of the pattern on and near boresight which is useful as it enables channel balance data to be extracted at no additional cost. Also, it is possible to scan the antenna so that its pattern is acquired twice (in the conventional and alternate spheres) to obtain a redundant dataset (as described in Chapter 8) which enables range multiple reflections to be suppressed by averaging of the measurements. The probe can be mounted so that, for the case of a waveguide probe at least, its radiating aperture is coincident with the origin of the measurement coordinate system. Thus a convenient arrangement is to define the axes such that the main beam is along the positive z-axis and the x- or y-axes are defined coincident and synonymous with the major linear polarisation axes.

This may appear to be a sensible choice when using rectangular OEWG probes; however things appear to be far less clear for the case of a non-aperture type probe, e.g. the LPDA discussed above. In that case, the active part of the antenna moves along the length of the array as a function of frequency. The resonant dipoles radiate with those longer elements behind acting as reflectors and with the smaller elements in front being parasitically coupled acting as directors. In practice when being characterised, such array antennas are generally installed within the calibration facility such that the furthest forward part of the antenna is coincident and synonymous with the origin of the spherical measurement coordinate system. Thus when the pattern data is acquired there will be a parabolic phase pattern that is superimposed on the measured probe pattern data that becomes progressively steeper at lower frequencies as the resonant dipole moves ever further away from the origin of the measurement coordinate system. However, when the LPDA probe is used to take SNF data, if the radius of the spherical near-field measurement is taken to extend from the origin of the SNF measurement coordinate system (i.e. the intersection of the θ- and ϕ-axes) to the tip of the probe then this parabolic phase function (which varies as a function of frequency and fixes the location of the active radiating element with respect to the tip of the array) ensures that the probe corrected far-field antenna data yields the correct far-field patterns. The tip of the probe is chosen as a mechanically convenient reference. However, in practice, it is possible to choose another arbitrary fiducial mechanical datum on the probe and providing the probe is characterised and then used with the SNF radius measured to the same point on the probe, then the displacement of the phase reference within the probe is correctly compensated for within the probe-compensated spherical near-field processing. If such a probe is used and calibrated probe patterns are *not* used to correct the SNF data then parallax effects, e.g., can become apparent. Further detailed information concerning probe characterisation and processing can be found in the open literature [10].

12.2.2 Channel-balance correction for antenna measurements

For the complete properties of the electromagnetic field to be determined uniquely, for near- and far-field antenna measurements, two orthogonal tangential field components must be sampled. This can be accomplished by using a linearly polarised probe with a single guided wave port and by rotating it about its axis by 90°, or alternatively by using a dual polarised probe with two orthogonal guided wave ports. An OEWG probe is an example of the former, whereas a quad-ridge open boundary horn is an example of the latter. If the reference signal is obtained by means of a directional coupler (i.e. a separate reference antenna is not utilised), with highly stable RF rotary joints employed within the guided wave path with a singularly polarised probe, then channel balance is perhaps not required for every measurement. However, if for whatever reason there is a rotary joint amplitude or phase variation, perhaps arising from thermal drift, or an imbalance between the ports within a dual polarised source antenna, or when measuring a circularly polarised antenna, etc., then in these cases a channel balance correction is required.

In most cases of interest a dual-port near-field probe is used with a pin diode switch mounted directly behind the probe. The objective of this test is to determine the amplitude and phase imbalance associated with the probe, connectors, adapters, cables, and switch ports from the common RF port at the switch to the probe aperture in order to correct for those in software. Since two orthogonal polarisations are measured and independently processed, any channel imbalance can be corrected for in the raw near- or far-field datasets as a pre-processing step. It is also important to realise that this can also be performed as an 'after the fact' correction if the network correction parameters were unknown at the time of the measurement.

To determine the probe network correction parameters, a test setup is required where the probe faces a linearly polarised antenna. An SGH is typically a good source antenna to use and the SGH and probe should be separated by several wavelengths, perhaps as many as 10–20. The latter step is a precaution to minimise the impact of probe to SGH unwanted interaction. It is further required that either the probe (most typically) or the SGH should be mounted on a rotation stage that enables rotation of the probe or SGH around the range z-axis. The intent of this rotation being pure rotation of the AUT or probe polarisation vector and that no (or very little) translation of the rotating element takes place. The SGH and probe should therefore be mounted coaxially and this condition should be maintained for the duration of the measurement. For the case of a planar facility, the source rotation aims to align the E-field vector along the x-axis of the antenna range, checking the X-port of the probe (Port 1) and then aligning the E-field vector along the y-axis and checking the Y-port of the probe (Port 2). For a spherical facility, the electric field would be aligned with the θ- and ϕ-axes. This ensures that the dual-port probe provides the same amplitude and phase data from Port 1 and Port 2. However, in some cases it is easier to rotate the near-field probe since the probe is often already mounted on a precision computer, controlled polarisation rotator. This is illustrated in Figure 12.15.

It is important to note that although what is described above will provide sufficient information for determining the network correction parameters, due to practical alignment limitations and finite measurement dynamic range, a better way to acquire the data for this test is to average the data points taken at $0°$, $-90°$, $-180°$ and $-270°$ polarisation orientation of the probe.

The above procedure is applicable to all forms of antenna measurements; however, when a polar spherical measurement system is utilised, an auxiliary channel balance measurement is not usually required as the crucial correction parameters are contained within the boresight cut and as such are sampled automatically within the pattern acquisition itself. However, when using an equatorial spherical system, cylindrical near-field system or a planar near-field system an auxiliary channel balance measurement is usually required. The subsequent section assumes that a polar spherical measurement is available, however, as this is merely equivalent to performing a polarisation cut, i.e. a χ-axis scan, the results and attendant analysis are the same.

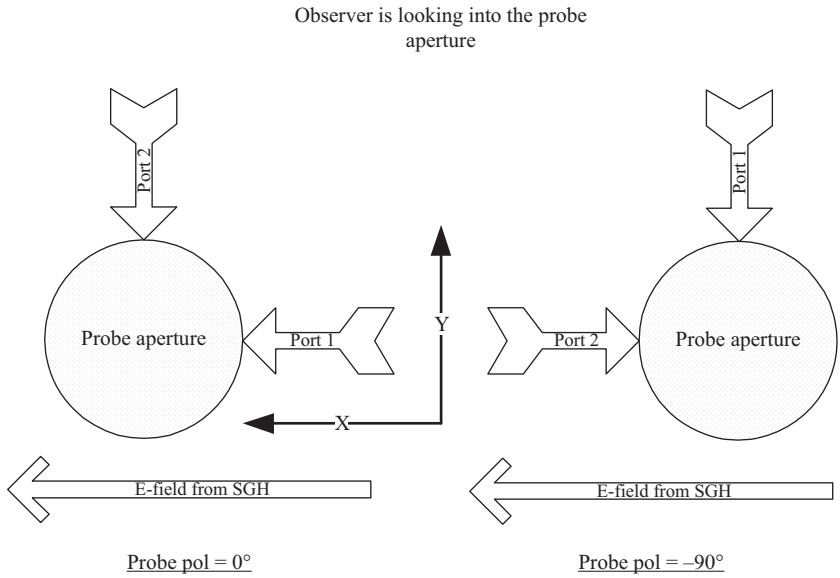

Figure 12.15 Diagram showing the probe aperture and SGH E-field vector for the probe balance measurement procedure

For a polar-pointing spherical measurement, the boresight scan (where $\theta = 0°$) involves taking ϕ_N measurements of essentially the same parameter with only a rotation of the polarisation reference. This is repeated for each orthogonal polarisation, i.e. once when the principal polarisation of the probe was aligned to the *x*-axis and again with the principal polarisation of the probe aligned with the *y*-axis (two χ values). Thus the channel balance correction factor can be determined from the difference between equivalent measurements. These techniques are described in detail in the following sections where it has been assumed that the probe is a linearly polarised antenna. When using circularly polarised probes, the correction procedure is more complex and beyond the scope of this discussion, as these instruments are expensive, typically more band-limited and are used only occasionally.

12.2.2.1 Channel balance correction for measurements of linearly polarised antennas

Figure 12.16 shows a boresight ($\theta = 0°$) ϕ cut. The channel balance correction factor can be determined from the 'weighted' mean difference between the respective cuts. Here, the weighting term is chosen to be proportional to the square of the field present in each cut, i.e. proportional to the power which is in accordance

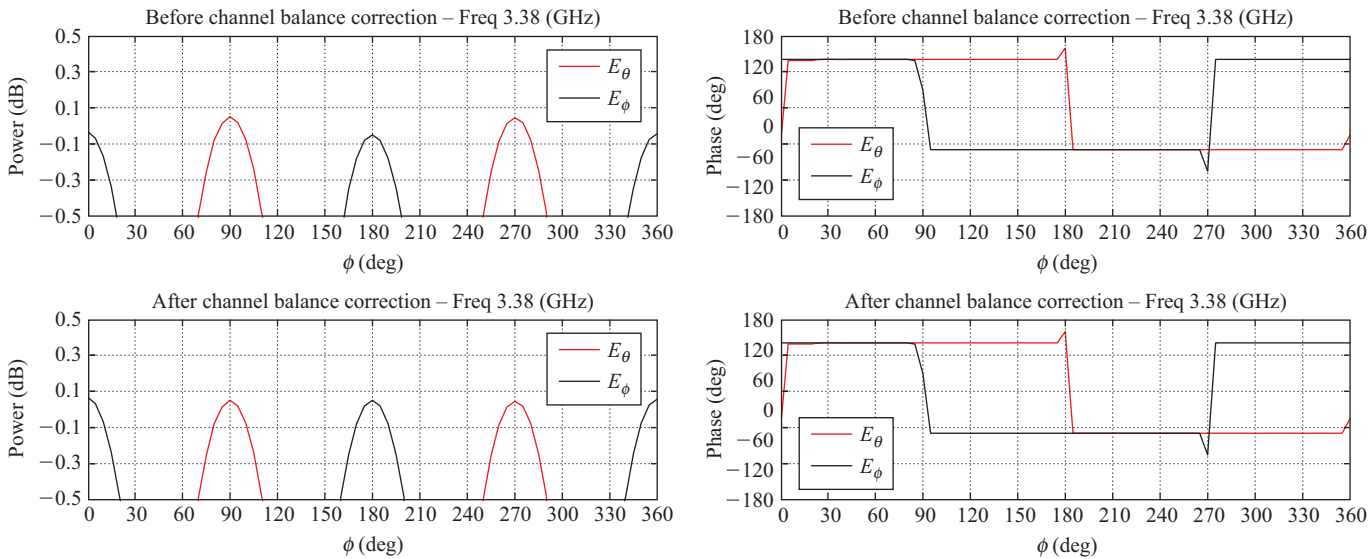

Figure 12.16 Example of channel balance correction

with the principal of least squares. The amplitude and phase channel balance correction terms can be expressed as

$$\mathrm{CB}|_{\mathrm{dB}} = \frac{\sum_{n=1}^{N}\left(E_\theta|_{\mathrm{dB}}(\phi_n) - E_\phi|_{\mathrm{dB}}\left(\phi_n + \frac{\pi}{2}\right)\right)w_n}{\sum_{n=1}^{N} w_n} \tag{12.1}$$

$$\mathrm{CB}|_{\mathrm{deg}} = \frac{\sum_{n=1}^{N}\mathrm{closest}\left(E_\theta|_{\mathrm{deg}}(\phi_n) - E_\phi|_{\mathrm{deg}}\left(\phi_n + \frac{\pi}{2}\right)\right)w_n}{\sum_{n=1}^{N} w_n} \tag{12.2}$$

Here, E_θ and E_ϕ are the signals measured at the two ports of the probe during the boresight cut with each individual cut consisting of N individual samples. The function closest 'wraps' the phases into modulo 2π. A detailed description of this function can be found in [11]. The least-squares weighting coefficient can be expressed as

$$w_n = (|E_\theta(\phi_n)| - \max(|E_\theta(\phi_n)|))\left(\left|E_\phi\left(\phi_n + \frac{\pi}{2}\right)\right| - \max\left(\left|E_\phi\left(\phi_n + \frac{\pi}{2}\right)\right|\right)\right) \tag{12.3}$$

Here, the function max returns the largest value in the cut, and is used here to normalise the peak of the respective cuts to 0 dB. This weighting coefficient is of particular importance from a practical perspective, as it protects the channel balance coefficient from being disturbed by the large phase differences that are usually encountered within the pattern nulls. The correction is applied to the polar spherical measured field components using

$$E_\phi(\theta,\phi)\,|_{\mathrm{corr}} = E_\phi(\theta,\phi)10^{(\mathrm{CB}|_{\mathrm{dB}}/20)}e^{j\mathrm{CB}|_{\mathrm{deg}}\pi/180} \tag{12.4}$$

The effect of channel balance is illustrated in Figure 12.16 which contains a boresight ϕ cut of the polar spherical measured field components before and after the correction is applied.

Figure 12.16 contains an example of a channel imbalance of approximately 0.1 dB which has been identified and subsequently corrected using the method described in this section. In this example, the channel imbalance was 0.0996 dB and 0.01009° at 3.38 GHz. Without this correction, a discontinuity is introduced on and near the boresight direction of the processed antenna pattern. Thus this error typically introduces a 'pinch' in the co-polar pattern on and near boresight, and can significantly raise, and even dominate, the level of the cross-polar pattern which is most evident in the inter-cardinal planes. This imbalance is a consequence of the singularity that is inherent within the polar-spherical polarisation basis.

12.2.2.2 Channel balance correction for measurement of circularly polarised antennas

The principle of channel balance correction is precisely the same when testing circularly polarised antennas as it is for linearly polarised antennas only in this case no weighting of the amplitude function is required as the amplitude is free from polarisation-induced trigonometric pattern nulls as shown in Figure 12.17. For the

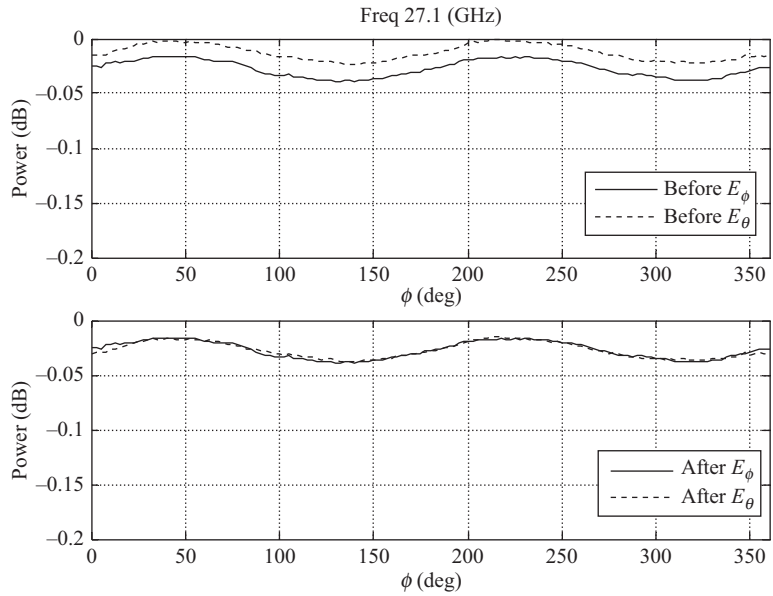

Figure 12.17 Example cuts of processed probe pattern boresight amplitude plot with and without amplitude channel balance correction

case of a CP probe, the phase dependency on boresight is linearly dependent upon the ϕ angle. This can be seen from inspection of Figure 12.18.

Here, the channel imbalance was -0.01464 dB and 1.073692°. Although this does not seem like a large amount, as the probe is CP, this will have a significant impact upon the measured cross-polar pattern. In practice, phase imbalance tends to be the more significant source of CP cross-polar pattern error. The determination of the channel balance involves the following steps:

1. Unwrap the phase in the $\theta = 0^\circ$ boresight ϕ cut by changing absolute jumps greater than or equal to π to their 2π complement.
2. Find the difference between the two phase cuts for equivalent points in the boresight ϕ cut.
3. Wrap the phase differences into the modulo 360° phase range.
4. Calculate the mean value of the wrapped differences.
5. Adjust the phase of one of the channels by the phase channel imbalance.

Amplitude channel balance values can be determined in the same way as was the case for linearly polarised probes. The analysis is somewhat simplified as the boresight amplitude function should be a constant and the average of the differences will not need to be weighted by the intensity function to protect the average from the effects of noise. Figures 12.19 and 12.20 illustrate the effects of channel balance correction on the resulting probe pattern correction files. Although the

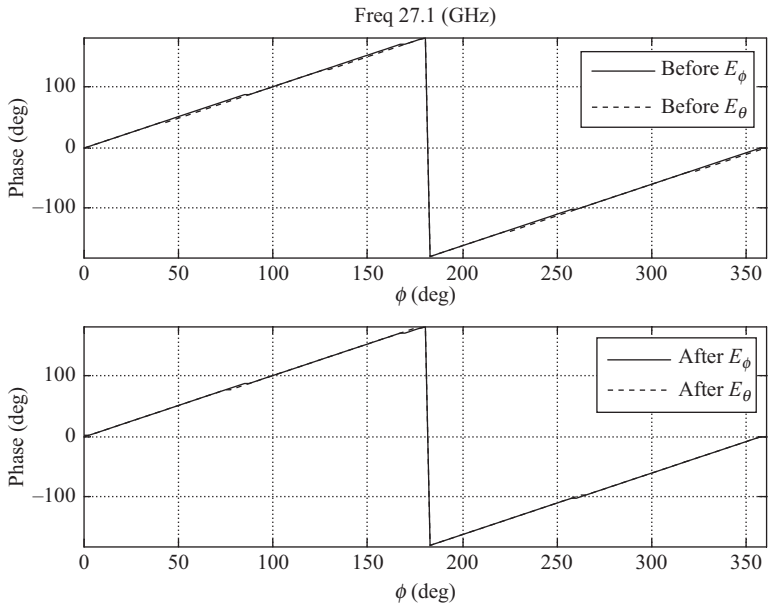

Figure 12.18 Example cuts of processed probe pattern boresight phase plot with and without phase channel balance correction

channel balance values are small, their impact is significant, particularly upon the cross-polar pattern.

12.2.3 Aperture diagnostics

The technique of microwave holographic diagnosis, i.e. the recovery of the antenna aperture illumination function, is now a well-established method of non-intrusive, non-destructive, characterisation of antenna assemblies as it can be harnessed to reveal faulty radiating elements or incorrectly adjusted transmit and receive modules within a phased array antenna, or an incorrectly aligned feed or reflector within a reflector antenna assembly. Although such diagnostic analysis is applicable to cylindrical and spherical near-field measurements, and some forms of far-field measurements, these techniques are most closely identified with the planar methodology. This is likely due to the attention that the technique has received in the open literature which has to a large extent been concerned with planar near-field test systems but perhaps also as the algorithm is most readily obtained from the plane wave spectrum (PWS) representation. Thus, in this section the analysis will commence using a PWS basis before links to other measurement geometries are established. The theoretical framework for the plane-to-plane transform has already been developed in Chapter 6. As shown earlier, knowledge of the tangential components of the electric field enables the *complete* electromagnetic six-vector to be determined *everywhere* within a half space. This, of course, enables the fields over

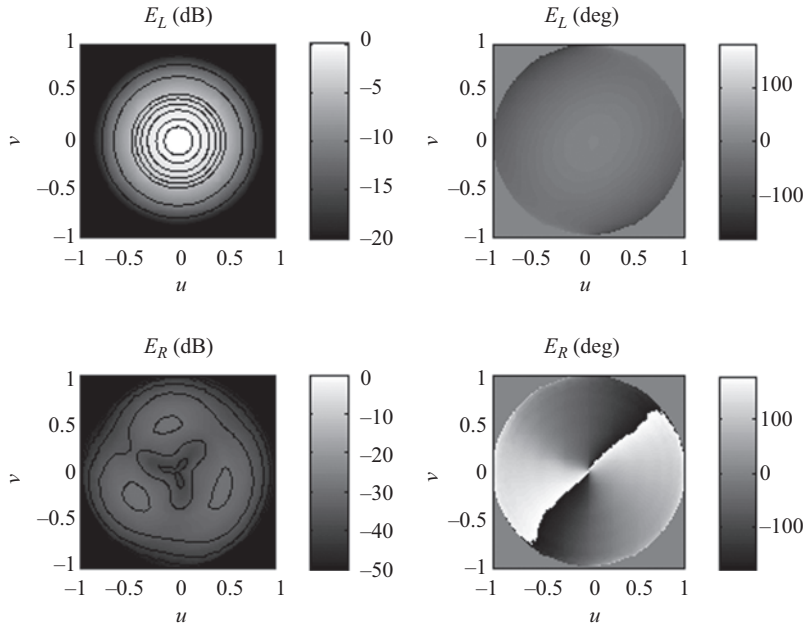

Figure 12.19 Probe patterns shown prior to channel balance correction. LHCP is shown at the top and RHCP on the bottom

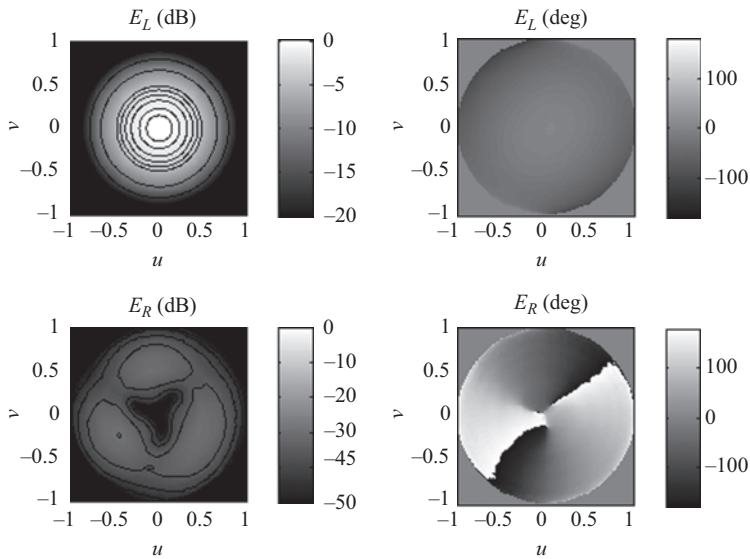

Figure 12.20 Probe pattern shown with channel balance correction applied. LHCP is shown at the top and RHCP on the bottom

one plane in space to be used to determine the field over another plane in space. The reconstruction of near-field data over a plane in space, other than the measurement plane, is accomplished by the application of a differential phase change. This can be seen to be analogous to a refocusing of the far-field image. Thus in summary, using the notation established in Chapter 6

$$F\left(k_x, k_y, z=0\right) = \int_{-\infty}^{\infty}\int_{-\infty}^{\infty} E(x,y,z=0)e^{j\left(k_x x + k_y y\right)}dx\,dy \tag{12.5}$$

and

$$E(x,y,z) = \frac{1}{4\pi^2}\int_{-\infty}^{\infty}\int_{-\infty}^{\infty} F\left(k_x, k_y, z=0\right)e^{-j\left(k_x x + k_y y + k_z z\right)}dk_x\,dk_y \tag{12.6}$$

Hence the field over one plane can be used to calculate the equivalently polarised field over the surface of another, parallel plane displaced by an amount z in the z-axis. When expressed compactly using $\Im$ operator notation, this reduces to

$$E(x,y,z) = \Im^{-1}\left\{\Im\{E(x,y,z=0)\}e^{-jk_z z}\right\} \tag{12.7}$$

This reconstructed plane can be located at any of an infinite number of planes that are in the region of space at or in front of the instrument's phase centre. However it is when the fields are reconstructed at a plane that is coincident with the AUT's 'aperture plane' that this process is of most utility. The antenna aperture can be conveniently thought of as that surface in space which represents the transition between the majority conduction current and displacement current regions defined by the presence of a charge distribution. A near-field measurement is typically constructed so that the field produced by the antenna is sampled over a region of space in which there is an absence of divergence contained within that field. Therefore, the plane-to-plane transform process results in knowledge of only the radiating components and provides no knowledge as to the stored energy component. Also, as it depends upon the solution of the Helmholtz equation in free space, this therefore cannot strictly be used to compute fields within a re-entrant surface.

To illustrate the physical interpretation of these expressions, let us consider the behaviour of the free-space Green's function, as in the limit of the far-field it behaves in a manner which is similar to that of a general far-field antenna pattern function. The free-space Green's function, which is a radial spherical mode and experiences a soft singularity when $r = 0$, can be expressed as

$$\psi = \frac{e^{-jk_0 r}}{r} \tag{12.8}$$

Clearly, as the amplitude of the free-space Green's function reduces by an amount that is inversely proportional to distance, this implies that the rate of change of amplitude with distance will tend to zero in the far-field as the distance tends to infinity. Conversely, the rate of change of the phase of the free-space Green's function is obviously independent of distance as it is a constant. Consequently, the corresponding angular spectra of two coplanar field distributions, i.e. two antenna

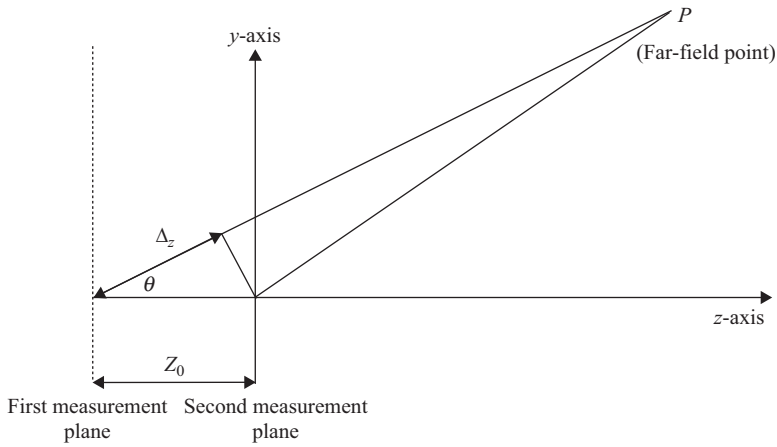

Figure 12.21 Schematic representation of plane-to-plane translation

apertures, spaced apart by a few wavelengths in z, will differ *only* by a phase factor. Displacing one plane by a distance z_0 in the z-axis will result in a change in path length of $z_0 \cos\theta$, where θ is the polar angle, i.e. that angle measured away from the positive z-axis, cf. Figure 12.21.

The free-space electrical length, i.e. the phase, is related to the physical length l by

$$\phi = k_0 l \tag{12.9}$$

where ϕ denotes the electrical length. Thus, the difference in phase between the two angular spectra will be characterised by

$$\phi = k_0 z_0 \cos\theta = k_z z_0 \tag{12.10}$$

which is in agreement with our rigorous analysis presented in the preceding chapters. By way of an example, Figure 12.22 contains the x-polarised electric near-field component that was acquired using as planar near-field test system with an antenna-to-probe separation of 3.25 λ. Diffraction effects are clearly visible in the measured near-field image.

The aperture illumination function is clearly revealed in the reconstructed amplitude plot shown in Figure 12.23. Some spectral leakage is evident and is a consequence of the finite scan plane size which is inevitable when testing with a planar near-field system. As will be shown below, this limitation can be overcome with spherical testing.

It is customary to present far-field antenna pattern functions in terms of spherical angles. Often, far-field pattern functions are tabulated as a function of the spherical angles azimuth (*az*) and elevation (*el*) rather than the polar spherical

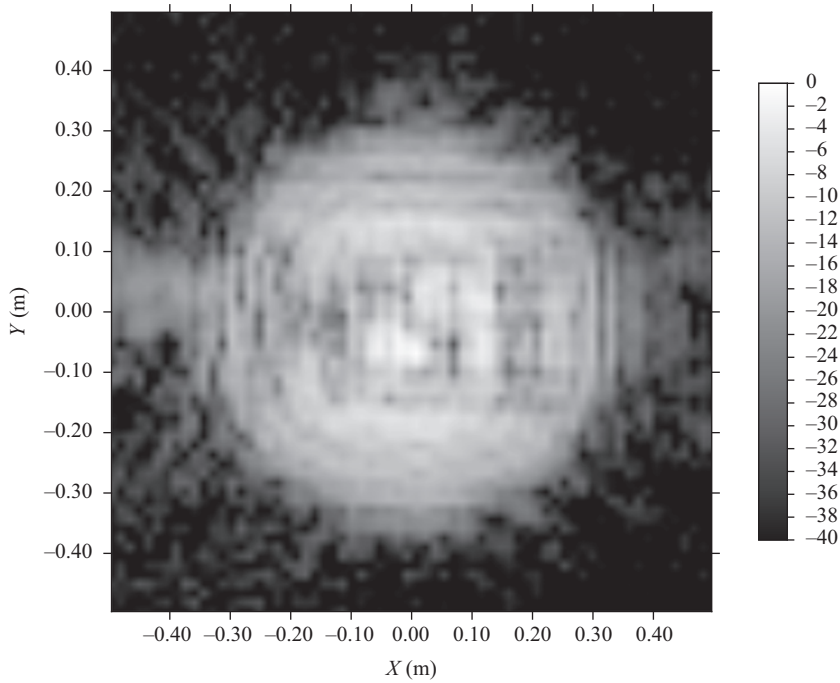

Figure 12.22 Measured near-field amplitude pattern of an X-band slotted waveguide planar array antenna (Picture courtesy of NSI-MI Technologies LLC)

angles θ and ϕ. The azimuth over elevation (*az/el*) grid can be thought of as being that grid that is most closely related to a positioner that consists of an upper azimuth rotator, to which the AUT is attached, and a lower elevation positioner upon which the azimuth rotator is mounted. As the AUT is attached to the azimuth positioner, the AUT will rotate about the azimuth axis that is therefore the polar axis. The field point is obtained by rotating the horizontal azimuth positioner and vertical elevation positioner through the angle *az* and elevation *el* where the order is unimportant. A detailed overview of coordinate systems, including the *az/el* system, can be found in the appendices. Here, it is sufficient to recall that *az* and *el* define the direction to the field point through

$$\underline{\hat{r}} = \sin(az)\cos(el)\underline{\hat{e}_x} + \sin(el)\underline{\hat{e}_y} + \cos(az)\cos(el)\underline{\hat{e}_z} \tag{12.11}$$

so that

$$az = \arctan\left(\frac{u}{w}\right) \tag{12.12}$$

$$el = \arcsin(v) \tag{12.13}$$

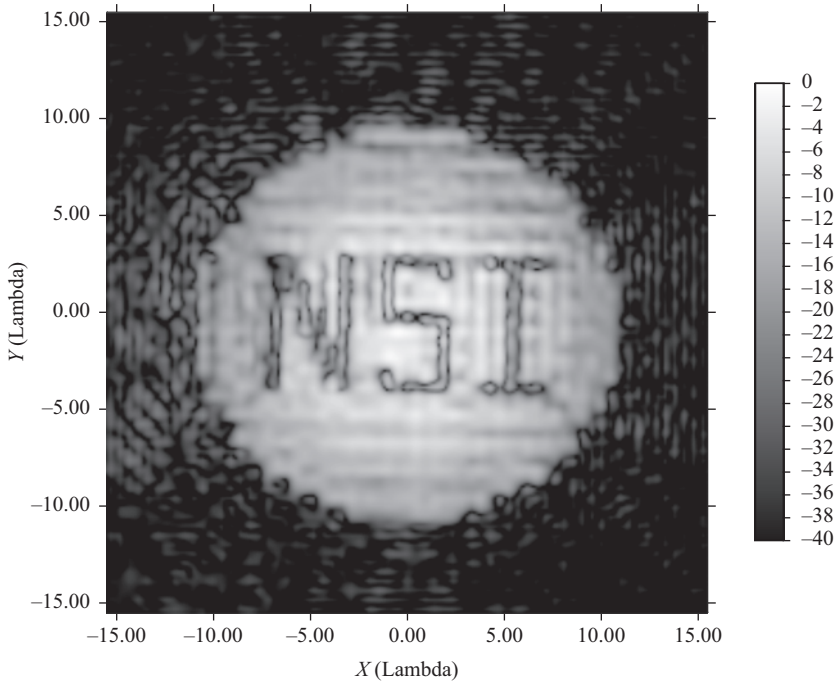

Figure 12.23 Reconstructed, probe-corrected aperture illumination function amplitude pattern of an X-band slotted waveguide planar array antenna (The letters 'NSI' visible is due to conducting tape applied to the surface of the AUT as way of demonstration) (Picture courtesy of NSI-MI Technologies LLC)

Let us assume that the far-field pattern is tabulated on a plaid monotonic equally spaced *az/el* grid. The integration required to obtain near-field parameters from far-field pattern functions must therefore be modified accordingly. As

$$\underline{E}(x,y,z) = \frac{1}{4\pi^2}\int_{-\infty}^{\infty}\int_{-\infty}^{\infty}\underline{F}\left(k_x,k_y,z=0\right)e^{-j\left(k_x x+k_y y+k_z z\right)}dk_x\,dk_y \tag{12.14}$$

Since $k_x = k_0\alpha$ and $k_y = k_0\beta$ then by differentiation we obtain

$$dk_x = \frac{2\pi}{\lambda}d\alpha \tag{12.15}$$

$$dk_y = \frac{2\pi}{\lambda}d\beta \tag{12.16}$$

Then

$$\underline{E}(x,y,z) = \frac{1}{\lambda^2}\int_{-\infty}^{\infty}\int_{-\infty}^{\infty}\underline{F}(\alpha,\beta)e^{-jk_0(\alpha x+\beta y+\gamma z)}d\alpha\,d\beta \tag{12.17}$$

As usual, the limits of integration can collapse to the visible region where $\alpha^2 + \beta^2 \leq 1$ without loss of generality as no reactive fields were sampled during the near-field measurement. The application of the change of variable formula for double integrals can be applied to the Fourier transform of the boundary conditions so that all quantities can be rewritten in terms of the angular spectrum. Using the initial boundary condition specified in a regular azimuth and elevation coordinate system where the transformation between direction cosine and azimuth and elevation angles could be expressed as (cf. Chapter 4 above):

$$\alpha = \sin(az)\cos(el) \tag{12.18}$$

$$\beta = \sin(el) \tag{12.19}$$

$$\gamma = \cos(az)\cos(el) \tag{12.20}$$

Thus

$$\underline{E}(x,y,z=0) = \frac{1}{\lambda^2}\int_{-\infty}^{\infty}\int_{-\infty}^{\infty}\underline{F}(\sin(az)\cos(el),\sin(el)) \times e^{-jk(\sin(az)\cos(el)x+\sin(el)y)}\left|\frac{\partial(\alpha,\beta)}{\partial(az,el)}\right| daz\, del \tag{12.21}$$

where

$$\left|\frac{\partial(\alpha,\beta)}{\partial(az,el)}\right| = \begin{vmatrix}\dfrac{\partial\alpha}{\partial az} & \dfrac{\partial\alpha}{\partial el}\\ \dfrac{\partial\beta}{\partial az} & \dfrac{\partial\beta}{\partial el}\end{vmatrix} = \frac{\partial\alpha}{\partial az}\cdot\frac{\partial\beta}{\partial el} - \frac{\partial\alpha}{\partial el}\cdot\frac{\partial\beta}{\partial az} \tag{12.22}$$

Thus

$$\frac{\partial\alpha}{\partial az} = \frac{\partial}{\partial az}(\sin(az)\cos(el)) = \cos(az)\cos(el) \tag{12.23}$$

$$\frac{\partial\beta}{\partial el} = \frac{\partial}{\partial el}(\sin(el)) = \cos(el) \tag{12.24}$$

$$\frac{\partial\alpha}{\partial el} = \frac{\partial}{\partial el}(\sin(az)\cos(el)) = -\sin(az)\sin(el) \tag{12.25}$$

$$\frac{\partial\beta}{\partial az} = \frac{\partial}{\partial az}(\sin(el)) = 0 \tag{12.26}$$

Hence

$$\left|\frac{\partial(\alpha,\beta)}{\partial(az,el)}\right| = \cos(az)\,\cos(el)\,\cos(el) - 0 \tag{12.27}$$

so that

$$\underline{E}(x,y,z) = \frac{1}{\lambda^2}\int_{-\pi/2}^{\pi/2}\int_{-\pi/2}^{\pi/2}\underline{F}(az,el)e^{-jk(\sin(az)\cos(el)x+\sin(el)y+\cos(az)\cos(el)z)} \cos(az)\,\cos^2(el)daz\,del \tag{12.28}$$

This expression will allow the determination of the propagating near-field, on a planar surface from far-field data that has been tabulated on the surface of a sphere, using an azimuth over elevation positioner system, i.e. the basis of spherical microwave holographic metrology (MHM). Crucially, this development enables MHM to be performed rigorously without the need to interpolate antenna patterns onto a regular direction cosine coordinate system. When implemented numerically, the integration is separable if the azimuth integral is evaluated first, as alpha is a function of azimuth and elevation whereas beta is a function of elevation only. When the range of azimuth and elevation angles represents a full sphere, this formula is required to be applied separately for the forward and backward half spaces. A similar procedure can be used to derive similar expressions for the case where the far-field pattern has been tabulated on a regular spherical grid. Here the direction cosines are related to the polar spherical angles through

$$\alpha = \sin\theta\cos\phi \tag{12.29}$$

$$\beta = \sin\theta\sin\phi \tag{12.30}$$

$$\gamma = \cos\theta \tag{12.31}$$

so that

$$\frac{\partial\alpha}{\partial\theta} = \frac{\partial}{\partial\theta}(\sin\theta\cos\phi) = \cos\theta\cos\phi \tag{12.32}$$

$$\frac{\partial\alpha}{\partial\phi} = \frac{\partial}{\partial\phi}(\sin\theta\cos\phi) = -\sin\theta\sin\phi \tag{12.33}$$

$$\frac{\partial\beta}{\partial\theta} = \frac{\partial}{\partial\theta}(\sin\theta\sin\phi) = \cos\theta\sin\phi \tag{12.34}$$

$$\frac{\partial\beta}{\partial\phi} = \frac{\partial}{\partial\phi}(\sin\theta\sin\phi) = \sin\theta\cos\phi \tag{12.35}$$

Hence

$$\left|\frac{\partial(\alpha,\beta)}{\partial(\theta,\phi)}\right| = \frac{\partial\alpha}{\partial\theta}\cdot\frac{\partial\beta}{\partial\phi} - \frac{\partial\alpha}{\partial\phi}\cdot\frac{\partial\beta}{\partial\theta}$$

$$= \cos\theta\cos\phi\sin\theta\cos\phi + \sin\theta\sin\phi\cos\theta\sin\phi \tag{12.36}$$

Or simplifying with trigonometric identities yields

$$\left|\frac{\partial(\alpha,\beta)}{\partial(\theta,\phi)}\right| = \sin\theta\cos\theta \tag{12.37}$$

Hence

$$\underline{E}(x,y,z) = \frac{1}{\lambda^2}\int_{-\pi}^{\pi}\int_{0}^{\pi/2}\underline{F}(\theta,\phi)e^{-jk_0(\alpha x+\beta y+\gamma z)}\sin\theta\cos\theta\,d\theta\,d\phi \tag{12.38}$$

Here, the limits of integration have been collapsed to denote integration over only the visible region of space. For cases where reactive fields are reliably known, that is to say typically theoretical or numerical cases, these limits can be expanded to include non-visible space where the polar angle can take on complex values. This expression is very useful. In addition to enabling microwave holography to be applied to spherical measurements, whether they are taken using a far-field range, a compact antenna test range (CATR) or a spherical range, they show how to relate the plane wave and spherical wave expansions to one another, and also show how to circumnavigate the soft singularity in the normal field component that is encountered on the $k_z = 0$ ($\theta = 90°$) circle. To illustrate this final point, the plane wave condition can be expressed as

$$\underline{k}\cdot\underline{F} = 0 \tag{12.39}$$

Thus the normal plane wave component can be expressed in terms of the tangential plane wave components as

$$F_z = -\frac{F_x\sin\theta\cos\phi + F_y\sin\theta\sin\phi}{\cos\theta} \tag{12.40}$$

and the normal near electric field component can be obtained from

$$E_z(x,y,z) = -\frac{1}{\lambda^2}\int_{-\pi}^{\pi}\int_{0}^{\pi/2}\left[\frac{F_x(\theta,\phi)\sin\theta\cos\phi + F_y(\theta,\phi)\sin\theta\sin\phi}{\cos\theta}\right.$$

$$\left.e^{-jk_0(\alpha x+\beta y+\gamma z)}\sin\theta\cos\theta\,d\theta\,d\phi\right] \tag{12.41}$$

Simplifying yields

$$E_z(x,y,z) = -\frac{1}{\lambda^2}\int_{-\pi}^{\pi}\int_{0}^{\pi/2}\left(F_x(\theta,\phi)\cos\phi + F_y(\theta,\phi)\sin\phi\right)e^{-jk_0(\alpha x+\beta y+\gamma z)}\sin^2\theta\,d\theta\,d\phi \tag{12.42}$$

Here, the soft singularity at the unit circle has been removed and the normal near-field component can be recovered without encountering a mathematically and numerically inconvenient division by zero error.

While the previous cases have considered providing the electric or magnetic fields over the surface of a plane in the near-field, in principle these expressions can be used to provide fields over an arbitrary shaped surface that does not pass into the negative half space, behind the radiating aperture. To do this, one has to abandon the efficient fast Fourier transform (FFT)-based techniques and instead harness the more flexible DFT as the z distance can become a function of the x- and y-axes coordinates such that

$$\underline{E}(x,y,z(x,y)) = \frac{1}{\lambda^2}\int_{-\infty}^{\infty}\int_{-\infty}^{\infty}\underline{F}(\alpha,\beta)e^{-jk_0(\alpha x+\beta y+\gamma z(x,y))}d\alpha\, d\beta \tag{12.43}$$

As usual, the limits of integration collapses to the visible region where $\alpha^2+\beta^2 \leq 1$. An illustration of this can be seen presented in Figure 12.24 which uses these expressions to recover the radiated field in the near vicinity of an X-band slotted waveguide planar array antenna. Here the aperture illumination function is shown together with the field as it passes through the x-z and y-z planes.

This plot contains the probe-corrected propagating power of the propagating field in the immediate vicinity of a circular array antenna, measured using a planar near-field facility. The data utilised within these figures was obtained from the generalised MHM algorithm developed within this section. For this example, the quasi far-field region was determined as beginning at a distance of circa 6 m from the origin, which lies outside the range plotted.

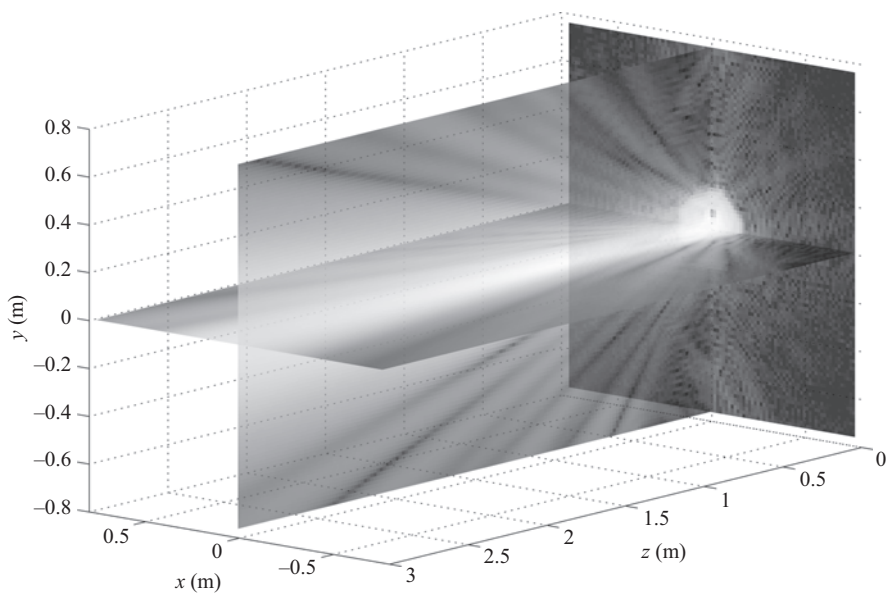

Figure 12.24 Power propagating in the near zone of an antenna

A note on semantics – sometimes writers denote the aperture illumination function as being a (or even, the) hologram. This is potentially confusing as a hologram is usually taken to mean (total recording) a quantity that contains both amplitude and phase information (i.e. total recording) and as such this is clearly not purely limited to the antenna aperture plane.

The above mathematical development shows that an aperture illumination function can be obtained from planar, cylindrical or spherical measurements. However, as spherical testing can enable an antenna to be characterised in the absence of truncation in the forward half space, as the wide-out pattern corresponds to the higher order propagating plane wave spectra, this would suggest that the best results could be obtained from spherical testing where the maximum theoretical resolution could be achieved. Planar scanning, as a result of the inevitable truncation, will result in a loss of resolution in the reconstructed near-field. The following comparison between holograms from simulated planar near-field measurements, and those of equivalent spherical near-field measurements illustrate this. The simulated configurations correspond to an effective radiating aperture of 23 (horizontal) $\times$ 21 (vertical) Hertzian dipoles. These dipoles are oriented along the x-axis. This aperture was uniformly excited, with the exception of a collection of dipoles that would produce the 'NSI' logo on the array face. Using this radiating aperture as source, the near-field was simulated on a regular planar and spherical grid, as if planar and spherical near-field measurements are acquired satisfying the respective sampling criteria.

The data presented in Figure 12.25 shows the dominant polarisation component, extracted for a horizontal cut of the holographic data at a distance of $z = 0$ for both the planar and spherical measurement simulations. Figure 12.26 shows the corresponding information, but at a distance of $z = 10\ \lambda$. These results show that a planar back projection taken from a spherical surface provides one with the ability to replicate measured data as if this were taken in the plane of interest. Slight discrepancies occur due to the finite size of the scan plane (and the associated truncation) as used for planar measurements and due to the interpolation that is performed in the intermediate steps of the conversion of spherical data to back-projected data.

12.2.3.1 Holographic diagnosis for scattering suppression

An alternative multi-path suppression technique that has been known of for many years is the aperture plane spatial filtering technique [12,13]. This technique centres upon transforming the electric fields back to the antenna aperture plane, using a conventional aperture diagnostics technique, cf. Section 12.2.3 and then truncating the electric fields outside of that aperture. This infinitely thin, two-dimensional, region of space would typically be chosen to be coincident and synonymous with the aperture plane of the AUT and be tightly constrained to that region. Thus, all the fields outside of the physical aperture of the antenna would be truncated, i.e. set to 0 V, whereupon the spatially filtered far-field pattern would be calculated in the usual way. Figures 12.27 and 12.28 contain comparisons of the horizontal and vertical cardinal cuts of a baseline unfiltered pattern, the planar-MARS filtered

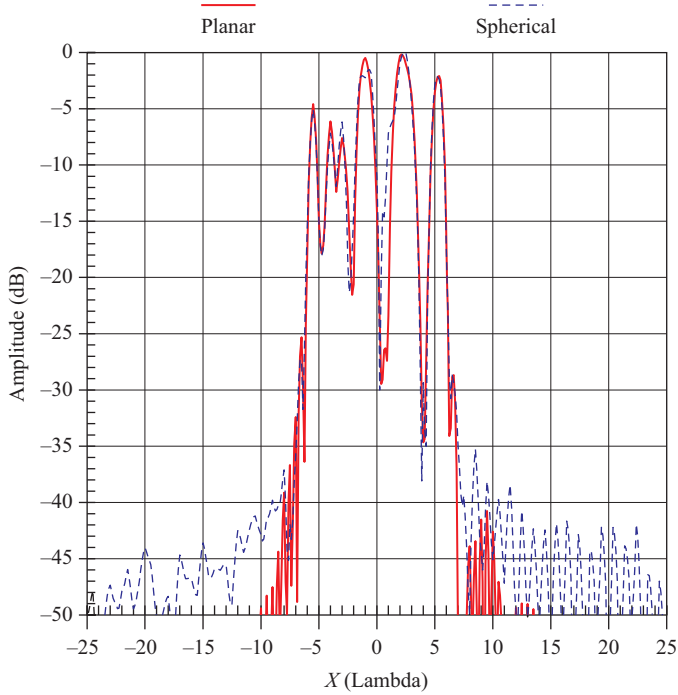

Figure 12.25 Horizontal cut comparing the holographic data (Z = 0) from planar and spherical measurement simulations

pattern, and the aperture plane spatial filtered pattern of a measurement of an X-band pyramidal horn. From inspection, it is clear that the P-MARS filtered measurement and the aperture plane filtered measurement are in encouraging agreement. However, at this point, it is worthwhile noting the differences between the respective techniques. The aperture plane spatial filtering technique requires the AUT to be an aperture-type antenna. If the antenna does not have a well-defined (i.e. tightly constrained aperture distribution that is well approximated by an infinitely thin) aperture then the effectiveness of the technique is limited or, in many cases, compromised. The pyramidal gain horn being considered here *is* an aperture-type antenna and as such constitutes an ideal candidate for this technique. However, even here, there are approximations. Any currents flowing on the exterior of the SGH will also radiate and contribute to the true far-field pattern. These will be removed from the aperture plane filtered far-field pattern thereby introducing an error. P-MARS does not impose such an aggressive filter as it effectively removes fields outside a three-dimensional volume of space that encloses the AUT. External currents such as those flowing down the exterior of a SGH, etc., are also not removed from the P-MARS filtered far-field pattern. Thus, the success of the mode filtering algorithm does *not* depend upon the AUT approximating an aperture-type

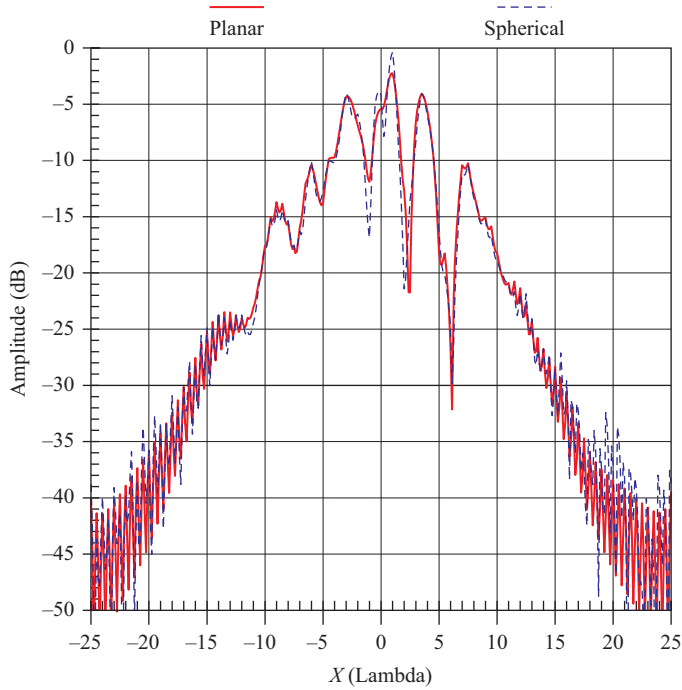

Figure 12.26 Horizontal cut comparing the holographic data (Z = 10 λ) from planar and spherical measurement simulations

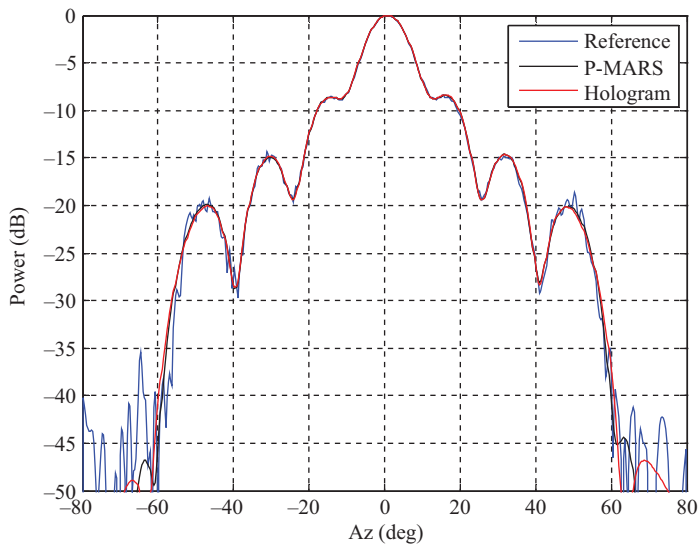

Figure 12.27 Comparison of azimuth cardinal cuts of reference pattern of X-band SGH, planar MARS filtered antenna and hologram filtered pattern

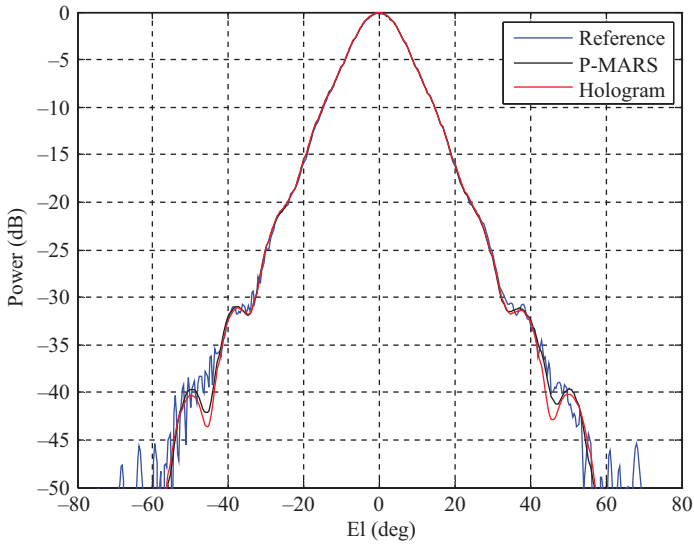

Figure 12.28 Comparison of elevation cardinal cuts of reference pattern of X-band SGH, planar MARS filtered antenna and hologram filtered pattern

antenna to a very high degree and, for example, would be equally effective for the case of an antenna that is spatially extended in the longitudinal z-dimension, i.e. a 'thick' antenna such as a log periodic dipole array antenna or an open-boundary, dual ridged horn. Additionally, if the aperture plane fields are truncated too aggressively in the transverse dimension then the fields at the edge of the filtered sampling interval can have a significant effect on the corresponding filtered far-field pattern as they may still have relatively large intensities. This means that a significant amount of care must be taken in order to ensure that the processed far-field pattern does not become unreliable.

12.2.4 Amplitude and phase drift correction: tie-scan correction

Electrical drift within the RF-guided wave path of the antenna test system can introduce significant measurement errors, particularly phase errors, on data acquired when test durations become protracted or when temperature fluctuations become excessive. As test frequencies increase, the sensitivity of the measurement system to this effect also increases significantly. This is especially true when the electrical length of the RF-guided wave path is long and the test and reference arms of the RF sub-system are of different lengths, which is generally the case. The situation can also be exacerbated by the electrical temperature stability of the particular RF cables that are used within the RF sub-system. Cable construction and the materials used all have an influence. This is illustrated in Figure 12.29, which presents a plot of the transmission phase through a fixed unit physical length of RF

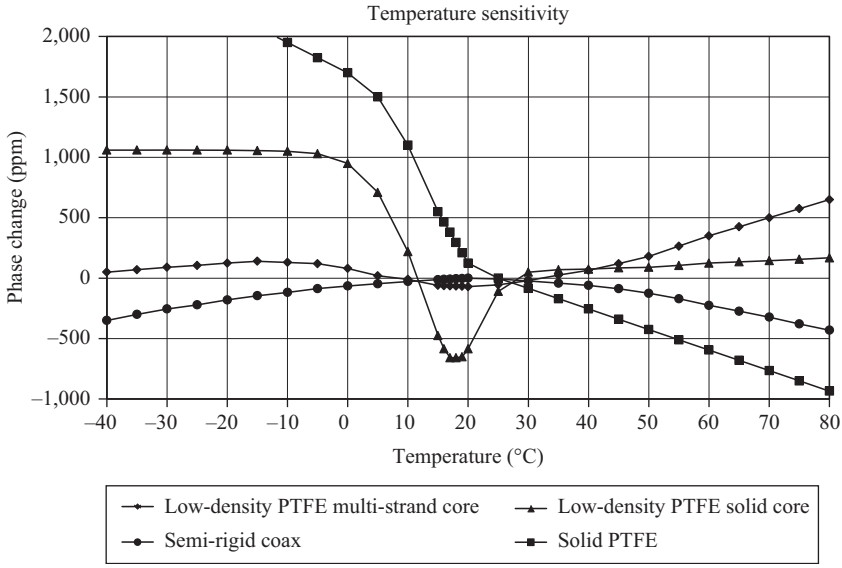

Figure 12.29 Thermal phase sensitivity of transmission line

transmission line of various different constructions. This throws into very sharp relief the benefits that can be had by the judicious selection of RF cables as well as the choice of temperature at which to test. Here, it can be seen that many commonly used polytetrafluoro-ethylene (PTFE) dielectric layer cables suffer a nonlinear phase change with temperature at around 20°C, which is unfortunate as this is precisely the temperature that many antenna test systems are specified to operate at. This is a direct consequence of PTFE undergoing a dimensional change with temperature that is most dramatic at about 19°C. This volumetric change impacts upon the dielectric and mechanical properties of the transmission line and this is the root cause of the transmission phase behaviour.

Generally then, when testing at millimetrewave or sub-millimetrewave frequencies, these effects cannot be ignored and some form of correction is needed. All forms of near-field systems are susceptible to these effects, with planar and cylindrical systems being perhaps the most vulnerable, with the effects being most pronounced when testing high-gain antennas. Most correction techniques involve a 'return to point' repeat measurement procedure being used to compensate for this electronic drift. Near-field measurements typically involve a raster type scan with typically the lighter faster axis being scanned with the heavier axis being stepped. For vertical plane rectilinear systems, this usually corresponds to the *y*-axis being scanned with the *x*-axis being stepped. Due to the generally quite large thermal mass of many indoor test environments, thermal drift effects tend to be comparatively slowly varying functions of time. Thus in many applications a *y*-axis scan can be assumed to be acquired with negligible drift in amplitude and phase arising

within the guided wave path from thermally induced fluctuations. However there may be a significant drift in the (stepped) *x*-axis as the total scan time will be significantly greater than the time taken to acquire a single *y*-axis cut. This clearly assumes no thermal stratification within the chamber, or at least that any thermal stratification that does not have sufficient time to be able to influence the RF-guided wave path. Providing this assumption holds then a 'tie-scan' compensation technique becomes viable. Tie scans involve a return to point calibration and correction scheme that consists of repeating the near-field measurement over a smaller sub-area of the total acquisition interval. Thus if acquisitions are made by scanning in the *y*-axis and stepping in the *x*-axis, at the end of a complete scan, a single *x*-axis cut is taken so as to 'tie' each of the individual *y*-axis cuts together (cf. Figure 12.30). To overcome finite sensitivity and in an attempt to increase the reliability of the correction terms, a set of *x*-axis cuts can be taken at varying *y*-axis positions. In the same way that we initially assumed that each of the individual *y*-axis scans are all acquired in the same state of electronic drift, here we have assumed that the *x*-axis cut is also acquired with the same state of electronic drift. This is not an unreasonable assumption as many modern measurement systems are capable of acquiring data on the fly with the probe in a continuous state of constant velocity motion with a cut taking perhaps only in a matter of a few seconds.

The correction factors can be obtained from the tie scans by noting that in essence, across the interval of the tie scan, we wish to replace the measured values in the complete scan with the values acquired within the tie scan as these values are assumed to be free from electronic system drift. Thus the correction factors can be

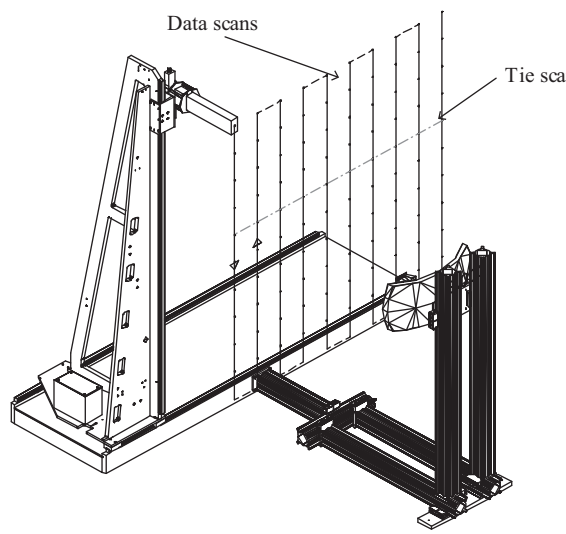

Figure 12.30 Schematic of 'tie-scan' return to point correction for electronic system drift as applied to a PNF acquisition system

expressed simply as

$$c(x) = \frac{E_t(x, y = y_0)}{E(x, y = y_0)} \tag{12.44}$$

where $c(x)$ can be used to correct the near-field data and E_t and E are assumed to be the same near electric field component. Here, y_0 is used to denote a constant, i.e. the y-axis value for the x-cut. That is to say, the correction factor c which is valid for all x and y positions across the scan plane is derived from the ratio of the tie scan (E_t) and the complete scan (E) over the interval of the tie scan. Unfortunately, as this correction strategy applies a global correction that is based on data obtained from a localised measurement, such correction schemes run the risk that when the tie scan, E_t, is measured at a point in the near-field patterns where there is a minimum (e.g. a null) where the signal-to-noise ratio (SNR) becomes small, the resulting correction term can, at best, introduce additional noise into the measurement, and at worst corrupt a complete near-field cut. This can be mitigated against, in part at least, by extending the tie scan to comprise a series of tie scans and by determining the least-squares weighted mean correction term, cf. channel balance correction expression that was developed in the preceding section, thus

$$c(x) = \frac{\sum_{n=1}^{N} \left[\frac{E_t(x, y=y_s)}{E(x, y=y_s)}\right] w_n}{\sum_{n=1}^{N} w_n} \tag{12.45}$$

Here, w_n is used to denote the weighting term which is equal to the amplitude squared with the summation being taken over the y-axis indices of each of the N tie scans taken at $y = y_s$, where y_s denotes the y-axis coordinates of the tie scans. Typically, N is set to a small value, e.g. between 5 and 10; however, in practice a degree of experimentation may be needed to establish a reasonable compromise between accuracy and the measurement time.

In practice multiple frequency near-field acquisitions are generally made with data being taken on the fly, that is to say, with the probe in continuous motion. Such schemes are not automatically compatible with this type of return to point-based correction schemes as at best only a single frequency within the complete acquisition will be repeated within the tie scan as the tie scans are being taken with the orthogonal axis in motion. However, providing one frequency point within the complete measurement is coincident and synonymous with an equivalent frequency point within the tie scan; thus this correction methodology may be extended so that all of the frequencies can be corrected. This can be accomplished if we assume that the amplitude drift is not frequency dependent, which is a good approximation, and that the phase change is a result of a change in the electric length of the transmission line. Thus the correction coefficients can be translated to other frequencies if first the phases are converted to an electrical length. For the frequency for which the measurement is repeated, the equivalent physical length can be computed from the phase change, denoted by Φ contained within $c_w(x, y)$, using

$$l = \frac{\lambda}{2\pi}\Phi \tag{12.46}$$

Thus for other frequencies the equivalent phase change can be computed using

$$\Phi_f = \frac{2\pi}{\lambda_f} l = \frac{\lambda}{\lambda_f} \Phi \tag{12.47}$$

Here, Φ_f denotes the phase change at the desired frequency, which is to say for the frequency where the data in the complete acquisition does not line up with any of the points within the tie scan. Thus the phase change as the desired frequency can be estimated from the phase change at the measured frequency.

Other techniques for compensating drift in near-field measurements exist. The proprietary, motion tracking interferometer method is a 'return to point' method that is capable of correcting planar near-field data for thermally induced amplitude and phase variations [14]. However, although this is a proven, effective method, as it is a proprietary, patented technology, it is not widely utilised outside of test systems that have been provided by the patent holder and as such it will not be discussed further within this text.

12.2.5 Alignment correction (in PNF, CNF, and SNF)

The normal aim of a range measurement process is to characterise the radiation pattern of the AUT at a very great, or infinite, distance with reference to an angular or other coordinate system defined with respect to a fixed (precision) fiducial mechanical interface. This data can then be utilised to establish the extent to which the instrument fulfils its requirements. The angular accuracy required is usually in the order of $\pm 0.02^\circ$, particularly when the antenna is to be mounted on a spacecraft intended for geostationary orbit. Such requirements place significant demands upon the antenna-to-range alignment which may not be deliverable through the use of a precision mechanical support and in these cases errors in the alignment need to be measured with the measured antenna patterns being compensated. The following section presents an overview of an approximate correction methodology before more rigorous techniques which are measurement geometry specific are developed.

12.2.5.1 Overview of antenna pattern rotation

A detailed introduction to coordinate systems for antenna pattern plotting, polarisation basis and the transformation between coordinate systems can be found presented in the appendices. Within this section an introduction to the numerical conversion of far-field antenna pattern data from one frame of reference to another is developed that enables, e.g., antenna-to-range alignment errors to be compensated for. These techniques can also be used to allow antennas that have been acquired in one range to be presented in the same form as data obtained from another system which is a commonly encountered problem.

In the case of applying a scalar (*no* polarisation change) rotation to an antenna pattern, the algorithm would be as follows:

1. Calculate the equivalent triad of Cartesian direction cosines (u, v, w) corresponding to each of the points in the pattern, i.e. directions in the raster grid of sampling nodes which is usually a grid of spherical angles, e.g. a plaid, monotonic and equally spaced grid of say θ and ϕ angles.

2. Transform the triad of direction cosines to compute the equivalent direction cosines in the other rotated frame of reference (u', v', w').
3. Calculate the equivalent spherical angles in the second rotated coordinate system. *Note*: this will generally represent an irregular non-rectilinear coordinate system.
4. Approximate the new rotated pattern function from the original dataset using whichever interpolating scheme is best suited to the underlying pattern function, e.g. bilinear and bicubic.
5. Plot new data using regular raster grid of spherical angles.

This generic process can be used to rotate an antenna pattern that has been tabulated in any of the conventional far-field plotting coordinate systems, e.g. azimuth over elevation, elevation over azimuth, polar spherical and true-view, direction cosine, cf. Chapter 4. Clearly, this can be repeated for each polarisation component.

In contrast, a vector rotation (as required to implement an alignment correction to an antenna measurement) changes both the pattern and polarisation. Unfortunately, the by-product of a scalar rotation is that the reference, i.e. observing, polarisation is rotated with the pattern by exactly the same amount as the pattern has been rotated – after all we did nothing to the polarisation, we merely rotated the pattern so it had no alternative but to be rotated with the pattern. Thus an inverse rotation must be applied to the polarisation basis in order that the observing polarisation can be returned to its original state. Fortunately, this can be accomplished simply by utilising the inverse of this equation to correct the field components. In summary, the algorithm for applying a vector rotation to an antenna pattern can thus be expressed as follows:

1. Resolve the far-field pattern (e.g. initially resolved onto a Ludwig III polarisation basis) onto a Cartesian polarisation basis.
2. Apply a scalar rotation to each of the three polarisation patterns (separately) using the algorithm detailed above.
3. Apply an inverse isometric rotation to the interpolated field components to complete the vector isometric rotation.
4. Resolve the far-field pattern back onto the desired polarisation basis (e.g. Ludwig III definition).

In order to illustrate the post-processing technique described above, simulated far-field patterns were obtained where a radiator was aligned to the axes of the simulation space, and again where it was rotated with respect to the simulation space. The purpose of this was to test the vector isometric rotation by taking the rotated data-set and computing the nominally aligned dataset that could then be compared with the nominally aligned reference set. To this end, a proprietary three-dimensional, full-wave CEM solver employing the finite difference time domain (FDTD) method was used to solve for the electric and magnetic fields. In this case, a simple OEWG section excited by the fundamental TE_{10} mode was modelled twice, once when the axes of the OEWG were aligned with the axes of the simulation space, and again with the OEWG section having been rotated through 30°

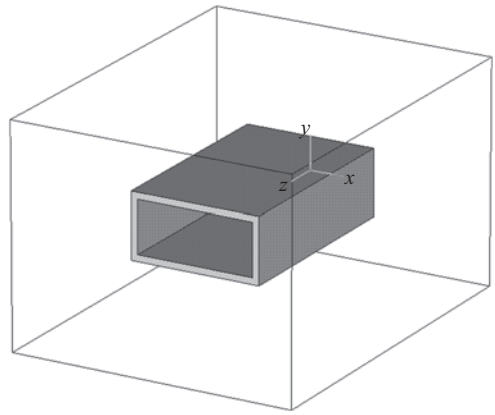

Figure 12.31 Nominally aligned waveguide section in problem space

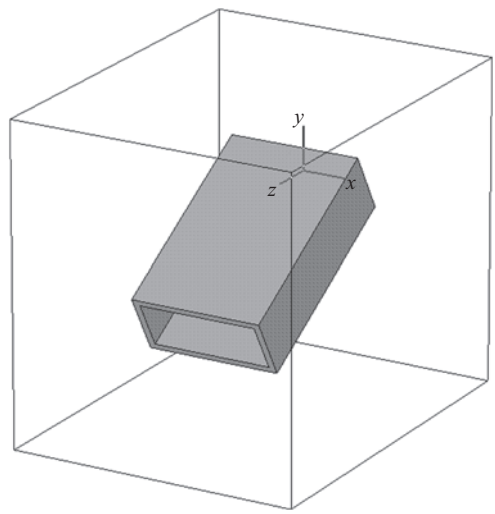

Figure 12.32 Rotated waveguide section shown in problem space

about the *x*-axis of the space. This can be seen illustrated schematically in Figures 12.31 and 12.32, respectively. The choice of an elementary OEWG section was made as this was both simple to model and the low-gain nature of the device enables pattern comparisons to be made over very nearly the complete far-field sphere.

The Cartesian components of the far-field patterns of the nominally aligned simulation can be seen presented in Figures 12.33 and 12.34. The Cartesian components of the far-field patterns of the rotated simulation can be seen presented in Figures 12.35 and 12.36. The alignment corrected Cartesian components can be

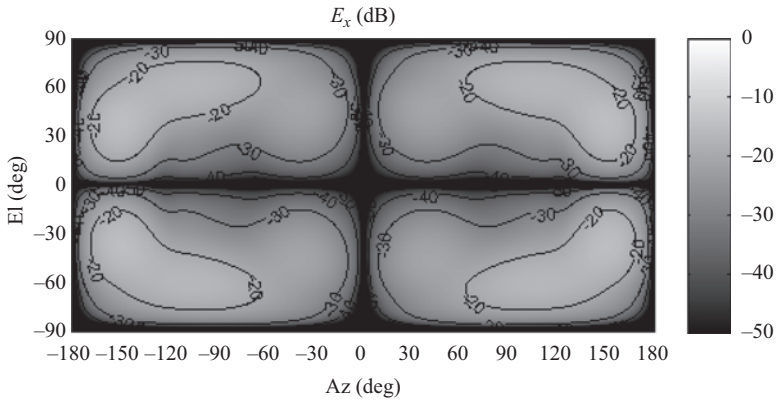

Figure 12.33 E_x polarised component of nominally aligned OEWG

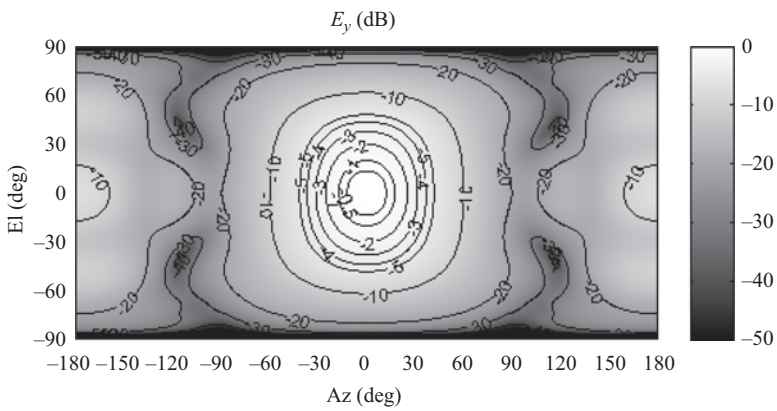

Figure 12.34 E_y polarised component of nominally aligned OEWG

found in Figures 12.37 and 12.38. Here, each of the plots has been tabulated using a regular azimuth over elevation coordinate system with data presented over the complete far-field sphere. From inspection, it is clear that the alignment-corrected patterns agree closely for each of the triad of Cartesian field components. Although not shown, the agreement between the resulting phase patterns was equally encouraging with only very minor differences being evident which result from the slightly different phase origins that were used in the respective CEM simulations.

12.2.5.2 Alignment correction in planar antenna measurements

For the case of the planar near-field to far-field transformation, the application of alignment correction data is handled rigorously by expanding the PWS on an

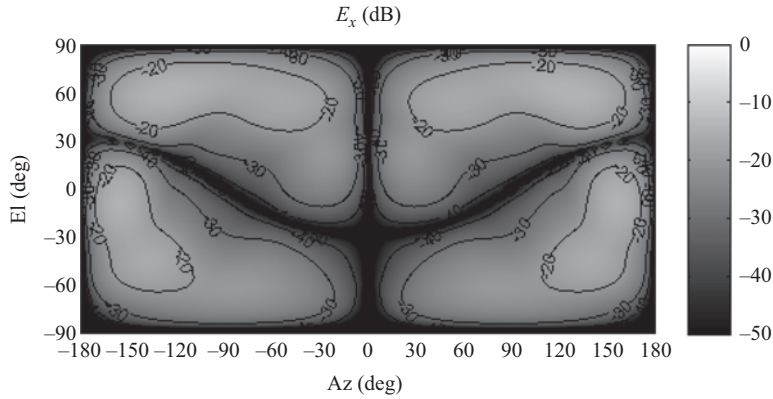

Figure 12.35 E_x polarised component of rotated OEWG

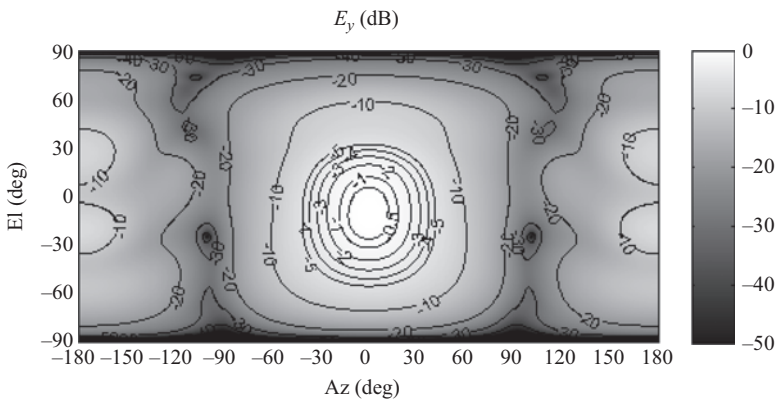

Figure 12.36 E_y polarised component of rotated OEWG

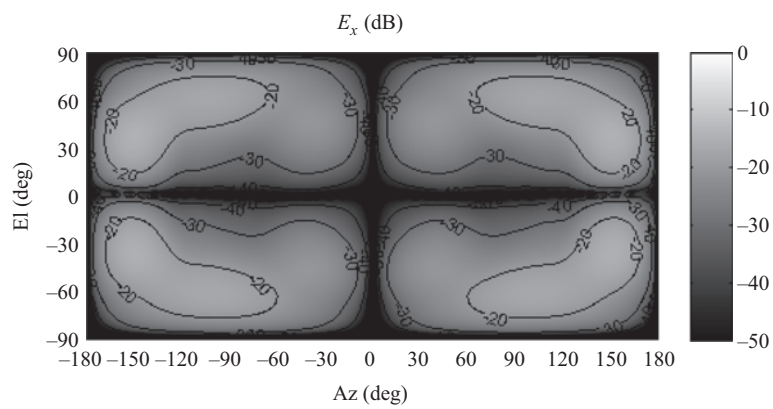

Figure 12.37 E_x polarised component of re-aligned OEWG

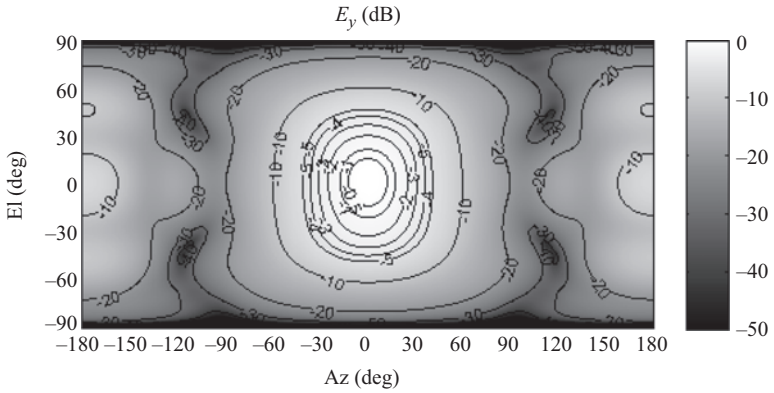

Figure 12.38 E_y polarised component of re-aligned OEWG

irregular grid in the range system. This irregular space corresponds to a regular angular domain in the antenna mechanical system. With the transformation of the measured Cartesian field components from the range polarisation basis into the antenna polarisation basis, the required isometric rotation is completed.

Let (x_p, y_p, z_p) represent the antenna electrical system (AES), that is to say the Cartesian polarisation basis onto which the vector antenna radiation pattern is to be resolved. Let (x_a, y_a, z_a) represent the antenna mechanical system (AMS), which is the system with which the antenna patterns are to be plotted (i.e. the observation coordinate system). Finally, let (x_r, y_r, z_r) represent the range-fixed system (RFS), i.e. the system in which the measurements are taken. The following definitions can be formed from the nine possible scalar products between the respective sets of axes. Let the mechanical alignment direction cosine matrix be represented by

$$\begin{bmatrix} x_a x_r & x_a y_r & x_a z_r \\ y_a x_r & y_a y_r & y_a z_r \\ z_a x_r & z_a y_r & z_a z_r \end{bmatrix} = [A] \tag{12.48}$$

Furthermore let the polarisation direction cosine matrix be represented by

$$\begin{bmatrix} x_p x_a & x_p y_a & x_p z_a \\ y_p x_a & y_p y_a & y_p z_a \\ z_p x_a & z_p y_a & z_p z_a \end{bmatrix} = [P] \tag{12.49}$$

Hence the antenna-to-range alignment can be corrected using

$$\lfloor k_{x_r}, k_{y_r}, k_{z_r} \rfloor = \lfloor k_{x_a}, k_{y_a}, k_{z_a} \rfloor \cdot [A] \tag{12.50}$$

or

$$\begin{bmatrix} k_{x_r} \\ k_{y_r} \\ k_{z_r} \end{bmatrix} = [A]^{-1} \cdot \begin{bmatrix} k_{x_a} \\ k_{y_a} \\ k_{z_a} \end{bmatrix} \tag{12.51}$$

The measured field components, when transformed to the far-field, can readily be resolved onto the desired polarisation basis using

$$\begin{bmatrix} E_{x_p} \\ E_{y_p} \\ E_{z_p} \end{bmatrix} = [P] \cdot [A] \cdot \begin{bmatrix} E_{x_r} \\ E_{y_r} \\ E_{z_r} \end{bmatrix} \tag{12.52}$$

Finally

$$\begin{bmatrix} k_{x_p} \\ k_{y_p} \\ k_{z_p} \end{bmatrix} = [P] \cdot [A] \cdot \begin{bmatrix} k_{x_r} \\ k_{y_r} \\ k_{z_r} \end{bmatrix} = [P] \cdot \begin{bmatrix} k_{x_a} \\ k_{y_a} \\ k_{z_a} \end{bmatrix} \tag{12.53}$$

In general, it is preferable to handle rotations in terms of direction cosine matrices as the requirement to know the *sense* and *order* of a sequence of angular rotation is avoided. The determinant of the above direction cosine matrix will be unity as we are only considering right-handed coordinate systems (the determinant will be negative if the transformation changes a right-handed coordinate system to a left-handed one, or vice versa). As developed above, these vector rotations can be thought of as being constructed from a scalar rotation of the pattern and an inverse scalar rotation of the polarisation vector, where the order of application is unimportant. The far-field antenna pattern function can be obtained without recourse to polynomial approximation by utilising the discrete Fourier transform (DFT) to compute the pattern in the exact direction required. The field components can then be rotated through the use of the plane wave condition which enables the complete field to be recovered from the tangential electric fields and through the inverse isometric rotation of the fields. Details of the acquisition of antenna-to-range alignment data in a planar facility can be found in [15].

To illustrate the alignment techniques discussed above, a low-gain pyramidal horn was acquired at two different orientations with respect to the range axes. A low-gain instrument is preferable here, as the signal levels are relatively high at large angles so that errors in the vector isometric rotation are clearly observable. The antenna-to-range alignment was measured for each case and then the data transformed. Figure 12.39 contains the far-field antenna pattern for the case where the AUT was nominally aligned to the range. Conversely, Figure 12.40 presents the far-field alignment-corrected pattern of an antenna that was grossly misaligned to the axes of the range.

Here, the far-field plots consist of Ludwig III vertical co-polarisation and cross-polarisation data tabulated on a regular 81-element by 81-element array in an azimuth over elevation coordinate system. The data has only been plotted out to $\pm 40^\circ$ in azimuth and elevation in order that the entire far-field dataset should be free from first-order truncation effects. Clearly, the co-polarised patterns are in good agreement with differences in the patterns being primarily a result of the difference in the chamber scattering which is a consequence of the different antenna orientation within the partially absorber lined anechoic chamber. The cross-polarised patterns are at a sufficiently low level that other measurement uncertainties prevent a sensible comparison to be made.

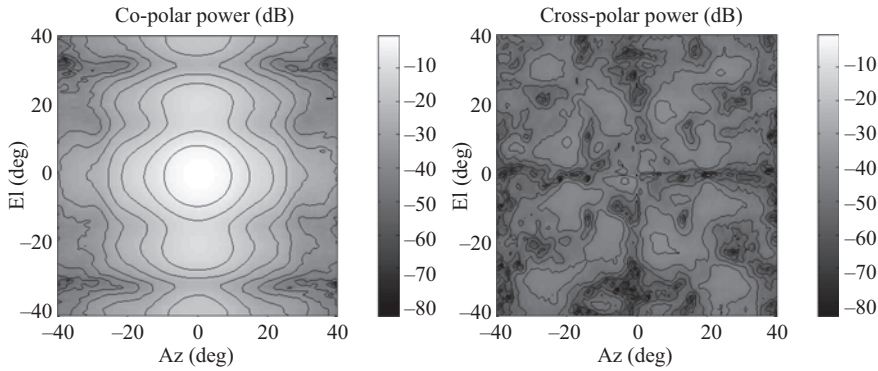

Figure 12.39 Far-field co-polar and cross-polar pattern of nominally aligned antenna measurement

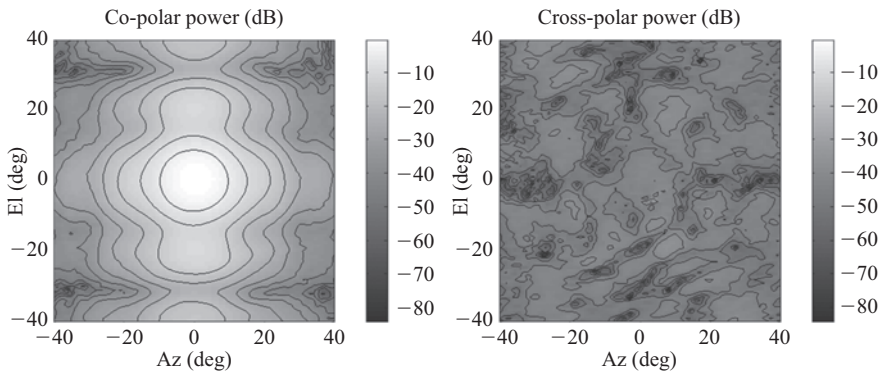

Figure 12.40 Far-field co-polar and cross-polar pattern of grossly miss-aligned measurement after active alignment correction has been applied

Microwave holographic metrology (MHM) or aperture diagnostics is a powerful technique that can also be usefully extended with the incorporation of active alignment correction. Figure 12.41 contains plots of reconstructed near-fields that were obtained from measurements of the same antenna as was measured and used to create Figure 12.24 only here; the data was acquired while the antenna was grossly misaligned in azimuth with respect to the axes of the range. This data was obtained by testing an X-band planar slotted waveguide array antenna that had an aperture with a circular profile.

Figure 12.41 illustrates the aperture illumination function of the circular array antenna in the absence of active alignment correction. Conversely, Figure 12.42 shows the reconstructed aperture illumination function once the near-field data has been corrected for the gross azimuth alignment error. Here, the residual small vertical phase taper evident on the corrected aperture phase function results from a

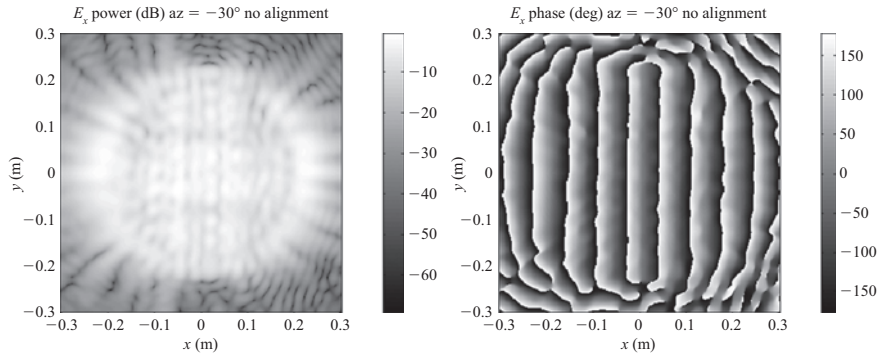

Figure 12.41 Reconstructed amplitude and phase function

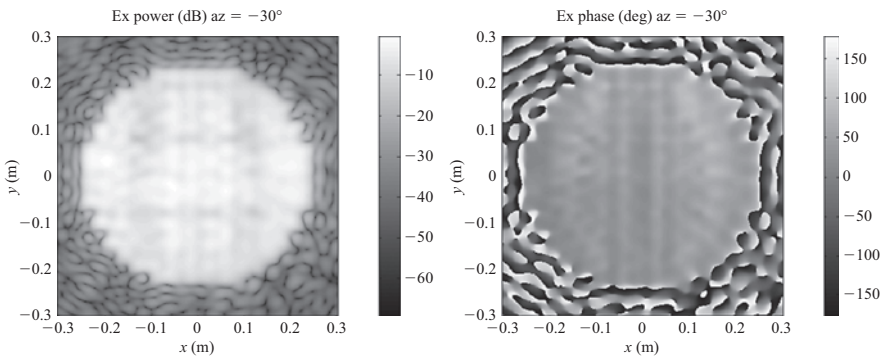

Figure 12.42 Reconstructed amplitude and phase function with active alignment correction applied

small elevation pointing error which was not compensated for within this processing. The differences between the two sets of results are not characterised by a simple linear phase taper. The uncorrected results are focused when $x = 0$, where the aperture plane and the translated measurement plane intersect, and become progressively diffracted as the magnitude of x increases and the two planes diverge in space. However, when corrected, the reconstructed image is focused, i.e. free from diffraction effects, as only then is the reconstructed plane coincident and synonymous with the antenna aperture plane. In this case the image shows a clear resemblance with the physical aperture as shown in Figure 12.43, cf. the staircase circular approximation visible in the aperture illumination function of the antenna.

12.2.6 Simple semi-empirical model of an open-ended rectangular waveguide probe

Rectangular open-ended waveguide (OEWG) probes are widely used on planar, cylindrical, and spherical near-field antenna measurement systems. They are

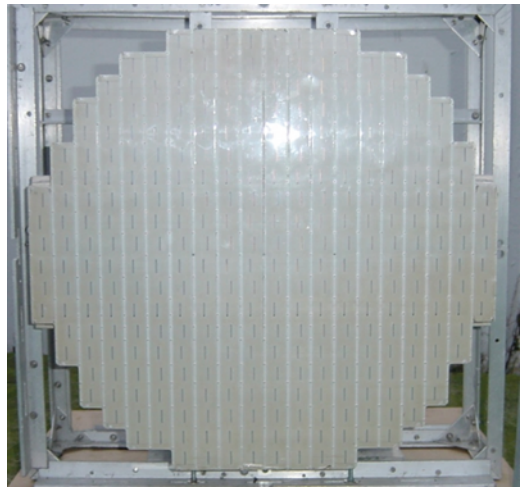

Figure 12.43 Photograph of circular slotted waveguide array antenna (Picture courtesy of SELEX ES)

typically inexpensive to fabricate, easy to mount on the measurement system and their patterns can be calculated fairly accurately to provide the data needed for probe pattern correction. This last point is valuable as, probe pattern compensation is generally required if reliable far-field data is to be obtained from near-field measurements and calibration can be an expensive and time consuming task that will provide the pattern at only a fixed number of frequency points. A commonly used formula for the pattern of an OEWG probe can be found presented in [16]. As this is an almost ubiquitously used semi-empirical model, the purpose of this section is not to supplant the original references [16,17] or re-derive the formulae from scratch, as that adds little value, but rather to provide a summary of the important expressions, their critical parameters and to illustrate the degree of agreement that can be attained between the OEWG model and a high quality pattern measurement. As it has been found that the gain values obtained from this formula are less reliable than the pattern information, being as they are more dependent upon manufacturing tolerances, only the pattern formula are addressed herein.

From (1A) in [16], it can be seen that, in the far-field, with the unimportant spherical phase factor and inverse r term suppressed, the electric fields for an OEWG probe can be expressed as

$$\underline{E}(\theta,\phi) = \frac{1}{k_0}\left[E_E(\theta)\sin\phi\,\underline{\hat{e}}_\theta + E_E(\theta)\cos\phi\,\underline{\hat{e}}_\phi\right] \tag{12.54}$$

Here, the full far-field pattern is obtained from the E- and H-plane pattern cuts using the assumption that the aperture is electrically small and can excite only certain specific spherical modes. Figure 12.44 presents a schematic

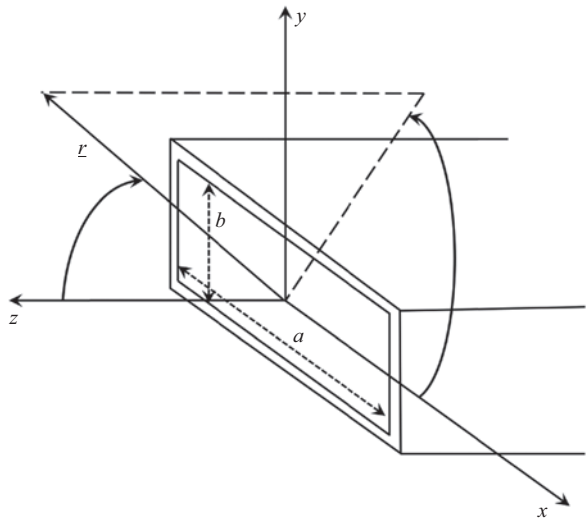

Figure 12.44 Coordinate system used for derivation of far-field pattern of OEWG probe

representation of the vertically polarised OEWG probe in its local coordinate system showing the definition of the attendant spherical angles. Here, a and b denote, respectively, the width and height of the *internal* dimensions of the waveguide section. The external dimensions differ, clearly, by the thickness of the walls of the waveguide sections.

Using (2) in [16], it can be shown that the E-plane pattern of the probe, $E_E(\theta)$, in the forward hemisphere when assuming the reflection coefficient at the aperture of the waveguide section is zero can be expressed as

$$E_E(\theta) = A_E \frac{\left[1 + \frac{\beta}{k_0}\cos\theta\right]}{1 + \frac{\beta}{k_0}} \operatorname{sinc}\left(\frac{k_0 b}{2}\sin\theta\right) \tag{12.55}$$

Similarly, taking (8) in [16], it can be shown that the H-plane pattern of the probe, $E_H(\theta)$, in the forward hemisphere when assuming the reflection coefficient at the aperture of the waveguide section is zero can be expressed as

$$E_H(\theta) = A_H \left[\frac{\cos\theta + \frac{\beta}{k_0}}{\left(\frac{\pi}{2}\right)^2 - \left(\frac{k_0 a}{2}\sin\theta\right)^2} + C_0\right] \cos\left(\frac{k_0 a}{2}\sin\theta\right) \tag{12.56}$$

Here, the normalised propagation constant is defined as

$$\frac{\beta}{k_0} = \sqrt{1 - \left(\frac{\pi}{k_0 a}\right)^2} \tag{12.57}$$

The normalisation constant A_E is given by

$$A_E = A_H\left[\left(\frac{2}{\pi}\right)^2\left(1+\frac{\beta}{k_0}\right)+C_0\right] \tag{12.58}$$

A_H by

$$A_H = -\frac{jk_0^2ab}{8} \tag{12.59}$$

The parameter C_0 is defined as being

$$C_0 = -\left(1+\frac{\beta}{k_0}\right)\left(\frac{2}{\pi}\right)^2+\sqrt{\frac{G_0}{A}} \tag{12.60}$$

where A is given by

$$A = \frac{\pi k_0^2ab}{8\left(\frac{\beta}{k_0}\right)} \tag{12.61}$$

where G_0 is given by

$$G_0 = \frac{4}{\int_0^{\pi}\left\{\left[\frac{\left(1+\frac{\beta}{k_0}\cos\theta\right)\sin\left(\frac{k_0b}{2}\sin\theta\right)}{\left(1+\frac{\beta}{k_0}\right)\frac{k_0b}{2}\sin\theta}\right]^2+\left[\left(\frac{\pi}{2}\right)^2\frac{\cos\theta\cos\left(\frac{k_0a}{2}\sin\theta\right)}{\left(\frac{\pi}{2}\right)^2-\left(\frac{k_0a}{2}\sin\theta\right)}\right]^2\right\}\sin\theta d\theta} \tag{12.62}$$

This expression can be evaluated numerically as it is a well behaved usually slowly varying function of angle as illustrated in Figure 12.45 for case of the OEWG probe treated below showing the integrand at the bottom and top of the WG frequency band. In each case this is a well-behaved smoothly varying function of polar angle.

Thus, once we have computed the spherical field components of the far-field pattern of the OEWG probe as the radial field component is identically zero, these formulae are sufficient for us to resolve the fields onto any desired polarisation basis. For example, the spectral fields can be computed from, cf. Chapter 4,

$$F_x = E_\theta\cos\phi - E_\phi\frac{\sin\phi}{\cos\theta} \tag{12.63}$$

$$F_y = E_\theta\sin\phi + E_\phi\frac{\cos\phi}{\cos\theta} \tag{12.64}$$

$$F_z = -\frac{\left(F_x\sin\theta\cos\phi + F_y\sin\theta\sin\phi\right)}{\cos\theta} \tag{12.65}$$

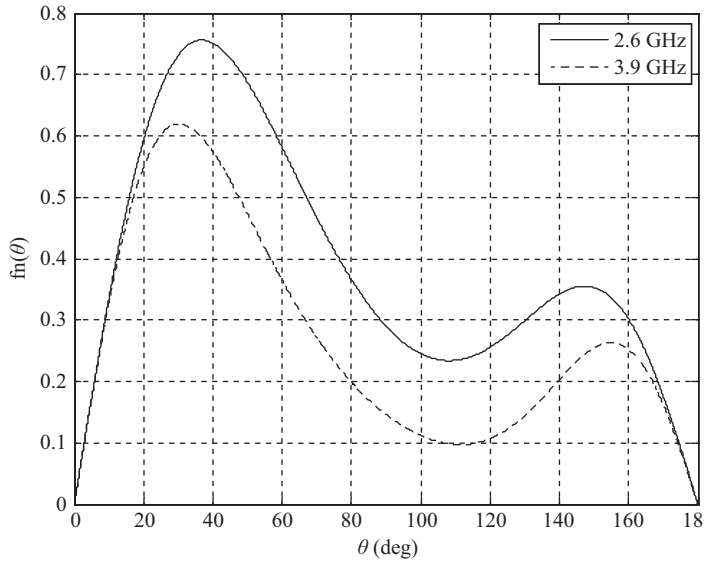

Figure 12.45 Plot of integrand at the bottom and top of the frequency band to be numerically integrated when determining the factor G_0. In each case, the function is a smoothly varying well behaved function of θ

Conversely, the azimuth and elevation electric field components can be obtained from

$$E_{az} = \frac{1}{\sqrt{1-(\sin\theta\sin\phi)^2}}\left(E_\theta\cos\phi - E_\phi\cos\theta\sin\phi\right) \tag{12.66}$$

$$E_{el} = \frac{1}{\sqrt{1-(\sin\theta\sin\phi)^2}}\left(E_\theta\cos\theta\sin\phi + E_\phi\cos\phi\right) \tag{12.67}$$

The spectral and Ludwig II components are explicitly determined here as these are two of the more commonly used polarisation bases for probe pattern correction.

By way of an illustration let us consider the example of an S-band open ended rectangular waveguide probe radiating at 3.2 GHz. For this case the width, $a = 0.07214$ m, and the height $b = 0.03404$ m. Assuming that the probe is vertically polarised in its local coordinate system, as shown in Figure 12.44, we can see the measured and modelled co-polar patterns presented in Figures 12.46 and 12.47 respectively. Conversely, Figures 12.48 and 12.49 contain, respectively, measured and modelled cross-polar patterns. Here, the electric field components have been resolved onto a Ludwig II azimuth over elevation polarisation basis and have been

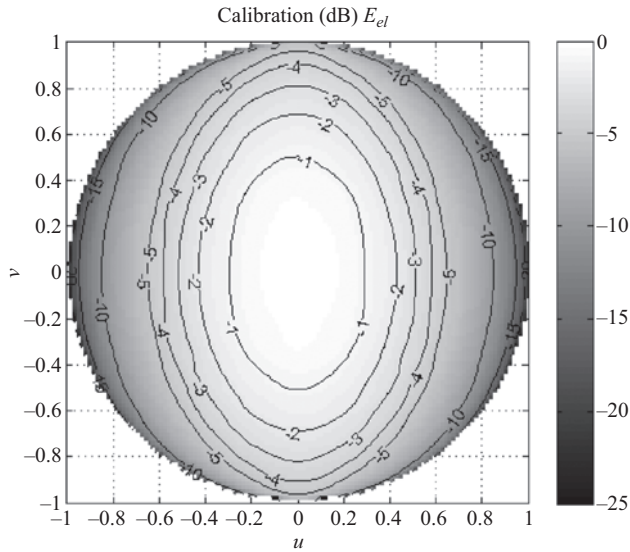

Figure 12.46 Far-field co-polar measured pattern of OEWG probe. Field resolved onto a Ludwig II azimuth and elevation polarisation basis and tabulated on a regular direction cosine plotting system

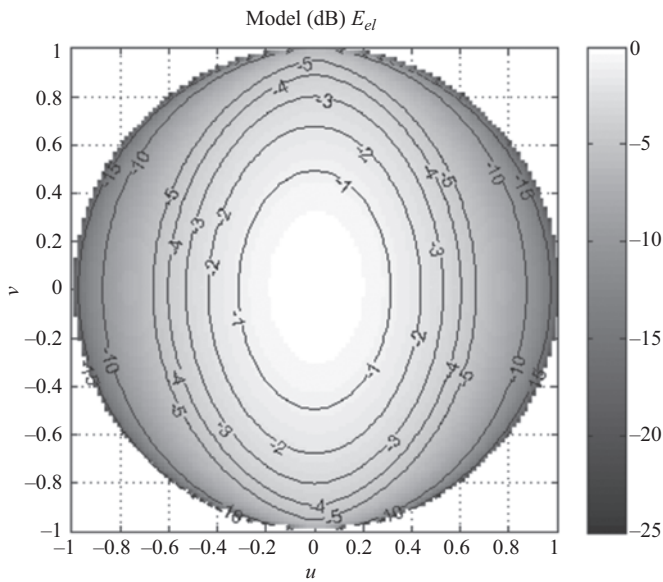

Figure 12.47 Far-field co-polar modelled pattern of OEWG probe. Field resolved onto a Ludwig II azimuth and elevation polarisation basis and tabulated on a regular direction cosine plotting system

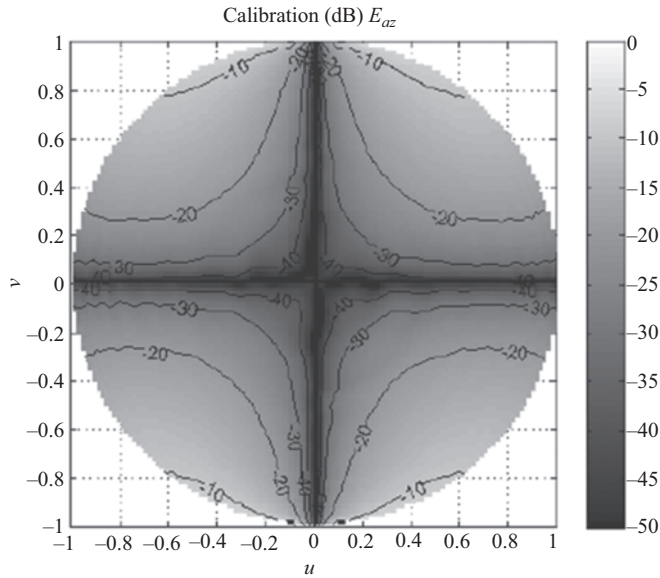

Figure 12.48 Far-field cross-polar measured pattern of OEWG probe. Field resolved onto a Ludwig II azimuth and elevation polarisation basis and tabulated on a regular direction cosine plotting system

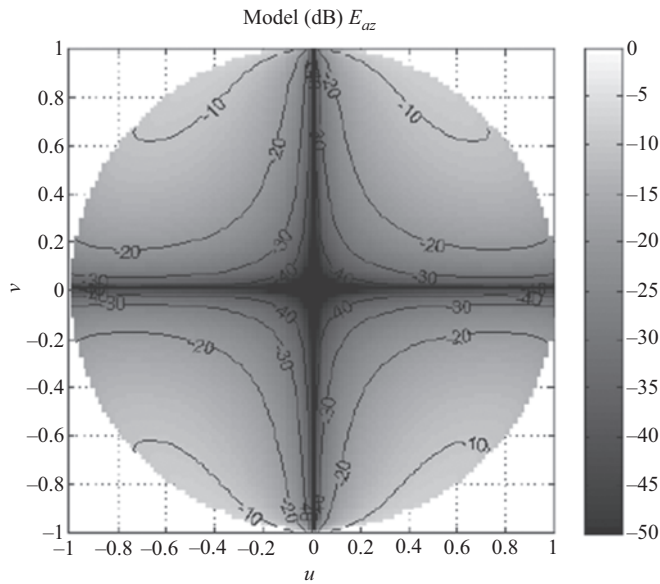

Figure 12.49 Far-field cross-polar modelled pattern of OEWG probe. Field resolved onto a Ludwig II azimuth and elevation polarisation basis and tabulated on a regular direction cosine plotting system

tabulated on a regular direction cosine plotting coordinate system. The peaks of the patterns have been normalised to 0 dB. From inspection of these patterns the co-polar patterns are in encouraging agreement however, the inter-cardinal cross-polar patterns do display differences, particularly for wider θ values. Thus, for many applications, these analytical models are found to be sufficient however they do not contain the effects of the absorber panel, manufacturing imperfections and the cross-polar pattern is not perfect thus for some more demanding testing campaigns there will be a need to use more sophisticated simulations or preferably calibrated pattern data.

12.2.7 Introduction to range reflection suppression

Reflections in antenna test ranges can often be the largest source of measurement error within the error budget of a given facility (cf. Chapter 10) often dominating all other errors. The very nature of indoor antenna measurements will inevitably result in the facility walls being illuminated to some degree by the radiating antenna. If not all of this power is absorbed, the scattered signal can become significant when compared with the direct signal, significantly degrading the performance of the facility. When making indoor antenna measurements, unwanted reflections are largely suppressed by lining the exposed surfaces of the interior of the test chamber and test equipment with electromagnetic absorbent, i.e. anechoic material. Such material, which typically comprises open cell carbon loaded foam, can be costly, bulky, delicate, and over time can shed particles of carbon. Most absorber is shaped specifically so that its performance is optimised for use across a predetermined range of frequencies. However this necessarily renders it less effective at other frequencies. For example tall pyramidal absorber may provide a smooth impedance transition between free-space impedance and a short circuit, that is to say the highly conductive metal screening at low frequencies and long wavelengths. However such tall pyramids and the large flat surfaces they comprise will present a sharp, highly discontinuous change in impedance which results in a comparatively reflective surface for high frequency, short wavelength and radiation. Also, while considerable effort can be devoted to optimising the design and placement of absorber within the test environment, it is not possible to place this material everywhere, and some surfaces are inevitably left exposed, e.g. lights, fire detection and suppression equipment and linear bearings.

Considerable attention has been paid to range multipath suppression in the open literature with significant effort, ingenuity and resourcefulness having been devoted to quantifying and subsequently correcting multipath contaminated measurements by means of hardware or software [18] time-gating, background subtraction [19], complex plane circular least-squares fitting (i.e. AAPC as outlined below [20]), aperture plane spatial filtering [21], signal encoding-based techniques, etc. It is not possible to present a detailed discussion of all of these techniques, so the following sections will provide an overview of two of the more successful, commonly deployed and practical frequency domain reflection suppression techniques. However before tackling this, a little attention will be devoted to illustrating

the impact of range reflections on measurements taken using a conventional spherical antenna test system.

12.2.7.1 Conventional methods for suppressing range reflections

Any antenna pattern can be characterised in a spherical range by scanning the azimuthal angle ϕ over the range $-180^\circ \leq \phi \leq 180^\circ$ and stepping the polar angle θ over the range $-180^\circ \leq \theta \leq 180^\circ$. Thus, the forward hemisphere of an antenna can be sampled twice, conventionally and again in the 'alternate' sphere configuration to obtain a redundant dataset (as described in Chapter 8). The relationship between these equivalent pairs of spherical angles can be expressed as, cf. Appendices, where it is assumed that the angles are modulo 360°

$$\theta = \begin{cases} \theta & \text{when } \theta \geq 0 \\ -\theta & \text{otherwise} \end{cases} \tag{12.68}$$

$$\phi = \begin{cases} \phi & \text{when } \theta \geq 0 \\ \phi \pm 180^\circ & \text{otherwise} \end{cases} \tag{12.69}$$

From this identity, it is clear that a very simple reflection test involves comparing θ cuts at $\phi = 0^\circ$ and $\phi = 180^\circ$. For a correctly aligned measurement system, the differences in the patterns are primarily due to the range reflections as everything, to the limits of repeatability (including drift) and random errors, will have remained the same. Subtraction of the two pattern cuts gives a preliminary estimate of expected error to signal ratio. This is perhaps the most straightforward range multipath assessment that is possible. Figure 12.50 contains a plot comparing θ cuts, solid line, for $\phi = 0^\circ$, and $\phi = 180^\circ$, dashed line, with the difference between the two cuts plotted using a dotted line.[2] Here, a very low-gain, i.e. circa 6 dBi, antenna was used so as to illuminate the walls of the chamber with comparatively high signal levels so as to reveal clearly the effects of multipath within the measurement. Here, a signal to error level of 30 dB is evident for the great circle cut.

This concept can be extended to cover all space if the alternate and conventional spheres are mapped into the same domain. The results of this for a forward hemisphere can be seen presented in Figure 12.51; dotted contours represent data taken in the conventional hemisphere, while black contours represent equivalent data taken using the alternate hemisphere which have been mapped onto the forward hemisphere. Contours are plotted in 3 dB increments from –50 dB upwards.

The average multipath level for the $\underline{\theta}$ and $\underline{\phi}$ polarisation was found to be at circa -52.4 dB and -51.4 dB levels, respectively. This can be thought of as representing the maximum change in room effects between the two configurations

[2]It is worthwhile noting that the $\phi = 180^\circ$ cut is reversed with respect to the $\theta = 0^\circ$ point before this subtraction is performed. Also, there is no need for an AUT that has a nominally symmetric radiation pattern with respect to the $\theta = 0^\circ$ point.

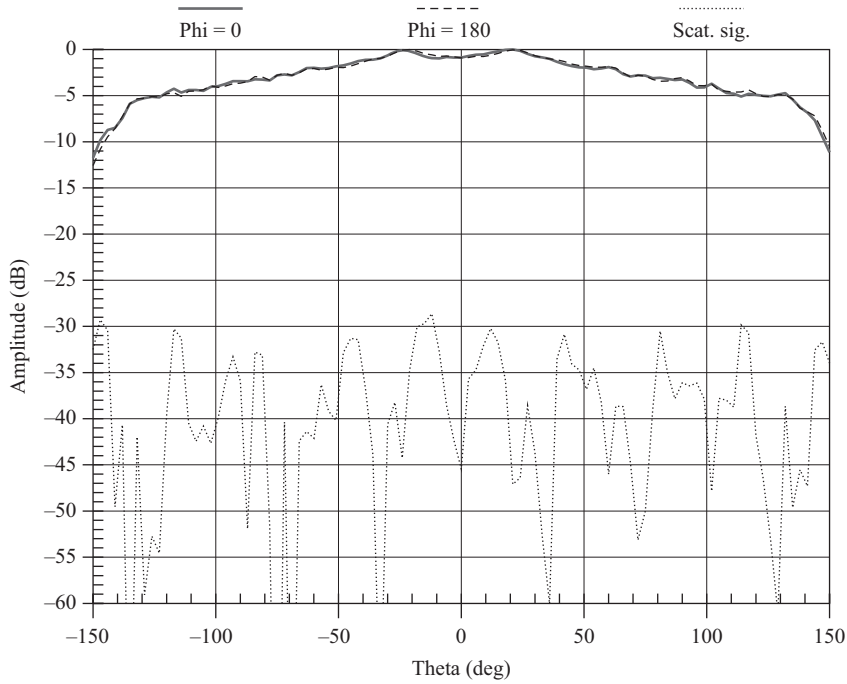

Figure 12.50 Typical results of a conventional reflection test for a low-gain S-band antenna

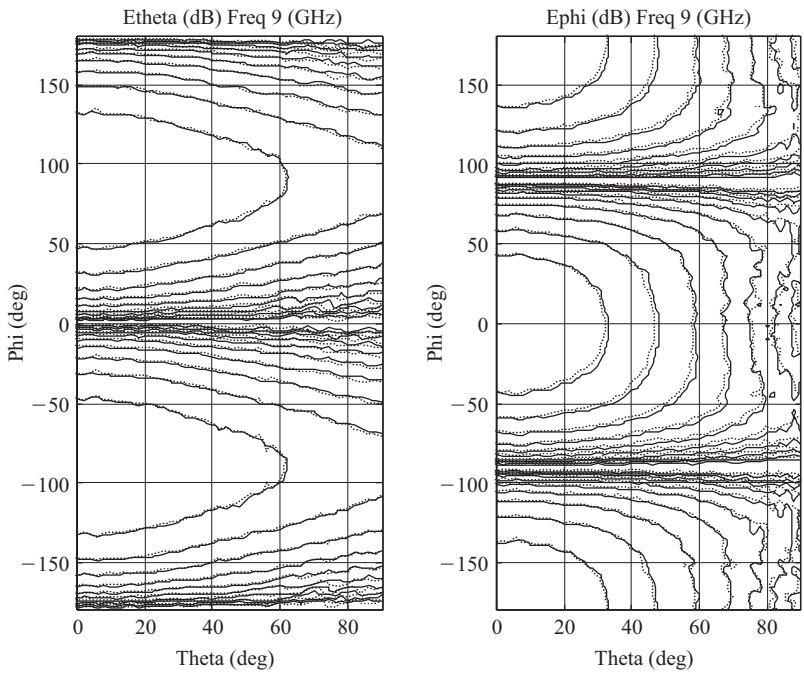

Figure 12.51 Comparison of conventional and alternate sphere pattern of a low-gain open-ended rectangular waveguide probe

assuming the spherical system is aligned perfectly and that the AUT does not deform under the effects of gravity. Similar tests such as these are commonly employed to assess and partially compensate for range multipath effects and have proved both illustrative and effective for many years. Sections 12.2.7.2 and 12.2.7.3 provide an introduction to two more sophisticated and far more potent methods that are now commonly employed in many antenna test ranges.

12.2.7.2 Advanced antenna pattern correction

As was described in Chapter 5, if phase information is available and if the error components within a particular measurement are not repeatable, an advanced antenna pattern correction (AAPC) [20] scheme can be followed where the two, say, spherical measurements are treated as two of a minimum of three datasets that can be used to provide an AAPC correction. At least one other dataset would be required, and this could be obtained from making a repeat measurement with the AUT displaced from the centre of rotation by some small known amount. Then, correcting for the resulting phase change in the far-field patterns and performing a correction across three such measurements using the AAPC processing as described below, a pattern correction is possible. Simply stated, AAPC is an Argand plane circular data-fitting technique. Here, the true value is assumed to be represented by a constant vector of fixed length and direction in the Argand (complex) plane, with the range multipath being represented by smaller magnitude vectors of equal length with different phases, i.e. arguments. In this way, it is self-evident that by making repeat measurements where only the phase of the interfering signal changes, by best fitting a circle in the Argand plane to the measured data at each point on the far-field sphere, we can attempt to reconstruct the underlying antenna pattern function in the absence of the scattered field. The derivation of the correction post-processing is based on finding the best fit circle to a set of three points. Let the points be described by x_1, y_1, x_2, y_2 and x_3, y_3, then the parameters of the circle can be obtained from

$$\begin{bmatrix} c_1 \\ c_2 \\ c_3 \end{bmatrix} = \begin{bmatrix} x_1 & y_1 & 1 \\ x_2 & y_2 & 1 \\ x_3 & y_3 & 1 \end{bmatrix}^{-1} \cdot \begin{bmatrix} -x_1^2 - y_1^2 \\ -x_2^2 - y_2^2 \\ -x_3^2 - y_3^2 \end{bmatrix} \tag{12.70}$$

where

$$\begin{bmatrix} x_1 & y_1 & 1 \\ x_2 & y_2 & 1 \\ x_3 & y_3 & 1 \end{bmatrix}^{-1} = \frac{1}{(y_2 - y_3)x_1 + x_3 y_1 - x_3 y_2 - x_2 y_1 + x_2 y_3} \times \begin{bmatrix} (y_2 - y_3) & -(y_1 - y_3) & (y_1 - y_2) \\ -(x_2 - x_3) & (x_1 - x_3) & -(x_1 - x_2) \\ (x_2 y_3 - x_3 y_2) & -(x_1 y_3 - x_3 y_1) & (x_1 y_2 - x_2 y_1) \end{bmatrix} \tag{12.71}$$

such that the coordinates of the origin of the circle and its radius are

$$h = -\frac{1}{2}c_1 \tag{12.72}$$

$$k = -\frac{1}{2}c_2 \tag{12.73}$$

$$r = \sqrt{h^2 + k^2 - c_3} \tag{12.74}$$

This algorithm was verified by locating the origin and radius of a circle that passes through three points on a plane as illustrated in Figure 12.52, where the stars represent the three points, the cross represents the origin of the circle and the plus represents the mean coordinate of the three points. Here, the left-hand plot illustrates the case where the three points are distributed roughly evenly around the perimeter of the circle where the mean coordinate roughly approximates the origin of the circle. The right-hand plot illustrates a worst case where the three points are closely spaced around the circumference and there is a significant difference between the origin of the best-fit circle and the mean coordinate.

Thus, if repeatable measurements cannot be obtained, the AAPC as it might be deployed in cases of high multipath, etc. can be used to assign a nominal value to the measurement data point that would be an average of the three measurements. Of course this implies that at least three times as many measurements will be needed to assign a value to any given data point. Usefully, AAPC can be used with planar, cylindrical, spherical near-field, or conventional far-field antenna measurement systems. While AAPC can significantly improve the quality of measured antenna patterns, it clearly requires the very careful displacement of an AUT and an extremely high degree of range repeatability in all other aspects in order for the least-squares fitting technique to prove effective. Section 12.2.7.3 introduces a more recently introduced range multipath extraction technique that is significantly more effective and efficient in terms of the amount of measured data that is required to apply the correction and is therefore significantly less intensive in terms of antenna test time.

12.2.7.3 Introduction to mathematical absorber reflection suppression

Mathematical absorber reflection suppression (MARS) has been used successfully and extensively to identify and extract range multipath effects in a great many spherical [22,23], cylindrical [24], and planar [21,25] near-field antenna measurement systems, as well as single [26] and dual [27] reflector CATRs and far-field systems [28]. As discussed above, in certain circumstances, multiple reflections within the chamber can become significant, e.g. when measuring lower gain antennas, wide-out side lobes or low cross-polarised patterns. Furthermore, any absorber which is used cannot be perfectly matched to illuminating fields for all directions, polarisations, and frequencies. Thus in some cases, the resulting scattering can impede the measurements taken.

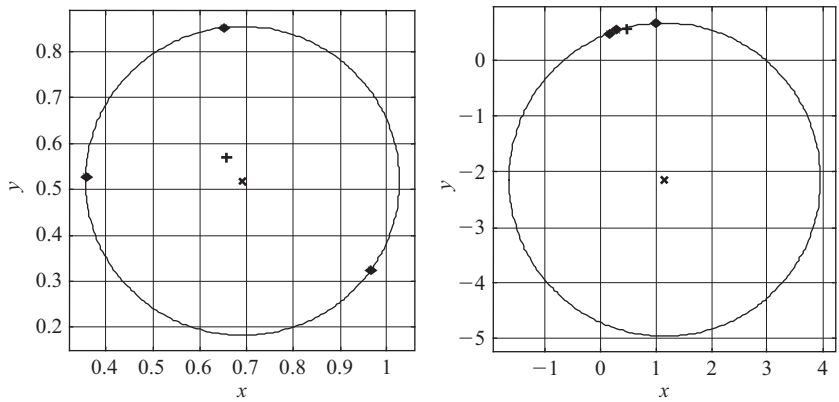

Figure 12.52 Two examples of best-fit circle

The spherical S-MARS technique was first implemented to support operations in a large hemi-spherical automotive test system [22]. The successful utilisation of the MARS technique was crucial as without this capability, scattering from the metallic floor, dielectric gantry, and radome could otherwise have degraded the quality of the results obtained from the test system. Following on from this, the S-MARS technique has been extended so that it can be used with other, more conventional spherical near-field antenna test systems. It has been found that the technique is sufficiently general to be used with polar and equatorial mode acquisitions, robotics positioning sub-systems utilising 'model tower' ϕ/θ and 'scanning arm' θ/ϕ arrangements, and to characterise linear and circularly polarised antennas, enabling meaningful results to be obtained from systems containing limited amounts, or even no absorber at all, as well as for use in improving the reflection performance in a traditional anechoic chamber. The large number and great variety of measurement configurations and antennas that have been found to be helped by the MARS technique indicated that the physical principle that underpins the process is sufficiently general in form to be extended to other measurement geometries. Thus, as the cylindrical near-field methodology is conceptually most closely related to the spherical case, and although the mathematical treatment is entirely separate and distinct, cylindrical MARS (C-MARS) has been implemented essentially as a corollary to S-MARS. In this way, it has been found that the underlying MARS technique is not a peculiarity of one particular modal basis or sampling scheme. Thus, although the actual mathematical operations *are* peculiar to the particular experimental geometry concerned, the underlying physical principles that enable a distinction to be made between those fields that are associated with the AUT and those arising from scattering are not. In each of the spherical, cylindrical, planar, and far-field implementations, a unique measurement and mathematical post-processing technique is implemented that requires only a minimum amount of detailed information about the AUT probe and range geometry; the processing is applied with the use of a mathematical operator that orthogonalises

those fields associated with the AUT from those fields associated with other spurious sources so that unwanted contributions can be effectively attenuated and filtered out.

The general mathematical absorber reflection suppression, that is to say MARS, principle comprises a measurement and post-processing technique that analyses the measured data before utilising a filtering process to suppress undesirable scattered fields. This frequency-domain technique is completely general requiring only a minimum amount of information about the AUT and measurement configuration. The technique is entirely generic in nature and can be applied to a variety of different antenna types, i.e. no specific *a priori* assumptions about the arrangement of current sources are made. Thus this technique is equally applicable to aperture and *non*-aperture type antennas. However it is assumed that the near-field antenna pattern function is spatially band-limited (i.e. the current sources occupy a finite region of space) and that the multiple reflections, arising from the various scatterers within the test environment, are outside of this finite region of space.

Generally when characterising an antenna it is installed within the system such that the majority of the current sources are situated about the origin of the range measurement coordinate system so that it is displaced in space as little as possible during the course of a measurement. As range multipath tends to disturb the fields illuminating the test antenna, the purpose of this strategy is to ensure that the field illuminating the test antenna vary as little as possible over the AUT during the course of the acquisition. However the MARS measurement technique adopts a fundamentally opposing strategy whereby the test antenna is deliberately displaced from the centre of rotation. This has the effect of making the differences in the illuminating field far more pronounced than would otherwise be the case, and it is exactly this greater differentiation that makes their identification and subsequent extraction feasible. It has been found that the larger the displacement, the more effective the filtering becomes. That is, until the separation is larger than the maximum dimension of the AUT whereupon the benefits of an increased separation can become negated by the increase in measurement time, the greater constraints of facility alignment, and in the cylindrical or planar cases unnecessary additional truncation.

All forms of MARS processing require the AUT to be offset from the conceptual origin of the measurement coordinate system by a distance at least equal to its largest dimension [24]. This displacement is illustrated schematically in Figure 12.54 for the SNF case. By way of a comparison, Figure 12.53 shows the same AUT located conventionally at the origin of the spherical measurement coordinate system. The conceptual minimum spheres are also shown for each of these cases which are centred about the intersection of the orthogonal θ- and ϕ-axes.

As expounded within the preceding chapters, it can be shown that the electromagnetic fields outside an arbitrary test antenna radiating into free space can be expanded onto a set of elementary orthogonal spherical or cylindrical mode coefficients (CMCs) and that these modes and coefficients can then be used to obtain

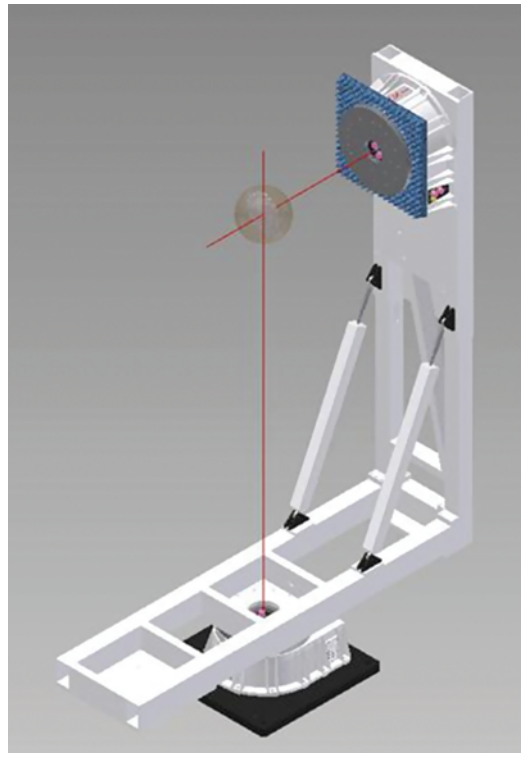

Figure 12.53 AUT measured conventionally at rotation origin with smaller MRE shown

the electric and magnetic fields everywhere in space outside of respectively a conceptual spherical or right circular cylindrical surface which encloses that radiator using modal orthogonality and the principle of linear superposition. The MARS measurement and post-processing technique utilises the classical near-field theory but implements the transformation in a subtly different way so as to be able to orthogonalise those mode coefficients that are associated with the AUT from those mode coefficients that cannot be associated with the AUT. An overview of the generic MARS processing algorithm is described below:

1. Take the two orthogonal tangential electric near-field components and compute the mode coefficients for each polarisation index.
2. Solve for the AUT's unknown mode coefficients using previously computed probe pattern mode coefficients. These mode coefficients are generally obtained from an *a priori* auxiliary probe pattern characterisation and a modal translation integral that places the probe at the measurement radius.
3. Compute the complete far electric field components from mode coefficients.
4. Apply a differential phase change to mathematically translate the AUT back to the origin of the measurement coordinate system.

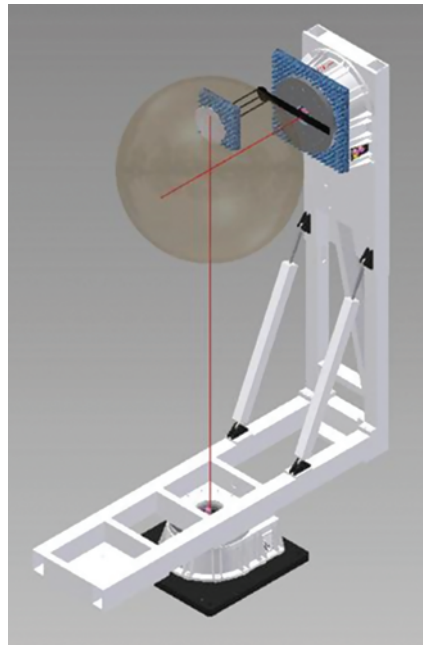

Figure 12.54 AUT measured with offset from rotation origin with larger MRE shown

5. Obtain the translated mode coefficients of the AUT for an AUT conceptually located at the origin of the measurement coordinate system.
6. Apply a two-dimensional mode-filtering function to suppress unwanted mode coefficients where the properties of the filter function are determined from the physical size of the AUT and the free-space propagation number.
7. Compute the complete far electric field pattern from the filtered mode coefficients to obtain the MARS-filtered AUT pattern function. Calculate magnetic fields from the electric fields and the plane wave condition.

Hence the MARS methodology is very closely related to that of the classical near-field measurement and transformation techniques using as it does the standard steps (i.e. steps 1, 2, 3) and merely deploying them in a subtly different way (i.e. step 4 is conventionally used within MHM, step 5 is closely related to step 1 and step 7 is the same as step 3). Thus while it is clear that the details of the modal basis, probe compensation and transformation algorithms will be different for each of the geometries, for any given radiator, the resulting electromagnetic six-vector field outside the respective excluded regions of space must equate *exactly*. The purpose of this section is merely to present an overview of the MARS methodology, with details of the spherical, cylindrical, planar, and far-field MARS implementations presented in the following coordinate system specific sections.

12.3 PNF topics

12.3.1 Bias leakage error

The detection and conversion of the RF signals to real and imaginary or amplitude and phase components within the RF sub-system can introduce a small bias error that imposes a very small constant signal on the recorded amplitude and phases of the near-field pattern. This can arise from a fault within the VNA or receiver; it more commonly arises within distributed RF sub-systems especially those that include imperfectly screened long test and reference cables, or when passing through bulkhead connector panels with a common ground. This signal may be very small, being as much as 50–100 dB below the peak near-field amplitude. However, during the near-field to far-field transform of the data for planar measurements (specifically within the Fourier transform, i.e. the FFT processing), this leakage signal is summed coherently within the integration in the on-axis direction. It is possible to conceptualise this bias leakage comprising a small amplitude plane wave with a size and shape equal to the near-field scan area, and which is propagating in the range z-axis (i.e. in the range boresight direction). In the far-field, for the plane-rectilinear case this corresponds to a two-dimensional Sinc function with its peak at $k_x = k_y = 0$, with trails of side lobes aligned with the cardinal axes. The beamwidth of this Sinc function will be inversely proportional with the scan area implying that for large acquisitions this phenomenon will appear mainly as a 'spike' within the far-field pattern. It can therefore produce a noticeable distortion in the main beam region if the measurement area is much larger than the AUT area. This can have a significant impact on gain measurements as this phenomenon would be present on both the SGH and AUT pattern measurements with the magnitude of the effect being different in each as the scan area of the respective near-field acquisitions would be different. Bias leakage error therefore impacts upon the antenna pattern and measured gain; however relative parameters such as axial ratio are typically unaffected.

The effects of this bias leakage can be minimised in a number of ways. It is possible to set all low values in the near-field pattern to 0 V, i.e. to a large negative value in dB. Alternatively, a far less intrusive and far more effective strategy is to estimate the bias leakage value and then to extract it from all of the measured near-field data points [29]. Fortunately, the amplitude and phase of the bias error can be determined from the data without additional measurements by examining the measured data at the extremes of the measurement area where the pattern amplitude is small. In this region, the pattern data should be dominated by noise (rather than by the antenna pattern) and as such the vector summation of the data will converge to the constant bias error. This can then be subtracted from the measured data thereby suppressing the effect of the bias leakage term.

Figure 12.55 contains a plane rectilinear near-field measurement of an SGH that was acquired at X-band using an older vector network analyser that exhibited an internal bias leakage fault.

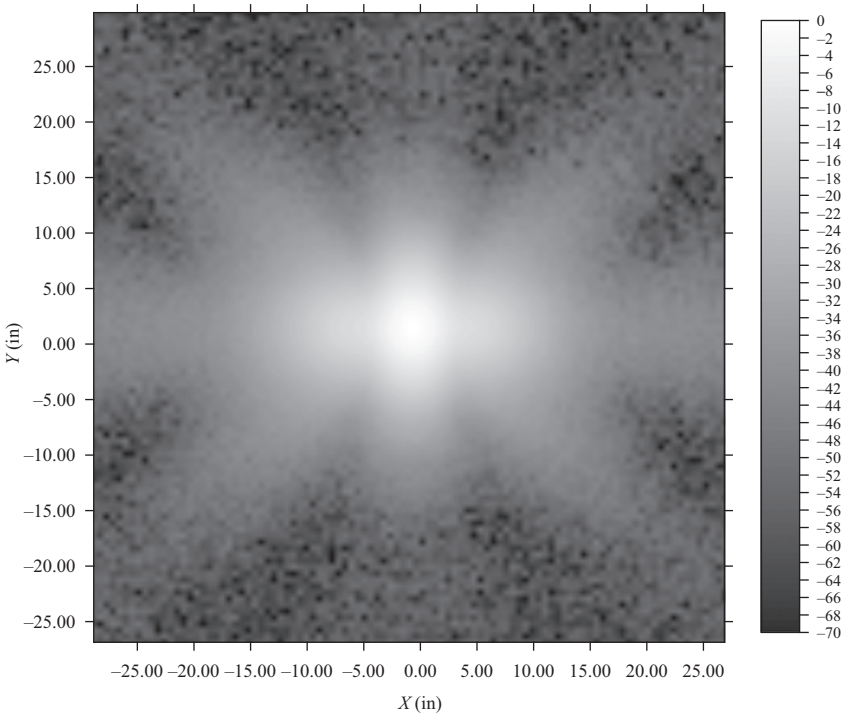

Figure 12.55 Example of a planar near-field measurement of an SGH acquired with an RF sub-system containing a small bias leakage error

From inspection of this near-field dataset, there is no obvious evidence of the bias leakage error as the amplitude of the error is small when compared with the pattern values. However, when the pattern was transformed to the far-field, the bias leakage error became apparent on the co-polar and cross-polar patterns. This can be seen in Figure 12.56 which contains a grey-scale plot of the far-field cross-polar pattern. Here, the bias leakage is visible as a single white pixel at azimuth = elevation = 0°.

From inspection of the near-field pattern, it can be seen that the noise floor of the measurement was circa −50 dB below the near-field peak. The amplitude and phase of the bias error were determined from the near-field pattern data by computing the vector sum of the measured data with amplitudes below −50 dB which converge to the constant bias leakage error. This value was subtracted from the measured near-field before the far-field pattern was recomputed. The resulting bias-leakage corrected far-field cross-polarised pattern can be seen in Figure 12.57.

Figure 12.58 contains a cardinal cut of the cross-polar pattern with and without the bias leakage error correction. Here it is evident that data corrected in this way greatly reduce the effect of the bias error leakage signal. Although the effect on the principal polarised pattern is less pronounced, if accurate gain values are needed,

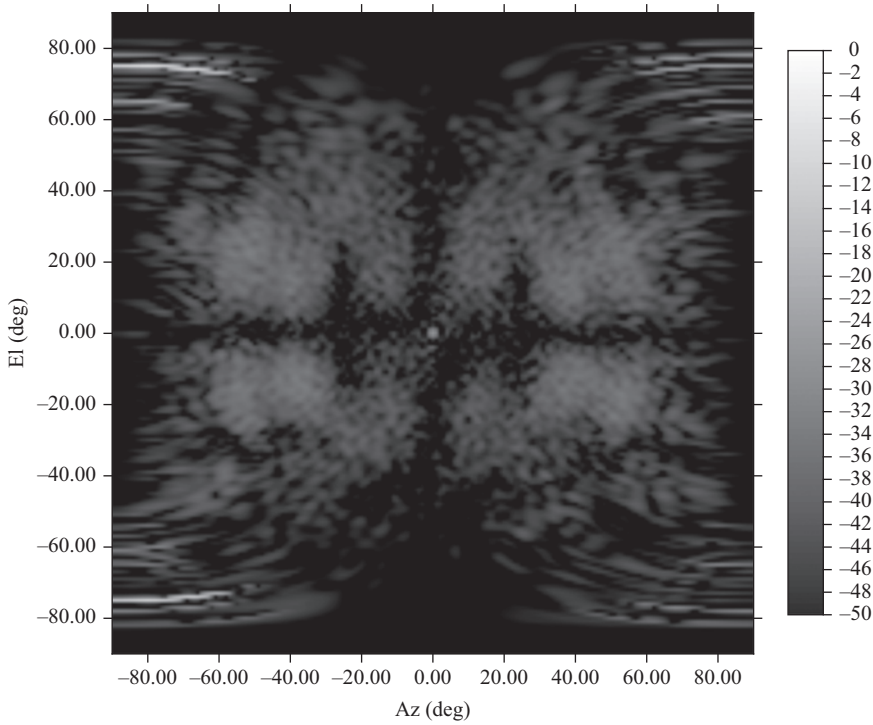

Figure 12.56 Far-field cross-polarised pattern of an SGH exhibiting a bias leakage error

this effect can comprise one of the most significant terms within the facility level uncertainty budget.

Bias error leakage has no effect on spherical data since a constant signal over the sphere does not produce or modify any of the calculated spherical modes. For the case of cylindrical near-field measurements, bias leakage corresponds to a cylindrical wave of height equal to the linear scan axes. This will therefore have an effect in purely the polar axis, as a constant signal over the cylinder will have no effect on the CMCs in the index domain.

12.3.2 Compensation for probe translation effects in dual polarised planar near-field antenna measurements

It is common practice to use a single linearly polarised near-field probe for planar near-field testing of antennas of arbitrary polarisation. During such an acquisition two orthogonally polarised datasets are measured. In keeping with the original near-field formulation that requires the use of two distinct probes, this is achieved by simple polarisation rotation of a single probe. These two orthogonal datasets are then independently processed to obtain probe-corrected far-field radiation pattern

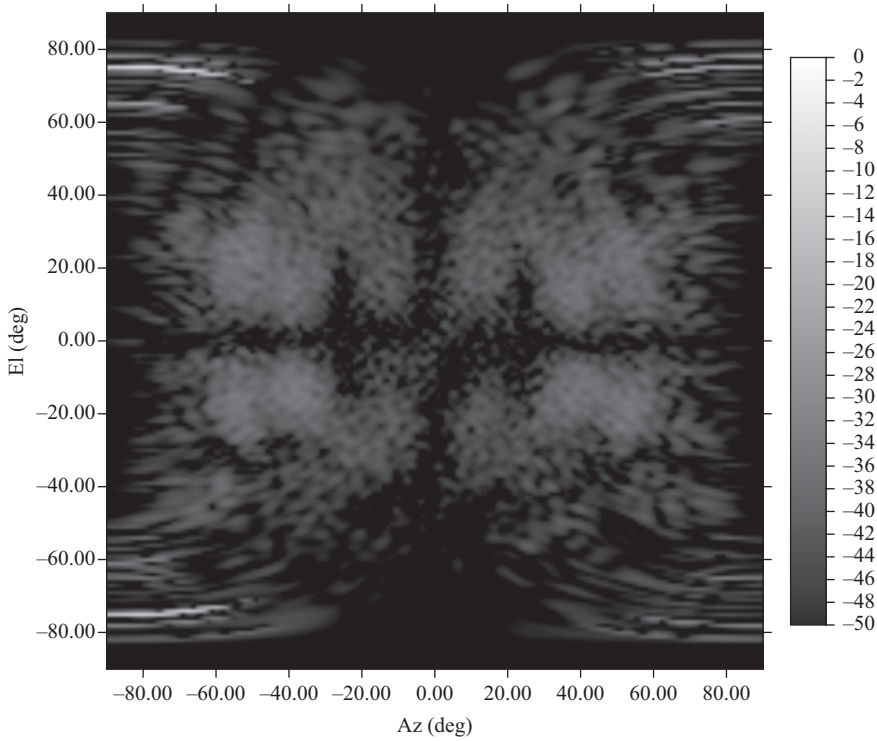

Figure 12.57 Far-field cross-polarised pattern of an SGH after correction of bias leakage error

information and can be combined to form slant linear or circular polarisation, depending on the polarisation definition required. This polarisation processing assumes only rotation of the probe and any translation (which is due to mechanical misalignment of the probe *z*-axis with respect to the axis of rotation) is usually neglected. For many low-frequency applications, i.e. lower than 40 GHz, this is a reasonable assumption and compensation is not required. However, for higher frequency applications the physical size of the probe makes mechanical alignment more challenging and when that probe is attached to a bulky millimetre-wave RF module, as illustrated in Figure 12.59, the alignment of the entire assembly becomes very challenging. Typically, the millimetrewave modules are installed on the polarisation stage, as shown here, as high-frequency RF rotary joints are not commercially available, and waveguide rotary joints tend to be prohibitively expensive and frequency band limiting.

However, mechanical alignment of the probe axis to be orthogonal to the scan plane is not as challenging and of less importance to the resulting far-field antenna pattern measurements since most rectangular OEWG probes have very broad radiation patterns, thus a slight non-orthogonality can be tolerated. This assumption is therefore not regarded as overly restrictive, but should be noted nonetheless.

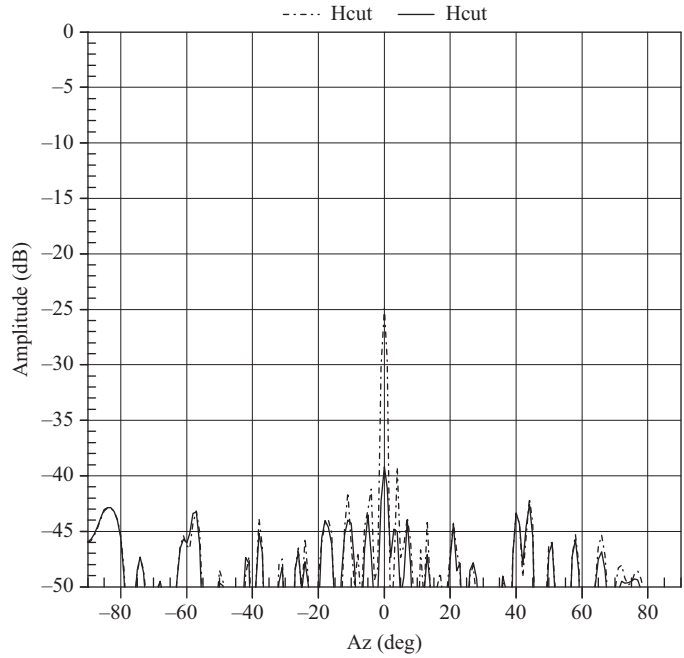

Figure 12.58 Far-field cross-polarised pattern of an SGH showing the effect of bias leakage correction. Dashed trace is before correction and the solid trace is after correction

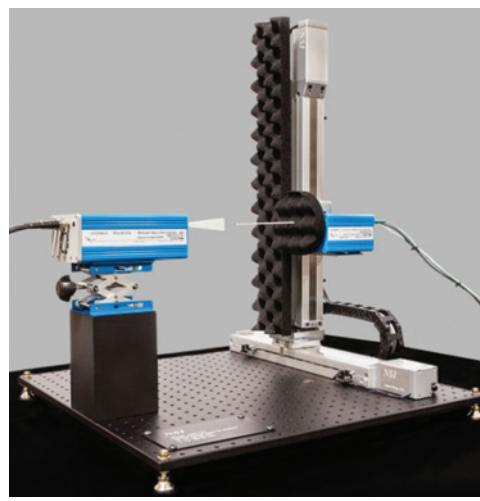

Figure 12.59 Typical near-field probe millimetrewave hardware and fixturing mounted on a planar near-field scanner (Picture courtesy of NSI-MI Technologies LLC)

Figure 12.60 depicts the typical probe translation observed during rotation from polarisation position #1 (Pol = 0°) to polarisation position #2 (Pol = 90°), where the axis of rotation is the *z*-axis. Measurement of the depicted offset distances defines vector $\underline{T} = \Delta x\hat{x} + \Delta y\hat{y}$ and therefore allows for compensation of the probe translation [30]. It is important to realise that although Figure 12.60 depicts the simple case of the probe being intersected by the *x*- and *y*-axes at the respective polarisation orientations, this is not true in general and in such cases $\Delta x \neq \Delta y$.

In Figure 12.61 the measured near-field intensity is shown for a CP horn antenna, measured with a linearly polarised (LP) open-ended rectangular

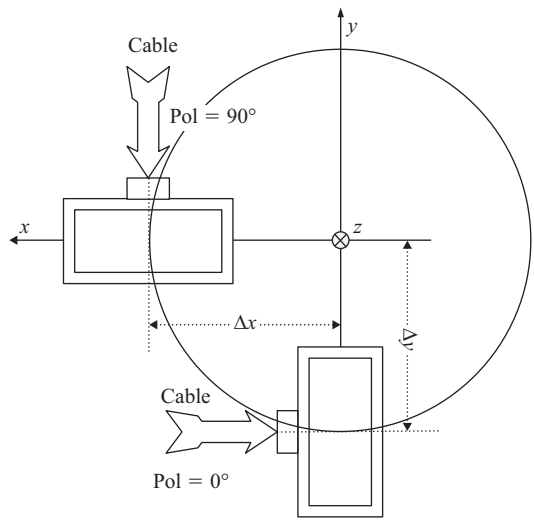

Figure 12.60 Probe translation from Pol = 0° position to Pol = 90° position

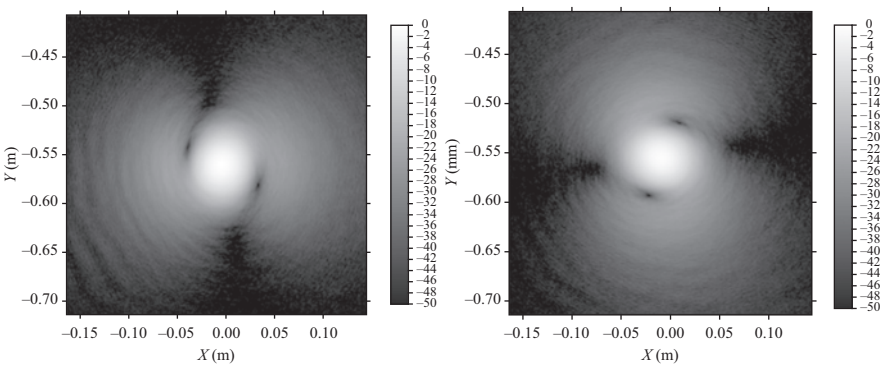

Figure 12.61 Near-field intensity for circularly polarised antenna measured with linearly polarised probe. T = 4 mm (x) – 4.5 mm (y). Dynamic range shown is 50 dB

waveguide probe at 94 GHz. In this instance Δx and Δy were measured mechanically and determined to be $\Delta x = 4$ mm (1.25 λ) and $\Delta y = -4.5$ mm (1.4 λ). Compensating for this probe translation distance, one obtains the far-field results depicted in Figure 12.62 (co-polarised) and Figure 12.63 (cross-polarised). Both these images also show a reference pattern, where a probe translation of less than 1 mm was present during polarisation rotation.

It is clear in this comparison what the impact of the correction is and that the reference pattern can be recovered with reasonable fidelity. As a second test case the same antenna was measured at 94 GHz but with an increased probe translation error of $\Delta x = 2.5$ mm (0.8 λ) and $\Delta y = -9.5$ mm (3 λ). Compensating for this probe translation distance was less successful and a sensitivity analysis indicated that the accuracy of the measured distances was insufficient. This fact again highlighted that this process becomes challenging if probes are physically small, and a self-calibrating technique that avoids recourse to cumbersome mechanical calibration has obvious benefits.

A highly effective, electrical self-comparison method can be employed to deduce the physical offsets. The method requires the near-field probe of interest and the AUT to be mounted and nominally aligned before performing a full

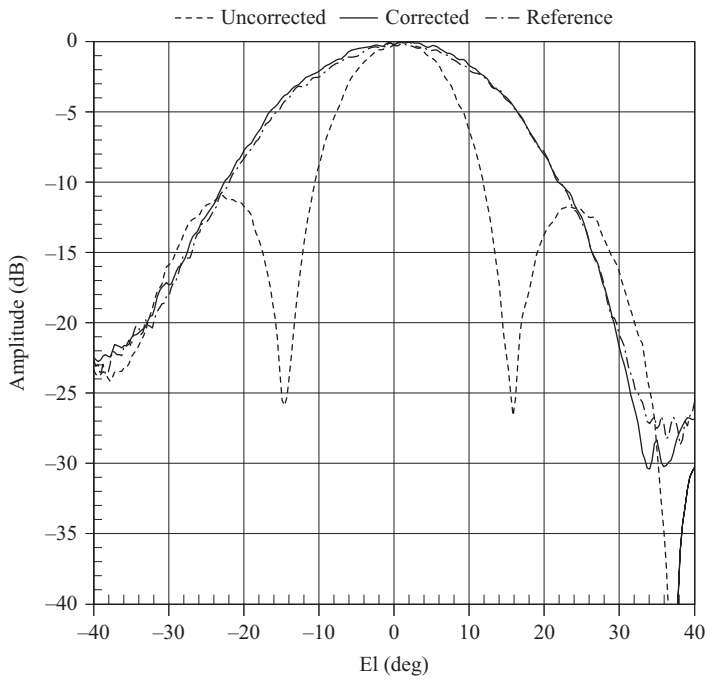

Figure 12.62 Elevation plane co-polarised patterns for 94 GHz CP horn: original uncorrected data (dashed curve); corrected (solid line); reference data (dashed-dot line). T = 4 mm (x) – 4.5 mm (y)

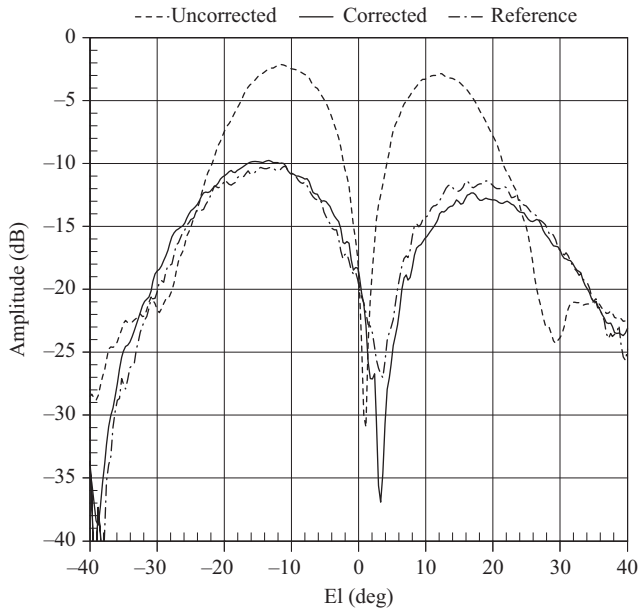

Figure 12.63 Elevation plane cross-polarised patterns for 94 GHz CP horn. Original uncorrected data (dashed line), corrected (solid) and reference data (dashed-dot line). T = 4 mm (x) – 4.5 mm (y)

near-field acquisition with the near-field probe polarisation positions 0° and 90° as depicted in Figure 12.60. Upon completion, far-field data can be calculated and a phase reference pattern extracted for both the horizontal (azimuth) and vertical (elevation) cardinal cuts can be computed. The measurement is then repeated, but in this second instance the near-field probe polarisation positions are set to 180° and 270° relative to that depicted in Figure 12.60. Using this second dataset, far-field data can again be extracted and respective phase reference patterns can again be computed. Comparison of these two sets of phase references (where the second set has to be phase reversed due to the inversion of the near-field probe) now provides a direct measure of the probe translation in Δx and Δy. The determination of the displacement vector $\underline{T}$ is illustrated using the example of a high-gain rectangular planar array antenna.

In the following example, probe translation values of $\Delta x = \Delta y = 3$ mm (0.23 λ at 23.25 GHz) were introduced as a controlled test distance. The test setup is shown in Figure 12.64 and the AUT was a linearly polarised (LP) slotted waveguide array, resonant at 23.25 GHz. The antenna was measured with a linearly polarised (LP) open-ended rectangular waveguide probe.

Transforming this data to the far-field, one obtains the data shown in Figure 12.65 (azimuth pattern) and Figure 12.66 (elevation pattern). In Figure 12.65 (overlay – dashed curve) and Figure 12.66 (overlay – dashed curve), the far-field data is obtained for the near-field probe positions 180° and 270°. The

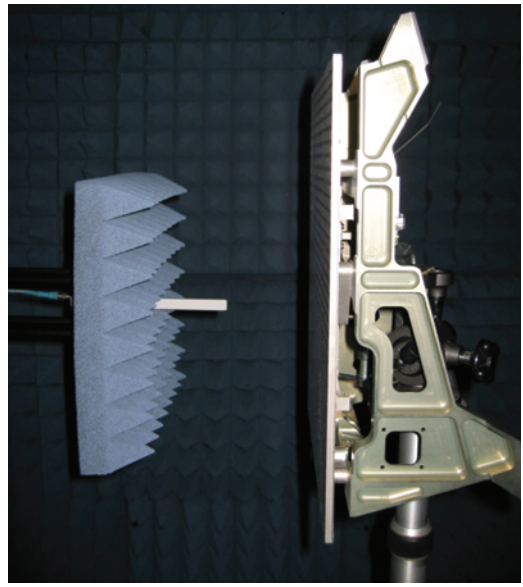

Figure 12.64 Linearly polarised slotted waveguide array measured with an open-ended waveguide probe

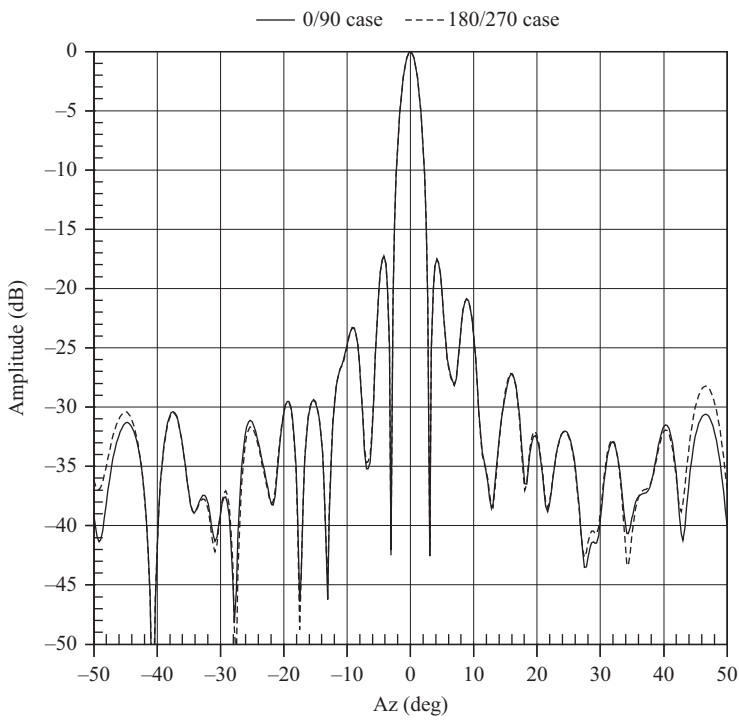

Figure 12.65 Azimuth linearly polarised co-polarised patterns: probe position 0/90 data (solid line) and probe position 180/270 data (dashed line)

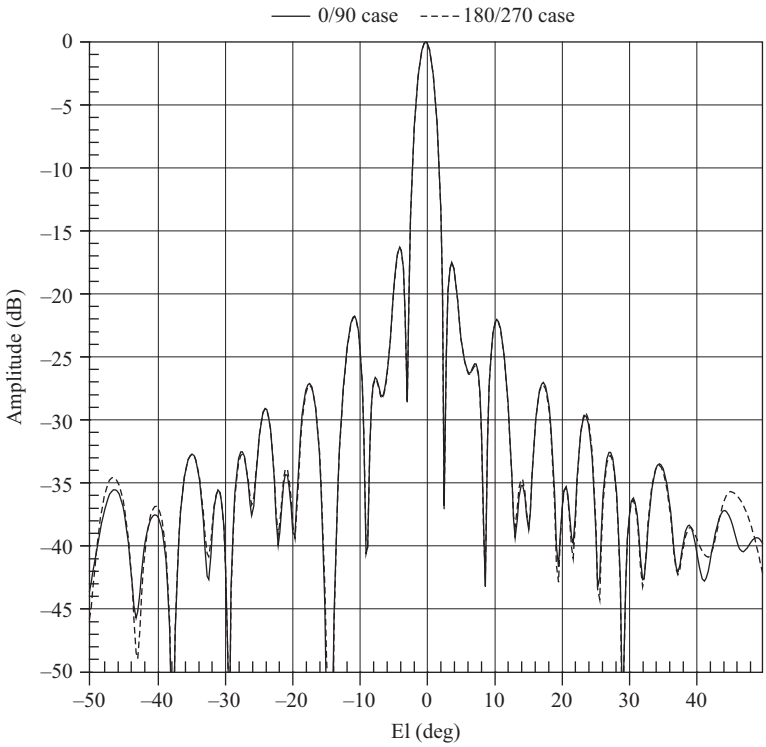

Figure 12.66 Elevation linearly polarised co-polarised patterns: probe position 0/90 data (solid line) and probe position 180/270 data (dashed line)

results clearly show no significant difference (despite the near-field probe translation).

However, when comparing far-field phase data, the effect of the probe translation is clear and is shown in Figure 12.67. This behaviour is a direct consequence of the shifting property of the Fourier transform.

Only the azimuth patterns are shown, but the elevation patterns display the same phase offset. The difference between the two phase functions is also shown and although this appears to be a linear function it is actually sinusoidal with respect to the azimuth angle, the function would be linear if the pattern were tabulated using a regular direction cosine coordinate system. This phase difference can be converted to a linear physical offset Δx using

$$\Delta x = \frac{\lambda \Delta \text{Phase}}{2\pi \sin\theta} \tag{12.75}$$

An analogous expression can be obtained to compute the value of Δy. Figure 12.68 shows the function obtained as well as an average value for Δx in mm (2.98 mm). Repeating this process for the elevation plane results in an average value for Δy in mm (3.04 mm) as shown in Figure 12.69. Both values closely resemble the

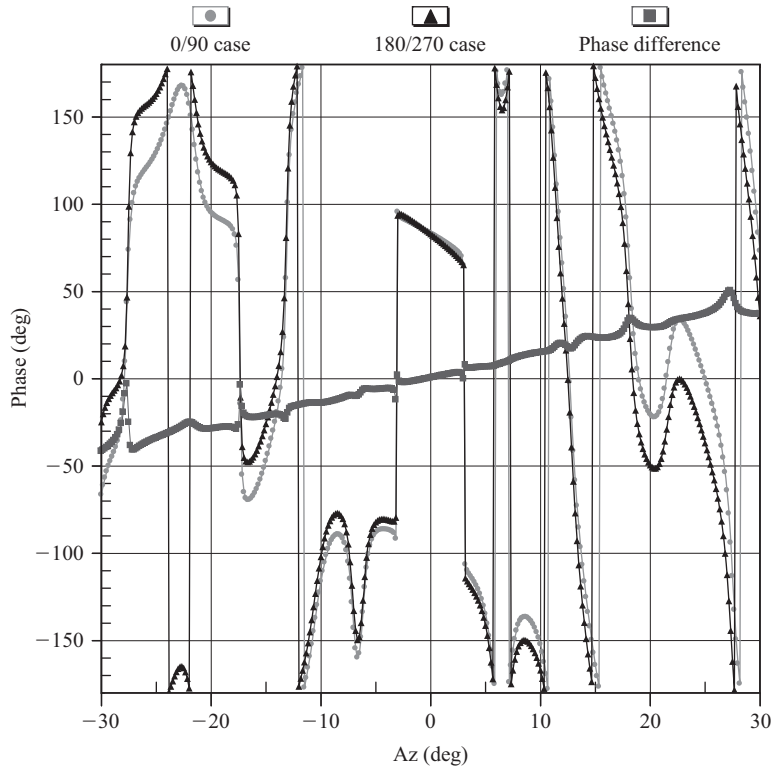

Figure 12.67 Far-field azimuth pattern phase data comparison showing the 3 mm probe translation effect

actual (mechanically measured) probe offset values of $\Delta x = \Delta y = 3$ mm. Using these values for correction of the probe translation, the azimuth and elevation phase patterns in Figures 12.70 and 12.71 are obtained. The original uncorrected data, the corrected data and the reference data is shown. The technique compensates successfully for the probe translation in both planes and one is able to recover the far-field phase.

This data therefore confirms that calculation of a phase reference position based on two near-field acquisitions can provide a measure of the near-field probe translation vector $\underline{T}$ without making any mechanical measurement. This type of calibration can be performed at a *single* frequency once a near-field probe has been mounted and the information can then be used for all subsequent measurements at *all* frequencies to correct for the probe translation.

The significance of this correction is that with the growing number of millimetrewave applications and the bulk of millimetrewave hardware directly attached to the near-field probe carriage, probe alignment becomes increasingly difficult and this method provides a highly effective and convenient way to correct for such anomalies. With ever decreasing wavelength, satisfactory mechanical alignment

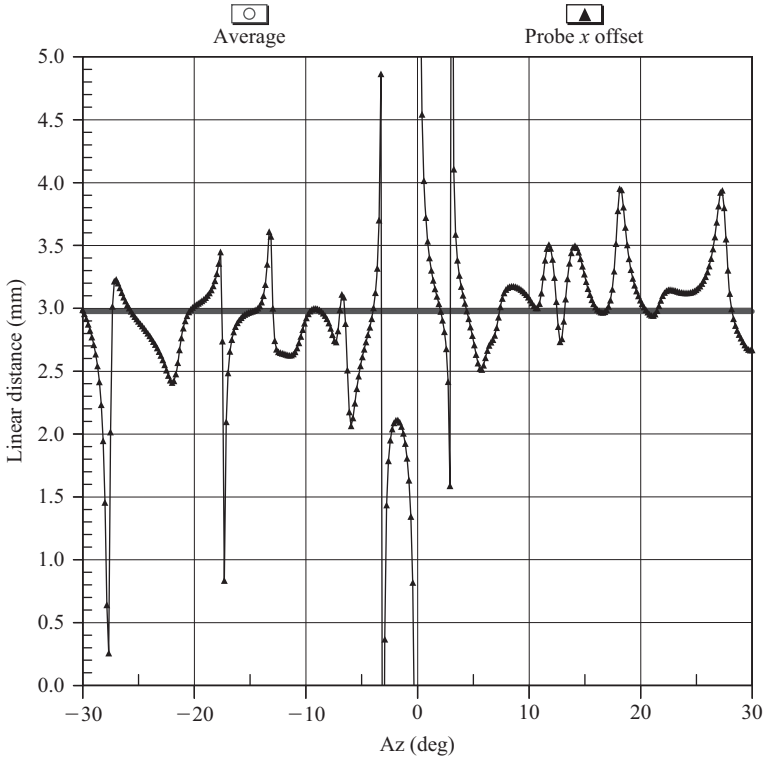

Figure 12.68 Probe offset Δx calculated from the phase difference function in Figure 12.67 – an average value of 2.98 mm

may ultimately become unfeasible and this technique provides a way to overcome this problem.

12.3.3 Introduction to phase-less near-field antenna measurements

The phase-retrieval problem arises in applications of electromagnetic theory in which wave phase is apparently lost or is impractical to measure and only intensity data is available. The experimenter can be faced with this difficulty when testing at high frequencies where RF instrumentation becomes prohibitively expensive and phase stability renders phase information unreliable, or when testing active antenna assemblies where direct access to the RF source is not possible. In the latter case, it is sometimes possible (although perhaps not convenient) to use a reference antenna that is in the same inertial frame of reference as the test antenna to obtain a phase reference. However, in cases where this is not convenient, or even possible, recourse to phase-retrieval techniques becomes unavoidable. The near-field methodology, as developed within the preceding chapters, requires holographic measurements to be made. In other words, in order that the respective modal expansions

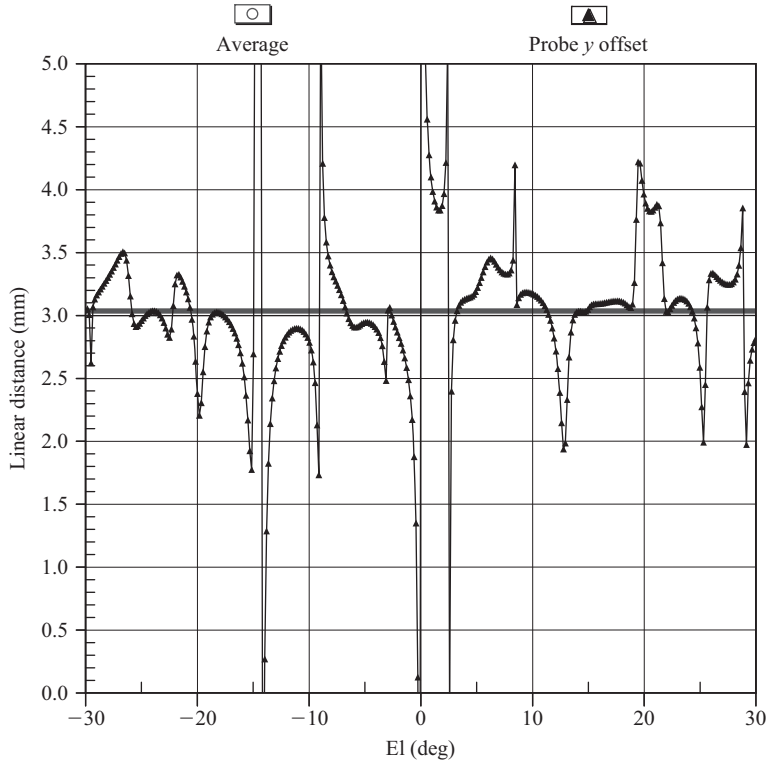

Figure 12.69 Probe offset Δy calculated from the phase difference function in the elevation plane – an average value of 3.04 mm

can be obtained, knowledge of both the amplitude and phase of the measured field must be available.

Many alternatives are available for recovering the phase from amplitude-only measurements. However, in the following sections only iterative computational phase-retrieval algorithms are discussed as these are typically the most readily implemented experimental arrangement and are therefore the approach that is most often encountered within the antenna measurements community. The following iterative phase recovery strategy has been implemented using planar (rectilinear, polar, bi-polar) and spherical near-field data. Although the exact details of the processing algorithm varies according to the measurement geometry concerned, the basic underlying technique remains unchanged and as such the following planar example can be translated to other measurement geometries. As the plane rectilinear near-field test systems are most commonly employed when testing high-frequency (and therefore most often high gain) antennas, this is the example that will be developed below.

The plane-to-plane (PTP) phase recovery algorithm essentially entails taking two amplitude-only measurements over parallel planes in the near-field of the test antenna that are separated by a known distance as illustrated in Figure 12.72.

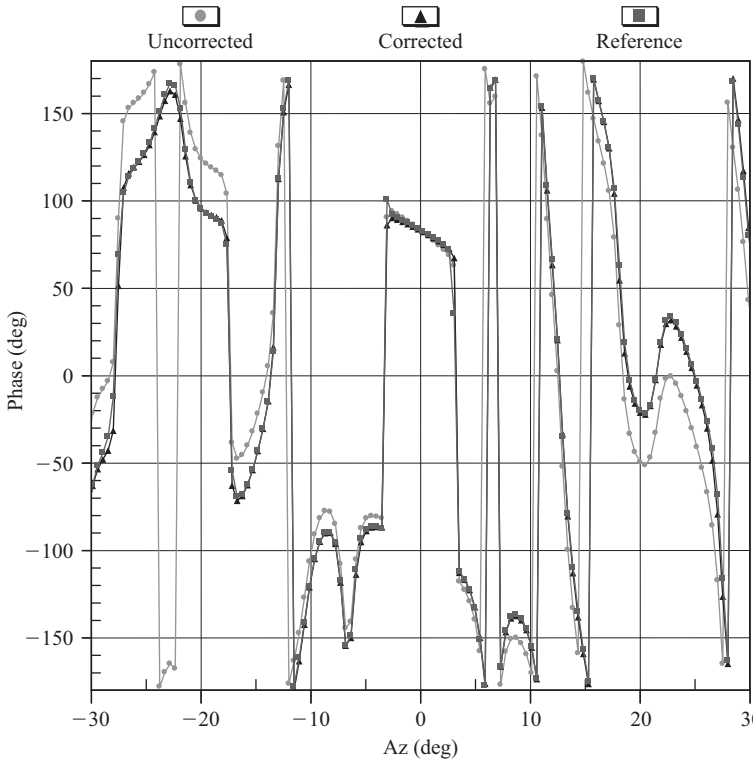

Figure 12.70 Far-field azimuth phase data comparison demonstrating the $\underline{T}$ = 2.98 mm (x) + 3.04 mm (y) probe translation correction

Essentially, we are using the plane-to-plane transform as used for MHM, developed above, to calculate the field over one plane in space from knowledge of that field over another plane in space. Now as was shown above, the angular spectrum and the boundary conditions, i.e. the measurement, are related to one another through the Fourier relationship

$$F(k_x, k_y) = \Im\{E(x, y, z = 0)\} = \int_{-\infty}^{\infty}\int_{-\infty}^{\infty} E(x, y, z = 0)e^{j(k_x x + k_y y)}dx\,dy \tag{12.76}$$

and

$$\begin{aligned} E(x, y, z) &= \Im^{-1}\left\{F(k_x, k_y)e^{-jk_z z}\right\} \\ &= \frac{1}{4\pi^2}\int_{-\infty}^{\infty}\int_{-\infty}^{\infty} F(k_x, k_y)e^{-j(k_x x + k_y y + k_z z)}dk_x\,dk_y \end{aligned} \tag{12.77}$$

Again, the nomenclature established in Chapter 6 has been adopted. Thus, if the field is known over one plane, which can be defined to be at $z = 0$, then the field

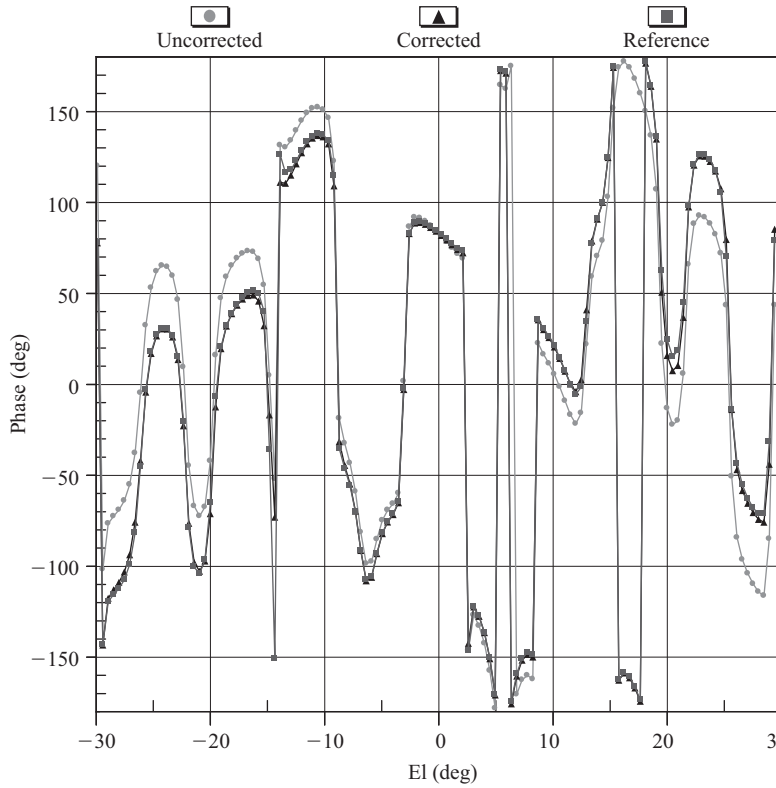

Figure 12.71 Far-field elevation phase data comparison demonstrating the $\underline{T} = 2.98$ *mm (x) + 3.04 mm (y) probe translation correction*

Figure 12.72 Measurement configuration of the PTP algorithm

over another parallel plane, i.e. the plane-to-plane transform, can be expressed as

$$E(x,y,z) = \Im^{-1}\left\{\Im\{E(x,y,z=0)\}e^{-jk_z z}\right\} \tag{12.78}$$

Here, as only knowledge of the propagating field is known, the limits of integration in the spectral domain are truncated to visible space to prevent the translated fields becoming swamped by exponentially increasing reactive fields. This equates to imposing a filter function on the spectral field components which removes all evanescent components. As these components decay exponentially away from the aperture, then as the field is propagated towards the aperture, they will exponentiate and could cause the algorithm to become unstable. In practice as the measurements are made outside the reactive near-field region, fields in invisible space will only enter into the algorithm through, e.g. numerical noise, AUT-to-probe multiple reflections. Using this plane-to-plane transform that can be implemented very efficiently using the FFT, the plane-to-plane phase-retrieval algorithm can be described as follows:

1. Measure the amplitude of the field over plane 1.
2. Measure the amplitude of the field over plane 2.
3. Use PTP transform to propagate the AUT aperture fields to plane 2 from plane 1. For the first iteration, i.e. as an initial guess, we assume that the phase is zero everywhere across plane 1. If the antenna is an electronically scanned array, then applying a linear phase taper to the phase function that corresponds to the direction of the scanned main beam direction can constitute a better initial guess for that case.
4. Replace the amplitude estimation at plane 2 with the measured amplitude at plane 2. Retain the phase function.
5. Use PTP to propagate the fields back to plane 1.
6. Replace the amplitude estimation at plane 1 with the measured amplitude at plane 1. Retain the phase function.
7. Repeat steps 3 to 6 until amplitude on plane 1 (or plane 2) has converged to within a prescribed tolerance.
8. Transform the fields to the far-field using standard near-field to far-field algorithm.

Figure 12.73 contains example plots of the measured amplitude taken across two parallel planar surfaces with a separation between the AUT and the probe of $z = 0.105$ m and $z = 0.235$ m, respectively, taken at millimetrewave frequencies.

In order to keep the relative pattern truncation constant between the two measured planes, the plane which is further from the AUT is, ideally, specified to be slightly larger than the nearer plane. However, in practice due to the physical constraints of the finitely large scanning positioning system, these two planes are often the same size. These amplitude patterns can be used with the plane-to-plane phase-retrieval algorithm as described above to reconstruct the associated phase-patterns. When the phase-retrieval algorithm has converged sufficiently, the measured amplitude and reconstructed phase functions can be transformed to the

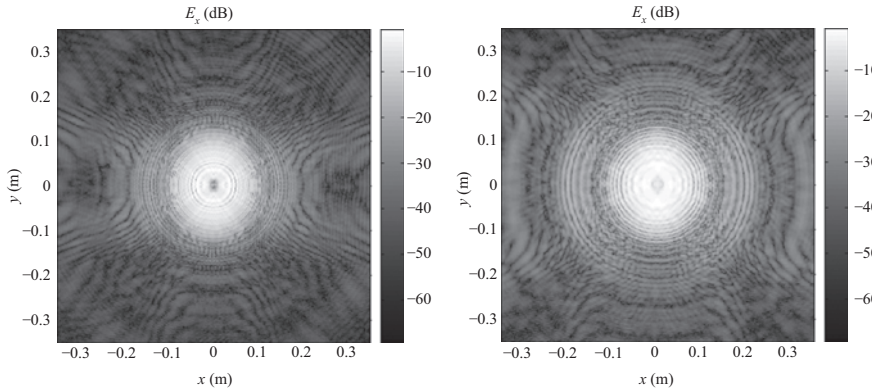

Figure 12.73 Near-field measurements taken over two different parallel planes

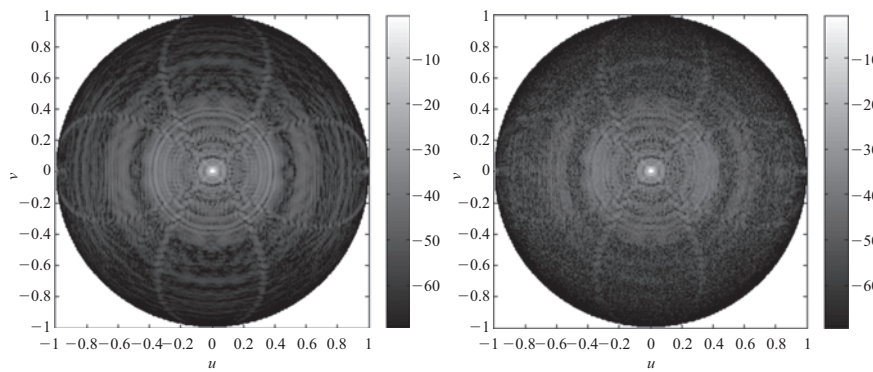

Figure 12.74 Comparison of angular spectrum obtained through direct measurement and phase-retrieval

angular spectrum. Figure 12.74 contains a comparison of the angular spectra obtained from a direct holographic measurement and from the plane-to-plane phase-retrieval algorithm. The figure on the right was derived using retrieved phase function.

Clearly, the angular spectra as recovered by conventional amplitude and phase, i.e. coherent, measurements agree with those obtained from phase recovery. However, the phase-retrieval patterns clearly contain a greater amount of speckle noise indicating a reduced SNR. This can perhaps be seen more in Figure 12.75 which contains cardinal cuts of the respective patterns together with the EMPL. Although the cuts agree, the impact of the noise is clearly illustrated in the EMPL that is perhaps as little as 20 dB below the pattern functions out to ~$\pm 25^\circ$ ($u = v = \pm 0.4$) and then less beyond this angular region.

Figure 12.76 contains the reconstructed aperture illumination function of the antenna as recovered from the coherent, amplitude and phase, measured data.

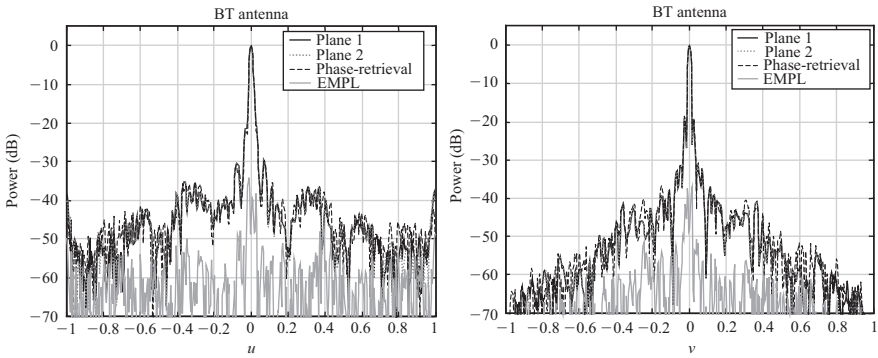

Figure 12.75 Measured and phase recovery

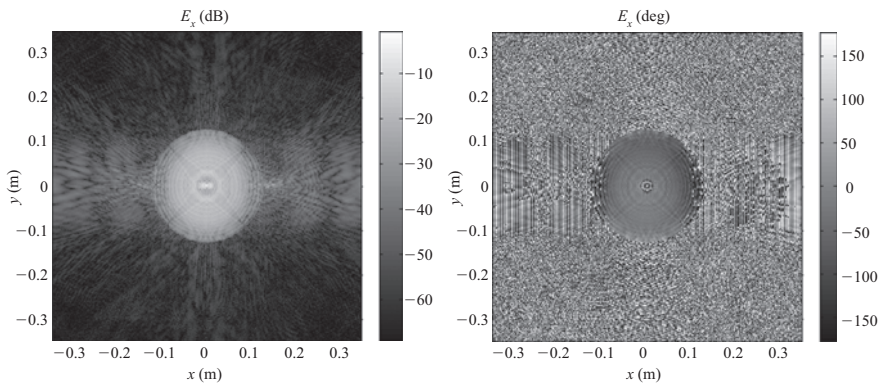

Figure 12.76 Aperture illumination function derived from coherent measurement. Amplitude is shown on the left and phase on the right

Conversely, Figure 12.77 contains the reconstructed aperture illumination function as recovered from the amplitude-only measurement and an application of the iterative plane-to-plane algorithm. Although encouraging, to obtain results with this limited degree of agreement took circa 20,000 iterations of the plane-to-plane phase recovery algorithm. In general, as the separation between the two measurement planes is increased the convergence rate increases, as the difference between the respective patterns is more significant; however the additional separation also increases truncation within the measurement system that will inevitably degrade the quality of the measurements. Clearly maintaining good alignment between the measurements is crucial to the success of the technique. The convergence rate of this algorithm is clearly very slow and an alternative algorithm with a faster rate of convergence is highly desirable. This therefore is the motivation for the inclusion of an aperture constraint that is currently the most widely used form of the phase recovery technique as it converges 100 times more rapidly [31]. However this efficiency is

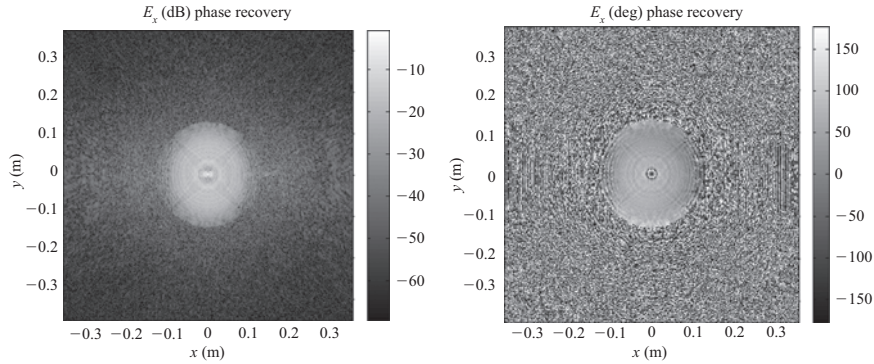

Figure 12.77 Aperture illumination function derived from coherent measurement and amplitude-only measurement. Amplitude is shown on the left and phase on the right

brought at the expense of having to impose an aperture constraint that, depending upon the exact characteristics of the AUT, may be limited in its applicability.

The concept of taking two amplitude-only measurements on sampling intervals in different regions of space can clearly be applied to cylindrical and spherical geometries with the spherical case having the distinct advantage that in principle the measured data need not suffer from errors associated with truncation. However the large number of surface-to-surface propagations, circa tens of thousands, render the computational effort significant, which perhaps explains why these implementations have been developed only comparatively recently.

12.3.4 Planar mathematical absorber reflection suppression

Due to the finite size of the planar sampling interval and thus the necessity to characterise primarily directional antennas, range multipath effects have typically been considered to be of lesser importance in planar than in the corresponding cylindrical, spherical or far-field measurement techniques. Clearly, the directional nature of the higher gain antennas that are generally tested using planar systems results in the region of greatest field intensities being concentrated on the parts of the chamber situated immediately behind the scan plane and on the scanning robot itself. As a result of cost considerations, it has become widespread practice to concentrate the placement of absorbent material around the scanner itself, leaving, in some cases, much of the remainder of the chamber uncovered. Thus in some circumstances multiple reflections within the chamber can become significant, especially when measuring lower directive antennas exhibiting broader patterns or low cross-polar patterns.

Typically, unwanted reflections are suppressed through the use of electromagnetic absorbing material, which tends to be costly, bulky and delicate, and can shed carbon dust. This absorber is usually shaped specifically so that its performance is optimised for use over a specific range of frequencies which necessarily

render it less effective outside the designated frequency band. While considerable effort is devoted to optimising the design and placement of this absorber, it is not possible to place the material everywhere, and some surfaces such as linear bearings, lighting, and closed circuit cameras are inevitably left exposed. As is always the case, any electromagnetic absorber which is used cannot be perfectly matched to fields incident from all directions, polarisations, and frequencies. Thus in some cases the resulting scattering can impede the measurements taken therein.

As presented within the preceding chapters, near-field methodologies require that far-field antenna parameters such as pattern, gain, directivity, and polarisation be derived analytically from measurements taken over a convenient smooth surface in the near-field of a radiator. For such parameters, which cannot be obtained directly from measurements made in the near-field, a transformation from one surface to another is necessitated. This transformation, of monochromatic but otherwise arbitrary waves, can be accomplished by representing the field at an arbitrary point in space as a summation of any elementary wave solutions to Maxwell's equations. Here, the mode coefficients to these solutions are determined by matching the fields over the surface on which the fields are known and by using mode orthogonality. Solving this modal expansion for the fields over the surface of a sphere with an infinite radius centred about the AUT results in the far-field pattern. A degree of mathematical convenience can be obtained from selecting a modal basis that is commensurate with the measurement geometry, i.e. by utilising plane waves, cylindrical waves or spherical waves respectively for the case where the measurements are taken over planar, cylindrical, or spherical surfaces. However, outside of the excluded regions, and as a consequence of the uniqueness principle, it is possible to equate the fields and thus express one mode set in terms of another. Here, the excluded region is that portion of space for which the spherical, cylindrical, or planar expansions are *not* valid. For the spherical case this corresponds to a spherical volume that is centred about the origin of the measurement coordinate system that has a radius large enough to enclose the majority of the current sources. For the cylindrical cases the excluded region corresponds (analogously) to a right cylinder of infinite length that is centred about the origin of the measurement coordinate system that again has a radius large enough to enclose the majority of the current sources. Conversely for the planar case, it corresponds to the half space that contains the radiator. While the mode sets can be equated in almost any homogeneous linear isotropic source or sink-free region of non-excluded space, by virtue of the simplification afforded by the commonality of coordinate system and polarisation bases it is perhaps most convenient to equate electric or magnetic far-fields. As near-field measurements are taken outside the reactive near-field region, and as such evanescent fields are not sampled, choosing the far-field for this transformation of mode bases imposes no additional assumptions, approximations or limitations. It is therefore possible to obtain cylindrical and/or spherical mode coefficients (SMCs) from planar near-field measurements thereby extending the possibility of applying the highly sophisticated and well-developed mode-spectrum-filtering techniques directly to the planar near-field methodology. This is a very attractive proposition as the success of such measurement and mode-

filtering techniques has been attested across a wide range of frequencies on numerous different antenna measurement systems and antenna types. The remainder of this section develops techniques for accomplishing this and illustrates the effectiveness of the planar MARS technique.

As developed above in the preceding sections, all forms of MARS processing require the AUT to be offset from the origin of the measurement coordinate system by a distance at least equal to its largest dimension. While it is clear for the cylindrical and spherical cases where the origin is, for the planar case this can at first appear to be less instantly apparent. The translation of origins that is required by MARS is identical to that which is required with reconstructing an antenna aperture illumination function. Thus

- for P-MARS, the displacement is the distance between the tip of the probe and the antenna aperture plane;
- for C-MARS, the displacement is the distance from the ϕ-axis to the centre of the antenna aperture plane;
- for S-MARS, the displacement is the distance from the intersection of the θ- and ϕ-axes to the centre of the antenna aperture.

This is illustrated schematically in Figure 12.78 which contains a combination of planar, cylindrical, and spherical near-field antenna test system. Thus, although conceptually the translation is identical between various geometries, in implementation and the definition it does differ subtly.

In principle, it is possible to obtain spherical mode coefficients (SMCs) or CMCs from the plane wave spectrum (PWS), thereby providing two mathematically independent formulations of the P-MARS processing. Both methods are treated in the remainder of this section; however we start by considering the cylindrical mode case first.

It has been shown earlier that it is possible to obtain probe pattern-corrected far-fields directly from planar near-field measurements on an azimuth over elevation coordinate system, by carefully selecting the direction cosines. The angular spectrum can be obtained directly from the sampled tangential near-field components using

$$\underline{F}_T\left(k_x, k_y, z = 0\right) = \int_{-\infty}^{\infty}\int_{-\infty}^{\infty} \underline{E}_T(x, y, z = 0) e^{j\left(k_x x + k_y y\right)} dx\, dy \tag{12.79}$$

Here, $\underline{E}_T$ denotes the two tangential orthogonal sampled near-field components, $k_x = k_0 \sin(az) \cos(el)$, $k_y = k_0 \sin(el)$, $k_z = k_0 \cos(az) \cos(el)$, where *az* and *el* are used to denote the azimuth and elevation angles respectively, and k_0 is the free-space propagation constant. In practice, this can be evaluated efficiently without recourse to approximation by implementing the two-dimensional integration as a series of *y*-axis one-dimensional integrations, before integrating this result as a series of one-dimensional *x*-axis integrals. Generally the measured spectral components are corrected for the directive and polarisation properties of the near-field probe and a detailed discussion of this is presented in Chapter 6 and in [32]. The

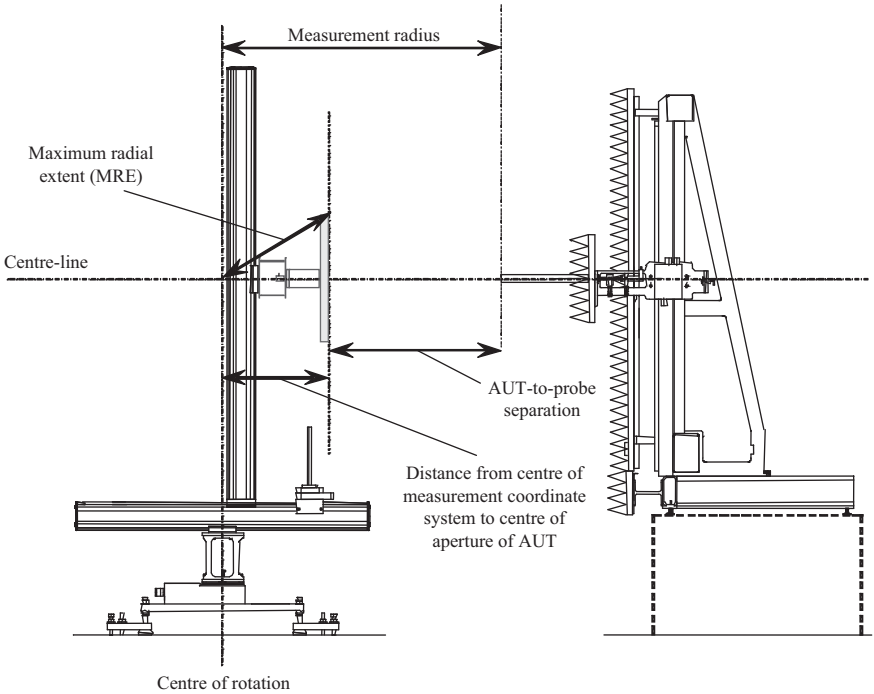

Figure 12.78 Extension of MARS to the planar geometry. S-MARS and C-MARS displacement compared with P-MARS displacement

propagating far-electric field can be obtained from the tangential angular spectra using the method of stationary phase and the plane wave condition

$$\underline{E}(k_x, k_y) \approx j\frac{e^{-jk_0 r}}{\lambda r}\frac{k_z}{k_0}\left[\underline{F}_T(k_x, k_y) - \frac{\underline{k_T} \cdot \underline{F_T}(k_x, k_y)}{k_z}\hat{\underline{e}}_z\right] \tag{12.80}$$

As all three Cartesian components of the far-electric field are known, it is a trivial matter to resolve these fields onto a Ludwig II azimuth over elevation polarisation basis. See appendices for a detailed treatment of the transformation of polarisation bases. An azimuth over elevation system has been chosen, since it has been shown previously within Chapter 7 that the equivalent CMCs can be obtained from this data through a simple inverse Fourier transform. Thus it is possible to obtain CMCs from a planar near-field measurement without approximation. Figure 12.79 contains a grey-scale plot of the amplitudes of the CMC modes for $s = 1$, i.e. B^1, from a planar measurement of an X-band SGH.

From inspection of Figure 12.79 it can be seen that there are significant amounts of power distributed across a wide range of CMCs. However it is clear that

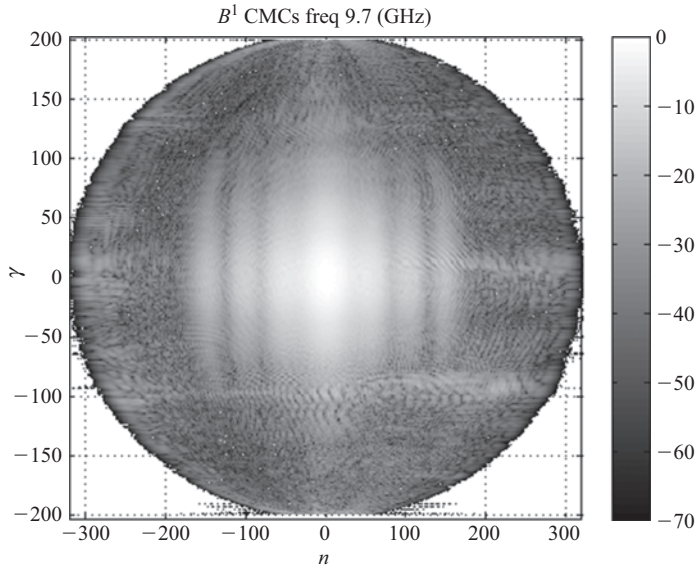

Figure 12.79 CMC amplitudes (dB) calculated from planar near-field measurement

there is very little power contained in modes outside the circle of radius $n^2 + (\gamma a)^2$ where a represents half the scan width of the planar near-field measurement. It is worth stating explicitly that this effect was *not* imposed by any conscious filtering of the CMCs, but rather is a natural consequence of the measurement process itself. Thus the larger the planar sampling interval, the higher the order of CMC that can be reconstructed from that dataset. Here, $n_{\max} = k_0 a = 203.2 \times 1.53 = 311$. For the cases of spherical and cylindrical near-field measurements, the highest order mode index is related to the MRE of the measurement. Thus as the AUT is displaced away from the origin of the measurement coordinate system, the highest order mode index increases proportionally with the MRE. For the planar case, the origin of the measurement coordinate system is usually defined as being the centre of the aperture of the scanning probe when in the centre of the scan plan (this can be dependent upon the phase reference used during the auxiliary probe pattern calibration). Thus for P-MARS it is the AUT-to-probe separation that is the *crucial* parameter; see Figure 12.78 for a schematic representation of these parameters. Figure 12.80 contains a grey-scale plot of the CMCs once the AUT has been mathematically translated back to the origin of the measurement coordinate system, i.e. the parabolic phase function that results from the finite non-zero AUT-to-probe separation has been removed from the far-field pattern. Here, it is clear that the CMCs associated with the AUT are confined to a narrow band which are tightly distributed about $n = 0$, i.e. in the centre of the plot with $|n| < 30$. As the total power

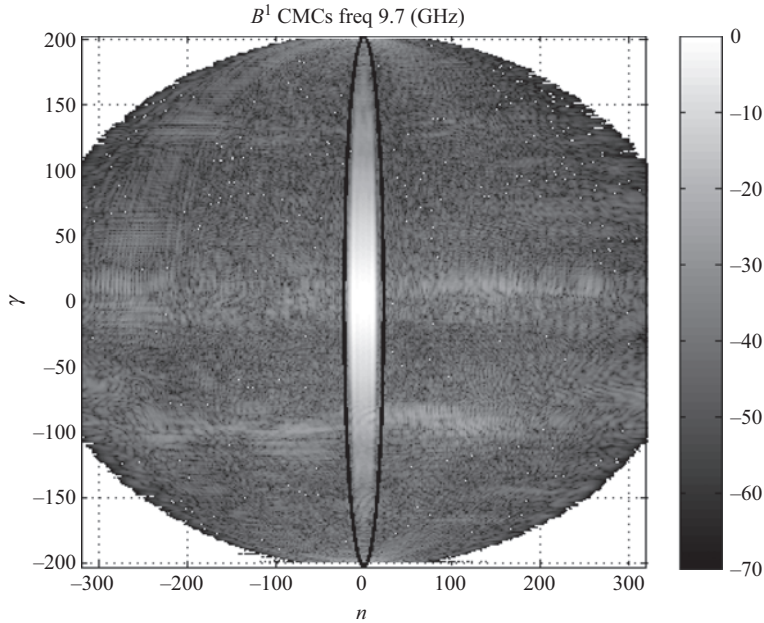

Figure 12.80 CMCs calculated from planar measurement after AUT translated to origin

radiated by the AUT must be conserved, the amount of power per mode must increase as the total number of modes associated with the AUT decreases. As the amount of noise per mode can be seen to be roughly constant, in this case at circa –60 dB with respect to the maximum level, the effective system SNR ratio of the measurement is increased.

Crucially, as has been observed previously with S-MARS and C-MARS, although the AUT has been translated back to the origin of the measurement coordinate system, and as such can be represented with only a comparatively small number of modes, this is not the case for the scatterers which are spatially extended and are represented by higher order modes. In effect, the contributions in the domain of the CMCs from the AUT and the scatterers are separated, i.e. displaced so that they no longer interfere with one another. This effect is clearly illustrated in Figure 12.80 in which the modes associated with scatterers can be seen outside the $|n| = 30$ mode range which is represented with a black ellipse. Consequently, any mode that is of higher order than that required to reconstruct the field of the AUT can be filtered out using a band-pass filter function as these modes cannot be part of the antenna's far-field radiation pattern. Although the filtering is normally based on the MRE of the antenna, this may be increased for analysis purposes up to a limit determined by the dimensions of the planar near-field dataset (cf. for conventional

spherical or cylindrical scanning this limit would be determined by the data point spacing). The mode-filtered far-field pattern can be obtained from the CMCs from a simple summation that can be evaluated using the FFT (cf. Chapter 7). The mode-filtering technique described above suppresses the effects of scattering principally in the *xz*-plane. However scattering artefacts that have a component in the *yz*-plane are essentially unaffected by this processing. Fortunately, it is a simple matter to repeat this processing once the filtered antenna pattern function has been rotated by 90° about the positive *z*-axis. Thus by implementing this processing in both horizontal and vertical axes, *all* of the range scattering effects can be very effectively suppressed.

To illustrate the effectiveness of this strategy, the repeatability between successive measurements where a single parametric change had been introduced is discussed. The intent being that the parametric change, i.e. the introduction of a scatterer, should be capable of being compensated for by P-MARS processing. Figure 12.81 shows an NSI-300V-12 × 12, vertical planar near-field antenna test system with 3.7 m × 3.7 m scan plane installed within a partially absorber lined chamber. This system was used to measure an X-band SGH.

Here, a baseline measurement was taken after which reflective aluminium foil was hung in the region of greatest field intensity, that is to say, it was placed on the rear wall immediately behind the scan plane. This arrangement can be seen presented in Figure 12.82. Here, the measurements were taken at the lower end of the X-band so that the AUT pattern would be as broad as possible and so that effects over a larger proportion of the forward hemisphere could be examined.

Figure 12.83 contains the far-field pattern of the scattering contaminated SGH measurement as obtained using conventional planar processing. Conversely, Figure 12.84 contains an equivalent plot of the same measured data after P-MARS processing has been applied.

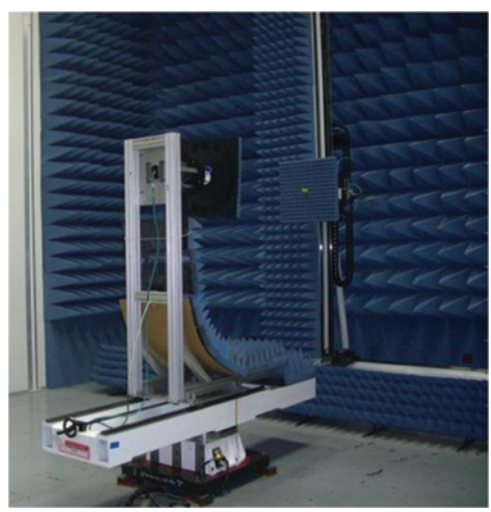

Figure 12.81 NSI-300V-12 × 12 system installed within a partially absorber lined chamber

Figure 12.82 NSI-300V-12 × 12 system installed within a partially absorber lined chamber. Artificial scatterer introduced is also shown

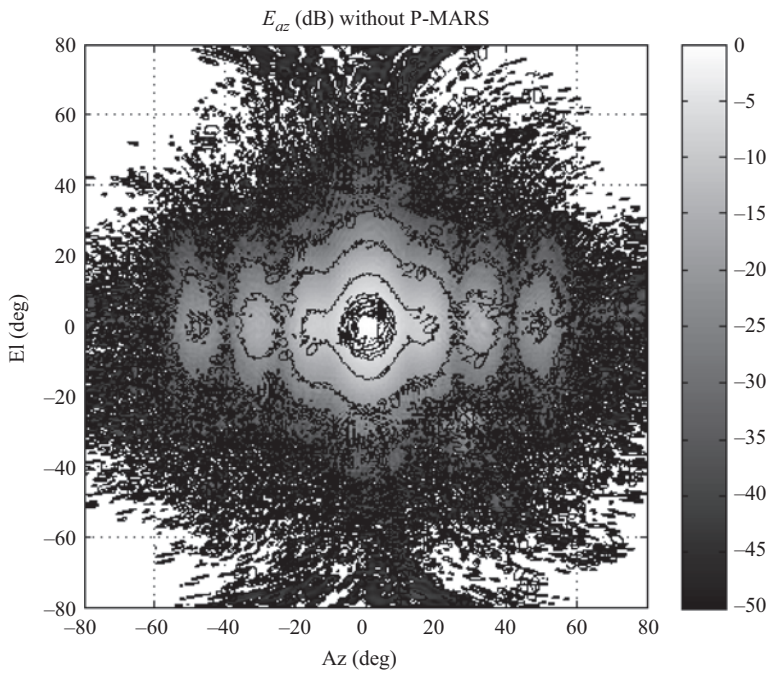

Figure 12.83 Measurement with reflector on back wall

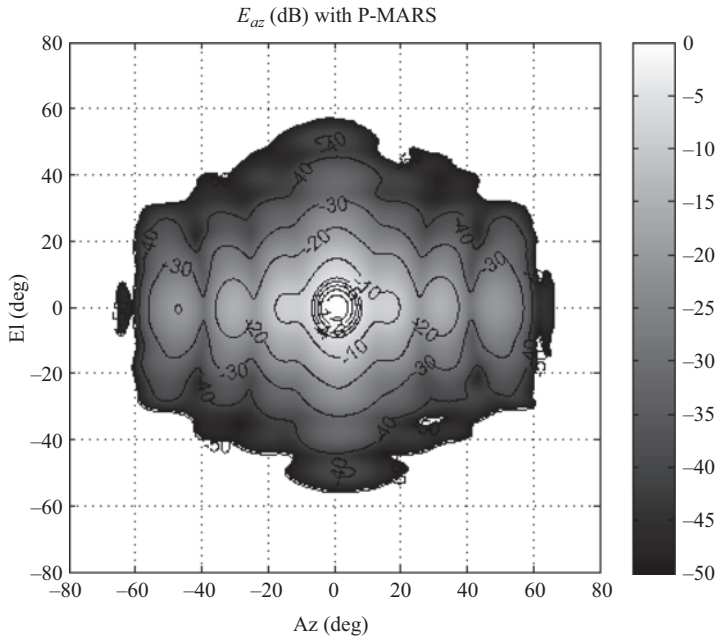

Figure 12.84 Measurement with reflector and P-MARS

As before, the high-frequency angular ripple has been effectively eradicated together with the spurious scattering that is clearly evident on the unfiltered results at $A = 25°$, $E = -25°$.

In principle, it is possible to obtain CMCs or SMCs from data derived from a planar near-field system. This would enable an alternative scattering suppression algorithm to be developed. Probe pattern-corrected far electric fields can be obtained directly from planar near-field measurements tabulated on a polar spherical coordinate system by carefully selecting the appropriate direction cosines such that $k_x = k_0 \sin\theta \cos\phi$, $k_y = k_0 \sin\theta \sin\phi$, $k_z = k_0 \cos\theta$, where θ and ϕ are used to denote the conventional polar and azimuthal spherical angles, and k_0 is the free-space propagation constant. In order that polar spherical far electric fields can be calculated, the spherical angles are determined using a lattice of points that is plaid, monotonic and equally spaced in θ and ϕ. As all three Cartesian components of the far electric field are known, it is a trivial matter to resolve these fields onto a polar spherical polarisation basis using

$$\begin{bmatrix} E_\theta \\ E_\phi \end{bmatrix} = \begin{bmatrix} \cos\theta\cos\phi & \cos\theta\sin\phi & -\sin\theta \\ -\sin\theta & \cos\phi & 0 \end{bmatrix} \cdot \begin{bmatrix} E_x \\ E_y \\ E_z \end{bmatrix} \tag{12.81}$$

The electromagnetic fields outside an arbitrary test antenna radiating into free space can be expanded onto a set of elementary orthogonal SMCs whereupon these

vector mode functions and associated mode coefficients can then be used to obtain the electric and magnetic fields everywhere in space outside of a conceptual spherical surface of radius ρ_0 which encloses that radiator. Specifically, in a source or sink-free simple linear homogeneous and isotropic region of space which is bounded by spherical surfaces and is centred at the origin of a spherical coordinate system, the electric field can be expressed as, cf. Chapter 8

$$\underline{E}(\underline{r}) = \frac{k}{\sqrt{\eta}} \sum_{n=1}^{\infty} \sum_{m=-n}^{n} \left[B^1_{mn} \underline{M}^{(4)}_{mn}(\underline{r}) + B^2_{mn} \underline{N}^{(4)}_{mn}(\underline{r}) \right] \tag{12.82}$$

where B^1_{mn} and B^2_{mn} are used to denote the transverse electric (with respect to the radial coordinate) and transverse magnetic wave coefficients, which are complex functions of m and n; $\underline{M}^{(4)}_{mn}(\underline{r})$ and $\underline{N}^{(4)}_{mn}(\underline{r})$ are, respectively, the transverse electric and transverse magnetic spherical vector wave functions which are dimensionless functions of m, n, r, θ, ϕ and in all cases the superscript (4) indicates spherical Hankel functions which represent radial outgoing waves that satisfy the radiation condition. The intrinsic impedance of the medium through which the field is propagating is denoted by η. In practice the n-summation of the spherical wave expansion has to be truncated at some finite value, say N, which is sufficiently large to ensure that the properties of the field have been accurately and precisely represented. As it was assumed in the formulation that the majority of the current sources are located within a sphere of radius ρ_0, spherical waves of order $N > k_0\rho_0$ represent the most complex constituents of the field structure; thus typically N is chosen so that (cf. Chapter 8)

$$N = \text{ceil}(k_0\rho_0) + n_1 \tag{12.83}$$

Here, ceil is used to denote a function that rounds to the nearest integer towards positive infinity, n_1 is a positive integer that depends upon the accuracy required (e.g. $n_1 = 10$). When deriving CMCs from planar near-field antenna measurements, it was found that the MRC was related to the maximum dimension of the acquisition plane. That is, the highest order mode coefficient was related directly to the size of the near-field sampling interval. This implies that for the complete spherical mode set to be calculated that represents the planar *measured* data, the maximum number of polar modes is

$$N = \text{ceil}\left(\frac{k_0 \sqrt{x^2_{\text{span}} + y^2_{\text{span}}}}{2} \right) + n_1 \tag{12.84}$$

Here, x_{span} and y_{span} are the x- and y-axes planar near-field measurement, spans respectively. Conventional spherical near-field theory states that the polar sample spacing is related to the maximum mode index using (cf. Chapter 8)

$$\Delta\theta = \frac{2\pi}{2N + 1} \tag{12.85}$$

Thus when determining SMCs from planar near-field antenna measurements, the polar sample spacing is required to be no less than

$$\Delta\theta = \frac{2\pi}{2\left(\text{ceil}\left(k_0\sqrt{x_{\text{span}}^2 + y_{\text{span}}^2}/2\right) + n_1\right) + 1} \tag{12.86}$$

Provided the planar near-field measurement is correctly spatially sampled, it is possible to compute far-field data that is tabulated across an arbitrarily finely sampled grid with no additional experimental burden. The ϕ-axis sample spacing can be obtained in a similar fashion; however, here the maximum radial extent (MRE) refers to the radius of a circular cylinder that is centred about the z-axis of the range (i.e. at a normal to the scan plane) and that is large enough to encompass the majority of the current sources. In the example discussed below, the two MRSs are the same and as such and the θ- and ϕ-axes increments are equal. Thus, by using these equations, it is therefore possible to obtain SMCs from a planar near-field measurement in a rigorous way, that is to say without recourse to approximation. The process is as follows: (1) measure planar near-field data on a plane offset from the origin, (2) calculate the θ and ϕ components of the far-field on a θ, ϕ grid, and (3) calculate the SMCs for this far-field data.

As developed in Chapter 8, SMCs are complex numbers that are functions of the polarisation index, and the n, m index. Figure 12.85 presents a grey-scale plot of the amplitudes of the TE SMCs which were obtained from a planar near-field measurement by using the data-processing chain described above.

In each of these plots, modes for which $|m| > n$ are (mathematically) undefined are represented with white space. The offset in the near-field measurement between the AUT and the probe causes the phase of the measured signals to vary more rapidly across the measurement plane and produce the broad distribution of modes shown in Figure 12.85, i.e. modes with significant amounts of power for higher order m and n indices. Conversely, Figure 12.86 contains an equivalent plot only in this case; the AUT has been mathematically translated back to the origin of the measurement coordinate system prior to the computation of the SMCs. Here, it is quite evident that as a direct consequence of this translation the AUT pattern is now represented by far fewer, lower order, SMCs than would otherwise have been the case. The modes associated with the AUT are within a very small region at the 'tip' of the plots in Figure 12.86 (i.e. where m and n are small). However, as has been the case for all other implementations of MARS, the modes associated with room scattering effects (which are spatially extended) can be seen to be represented by higher order mode coefficients. These appear as low-level 'trails' in the regions beyond the tip in Figure 12.86. This is evident from inspection of Figure 12.87 in which the 'trails' outside the 'tip' are absent. These SMCs were obtained from the same experimental setup that was used to generate the data presented in Figure 12.86; only in this instance a large scattering object was removed from the chamber prior to taking the near-field data. In effect, the contributions in the SMC domain of the AUT and the scatterers are

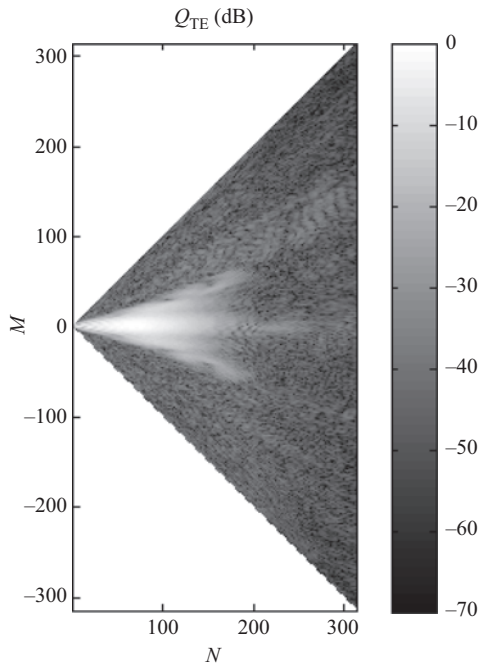

Figure 12.85 SMCs derived from planar near-field measured data AUT-to-probe separation ≫ 0

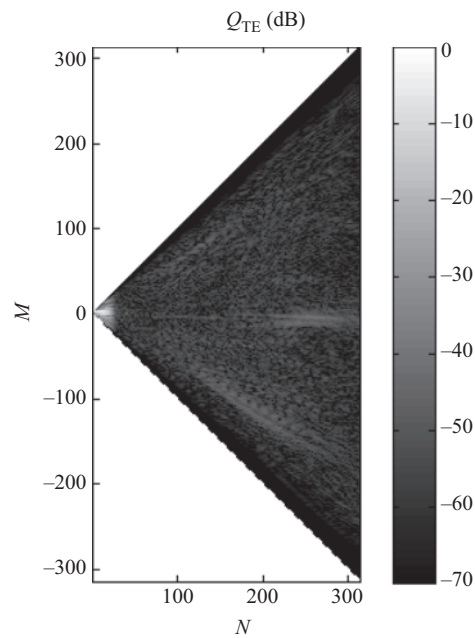

Figure 12.86 SMCs derived from planar near-field measured data AUT-to-probe separation = 0

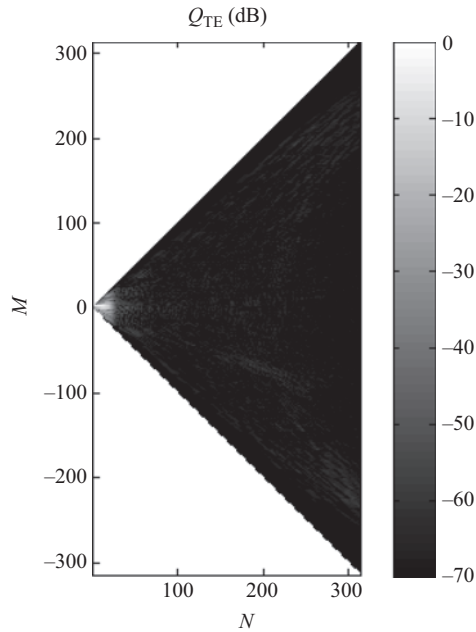

Figure 12.87 SMCs for AUT located at origin derived from PNF data, no scatterer present

separated so that they do not interfere and are effectively orthogonalised from one another. Thus by filtering out the higher order modes that cannot be associated with the AUT itself, which can be calculated based on knowledge of the physical size of the antenna and the associated mode cut-off number, room scattering can be suppressed. Hence any coefficients outside of the $k_0 r_{t0}$ region of mode space can be removed without prejudice to the underlying far-field antenna pattern function. Here, r_{t0} denotes the conceptual minimum possible MRS that just circumscribes the AUT. Once the filtered SMCs are obtained, the far-field pattern can be obtained using standard efficient spherical processing. Although the filtering is normally based on the size of the antenna, this may be increased for analysis purposes up to a limit determined by the angular sample spacing. Crucially, for the planar MARS implementation, this angular spacing can be freely specified by the user and is completely independent of the *x*-, *y*-near-field sample spacing. It is clear that the SMCs associated with the AUT are confined to a region that is tightly distributed about low-order polar modes. As the total power radiated by the AUT must be conserved, the amount of power per mode must increase as the total number of modes associated with the AUT decreases. As the amount of noise per mode can be seen to be roughly constant, in this case at circa –50 dB with respect to the maximum level, the effective

system SNR of the measurement is significantly increased through this processing. Planar testing is known to admit greater and greater amounts of spurious noise into the measurement as the scan plane is progressively enlarged (as is required when testing wide-out side lobes); however P-MARS processing can be seen to provide a highly effective method of compensating for this undesirable, and frequently encountered, effect.

Figure 12.88 contains an equivalent antenna diagram only here, the planar MARS processing has been implemented using the spherical mode-based processing described above, termed second generation P-MARS processing. The resulting MARS-processed far-fields that have been obtained using the first and second generations of the planar MARS are clearly in very encouraging agreement with one another with the scattering being very effectively suppressed in both.

In order that the degree of agreement could be further verified, contour (iso-level) pattern plots were overlaid where the contours were plotted at the –40, –30, –20, –10, –5, –4, –3, –2 dB levels with each pattern being normalised to 0 dB at the peak of the pattern, as shown in Figure 12.89. Here, grey contours are used to represent CMC-based P-MARS-processed results, while black contours are used to denote SMC-based P-MARS results. Again, the degree of agreement is encouraging with contours being in good agreement down to the –40 dB level over all angles. Some small differences are evident and these are largely a result of the difference between the included region respectively by the cylindrical and spherical implementations. The cylindrical-based processing uses the intersection of two

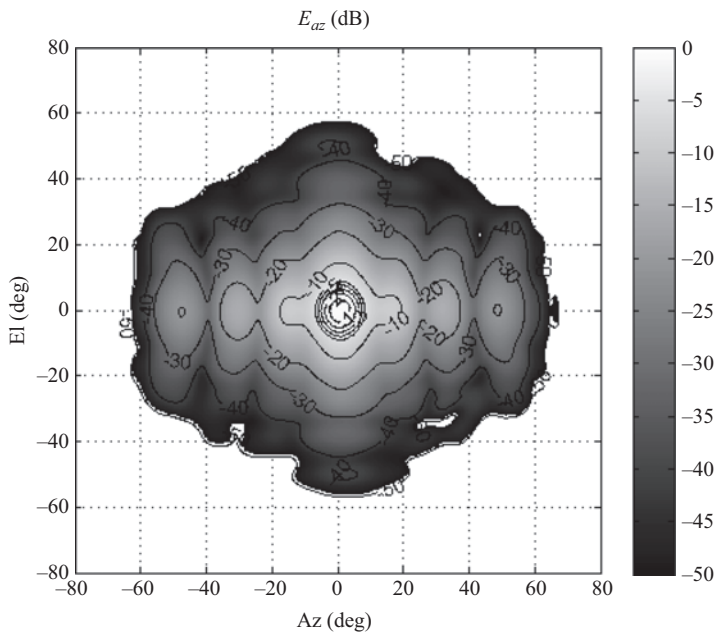

Figure 12.88 Measurement with reflector on back wall, processed using SMC-based P-MARS

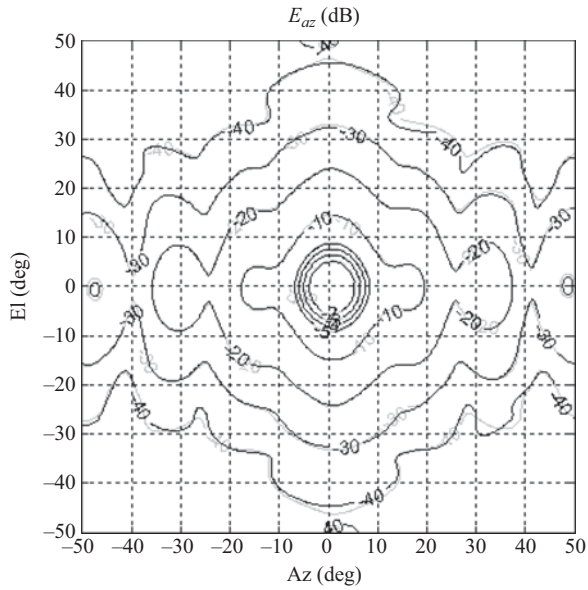

Figure 12.89 Comparison of P-MARS results obtained using SMC- and CMC-based processing algorithms

orthogonal right circular cylindrical surfaces to define the included region, whereas the spherical-based processing uses a single spherical surface to define the included region. As these two regions of space are subtly different, and as the degree of scattering is severe, some small differences are expected.

That being noted, the degree of agreement obtained is very encouraging which is significant as the respective mathematical formulations and computational implementations are entirely separate and distinct. Specifically, the only commonality between methods is the underlying physical MARS principle.

As has been demonstrated in the preceding sections, MARS processing can be used with a very high degree of confidence since all the steps in the measurement and analysis are consistent with the well-established principles of standard near-field theory and measurement technique, and all comparisons to date have proved overwhelmingly positive. The translation of the far-field pattern to the origin with the application of a differential phase shift is rigorous. The selection of the mode cut-off for the translated antenna pattern is based on the physical dimensions of the AUT and its translated location and does not rely on any particular pre-assumed characteristics of the current distribution. The results of the MARS processing will reduce, but clearly cannot entirely eliminate, the effect of the scattering. The final result with MARS processing can be degraded if the sampling of the near-field data is too coarse, but this is also true for regular near-field processing with, importantly, this parameter being controlled by the user. The MARS measurement and post-processing scheme holds for general source geometries, and has been found to be very robust with respect to truncation of the measured near-field data. As has been demonstrated, this novel

frequency domain measurement and processing technique is entirely general and can be used to achieve acceptable results with the use of minimal absorber or even without the use of an anechoic chamber, irrespective of whether testing high- or low-gain antennas. MARS has been found to improve the reflection levels in traditional anechoic chambers allowing improved accuracy as well as offering the ability to use existing chambers down to lower frequencies than the absorber might otherwise suggest. As it is not possible to take planar near-field measurements with an AUT-to-probe separation of 0 m, in essence one is always taking a measurement that is, to some degree at least, amenable for MARS processing, all that this costs is some additional processing time, which is typically measured in a few seconds. As larger AUT-to-probe separations are often utilised to minimise other measurement effects such as AUT-to-probe multiple reflections, MARS type measurements are often acquired and in those cases even the additional acquisition time is not a detractor.

12.4 CNF topics

12.4.1 Cylindrical mathematical absorber reflection suppression

The electromagnetic fields outside an arbitrary test antenna radiating into free space can be expanded into a set of orthogonal CMCs and these modes and coefficients can then be used to obtain the electric and magnetic fields everywhere in space outside of a conceptual cylindrical surface which encloses the radiator (cf. Chapter 7). This can be seen illustrated in Figure 12.90. As has been shown above, the CMCs are determined from the measured data in a very efficient manner through the use of the FFT. Once obtained, these mode coefficients are corrected for the spatial filtering properties of the near-field probe to determine the true AUT-transmitting CMCs. A highly efficient FFT-based summation process is then utilised to obtain the asymptotic far electric fields. Parameters such as co-polar pattern, cross-polar pattern, axial ratio, tilt angle, directivity, and gain of the AUT-can be obtained from the electric field where the resulting pattern data is, by virtue of this transform, naturally tabulated on a regular azimuth over elevation coordinate system and resolved onto a Ludwig II azimuth over elevation polarisation basis, cf. Appendices.

As derived in Chapter 7, when expressed in component form, and when assuming an infinitesimal Hertzian dipole probe is employed as a near-field probe (this assumption is merely introduced to simplify the pedagogy), the two sets of orthogonal CMCs $B_n^{(1)}(\gamma), B_n^{(1)}(\gamma)$ can be obtained from

$$B_n^1(\gamma) = \frac{-1}{4\pi^2 k_\rho^3 H_{-n}^{(2)'}\left(k_\rho \rho_0\right)} \int_{-\infty}^{\infty} \int_0^{2\pi} \left(\frac{n\gamma}{\rho_0} E_z(\rho_0, \phi, z) + k_\rho^2 E_\phi(\rho_0, \phi, z) \right) e^{jn\phi} e^{j\gamma z} d\phi \, dz \tag{12.87}$$

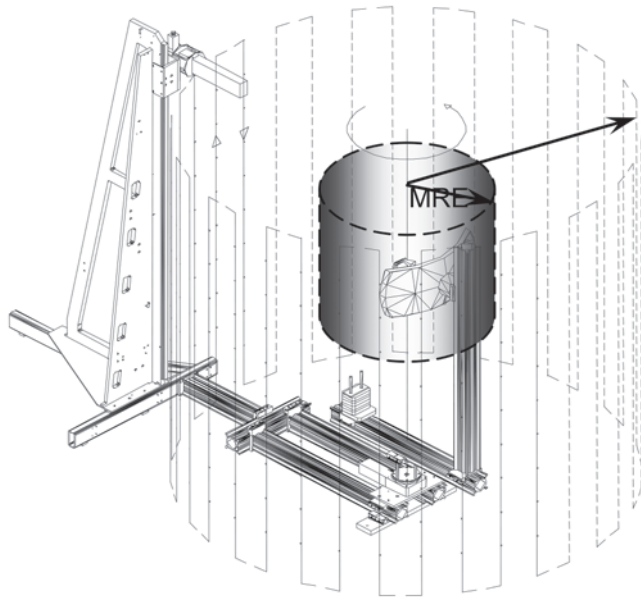

Figure 12.90 Cylindrical measurement system showing conceptual cylindrical maximum radial extent

$$B_n^2(\gamma) = \frac{k}{4\pi^2 k_\rho^2 H_n^{(2)}\left(k_\rho \rho_0\right)} \int_{-\infty}^{\infty} \int_0^{2\pi} E_z(\rho_0, \phi, z) e^{jn\phi} e^{j\gamma z} d\phi \, dz \tag{12.88}$$

The maximum mode index N is given by

$$N = \text{ceil}(k_0 r_t) + n_1 \tag{12.89}$$

Here, ceil is used to denote a function that rounds to the nearest integer towards positive infinity, n_1 is a positive integer that depends upon the accuracy required (e.g. $n_1 = 10$ is a commonly used value), N is the maximum cylindrical mode index required to represent the radiated fields, r_t is the maximum radial extent (MRE or MRC), and $\delta\phi$ is the sample spacing in the angular axis. The MRC is a conceptual cylinder that is coaxial with the measurement cylinder, that extends to $\pm\infty$, and that encloses the majority of the current sources. Unfortunately, in practice for some antennas the size of the MRC may not be obvious but often can be approximated with a conservative, that is to say pessimistically large, value. As only propagating modes can contribute to the far-field pattern, the Fourier variable γ can be restricted to $\pm k_0$ with no loss of rigour as these represent the highest order propagating mode coefficients. This also places a limit on the sample spacing required to obtain alias free data. As the sample spacing δ_z (i.e. the resolution) in the linear axis is determined from the maximum value of γ, we can write that $\delta_z = \lambda/2$, where λ is used to denote the free-space wavelength, cf. the planar analogue. Similarly, the

sample spacing in the angular dimension is obtained from the highest order cylindrical mode index such that (cf. Chapter 7)

$$\delta\phi = 2\pi/(2N+1) \tag{12.90}$$

Clearly then, by displacing the AUT away from the centre of rotation, the MRC is increased. This decreases the sample spacing which increases the amount of data needed and therefore correspondingly increases the amount of time required to acquire the complete near-field dataset. The last remaining parameter that needs to be determined is the range length, i.e. the radius of the conceptual measurement cylinder. This is specified as being the larger of the two following requirements [33]:

$$\rho_0 \geq \begin{cases} r_t + r_p + 10/k_0 \\ r_t + 3\lambda \end{cases} \tag{12.91}$$

where r_p is the MRE of the probe. This quantity would have been determined during the probe's auxiliary pattern calibration. Typically, for an electrically small probe, the measurement radius must be several wavelength larger than the MRC to ensure that only propagating fields are sampled and measurement are taken in the propagating near-field and not in the reactive near-field of the AUT. Once the probe-corrected electric far-fields have been determined, the phase reference can be displaced by means of the application of a simple differential phase change, i.e.

$$\underline{E}_t(r \to \infty, \theta, \phi) = \underline{E}(r \to \infty, \theta, \phi) e^{j\underline{k}_0 \cdot \underline{r}} \tag{12.92}$$

Here, $\underline{r}$ denotes the displacement vector between the centre of the measurement coordinate system and the centre of the aperture of the AUT. Crucially, while in principle all we have done is to mathematically translate the AUT back to the centre of the measurement coordinate system; this has the corresponding effect of significantly reducing the number of CMCs that are required to represent the radiated field. That is, we have reduced the MRC to a conceptual (i.e. optimised) minimum value. The equivalent CMCs that represent the displaced antenna can be obtained directly from an inversion of the Fourier relationship that connects the CMCs and the far-fields. Again, this can be evaluated numerically through the use of the one-dimensional inverse FFT (cf. Chapter 7). Once the CMCs for the now ideally centrally located AUT have been recovered, any mode representing fields outside the ideal MRC can be filtered out, thus removing contributions that are not associated with the AUT. This is determined using (cf. Chapter 7)

$$n^2 + (\gamma r_{t0})^2 > (k_0 r_{t0})^2 \tag{12.93}$$

Here, r_{t0} denotes the optimum MRC, rather than the actual MRC as determined from the near-field measurement where $r_t > r_{t0}$. Thus any CMCs corresponding to fields that are exterior to this reduced region of space can be safely filtered out using a band-pass filter function without compromising the integrity of the underlying antenna pattern function, irrespective of its complexity. When expressed

mathematically, the mode filter becomes

$$B_n^s(\gamma)|_{s=1,2} = \begin{cases} B_n^s(\gamma) & n^2 + (\gamma r_{t0})^2 \leq (k_0 r_{t0})^2 \\ 0 & \text{elsewhere} \end{cases} \tag{12.94}$$

Here, s denotes the polarisation index of the CMCs and r_{t0} the optimum MRC, rather than the actual MRC as taken from the near-field measurement. The mode cut off is based on the fact that modes above a certain index number are spatially exponentially attenuated and do not contribute to the far-field. Thus in effect, the mode cut-off is determined by the *physical* dimensions of the AUT. The final step in the processing is to reconstruct the filtered far-field antenna pattern from the filtered CMCs. Thus, the cylindrical MARS algorithm can be summarised as follows:

1. Take the two orthogonal tangential electric cylindrical near-field components (E_ϕ, E_z) and perform a 2-D FFT on each component.
2. Compute $B_n^1(\gamma)$ and $B_n^2(\gamma)$ from the results of the 2-D FFT of each measured field component.
3. Solve for the antenna's unknown CMCs using previously computed probe pattern coefficients.
4. Perform a 1-D FFT to obtain the far-field azimuth antenna pattern for a particular elevation angle. Compute the complete far-field pattern by repeating this for each discrete elevation angle.
5. Apply a differential phase change to mathematically translate the AUT back to the origin of the measurement coordinate system.
6. Perform a 1-D IFFT to obtain the translated CMC of the AUT for a particular γ. Repeat this for each discrete value γ.
7. Apply two-dimensional mode-filtering function to suppress unwanted CMCs.
8. Perform a 1-D FFT to obtain far-field azimuth antenna pattern for a particular elevation angle. Compute the complete far-field pattern by repeating this for each discrete elevation angle to obtain the MARS-filtered AUT pattern function.

While a certain degree of effort is required to calculate the CMCs from the far-field pattern, and then reconstruct the far-field pattern from the filtered set of CMCs, as neither of these operations require us to compute a Hankel function (or their derivatives), and since the transforms are evaluated with the FFT, these operations are very cost-effective in terms of computational effort, especially when compared to other alternative strategies. In order that range multipath can be effectively suppressed, previously, it has been shown that the magnitude of the displacement in the y-axis (i.e. at a normal to the aperture plane of the AUT) should be greater than the diameter of the conceptual optimum MRC. The remainder of this section is devoted to demonstrating the effectiveness of the MARS technique and illustrating the impact that changing the location of an antenna in a facility has on the CMC.

To illustrate this powerful measurement and data transformation technique, let us consider using a small combination near-field antenna measurement system to

take a series of cylindrical near-field measurements where specific known scatterers have been introduced into the test environment. Figure 12.91 shows an NSI-200V-3 × 3 combination planar/cylindrical/spherical system testing a 0.3 m (12″) wide by 0.29 m (11.6″) high X-band slotted waveguide planar array antenna.

Here, a small removable reflecting plate was installed within the chamber at a specular point to maximise the scattering and create a 'worst case' configuration that could be compared against the nominal baseline equivalent case. It is also worth noticing that much of the scanner's aluminium structure was not covered with absorber which further exacerbates the scattering. The following results were obtained when testing the slotted waveguide array antenna at a frequency of 9.2 GHz with a measurement radius of 0.625 m (24.625″) and an MRC of 0.40 m (16″). As can be seen from the figure, a WR90 OEWG probe was used to sample the near-fields as good theoretical probe patterns are available for this instrument. In addition to this, and as shown above, for the purposes of cylindrical MARS testing, the displacement between the centre of the range measurement coordinate system and the AUT, and the conceptual minimised MRC are also needed. These were 0.38 m (15″) and 0.16 m (6.3″) respectively. This arrangement can be seen presented schematically in Figure 12.92.

Figures 12.93 and 12.94 contain virtual reality three-dimensional grey-scale plots of the measured horizontally polarised, principle electric field distributions, without and with the scatterer present, respectively. Here, the fields scattered by the reflecting plate are evident in the cylindrical measured fields and are manifest as a large amplitude spurious lobe that is directed away from the boresight direction that can be expected to have a significant impact upon the resulting far-field pattern.

Standard cylindrical near-field theory can be used to derive the equivalent CMCs. As derived above, CMCs are complex numbers that are functions of the polarisation index, the ϕ index n and the Fourier variable γ. Figure 12.95 contains a plot of the amplitudes of the CMC modes for $s = 1$, i.e. B^1, for this measurement which were generated by the regular cylindrical processing of the measured cylindrical near-field data.

The offset of the AUT in the near-field measurement causes the phase of the scattered signals to vary rapidly over the measurement cylinder and to produce the higher order modes shown. Clearly, the CMCs obtained from the near-field measured data shown in Figure 12.96 contain contributions from both the AUT and the scatterer. In the domain of the CMCs, these two sources are interfering constructively and destructively as a function of mode index. This effect is clearly visible when comparing with Figure 12.95 where the interference fringes are largely absent as the reflecting plate is absent from the measurement (although the interference from the un-absorber covered scanner is still present).

After applying the differential phase change to the equivalent far-field pattern to mathematically displace the AUT so that its phase centre (i.e. aperture) is coincident and synonymous with the origin of the cylindrical measurement coordinate system, the contributions in the domain of the CMCs are separated, i.e. displaced so that they no longer interfere with one another. This is clearly evident by comparing Figures 12.97 and 12.98 where the low-order CMCs are in excellent

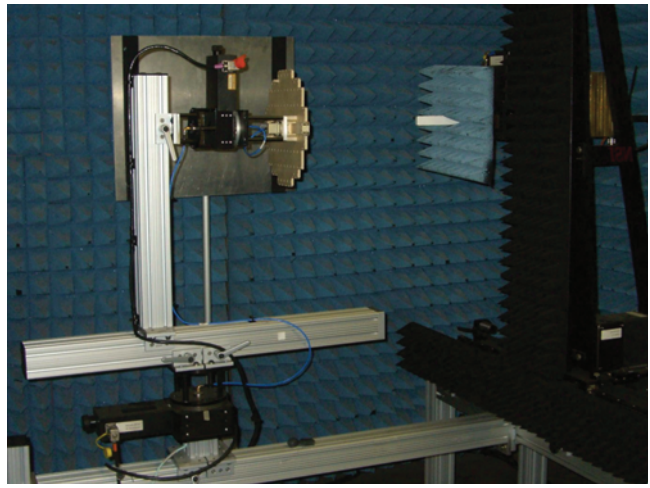

Figure 12.91 NSI-200V-3 × 3 planar/cylindrical/spherical near-field system measuring a slotted array antenna in the presence of a reflecting plate

agreement. Conversely, the higher order CMC are very different as the modes associated with the scattered fields have been redistributed to this region of mode space.

Here, modes associated with the AUT are tightly distributed about the $n = 0$, i.e. in the centre of the plot, while the modes associated with the scatterer can be seen to be distributed about the $n = -75$ mode index. Thus the two sources have been separated, i.e. orthogonalised in the CMC domain. Furthermore, as the mode coefficients associated with the AUT are within the $k_0 r_{t0}$ region of mode space, any coefficients outside of this region of the domain can be removed without prejudice to the far-field antenna pattern function. Although the filtering is normally based on the aperture size of the antenna, this may be increased for analysis purposes up to a limit determined by the near-field data point spacing as shown here. Figures 12.99 and 12.100 contain plots of the CMCs after filtering and clearly illustrate the similarity in the mode domain between the two measurements despite the differences in the respective test environments, which suggests that the corresponding far-field patterns should be in similarly encouraging agreement. In this case, the minimum cylinder which contains the translated antenna aperture causes the cylindrical MARS processing to filter out all higher order modes above $|N| = 31$ as these modes cannot be part of the antenna's far-field radiation pattern. Although not shown herein, similar plots can be created for the linearly independent set of B^2 CMCs with similar phenomena being observed.

Figures 12.101 and 12.102 contain plots of the probe-corrected far-field pattern of the AUT that is obtained from the cylindrical near-field data prior to cylindrical MARS filtering without and with the reflecting plate respectively. Here, it is clear

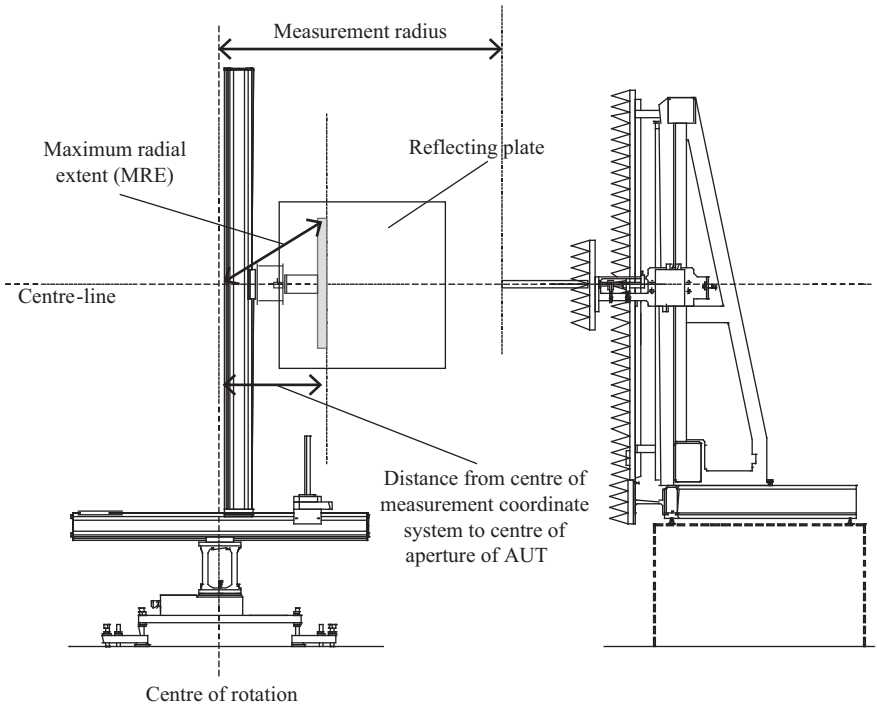

Figure 12.92 Schematic of NSI-200V-3 × 3 PCS system configured for taking a C-MARS measurement

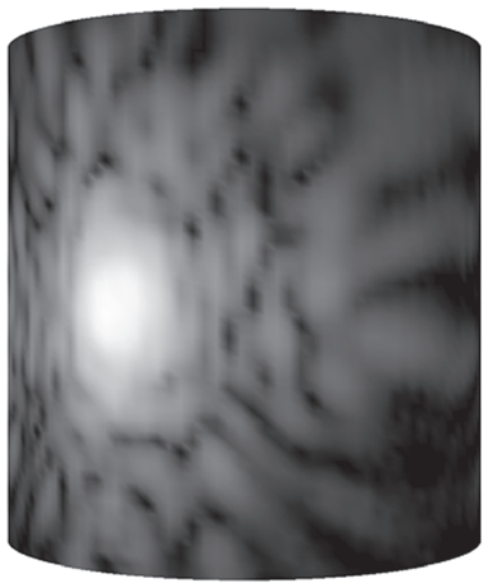

Figure 12.93 Virtual reality three-dimensional grey-scale plot of the measured horizontally polarised, principle, electric field, without scatterer

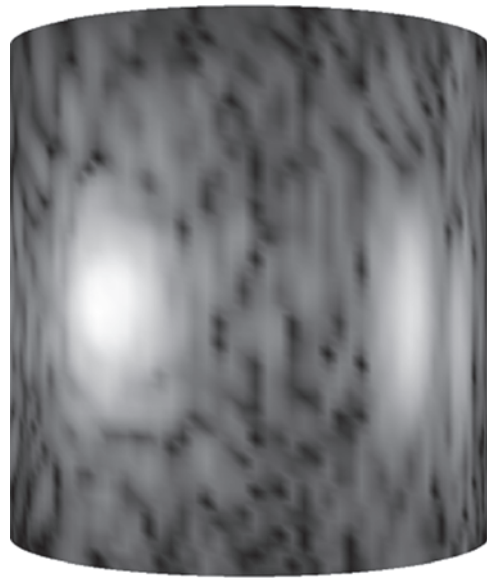

Figure 12.94 Virtual reality three-dimensional grey-scale plot of the measured horizontally polarised, principle, electric field, with scatterer

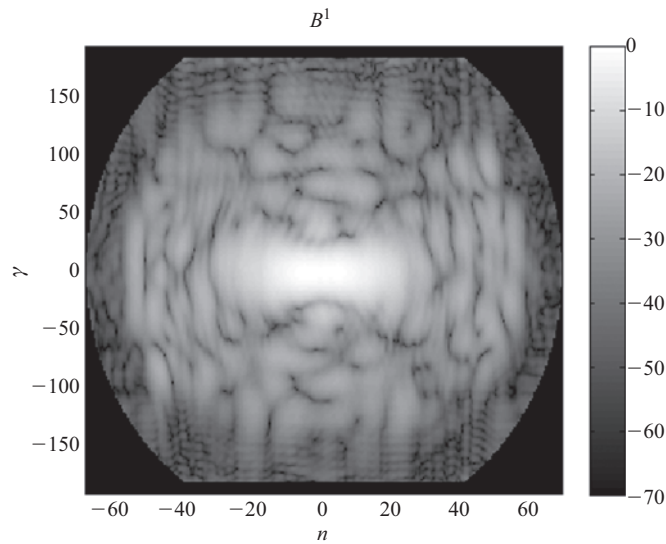

Figure 12.95 B^1 CMCs derived directly from measured near-field data without scatterer

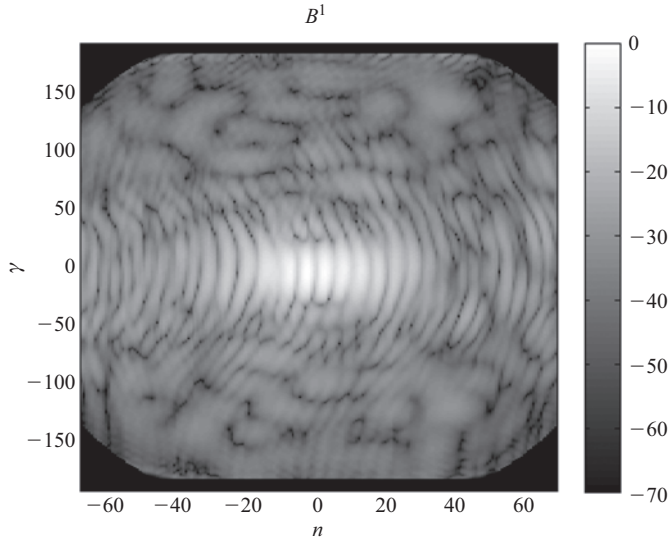

Figure 12.96 B^1 *CMCs derived directly from measured near-field data with scatterer*

that with the reflecting panel, the measurements contain significant range multipath with a large response being visible at $az = 80°$, $el = 0°$ originating from the spectral reflection from the panel. The reflections at –150° to –70° in *az* were most likely a result of additional scattering coming from an RF equipment rack that was situated immediately outside the small test chamber that was used for this test campaign.

Figures 12.103 and 12.104 contain equivalent plots that were obtained using the same cylindrical near-field dataset as was used in Figures 12.101 and 12.102 only this time; the cylindrical MARS process was employed to filter out artefacts arising from range multipath in each measurement. From inspection, it is quite evident that the main specular reflection that was evident at $az = 80°$, $el = 0°$ has been almost completely suppressed. Furthermore, the high-frequency angular ripple that was evident in the unfiltered results is clearly absent in this result, which is very encouraging. Due to the large measurement radius and the comparatively short travel of the linear scan axis (3′ or 900 mm), these patterns suffer a significant amount of truncation in the elevation plane and the pattern data at larger angles is rendered unreliable as a result of the onset of the first-order truncation effect. From inspection of Figure 12.105, which contains an azimuth cardinal cut of the far-field pattern with and without MARS processing, it is very evident from a comparison of the respective azimuth cuts that the spurious specular reflection at 80° has been suppressed by *more* than 25 dB. Again, it is clear that the overall spurious high-frequency ripple that is evident on the solid unprocessed trace can be seen to have been suppressed on the dotted, MARS-filtered trace.

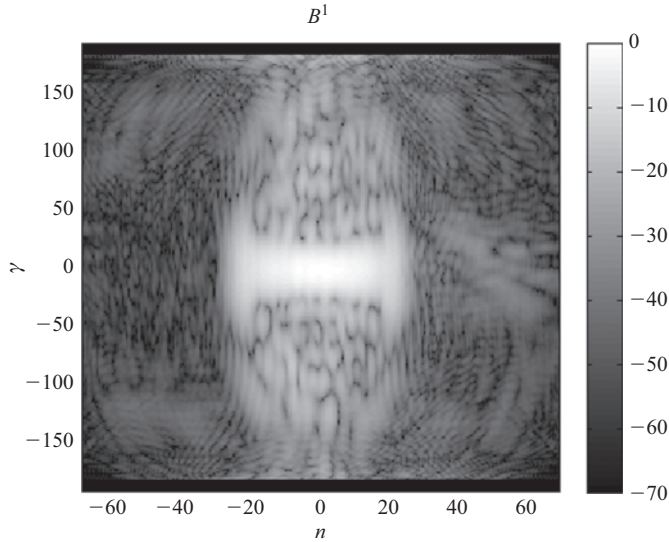

Figure 12.97 B^1 *CMCs derived directly from measured near-field data without scatterer – AUT translated to origin*

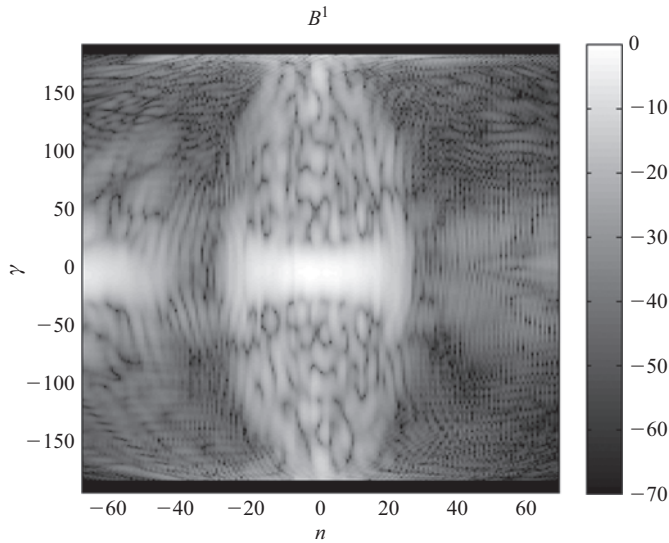

Figure 12.98 B^1 *CMCs derived directly from measured near-field data with scatterer – AUT translated to origin*

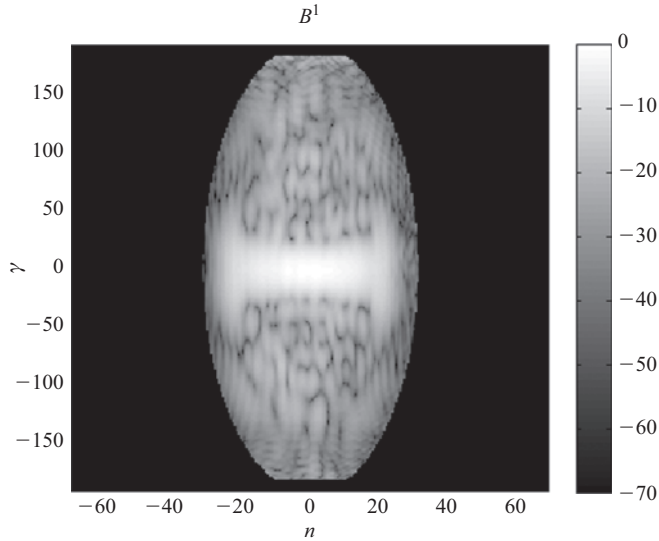

Figure 12.99 B^1 *CMCs derived directly from measured near-field data without scatterer – AUT translated to origin with MARS filtering applied*

For further illustration Figure 12.106 contains a comparison plot of the AUT measured without the reflecting plate, which is used as a reference 'truth model', and the MARS-filtered measurement with the reflecting plate. Here, solid contours (i.e. iso-levels) are used to denote the cylindrical MARS-filtered antenna pattern without the reflecting plate, while the dotted contours denote the cylindrical MARS-filtered antenna pattern with the reflecting plate. The respective sets of contours have been plotted at –40, –30, –20, –10, –5, –3, –2, –1 dB levels. Again the degree of agreement is very encouraging with differences becoming visible at large elevation angles where the pattern data is outside the range of validity and for regions of lower field intensities.

We can obtain a more concise graphical display by selecting the $\gamma = 0$ CMCs which correspond to the maximum amplitude and plot a graph of the mode amplitude versus the mode number n. Table 12.1 shows a mode plot for the reference truth model data (cf. Figure 12.99 for $\gamma = 0$).

Here, the groupings of CMCs that are associated with the reflecting plate are absent and the equivalent far-field azimuth plot is also free of the large specular response that is clearly present within the unfiltered pattern data. Table 12.2 contains similar data from a series of measurements that were taken with the reflecting plate installed within the chamber. During each of these measurements, the only parametric change that was introduced was in the displacement between the origin of the measurement coordinate system and the phase centre of the AUT. The purpose of this was to try and establish a relationship between this displacement and the location of the scattering CMCs.

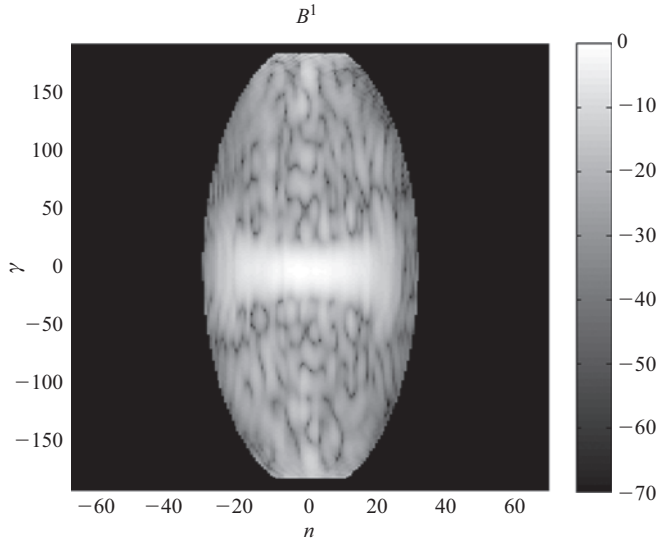

Figure 12.100 *B^1 CMCs derived directly from measured near-field data with scatterer – AUT translated to origin with MARS filtering applied*

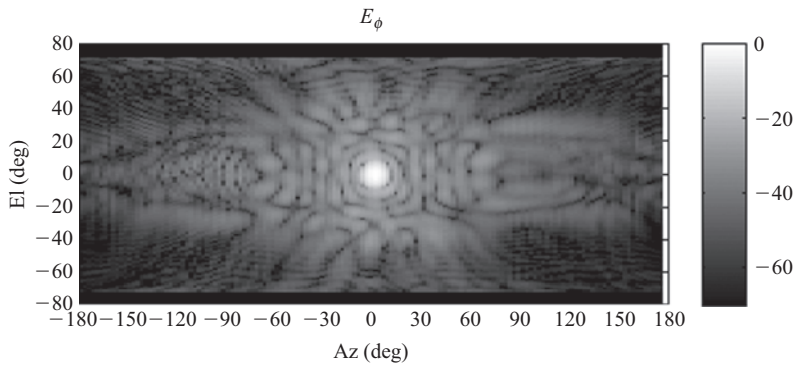

Figure 12.101 *Far-field pattern of X-band slotted waveguide array antenna without scatterer*

From inspection of the figures contained in Table 12.2, it can be seen empirically that the centre of the distribution of CMCs that are associated with the scatterer (plotted as a dotted trace and shown on the left-hand side of the mode plots) are approximately located at

$$n = k_0 \Delta z \tag{12.95}$$

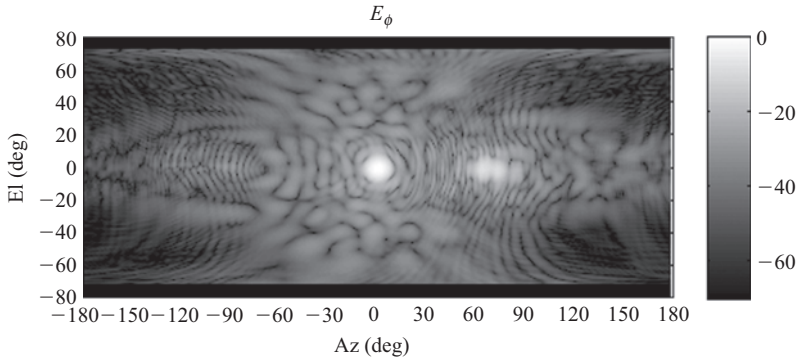

Figure 12.102 Far-field pattern of X-band slotted waveguide array antenna with scatterer

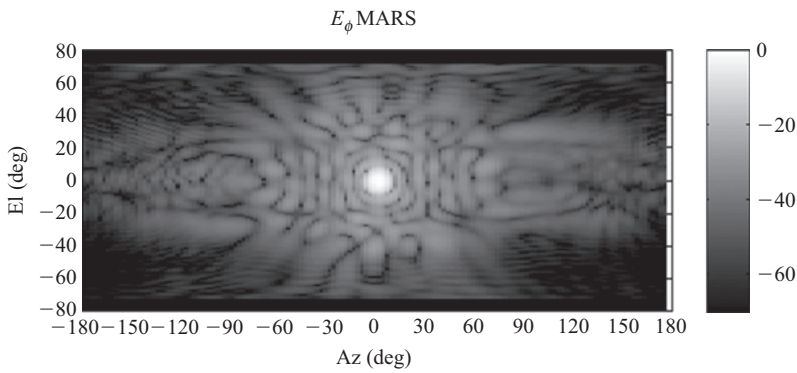

Figure 12.103 Far-field pattern of X-band slotted waveguide array antenna without scatterer and with MARS processing

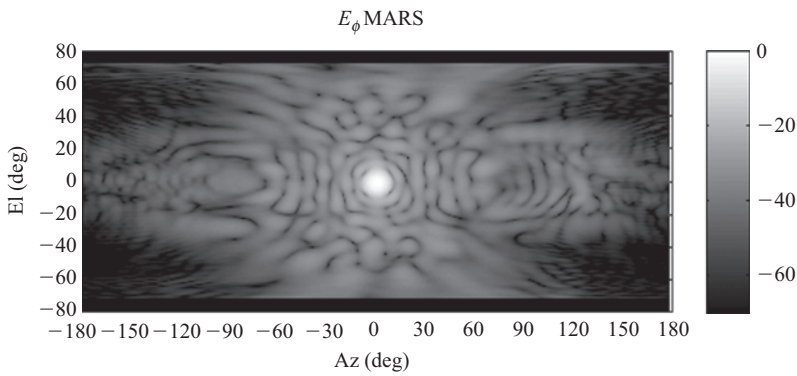

Figure 12.104 Far-field pattern of X-band slotted waveguide array antenna with scatterer and with MARS processing

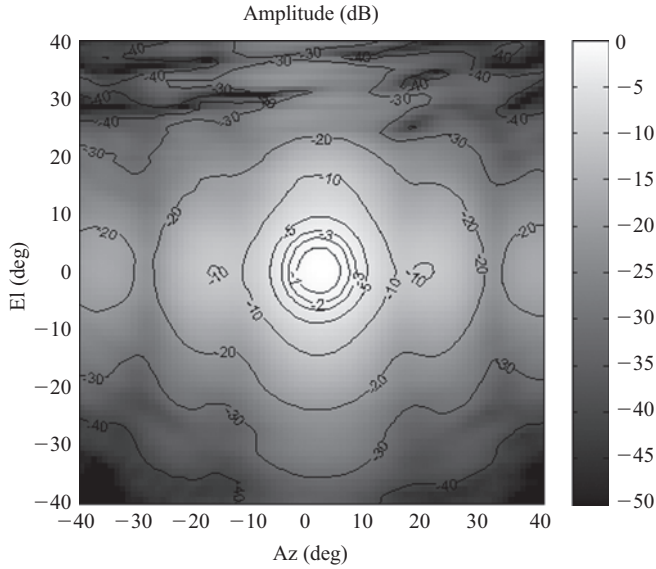

Figure 12.105 Far-field pattern of X-band slotted waveguide array shown before and after MARS processing

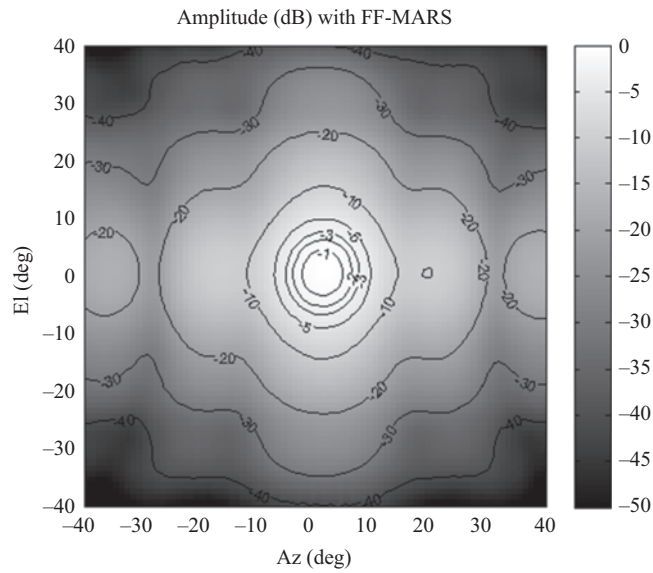

Figure 12.106 Comparison of MARS-filtered pattern without plate and MARS-filtered pattern with plate results

Table 12.1 Cylindrical MARS results without reflecting plate

Δz	CMCs @ $\gamma = 0$	Far-field azimuth cut
9.5″	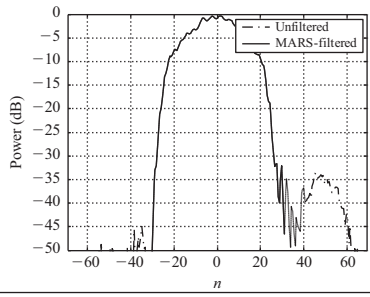	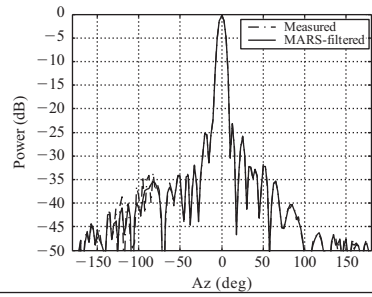

Here, Δz denotes the offset between the centre of rotation and the AUT. Strictly, the modes are located at negative mode indices but this is only an artefact of the location of the reflecting plate within the chamber. If the scatterer were to be located on the opposite side of the chamber, then the distribution would correspond to positive mode indices. Crucially, irrespective of where the scattered modes are, the effect of the MARS process is to move modes that are associated with scattering object to larger magnitude mode indices, i.e. their distributions move away from $n = 0$. By way of confirmation, using the sampling theorem to obtain the highest order mode coefficient for the measurements presented in Table 12.2, and rounding towards the nearest largest integer, yields the following results: ($\Delta z = 8.0''$, $n = 40$), ($\Delta z = 9.5''$, $n = 47$), ($\Delta z = 12.0''$, $n = 59$), ($\Delta z = 13.0''$, $n = 64$), ($\Delta z = 15.0''$, $n = 74$). All of these results are in agreement with the experiment. Thus we would want to ensure that Δz is sufficiently large so that lowest order modes associated with the scatterer are outside the mode spectrum occupied by the AUT. When $\gamma = 0$, once translated back to the origin of the measurement system, the AUT always occupies the mode spectrum

$$-k_0 r_{t0} \leq n \leq k_0 r_{t0} \tag{12.96}$$

where r_{t0} is the maximum radial extent (this is the conceptual MRE when the AUT is optimally installed in the range coincident and synonymous with the origin of the measurement coordinate system). Hence we need to ensure that the following condition is satisfied:

$$k_0 \Delta z \gg k_0 r_{t0} \tag{12.97}$$

Stated simply, the displacement must be larger than the diameter of the conceptual optimum MRC. In this case, this corresponds to ensuring that the displacement is at least as large as the diameter of the AUT and preferably a little larger.

Table 12.2 Cylindrical MARS results with reflecting plate

Δz	CMCs @ $\gamma = 0$	Far-field azimuth cut
8″	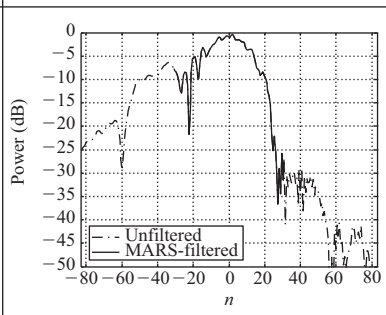	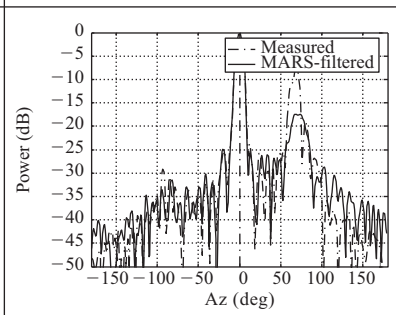
9.5″	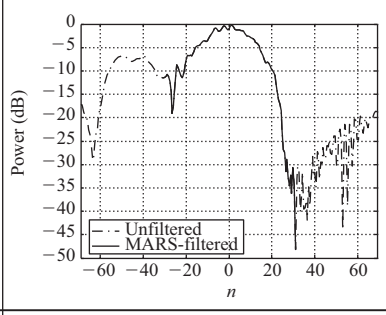	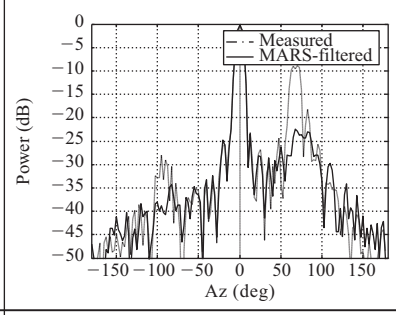
12″	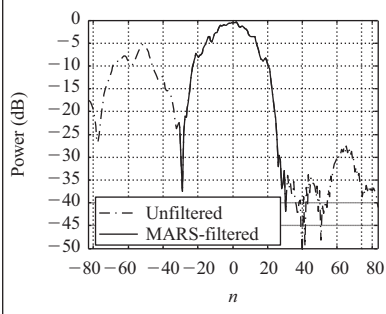	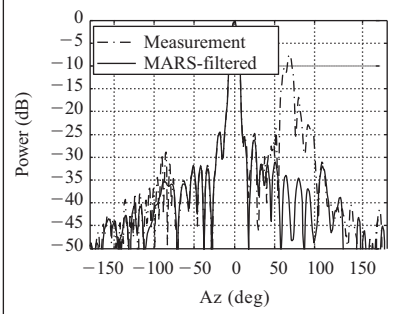
13″	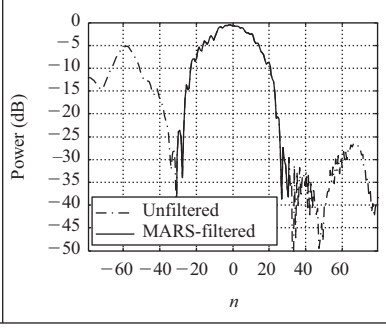	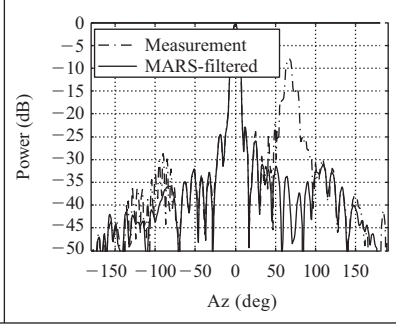

(Continues)

Table 12.2 (*Continued*)

15″	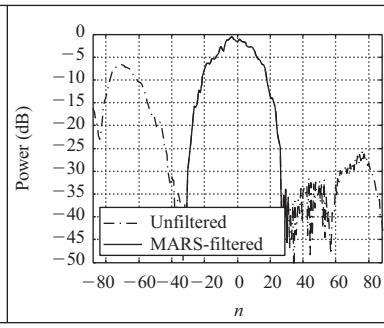	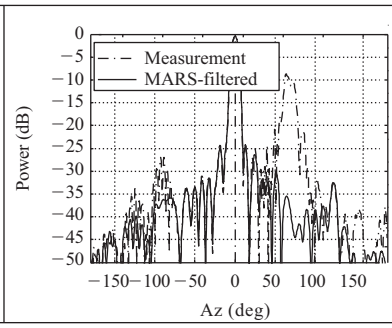

12.4.2 Application of C-MARS to far-field and CATR measurements – FF-MARS

Although it is perhaps not immediately apparent, the above C-MARS technique can, with only minor modification, be extended for use with far-field antenna measurements consisting of only a single great circle cut. This section introduces the far-field MARS technique and illustrates how cylindrical mode expansion-based techniques can be used with far-field measurements.

The enduring popularity of the direct far-field antenna range measurement technique is attributable to the ease and simplicity with which asymptotic far-field antenna pattern data can be obtained using relatively simple test equipment. However the absence of an obligation to undertake intensive mathematical transformations or involved digital signal processing has resulted in a tendency for far-field measurements to receive comparatively little or, in some cases, no additional post-processing. Many of the more sophisticated data post-processing techniques and analyses whose usage have become commonplace when considering near-field antenna measurements are equally applicable and beneficial to direct far-field range measurements. Indeed, in certain circumstances, these can be of even greater utility than in their original area of application and one of these is MARS. MARS processing requires phase information; however many modern direct far-field antenna measurement facilities are equipped with vector network analysers, making the phase data readily available. The acquisition of phase data implies a higher degree of system stability than amplitude-only measurements, although this only need be maintained for the duration of a single cut which can be as brief as a few seconds. The MARS technique is entirely generic in nature, and can be applied to a variety of different antenna types with no *a priori* assumptions being made about the distribution of currents over the AUT.

Far-field MARS is very closely related to the spherical and particularly the cylindrical MARS implementations. Spherical MARS has been available for use with

far-field ranges and CATRs for some time; however the existing implementation as expounded above relies on the acquisition of a complete two-dimensional antenna pattern function, i.e. $\underline{E}(\theta, \phi)$. Conversely, the FF-MARS implementation as introduced here enables MARS-processed results to be obtained from only a single one-dimensional far-field pattern cut, i.e. $\underline{E}(\phi)$ with θ arbitrary but fixed for the duration of the cut. This is significant, as one of the great strengths of the far-field methodology is its ability to provide a single antenna pattern cut, minimising the required measurement time. Here, a right-handed coordinate system is used with θ measured from the positive z-axis, ϕ measured from the positive x-axis in the xy plane with the antenna being equatorial pointing – which is consistent with conventional cylindrical near-field theory as expounded above. One of the recognised shortcomings of making single-cut far-field measurements is that range multipath can degrade the accuracy of the measurement results. All versions of MARS require phase *and* amplitude data; however the ability to apply MARS processing to a single cut minimises the measurement duration. This relaxes requirements for thermal and structural stability that may not be possible to achieve over the time needed to take a full two-dimensional raster scan – often the case when using outdoor far-field facilities. An additional requirement is that the acquired far-field great circle pattern data must be tabulated on a monotonic equally spaced angular grid where the sample spacing is dependent upon the frequency and the MRE. In this case, the MRE is defined to be the radius of a conceptual cylinder that is centred about the origin of the measurement coordinate system and that is sufficiently large to encompass the majority of the current sources.

Typically, for reasons already discussed an antenna is installed within a near-field or far-field facility such that it is displaced in space as little as possible during the course of a measurement. Clearly, displacing the AUT from the centre of rotation will necessarily increase the MRE and from inspection of the following equation it is clear that this will correspondingly decrease the angular data point spacing as

$$\Delta\theta = \frac{2\pi}{2(\mathrm{ceil}(k_0\rho_0) + n_1) + 1} \tag{12.98}$$

Here, again ceil is used to denote a function that rounds to the nearest integer towards positive infinity, n_1 is a positive integer that depends upon the accuracy required (e.g. $n_1 = 10$), k_0 is the free-space wave number, and ρ_0 is the MRE. However, as only a single cut is required, the additional data will not typically affect the duration of the measurement providing the measurements are taken on-the-fly and the receiver is sufficiently fast to be able to acquire the data before the next sample point is encountered. Modern VNAs and receivers are sufficiently fast that this should not increase measurement times in all but the most demanding multiplexed applications where a great many frequencies and/or beam states are acquired. Displacing the AUT in this way also has an implication for the Rayleigh far-field criterion [9] since this can also be expressed in terms of the MRE. It can also be seen that increasing the MRE will similarly increase the required range

length, i.e. the minimum required separation between the AUT and the remote source antenna, as

$$R = \frac{2D^2}{\lambda} \approx \frac{2(2\rho_0)^2}{\lambda} = \frac{8\rho_0^2}{\lambda} \tag{12.99}$$

Once a far-field great circle pattern cut has been acquired using a sufficiently finely spaced abscissa to satisfy the sampling criteria, the AUT has to be mathematically translated back to the origin of the measurement coordinate system by means of a differential phase change, thus

$$\underline{E}_t(r \to \infty, \theta, \phi) = \underline{E}(r \to \infty, \theta, \phi) e^{j\underline{k}_0 \cdot \underline{r}} \tag{12.100}$$

Here, $\underline{r}$ denotes the displacement vector between the centre of the measurement coordinate system and the centre of the current sources, e.g. the aperture of the AUT. In the true far-field this expression is exact. However, for the case of a measurement taken at a large but finite range length where the separation is sufficiently large to satisfy the far-field condition, this relation still remains a very good approximation. This mathematical translation has the effect of reducing the number of mode coefficients, of any elementary kind, that are required to represent thefar-field pattern. The equivalent CMCs can be obtained from far electric fields using standard cylindrical near-field theory (cf. Chapter 7)

$$B_m^1(k\cos\theta) = -\frac{j^{-m}}{4\pi k \sin\theta} \int_0^{2\pi} \underset{r\to\infty}{E_\phi}(r, \phi, \theta) e^{-jm\phi} d\phi \tag{12.101}$$

$$B_m^2(k\cos\theta) = -j\frac{j^{-m}}{4\pi k \sin\theta} \int_0^{2\pi} \underset{r\to\infty}{E_\theta}(r, \phi, \theta) e^{-jm\phi} d\phi \tag{12.102}$$

Here, ϕ represents a rotation about the vertical axis, while θ is measured away from the positive vertical axis. For a fixed measurement radius and frequency, these mode coefficients are complex numbers that do not vary with any of the scanning coordinates and are instead functions of the angular index n, and $\gamma = k\cos\theta$ is the Fourier variable which is the conjugate of the linear spatial variable z, such that $-\infty \leq n \leq \infty$, $-\infty \leq \gamma \leq \infty$. Strictly, these equations are only valid in the true (asymptotic) far-field. However, provided the measurements are taken with a finite but sufficiently large range length that guarantees the far-field condition is satisfied, then these integrals may be used with a high degree of confidence. Similarly, probe pattern correction can be effectively ignored since in the far-field the MRE only subtends a very small angular range as seen from the remote source antenna. That is, the probe (remote source antenna) pattern is effectively constant over the sphere containing the AUT that is centred about the origin of the measurement coordinate system.

From examination of these equations, it is clear that for a fixed value of θ, it is possible to deduce all CMCs for a corresponding value of γ. It is this observation

that allows the MARS technique to be extended and applied to one-dimensional far-field applications as when processing great circle far-field cuts, where the polar angle $\theta = \pi/2$ radians. It is also clear that the TE and TM CMCs are uncoupled from one another and that the θ- and ϕ-polarised electric fields are also uncoupled from one another. Crucially, this enables far-field MARS processing to be applied to only a *single* far electric field component. Thus dual polarised acquisitions are not required in all instances, cutting measurement time in half when cross-polar pattern information is not required. Strictly, as only far-field applications are being considered, only a single value of γ is used and this dummy variable (together with its Fourier conjugate variable z) can be omitted from the notation. Its retention here is merely intended to show how this application relates to the more general, and very well-established, cylindrical formulation.

Once the CMCs for the (now ideally centrally located) AUT have been recovered, any mode representing fields outside the ideal conceptual minimum MRE (r_{t0}) can be filtered out, removing contributions that are not associated with the AUT. Thus from standard cylindrical theory, it is possible to filter out all higher order modes without affecting the integrity of the underlying antenna pattern function. When expressed mathematically, the band-pass brick-wall mode-filtering function can be expressed as

$$B_n^s(\gamma)|_{s=1,2} = \begin{cases} B_n^s(\gamma) & n^2 + (\gamma r_{t0})^2 \leq (k_0 r_{t0})^2 \\ 0 & \text{elsewhere} \end{cases} \tag{12.103}$$

Here, it is clear that the CMCs associated with the AUT are confined to a narrow band that is tightly distributed about the $n = 0$ coefficient. As the total power radiated by the AUT must be conserved, the amount of power per mode must increase as the total number of modes associated with the AUT decreases. As the amount of noise per mode can be seen to be roughly constant with respect to the maximum level, the effective system SNR of the measurement is significantly increased. Crucially, as has been observed previously with *all* other MARS implementations, although the AUT has been translated back to the origin of the measurement coordinate system, this is not the case for the scatterers which are spatially extended and are represented by many *higher* order modes. In effect, the contributions in the CMC domain of the AUT and the scatterers are separated so that they do not interfere and are in essence orthogonalised from one another. The MARS-processed asymptotic far-field pattern can be obtained from a simple summation of CMCs. As these transforms and their inverse operations can be evaluated using the one-dimensional FFT, this makes the FF-MARS algorithm very efficient in terms of computational effort and resources. In summary, the FF-MARS algorithm can be described as follows:

1. Take a direct acquisition of the one-dimensional far electric field amplitude and phase pattern functions with the AUT offset from the origin.
2. Apply a differential phase change to mathematically translate the AUT to the origin of the measurement coordinate system.

3. Obtain the translated mode coefficients of the AUT for an AUT conceptually located at the origin of the measurement coordinate system.
4. Apply band-pass mode-filtering function to suppress unwanted higher order CMCs where the properties of the filter function are determined from the physical size of the AUT and the free-space propagation number.
5. Compute the complete far electric field pattern from the filtered mode coefficients to obtain the MARS-filtered AUT pattern function.

Results of the far-field MARS processing when used with a CATR can be seen presented in Chapter 5 (Section 5.4.5.1). The far-field MARS technique can be extended for use with two-dimensional antenna patterns. The FF-MARS technique was formulated for use with great-circle cuts. As every elevation cut in an azimuth over elevation measurement is a great circle cut, it is conceivable that FF-MARS can be used to suppress scattering in the elevation axis. Conversely, for the case of measurements taken using an elevation over azimuth coordinate system, FF-MARS would be applied to the azimuth axis.

Figure 12.107 contains a far-field measurement of an X-band SGH that was acquired using a far-field range and an azimuth over elevation positioner. Here, as a result of the chamber absorber layout, some scattering was evident in the elevation axis, cf. the distortion that is clearly evident for large elevation angles. Far-field MARS processing was applied in the elevation axis yielding the results presented in Figure 12.108. Here, it is evident that the effects of range reflections that were

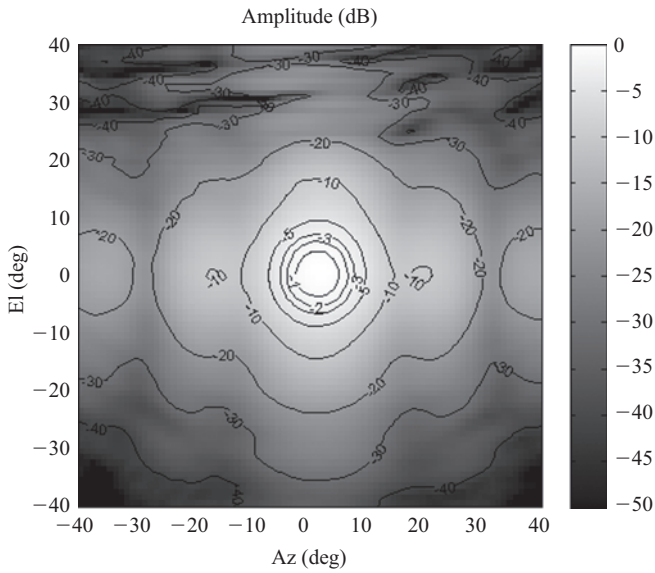

Figure 12.107 Azimuth over elevation measurement without FF-MARS processing

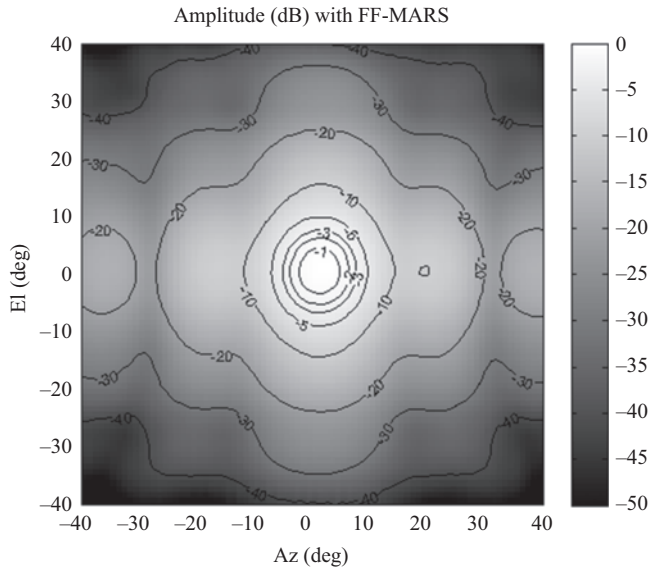

Figure 12.108 Azimuth over elevation measurement with FF-MARS processing applied

hitherto degrading the measurements have been successfully removed yielding a high-quality result.

Far-field MARS as implemented here only suppressed range reflections in one axis. As two-dimensional data is available, it would be preferable for this suppression to be applied in both axes. In practice this can be accomplished using the spherical MARS technique that is developed below. As the spherical near-field formula is equally valid for near- and far-field data, S-MARS can automatically be used with two-dimensional far-field data.

12.5 SNF topics

12.5.1 Spherical near-field electrical alignment

Within the development of the spherical mode expansion-based near-field to far-field transform, it was assumed that the sampled near-fields were tabulated on a plaid, monotonic and equally spaced spherical grid. This arrangement is shown in Figure 12.109.

For this to be a valid assumption, the mechanical rotators employed within the spherical positioning system must be correctly aligned and the probe placed in the proper location and orientated correctly when taking spherical near-field measurements. This alignment is usually accomplished using optical instruments such as theodolites and autocollimators and ideally it should be carried out with the AUT mounted on the rotator [34]. In this way any gravitational deformation that is

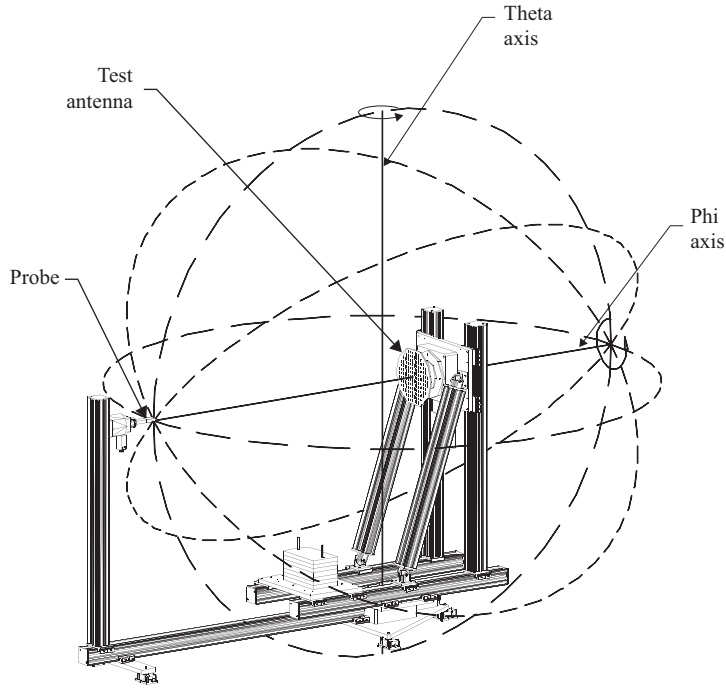

Figure 12.109 Schematic of spherical measurement system showing correctly aligned axes and probe position

induced by the mass of the AUT can be taken into account within the alignment process allowing the spherical positioning structure to be correctly aligned. In some cases it may be impractical to place the alignment mirrors on the AUT or optical instruments may not be available. In these cases, it is desirable to confirm the spherical alignment using electrical measurements on the actual AUT and probe. If the rotation stages are not correctly aligned, the radial distance will change as the AUT is rotated, and the measurement points will not be taken on a regular plaid and equally spaced intervals in θ and/or ϕ. The resulting data will therefore not produce correct results when processed using standard spherical mode expansion-based techniques. The extent to which this error enters into the far-field pattern will depend upon the exact nature and magnitude of the alignment imperfection and it may not be convenient or even possible to correct for these errors during post-processing.

That being said, in many cases, the spherical rotators are aligned using a combination of mechanical and optical devices before the AUT is mounted for measurements. It is therefore assumed that the rotator remains perfectly aligned when the antenna is mounted and measurements are performed. In these cases, it would be very desirable to have electrical measurements, i.e. those derived from the measured amplitude and phase data, which can be used to verify the alignment

of the rotators with the actual AUT in place. This would enable the effects resulting from gravitation deformation to be quantified or corrected. Such electrical measurements can also be used in place of the mechanical/optical procedures when appropriate, and can be used periodically during a measurement campaign to ensure continued alignment. These electrical measurements and the accompanying post-processing are presented below. Detailed information on the sensitivity to alignment errors and measurement geometry can be found in the open literature [35,36]. Various alignment errors can be considered within a spherical measurement system. These can be summarised as follows:

1. Non-orthogonality of the θ- and ϕ-axes,
2. θ-zero error,
3. x-zero error,
4. y-zero error,
5. Non-intersection of the θ- and ϕ-axes,
6. Probe axis not parallel to the z-axis.

These six cases can be seen illustrated schematically for a ϕ over θ (also sometimes referred to as a 'roll over azimuth' or 'model tower') positioner system in Figures 12.110–12.115, respectively.

Within the open literature a great deal of information can be found describing the ways in which spherical positioners can be aligned [34,32–38] and it is not the intent to repeat these procedures here. For the purposes of developing the electrical alignment procedure below, it is merely necessary to assume that the rudimentary course mechanical spherical alignment has been completed. Once these initial mechanical and optical alignments have been completed, the AUT can be installed on the ϕ-axis positioner and the electrical tests can commence.

The electrical alignment measurements consist of acquiring two principal polarisation θ-cuts across the main beam region of the pattern (down to circa -20 dB below the pattern peak) for $\phi = 0^\circ$ and $\phi = 180^\circ$ with a finely spaced abscissa, circa better than 0.5° sample spacing. These measurements, when processed appropriately, enable the derivation and compensation of the θ-zero error, and a calculation of the intersection error. As defined above, the θ-zero error is the misalignment between defined zero position of θ rotator and the true zero, whereas the non-intersection error is the offset between θ-axis rotator and the ϕ-axis rotator. Figures 12.116 and 12.117 contain plots of the measured amplitude and phase θ-scans taken at $\phi = 0^\circ$ and $\phi = 180^\circ$ for an X-band 15 dB gain horn showing typical alignment data with θ-zero, x-zero, and non-intersection errors. Here, the 180° scan has been inverted to enable it to be directly compared with the 0° scan.

The amplitude difference and part of the phase difference are due to the combined x-zero and θ-zero errors. This is because the antenna is fixed to the ϕ-axis, the pattern is rotated about the ϕ-axis for the 180° scan, and the position of the probe relative to the antenna is changed. The θ-zero error can be established by taking half the difference between the electrical antenna pointing. This is true even if the AUT is not perfectly aligned to the axes of the range. In practice there are several avenues available for the computation of the pointing of the pattern. It is

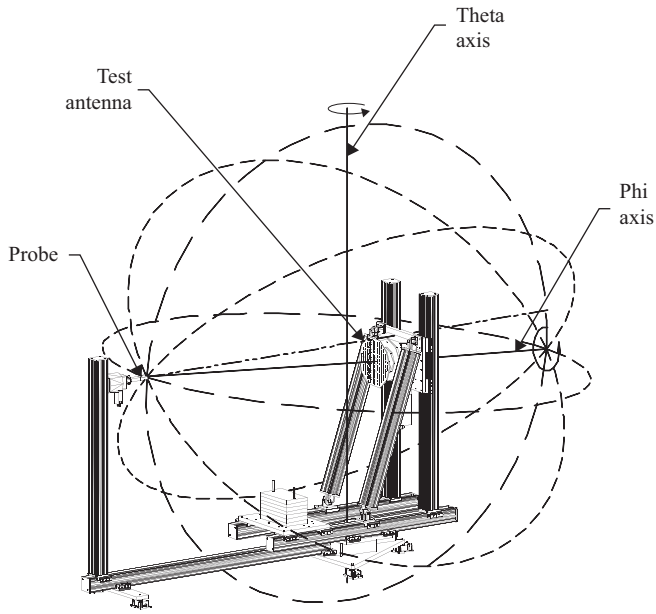

Figure 12.110 Schematic of spherical measurement system showing non-orthogonality of θ- and ϕ-axes alignment error

possible to fit a function, e.g. a low-order polynomial, to the peak of the pattern and then to solve for the point of inflection that is simultaneously also the largest pattern value. This would be performed for both the $\phi = 0^\circ$ and the $\phi = 180^\circ$ cuts. Alternatively, it is possible to compute the difference between the cuts. By calculating the dB difference of the linear amplitudes, an error to signal level can be obtained for the main beam region, i.e. for parts of the pattern that are 10 dB and higher with respect to the peak of the pattern. The degree of agreement attained can be represented by a single RMS value that is computed across this region of the pattern. By sequentially sifting one cut with respect to the other, it is possible to minimise this function thereby simultaneously minimising the difference in the pointing between the respective cuts. In practice this non-local iterative optimisation scheme is found to yield the best result as it is inherently robust to measurement noise, etc. Once the value of the θ-zero error is determined, it can be added to the θ-axis encoder readout value (i.e. the index offset) and acquisitions can be taken with the pole of the spherical measurement system correctly aligned. Once the θ-zero error has been minimised, it is possible to repeat the acquisition of the two θ cuts and the axis intersection error can be determined. In principle it is possible to minimise the number of acquisitions that are taken by merely correcting the original cuts for the θ-zero error before performing the additional processing. However, acquiring fresh measurements enables a practical confirmation of the

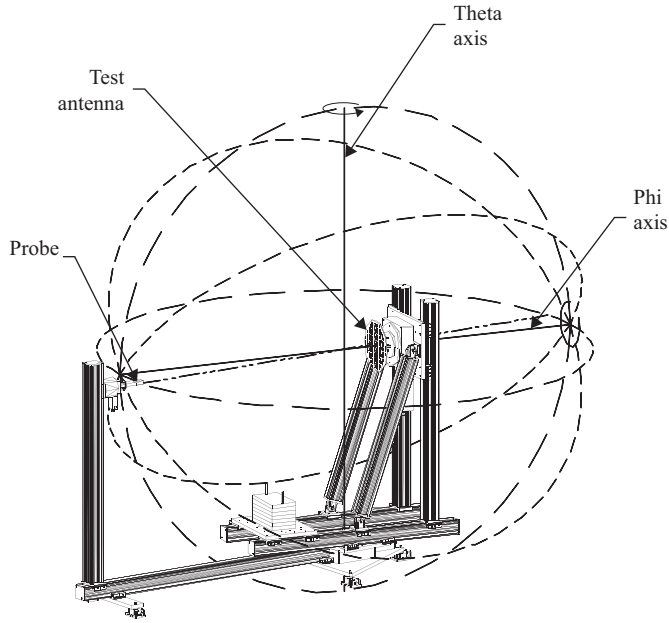

Figure 12.111 Schematic of spherical measurement system showing θ-zero alignment error

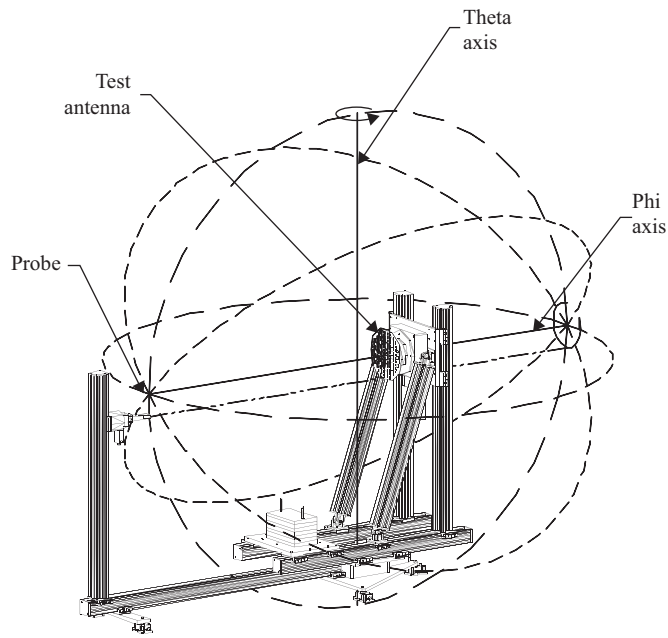

Figure 12.112 Schematic of spherical measurement system showing x-zero alignment error

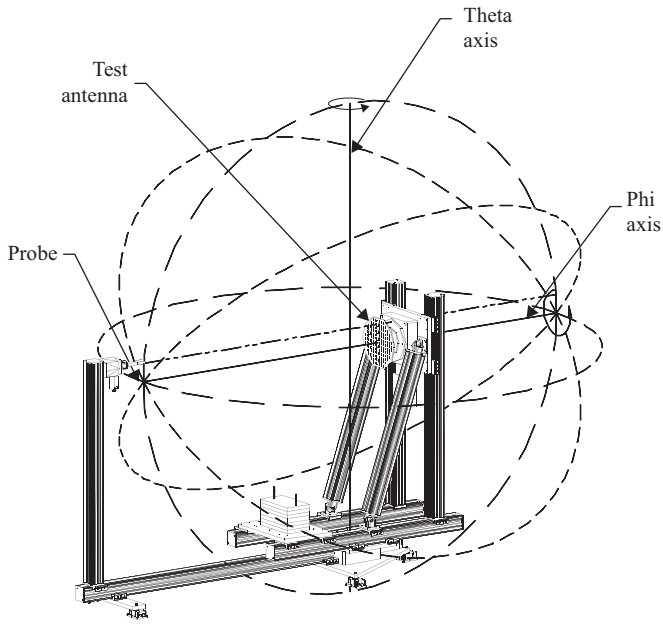

Figure 12.113 Schematic of spherical measurement system showing y-zero alignment error

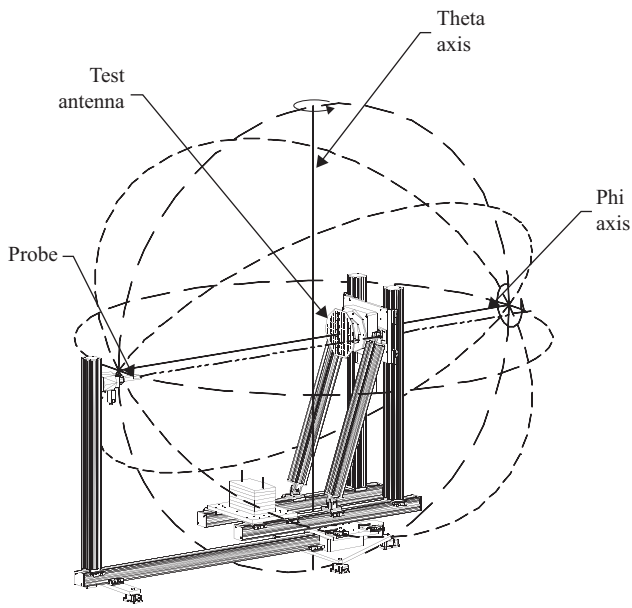

Figure 12.114 Schematic of spherical measurement system showing non-intersection of θ- and ϕ-axes alignment error

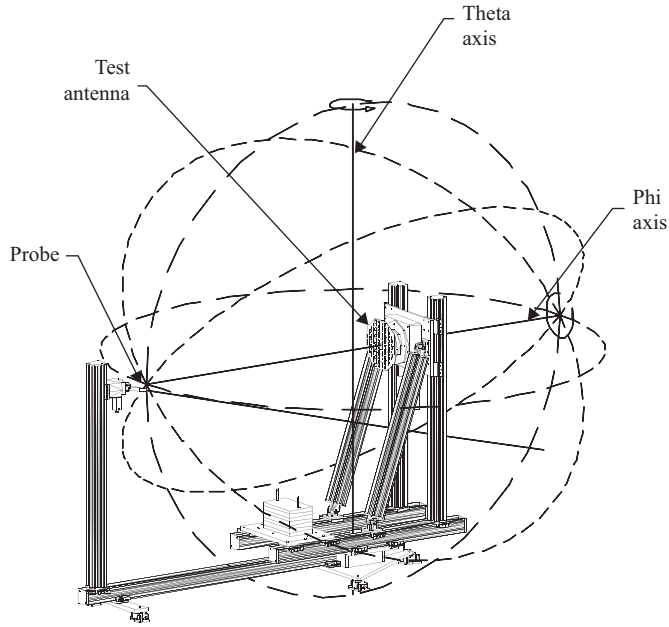

Figure 12.115 Schematic of spherical measurement system showing probe axis alignment error

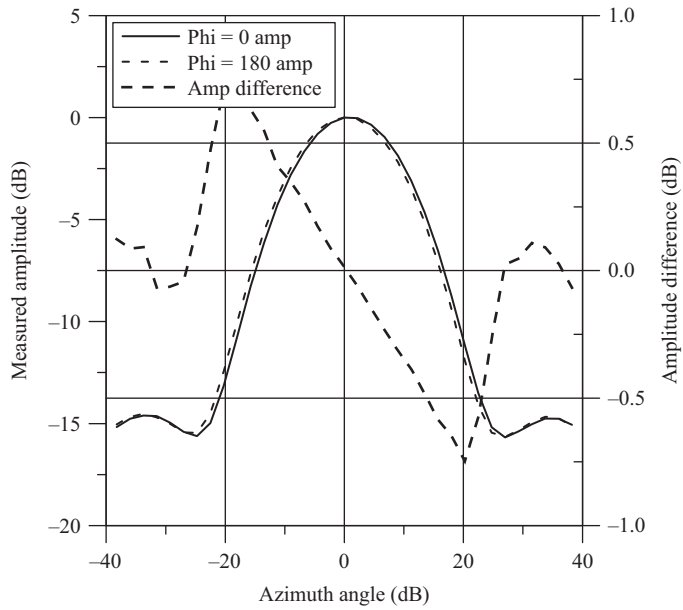

Figure 12.116 Comparison of $\phi = 0°$ and $180°$ cuts together with amplitude difference

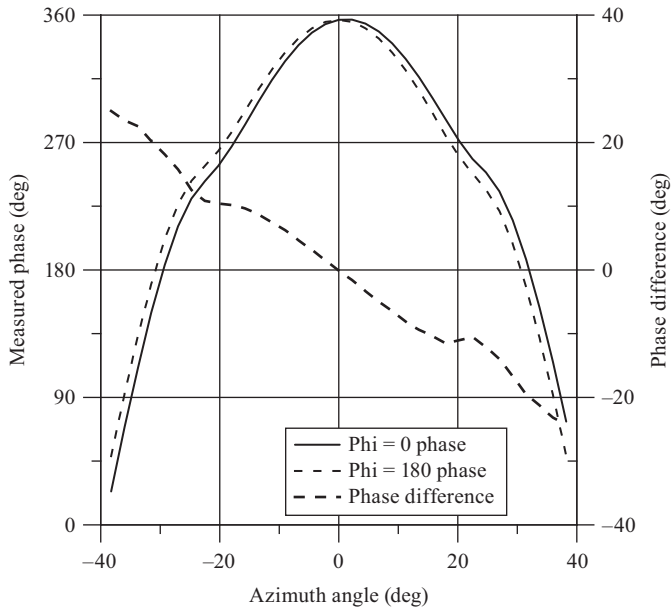

Figure 12.117 Comparison of $\phi = 0^\circ$ and 180° cuts together with phase difference

correct application of the θ-zero value to be obtained, and requires only a minimal amount of range time. The derivation of the axis intersection, as illustrated in Figure 12.118, is obtained from inspection of the difference in the respective phase plots once the θ-zero error has been removed as illustrated in Figure 12.119. Here, Figure 12.118 shows a non-intersection error which is the offset between θ-axis of rotator and the ϕ-axis of the spherical AUT rotator.

Here, the intersection error can be obtained from the slope of the phase difference plot using

$$\Delta_{\text{Int}} = -\frac{\lambda \Delta_\phi}{2\pi \sin(\theta)} \tag{12.104}$$

Here, the peak-to-peak phase change is denoted by Δ_ϕ. This is the peak-to-peak phase change across the angular range of $-\theta$ and $+\theta$. Thus for the example of an X-band (10 GHz, $\lambda = 3$ cm $= 1.18''$) pyramidal horn shown in Figure 12.119, the peak-to-peak phase change $\Delta_\phi = 24.4^\circ$ between -40° and $+40^\circ$; thus we may write that the intersection error when expressed in inches is

$$\Delta_{\text{Int}}(\text{Inch}) = -0.005\Delta_\phi = -0.122'' \tag{12.105}$$

For this case, this corresponds to an intersection error of approximately one-tenth of a wavelength. Here, for the case of receivers that use the positive time convention

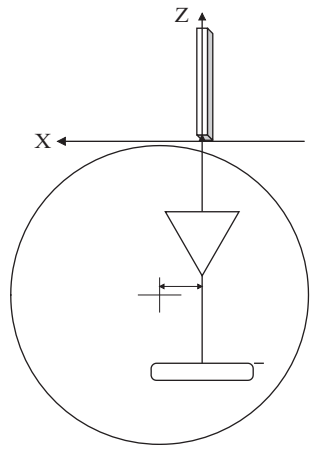

Figure 12.118 Spherical near-field electrical alignment with non-intersecting θ/ϕ axes only

of exp($j\omega t$), the phase will decrease with increasing distance between the AUT and the probe. For this time convention and the phase difference as defined in the equation above, an offset error in the $+x$ direction as shown in the example treated here produces a negative phase difference slope which explains the negative sign in the equations quoted above. In this way, fine alignment adjustments can be made to the spherical positioners, e.g. with the use of shim stock. A similar process can be used to obtain the intersection error on the y-axis.

Electrical alignment is a fast and accurate addition to the spherical alignment process. Crucially, only measurements of the principally polarised field-component are required. No optical alignment tools are required, with only two one-dimensional scans being required making the process very fast, with potentially the measurement and processing being fully automated allowing the alignment to converge quickly. Most significantly, the system is aligned with the actual weight loading of the AUT and probe with an accuracy that is approximately equal to that which can be attained using optical instruments.

12.5.2 The radial distance to MRS ratio

In the previous section, techniques for aligning the rotator within a spherical near-field system were discussed. In addition to these alignments, for the spherical near-field to far-field transform to be valid, the measurement radius must also be known. If there is an error within the values used within the transform, this will manifest itself within the far-field pattern. This section illustrates the impact that such errors can have and provides guidelines for the accuracy with which these values must be known.

To illustrate this, a narrow beam slotted waveguide array antenna with a gain of circa 35 dB radiating at 9.375 GHz was acquired. Here, AUT and the probe were

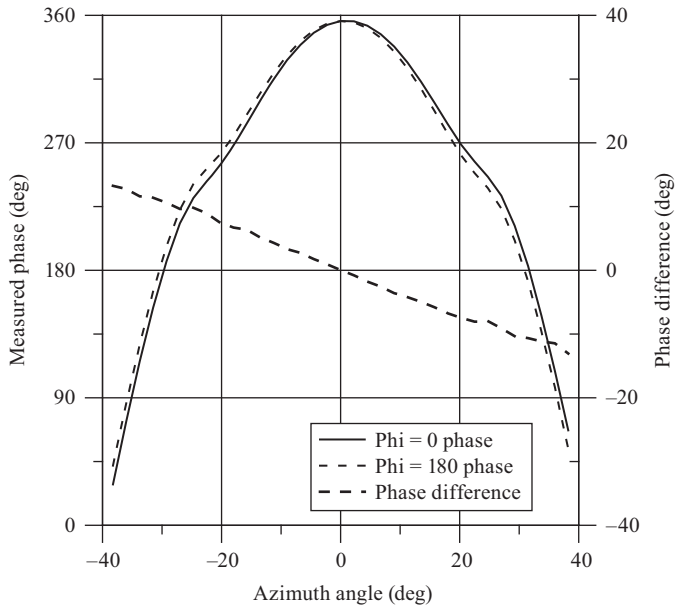

Figure 12.119 Spherical near-field electrical alignment data with non-intersecting θ/ϕ axes only

linearly polarised with on-axis axial ratios of 40 dB or more. Near-field data were obtained for two measurement radii. The first spherical near-field dataset was taken at a measurement radius of twice the MRS of the AUT; the second dataset was for a measurement radius at four times the MRS. By acquiring the antenna with a measurement radius specified in terms of the MRS, it allows the results to be translated to other antennas of different sizes operating at different frequencies. Each of these datasets were transformed to the far-field using a standard spherical mode expansion-based transform as developed above within Chapter 8. To illustrate the effect of an error in the measurement radius, these datasets were transformed to the far-field; only this time the measurement radius used by the spherical transform was increased by half a wavelength. The resulting far-field patterns were compared with differences being presented in terms of a difference level. These far-field patterns can be seen respectively in Figures 12.120 and 12.121.

Here, the solid trace denotes the far-field pattern as obtained from the spherical transform when using the correct measurement radius. The trace containing the crosses was derived using the same near-field data only here; the measurement radius used within the transformation was specified as being too large by half a wavelength at X-band. Here, as expected, the largest differences are evident in the region of the main beam. The dataset containing the measurement radius error exhibits a broadening of the main beam (corresponding to a reduction in apparent gain and directivity) with the first nulls being partially filled in. Such effects are

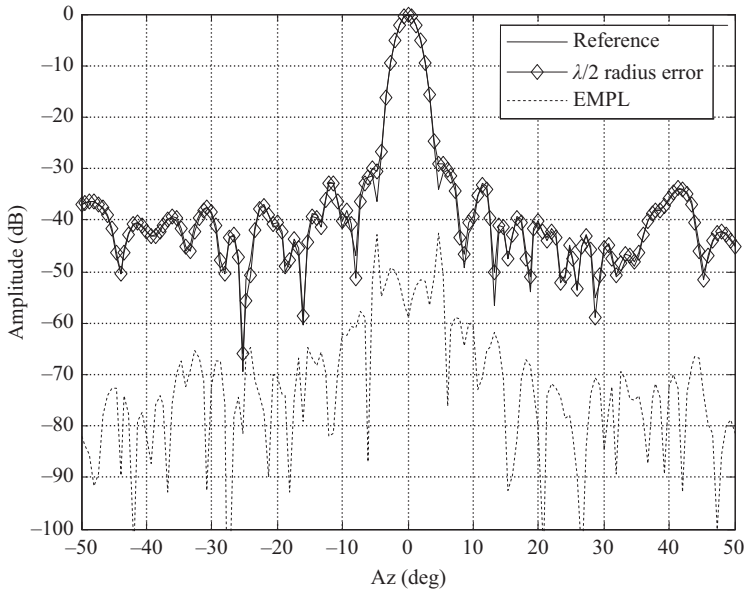

Figure 12.120 Example of half wavelength measurement radius error on SNF measurement taken at a range length of 2 MRE

generally most pronounced for large aperture high-gain antennas such as that which was used here. The effects are less dramatic at wide out pattern angle as the projected aperture is smaller and the corresponding range length effects are less critical. Figure 12.121 contains an equivalent result for the measurement when taken at twice the range length. Here, the same observations can be made; however it is quite clear that they are far less pronounced. This is particularly evident from inspection of the EMPL which is circa 10 dB lower than was the case for the reduced range length measurement. In general, it is found that the accuracy and precision with which the measurement radius is needed to be known reduces as the ratio of the range length to the MRS increases. Thus, irrespective of the frequency, and the size of the AUT, as the ratio of the range length to the MRS becomes large, the contributions those errors have to the facility level uncertainty budget become progressively less pronounced.

However, as far-field phase is generally not important for most antenna measurements, uncertainties within the AUT-to-probe separation are often unimportant when testing using a planar near-field test system. Thus when testing using a cylindrical near-field system, range-length errors typically only manifest themselves within one of the far-field dimensions, i.e. the ϕ-axis as this axis is conceptually equivalent to the spherical case discussed above.

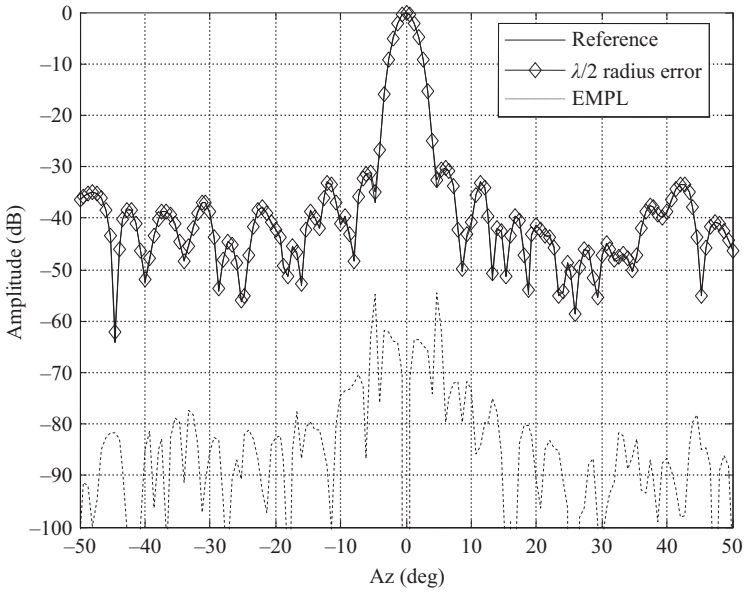

Figure 12.121 Example of half wavelength measurement radius error on SNF measurement taken at a range length of 4 MRE

12.5.3 Spherical mathematical absorber reflection suppression

The electromagnetic fields outside an arbitrary test antenna radiating into free space can be expanded onto a set of elementary orthogonal SMCs as was outlined in Chapter 7 and in Section 12.3.4. When this spherical mode expansion techniques are combined with the MARS processing algorithm presented above, a highly effective method for suppressing spurious scattered fields can be obtained.

The effectiveness of this strategy can be demonstrated through the use of a series of self-comparison (i.e. repeat) measurements that are used to evaluate the effects of error sources on the measurements of an SGH that was acquired within an anechoic chamber of finite, but changeable, quality. To further illustrate the impact of the post-processing, spherical measurements using two different acquisition modes can be compared that significantly alter the way in which the walls of the chamber are illuminated by the AUT during the acquisition which provides additional conformation of the effectiveness of the processing. Figure 12.122 contains a picture of an anechoic chamber that was lined with 7.62 cm (3″) wedge absorber in the central region which is the region where the largest field intensities can reasonably be expected to be encountered. A WR284 OEWG probe was used to acquire data within this chamber before the absorber treatment in the central region was exchanged for taller, 20 cm (8″) pyramidal absorber which is shown in Figure 12.123. By exchanging the absorber it would be expected that the scattering

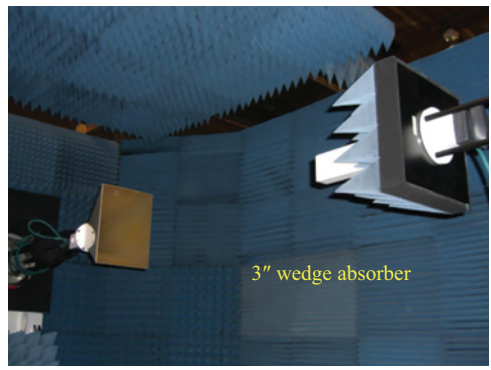

Figure 12.122 WR284 SGH acquired in chamber with 3″ wedge absorber lining

properties of the chamber would be significantly affected. Pyramidal absorber tends to have more improved forward scattering properties than equivalently sized wedge absorber.

In addition to this, and as discussed in Chapter 8 and in the appendices of this text, repeat measurements were made in each of these chamber configurations where $0° \leq \theta \leq 180°$ with $0° \leq \phi \leq 360°$ and again where $-180° \leq \theta \leq 180°$ with $0° \leq \phi \leq 180°$. Each of these spherical acquisition schemes results in a complete sphere of near-field data being recorded. However, in the first case the boresight direction of the AUT only illuminates one half of the chamber, whereas in the second case the boresight direction passes around the entire chamber. Thus assuming that the near-field system is correctly aligned, then differences in the absorber configuration and scattering characteristics of the chamber will influence the measurements differently.

Measured near electric fields for a principally horizontally polarised (E_θ) probe and a vertically polarised (E_ϕ) probe, for a 180° span in θ acquisition (Phi_360[3]), can be found presented in Figures 12.124 and 12.126. Similarly, Figures 12.125 and 12.127 contain equivalent measured data that was obtained from a 360° θ acquisition (Phi_180[3]). Although these measurements contain the fields radiated by the same antenna in the same chamber with the same blockage and probe effects, the range reflections that are contained within these datasets will be quite different. Here, the near electric fields have been presented as grey-scale plots having been resolved onto a polar spherical polarisation basis and tabulated on a regular polar spherical coordinate system.

Although the angular ranges of the spherical near-field acquisition intervals differ between these two measurements, equivalent probe pattern-corrected far-field data can be derived and compared. Figures 12.128 and 5.129 contain grey-scale plots of the probe pattern-corrected far electric fields of the SGH having been resolved onto a Ludwig II azimuth over elevation polarisation basis and having

[3]Refer to Chapter 7, Section 7.9.

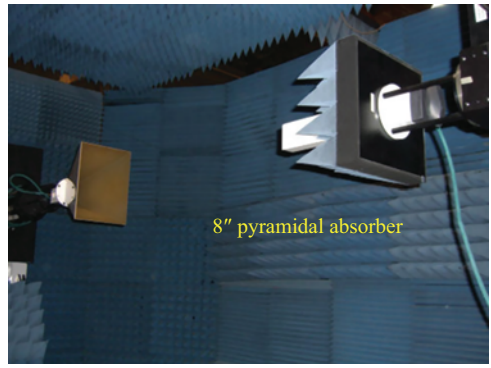

Figure 12.123 WR284 SGH acquired in chamber with 8″ pyramidal absorber lining

been tabulated on a regular nadir-centred azimuth over elevation coordinate system which were derived from the single-sided (Phi_360) and dual-sided (Phi_180) near-field acquisitions. These patterns were derived by using standard spherical processing.

As expected, the respective far-field patterns are in encouraging agreement, as they should be; however some second-order differences are present. These can be better seen by comparing the great circle azimuth cuts which can be found presented in Figures 12.130 and 12.131. Figure 12.130 contains three traces. The solid trace is the great circle far-field cut as obtained from the single-sided (Phi_360) cut. The dashed trace was derived from the double-sided (Phi_180) cut. Finally, the dotted trace denotes the difference between these cuts when expressed in dB form. Figure 12.131 is an equivalent plot for the case where the SGH was acquired in a chamber with 8″ pyramidal absorber. By comparing Figures 12.130 and 12.131, it is clear that the difference between the single-sided (Phi_360) cut and the double-sided (Phi_180) cut are larger for the case where the SGH was acquired with 3″ wedge absorber than is the case when the SGH was acquired with 8″ pyramidal absorber. This is evidenced by the lower difference level (i.e. a larger negative number is shown in the plot subtraction in Figure 12.131 than can be seen in Figure 12.130).

Figures 12.132 and 12.133 contain equivalent pattern cuts; only in this case spherical MARS processing has been applied in order that the spurious range reflection can be suppressed. From inspection of these figures, it is clear that the degree of agreement attained between the respective patterns is significantly better than was previously the case. Here, it is clear that the difference levels, i.e. the dotted traces, have decreased by circa 15–20 dB from the baseline case as obtained with standard spherical processing. This improvement in agreement between the single-sided (Phi_360) cut and the double-sided (Phi_180) cut provides strong encouragement that the MARS processing is effectively attenuating range reflections. This is also supported by the improvement in the symmetry that can be seen

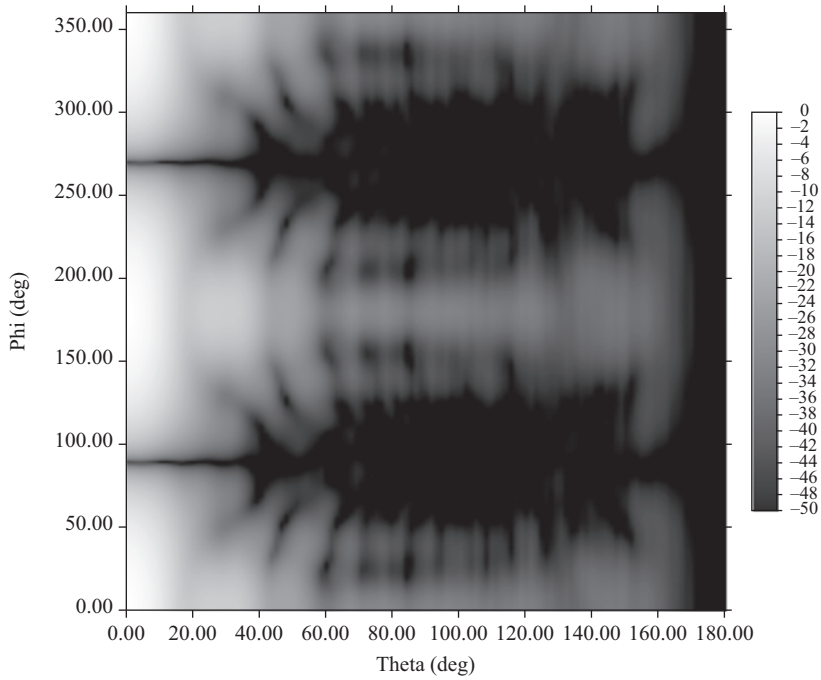

Figure 12.124 $E_\theta(H)$ *polarised measured near electric field. AUT boresight illuminates only the positive* θ *sides of the chamber*

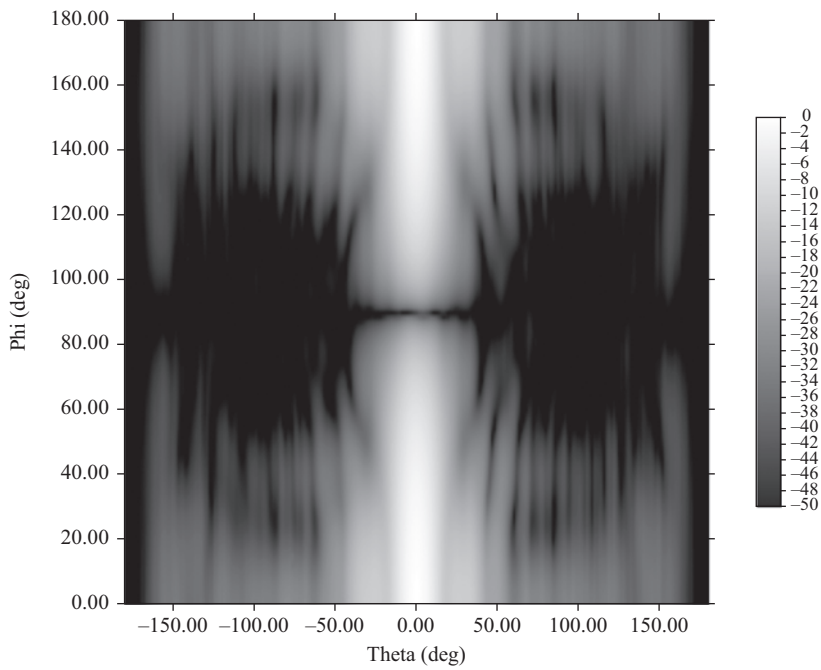

Figure 12.125 $E_\theta(H)$ *polarised measured near electric field. AUT boresight direction illuminates both the positive* θ *and negative* θ *sides of the chamber*

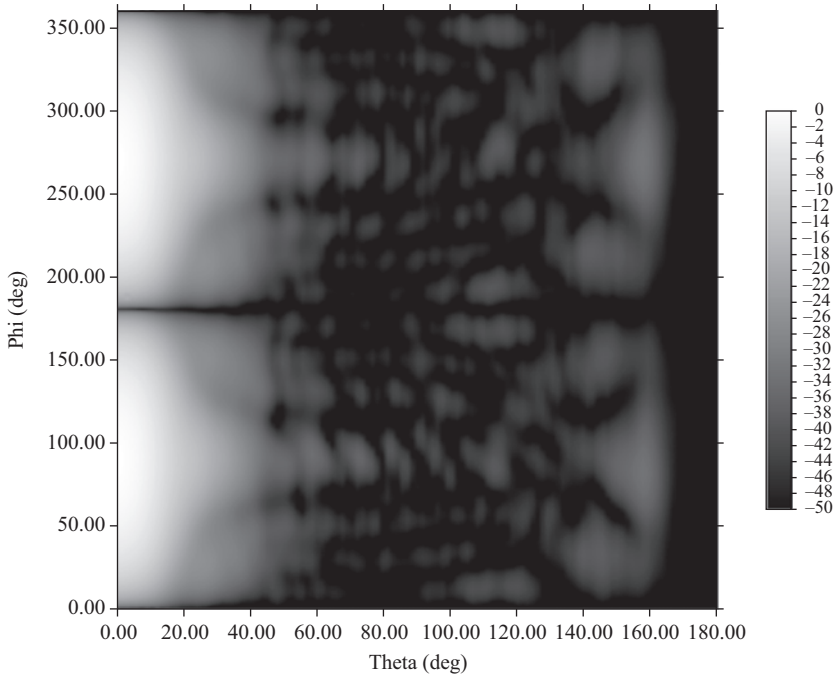

Figure 12.126 $E_\phi(V)$ polarised measured near electric field. AUT boresight illuminates only the positive θ sides of the chamber

in the patterns, and the absence of high angular frequency ripple that is not realisable from a small aperture antenna such as the SGH being tested here.

An illustration of the MARS processing can be obtained from the mode plots. Figure 12.134 contains a spherical mode plot that shows the normalised power contained within the n modes for the $m = 1$ index. The solid trace shows the mode plot that was obtained from the SMCs that were derived from the measured spherical near-field data. The dashed trace contains an equivalent mode plot for the case where the AUT has been mathematically translated back to the origin of the measurement coordinate system. As the corresponding conceptual MRS has been decreased by this translation, fewer modes are required to represent the AUT. The higher order modes, i.e. modes with indices higher than approximately $n = 11$ however, cannot be associated with the AUT and can be filtered out without affecting the fidelity of the underlying antenna pattern function. The corresponding MARS-filtered mode plot can be seen represented by the dotted trace.

The difference in behaviour of modes associated with the AUT and modes that result from range reflections and noise are not easy to ascertain from inspection of plots of the SMCs. However, as the underlying physics is in common between the various implementations of the MARS measurement and post-processing, further

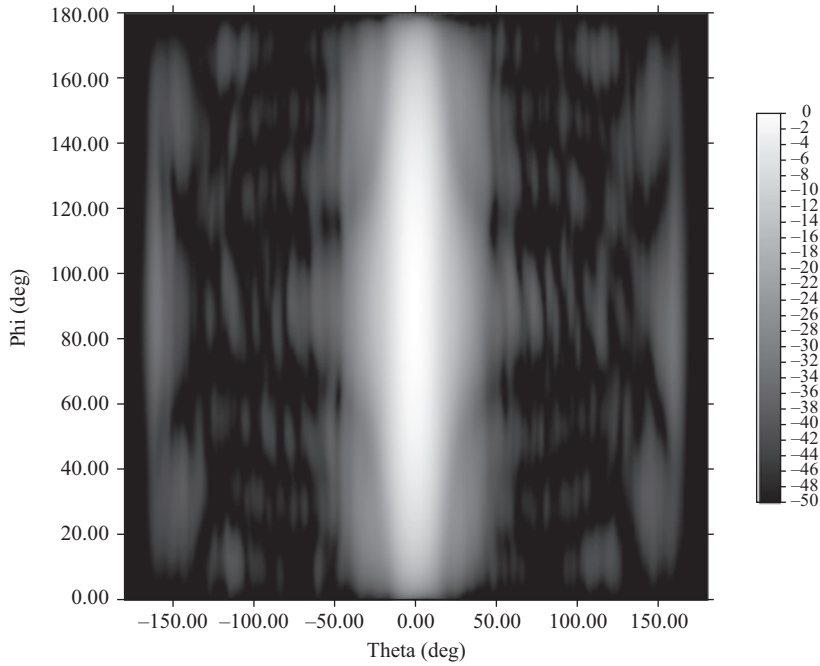

Figure 12.127 *$E_\phi(V)$ polarised measured near electric field. AUT boresight direction illuminates both the positive θ and negative θ sides of the chamber*

explanation will be left to the subsequent sections where these observations are more immediately apparent.

12.5.3.1 MARS with a stationary AUT and an articulated mm-wave spherical antenna test system

The articulated spherical near-field antenna test system presented in Chapter 8 and illustrated in Figure 8.12 [39] is unusual in the fact that the AUT remains entirely at rest for the duration of the spherical near-field acquisition with, instead, the near-field probe traversing the spherical sampling surface. This means that the AUT rather than the probe remains fixed in its orientation with respect to the chamber and any likely sources of scattering. However, as the probe still moves, and consequently the signal path changes throughout the measurement the scattering suppression techniques developed above should remain effective at removing spurious signals. To illustrate this, a stationary mm-wave low gain AUT was acquired in an open non-anechoic laboratory environment with the results being courtesy of Universitié Nice Sophia Antipolis. Here, only a small physical offset was required to achieve full spherical mode orthogonalisation. The far-field cylindrical mode processed results can be seen presented in Figure 12.135. Here, the red trace denotes the far-field pattern as measured which clearly exhibits a significant

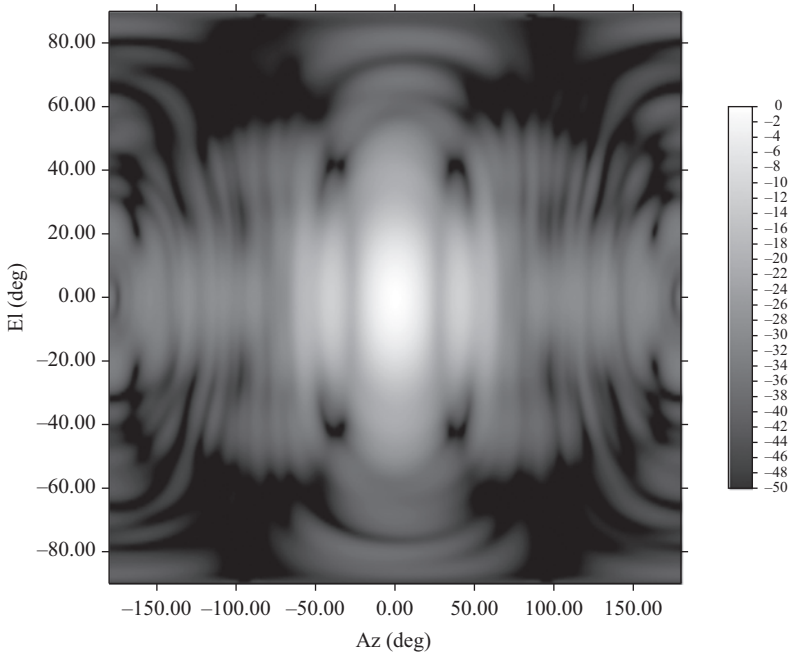

Figure 12.128 Far-field $E_{az}(H)$ polarised far-field pattern derived from measurements where the AUT boresight illuminates only the positive θ sides of the chamber

amount of scattering. Conversely, the blue trace corresponds to the mode filtered pattern where the high angular frequency ripple has been very effectively extracted. The behaviour of the corresponding CMCs can be seen presented in Figure 12.136. Here, the red CMC plot corresponds to the modes obtained prior to mathematically translating the AUT to the origin of the measurement coordinate system, the blue trace represents the amplitude of the CMCs once they have been translated to the origin and the purple trace represents those modes once they have been filtered. As usual, the mode filter was determined by the conceptual minimum MRE of the AUT and the frequency of operation. Here, crucially, the behaviour of the modes exactly mirrors the behaviour that is typically observed during a conventional measurement in which the AUT is rotated thereby confirming the applicability of the mode filtering technique to this area of application.

12.5.3.2 Generalised far-field MARS – matrix inversion method

So that we may develop the generalised post-processing let us start by taking the standard transmission equation presented above which relates CMCs to far-fields where, as per the usual convention, the unimportant far-field spherical phase factor and inverse *r* term have been suppressed. Thus, for the case of the great circle cut

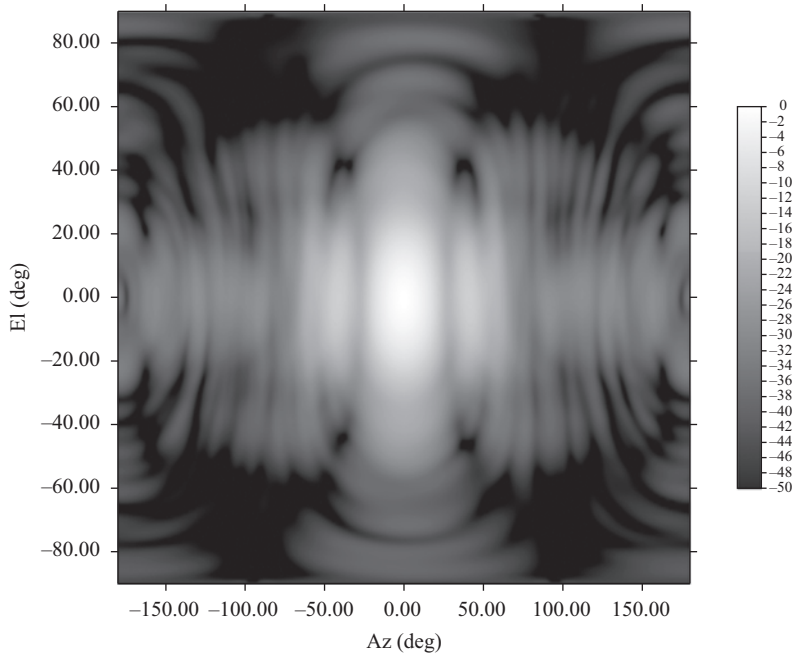

Figure 12.129 Far-field $E_{az}(H)$ polarised far-field pattern derived from measurements where the AUT boresight direction illuminates both the positive θ and negative θ sides of the chamber

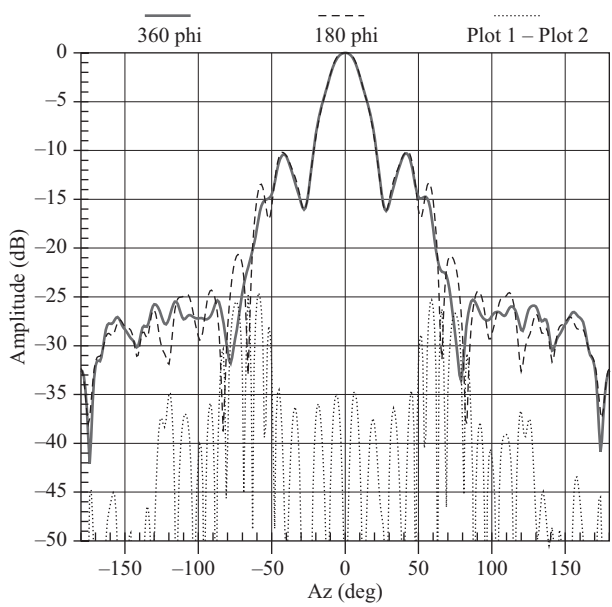

Figure 12.130 Comparison of far-field azimuth cuts that were acquired in chamber with 3″ wedge absorber

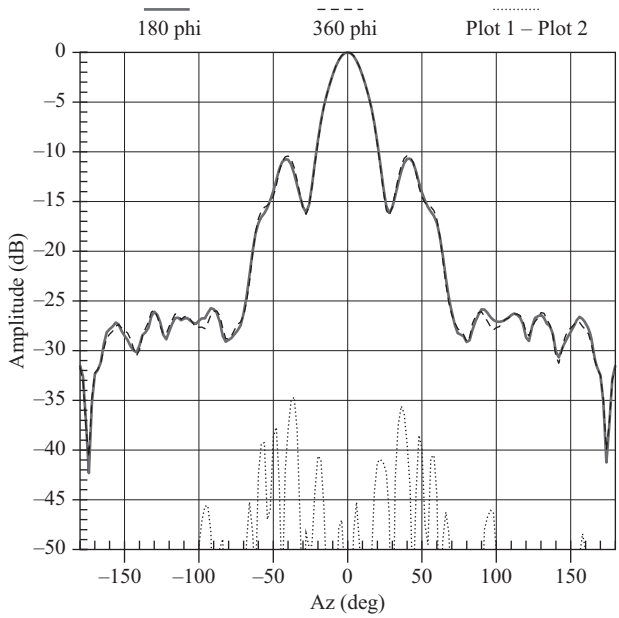

Figure 12.131 Comparison of far-field azimuth cuts that were acquired in chamber with 8″ pyramidal absorber

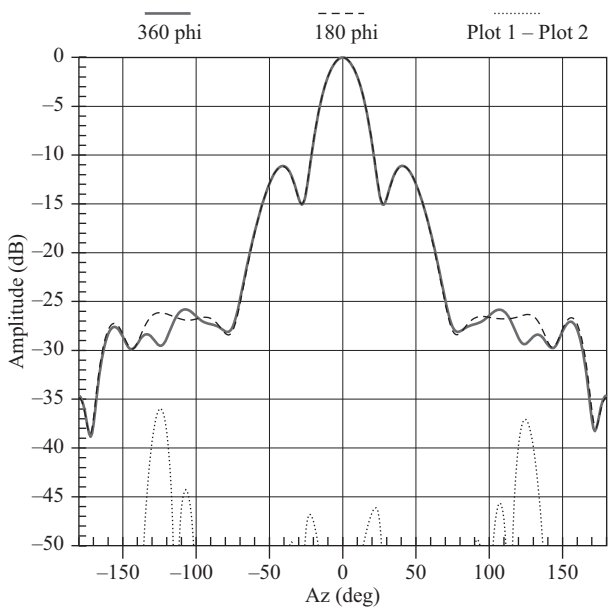

Figure 12.132 Comparison of far-field azimuth cuts that were acquired in chamber with 3″ wedge absorber with MARS processing applied

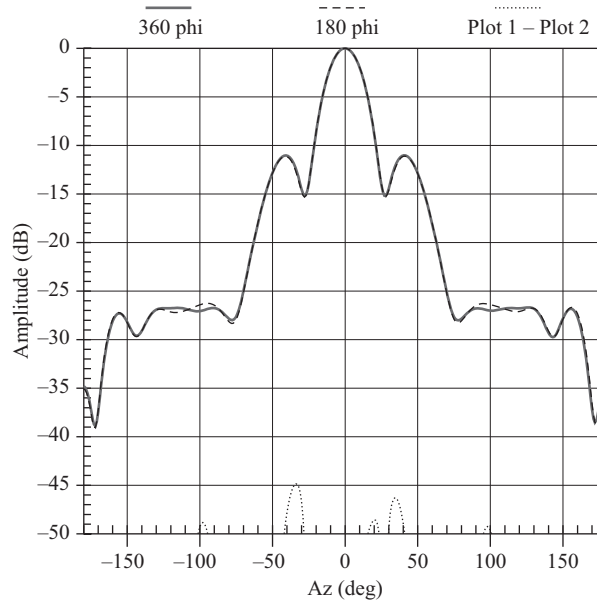

Figure 12.133 Comparison of far-field azimuth cuts that were acquired in chamber with 8″ pyramidal absorber with MARS processing applied

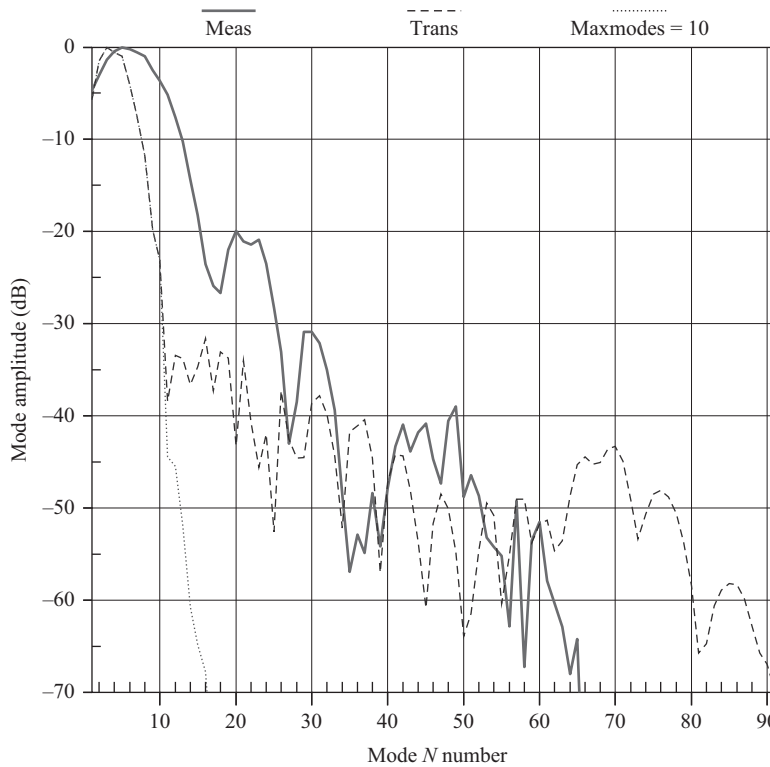

Figure 12.134 Spherical mode plot for m = 1

where $\theta = 90^\circ$ we may write that

$$E_\theta(\phi) = 2jk_0 \sum_{n=-\infty}^{\infty} (-j)^n B_n^2 e^{jn\phi} \tag{12.106}$$

With no loss of generality, we may rewrite this summation in the form of a matrix multiplication yielding

$$\begin{bmatrix} E_{\theta,\phi_1} \\ E_{\theta,\phi_2} \\ \vdots \\ E_{\theta,\phi_{n_\phi}} \end{bmatrix} = 2jk_0[M] \cdot \begin{bmatrix} B_1^2 \\ B_2^2 \\ \vdots \\ B_n^2 \end{bmatrix} \tag{12.107}$$

The matrix of basis functions M which has n_ϕ rows by n_n columns is defined as

$$[M] = \begin{bmatrix} -je^{j\phi_1} & (-j)^2 e^{j2\phi_1} & \cdots & (-j)^{n_n} e^{jn_n\phi_1} \\ -je^{j\phi_2} & (-j)^2 e^{j2\phi_2} & \cdots & (-j)^{n_n} e^{jn_n\phi_2} \\ \vdots & \vdots & \ddots & \vdots \\ -je^{j\phi_{n_\phi}} & (-j)^2 e^{j2\phi_{n_\phi}} & \cdots & (-j)^{n_n} e^{jn_n\phi_{n_\phi}} \end{bmatrix} \tag{12.108}$$

Here, the elements within the matrix M have a magnitude of unity with only the phase varying from element to element. Inverting this expression and

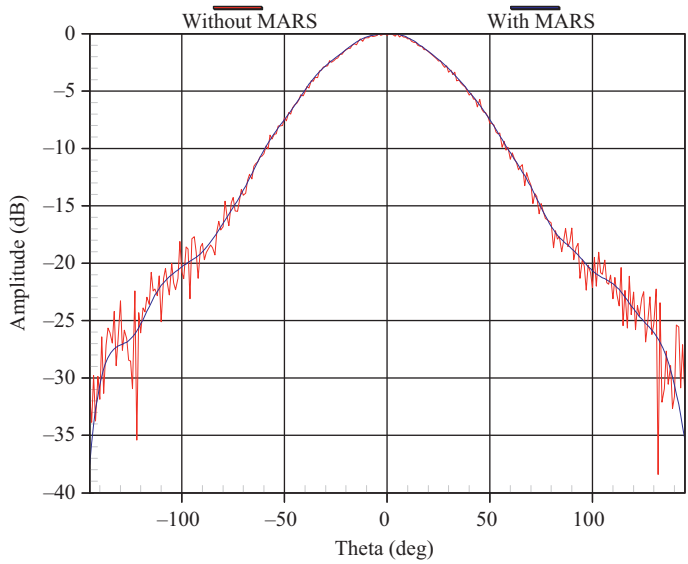

Figure 12.135 Comparison of far-field measured pattern in a non-anechoic environment with the same pattern having been processed. Result courtesy of Universitié Nice Sophia Antipolis

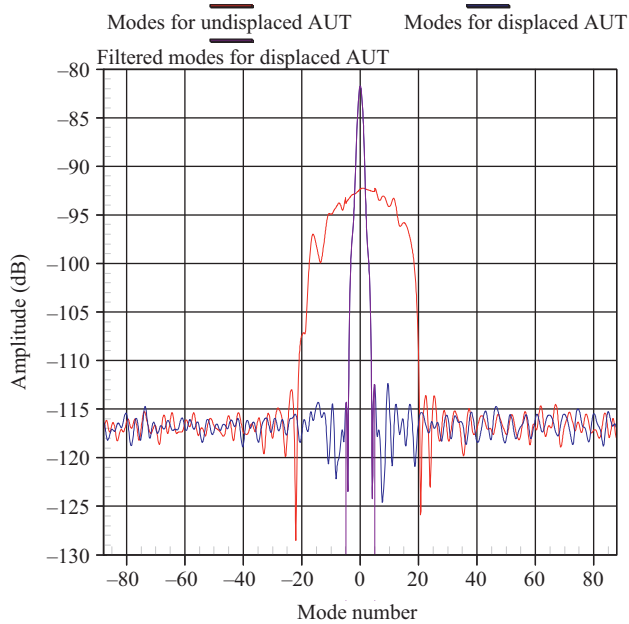

Figure 12.136 Plot of cylindrical mode coefficients for mm-wave AUT with and without mode filtering. Results courtesy of Universitié Nice Sophia Antipolis

simplifying yields

$$\begin{bmatrix} B_1^2 \\ B_2^2 \\ \vdots \\ B_n^2 \end{bmatrix} = -\frac{j}{2k_0}[M]^{-1} \cdot \begin{bmatrix} E_{\theta,\phi_1} \\ E_{\theta,\phi_2} \\ \vdots \\ E_{\theta,\phi_{n_\phi}} \end{bmatrix} \tag{12.109}$$

This matrix equation expresses the unknown CMCs in terms of the far-field points. A similar expression can be obtained for the orthogonal field component and second independent set of CMCs. In inverting this system of equations, we have assumed that the matrix M is a non-singular square matrix and the superscript -1 denotes the matrix inverse such that by definition $M^{-1}M = I$, where I is the identity matrix. In general, the matrix M will *not* be square and we will need to find the solution of this system of equations using some degree of estimation. Fortunately, we can find a pseudo-inverse matrix by using the principle of least squares to obtain an approximate solution. Thus, by multiplying by the Hermitian (conjugate) transpose of M, we may write that

$$M^T Mb = M^T v \tag{12.110}$$

Here, v is a column vector set of measurements, M is a matrix of basis functions, i.e. wave functions, and b is a column vector set of unknown mode coefficients and M^T is the Hermitian transpose of M. Thus when the columns of M are linearly independent, the product $M^T M$ is invertible and we may write that

$$b = \left(M^T M\right)^{-1} M^T v = M^P v \tag{12.111}$$

where M^P denotes the pseudo-inverse matrix. Thus, we can obtain the set of unknown mode coefficients from the set of measurements using

$$\begin{bmatrix} B_1^2 \\ B_2^2 \\ \vdots \\ B_n^2 \end{bmatrix} = -\frac{j}{2k_0} M^P \cdot \begin{bmatrix} E_{\theta,\phi_1} \\ E_{\theta,\phi_2} \\ \vdots \\ E_{\theta,\phi_{n_\phi}} \end{bmatrix} \tag{12.112}$$

Although this looks to be a reasonable strategy, the difficulty associated with this approach is that the matrix M will, for any practical measurement, be fairly large. However, as the far-field measured data comprises a pattern cut, this matrix will likely be much smaller than would otherwise be the case if instead two-dimensional pattern data were under consideration. That being said, alternative more efficient methods for computing the pseudo inverse are generally needed with the iterative conjugate gradient (CG) method [40] or least squares conjugate gradient (LSQR) method [41] being popular choices. The LSQR method is a particular implementation of the CG method which offers a numerically stable and computationally efficient solution for the inversion of the matrix M. A detailed treatment of the LSQR is beyond the scope of this text however and it is instead left to the open literature, cf. [41].

When constructing the matrix of basis functions consideration must be taken as to the number and range of CMCs that are needed. The highest order cylindrical mode that can be computed from the far-field measured data can be determined from the arithmetic mean sample spacing using

$$n_{\max} = \text{ceil}\left(\frac{\pi}{|\Delta\phi|}\right) \tag{12.113}$$

Here, ***ceil*** is used to denote a function that rounds to the nearest integer towards positive infinity. In this case, $\Delta\phi$ is taken to be the arithmetic mean angular sample spacing between the data points. Providing that the data points are not *too* unevenly distributed, and without a strict definition for what comprises a reasonable distribution, this formula will provide a reliable estimate of the highest order mode that can be computed. Thus, the range of modes will span $-n_{\max} \leq n \leq n_{\max}$. As this algorithm does not utilise the FFT there is no need to have the number of modes equal an integer power of two. Thus, we are free to choose the number of

modes, N, as being

$$N = 2n_{\max} + 1 \tag{12.114}$$

As before, the computed modes can be filtered using a band-pass windowing function so that only those modes which are associated with the AUT are retained whereupon the filtered far-fields can be obtained from an application of (12.69). Although we can, for the sake of computational efficiency, use the pre-computed M matrix so that the filtered fields are reconstructed at the measurement points, we are of course free to choose a different M matrix so that the reconstructed far-field points can be tabulated on an, e.g. equally spaced, grid of our choosing.

Figures 12.137 and 12.138 contain, respectively, plots of the great-circle far-field co-polar amplitude and phase patterns of the AUT. Here, the red unperturbed (reference) traces were taken without the reflecting plate, cf. Figure 12.137. Conversely, the blue traces were taken with the reflecting plate installed within the chamber and they clearly show the effects of the additional scattering as a spurious large amplitude side lobe which is visible in the plot at around $\theta = 50°$. The magenta trace represents the conventional interpolation and FFT-based mode filtering post-processing as presented above whereas the black trace denotes the more sophisticated inverse-matrix-based post-processing technique.

From inspection of these plots, it can be seen that the effects of the spurious scatterer have been very effectively suppressed in both the amplitude and phase plots as the unperturbed and processed perturbed traces are clearly in very encouraging agreement. The algorithm in effect uses the data points to function fit a spectrum of CMCs to the measured data and has the effect that the algorithm can more effectively suppress the effects of random noise within the measurement.

This section presents a very general post-processing technique that requires only a minimum amount of information about the AUT and measurement geometry, which suppresses reflections and noise in a far-field one-dimensional frequency domain antenna pattern measurement where the data has not necessarily been acquired on an equally spaced abscissa. This technique is entirely generic in nature, can be applied to a variety of different antenna types with no specific *a priori* assumptions being made about the distribution of the currents over the AUT. This is valuable as many far-field measurement facilities, as a result of the implementation of the positioning, control and software sub-systems, are only able to tabulate measurements on an irregularly spaced angular grid.

12.5.4 Rotary joint wow correction for LP antennas

In essence, the $\theta = 0°$ cut represents a sequence of repeat measurements of the same part of the probe pattern. The sinusoidal variation with the ϕ angle that is observed across this cut is merely an artefact of the polarisation basis that the pattern is resolved onto, i.e. the probe is rotating in phi, while the remote source antenna remains fixed. If instead the pattern was resolved onto a Ludwig III polarisation basis, this corresponds to the case where the probe and remote source antenna are rotating in unison, and this sinusoidal variation is removed. Thus in a

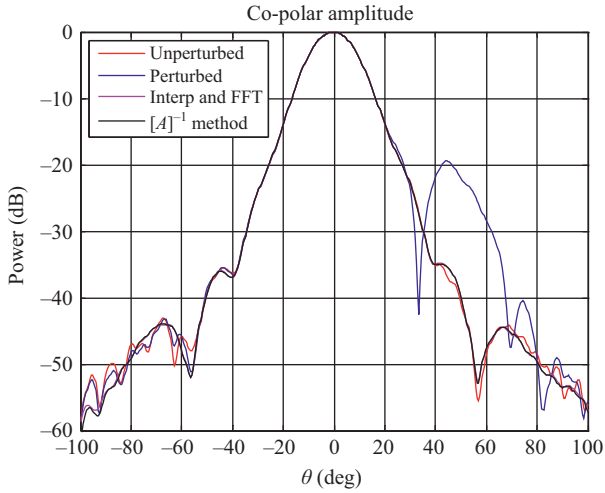

Figure 12.137 Far-field amplitude plot of horn measured unperturbed and perturbed and compared against two different scattering suppression algorithms

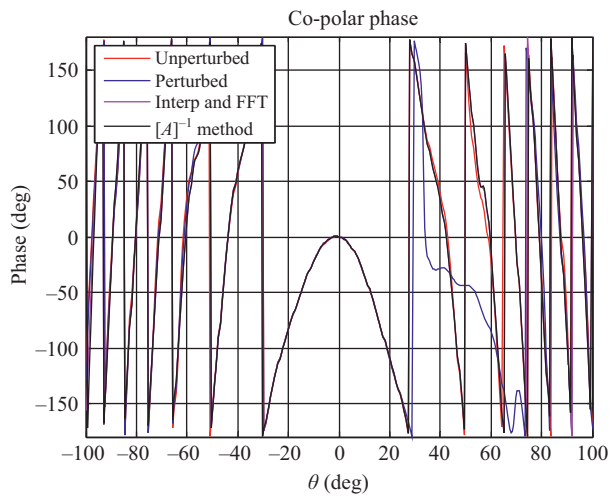

Figure 12.138 Far-field phase plot of horn measured unperturbed and perturbed and compared against two different scattering suppression algorithms

perfect system, the boresight co-polar component, amplitude, and phase, should be constant for all ϕ angles. In practice, small variations will be seen and these can arise from imperfections in the orientation of the antenna, alignment errors, multipath errors, or rotary joint errors, as channel balance errors should have been

corrected previously (see above). Thus the rotary error can be defined to be

$$f(\phi) = E_{\text{co}}(\theta, \phi)|_{\theta=0} \tag{12.115}$$

Thus the rotary joint error can be corrected using

$$E_{\text{co}}(\theta, \phi)|_{\text{corrected}} = \frac{E_{\text{co}}(\theta, \phi)}{f(\phi)} \tag{12.116}$$

$$E_{\text{cr}}(\theta, \phi)|_{\text{corrected}} = \frac{E_{\text{cr}}(\theta, \phi)}{f(\phi)} \tag{12.117}$$

It is important to note that strictly this method only works for cases where the measurements are taken in the far-field using a polar spherical phi over theta antenna measurement system where the antenna has been carefully aligned to the axes of the range.

12.6 Power parameter definitions and their measurement

In this section we provide formal definitions of the power parameters: Directivity, Gain, Effective Isotropic Radiated Power (EIRP) and Saturating Flux Density (SFD). We then present the methods available to measure these parameters using both far-field and near-field techniques. In principle these parameters can be obtained with any of the measurement techniques that have been established above (with, as is noted below, the exception of the three-antenna gain method). As such, this section could have been included within Section 12.2. However, as the measurement of power parameters constitutes such an important topic within modern antenna range measurements it has been assigned a specific section to itself.

12.6.1 Directivity

The maximum directivity (D) of an antenna is equal to the ratio of its maximum radiation intensity (often defined as the boresight direction) over that of an isotropic antenna radiating the same power [1]. Thus

$$D = \frac{\text{Radiation intensity at max radiation pattern direction (W/unit solid angle)}}{\text{Radiation intensity of an isotropic antenna (W/unit solid angle)}} \tag{12.118}$$

Or equivalently

$$D = \frac{\text{Radiation intensity at max radiation pattern direction (W/unit solid angle)}}{\frac{\text{Total radiated power}}{4\pi}\ \text{(W/unit solid angle)}} \tag{12.119}$$

Since the magnitude variations of the radiated field are $1/r$ radiation, intensity (power per unit solid angle – W/Steradian) can be expressed as

$$U = r^2 S \tag{12.120}$$

Here r is the radius and S is the average power flux density and is given by the real part of the Poynting vector (W/m^2) and thus U is independent of r. The radiation intensity is related to the far electric field through

$$U(\theta,\phi) = \frac{r^2}{2Z_0}|\underline{E}(r,\theta,\phi)|^2 \tag{12.121}$$

In the far-field, it is possible to describe the electric (and magnetic) fields as

$$\underline{E}(r,\theta,\phi) = \frac{e^{-jk_0 r}}{r}\underline{E}(\theta,\phi) \tag{12.122}$$

where

$$\underline{E}(\theta,\phi) = \frac{\pi}{jk_0\lambda^2}\int_S \left[\hat{\underline{r}} \times \left(\underline{n} \times \underline{E}_s\right) + Z\hat{\underline{r}} \times \left\{\left(\underline{n} \times \underline{H}_s\right) \times \hat{\underline{r}}\right\}\right] e^{jk_0\hat{\underline{r}}} \cdot \underline{r}_0 ds_0 \tag{12.123}$$

Thus the radiation intensity can be expressed as

$$U = \frac{1}{2Z_0}|\underline{E}(\theta,\phi)|^2 \tag{12.124}$$

Or in terms of the conventional orthogonal polar spherical polarisation basis

$$U(\theta,\phi) = \frac{1}{2Z_0}\left(|E_\theta(\theta,\phi)|^2 + |E_\phi(\theta,\phi)|^2\right) \tag{12.125}$$

The total power is obtained by integrating the radiation intensity over the far-field sphere, thus

$$P_{\text{rad}} = \oint_\Omega U d\Omega \tag{12.126}$$

Here, Ω is the elemental solid angle where $d\Omega = \sin\theta\, d\theta\, d\phi$. Now, the directivity can be expressed as

$$D = \frac{U}{U_0} \tag{12.127}$$

Here, U_0 is taken to denote the radiation intensity of an isotropic source.

$$P_{\text{rad}} = \oint_\Omega U_0\, d\Omega = U_0 \oint_\Omega d\Omega = 4\pi U_0 \tag{12.128}$$

Finally

$$D = \frac{4\pi U}{P_{\text{rad}}} \tag{12.129}$$

and this provides one with a convenient way of calculating directivity from any measured far-field result obtained over a spherical surface. (Within this definition it has been assumed that the field points represent peak values. If the RMS values had been used, the expression for directivity would remain unchanged; however other quantities would differ by a factor of one half.) Typically, directivity is expressed in logarithmic terms whereby

$$D|_{\text{dB}} = 10\log_{10}(D) \tag{12.130}$$

By way of an elementary illustration, for a uniformly illuminated rectangular aperture of cross-sectional area $A = ab$, we may write that the directivity in dBi, that is to say the directivity expressed in dB relative to an isotropic radiator and hence the subscript i, is

$$D|_{\text{dB}} = 10\log_{10}\left(\frac{4\pi}{\lambda^2}\eta ab\right) \tag{12.131}$$

where η is a dimensionless quantity that varies such that $0 \leq \eta \leq 1$, and which is used to denote the aperture efficiency. Setting the aperture efficiency equal to unity, we can plot the theoretical peak directivity of an aperture of fixed size as a function of frequency. This is depicted in Figure 12.139.

This is a peak directivity which would reduce with less ideal aperture efficiency. For example the aperture efficiency is approximately 0.81 for the case of an aperture that is illuminated by the fundamental TE_{10} mode. Conversely, Figure 12.140 contains a graph of directivity which has been plotted as a function of frequency where the directivity value has been obtained from a pattern integration that has been performed on measured data. This data is denoted with circular markers. A second trace has been plotted on this graph which depicts the Naval Research Laboratory (NRL) calculated directivity value. This data is denoted with triangular markers. Here, as is generally the case, the WR62 rectangular pyramidal SGH was manufactured in accordance with the requirements of Naval Research Laboratory, NRL Report 4433 [42].

Here, the worst-case difference between the measured directivity and the predicted directivity value was 0.17 dB with the mean average difference being just 0.09 dB.

At this point it is worthwhile to briefly examine the behaviour of the flow of power in the far-field. As stated above, the average power flux density can be given by the real part of the Poynting vector and is given by

$$\underline{S} = \frac{1}{2}\text{Re}\{\underline{E}^* \times \underline{H}\} \tag{12.132}$$

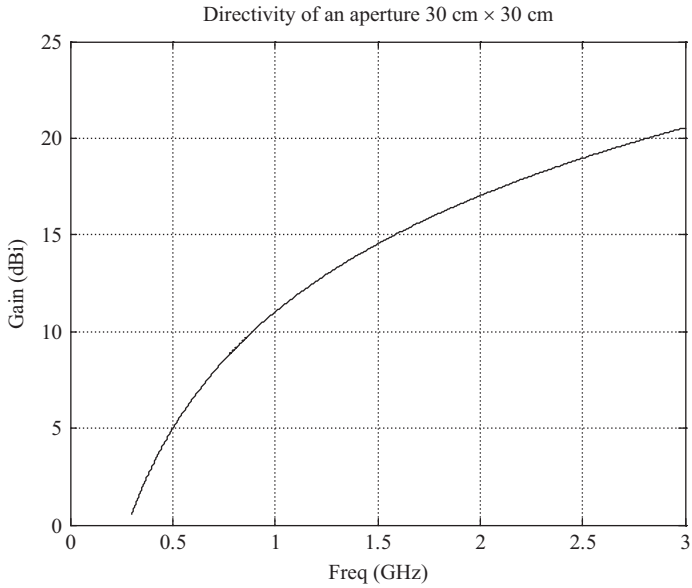

Figure 12.139 Directivity of a uniformly illuminated square aperture

Here, the asterisk denotes the complex conjugate. In the far-field

$$\underline{H} = \frac{1}{Z_0}(\hat{\underline{u}}_r \times \underline{E}) \tag{12.133}$$

Thus assuming that Z_0 is real, in the far-field we can write that

$$\underline{S} = \frac{1}{2Z_0}\mathrm{Re}\{\underline{E}^* \times (\hat{\underline{u}}_r \times \underline{E})\} \tag{12.134}$$

Now using standard vector relations, we can write that

$$\underline{E}^* \times (\hat{\underline{u}}_r \times \underline{E}) = (\underline{E}^* \cdot \underline{E})\hat{\underline{u}}_r - (\underline{E}^* \cdot \hat{\underline{u}}_r)\underline{E} \tag{12.135}$$

In the far-field, the plane wave condition applies and the field is transverse. That is to say

$$\underline{E} \cdot \hat{\underline{u}}_r = \underline{H} \cdot \hat{\underline{u}}_r = 0 \tag{12.136}$$

Thus

$$\underline{S} = \frac{1}{2Z_0}\mathrm{Re}\{(\underline{E}^* \cdot \underline{E})\hat{\underline{u}}_r\} \tag{12.137}$$

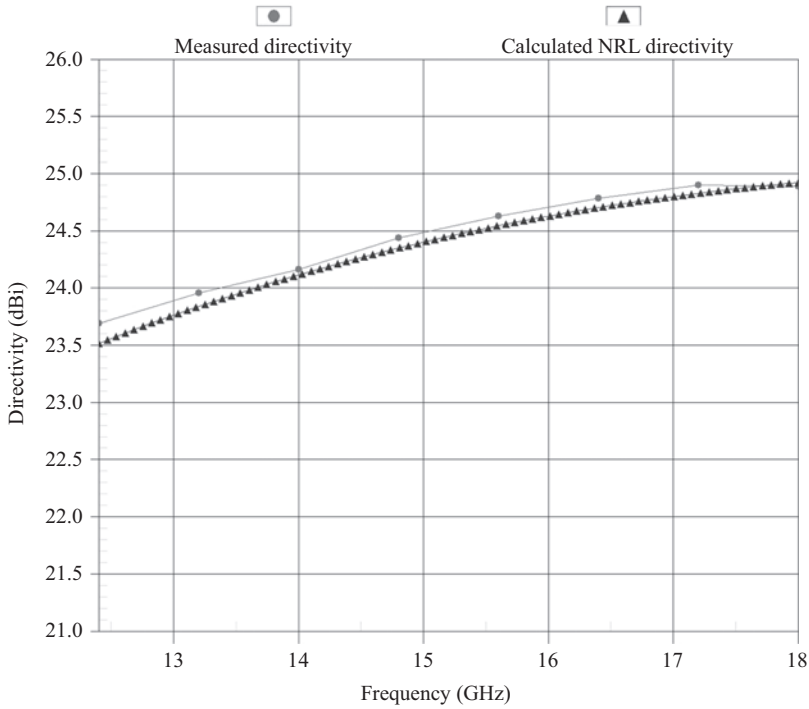

Figure 12.140 Plot of directivity as calculated from an SNF measurement versus NRL directivity plots for a WR62 SGH

Or

$$\underline{S} = \frac{|\underline{E}|^2}{2Z_0}\hat{\underline{u}}_r \tag{12.138}$$

where $|\underline{E}|^2$ is always real and positive. This means that in the far-field power is always flowing directly away from the antenna in the radial direction. As has been shown earlier, cf. Chapters 6–8, in the far-field it is possible to describe the electric (and magnetic) fields in the form of a product of an angularly dependent vector pattern function, an inverse r term, and a radially dependent complex exponential

$$\underline{E}(r,\theta,\phi) = \frac{e^{-jk_0 r}}{r}\underline{E}(\theta,\phi) \tag{12.139}$$

Thus as the magnitude of a complex exponential is unity, we may express this as

$$\underline{S} = \frac{|\underline{E}(\theta,\phi)|^2}{2r^2 Z_0}\hat{\underline{u}}_r \tag{12.140}$$

Hence we can also see that $\underline{S}$ decreases as $1/r^2$.

12.6.2 Gain

As indicated above, gain and directivity are very closely related. Gain in a direction (θ, ϕ) is given by [43]

$$G(\theta,\phi) = 4\pi \frac{\text{Power radiated per unit solid angle in direction } (\theta,\phi)}{\text{Total power accepted from the source}} \tag{12.141}$$

This includes dissipative losses within the antenna but does not include transmission line mismatch or polarisation mismatch losses. Perhaps the primary reason that this definition did not include reflection losses in the formulation of the antenna gain is that in principle it is always possible to construct a feeding network that perfectly matches the transmission line to the terminals of the antenna thereby avoiding mismatch losses. By way of comparison, when expressed in a similar form, directivity in the direction (θ, ϕ) is given by

$$D(\theta,\phi) = 4\pi \frac{\text{Power radiated per unit solid angle in direction } (\theta,\phi)}{\text{Total power radiated by antenna}} \tag{12.142}$$

This does not include dissipative losses within the antenna. The gain and directivity of an antenna can be related to one another through the efficiency, e, of the antenna. Thus let

$$G(\theta,\phi) = eD(\theta,\phi) \tag{12.143}$$

Here, e is the antenna radiation efficiency which again is a dimensionless real quantity. As, for a passive antenna, efficiency can never be greater than unity, the gain value should always be less than the value of directivity (experimental errors aside) such that $0 \leq e \leq 1$. When the efficiency is unity this implies that the gain and directivities are equal. Thus when expressed in decibel form, directivity and gain can be related through

$$G(\theta,\phi)|_{\text{dB}} = D(\theta,\phi)|_{\text{dB}} - e|_{\text{dB}} \tag{12.144}$$

12.6.2.1 Gain measurement

There are three techniques commonly used for measuring gain and they are outlined in this section.

The gain substitution method

This technique is by far the one used most commonly in industry today and involves comparing the AUT to a calibrated standard gain antenna. This gain measurement technique can be used effectively with any of the near-field test geometries that are developed above. Starting with the Friis transmission formula [44] for reflection-less and polarisation-matched directional radiation and reception

for two antennas, which are in the far-field of one another, we can write

$$\frac{P_r}{P_t} = \left(\frac{\lambda}{4\pi R}\right)^2 G_{0t} G_{0r} \tag{12.145}$$

where the factor $\left(\frac{\lambda}{4\pi R}\right)^2$ is the free-space loss factor and polarisation mismatch is ignored. In the far-field, if the gain of one antenna is known and the separation R is also available, then this equation can be used directly to compute the gain of the AUT. This is known as the direct gain method. However, for the case where near-field data has been transformed to the far-field, R is infinite. The gain substitution method enables us to sidestep this as we will now illustrate. Therefore, in logarithmic form, we can write for the gain standard, e.g. an SGH

$$(G_{0t\mathrm{SGH}})_{\mathrm{dB}} + (G_{0r\mathrm{probe}})_{\mathrm{dB}} = 20\log_{10}\left(\frac{4\pi R}{\lambda}\right) + 10\log_{10}\left(\frac{P_{r\mathrm{probe}}}{P_{t\mathrm{SGH}}}\right) \tag{12.146}$$

and for the test antenna

$$(G_{0t\mathrm{AUT}})_{\mathrm{dB}} + (G_{0r\mathrm{probe}})_{\mathrm{dB}} = 20\log_{10}\left(\frac{4\pi R}{\lambda}\right) + 10\log_{10}\left(\frac{P_{r\mathrm{probe}}}{P_{t\mathrm{AUT}}}\right) \tag{12.147}$$

If the separation between the probe and the gain standard is the same as that between the probe and the test antenna and further supposing that the frequency remains fixed and that the same amount of power was supplied to the gain standard as to the test antenna, then these expressions reduce to

$$(G_{0t\mathrm{SGH}})_{\mathrm{dB}} - 10\log_{10}(P_{t\mathrm{SGH}}) = (G_{0t\mathrm{AUT}})_{\mathrm{dB}} - 10\log_{10}(P_{t\mathrm{AUT}}) \tag{12.148}$$

Thus the gain of the AUT can be expressed in terms of the gain of the gain standard and the ratio of the transmitted powers when the antennas are polarisation matched

$$(G_{0t\mathrm{AUT}})_{\mathrm{dB}} = (G_{0t\mathrm{SGH}})_{\mathrm{dB}} + 10\log_{10}\left(\frac{P_{t\mathrm{AUT}}}{P_{t\mathrm{SGH}}}\right) \tag{12.149}$$

where $G_{0t\mathrm{AUT}}$ is the gain of the test antenna, $G_{0t\mathrm{SGH}}$ is the gain of the gain standard, $P_{t\mathrm{AUT}}$ is the transmitted power into the test antenna and $P_{t\mathrm{SGH}}$ is the transmitted power into the gain standard.

Here, as required the separation R is removed from these equations. This technique utilises a gain standard (with known gain) to determine absolute gain of the test antenna. Therefore by transforming an acquisition of the SGH and noting the power on boresight and by performing the same operation on the test antenna, the gain of the test antenna can be computed by normalising further test antenna

far-field patterns by the quantity

$$10 \log_{10}\left(\frac{P_{t\mathrm{AUT}}}{P_{t\mathrm{SGH}}}\right) \tag{12.150}$$

Since the powers are the powers recorded during different measurements (one involving the AUT and the probe and the other involving the SGH and the probe) and noting that the power ratio can be expressed in terms of the peaks (denoted by E_t below) of the un-normalised AUT and SGH pattern measurements, we may write that

$$(G_{0t\mathrm{AUT}})_{\mathrm{dB}} = (G_{0t\mathrm{SGH}})_{\mathrm{dB}} + (E_{t\mathrm{AUT}})_{\mathrm{dB}} - (E_{t\mathrm{SGH}})_{\mathrm{dB}} \tag{12.151}$$

The following comprises a simple example of a gain transfer measurement. Figure 12.141 contains the far-field azimuth cut of an X-band SGH plotted at 9.375 GHz.

Here, the peak of the pattern was 54.7 dB. This value has no reference and is only of value providing the RF sub-system remains invariant between measuring the AUT and the SGH. That is to say, no amplifiers, attenuators, and cables are changed, the source power is held constant and the frequency is stable. Most SGHs are designed and built to meet the requirements of NRL Report 4433 [45] and are provided with either a theoretical gain versus frequency curve, as shown in Figure 12.142, or a representative measured gain versus frequency curve with frequency coverage being based on standard 'WR' waveguide bands, cf. Table 1.3 in Appendix 1.2 with a stated typical gain accuracy. In this case the stated gain accuracy across the band was ± 0.5 dB. This uncertainty is due to several factors including manufacturing tolerances fabricating the horn and losses in the waveguide to coaxial adapter. This is a fairly typical value for this frequency and in many applications; the largest uncertainly in the gain error budget is the accuracy of the calibrated standard antenna.

Here, the gain of the SGH shown in Figure 12.143 at 9.375 GHz can be seen to be circa 22 dBi ± 0.5 dB. The SGH was replaced with the AUT and its pattern was acquired and transformed to the far-field. The un-normalised boresight far-field pattern of the AUT can be seen presented in Figure 12.144 where the peak of the pattern was 58.6 dB.

Thus, this makes the calculated gain of the AUT = SGA gain + AUT max far-field value – SGA max far-field value so that

$$\text{AUT gain (dB)} = 22 \text{ dB} + 58.6 \text{ dB} - 54.7 \text{ dB} = 25.9 \text{ dB} \tag{12.152}$$

Remembering the uncertainty associated with the calibration of the standard gain antenna, the gain of the AUT is 25.9 ± 0.5 dB. Strictly this is the realised gain of the AUT, not the actual gain of the antenna, as a mismatch correction was not performed to take account of the reflection losses within the measurements. A useful check is to compare the calculated gain of the AUT with the calculated directivity of the AUT. In this case the pattern integration indicated that the directivity of the AUT was 26.1 dB. Ignoring the, comparatively large, uncertainty

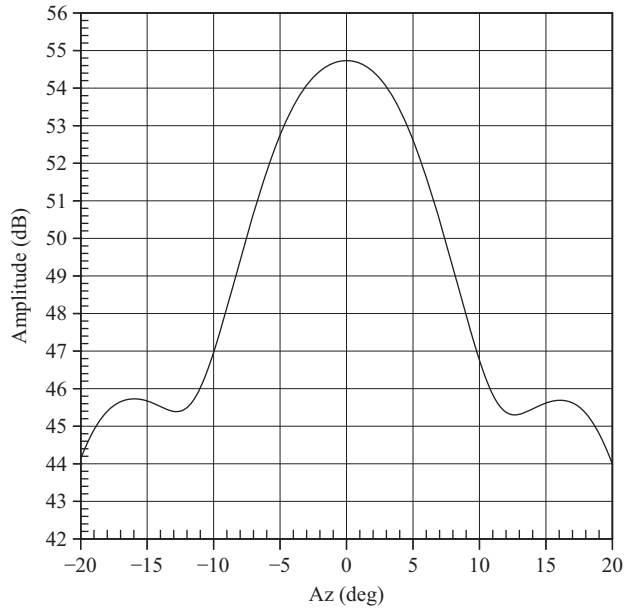

Figure 12.141 Un-normalised far-field pattern of SGH at 9.375 GHz

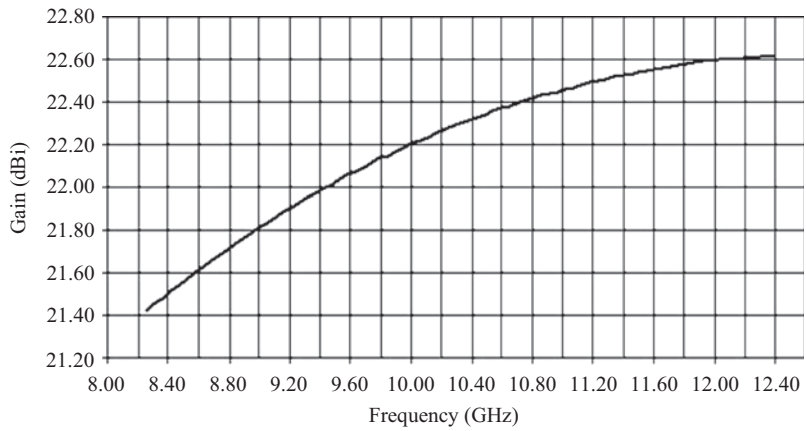

Figure 12.142 Theoretical gain curve for a WR90 gain horn

in the measurement for one moment, this makes the efficiency of the AUT −0.2 dB ± 0.5 dB. Here, as the uncertainties are comparatively large when compared to the losses, it is possible that the calculated gain value could become slightly larger than the calculated directivity value.

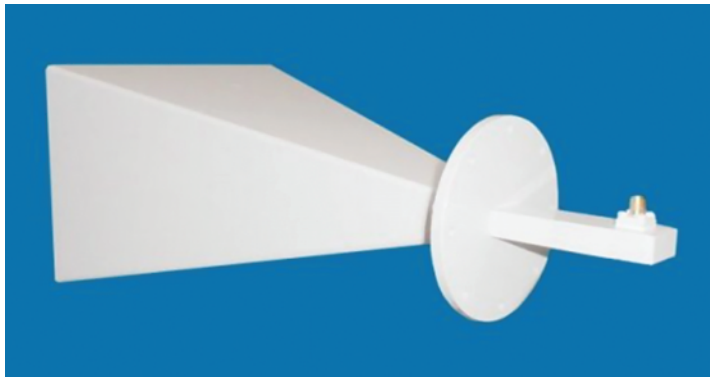

Figure 12.143 WR90 gain horn shown complete with coaxial to WG transition

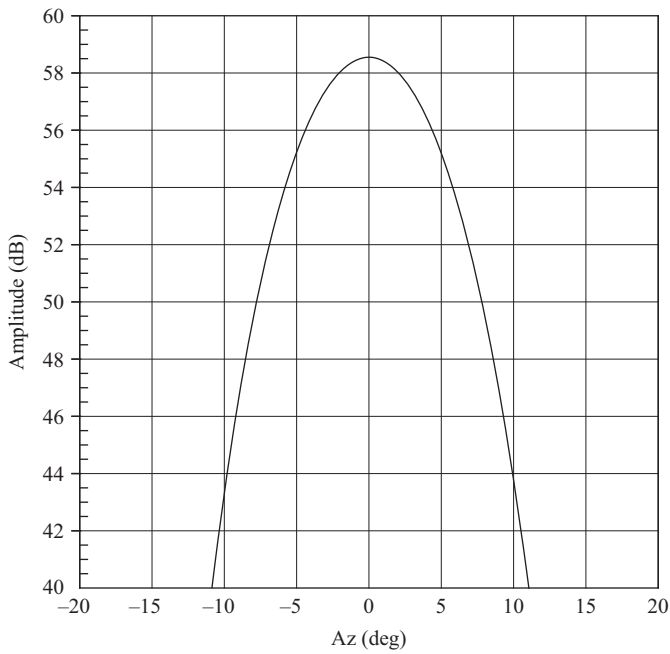

Figure 12.144 Un-normalised far-field pattern of AUT at 9.375 GHz

Near-field issues

A question that often arises is: does the AUT-to-range illuminator distance need to be exactly the same for the AUT measurement and the SGH measurement if measurements are being taken in the near-field? The short answer is that the distance does not enter into the gain equation because in the near-field theory, planar, cylindrical, or spherical, the measurement distance only affects the probe correction

and this has been handled before the gain is calculated as part of the near-field to far-field transformation process. Actually, the distance between the probe and the origin of the reference measurement coordinate system (which is usually the same as the AUT coordinate system) does enter into the planar, cylindrical, and spherical equations and it arises for the same conceptual reason. In the development of the theory, as shown above, the AUT is described by a spectrum of waves that are mathematically referenced to the reference coordinate system. The probe is also described by a spectrum of waves that are mathematically referenced to the reference coordinate (not the coordinates centred at the probe). The coupling between the AUT waves and the probe waves is then just the product of the complex coefficients of the probe and AUT waves since they are both described in the same coordinate system. There is a step in the probe correction process, referred to as the translation of centres, which calculates the complex coefficients for the probe in the reference coordinate system from the similar coefficients in its own coordinate system. In the spherical case, a small probe like an OEWG can be described in its own coordinate system with very few modes, but in the translated and rotated reference system it requires a far larger number of modes. This is also true of the cylindrical case. The mathematics for the translation of centres process in spherical is complex but it is handled automatically by the transformation software and the user is not aware of the process. Thus in the planar, cylindrical, and spherical cases, the translation of centres process does not change the far-field peak value. If the input power level to the AUT stays the same, the far-field peak should be independent of the measurement radius and where the current sources were located within the MRS (sphere) or MRC (cylinder) and therefore does not enter into the gain equation. Thus the SGH does not have to be located in the same position as each AUT of interest to obtain valid gain data. As long as each AUT of interest (and the SGH) is enclosed by a conceptual spherical surface and sampled at the density prescribed by the MRS when measured, the absolute distance from the probe to the AUT and its position with respect to the coordinate system origin are irrelevant. However multiple reflections between the AUT and probe can result in a standing wave pattern being setup and this can affect the measured peak of the pattern but this is not strictly an artefact of the range length in a mathematical sense.

Another feature of the gain measurement process using the transformation software that is not immediately apparent is that for comparison gain measurements to a gain standard, the polarisation of the standard and the AUT do not have to be the same. In point of fact, as any realised antenna is never perfectly linearly polarised, or perfectly circularly polarised, in principle they can never be perfectly polarisation matched. Since the far-field peak is a power quantity rather than a field quantity, a linear gain standard can be used to measure a circularly polarised antenna and there is no modification in the gain equation to account for the difference in polarisation. If the SGH is much smaller than the AUT, which is often the case, then multiple reflection and truncation errors can become more significant. We address these sources of uncertainty in Chapter 8 and describe techniques for the determination and compensation of these uncertainties in detail.

The direct gain measurement method

This technique is common for near-field systems since it requires reasonable proximity between the source and receive ports. But it is equally applicable to the gain of small feed antennas measured in a far-field anechoic chamber. The direct gain measurement method is based on a direct application of the near-field equations, and hence the name. In this case, the near-field probe or the far-field range source antenna is used as a gain standard. Thus for this method to be used, an auxiliary gain calibration must have been performed on the near-field probe or source antenna. Direct gain measurements are typically faster than gain comparison, i.e. substitution, measurements since only a single near-field or far-field data point acquisition is required. Direct gain measurements are made by first making a bypass measurement where the bypass measurement is a way of calibrating out the effects of cable losses within the RF sub-system. Thus for this method to be viable, the separation between the AUT and probe cannot be too great, otherwise the technique becomes rather inconvenient with guided wave path losses ultimately limiting viability. The normalisation that is required to relate the peak of the far-field pattern to the input power is achieved by connecting the probe cable directly to the AUT cable so as to bypass both the AUT and the probe. Note that if this connection requires an additional cable, the losses in this cable must be accounted for. The computed far-field peak and bypass measurement represent a power ratio measurement. The direct gain equation can therefore be expressed as

$$(G_{0t\mathrm{AUT}})_{\mathrm{dB}} = (E_{t\mathrm{AUT}})_{\mathrm{dB}} - (\mathrm{Bypass})_{\mathrm{dB}} - \left(G_{0t\mathrm{probe}}\right)_{\mathrm{dB}} \tag{12.153}$$

The generalised case of an antenna and SGH that is not polarisation matched can be found in [46] but is beyond the scope of this discussion. This direct connection gain calibration method is used as the basis of the near-field three-antenna gain method which is discussed in the following section once the analogous far-field case is treated.

12.6.2.2 Three-antenna gain method

The three-antenna near-field gain method is an extension of the direct gain method except that the probe gain is not known. Thus in the event that a gain standard is not available, and two identical antennas are also not available, or practical, then the three-antenna gain measurement method must be utilised instead, where the assumption is that during each of these three measurements the transmitted power and frequency was held constant. More details concerning the two identical antenna gain measurement method can be found in [47]. However, as no two antennas are ever truly identical herein only the general three-antenna gain method is discussed. Near-field measurements are then taken on antenna combinations 1 and 2, 1 and 3, and 2 and 3. Antenna 1 is taken to be the AUT; antennas 2 and 3 are assumed to be non-identical probes. Conversely, for the far-field case, recasting the above equations for the measurement of the three combinations of antennas 1,

2, and 3, we obtain the following three simultaneous equations that we can subsequently solve:

$$(G_1)_{\text{dB}} + (G_2)_{\text{dB}} = 20\log_{10}\left(\frac{4\pi R}{\lambda}\right) + 10\log_{10}\left(\frac{P_{r2}}{P_{t1}}\right) \tag{12.154}$$

$$(G_1)_{\text{dB}} + (G_3)_{\text{dB}} = 20\log_{10}\left(\frac{4\pi R}{\lambda}\right) + 10\log_{10}\left(\frac{P_{r3}}{P_{t1}}\right) \tag{12.155}$$

$$(G_2)_{\text{dB}} + (G_3)_{\text{dB}} = 20\log_{10}\left(\frac{4\pi R}{\lambda}\right) + 10\log_{10}\left(\frac{P_{r3}}{P_{t2}}\right) \tag{12.156}$$

From these three questions, we can solve for the gains of the three antennas providing that R and λ are held constant. Subtracting the last two equations, we obtain

$$(G_1)_{\text{dB}} - (G_2)_{\text{dB}} = 10\log_{10}\left(\frac{P_{r3}}{P_{t1}}\right) - 10\log_{10}\left(\frac{P_{r3}}{P_{t2}}\right) \tag{12.157}$$

Hence adding this to the first equation yields

$$2(G_1)_{\text{dB}} = 20\log_{10}\left(\frac{4\pi R}{\lambda}\right) + 10\log_{10}\left(\frac{P_{r2}}{P_{t1}}\right) + 10\log_{10}\left(\frac{P_{r3}}{P_{t1}}\right) - 10\log_{10}\left(\frac{P_{r3}}{P_{t2}}\right) \tag{12.158}$$

Or

$$(G_1)_{\text{dB}} = \frac{1}{2}\left[20\log_{10}\left(\frac{4\pi R}{\lambda}\right) + 10\log_{10}\left(\frac{P_{r2}}{P_{t1}}\right) + 10\log_{10}\left(\frac{P_{r3}}{P_{t1}}\right) - 10\log_{10}\left(\frac{P_{r3}}{P_{t2}}\right)\right] \tag{12.159}$$

Subtracting the first two equations yields

$$(G_2)_{\text{dB}} - (G_3)_{\text{dB}} = 10\log_{10}\left(\frac{P_{r2}}{P_{t1}}\right) - 10\log_{10}\left(\frac{P_{r3}}{P_{t1}}\right) \tag{12.160}$$

Thus

$$2(G_2)_{\text{dB}} = 20\log_{10}\left(\frac{4\pi R}{\lambda}\right) + 10\log_{10}\left(\frac{P_{r3}}{P_{t2}}\right) + 10\log_{10}\left(\frac{P_{r2}}{P_{t1}}\right) - 10\log_{10}\left(\frac{P_{r3}}{P_{t1}}\right) \tag{12.161}$$

Or

$$(G_2)_{\text{dB}} = \frac{1}{2}\left[20\log_{10}\left(\frac{4\pi R}{\lambda}\right) + 10\log_{10}\left(\frac{P_{r3}}{P_{t2}}\right) + 10\log_{10}\left(\frac{P_{r2}}{P_{t1}}\right) - 10\log_{10}\left(\frac{P_{r3}}{P_{t1}}\right)\right] \tag{12.162}$$

Finally, subtracting the first and last equations yields

$$(G_1)_{\text{dB}} - (G_3)_{\text{dB}} = 10\log_{10}\left(\frac{P_{r2}}{P_{t1}}\right) - 10\log_{10}\left(\frac{P_{r3}}{P_{t2}}\right) \tag{12.163}$$

Or

$$(G_3)_{\text{dB}} - (G_1)_{\text{dB}} = 10\log_{10}\left(\frac{P_{r3}}{P_{t2}}\right) - 10\log_{10}\left(\frac{P_{r2}}{P_{t1}}\right) \tag{12.164}$$

Hence adding yields

$$2(G_3)_{\text{dB}} = 20\log_{10}\left(\frac{4\pi R}{\lambda}\right) + 10\log_{10}\left(\frac{P_{r3}}{P_{t1}}\right) + 10\log_{10}\left(\frac{P_{r3}}{P_{t2}}\right) - 10\log_{10}\left(\frac{P_{r2}}{P_{t1}}\right) \tag{12.165}$$

Or

$$(G_3)_{\text{dB}} = \frac{1}{2}\left[20\log_{10}\left(\frac{4\pi R}{\lambda}\right) + 10\log_{10}\left(\frac{P_{r3}}{P_{t1}}\right) + 10\log_{10}\left(\frac{P_{r3}}{P_{t2}}\right) - 10\log_{10}\left(\frac{P_{r2}}{P_{t1}}\right)\right] \tag{12.166}$$

Grouping these simultaneous expressions together and writing them in terms of the free-space loss factor yields

$$(G_1)_{\text{dB}} = \frac{1}{2}\left[10\log_{10}\left(\frac{P_{r3}}{P_{t1}}\right) + 10\log_{10}\left(\frac{P_{r2}}{P_{t1}}\right) - 10\log_{10}\left(\frac{P_{r3}}{P_{t2}}\right) - 20\log_{10}\left(\frac{\lambda}{4\pi R}\right)\right] \tag{12.167}$$

$$(G_2)_{\text{dB}} = \frac{1}{2}\left[10\log_{10}\left(\frac{P_{r2}}{P_{t1}}\right) + 10\log_{10}\left(\frac{P_{r3}}{P_{t2}}\right) - 10\log_{10}\left(\frac{P_{r3}}{P_{t1}}\right) - 20\log_{10}\left(\frac{\lambda}{4\pi R}\right)\right] \tag{12.168}$$

$$(G_3)_{\text{dB}} = \frac{1}{2}\left[10\log_{10}\left(\frac{P_{r3}}{P_{t1}}\right) + 10\log_{10}\left(\frac{P_{r3}}{P_{t2}}\right) - 10\log_{10}\left(\frac{P_{r2}}{P_{t1}}\right) - 20\log_{10}\left(\frac{\lambda}{4\pi R}\right)\right] \tag{12.169}$$

Here, the assumption is that during each of these three measurements, the transmitted power was held constant so that

$$P_{t1} = P_{t2} = P_{t3} \tag{12.170}$$

Thus the individual gains can be obtained from the three separate antenna measurements without *a priori* knowledge of a gain standard provided the free-space loss factor can be determined. On a far-field range, the AUT-to-probe separation can be measured and although it is generally quite large, particularly for the case of an outdoor range, it is still finite and these equations can be used directly. However, when working with asymptotic far-field parameters, such as those derived from

near-field measurements, R is assumed to be infinitely large and as such we need to adopt a slightly different tact. Generally when using a near-field range, this is accomplished by means of three direct cable connection gain measurements. As three measurements are taken, where one of these antennas is the probe, the other is the AUT and the third is another antenna that is different from the first two; it is worth highlighting that this method is therefore not well suited to planar or cylindrical near-field measurements or CATR measurements. This follows from recalling that for the planar or cylindrical cases, the near-field probe antenna is typically a low-gain broad beam antenna. This therefore means that when it is used in the position of the test antenna, its measurement will be grossly truncated resulting in inaccurate far-field patterns and unreliable pattern peaks. For the case of a CATR, the probe is the feed of a single- or dual-reflector assembly whose pattern is generally optimised so as to ensure correct illumination of the sub- and/or main reflector. This means that when the AUT is used to replace this feed, the CATR will likely be illuminated in a less than optimum way. Thus, the three-antenna gain measurement technique is most often encountered, and most successfully deployed, when taking spherical near-field or far-field measurements. The remainder of this section is devoted to developing this highly accurate gain measurement technique. Restating the equation for the near-field direct gain calibration method yields

$$G_1 + G_2 = E_{1,2} - \text{Bypass}_{1,2} \tag{12.171}$$

Here, the subscripts 1 and 2 on the Gains denote the gains of antennas 1 and 2, with the far-field peak of antenna 1 when tested with antenna 2 being denoted with the subscript 1,2. In this case, as before, all quantities are in dB form. We can write down similar expressions for the remaining combinations of measurements obtaining

$$G_1 + G_2 = E_{1,2} - \text{Bypass}_{1,2} = M_{1,2} \tag{12.172}$$

$$G_1 + G_3 = E_{1,3} - \text{Bypass}_{1,3} = M_{1,3} \tag{12.173}$$

$$G_2 + G_3 = E_{2,3} - \text{Bypass}_{2,3} = M_{2,3} \tag{12.174}$$

where the $M_{i,j}$ are merely convenient constants. As for the far-field case, and using a similar strategy, we are able to solve these three simultaneous equations to obtain the respective gains in terms of the measured quantities. Solving yields

$$G_1 = \frac{1}{2}\left(M_{1,2} + M_{1,3} - M_{2,3}\right) \tag{12.175}$$

$$G_2 = \frac{1}{2}\left(M_{1,2} + M_{2,3} - M_{1,3}\right) \tag{12.176}$$

$$G_3 = \frac{1}{2}\left(M_{1,3} + M_{2,3} - M_{1,2}\right) \tag{12.177}$$

Each of these three separate measurements requires a bypass measurement; however, if the test system is stable, and generally this is the case, we can assume that these bypass measurements are all the same with only a minor degradation in accuracy. In this case these equations and the practical measurements that they are predicated upon are significantly simplified yielding

$$G_1 = \frac{1}{2}\left(E_{1,2} + E_{1,3} - E_{2,3} - \text{Bypass}\right) \tag{12.178}$$

$$G_2 = \frac{1}{2}\left(E_{1,2} + E_{2,3} - E_{1,3} - \text{Bypass}\right) \tag{12.179}$$

$$G_3 = \frac{1}{2}\left(E_{1,3} + E_{2,3} - E_{1,2} - \text{Bypass}\right) \tag{12.180}$$

where strictly we have assumed that

$$\text{Bypass}_{1,2} = \text{Bypass}_{1,3} = \text{Bypass}_{2,3} = \text{Bypass} \tag{12.181}$$

By way of an illustration [47], at X-band, the gain comparison method has been found to be able to achieve an uncertainty of circa ±0.32 dB, whereas the three-antenna gain method achieved an uncertainty of circa ±0.14 dB. When using the gain comparison method, the difference between the representative gain curve, which in this case was the NRL gain curve [45] and the actual realised gain of the gain standard, is typically the largest single uncertainty in the facility-level gain uncertainty budget. Strictly, so as to be able to attain the very highest levels of accuracy, the mismatch formula as developed in Chapter 8 should be applied to each of these measurements. With mismatch correction applied, these results could be significantly improved upon.

12.6.3 Equivalent isotropically radiated power (EIRP)

Equivalent isotropically radiated power (EIRP) is a system power parameter and is obtained from the product of the antenna gain and the net input power accepted by the antenna [48]. Another way to interpret this is to say, the EIRP quantity is the power that an isotropic radiator will have to transmit to lead to the same power density that the AUT will affect at a specific angle of interest. If we consider the polarisation matched case of the Friis transmission equation then we may write that

$$\frac{P_r}{P_t} = \left(1 - |\Gamma_t|^2\right)\left(1 - |\Gamma_r|^2\right)\left(\frac{\lambda}{4\pi R}\right)^2 G_t G_r \tag{12.182}$$

where P_r denotes the power received, P_t denotes the power transmitted, and $G_{t/r}$ are the gains of the transmit and receive antennas. When we assume that our AUT is the transmitter, then we can write the EIRP as

$$EIRP = P_t G_t\left(1 - |\Gamma_t|^2\right) = \left(\frac{4\pi R}{\lambda}\right)^2 \frac{P_r}{(1 - |\Gamma_r|^2)G_r} \tag{12.183}$$

Thus a very convenient measurement technique is to set up a standard gain antenna as receiver in the far-field of our AUT and to then determine EIRP by measuring the power at the port of the standard gain receiving antenna. Since the distance is known, the EIRP can be calculated. The convenience of this approach is that the AUT can remain intact and no port disconnection is needed. A near-field EIRP technique as it applies to the planar coordinate system is presented in Equation (32) of [46]. This technique relies on a complex integration of the measured near-field power, the near-field probe gain, and a single power measurement at a reference location. It provides a convenient approach to measuring EIRP for active antennas on planar near-field ranges, but is not discussed in detail here. For the case of the CATR-based EIRP measurements, see Chapter 5, Section 5.5.2.4.

12.6.4 Saturating flux density (SFD)

Saturating flux density is the flux required to saturate the receiver of the AUT and is determined on a far-field range as

$$S_0 = \frac{P_i G_S}{4\pi d^2} \tag{12.184}$$

where P_i is the input power to the source antenna, G_S is the gain of that source antenna, and d is the distance separating the AUT and the source antenna. The philosophy of this measurement is to determine the saturation level of the receiver and this is typically achieved by gradually increasing the input power level P_i. This process continues as long as the receiver response linearly tracks the increase in power of the transmitter and is terminated once the receiver is saturated. Thus, SFD can be interpreted as being the receive system parameter analogy of the transmit system parameter EIRP. For CATR-based measurement see Chapter 5, Section 5.5.2.5.

A near-field SFD technique as it applies to the planar coordinate system is presented in Equation (39) of [46]. This technique relies on a complex integration of the measured near-field power, the near-field probe gain and a single transmitting probe power measurement at a reference location. It provides a convenient approach to measuring SFD for active antennas on planar near-field ranges, but is not discussed in detail here.

12.7 Summary

This chapter has presented a number of more advanced measurement correction and post-processing techniques that are commonly encountered within the modern antenna test community. Some of these techniques enable existing facilities to be used with greater accuracy and precision, whereas other, through significant ingenuity, allows additional diagnostic information to be extracted. In each case, these sections illustrate the great power and flexibility that is routinely afforded to the modern practitioner.

12.7.1 Summary of MARS

As has been demonstrated within each of the preceding sections that have focused specifically on planar, cylindrical, and spherical measurement topics, MARS processing can be used with a very high degree of confidence since all the steps in the measurement and analysis are consistent with the well-established principles of standard near-field theory and measurement technique, and all comparisons to date have proved overwhelmingly positive. The translation of the far-field pattern to the origin with the application of a differential phase shift is rigorous. The selection of the mode cut-off for the translated antenna pattern is based on the physical dimensions of the AUT and its translated location and does not rely upon any particular pre-assumed characteristics of the current distribution. The results of the MARS processing will reduce, but clearly cannot entirely eliminate, the effect of the scattering. The final result with MARS processing can be degraded if the sampling of the near-field data is too coarse, but this is also true for regular near-field processing with, importantly, this parameter being controlled by the user. The MARS measurement and post-processing scheme holds for general source geometries, and has been found to be very robust with respect to truncation of the measured near-field data. As has been demonstrated, this novel frequency domain measurement and processing technique is entirely general and can be used to achieve acceptable results with use of minimal absorber or even without the use of an anechoic chamber, irrespective of whether testing high- or low-gain antennas. MARS has been found to improve the reflection levels in traditional anechoic chambers allowing improved accuracy as well as offering the ability to use existing chambers down to lower frequencies than the absorber might otherwise suggest.

References

[1] Yaghjian A.D., *Approximate Formulas for the Far Fields and Gain of Open-Ended Rectangular Waveguide*, NBSIR 83-1689; 1983

[2] Gregson S.F., Parini C.G., McCormick J., *Principles of Planar Near-Field Antenna Measurements*. London, UK: IET Press; 2007. p. 263. ISBN 978-0-86341-736-8

[3] Pozar D.M., *Microwave Engineering*, 2nd edn. New York, USA: John Wiley & Sons; 1998. p. 123. ISBN 0-471-17096-8

[4] Newell A.C., Gregson S.F., Gentle D., Miller P.R., 'The effect of the absorber collar on open ended waveguide probes', *Antenna Measurement Techniques Association Conference*, Salt Lake City, Utah; October 2009

[5] Olver A.D., Clarricoats P.J.B., Kishk A.A., Shafai L., 'Microwave Horns and Feeds', *IEE Electromagnetic Waves Series 39*. London, UK. 1994. p. 100. ISBN 0-85296-809-4

[6] Olver A.D., Clarricoats P.J.B., Kishk A.A., Shafai L., 'Microwave Horns and Feeds'. *IEE Electromagnetic Waves Series 39*. London, UK. 1994. p. 222. ISBN 0-85296-809-4

[7] Newell A.C., Pelland P., 'Measuring low cross polarization using a broad band, log periodic probe', AMTA, Seattle; October 2012
[8] Gentle D., Miller P.R., 'Antenna calibrations at NPL', *Antenna Measurement Techniques Association Conference*, Monterey Bay, California; October 1999
[9] Newell A.C., Baird R.C., Wacker P.F., 'Accurate measurement of antenna gain and polarization at reduced distances by an extrapolation technique', *IEEE Transactions on Antennas and Propagation*. 1973;**AP-21**(4): 418–431
[10] Repjar A.G., Newell A.C., Francis M.H., 'Accurate determination of planar near-field correction parameters for linearly polarized probes', *IEEE Transactions on Antennas and Propagation*. 1988;**36**(6):855–868
[11] Gregson S.F., Parini C.G., McCormick J., *Principles of Planar Near-Field Antenna Measurements*. London, UK: IET Press; 2007. p. 211. ISBN 978-0-86341-736-8
[12] Cano-Fácila F.J., Sierra-Castañer M., Besada J.L., 'New applications of diagnostic techniques in antenna measurements', *AMTA Proceedings*, Salt Lake City; November 2009
[13] Gregson S.F., Newell A.C., Hindman G.E., Carey M., 'Extension of the mathematical absorber reflection suppression technique to the planar near-field geometry', *AMTA Proceedings*, Atlanta, Georgia; October 2010
[14] Slater D., 'A 550 GHz near-field antenna measurement system for the NASA submillimeter wave astronomy satellite', *Antenna Measurement Techniques Association Conference*, Long Beach, California; 3–7 October 1994
[15] Gregson S.F., Parini C.G., McCormick J., *Principles of Planar Near-Field Antenna Measurements*. London, UK: IET Press; 2007. p. 289. ISBN 978-0-86341-736-8
[16] Yaghjian A.D., Approximate Formulas for the Far Fields and Gain of Open-Ended Rectangular Waveguide, NBSIR 83-1689; 1983
[17] Yaghjian A.D., 'Approximate formulas for the far fields and gain of open-ended rectangular waveguide', *IEEE Transactions on Antennas and Propagation*. 1984;**AP-32**(4):378–384
[18] Leibfritz M.M., Blech M.D., Landstorfer F.M., Eibert T.F., 'A comparison of software- and hardware-gating techniques applied to near-field antenna measurements'. *Advances in Radio Science*. 2007;**5**:43–48
[19] Knott E.F., *Radar Cross Section Measurements*. Raleigh, USA: SciTech Publishing; 2006. p. 377. ISBN 0442005369
[20] van Norel J., van Gastel A.H., Vokurka V.J., Neve J., Coroller J.F., 'Application of flexible scanning in advanced APC-techniques', *AMTA 16th Annual Meeting & Symposium*, Long Beach, California; October 1994
[21] Gregson S.F., Newell A.C., Hindman G.E., Carey M.J., *Extension of the Mathematical Absorber Reflection Suppression Technique to the Planar Near-Field Geometry*, AMTA, Atlanta, GA; October 2010
[22] Hindman G.E., Newell A.C., *Reflection Suppression in a Large Spherical Near-Field Range*, AMTA, Newport, RI; October 2005

[23] Hindman G.E., Newell A.C., *Reflection Suppression to Improve Anechoic Chamber Performance*, AMTA Europe, Munich, Germany; March 2006
[24] Gregson S.F., Newell A.C., Hindman G.E., *Reflection Suppression in Cylindrical Near-Field Antenna Measurement Systems – Cylindrical MARS*, AMTA, Salt Lake City, UT; November 2009
[25] Gregson S.F., Newell A.C., Hindman G.E., Pelland P., *Range Multipath Reduction in Plane-Polar Near-Field Antenna Measurements*, AMTA, Seattle; October 2012
[26] Gregson S.F., Dupuy J., Parini C.G., Newell A.C., Hindman G.E., *Application of Mathematical Absorber Reflection Suppression to Far-Field Antenna Testing*, LAPC, Loughborough; November 2011
[27] Gregson S.F., McCormick J., Kerse B.J., Newell A.C., Hindman G.E., 'Computational and experimental verification of far-field mathematical absorber reflection suppression', *6th EuCAP*, Prague; March 2012
[28] Gregson S.F., Williams B.M., Masters G.F., Newell A.C., Hindman G.E., *Application of Mathematical Absorber Reflection Suppression to Direct Far-Field Antenna Range Measurements*, AMTA, Denver; October 2011
[29] Newell A.C., Guerrieri J., MacReynolds K., 'Methods to estimate and reduce leakage bias errors in planar near-field antenna measurements', *AMTA Proceedings*, Cleveland, Ohio; October 2002
[30] Janse van Rensburg D.J., 'Compensation for probe translation effects in dual polarized planar near-field antenna measurements', *AMTA 30th Annual Meeting & Symposium*, Boston, MA; November 2008
[31] Gregson S.F., Parini C.G., McCormick J., *Principles of Planar Near-Field Antenna Measurements*. London, UK: IET Press; 2007. p. 303. ISBN 978-0-86341-736-8
[32] Gregson S.F., Parini C.G., McCormick J., *Principles of Planar Near-Field Antenna Measurements*. London, UK: IET Press; 2007. p. 296. ISBN 978-0-86341-736-8
[33] Hansen J.E. (ed.), *Spherical Near-Field Antenna Measurements*. London, UK: Peter Peregrinus (on behalf of IEE); 1988
[34] Zieg S.W., 'A precision optical range alignment technique', *AMTA Symposium*, New Mexico; October 1982. pp. 1–20
[35] Newell A.C., Hindman G.E., Stubenrauch C., 'The effect of measurement geometry on alignment errors in spherical near-field measurements', *AMTA Proceedings*, Monterey Bay, California; 1999
[36] Newell A.C., Hindman G.E., 'The alignment of a spherical near-field rotator using electrical measurements', *AMTA Proceedings*, Boston, Massachusetts; 1997
[37] Demas J., 'Low cost and high accuracy alignment methods for cylindrical and spherical near-field measurement systems', *AMTA Proceedings*, Newport, Rhode Island; 2005
[38] Hansen J.E. (ed.), *Spherical Near-Field Antenna Measurements*. London, UK: Peter Peregrinus (on behalf of IEE); 1988. p. 218
[39] Ferrero F., Benoit Y., Brochier L., Lanteri J., Dauvignac J.-Y., Migliaccio C., Gregson S.F, 'Spherical scanning measurement challenge for future

millimeter wave applications', *AMTA Proceedings*, Long Beach, California; October 2015

[40] Hestenes M.R., Stiefel E., 'Methods of conjugate gradients for solving linear systems', *Journal of Research of the National Bureau of Standards*. 1952;**49** (6):409–436

[41] Paige C.C., Saunders M.A., 'LSQR: an algorithm for sparse linear equations and sparse least squares', *ACM Transactions on Mathematical Software*. 1982;**8**(1):43–71

[42] *Design and Calibration of Microwave Antenna Gain Standards*. NRL Report 4433, 2 September 1954

[43] IEEE Std 145-1993, *IEEE standard definitions of terms for antennas*

[44] Balanis C.A., *Antenna Theory Analysis and Design*. New York, USA: John Wiley & Sons; 1997

[45] Slayton W.T., *Design and Calibration of Microwave Antenna Gain Standards*, Naval Research Laboratory, Microwave Antennas and Components Branch, Electronics Division, Washington, DC, NRL Report 4433, 9 November 1954

[46] Newell A.C., Ward R.D., McFarlane E.J., 'Gain and power parameter measurements using planar near-field techniques', *IEE Transactions on Antennas and Propagation*. 1988;**36**(6):792–803

[47] Masters G.E., Pelland P., 'Selection criteria for near-field gain techniques', *AMTA Symposium*, Columbus, OH; 2013

[48] Stutzman W.L., Theil G.A., *Antenna Theory and Design*, 2nd edn. New York, USA: John Wiley & Sons; 1998. p. 80. ISBN 0-471-02590-9

This page intentionally left blank

Chapter 13

Electromagnetic modelling of antenna measurement ranges

13.1 Introduction

The development of general-purpose tools for the simulation of antenna measurement systems is of interest for several reasons. It would enable an engineer to:

1. Design and optimise a proposed new antenna systems system, especially Compact Antenna Test Ranges (CATR)
2. Plan and optimise a measurement campaign before committing valuable facility time,
3. Assess error terms within the facility error budget,
4. Verify correction algorithms, e.g. probe pattern correction, position correction, etc. which can constitute a crucial constituent of any post-processing algorithm.

However, in general, it is difficult to obtain closed form, functional, solutions for the electromagnetic field at an arbitrary point in space from knowledge of the tangential electric or tangential magnetic fields over a closed surface for anything but the simplest of configurations. This is especially true when the closed surface, is not coincident with the aperture of the radiating structure, as is the case for near-field antenna measurements. Matters are further complicated if the sampling surface is not a canonical surface (e.g. sphere, cylinder, plane) as is often the case when simulating data that includes imperfections in the measurement system. As such, recourse to alternative methods, typically numerical techniques, becomes unavoidable.

In essence, any antenna measurement can be simulated by evaluating the complex coupling coefficient between the antenna under test (AUT) and the probe, feed or remote source antenna. This must be done at each point over the simulated acquisition surface for each sampled polarisation for the frequency at which the measurement is to be taken. In principle then, it would be possible to obtain the mutual coupling coefficient (S_{21}) between a given mode in the waveguide port in the AUT and a given mode in the waveguide port in the scanning probe, feed or remote source antenna from a three-dimensional electromagnetic full-wave solver for each of the positions at which field samples are to be recorded. This approach would have the advantage of potentially introducing the least number of assumptions and approximations, and therefore could, in theory, yield the most accurate predications.

Unfortunately, although many solvers are available employing say, the finite difference time domain (FDTD) method, the finite element methods (FEM), the method of moments (MoM), etc. they are generally inappropriate for simulating problem spaces as electrically large as those needed to enclose a complete near-field measurement system, including chamber, absorber, cranes, etc. This is a direct consequence of the extended processing times and the amount of computer resources required. Hence, an alternative less general, but more efficient, techniques is often required. Thus, the remainder of this chapter is devoted to the development of a variety of simulation techniques that become successively more sophisticated as their ability to mimic measurement facilities improves. However, this chapter is not intended to be an exhaustive survey of all the possible simulation techniques open, instead the writers have concentrated on a small selection of those methods that extend the near-field method and offer the greatest utility whilst requiring the minimum of computational and intellectual effort.

The CATR is a virtually unique form of antenna system as its design relies far more on the use of CEM than any other variety of test system. It is right therefore that this chapter kicks off with a development and presentation of first classical and then more modern simulation techniques. Here, the simulation is considered in terms of representing a coupling problem. Attention is then turned to the simulation of cylindrical and spherical test systems where the use of these modes is illustrated with the verification and validation of more modern measurement correction techniques, i.e. MARS. Use of full-wave three-dimensional CEM solvers is then introduced and used to highlight near-field probe effects.

13.2 Simulation of a compact antenna test range

This coupling calculation must be accomplished for each point within the simulated CATR quiet-zone (QZ), for each sampled polarisation, and for each frequency at which the measurement is to be taken. In principle then, it would be possible to obtain the mutual coupling coefficient, S_{21}, between a given mode in the waveguide port in the feed and a given mode in the waveguide port of the test antenna from a three-dimensional computational electromagnetic (CEM) full-wave solver. This approach would have the advantage of, potentially, introducing the least number of assumptions and approximations and therefore could in principle yield the most accurate predictions. Unfortunately, at the present time, although many solvers are available, these are generally considered inappropriate for simulating problem spaces as electrically large as those needed to enclose a complete CATR system, as illustrated in Figure 13.1, particularly at higher frequencies, e.g. short cm-wave, mm-wave frequencies and above and especially when that simulation is to be incorporated within a design optimisation process. This limitation is merely a consequence of the extended processing times and the large amounts of computer resources that are typically required. Hence, alternative, perhaps less generally applicable, but more computationally efficient techniques are required. However, the significance that the reflector edge treatment has on the quality of the pseudo-

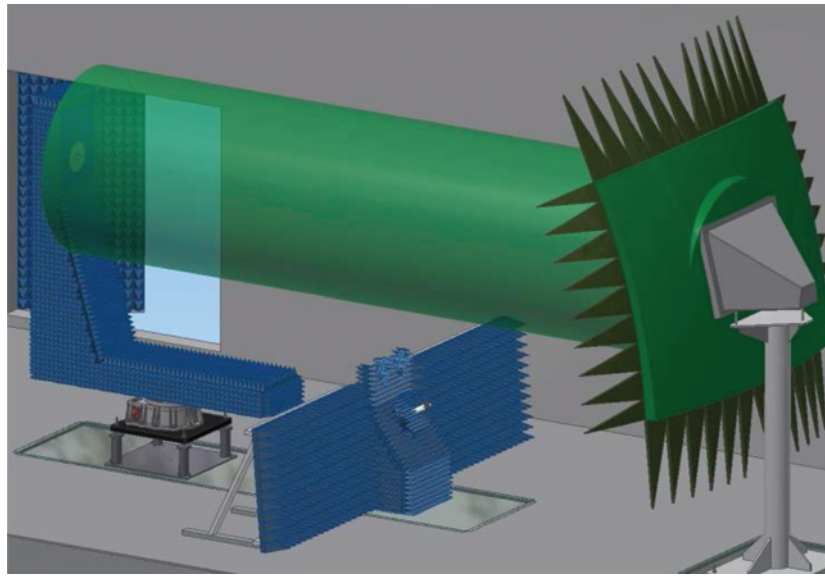

Figure 13.1 Schematic representation of serrated edge single offset-reflector with a 2 m × 2 m quiet-zone. Image courtesy of NSI-MI Technologies LLC

plane wave in the CATR QZ, as expounded above, means that special emphasis must be placed upon the successful validation and verification of any performance prediction software that is harnessed in the design of a CATR.

A schematic representation of the geometry of a CATR configuration is presented in Figure 13.1. Here, the parabolic reflector had a 3.6576 m (12 ft) focal length. The surface profile of the CATR was assumed to be formed from a concave paraboloidal surface. The reflector surface must be a paraboloid of revolution so that the, assumed spherical, incident wave propagating from the focus of the reflector is collimated into a pseudo-plane-wave. The CATR reflector included serrations formed from triangular petals. The phase centre of the feed was placed at the focus of the offset reflector and the feed was tilted up in elevation by 28°. An 11 dBi gain WR430 circular choked waveguide was used for the feed with far-field data being provided by a proprietary full-wave three-dimensional CEM solver using the finite-difference time-domain technique. The origin of the CATR co-ordinate system was located at the (virtual) vertex of the parabolic reflector with the QZ simulations being computed over a transverse plane at $z = 1.8f$, where f was the focal length of the reflector. Although, as we shall see, this is a sub-optimal CATR design, it does serve as a suitable case to illustrate several common modelling methods allowing a detailed comparison to be performed.

The field illuminating the reflector is determined from the far-field pattern function of the CATR feed by reintroducing the spherical phase function and the inverse r term. The corresponding magnetic field (as required by some of the field propagation models described below) can be calculated from the electric field

assuming the TEM far-field condition. Thus, each of the CATR simulations assumes that the reflector is in the far-field of the feed, which was a condition easily satisfied by the electrically small feed antenna. This pattern could be derived from CEM simulation or from empirical range measurement. When introducing the feed into the CATR model, it is assumed that the phase centre of the feed is coincident and synonymous with the focus of the CATR paraboloidal reflector so as to avoid defocusing of the point source CATR. Also, as a result of the requirement to minimise feed induced blockage, an offset reflector design is generally harnessed. Here, it is assumed that the (virtual) vertex of the reflector is coincident with the bottom edge of the reflector. Thus, the feed is required to be tilted up in elevation so that the boresight direction is orientated towards the centre of the reflector surface. A vector isometric rotation can be used to implement this pattern rotation [1]. In practice, as a result of the spherical loss, the feed is usually tilted up a little beyond the geometrical centre of the reflector so as to equalise the reflector illumination. In the subsequent simulations, this was not done and the resulting QZ predictions are therefore slightly sub-optimum. This compromise was admitted on the basis that it enabled a wider range of simulations to be directly compared.

13.2.1 Point source CATR

The surface profile of the point source CATR is assumed to be formed from a concave paraboloidal surface. The surface of a paraboloidal reflector is formed from rotating a parabola about its axis. The reflector surface must be a paraboloid of revolution so that the, assumed spherical, wave propagating from the focus of the reflector is collimated into a plane wave. When expressed in Cartesian coordinates, the equation of a convex parabola can be expressed as

$$z(x,y) = -\frac{(x^2+y^2)}{4f} \tag{13.1}$$

Here, f denotes the focal length and it is assumed that the xy-plane is perpendicular to the orientated z-axis of rotation. The origin of this Cartesian coordinate system is at the vertex of the paraboloidal surface. This can be converted to a (non-truncated) concave surface profile (concave on the positive z-half-space) by reversing the sign of z such that

$$z(x,y) = \frac{(x^2+y^2)}{4f} \tag{13.2}$$

The truncation of the CATR reflector surface is considered in a subsequent section. Within the software, the surface profile is typically represented with an array of points that are tabulated as a function of the x- and y-axes which are assumed to be plaid, monotonic and equally spaced. In this way, deformations in the surface profile can be incorporated with the deformations being derived from measurement (e.g. from three-axis surface profile measurements) or introduced numerically (e.g. as a result of thermo-elastic deformation analysis as discussed below). This provides the model with a great degree of flexibility as imperfection in manufacture can be readily incorporated into the analysis.

A crucial feature of the CATR QZ performance prediction is the effect that the truncation of the offset-reflector will have on the collimated fields, that is to say, edge diffraction effects. The underlying field propagation method, as developed below, introduces this automatically in a natural way that is reliable providing the reflector is more than a few wavelengths across. In practice, this can be incorporated into the model by reducing the limits of integration to only include the region inside an arbitrarily shaped closed polygon that lies in the *xy*-axis. In this way, the reflector is 'cookie-cut' into the requisite shape. This can also be accomplished by setting the reflected electric fields to zero on the exterior of this polygon, which is also equivalent to setting the reflection coefficient of the reflector to zero.

This is the basis of the *physical optics* approximation and it is used extensively when treating electromagnetic scatting problems. Thus, as will be shown below, the surface current will only be assigned a value over the illuminated region of the reflector surface. Therefore, in the shadow region that is cast by the surface, the currents are assumed to be identically zero. Therefore, we can expect that this method will be unsuitable for predicting the fields in the deep shadow region where these neglected currents can be reasonably expected to form the majority of sources. This region is outside of the area of interest when modelling the QZ performance of a CATR however.

13.2.2 Illumination of the CATR reflector

The field illuminating the CATR reflector is derived from the assumed known far-field pattern of the feed. This pattern could be derived from CEM simulation, or from empirical range measurement. When introducing the feed into the CATR model, it is assumed that the phase centre of the feed is coincident and synonymous with the focus of the CATR paraboloidal reflector. Also, as a result of the requirement to minimise feed-induced blockage, an offset reflector design is harnessed. Here, it is assumed that the vertex of the reflector is coincident with the bottom edge of the main reflector. Thus, the feed is required to be tilted up in elevation so that the boresight direction is orientated towards the centre of the reflector surface. In practice, as a result of the spherical loss, the feed is tilted up a little beyond the geometrical centre of the reflector so as to equalise the reflector illumination. This arrangement is illustrated in Figure 13.1. From the perspective of the simulation, all that is needed to be known is the elevation tilt angle, the focal length of the reflector and the far-field pattern of the CATR feed antenna. Let us assume that the far-field pattern of the feed can be expressed as

$$\underline{E}\,(r,\theta,\phi) = \left[E_\theta(\theta,\phi)\underline{\widehat{e}}_\theta + E_\phi(\theta,\phi)\underline{\widehat{e}}_\phi\right]\frac{e^{-jk_0 r}}{r} \tag{13.3}$$

where we have reintroduced the, usually suppressed, spherical wave amplitude and phase factors and assumed a, suppressed, positive time dependency. For electrically small feeds, this far-field assumption is a reasonable one, and in fact it can also be shown to be reliable even for electrically larger antennas, such as corrugated horns, providing they exhibit a Gaussian pattern since the Fourier transform of a Gaussian is also a Gaussian resulting in the behaviour of the feed being comparatively

invariant of distance in the quasi far-field, even when the field point on the CATR reflector surface is not in the true far-field. We can also assume that this is a TEM wave so that the magnetic field can be obtained from the electric field using

$$\underline{H} = \frac{1}{Z_0}\widehat{\underline{u}} \times \underline{E} \tag{13.4}$$

and, the plane-wave condition applies locally so that

$$\underline{E} \cdot \widehat{\underline{u}} = \underline{H} \cdot \widehat{\underline{u}} = 0 \tag{13.5}$$

Here, $\widehat{\underline{u}}$ is the unit vector in the direction of propagation and Z_0 is the impedance of free space, or characteristic impedance, of free space where $Z_0 = c\mu_0$. Here, c is used to denote the speed of light in a vacuum and μ_0 is the permeability of free space which has the exactly defined value of $4\pi \times 10^{-7}$. As noted above, the far-field phase is assumed to be referenced to the 'phase centre' of the feed [2]. That is to say, when the feed was characterised, or simulated, the origin of the measurement (or simulation) was coincident and synonymous with the phase centre of the feed. In practice, this is seldom the case and it is assumed that a differential phase change is applied to the far-field pattern prior to it being used. Here, the phase function fitting that is a pivotal part of the optimisation is performed only out to the maximum polar angle as subtended at the feed, cf. the maximum value of θ_f as derived below. Fields at wider pattern angles will not illuminate the CATR reflector and as such their functional form is unimportant as they are assumed to be absorbed by the, assumed, perfectly impedance matched anechoic environment. The feed pattern is assumed to be tabulated in a polar-pointing spherical coordinate system that is known relative to an arbitrary, but known, fiducial mechanical datum. Typically, the positive z-axis will be at a normal to the aperture of the feed, with the x- or y-axes being aligned, respectively, with the principal electric field vector for the case of an x-polarised or y-polarised feed. The far-field Cartesian components of the feed can be obtained from the far-field polar spherical components using the standard formula

$$\begin{bmatrix} E_x(\theta,\phi) \\ E_y(\theta,\phi) \\ E_z(\theta,\phi) \end{bmatrix} = \begin{bmatrix} \cos\theta\cos\phi & -\sin\phi \\ \cos\theta\sin\phi & \cos\phi \\ -\sin\theta & 0 \end{bmatrix} \cdot \begin{bmatrix} E_\theta(\theta,\phi) \\ E_\phi(\theta,\phi) \end{bmatrix} \tag{13.6}$$

As the feed will be displaced and rotated with respect to the axes of the CATR, it is necessary to determine the Cartesian field component of the field radiated by the feed at the tabulating points across the parabolic surface of the CATR reflector. This is accomplished as follows. The displacement of the reflector sampling point from the focus, i.e. the feed phase centre, can be obtained from

$$r = \sqrt{x^2 + y^2 + (z - f)^2} \tag{13.7}$$

Here, x, y and z are the coordinates across the surface of the reflector such that $z = z(x, y)$. The Cartesian components of the unit vectors in the direction of the field point can then be obtained respectively from

$$u = \frac{x}{r} \tag{13.8}$$

$$v = \frac{y}{r} \tag{13.9}$$

$$w = \frac{(z-f)}{r} \tag{13.10}$$

This represents the direction from the focus to each point across the surface of the parabolic reflector. Thus

$$\underline{E}\,(r,\theta,\phi) = \left[E_\theta(\theta,\phi)\underline{\hat{e}}_\theta + E_\phi(\theta,\phi)\underline{\hat{e}}_\phi\right]\frac{e^{-jk_0\sqrt{x^2+y^2+(z-f)^2}}}{\sqrt{x^2+y^2+(z-f)^2}} \tag{13.11}$$

Here, however, it is assumed that the field components radiated by the feed are in the CATR coordinate system however in fact, this is not the case. In general, an angular rotation of the feed can be incorporated through the use of a direction cosine matrix. Thus, let the feed rotation be defined by the 3 × 3 homogeneous normalised matrix [*A*] such that, cf. Appendices,

$$\begin{bmatrix} u'_f \\ v'_f \\ w'_f \end{bmatrix} = [A]\cdot\begin{bmatrix} u_f \\ v_f \\ w_f \end{bmatrix} \tag{13.12}$$

where the primed variables represent the rotated coordinate system. The derivation of the matrix [*A*] is presented below in a subsequent section. Next, we need to compute the unit direction cosines of the feed coordinate system in the CATR coordinate system. Thus, using the direction cosine matrix, the *z*-directed unit vector in the feed coordinate system will become

$$\begin{bmatrix} u'_w \\ v'_w \\ w'_w \end{bmatrix} = [A]\cdot\begin{bmatrix} 0 \\ 0 \\ 1 \end{bmatrix} \tag{13.13}$$

in the CATR coordinate system. Here, the '*w*' subscript is used to signify that these components relate to the *z*-directed unit vector. The polar angle, θ_f, subtended at the feed by each point across the reflector can be obtained from the definition of the dot product as

$$\theta_f = \arccos\left(\left(u\underline{\hat{e}}_x + v\underline{\hat{e}}_y + w\underline{\hat{e}}_z\right)\cdot\left(u'_w\underline{\hat{e}}_x + v'_w\underline{\hat{e}}_y + w'_w\underline{\hat{e}}_z\right)\right) \tag{13.14}$$

Note: the maximum value of θ_f is used to determine the pattern angle that is used when determining the phase centre of the feed. Similarly, we can write the remaining unit vectors in the CATR coordinate system as

$$\begin{bmatrix} u'_u \\ v'_u \\ w'_u \end{bmatrix} = [A]\cdot\begin{bmatrix} 1 \\ 0 \\ 0 \end{bmatrix} \tag{13.15}$$

$$\begin{bmatrix} u'_v \\ v'_v \\ w'_v \end{bmatrix} = [A] \cdot \begin{bmatrix} 0 \\ 1 \\ 0 \end{bmatrix} \tag{13.16}$$

Thus, the azimuthal, ϕ_f, angle can be obtained using

$$\phi_f = \arctan\left(\frac{\left(u\underline{\hat{e}}_x + v\underline{\hat{e}}_y + w\underline{\hat{e}}_z\right) \cdot \left(u'_v\underline{\hat{e}}_x + v'_v\underline{\hat{e}}_y + w'_v\underline{\hat{e}}_z\right)}{\left(u\underline{\hat{e}}_x + v\underline{\hat{e}}_y + w\underline{\hat{e}}_z\right) \cdot \left(u'_u\underline{\hat{e}}_x + v'_u\underline{\hat{e}}_y + w'_u\underline{\hat{e}}_z\right)}\right) \tag{13.17}$$

Thus, the angles to the points on the reflector with respect to the feed are known. If the feed pattern is known on a plaid monotonic and equally spaced (θ, ϕ) grid, piecewise polynomial interpolation can be used to approximate the amplitude and phase patterns at the interleaving points (θ_f, ϕ_f) [3]. The final stage is to rotate the Cartesian components of the field onto the CATR coordinate system. This is accomplished again by using the transformation

$$\begin{bmatrix} E'_x \\ E'_y \\ E'_z \end{bmatrix} = [A] \cdot \begin{bmatrix} E_x \\ E_y \\ E_z \end{bmatrix} \tag{13.18}$$

Only here it is the field components as opposed to the direction components that are being rotated. In this way, the field from the feed that illuminates the reflector is transformed into the CATR coordinate system. The same transformation can be used to rotate the magnetic fields if these are required, e.g. as needed by the Kirchhoff–Huygens or current element methods, thus,

$$\begin{bmatrix} H'_x \\ H'_y \\ H'_z \end{bmatrix} = [A] \cdot \begin{bmatrix} H_x \\ H_y \\ H_z \end{bmatrix} \tag{13.19}$$

Any number of angular definitions for describing the relationship between the two coordinate systems exists. However, the direction cosine matrix that relates the feed and CATR coordinate system is produced from multiplying out two rotation matrices. The first transformation rotates the feed by 180° about the vertical y-axis so that the feed points towards the reflector with the second rotation being about the positive x-axis so that the feed point up in elevation towards the centre of the reflecting surface.

13.2.3 Calculation of the reflected electric field

The field reflected by the CATR reflector can be computed by the General Law of Reflection. Locally therefore, at the elemental point, the field will be of the form of a TEM plane-wave propagating in the direction $\underline{r}'$. As the field is a local plane wave and assuming that the reflecting surface is locally planar and is made from a perfectly conducting (PEC) material, the normal electric field component will be unchanged upon reflection. Thus, if a homogeneous plane wave is incident on a perfect electrical conducting (PEC) flat surface of infinite extent, the reflected elemental electric field constitutes a similar plane wave and the reflected field can be obtained from the incident field thus we may write that

$$\underline{E}_r = -\underline{E}_i + 2(\hat{\underline{n}} \cdot \underline{E}_i)\hat{\underline{n}} \tag{13.20}$$

Here, $\underline{E}_i$ denotes the incident fields and $\underline{E}_r$ denotes the reflected field. This states that, if a homogeneous plane wave is incident on a perfect electrical conducting (PEC) flat surface of infinite extent, the normal component of the reflected field is unchanged upon reflection whilst the tangential components of the electric field are reversed in sign. From the law of reflection, i.e. the angle of incidence equals the angle of reflection.

$$\theta = \arccos(\hat{\underline{n}} \cdot \hat{\underline{u}}_i) = \arccos(\hat{\underline{n}} \cdot \hat{\underline{u}}_r) \tag{13.21}$$

Thus, it is possible to write the general statement of reflection as

$$\hat{\underline{u}}_r = \hat{\underline{u}}_i - 2(\hat{\underline{n}} \cdot \hat{\underline{u}}_i)\hat{\underline{n}} \tag{13.22}$$

Here, $\hat{\underline{u}}_i$ denotes the direction of propagation of the incident plane wave and $\hat{\underline{u}}_r$ represents the direction of propagation of the reflected, specular, plane wave. This can be taken to represent the general form of the law of reflection with the scattered field being a plane wave as the material is assumed to be infinite in extent in the tangential direction and the material properties do not vary across this surface.

13.2.4 Calculation of the local surface unit normal and elemental surface area

In order that the field reflected by the CATR reflector can be obtained, we must first compute the local surface unit normal. This section develops techniques for obtaining these quantities from, in principle, a surface that is specified numerically. Let the surface over which the electric field is known to be expressed as

$$g(x, y, z) = 0 \tag{13.23}$$

The outward-pointing surface normal can be formed from the cross product of two non-parallel tangent vectors. Thus, provided that the Cartesian coordinates are tabulated such that

$$x = f_1(u, v) \tag{13.24}$$

$$y = f_2(u, v) \tag{13.25}$$

$$z = f_3(u, v) \tag{13.26}$$

then two tangential vectors $\underline{a}$ and $\underline{b}$ can be formed from

$$\underline{a} = -\frac{dx}{du}\hat{\underline{i}} - \frac{dy}{du}\hat{\underline{j}} - \frac{dz}{du}\hat{\underline{k}} \tag{13.27}$$

$$\underline{b} = -\frac{dx}{dv}\hat{\underline{i}} - \frac{dy}{dv}\hat{\underline{j}} - \frac{dz}{dv}\hat{\underline{k}} \tag{13.28}$$

Here, the $\hat{\underline{i}}$, $\hat{\underline{j}}$ and $\hat{\underline{k}}$ denote unit vectors in the x-, y- and z-axes respectively. Hence, the surface unit normal can be obtained from

$$\hat{\underline{n}} = -\frac{\underline{a} \times \underline{b}}{|\underline{a} \times \underline{b}|} \tag{13.29}$$

The inward-pointing unit surface normal is assumed to be anti-parallel with this vector. Finally, the elemental area, which will be needed when propagating the reflected field to the QZ (via the vector-Huygens formula, etc.), can be found by evaluating

$$da = |\underline{a} \times \underline{b}| \tag{13.30}$$

Thus, the surface unit normal and elemental area is obtained in a form that can be used with the general law of reflection, as developed above, and the field propagation methods presented in the following sections treat the field propagation from reflector to the CATR QZ.

13.2.5 Electromagnetic field propagation

The preceding sections enable the field reflected by a perfectly conducting smooth surface to be computed from the far-field pattern of the feed antenna and from the geometry of the point source CATR. The following sections present a number of methods for propagating those reflected fields to the CATR QZ using two-dimensional surface integration methods with varying degrees of complexity, computational effort and accuracy.

13.2.5.1 Vector-Huygens method (plane-wave spectrum method)

Once the field reflected by the main reflector is known across the surface of the reflector, the vector-Huygens method can be used to compute the field across the QZ. The vector-Huygens method is a powerful technique for determining the field in a source and sink free region outside a surface from the knowledge of the field distribution over that surface. It is applicable to arbitrary but smoothly shaped (not necessarily planar) apertures over which the tangential components of the electric fields are prescribed. The vector-Huygens principle can be obtained directly from the coordinate free form of the conventional plane-rectilinear near-field to far-field transformation by collapsing the area of the aperture plane until in the limit, it becomes a single elemental, i.e. infinitesimal, Huygens source. The geometry of the vector-Huygens formula is presented in Figure 13.2.

When expressed mathematically, providing the scalar product of the surface unit normal $\underline{\hat{n}}$ and the vector to the field point $\underline{\hat{u}}_{r''}$ are positive, the electric field at a point P radiated by a closed Huygens surface S_H that is in the far-field of the infinitesimal Huygens element is given by [4]

$$d\underline{E}(P) = j\frac{e^{-jkr''}}{\lambda r''}\left[\underline{\hat{u}}_{r''} \times \left(\underline{E}_a \times \underline{\hat{n}}\right)\right] da \tag{13.31}$$

Here, point P located at (x, y, z) must be in the far-field of the infinitesimal radiating elemental Huygens source, which results in the field point being removed from the Huygens source by a few wavelengths. This formula can be seen to have been obtained from the coordinate-free form of the planar near-field to far-field transform (with probe pattern correction omitted) for the case where the scan plane

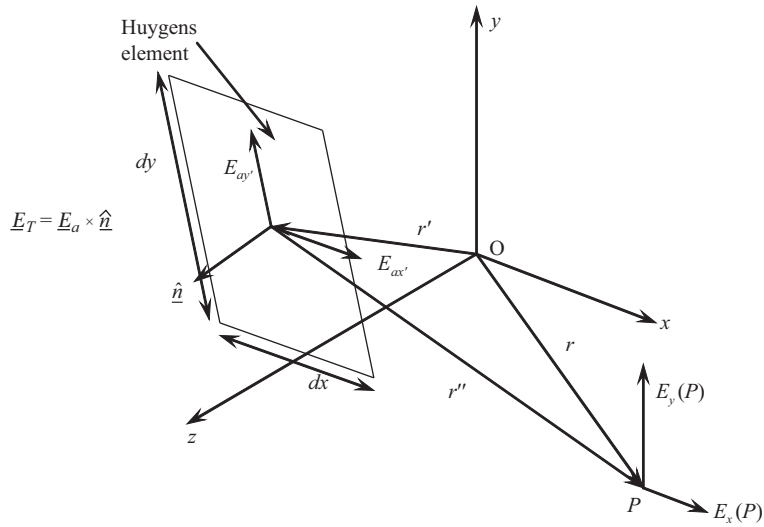

Figure 13.2 Illustration of vector-Huygens formulation

has reduced to an infinitesimally small region of space, *da*, where we can assume that the amplitude and phase remains constant across this interval. Thus, the total field at a point in space can be expressed by integrating across the complete radiating aperture thus the electric field can be obtained from

$$\underline{E}(P) = \frac{j}{\lambda}\int_S \left[\hat{\underline{u}}_{r''} \times \left(\underline{E}_a \times \hat{\underline{n}}\right)\right] \frac{e^{-jkr''}}{r''} da \tag{13.32}$$

Here, *S* denotes the finitely large aperture and *da* is the elemental surface area. Although the field point must be in the far-field of the infinitesimal Huygens element, it can still be in the near-field of the complete radiating aperture. Thus, for the purposes of simulating a CATR, providing the QZ is more than a couple of wavelengths from the reflector (which it always will be) the results will be valid. Crucially, as the surface unit normal is permitted to vary across the aperture *S*, this expression can be used to calculate the electric fields at the observation point *P* as radiated from smooth non-planar apertures. Furthermore, provided that the observation point is displaced by more than a few wavelengths from the radiating aperture, i.e. the reflector, then the field points can be distributed arbitrarily throughout space. This makes this form of field transport particularly effective for the purpose of simulating near-field measurements, whether they are planar (rectilinear, polar or bi-polar), cylindrical or spherical in geometry. For the purposes of computing, the QZ performance using the vector-Huygens formula as expounded above, $\underline{E}_a$ is taken to be the reflected electric field, $\underline{E}_r$ which was determined from the incident field. The sample spacing should satisfy Nyquist locally, that is to say, there must be at least one sampling node per half-wavelength across the surface of the parabolic reflector. Furthermore, when

computing the field across the QZ, at least one sample is needed per half-wavelength across the sampling surface. That is to say, the sample spacing is related to the free space wavelength through

$$\delta x = \delta y = \frac{\lambda}{2} \tag{13.33}$$

In order that the accuracy of the method is guaranteed, sample spacings of a sixth of a wavelength or finer are generally used.

13.2.5.2 Kirchhoff–Huygens method

Once the field reflected by the main reflector is known across the surface of the reflector, the Kirchhoff–Huygens method can be used to compute the field across the QZ. The Kirchhoff–Huygens method is another powerful technique for determining the field in a source and sink free region outside a surface from knowledge of the field distribution over that surface. It is applicable to arbitrary but *not* necessarily smoothly shaped apertures over which the tangential components of the electric *and* magnetic fields are prescribed. The Kirchhoff–Huygens method is, in essence, a direct integral of Maxwell's equations. The geometry of the Kirchhoff–Huygens formula is presented in Figure 13.3.

The general vector Kirchhoff–Huygens formula can be expressed as [5]

$$\underline{E}_p = \frac{1}{4\pi}\int_S \left[-j\omega\mu(\hat{\underline{n}} \times \underline{H}) + \left\{(\hat{\underline{n}} \times \underline{E}) \times \hat{\underline{r}}' + (\hat{\underline{n}} \cdot \underline{E})\hat{\underline{r}}'\right\}\left(jk_0 + \frac{1}{r'}\right)\right]\frac{e^{-jk_0 r'}}{r'}\,da \tag{13.34}$$

In addition to the reflected electric fields $\underline{E}$, this expression requires knowledge of the tangential components of the reflected magnetic fields $\underline{H}$. These can be

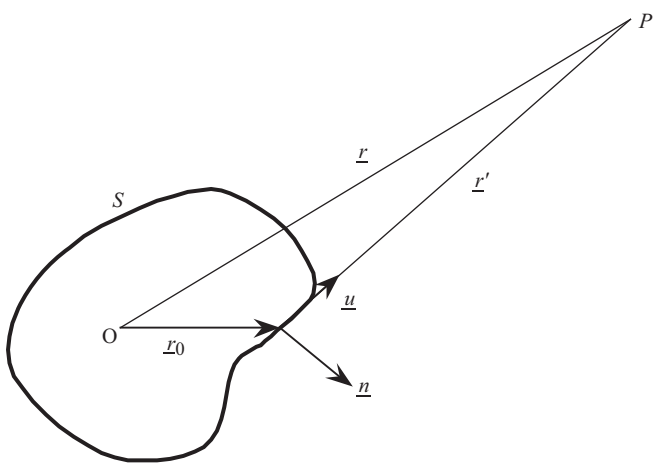

Figure 13.3 Illustration of Kirchhoff–Huygens formulation

computed from the incident magnetic fields as from the method of images (and assuming the parabolic reflector is locally planar) we can write that

$$\underline{n} \times \underline{H}_i = \underline{n} \times \underline{H}_r \tag{13.35}$$

The Kirchhoff–Huygens theory is exact, provided that the field is known exactly over a closed surface although this additional rigour is sought at the expense of additional computational effort. The closed surface can take the form of an infinite plane together with an infinite radius hemisphere. If the source is finite, then, from the radiation condition, it can be seen that no contribution to the total field arises from any part of the hemispherical portion of the surface.

13.2.5.3 Current element method

The current element method is an alternative field propagation method to those developed above. The current element method replaces the fields with an equivalent surface current density $\underline{J}_s$ which is used as an equivalent source to the original fields. The surface current density across the surface of the reflector can be obtained from the magnetic fields and the surface unit normal using [6]

$$\underline{J}_s = 2\hat{\underline{n}} \times \underline{H}_i = 2\hat{\underline{n}} \times \underline{H}_r \tag{13.36}$$

The current density approximation for $\underline{J}_s$ (as embodied by the above expression) is known as the *physical-optics* approximation. The fields radiated by an electric current element can be expressed as [6]

$$d\underline{H}(P) = \frac{1}{4\pi}\left[\underline{J}_s \times \nabla\psi\right] da \tag{13.37}$$

Here, we are computing the elemental magnetic field from the vector potential where

$$\psi = \frac{e^{-jk_0 r'}}{r'} \tag{13.38}$$

so that [5,6]

$$\nabla\psi = \left(jk_0 + \frac{1}{r'}\right)\psi\hat{\underline{u}} \tag{13.39}$$

Thus,

$$d\underline{H}(P) = \frac{1}{4\pi}\left(jk_0 + \frac{1}{r'}\right)\frac{e^{-jk_0 r'}}{r'}\left[\underline{J}_s \times \hat{\underline{u}}\right] da \tag{13.40}$$

This is an exact expression. Integrating the elemental magnetic field results in the total magnetic field

$$\underline{H}(P) = -\frac{1}{4\pi}\int_S \left(\hat{\underline{u}} \times \underline{J}_s\right)\frac{1 + jk_0 r'}{r'^2} e^{-jk_0 r'} da \tag{13.41}$$

The corresponding elemental electric fields can be obtained, approximately, from the elemental magnetic fields using the far-field TEM condition. That is to say, approximately,

$$d\underline{E} = Z_0(d\underline{H} \times \hat{\underline{u}}) \tag{13.42}$$

As before, the total electric and magnetic fields can be obtained from the elemental fields by integrating across the surface of the parabolic reflector.

13.2.5.4 Geometric optics method

Geometrical optics (GO), or ray optics takes the Lagrangian point of view by considering the transportation of energy quanta from a point of emission to a point of absorption and is applicable to problems where the frequency is sufficiently high to enable the wave properties of light to be ignored giving rise to an infinite frequency approximation. Thus, GO is an incomplete treatment of the physical phenomena and needs to be augmented to include diffraction effects that are so crucial when predicting the QZ of a CATR. In practice, this can be implemented by incorporating a geometrical theory of diffraction (GTD) correction through the principle of linear superposition with a detailed treatment of GO and GTD being presented within [7]. By simple ray tracing, it is clear that geometrical optics is incapable of correctly predicting a nonzero field in the shadow region. This situation is illustrated in Figure 13.4.

By including diffracted rays, we can account for a nonzero field in the shadow region and in addition, modify the geometrical optics field in the illuminated region. By adding diffracted rays, we correct the deficiency in the GO that predicts

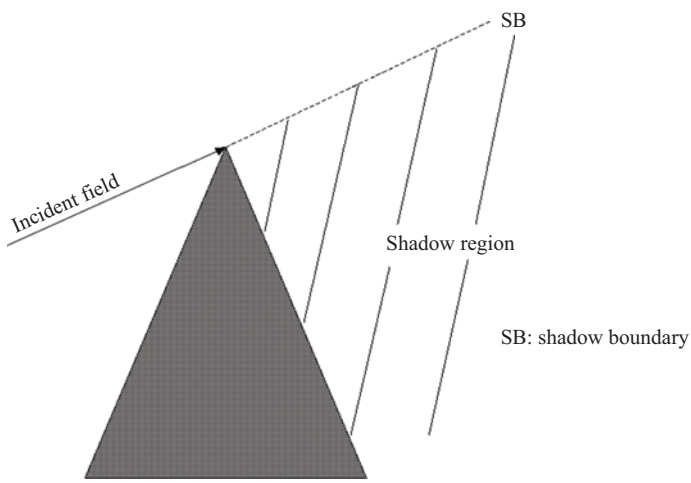

Figure 13.4 Illustration of GO illumination and shadow region

zero field in the shadow regions. The geometrical theory of diffraction (GTD) was developed by Keller [8] and can be summarised as follows:

1. The diffracted field propagates along rays that are determined by a generalisation of Fermat's principle to include points on the boundary surface in the ray trajectory.
2. Diffraction like reflection and transmission is a local phenomenon at high frequencies, i.e. it depends only on the nature of the boundary surface and the incident field in the immediate neighbourhood of the point of diffraction.
3. The diffracted wave propagates along its ray so that
   - the power is conserved in a tube,
   - the phase delay along the ray path equals the product of the wave number of the medium and the distance.

Keller postulated that diffracted rays exist and that they are produced when geometrical optics rays illuminate edges, corners and vertices of boundary surfaces or when GO rays graze surfaces, in fact, whenever a structure causes a discontinuity in a GO field by creating shadow regions. If a plane wave is illuminating an object, the nature of the diffracted wave depends on the scattering structure and the direction of incidence. As an example, when the incident wave is propagating in a direction normal to the edge of a wedge, the diffracted wave is cylindrical Figure 13.5(a). If the incident rays in the direction of propagation of the incident wave are oblique to the edge [Figure 13.5(b)], the diffracted wave is conical. This means that the diffracted wavefronts are parallel cones with the edge as their common axis. Keller's law of diffraction is thus defined as 'A diffracted ray and the corresponding incident ray make equal angles with the edge at the point of diffraction, provided they are in the same medium [8]. They lie in opposite sides of the plane normal to the edge at the point of diffraction'.

As with all GO rays, however, the problem is to determine the initial values of the amplitude, phase and polarisation at the point where the ray is launched, that is, the point of diffraction. Following the analogy of GO reflected rays, Keller's

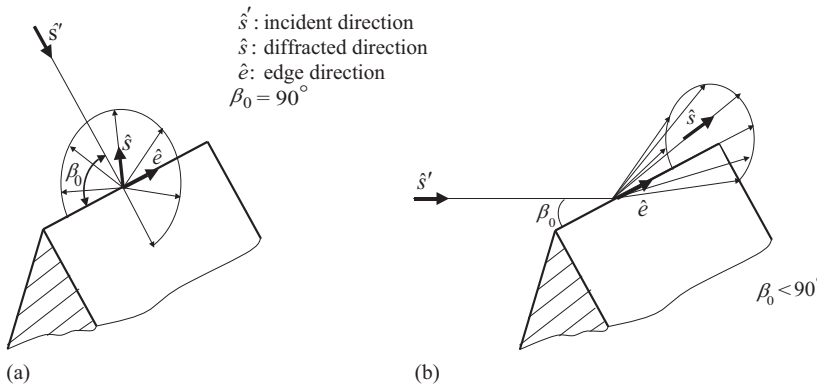

Figure 13.5 Illustration of GO illumination and shadow region

diffracted rays are determined by the field incident on the diffraction point multiplied by a diffraction coefficient, a spreading factor and a phase term. The diffracted field will, in general, have the form:

$$\underline{E}^d = \underline{E}^i(Q) \cdot \underline{\underline{D}}A(l)e^{-jkl} \tag{13.43}$$

where $E^i(Q)$ is the field incident on the point of diffraction Q on an edge, D is the dyadic diffraction coefficient, $A(l)$ is the spreading factor and l is the distance from Q to the field point [19]. In this form, GTD could predict the diffracted fields in regions away from the shadow boundary, but become singular in the transition regions surrounding such boundaries.

In 1974, Kouyoumjian and Pathak wrote a landmark paper [9] defining the uniform theory of diffraction (UTD). They described an asymptotic analysis and found that, by multiplying the diffraction coefficient by a transition function, the diffracted fields remain bounded across the shadow boundaries. The form of the transition function is such that it approaches zero at the same rate as that at which the diffraction coefficients become singular at the shadow boundaries, so that the resultant diffracted fields remain bounded at the shadow boundaries. Kouyoumjian and Pathak had thus succeeded in developing a ray-based uniform diffraction theory; that is, one that is valid everywhere in space. However, UTD still suffers from some of the shortcomings of the GTD; namely, the theory fails when the incident field is not a ray optical field and it cannot be applied when reflection and diffraction no longer are local phenomena.

13.2.6 Comparison of CATR CEM simulation methods with full-wave simulations

The four different CEM modelling techniques described above can all be used to compute CATR QZ performance for the CATR configuration presented above. The now five simulations all used the same feed pattern and geometry with only the field propagation method and reflection calculation changing between the various simulations. The simulation techniques used were as follows: geometrical optics with geometrical theory of diffraction edge correction (GO + GTD), vector-Huygens (VH), Kirchhoff–Huygens (KH), current elements (CE) and FEKO physical optics (FEKO). Thus, Figure 13.4(a) presents a comparison of the CATR QZ amplitude predictions for the five simulations for the horizontally polarised electric field component (*Ex*) in terms of iso-levels (contours) where each of the patterns was normalised to 0 dB at the peak of the pattern. Here, red contours denote GO + UTD, magenta contours denote VH, cyan contours denote KH, blue contours denote CE-based field propagation whilst black contours represent the results from FEKO using PO. Similarly, Figure 13.4(b) contains an equivalent plot for the vertically polarised (cross-polar) electric field component (*Ey*).

From inspection of these plots, it is clear that the VH-, KH- and CE-based methods are in very good agreement with GO + GTD being in only slightly less close agreement with the main difference being the presence of additional ripple on

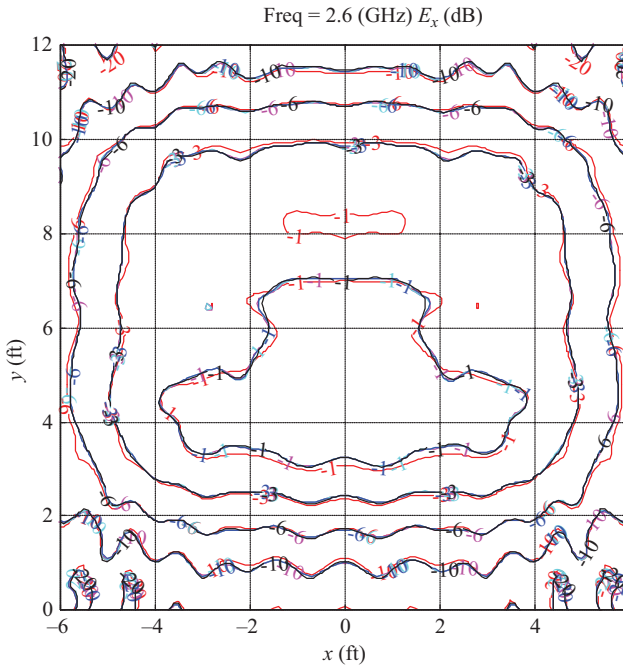

Figure 13.6 Comparison of CATR QZ x-polarised electric field using various simulation methods

the GO + GTD QZ predictions. General levels and shape of the patterns for both *x*- and *y*-polarised amplitude plots are very encouraging (Figures 13.6 and 13.7). Some asymmetry is apparent in the GO + GTD simulations on the *y*-polarised patterns, which is erroneous as the model is inherently symmetrical in the *yz*-plane. Although not shown due to the need for brevity, better agreement can be attained at higher frequencies where the GO assumption becomes an increasingly good approximation of the physics. Additionally, the CATR feed model is not perfectly symmetrical which is a consequence of small numerical imperfections within the finite difference time domain CEM model that was used to generate the feed pattern predictions. Figures 13.8–13.15 contain horizontal and vertical amplitude and phase plots through the QZ that are intended to enable a more critical assessment of the degree of agreement to be attained.

Here, it is clear that all of the principal polarised cardinal cuts are in good agreement with the general pattern shapes and features being in close agreement. General cross-polar levels are also in excellent agreement, with only the null-depth changing between the respective simulations. As can be seen, the CE and FEKO PO models are closest in agreement, especially in the very demanding vertical cross-polar cut (where the levels are circa 70 dB below the peak). The phase patterns are also in very good agreement confirming the adoption of the same

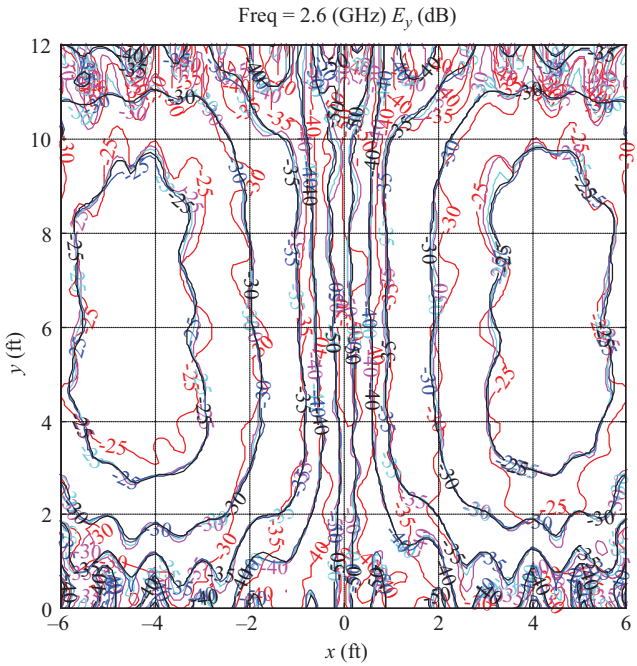

Figure 13.7 Comparison of CATR QZ y-polarised electric field using various simulation methods

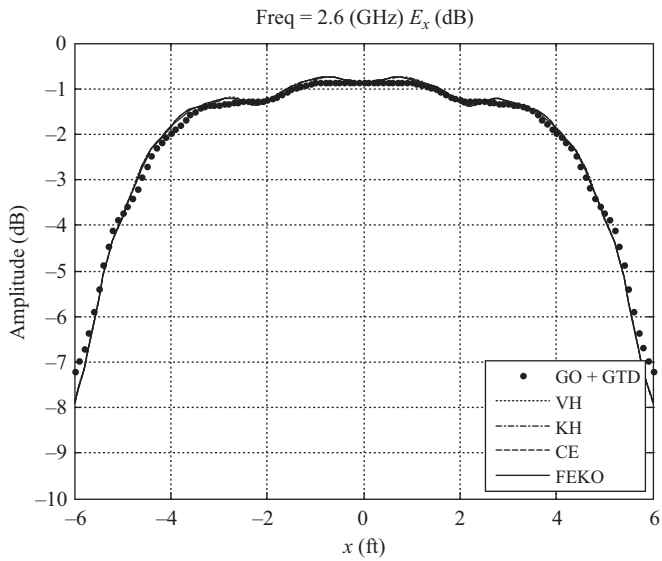

Figure 13.8 Horizontal cut through QZ of the amplitude of H-pol fields

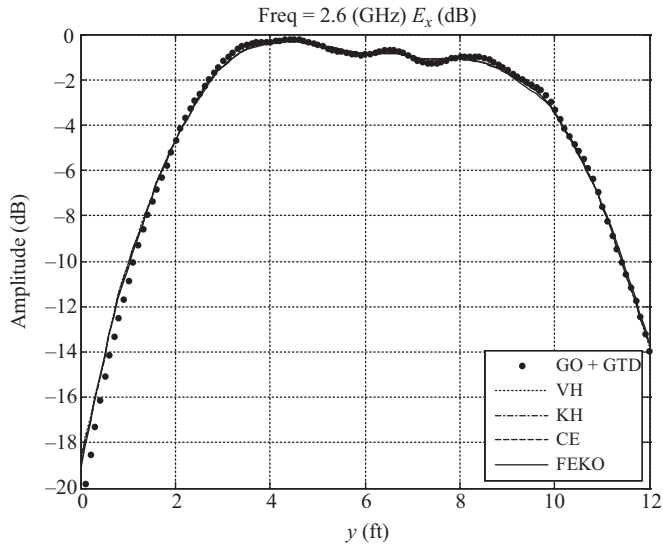

Figure 13.9 Vertical cut through QZ of the amplitude of H-pol fields

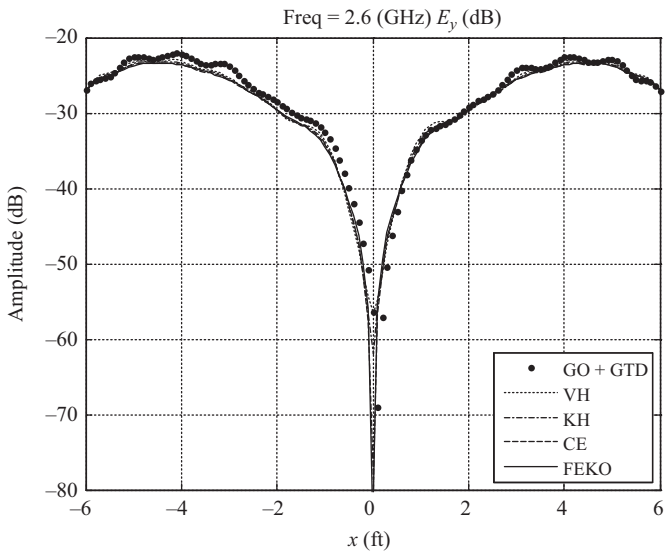

Figure 13.10 Horizontal cut through QZ of the amplitude of V-pol fields

(suppressed) time dependency. Some small phase differences are evidently becoming progressively more noticeable in regions of low field intensity where it is difficult to control the phase, e.g. in nulls and towards the extremities of the QZ. From inspection of the cross-polar iso-level plots and the cardinal cuts, some

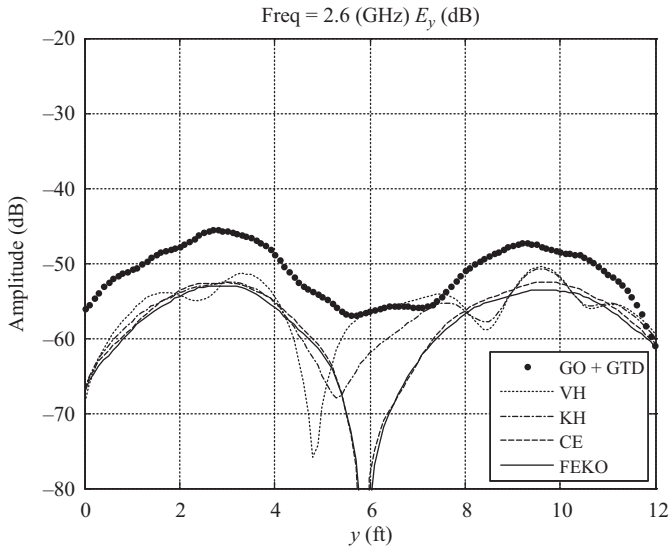

Figure 13.11 Vertical cut through QZ of the amplitude of V-pol fields

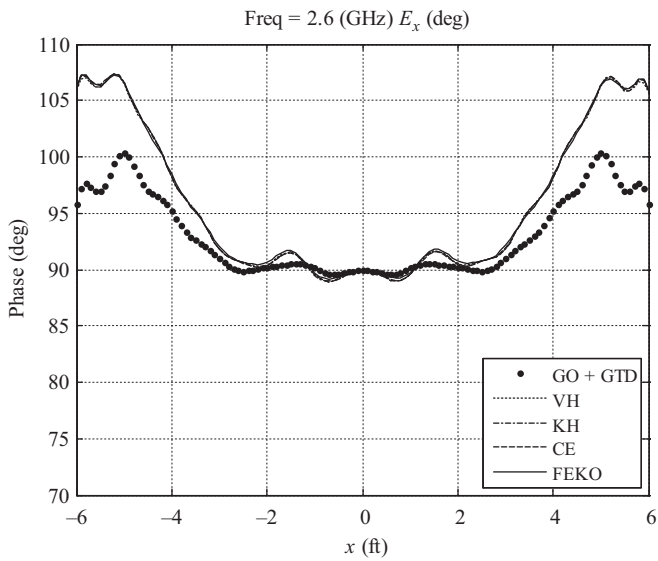

Figure 13.12 Horizontal cut through QZ of the phase of H-pol fields

differences in symmetry (left to right) are evident in the GO + GTD predictions (these are most noticeable in the cross-polar patterns). As both the feed and reflector are symmetrical in this axis, as the offset is in the vertical axis, symmetry should not be broken here and this is an indication that the method is being used at

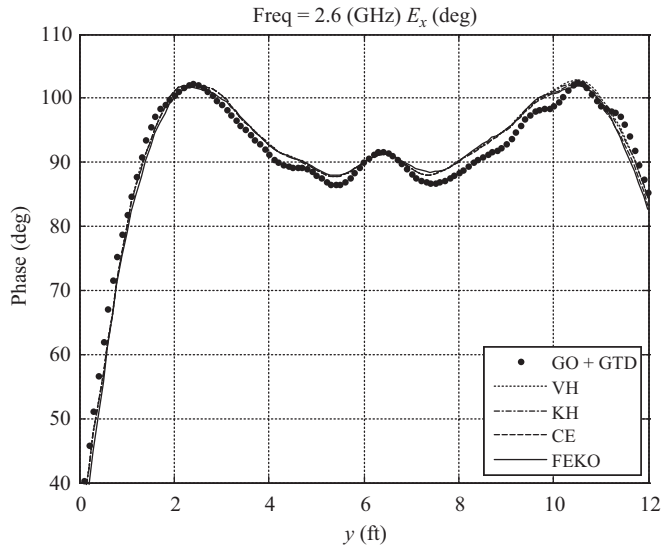

Figure 13.13 Vertical cut through QZ of the phase of H-pol fields

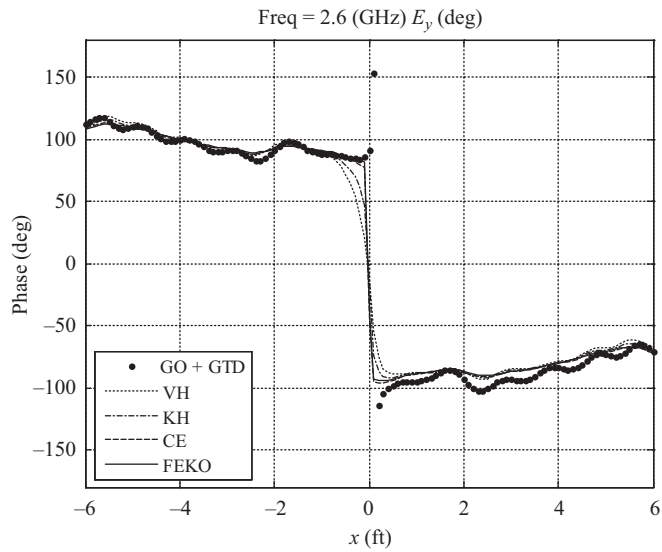

Figure 13.14 Horizontal cut through QZ of the phase of V-pol fields

too low a frequency. The VH, KH, CE and FRKO PO models exhibit a very good degree of symmetry in this axis.

Clearly, each of the five different CATR QZ simulations can be seen to be in very good agreement with one another. Furthermore, from inspection of the CE and

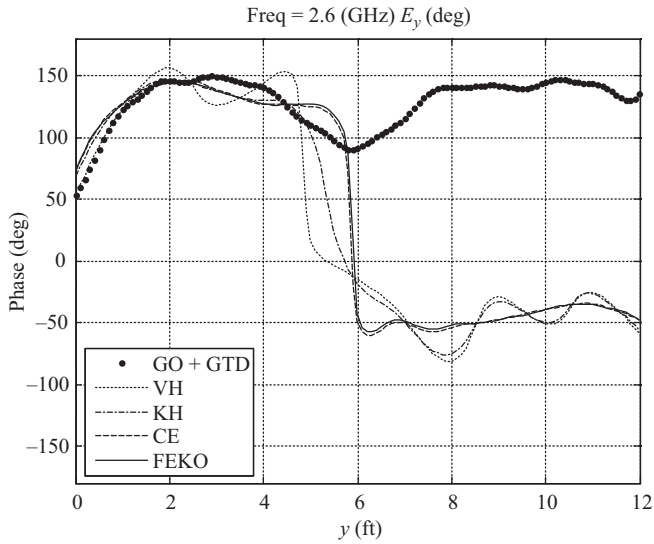

Figure 13.15 Vertical cut through QZ of the phase of V-pol fields

FEKO PO models, it could be seen that these arguably demonstrated the closest agreement with the GO + GTD result exhibiting the largest differences due to the low frequency of the simulation and resulting inapplicability of the method. These observations however are merely qualitative and it is preferable to instead adopt quantitative holistic pattern comparison techniques [11]. Many attempts to produce objective quantitative measures of correspondence between data sets that can be used to assess the accuracy, sensitivity and repeatability associated with the production of that data have been reported in the open literature [11–13]. In these, a variety of statistical methods have proved successful in the robust assessment of similarity between antenna pattern functions where the comparison has been found to be complicated: the large amount of interferometric, i.e. complex, data which is used to represent the QZ performance and the huge dynamic range of that data, which in this case is greater than 70 dB. This, however, is the first time that these sophisticated techniques have been harnessed to assess near-field data. Two commonly used techniques for the comparison of electromagnetic data are the root mean square (RMS) difference and the ordinal measure of correspondence [11]. Table 13.1 contains a comparison of the RMS difference (in dB) which is a conventional interval assessment technique. The larger the negative value of the RMS value, the better the agreement with −300 dB corresponding to perfect agreement between the data sets. Conversely, Table 13.2 contains an equivalent set of comparisons using the ordinal measure of correspondence k, where zero represents no similarity and unity represents perfect agreement such that $0 \leq k \leq 1$ [18].

Each of these comparison techniques is commutative, and as a consequence of this, the tables exhibit symmetry as their elements are equal to their transpose elements, i.e. $A_{j,k} = A_{k,j}$. The values of the elements in the leading diagonal merely

Table 13.1 Mean RMS difference, QZ patterns

	GO	VH	KH	CE	FEKO
GO	**−300.00**	**−39.39**	**−39.20**	**−38.90**	**−38.95**
VH	−39.39	**−300.00**	**−56.41**	**−53.50**	**−49.13**
KH	−39.20	−56.41	**−300.00**	**−55.65**	**−52.38**
CE	−38.90	−53.50	−55.65	**−300.00**	**−50.82**
FEKO	−38.95	−49.13	−52.38	−50.82	**−300.00**

Table 13.2 Ordinal measure of correspondence, QZ patterns

	GO	VH	KH	CE	FEKO
GO	**1.00**	**0.82**	**0.81**	**0.80**	**0.80**
VH	0.82	**1.00**	**0.98**	**0.96**	**0.95**
KH	0.81	0.98	**1.00**	**0.97**	**0.97**
CE	0.80	0.96	0.97	**1.00**	**0.99**
FEKO	0.80	0.95	0.97	0.99	**1.00**

represent a perfect agreement between the patterns being compared and have no significance further than that. Thus, in each case, the comparison of five simulations (yielding complex dual polarised) data arrays with 121 by 121 elements has been successfully reduced to the assessment of ten quantitative numbers (i.e. the elements of the upper triangular matrix shown in bold typeface in Tables 13.1 and 13.2). However, while Table 13.1 was derived from comparing the amplitudes of the E_x- and E_y-polarised QZ data, Table 13.2 was produced from comparing the amplitude *and* phase patterns of *both* the E_x- and E_y-polarised QZ fields thereby comprising a far more holistic comparison of much larger data sets.

From inspection of the first row of Tables 13.1 and 13.2, it is clear that the GO + GTD method is in less encouraging agreement than the other methods in this study and is essentially an outlier. This is expected and ties in with the results of the visual inspection. From the results shown in Table 13.2, it is clear that CE and FEKO PO are in very good agreement with a k value of 0.99. The KH and VH methods are similar and this too is revealed within the ordinal assessment as shown in Table 13.2. The results of the interval assessment are less clearly defined and stems from the large dynamic range and the very localised region and low level (i.e. in the vicinity of the cross-polar null) where the largest differences are manifest.

At route, almost all data assessment techniques depend on reducing the dimensionally of the data being assessed to make them more easily accessible. Electromagnetic data may contain tens or hundreds of thousands of individual complex vector data points and the quantitative assessment of such large data sets become close to impossible without distilling the data down to more manageable levels. Clearly, such data reduction techniques almost always involve the loss of some information. However, it should be borne in mind that all inferential

statistical methods, be they nominal (i.e. categorical), ordinal, interval or ratio abstract the data to assess specific attributes or features so in all forms of statistical data assessment information is lost about the specific nature of the sets being examined. Thus, the choice of assessment technique must be steered by an informed understanding of the nature of the parameters that are to be assessed.

13.2.7 Assessment of CATR QZ predictions

The widely accepted criteria for specifying the quality of this pseudo-plane is to insure that the wave should have less than a 1 dB amplitude taper, less than a ± 0.5 dB amplitude ripple and less than a $\pm 5^\circ$ phase ripple, cf. Chapter 5. The amplitude taper is measured as the variation of a quadratic function that is typically found from a least-squares best fit through the amplitude data over a cut through the QZ. The amplitude ripple is then measured by determining the variation of the amplitude about this second-degree polynomial function. A detailed treatment of the least-squares function fit that can be used for this purpose can be found presented in [14]. The phase ripple is characterised by the deviation from a best-fit straight line across the QZ and is expressed in decimal degrees. Of course, in practical measurements the accuracy depends upon the linearity of the QZ probe's translation stage and the stability of the guided wave path, granted, but that can be verified if need be. The only additional requirement is that we maintain the same relative correction across all frequencies. These linear cuts are typically acquired across horizontal, vertical or inter-cardinal cuts that are transverse to the *z*-axis of the range and are repeated for various *z*-positions downrange. The maximum dimensions within a volume of space, typically cylindrical in shape, throughout which this specification can be met determines the physical size of the CATR QZ. Amplitude taper and amplitude ripple parameters are illustrated in Figure 13.16 with the phase ripple being analogous to the amplitude pattern without the quadratic taper. These field properties are generally measured as part of the CATR installation using a procedure based upon a field probe scanner. The final facility acceptance is typically predicated upon the vendor being able to successfully

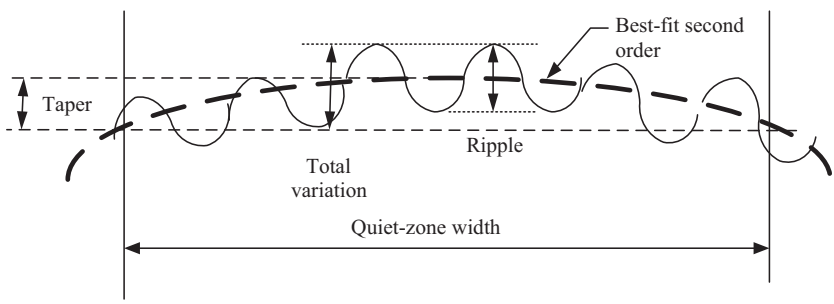

Figure 13.16 Illustration of CATR amplitude taper and amplitude ripple specifications in the QZ

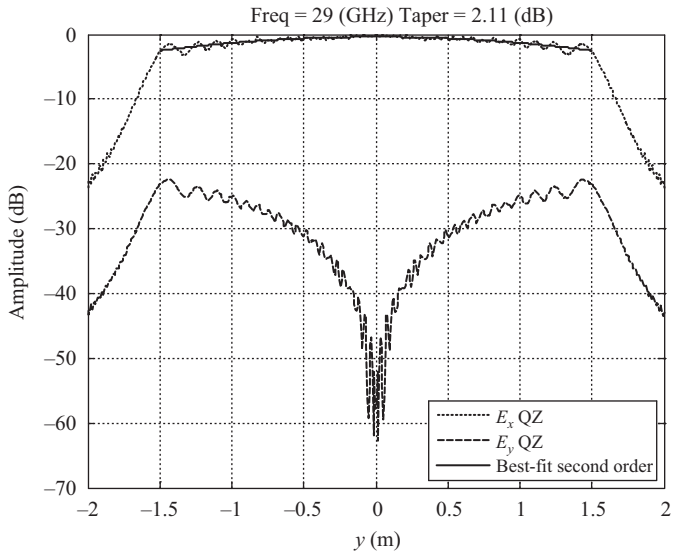

Figure 13.17 Co-polar and x-polar QZ field in the y-plane at x = 4 m (Centre of CATR)

demonstrate that these requirements have been met or exceeded at a number of specified frequencies across the intended frequency range for the facility.

For the QMUL sector-shaped CATR shown schematically in Figures 5.14 and 5.60, Figure 13.17 contains an example of the simulated QZ performance when presented in the form of a cut of the offset plane QZ co-polar and cross-polar field in the vertical, *y*-plane, at $x = 4$ m for the QMUL sector-shaped point source CATR.

Figures 13.18 and 13.19 present, respectively, expanded views of the QZ amplitude and phase in the *y*-plane at $x = 4$ m.

The amplitude taper, amplitude ripple and phase ripple results can be calculated for a range of *x*-axis and *y*-axis spans so that the CATR QZ volume can be estimated. Table 13.3 presents an example of this for the case of the QMUL CATR, cf. Figure 5.60, for the case of the vertical *y*-axis cut at a distance in *Z* from the vertex to the CATR QZ cut = 1.136 × focal length = 6.13 (m). Similar results can be obtained for the horizontal *x*-axis cut or for any other intercardinal cut.

From inspection of Tables 13.3 and 13.4, it is clear that the CATR QZ meets the standard specification across a vertical cut that spans 1.25 m and a horizontal cut that spans 1.00 m when operating at a frequency of 29 GHz at a down-range position of 13.13 m as measured from the virtual vertex of the parabolic reflector. Assuming an elliptical cross-section for the CATR QZ then this corresponds to an area of 0.98 m^2. It is typical for a side-fed CATR to suffer from slightly degraded performance in the plane of the offset as the CATR QZ pseudo-plane wave is typically less symmetrical in this axis. The improved results in the vertical cut mainly arise from the greater symmetry observed in this plane. Clearly, if the feed were offset in the *y*-axis instead of the *x*-axis, then this situation would be reversed.

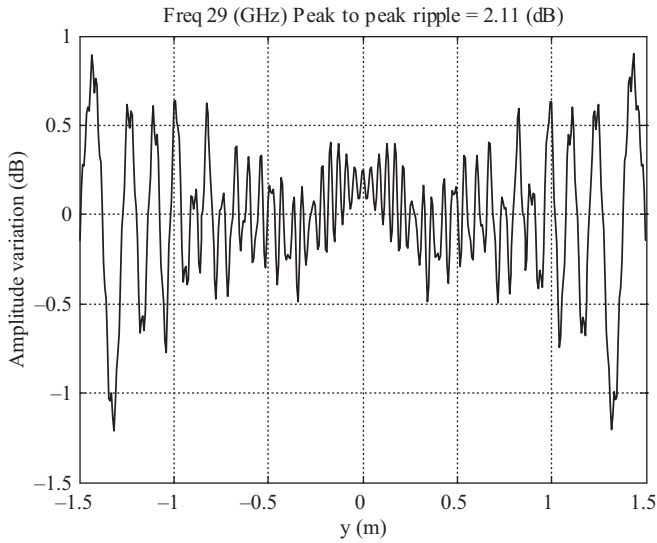

Figure 13.18 Expanded view of the QZ amplitude in the y-plane at x = 4 m

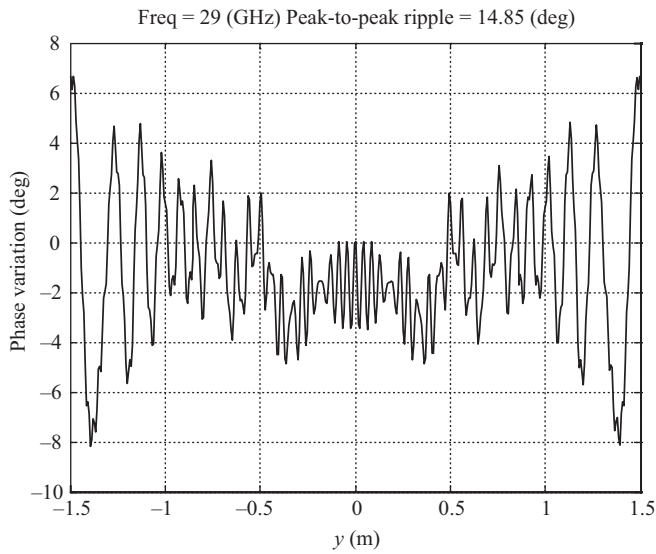

Figure 13.19 Expanded view of the QZ phase in the y-plane at x = 4 m

In practice, this assessment would be repeated at various locations down range so as to be able to establish a three-dimensional, elliptical, volume for the QZ. Once this has been completed, this assessment would be conducted across a range of frequencies over which the CATR would be used.

Table 13.3 Summary of CATR QZ results for QMUL CATR at 29 GHz – vertical cut

CATR QZ Span (m)	Amplitude Taper (dB)	Peak-to-peak Amplitude Ripple (dB)	Peak-to-peak Phase Ripple (deg)
3.00	2.11	2.11	14.85
2.75	2.13	1.79	12.42
2.50	1.46	1.41	10.53
2.25	1.16	1.41	8.46
2.00	0.94	1.14	8.15
1.75	0.78	1.16	8.15
1.50	0.65	0.96	7.25
1.25	0.50	0.91	6.87
1.00	0.48	0.81	6.87

Table 13.4 Summary of CATR QZ results for QMUL CATR at 29 GHz – horizontal cut

CATR QZ span (m)	Amplitude taper (dB)	Peak-to-peak amplitude ripple (dB)	Peak-to-peak phase ripple (deg)
3.00	3.07	7.05	20.66
2.75	2.03	1.92	16.73
2.50	1.77	1.91	12.46
2.25	1.46	1.85	12.03
2.00	1.24	1.27	10.51
1.75	1.03	1.24	8.59
1.50	0.82	1.25	8.59
1.25	0.65	1.12	7.95
1.00	0.53	1.03	7.95

Unfortunately, in many cases, it is not directly apparent how a given CATR QZ performance specification, when expressed in terms of amplitude taper, amplitude ripple and phase ripple will manifest itself on the resulting far-field antenna pattern measurement. Previous work in this area is relatively limited. In the early days of CATR development, the specification of QZ field amplitude taper of 1 dB and ripple as being less than ± 0.5 dB in amplitude and $\pm 5^\circ$ in phase was determined from a heuristic viewpoint. This is illustrated through taking scans of QZ amplitude and phase ripple and demonstrating that antennas measured in such QZ where comparable to outdoor far-field measurements. Later, computational techniques began to be used and in [15] the coupling between the AUT and CATR is expressed in terms of CATR modelling using geometrical optics (GO) and geometric theory of diffraction (GTD) and plane-wave spectra coupling to the AUT. This work was used to illustrate the design of a CATR in terms of its reflector edge illumination and edge treatment and is discussed in detail in Chapter 5, Section 5.4. The following sections present an end-to-end simulation process that can be used to determine the actual error that would be seen for a given CATR antenna combination.

13.2.8 Inclusion of feed spill-over in CATR quiet-zone

The CATR QZ performance prediction model, as developed above, can also incorporate the effects of feed spill-over. The total field is obtained using the principle of linear superposition which can be expressed as,

$$\underline{E}_{\text{total}}(x,y,z) = \underline{E}(x,y,z) + \underline{E}_{\text{feed}}(x,y,z) \tag{13.44}$$

Here, $\underline{E}$ represents the electric field in the QZ that was reflected from the CATR reflector, while $\underline{E}_{\text{feed}}$ represents the field in the QZ resulting from direct illumination from the feed. The field illuminating the QZ that is emanating from the feed is calculated in exactly the same way as the field illuminating the CATR reflector, as presented above in Section 13.2.2. The field propagation methods presented above, e.g. vector-Huygens formula correctly normalises the amplitude and phase patterns so that they may be combined with the field directly radiated by the feed without further normalisation. As scattering from chamber walls, etc. are not included within the simulation and only direct path illumination from the CATR feed is considered, i.e. blockage from the feed support structure is also omitted, thus this can be considered to represent a first-order model capable of providing a worst-case, upper bound performance prediction. The effect of the feed spillover within the CATR QZ is to introduce a high spatial frequency ripple which is caused by the constructive and destructive interference resulting from the linear superposition of fields radiated by the feed and those reflected by the CATR reflector. This can be seen illustrated in Figures 13.20 and 13.21 which contain respectively the *x*- and *y*-polarised tangential electric field components plotted across a plane that is transverse to the *z*-axis of the CATR. By comparison with Figures 13.6 and 13.7 which contain equivalent plots in the absence of feed spill-over, it is clear that the principally polarised *x*-polarised pattern has changed very little; however, the *y*-polarised pattern has a high spatial frequency ripple super-imposed on the pattern. The feed spill-over is at a much lower level than the principal polarisation of the CATR pseudo-plane-wave, however that is not the case for the orthogonal polarisation where the interfering fields are more similar. Here, the offset is in the *y*-axis and thus the ripples are predominantly evident in the *y*-axis. If instead the offset were in the *x*-axis, then correspondingly, the ripple would also be evident in the *x*-axis.

Ordinarily, a great deal of time, trouble and ingenuity is invested in making certain that there is no direct illumination of the CATR QZ by the CATR feed with techniques for minimising this being discussed in detail in Chapter 5. However, the results presented in this section provide an upper bound for this error and a method of incorporating it into range simulations. Furthermore, post-processing methods for extracting any stray fields that do illuminate the CATR QZ are presented below.

13.2.9 End-to-end simulation of CATR measurement process

As noted above and following the development presented in [16], the coupling of the pseudo-plane wave into the aperture of an AUT creates the classical measured

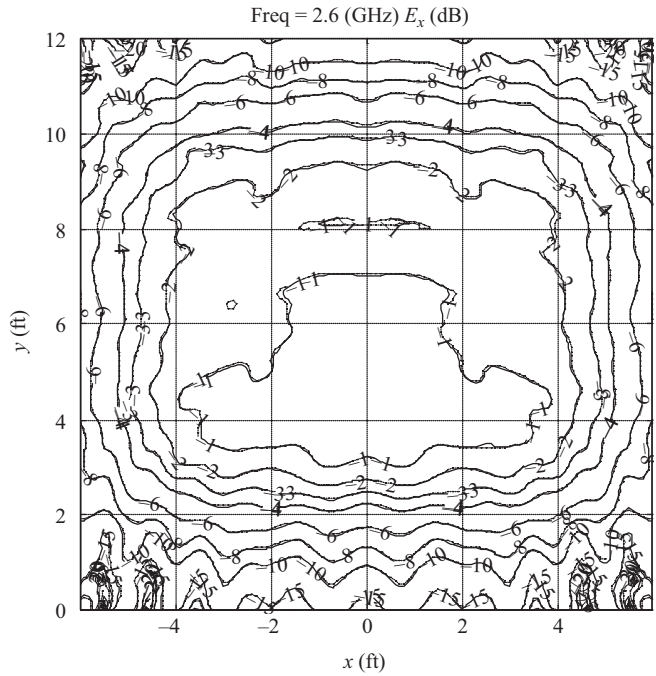

Figure 13.20 Comparison of CATR QZ x-polarised electric field including feed spillover using FEKO PO and current element methods

'far-field' radiation pattern. Assuming the electric and magnetic fields radiated by a given antenna over a convenient enclosing surface are known then, it is possible to create a perfect plane wave and to use that to tap off the far-field pattern at a specific far-field angular direction by evaluating the reaction integral between the pseudo-plane wave and the AUT [16] (Figure 13.22).

The reaction theorem is a well-known method for analysing coupling problems. This theorem states that, provided the electric and magnetic field vectors ($\underline{E}_1$, $\underline{H}_1$) and ($\underline{E}_2$, $\underline{H}_2$) are of the same frequency and monochromatic than the mutual impedance, Z_{21}, between two radiators, antennas 1 and 2, in the environment described by ε, μ can be expressed in terms of a surface integration,

$$Z_{21} = \frac{V_{21}}{I_{11}} = -\frac{1}{I_{11}I_{22}} \int_{S_2} (\underline{E}_2 \times \underline{H}_1 - \underline{E}_1 \times \underline{H}_2) \cdot \hat{\underline{n}}\, ds \tag{13.45}$$

Here, $\underline{n}$ is taken to denote the outward pointing surface unit normal. Subscript 1 denotes parameters associated with antenna 1, whilst subscript 2 denotes quantities associated with antenna 2, i.e. S_2 is a surface that encloses antenna 2, but not antenna 1. Here, I_{11} is the terminal current of antenna 1 when it transmits and similarly, I_{22} is the terminal current of antenna 2 when it transmits. Note that this integral does *not* compute transferred power as there are no conjugates present and as such, crucially, phase information is preserved. From

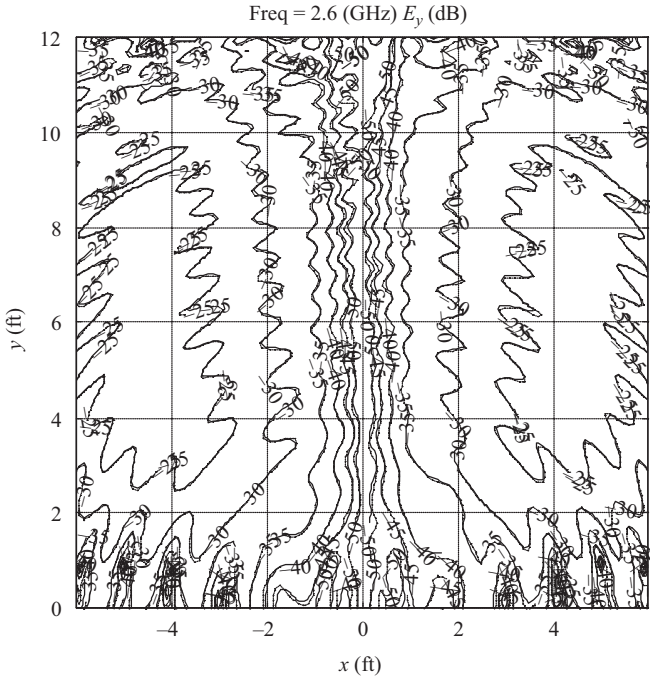

Figure 13.21 Comparison of CATR QZ y-polarised electric field including feed spillover using FEKO PO and current element methods

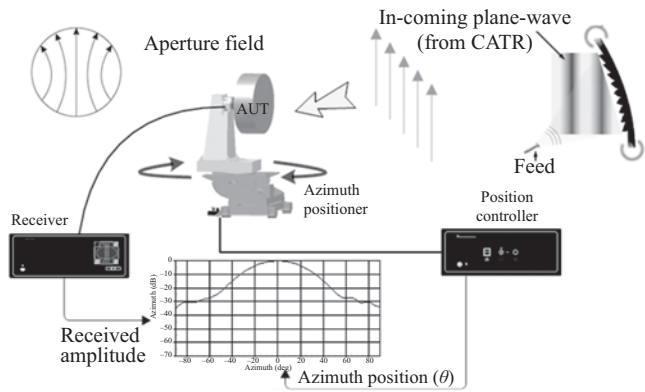

Figure 13.22 Illustration of CATR measurement process

reciprocity, the mutual impedance, $Z_{12} = Z_{21}$, and is related to the coupling between two antennas. Clearly then the mutual impedance will also be a function of the displacement between the antennas, their relative orientations, and their respective polarisation properties. As an admittance is merely the reciprocal of an impedance, an admittance matrix [Y] representing this two-port coupled systems

can be readily populated so that

$$[Y] = \begin{bmatrix} Y_{11} & Y_{12} \\ Y_{21} & Y_{22} \end{bmatrix} \tag{13.46}$$

It is well known that the re-normalised scattering matrix, $[S_\Omega]$, can be calculated from this admittance matrix and is used to describe what fraction of the signal is transmitted, or reflected at each port of the coupled system,

$$[S_\Omega] = \sqrt{[Y_\Omega]}([Z] - [Z_\Omega])([Z] + [Z_\Omega])^{-1}\sqrt{[Z_\Omega]} \tag{13.47}$$

Here, $[Y_\Omega] = [Z_\Omega]^{-1}$ and is a diagonal matrix with the desired normalising admittance as the diagonal entries, i.e. the admittance of the attached transmission line which in this case will be equal to the port impedance $Z_1 = Z_2 = Z_{\text{TE}}$. The elements $S_{12} = S_{21}$ of $[S_\Omega]$ are the complex transmission coefficients for the coupled antenna system which are taken to represent a single point in the far-field measurement. When utilising this procedure to simulate CATR measurements it is crucial to recognise that the fields illuminating the AUT from the CATR only need to be computed once per frequency. This is also true for the fields radiated by the AUT. Thus, in principle, it is possible to simulate measured cuts and patterns in a computationally efficient manner allowing simulation of many different test configurations. This will be further examined in the following section.

As stated here, the coupling of the pseudo-plane wave into the aperture of an AUT creates the classical measured 'far-field' radiation pattern and can be evaluated by evaluating the reaction integral. This integration can be performed across any convenient free-space closed surface a powerful, generic, CATR modelling procedure can be developed if a spherical surface is utilised. Figures 13.23 and 13.24 illustrate respectively the *x*- and *y*-polarised electric near-fields of an AUT sampled across the surface of the sphere of a radius of 0.6096 m. Here, the amplitude patterns are presented in terms of false-colour plots over the conceptual spherical integrating surface. Although not shown, the *z*-polarised electric field and corresponding magnetic fields were also obtained. The corresponding far-fields were also determined and are shown below where they are used as a 'truth' model against which the CATR measurement simulation can be gauged.

Figures 13.25 and 13.26 present equivalent plots for the case where the AUT has been rotated by 40° about the positive *y*-axis as would be required when evaluating the corresponding 'measured' far-field pattern value at this angle.

Although any closed surface could be used, the advantage of the spherical integration surface is that a general compound rotation about the *x*-, *y*- and *z*-axes can be implemented without the need to compute fields outside this sampling interval, i.e. domain. Such vector isometric rotations can be implemented either approximately through approximation or rigorously by expanding the fields onto a set of spherical vector mode functions and by rotating those functions. In most cases, the choice is unimportant as the near-fields can be grossly oversampled, to improve the accuracy of the numerical integration, so that the use of approximation typically introduces only second-order errors. However, if the fields are sampled on

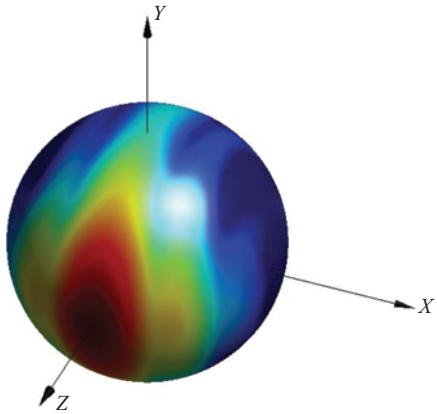

Figure 13.23 E_x*-polarised AUT near-field amplitude pattern*

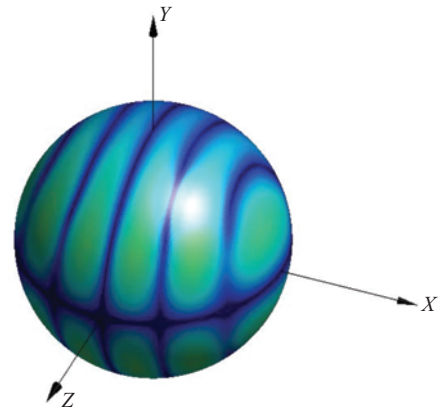

Figure 13.24 E_y*-polarised AUT near-field amplitude pattern*

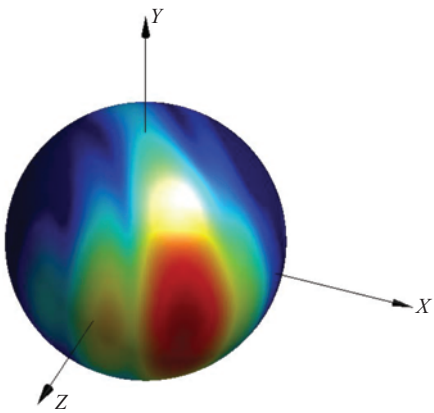

Figure 13.25 E_x*-polarised rotated AUT near-field amplitude pattern*

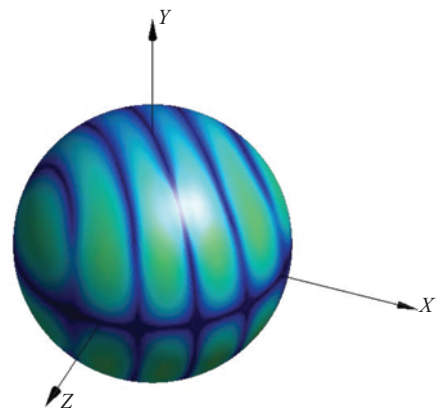

Figure 13.26 E_y*-polarised rotated AUT near-field amplitude pattern*

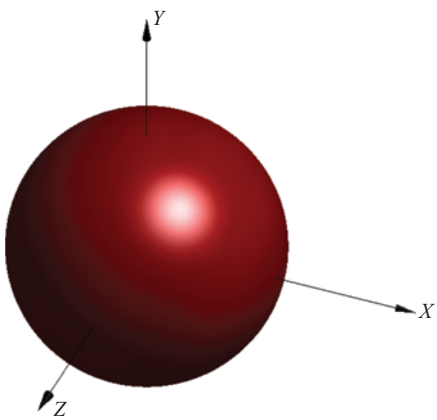

Figure 13.27 E_x*-polarised QZ amplitude patterns in the centre of CATR QZ*

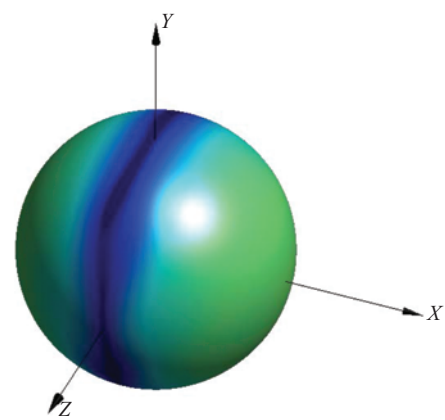

Figure 13.28 E_y*-polarised QZ amplitude patterns in the centre of CATR QZ*

an azimuth over elevation tabulating coordinate system the pattern rotation is reduced to a cyclic permutation of the column elements within the data array thereby eliminating this source of error. Thus, in this case, the number of points in the azimuth axis of the near-field data was set equal to the number of points in the required far-field great-circle azimuth simulated measurement cut. The adoption of an elevation over azimuth coordinate system would enable the elevation cut to be obtained in a similarly rigorous fashion.

Figures 13.27 and 13.28 present, respectively, the E_x- and E_y-polarised fields of the pseudo-plane wave as created by the CATR. Although the CATR QZ data presented above were sampled across the surface of a plane that was transverse to the z-axis of the range, in principle fields can be computed at any point in space providing that point is more than a few wavelengths from the surface of the reflector and outside of the deep shadow region. Consequently, it is possible to place the spherical integrating surface in various positions throughout the QZ. This corresponds to making a measurement with the AUT located at different positions within the QZ. Thus, Figures 13.29 and 13.30 present corresponding CATR QZ data for the case where the sphere was translated to the bottom of the QZ where the zenith of the sphere was aligned with the bottom of the CATR reflector (before the serrations started). Figures 13.31 and 13.32 show equivalent patterns for the case where the origin of the sphere was aligned with a projection of the vertex of the parabolic reflector, i.e. the sphere located half outside of the CATR QZ in what is far from an optimum position to more clearly illustrate the change in the CATR pseudo-plane wave. Here, it is possible to clearly see the degradation in the performance of the pseudo-plane wave at the extremities as the uniformity in the amplitude of the x-polarised electric field is greatly reduced. Thus, by computing the reaction of the sequentially rotated AUT with the translated CATR fields, it is possible to compute, in a very general sense, the simulated far-field CATR measurement of a given AUT when tested in a variety of locations within the range.

Thus, by computing the reaction of the sequentially rotated AUT (as illustrated in Figures 13.25 and 13.26) with the translated CATR fields (as illustrated in Figures 13.27–13.30), it is possible to compute, in a very general sense, the simulated far-field CATR measurement of a given AUT can be predicted. Figures 13.33–13.38 show examples of the results of this calculation. In these plots, the solid trace that can be seen in Figure 13.33 contains a plot of the ideal far-field pattern of the 2.6 GHz AUT (that was used to compute the spherical near-fields shown in Figures 13.27 and 13.28). The dotted trace corresponds to specifying the pseudo-plane wave as being that of a perfect TEM wave propagating in the z-axis and then using the reaction integral to evaluate the coupled fields. This process of rotating and integrating implements a spherical near-field to far-field transform. The agreement between the solid and dotted traces for the amplitude and phase plots confirms the validity of the approach. The dashed trace denotes the simulated measured far-field pattern that is obtained when using the pseudo-plane wave that is generated by the offset parabolic reflector CATR. Here, from inspection, the agreement between the simulated measured far-field pattern and the ideal far-field amplitude and phase patterns is very encouraging. This is further corroborated by

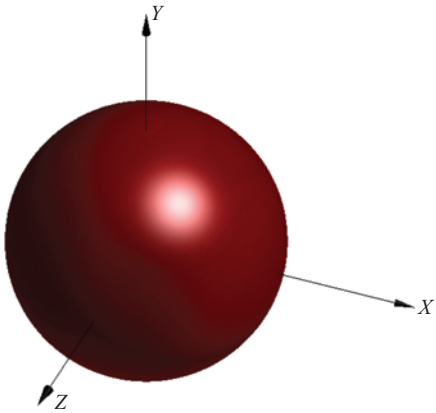

Figure 13.29 *E_x-polarised QZ amplitude patterns at the bottom of the CATR QZ*

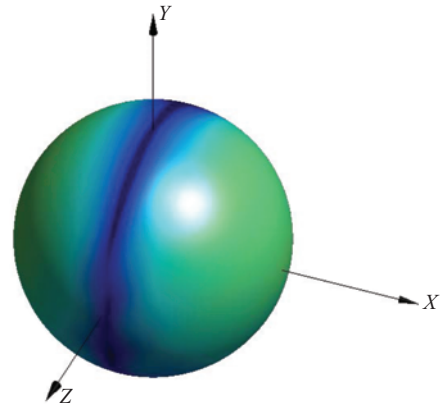

Figure 13.30 *E_y-polarised QZ amplitude patterns at the bottom of the CATR QZ*

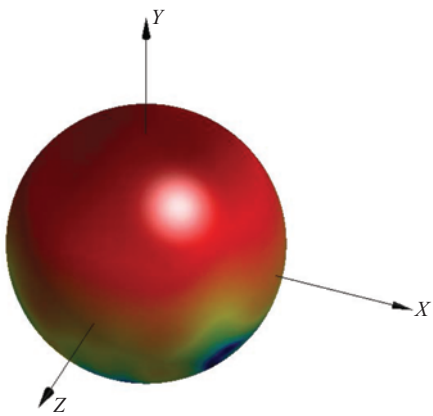

Figure 13.31 *E_x-polarised QZ amplitude patterns at the projection of the vertex of the CATR reflector*

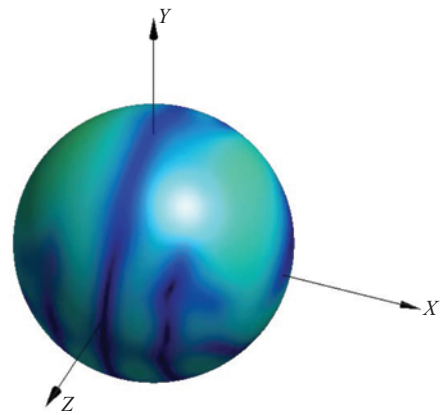

Figure 13.32 *E_y-polarised QZ amplitude patterns at the projection of the vertex of the CATR reflector*

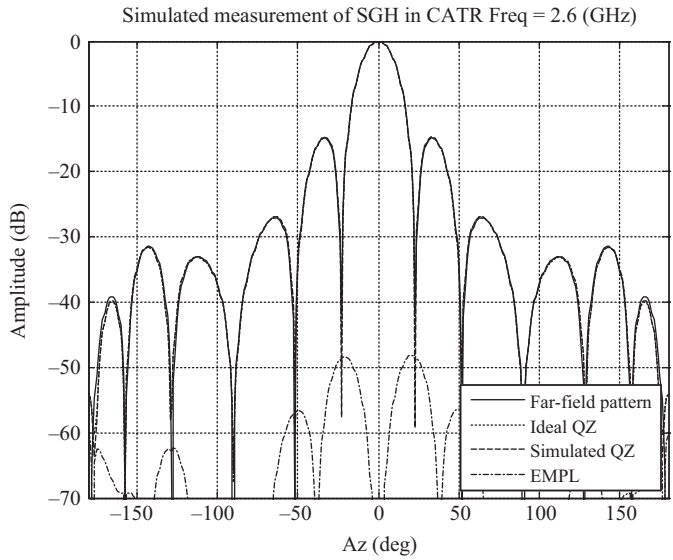

Figure 13.33 Comparison of E_x-polarised QZ amplitude patterns with AUT in the centre of QZ

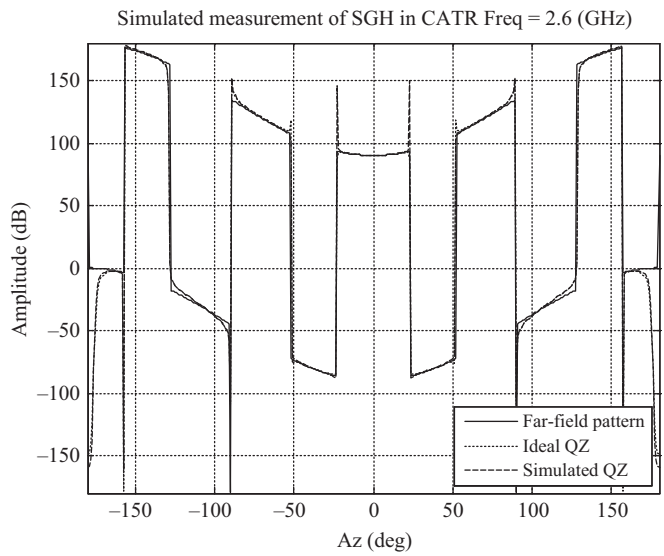

Figure 13.34 Comparison of E_y-polarised QZ amplitude patterns with AUT in the centre of QZ

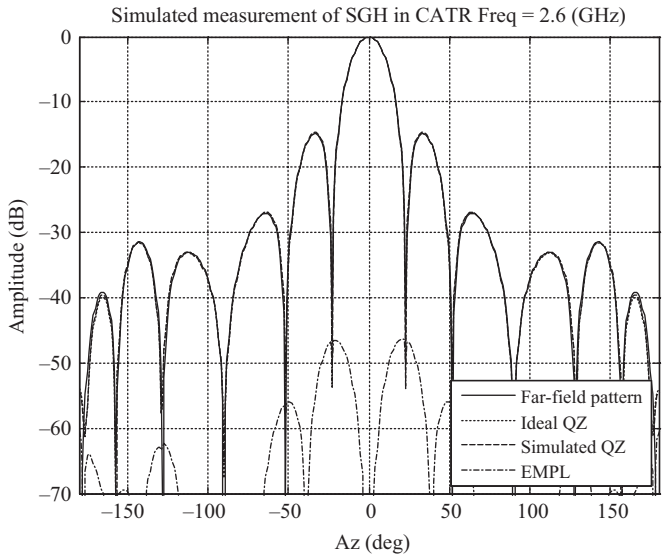

Figure 13.35 Comparison of E_x-polarised QZ amplitude patterns with AUT at the bottom of QZ

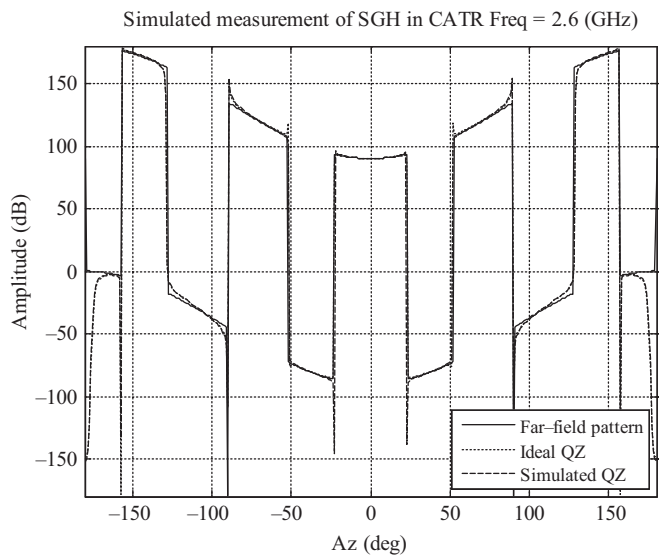

Figure 13.36 Comparison of E_y-polarised QZ amplitude patterns with AUT at the bottom of QZ

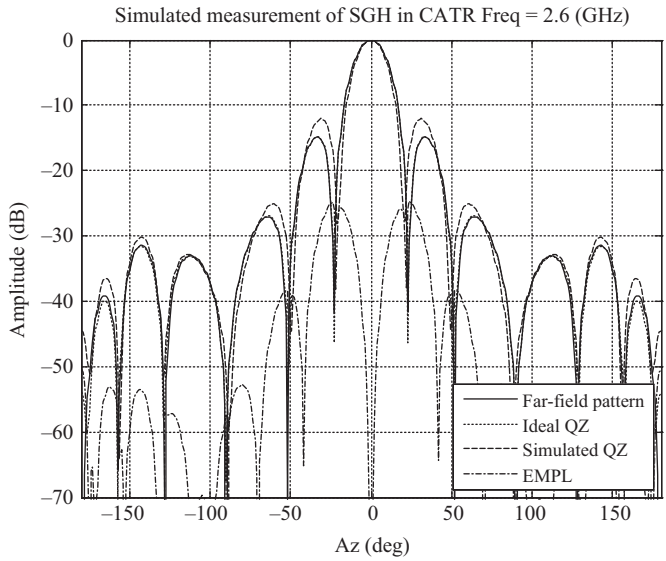

Figure 13.37 Comparison of E_x-polarised QZ amplitude patterns with AUT at the vertex of the reflector – outside of QZ

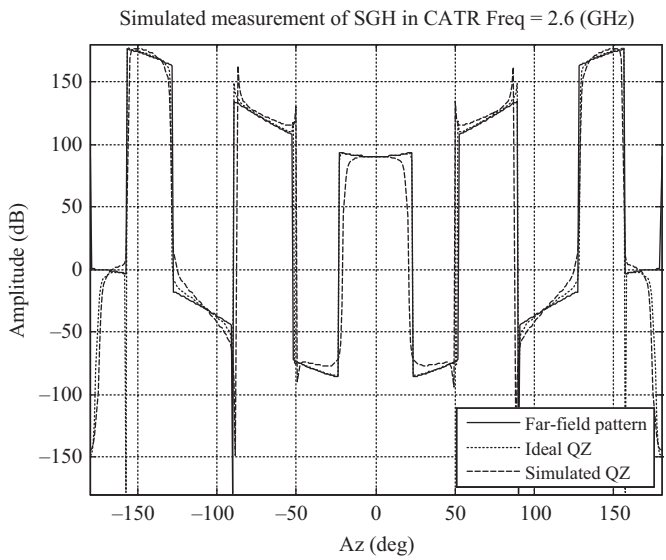

Figure 13.38 Comparison of E_y-polarised QZ amplitude patterns with AUT at the vertex of the reflector – outside of QZ

the low level of the equivalent multipath level (EMPL) trace, shown as a dash-dotted line. The EMPL is a quantitative objective measure of the adjacency between two patterns with a better agreement being denoted with increasing large negative dB values. Here, the peak EMPL between the ideal and simulated measured far-field pattern is circa −48 dB. Indeed, the EMPL is a valuable measure of similarity as the agreement between the respective traces is so good that differences are difficult to assess otherwise. When the AUT is translated to the lower edge of the CATR QZ, it can be seen that the degree of agreement slightly degrades as the EMPL level, as shown in Figure 13.35, increases by circa 2 dB. However, once the AUT is translated so as to be situated level with the vertex of the reflector, i.e. outside of the classical QZ region, it is clear that from inspection of Figure 13.37 that the simulated CATR measurement is grossly distorted with significant differences becoming apparent and the peak EMPL level increasing to circa −26 dB. This is to be expected and is further confirmation that this new CATR measurement simulation is producing reliable results.

Crucially, the CATR simulation technique is also able to provide phase data. This is a crucial feature of the very general simulation technique as in principle the simulated data may be needed to examine and verify additional post-processing techniques, as discussed below. Thus, in addition to being able to provide conventional CATR QZ performance predictors such as amplitude taper, amplitude and phase peak-to-peak ripple, within this section we have shown that it is also possible to provide full-sphere simulated measured data for a given CATR AUT combination.

13.2.10 Effect of amplitude taper, amplitude ripple and phase ripple on CATR measurements

As noted above, the CATR specification of QZ field amplitude taper of 1 dB and ripple as being less than ±0.5 dB in amplitude and ±5° in phase was determined mainly from a heuristic viewpoint. The simulation technique described in Section 13.2.9 provides a means for examining the effects of these specifications in detail thereby allowing the correlation of CATR QZ performance specifications with far-field AUT measurement uncertainties. The method for establishing this is the topic for the remainder of this section.

As noted above the coupling of the pseudo-plane wave into the aperture of an AUT creates the classical measured 'far-field' radiation pattern. Assuming the electric and magnetic fields radiated by a given antenna over the convenient enclosing surface are known then, it is possible to create a perfect plane wave and to use that to 'measure' the far-field pattern at a specific far-field direction be evaluating the reaction integral between the plane wave and the AUT. Clearly, the electric and magnetic fields of a perfect x-polarised plane wave propagating in the positive z-direction can be expressed as

$$\underline{E}(x,y,z) = A(x,y)e^{-jk_0 z}\underline{\hat{e}}_x \tag{13.48}$$

Here, we have assumed a positive, suppressed, time dependency, A is the complex wave amplitude and k_0 is the free-space propagation constant. Thus, we

can create a plane wave with amplitude taper, amplitude ripple and phase ripple of our choosing using, for example,

$$A(x,y) = \sin\left(\frac{n_x \pi x}{L_x}\right)\sin\left(\frac{n_y \pi y}{L_y}\right) \tag{13.49}$$

Here, n_x, n_y denote the number of ripples in the x- and y-axes across the QZ, respectively, and L_x, L_y denote the width of the CATR QZ in the x- and y-axes. Similar expressions can be used to perturb the phase function. The corresponding magnetic fields can be obtained from the TEM condition specifically

$$\underline{H}\,(x,y,z) = \frac{1}{Z_0}\widehat{\underline{u}} \times \underline{E}\,(x,y,z) \tag{13.50}$$

Here, Z_0 is the characteristic impedance of free space. Thus, with the use of the plane-wave equations, we are able to create a plane wave with amplitude taper, amplitude ripple and phase ripple of our choosing using the definitions set out above. For the simulations presented, the case of a simulated WR90 pyramidal horn AUT was utilised. Here, the pyramidal horn had an aperture dimension of width 0.144 m and height 0.194 m with a horn length of 0.378 m, which is excited by the fundamental TE_{10} mode and radiating at 8 GHz. The near electric and magnetic fields were computed across the surface of an enclosing integrating surface of radius 0.91 m. In the sections that follow, the properties of $A(x, y)$ are specified in terms of the CATR QZ performance parameters defined above across a 1.83 m diameter cylindrical QZ that corresponded to the spherical integrating surface. The following sections examine each of these CATR QZ parameters individually and in each case observe the effect that a variation has on the corresponding 'measured' antenna pattern.

13.2.10.1 Amplitude taper

Figure 13.39 contains a great circle azimuth far-field pattern cut of the simulated pyramidal horn antenna. The dotted trace shows the equivalent simulated 'measured' far-field cut for the case where the illuminating plane wave had an amplitude taper of 0.25 dB. Here, the amplitude ripple was 0 dB, and the phase ripple was 0°. The AUT was offset from the origin of the measurement coordinate system by 0.6096 m thereby insuring that the AUT traversed much of the assumed CATR QZ region. In this case, the ratio of the maximum radial extent of the AUT to the CATR QZ was 75.3%. The impact of increasing or decreasing the utilisation of a CATR QZ is examined in a subsequent section. The agreement between the true model supplied by the ideal far-field pattern and the simulated measurement is very encouraging. The difference level, denoted by the dashed trace, was computed and is not shown as it was below the −60 dB vertical lower limit of the plot. The RMS difference level was computed over the entire great circle cut (and not just across the angular region shown in Figure 13.39) and was found to be −74.75 dB. Figures 13.40–13.42, respectively, present equivalent results for the case of 0.5, 1.0 and 1.5 dB amplitude taper with the RMS difference levels being −68.64, −62.76 and −59.28 dB. Please

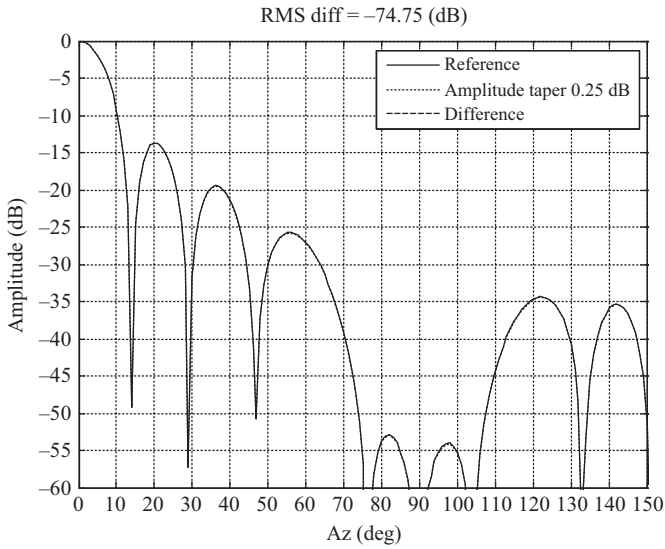

Figure 13.39 0.25 dB amplitude taper across QZ

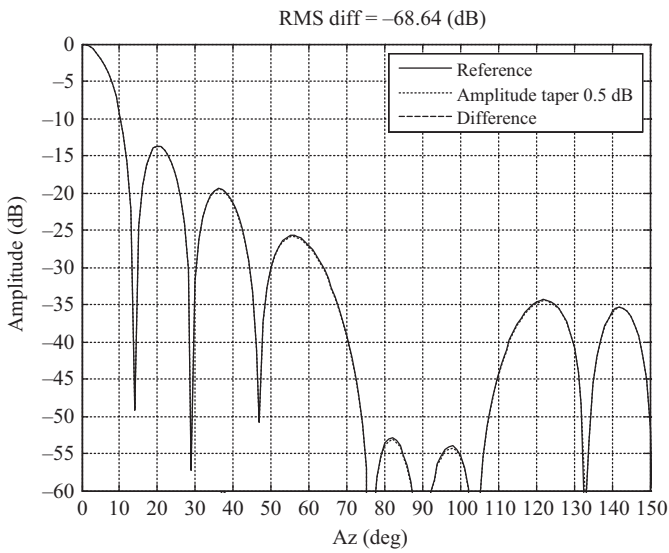

Figure 13.40 0.5 dB amplitude taper across QZ

be aware that for some of these figures the difference levels are sufficiently small that the trace is below the minimum *y*-axis limit.

This is a very interesting result as it is clear that even for the case of a 1.5 dB taper, which is significantly greater than the generally accepted upper bound for

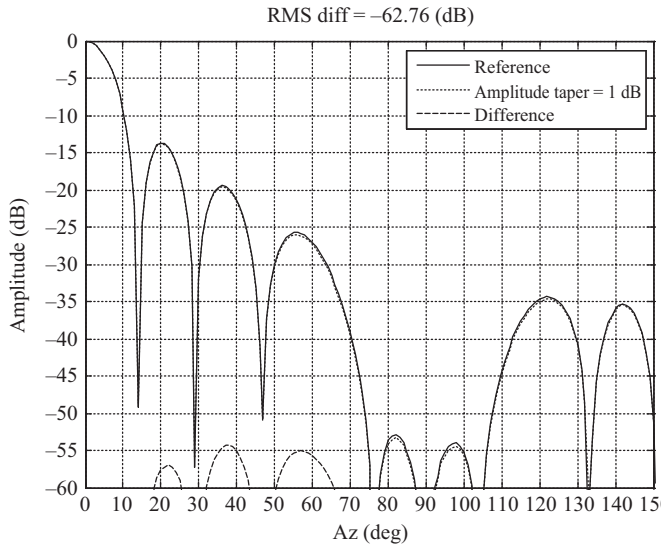

Figure 13.41 1.0 dB amplitude taper across QZ

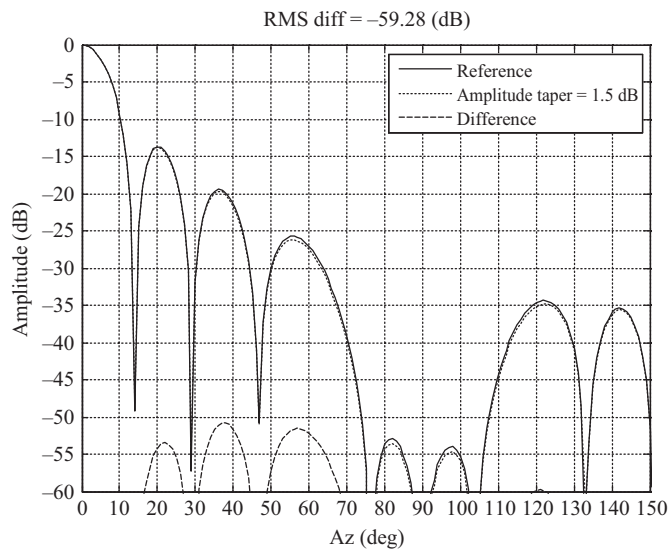

Figure 13.42 1.5 dB amplitude taper across QZ

this parameter, the RMS difference level was well below many of the other typically observed terms within the range uncertainty budget. Furthermore, the differences were mostly evident in the wide-out pattern and back-lobes which can be a region of lesser interest in many commonly encountered applications.

13.2.10.2 Amplitude ripple

The next parameter that can be investigated is amplitude ripple. In this case, the amplitude taper and phase ripple are each set to zero. As with the case of the amplitude taper, the AUT was offset from the origin of the measurement coordinate system by 0.6096 m. Figures 13.43–13.46 contain simulations of far-field 'measurements' with changing amplitude ripple. In addition to the amplitude of the ripple, the spatial frequency of the ripple must be taken into account and this is examined below. However, for the simulations presented here, 5 ripples were assumed across the CATR QZ which is realistic, especially for lower frequency CATR performance. From inspection of these results, it is evident that the amplitude ripple has a far greater impact on the resulting far-field 'measurements' than was the case for the amplitude taper. Here, the RMS difference level, i.e. the RMS value of the dashed trace, was −56.86, −50.68, −44.39 and −37.81 dB for the 0.25, 0.5, 1.0 and 2.0 dB amplitude peak-to-peak ripple cases respectively with the difference levels increasing towards the boresight direction. Here, even for the 1 dB case, the agreement between the ideal pattern and the simulated measurement is good with the differences being most evident in the change in the level of the nulls depth with smaller differences appearing in the side lobe levels.

13.2.10.3 Phase ripple

The last parameter that was investigated was the phase ripple. Here, the amplitude taper and amplitude ripple wereset to zero. Again, the AUT was offset from the origin of the measurement coordinate system by 0.6096 m. The peak-to-peak phase

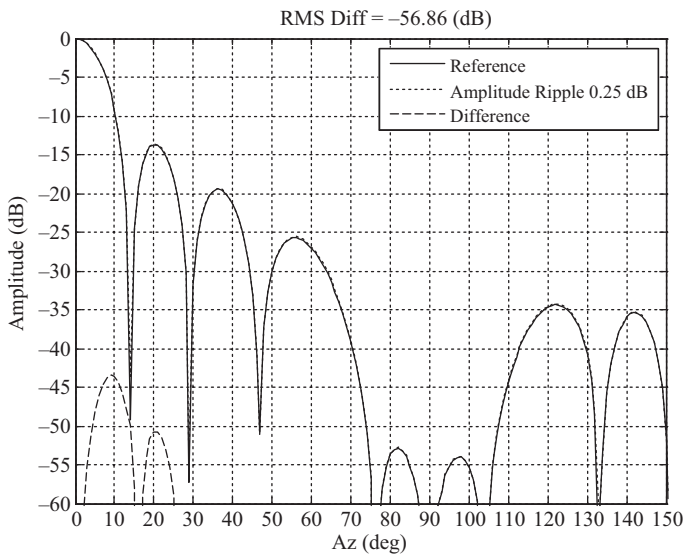

Figure 13.43 0.25 dB peak-to-peak amplitude ripple

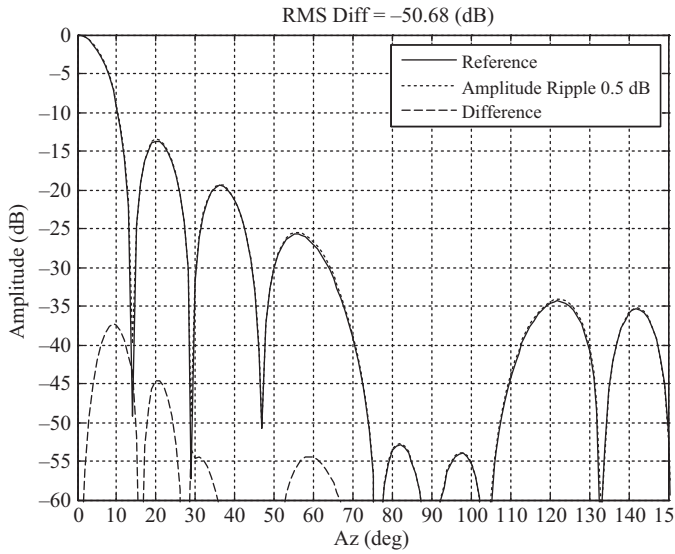

Figure 13.44 0.5 dB peak-to-peak amplitude ripple

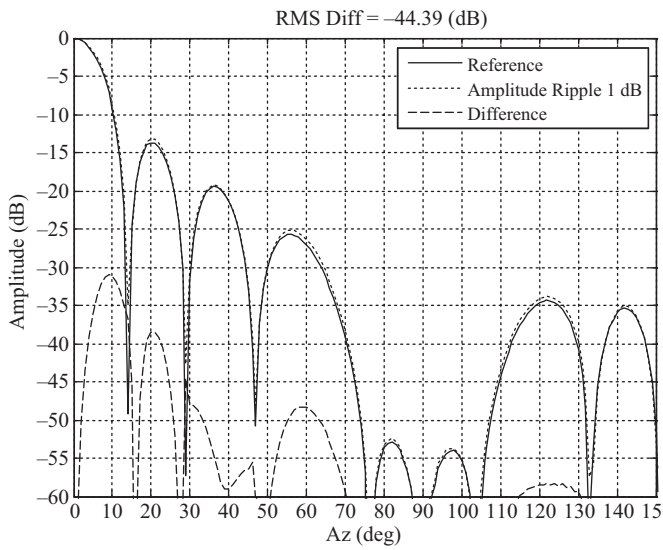

Figure 13.45 1 dB peak-to-peak amplitude ripple

ripple was set to 2.5°, 5.0°, 7.5° and 10.0°, and the simulated 'measurement' results can be found presented, respectively, in Figures 13.47–13.50.

As before, a spatial frequency of 5 wavelengths across the QZ was used in these simulations. As with previous cases, the amplitude difference level can be

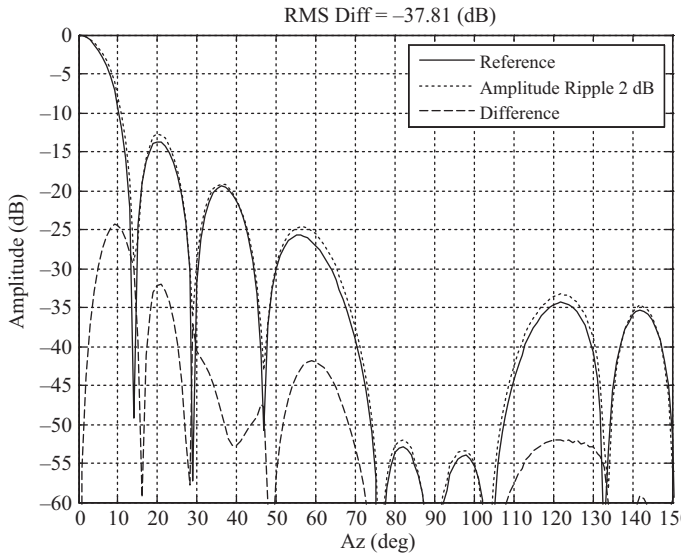

Figure 13.46 2 dB peak-to-peak amplitude ripple

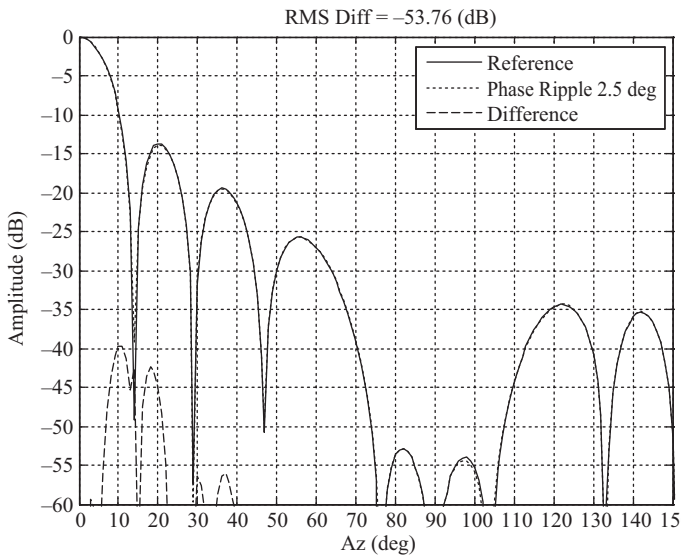

Figure 13.47 2.5° peak-to-peak phase ripple

seen plotted and is denoted by the dashed trace with the RMS difference level also being computed. Here, the RMS difference level was, respectively, −53.76, −47.71, −44.26 and −41.38 dB for the 2.5°, 5.0°, 7.5° and 10.0° peak-to-peak phase ripple cases. As was the case for the amplitude ripple, the greatest

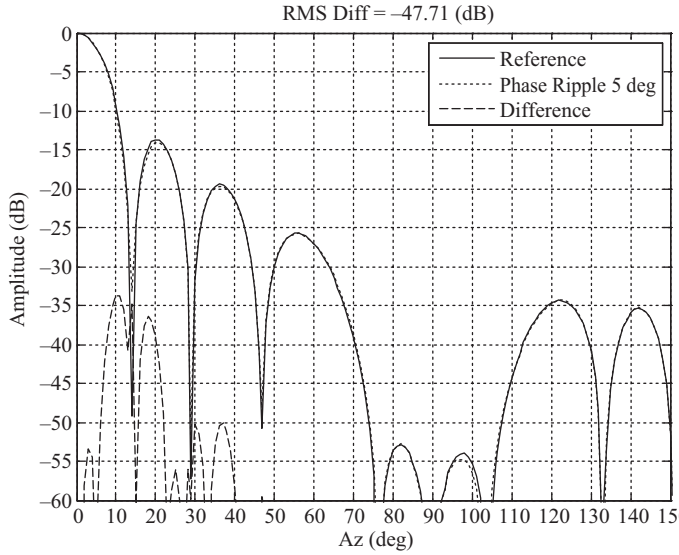

Figure 13.48 5° peak-to-peak phase ripple

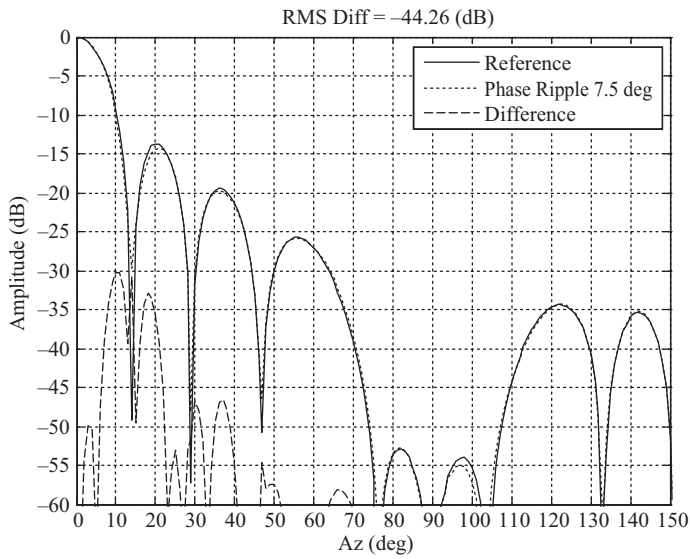

Figure 13.49 7.5° peak-to-peak phase ripple

differences can be seen in the near-in far-field pattern, however, the change in the null depth levels is less pronounced in this case. Otherwise, it is interesting to note that the impact that the phase ripple has on the 'measured' far-field patterns is very comparable with the impact that the amplitude ripple has with the 1 dB

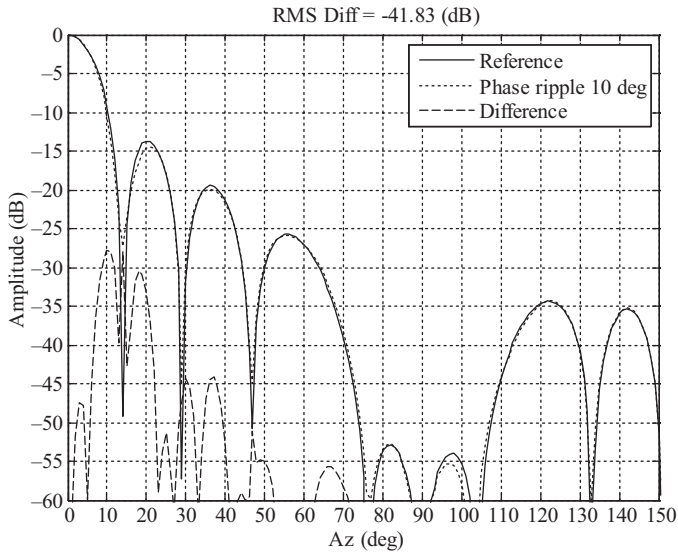

Figure 13.50 10° peak-to-peak phase ripple

ripple and 10° phase ripple both resulting in RMS difference levels of circa −44 and −41 dB, respectively. This agrees with theory as a maximum phase error of 10° or a maximum amplitude error of 1 dB could be produced by the same error level.

13.2.10.4 Spatial frequency of QZ ripple

The previous sections considered the effect of amplitude and phase ripple on resulting far-field measurements. However, no consideration was given to the effect of the spectral content of that ripple. In this section, that question is addressed. Here, simulations were repeated only in this case the spatial wavelength of the ripple was varied and the effect on the resulting 'measured' far-field patterns assessed. Figures 13.51 and 13.52 present the far-field amplitude and phase great circle cut for the case of a 1 dB amplitude taper, a 1 dB amplitude ripple and a 10° phase ripple with a spatial frequency of 5, 10, 20, 30 and 40 wavelengths per CATR QZ diameter. The respective plots have been overlaid with the far-field phase patterns being compensated for the physical offset of the AUT in the measurement coordinate system so that the character of the phase patterns is more clearly discernible.

From inspection of Figure 13.51, it is evident that as the spatial frequency of the ripple increases, the location of the maximum difference between the simulated 'measured' pattern and the reference pattern increases in angle with low spatial frequency ripple having a greater effect in the main beam region. For example, the 20 ripple case had the largest impact on the 20° side lobe. The 5, 10, 20, 30 and 40 ripple cases resulted in a RMS difference level of, respectively, −38.41, −39.82, −40.87, −41.62 and −43.23 dB justifying the use of the 5 ripple case considered

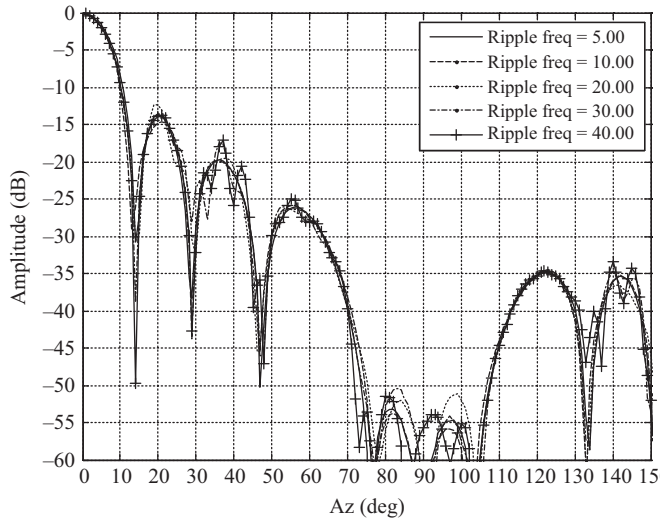

Figure 13.51 Far-field plot of simulated 'measured' amplitude pattern with varying spatial frequency ripple

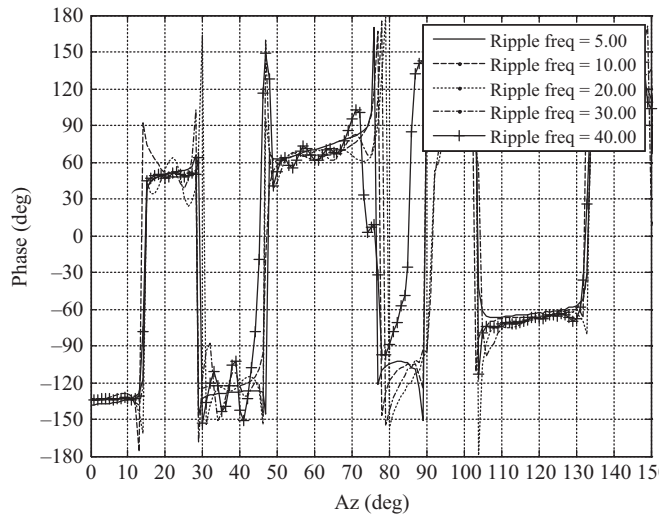

Figure 13.52 10° far-field plot of simulated 'measured' phase pattern with varying spatial frequency of ripple

above as a reasonable worst-case upper bound. In practice, the amplitude and phase ripple of a real CATR will have a far more complex spectral structure than that considered here. However, the purpose of this work was to establish and verify simple design rules and this is sufficient for that purpose.

13.2.10.5 Combined specification and effect of AUT position in CATR QZ

In addition to verifying the effect of the various CATR QZ specifications on the resulting far-field antenna pattern, it is also possible to examine the effect that the position that the AUT has within the CATR QZ has on the accuracy of the ensuing measurement. As before, we can select an upper bound CATR QZ specification of 1 dB amplitude taper, 1 dB amplitude ripple and 10° phase ripple for the case where the AUT is located at the origin of the measurement coordinate system and again when it is offset from the origin by 0.61 m. Thus, Figure 13.53 shows the amplitude pattern for the case where the AUT was located at the origin of the CATR QZ with 5 ripples while Figure 13.54 shows the equivalent case only here the AUT had been offset by 61 cm. It is very evident that the RMS difference level has significantly increased as the AUT traverses across a larger portion of the QZ. Figures 13.55 and 13.56 are equivalent plots only here the case of 10 ripples has been treated with a similar behaviour being evident.

For the case where the AUT is offset by 61 cm we find that for the case where we have a 1 dB amplitude taper, 1 dB amplitude ripple and 10° phase ripple we obtain a RMS difference level of −39.82 dB (Figure 13.56). Thus, if we wish to know the effect that this would have on a −20 dB side lobe we can compute this using the standard formula, cf. Chapter 10, $20\log_{10}(1 + 10\text{^}((-39.82 + 20)/20)) = 0.84$ dB. However, for the case where the AUT is offset by 75 cm so that it traverses much of the QZ, i.e. 91.8% utilisation, we obtain a higher RMS difference level of −38.98 dB. Here, the effect that this would have on a −20 dB side lobe would be $+20\log_{10}(1 + 10\text{^}((-38.98 + 20)/20)) = +0.93$ dB and, $20\log_{10}$

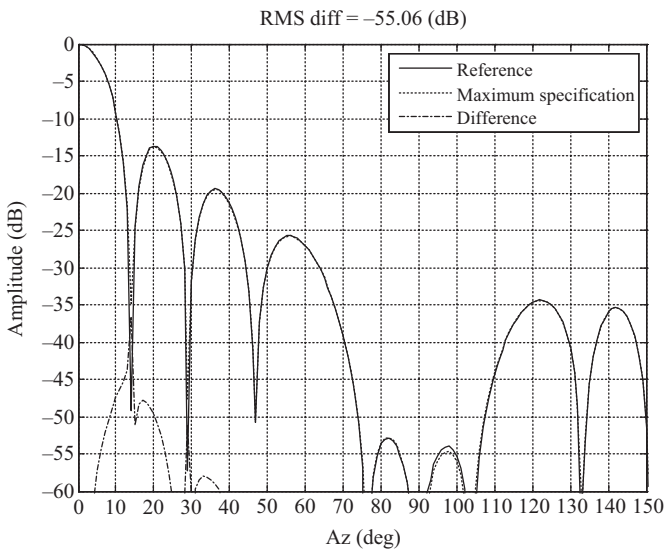

Figure 13.53 AUT at the origin of the measurement coordinate system, 5 ripples

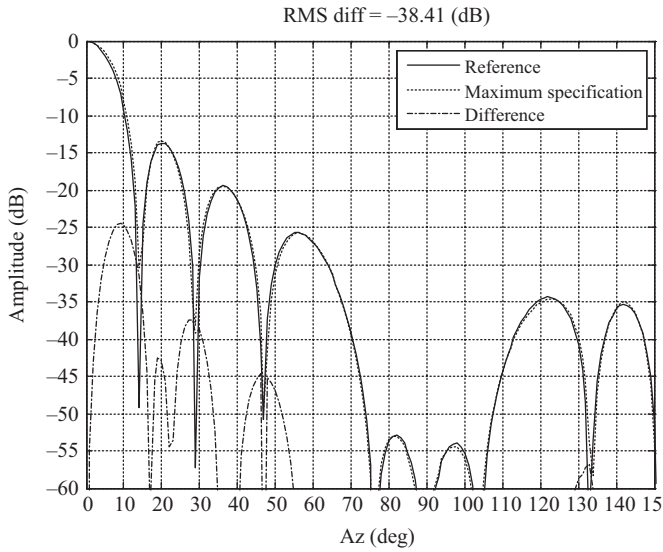

Figure 13.54 AUT offset from the origin of the measurement coordinate system by 61 cm, 5 ripples

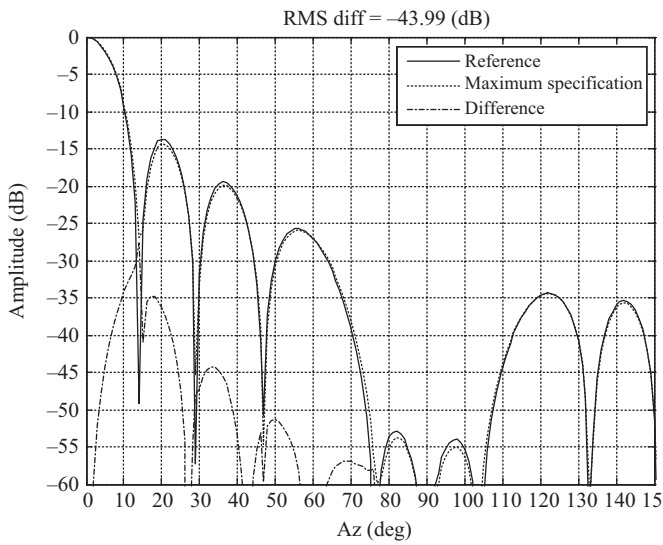

Figure 13.55 AUT at the origin of the measurement coordinate system, 10 ripples

(1 − 10^((−39.82 + 20)/20)) = −1.04 dB. This approximates the ±1 dB value which is the accepted rule of thumb that is often stated (and never derived from theory) that originates from what one typically sees in practice. We can of course change these values subtly by displacing the AUT by a greater or lesser degree and

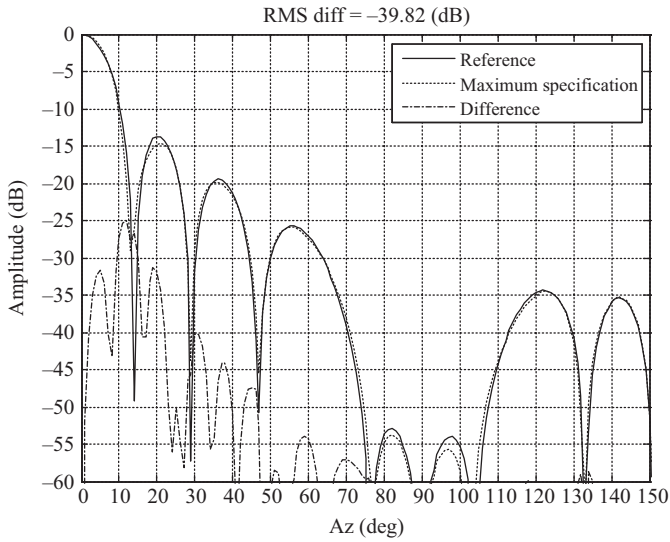

Figure 13.56 AUT offset from the origin of the measurement coordinate system by 61 cm, 10 ripples

by adjusting the spatial frequency of the amplitude and phase ripple as has been illustrated above. However, the results obtained above are largely insensitive to these parameters and are sufficient for the purposes of generally specifying a given CATR.

13.2.11 Use of CATR EM model to verify post-processing and error correction techniques

A flexible range simulation model can, as illustrated in the above sections, prove invaluable when designing a new facility, verifying the impact of a known error on a given measurement or when optimising a planned measurement campaign. However, one of the other applications of this sort of tool is in harnessing it to carefully and precisely verify and validate new or existing post-processing or error correction techniques. This is illustrated in this and the next section when the CATR simulation is used to verify mode filtering-based scattering suppression technique in three areas of application. First, the ability of the measurement and mode filtering technique for attenuating spurious range reflections is verified before its utility for suppressing amplitude and phase ripple in the CATR pseudo-plane wave is examined, and finally, its ability to compensate for the direct illumination of the CATR QZ by the feed is determined.

13.2.11.1 CEM verification of scattering suppression with mode filtering

Once the far-field great circle antenna pattern cut has been acquired and the AUT mathematically translated back to the origin of the measurement coordinate system

by means of a differential phase change, the equivalent cylindrical mode coefficients (CMCs) can be deduced from far electric fields numerically using standard cylindrical near-field theory, cf. Chapter 7. This procedure incorporates a highly efficient algorithm that relies upon an inverse fast Fourier transform (IFFT). These CMCs can then be filtered using a carefully chosen band-pass filter function to remove artefacts that are not associated with the AUT whereupon the processed far-field pattern can be recovered from the reduced set of CMCs using a FFT-based summation procedure.

Utilising the configuration used within the previous sections, Figure 13.57 presents the CMCs as obtained from a simulated CATR measurement of a WR90 pyramidal horn that is shown in Figure 13.58. Here, the aperture of the horn was located at the origin of the measurement coordinate system. The dotted trace shows the equivalent CMCs that were computed from the simulated far-field 'measurement'. The highest order CMC that is associated with the AUT can be computed from the standard cylindrical sampling theorem as frequency and radius of a conceptual cylinder that is centred about the rotation axis and is large enough to enclose the majority of the current sources. The far-field data is sampled sufficiently finely to enable a large number of higher order modes to be computed; however, the finite size of the radiator means that only a subset of these modes is required to accurately represent the radiator explaining the limited span of the black trace, which represents this retained, finite, set of cylindrical modes.

The dotted-trace shown in Figure 13.58 presents the far-field pattern of this ideal measurement and represents the reference pattern, i.e. our 'truth' model. A large amplitude scatterer was then introduced into the measurement simulation. This comprised a plane wave propagating at 30° in azimuth with respect to the

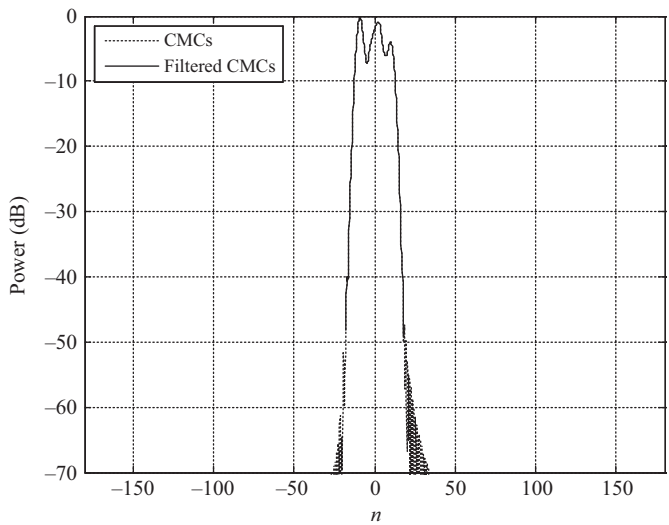

Figure 13.57 Cylindrical mode coefficients for 0 m AUT offset case

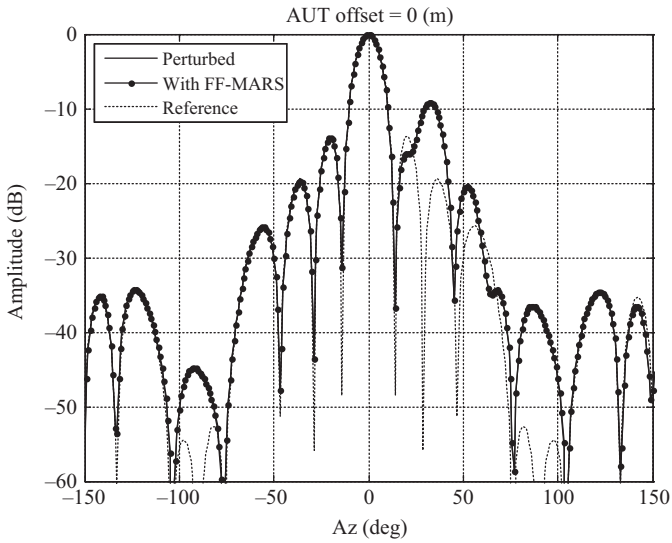

Figure 13.58 Far-field amplitude pattern for 0 m AUT offset case

boresight direction of the range with maximum amplitude that was only 6 dB below that of the CATR pseudo-plane wave. The perturbed simulated measurement in the presence of this spurious signal can be seen plotted in Figure 13.58 as the black-trace. Finally, the black trace with dots represents the processed pattern. Here, the perturbed and processed traces are effectively identical. The absence in AUT offset in this simulated measurement means that the CMCs associated with the AUT and the scatterer are not displaced from one another when transformed to the cylindrical mode domain, as is apparent from inspection of Figure 13.57. Consequently, the band-pass filter that is applied in the mode domain does not attenuate the unwanted scattered fields.

However, Figure 13.60 contains an equivalent simulated measurement only in this case the AUT aperture has been displaced from the origin by 30 cm in the z-axis. When translated back to the origin and transformed to the cylindrical mode domain, as is shown in Figure 13.59, it is clear that there is some degree of separation between the modes associated with the AUT (modes grouped around $n = 0$) and those associated with the scatterer (the emergent group of modes centred around $n = 30$). As before, from standard cylindrical near-field theory, cf. Chapter 7, it is well known that the highest order CMC that can be produced by a radiator when situated at the origin of the measurement coordinate system is $N = k_0 a = 18$ in this case where k_0 is the free space propagation constant and a denotes the radius of the minimum cylinder – as was defined above. Thus any higher order mode can be filtered out without affecting the properties of the underlying AUT irrespective of the complexity of that AUT pattern. Consequently, when filtered and transformed back to the angular domain, there is correspondingly

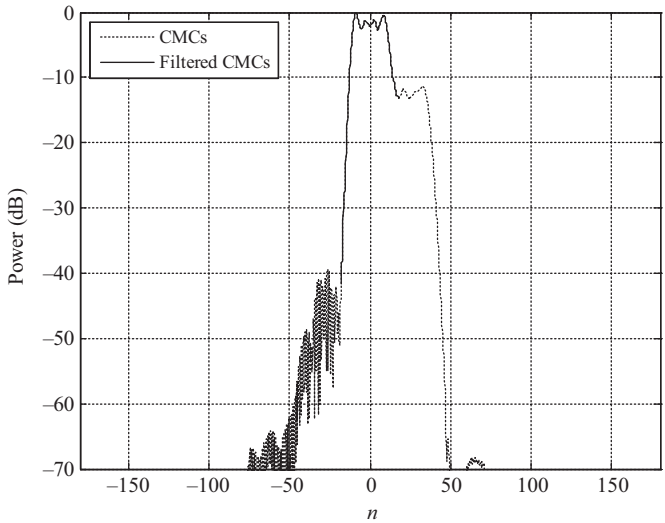

Figure 13.59 Cylindrical mode coefficients for 0.30 m AUT offset case

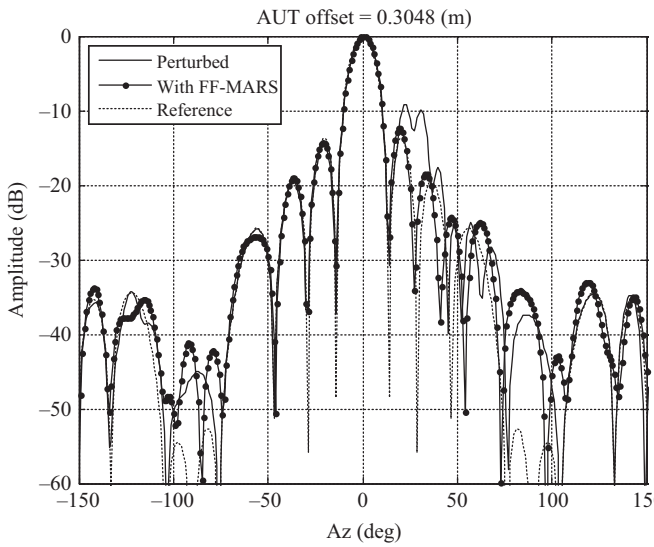

Figure 13.60 Far-field amplitude pattern for 0.30 m AUT offset case

some degree of suppression of the scattered signal. Here in Figure 13.60, it is clear that the processed pattern (solid line with doted markers) is in better agreement with the reference pattern (dotted-trace).

However, as the mode spectra are not completely separated, cf. Figure 13.59, the suppression is not complete. Thus, as the AUT is successively translated away

from the origin of the measurement coordinate system, as the results in Figures 13.61 and 13.63, the degree of mode separation, (i.e. orthogonalisation) increases, as is confirmed by inspection of Figures 13.60 and 13.62. Thus, the spurious scattered signal is attenuated ever more effectively as the displacement is increased until the respective mode spectra do not overlap and are effectively orthogonalised. From inspection of Figure 13.62, it is quite clear that the processing is having a very significant effect on the far-field pattern and is very effectively suppressing the artefacts that are associated with the spurious scatterer as the solid trace with dotted markers (processed pattern) is in very close agreement with dotted (reference) trace. Some small differences are evident in regions of very low field intensity, i.e. for parts of the pattern that are below, for example, –50 dB.

It is also interesting to note how translating the AUT across progressively larger regions of the CATR QZ also increases the general error level of measurement. The predicted CATR pseudo-TEM wave used within these measurement simulations includes amplitude taper stemming from the feed pattern and amplitude and phase ripple primarily emanating from fields diffracting from the knife-edge of the CATR reflector both of which mean that the QZ is of a finite quality and size. Thus, as the AUT is progressively offset from the origin the measurement also occupies a larger and larger region of space placing ever greater demands upon the quality of the CATR QZ. This means that although the effectiveness of the processing increases as the AUT offset is increased, other CATR QZ-related errors increase eventually compromising the measurement technique (Figure 13.64). Although not treated within these simulations, positioner alignment is also known to become more critical as the magnitude of the AUT offset increases. Thus, although it is preferable to offset the AUT by an amount that is equivalent to the

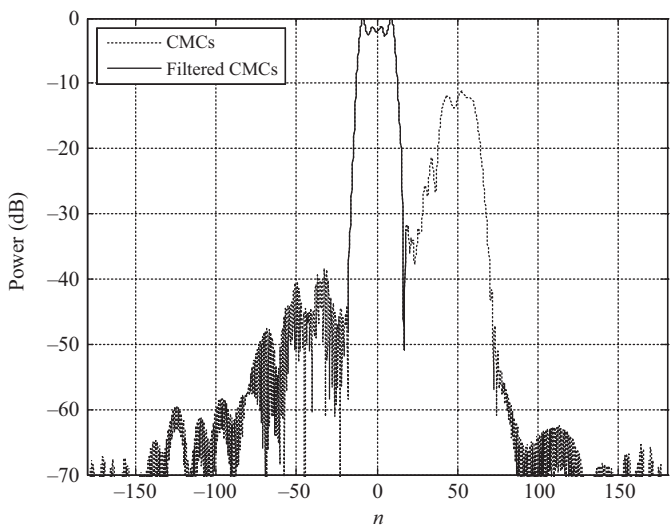

Figure 13.61 Cylindrical mode coefficients for 0.61 m AUT offset case

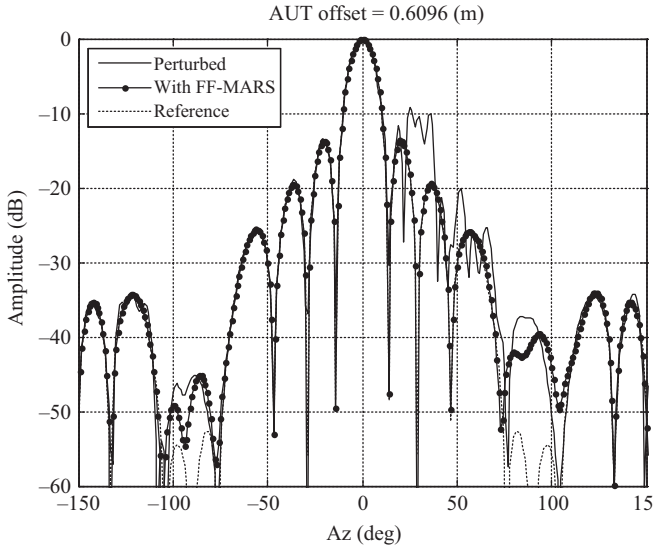

Figure 13.62 Far-field amplitude pattern for 0.61 m AUT offset case

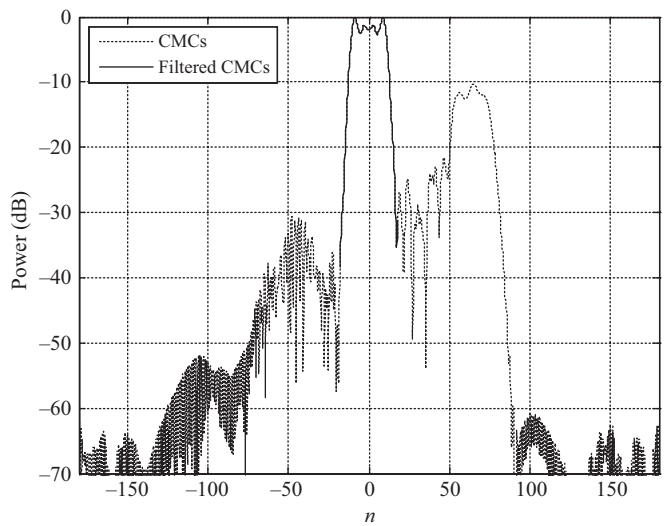

Figure 13.63 Cylindrical mode coefficients for 0.76 m AUT offset case

maximum dimension of the AUT, as this is an engineering compromise between maximising suppression and minimising CATR QZ with larger translations generally being undesirable.

As an additional test, the 0.61 m AUT offset case was reprocessed using a cosine squared window function. This mode filter imposes less of a discontinuity in

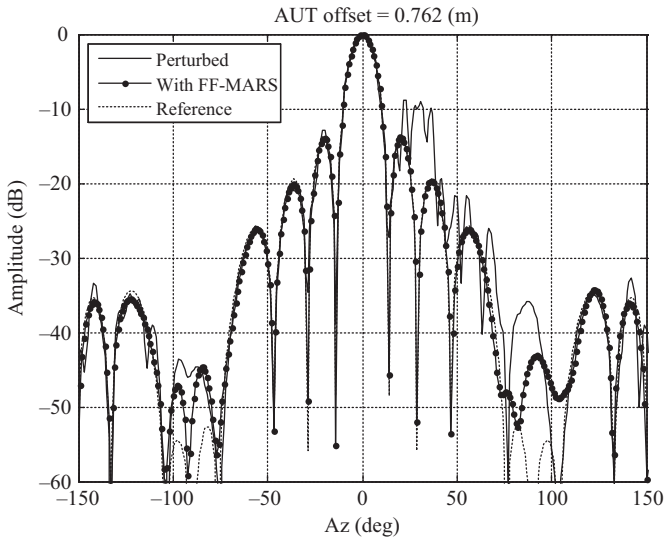

Figure 13.64 Far-field amplitude pattern for 0.76 m AUT offset case

the mode domain than the brick-wall bandpass filter that is often used and has been seen to provide a minor improvement in the filtered far-field patterns.

From the comparison of Figures 13.65 and 13.62, it can be seen that the degree of agreement attained between the reference pattern and the filtered pattern is

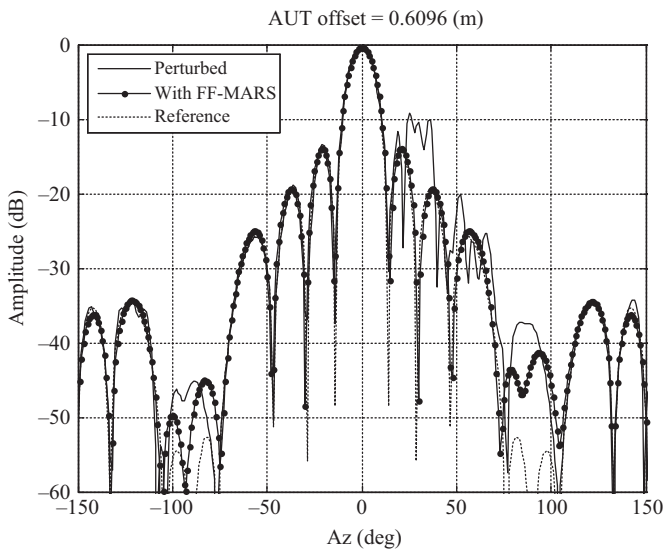

Figure 13.65 Far-field amplitude pattern for 0.61 m AUT offset case with cosine squared CMC window function

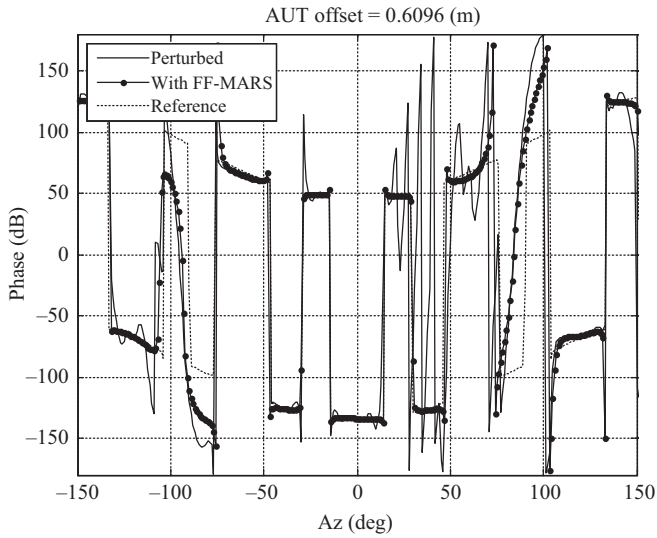

Figure 13.66 Far-field phase pattern for 0.61 m AUT offset case with cosine squared CMC window function

marginally improved, especially for the back-lobes. For the sake of completion, Figure 13.66 presents a comparison of the reference and filtered phase plots. Here, it can be seen that the agreement attained is very encouraging everywhere except the region of low amplitude where it is more difficult to control phase, i.e. in the null region around $\pm 90°$. This sort of very detailed analysis of the performance of a new post-processing technique is possible through experimental means however its undertaking is significantly simplified when the computational analysis is available as is the case here.

13.2.11.2 CEM verification of amplitude and phase ripple suppression with mode filtering

As presented above, the widely accepted criteria for specifying the quality of this pseudo-plane is to insure that the wave should have less than a 1 dB amplitude taper, less than a ± 0.5 dB amplitude ripple and less than a $\pm 5°$ phase ripple. The amplitude taper is largely governed by the pattern of the feed antenna with the amplitude and phase ripple resulting from the edge design of the reflector. Generally, these are properties that are fixed at the time of manufacture with there being relatively little scope for adjusting these effects afterwards. It is possible to select a feed with a different pattern, to add absorbing treatment to the edge of the reflector and in some cases; the reflector has even been extended however these are the exceptions rather than the norm. Within Chapter 5, a number of methods for improving measured CATR patterns were presented. Although this technique was conceived as providing a method for suppressing spurious reflections within

antenna ranges, as discussed above, as edge diffraction effect can be conceptualised as resulting from the presence of additional undesirable current sources, it has been found that this form of mode filtering can be used to further enhance the performance of existing CATRs where the option of extending or reshaping the termination of the reflector is not a viable option.

As was the case in the prior section, here, we shall use the simulation method presented in the previous section to predict the 'measured' far-field antenna pattern for a known antenna assuming a CATR with a defined amplitude ripple and phase ripple. We will then apply the far-field processing to the simulated 'measured' far-fields to identify and then extract the effects of the ripple from the measurement. In order that the effectiveness of the technique could be verified a number of simulations were run, and as before, in each case an *x*-band SG90 pyramidal horn was used as the AUT. This antenna was positioned offset from the origin of the measurement coordinate system by 0.61 m. The electromagnetic six-vector field was computed over the surface of a conceptual integrating sphere with a radius of 0.91 m with a data point spacing of 1° in the θ and ϕ at a frequency of 8 GHz. The CATR pseudo-TEM wave was then fashioned using the methodology set out above with the amplitude and phase ripple being varied for each case. As with the AUT, a spherical sampling surface of 0.91 m radius was used. Five test cases are considered. For these simulations, all parameters were held consistent with the exception of the spatial frequency of the amplitude and phase ripple across the pseudo-plane wave, which was varied from 10 ripples to 50 ripples in increments of 10. The amplitude taper of the pseudo-plane wave was set to 0 dB (i.e. no amplitude taper) as this is not a property that this processing is able to mitigate, however and as was noted above this has a comparatively benign effect on the measurement. These far-field amplitude and phase results are presented in Figures 13.67–13.76 inclusive. Here, the reference, ideal, far-field patterns are denoted with solid lines, the perturbed patterns are denoted with dotted lines and the processed patterns are represented by solid lines with a cross. The difference level is shown on the amplitude plots with a dashed-dotted line.

From inspection of these plots, it is evident that processing is very effectively compensating for the errors in the far-field pattern that are introduced by the ripple in pseudo-plane wave for cases where the spatial frequency is higher. Table 13.5 summarises these results and from inspection of the results shown it is clear that for the cases where the spatial frequency is circa 30 ripples across the 1.8 m CATR QZ or more, then the measurement errors are very effectively being identified and extracted with a circa 20 dB improvement in the RMS difference level being achieved.

Conceptually, amplitude and phase ripple across the pseudo-plane wave can be considered to result from the interference of two, or more, planewave propagating in different directions interfering constructively and destructively across the plane. The larger the angle between the directions of propagation of these waves, the higher the spatial frequency of the ripple in resulting interference pattern. When the direction of the arrival of these plane waves is close to that of the ideal pseudo-plane wave, it is going to be very difficult for the processing to extract the

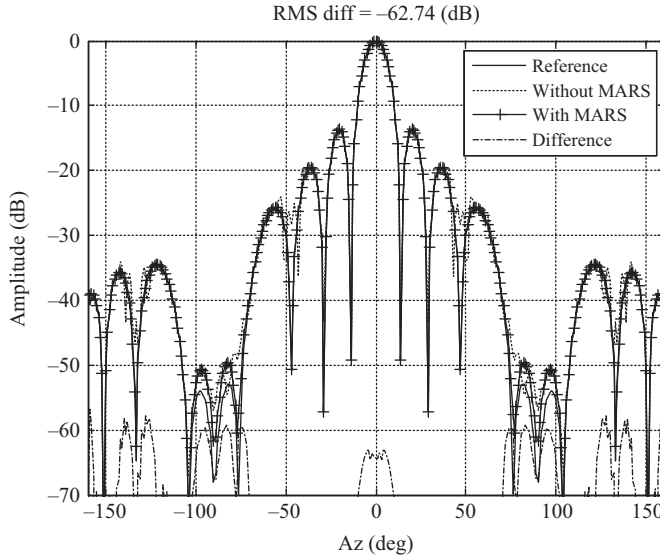

Figure 13.67 FF amplitude plot for 50 ripples across QZ

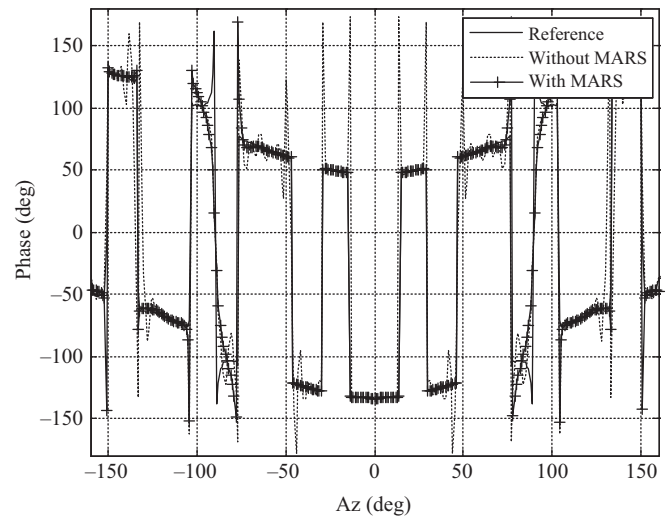

Figure 13.68 FF phase plot for 50 ripples across QZ

undesired wave. However, when the direction of arrival is larger, and the spatial frequency of the interference pattern is higher, this wave can be far more easily differentiated from the ideal pseudo-plane wave when viewed in the mode domain.

In order that this could more easily examined, the CMCs plots are presented in Figures 13.77–13.81 inclusive and which correspond to the 50, 40, 20, 20 and 10

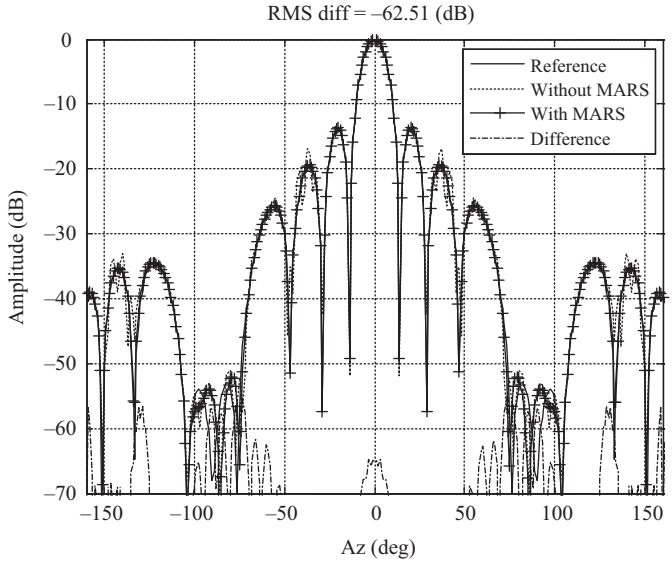

Figure 13.69 FF amplitude plot for 40 ripples across QZ

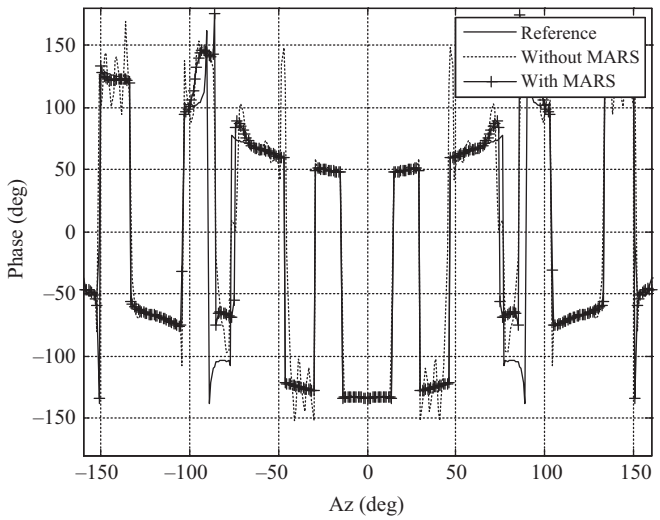

Figure 13.70 FF phase plot for 40 ripples across QZ

ripple cases, respectively. Here, the dotted trace represents the CMCs that are computed from the far-field pattern data once the AUT has been translated back to the origin of the measurement coordinate system. The solid trace represents those CMCs that, by virtue of the cylindrical sampling theorem, correspond to the AUT alone.

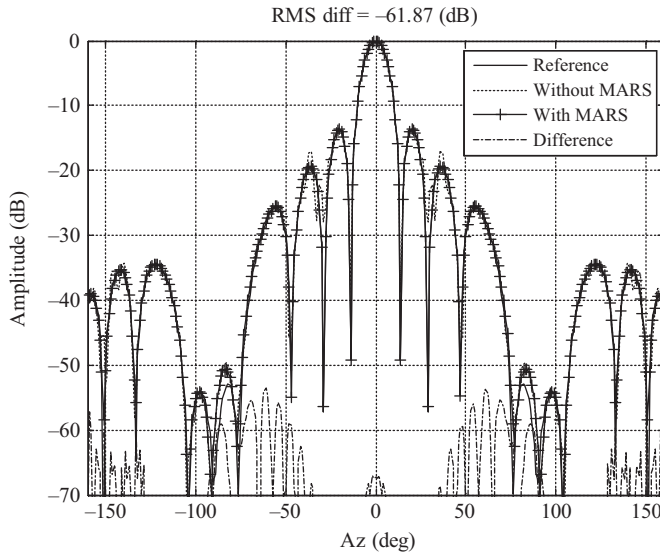

Figure 13.71 FF amplitude plot for 30 ripples across QZ

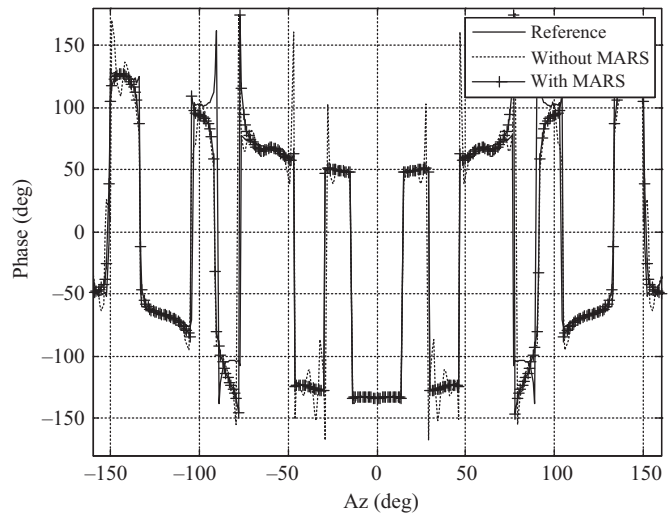

Figure 13.72 FF phase plot for 30 ripples across QZ

Here, and as was developed within Chapter 7, CMC are complex numbers that are functions of frequency, where the polarisation index, and the azimuthal index which do not vary with any of the scanning coordinates. The cylindrical mode cut-off is determined by evaluating when $|n| \leq \text{ceil}(k_0 r_{t0}) + n_s$, where n is the highest

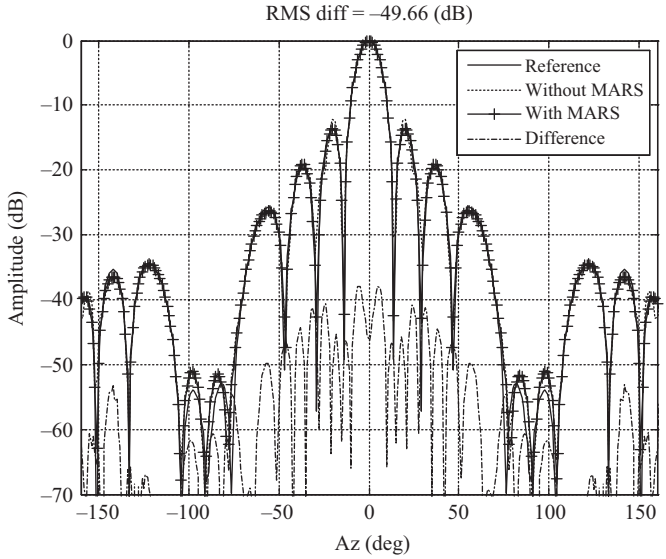

Figure 13.73 FF amplitude plot for 20 ripples across QZ

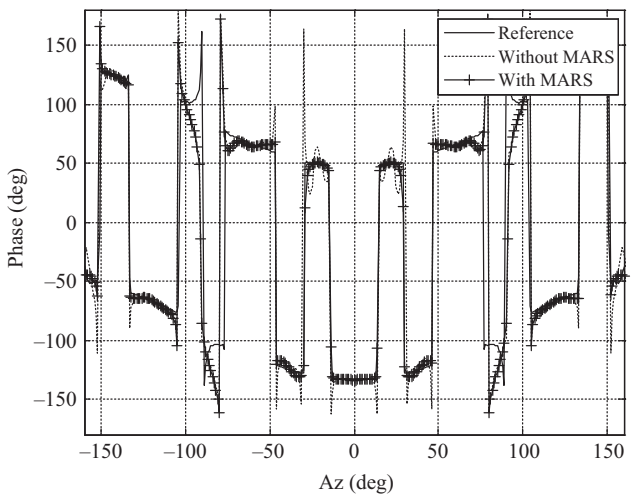

Figure 13.74 FF phase plot for 20 ripples across QZ

order cylindrical mode index associated with the AUT. Here, r_{t0} denotes the maximum radial extent (MRE), k_0 is the free space propagation number, n_s is a positive integer that is used as a safety margin that depends upon the accuracy required and ceil is a function that rounds towards positive infinity. The MRE is the

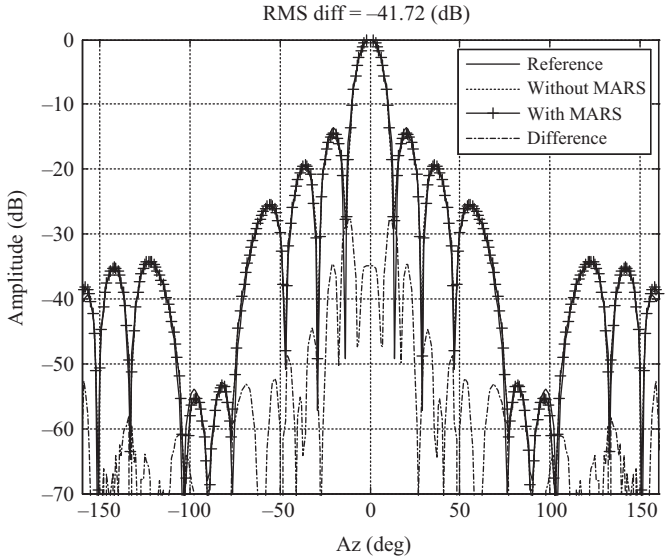

Figure 13.75 FF amplitude plot for 10 ripples across QZ

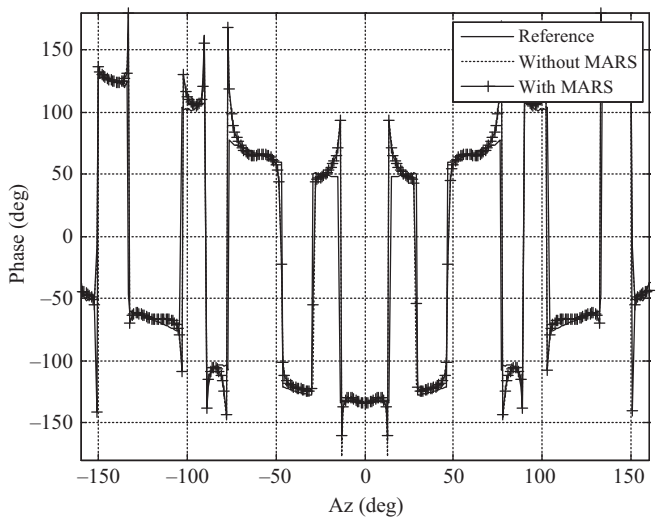

Figure 13.76 FF phase plot for 10 ripples across QZ

radius of a conceptual cylinder that is centred about the origin of the measurement coordinate system that is large enough to circumscribe the majority of the current sources in the AUT, cf. Chapters 7 and 8. Thus, by knowing the physical size of the AUT, the frequency then it is possible to set the limit of the band-pass mode filter

Table 13.5 Summary of results showing improvement provided by FF-MARS processing as CATR QZ ripple spatial frequency changes

No. of ripples across QZ	RMS diff without (dB)	RMS diff with (dB)	FF-MARS change (dB)
50	−42.8	−62.7	19.9
40	−42.8	−62.5	19.7
30	−41.3	−61.9	20.5
20	−40.8	−49.7	8.9
10	−39.8	−41.7	1.9

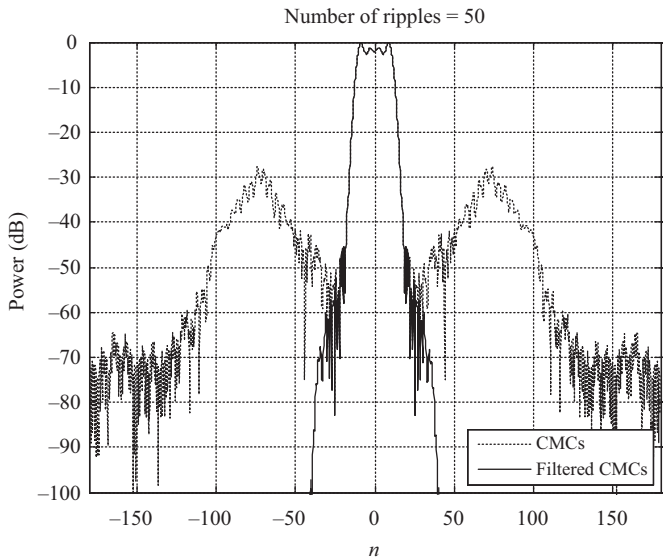

Figure 13.77 CMC plot for 50 ripple cases

function. Here, a $\cos^2$ mode filter function is used so as to match as many derivatives of the windowing function to zero as possible as this is known to improve the phase results of the resulting processed far-field pattern.

From inspection of these figures, i.e. Figures 13.77–13.81 inclusive, it is clear that as the spatial frequency of the ripple on the CATR pseudo-plane wave increases, so too does the amount of power present in the higher order modes of the cylindrical mode expansion, cf. Figure 13.77. Conversely, as the spatial frequency decreases those modes associated with the ripple gradually shift to lower order mode coefficients and increasingly coexist with those modes associated with the AUT rendering their extraction through mode filtering ineffectual, cf. Figure 13.81. However, as the spatial frequency of the ripple increases, corresponding conceptually to incoming waves at wider angles of incidence, the mode spectra shift

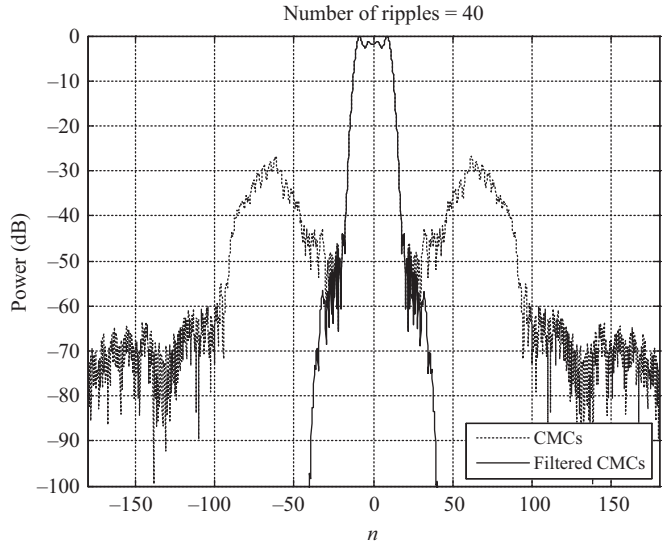

Figure 13.78 CMC plot for 40 ripple cases

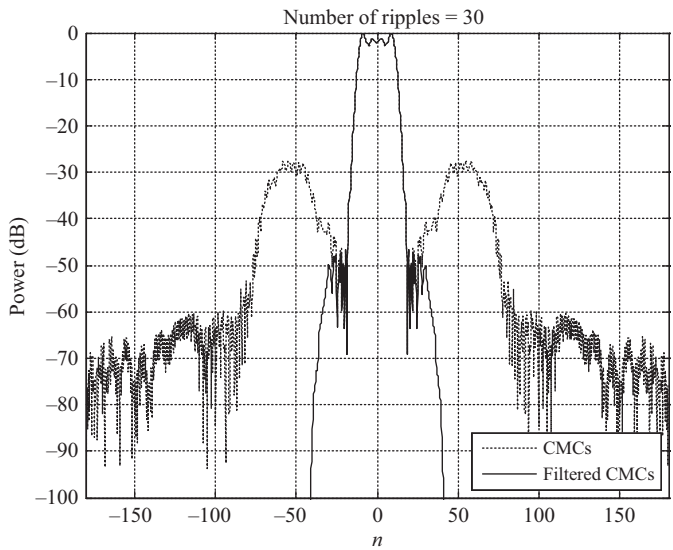

Figure 13.79 CMC plot for 30 ripple cases

towards higher order mode spectra whereupon they can be extracted with the application of a band-pass mode filter.

This section has presented a method for suppressing the effects of imperfections within the uniformity of the pseudo-plane wave through post-processing of

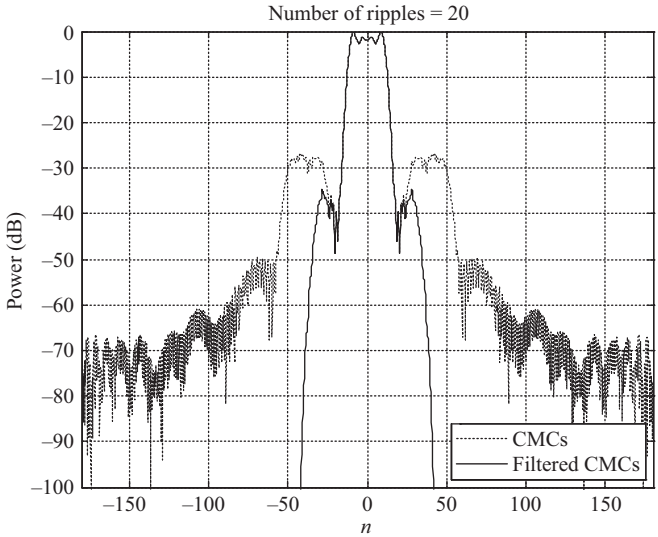

Figure 13.80 CMC plot for 20 ripple cases

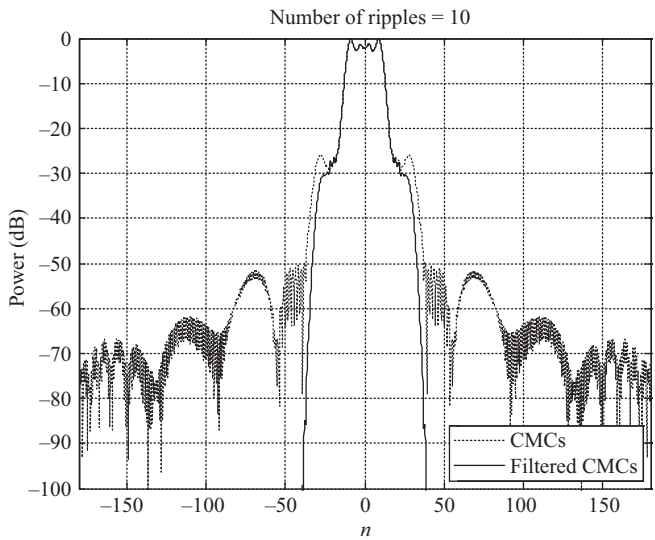

Figure 13.81 CMC plot for 10 ripple cases

measured antenna pattern data using a mode filtering-based algorithm. The price of this correction method is that the AUT must be offset from the origin of the measurement coordinate system meaning that the antenna will traverse across a larger portion of the CATR QZ however as the amplitude and phase ripple in the CATR

pseudo-plane wave are being suppressed and, as was shown above, as the amplitude taper is a relatively benign second-order effect, then providing the CATR is sufficiently large to accommodate the AUT then this provides a very feasible method for improving the accuracy of measurements taken within a given facility.

13.2.12 CEM verification of scattering suppression and feed spill-over with mode filtering

Direct illumination of the CATR QZ is usually minimised through the use of absorber collars on the feed and/or baffles positioned within the chamber, cf. Chapter 5. However, feed spillover effects are seen, to some extent, in many ranges with the widely employed offset reflector configuration and low gain feed making this to some extent almost unavoidable with dual reflector CATRs being perhaps the most susceptible designs. Typically, CATR QZ field probing involves using a planar near-field scanning system, cf. Chapter 6, to measure the horizontal and vertically polarised components of the electric field across a plane that is transverse to the boresight, i.e. *z*-axis, of the range. It can be seen that the *x*- and *y*-polarised components of the field radiated by the feed in the CATR QZ are generally comparatively small (e.g. 40 dB down) when compared to the pseudo-plane wave formed by reflection from the reflector itself. However, the *z*-polarised component of the field radiated by the feed-in CATR QZ, which in practice is not normally characterised during range commissioning or validation activities can be significant and in this case was circa 15–20 dB *greater* than the longitudinal component of the pseudo-plane wave, thereby dominating this polarisation. Figure 13.82 shows the amplitude of the *z*-polarised electric field radiated by the feed in the CATR QZ where the levels have been plotted normalised relative to the peak of the pseudo-plane wave, i.e. the E_x component in this case. Crucially, it is the entire electromagnetic six-vector of the pseudo-plane wave formed by the CATR that couples into the aperture of the test antenna that produces the measured far-field antenna pattern function. As developed above, the actual coupling can be determined using the reaction integral which is based upon a reciprocity relationship. This suggests that on boresight feed spillover related effects could be comparatively small. However, as the AUT is rotated so that its aperture plane aligns more closely with the *z*-axis of the range then the coupled power can increase meaning that feed spillover effects become more pronounced on the wideout antenna pattern function.

The existing QMUL CATR EM model, as presented above, was used to compute the fields radiated by the CATR at 8 GHz with and without direct illumination of the QZ by the feed. The coupling of these fields into the AUT was then obtained from a numerical evaluation of the reaction integral, which produced a simulated CATR measurement. As before the AUT was offset from the origin of the measurement coordinate system by an amount that was larger than the maximum dimension of the AUT and in this case a 0.61 m displacement in the *z*-axis was used which is at a normal to the aperture plane of the AUT which is also orthogonal to the vertical azimuth rotation axis of the CATR. Figures 13.83 and 13.84 present azimuth and elevation far-field AUT patterns.

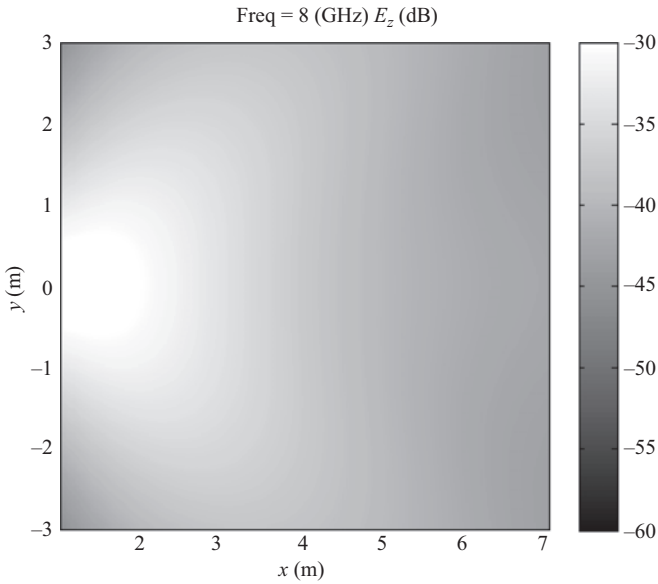

Figure 13.82 Longitudinal component of field radiated by feed-in CATR QZ plotted across a plane transverse to the range boresight

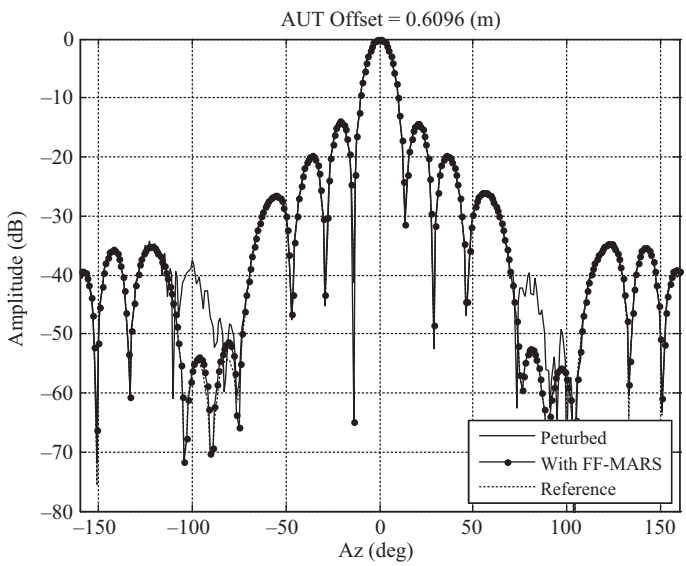

Figure 13.83 Far-field azimuth cut showing feed spill-over and its suppression with MARS processing

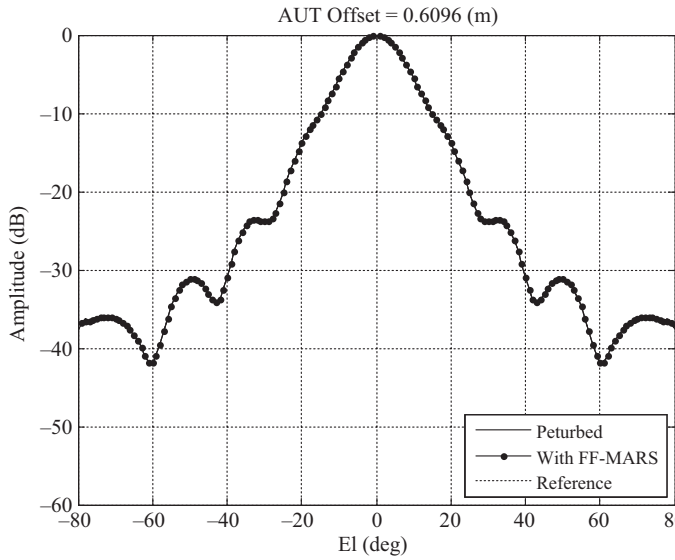

Figure 13.84 Far-field elevation cut showing very little effect arising from feed spill-over

Here, the dotted trace denotes the reference ideal far-field patterns which are shown plotted against the perturbed simulated 'measured' fields which are denoted by the black traces. As expected, these differ most significantly in the region of the wide-out antenna side lobes. Standard mode filtering processing was again used to suppress the effects of the feed spill-over with the results of the processing being denoted with the solid trace with dotted markers. As expected feed spill-over had the largest impact in the horizontal plane as this is the plane in which the feed was offset. From inspection of Figure 13.83, it is clear that the processing has significantly reduced the effect of the feed spill-over (by circa 15 dB around $\pm 90^{\circ}$) with the reference and processed patterns yielding very good agreement with the ideal reference pattern. This illustrates effectively that the mode filtering is capable of suppressing CATR feed spill-over, which can be a major issue particularly in dual reflector CATRs.

13.2.12.1 Summary

The PO-based CATR simulation techniques presented herein, particularly the CE-based method, provides a highly accurate, computationally efficient, simulation tool for the design and evaluation of offset serrated reflector CATRs. The method outlined is sufficiently general to allow the incorporation of measured or modelled feeds, reflector surface deformations, generic serration designs, and enables the simulation of CATRs varying in physical size from a few centimetres to many metres across and operating from a few GHz to mm-wave frequencies.

13.3 Full-wave three-dimensional CEM simulations

The development of general-purpose purpose tools for the simulation of a near-field measurement is of interest for several reasons. It can enable one to plan and optimise a measurement campaign *a priori*, to verify correction algorithms, new transform algorithms, post-processing, etc., and can be used to assess error terms within the range uncertainty budget. The problem is, however, that these are rather large electrical problems, and even larger if one also considers the test chamber. However, there are some electrically smaller problems that are tractable and these can be used to distil more information on the subtler nature of near-field measurements. Some of the more important cases are considered in the following sections.

13.3.1 Full-wave simulation of a PNF measurement z-cut

As described above, a full-wave three-dimensional CEM solver can be used to simulate a general antenna measurement. Here, a method of moments-based commercially available tool was used to simulate the measurement of an *x*-band standard gain horn by an *x*-band open-ended rectangular waveguide probe. Here, to simplify the simulation no absorber collar was used on the probe or the SGH however that can in principle be included if more accurate simulations are required. The absorber was omitted so as to be able to keep the simulation times to reasonable limits. The difficulty associated with simulating a near-field measurement involving acquisitions taken over two-dimensional surfaces is that a new simulation must be run for every position of the probe. This means that an $n \times m$ point measurement would take $2 \times n \times m$ individual simulations for a single frequency if dual polarised acquisitions were needed, which is generally the case. For the configuration treated here, namely, that of a one-dimensional *z*-axis cut the number of simulations is far more manageable – although not inconsiderable if a reasonably fine resolution is required, especially when the AUT and probe are close and within the reactive near-zone.

For the configuration illustrated in Figure 13.85, the frequency domain finite element full-wave solver was used to compute the forward transmission scattering coefficient, S_{21} for the SG90 (aperture size 14.4 cm by 19.4 cm) and OEWG90 combination between a port within the waveguide section of each antenna. The amplitude and phase of the S_{21} transmission coefficient are presented in Figures 13.86 and 13.87, where here the AUT-to-probe separation (z) runs from 0.0 to 1.0 m.

For the case of the very near-field, i.e. when $z \leq \lambda$, the field is greatly dominated by the reactive near-fields that, in the absence of a probe into which to couple, would not propagate away from the AUT and would remain stored. Here, however, for the case when the rectangular waveguide probe is in close proximity to the SGH those stored fields can couple into the probe producing the result shown here. Outside of this reactive near-field, the fields behave more predictably with the field on boresight reaching maximum field intensity. This is an important, and very real effect, which imposes a limit on the power handling requirements when performing high power testing in the near-field, and particularly when performing planar near-field testing

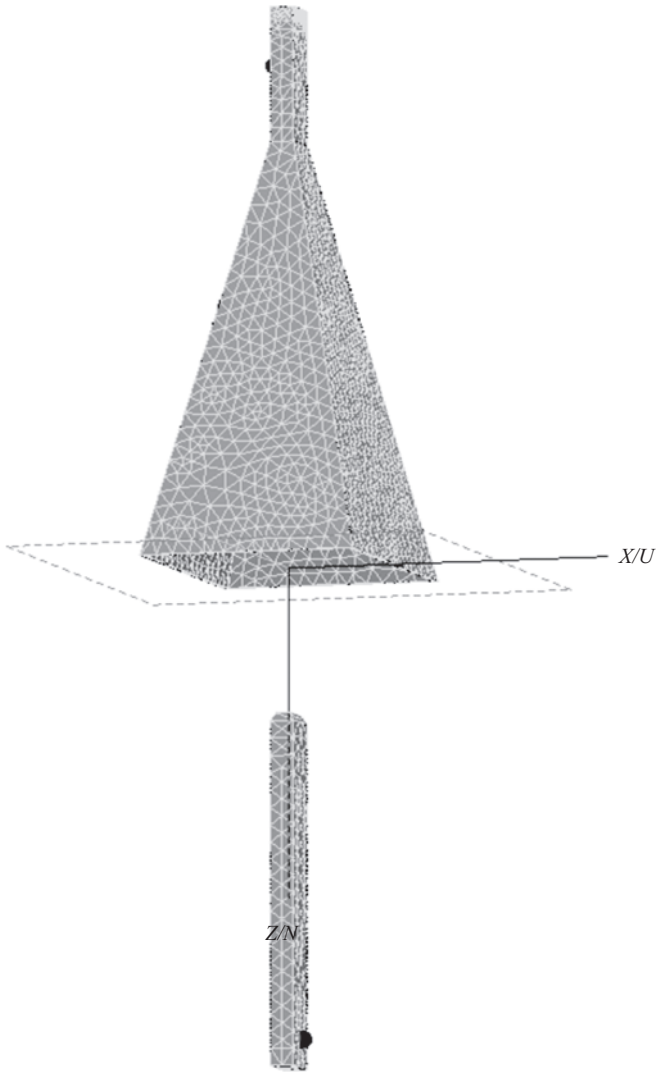

Figure 13.85 Model shown at the 10 cm separation between the probe and the SGH

when the probe is likely to come into closer proximity to the AUT. Around this region, the ripple that is evident is a result of multiple reflections between the AUT and the probe that can often contribute to uncertainties in gain measurements, and as expected the amplitude of this ripple decreases with increased separation. This is the reason why increasing the AUT-to-probe separation generally helps to reduce the uncertainty in a gain measurement. Further out, and in the limit as the far-field

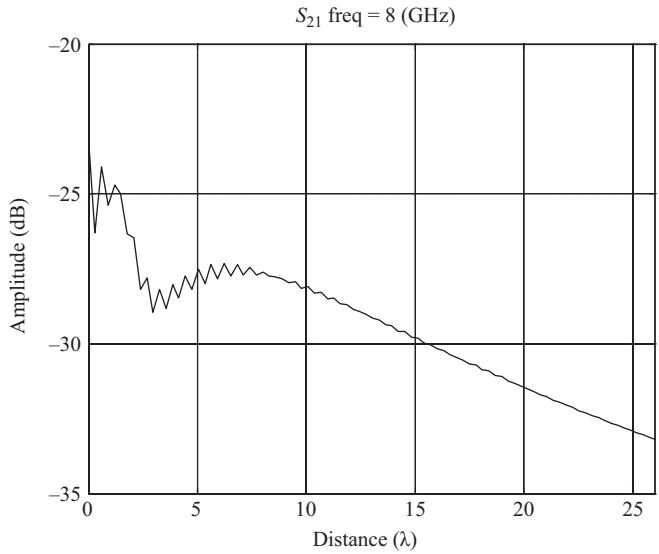

Figure 13.86 Magnitude of coupling between probe and SGH plotted on boresight as a z-cut

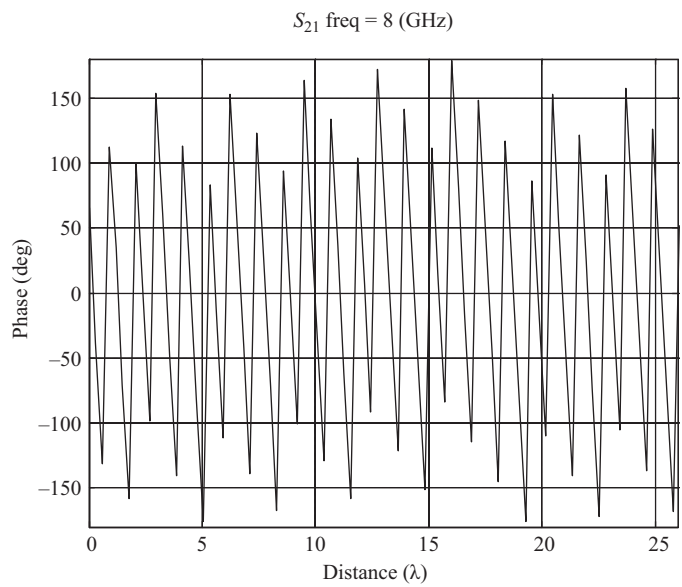

Figure 13.87 Phase of the coupling between probe and SGH plotted on boresight as a z-cut

condition becomes an increasingly good approximation, the trace approaches the form of

$$\lim_{R\to\infty}(|S_{21}|) = \frac{P_R}{P_T} = \left(\frac{\lambda}{4\pi R}\right)^2 G_T G_R \tag{13.51}$$

Thus, this formula can be used when performing link budget calculations providing the AUT to probe separation is reasonably large, as is often the case when for spherical testing. The positive assumed time dependency is evident in Figure 13.87 as the phase function becomes progressively more negative as the physical separation between the AUT and the probe increases.

13.3.2 Full-wave simulation of a PNF measurement xy-scan

In this section, the results of a conventional *xy*-plane rectilinear near-field acquisition are considered and are illustrated schematically in Figure 13.88. As was the

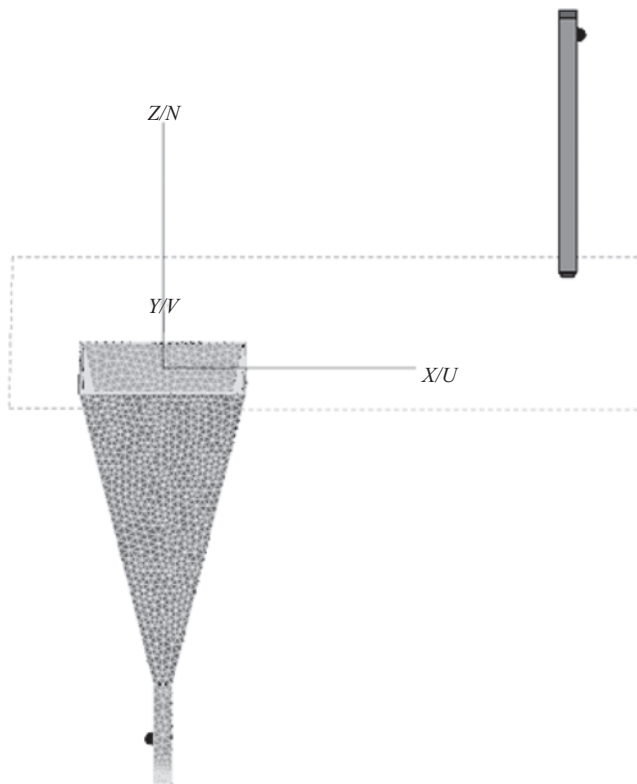

Figure 13.88 Planar-near-field measurement model shown with a 10 cm separation in the z-axis between the probe and the SGH with an offset in the xy position

case in the previous section, a frequency domain moment method-based proprietary full-wave three-dimensional EM solver was used to simulate the measurement of an *x*-band (WR90) pyramidal horn by an *x*-band WR90 rectangular waveguide probe testing at 8.2 GHz. One complete full-wave EM simulation is required per point within the simulated plane rectilinear acquisition meaning that in this case, assuming half-wavelength sample spacing, required $31 \times 31 = 961$ individual S_{21} simulations – and this assumed the use of symmetry to minimise the computational effort. As before, this number is doubled for the case where a second polarisation is needed. Thus, this is a very computationally intensive simulation. However, it is also a very accurate one as it includes: multiple reflections between AUT and probe and evanescent coupling.

The results of this simulation are presented in Figures 13.89 and 13.90 which, respectively, show the amplitude and phase of the transmission coefficient S_{21} in the form of a greyscale checkerboard plot. Here, the largest field intensity can be seen in the centre of the simulated 'measurement' where the probe is passing over the aperture of the rectangular pyramidal horn. The field outside of this projected aperture is far lower, with diffraction effects also being clearly visible which agrees with what one would generally expect to see in practice as the measurement is taken across a plane that is parallel to but displaced from the aperture plane of the AUT. The phase plot shows a relatively flat phase function across the aperture of the AUT with the phase changing outside of this region. Again, this agrees with our expectations as we are in essence cleaving a plane through a series of concentric spherical constant phase surfaces, cf. imagine taking a cut through an onion.

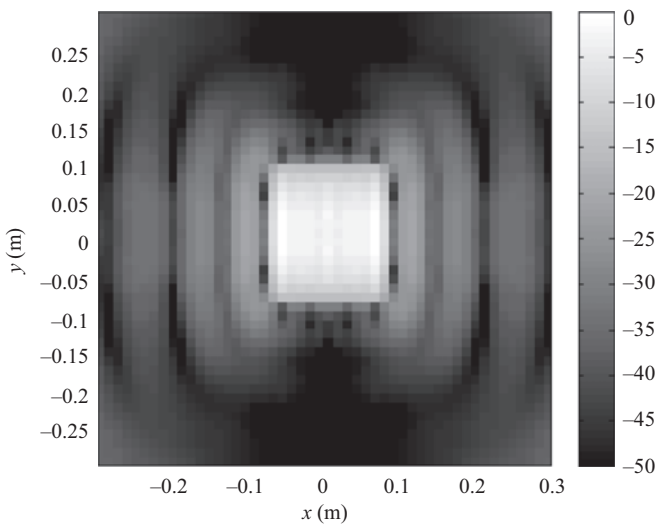

Figure 13.89 Simulated E_x-polarised amplitude pattern measurement including OEWG probe effects

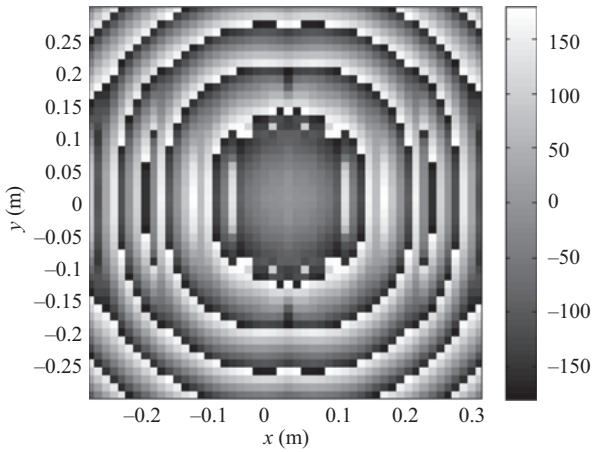

Figure 13.90 Simulated E_x-polarised phase pattern measurement including OEWG probe effects

By way of comparison, Figures 13.91 and 6.92 contain results that are equivalent to those shown in Figures 13.89 and 13.90 however here, an infinitesimal Hertzian dipole probe was used as opposed to a finitely large rectangular OEWG probe. Although the respective results are similar, some differences do exist and it is important recognise them and as such plots containing horizontal and vertical cuts through the amplitude patterns is presented in Figures 13.93 and 13.94,

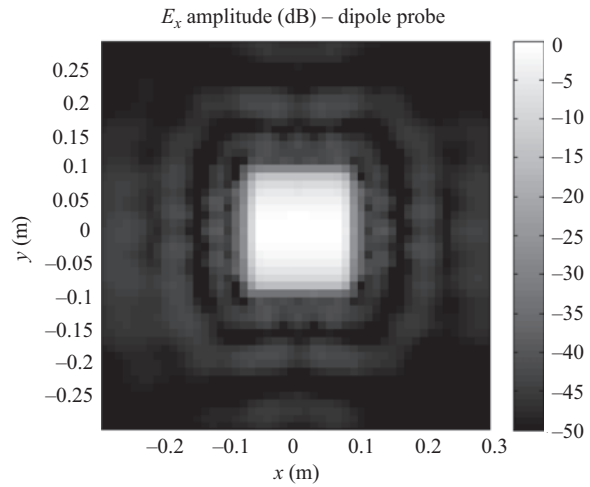

Figure 13.91 Simulated E_x-polarised amplitude pattern measurement assuming ideal Hertzian dipole probe

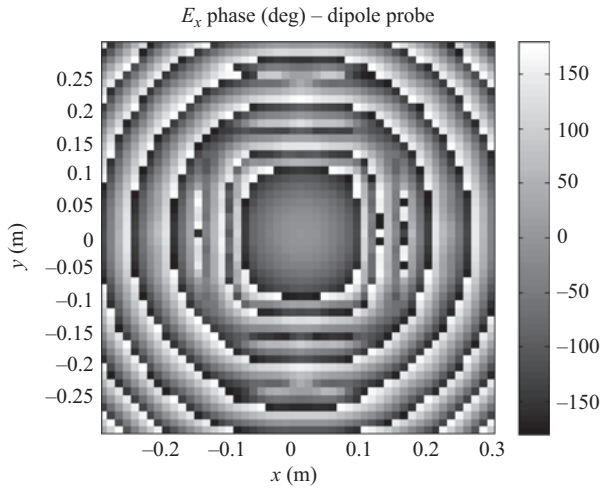

Figure 13.92 Simulated E_x-polarised phase pattern measurement assuming ideal Hertzian dipole probe

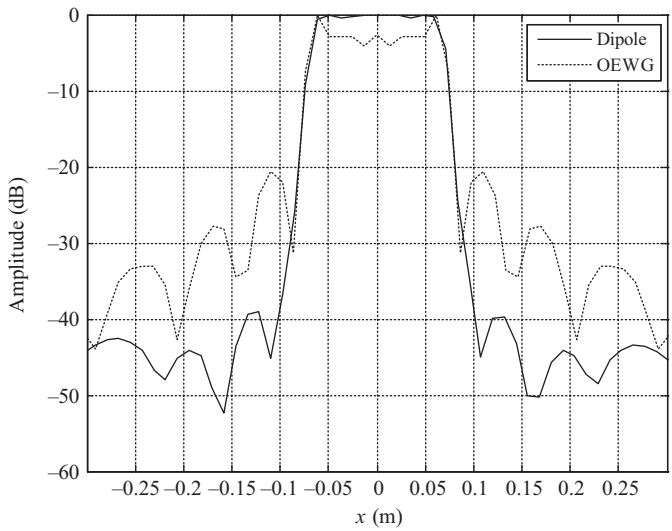

Figure 13.93 Comparison of horizontal cut through simulated E_x-polarised amplitude pattern using OEWG and dipole probes

respectively. Here, the solid trace denotes the field sampled using a dipole probe, i.e. that used by theory, with the OEWG probe results being represented by the dotted trace. From inspection of these plots is it evident that the simulated OEWG measurement contains a larger amount of ripple outside of the geometric projection of

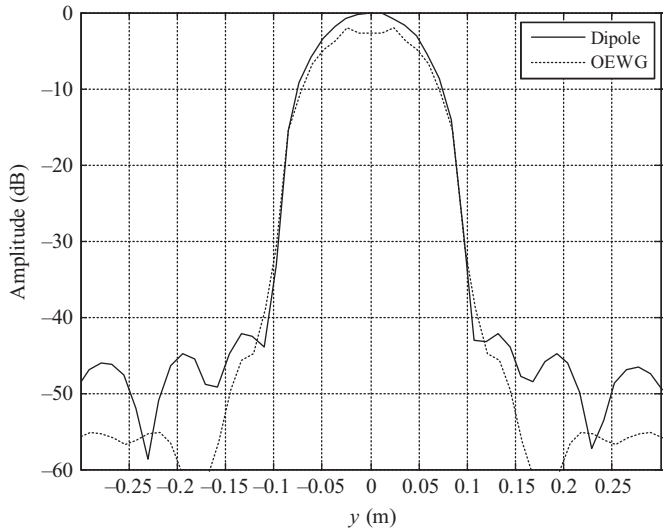

Figure 13.94 Comparison of vertical cut through simulated E_x-polarised amplitude pattern using OEWG and dipole probes

the aperture of the AUT. This is a result of multiple reflections, i.e. between the AUT and the probe. As observed above, this is a real effect and is something that is seen in practical measurements. However, due to the extended processing time required, it is something that is usually absent from most measurement simulations. From inspection of the respective phase plots, it is evident that this coupling has upset the measured phase although this is far less obvious. The second effect that is clear is the change in the shape of the pattern cuts. This is a consequence of the convolution between the fields in the AUT and the fields in the probe. In essence, the dipole probe performs an average of the field incident upon it. As the probe is infinitesimally small, this averaging is also infinitesimal resulting in the dipole probe sampling the field at a *single* point in space, with a single direction of polarisation. However, the OEWG has a finitely large aperture meaning that this averaging is performed over a finitely large region of space. The coupling of the field into the aperture of the OEWG probe results in the measured signal being a combination of the field associated with the AUT and the field associated with the probe.

The central task of many near-field to far-field transformation algorithms, as developed within the preceding chapters, concerns compensating for this probe pattern effect. Thus, one of the great utilities of this measurement simulation approach is that probe effects are included enabling the data provided to be used for the purposes of accurately and precisely verifying complete transformation algorithms. Unfortunately, the simulation times involved can be prohibitive thereby providing motivation for the development and use of the measurement simulation

techniques developed in the following sections which culminate with final sections of this chapter developing general-purpose methods for the simulation of, in the example considered, generic spherical near-field measurements that contain probe pattern effects. However, before these are developed the following section considers another use for full-wave three-dimensional CEM solvers which is connected with the measurement of gain.

13.3.3 Simulation of a pyramidal standard gain horn

The calibration of a standard gain horn by the three antenna method is highly accurate approach for determining the gain and polarisation properties of the antennas involved. However, it is time-consuming practice and this is especially true if mismatch correction is applied to each antenna, as indeed it should be, and the gain is required to be known at many frequency points across the band. This can become even more demanding in cases where the frequency of operation of the horn spans several waveguide bands where it is possible that additional antennas would be required by the calibration. In cases such as these, or in less demanding applications where lower accuracies are required, it is often attractive to resort to analytical methods or computational simulations to estimate the gain of the standard antenna.

Figure 13.95 contains a plot of gain as a function of frequency for the WR90 pyramidal gain horn that is presented in Figure 13.85. Here, the gain as estimated by the frequency domain moment method full-wave solver can be seen denoted by the dotted trace. A measurement of the gain of this horn is also plotted and denoted with the dashed line, and finally, the Navy Research Labs (NRL) curve is denoted

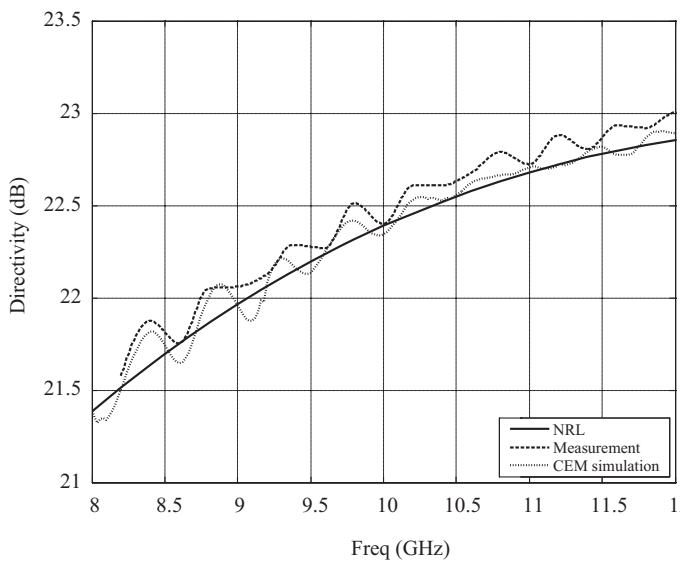

Figure 13.95 Model plot of gain as a function of frequency for a pyramidal gain horn, comparison of measured and theoretical gain values

with the solid trace. This derives from (4) (and the associated expressions) in the appendix of the Navy Research Laboratories (NRL) Report 4433. The pyramidal horn can be approximated as an aperture antenna and by utilising analytical methods formula for the boresight gain can be derived. This is the basis of the NRL curve. From inspection, it is clear that the average level of the NRL curve agrees with the results of the full-wave solver, the ripple that is present in both the measurement and the simulation is absent. This ripple is a result of the mismatch that is encountered at the aperture of the horn and is a real effect. Thus, although very convenient, the NRL curve will inherently have an uncertainty associated with it that is, for this example, on the order of ± 0.5 dB. If this is acceptable, then this is a very convenient way to determine the gain of an NRL compliant SGH that is routinely used in many commercial and educational applications. It is worth noting that some authors incorrectly state the formula for the gain of the SGH resulting in lower estimated gains than those stated here so some caution is needed on the part of the reader.

It is worth noting that deviations in geometry due to manufacturing tolerance and variations in material properties will impact upon the predicted gain values; however, these are generally less significant for the case of a medium-to-high gain SGH than would be the case for a low-gain standard antenna such as an open-ended rectangular waveguide probe.

13.3.4 Full-wave simulation of a spherical test system

The use of electromagnetic simulation and a digital twin enables a far greater degree of freedom and control in the way in which one may perturb a given, otherwise ideal, measurement configuration. To achieve this, the key is to build a suitable model and select an appropriate full-wave solver with sufficient modelling accuracy, flexibility and efficiency to demonstrate the phenomena under investigation. For a spherical simulation, the ultimate goal is to recreate the measurement configuration in the antenna test range using a general-purpose full-wave three-dimensional CEM solver to obtain the simulated field pattern over the full 4π steradian sphere, and this inevitably involves a huge amount of computational effort. The modelled system is presented in Figure 13.96. Here, the simulation recreates a measurement that is intended to verify the mode filtering-based scattering suppression technique presented in Chapter 4, Section 4.4.5.1.

Here, the AUT is shown offset from the origin of the measurement coordinate system ($x = y = z = 0$) by 0.36 m. An open-ended rectangular waveguide antenna is used as a probe in this schematic. A metal plate is introduced to perturb the system with the introduction of known scattering. The transmission scattering parameter S_{21} between the two waveguide ports of the AUT and the probe are simulated for each orientation of the AUT as it is sequentially rotated around the origin. In this way, a very general replica, i.e. digital-twin, of the antenna range measurement can be constructed and used, not only for examination of the scattering suppression technique, as discussed herein, but also in principal probe effects and any other antenna measurement artefact of interest.

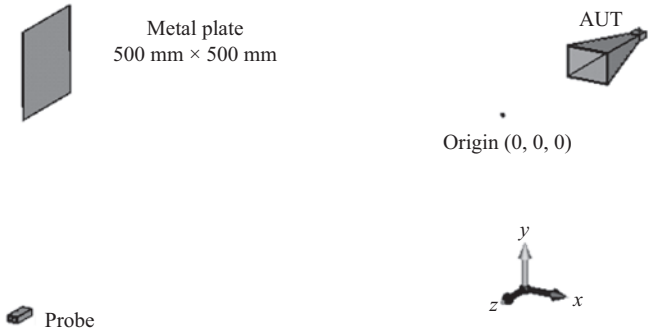

Figure 13.96 Schematic representation of the three-dimensional transmission model showing the probe (remote source antenna), the offset AUT and the metallic plate which is introduced to perturb the system with spurious reflected fields

A WR75 standard gain horn (SGH) radiating at 13 GHz was selected to represent the AUT for the purpose of this simulation for several practical reasons. Firstly, the antenna geometry is comparatively simple and mechanically rigid and, as has been shown previously, very encouraging agreement has been attained between CEM simulation and actual range measurement. This reduces the number of potential sources of uncertainties when comparing the simulated data with the measured data and presents a significant advantage when compared to antennas comprising complex mechanical configurations containing dispersive materials. Secondly, as a scatterer is to be included within the model as a parametric change that is to be subsequently extracted, the model rapidly becomes an electrically large structure. The proprietary Integral Equation Solver was selected as it is a solver that is specifically intended to treat this sort of electrically large metallic structure. The essence of the scattering suppression technique is to measure the antenna with its aperture offset from the rotation centre by a certain known amount that is at least twice the conceptual minimum MRE, so that the authentic modes associated with the AUT and the higher order modes associated with the scatterer can be separated in the mode domain. Thus, the CEM model is required to recreate this situation by simulating the AUT with its aperture offset away from the rotation origin and acquire its far-field amplitude and phase at $\theta = 0^\circ$ and $\phi = 0^\circ$ for every point on the far-field cut which corresponds to each rotated position of the AUT, thus for N_θ points, N_θ individual simulations are required.

Figure 13.97(a) shows the perspective view of the model for a WR75 SGH. Figure 13.97(b) illustrates the AUT when offset along the *Z*-axis and rotated to a series of different θ positions with the rotation centre located at the origin. Here, it is worth noting that the SGH was modelled with a waveguide to coax transition. In addition to improving the accuracy of the model, the auxiliary reason for this is due to the fact that both the time domain solver and integral equation solver require the waveguide port be aligned with a Cartesian axis. When the antenna is rotated to different θ angles, as shown in Figure 13.97(b), the waveguide section and port do

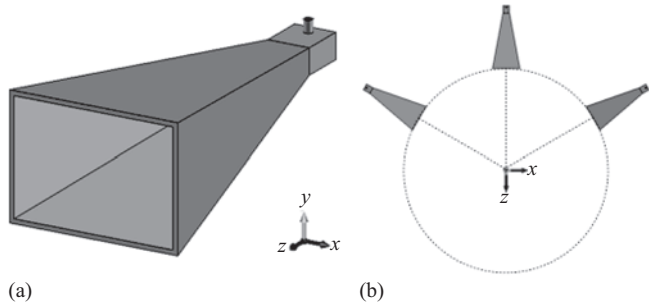

Figure 13.97 (a) Perspective view of the EM model of a WR75 SGH with waveguide to coax transition. (b) Plan view of an offset AUT at a series of different rotation angles with the aperture offset from the rotation centre

not align to the *x*-, *y*-, *z*-axes. For the case of the time-domain solver this means that the simulation cannot be run and in the case of the integral equation solver very poor results are obtained. Conversely, the frequency domain solver can accommodate a waveguide port which is not aligned to the Cartesian axis; however, it is not computationally efficient for large electrical problems such as the one under consideration here. One approach that can be used to overcome this problem is to include a waveguide to coax transition so that as the AUT is rotated, the coax port will remain normal to the *y*-axis of the model.

As mentioned in the previous section, the modelling will involve the simulation of the offset antenna at a series of different rotation angles with the far-field exported at $\theta = 0^\circ$ and $\phi = 0^\circ$. A macro was developed so as to automatically generate the modelling file for each rotation position. A second macro was developed to export the far-field data at $\theta = 0^\circ$ and $\phi = 0^\circ$. To ensure both the model and the macros work correctly, simulations were initially run without the scatterer. Thus, the SGH was first simulated to obtain its far-field pattern without any rotation using both the time-domain and the integral equation solver. The resulting simulated far-field patterns were found to agree with one another, providing confidence that reliable data had been obtained. The simulation was then run for the rotated AUT case as illustrated in Figure 13.97(b) with the far-field at $\theta = 0^\circ$ and $\phi = 0^\circ$ being extracted for each rotation case. These data sets were then combined together to form the great circle far-field pattern of the offset AUT. One critical setup when exporting the far-field point for each rotation case was to specify the far-field origin correctly. The far-field origin should be coincident with the rotation origin so that there is single consistent phase reference for each rotation case. If the model is configured correctly, clearly we can expect to obtain the same amplitude pattern from the two simulation methods. The comparison results are presented in Figure 13.98(a) which confirmed this. Here, the dashed trace denotes the far-field of the rotated AUT. Conversely, the conventionally simulated far-field pattern of the SGH is plotted in a solid trace and constitutes the reference.

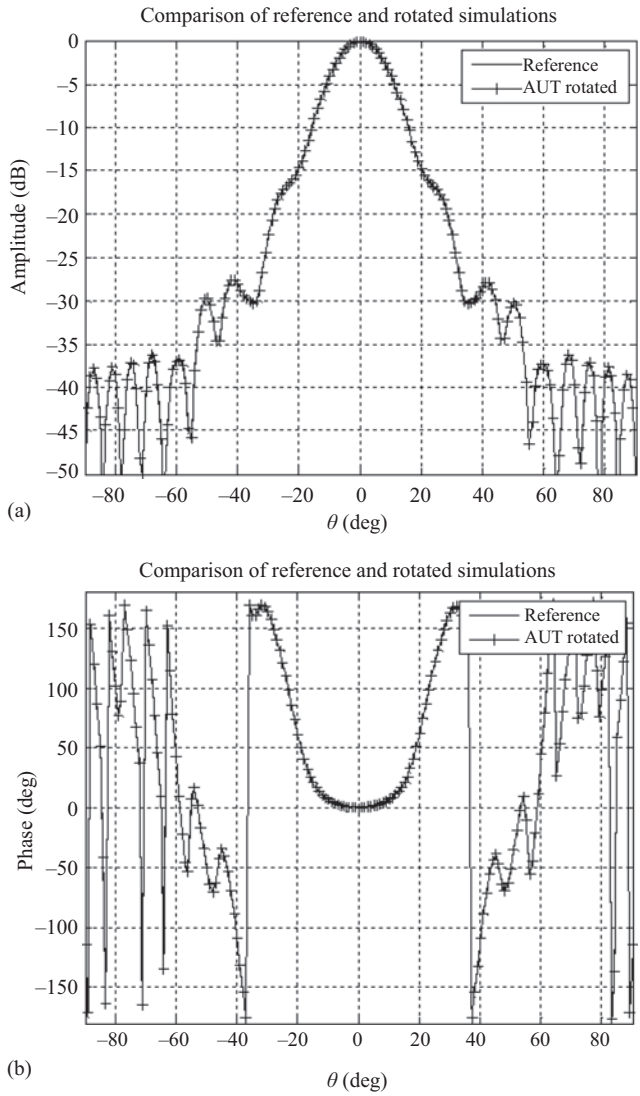

Figure 13.98 Results comparison at 13 GHz: (a) comparison of simulated amplitude patterns and (b) comparison of simulated phase patterns

Similarly, the reference and corrected displaced simulated phase patterns are presented in Figure 13.98(b) confirming the mathematical translation formula is reliable. In order that the scattering suppression technique presented above could be verified, the simulation was rerun, only this time a reflecting plate was introduced into the simulation as illustrated in Figure 13.99.

A square metallic plate 500 mm by 500 mm was introduced into the model and used as a large scatterer. This arrangement is shown schematically in Figure 13.99.

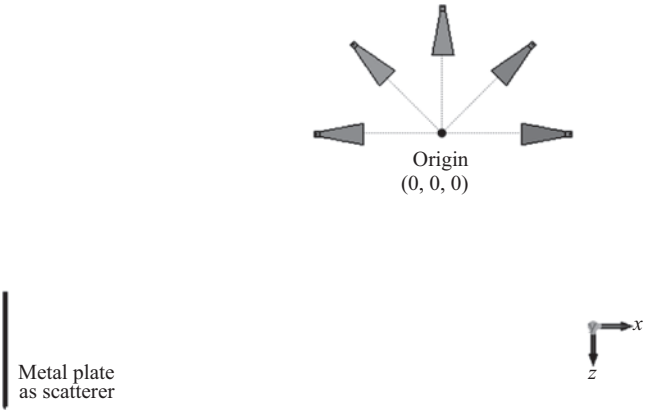

Figure 13.99 Offset AUT with scatterer at different rotation positions (plan view)

Here, the centre of the reflecting plate was located at (−2000, 0, 1000 mm) and was used to simulate a highly exaggerated scatterer. The AUT was offset by 360 mm from the rotation origin (0, 0, 0). Figure 13.100 illustrates the model for the offset AUT at different rotation angles with the scatterer in place. For each rotation position, the far-field of the combined structure, including both the rotated offset antenna and the scatterer, was simulated.

Clearly, although the CEM simulation will provide the far-field pattern of the combined structure over the full 4π steradian far-field sphere, only the point at $\theta = 0^\circ$ and $\phi = 0^\circ$ is of interest here, as it is this single point that is used to populate the simulated 'measured' far-field pattern cut. In Figure 13.100(a), the dotted trace denotes the free-space far-field amplitude pattern of the AUT as computed in this manner and this is plotted in the background and is used as the absolute truth-model. The solid trace denotes the simulated perturbed far-field pattern with the scatterer present. The simulated perturbed far-field pattern is then filtered using the conventional scattering suppression filter as described above with the mode-filtered amplitude pattern plotted in dashed. From inspection, it can be seen that the scattering due to the presence of the metallic plate has been effectively removed with the resulting pattern agreeing well with the reference data set. By way of a further illustration, Figure 13.100(b) compares the amplitude of the CMCs of the free space horn antenna, the antenna with the scatterer before and after filtering. Here, it is clear that the modes associated with the metallic plate are displaced towards higher mode indices meaning that the mode filtering effectively extracts their influence from the mode-filtered far-field antenna pattern. This is a relatively simple illustration of the way in which three-dimensional full-wave CEM solvers can be used to simulate antenna measurements in such a way as to permit careful verification and validation of, for example, sophisticated measurement and post-processing techniques. The great power here is that the measurement configuration can be very carefully and precisely controlled allowing close examination of any aspect of the system. Further information on this modelling can be found in the open literature [15].

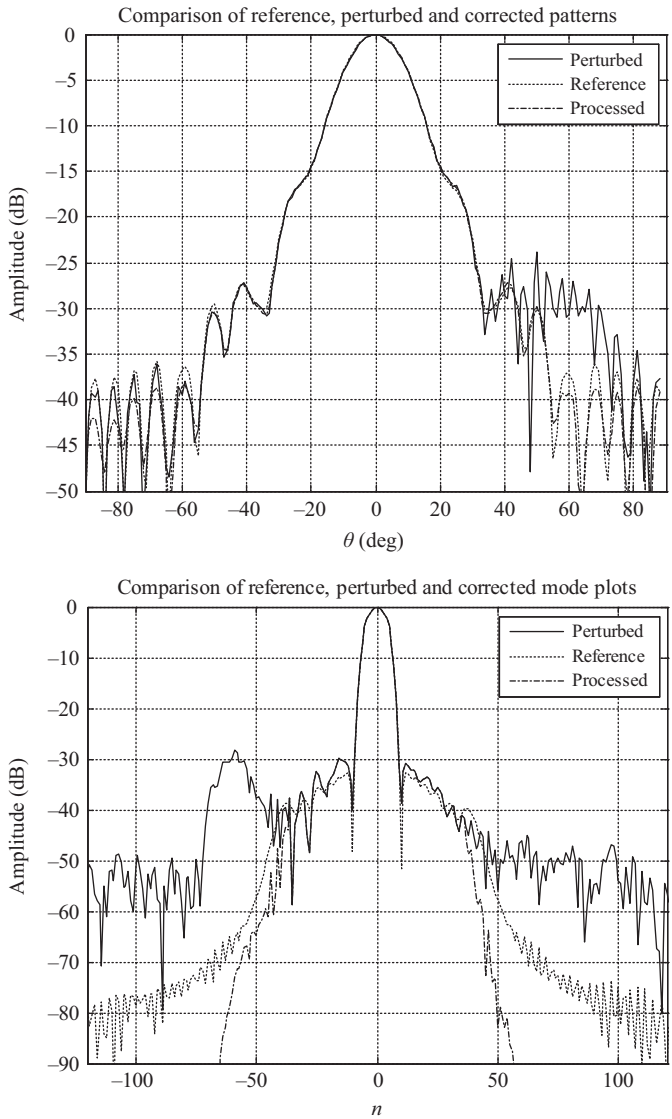

Figure 13.100 Offset (a) amplitude of far-field pattern with and without scattering suppression with far-field pattern at 13 GHz of the horn antenna as reference; (b) amplitude of the cylindrical mode coefficient (CMC) of the AUT with and without filtering compared with that of the horn antenna in free space

13.4 Simulation of a cylindrical near-field antenna test system

As expounded above, as a result of the potentially long simulation times and the often not inconsiderable amounts of computer resources required means that

switching to less general, but more efficient modelling approaches becomes very attractive. For the case of the cylindrical near-field measurement, it is possible to harness the plane-wave spectrum (PWS) method, as developed in Chapter 6 to reconstruct the radiated near electric field across a cylindrical surface from the far-field antenna pattern by evaluating two-dimensional radiation integrals with a given impressed source. Alternatively, and in many cases, a more convenient method is, assuming the orthogonal tangential near electric field components are known, to compute the PWS from a two-dimensional Fourier transform of an aperture illumination function, which can be implemented efficiently using the fast Fourier transform algorithm (FFT),

$$F_x(u,v) = \int_{-\infty}^{\infty}\int_{-\infty}^{\infty} E_x(x,y,z=0)e^{jk_0(ux+vy)}dxdy \tag{13.52}$$

$$F_y(u,v) = \int_{-\infty}^{\infty}\int_{-\infty}^{\infty} E_y(x,y,z=0)e^{jk_0(ux+vy)}dxdy \tag{13.53}$$

Here, E_x and E_y denote the x- and y-polarised component electric fields, respectively, F_x and F_y denote the x- and y-polarised components of the plane-wave spectra, k_0 is the free space propagation constant, and u, v and w are the x-, y- and z-axes orientated direction cosines, which can be related to conventional azimuth and elevation spherical coordinates that are often used to tabulated far-field antenna patterns through $u = \sin(\text{Az})\cos(\text{El})$, $v = \sin(\text{El})$, and $w = \cos(\text{Az})\cos(\text{El})$. Alternatively, and as described above, the PWS could be obtained from an auxiliary measurement, prior simulation or from a convenient analytical model. In this chapter, a simple aperture illumination function was used consisting of a uniformly illuminated square aperture cut in an infinitely thin perfectly conducting infinite extent ground plane is used throughout. With the PWS known, the radiated cylindrical near-field can then be reconstructed across the surface of a right hemi-cylinder where $z > 0$ using

$$\underline{E}(x,y,z) = \frac{1}{\lambda^2}\int_{-\infty}^{\infty}\int_{-\infty}^{\infty}\left[\left(\underline{\hat{u}}_x - \underline{\hat{u}}_z\frac{u}{w}\right)F_x(u,v) + \left(\underline{\hat{u}}_y - \underline{\hat{u}}_z\frac{v}{w}\right)F_y(u,v)\right] e^{-jk_0(ux+vy+wz)}dudv \tag{13.54}$$

Here, F_x and F_y are, respectively, the x- and y-polarised plane-wave spectra, the conventional Cartesian and cylindrical coordinates are related by $x = \rho\cos\phi$, $z = \rho\sin\phi$ where $0 \leq \phi \leq 2\pi$, $-\infty \leq y \leq \infty$ and $\rho \geq 0$ and fixed for a given measurement, with the linear axis of the cylindrical system being aligned with the vertical y-axis. Here, the reconstructed Cartesian near electric field components $\underline{E}$ are sampled using a monotonic plaid and equally spaced ϕ, y, grid with this equation representing a discrete Fourier transform that can be numerically evaluated. Unfortunately, this expression is not in a form that is amenable for implementation with the fast Fourier transform (FFT) making this the more computationally expensive task required by the simulation. The near electric field can be resolved onto a conventional cylindrical polarisation basis using, cf. Chapter 7.

$$\begin{bmatrix} \underline{\hat{e}}_\rho \\ \underline{\hat{e}}_\phi \\ \underline{\hat{e}}_z \end{bmatrix} = \begin{bmatrix} \cos\phi & \sin\phi & 0 \\ -\sin\phi & \cos\phi & 0 \\ 0 & 0 & 1 \end{bmatrix} \cdot \begin{bmatrix} \underline{\hat{e}}_x \\ \underline{\hat{e}}_y \\ \underline{\hat{e}}_z \end{bmatrix} \tag{13.55}$$

Once the orthogonal tangential electric field components are obtained, the resulting near-field data is in a form that is immediately suitable for processing with a standard cylindrical near-field to far-field transformation as developed within Chapter 7. Cylindrical near-field data obtained in this way is valid for the forward half-space only, cf. Chapter 6. However, if auxiliary angular spectra for the corresponding back half-space are available, and assuming the radiating antenna is thin, then, in principle, it is possible to provide data over the complete cylindrical scanning surface. However, for many cases of interest, this is not necessary including the examples presented in the following sections which use this method to usefully investigate and optimise many aspects of a given CNF measurement or post-processing activity.

13.4.1 CEM verification of scattering suppression with mode filtering

Figure 13.101 contains a greyscale plot of the ϕ-polarised component of the near electric field of a uniformly illuminated square aperture of side 0.356 m cut in an infinitely thin perfect electric conducting (PEC) ground-plane of infinite extent that is coincident and synonymous with the *xy*-plane as computed using the PWS-based simulation method developed within the preceding section.

The two orthogonal tangential near electric field components (one of which is shown in Figure 13.101) can be used to obtain the TM and TE CMCs using standard cylindrical processing, cf. Chapter 7. The resulting TE CMCs are presented in Figure 13.102. CMCs are complex numbers that are functions of the polarisation index, the azimuthal index n, the polar direction cosine γ, the frequency and are all variables which do not vary with any of the scanning coordinates. Figure 13.102 contains a greyscale checkerboard plot of the magnitude of the CMCs as obtained using standard cylindrical near-field processing.

Figure 13.103 presents an equivalent set of CMCs to those shown in Figure 13.102, i.e. for the same AUT, only here the AUT has been mathematically translated to the origin of the cylindrical measurement coordinate system. Prior to the translation, the AUT had been displaced away from the origin of the measurement coordinate system in the *z*-axis direction, cf. Figure 13.101, by 0.36 m (14″) with the distance corresponding approximately to the largest dimension of the aperture of the AUT. The displacement of the AUT from the measurement origin produces a far more complex phase variation within the measured cylindrical near-fields. The greater the complexity of the phase function, the greater the need for power within higher order CMCs and thus the broader distribution of cylindrical modes.

Here, the black ellipse plotted in Figure 13.103 denotes the highest order CMCs required by the standard cylindrical sampling theorem to represent a radiator

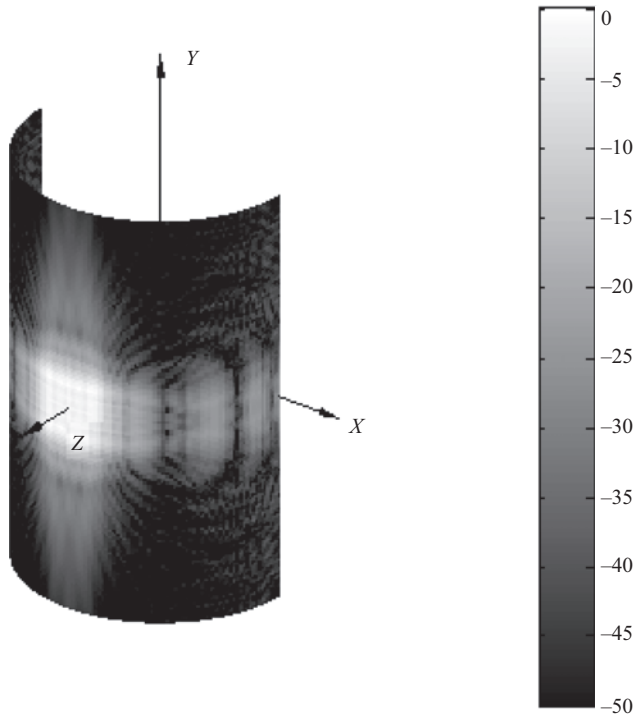

Figure 13.101 Simulated ϕ-polarised near electric field component plotted over conceptual cylindrical acquisition surface. AUT displaced away from the origin of the measurement coordinate system in the z-axis direction by 0.36 m

of a given size, cf. Chapters 7 and 8. This mode cut-off is determined when $n^2 + (\gamma r_{t0})^2 \geq (k_0 r_{t0})^2$. Here, r_{t0} denotes the maximum radial extent (MRE), n is the mode index and γ is the Fourier variable which is conjugate of the linear spatial variable. Here, the MRE is the radius of a conceptual cylinder that is coaxial with the cylindrical sampling surface that is large enough to circumscribe the majority of the current sources. As a consequence of the exponential decrease in the reactive modes, any mode not within this ellipse can be filtered out without impacting the integrity of the underlying antenna pattern function, irrespective of the complexity of that pattern. This generality is at the heart of the utility of the cylindrical mode filtering technique that is initially examined in Chapter 5, when considering the MARS technique and then developed fully below. However, the intent here is primarily focused upon using the verification of this post-processing technique to illustrate the utility of the CNF simulation.

To illustrate the effectiveness of the cylindrical mode filtering technique, an additional spurious, source can be introduced within the near-field simulation shown in Figure 13.101. The modified cylindrical near-fields are presented in

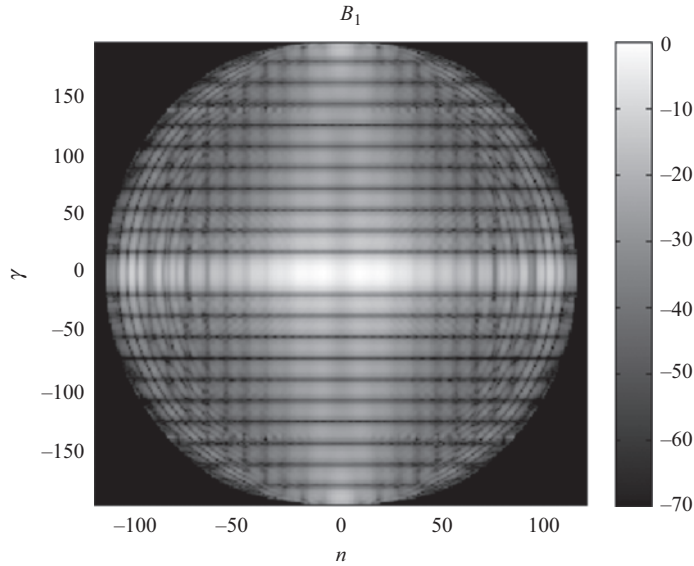

Figure 13.102 Amplitude plot of CMCs for the case of an AUT when its aperture is displaced from the measurement origin

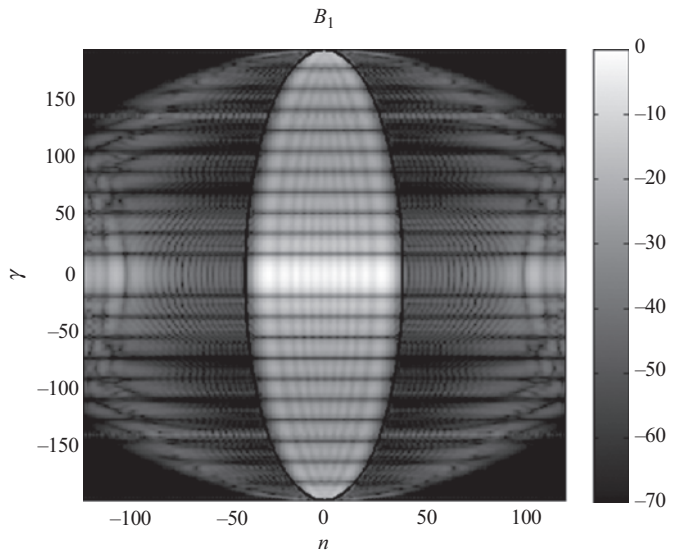

Figure 13.103 Amplitude plot of CMCs for the case of an AUT when its aperture is located at the measurement origin

Figure 13.99. This took the form of an additional radiator located at a different position in space and pointing in a different direction to that of the AUT. This additional source is the reason for the apparent asymmetry visible within the CNF data (Figure 13.104).

Prior to translating the AUT those modes associated with the AUT and those modes associated with the spurious source coexist through a linear superposition. However once the AUT is translated back to the origin of the measurement coordinate system, these mode spectra separate in the mode domain with the spurious modes appearing to shift towards larger absolute mode indices, i.e. $|n|$, as can be seen shown to the left- and right-hand sides of Figure 13.105.

As these modes lie outside of the black ellipse which is again used to denote the upper bounds of the standard cylindrical sampling theorem they can be safely filtered out without impacting upon the underlying AUT pattern whereupon the now processed far-field pattern can be obtained from a summation of the remaining antenna modes. Figure 13.106 contains a plot of the far-field pattern as obtained using the standard cylindrical near-field to far-field transform, i.e. without cylindrical mode-based processing. This pattern clearly shows the effects of the presence of the spurious source.

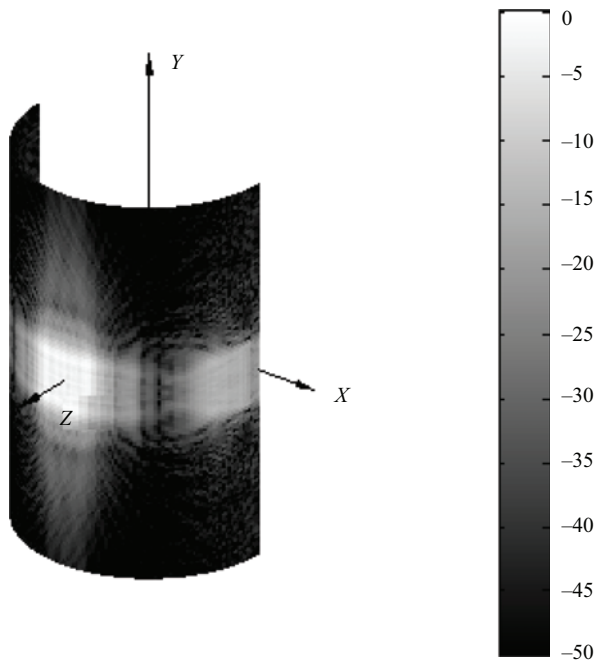

Figure 13.104 Simulated ϕ-polarised near-field component plotted over conceptual cylindrical acquisition surface with spurious radiator present (50 dB scale)

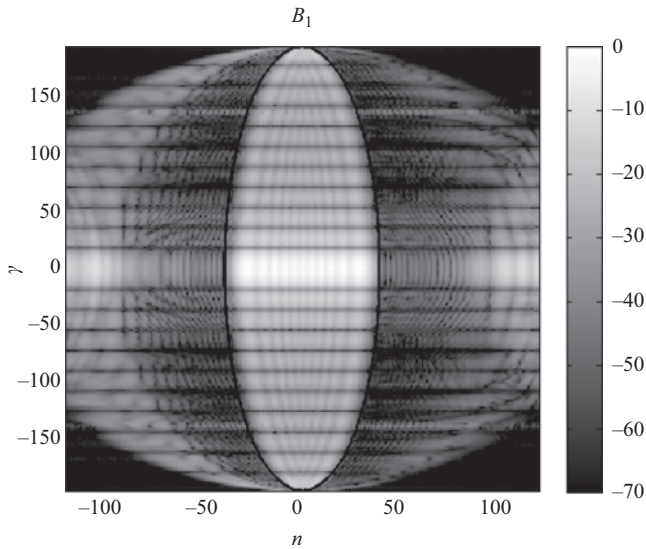

Figure 13.105 ϕ-polarised near-field component with spurious radiator present (50 dB scale) showing scattered power in higher order CMCs

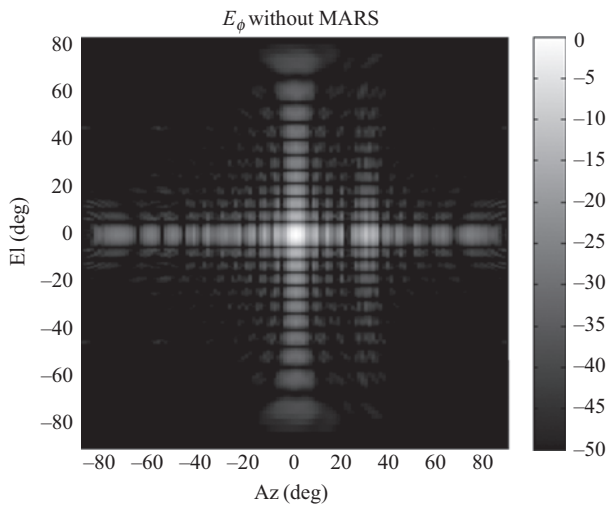

Figure 13.106 Far-field pattern of AUT obtained using standard cylindrical near-field processing showing presence of spurious source, i.e. without C-MARS processing wrong figure! this is a copy of 6.107 below

In contrast, Figure 13.107 shows the equivalent far-field pattern with mode processing having been applied with the spurious signal clearly being largely attenuated across a wide range of azimuth, *and* elevation, angles.

By way of further comparison, Figures 13.108 and 13.109 contain great circle azimuth amplitude and phase cuts, respectively, that compare these patterns to

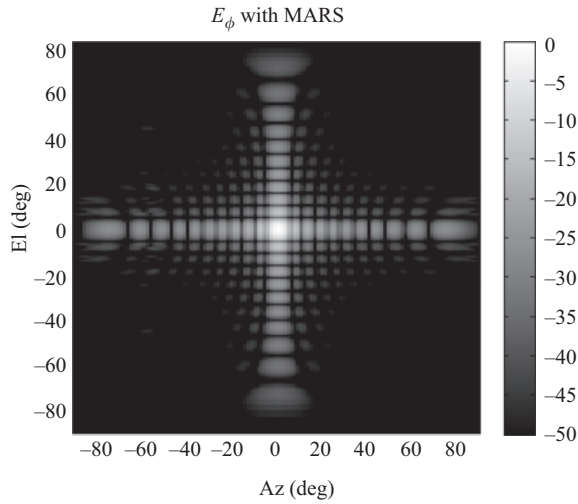

Figure 13.107 Far-field pattern of AUT obtained using C-MARS processing

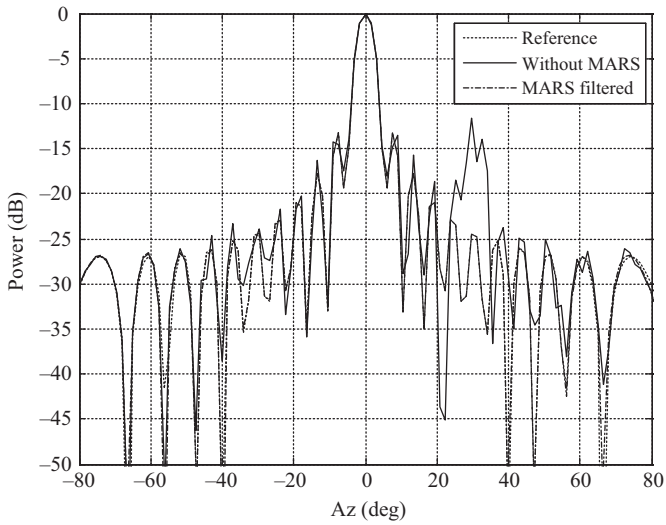

Figure 13.108 Azimuth amplitude cut comparing reference to patterns without and with processing

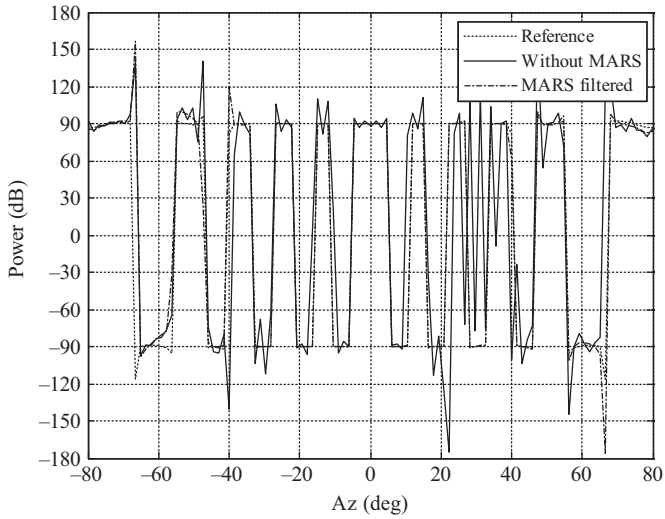

Figure 13.109 Azimuth phase-cut comparing reference to patterns without and with processing

reference far-field pattern data. This provides additional confirmation of the effectiveness of the filtering process showing a circa 12 dB attenuation of the spurious signal in the vicinity of the peak at a direction of 30° from boresight and crucially demonstrates that the remaining pattern is reliable. A similar effect can be seen within the phase patterns where the solid, unfiltered results show significant ripple with the dotted reference and dashed cylindrical filtered traces being in very impressive agreement with one another. This simulation recreates and reconfirms results that have previously been obtained empirically below. This exercise was completed in 10° steps with the spurious radiator being orientated sequentially at 10°, 20°, 30°, 40° and 50° in azimuth. Although not shown, as a consequence of available space, in each case a similar degree of suppression was obtained, irrespective of the azimuthal angular orientation of the radiator.

As a way of further examining the effectiveness of cylindrical mode processing, a simulation was constructed where the spurious signal had been orientated to point predominantly in elevation with the greatest effects being seen around 30° in elevation. Figure 13.110 presents the simulated cylindrical near-field data set, where the additional radiator is placed to the side of the AUT and is tilted up in elevation. As is discussed below, this form of mode filtering is generally thought to have the greatest effect in the angular axis as this is the axis which most closely corresponds to the mode index. Hence, this configuration can be considered to be a very demanding test case which is the principal reason it was chosen.

Figure 13.111 presents the corresponding far-field pattern as obtained, again, from standard cylindrical near-field processing showing the spurious signal.

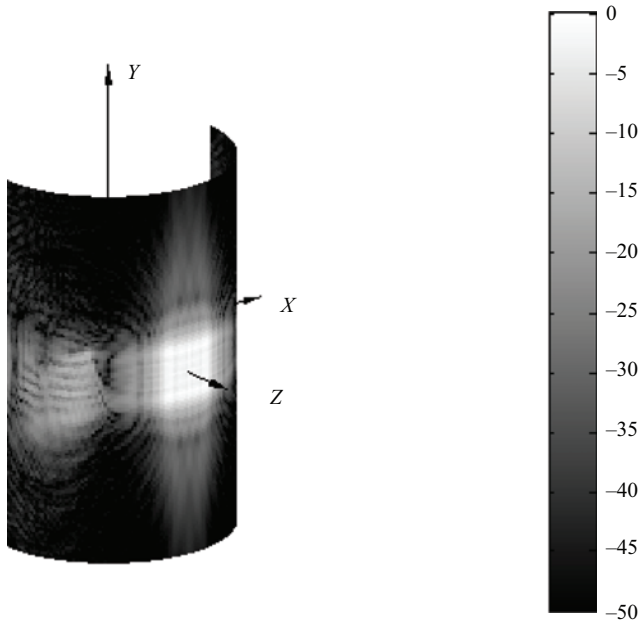

Figure 13.110 Simulated ϕ-polarised electric near-field component plotted over conceptual cylindrical acquisition surface with spurious radiator included (50 dB scale)

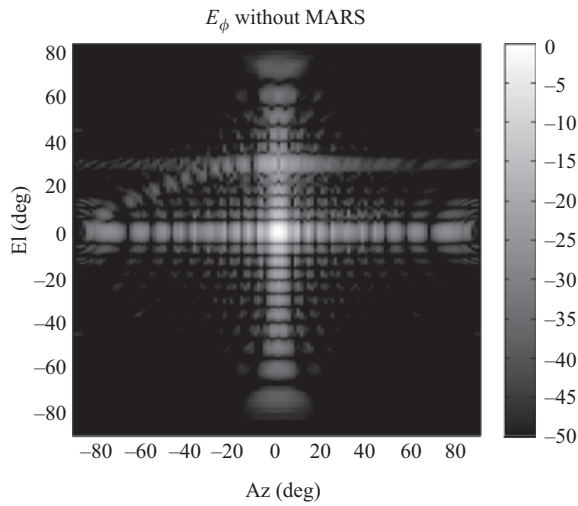

Figure 13.111 Far-field pattern of AUT obtained from standard CNF to FF transform – without MARS processing

Conversely, Figure 13.112 contains a directly equivalent far-field greyscale checkerboard plot to that shown in Figure 13.111, here however, standard processing has been utilised. From inspection, it is evident that the spurious trail of side lobes from the additional radiator has been effectively suppressed. So that a more complete picture of the effectiveness of the cylindrical processing can be obtained, this exercise can be repeated using different azimuthal angles for the spurious scattering source.

In this case, the spurious radiator was offset in the *x*-axis with respect to the AUT. It is the small horizontal displacement that enabled the algorithm to succeed. Some small residuals of the spurious source do still persist however their artefacts are low level, circa −40 dB level and are very wide-out. This is a consequence of the comparatively small change in their mode structure under translation allowing their modes to remain within the ellipse that is defined by the sampling theorem. However, had the additional spurious source not been displaced by at least some small amount in the *x*-axis from the AUT then the cylindrical mode-based processing would have been far less effectiveness. In practice, this implies that processing can be effective in suppressing scattering originating from the walls of the test chamber but will be far less effective in compensating from scatterers located along the vertical centre-line of the test chamber. However, for that specific case, the more recently developed two-dimensional cylindrical processing algorithm could be used instead (see Section 12.4.2, Figure 12.110). However, as cylindrical measurements are typically deployed to measure antennas with higher gain in the elevation axis, this means that there is generally less power radiating in wide elevation angles meaning that lower field intensity illuminates these parts of the test environment. If this were not the case then the cylindrical technique itself would be rendered inaccurate as a result of excessive truncation in the measured near-fields.

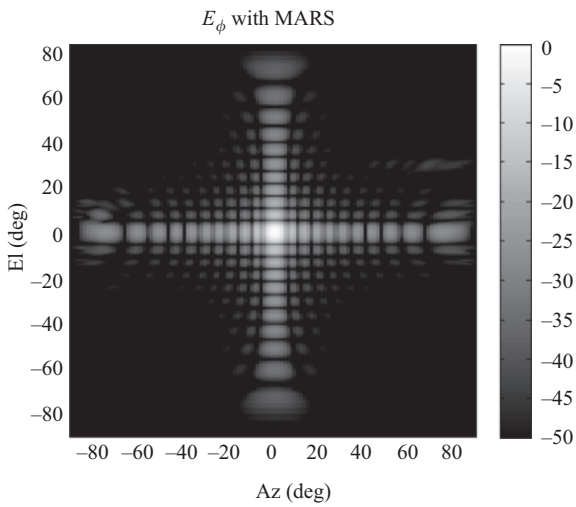

Figure 13.112 Far-field pattern of AUT obtained using MARS processing

13.4.2 CEM verification of improvement in signal-to-noise ratio

In a number of previous studies, it has been shown that cylindrical processing is able to increase the effective far-field system signal-to-noise ratio (SNR) in a given measurement. This is possible as noise power is distributed broadly evenly across the mode spectra whereas modes associated with the AUT are bounded within the mode domain once the translation of origins has been applied. As the translation of origins has the effect of reducing the power distribution of modes associated with the AUT to a minimum, an effective increase in the SNR is generally achieved. This increase in SNR is separate and in addition to that which is ordinarily provided by the transform gain. Figure 13.113 shows the baseline CNF data plotted as a greyscale checkerboard plot, cf. Figure 13.101.

Figure 13.114 shows the same basic pattern, only here addition random noise has been incorporated. In this case, noise was added such that the amplitude was normally distributed with a distribution of 2 standard deviations (2σ) about a mean value of -46 dB with a uniformly distributed phase error. This corresponds closely to what is seen in practice. Modern receivers and vector network analysers (VNA) recover phase from a ratio of two complex measurements each possessing nominally the same error distribution. The distributions approximately cancel resulting in the uniform 360° phase distribution encountered in practice. The mean amplitude noise signal level was selected as this is a typical value for a chamber lined with poorly performing 12″ pyramidal absorber. The, rather drastic, effect that this has on the CNF data is illustrated in Figure 13.114. Figure 13.115 presents the CMCs

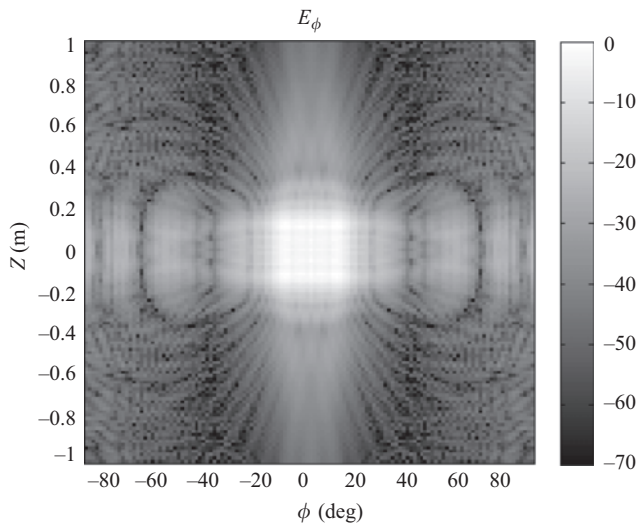

Figure 13.113 Greyscale checkerboard plot of simulated ϕ-polarised electric near-field component without spurious random signal added

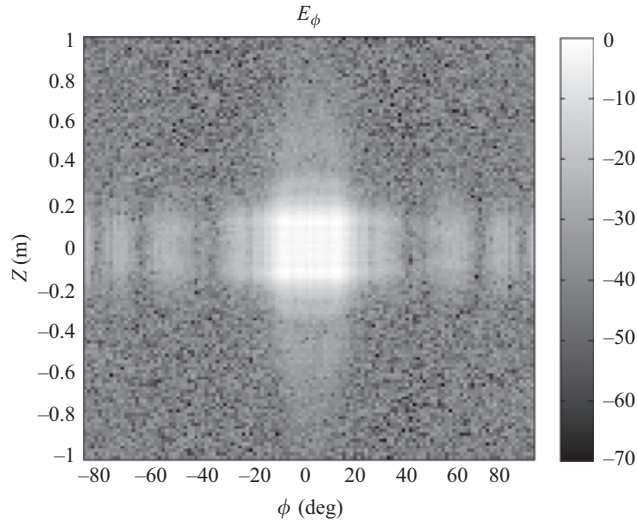

Figure 13.114 Greyscale checkerboard plot of simulated ϕ-polarised electric near-field component with spurious random signal added

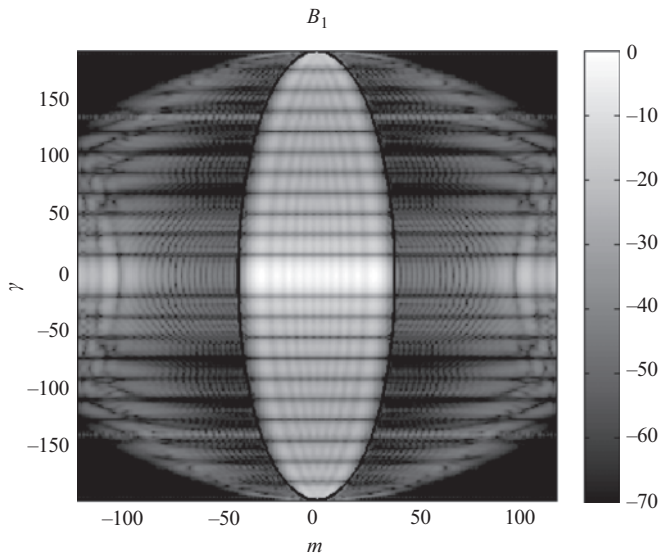

Figure 13.115 CMCs of AUT in the absence of noise

for the AUT for the case in the absence of noise whereas Figure 13.116 contains an equivalent plot for the noise-contaminated case. Here, power contained in spurious random noise outside the black ellipse corresponds to CMCs that are excluded by the cylindrical mode-based processing.

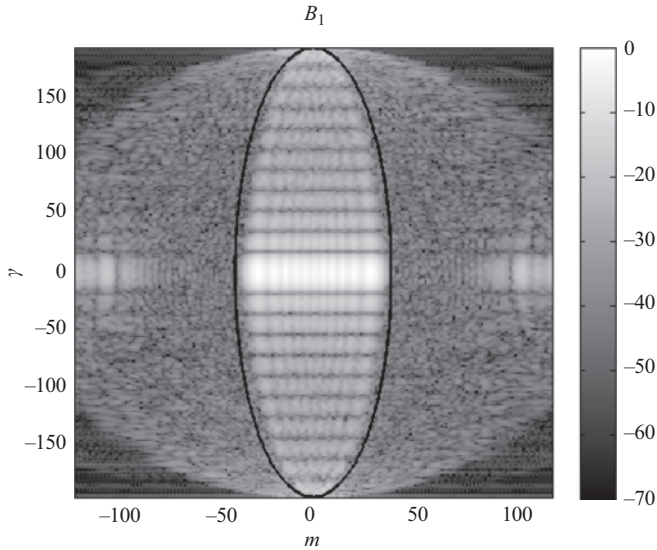

Figure 13.116 CMCs of AUT in the presence of noise

The corresponding far-field pattern obtained using standard cylindrical processing is presented in Figures 13.117–13.119 which clearly shows an increase in the background noise level, especially in the regions away from the principal planes over the uncontaminated result shown in Figure 13.117.

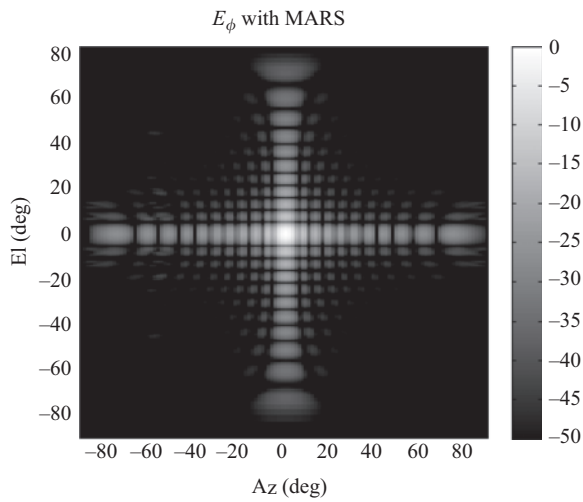

Figure 13.117 Far-field pattern of AUT without C-MARS processing of AUT in the absence of noise

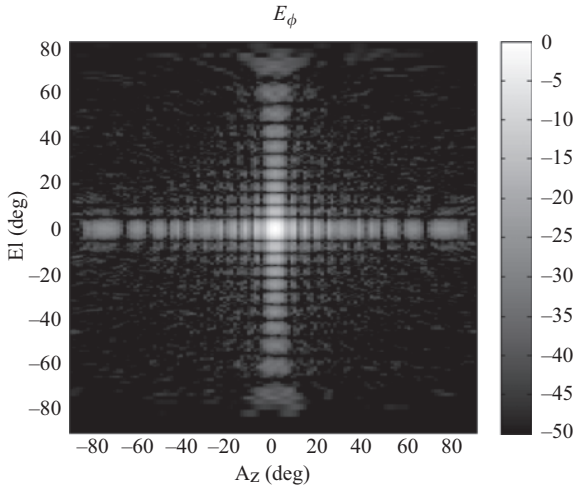

Figure 13.118 Far-field pattern of AUT without C-MARS processing in the presence of noise

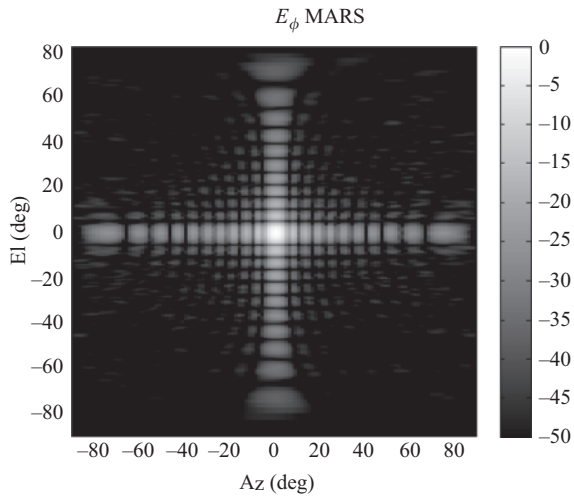

Figure 13.119 Far-field pattern of AUT with noise with C-MARS processing

Conversely, the equivalent cylindrical processed, i.e. filtered, result is presented in Figure 13.119.

From a comparison of Figure 13.119 with a noise-free result, that of Figure 13.117, it is clear that cylindrical processing has significantly reduced the background noise level. By way of further confirmation, the RMS difference level

between the reference and noise-contaminated result was computed and was found to be −49.9 dB. When the RMS difference level was computed between the reference and processed noise-contaminated result the level was found to be −57.5 dB which corresponds to an overall improvement in signal to error level of greater than 7.5 dB. Again, this is an encouraging result. Here, the comparisons are made in the far-field, meaning that this improvement in the RF link budget is in addition to any improvement yielded by the gain of the cylindrical near-field to far-field transform.

13.4.3 CEM verification of suppression of second-order truncation effect

The third widely reported capability of the cylindrical mode-based processing is the ability to suppress second-order truncation effects, i.e. spectral leakage giving rise to Gibbs ripple [17]. Cylindrical mode truncation is introduced by the presence of an artificial sharp discontinuity at the boundary of the finite sampling interval in y. This boundary is a consequence of the finitely long linear-axis and necessitates the use of a larger number of higher order CMCs to represent this discontinuous behaviour within the measured near electric fields. As the processing removes higher order CMCs this means that it also suppresses Gibbs like phenomena. To illustrate and examine this more closely, a number of simulations are presented in this section with respectively linear spans of 2.0, 1.4 and 1.0 m. These correspond to a maximum valid elevation pattern angle of circa 68°, 57° and 44°, respectively. Each CNF data set was transformed into the far-field using the standard cylindrical near-field to far-field transformation (Figures 13.120, 13.122 and 13.124,

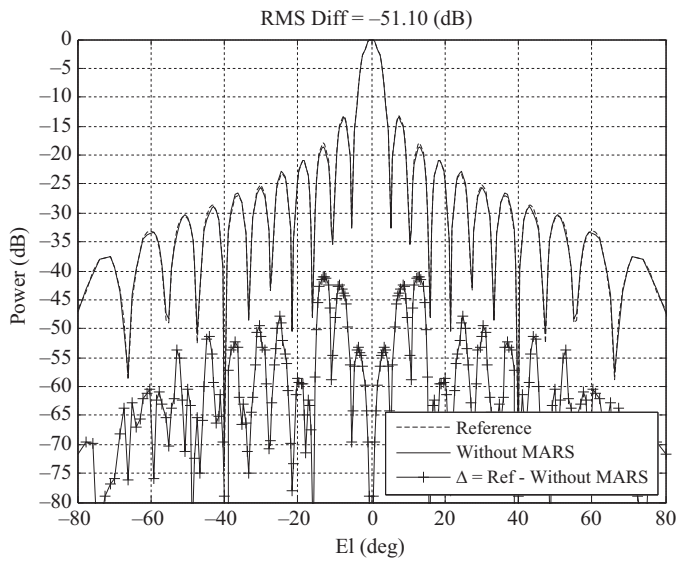

Figure 13.120 2.0 m truncation test Δ computed without processing

respectively). This was repeated using cylindrical processing with the results being shown in Figures 13.121, 13.123 and 13.125, respectively. The elevation boresight pattern cuts are compared and the RMS difference levels indicated.

In Figure 13.120 Figure 13.122 and Figure 13.124, the dotted trace denotes the reference far-field pattern, the black trace is the truncated far-field pattern obtained using standard cylindrical processing, and the black trace with crosses represents the difference level between these two patterns when expressed in dB form. Conversely, Figure 13.121, Figure 13.123 and Figure 13.125, the dotted trace denotes the reference far-field pattern, the black trace is the truncated far-field pattern obtained using MARS processing, and the black trace with crosses represents the difference level between these two patterns when expressed in dB form. In each case, the patterns show a significant improvement in the degree of agreement attained within the valid elevation angle for the case where cylindrical processing has been applied. This is expected as, cf. Figure 13.125 the black (without processing) trace can be seen to be most obviously different to the solid (with processing) trace mainly in the vicinity of the peaks of the side lobes. This result is also confirmed by comparing the RMS difference levels obtained, respectively, with and without applying the processing. Here, there was a 20, 12 and 5 dB improvement in the RMS difference levels, respectively, for the respective cases of a 2.0, 1.4 and 1.0 m linear scan. The degradation with decreasing span is a direct consequence of the increasing impact of the first order truncation effect which is revealed by the larger differences in the wide-out pattern. Although not shown, due to the constraints of space, the azimuth patterns do show some variation with linear

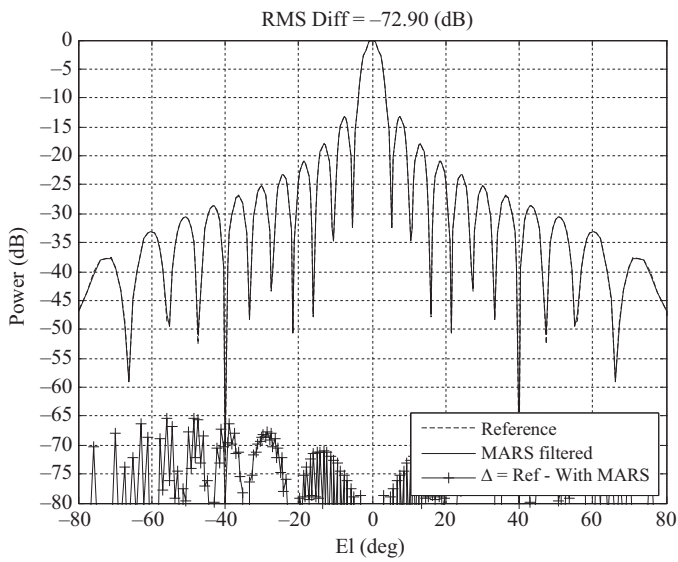

Figure 13.121 2.0 m truncation test Δ computed with processing

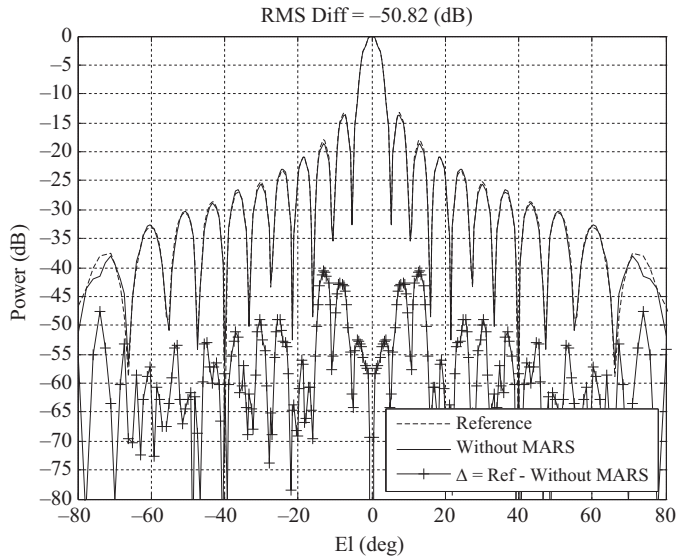

Figure 13.122 1.4 m truncation test Δ computed without processing

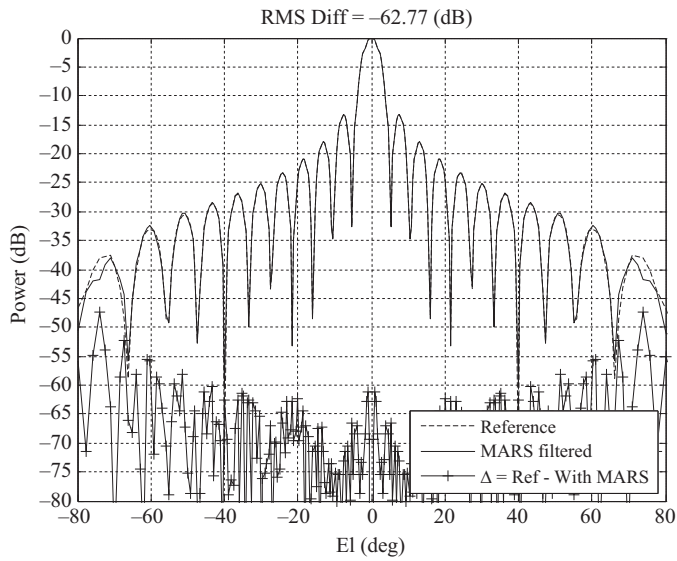

Figure 13.123 1.4 m truncation test Δ computed with processing

span, and is a natural consequence of the anti-reductionist relationship that exists between the near- and far-fields, although that difference is small.

As shown in this and the preceding sections, the CEM model has been able to provide further confirmation of the effectiveness of the cylindrical processing,

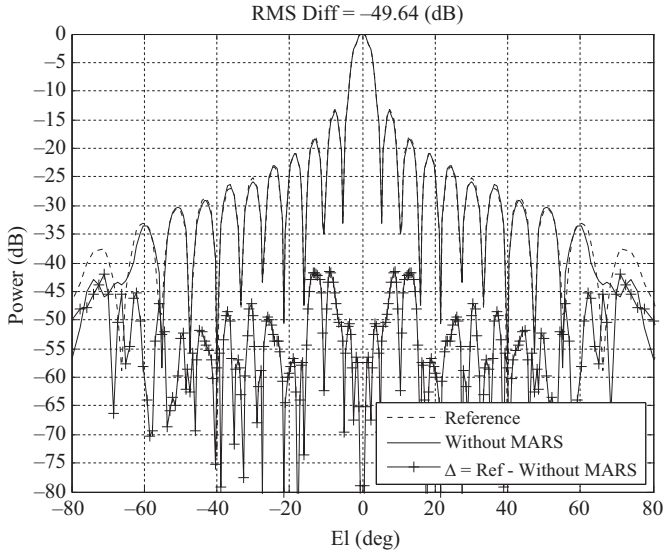

Figure 13.124 1.0 m truncation test Δ computed without processing

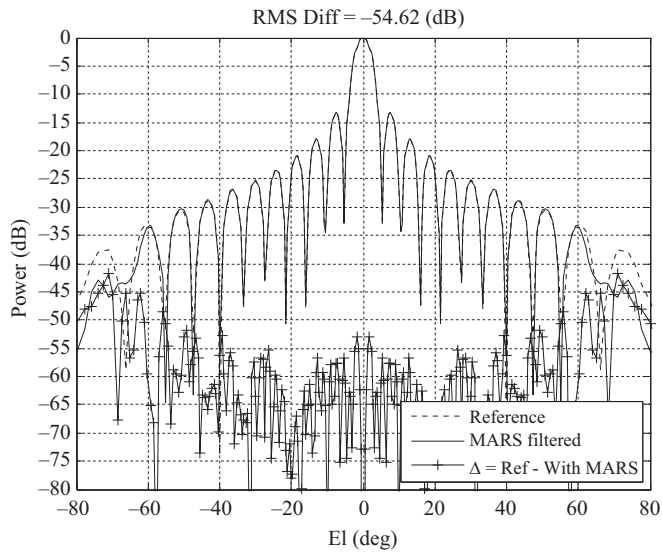

Figure 13.125 1.0 m truncation test Δ computed with processing

showing that it can be used with a very high degree of confidence to improve the quality of measurements taken using cylindrical near-field test systems.

13.5 Simulation of a spherical near-field antenna test system

Spherical near-field measurement systems can be simulated in a similar method to those used above to treat the cylindrical case. Thus, the radiated near-field can be reconstructed across the surface of a hemisphere where $z > 0$ using

$$\underline{E}(x,y,z) = \frac{1}{\lambda^2}\int_{-\infty}^{\infty}\int_{-\infty}^{\infty}\left[\left(\underline{\hat{u}}_x - \underline{\hat{u}}_z\frac{u}{w}\right)F_x(u,v) + \left(\underline{\hat{u}}_y - \underline{\hat{u}}_z\frac{v}{w}\right)F_y(u,v)\right]e^{-jk_0(ux+vy+wz)}dudv \tag{13.56}$$

As before, F_x and F_y are, respectively, the x- and y-polarised angular spectra, the conventional Cartesian and spherical coordinates are related by

$$x = r\sin\theta\cos\phi \tag{13.57}$$

$$y = r\sin\theta\sin\phi \tag{13.58}$$

$$z = r\cos\theta \tag{13.59}$$

where $0 \leq \theta \leq \pi/2$, $0 \leq \phi \leq 2\pi$, and $r \geq 0$. The reconstructed Cartesian near electric field components are typically sampled using a monotonic plaid and equally spaced θ, ϕ grid. The near electric field can be resolved onto a conventional spherical polarisation basis using

$$\begin{bmatrix} E_\theta \\ E_\phi \end{bmatrix} = \begin{bmatrix} \cos\theta\cos\phi & \cos\theta\sin\phi & -\sin\theta \\ -\sin\phi & \cos\phi & 0 \end{bmatrix} \cdot \begin{bmatrix} E_x \\ E_y \\ E_z \end{bmatrix} \tag{13.60}$$

Thus, the resulting spherical near-field data is in a form that is immediately suitable for processing with a standard spherical near-field to far-field transformation developed above.

A result of the application of this simple procedure is illustrated in Figures 13.126 and 13.127, which contains therefore a greyscale plot over a conceptual spherical measurement surface of the θ- and ϕ-polarised components, respectively, of the near electric field of a uniformly illuminated square aperture of side 0.356 m cut in an infinitely thin PEC ground-plane of infinite extent that is coincident and synonymous with the xy-plane. This plane was offset from the origin of the spherical measurement coordinate system by 0.51 m in the z-direction to form a conventional spherical mode filtering type measurement configuration, cf. the cylindrical case treated within the preceding section.

As developed within Chapter 8, the standard spherical transmission formula permits the AUT and the probe to be described by spherical mode coefficients that

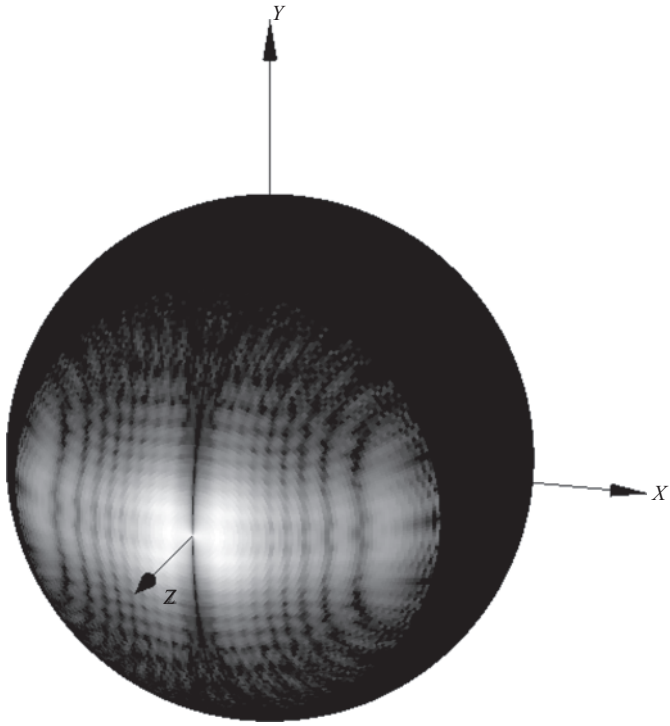

Figure 13.126 Simulated θ-polarised near electric field component plotted over the spherical surface, 50 dB amplitude scale of a uniformly illuminated square aperture of side 0.356 m

are the complex coefficients of basis functions that are elementary solutions of Maxwell's equations for a spherical coordinate system. In principle, the spherical transmission equation is valid for any arbitrary test antenna and certain probe combinations at any separation distance between the spherical coordinate system origin and the probe that is outside of the minimum sphere of radius ρ_0 that will completely enclose the majority of the current sources. In a linear isotropic and homogeneous source or sink-free space which is enclosed by a spherical surface and which is located at the origin of an inertial frame of reference, the electric field can be expressed as

$$\underline{E}(r,\theta,\phi) = k_0\sqrt{Z}\sum_{n=1}^{\infty}\sum_{m=-n}^{n}\left[Q^{(3)}_{TEmn}\underline{F}^{(3)}_{TEmn}(r,\theta,\phi) + Q^{(3)}_{TMmn}\underline{F}^{(3)}_{TMmn}(r,\theta,\phi)\right] \tag{13.61}$$

Here, $Q^{(3)}_{TMmn}$ and $Q^{(3)}_{TEmn}$ denote the transverse magnetic (TM) and transverse electric (TE) spherical mode coefficients, which are complex values of n and m, $\underline{F}^{(3)}_{TMmn}$ and $\underline{F}^{(3)}_{TEmn}$ are TM and TE spherical vector wave-functions which are

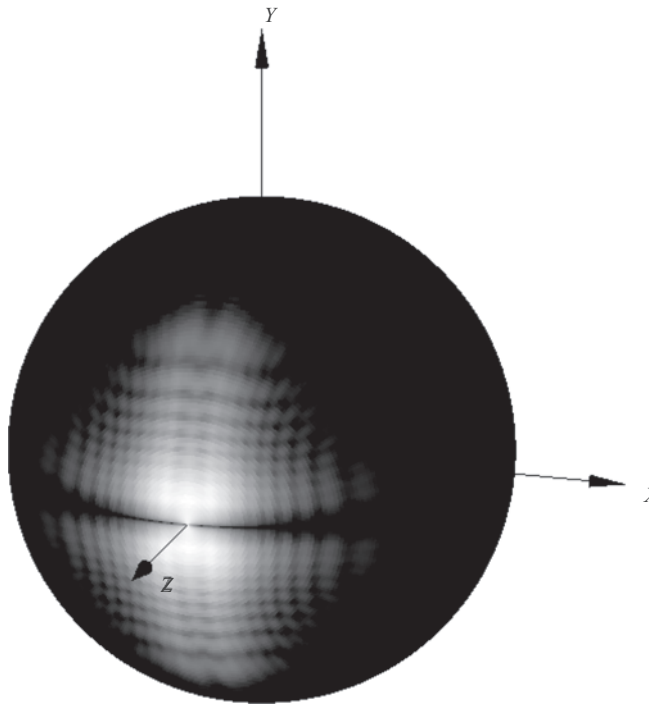

Figure 13.127 Simulated ϕ-polarised near electric field component plotted over the spherical surface, 50 dB amplitude scale of a uniformly illuminated square aperture of side 0.356 m

functions of n, m, r, θ and ϕ. Here, spherical Hankel functions are used to represent radial outgoing waves. The spherical mode coefficients (SMC) are complex numbers that are functions of frequency, the polarisation index, the polar index n and the azimuthal index m such that $0 \leq n \leq \infty$ and $-n \leq m \leq n$ which do not vary with any of the scanning coordinates. As was developed above, by using mode orthogonality, this expression can be inverted whereby the two orthogonal tangential near electric field components (as illustrated in Figures 13.126 and 13.127) can be used to obtain the TM and TE SMCs using standard spherical processing. The resulting TE SMCs are presented in Figure 13.128.

Conversely, Figure 13.129 presents an equivalent set of SMCs to those shown in Figure 13.121, i.e. for the same AUT, only here the AUT has been mathematically translated back to the origin of the spherical measurement coordinate system. Prior to the translation, the AUT had been displaced away from the origin of the measurement coordinate system in the z-axis direction by 0.51 m (20″). The displacement of the AUT from the measurement origin produces a far more complex phase variation within the measured spherical near fields. The greater the complexity of the phase function, the greater the need for power within higher order

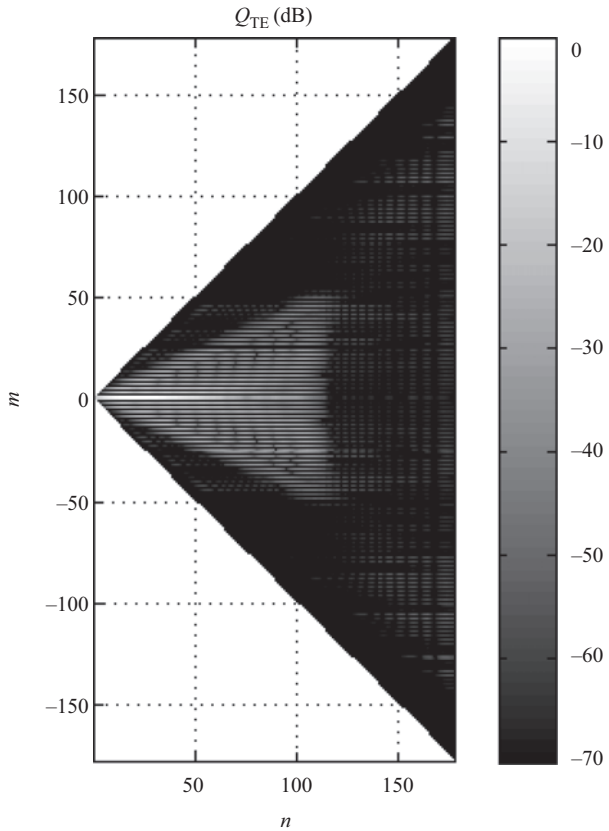

Figure 13.128 Amplitude plot of TE SMCs for an AUT when its aperture is displaced from the measurement origin

SMCs and thus the broader the distribution of the associated spherical mode spectrum. In Figure 13.129, the vertical line denotes the highest order SMCs required by the standard spherical sampling theorem to represent a radiator of a given electrical size. This mode cut-off is determined by evaluating $n = \text{ceil}(k_0 r_{t0}) + n_s = 55 + n_s$, where n is the highest order polar mode index associated with the AUT. Here, r_{t0} denotes the maximum radial extent (MRE), k_0 is the free space propagation number, and n_s is a positive integer that is used as a safety margin that depends upon the accuracy required and ceil is a function that rounds towards positive infinity. The MRE is the radius of a conceptual sphere that is centred about the origin of the measurement coordinate system that is large enough to circumscribe the majority of the current sources in the AUT. As the behaviour of the SMCs in the model is consistent with what is encountered experimentally, we can now examine the behaviour for the case where a spurious radiator is incorporated within the measurement simulation. This perturbed spherical near-field data

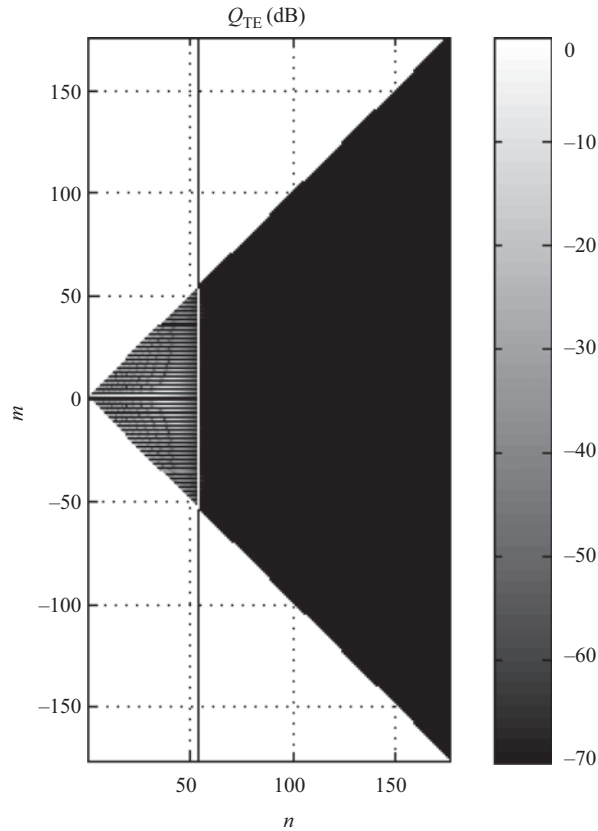

Figure 13.129 Amplitude plot of TE SMCs for an AUT when its aperture is at the measurement origin

set can be transformed, using standard spherical processing, and the resulting SMCs is presented in Figure 13.130 for the case where the AUT has been mathematically translated (by 0.51 m) back to the origin of the measurement coordinate system. Here, the SMCs associated with the AUT can be seen towards the 'tip' of the spectrum pattern in the vicinity of lower order m and n mode indices. Conversely, the modes associated with the scatterer, seen towards the right of the plot, have been displaced towards higher order modes, cf. especially in the region where $n > 100$.

These higher order modes can be filtered out as they correspond to modes that, as a consequence of the spherical sampling theorem, cannot be associated with the AUT. In this case, using the sampling theorem set out above, this corresponds to a polar mode index of circa 55. This is represented in Figure 13.131 with the vertical line. Once filtered using a low pass mode filter function such that

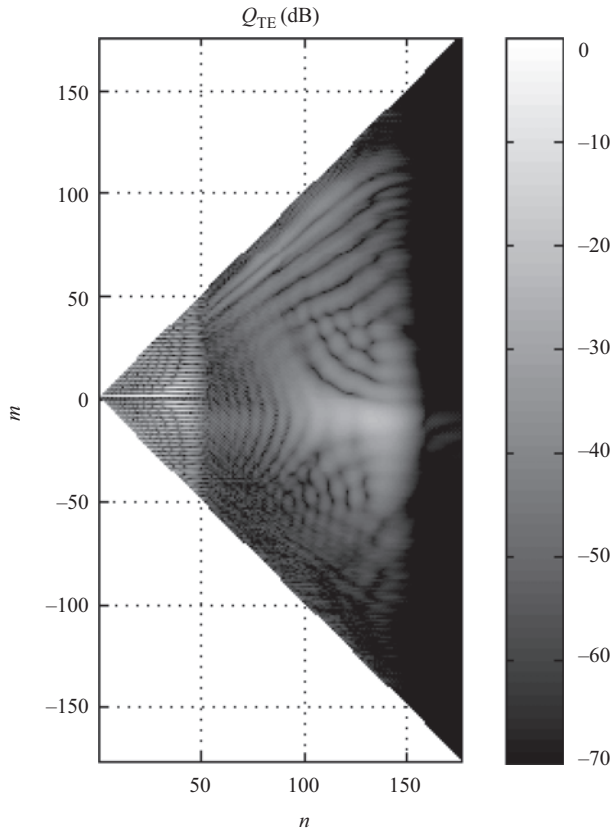

Figure 13.130 Amplitude plot of SMCs showing mode orthogonalisation after AUT translated to origin. With spurious radiator

$$Q^{(3)}_{TEmn}\Big|_{\text{Filtered}} = Q^{(3)}_{TEmn} f_m f_n \tag{13.62}$$

$$Q^{(3)}_{TMmn}\Big|_{\text{Filtered}} = Q^{(3)}_{TMmn} f_m f_n \tag{13.63}$$

where

$$f_m = \begin{cases} 0.5^{(|m|-m_{\max})} & \text{when } |m| > m_{\max} \\ 1 & \text{elsewhere} \end{cases} \tag{13.64}$$

$$f_n = \begin{cases} 0.5^{(n-n_{\max})} & \text{when } n > n_{\max} \\ 1 & \text{elsewhere} \end{cases} \tag{13.65}$$

Here, $m_{\max}$ and $n_{\max}$ denote the highest order azimuthal and polar modes as determined by the spherical sampling theorem. This filtering corresponds to a linear attenuation when expressed in dB form. The resulting filtered mode function,

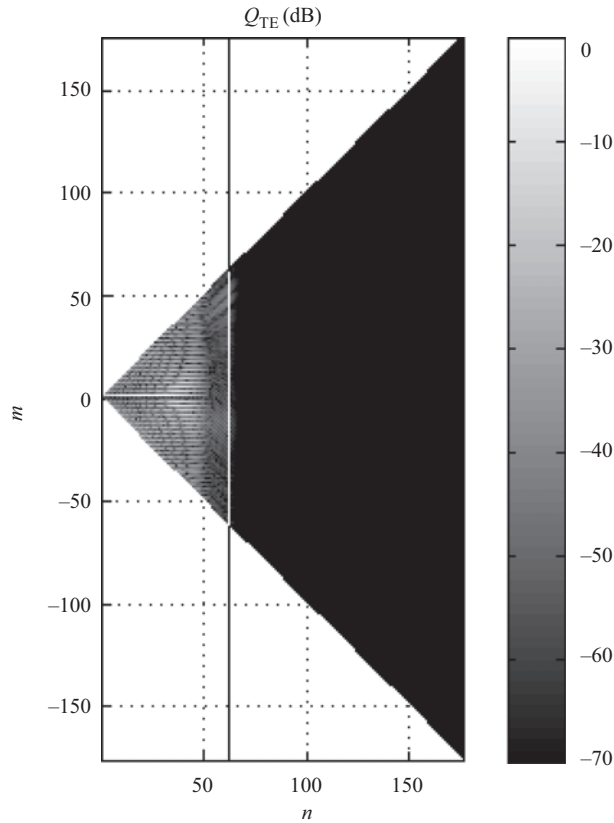

Figure 13.131 Amplitude plot of SMCs with S-MARS filtering applied

i.e. Figure 13.131, is found to be in good agreement with the reference result, Figure 13.129. Here, this mode filter was applied and the higher order modes were attenuated. Crucially, as the mode filter only acts upon higher order modes, the integrity of the underlying antenna pattern function is preserved irrespective of the complexity of that pattern making spherical mode processing equally effective with high and low gain antennas. Figure 13.132 shows a plot of the amplitude of the power contained within the n mode index for $m = 1$ which corresponds to taking a 'horizontal' cut that passes through the centre of the plot shown in Figure 13.130. Here, the blue trace represents a cut through the mode space prior to the AUT being translated back to the origin of the measurement coordinate system. The red trace represents the same data only here the AUT has been mathematically translated back to the origin of the measurement coordinate system prior to the SMCs being computed. The vertical magenta line denotes the $n = 55$ mode and lastly, the black trace represents the SMCs once the filter has been applied. By way of a comparison, Figure 13.133 shows the SMCs for the case where the AUT has been

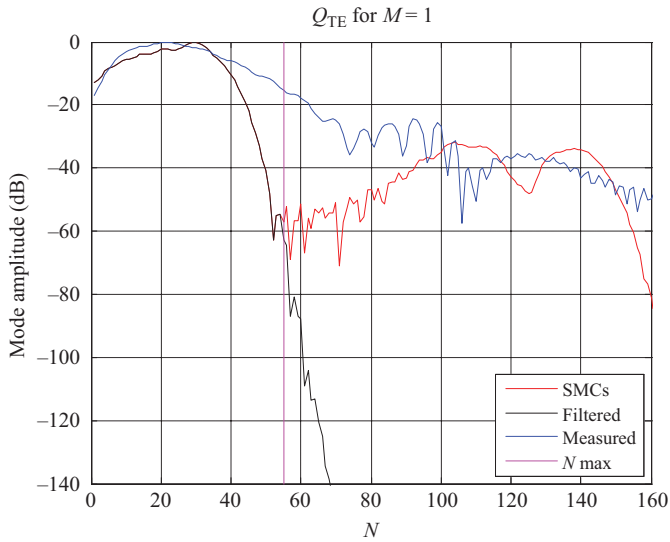

Figure 13.132 Plot illustrating the effect of processing on the SMCs

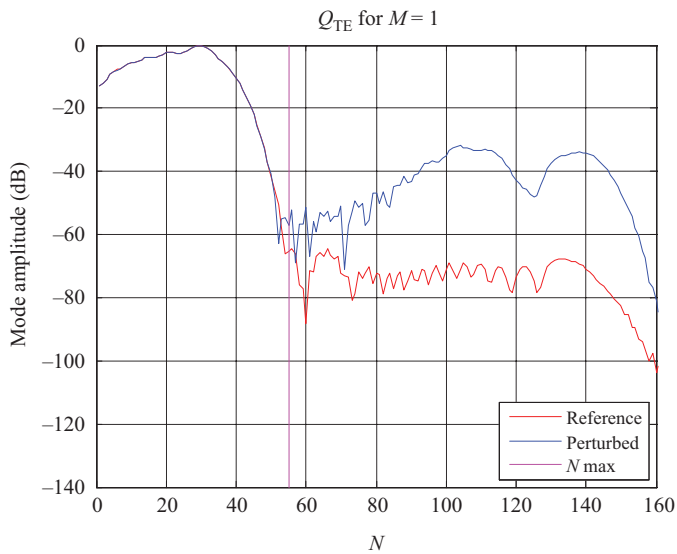

Figure 13.133 Comparison of SMCs with and without being perturbed by spurious scattering

translated back to the origin of the measurement coordinate system but where the simulated measurement has *not* been perturbed by the introduction of the spurious scatterer. As expected, it is evident from inspection of Figure 13.133 that the low-order modes, i.e. those modes associated with the AUT (i.e. where $n < 55$) are in

very close agreement; however the higher order modes, i.e. those modes which are predominately associated with the scatterer, diverge significantly.

Figure 13.134 shows the resulting far-field pattern that is obtained from using standard spherical near-field to far-field transformation to process the scatterer contaminated spherical near-field data. The effect of the spurious scatterer is evident in the pattern. Conversely, Figure 13.135 presents the result of applying the processing

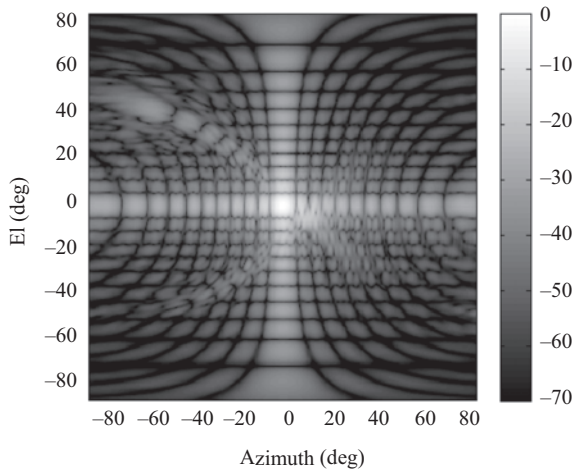

Figure 13.134 Far-field pattern with scatterer included using standard spherical processing

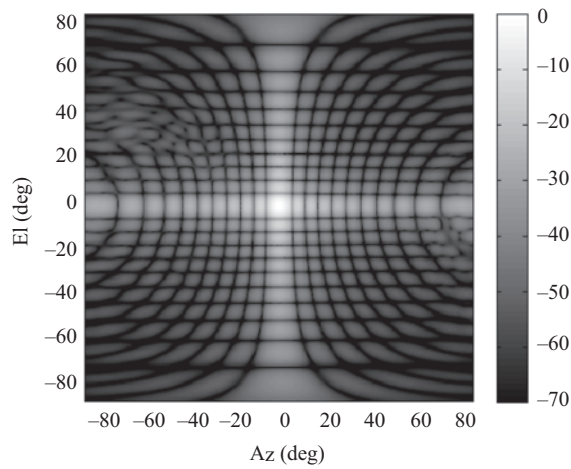

Figure 13.135 Equivalent far-field pattern obtained using S-MARS processing

to the same data set that was used to create Figure 13.134. Here, it is clear that the spurious scatter has been very effectively extracted from the processed far-field data.

Although this is clearly a very powerful method, the difficulty associated with the simulation technique presented within this section, and the preceding ones on CNF testing, is that no account of the directive or polarisation properties of the scanning probe are taken into account. Verifying the effectiveness of the probe compensation within any transformation algorithm that is intended for general-purpose use is absolutely critical. The remaining sections within this chapter show how this can be introduced into the model in a straight forward way with the use of the planar transmission formula and appropriate vector isometric rotations of the respective patterns.

13.5.1 Polar mode spherical acquisition simulation with arbitrary probe

In this section, together with the final section in this chapter, we consider the problem of generating simulated near-field measurements with probe effects included so that a more rigorous verification of transformation algorithms and post-processing techniques can be undertaken. The previous sections in this chapter used the PWS method to create near-field simulations. In this section, we will use the planar transmission formula to provide more complete simulations. The planar transmission equation is used for the simulation rather than the spherical transmission equation despite both being equally valid and accurate expressions for the transmission between a test antenna and a probe at any arbitrary near-field position and relative orientation as the planar equation is much more stable and easier to manipulate numerically. Additionally, this method can be used without modification for both first-order and higher-order probes, cf. Chapter 8. Thus, and as was shown in Chapter 6, provided that the angular spectrum of the AUT and the sampling near-field probes are known then the antenna-to-antenna coupling formula can be used to compute the 'measured' field by convolving together the respective patterns

$$\begin{bmatrix} S_x \\ S_y \end{bmatrix} = \frac{j}{\lambda} \begin{bmatrix} B_x(-\alpha,\beta) & B_y(-\alpha,\beta) \\ C_y(-\beta,-\alpha) & -C_x(-\beta,-\alpha) \end{bmatrix} \cdot \frac{1}{\gamma} \begin{bmatrix} (1-\beta^2) & \alpha\beta \\ -\alpha\beta & -(1-\alpha^2) \end{bmatrix} \cdot \begin{bmatrix} A_x(\alpha,\beta) \\ A_y(\alpha,\beta) \end{bmatrix} \frac{e^{-jk(\alpha x_0+\beta y_0+\gamma z_0)}}{\gamma} \tag{13.66}$$

Here, S is the received field, B and C denote the probe pattern functions, A is the AUT plane wave spectral components, α, β and γ are respectively the x-, y- and z-orientated direction cosines, j is the imaginary unit, k_0 is the free-space propagation constant, λ is the wavelength and z_0 is the separation between the AUT and the probe (which is assumed to be the same for both probes 'B' and 'C'). Note that each probe is x co-polar in their respective local coordinate systems. The intention of this is that if a single port probe (SPP) has been used to characterise the AUT, then the same probe pattern can be used for probe B and probe C. For the purposes

of this simulation, unless a probe misalignment is intended to be included, x_0 and y_0 are zero. The 'measured' field at a *single* point in the near-field for the combination of the AUT and probe is obtained by evaluating the integral

$$\underline{E}\,(x=0, y=0, z=z_0) = \frac{1}{\lambda^2}\int_{-\infty}^{\infty}\int_{-\infty}^{\infty}\underline{S}\,(\alpha,\beta)e^{-jk_0(\alpha x+\beta y+\gamma z)}d\alpha d\beta \qquad (13.67)$$

Thus, for each point in the simulated 'measured' spherical near-field, this integral needs to be evaluated using a differently orientated AUT, i.e. $A_x(\alpha, \beta)$, $A_y(\alpha, \beta)$, pattern. The AUT far-field pattern is then rotated mathematically about the z-axis to simulate a ϕ-rotation and about the y-axis to simulate a θ-rotation using a vector isometric rotation. This PWS represents the AUT rotated in ϕ and θ as it is in a spherical near-field measurement for a given point in the simulated spherical measurement. However, with the AUT being rotated, using a vector isometric rotation, in θ and ϕ this results in the near electric field components E_x and E_y automatically denoting, respectively, the E_θ and E_ϕ field components. Thus, previously measured patterns for both the antenna under test (AUT) and the probe can be used to calculate arbitrary, e.g. SNF data. Alternatively, it is possible to utilise simulated patterns for the probe and AUT in the event this is more convenient. The necessary vector isometric rotation of antenna pattern is treated in detail below within the Chapter 4. The utility of this simulation method is harnessed in Chapter 8 where it is used to examine the effects of using non-first order probes for spherical near-field scanning.

13.5.2 Equatorial mode spherical acquisition simulation with an arbitrary probe

The details of the polar mode simulation algorithm have been described in detail in the previous section and will merely be summarised here with the necessary modification to enable the simulation of equatorial mode spherical near-field data being highlighted. As detailed above, previously measured spherical near-field data for both the AUT and a scanning probe is used to calculate the far-field patterns of both antennas over a full far-field sphere. The AUT far-field pattern is then rotated mathematically about the z-axis to simulate a ϕ-rotation and about the y-axis to simulate a θ-rotation. The transmitting PWS over the forward hemisphere on a direction cosine grid is then derived from the rotated pattern. This PWS represents the AUT rotated in ϕ and θ as it is in a spherical near-field measurement. Whilst this approach is effective for simulating polar mode spherical near-field measurements, a different approach is needed when simulating equatorial measurements as in this case the boresight direction of AUT is assumed to nominally point in the $\theta = 90^\circ$ equatorial region. Thus, an additional step is required in the simulation software to implement this change in the antenna-to-range alignment. A number of strategies could be adopted however perhaps the simplest is to recognise that the elevation over azimuth (α, ε) coordinate system corresponds closely to a conventional spherical system when used in equatorial mode. Thus, by specifying the

required (θ, ϕ) pattern angles and by mapping these to the corresponding (α, ε) angles, i.e. $\alpha = \theta - 90^\circ$, $\varepsilon = \phi$, the AUT far-field pattern is then rotated mathematically about the negative y-axis to simulate a α-rotation and then about the x-axis to simulate a ε-rotation where the rotations are applied sequentially in that order. This insures that the directions and unit vectors are correctly preserved. Although it is possible to use an equatorial mode far-field antenna pattern as the basis for the simulation, this technique has the inherent advantage that when comparing results with the existing polar-mode simulations the same AUT patterns can be used with either software with no external additional changes being required. The remainder of the processing is in common with the polar-mode simulation. Thus, as before, the far-field probe pattern is rotated about its z-axis to simulate a χ-rotation and its receiving PWS calculated on the same k-space grid as the AUT. The calculation of a receiving PWS for the rotated OEWG probe is repeated. For the remaining steps in the simulation a computer program was developed to use the rotated plane-wave spectra of the AUT and one of the probes to calculate the output of the probe for a specified x, y, z position of the probe. When $x = y = 0$, the probe is at the equator of the measurement sphere and the AUT is positioned at the origin of the sphere or along the x-axis. Offset positions of the AUT can be simulated by selecting non-zero values for x and y or using a z-offset when calculating the AUT far-field pattern. The z-position of the probe defines the measurement radius. The probe output is produced using the planar near-field transmission equation.

$$\underline{E}(x,y,z,\theta,\phi,\chi) = \frac{1}{\lambda^2}\int_{-\infty}^{\infty}\int_{-\infty}^{\infty}\underline{S}(\alpha,\beta,\chi)e^{-jk_0(\alpha x+\beta y+\gamma z)}d\alpha d\beta \tag{13.68}$$

where $\underline{E}(x, y, z, \theta, \phi, \chi)$ is the measured output amplitude and phase for the probe at (x, y, z) and rotated about the probe axis by the angle χ and the AUT rotated by θ, ϕ. The rotation angles θ, ϕ and χ have been added as variables to the probe output, the AUT spectrum and the probe receiving spectrum to show that the planar transmission equation will be used to produce simulated spherical near-field data at arbitrary θ and ϕ positions on the measurement sphere with arbitrary χ rotations of the probe. The planar transmission equation is used for the simulation rather than the spherical transmission equation since both are equally valid and accurate expressions for the transmission between a test antenna and a probe at any arbitrary near-field position and relative orientation. The planar equation is much easier to calculate numerically and can be used *without* modification for both first-order *and* higher-order probes. An example of the equatorial spherical near-field simulation of an x-band slotted waveguide array antenna is presented in Figures 13.136 and 13.137.

By way of comparison, an equivalent polar mode simulation of the same antenna being measured in polar mode is presented in Figures 13.138 and 13.139. In each case, it is important to recognise that only a half-space may be simulated, as the PWS method is utilised. The back half-space may be simulated similarly providing the PWS is well behaved.

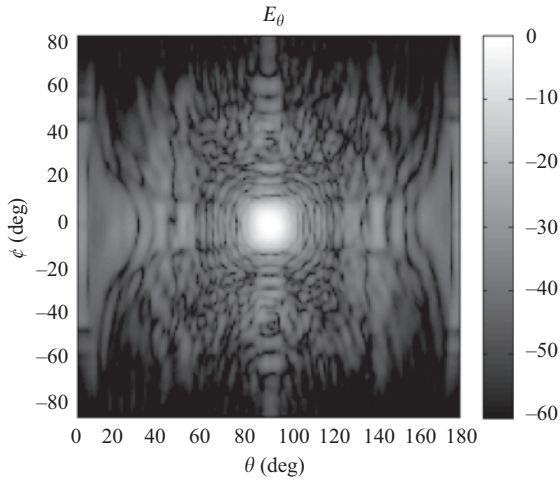

Figure 13.136 *E_θ-polarised simulated equatorial mode SNF measurement of x-band waveguide array measured with an open-ended rectangular waveguide probe*

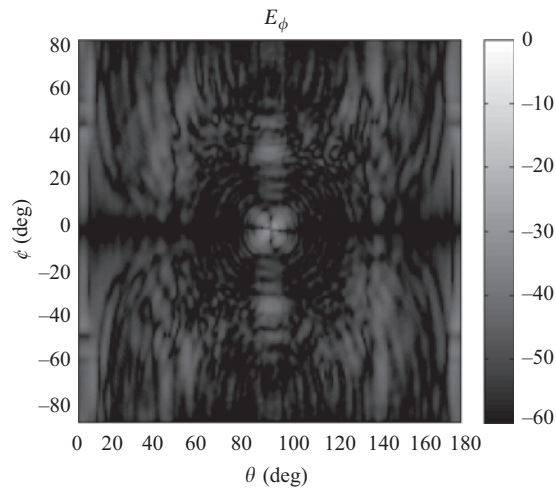

Figure 13.137 *E_ϕ-polarised simulated equatorial mode SNF measurement of x-band waveguide array measured with an open-ended rectangular waveguide probe*

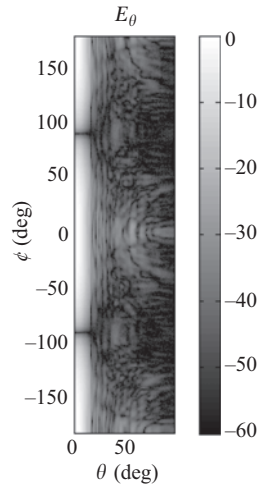

Figure 13.138 *E_θ-polarised simulated polar mode SNF measurement of x-band waveguide array measured with an open-ended rectangular waveguide probe*

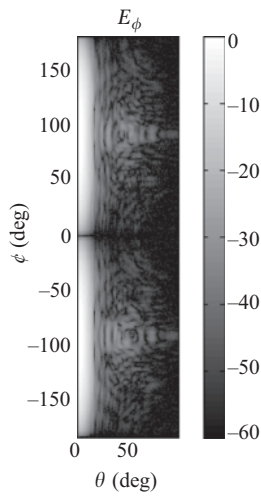

Figure 13.139 *E_ϕ-polarised simulated polar mode SNF measurement of x-band waveguide array measured with an open-ended rectangular waveguide probe*

13.6 Summary

In summary, many different CEM tools are available. Various tools can be used in different applications depending upon the accuracy needed and the nature of the problem being concerned. Although measurement and simulation are seen as different disciplines, these tools are an invaluable aid to the experimentalist with the skill being to know which tool to use in any given case.

References

[1] Gregson S.F., McCormick J., Parini C.G. Principles of Planar Near Field Antenna Measurements, IET Electromagnetic Waves Series; London; IET; 2007. pp. 257–259. ISBN-978-0-86341-756-8.
[2] Clarricoats P.J.B., Olver A.D. "Corrugated horns for microwave antennas", IEE EM Waves Series; 1984, pp. 124–126. ISBN 0-86341-003-0.
[3] Gregson S.F., McCormick J., Parini C.G. Principles of Planar Near Field Antenna Measurements, IET Electromagnetic Waves Series; London; IET; 2007. pp. 310–320. ISBN-978-0-86341-756-8.
[4] Gregson S.F., McCormick J., Parini C.G. Principles of Planar Near Field Antenna Measurements, IET Electromagnetic Waves Series; London; IET; 2007. pp. 346–349. ISBN-978-0-86341-756-8.
[5] Gregson S.F., McCormick J., Parini C.G. Principles of Planar Near Field Antenna Measurements, IET Electromagnetic Waves Series; London; IET; 2007. pp. 349–354. ISBN-978-0-86341-756-8.
[6] Rudge A.W., Milne K., Olver A.D., Knight P. "The handbook of antenna design Volume 1", IEE; 1982, pp. 74–76. ISBN 0-906048-82-6.
[7] Keller J.B., Hansen E.B. "Survey of Theory of Diffraction of Short Waves by Edges", Acta Phys. Polon., Vol. 27, pp. 217–234, 1965.
[8] Keller J.B. "Geometrical Theory of Diffraction", J. Opt. Soc. America, Vol. 52, No. 2, pp. 116–130, 1962.
[9] Kouyoumjian R.G., Phatak P.H. "A Uniform Geometrical Theory of Diffraction for an Edge in a Perfectly Conducting Surface", Proc. IEEE, Vol. 62, pp. 1448–1461, 1974.
[10] Gregson S.F., McCormick J., Parini C.G. "Principles of Planar Near-Field Antenna Measurements", IET Press, 2007. ISBN 978-0-86341-736-8.
[11] Gregson S.F., Newell A.C., Feat C., Viguier Vigi F. "The Use of Statistical Image Classification In Assessing Antenna Pattern Measurements", AMTA, Columbus, OH, 2013.
[12] McCormick J., Gregson S.F., Parini C.G. "Quantitative Measure of Comparison between Antenna Pattern Data Sets", IEE Proc. Microw. Antennas Propag., Vol. 152, No. 6, 2005.
[13] Gregson S.F., McCormick J., Parini C.G. "Principles of Planar Near-Field Antenna Measurements", IET Press, 2007. ISBN 978-0-86341-736-8.

[14] Parini C.G., Dubrovka R., Gregson S.F. "CATR Quiet Zone Modelling and the Prediction of 'Measured' Radiation Pattern Errors: Comparison using a Variety of Electromagnetic Simulation Methods", AMTA, October 2015.
[15] Tian Z., Gregson S.F. "Examination of the Effectiveness of Mode Orthogonalisation and Filtering for Scattering Suppression in Antenna Measurements Through Computational Electromagnetic Simulation", European Conference on Antennas and Propagation, Krakow, Poland, April 2019.
[16] Philippakis M., Parini C.G. "Compact Antenna Range Performance Evaluation Using Simulated Pattern Measurements", IEE Proc. Microw. Antennas Propag., Vol. 143, No. 3, pp. 200–206, 1996.
[17] Hazewinkel, Michiel, ed., "Gibbs phenomenon", Encyclopaedia of Mathematics, Springer/Kluwer Academic Publishers, 1994. ISBN 978-1-55608-010-4.
[18] Gregson S.F., Parini C.G., McCormick J. "Principles of Planar Near-Field Antenna Measurements", IET Press, EM Waves Series 53, UK, 2007, Section 8.5. ISBN 978-0-86341-736-8.
[19] Rudge A.W., Milne K., Olver A.D., Knight P. "The handbook of antenna design Volume 1", IEE; 1982, pp. 94. ISBN 0-906048-82-6.

Appendix A

A.1 IEEE standard letter designations for radar-frequency bands (Table A.1)

Table A.1 contains a summary of the IEEE standard radar band frequency designations [1]. Table A.2 contains a microwave frequency classification band comparison that shows how the IEEE band designations relate to equivalent band designations as defined by other governing bodies, specifically the International Telecommunication Union and the convention adopted by the Electronic Countermeasures Community.

Here, HF is High Frequency, VHF is Very High Frequency, UHF is Ultra High Frequency, SHF is Super High Frequency, EHF is Extremely High Frequency, THz is Terahertz. The IEEE frequency bands tend to be adopted within civilian-oriented radar communities and the ITU (International Telecommunications Union) frequency bands tend to be in common usage within the radar and radio communities, whereas the European Union (EU), North Atlantic Treaty Organisation (NATO) and the United States (US) military have agreed on a set of ECM (Electronic Countermeasures) frequency bands for electromagnetic frequencies that are used primarily for radar applications.

A.2 Standard rectangular waveguide bands and selected properties (Table A.3)

Many of the parameters associated with rectangular waveguides have been standardised so that uniformity can be insured across the microwave industry. Table A.3 presents a summary of reference data for many standard waveguide sizes. The waveguide name WR stands for Waveguide Rectangular, and the number is the inner dimension width of the waveguide specified in hundredths of inches (0.01 inch) which are rounded to the nearest hundredth of an inch.

A.3 Care and use of microwave coaxial connectors

Figure A.1 contains five of the most commonly encountered microwave coaxial connectors. Male plugs are shown on the top row, and female jacks are shown on the bottom row. The names of each type of adapter is given under the respective pictures.

Figure A.2 provides the frequency range of each of these commonly used microwave adapters with maximum, and nominal upper limits provided.

When handling microwave coaxial connectors the following handling guidelines are recommended: protect during storage, inspect visually for damage, clean

Table A.1 IEEE standard radar band nomenclature

Band designation	Nominal frequency range
HF (high frequency)	3–30 MHz
VHF (very high frequency)	30–300 MHz
UHF (ultra-high frequency)	300–1,000 MHz (the official ITU designation extends to 3,000 MHz, however in practice the upper limit is usually taken to be 1,000 MHz)
L-band	1–2 GHz
S-band	2–4 GHz
C-band	4–8 GHz
X-band	8–12 GHz
Ku-band	12–18 GHz
K-band	18–27 GHz
Ka-band	27–40 GHz
V-band	40–75 GHz
W-band	75–110 GHz
Millimetre wave band	110–300 GHz (the term millimetre-wave can also be used to refer to *V*- and *W*-bands, and even the upper part of *Ka*-band)

Table A.2 Microwave frequency classification band comparisons

IEEE		ITU		Common usage		ECM	
Band	**Frequency in GHz**	**Band**	**Frequency in GHz**	**Band**	**Frequency in GHz**	**Band**	**Frequency in GHz**
HF	0.003–0.03	HF	0.003–0.03	HF	0.003–0.03	A	0.0–0.25
VHF	0.03–0.3	VHF	0.03–0.3	VHF	0.03–0.3	B	0.25–0.5
UHF	0.3–1.0	UHF	0.3–3.0	UHF	0.3–1.0	C	0.5–1.0
L	1.0–2.0	SHF	3.0–30.0	L	1.0–2.0	D	1.0–2.0
S	2.0 –4.0	EHF	30.0–300.0	S	2.0–4.0	E	2.0–3.0
C	4.0–8.0			C	4.0–8.0	F	3.0–4.0
X	8.0–12.0			X	8.0–12.4	G	4.0–6.0
Ku	12.0–18.0			Ku	12.4–18.0	H	6.0–8.0
K	18.0–27.0			K	18.0–26.5	I	8.0–10.0
Ka	27.0–40.0			Ka	26.5–40.0	J	10.0–20.0
				Q	33.0–50.0	K	20.0–40.0
V	40.0–75.0			V	50.0–75.0	L	40.0–60.0
W	75.0–110.0			W	75.0–110.0	M	60.0–100.0
mm	110.0–300.0						
		THz	300.0–3000.0				

Table A.3 Standard rectangular waveguide bands

WR designation	WG designation	Recommended low-frequency GHz	Recommended upper frequency GHz	TE10 cut-off frequency GHz	Guide wavelength mm at cut-off frequency	Inside dimension *x* inch	Inside dimension *y* inch	Inside dimension *x* mm (approximate)	Inside dimension *y* mm (approximate)	Attenuation dB/30.5 m at recommended low frequency	Attenuation dB/30.5 m at recommended upper frequency	Material
WR2300	WG00	0.32	0.49	0.257	1168.400	23.0000	11.5000	584.200	292.100	0.04	0.027	Aluminium
										0.046	0.031	Brass
WR2100	WG0	0.35	0.53	0.281	1066.800	21.0000	10.5000	533.400	266.700	0.046	0.031	Aluminium
										0.053	0.036	Brass
WR1800	WG1	0.41	0.63	0.328	914.400	18.0000	9.0000	457.200	228.600	0.058	0.039	Aluminium
										0.067	0.045	Brass
WR1500	WG2	0.49	0.75	0.393	762.000	15.0000	7.5000	381.000	190.500	0.076	0.051	Aluminium
										0.088	0.059	Brass
WR1150	WG3	0.64	0.96	0.513	584.200	11.5000	5.7500	292.100	146.050	0.113	0.077	Aluminium
										0.131	0.089	Brass
WR975	WG4	0.75	1.12	0.605	495.300	9.7500	4.8750	247.650	123.825	0.147	0.099	Aluminium
										0.171	0.114	Brass
WR770	WG5	0.96	1.45	0.766	391.160	7.7000	3.8500	195.580	97.790	0.205	0.14	Aluminium
										0.238	0.162	Brass
WR650	WG6	1.12	1.70	0.908	330.200	6.5000	3.2500	165.100	82.550	0.273	0.181	Aluminium
										0.316	0.209	Brass
WR510	WG7	1.45	2.20	1.157	259.080	5.1000	2.5500	129.540	64.770	0.38	0.258	Aluminium
										0.44	0.3	Brass
WR430	WG8	1.70	2.60	1.372	218.440	4.3000	2.1500	109.220	54.610	0.502	0.334	Aluminium
										0.583	0.388	Brass
WR340	WG9A	2.20	3.30	1.736	172.720	3.4000	1.7000	86.360	43.180	0.682	0.475	Aluminium
										0.791	0.551	Brass
WR284	WG10	2.60	3.95	2.078	144.272	2.8400	1.3400	72.136	34.036	0.95	0.651	Aluminium
										1.102	0.755	Brass

(Continues)

Table A.3 (*Continued*)

WR designation	WG designation	Recommended low-frequency GHz	Recommended upper frequency GHz	TE10 cut-off frequency GHz	Guide wavelength mm at cut-off frequency	Inside dimension *x* inch	Inside dimension *y* inch	Inside dimension *x* mm (approximate)	Inside dimension *y* mm (approximate)	Attenuation dB/30.5 m at recommended low frequency	Attenuation dB/30.5 m at recommended upper frequency	Material
WR229	WG11A	3.30	4.90	2.577	116.332	2.2900	1.1450	58.166	29.083	1.21	0.859	Aluminium
										1.404	0.996	Brass
WR187	WG12	3.95	5.85	3.152	95.098	1.8720	0.8720	47.549	22.149	1.784	1.238	Aluminium
										2.069	1.436	Brass
WR159	WG13	4.90	7.05	3.712	80.772	1.5900	0.7950	40.386	20.193	1.987	1.485	Aluminium
										2.304	1.722	Brass
WR137	WG14	5.85	8.20	4.301	69.698	1.3720	0.6220	34.849	15.799	2.531	2	Aluminium
										2.935	2.32	Brass
WR112	WG15	7.05	10.00	5.260	56.998	1.1220	0.4970	28.499	12.624	3.546	2.757	Aluminium
										4.113	3.198	Brass
WR90	WG16	8.20	12.40	6.557	45.720	0.9000	0.4000	22.860	10.160	5.536	3.834	Aluminium
										6.419	4.446	Brass
WR75	WG17	10.00	15.00	7.869	38.100	0.7500	0.3750	19.050	9.525	6.55	4.579	Aluminium
										7.595	5.311	Brass
WR62	WG18	12.40	18.00	9.488	31.598	0.6220	0.3110	15.799	7.899	8.254	6.073	Aluminium
										9.572	7.042	Brass
WR51	WG19	15.00	22.00	11.571	25.908	0.5100	0.2550	12.954	6.477	11.271	8.174	Aluminium
										13.071	9.479	Brass
WR42	WG20	18.00	26.50	14.051	21.336	0.4200	0.1700	10.668	4.318	17.652	12.979	Aluminium
										20.47	15.052	Brass
WR34	WG21	22.00	33.00	17.357	17.272	0.3400	0.1700	8.636	4.318	21.567	15.016	Aluminium
										25.011	17.413	Brass
WR28	WG22	26.50	40.00	21.077	14.224	0.2800	0.1400	7.112	3.556	29.317	20.104	Aluminium
										33.998	23.314	Brass

Table A.3 (*Continued*)

WR designation	WG designation	Recommended low-frequency GHz	Recommended upper frequency GHz	TE10 cut-off frequency GHz	Guide wavelength mm at cut-off frequency	Inside dimension *x* inch	Inside dimension *y* inch	Inside dimension *x* mm (approximate)	Inside dimension *y* mm (approximate)	Attenuation dB/30.5 m at recommended low frequency	Attenuation dB/30.5 m at recommended upper frequency	Material
WR22	WG23	33.00	50.00	26.346	11.379	0.2240	0.1120	5.690	2.845	41.285	28.096	Aluminium
										47.877	32.582	Brass
WR19	WG24	40.00	60.00	31.391	9.550	0.1880	0.0940	4.775	2.388	51.928	36.459	Aluminium
										60.219	42.281	Brass
WR15	WG25	50.00	75.00	39.875	7.518	0.1480	0.0740	3.759	1.880	76.705	52.468	Aluminium
										88.952	60.845	Brass
WR12	WG26	60.00	90.00	48.372	6.198	0.1220	0.0610	3.099	1.549	104.836	70.368	Aluminium
										121.575	81.603	Brass
WR10	WG27	75.00	110.00	59.014	5.080	0.1000	0.0500	2.540	1.270	134.527	94.762	Aluminium
										156.006	109.892	Brass
WR8	WG28	90.00	140.00	73.768	4.064	0.0800	0.0400	2.032	1.016	204.896	131.637	Aluminium
										237.611	152.655	Brass
WR7	WG29	110.00	170.00	90.791	3.302	0.0650	0.0325	1.651	0.825	284.484	180.543	Aluminium
										329.906	209.37	Brass
WR5	WG30	140.00	220.00	115.714	2.591	0.0510	0.0255	1.295	0.648	410.739	258.471	Aluminium
										476.32	299.74	Brass
WR4	WG31	170.00	260.00	137.242	2.184	0.0430	0.0215	1.092	0.546	502.489	334.24	Aluminium
										582.719	387.608	Brass
WR3	WG32	220.00	325.00	173.571	1.727	0.0340	0.0170	0.864	0.432	682.021	477.235	Aluminium
										790.918	553.433	Brass
WR2		325.00	500.00	295.071	1.016	0.0200	0.0100	0.508	0.254	2322.744	1105.531	Aluminium
										2693.61	1282.047	Brass
WR1.5		500.00	750.00	393.428	0.762	0.0150	0.0075	0.381	0.191	2315.647	1619.073	Aluminium
										2685.38	1877.585	Brass
WR1		750.00	1100.00	590.143	0.508	0.0100	0.0050	0.254	0.127	4254.116	2996.634	Aluminium
										4933.358	3475.098	Brass

Figure A.1 Microwave coaxial connectors

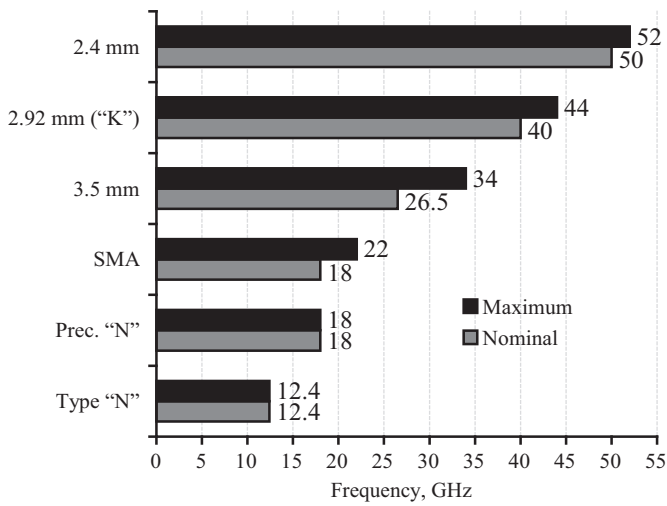

Figure A.2 Microwave coaxial connectors frequency range

to remove metal flakes, dust and oil, do not touch mating surfaces, gauge pin depth and male pin size, make connections using male nut (do not rotate the device), use correct torque. Table A.4 contains commonly recommended torque values for these connectors. Finally, Table A.5 contains a summary of the mechanical compatibility of these connectors.

Table A.4 Typical recommended torque values for standard coaxial connectors

Connector type	Torque (SI NM)	Torque (imperial lb in)
Type-N	1.36	12
SMA	0.56	5
Precision 3.5 mm	0.90	8[a]
Precision 2.4 mm	0.90	8[a]
Precision 1.85 mm	0.90	8

[a]Use SMA torque value to connect male SMA to female 3.5 mm, use 3.5 mm torque value to connect male 3.5 mm to female SMA. Finally, Table A.5 contains a summary of the mechanical compatibility of these connectors.

Table A.5 Common microwave connector mating compatibility matrix

	Male (plug)				
Female (Jack)	**"N"**	**SMA**	**3.5 mm**	**2.92 mm**	**2.4 mm**
"N"	YES	NO	NO	NO	NO
SMA	NO	YES[a]	YES	YES	NO
3.5 mm	NO	YES[a]	YES	YES	NO
2.92 mm	NO	YES[a]	YES	YES	NO
2.4 mm	NO	NO	NO	NO	YES

[a]SMA are not precision adapters and there is risk of damage.

A.4 Reflection coefficient, return loss, transmission loss as a function of VSWR

The magnitude of the voltage reflection coefficient can be obtained from the voltage standing wave ratio since,

$$|\Gamma| = \frac{\text{VSWR} - 1}{\text{VSWR} + 1} \tag{A.1}$$

Note, as the current reflection coefficient is merely the negative of the voltage reflection coefficient, we shall avoid its use. Return loss in dB is defined as

$$\text{RL}|_{\text{dB}} = -20 \log_{10}|\Gamma| \tag{A.2}$$

Transmission loss in dB is therefore defined as

$$\text{TL}\big|_{\text{dB}} = -10 \log_{10}(1 - |\Gamma|^2) \tag{A.3}$$

Table A.6 Voltage reflection coefficient, return loss, transmission loss, percentage power reflected and percentage power transmitted as a function of VSWR

VSWR	Voltage reflection coefficient	Return loss (dB)	Transmission loss (dB)	% Power reflected	% Power transmitted
1.00	0.0000	∞	0.00	0.0	100.0
1.01	0.0050	46.06	0.00	0.0	100.0
1.02	0.0099	40.09	0.00	0.0	100.0
1.03	0.0148	36.61	0.00	0.0	100.0
1.04	0.0196	34.15	0.00	0.0	100.0
1.05	0.0244	32.26	0.00	0.1	99.9
1.06	0.0291	30.71	0.00	0.1	99.9
1.07	0.0338	29.42	0.00	0.1	99.9
1.08	0.0385	28.30	0.01	0.1	99.9
1.09	0.0431	27.32	0.01	0.2	99.8
1.10	0.0476	26.44	0.01	0.2	99.8
1.12	0.0566	24.94	0.01	0.3	99.7
1.14	0.0654	23.69	0.02	0.4	99.6
1.16	0.0741	22.61	0.02	0.5	99.5
1.18	0.0826	21.66	0.03	0.7	99.3
1.20	0.0909	20.83	0.04	0.8	99.2
1.25	0.1111	19.08	0.05	1.2	98.8
1.30	0.1304	17.69	0.07	1.7	98.3
1.35	0.1489	16.54	0.10	2.2	97.8
1.40	0.1667	15.56	0.12	2.8	97.2
1.45	0.1837	14.72	0.15	3.4	96.6
1.50	0.2000	13.98	0.18	4.0	96.0
1.55	0.2157	13.32	0.21	4.7	95.3
1.60	0.2308	12.74	0.24	5.3	94.7
1.65	0.2453	12.21	0.27	6.0	94.0
1.70	0.2593	11.73	0.30	6.7	93.3
1.75	0.2727	11.29	0.34	7.4	92.6
1.80	0.2857	10.88	0.37	8.2	91.8
1.85	0.2982	10.51	0.40	8.9	91.1
1.90	0.3103	10.16	0.44	9.6	90.4
1.95	0.3220	9.84	0.48	10.4	89.6
2.00	0.3333	9.54	0.51	11.1	88.9
2.10	0.3548	9.00	0.58	12.6	87.4
2.20	0.3750	8.52	0.66	14.1	85.9
2.30	0.3939	8.09	0.73	15.5	84.5
2.40	0.4118	7.71	0.81	17.0	83.0
2.50	0.4286	7.36	0.88	18.4	81.6
2.60	0.4444	7.04	0.96	19.8	80.2
2.70	0.4595	6.76	1.03	21.1	78.9
2.80	0.4737	6.49	1.10	22.4	77.6
2.90	0.4872	6.25	1.18	23.7	76.3
3.00	0.5000	6.02	1.25	25.0	75.0
3.10	0.5122	5.81	1.32	26.2	73.8

Table A.6 (*Continued*)

VSWR	Voltage reflection coefficient	Return loss (dB)	Transmission loss (dB)	% Power reflected	% Power transmitted
3.20	0.5238	5.62	1.39	27.4	72.6
3.30	0.5349	5.43	1.46	28.6	71.4
3.40	0.5455	5.26	1.53	29.8	70.2
3.50	0.5556	5.11	1.60	30.9	69.1
3.60	0.5652	4.96	1.67	31.9	68.1
3.70	0.5745	4.81	1.74	33.0	67.0
3.80	0.5833	4.68	1.81	34.0	66.0
3.90	0.5918	4.56	1.87	35.0	65.0
4.00	0.6000	4.44	1.94	36.0	64.0
4.20	0.6154	4.22	2.07	37.9	62.1
4.40	0.6296	4.02	2.19	39.6	60.4
4.60	0.6429	3.84	2.32	41.3	58.7
4.80	0.6552	3.67	2.44	42.9	57.1
5.00	0.6667	3.52	2.55	44.4	55.6
5.20	0.6774	3.38	2.67	45.9	54.1
5.40	0.6875	3.25	2.78	47.3	52.7
5.60	0.6970	3.14	2.89	48.6	51.4
5.80	0.7059	3.03	3.00	49.8	50.2
6.00	0.7143	2.92	3.10	51.0	49.0
6.20	0.7222	2.83	3.20	52.2	47.8
6.40	0.7297	2.74	3.30	53.3	46.7
6.60	0.7368	2.65	3.40	54.3	45.7
6.80	0.7436	2.57	3.50	55.3	44.7
7.00	0.7500	2.50	3.59	56.3	43.8
7.50	0.7647	2.33	3.82	58.5	41.5
8.00	0.7778	2.18	4.03	60.5	39.5
8.50	0.7895	2.05	4.24	62.3	37.7
9.00	0.8000	1.94	4.44	64.0	36.0
9.50	0.8095	1.84	4.63	65.5	34.5
10.00	0.8182	1.74	4.81	66.9	33.1
11.00	0.8333	1.58	5.15	69.4	30.6
12.00	0.8462	1.45	5.47	71.6	28.4
13.00	0.8571	1.34	5.76	73.5	26.5
14.00	0.8667	1.24	6.04	75.1	24.9
15.00	0.8750	1.16	6.30	76.6	23.4
20.00	0.9048	0.87	7.41	81.9	18.1
25.00	0.9231	0.70	8.30	85.2	14.8
30.00	0.9355	0.58	9.04	87.5	12.5
35.00	0.9444	0.50	9.66	89.2	10.8
40.00	0.9512	0.43	10.21	90.5	9.5

The percentage of the reflected power can be obtained from the voltage reflection coefficient using

$$P_{\mathrm{R}}\big|_{\%} = 100|\Gamma|^2 \tag{A.4}$$

Similarly, the percentage of the power transmitted can be obtained using

$$P_{\mathrm{T}}\Big|_{\%} = 100\left(1 - |\Gamma|^2\right) \tag{A.5}$$

These expressions were used to generate table (Table A.6). Note: in some texts, transmission loss can be referred to as mismatch loss.

Index

Theory and Practice of Modern Antenna Range Measurements

2nd Expanded Edition, Volume 2

This greatly expanded, co-authored, two-volume text provides a comprehensive introduction and explanation of both the theory and practice of modern antenna measurements, from their most basic postulates and assumptions, to the intricate details of their applications in various demanding modern measurement scenarios.

Starting with an initial examination of the properties of antennas that allow them to enhance the free-space interaction of electronic systems, the authors then introduce direct far-field and indirect far-field forms of antenna measurements and their various implementations. Detailed descriptions are given of the direct far-field measurement technique CATR (Compact Antenna Test Ranges), Body-Centric measurements, and detailed developments of standard planar, cylindrical, spherical and non-canonical near-field techniques; and includes a through treatment of near-field range error budgets which are an indispensable part of antenna metrology. The books conclude with recent advances in measurement techniques such as aperture diagnostics, phase-less antenna metrology, error correction, and range multi-path suppression techniques. Extensive examples illustrate the concepts and techniques covered.

This second edition is thoroughly expanded and now includes new chapters on near-field to far-field transforms from non-canonical surfaces, electromagnetic modelling of CATRs and near-field antenna measurement systems. In addition there is an expanded chapter on coordinate systems, polarization bases and antenna pattern plotting and new sections on more specialized topics such as 5G and Radome measurements.

About the Authors

Professor Clive Parini is Professor of Antenna Engineering at Queen Mary University of London, UK.

Professor Stuart Gregson is Director of Operations & Research at Next Phase Measurements and an Honorary Visiting Professor in the School of Electronic Engineering and Computer Science of Queen Mary University of London, UK.

Dr John McCormick is an Antenna Engineer with Leonardo MW, Edinburgh, UK.

Dr Daniël Janse van Rensburg is Snr VP of RF Products and Applications at NSI-MI Technologies, Suwanee, Georgia, USA. He is also Adjunct Professor at the University of Ottawa, Canada.

Professor Thomas Eibert is Professor of High-Frequency Engineering at the Technical University of Munich, Germany.

ISBN 978-1-83953-128-6

9 781839 531286

SciTech Publishing an imprint of the IET
The Institution of Engineering and Technology
theiet.org
978-1-83953-128-6